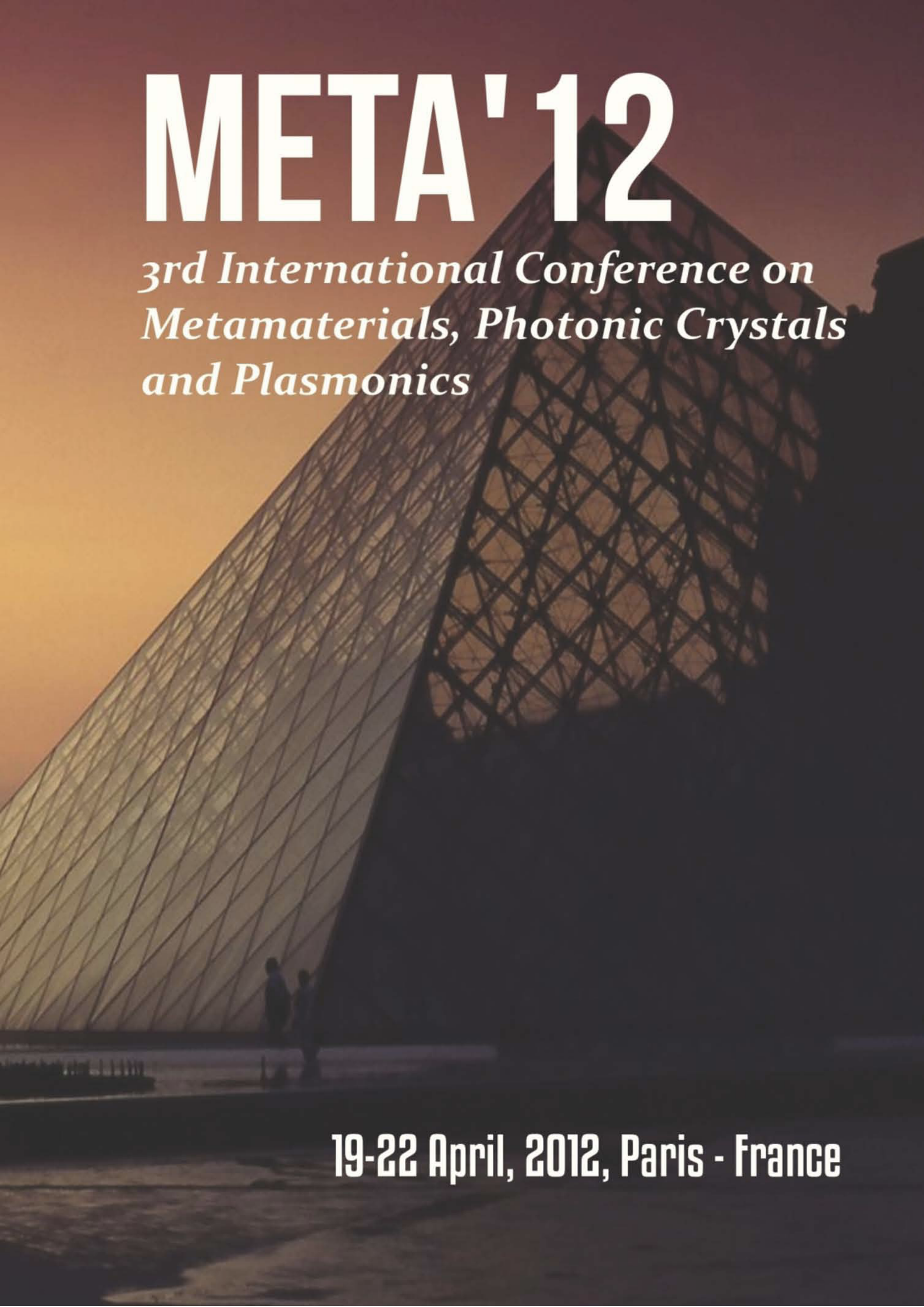

META'12

3rd International Conference on Metamaterials, Photonic Crystals and Plasmonics

19-22 April, 2012, Paris - France

ISBN: 978-2-9545460-5-6
ISSN: 2429-1390

META'12, Paris – France

3rd International Conference on Metamaterials, Photonic Crystals and Plasmonics

Edited by

Saïd Zouhdi | University Paris-Sud, France
&
Xavier Begaud | Telecom Paristech, France

Organizers

META'12 General Chair
Said Zouhdi, Paris Sud University, France

META'12 General co-Chair
Xavier Begaud, Telecom Paristech, France

Organizing Committee
L. Bernard, France
Y. Bernard, France
E. Berthelot, France
R. Corcolle, France
J. C. Cousin, France
L. Daniel, France
O. Dubrunfaut, France
A. C. Lepage, France
L. Santandrea, France
J. Sarrazin, France

International Advisory Committee
N. Engheta (Chair), USA
M. Fink, France
S. He, Sweden
T. Itoh, USA
Y. Kivshar, Australia
R. Marques, Spain
G. Milton, USA
S. Noda, Japan
M. Notomi, Japan
Y. Rahmat-Samii, USA
V. Shalaev, USA
A. Sihvola, Finland
M. Sorolla, Spain
S. Tretyakov, Finland
J. C. Vardaxoglou, UK
A. Vinogradov, Russia
M. Wegener, Germany
N. Zheludev, UK
R. Ziolkowski, USA

Technical Program Committee
S. Maier (Chair), UK
T. Akalin, France
W. L. Barnes, UK
S. Bozhevolnyi, Denmark
K. Busch, Germany
C. T. Chan, Hong Kong
A. Dmitriev, Sweden
I. El-Kady, USA
W. Fritzsche, Germany
F. J. Garcia, Spain
O. Hess, UK
R. Hillenbrand, Spain
D. Kim, Republic of Korea
J. Krenn, Austria
K. Leosson, Iceland
M. McCall, UK
L. M. Moreno, Spain
P. Nordlander, USA
T. Odom, USA
R. Quidant, Spain
D. R. Smith, USA
T. Tanaka, Japan
J. K. W. Yang, Singapore
A. V. Zayats, UK
X. Zhang, USA

Special Session Organizers
D. Pawlak, Poland
H. Giessen, Germany
N. Liu, USA
T. Vo-Dinh, USA
R. C. Gauthier, Canada
H. Fernandes, Brazil
B. Ravelo, France
M. Mojahedi, Canada
N. Zheludev, UK
V. Shalaev, USA
A. Chipouline, Germany
V. Fedotov, UK
R. Colombelli, France
Y. De Wilde, France
J. Li, City, Hong Kong
J. Christensen, Spain
T. Akalin, France
M. Qiu, Sweden
M. Yan, Sweden
Y. Zhang, China
X. Chen, UK
T. W. Odom, USA
K. Leosson, Iceland
A. de Lustrac, France
S. N. Burokur, France
P. Lalanne, France
L.Zhou, China
J. Hao, France
A. Urbas, USA
F. Martin, Spain
S.-H. Oh, USA
A. Brolo, Canada
D. Felbacq, France
S. Weiss, USA
A. Zaghloul, USA
M. Hoque, USA
H. Wang, Singapore
C.-W. Qiu, Singapore

Sponsors & Supporters

We wish to thank the following organizations for their contribution to the success of this conference:

TELECOM PARISTECH, France
SUPELEC, France
GDR Ondes, France
IOP Publishing, UK
EPL, UK
CST, France
IEEE-APS, USA
URSI, Belgium

Contents

Controlling the hybridization in stacked split-ring resonators

Withawat Withayachumnankul[1,2,*], Christophe Fumeaux[1], and Derek Abbott[1]

[1]School of Electrical & Electronic Engineering, The University of Adelaide, Adelaide, SA 5005, Australia
[2]Faculty of Engineering, King Mongkut's Institute of Technology Ladkrabang, Bangkok 10520, Thailand
*corresponding author, E-mail: withawat@eleceng.adelaide.edu.au

Abstract

The influence of dielectric layers on the hybridization of stacked split-ring resonators (SRRs), or SRR dimers, is investigated in this article. It is found that when the permittivity of the layer between the two SRRs is higher than that of free space, the electric dipole-dipole interaction plays a dominant role in determining the modes of resonance. On the other hand, for the case of a free-space intermediate layer, the resonance modes are mainly determined by the magnetic dipole interaction. As a consequence, this near-field effect exerts a great impact on the far-field characteristics, i.e., the resonance behavior and chiral optical activity. A Lagrangian formalism is used to characterize the interplay between the magnetic and electric couplings. The results suggest an additional degree of freedom to control the behavior of this fundamental metamaterial element.

1. Introduction

Metamaterials are defined as a group of man-made materials with customizable electromagnetic properties. Typically, a metamaterial consists of subwavelength metallic resonators usually aligned in a 2D or 3D periodic arrangement. The response of metamaterials is controlled by the geometries, dimensions, and materials of these resonators. In addition to that, near-field interactions between neighboring resonators also have significant effects on the response of metamaterials. The hybridization in metamaterials introduced by intercell couplings leads to new phenomena, including multiple or continuum modes of resonance [1, 2].

This hybridization has been observed in a 'magnetic dimer' that is composed of two stacked SRRs with their gaps orthogonally aligned [3]. Although only one ring is directly excited, the other ring establishes an oscillating current via the magnetic coupling between the resonators. Effectively, the SRR hybridization causes resonance splitting and a strong chiral optical activity. The concept of magnetic dimer has been extended to the case where the second ring can be freely twisted around its axis [4, 5]. This configuration, known as stereometamaterial, allows the electric dipole coupling to support or counteract the magnetic coupling depending on the twist angle. The optical activity arising from this chiral metamaterial can be fully characterized through the Jones calculus employing a Lagrange model with phase retardation [6].

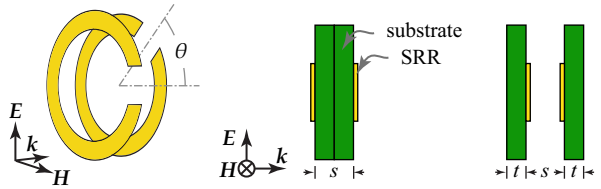

Figure 1: Schematic of SRR dimers. (a) Orientation of two resonators in perspective view. (b) Back-to-back configuration in side view. (c) Front-to-front configuration in side view. The twist angle θ can vary from 0° to 180°. The substrate thickness, t, and separation between SRRs, s, are 1.6 and 3.2 mm, respectively.

In this article, the influence of the supporting dielectric on stereometamaterials or SRR dimers is investigated in detail. Changing the permittivity of the dielectric in the vicinity of the dimers affects the local distribution of the induced electric field. Implicitly, the hybridization or near-field interactions in the dimers can be manipulated. The effects are manifested through a change in the resonance mode, strength, and position. Consequently, the state of polarization is greatly affected. Although the effect of the dielectric on SRR dimers has been mentioned briefly in [5], in contrast to this study, it does not focus on a difference in physical interactions nor discusses a difference in chiral optical properties.

The study begins with an observation on the hybridization effect under the influence of dielectric in Sec 2. Section 3 presents an analysis of the results through a dipole interaction model, together with a Lagrangian formalism. Section 4 demonstrates the impact of the supporting dielectric on the chiral optical activity of SRR dimers.

2. Observation of the hybridization effect

An individual SRR in a dimer used in the experiment has an inner radius, outer radius, and gap width of 2.5, 3.0, and 1.0 mm, respectively. Each SRR is made of copper with a thickness of 0.035 mm. It is printed on an FR4 substrate with a relative permittivity of 4.1, a loss tangent of 0.02, and a thickness of 1.6 mm. As illustrated in Fig. 1(a), a SRR dimer is formed by stacking coaxially two identical SRRs with a separation of 3.2 mm. The second SRR in

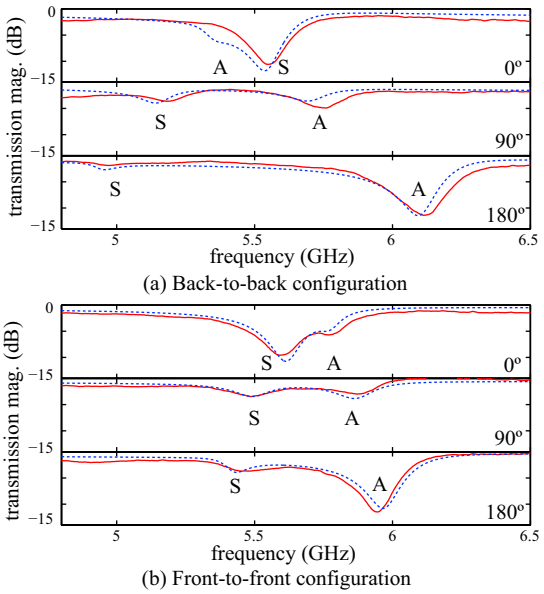

Figure 2: Transmission profiles of SRR dimers. (a) Back-to-back configuration. (b) Front-to-front configuration. The twist angle varies from 0°, 90°, to 180°. The dotted lines are from the simulation, and the solid lines are from the experiment. Two modes of resonance, symmetric and asymmetric, are denoted by 'S' and 'A', respectively.

a dimer can be twisted with respect to the first SRR. Two different forms of stacking are investigated as indicated in Figs. 1(b,c). In the back-to-back configuration, the substrates fill the space between the two SRRs, and in the front-to-front configuration the dielectric in-between the SRRs is free space. Periodic duplications of a dimer form a planar array with a lattice constant of 20 mm.

The measurement is performed in an anechoic chamber with transmitting and receiving microwave horn antennas that are connected to a vector network analyzer, Agilent Technologies N5230A. As indicated in Fig. 1(a), the E-field polarization is always perpendicular to the gap of the SRR on the side of incidence. The measured sample transmission is normalized by the free-space transmission to remove any system dependence. As a complement, the simulation is performed by using CST Microwave Studio and cross-validated with HFSS. To replicate an infinite planar array of dimers, unit-cell boundary conditions are utilized for the transverse boundaries. A plane wave incident normally to the array is transmitted and received by two Floquet ports.

The numerical and experimental results compared in Fig. 2 are in good agreement. Note that in the simulation for the front-to-front configuration the separation s is increased to 4 mm to reflect the experimental inaccuracy. In both of the configurations, the transmission profiles clearly show resonance splitting as the twist angle varies from 0° to 180°. The different modes of resonance labelled 'S' and 'A' in Fig. 2 are deduced from the simulated surface current distribution on the dimer. For the symmetric (S) and asymmetric (A) modes, the current loops in the two rings are parallel and anti-parallel, respectively. The back-to-back configuration shows relative resonance strengths and mode orientation similar to that observed earlier [4]. However, the relative strengths and orientation are different for the front-to-front configuration, particularly at the twist angle of 0°.

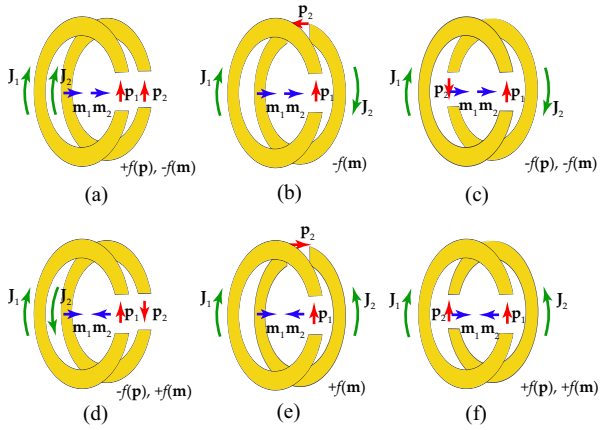

Figure 3: Instantaneous surface current and dipole moments. The twist angle equals 0°, 90°, and 180° in (a,d), (b,e), and (c,f), respectively. The resonance mode is symmetric in (a,b,c) and asymmetric in (d,e,f). The surface current density, electric and magnetic moment are represented by $\mathbf{J}_{\{1,2\}}$, $\mathbf{p}_{\{1,2\}}$, and $\mathbf{m}_{\{1,2\}}$, respectively. The effect of dipole interactions on the resonance frequency is indicated.

3. Analysis

3.1. Dipole-dipole interaction model

The hybridization effect observed in the previous section can be explained via a dipole-dipole interaction model [4]. Essentially, an excited SRR develops an electric dipole across the gap and a magnetic dipole in the axial direction. Two identical SRRs aligned coaxially as in a SRR dimer mutually interact through these dipoles, leading to resonance splitting. A resonance frequency is governed by the relative orientation of dipoles and their moments. Specifically, a pair of transversely coupled dipoles with their moments in parallel and anti-parallel tends to shift the resonance up and down, respectively, whilst a pair of longitudinally coupled dipoles behalves vice versa. The net effect takes into account the separated electric and magnetic dipole interactions. For a SRR dimer, the alignment of the two magnetic dipoles is longitudinal, whilst that of the two electric dipoles is transversal.

Figure 3 illustrates the model current and electric/magnetic moments in the SRR dimer. At the twist angle of 0°, for the symmetric mode in Fig. 3(a) the electric dipole interaction tends to shift up the resonance, whilst the magnetic interaction acts oppositely. The situation reverses for the asymmetric mode in Fig. 3(d). Therefore, from the results in Fig. 2 at the angle of 0°, it can be deduced that

for the back-to-back configuration, the electric dipole interaction determines the resonance modes, whilst for the front-to-front configuration the magnetic dipole interaction assumes the role. This is supported by the fact that the electric field tends to couple into a dielectric with a high permittivity. Figures 3(b,e) show that at the angle of 90° the two electric dipoles are aligned orthogonally. The hybridization is therefore solely determined by the magnetic coupling. Hence, the modes are not influenced by the dielectric layers. This explains the similarity of the mode orientation in the two configurations at 90° in Fig. 2.

In Figs. 3(c,f), at the twist angle of 180°, the effects from electric and magnetic dipole interactions become constructive. In this case, the resonance frequency is always decreased and increased for the symmetric and asymmetric modes, respectively. The reinforcing electric and magnetic coupling effects cause a large resonance separation observed in both of the configurations at 180° in Fig. 2. A smaller separation for the front-to-front configuration is attributed to a weak electric dipole coupling through free space. As for the resonance strength, parallel dipole moments are preferentially coupled to the excitation field. This explains the relatively strong resonance observable in the symmetric mode at 0° and asymmetric mode at 180°.

It is clear that the interplay between the electric and magnetic interactions, and hence the mode orientation and resonance strength, can be controlled by changing the permittivity of the supporting dielectric. In particular, the presence of the intermediate dielectric layer in the back-to-back configuration reinforces the electric coupling between the two SRRs. On the other hand, a low permittivity of intermediate free space and a high permittivity of the backing substrates in the front-to-front configuration weaken the transverse electric dipole coupling to the point that the magnetic coupling becomes dominant.

3.2. Lagrangian formalism

The near-field interactions within the SRR dimer can be quantitatively characterized on the basis of a quasistatic approximation [7]. According to the Lagrangian formalism, the frequencies for the symmetric and asymmetric resonances in a SRR dimer are described as, respectively, [4, 5]

$$\omega_s = \omega_0\sqrt{\frac{1+\kappa_E}{1+\kappa_H}} \quad (1)$$

$$\omega_{as} = \omega_0\sqrt{\frac{1-\kappa_E}{1-\kappa_H}}\,, \quad (2)$$

where $\kappa_E = \kappa_{E0}\cos\theta$ and κ_H represent the electric and magnetic coupling coefficients, respectively. The resonance frequency of the uncoupled SRR is represented by ω_0, which is slightly different for the two configurations due to a difference in the substrate thickness, i.e., $\omega_{0,\mathrm{b2b}} = 5.49$ GHz and $\omega_{0,\mathrm{f2f}} = 5.65$ GHz. The cosine term for κ_E reflects a change in the electric dipolar coupling strength following the twist angle. This model does not consider the effects from inter-dimer coupling or multipole interactions. Such a consideration is not critical, since the neighbour coupling changes the response only slightly [8] and the multipole effect is not observed in the transmission results [5].

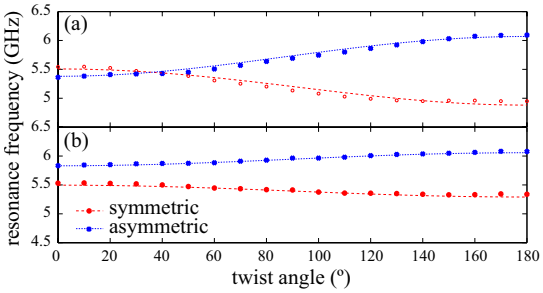

Figure 4: Resonance frequencies of SRR dimers as a function of the twist angle. (a) Back-to-back configuration, and (b) Front-to-front configuration. The numerical results are represented by the markers, and the analytical fittings by the lines.

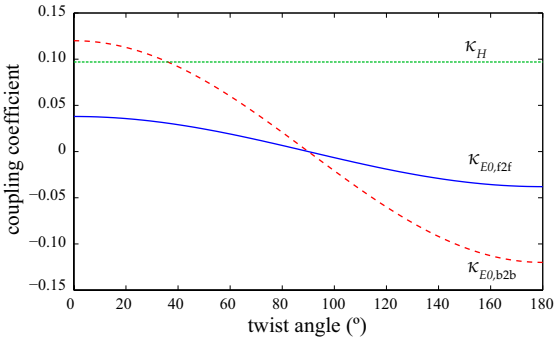

Figure 5: Coupling coefficients as a function of the twist angle. The coefficients are obtained by fitting the numerical results in Fig. 4 with Eq. 1. The subscriptions b2b and f2f denote the back-to-back and front-to-front configuration, respectively.

Figure 4 shows the resonance frequencies obtained from simulation as a function of the twist angle. The accompanying analytical curves are obtained by fitting Eq. 1 to the numerical data. The electric coupling coefficients κ_{E0}, i.e., κ_E at 0° twist angle, are estimated as 0.120 for the back-to-back configuration and 0.038 for the front-to-front configuration. The magnetic coupling coefficient $\kappa_H = 0.097$ is fixed regardless of the dielectric arrangement. It is clear that the electric coupling coefficient can be varied greatly by changing the dielectric permittivity.

Figure 5 further elucidates the variation in the near-field coupling coefficients with respect to the twist angle and the dielectric configuration. It shows that the electric coupling strength in the back-to-back configuration is larger than the magnetic coupling strength at a small twist angle. At 36° the electric and magnetic coupling strengths are equal, resulting in a mode crossing observable in Fig. 4. This crossing is not observed in the front-to-front configuration, as its absolute electric coupling coefficient is well below the

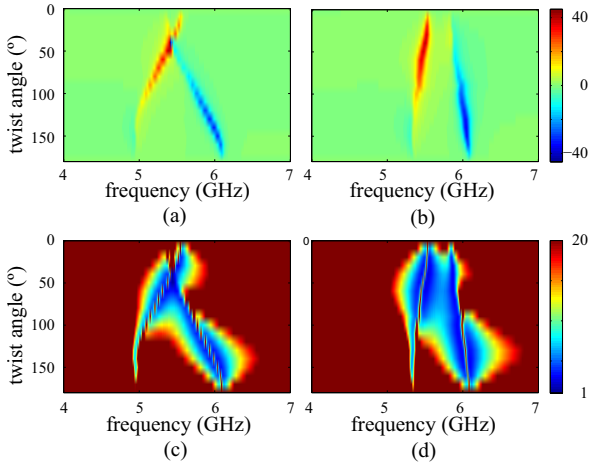

Figure 6: Polarization characteristics as a function of the frequency and twist angle. (a,b) Tilt angle, and (c,d) Axial ratio. The left column belongs to the back-to-back configuration, whilst the right column belongs to the front-to-front configuration. The tilt angle is with respect to the incident electric field polarization and with the positive sign in the clockwise direction. The axial ratio is capped at 20 for clarity.

magnetic coefficient at any angle.

4. Chiral optical activity

Since a SRR dimer with a twist angle not equal to 0° or 180° is chiral, it can exhibit a degree of optical activity, i.e., the structure imparts polarization rotation and phase retardation to the incident wave. In summary, the incident wave with an electric field polarized across the gap of the first SRR induces the oscillating current, which builds up a magnetic dipole along the axis of that SRR. The accumulated energy can be transferred to the second coaxial SRR through the near-field coupling mechanisms discussed earlier. As a result, the second SRR develops its own electric dipole source with a polarization different from the incident field polarization. Thus, in effect, this hybridized SRR dimer can change the polarization state of the incident wave. This section compares the optical activities of SRR dimers in the two configurations.

The polarization characteristics exhibited by the SRR dimer with the back-to-back and front-to-front configurations are shown in Fig. 6. In general, the resonance mode and twist angle in either configuration have a strong impact on the polarization state of the transmitted wave. Figure 6 further provides an overview of the influence of dielectric layers on the polarization behaviors. It is obvious that the tilt angle and axial ratio for the two configurations are significantly different, particularly below the twist angle of 90°. As an example, the polarization ellipses at a set of frequencies and twist angles are compared in Fig. 7. In Fig. 7(a) the electric dipoles dominate the near-field activity in the back-to-back configuration, and the transmitted

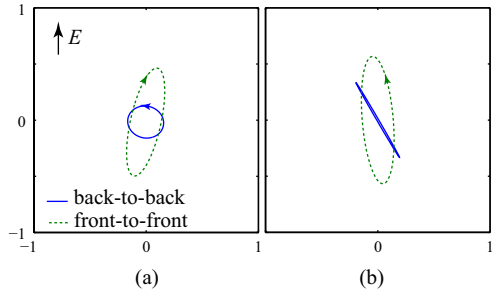

Figure 7: Comparison of polarization ellipses in two different SRR dimers. The polarizations are observed at the frequency and twist angle of (a) 5.44 GHz and 40° and (b) 5.93 GHz and 130°, respectively. The electric field vector shows the incident polarization.

wave is nearly circularly polarized. Reducing the influence of electric dipoles changes the polarization to ellipse with an inverse rotation direction. In the second case in Fig. 7(b), the transmitted wave can be altered between the linear and elliptical polarizations via a change in the dielectric. Note that the direction of polarization rotation in a SRR dimer can be reversed in its mirrored structure.

5. Conclusion

In conclusion, the permittivity of neighboring dielectric layers has a strong impact on the hybridization in a SRR dimer. A high-permittivity dielectric mediating the dimer strengthens the electric near-field interaction. In effect, this electric dipolar interaction is mainly responsible for the resonance splitting and determines the modes of resonance. As the intermediate dielectric is replaced by free space, the strength of the magnetic interaction surpasses that of the electric interaction. Hence, the modes of resonance are governed by magnetic dipoles. A quantitative analysis carried out via the Lagrangian formalism confirms this explanation. This controllable near-field behavior is shown to have a large impact on the far-field polarization activity. An implication of this study is the ability to actively manipulate the response of SRR dimers or other chiral metamaterials for optical devices. It shifts away from SRR twisting by offering an opportunity to optically or electrically control the dielectric.

Acknowledgement

The authors acknowledge B. Pullen, I. Linke, and P. Simcik for their technical assistance. WW acknowledges the Australian Post-Doctoral Fellowship from the Australian Research Council (ARC) through Discovery Project DP1095151.

References

[1] H. Liu, Y. Liu, T. Li, S. Wang, S. Zhu, and X. Zhang, "Coupled magnetic plasmons in metamaterials," *Phys-*

ica Status Solidi (B), vol. 246, no. 7, pp. 1397–1406, 2009.

[2] H. Liu, D. Genov, D. Wu, Y. Liu, J. Steele, C. Sun, S. Zhu, and X. Zhang, "Magnetic plasmon propagation along a chain of connected subwavelength resonators at infrared frequencies," *Physical Review Letters*, vol. 97, no. 24, art. no. 243902, 2006.

[3] H. Liu, D. Genov, D. Wu, Y. Liu, Z. Liu, C. Sun, S. Zhu, and X. Zhang, "Magnetic plasmon hybridization and optical activity at optical frequencies in metallic nanostructures," *Physical Review B*, vol. 76, no. 7, art. no. 073101, 2007.

[4] N. Liu, H. Liu, S. Zhu, and H. Giessen, "Stereometamaterials," *Nature Photonics*, vol. 3, no. 3, pp. 157–162, 2009.

[5] D. Powell, K. Hannam, I. Shadrivov, and Y. Kivshar, "Near-field interaction of twisted split-ring resonators," *Physical Review B*, vol. 83, no. 23, art. no. 235420, 2011.

[6] H. Liu, J. Cao, S. Zhu, N. Liu, R. Ameling, and H. Giessen, "Lagrange model for the chiral optical properties of stereometamaterials," *Physical Review B*, vol. 81, no. 24, art. no. 241403, 2010.

[7] I. Sersic, M. Frimmer, E. Verhagen, and A. Koenderink, "Electric and magnetic dipole coupling in near-infrared split-ring metamaterial arrays," *Physical Review Letters*, vol. 103, no. 21, art. no. 213902, 2009.

[8] J. Liu, M. He, S. Chen, C. Huang, L. Zhou, and Y. Zhu, "Electromagnetic interaction in stacked split ring resonator arrays," *Journal of Physics: Condensed Matter*, vol. 23, no. 21, art. no. 215303, 2011.

Tunable Broadband Plasmonic Perfect Absorber at Visible Frequencies

M. Keshavarz Hedayati[1], F. Faupel[2], and M. Elbahri[1,3]*

[1] Nanochemistry and Nanoengineering, Institute for Materials Science, Faculty of Engineering, University of Kiel, Kaiserstrasse 2, 24143 Kiel, Germany

[2] Multicomponent Materials, Institute for Materials Science, Faculty of Engineering, University of Kiel, Kaiserstrasse 2, 24143 Kiel, Germany

[3] Helmholtz-Zentrum Geesthacht, Institute of Polymer Research, Nanochemistry and Nanoengineering, Max-Planck-Str.1, 21502, Geesthacht, Germany

*corresponding author: me@tf.uni-kiel.de

Abstract

Metamaterials and plasmonics as a new pioneering field in photonics joins the features of photonics and electronics by coupling photons to conduction electrons of a metal as surface plasmons (SP). This concept haven been implemented for variety of application including negative index of refraction, magnetism at visible frequencies, cloacking devices amongst others. In the present work, we used plasmonic hybrid material in order to design and fabricate a broad-band perfect plasmonic metamaterial absorber in a stack of metal and Copper-PTFE (Polytetrafluoroethylene) nanocomposite showing average absorbance of 97.5% in whole visible frequencies. Our experimental results showed that the absorption peak of the stacks can be tuned upon varying the thickness and type of the spacer layer due to the sensitivity of plasmon resonance to its environment. To the best of our knowledge this is the first report of plasmonic metamaterial absorber based on copper with absorption around 100% in entire visible and NIR.

1. Introduction

The general attention in solar use fast raised in the mid-70's due to the renewed interest in substitute energy resources which resulted from the "oil crisis" [1]. Graded structure made of metal-dielectric composite along with anti-reflectors were the basic of the developed structure for solar absorption which were fabricated by electroplating or vacuum deposition methods (Details can be found in [1]). Nowadays, due to the fast growing field of nanotechnology and great demand for nanoscale system, the trends to realize a system showing black absorption for solar and sensoric purposes with sub-wavelength dimension increased. However, so far most of the applied techniques (e.g. perforated metallic films[2], grating structured systems [3] and metamaterials [4-6]) are either costly or has low fabrication tolerance and their absorption resonance is narrow-band which limits their utility for energy harvesting. Recently, we show experimentally for the first time fabrication of a broadband perfect plasmonic absorber in a stack of gold and gold-SiO_2 nanocomposite showing nearly 100% absorbance at visible frequencies [7-8]. In this report, we implemented the same idea but in a polymeric nanocomposite and replacing Gold with a Copper to reduce significantly the material cost. In copper based absorber, the bandwidth is broader and since the Copper is cheaper than Gold, the new developed absorber is more cost effective for practical application. In addition, the average value of absorption in visible spectrum is above 97% which is the best reported broad band plasmonic perfect absorber so far.

2. Experimental procedure

A cylindrical vacuum chamber was used for sputtering of the metal and polymeric film. By installing two magnetron with an angle of 50º, co-sputtering was done in order to make a nanocomposite out of a Copper and PTFE targets. Simultaneous sputtering from different sources allows deposition of nanocomposites with different filling factors (ff) and thicknesses. For acquiring a uniform thickness for the film and homogeneous metal distribution for the composite, all depositions were done on the samples attaching to a rotatable sample holder. For dielectric deposition (PTFE in this case) a RF power and for conductive targets (Copper) a DC power supply were used. The details of co-sputtering methods can be found in our former reports [9]. Thickness measurements was performed using Dectak 8000 profilometer. Optical analysis carried out by a UV-Vis-NIR spectrometer (Lambda900, Perkin Elmer). Although Aluminum was used as a mirror for reflection measurement, the data was normalized to a perfect reflector in order to achieve absolute value of reflection. Since all the base film thickness was 100nm which is far greater than the skin depth of copper, it was assumed that the transmission is zero. Therefore, all calculation of absorbance is based on: A+R= 100%, where A stands for absorption and R is reflection.

3. Results and discussion

Schematic of the structure which was used in this work is shown in Figure 1 (a). It is composed of an optically thick copper film as base layer (100nm) and a nearly percolated Copper-PTFE nanocomposite as top layer which are separated by a dielectric inter-layer (PTFE). TEM of the nanocomposite used in this work presented in Figure 1 (b). One can see that the distance between the particles are very small and the composite is near-percolation.

Figure 1(a): Schematic draw of the perfect absorber structure

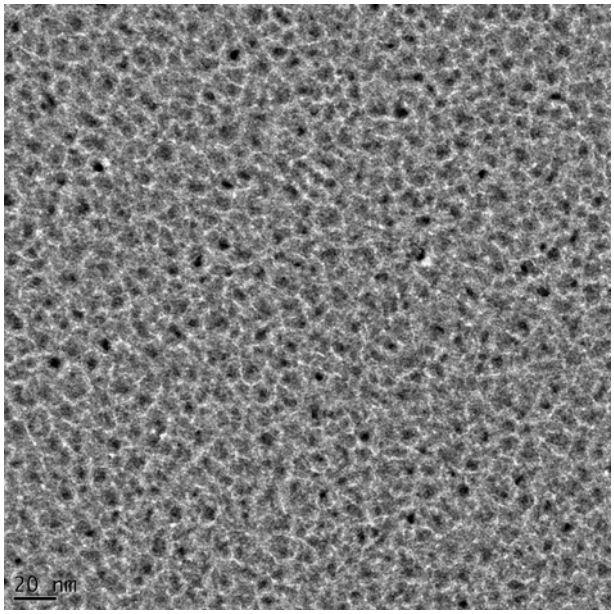

Figure 1(b): Top-view TEM image of the near percolated copper-PTFE nanocomposite.

Figure 1(c): Photo of the perfect black absorber in comparison with bare copper film.

Figure 1 (c) show the photograph of the optimized sample compare to the bare copper film where one can see the black appearance of the highly absorber system compare to the shiny surface of metallic film. Optical measurements showed that 20nm spacer layer of PTFE gives the best performance of the device and thickening or thinning the thickness of interlayer reduced (increases) the absorption (the reflection) of system. Figure 2a shows the absorption spectra of 20nm Cu-PTFE composite on 100nm copper base layer separated with different thickness of interlayer. It is obvious that changing the spacer layer thickness from the optimum value of 20nm will alter the efficiency of the device and the absorption drop. We attributed the drop to the lack of coupling of the top nanoparticles and the base layer. Indeed, in such a system, excitation of anti-parallel currents between nanoparticles (embedded within the nanocomposite) and base layer (known as magnetic resonance) induced by dipole–image interaction will trap the light within the inter-layer. However, it seems that upon increment or decrease of spacer-layer thickness, dipole-image interaction becomes less efficient and results in a drop in absorption [6-7]. Deposition of the composite on a bare base layer further support the mentioned idea in a sense that when there is no distance between the film and nanoparticles, no light can be confined and therefore the reflection enhances (Figure 3 (green curve).

The optical response of such a stack is not only dependent on the spacer layer thickness rather than the filling factor of the composite plays a crucial role in the efficiency of film. UV-vis measurement of the samples prepared with different filling factor showed that the best performance achieved when the ratio of sputtering rate of copper to PTFE is 2.33. On the other hand, changing the sputtering ratio to 2.0 or 2.66 reduce the overall absorption of the device. Figure 2 (a) shows the absorption spectra of the stacks with different sputtering ratio of Copper and PTFE. It is obvious the highest absorption is happened when the ratio is 2.33. When the ff raises far above the percolation threshold the reflectivity of the upper layer goes up and consequently the optical response of the stacks become similar to thick copper film. In other word, as soon as the

composite starts turning to a continuous metal film, the light can not pass through the top layer anymore and it acts as a metal reflector. Therefore the absorption of the structure dramatically drops. Comparing the current results with our previously report on gold base perfect absorber, one can see that the broadness of the peak is more than that of gold one. In other words, the average value of absorption in the visible range (400-750nm) is around 97% which shows the higher efficiency of Copper-absorber compared to Gold one which shows the higher efficiency of former one. In fact, the filling factor of optimized condition in copper system (70%) is far above that of gold (40%) and therefore it is expected to be highly reflective. However, a broader resonance and perfect absorption was observed which we attributed to the plasmonic damping of copper which occurs due to interaband processes via electron photon as well as electron-electron scattering [10].

The role of magnetic resonance in the high absorption of the structure was shown in our last work [7] however one can not role out the significance of interference in the low reflectivity of such a structure. The influence of interference in perfect absorber has been recently studied by Chen [11]. He showed in a typical metamaterial absorber there is minor near-field interaction or magnetic response among the neighboring metal structures. In addition, the surface currents with anti-parallel directions originated from the interference and superposition, rather than excited by the magnetic component of the incident electromagnetic fields [11]. We believe that Chen's theory might hold for grating on a film or resonator designed for MIR range of frequencies but it can not be applied in our structure. Because in our device, the inter-particles distance is less than 5nm (Figure 1 (b)) and hence one can not neglect the huge light confinement between the particles beside the light trapping in the interface [12]. In addition, the resonance band of our system is few hundred nanometers (i.e. very broad low reflection) which can not be explained only by interference phenomena.

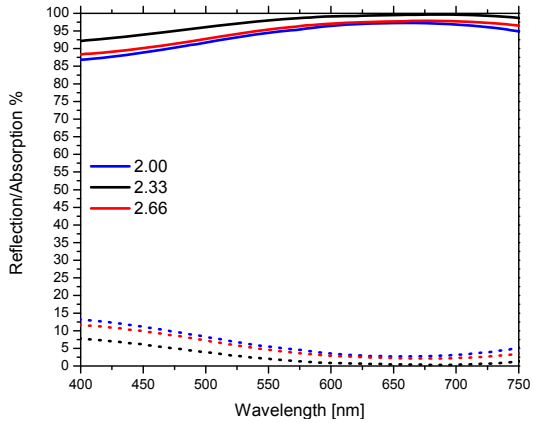

Figure 2(a): Absorption (solid lines) and reflection (dot lines) spectra of the near percolation nanocomposite with three different sputtering ratio of polymer and metal on a 100 nm gold film coated with 20nm PTFE layer as spacer

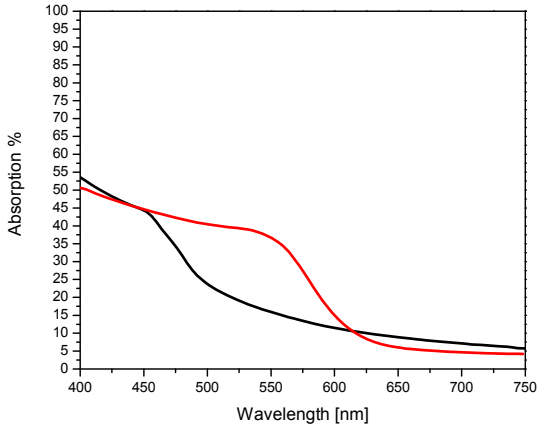

Figure 2(b): Absorption spectra of 20nm Cu-PTFE composite (black) with sputtering ratio of 2.0 on 20nm PTFE on glass in comparison of 100nm copper film (red).

Measuring the optical response of the metal alone as well as the composite film with the same condition deposited on glass substrate showed that the high absorption of the system is not originated neither from the composite alone nor from the metal. Figure 2 (b) shows the absorption spectra of composite and bare copper film on glass. It is clear that the average absorption value in both cases is less than 30% which is far below the 97% of copper-perfect absorber. This results further support the idea of plasmon coupling in the highly absorber structure and shows that the Ohmic losses of the device within the metallic particles due to the localized particles plasmon resonance of copper nanoparticles is not the dominating process of the overall absorption.

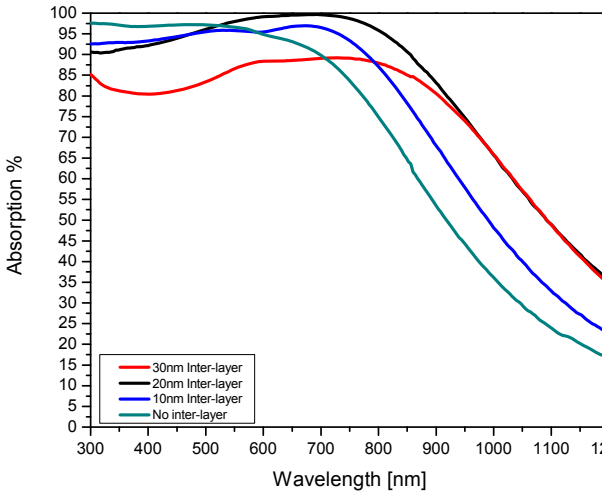

Figure 3: Absorption spectra of 20nm Cu−PTFE composite on PTFE spacer layer with different thickness on 100nm Cu. Green curve show the composite on a base layer without any inter-layer for comparison.

In addition, the optical study of the system with different spacer layer thickness further support the significant role of dipole-image interaction in perfect absorption of our

developed system (Figure 3). As it was mentioned above, increasing the distance between the metal film and the nanocomposite by adding a thick spacer layer, disturbs the resonant condition and results in a weaker coupling. Different to our previous report[7] a critical spacer layer of 20nm was observed where the absorption width and intensity is maximized. The significant drop in the absorption observed when the thickness of spacer layer exceeds 50nm which we attributed to the lack of efficient dipole-dipole interaction. Indeed, the difference of spacer layer in Gold and Copper system can be attributed to two effects. Firstly, the refractive index of PTFE is less than that of SiO_2. Secondly, the plasmon resonance of Gold and Copper response differently to the certain dielectric [13]. Beside the two mentioned parameters, the ratio of gold to SiO_2 matrix in gold-perfect absorber was less than the ratio of Copper in PTFE in copper-one. Indeed, all of the difference originated from the different plasmon resonance of Gold and Copper.

4. Conclusions

In summary, we have developed and studied a new plasmonic metamaterial with almost perfect absorption of light in visible frequencies. Structure out of polymer matrix of composite and spacer layer and Copper as a metallic component showed that the perfect absorption can be achieved with other system rather than Gold. However the thickness of the inter-layer and the filling fraction of metal should be varied depends on its dielectric function. We concluded that interference theory can not explain the broad-band perfect absorption of our developed system since both the particle size and inter-particles distance is too small that one can not neglect the strong electrical filed confinement within the structure. Due to the simple fabrication technique that we employed, the production cost is very low compare to the competitive methods such as e-beam lithography. In addition, the higher fabrication tolerance of our highly absorber structure makes it an outstanding candidate for future application in photovoltaic and sensor.

Acknowledgements

Funding by the German Research Foundation (DFG) through the projects EL 554/1-1 and SFB 677 (C1,C9) are acknowledged. M.E. would like to thank the Initiative and Networking Fund of the Helmholtz Association's (grant No. VH-NG-523) for providing the financial base for the start-up of his research group.

References

1. Niklasson, G.A., Granqvist, C.G., “Review Surfaces for selective absorption of solar energy: an annotated bibliography 1955-1981,” J. Mater. Sci., Vol. 18, 3475-3534, 1983.
2. Teperik, T. V., García de Abajo, F. J. A., Borisov, Abdelsalam, G., M., Bartlett, P. N., Sugawara, Y. J., Baumberg, J., “Omnidirectional absorption in nanostuctured metal surfaces,” Nat. Photon. Vol. 2, 299, 2008
3. Sun, Z., Zuo, X., “Tunable Absorption of Light via Localized Plasmon Resonances on a Metal Surface with Interspaced Ultra-thin Metal Gratings,” Plasmonics, Vol. 6, 83, 2010.
4. Hao, J., Wang, J., Liu, X., Padilla, W. J., Zhou, L., Qiu, M., “ High performance optical absorber based on a plasmonic metamaterial,” Appl. Phys. Lett., Vol. 96, 251104, 2010.
5. Landy, N. I., Sajuyigbe, S. J., Mock, J., Smith, D. R., Padilla, W. J., “Perfect metamaterial absorber,” Phys. Rev. Lett. Vol. 100, 207402, 2008.
6. Liu, N., Mesch, M., Weiss, T., Hentschel, M., Giessen, H., “Infrared Perfect Absorber and Its Application As Plasmonic Sensor,” Nano Lett., Vol. 10, No. 7, 2342-2348, 2010.
7. Hedayati, M. K., Javaherirahim, M., Mozooni, B., Abdelaziz, R., Tavassolizadeh, A., Chakravadhanula, V.S.K., Zaporojtchenko, V., Strunkus, T., Faupel, F., Elbahri, M., “ Design of a Perfect Black Absorber at Visible Frequencies Using Plasmonic Metamaterials,” Adv. Mater. Vol. 23, 5410-5414, 2011.
8. Elbahri, M., Hedayati, M.K., Faupel, F., Strunkus, T., Zaporojtchenko, V., “Absorberschicht für den VIS- und/oder NIR-Spektralbereich, ” DE Patent (pending)
9. Schürmann, U, Takele, H., Zaporojtchenko, V., Faupel, F., “Optical and electrical properties of polymer metal nanocomposites prepared by magnetron co-sputtering, ” Thin solid Films, Vol. 515, 801-804.
10. J.-Y. Bigot, J.-C. Merle, O. Cregut, and A. Daunois, Electron Dynamics in Copper Metallic Nanoparticles Probed with Femtosecond Optical Pulses, Phys. Rev. Lett. 75, 4702–4705 (1995)
11. Chen, H., “Interference theory of metamaterial perfect absorbers,” arXiv:112.5168v1.
12. Ducourtieux, S., Podolskiy V.A,, Grésillon, S., Buil, S., Berini, B., Gadenne, P., Boccara, A.C., Rivoal, J.C., Bragg, W.D., Banerjee, K., Safonov, V.P., Drachev, V.P., Ying, Z.C., Sarychev, A.K., Shalaev, V.M., “Near-field optical studies of semicontinuous metal films, ” Phys. Rev. B, Vol. 64, 165403-165417, 2001.
13. Murray, W., Barnes, W., “Plasmonic Materials, ” Adv. Mater., Vol. 19, 3771–3782, 2007.

Plasmonic Metal Displacement Deposition on Porous Silicon for SERS Substrate Fabrication

Hanna Bandarenka*[1], Ksenya Artsemyeva[1], Sergei Redko[1], Andrei Panarin[2], Sergei Terekhov[2], Inna Khodasevich[2], Valentin A. Orlovich[2], and Vitaly Bondarenko[1]

[1]Department of Micro- and Nanoelectronics, Belarusian State University of Informatics and Radioelectronics, Minsk, Belarus
[2]B.I. Stepanov Institute of Physics, National Academy of Sciences of Belarus, Minsk, Belarus
*corresponding author, E-mail: h.bandarenka@gmail.com

Abstract

Displacement technique was applied to form silver and copper plasmonic deposits for the surface enhanced Raman spectroscopy application. Porous silicon was used as a template for the metal deposition. Morphology of the obtained samples was studied with scanning electron microscopy. Raman spectra of the CuTMpyP4 molecules adsorbed on the metal structures were taken and their dependences on the porous silicon morphology and the deposition regimes were determined. Surface enhancement of Raman signal was detected from the following substrates: (i) the Ag nanoparticles deposited on porous silicon, (ii) the Cu porous film formed by complete displacement of the porous silicon skeleton with copper atoms.

1. Introduction

Successful application of nanosized metallic structures has been attracting a great interest since the beginning of the nanotechnology development. One of the most prospective using approaches of such materials is the detection of the extremely small amount of substances by the surface enhanced Raman spectroscopy (SERS). The Raman signal of molecules adsorbed on the nanorough metallic films is significantly magnified [1-3]. The mechanism of the effect has the electromagnetic nature and is caused by the modification of the incident field intensity near the metallic boundary due to excitation of the surface plasmons in the roughness nanoparticles (NPs). An enhancement factor of about 14 orders of magnitude, as compared with conventional non-resonant RS, can be achieved [4]. For the last decade a lot of papers have been published on the use of SERS in such analytical applications as medical diagnostics, quality control of medicines and food products, and the analysis of complex mixtures [5–8]. Despite on it SERS-based devices production has not found so wide distribution as it might be. The fabrication process of the SERS substrates needs to be simple, cheap, repeatable, and compatible with the Si technology and results in the stable product of high sensitivity. Traditionally SERS substrates have been forming by electrochemical roughening of the metallic electrodes or aggregation of the colloidal NPs. The first substrates show low degradation and repeatability but not very high SERS activity. On the other hand, aggregates of NPs can be easily produced and often provide the strong Raman enhancement, however the open problem is to achieve its stability. Several methods for the formation of the metallic substrates have been also considering since SERS activity had been found to depend on size, shape, and interspacing of NPs [9]. But practically electron-beam lithography [10], nanosphere lithography [11], or films over nanospheres technology [12] are costly and require special equipment and professional level staff. Recently, it has been proposed to roughen the plasmonic films by the metal displacement deposition on porous silicon (PS) templates obtained after the electrochemical anodization of monocrystalline Si [13-15]. The least complicated liquid processing and Si-based technology are among the principal advantages of the method. The deposition mechanism is based on the redox reaction between Me^{n+} cations and Si atoms of the PS immersed into the aqueous solutions of metal salt. It is quite important that the noble metals and copper might be deposited in this way because their rough films promote the greatest enhancement of the SERS signal. Raman intensity has been found to strongly depend on the morphology of PS and metal deposition regimes. Our work [16] has shown that the use of macroPS covered with the plasmonic metal NPs by displacement deposition provides the higher SERS signal in comparison with mesoPS. We suggest that metallized macropores has the similar structure to the fundamentally new plasmonic materials [17, 18] that presents nanosized vias ("antiNPs") embedded in a periodic manner in the metal film. Such structures have a very intensive component of the local field in a circle at the entrances to nanovias. It is radically different from the plasmon modes in nanorough films and creates conditions for more significant increase in the SERS signal. Moreover the ethanol addition to the metal salt solution has been found to promote better SERS-active substrates formation. We have used macroPS of 10 um thickness and the wet ability improvement of the solution has allowed deeper but not complete pore walls covering with metal atoms [16]. In the present research we have optimized the structural parameters of macroPS template, the composition of metal salt solution and the deposition regimes to produce SERS-active substrates. Silver and copper have been used as plasmonic

metals for the following reasons. Ag-based substrates demonstrate the strongest enhancement of the Raman signal intensity while the weaker SERS-activity of copper is compensated by its low price.

2. Experimental

Boroh doped 100 mm monocrystalline silicon wafers with (100) orientation and 0.3-12 Ohm·cm resistivity were used as initial substrates. Organic clean of the Si wafers was performed for 10 min with a hot (75^0C) solution of NH_4OH, H_2O_2 and H_2O mixed in a volume ratio of 1:1:4. Then the wafers were dried in a centrifuge and cut into a number of rectangular 3x3 cm samples. Just before PS formation each experimental sample was immersed into 5% HF solution for 30 s to remove the native oxide. Immediately after oxide removal, the Si sample was placed in an electrolytic cell made of Teflon. The active opening of the cell had a round shape and an area of 3 cm^2. Uniform PS layers were formed by electrochemical anodization of silicon samples in the electrolytes consisted of HF, DMSO and C_3H_7OH. Anodization was performed at current density of 7-8 mA/cm^2 for 5-85 min. A spectrally pure graphite disk was used as a contact electrode to the back side of the samples during the electrochemical treatment. Platinum spiral wire was used as a cathode electrode. The equipment for the conduction of the electrochemical process was the potentiostat/galvanostat AUTOLAB PGSTAT302. Gravimetric method was applied to determine the porosity of PS. Mass measurements were performed with Sartorius CP225D micro/analytical electronic balance that provided the instrumental error no more than 10 ug.

After PS formation the HF solution was removed and the electrolytic cell was thoroughly rinsed with deionized water for 3 min and C_3H_7OH for 5 min to clean the pores from the electrolyte reagents. The cell was then filled with the diluted HF solutions of $AgNO_3$ or $CuSO_4$ for 40-180 min at 25^0C. The HF addition provided SiO_2 removing from the porous surface and continuous displacement process of the PS skeleton with the metallic atoms. Than the solution was removed, the sample surface was rinsed 3 times for 30 s with deionized water and dried on the air for 30 min.

For the SERS measurements the 0.02 ml drop of the 10^{-6} M CuTMpyP4 solution was poured on each piece. After its drying on the air the round spot of 1 cm diameter was observed on the metallic surface.

Raman spectra were registered with spectrometers SpectraPro 500 I and T64000 (Jobin-Yvon), equipped with a CCD-detectors. The sources of continuous excitation were helium-cadmium laser Liconix (λ_{exc}=441.6 nm), Ar^+-laser Stabilite 2017 (Spectra-Physics) (λ_{exc}=457.9, 488.0 and 514.5 nm) and a semiconductor laser (λ_{exc}=532 nm). The accuracy of the frequencies in the SERS spectra did not extend beyond 1 cm^{-1}. SERS spectra were recorded during continuous rotation of the sample for signal averaging.

The morphology and structure of the samples were studied with the scanning electron microscope (SEM) Hitachi S-4800 that provided the resolution of 1 nm. The elemental composition of samples was determined using SEM Cambridge Instruments Stereoscan-360 with a Link Analytical AN 10000 energy dispersive X-ray analyzer.

3. Results and Discussion

3.1. Ag/macroPS-based SERS substrates

In order to provide the formation of the macropores in Si suitable for full coverage with Ag NPs by displacement deposition, monocrystalline Si wafers of 12 Ohm·cm resistivity were used. The electrolyte and the current density were the same as in [16] but the anodizing time was reduced to 5 min to grow the shorter pores. Ag deposition was performed from the aqueous solution of 10^{-3}M $AgNO_3$ and 1 M C_2H_5OH. We suggest that higher SERS signal intensity from the substrates formed with ethanol in the paper [16] was observed because of better Ag atoms penetration in the depth of PS. Figure 1 shows SEM images of top (a-c) and cross section (d-f) views of macroPS after 40 (a, d), 120 (b, e) and 200 (c, e) time periods of Ag deposition.

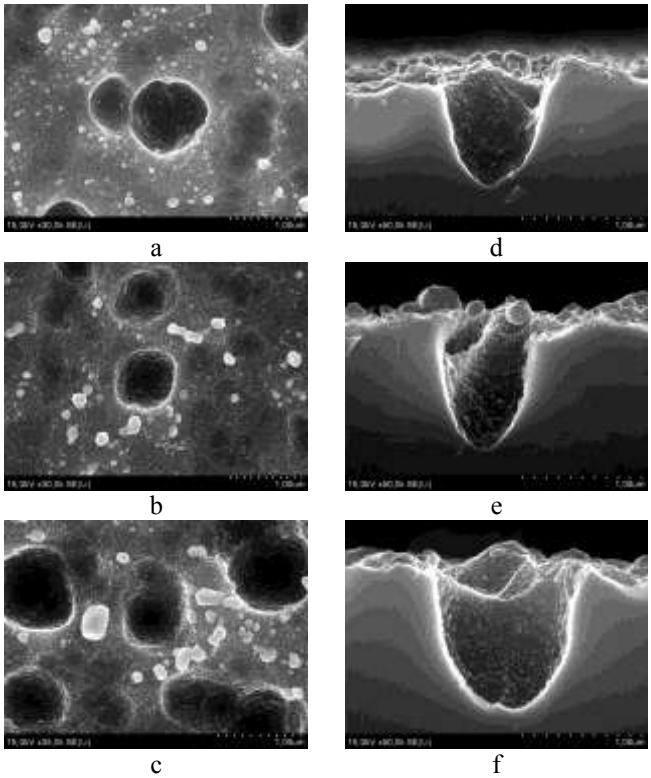

Figure 1: SEM top (a, b, c) and cross section views (d, e, f) of macroPS after 40 (a, d), 120 (b, e) and 200 (c, f) min of Ag displacement deposition.

The diameters of the macropores varied from 700 to 1500 nm and the thickness was about 1000 nm. Ag covered the whole surface of the pore walls as quasi continuous film consisted of NPs of 30-60 nm diameters. The least density of Ag particles is observed on the sample formed during 40 min of deposition (Fig. 1 a, b). The tightly packed Ag films were obtained by the prolonged displacement process of 120 and 200 min duration. The concentration of NPs was found to be almost constant for these times of deposition. We suggest it was caused by the limitation of the electrons for

Ag reduction supplied from the Si skeleton. During the deposition process the surface of the pores was oxidized to SiO_2 that permitted further solution contact with pure Si. Remarkable, the biggest NPs on the outer surface of PS deposited for 120 min were partially connected into chains while the 200 min process resulted in the aggregates coalescence.

To reveal the SERS intensity in dependence on the morphology of Ag films it was necessary to study the Raman spectra of each sample presented on the Figure 1. Figure 2 shows the SERS spectra of the 10^{-6} M CuTMpyP4 molecules obtained from the substrates fabricated by Ag displacement deposition on macroPS for 40 (a), 120 (b) and 200 (c) min. The spectrum of 120 min substrate (Fig. 2 b) demonstrates the Raman intensity of 1.5 times more than two others (Fig. 2 a, c). As the inner surface of the pores was not significantly differ for all times of Ag deposition the enhancement of the signal had to be caused by the outer morphology. Ag chains on the Fig.1 b formed so-called "hot spots" in the points of NPs connections that promoted the plasmon's coupling. Therefore, strong local field enhancement areas appeared.

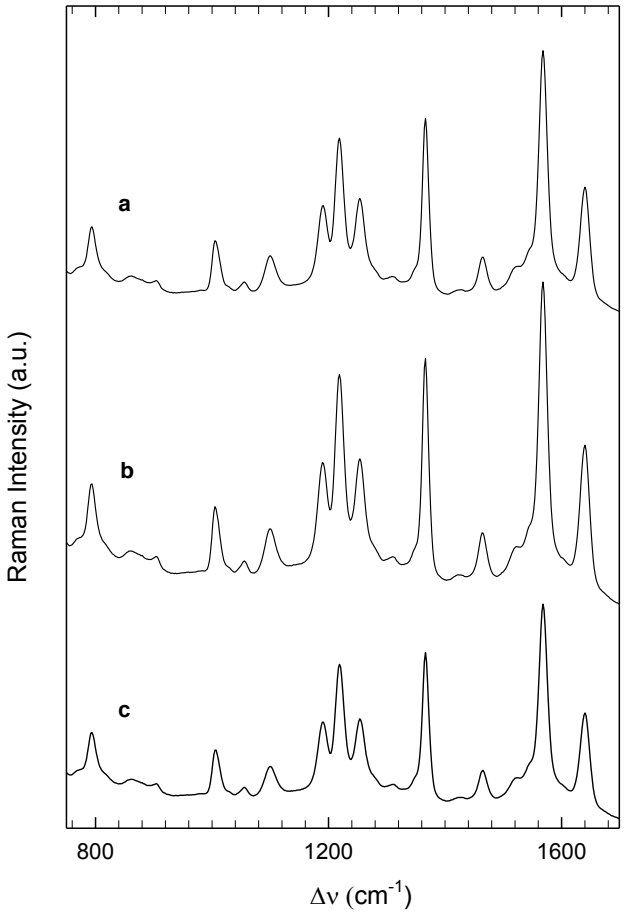

Figure 2: SERS spectra of 10^{-6} M CuTMpyP4 molecules obtained from the substrates fabricated by Ag displacement deposition on PS for 40 (a), 120 (b) and 200 (c) min.

3.2. Porous Cu-based SERS substrates

To obtain the active SERS substrates based on the copper displacement deposition on PS, the specific type of macropores was formed. Figure 3 presents top (a) and cross section (b) views of such PS. It consisted of macropores of 700-1000 nm diameter and Si 80-100 nm walls. Moreover the sponge of nanoporous silicon partially covered the macroporous skeleton. The principal difference of copper deposition from the silver processing was in the solution composition that consisted of copper salt ($CuSO_4$), hydrofluoric acid (HF), isopropyl (C_3H_7OH) and water (H_2O). HF provided removing of SiO_2 under the copper deposit and continuous supplying of the electrons for Cu atoms reduction [19, 20]. In that way the complete displacement of Si skeleton with metal occurred. We observed the separation of copper porous membrane from the Si substrate after the end of the process. Figure 4 presents cross section (a), top (b) and bottom (c) views of the free copper membrane. The thickness of two-layers film was about 8 um. The top part shows the layer of connected large faceted pillars of about 2.5-3 um diameter and 5 um height. The pillars were parallel to each other and grew alone the initial PS pore direction. On the other hand, the bottom layer of the metallic membrane looks like highly porous sponge of 3 um thickness.

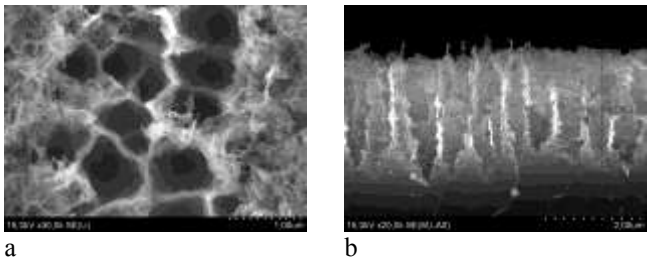

a b

Figure 3: SEM top (a) and cross section (b) views of PS used as a template for copper SERS-active substrate formation.

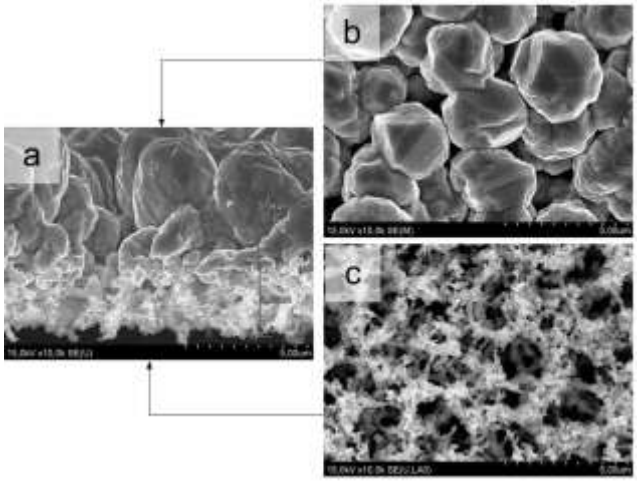

Figure 4: SEM cross section (a), top (b) and bottom (c) views of the copper porous film fabricated by Cu displacement deposition on PS for 180 min.

The elemental composition of the copper porous membrane was revealed by X-ray microanalysis. Figure 5 shows the X-ray microanalysis spectra of top (a) and bottom (b) sides of the copper porous film. The film was almost completely consisted of copper atoms with not significant additions of Si, O, and C. The oxygen presence is observed because of Cu_2O formation during the deposition and drying on the air [21]. Silicon atoms were obviously incorporated from the PS skeleton but they might be ignored due to very small amount. Carbon probably was absorbed by the porous structure of copper from the environment.

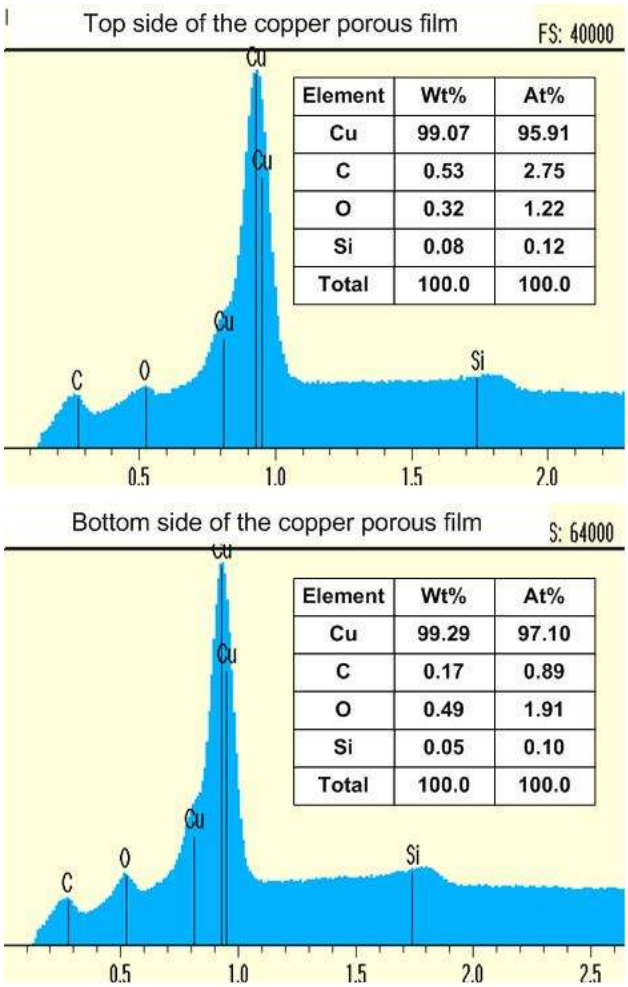

Figure 5: X-ray microanalysis spectra of the top (a) and bottom (b) sides of the copper porous film.

The SERS measurements were performed for both of sides of the porous copper membrane. Since water did not wet the surface of the porous Cu film (solution formed on the surface a ball shaped drop), the CuTMpyP4 precipitated from aqueous-alcoholic solution (in 1:1 ratio by volume). Figure 6 shows SERS spectra of 10^{-6} M CuTMpyP4 molecules obtained from the top (a) and the bottom (b) sides of porous copper membrane fabricated by Cu displacement deposition on PS. The intensity from the top side was three orders of magnitude higher in comparison with bottom side. The structure of the top of copper film was similar to the Si nanopillars array covered with copper that demonstrated the SERS activity in the paper [22]. So the enhancement was likely to be caused by two reasons: (i) plasmons concentration on the tips of copper pillars; (ii) the "hot spots" in the copper pillars connections.

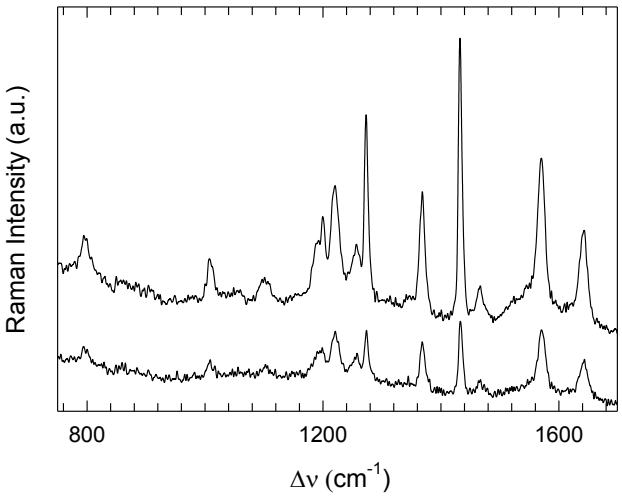

Figure 6: SERS spectra of 10^{-6} M CuTMpyP4 molecules obtained from the top (a) and bottom (b) sides of porous copper membrane fabricated by Cu displacement deposition on PS.

4. Conclusions

SERS-active substrates on the base of PS templates were fabricated by displacement deposition of silver and copper. The SERS efficiency of Ag/macroPS substrates was found to strongly depend on the morphology of silver deposit on the outer surface of PS. The studied structures consisted of monocrystalline Si with macropores of about 1000 nm depth and 700-1500 nm diameters. The walls of the pores and the outer surface of the PS were uniformly covered with connected Ag NPs of 30-60 nm diameters. The best results were obtained from the structures that contained the chains of Ag NPs on the top of PS.

Specific type of PS was used for copper deposition. It presented the macroporous silicon partially covered with sponge of nanoporous Si. The HF-containing solution for copper deposition provided the complete conversion of PS into free porous copper film. The structure of the two-layers copper film determined the intensity of the SERS signal. The large faceted pillars of the top copper layer showed higher intensity than the bottom copper sponge layer. The presented results reveal a new prospective ways of the SERS-active substrates technology including fabrication of nanovias, nanoporous metal films, and bimetallic Cu/Ag substrates.

Acknowledgements

The present research has been supported in parts by the Belarusian Republican Foundation for Fundamental Research under the projects T10M-089 and T11OB-057.

References

[1] M. Fleischmann, P.J. Hendra, A.J. McQuillan, Raman spectra of pyridine adsorbed at a silver electrode, *Chem. Phys. Lett.* 26: 163–166, 1974.

[2] D.L. Jeanmaire, R.P. Van Duyne, Surface Raman spectroelectrochemistry: 1. Heterocyclic, aromatic, and aliphatic-amines adsorbed on anodized silver electrode, *J. Electroanal. Chem.* 84: 1–20, 1977.

[3] M.G. Albrecht, J.A. Creighton, Anomalously intense Raman-spectra of pyridine at a silver electrode, *J. Am. Chem. Soc.* 99: 5215–5217, 1977.

[4] K. Kneipp, Y. Wang, H. Kneipp, I. Itzkan, R.R. Dasari, M.S. Feld, Population pumping of excited vibrational states by spontaneous surface-enhanced Raman scattering, *Phys. Rev. Lett.* 76: 2444–2447, 1996.

[5] S.C. Ponzaru, I. Pavel, N. Leopold, W. Kiefer, Identification and characterization of pharmaceuticals using Raman and surface-enhanced Raman scattering, *Raman Spectrosc.* 35: 338–346, 2004.

[6] J.M. Reyes-Goddard, H. Barr, N. Stone, Photodiagnosis using Raman and surface enhanced Raman scattering of bodily fluids, *Photodiag. Photodyn. Ther. 2*: 223–233, 2005.

[7] J. Kneipp, H. Kneipp, K. Kneipp, SERS - a single-molecule and nanoscale tool for bioanalytics, *Chem. Soc. Rev.* 37: 1052–1060, 2008.

[8] K. Hering, D. Cialla, K. Ackermann, T. Dorfer, R. Moller, H. Schneidewind, R. Mattheis, W. Fritzsche, P. Rosch, J. Popp, SERS: a versatile tool in chemical and biochemical diagnostics, *Anal. Bioanal. Chem.* 390: 113–124, 2008.

[9] C.L. Haynes, R.P. Van Duyne, Nanosphere lithography: a versatile nanofabrication tool for studies of size-dependent nanoparticle optics, *J. Phys. Chem. B* 105: 5599–5611, 2001.

[10] N. Félidj, J. Aubard, G. Lévi, J.R. Krenn, M. Salerno, G. Schider, B. Lamprecht, A. Leitner, F.R. Aussenegg, Controlling the optical response of regular arrays of gold particles for surface-enhanced Raman scattering, *Phys. Rev. B* 65: 075419, 2002.

[11] J.C. Hulteen, R.P. Van Duyne, Nanosphere lithography: a materials general fabrication process for periodic particle array surfaces, *J. Vac. Sci. Technol. A* 13: 1553–1558, 1995.

[12] L. Baia, M. Baia, J. Popp, S. Astilean, Gold films deposited over regular arrays of polystyrene nanospheres as highly effective SERS substrates from visible to NIR, *J. Phys. Chem. B* 110: 23982–23986, 2006.

[13] Lin H., Mock J., Smith D., Gao T. and Sailor M.J., Surface-Enhanced Raman Scattering from Silver-Plated Porous Silicon, *J. Phys. Chem. B* 108: 11654-11659, 2004.

[14] Jiang W. F., Shan W.W., Ling H., Wang Yu. C., Cao Y. X. and Li X. J., Surface-enhanced Raman scattering of patterned copper nanostructure electrolessly plated on arrayed nanoporous silicon pillars, *J. Phys.: Condens. Matter* 22: 415105-415109, 2010.

[15] A. Panarin, S. Terekhov, K. Kholostov, V. Bondarenko, SERS-active substrates based on n-type porous silicon, *Applied Surface Science* 256: 6969-6976, 2010.

[16] A. Panarin, S. Terekhov, K. Kholostov, V. Bondarenko, P.-Y. Turpin, *Proc. Nanomeeting: Phys., Chem. and Appl. of Nanostructures*, Minsk, Belarus, 2009.

[17] T. A. Kelf, Y. Sugawara, R. M. Cole, and J. J. Baumberg, Localized and delocalized plasmons in metallic nanovoids, *Phys. Rev. B* 74: 245415-1 - 245415-12, 2006.

[18] T.V. Teperik et al., Strong coupling of light to flat metals via a buried nanovoid lattice: the interplay of localized and free plasmons, *Opt. Express* 14: 1965-1972, 2006.

[19] H. Bandarenka, S. Redko, P. Nenzi, M. Balucani, Copper Displacement Deposition on Nanostructured Porous Silicon, *Nanotech 2011: Technical Proc. of the 2011 NSTI Nanotechnology Conference and Expo*, 2, pp. 269-272, 2011.

[20] M. Balucani, P. Nenzi, C. Crescenzi, P. Marracino, F. Apollonio, M. Liberti, A. Densi, C. Colizzi, Technology and Design of Innovative Flexible Electrode for Biomedical Applications, *Proc. Electronic Components and Technology Conference*, pp. 1319-1324, 2011.

[21] H. Bandarenka, S. Prischepa, M. Balucani, R. Fittipaldi, A. Vecchione, C. Attanasio, *Book of abstracts: 2009 EMRS Fall Meeting*, p. 204, 2009.

[22] W. F. Jiang, W. W. Shan, H. Ling, Y. S. Wang, Y. X. Cao, and X. J. Li, Surface-enhanced Raman scattering of patterned copper nanostructure electrolessly plated on arrayed nanoporous silicon pillars, *J. Phys.: Condens. Matter* 22: 415105 (5pp), 2010.

Antenna array directivity enhanced by metamaterial-based subwavelength cavity

Mondher LABIDI, Belgacem Aouedi, Jamel BELHADJ TAHAR and Fethi CHOUBANI

6'Tel Research Unit, Higher School of Communications of Tunis,
Sup'Com University of Carthage, Tunisia
mondher.labidi@supcom.rnu.tn

Abstract

In this paper we study the influence of metamaterials on the performances of an array of 2 × 4 microstrip patch antenna operating at about 10 GHz. For this purpose, metamaterials are based on Artificial Magnetic Conductor (AMC) and on inductive and capacitive planar structures. These structures providing High Impedance Surfaces (HIS) and Partially Reflective Surfaces (PRS). Application of these structures allows to improve the performance of antenna, increase the gain and offer a good directivity.

1. Introduction

Feresidis [1] and Zhou [2] showed that the half wavelength restriction of a Fabry-Perot cavity antenna can be reduced to respectively a quarter wavelength and a tenth (10th) wavelength by using a novel type of metamaterial-based resonant cavity in order to design compact directive electromagnetic sources based on a single radiating antenna.

In this study, we present the properties and characterization of an optimized cavity of a circular patch antenna at about 10 GHz. The latter consists of an Artificial Magnetic conductor (AMC) surface with reflection phase zero instead of a Perfect Electric Conductor (PEC) surface and a Partially Reflective Surface (PRS) with a reflection phase equal to 180°. This idea has been pushed further by Zhou et al. to present the advantage of the dispersive characteristics of metamaterials, made of capacitive and inductive grid. The cavity is composed of a substrate, a high impedance surface (HIS) and a partially reflective surface (PRS). The high impedance surface (HIS) [3-4] consists of periodic metallic patterns printed on a dielectric substrate; they have very interesting electromagnetic properties, because they allow the propagation of electromagnetic waves along the surface only for certain frequency bands.

Microstrip patch antennas are versatile in terms of their geometrical shapes and implementations. Inhibiting characteristics of a single microstrip patch, like low gain and smaller bandwidth, make it more popular for array configuration. Antenna arrays acts in microwave communications because of their high gain, good directivity and extensive coverage area. In this study, a 2 x 4 linear patch antenna array is studied. Simulation results of the array of patch antenna in the presence of Fabry-Perot cavity confirm that a drastic enhancement of the antenna directivity is obtained and a deflection of the antenna beam of about ± 20° and a gain of ± 18 dB are observed.

This paper is organized as follows; Section 1 presents an introduction to metamaterials based on the application of Fabry-Perot Cavity to the antenna. In section 2 we introduce the model of cavity in use. Moreover, the characteristics optimization of the array of patches is presented in section 3 and the conclusion is drawn in section 4.

2. Design of Fabry-Perot cavity

In 2005, Feresidis proposed for the realization of Fabry-Perot cavity, a totally reflective surface having the characteristic of reflecting waves with zero phase at its resonance frequency [1]. The cavity studied later by the team Feresidis was fueled by a patch antenna (microstrip patch antenna). But this structure was more compact than most any voids created by Von Trentini. Indeed, with the phase reflection near to zero, the thickness of the cavity was reduced by a factor of two.

In [5], Mondher et al. have proposed a new subwavelength resonant cavity for optimizing the directivity of a single antenna. The subwavelength resonant cavity proposed in this paper, is optimized to operate in X-band [8.2 GHz; 12.4 GHz]. It consists of an Artificial Magnetic Conductor (AMC) composed of a PEC surface and a Partially Reflective Surface (PRS) [6]. The latter consists of a capacitive metallic square patch milled on one face and an inductive metallic mesh on the other. This cavity is optimized to obtain a phase shift of the reflection coefficient between -180° and 180°. As shown in Fig 1, the PRS is placed on Rogers R04232 substrate of 0.81 mm thick (ε_r = 3.2 and tangδ = 0.0018

The width of the mesh is (*w*) is equals to 1.2 mm, the width of the square patch is a = 3.8 mm. Both (the mesh and patch) have a periodicity of 4 mm. The gap spacing between two patches is g. To study the effect of variation of this gap width g between the patches on the reflection coefficient phase, several simulations were made on a unit cell with a =

4 mm, w = 1.2 mm. The AMC behavior extends over a wide frequency range (30%) in which the phase remains between -90° and 90°.

The PRS study in this work presents a very high reflectivity with a phase $\emptyset_{PRS}$ close to -150°. The combination of the $\emptyset_r$ at the surface of the substrate and this negative phase above a conventional ground plane leads to the design of the cavity since at resonance the cavity thickness h is determined by:

$$h = \frac{\lambda}{4\pi}(\phi_{PRS} + \phi_r) \pm N\frac{\lambda}{2} \qquad (1)$$

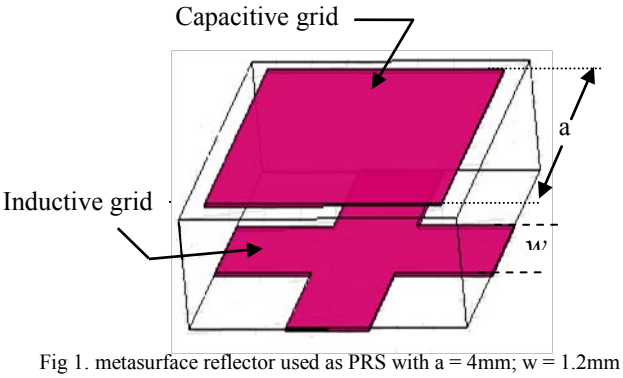

Fig 1. metasurface reflector used as PRS with a = 4mm; w = 1.2mm

Fig. 2 (a) shows the variation of the transmission coefficient phase, Fig. 2(b) depicts the variation of the reflection coefficient phase. As shown in these figures we can note that the variation of the gap spacing (g) causes a variation of the resonance frequency, increasing the gap width causes a decrease in the value of the capacitance between two cells. At a particular frequency we can note that the phase of the PRS increases with an increase of the gap spacing. As shown in Fig.2 several prototypes of subwavelength cavity have been simulated with several values of spacing gap "g". For the PRS, 25 x 13 unit cells have been simulated, the overall dimensions of the prototype are $100\,mm \times 52\,mm \times 1.2\,mm$. The unit cell consists of the metamaterials PRS has a dimensions of $4\,mm \times 4\,mm \times 35\mu m$ include the spacing gap between two capacitive grid of $g = 0.2\ to\ 0.8\,mm$ respectively.

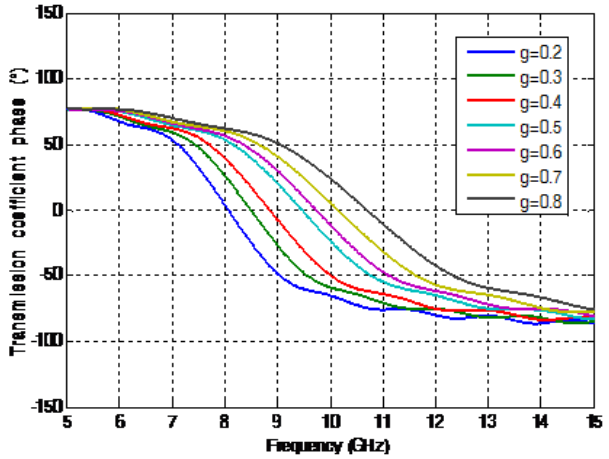

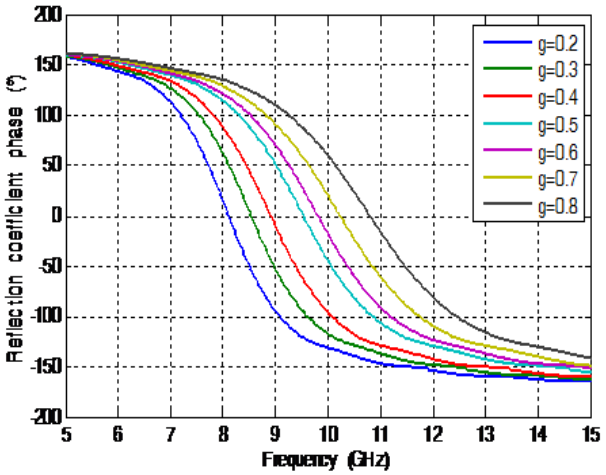

Fig.2 (a) and (b) show the variation of the transmission and reflection coefficients phase respectively

3. 2× 4 Antenna array design

An array consists of two or more antenna elements that are spatially arranged and electrically interconnected to produce a directional radiation pattern. The interconnection between elements, called the feed network, can provide fixed phase to each element or can form a phased array. In optimum and adaptive beam forming, the phases (and usually the amplitudes) of the feed network are adjusted to optimize the received signal. The geometry of an array and the patterns, orientations, and polarizations of the elements influence the performance of the array.

They show superior performance to the normal metal devices. Application of the metamaterials in the antenna domain present a high gain and a good directivity but an effort toward miniaturization is strongly desirable to allow the use of small size and easy handling cryocoolers, attractive for the realization of superconducting systems in radar and satellite applications [7].

The prototype of antenna array is composed as follow, the patch and the ground plane are assumed as perfect conductors deposited on $0.5\,mm$ thick Plexiglas substrate with dielectric constant ε_r = 3.4. A 2 × 4 microstrip patch antenna array is designed on a 100 × 52 mm^2 to operate near to 10 GHz where the PRS exhibits low reflection phase values. In case of linear polarized (LP) antenna. Our study focused on the patch antenna and antenna array. Their structures are illustrated in Fig.3 (a) and (b) below. The square patch element has a dimensions of Lp = Wp = 8 mm. The array is fed via microstrip transmission lines acting as $\lambda/4$ as shown in Fig.3. Different spacing, S, between two elements have been considered, $S = \lambda/2, S = \lambda$ and $S = 2\lambda$. We can note that an increase in S gives rise to a more directivity. In this study the spacing between two elements $S \sim 0.5\,\lambda$ is considered since it is more directive than the other cases. The Fabry-perot cavity is placed above the patch antenna array so as to study its effect on the radiation characteristics

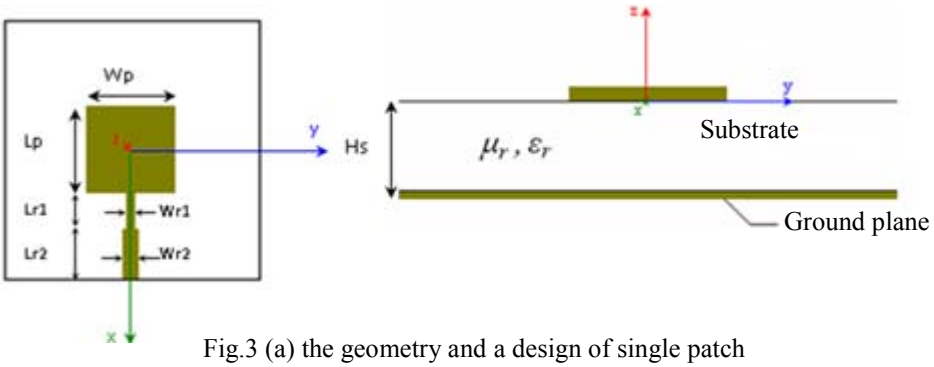

Fig.3 (a) the geometry and a design of single patch

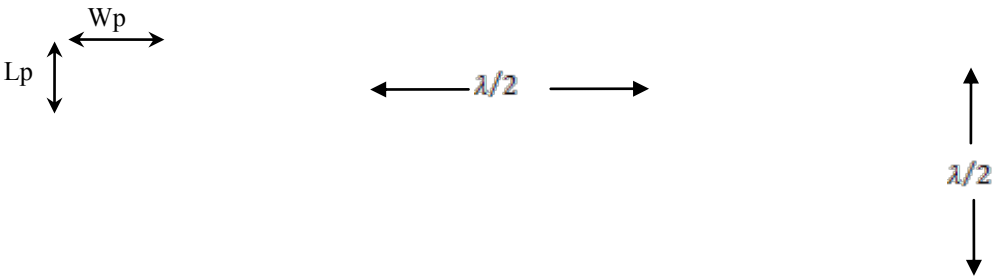

Fig.3 (b) Schematic of 2 x 4 patch antenna array

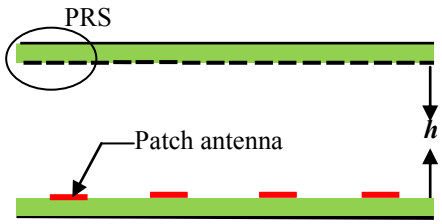

Fig.3 (c) Schematic of metamaterials based compact cavity antenna

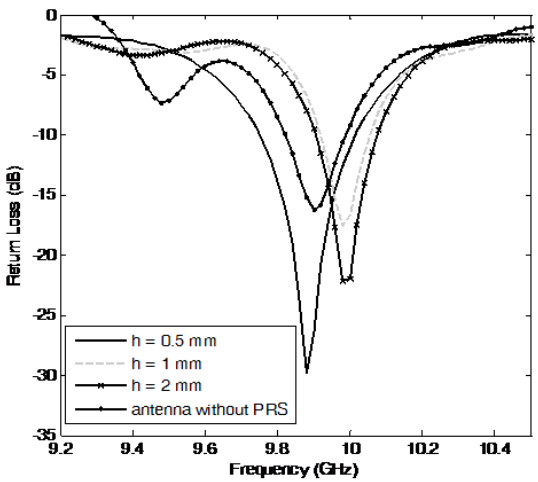

Fig.4 Calculated return losses of multisource cavity

The layout of the 8 patches array and the FP cavity is shown in Fig.3 (b) and (c).The idea is to study the antenna array without metamaterials in the first part and to show the effect of the metamaterials application to the antenna performances. Here we limited to mention that the gain of the 8 array is 12.2 dB higher than the single element and have a return loss of -16 db at 9.7 GHz as shown in Fig.4. In the second part, several prototypes of the subwavelength cavity have been simulated using Ansoft HFSS. First prototypes of antennas with distance $h = 0.5\ mm$ to the metamaterial PRS is considered as shown in Fig.3 (c), this prototype will assure no deflection of the beam since it exists no phase shift of the metamaterial. The second and third prototype, the optimized cavity thicknesses are $h = 1\ mm$ and $h = 1.5\ mm$ with $a = 3.8mm, w = 1.2\ mm$ and $g = 200\mu m$.

The S_{11} parameter and the gain associated to the patch antenna array in X-band are represented in Fig.4, 5 and 6.

Fig.5 shows the radiation Patterns for the E-plane ($\emptyset = 90°$) in (a) and for H-plane ($\emptyset = 0°$) in (b). We can notice that the secondary lobes are much lower than for the antenna array alone. Table1 summarizes the resonant frequencies and the radiation pattern for different thickness h of the cavity.

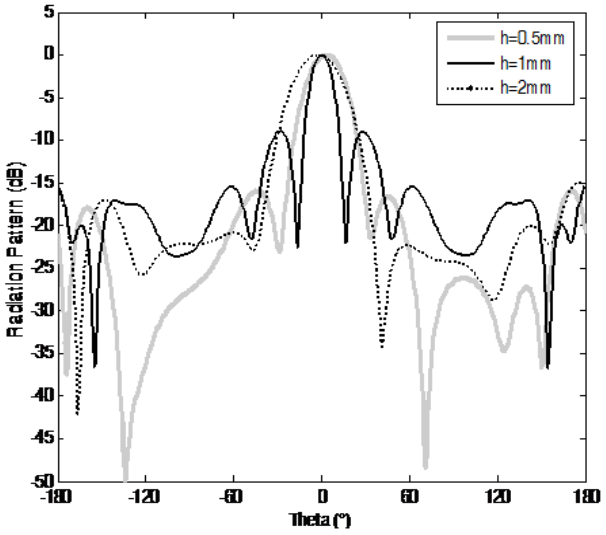

(a)

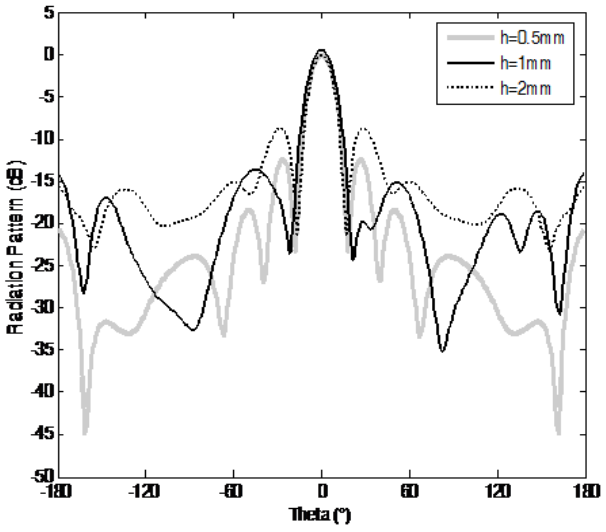

(b)

Fig.5 Calculated: (a) E and (b) H-planes radiation patterns of the antenna array for a cavity thikness $h = 0.5\ mm, h = 1\ mm$ and $h = 2\ mm$.

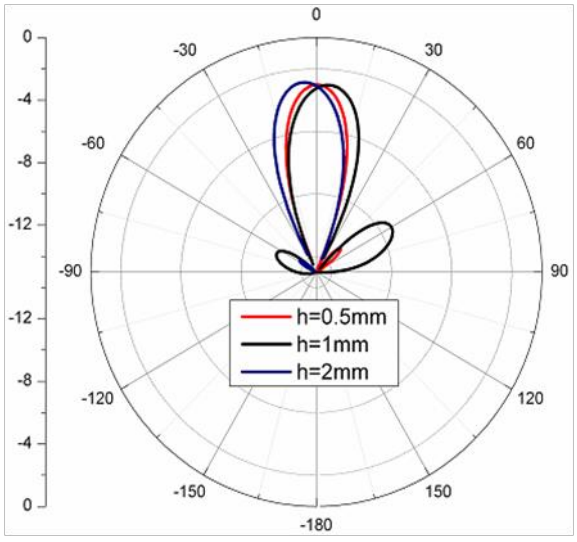

(a)

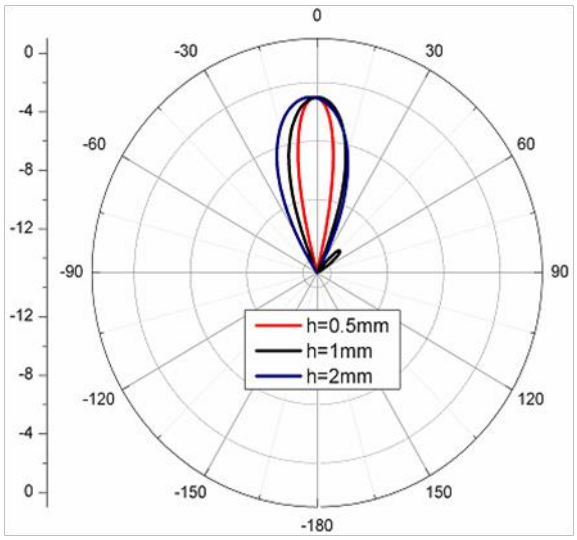

(b)

Fig.6. Far-field radiation pattern of the antenna array: (a) in the E($\emptyset = 90°$) and (b) in the H ($\emptyset = 0°$) planes for a cavity thikness $h = 0.5\ mm, h = 1\ mm$ and $h = 2\ mm$.

As shown in Fig.6 (a) and (b), for an optimized cavity thickness h =0.5 mm, a= 3.8mm, w = 1.2 mm and g = 200 µm, the beam is normal to the plane of the antenna array and shows no deflection. For a cavity thickness of h = 1 mm and h = 1.5 mm, with this regular variation of h, a deflection of antenna beam of about 17° and -10° can be observed in Fig.6 (a) in the E-plan $(\emptyset = 90°)$.

Table1. Resonant frequencies and the radiation pattern for different thickness h of the cavity.

	f_{res} (GHz)	S_{11} (dB)	Gain (dB)	Aperture at -3 dB (°)
Antenna without PRS	9.9	-16.21	12.2	60
$h = 0.5\ mm$	9.88	-29.87	18.5	16.8
$h = 1\ mm$	9.98	-17.51	17	22
$h = 1.5\ mm$	9.98	-22.18	15.8	27

4. Conclusions

A 2 × 4 linear antenna array composed of square patch elements is discussed and antenna array characteristics are improved by metamaterials based planr artificial magnetic conductor. A Fabry-Perot cavity and adequate arrangement of antenna geometry is a solution to miniaturize radiation and enhance the directivity of metamaterials based cavity antennas.

References

[1] Feresidis, A.P., Goussetis, G., Wang,S., and Vardaxoglou,J.C. “Artificial magnetic conductor surfaces and their application to low-profile highgain planar antennas”, IEEE Trans. Antennas Propag., pp. 209–215, 2005.

[2] Zhou, L., Li, H., Qin, Y., Wei, Z., and Chan, C.T.“Directive emissions from subwavelength metamaterial-based cavities”, Appl. Phys. 2005.

[3] R.F.J.Broas,D.Sievenpiper,E.Yab lonovitch, “A high-impedance ground plane applied to a cell phone hand set geometry”, IEEE Trans. Microw. Theory Tech. 1262–1265, 2001.

[4] D. Sievenpiper, L. Zhang, R.F.J. Broas, N.G. Alexópoulos, E. Yablonovitch, “High-impedance electromagnetic surfaces with a forbidden frequency band”, IEEE Trans. Microw. Theory Tech. 2059–2074, 1999.

[5] M. LABIDI, N. DAKHLI, J. BELHADJ TAHAR and F. CHOUBANI, “Circular patch antenna directivity enhanced by Left-handed Material cavity”, In proceeding of PIERS 2011.

[6] A. Ourir, A. de Lustrac, J.-M. Lourtioz, “Optimization of metamaterial based subwavelength cavities for ultracompact directive antennas”, Microwave Opt. Technol. Lett. 2573–2577, 2006.

[7] A. Ourir, A. de Lustrac, J.-M. Lourtioz, “All-metamaterial-based subwavelength cavities($\lambda/60$) for ultrathin directive antennas”, Appl. Phys. Lett.

Time domain investigation of the tunneling modes in photonic heterostructure containing single negative materials

Liwei Zhang[1, 3*], Guiqiang Du[2, 3], Yewen Zhang[3]

[1] School of Physics and Chemistry, Henan Polytechnic University, Jiaozuo 454000, China
[2] School of Space Science and Physics, Shandong University at Weihai, Weihai 264209, China
3 MOE Key Laboratory of Advanced Micro-structure Materials, Department of Physics, Tongji University, Shanghai 200092, China
*corresponding author, E-mail: lwzhang@hpu.edu.cn

Abstract

We present a theoretical investigation into the energy transport and transient wave propagation in the metamaterial tunneling structures consisting of ε-negative (ENG) and μ-negative (MNG) materials. It is proved that the conjugated matched ENG/MNG bilayer and the (zero index material doped) photonic crystal heterostructure can work as a sub-wavelength resonator at tunneling frequency. While the tunneling modes need a certain time to achieve to the steady state and the charge up characteristic time increase (nearly) exponentially with the thickness of the structures. Under the steady state, the waves in the single negative material structures are not evanescent, but a hybrid of traveling wave and reactive standing wave. The phase difference between the electric field and magnetic field varies with the position and time. The investigation of transient wave propagation in the metamaterial tunneling stuctures will help us to understand the interaction process between wave and metamaterial and to design special functional apparatus.

1. Introduction

Recently, metamaterials with non-positive permittivity and/or permeability have attracted people's interest due to their unique electromagnetic (EM) properties[1-8]. Besides double-negative metamaterials (ε<0, μ<0) [1,2], single negative metamaterials including ε-negative (ENG) materials (ε<0, μ>0) and μ-negative (MNG) materials (ε>0, μ<0) [3-6] and zero-index metamaterials (ZIMs)[7-9] in which ε=μ=0 or ε=0, μ≠0(ε≠0, μ=0) also deserve special attention. Based on the Maxwell equations, the fields inside a matched ZIM(ε=μ=0) should be homogeneous [10]. One of the most important features of metamaterials is the amplification of the amplitude of evanescent waves, and the double-negative metamaterials are used to realize perfect lens[2]. Furthermore, it was demonstrated that the enhancement of the evanescent waves also exists in an ENG/MNG bilayer and the (ZIM doped) photonic crystal heterostructure at zero average parameters[3,5]. The tunneling structures can work as a subwavelength resonator since the tunneling mode is independent of the scaling. In fact, the tunneling mode needs a certain time (which can be described with charging up characteristic time (CT) τ) to achieve to the steady state, the CT increases (nearly) exponentially with the thickness of the conjugate matched ENG/MNG bilayer[11,12]. In Ref 13 and 14, the tunneling time of electromagnetic planar wave propagating through the metamaterial structure are studied. In this paper, we study the transient wave propagation and energy transportation in the (ZIM doped) photonic heterostructure containing single negative materials.

2. Model and theory

For the sake of simplicity, we first consider the ENG/MNG bilayer, and a TM plane wave (E_x, H_y) is incident normally on the bilayer, which is shown in the inset of Fig. 1. After applying the boundary conditions on the three interfaces of the bilayer and some mathematical manipulation, the complete tunneling condition for the ENG/MNG bilayer can be expressed as[3]:

$$\sqrt{|\mu_1 \cdot \varepsilon_1|}d_1 = \sqrt{|\mu_2 \cdot \varepsilon_2|}d_2 \quad \text{and} \quad \sqrt{|\mu_1|/|\varepsilon_1|} = \sqrt{|\mu_2|/|\varepsilon_2|} \qquad (1)$$

where d_1 and d_2 are the thickness of ENG and MNG slabs, respectively. As a special case, a conjugate matched bilayer is denoted by $\varepsilon_1 = -\varepsilon_2 = -\varepsilon$, $\mu_1 = -\mu_2 = \mu$ and d_1=d_2=d, we have $k_i = jk = j\omega\sqrt{\mu\varepsilon}$, ($i$=ENG, MNG). Where the bilayer possess zero average permittivity and zero average permeability. The steady state electromagnetic (EM) fields in the bilayer can be expressed as follows.

In Region ENG :

$$E_{x1} = E_0 \cosh(kz) - j\frac{\eta}{\eta_0} E_0 \sinh(kz) = |E_{x1}| e^{j\theta_{E1}}$$

$$H_{y1} = \frac{E_0}{\eta_0}\cosh(kz) + j\frac{E_0}{\eta}\sinh(kz) = |H_{y1}| e^{j\theta_{H1}} \qquad (2)$$

Region MNG:

$$E_{x2} = E_0 \cosh[k(z-2d)] + j\frac{\eta}{\eta_0} E_0 \sinh[k(z-2d)] = |E_{x2}| e^{j\theta_{E2}}$$

$$H_{y2} = \frac{E_0}{\eta_0}\cosh[k(z-2d)] - j\frac{E_0}{\eta}\sinh[k(z-2d)] = |H_{y2}| e^{j\theta_{H2}} \qquad (3)$$

where E_0 is the incident electric field amplitude and the wave impedance in free space and single negative material are $\eta_0 = \sqrt{\mu_0/\varepsilon_0}$ and $\eta = \sqrt{\mu/\varepsilon}$ respectively. It is easy to prove that the average power flow $p = 1/2|Exi \cdot Hyi|\cos\theta_i = E_0^2/2\eta_0$ in all the regions is constant, Where $\theta_1 = \theta_{E1} - \theta_{H1}$ and $\theta_2 = \theta_{E2} - \theta_{H2}$, respectively. In our previous paper [12] it is shown that ENG/MNG can work as

a special resonator, there is a substantial amount of EM energy (W_{EM}) stored in the bilayer. It takes a certain amount of time for the fields at ENG/MNG interface and the exit of MNG slab to reach to its steady state which can be descried by charging up process. The charging up process of the resonator with a rectangular waveform signal follows 1-exp(-αt) [15], where the charging up coefficient α=ω/2Q and the charging-up time is: $\tau/T = 2\left[\sinh(2kd)/2 + \arctan\left(e^{2kd}\right) - \pi/4\right]/\pi$ [12], where Q is the quality factor of the resonator, T is the cycle of the wave and d is the thickness of the slab. It increases exponentially with the thickness of the slab, corresponding to the increase of Q factor of the tunneling mode as shown in Fig.1(a) (the solid line). According to the theory[5], the (ZIM doped) photonic heterostructure containing single negative material can also possess complete tunneling mode under zero average parameters. And the transient wave propagation in the tunneling structures is studied by FDTD method.

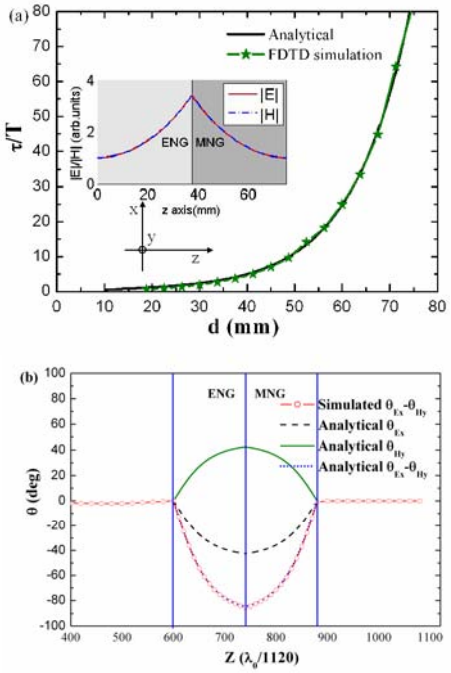

Figure 1. (a) The analytical and FDTD simulated charging up characteristic times τ/T vs thickness d of the conjugated matched ENG/MNG slabs, the inset is the steady state EM fields distribution at tunneling frequency (b) The phases of electric and magnetic fields and their phase difference, where f_0 = 1GHz, ε/ε$_0$ = 2, μ/μ$_0$ = 2, d = 37.5mm.

3. Results and discussions

Consider an example where the Drude models for the permittivity and permeability in the lossless ENG and MNG slabs are: $\varepsilon_1/\varepsilon_0 = 2 - 4/f^2$, $\mu_1/\mu_0 = 2$, $\mu_2/\mu_0 = 2 - 4/f^2$, $\varepsilon_2/\varepsilon_0 = 2$, where f is frequency measured in GHz and $d_1 = d_2 = 37.5mm$. According to the conjugate matched condition Eq.(1), the bilayer exhibits a complete tunneling mode at f_0=1GHz. The conjugate matched ENG and MNG bilayer shown in the inset of Fig. 1 is modeled by using FDTD method[16]. The amplitude and phase profiles of steady state electric and magnetic fields are plotted in Fig. 1 In simulation, the problem space is 1500 cells long, where $\Delta z = \lambda_0/1500$ with $\lambda_0 = 300mm$. A plane sinusoidal wave is launched at about a half wavelength away from the surface of ENG with a rectangular waveform. The thicknesses of the ENG and MNG layers are $d_{ENG} = d_{MNG} = 187.5\Delta z$, the time step is set to be $\Delta t = 0.5\Delta z/c = 1/3ps$. As from the time histories of the electric field and magnetic field in Ref.11, it is shown that the charging up process of the resonator with a rectangular waveform signal follows 1-exp(-αt). As verification to this theory, we have also computed the charging up characteristic time τ/T in the transient process simulations and plotted it in Fig. 1(a) as well. The analytical and simulated results agree to each other very well. It can be seen in Fig. 1(a) that the charging up characteristic time increases 'exponentially' with the thickness of the slab. It is due to the 'exponential' increase of the reactive field inside the bilayer, leading to a substantial increase of the Q factor.

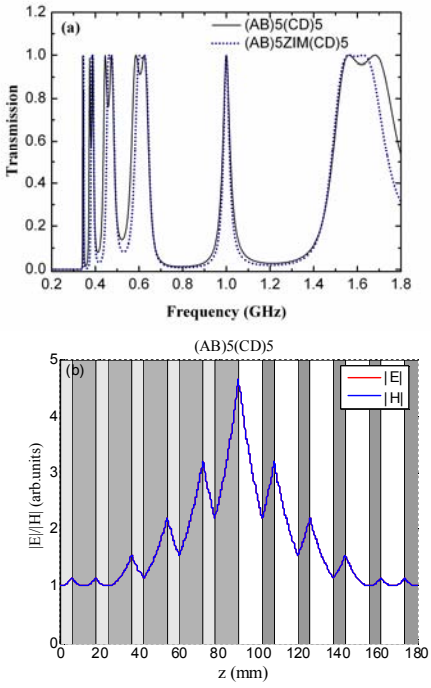

Figure 2. (a) Transmittances of the photonic heterostructure $(AB)_5(CD)_5$ (black solid line)and the ZIM doped heterostructure $(AB)_5ZIM(CD)_5$ (blue dotted line). (b) The steady state EM field distribution corresponding to the heterostructure tunneling mode.

It is interesting to observe that the phases (θ_{Ex}, θ_{Hy}) of *Ex* and *Hy* vary in an opposite way inside the ENG and MNG slabs – not being constant for typical evanescent waves. The phase variations of EM fields inside the ENG slab are completely 'compensated' inside MNG slab. Moreover the phases of EM fields remain the same at the entrance and exit of the bilayer, which is the resonance condition. The thickness of bilayer is much shorter than the wavelength

(2d=λ_0/4) which indicates that the conjugate matched ENG/MNG bilayer is a unique sub-wavelength open-cavity resonator. The phase difference θ_i between *E* field and *H* field starts with zero at the entrance to ENG slab, indicating a pure travelling wave, then increases inside the ENG slab, suggesting that the electric field starts to decouple with the magnetic field – becoming partly reactive. The phase difference reaches to its maximum, corresponding to a strongest reactive field or standing wave at the ENG/MNG interface. The phase difference starts to fall inside the MNG slab, indicating the dropping of reactive field, and reaches to zero at the exit of MNG slab – back to a pure travelling wave. It indicates clearly that the electromagnetic fields inside the conjugate matched ENG/MNG bilayer is a hybrid of travelling wave and reactive standing wave with the ratio between them varying with the position.

It was shown that a one-dimensional photonic crystal stacked by alternating MNG layer and ENG layer can possess photonic bandgaps originating from the interaction of evanescent-wave-based interface modes[5,6]. While the photonic heterostructure $(AB)_m(CD)_n$ (as show in Fig. 2(b)) and the ZIM doped photonic heterostructure $(AB)_mZIM(CD)_n$ (as show in Fig. 5) possess complete tunneling mode without phase shift under the zero average permittivity and average permeability condition. And the tunneling structures can also work as a sub-wavelength resonator[5], where $A(C)$ and $B(D)$ indicate ENG materials and MNG materials respectively and $m(n)$ is the period number. In addition the photonic heterostructure $(AB)_m(CD)_n$ can be a effective ENG_{eff}/MNG_{eff} bilayer under the tunneling condition. According to the effective medium theory, the effective permittivity ε_{eff} and the effective permeability μ_{eff} of the periodic ENG-MNG layered structures under normal incident condition can be written as $\varepsilon_{eff} = (\varepsilon_{A/C} d_{A/C} + \varepsilon_{B/D} d_{B/D}) / (d_{A/C} + d_{B/D})$, $\mu_{eff} = (\mu_{A/C} d_{A/C} + \mu_{B/D} d_{B/D}) / (d_{A/C} + d_{B/D})$ [17]. Here we use Drude model to describe the isotropic metamaterials, that are $\varepsilon_{A/C} = 1 - 4/f^2$, $\mu_{A/C} = 3$ in ENG materials and $\varepsilon_{B/D} = 3$, $\mu_{B/D} = 1 - 4/f^2$ in MNG materials. $\varepsilon_{ZIM} = \mu_{ZIM} = 1 - 1/f^2$, at about 1.0GHz, ZIM posses zero effective parameter. The thicknesses of ENG , MNG and ZIM slabs in the two tunneling structures are assumed to be $d_A = d_D = 6mm$, $d_B = d_C = 12mm$, $d_{ZIM} = 15mm$ respectively. We consider the transverse electric wave case, e.g., the electric field lies in the y direction. The treatment for the transverse magnetic wave is similar. The transmittance and field distributions of the structure can be obtained by means of the transfer matrix method[18].

As shown in Fig.2(a), the photonic heterostructure $(AB)_5(CD)_5$ (black solid line) and the ZIM doped heterostructure $(AB)_5ZIM(CD)_5$ (blue dotted line) possess complete tunneling mode at 1.0GHz. The steady state EM fields distribution corresponding to the tunneling mode is shown in Fig.2(b). It is shown that the EM fields concentrate on the interface and the evanescent fields are seemed to be amplified in single negative materials. It is worth to note that the establishment of the tunneling mode will also need a certain time to achieve to the steady state.

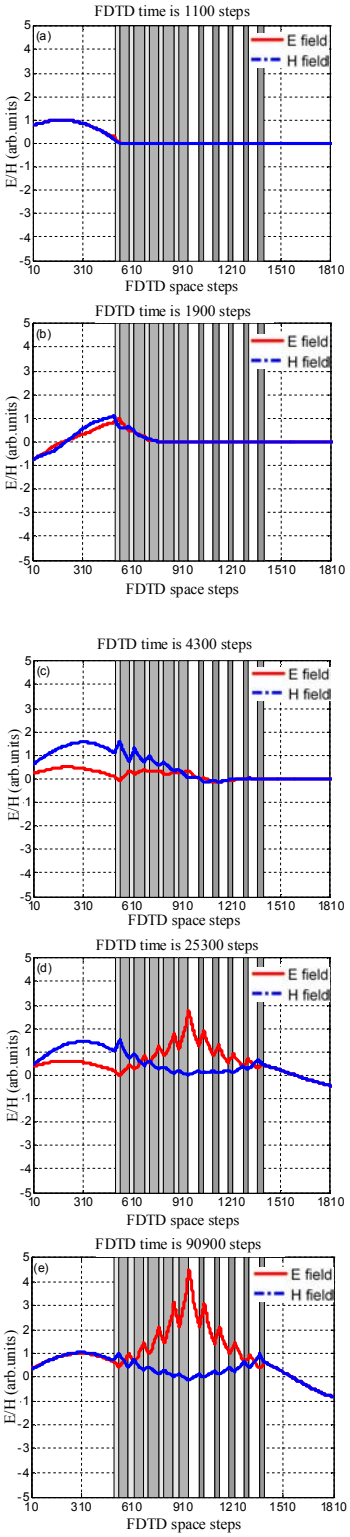

Figure 3. Snapshots of the electric field and magnetic field profiles at different moments of transient wave propagation: (a) a wave come from the free space to the heterostructure, (b)at entering $(AB)_5$, (c) at entering $(CD)_5$, (d) at building-up of the reactive field, (e) reaching to the steady state.

In order to study the transient wave propagation process, the time histories of the electric field and magnetic fields at any position of the tunneling mode are simulated, which are not show here since they are similar to that in Fig.2 in Ref.12. The detailed transient wave propagation through the photonic heterostructure is further investigated by observing the animation of electric and magnetic fields. Some snapshots of the field profiles in sequence are shown in Fig. 3. Fig. 3(a) shows when the incident wave enters into the photonic heterostructure $(AB)_5(CD)_5$ with the reflection at the air-ENG interface – the phases of electric and magnetic fields being split, which indicates that the phase difference appears. Fig. 3(b) shows when the wave reaches to ENG/MNG photonic crystal, a further reflection occurring at the ENG/MNG interfaces. Fig. 3(c) shows a moment when the attenuated wave tunnels through the heterostructure with more reflection. Fig. 3(d) shows a moment of the reactive fields being built up inside the heterostructure due to the multiple reflections and transmissions. Fig. 3(e) shows a moment of the steady complete tunneling state being reached – indicating a complete transparency of the heterostructure to the incident wave.

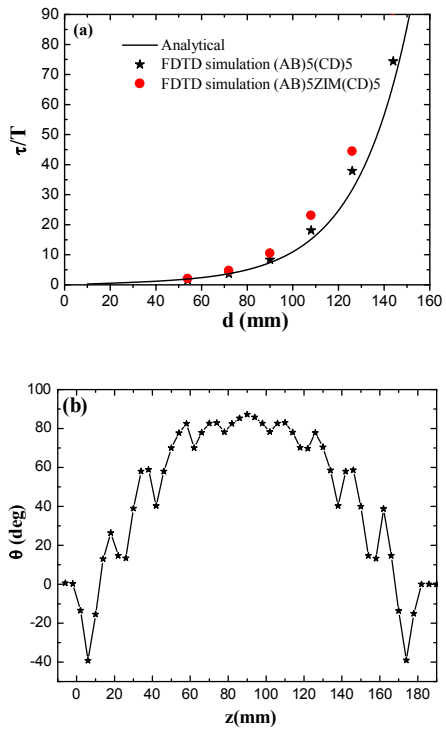

Figure 4. (a) The analytical and FDTD simulated characteristic times τ/T vs the thickness of the photonic crystal (AB)*n*, *n* is the period number, the black solid line is the analytical results, in which the effective parameters(i.e. ε_{eff}, $\mu_{eff,}$ and d) are used, the stars (solid circles) represents the FDTD simulated CTs based on (AB)*n*(CD)*n* ((AB)nZIM(CD)n) structure. (b)The phase difference between the electric field and magnetic fields in the photonic heterostructure $(AB)_5(CD)_5$ at the resonance frequency.

In Fig. 4. (a), the analytical and FDTD simulated characteristic times τ/T vs the thickness of the photonic crystal (AB)*n* are shown, where *n* is the period number. The black solid line is the analytical results, in which the effective parameters (i.e. ε_{eff}, $\mu_{eff,}$ and d) are used, the stars (solid circles) represents the FDTD simulated characteristic times based on (AB)*n*(CD)*n* ((AB)nZIM(CD)n) structure. It is shown that the CT is larger than that of ENG/MNG bilayer because of multiple reflection. Fig.4(b) shows the phase difference between the electric field and magnetic fields in the photonic heterostructure $(AB)_5(CD)_5$ at the resonance frequency. It is interesting to notice that the phase differences are nearly symmetrical relative to the heterostructure interface where the phase difference is maximum. In fact, it is observed that the phase differences at any position also vary with time in the transient process. So under the steady state, the waves in the single negative material structures are also not evanescent, but a hybrid of traveling wave and reactive standing wave, and the phase difference between the electric field and magnetic field varies with the position. While the steady state phase difference between electric field and magnetic field is zero at the entrance and exist of the tunneling structure which indicates the complete transparency.

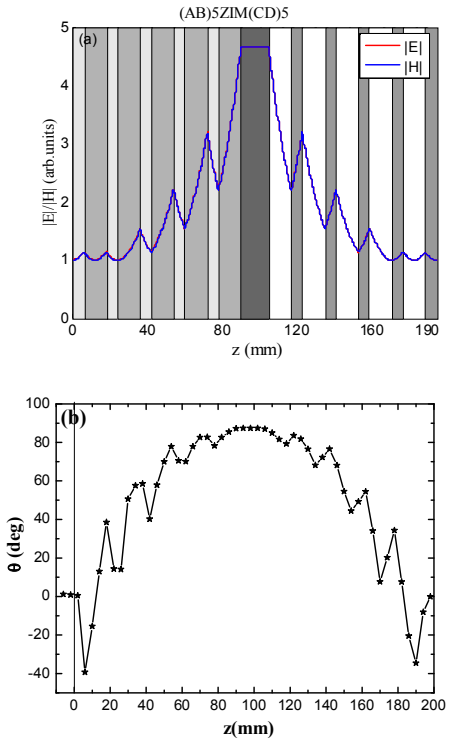

Figure 5. (a) The steady state EM field distribution in the ZIM doped heterostructure (AB)5ZIM(CD)5 at the tunneling mode. (b)The phase difference between the electric field and magnetic fields in the heterostructure (AB)5ZIM(CD)5 at resonance frequency.

Fig. 5. (a) shows the steady state EM field distribution in the ZIM doped photonic heterostructure $(AB)_5ZIM(CD)_5$ at the tunneling frequency. It is clear that the fields in single negative material are also amplified and the fields are all uniform in the ZIM material. The phase difference between the electric field and magnetic fields in the heterostructure (AB)5ZIM(CD)5 at resonance frequency are also shown in

Fig.5(b), it is also shown that the EM fields inside the structure is a hybrid of travelling wave and reactive standing wave with the ratio between them varying with the position. The phase difference is the same in all the ZIM material and the phase difference is a maximum. It is found that the phase difference in the tunneling structures compensates the field amplitude at very position to keep the power flow constant.

4. conclusions

In conclusion, the transient establishment process of the tunneling mode in the photonic crystal heterostructures containing single negative material are studied by FDTD method. It is shown that the conjugate matched ENG/MNG and the (ZIM doped) photonic crystal heterostructure can work as a sub-wavelength resonator at tunneling frequency. While the tunneling modes need a certain time to achieve to steady state and the CT increases (nearly) exponentially with the thickness of the ENG/MNG bilayer, the CT of the (ZIM doped) photonic crystal heterostructure is larger than that of ENG/MNG bilayer due to multiple interface reflection. Under steady state, the waves in the single negative material are a hybrid of traveling wave and reactive standing wave, and the phase difference between the electric field and magnetic field varies with the positions.

Acknowledgements

This research was supported by 973 Research program of China (No. 2011CB922001), by NFSC (Nos.10904032 and 11004121)

References

[1] V. G. Veselago, "The Electrodynamics of Substances With Simultaneously Negative Values of ε and μ," *Soviet. Physics. Uspekhi ,* Vol. 10, No.4, 509-514, 1968.

[2] N. Engheta, R. W. Ziolkowski, Metamaterials-physics and engineering explorations (Wiley IEEE press, 2006)

[3] A. Alù and N. Engheta, "Pairing an epsilon-negative slab with a mu-negative slab: resonance, tunneling and transparency," *IEEE Trans. Antennas Propagat.* vol. 51, no. 10, pp.2558-2571, Oct.2003

[4] Z. W. Liu, H. Lee, Y. Xiong, C. Sun, X. Zhang, "Far Field Optical Hyperlens Magnifying Sub Diffraction Limited Objects," *Science*, Vol. 315, No. 5819, 1686, 2007.

[5] G. S.Guan, H. T. Jiang, H. Q. Li, Y. W.Zhang, H. Chen, S.Y.Zhu, "Tunneling modes of photonic heterostructures consisting of single-negative materials," *Appl. Phys. Lett.* Vol. 88, No. 21, 211112, 2006.

[6]Y. H. Chen, "Defect modes merging in one-dimensional photonic crystals with multiple single-negative material defects," *Appl. Phys. Lett.* **92** (1), 011925(2008)

[7] D. A. Powell, A. Alù, B. Edwards, A.Vakil, Y. S. Kivshar, and N. Engheta, "Nonlinear control of tunneling through an epsilon-near-zero channel,"*Phys. Rev. B* Vol. 79, No. 24, 245135, 2009.

[8] J. M. Hao, W. Yan, and M. Qiu, "Super-reflection and cloaking based on zero index metamaterial," *Appl. Phys. Lett.* Vol. 96, No.10, 101109, 2010.

[9] V. C. Nguyen, L. Chen, and K. Halterman, "Total transmission and total reflection by zero index metamaterials with defects," *Phys. Rev. Lett*. **105** (23), 233908 (2010).

[10] R. W. Ziolkowski,"Propagation in and scattering from a matched metamaterial having a zero index of refraction," *Phys. Rev. E* Vol. 70, No.4, 046608, 2004.

[11] A.Alù, N. Engheta, R. W. Ziolkowski, Finite-difference time-domain analysis of the tunneling and growing exponential in a pair of ε-negative and μ-negative slabs, " *Phys. Rev. E* Vol.74, No.1, 016604, 2006.

[12]L. W. Zhang, Y. W. Zhang, X. D. Chen, X. M. Liu, H. Chen, "Energy transport in a metamaterial subwavelength open-cavity resonator," *Opt. Lett.* Vol. 36, No. 12, 2224-2226, 2011.

[13]I. Ilic´, P. P. Belicev, V. Milanovic´, J. Radovanovic, "Analysis of tunneling times in absorptive and dispersive media," *J. Opt. Soc. Am. B* Vol. 25, No. 11, 1800-1804, Nov. 2008

[14]P. P. Beličev,I. Ilić, V. Milanović,J. Radovanović, L. Hadžievski, "Tunneling times in metamaterials with saturable nonlinear ity," *Phys. Rev. A* Vol. 80, No.2, 023821, 2009.

[15]T. L. Floyd, Electric Circuit Fundamentals, (Prentice Hall, 7 edition 2006)

[16]D. M. Sullivan, Electromagnetic Simulation Using the FDTD Method, (IEEE Press: New York, 2000).

[17]A. Lakhtakia, and C. M. Krowne, "Restricted equivalence of paired epsilon-negative and mu-negative layers to a negative phase-velocity material (alias left-handed material)," *Optik*, Vol. 114, No.7, 509-514, 2003.

[18] N. H. Liu, S. Y. Zhu, H. Chen, and X. Wu, "Superluminal pulse propagation through one-dimensional photonic crystals with a dispersive defect," *Phys. Rev. E* Vol. 65, No.4, 046607, 2002.

Wave propagation in lossy MTMs surrounded by linear and nonlinear media with arbitrary nonlinearity

Zeyad I.Al-Sahhar[1], Hala J. El-Khozondar[2], Mohammed M. Shabat[3]

[1]Physics Department, Al-Aqsa University, Gaza, Palestine
[2]Electrical and Computer Engineering Department, Islamic University, P.O.Box 108, Gaza, Palestine
[3]Physics Department, Islamic University, P.O.Box 108, Gaza, Palestine
*corresponding author: hkhozondar@iugaza.edu.ps

Abstract

The dispersion relation in a system consists of a lossy metamaterials (MTMs) film surrounded by a linear substrate and a nonlinear cladding with an arbitrary nonlinearity is derived. The surface plasmonic (SP) wave at the interfaces between metamaterials (MTMs) and the nonlinear cover is recovered by taking certain limits. Results are presented by plotting the SP frequency as a function of the nonlinearity at chosen damping factors. Both the real and imaginary parts are studied. For comparison, the imaginary part is set to zero and curves are reproduced.

1. Introduction

Left-handed materials (LHMs) or double negative materials (DNMs) are predicted by Veselago [1]. He predicted that reversals of a number of fundamental electromagnetic phenomena would occur as a consequence of the change of sign in the refractive index. He also shows that the imaginary part of the permittivity and permeability are not zero. This implies that transmission loss exists in any MTMs. Theoretical study of the loss is a difficult problem which lead to a confusion result that MTMs are not transparent [2]. Experiments approved that the loss in the MTMs is as low as in the conventional materials [3]. However, the presence of dissipation cannot be ignored. It is also found that MTMs play an important role in improving the characteristics of optical isolator [4] and sensors [5].

Surface waves at the interface between MTMs and dielectric media vary in their propagation behaviors from those at the interface between two unlike conventional dielectric media. Electromagnetic Surface Waves of a Ferrite Slab Bounded by MTMs presented a new set of behavior [6]. Nonlinear waveguide devices, on the other hand, have been extensively investigated, *i. e.*, [7]. Most work is interested in Kerr like nonlinear materials with the refractive index proportional with the intensity of the fields [8]. A more general case is the permittivity of the media arbitrary depends on the intensity of the field, I^{β}, where β is an arbitrary number [9].

2. Schematic of the model

The proposed asymmetric slab waveguide is illustrated in Fig. 1. It consists of three layers. The film made of MTMs having width d bounded by a nonlinear cladding with an arbitrary nonlinearity and a linear substrate.

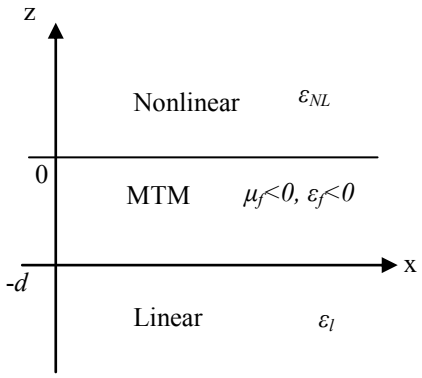

Figure 1: Asymmetric waveguide consists of MTM film surrounded by Nonlinear cladding and Linear substrate.

The MTMs film has negative permittivity ε_f and negative permeability μ_f. Both ε_f and μ_f are function of the frequency (ω) as follows:

$$\varepsilon_f = 1 - \frac{1}{\Omega^2 + j\,\Omega\Gamma} \tag{1}$$

$$\mu_f = 1 - \frac{F\Omega^2}{\Omega^2 - \Omega_r^2 + + j\Omega\Gamma} \tag{2}$$

where $\Omega = \omega/\omega_p$, $\Omega_r = \omega_r/\omega_p$ and $\Gamma=\gamma/\omega_p$, ω_r is the resonance frequency, ω_p is the plasma frequency and γ is the damping factor. The values of the parameters Ω_r and F are chosen to fit the experimental data [10] : $\Omega_r = 0.4$ and $F = 0.56$.

The permittivity for the nonlinear cladding is defined as

$$\varepsilon_{NL}(E) = \varepsilon + \alpha \left|E\right|^{\beta} \tag{3}$$

where ε is the linear part of the response, α is a nonlinear susceptibility, and β is the nonlinearity power. The linear substrate is dielectric with linear positive ε_l and μ_l.

3. Fields and dispersion equation

In this study, we only considered transverse Magnetic fields (TM). The TM fields are assumed to have the following forms:

$$\vec{E}\left(r,t\right)=\frac{1}{2}\left(jE_x\,x+E_z\,z\right)e^{j\left(kx-\omega t\right)}, \qquad (4)$$

$$\vec{H}=H_y\;e^{j\left(kx-\omega t\right)}y, \qquad (5)$$

where $k=n_{eff}\,k_0$ is the x component of the wave vector, n_{eff} is the effective refractive index and k_0 is the wave number in free space. For the nonlinear material, we consider the general D-E relation

$$\vec{D}=\varepsilon_{NL}\left(E\right)\vec{E} \qquad (6)$$

Applying the fields as defined in equation (4) and equation (5) into Maxwell's and applying the boundary conditions, the dispersion relation can easily be expressed as follows

$$\left(\frac{\omega\varepsilon_{NL}\varepsilon_f}{c}\right)^2\mu_f Q^2-2\varepsilon_{NL}\varepsilon_f^2k^2Q^2+\left(\varepsilon+\frac{2}{\beta+2}\alpha E_0^{\beta}\right)\left(q_f^2\varepsilon_{NL}^2P^2+k^2\varepsilon_f^2Q^2\right)=0. \qquad (7)$$

where $Q=q_f\,\varepsilon_l+q_l\varepsilon_f\,\tanh\left(q_f d\right)$, $q_f^2=k^2-\frac{\omega^2}{c^2}\mu_f\,\varepsilon_f$,

$P=q_l\varepsilon_f+q_f\,\varepsilon_l\,\tanh\left(q_f d\right)$, $q_l^2=k^2-\frac{\omega^2}{c^2}\varepsilon_l$ .The dispersion relation (equation (7)) relates the transverse wave numbers for each media. It is an implicit equation that gives the surface Plasmon dispersion relation. The field strength E_0 at the film and nonlinear dielectric interface appears and it can alter the dispersion equation. In this work, we study the special case where $q_f d\to\infty$. In this case, $Q=P=q_f\,\varepsilon_l+q_l\varepsilon_f$ and equation (7) becomes

$$\left[\left(\frac{\omega\varepsilon_{NL}\varepsilon_f}{c}\right)^2\mu_f-2\varepsilon_{NL}\varepsilon_f^2k^2+\left(\varepsilon+\frac{2}{\beta+2}\alpha E_0^{\beta}\right)\left(q_f^2\varepsilon_{NL}^2+k^2\varepsilon_f^2\right)\right]P^2=0. \qquad (8)$$

Setting P^2=0 recovers the standard surface Plasmon modes at LH/linear dielectric interface. While equating first term to zero produce surface Plasmon dispersion at LH/nonlinear dielectric regions,

$$\omega_{sp}=ck\left\{\frac{2\varepsilon_{NL}^3+\beta\varepsilon\varepsilon_{NL}^2-\left(\beta+2\right)\varepsilon_f^2\varepsilon_{NL}-\beta\varepsilon_f^2\alpha E_0^{\beta}}{\varepsilon_f\,\varepsilon_{NL}^2\left[2\alpha E_0^{\beta}+\left(\beta+2\right)\left(\varepsilon-\varepsilon_f\right)\right]}\right\}^{1/2} \qquad (9)$$

4. Numerical Calculations and Discussion

The surface Plasmon dispersion equation (9) is solved numerically. The surface-plasmon frequency Ω_{sp}, ω_{sp}/ω_p, as a function αE_0^{β} is solved numerically for different set of nonlinearity β while keeping the damping frequency Γ fixed. In the calculations, we take ω_p = 1.36x10^{16}, ck/ω_p = 0.4, ε = 2.0 and α = 6.379x10^{-12} m^{2}V^{-2}. Fig. 2. illustrates the effects of different nonlinearity by showing Ω_{sp} as a function αE_0^{β} for different values of β at Γ = 0.01. The set of values of β are chosen to be β_1 =1.5, β_2= 2, β_3= 2.5 and β_4= 3.

We see that the SP frequency depends on the nonlinearity. It has different behaviors when $\alpha>0$, self-focusing, for $\alpha<0$, self-defocusing. Fig. 2.a. shows the real part of Ω_{sp}. It displays that when $\alpha>0$ the frequency decreases with αE_0^{β} monotonically. While for $\alpha<0$, the frequency exhibits a bierfringent behavior. It seems that Ω_{sp} has two values at the same value of αE_0^{β} . Considering the imaginary part, we get reasonable values only when $\alpha<0$ as in Fig. 2.b. In this case, we get bierfringent behavior except at the maximum value of $\left|\alpha\right|E_0^{\beta}$. We also notice a discontinuity occurs for β_3 and β_4 for both real and imaginary part at Ω_{sp} range from 0.548 to 0.552. These discontinuities correspond to the stopping bands where the SP signals cannot propagate.

The same calculation has performed with larger value of absorption, *e.g.* Γ = 0.025. The results exhibited in Fig. 3. The real part, Fig. 3.a. shows that frequency passes for the region $\alpha<0$. The bierfringent behavior moves to the smaller values of $\left|\alpha\right|$. The imaginary part, Fig. 3.b. also has the frequency in the region $\alpha<0$. The discontinuity appears in both real and imaginary parts for β_4 for Ω_{sp} ranges from 0.538 to 0.542. Thus as the absorption increases, the discontinuities appears only for high order of nonlinearity. In this case stopping band occurs only for β_4 with slightly smaller values of frequencies. In this case, we can see that the bierfringent behavior except at the maximum value of $\left|\alpha\right|E_0^{\beta}$.

At a larger value of absorption, Γ = 5, the real part shows that the dispersion equation has only solution for α < 0 with the appearance of strong bierfringent behavior as it appears in figure 4.a. Figure 4.b. shows that the solution of the imaginary part appears only when $\alpha<0$. We have not notice any bierfringent behavior in this region. This indicates that for stronger absorption the only solution occurs for defocusing with the appearance of bierfringent in the real part. It is also noticeable that the discontinuities disappear.

For comparison, we plot the dispersion relation when Γ = 0 in figure 5. The plot has two regions for $\alpha>0$ and $\alpha<0$ and the bierfringent behavior disappear as expected. Since the bierfringent behavior appears in the presence of the absorption. Moreover, the discontinuities appear as expected.

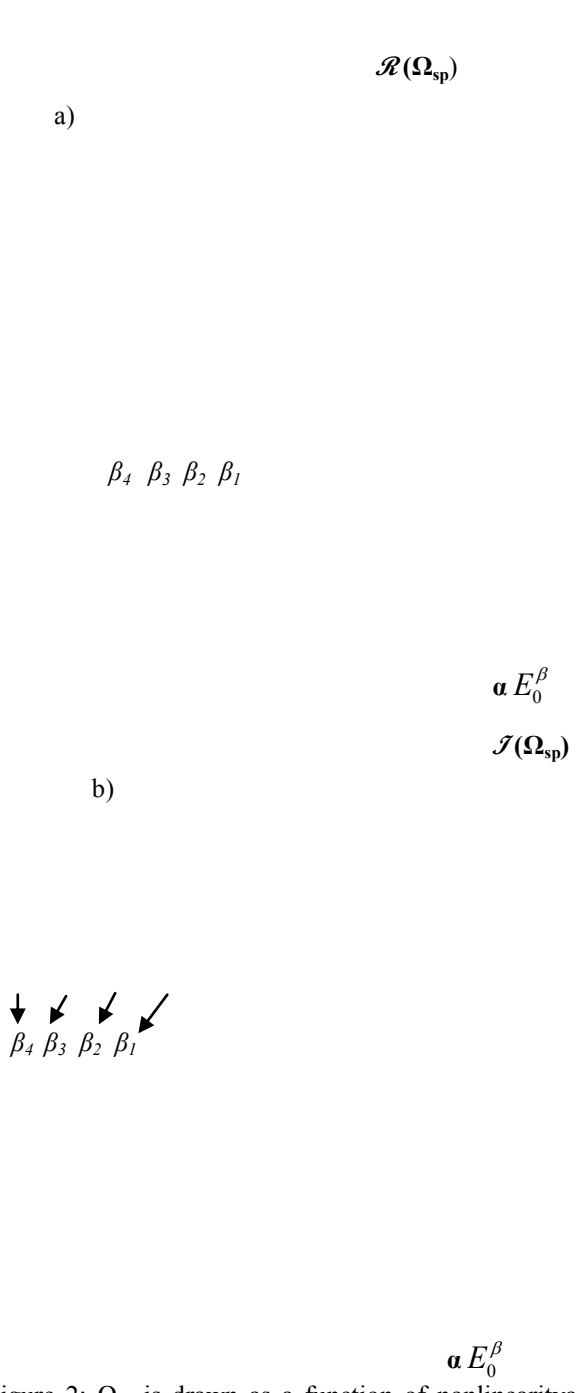

Figure 2: Ω_{sp} is drawn as a function of nonlinearityat Γ = 0.01. a) real part and b) imaginary part.

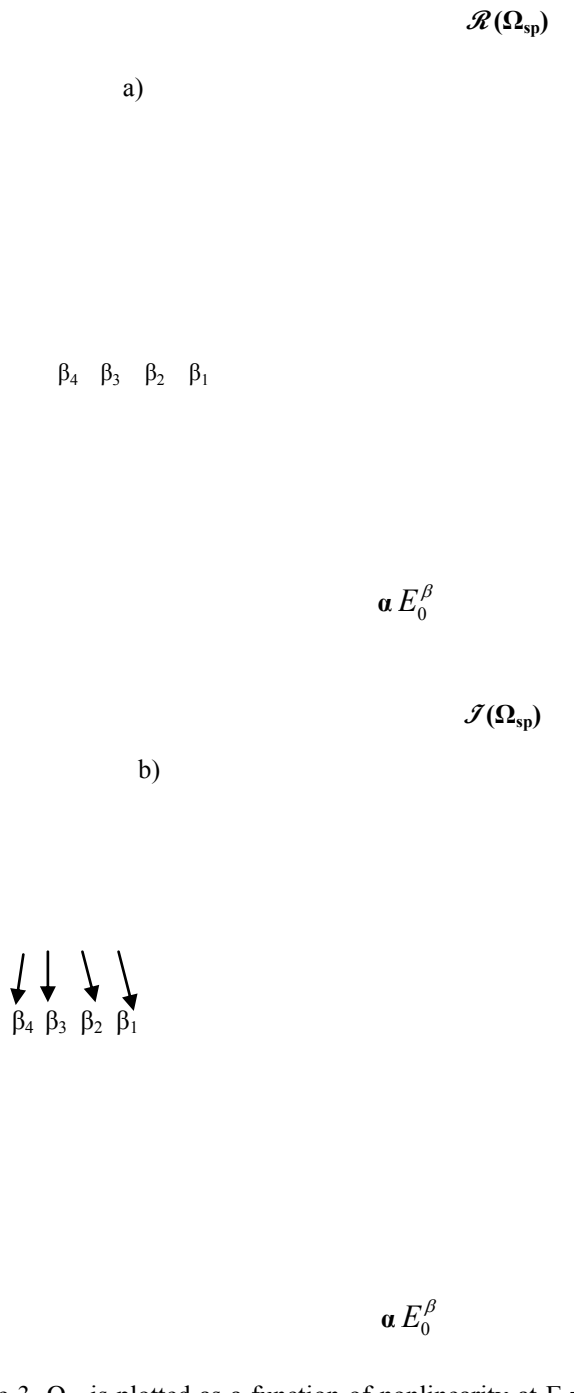

Figure 3. Ω_{sp} is plotted as a function of nonlinearity at Γ = 0.025. a) real part and b) imaginary part.

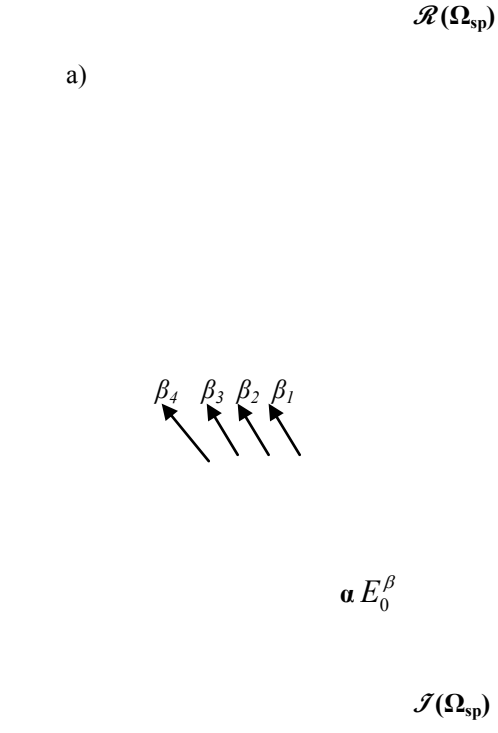

Figure 4. Ω_{sp} depends on the nonlinearity at $\Gamma = 5$. a) real part and b) imaginary part.

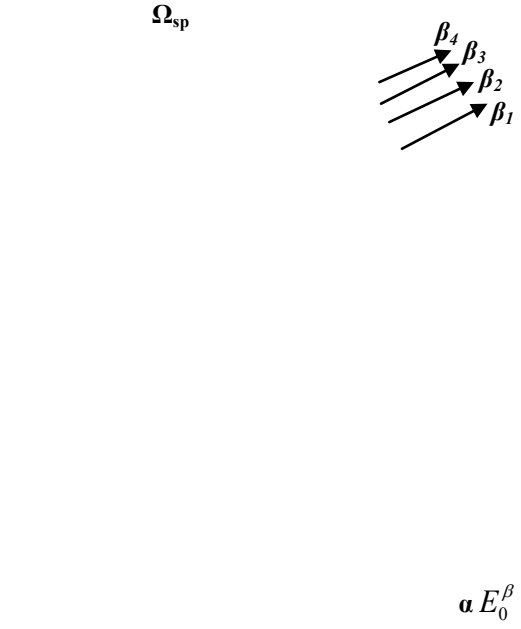

Figure 5. Ω_{sp} as a function of nonlinearity at $\Gamma = 0$.

5. Conclusion

The considered configuration is made of dielectric substrate, lossy MTMs film and nonlinear cover with arbitrary nonlinearity. The dispersion relation for the surface palsmoinc (SP) wave at the interfaces between metamaterials (MTMs) and the nonlinear substrate is recovered by taking certain limits. The dispersion equation is numerically solved. Results are presented by plotting the SP frequency as a function of the nonlinearity at chosen damping factors. Both the real and imaginary parts are plotted. Results also display the wave frequency as a function of propagation factor at different values of nonlinearity. For comparison, the imaginary part is set to zero and curves are reproduced. Results demonstrate that SP might have discontinuity at certain values of the power of nonlinearity. For example, when the loss Γ=0.01 discontinuity appears at β=2.5, 3. While when Γ=0.025, the discontinuity appears only when β=3.

References

[1] V. G. Veselago, The Electrodynamics Of Substances With Simultaneously Negative Values of ε and μ, *Soviet Physics USPEKHI*,vol. 10: 509-514, 1968.

[2] N. Garcia and M. Nieto-Vesperinas, Is there an experimental verification of a negative index of refraction yet? *Optics Letter*, vol. 27: 885-887, 2002.

[3] C.G. Parazzoli, R. B. Gregor, K. Li, B. E. C. Koltenbah, M. H. Tanielian, Experimental verification and simulation of negative index of refraction using Snell's law, 2002 preprint.

[4] R. J. El-Khozondar, H. J. El-Khozondar, and M. M. Shabat, Applications of Metamaterials in Optical Waveguide Isolator, *Journal of Al-Aqsa University series of natural science*12:35-50, 2008.

[5] H. J. El-Khozondar, S. A. Taya, M. M. Shabat, E. M. Mehjez, Optical Waveguide Sensors Using Double Negativity Guiding Layer, *Materials*, vol. 3, 2010.

[6] H. J. El-Khozondar, Z. Al-Sahhar, M. Shabat, Electromagnetic surface waves of a ferrite slab bounded by metamaterials, *AEU* 64:1063–1067, 2010.

[7] A. Sukhorukov, Y. S. Kivshar, H. S. Eisenberg, and Y.Silberberg, Spatial optical solitons in waveguide arrays, *IEEE J. Quantum Electronics* 39: 31-50, 2003.

[8] G. I. Segeman, C.T. Seaton, Nonlinear integrated optics, *J. Appl. Physics* 58: R57-R78, 1985.

[9] Yin, H., Xu, C., Hui, P. M., "Exact surface plasmon dispersion relations in a linear-metal-nonlinear dielectric structure of arbitrary nonlinearity", *Applied Physics Letters* 94: 221102-1-3, 2009.

[10] D. R. Smith, W. J. Padilla, D. C. Vier, S. C. Nemat-Nasser, and S. Schultz, Composite Medium with Simultaneously Negative Permeability and Permittivity, *Physical Review Letters* 84: 4184-4187, 2000.

[11] D. R. Smith, Willie J. Padilla, D. C. Vier, S. C. Nemat-Nasser, and S. Schultz, Composite Medium with Simultaneously Negative Permeability and Permittivity, *Phys. Rev. Lett.* 84: 4184-4187, 2000.

Surface waves at the interface between tunable LC-MTMs and Nonlinear media

Hala J. El-Khozondar[1], Rifa J. El-Khozondar[2], Said Zouhdi[3]

[1]Department of Electrical Engineering, IUG, P. O. Box 108, Gaza, Palestine.
[2]Physics Department, Al-Aqsa University, P.O. box 4051, Gaza, Palestine
[3]Laboratorie do Génie Electrique de Paris, Université Paris Sud 11, France
*corresponding author: hkhozondar@iugaza.edu

Abstract

The surface waves propagation at the interface between tunable metamaterials (MTMs) and Nonlinear media is investigated. Tunable MTMs has refractive index which can be tuned to negative-zero-positive values. Nonlinear materials are assumed to have Kerr-like refractive index. The dispersion equation is analytically derived and solved numerically. Results display the different behavior of the propagating waves as the refractive index is tuned.

1. Introduction

Materials exhibiting negative permittivity and permeability are a popular topic of current research due to their recent physical realization as metamaterials [1]. Recent research has focused both on the behavior of these metamaterials as well as on the incorporation of negative permittivity and permeability into electromagnetic theory [2]. Veselago [3] predicted theoretically several extraordinary electromagnetic phenomena of MTMs; *i.e.*, a reversed Doppler effect, reversed Čerenkov radiation, and a negative index of refraction. To date, the range of imaginable applications extends to important applications in communications; *e.g*., antenna design, vehicle coatings for altering radar cross section properties, and lenses [4]. Moreover, tremendous interest has been given to MTMs because of their important applications in sensors [5]and isolators[6-7].

Most recent work has been done by Werner *et al.* to show that it is possible to create tunable MTMs at near infrared waves having index varies from negative through zero to positive using Liquid crystals (LC) [8]. We will refer to this structure as tunable LC-MTMs.

The propagation of light in media characterized by intensity dependent refractive index, nonlinear media, was a subject of investigation in nonlinear optics. Nonlinear materials with dielectric constant depend on the intensity of the field have been suggested for several applications; *e.g.* [9-10]. In this work, the proposed structure consists of two media, one is the tunable LC-MTMs and the other is the nonlinear media.

The focus of section 2 is on the proposed structure. The theory of the problem will be covered in section 3. Results and discussion are presented in section 4. The conclusion is given is section 5.

2. Model representation

The proposed structure consists of two layers plane waveguide as in Figure 1. The substrate consists of tunable LC-MTMs and the cladding is nonlinear media as shown in Fig. 1.

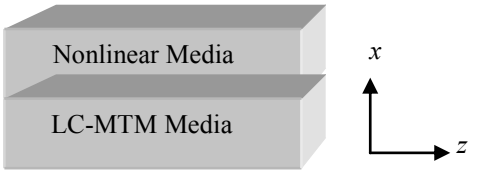

Figure 1. Proposed two layers waveguide structure

We here consider LC-MTMs with complex permittivity ε_{MTM} and complex permeability μ_{MTM} which can be tuned by changing the permittivity of the LC, ε_{LC} [11]. The nonlinear layer has a nonlinear index of refraction given by $n_{NL}= n_c+\alpha |E_y|^2$, where n_c is the linear part of the refractive index, α is the nonlinear coefficient, E_y is the only nonzero component of the electric field.

3. The fields and field equations

We consider only s-polarized waves propagating in the *z*-direction. Thus, the fields can be written as follows

$$\vec{E} = \left(0, E_y, 0\right) e^{-j\beta z} e^{j\omega t} \tag{1}$$

$$\vec{H} = \left(H_x, 0, H_y\right) e^{-j\beta z} e^{j\omega t} \tag{2}$$

where β is the propagation constant, ω is the wave frequency, $\beta= n_{eff} k_0$, n_{eff} is the effective refractive index,$k_0 =\omega/c$ and c is the speed of light.

Applying the fields in equations (1) and (2) into Maxwell's equations we obtain the fields in each region as follows

For $x \geq 0$,

$$E_y = \frac{q}{\sqrt{\Lambda}} \sec h\left(q(x+x_0)\right) \tag{3}$$

where $q = k_0\sqrt{n_{eff}^2 - n_{MTM}^2}$ and $\Lambda = \frac{k_0^2}{2}\alpha$.

For $x \le 0$,

$$E_y = Ae^{-px} \tag{4}$$

where $p = k_0\sqrt{n_{eff}^2 - n_{LC}^2}$.

Solving the boundary condition problem will result in the dispersion equation

$$\frac{\alpha E_y^2}{2} = \frac{1}{k_0^2}\left(q^2 - \frac{\mu_{MTM}^2}{\mu_{NL}^2}\frac{q^4}{p^2}\right), \tag{5}$$

where $\alpha E_y^2 / 2$ is called nonlinearity parameter.

Equation (5) contains explicitly the refractive index for each media and explains the behavior of the propagated wave at the interface between the two media in terms of refractive indices.

4. Results and Discussion

The dispersion equation (5) is solved numerically. Table 1lists the values of MTM parameters, n_{MTM} and μ_{MTM} for λ=1.4μm at different ε_{LC} [8]. For nonlinear media, n_c=1 and μ_{Nl}=1.

Table 1: MTM-Parameters for different values of ε_{LC}.

ε_{LC}	n_{MTM}	μ_{MTM}
2	-1+j0.9	4+j6
2.5	0.05+j0.3	-5+j4
2.6	0.15+0.6	-4+j4

The plot of the effective refractive index as a function of the nonlinear term $\alpha E_y^2 / 2$ at different values of the ε_{LC} is displayed in Fig. 2. We see that the behavior of the propagating wave changes with changing the nonlinear term.

Fig. 2 (a) shows that the real part of the n_{eff} changes monotonically with the nonlinearity term. It also shows that the real part of the n_{eff} varies as the value of ε_{LC} changes. For the same range of nonlinear term, the allowed range for the propagating waves extends as ε_{LC} increases.

Fig. 2 (b) shows that the imaginary part of n_{eff} varies as the nonlinear term changes. Moreover, as ε_{LC} increase the imaginary part of n_{eff} goes from negative to positive.

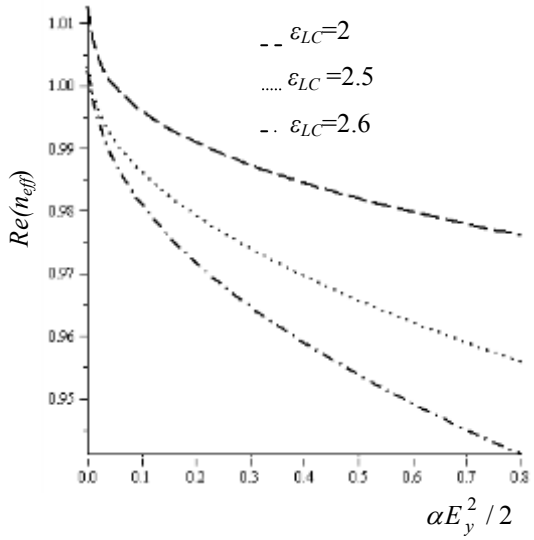

Figure 2. a) the real part of n_{eff} as function of the nonlinearity parameters. b) the imaginary part of n_{eff} as function of the nonlinearity parameters

5. Conclusions

In conclusion, we see that surface wave propagating at the boundary between LC-MTMs and Nonlinear Media can assume different behavior as LC-MTMs refractive index has different values. This indicates that this structure is promising for wide range of application.

Acknowledgements

This work is supported by Al-Maqdisi program for higher education and research, the fifth French-Palestinian grant.

References

[1] D. R. Smith, W. J. Padilla, D. C. Vier, D. C. Nemal-Nasser, and S. Schultz, Composite medium with simultaneously negative permeability and permittivity, *Phys. Rev. Lett*. 84:4184-4187, 2000.

[2] J. A. Kong, Electromagnetic wave interaction with stratified negative isotropic media, *J. Electromagnetic Waves and Applications* 15:1319-1320, 2001.

[3] V. G. Veselago, The electrodynamics of substances with simultaneously negative values of ε and μ, *Soviet Physics* 10: 509–514, 1968.

[4] J. B. Pendry, Negative refraction makes a perfect lens, *Phys. Rev. Lett*. 85: 3966-3969, 2000.

[5] H. J. El-Khozondar, S. A. Taya, M. M. Shabat, E. M. Mehjez, Lossy Double Negative Guiding Layer Optical Sensors, *Opto-electronics Review* 19: 277-281, 2011.

[6] H. J. El-Khozondar, R. J. El-Khozondar, M. Shabat, A. Koch, Coupling Efficiency of Metamaterial Magnetooptical Integrated Isolator, *Proceedings OPTO 2009 &I RS*^{2} 2009: 65-70, 2009.

[7] R. J. El-Khozondar, H. J. El-Khozondar, M. Shabat, Applications of Metamaterials in Optical Waveguide Isolator, *Journal of Al-Aqsa University series of natural science* 12: 35-50, 2008.

[8] D. H. Werner, D.-H Kwon, I.-C. Khoo, A. V. Kildishev, V. M. Shalaev, Liquid crystal clad near-infrared metamaterials with tunable negative-zero positive refractive indices, *Optics Express* 15: 3342-3347, 2011.

[9] H. J. El-Khozondar, Hydrostatic Stress Effect on the Optical Performance and the Stress Sensitivity of Optical Nonlinear Waveguide, *An - Najah Univ. J. Res. (N. Sc.)* 22: 1-16, 2008.

[10] H. J. El-Khozondar, R. J. El-Khozondar, Temperature sensitivity enhancement of nonlinear optical channel waveguide sensors using thermal-stress effect, *Islamic university journal for natural science and Engineering* 16: 15-27, 2008.

Visible negative refraction in natural indefinite medium: MgB_2

Jingbo Sun[1], Bo Li[2], Ji Zhou[1,*]

[1]State Kay Lab of New Ceramics and Fine Processing, Department of Materials Science and Engineering, Tsinghua University, Beijing China
[2] Research Institute for Advanced Materials, Graduate School at Shenzhen, Tsinghua University, Shenzhen China
*corresponding author, E-mail: zhouji@mail.tsinghua.edu.cn

Abstract

In this work, we report an intrinsic indefinite permittivity in crystalline MgB_2 that exhibits a negative group refraction for the blue-purple light. Based on the ellipsometry data of a crystalline MgB_2 sample, the equifrequency contour (EFC) is mapped and verified to be hyperbolic which enables a negative refraction for all incident angles. The indefinite dielectric tensor is attributed to the two Drude dispersions with different plasma frequencies between two crystal directions, which originates from the strong anisotropic crystal structure. Numerical simulations are also performed to demonstrate the negative refraction behaviour and the focusing property as a hyperlens. It is, for the first time, demonstrated that an all-angle negative refraction is able to occur in natural materials at visible frequency range.

1. Introduction

The concept of negative refraction has caused an excitement in physic community because of its unique property and the significant application as a perfect lens. Up to now, almost all present methods to realize the negative refraction were established by metamaterial, such as left-handed materials[1-3], photonic crystals[4, 5], chiral media[6], and artificially indefinite media[7, 8], which require a fine fabrication technology. For the optical region, however, the fabrication of these artificial media is really challenging[2,3, 7-10]. By contrast, nature materials may provide a shortcut for obtaining the bulk optic negative index materials, avoiding the use of the artificial engineering. So far, negative refractions in nature materials are mainly from single crystals with anisotropic permittivity, for example, infrared negative refraction in Al_2O_3[11] and ultra-violet (UV) negative refraction in graphite[12]. For visible frequency, the negative refraction can just be partially achieved from birefringence crystal[13-15], which has a strict limit to the incident angles.

MgB_2, famous for its high transition temperature (T_c=39K), is a rising star among the superconductors, which starts the research on high temperature superconductors[16-19]. In contrast to a lengthy siege of the doped MgB_2 to further improve the performances as a superconductor[20, 21]; few attentions have been paid to its strong anisotropic optical property brought by the graphitelike structure[22]. Fortunately, this illuminates our study on the negative refraction in natural indefinite media, which encourages us to investigate the optical refraction in high temperature superconductors with layered structure. In this letter, we reveal, for the first time, an all-angle broadband visible negative refraction in the natural indefinite medium: MgB_2. Its intrinsic indefinite dielectric property arises from two Drude dispersions at two crystal orientations with different plasma frequencies. This work also paves a new way for the study of the negative refraction material in nature.

2. Indefinite dielectric property in MgB_2

The analogy for MgB_2, structurally, electronically, can be addressed through the investigation of graphite, which exhibits a negative refraction in the UV region. The crystal structure of MgB_2 may be regarded as that of a graphite intercalation compound (GIC) with carbon replaced by boron (its neighbor in the Periodic Table) [23]. And the Mg atoms are completely intercalated in the graphitelike boron planes. The anisotropic dielectric properties are determined by two distinct types of electronic bands: the strongly covalent two dimensional (2D) σ bands derived from the hybridized sp_xp_y B orbitals and the 3D π bands made of p_z orbitals[16, 18, 22-24]. Different from graphite where the σ-bonding states are completely filled, providing a strong covalent bonding, the in-plane σ bands of MgB_2 retain their 2D covalent character, but exhibit metallic hole-type conductivity[23]. The coexistence of the 2D metallic-type covalent band in-plane and the 3D interlayer conducting bands is a peculiar feature of MgB_2, both of which can be approximately described by Drude model[22].

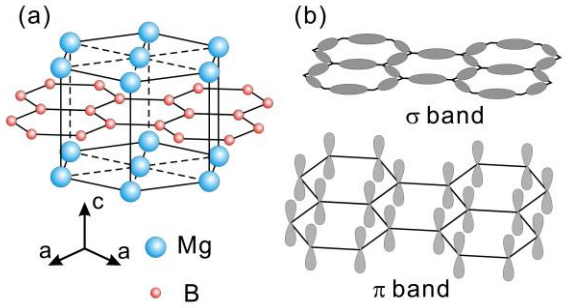

Figure 1: Crystal structure of MgB_2 and electronic states at the Fermi level. (a) The structure of MgB_2 contains graphitelike layers of B, which are intercalated by hexagonal close-packed layers of Mg. (b) σ-bonding states at the Fermi level formed by the hybridized sp_xp_y B orbitals and (c) π bands made of p_z B orbitals.

Previous studies present the anisotropic optical dielectric spectra of MgB_2 between 100 THz and 900 THz at room temperature, obtained on single crystals by spectroscopic ellipsometry measurements[19], as shown in Fig 2. Qualitatively, both the in-plane and the *c*-axis spectra exhibit a similar metallic behavior, characterized by the Drude model. However, one can see a strong anisotropy. There is a broad plasma edge of the red cure at about 490 THz, where the dielectric function $\varepsilon_{1,a}$ almost reaches zero. However, it then varies nonmonotonically while remaining negative at least up to 900 THz. On the contrary, the *c*-axis plasma edge is significantly sharper and is higher in frequency by about 130 THz. Correspondingly, $\varepsilon_{1,c}$ behaves monotonically and crosses zero at $\omega_{p,c}$ (627 THz). For the frequency range above 627 THz, the MgB_2 crystal is an indefinite media with $\varepsilon_c>0$ and $\varepsilon_a<0$, which may exhibit a negative refraction for blue or purple light with certain polarization.

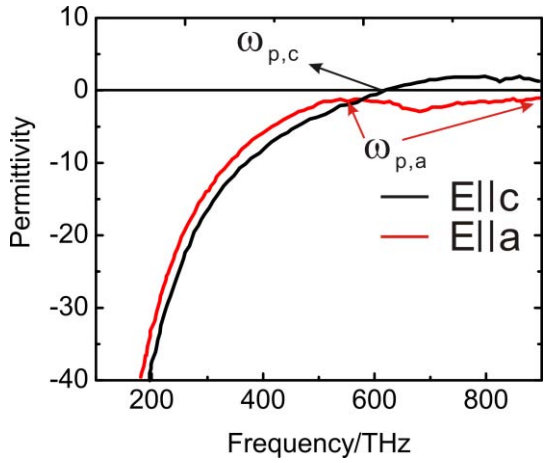

Figure 2: Optical anisotropic spectra at 300K obtained by the ellipsometry on a monocrystalline MgB_2 sample with dimensions (a×b×c) of 0.7×0.5×0.27 mm^3. The sample is kept in the flow of dry nitrogen in order to avoiding the deterioration caused by the air moisture. The *a*-axis and the *c*-axis spectra are shown by the red and black lines, respectively[19].

3. Negative refraction in MgB_2

3.1. Theory

The refraction property of MgB_2 can be analyzed by its ellipsoid of wave normals. For an incident ray of certain frequency with a linear polarization, the 3D-ellipsoid of wave normals degenerates into a 2D-equifrequency contour (EFC) in the E-plane. Usually, a single crystal with anisotropic permittivity can be described by a dielectric tensor below:

$$\tilde{\varepsilon} = \varepsilon_0 \begin{pmatrix} \varepsilon_{xx} & 0 & 0 \\ 0 & \varepsilon_{yy} & 0 \\ 0 & 0 & \varepsilon_{zz} \end{pmatrix},$$

Considering a TM (H field polarised along y-axis) electromagnetic wave with its wave vector *k* lying in the x-z plane incident on the crystal at an angle of θ_i, the general format of E field and H field of the TM wave can be written as:

$$\vec{E}(r) = E_0 e^{j(\vec{k}\bullet\vec{r}-wt)}, \qquad \vec{H}(r) = H_0 e^{j(\vec{k}\bullet\vec{r}-wt)}$$

According to Maxwell's equations,

$$\nabla\times\vec{E} = -\frac{\partial\vec{B}}{\partial t}, \quad \nabla\times\vec{H} = \frac{\partial\vec{D}}{\partial t},$$

we can write:

$$\vec{E}_0 = \frac{1}{\omega\varepsilon_0}\begin{pmatrix} \frac{k_z H_0}{\varepsilon_{xx}} & 0 & \frac{-k_x H_0}{\varepsilon_{zz}} \end{pmatrix}.$$

For TM wave, the H field is

$$\vec{H}_0 = \begin{pmatrix} 0 & H_0 & 0 \end{pmatrix}$$

Then, we can write down the Poynting vector as

$$\vec{S} = \frac{1}{2}\frac{1}{\omega\varepsilon_0}\begin{pmatrix} \frac{k_x {H^2}_0}{\varepsilon_{zz}} & 0 & \frac{k_z {H^2}_0}{\varepsilon_{xx}} \end{pmatrix} \qquad (9)$$

As a result, the refraction angle for the Poynting vector S_r can be determined by

$$\frac{S_x}{S_z} = \frac{\varepsilon_{xx} k_x}{k_z \varepsilon_{zz}}. \qquad (11)$$

Working from the Maxwell's equations, we can summarize the dispersion relationship as:

$$\frac{{k_x}^2}{\varepsilon_{zz}} + \frac{{k_z}^2}{\varepsilon_{xx}} = \frac{\omega^2}{c^2}.$$

Then, we can find

$$-\left(\frac{dk_x}{dk_z}\right)^{-1} = \frac{S_x}{S_z}. \qquad (12)$$

Based on this result, we derive that the Poynting vector S_r is parallel to the normal of the EFC, and the refraction property is determined by the monotonicity of the EFC. A monotone decreasing EFC of the isotropic media (Fig. 3 (a)) forms a positive refraction. Conversely, a monotone increasing EFC may result in a negative refraction of Poynting vector, like the hyperbolic EFC of the indefinite medium (Fig. 3 (b)). Moreover, the quadratic function type of equation decides that the EFC is monofonic at each quadrant, which means we can determine the monotonicity of the EFC by either part on it in mathematics.

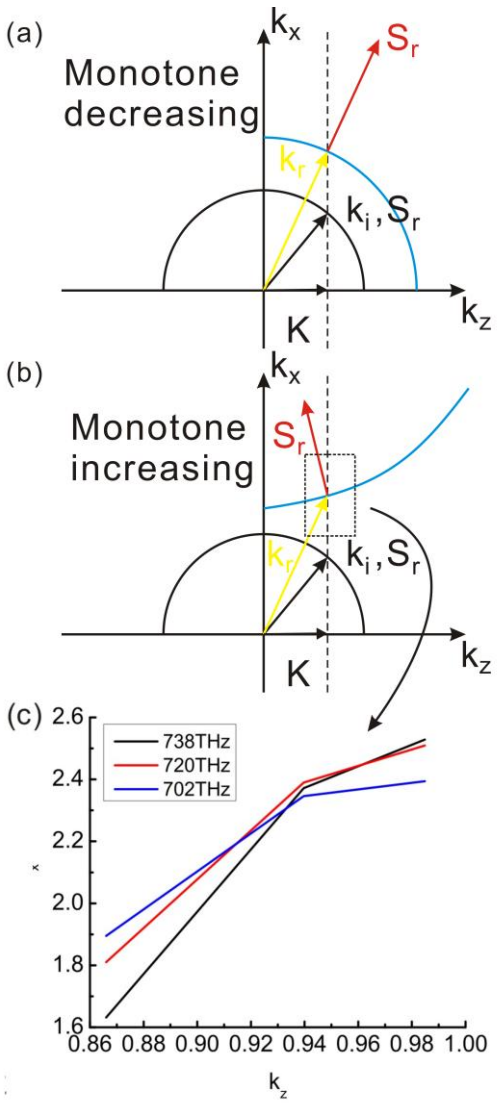

Figure 3: Schematic illustration of the relation between the refraction property and the monotonicity of the EFC. A TM wave with k_i along x-z plane is incident from air (circular black EFC) to a medium (blue EFC). The boundary condition requires that the components of the wave vectors (k_i & k_r) parallel to the interface **K** are equal in both media. Thus, the refracted wave vector k_r and Poynting vector S_r is determined by Maxwell's equations and the S_r is along the direction of the normal of EFC. (a) The EFC of an isotropic media is a circle which is monotone decreasing in the corresponding quadrant, resulting in a positive refraction. (b) The EFC of an indefinite medium is a hyperbola which is monotone increasing in the corresponding quadrant, resulting in a negative refraction. (c) The EFC of MgB_2 at three frequency points 738THz, 720THz and 702THz, mapped by the ellipsometry data in Ref. 19.

3.2. Ellipsometry results

Here we use ellipsometry to explore the monotonicity of the EFC. The EFC can be measured and mapped based on the ellipsometry measurement of $\rho(\theta_i)=\tan(\Psi)\cdot\exp(i\Delta)$ which displays the reflectance ratio of two polarization (r_p/r_s) under different incident angles. Ref. 19 supplies the raw data (Ψ & Δ) of the ellipsometer for incident angles of 60°, 70° and 80° at the range of 150THz ~ 900THz. According to Fig. 2, MgB_2 is an indefinite material above 627THz. Therefore, we can use three sets of data at 738THz, 720THz and 702THz to map the three EFCs of MgB_2 under the orientation shown in Fig. 4(a) at each frequency. According to the Fresnel reflection theory, the raw data obtained from the ellipsometer (r_p/r_s vs θ_i) can be transformed into the EFC curve of (k_x vs k_z)[12] and the results are shown in Fig. 3(c). We find that each EFC in Fig. 3(c) is an increasing function with respect to k_z from sin (60°) to sin (80°), which means that the EFC of MgB_2 is monotone increasing. As a result, the MgB_2 exhibits the negative refraction behaviour for TM wave at all incident angles.

This result can also be verified by the analysis of the crystal optics. The MgB_2 is a uniaxial crystal whose dielectric tensor is characterized by two independent dielectric functions, including the ordinary dielectric function $\varepsilon_a(\lambda)$, which describes light polarized along the B-layer planes, and the extraordinary dielectric function $\varepsilon_c(\lambda)$, which describes light polarized perpendicular to the B-layer planes. The optic axis (*c*-axis) is perpendicular to the hexagonal B-layer. If the crystal is oriented as shown in Fig. 4(a), the optic axis parallel to both the sample surface and the plane of incidence, $\varepsilon_{xx}=\varepsilon_{yy}=\varepsilon_a$, $\varepsilon_z=\varepsilon_c$. The incident TM wave propagating along the x-axis is modulated by the anisotropic permittivity of the crystal. At the frequency range above 627THz, the dielectric tensor is indefinite: $\varepsilon_a<0$, $\varepsilon_c>0$. Therefore, the monotone increasing EFC of the MgB_2 is hyperbolic, as shown in Fig. 3(b, c), and the Poynting vector S_r is parallel to the normal of the EFC. Negative light refraction is achieved from this hyperbolic dispersion, even though the phase velocity remains positive.

4. Simulation results

The negative refraction behavior of the crystal is simulated by using Ansoft HFSS 11, commercial software based on the finite element theory. We numerically simulated the propagation of light in MgB_2, whose principle axis (*c*-axis) is along z direction (Fig. 4). A TM wave (magnetic field is polarized along the y-axis) at the frequency of 738THz is incident on the MgB_2 from two different sources. Perfect M boundary conditions are applied along the y-axis, and open boundaries are applied along the x- and z-axis. The distribution of the magnetic field is plotted in Fig. 4 (b) and (c). Fig. 4(b) shows a TM Gauss beam incident on the MgB_2 with an angle of 45°. There is a notable negative refraction at the interfaces, with a refraction angle of about 30°. Focus performance of the MgB_2 as a hyperlens is shown in Fig. 4(c). A TM wave from a cylindrical source (r= 300nm) is focused twice and forms an image at the other side of the MgB_2 lens. The width of the image is about 660nm which is almost equal to the diameter of the source. However, the image on the x direction is extruded because of the hyperbolic dispersion.

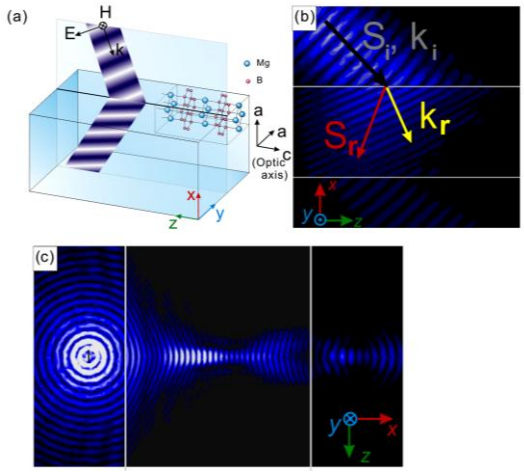

Figure 4: The orientation of the single crystalline MgB_2 when the negative refraction occurs and the simulation results of the negative refraction and focusing property at 738 THz (ε_{a1} = -2 and ε_{c1} = 2) of the sample by using HFSS. (a) The MgB_2 crystal is oriented as optic axis parallel to both the sample surface and the plane of incidence. A TM wave with H field polarized along y axis incident on the crystal may experience a negative refraction in it. (b) The refracted wave vector (yellow arrow) and Poynting vector (red arrow) is determined by Maxwell's theorem. The Poynting vector is negatively refracted, although the phase vector remains positive. (c) The focusing property of MgB_2 as a hyperlens.

5. Conclusions

In conclusion, we demonstrate that an all angle negative refraction at visible frequency can be realized by MgB_2, a naturally existed indefinite medium. This intrinsic indefinite permittivity is attributed to two Drude dispersions with different plasma frequencies between the directions perpendicular and parallel to the atomic plane in the MgB_2 structure. Moreover, an all angle negative refraction is verified through its hyperbolic equifrequency contour mapped by the reported data obtained in the ellipsometry measurement.

Since the frequency range between the two plasma frequencies ($\omega_{a,\,p}$-$\omega_{c,\,p}$) covers a relatively wide range from blue to purple, as shown in Fig. 2, the all-angle negative refraction can occur over quite a broad waveband. Based on the hyperbolic dispersion relation, monocrystalline MgB_2 can be valid for the evanescent modes, which preserve the information contained in the high spatial frequencies and are essential for super-resolution applications. As a homogenous material, it avoids severe wave scattering caused by the inner structures in those artificially engineered material. On the other hand, this intrinsic negative-index avoids complicated design and fine fabrication techniques. Hope that our work may be helpful for the further study of negative refraction in nature material and the potential applications in hyperlens and other devices based on natural indefinite media.

Acknowledgements

This work is supported by the National Science Foundation of China under Grant Nos. 90922025, 51032003, 50921061, and 10774087.

References

[1] C. M. Soukoulis, S. Linden, M. Wegener, Science 315: 47-49, 2007.
[2] G. Dolling, , M. Wegener, C. M. Soukoulis, S. Linden. Opt. Lett. 30: 53-55, 2005.
[3] V. M. Shalaev, Optical negative-index metamaterials. *Nat. Photon.* 1: 41-48, 2007.
[4] E. Cubukcu, K. Aydin, E. Ozbay, S. Foteinopoulou, C. M. Soukoulis, Nature 42: 604-605, 2003.
[5] A. Berrier, M. Mulot, M. Swillo, M. Qiu, L. Thylen, S. Anand, Phys. Rev. Lett. 93: 073902-073905, 2004.
[6] J. B. Pendry, Science 306: 1353-1355, 2004.
[7] A. J. Hoffman, L. Alekseyev, S. S. Howard, K. J. Franz, D. Wasserman, V. A. Podolskiy, E. E. Narimanov, D. Sivco and C. Gmachl, Nat. Mater. 6: 946-950, 2007.
[8] J. Yao, Z. Liu, Y. Liu, Y. Wang, C. Sun, G. Bartal, A. M. Stacy, X. Zhang, Science 321: 930, 2008.
[9] J. Valentine, S. Zhang, T. Zentgraf, E. Ulin-Avila, D. A. Genov, G. Bartal, X Zhang, Nature 455: 376-379, 2008.
[10] C. G. Meca, J. Hurtado, J. Marti, A. Martinez, Phys. Rev. Lett. 106: 067402-067405, 2011.
[11] R. Wang, J. Sun, J. Zhou, Appl. Phys. Lett. 97: 031912-031914, 2010.
[12] J. Sun, J. Zhou, B. Li, F. Kang, Appl. Phys. Lett. 98: 101901-101903, 2011.
[13] Y. Zhang, B. Fluegel, A. Mascarenhas, Phys. Rev. Lett. 91: 157404-157407, 2003.
[14] Kang L, Zhao Q, Li B, J. Zhou, H. Zhu, Appl. Phys. Lett. 90: 181931-181933, 2007.
[15] X. L. Chen, M. He, Y. X. Du, W. Y. Wang, D. F. Zhang, Phys. Rev. B. 72: 113111-113114, 2005.
[16] J. Nagamatsu, N. Nakagawa, T. Muranaka, Y. Zenitani, and J. Akimitsu, Nature 410: 63-64, 2001.
[17] D. G. Hinks, H. Claus, J. D. Jorgensen, Nature 411: 457-460, 2001.
[18] J. Kortus, I. I. Mazin, K. D. Belashchenko, V. P. Antropov, L. L. Boyer, Phys. Rev. Lett. 86: 4656-4659, 2001.
[19] C. Buzea, T. Yamashita, Supercond. Sci. Technol. 14: R115-R146, 2001.
[20] Yeoh, WK; Horvat, J; Kim, JH, et al. Appl. Phys. Lett. 90: 122502-122504, 2007.
[21] Shen, TM; Li, G; Cheng, CH, Y. Zhao. Supercond. Sci. Technol. 19: 1219-1224, 2006.
[22] V. Guritanu, A. B. Kuzmenko, D. Marel, S. M. Kazakov, N. D. Zhigadlo, J. Karpinski, Phys. Rew. B 73: 104509-104519, 2006.
[23] K. D. Belashchenko, M.Schilfgaarde, V. P. Antropov, Phys. Rew. B 64: 092503-092506, 2001.
[24] J. M. An, W. E. Pickett, Phys. Rew. Lett. 86: 4366-4369, 2001.
[25] P. Ravindran, P. Vajeeston, R. Vidya, A. Kjekshus, H. Fjellvag, Phys. Rew. B 64: 224509-224523, 2001.

[26] I. T. Belash, A. D. Bronnikov, O. V. Zharikov, and A. V. Pal'nichenko, Synth. Met. 36: 283-302, 1990.
[27] R. Ngarajan, C. Mazumdar, Z. Hossian, S. K. Dhar, K. V. Gopalakrishnan, L. C. Godart, B. D. Padalia and R Vijayraghavan, Phys. Rew. Lett. 72: 274-277, 1994.
[28] R. J. Cava, H. Takagi, H. W. Zandbergen, J. J. Krajewski, W. F. Peck Jr, T. Siegrist, B. Batlogg, R. B. van Dover, R. J. Felder, K. Mizuhashi, J. O. Lee, H. Eisaki, S. Uchida, Nature 367: 252-253, 1994.
[29] C. Mirri, L. Baldassarre, S. Lupi, M. Ortolani, R. Fittipaldi, A. Vecchione, P. Calvani, Phys. Rew. B 78: 155132-155137, 2008.
[30] J. K. Burdett, G. V. Kulkarni, Phys. Rew. B 40: 8908-8932, 1989.
[31] L. G. Johnson, & G. Dresselhaus, Phys. Rev. B. 7: 2275-2285, 1973.
[32] E. A. Taft, & H. R. Philipp, Phys. Rev. 138: A137-A202, 1964.
[33] Edward, D. P. *Handbook of Optical Constants of Solids II*, Academic Press, INC., 1991.

Light tunable megnetic metamaterials

P. V. Kapitanova[1], S. I. Maslovski[1,2], I. V. Shadrivov[1,3],
P. M. Voroshilov[1], D. S. Filonov[1], P. A. Belov[1,4], and Y. S. Kivshar[1,3]

[1]National Research University of Information Technologies, Mechanics and Optics, St. Petersburg 197101, Russia, kapitanova.poli@phoi.ifmo.ru
[2]Instituto de Telecomunicações, Universidade de Coimbra, Pólo II, 3030-290 Coimbra, Portugal
[3]Nonlinear Physics Centre, Research School of Physics and Engineering, Australian National University, Canberra ACT 0200, Australia
[4]Queen Mary University of London, Mile End Road, London E1 4NS, UK

Abstract— The paper present a new approach for designing electromagnetic metamaterials which can be tuned by light. The results of experimental study of magnetic resonance behavior of a tunable split-ring resonators loaded by a varactor diode and biased by a photodiode operated in photovoltaic mode are presented.

Past several years seen a tremendous increase of the interest in the study of tunable, nonlinear and active metamaterial structures. In particular, various efforts are being made to achieve tunability of the metamaterial properties, either externally [1] or by employing their nonlinear response [2]. At microwave frequencies, a split-ring resonator (SRR) loaded with a varactor diode can be considered as a tunable nonlinear meta-atom. The varactor diode can operate in either bias-free or biased regimes [3, 4], and subsequently create a bulk nonlinear metamaterial [5] allowing a power-induced control of the wave transmission and other intrigueing possibilities. The proposed biased regime allows significant tuning of the resonan however, is not practical for application in bulk structures, since the required circuitry becomes too cumbersome.

In this work we overcome this problem with a novel concept for creating light tunable metamaterials. We study experimentally SRRs with varactor diodes, which biasing is supplied by photodiodes operated in the photovoltaic mode, and demonstrate that SRR's magnetic resonance can be tuned by changing the intensity of an external light source. We employ coupled SRRs to demonstrate enhancement of the resonant response and switching between the bright and dark modes.

To study the tunability of such metamaterials with external light, first we consider a single light-tunable SRR. The schematic of the SRR structure is shown in Fig. 1(a). The SRR is printed on a dielectric FR4 substrate with $\varepsilon_r \approx 4.4$ and thickness of 1.5 mm. We use SRRs identical to those described in Ref. [3]. To achieve tunability we solder a Skyworks^{TM} SMV1233 varactor diode in additional gap in the outer ring of the SRR. The bias voltage for the varactor diode is produced by a BPW-34-S photodiode from Opto Semiconductors^{TM} that operates in the photovoltaic mode. Chip inductors connected in series with the photodiode are used to avoid shortening of the varactor

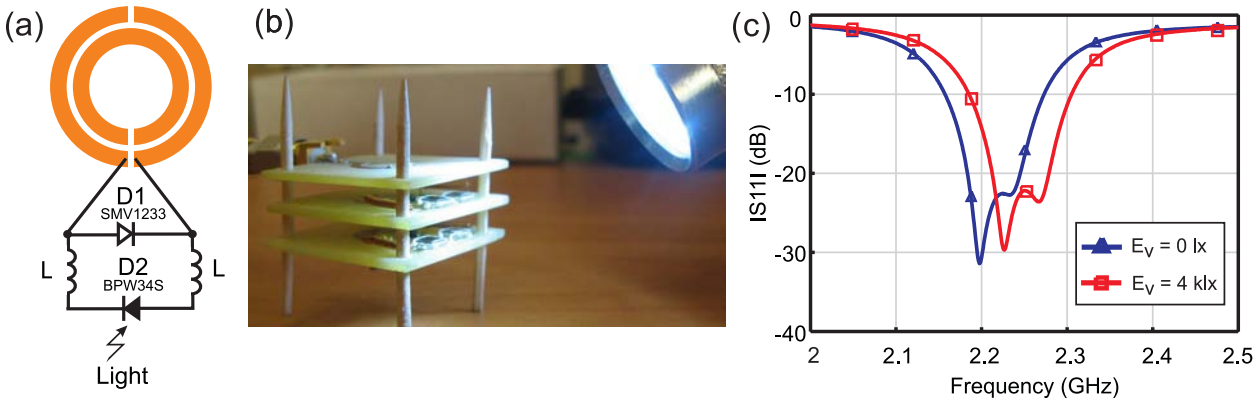

Figure 1: (a) Schematic of the light-tunable SRR. (b) Photograph of tunable SRRs (two lower boards) excited by a symmetric loop antenna (top board). (c) Switching between the dark and bright mode achieved by illuminating the photodiodes in the structure.

by the large parasitic capacitance of the photodiode. The inductors and photodiode are soldered to small metallic patches near the SRR that do not affect the magnetic resonance of the SRR.

As the voltage produced by the photodiode depends on the intensity of the incident light, the capacitance of the varactor changes with the light intensity. In turn, the resonant frequency of the SRR depends on the total loading capacitance in the entire resonator structure. The resonant frequency of the SRR becomes dependent on the intensity of the incident light. To measure the magnetic response of the fabricated particle we excite the SRR with an external magnetic field. We designed symmetric microstrip loop antenna for these measurements. The antenna was fixed 5 mm above the plane of the SRR and connected to the vector network analyzer. From the measurements of the reflection coefficient we observe a shift in the resonant frequency of the SRR from 2.276 GHz to 2.29 GHz when the light intensity illuminating the photodiode increases from 0 lx to 4 klx.

The sensitivity of the studied meta-atoms to the external light may be also increased using *a qualitatively different approach*. Instead of meta-atoms formed by single SRRs, one may consider structures composed of several coupled resonators. In the case of two coupled SRRs (we place the SRRs in parallel planes with their axes coinciding, see Fig. 1 (b)) there exist two normal modes, one has currents in both SRRs circulating in the same direction (even mode) and another mode with currents circulating in the opposite directions (odd mode). When such a pair is placed into a uniform external magnetic field, the even mode couples strongly to the external field, while the odd mode is not excited at all. Therefore, the even mode is called bright mode and it is associated with strong total magnetic moment, strong scattering, and a lower frequency; and the odd mode is called dark mode, and it has vanishing magnetic moment and scattering, as well as higher frequency. The splitting of the resonant frequencies of these modes is controlled by the strength of coupling that can be adjusted by changing the separation between the two interacting SRRs.

In our work we fine-tune the coupling and, respectively, the splitting of the resonant frequencies in the pair of SRRs without applied light so that it is equal to the shift in the resonant frequency of an isolated SRR when the intensity of light is changed. As a result, in such structure by changing the light intensity it becomes possible to switch between the bright and dark modes for the fixed frequency of the electromagnetic wave. Fig. 1 (c) demonstrates the light-induced switching between the bright and dark modes for the case when the SRRs are separated by $d = 8$ mm. When the illumination strength is changed from 0 lx to 4 klx, the resonant curve shifts to the right. As a result, if the external electromagnetic wave with the frequency around 2.23 GHz interacts with the dark mode when the photodiode is not illuminated by light, then by switching the light on, the properties of the coupled SRRs change so that the electromagnetic wave excites the bright mode. In other words, initially nonmagnetic meta-particle will acquire a significant magnetic response.

In conclusion, we have suggested and demonstrated experimentally a novel approach for tunability of meta-atoms, the key elements of electromagnetic metamaterials. We have fabricated split-ring resonators loaded with varactors, which are biased by photodiodes and demonstrated a shift of the magnetic resonance by an external light source. We have employed several approaches of collective SRR response to enhance this tunability. We believe this approach can be useful for creating bulk metamaterials which properties can be controlled by reconfigurable light sources.

The authors acknowledge a support from the Ministry of Education and Science of the Russian Federation, Dynasty Foundation (Russia), the Engineering and Physical Sciences Research Council (UK), and the Australian Research Council (Australia).

REFERENCES

1. W.J. Padilla, A.J. Taylor, C. Highstrete, M. Lee, and R.D. Averitt, Phys. Rev. Lett. **96**, 107401 (1996).
2. A.A. Zharov, I.V. Shadrivov, and Yu.S. Kivshar, Phys. Rev. Lett. **91**, 037401 (2003).
3. I.V. Shadrivov, S.K. Morrison, and Yu.S. Kivshar, Opt. Express **14**, 9344 (2006).
4. B. Wang, J. Zhou, T. Koschny, and C. M. Soukoulis, Opt. Express **16**, 16058 (2008).
5. I.V. Shadrivov, A.B. Kozyrev, D.W. Van Der Werde, and Yu.S. Kivshar, Opt. Express **16**, 20266 (2008).

Microwave scattered and absorbed powers by a multilayered zero-index anisotropic metamaterial-semiconductor cylinder

Liudmila Nickelson[1] and Juozas Bucinskas[2]

[1]State Research Institute Center for Physical Sciences and Technology, Vilnius, Lithuania
[2]Faculty of Physics, Vilnius University, Sauletekio 9, LT-10222, Vilnius, Lithuania
*corresponding author, E-mail: lucynickelson@gmail.com

Abstract

Abstract—We present here dependencies of scattered and absorbed powers of incident perpendicularly and parallel polarized microwaves by a multilayered cylinder. We consider here the normal (angle θ=90^0) and oblique (angles θ=60^0, 30^0, 5^0) incidence of microwave on the cylinder. The one consists of a glass core that is coated by the six anisotropic metamaterial and lossy *n*-Si semiconductor alternative layers. Here is presented characteristics of cylinder with the semiconductor external layer. The dispersion dependency of *n*-Si losses was taken into account. The metamaterial is a uniaxial anisotropic medium with the electric and magnetic plasma resonances in the frequency range from 1 till 4 GHz. The anisotropic metamaterial can include the constitutive parameters equal to zero. The multilayered cylinder has the external radius equal to 2 mm. The glass core has a radius equal to 0.5 mm. The thickness of all layers is the same. We have compared the scattered and absorbed power dependencies on the microwave polarization, the angle of microwave incidence (the normal and oblique directions of the incidence to the z-axis) and the *n*-Si specific resistivity. We discovered specific dependencies of scattered and absorbed powers on the parameters.

1. Introduction

The stream of articles devoted to the study of metamaterial scattering (reflecting) structures points that there is a need for development devices possessing unique characteristics. Many applications in modern technologies require the use of special materials with a strong electromagnetic (EM) response. The properties of special composite materials can be strikingly different from the properties of the constituent materials [1]. A composite material can be formed by compounding layers of two or more materials. The resulting composite material has more useful applications than the constituent materials alone. Advanced composite materials can achieve some novel superior properties, for example, electro-optic ones [2], excellent microwave absorption [3], ensure EM compatibility and immunity (insusceptibility) [4]. The multilayer shielding structures with both absorbing and reflecting composite layers are studied in [4].

The importance of diffraction problems for scattering structures made from special composites are based on their great practical utility for many applications, such as reflector antennas, the analysis of structures in the open space, electromagnetic defence of structures, high frequency telecommunications and invisibility cloaks technology [5-11]. The algorithm for exploring the scattering properties of single isotropic and bi-isotropic metamaterial cylinders is proposed in [5]. The enhanced resonant scattering and focusing properties were found in the last article. The full-wave EM scattering theory to study the scattering from infinitely long cylinders with cylindrically anisotropic coatings is given in [6].

The challenging new phenomena are usually discovered when composites contain metamaterials with very low, very large, or negative constitutive parameters. At the moment is an increased interest to the zero-index metamaterials. The metamaterials are attractive due to their unconventional constitutive parameters and different anomalous effects. Zero-index metamaterial may have the epsilon-near-zero (ENZ) or (and) mu-near-zero (MNZ) at some frequencies. Zero - index metamaterials are strongly dispersive media [7-11].

Here we give dependencies of total scattered and absorbed microwave powers of infinite multilayered glass-metamaterial-semiconductor cylinder on the frequency range. The metamaterial is qualified by the tensors of permittivity and permeability. The tensor's components are equal to zero at certain frequencies and the matter can be a zero-index metamaterial.

2. Problem formulation and parameters

In present article we demonstrate our calculation results that based on the rigorous electrodynamical solution of diffraction problem about the microwave scattering by an infinite multilayered cylinder. The solution of Maxwell's equations for the multilayer cylinder was carried out by the partial area method [12-14]. The central core of multilayered cylinder made of glass material. The glass core is coated by a sandwich semiconductor-metamaterial cover. The multilayered cylinder consists of seven concentric surfaces with radii R_j, j=1, 2,..., N (Fig. 1). The every j-th region is filled with a material having the permittivity ε_j and the permeability μ_j. Numbering of layers is going from outside layer to the inner one. Thus R_1 is the outside radius of the cylinder. In our calculations N = 7, i.e. the glass core with radius R_7 is coated with 6 layers of metamaterial and *n*-Si alternately. The radius of glass core is R_7=0.5 mm. The first layer that coated the glass core is a metamaterial layer. The thickness of every layer is equal to 0.25 mm and the

outer radius of the multilayered cylindrical structure is R_1=2 mm.

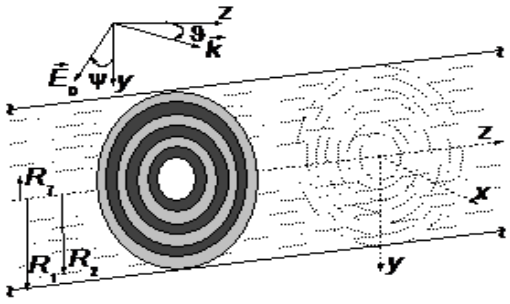

Figure 1: *N*-layered glass-anisotropic metamaterial-semiconductor cylinder model and designations.

As it is known, a semiconductor material with some relatively small specific resistivity is the dispersive lossy material. The imaginary part of semiconductor permittivity Im(ε_s) depends on the operating frequency f and the semiconductor material specific resistivity ρ. The n-Si permittivity ε_s is determined by the expression:

$$\varepsilon_s = 11.8 - \mathrm{i}/(\omega\varepsilon_0\rho), \qquad (1)$$

where $\omega = 2\pi f$ is an angular frequency of incident microwave, ε_0 is the electric constant. The semiconductor losses depend on the frequency and this fact strongly affects on the absorbed power into semiconductor layers. The glass and the n-Si permeabilities are equal to $\mu_g = \mu_s = 1$.
The incident plane harmonic monochromatic microwave

$$\boldsymbol{E}^{in} = \boldsymbol{E_0}\exp\left(\mathrm{i}(\omega t - \sqrt{\varepsilon\mu}\,\boldsymbol{kr})\right) \qquad (2)$$

propagates in the plane $x0z$ and the direction of microwave propagation describes by an angle θ between the z-axis and the wave vector $\boldsymbol{k}$ (Fig. 1). Here $\boldsymbol{E_0}$ is the amplitude of the electric field of an incident microwave. The vector $\boldsymbol{E_0}$ determines the polarization of the incident microwave. The direction of vector $\boldsymbol{E_0}$ defined by the angle ψ that is between the vector $\boldsymbol{E_0}$ and the y-axis. The EM wave has the parallel polarization when the angle ψ is equal to 90°. The EM wave has the perpendicular polarization when ψ is equal to 0°. The module of the amplitude of incident microwave $|\boldsymbol{E_0}|$=1. Here $(\boldsymbol{E_0}\ \boldsymbol{k})=\theta$, $(\boldsymbol{E_0}\ \boldsymbol{n_y}) = \cos\psi$, $\boldsymbol{k} = k_x\,\boldsymbol{n_x}+k_z\,\boldsymbol{n_z}$, where $\boldsymbol{n_x}$, $\boldsymbol{n_y}$, $\boldsymbol{n_z}$ are the unit vectors. The cylinder is placed in an air medium with the permittivity and the permeability $\varepsilon=\mu$=1. Boundary conditions on all surfaces separating different media are the standard ones. The equality of tangent components of the electric and magnetic fields on the glass- metamaterial, every metamaterial–semiconductor, as well as the semiconductor–air surfaces are required [12].

3. Results and discussions

The computer program for calculations has created in FORTRAN language. Our computer program allows take into account a large material attenuation [12-14]. Here the constitutive parameters of the uniaxial electrically and magnetically anisotropic metamaterial were taken from the article [15]. In the last article was considered an anisotropic lossless metamaterial slab. For this reason there were given only the real parts of the permittivity $\varepsilon_{r,ij}=(\varepsilon_{xx}, \varepsilon_{xx}, \varepsilon_{zz})$ and permeability $\mu_{r,ij}=(\mu_{xx}, \mu_{xx}, \mu_{zz})$ tensor components. The tensor components of the relative permittivity and the relative permeability are described by following formulae [15]:

$$\varepsilon_{xx}=1-\omega^2_{epxx}/\omega^2, \qquad \varepsilon_{zz}=1-\omega^2_{epzz}/\omega^2, \qquad (3)$$
$$\mu_{xx}=1-\omega^2_{mpxx}/\omega^2, \qquad \mu_{zz}=1-\omega^2_{mpzz}/\omega^2. \qquad (4)$$

The values of tensors' components ε_{xx}, ε_{zz},. μ_{xx}, μ_{zz} become equal to zero at the operating frequency f equal to the metamaterial electric f_{epxx}=3.46 GHz, f_{epzz}=2.5 GHz and magnetic f_{mpxx}=2.45 GHz, f_{mpzz}=2 GHz plasma resonance frequencies. The core of our multilayered cylinder is made of acrylic glass with the permittivity ε_{glass}=3.8- i0.0005. The semiconductor layers were made of electronic type silicon (n-Si) with the specific resistivities ρ= 100, 30, 10 Ω·m. We take into account the dispersion of semiconductor by formula (1). The calculations of the total scattered W^s and total absorbed W^a powers were fulfilled using method of article [12]. Under the term "total power" we mean the sum power (scattered or absorbed) by the all layers and the core of multilayered cylinder. The dependencies of total W^s and W^a powers that are normalized to the unit length of multilayered cylinder and through one oscillation period are presented in Figs 2 9. Dependencies for the incident perpendicular polarized microwave are shown in Figs 2(a) 9(a). Dependencies for the incident parallel polarized microwave are given in Figs 2(b 9(b). esi gnations in ig s 2 correspond: curve 1 (line with empty squares) for ρ=100 Ω·m; curve 2 (line with empty circulars for ρ=30 Ω·m; curve 3 (line with empty triangulars for ρ= 10 Ω·m. We explored the dependencies from 1 till 40 GHz. Here we present our calculations in the most interesting microwave range where happened uniaxial anisotropic metamaterial resonances from 1 till 4 GHz. We would like to pay your attention that the upper part of the resonance peaks has been cut to see better the character of dependencies along of the metamaterial resonance frequencies (Figs 2 9).

3.1 Scattered power in the anisotropic metamaterial resonances' frequency range

The scattered power W^s presented for three values of the n-Si specific resistivity ρ at two polarizations and four angles θ=90° (Fig. 2), θ=60° (Fig. 3), θ=30° (Fig. 4) and θ=5° (Fig. 5) of microwave incidence.

The specific resistivity ρ varies within ten times in our calculations. The imaginary part of the semiconductor permittivities Im (ε_s) changes from 0.18 till 1.8 at f=1 GHz. The scattered power depends weakly on the specific resistivity (Figs 2 5) in spite of the large Im (ε_s).
Analysis of the scattered power dependencies of multilayered cylinder shows that there are strongly expressed resonance peaks. We see that these peaks are on other frequencies than the anisotropic metamaterial resonances that is calculated by formulae (3) and (4) but all resonances are in the same frequency range between 1 and 4 GHz.

The comparison of scattered powers for the microwave perpendicular (Fig. 2(a)) and parallel (Fig. 2(b)) polarizations at θ=90^o shows the significantly different features the ones. We see three W^s resonances for both microwave polarizations. The central resonance frequencies of the W^s resonances for the perpendicular polarized microwave are observed at frequencies equal to 2.28, 2.92 and 3.26 GHz. The central resonance frequencies of W^s resonances for the parallel polarized microwave are at f= 1.2, 2.13 and 2.4 GHz.

The scattered power resonances are very narrow for the incident microwave with the parallel polarization. The last properties can be useful for working out of precision sensor devices.

The comparison of Figs 2(a) 5(a) shows that the smaller the angle θ is the more complex the W^s resonance distributions are in the frequencies between 1 and 4 GHz. We see that the values of scattered power minima decrease with decreasing of angle θ. This decrease is the particularly noticeable at frequencies between 3 and 4 GHz.

There are six resonances of scattered power for both microwave polarizations at the oblique incidence of microwave. The central resonance frequencies of perpendicular and parallel polarized microwaves are at frequencies equal to 1.2, 2.13, 2.28, 2.4, 2.92 and 3.26 GHz when θ=60^0, 30^0 and 5^0 (Figs 3-5).

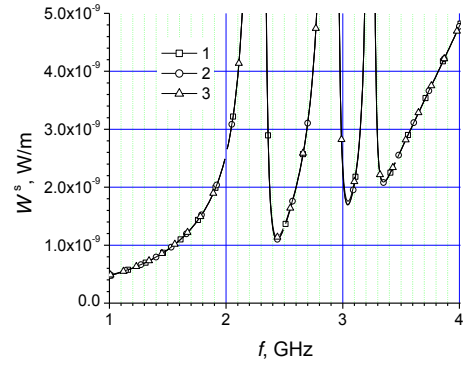

(a)

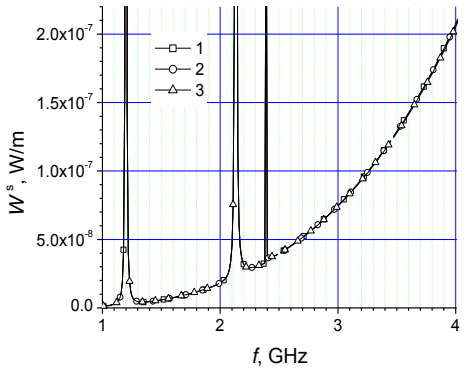

(b)

Figure 2: Scattered power of multilayered cylinder on the frequency of incident (a) perpendicular and (b) parallel polarized microwave at θ=90^0.

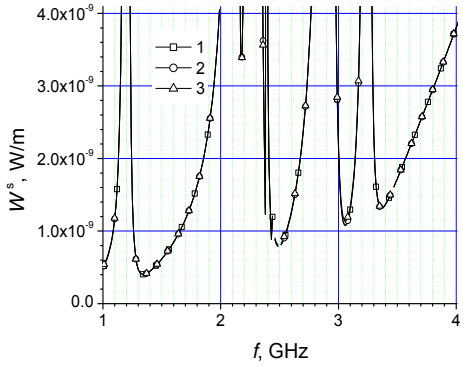

(a)

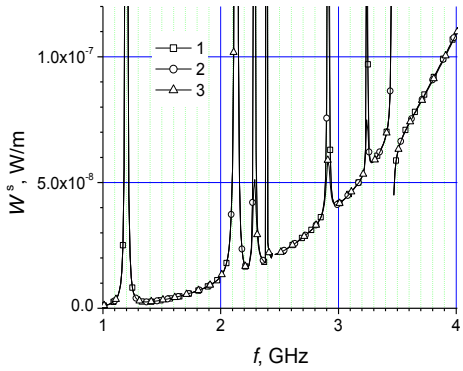

(b)

Figure 3: Scattered power of multilayered cylinder on the frequency of incident (a) perpendicular and (b) parallel polarized microwave at θ=60^0.

We can see that the central resonance frequencies at the oblique microwave incidence for the every of polarizations (Figs 3-5) are equal to the sum of all resonance frequencies at the normal microwave incidence (Fig. 2). It is possible to determinate the value θ, i.e. the location of a microwave radiation source, thanks to the knowledge of scattered power minimum values.

The less θ is the smaller scattered powers are at the certain frequencies. As an example, the scattered power is approximately zero and the cylinder become invisible at frequencies equal to 3.1 and 3.4 GHz when θ=5^o (Fig. 5).

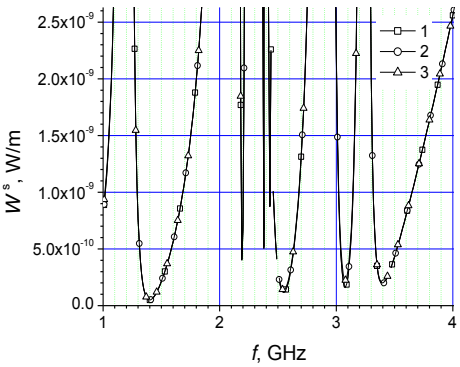

(a)

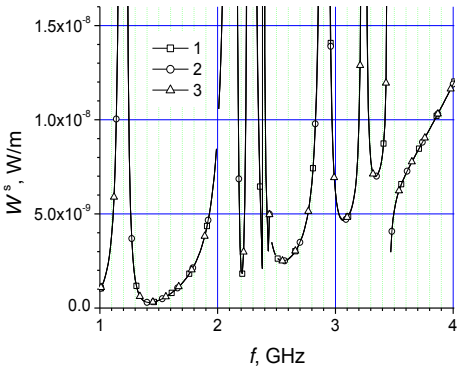

(b)

Figure 4: Scattered power of multilayered cylinder on the frequency on the frequency of incident (a) perpendicular and (b) parallel polarized microwave at θ=30^0.

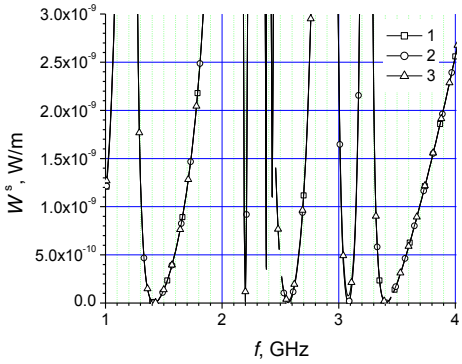

(a)

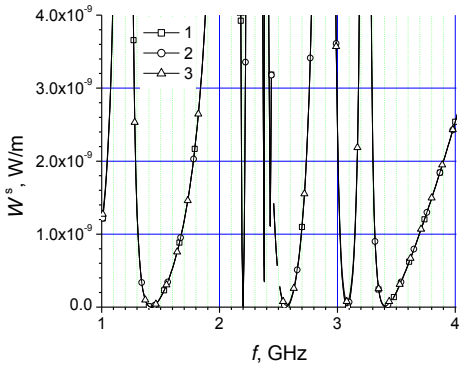

(b)

Figure 5: Scattered power of multilayered cylinder on the frequency of incident (a) perpendicular and (b) parallel polarized microwave at θ=5^0.

The scattered power dependencies on the polarization and the angle θ of microwave are given in Figs 2 and 3. We also see the resonance peaks are narrower for the microwave with the parallel polarization at θ =90^o (Fig. 2), θ =60^o (Fig. 3), θ =30^o (Fig. 4). This fact can be used to detect the polarization of incident microwave.

We would like to pay your attention on an interesting detail. The scattered power distributions on the frequency for the perpendicular and parallel polarizations are approximately similar at small angles θ. This can be explained by the fact that the configuration of falling EM fields becomes identical. We see that the W^s resonance pictures for both microwave polarizations are very similarly at θ=5^0 (Fig 6 (a, b)).

3.2 Absorbed power in the anisotropic metamaterial resonances' frequency range

The absorbed power W^a presented for three values of the *n*-Si specific resistivity ρ at two polarizations of incident microwave and four angles of incidence θ =90^o (Fig. 6), θ =60^o (Fig. 7), θ =30^o (Fig. 8) and θ =5^o (Fig. 9).

We see that W^a substantially depends on the specific resistivity of semiconductor material. This dependence is fairly large in the frequency intervals between the W^a resonance frequencies. As we explored dependencies till 40 GHz we can remark that W^a dependence on ρ is also strong between 5 and 40 GHz. We see in Fig. 6(a) the smaller specific resistivity the wider resonance curve for the perpendicular polarized microwave. The comparison of absorbed power for both polarizations when θ =90^o shows that there is the noticeable difference in their distributions. The central resonance frequencies are 2.3, 2.9 3.25 GHz for the incident microwave with the perpendicular polarization and 1.2, 2.1, 2.4 GHz for the incident microwave with the parallel polarization. The W^a resonance frequencies do not move with the changing of value ρ for both polarizations. All W^a resonance curves are very narrow for the parallel polarized microwave at θ=90^o. The absorbed power for the microwave with the parallel polarization depends stronger on the *n*-Si specific resistivity than for microwave with the perpendicular one at the frequency intervals between W^a resonance frequencies (see Fig. 6(a, b)). As an example, frequencies can be between 1.4 and 1.9 GHz or 2.5 and 2.8 GHz. Absorbed power dependencies Fig. 6(b) can be used for the precision determination of semiconductor specific resistivity of multilayered cylinder when the incident parallel polarized microwave impinges at θ=90^0.

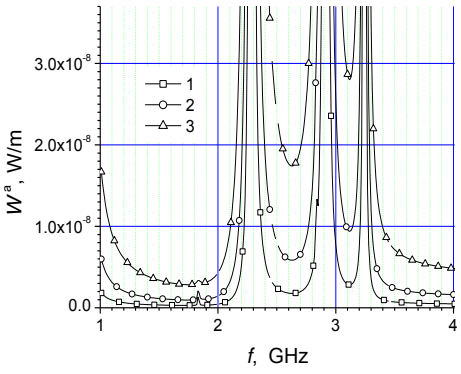

(a)

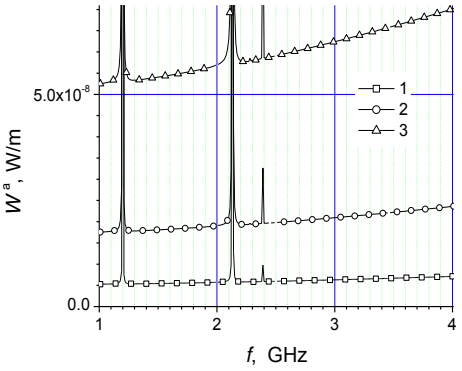

(b)

Figure 6: Absorbed power of multilayered cylinder on the frequency of incident (a) perpendicular and (b parallel polarized microwave at θ=90^0.

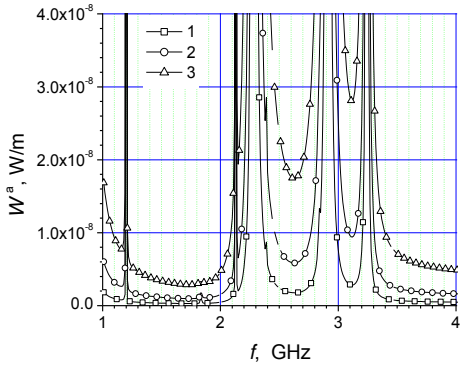

(a)

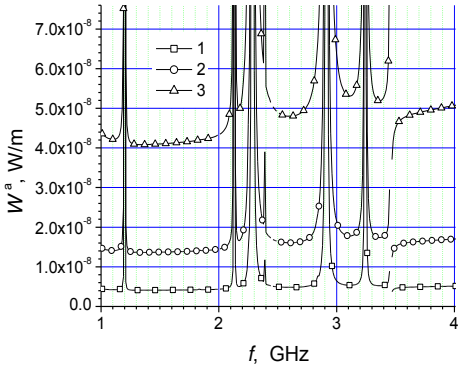

(b)

Figure 7: Absorbed power of multilayered cylinder on the frequency of incident (a) perpendicular and (b) parallel polarized microwave at θ=60^0.

In this case we have to know the incident microwave polarization, angle θ, main parameters of other cylinder materials and geometrical sizes.

In Fig. 6 are three resonances while in Figs 7 9 are six resonances. The values of W^a resonance frequencies match with the W^s resonance frequencies.

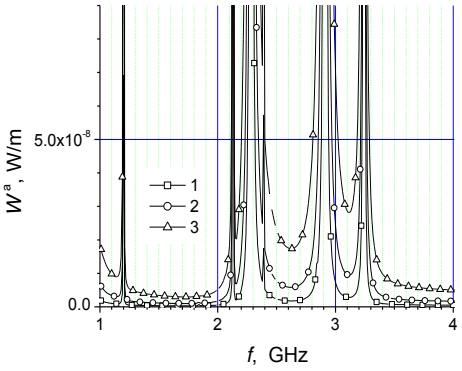

(a)

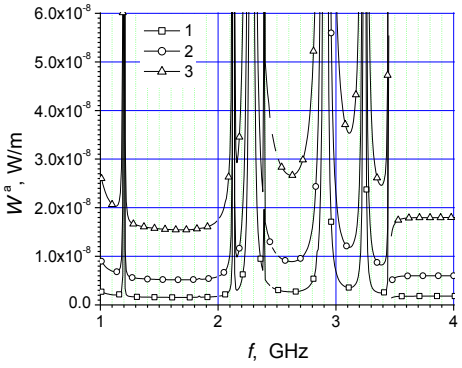

(b)

Figure 8: Absorbed power of multilayered cylinder on the frequency of incident (a perpendicular and (b) parallel polarized microwave at θ=30^0.

The larger value of specific resistivity is the wider resonance curves are for the perpendicular polarized microwave at different angles θ (Figs 7(a), 8(a)). The location of resonance frequencies practically do not depends on the semiconductor specific resistivity for the parallel polarized microwave (Figs 6(b) 9(b). The numbers of absorbed power resonances become larger with the reduction of the incident angle θ.

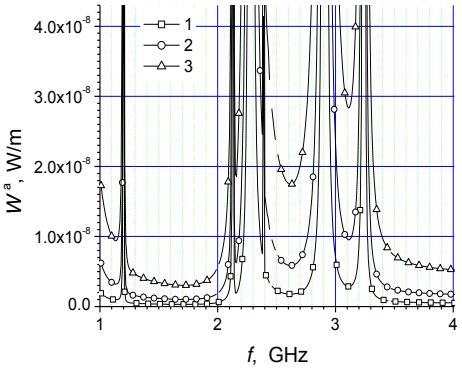

(a)

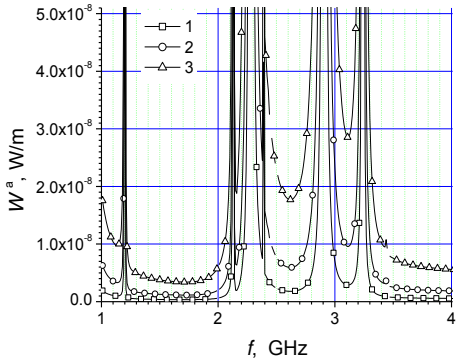

(b)

Figure 9: Absorbed power of multilayered cylinder on the frequency of incident (a) perpendicular and (b parallel polarized microwave at θ=5^0.

We can also see that the distribution of absorbed power for both polarizations is similar at the small incident angles, i.e. when $\theta = 5^0$ (Fig. 9(a, b)). The reason of this is the same as for the scattered power (Fig. 5(a, b)), i.e. the incident EM field configurations are similar for both polarizations when θ is small.

4. Conclusions

1. Analyses of scattered and absorbed microwave powers of multilayered cylinder that consists of the glass core coated with six uniaxial anisotropic metamaterial-semiconductor layers is carried out on the base of the rigorous solution of the boundary diffraction problem.
   2. Resonances of multilayered metamaterial-semiconductor cylinder are in the same frequency range as resonances of the metamaterial. We can observe three and six resonances of the multilayered cylinder at normal (θ=90^0) and oblique (θ=60^0, 30^0, 5^0) microwave incidence correspondingly instead of four resonances of the uniaxial anisotropic metamaterial.
3. The microwave power dependencies on the *n*-Si specific resistivity, the incident microwave polarization and the incident angle of microwave are implemented.
4. A magnitude of absorbed power is strongly dependent on the *n*-Si material specific resistivity at the frequency intervals between the frequencies of multilayered cylinder resonances. These dependencies are especially strong for parallel polarization at θ=60^0 and 90^0. The dependence on the specific resistivity shows that this multilayered cylindrical structure can be used for creating of microwave semiconductor sensor.
5. There are narrow resonances of the scattered and absorbed powers of parallel polarized microwave at θ=90^0. These resonances can be used for the determination of microwave polarization.

References

[1] G.W. Milton, *The theory of composites,* Cambridge university press, New York, 2002.

[2] R. L. Nelson, R. W. Boyda, Enhanced electro-optic response of layered composite materials, *Applied physics letters* 74: 2417–2419, 1999.

[3] D. Micheli, C. Apollo, R. Pastore, R. Bueno Morles, M. Marchetti, G. Gradoni, Electromagnetic Characterization of Composite Materials and Microwave Absorbing Modeling. *In book: Advances in Nanocomposites - Synthesis, Characterization and Industrial Applications*. ISBN 978-953-307-165-7, InTech, Ch.16: pp. 359–384, 2011.

[4] M. Y. Koledintseva, J. Drewniak, R. DuBroff, K. Rozanov, B. Archambeault, Modeling of shielding composite materials and structures for microwave frequencies, *PIER B* 15: 197–215, 2009.

[5] C. W. Qiu, H.-Y. Yao, S.-N. Burokur, S. Zouhdi, L.-W. Li, Electromagnetic scattering properties in a multilayered metamaterial cylinder, *IEICE Trans. Commun.* E90-B: 2423–2429, 2007.

[6] Y. Ni, L. Gao, C.-W. Qiu, Achieving Invisibility of Homogeneous Cylindrically Anisotropic Cylinders, Plasmonics 5:251–258, 2010.

[7] H. Oraizi, A. Abdolali, N. Vaseghi, Introduction of a New class of materials called double zero media having the real parts of epsilon and mu equal to zero, *PIERS Proceedings*, Moscow, Russia, pp. 348–350, 2009.

[8] H. Zhou, Z. Pei, S. Qu, S. Zhang, and J. Wang, A planar zero-index metamaterial for directive emission, *J. of Electromagn. Waves and Appl.* 23: 953–962, 2009.

[9] N. M. Litchinitser, A. I. Maimistov, I. R. Gabitov, R. Z. Sagdeev, V. M. Shalaev, Metamaterials: electromagne- tic enhancement directive emission, *Optics Letters* 33: 2350–2352, 2008.

[10] A. Alú, Restoring the physical meaning of metamaterial constitutive parameters, *Physical Review B* 83: 081102-(1–4), 2011.

[11] M. Silveirinha, N. Engheta, Design of matched zero-index metamaterials using nonmagnetic inclusions in epsilon-near-zero media, *Physical Review B* 75: 075119-(1–10), 2007.

[12] J. Bucinskas, L. Nickelson, V. Sugurovas, Microwave diffraction characteristic analysis of 2D multilayered uniaxial anisotropic cylinder, *Progress In Electromagn. Research*, PIER109: 175–190, 2010.

[13] J. Bucinskas, L. Nickelson, V. Sugurovas, Microwave scattering and absorption by a multilayered lossy metamaterial-glass cylinder, *Progress In Electromagn. Research*, PIER105: 103–118, 2010.

[14] L. Nickelson, J. Bucinskas, Microwave diffraction dependencies of a conductor cylinder coated with twelve glass and semiconductor layers on the *n*-Si specific resistivity. *Electronics and Electrical Engineering*, 115: 47–50, 2011.

[15] S.-H. Liu, C.-H. Liang, W. Ding, L. Chen, W.-T. Pan, Electromagnetic wave propagation through a slab waveguide of uniaxially anisotropic dispersive metamaterial, *Progress In Electromagn. Research*, PIER 76: 467–475, 2007.

New Equipment for SHF Electric Field Visualization

Igor A. Karpov, Mikhail R. Trunin and Egil D. Shoo
Institute of Solid State Physics, RAS, 142432 Chernogolovka, Moscow distr., karpow@issp.ac.ru

Abstract **We present the operation and design of newly developed fully automatic equipment for visualization of *SHF* electric fields. This equipment enables to obtain patterns of *SHF* fields around different objects including metamaterial product and to study field patterns of various developed *SHF* antennas and other objects, which interact with surrounding *SHF* electromagnetic field. Moreover, with scaled sizes of developed products whose interaction with electromagnetic wave is crucial for practical applications, our equipment can be used for testing of antennas and other interacted with electromagnetic radiation devices, not only at *SHF*, but also at radio frequencies. The performance of our innovative equipment was demonstrated during the investigation of the metamaterial cloak. The frequency behavior of the cloak reveal the frequency bands with maximum efficiency of the meta-material cloak.**

Index Terms **Equipment, Metamaterial, Microwave, *SHF* field pattern**

I. INTRODUCTION

The increasing interest has been manifested recently by many researchers to investigation of metamaterials, which composed of a great number of structural metaatom units ordered into a crystal-like packing. Such materials differ from common crystals by the size of their structural units - metaatoms, which is much larger than the structural units of standard crystalline matters as atoms, ions or molecules. Hence, each metamaterial metaatom consists of a large number of ordinary atoms and molecules, though this is not the only difference between meta- and ordinary materials. Metaatoms do not necessarily consist of a single type of molecule or atom, but they can also include several different materials filling the metaatom space in a prearranged way. Such metaatoms of a single or several different types are further packed into a specific predetermined spatial lattice structure to form metamaterial [1 - 3]. In short, metamaterial is man-made material composed of a single or more substances prearranged in a specified sequence to obtain the required properties.

The size and structure of the metamaterial as well as its metaatoms depend on the electromagnetic radiation wavelength affecting the metamaterial. The shorter the electromagnetic radiation wavelength, the smaller should be the size of metamaterial metaatoms. For the optical range the size of metaatoms can reach 50-200 nm which is fairly achievable for modern lithographic and material processing equipment used in microelectronics to create large-scale integration circuits, for instance, computer microprocessors. For the SHF range the size of metaatoms is appreciably larger, reaching units and even tens of millimeters [4 – 7]. As a result, SHF metaatoms can be observed by the unaided eye.

II. DESCRIPTION OF EQUIPMENT

We have developed a pioneering experimental equipment for investigation of the properties and measurement of characteristics of SHF metamaterials (Fig.1). This equipment enables us in polar coordinates to obtain the characteristics of SHF electromagnetic flow in

Manuscript received 15 November 2011. This work was supported by State contract 02.740.11.0216 and Program of Russian Academy of Science “New materials”.

I. A. Karpov is with the Institute of Solid State Physics of RAS, Chernogolovka, Moscow district, 142432, Russia (corresponding author; phone: 7(496)522-84-55; fax: 7(496)522-81-60; e-mail: karpow@issp.ac.ru).

E. D. Shoo is with the Institute of Solid State Physics of RAS, Chernogolovka, Moscow district, 142432, Russia (e-mail: shoo@issp.ac.ru).

the vicinity of the metamaterial sample and reproduce the pattern of its surrounding electromagnetic SHF field.

The measuring chamber of the device consists of two horizontal plane-parallel copper discs (1) with a clearance between them where the metamaterial sample is placed. SHF power

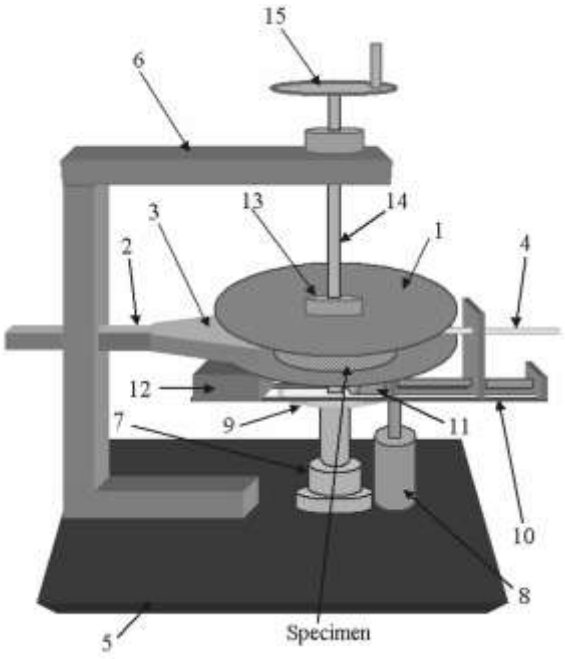

Fig. 1. The scheme central part of the equipment for SHF electric field visualization. **1**–Two parallel copper disks; **2**–Supply SHF waveguide; **3** – Megaphone; **4**–Antenna-probe; **5**–Plate-foundation; **6**–Stand; **7**–Support-axle; **8**–Stepping motor for circular transference of antenna-probe; **9**–Disk with gearing; **10**–System for radial transference of antenna-probe; **11**–Stepping motor for radial transference of antenna-probe; **12**–Counterbalance; **13**–Support of upper disk; **14**–Worm-and-worm pair for hand vertical transference of upper disk; **15**–Handle for hand vertical transference of upper disk.

is supplied from the generator into the measuring chamber by means of a waveguide megaphone (3) aimed at the metamaterial sample placed in the center of the measuring chamber. The value of the SHF field in the vicinity of the sample can be analyzed by usage of an antenna-probe (4) that is a coaxial cable ending with a prominent central wire bent upward. This bent upward wire (rod antenna) is moved by two computer-controlled step motors (8 and 11) along the circular arc as well as in the radial direction that allows to do step-defined measurements of the SHF fields in the measuring chamber in polar coordinates.

The SHF field values taken by the antenna-probe are transferred to a computer-connected vector network analyzer (Fig.2). The color image of the electrical component of the SHF electromagnetic field in the vicinity of the metamaterial sample is formed on the computer

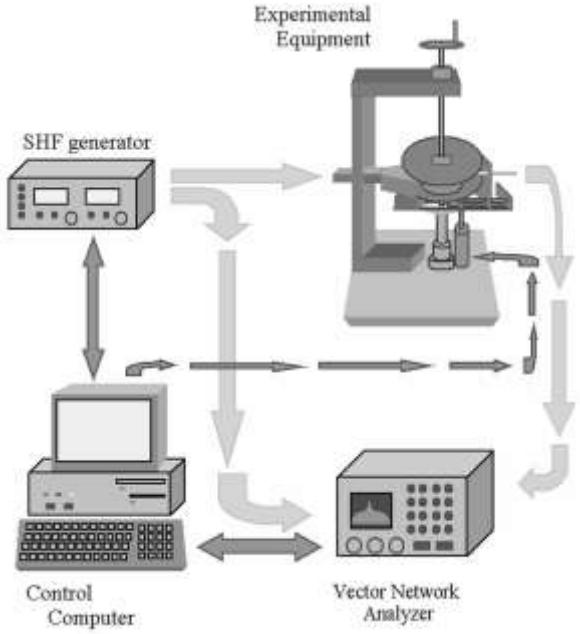

Fig. 2. The scheme of principal connections between important component of equipment.

screen by a special processing program. The picture color corresponds to the SHF field value in a predefined way.

Therefore, this measuring equipment enables us to get the computer display visualization of the spatial pattern of the SHF field value in the vicinity of the metamaterial sample. This pattern is depicted in prearranged colours with a predefined step, the value of which can be changed before beginning of each measurement within a certain interval.

III. METAMATERIAL FOR TESTING

The authors of [7] describe the design of a metamaterial product that allows the waves of the SHF electromagnetic field to turn round their created ring-shaped metamaterial object as

well as the objects placed inside that ring-shaped cloak.

Due to the authors of [7] such metamaterial design should ideally prevent wave reflection and scattering because the whole wave passes through the cloak as through an empty waveguide. Therefore, it appears as an "empty space illusion" as if there was no object on the way of the SHF wave. Since the SHF wave does not penetrate inside the ring, any objects can be placed there and their presence inside the ring will have no effect on the SHF wave propagation pattern. This masking effect is demonstrated for a copper cylinder 5 cm in diameter and 1 cm high placed inside the ring-shaped metamaterial cloak, which is totally opaque for electromagnetic waves.

In the case of an uncloaked cylinder we can see a distinct shadow behind the cylinder and color intensification of the field pattern in front of the cylinder due to wave reflection. The map of the SHF field with a copper cylinder surrounded by a metamaterial ring shows a smeared shadow behind the object, the reflection in front of the object also diminishes it which is confirmed by the attenuation of the intensity of the field pattern on the same side of the object.

In the ideal case the shadow of copper cylinder, which is placed in the center of metamaterial ring, has to be entirely disappeared. However, it does not occur: nevertheless a smeared shadow is seen behind the cloak with the copper cylinder inside. The authors explain this by a few losses in the meta-material.

Indeed, metamaterial consists of a great number of metaatoms, namely, split ring resonators (SRR), made of thin copper foil of 17 micrometer thick, placed on flexible dielectric "Duroid 5870" which is 381 micrometer thick polyethylene terephthalate film reinforced with glass fiber powder. As copper is not a perfect conductor (not a superconductor) and has electric resistance, the latter causes most of the losses. Dielectric is not perfect too: its dielectric loss tangent is equal to 0.0012 at the 10 GHz frequency. There are other typical losses for any imperfect (not theoretically calculated) object, and this is in agreement with the data of work [7].

Since this metamaterial sample seems to be a fairly interesting research object and its sizes and parameters are clearly and unambiguously indicated in the mentioned above paper, we chose it for testing of our new equipment (Fig.3) that allows to visualize SHF waves spatial expansion patterns, or more specifically, their electric component. The exterior view of cloak with a copper cylinder inside is shown in Fig.4.

Fig. 3. The outward appearance of our new equipment for SHF electric field visualization.

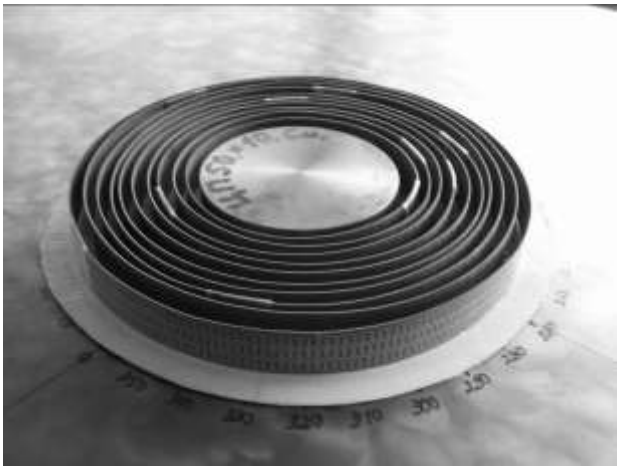

Fig. 4. The outward appearance of ring-like metamaterial cloak with copper cylinder inside.

IV. EXPERIMENT

We made a metamaterial object following the description given in [7]. The sample was placed in the measuring chamber center of our

equipment for visualization of the SHF electric field pattern. SHF power was supplied by the coaxial cable (Fig.5) from the first port of a "P4M-18" Vector Network Analyzer to the first power divider (left power divider in Fig.5).

Then the power divider splits the signal between two parts: the reference and the measuring signals. The signal of the measuring channel is supplied through a doorknob transformer and a waveguide piece to a brass megaphone with an outflow face of 1 x 20 cm. From the megaphone the SHF signal with vertical polarization of the electric component is supplied to the measuring chamber, which

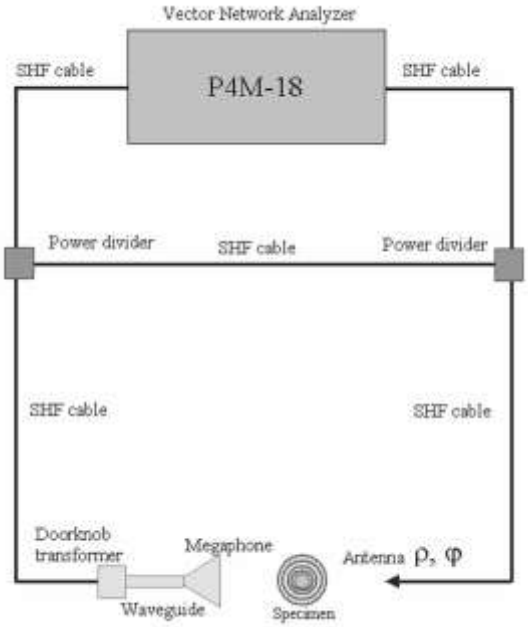

Fig. 5. The SHF circuit scheme of our new equipment.

represents the 11 - 12 mm spacing between two parallel copper disks. After passing through the measuring chamber the SHF signal is collected by a rod antenna moving along the radius as well as the circular arc (in the polar coordinates). Then the signal collected by the rod antenna is transmitted by the phase stabilized coaxial cable to the second power divider (right power divider in Fig.5) where it is summed and interferes with the reference channel signal. By the coaxial cable the interfered signal gets to the second measuring port of the "P4M-18" Vector Network Analyzer that analyzes the signal by measuring its amplitude and phase. Our special computer program for these measurements using "Visual Basic 6.0" draws on computer display the SHF electric field pattern inside the measuring chamber in prearranged colors. The aubergine-purple color corresponds to the minima (negative maxima) of the SHF electric field and the red color to the positive maxima. The zero of electric field strength is represented by the aquamarine experimental points on the SHF electric field pattern.

We have studied SHF field patterns in the empty chamber and for the case with a copper cylinder 50 mm in diameter and 10 mm high

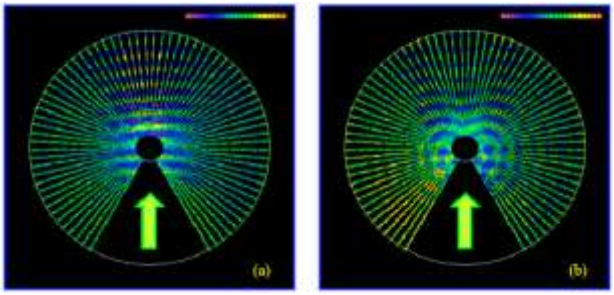

Fig. 6. (Colour.) SHF electric field patterns for empty measuring chamber (left) and for measuring chamber with Cu cylinder in the centre (right). The SHF field frequency is 10 GHz.

placed in the center of the measuring chamber at 10 GHz frequency (Fig.6).

We have also received a series of patterns of the SHF field electric component for the meta-material cloak at different frequencies and a series of similar SHF filed patterns at the same frequencies for the case with the copper cylinder 50 mm in diameter and 10 mm high placed inside the metamaterial cloak. During the experiments on the both SHF field patterns, the "empty" metamaterial cloak as well as that with the copper cylinder inside, was placed in the center of the measuring chamber of our equipment. The patterns of the SHF field electric component are shown in Figs.7-10.

We have also obtained the frequency dependences of the SHF electric field strength in the points along the 70 mm radius (the radius of the internal points row on the pattern of the SHF field with metamaterial cloak) at a 15 degree interval, the first curve corresponding to the 30 degree azimuth and the last to the 330 degree azimuth. The curves for twenty-one

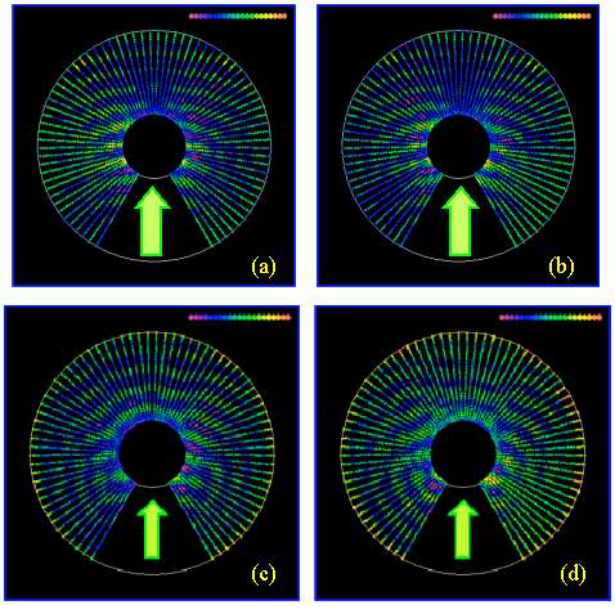

Fig. 7. (Colour.) Ideal and not ideal camouflage cases. SHF electric field at 8.0 GHz (above) and 7.3 GHz (below): left pictures are for metamaterial without Cu cylinder; right pictures are for metamaterial with Cu cylinder. Almost ideal camouflage of metamaterial sample both without Cu cylinder and with Cu cylinder can see at upper pictures. The camouflage at lower pictures is not ideal.

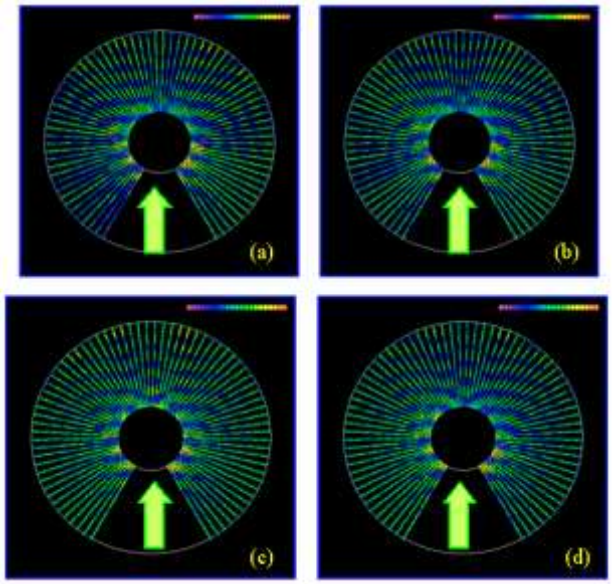

Fig. 8. (Colour.) Not ideal case of camouflage and the appearance of SHF field local minimum. SHF electric field at 8.2 GHz (above) and 8.5 GHz (below): left pictures are for metamaterial without Cu cylinder; right pictures are for metamaterial with Cu cylinder. On below pictures can see the violet spots of SHF field local minimum behind the metamaterial sample.

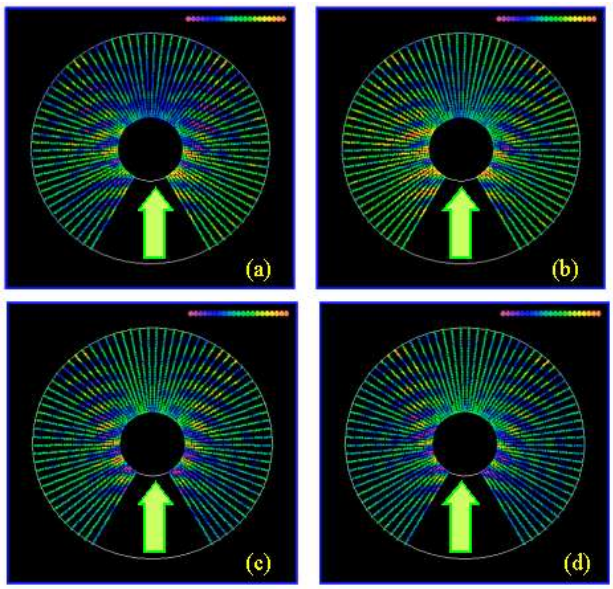

Fig. 9. (Colour.) The bifurcation of SHF stream. SHF electric field at 7.5 GHz (above) and 7.8 GHz (below): left pictures are for metamaterial without Cu cylinder; right pictures are for metamaterial with Cu cylinder. SHF stream doubles behind metamaterial sample: at increase of frequency the bifurcation becomes clearer and less depends on the presence of Cu cylinder within metamaterial sample.

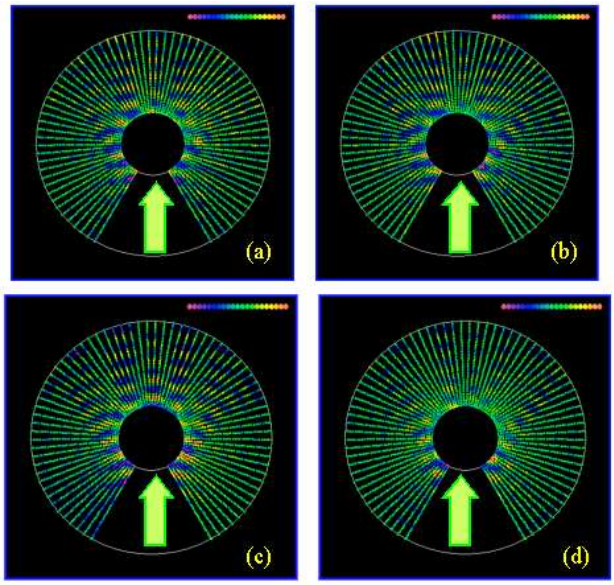

Fig. 10. (Colour.) The splitting of SHF stream into five parts. SHF electric field at 8.3 GHz (above) and 8.4 GHz (below): left pictures are for metamaterial without Cu cylinder; right pictures are for metamaterial with Cu cylinder. SHF stream splits into five parts behind the metamaterial sample: at increase of frequency the splitting becomes clearer in the case without Cu cylinder and less clear in the case with Cu cylinder.

coordinate points were obtained for the case of "empty" metamaterial cloak as well as that with the copper cylinder inside. Pointwise subtraction of curves for the cases of meta-material cloak with and without copper cylinder gives the differential curves for the frequency dependences of SHF electric field strength in each of the twenty-one coordinate points. The curves are shown on the diagram (Fig.11).

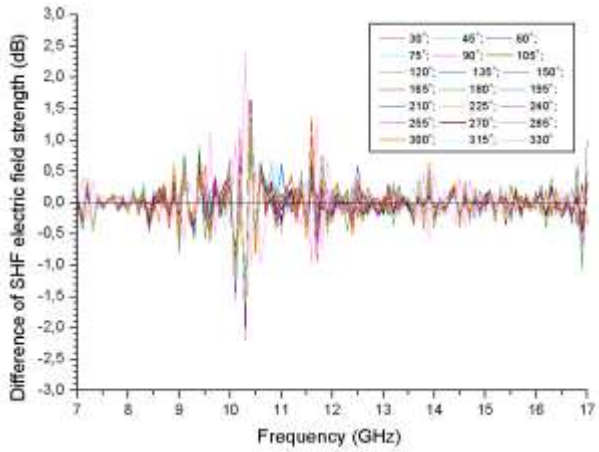

Fig. 11. (Colour.) Diagram of the differential curves for the frequency dependences of SHF electric field strength in each of the twenty-one coordinate points.

V. DISCUSSION

It is well seen from the diagram (Fig. 11) that at some frequencies all the twenty-one curves approach to zero. That signifies the minimal difference in SHF electric field strength between the case of "empty" metamaterial cloak and that of metamaterial cloak with a copper cylinder inside at this frequency range in all the coordinate points studied. And this, in one's turn, indicates that at the frequencies where all the curves of the diagram in Fig.11 approach to zero value of the SHF electric field strength the metamaterial cloak has the maximum camouflage ability with respect to case of the copper cylinder inside.

For the ideal metamaterial cloak at frequencies where the difference in SHF electric field strength between the case of "empty" metamaterial cloak and that of meta-material cloak with a copper cylinder inside is close to zero (Fig. 11), the difference in the SHF electric field strength should be expected to become zero. However, since metamaterial cloak is not perfect and possesses losses, the SHF field patterns for the cloaks with and without a copper cylinder do not coincide but exhibit only slight differences. Hence, it is seen that neither of the twenty-one frequency dependencies taken in different coordinate points turn to zero at any frequency. All the curves only approach to zero at some frequencies. However, the efficiency of the metamaterial cloak at some frequencies can be appreciated by the approach of the curves to the zero value of the difference in SHF electric field strength between the case of "empty" metamaterial cloak and that of metamaterial cloak with a copper cylinder inside. When the curves are nearest the zero value of the difference in SHF electric field strength, the camouflage properties of the cloak are maximal, whereas at the frequencies where the curves are farthest from the zero value of the difference in SHF electric field strength, the camouflage properties of the cloak are minimal.

VI. CONCLUSION

Thus, we have created new automatized equipment that enables to obtain spatial propagation patterns of SHF wave electric field components in prearranged colors that allows us to investigate SHF field patterns around various objects, for instance, metamaterial product, phased gratings, various antennas. All this can be useful for development and testing of such objects.

We have demonstrated the efficiency of our new equipment in studies of SHF field patterns around metamaterial camouflage cloak suggested by the American authors in [7].

Using our innovative equipment, we have also demonstrated SHF field patterns around the metamaterial cloak suggested in [7] in the frequency range from 7 GHz to 15 GHz and revealed the frequencies at which the camouflage properties of the metamaterial cloak are maximum.

ACKNOWLEDGMENT

I. A. Karpov thanks engineers and mechanicians of Electron kinetics laboratory (Head is Prof. M. R. Trunin) for manufacture of mechanical components and assembling of them in order to creation of described equipment; Firm "Electroprivod" (St. Petersburg) for delivery of stepping motors and machinery of precise travels; Research-and-production firm "Micran" (Tomsk) for delivery of Vector Network Analyzer "P4M-18" and all other SHF components for our equipment; Firm "KTC-MicroComplete" (Moscow) and Firm "EASCA" (China) for production of meta-material pattern. The individual gratitude is to Programmer Mr. E. D. Shoo for creation of programs on "Visual Basic 6.0" for our new equipment.

REFERENCES

[1] Three-dimensional optical metamaterial with a negative refractive index. Jason Valentine, Shuang Zhang, Thomas Zentgraf, Erick Ulin-Avila, Dentcho A. Genov, Guy Bartal & Xiang Zhang Nature, Vol. 455, 2008, p. 376 – 380.

[2] Far-field optical hyperlens magnifying sub-diffraction-limited objects. Zhaowei Liu, Hyesog Lee, Yi Xiong, Cheng Sun, Xiang Zhang Science Vol. 315, 2007, p. 1686.

[3] Super-resolution imaging using a three-dimensional metamaterials nanolens. B. D. F. Casse, W. T. Lu, Y. J. Huang, E. Gultepe, L. Menon, and S. Sridhar Applied Physics Letters **96**, 023114 2010.

[4] Slow microwave waveguide made of negative permeability metamaterials. Wentao T. Lu, Savatore Savo, B. Didier, F. Casse and Srinivas Sridhar Microwave and optical technology letters Vol. 51, No. 11, November 2009, p. 2705 – 2709.

[5] Slow microwaves in left-handed materials. E. Di Gennaro, P. V. Parimi, W. T. Lu and S. Sridhar, J. S. Derov and B. Turchinetz Physical Review B **72**, 033110 2005, 4p.

[6] Modulating and tuning the response of metamaterials at the unit cell level. Aloyse Degiron, Jack J. Mock, and David R. Smith Optics express, Vol. 15, No. 3, 2007, p. 1115 – 1127.

[7] Metamaterial Electromagnetic Cloak at Microwave Frequencies. D. Schurig, J. J. Mock, B. J. Justice, S. A. Cummer, J. B. Pendry, A. F. Starr, D. R. Smith Science 314, 2006, p. 977 – 980.

Below/Above Cutoff Dual Metamaterial Band in Cylindrical Media

S. A. Hassani Gangaraj*, M. Tayarani, A. Abdolali

Department of Electrical Engineering, Iran University of Science and Technology, Tehran, Iran
*corresponding author, E-mail: Ali.Gangaraj@Gmail.Com

Abstract

In this paper we have considered a magnetic anisotropic media in cylindrical coordinate with scalar permittivity and diagonal tensor permeability. A PEC (Perfect Electric Conductor) boundary condition assumed at the radius ρ = a . We have solved the Maxwell equations inside the medium for radius less than a. Actually this structure is an anisotropic cylindrical waveguide. Then, we have extracted the characteristic equations for dominant TE and TM modes for such a structure. By focusing on these equations we have achieved several analytical conditions for different situations of wave propagation such as left hand, right hand or even evanescent mode depending on different signs of cylindrical permeability components. After that, we have focused on the left hand property and we achieved below/above cutoff dual metamaterial band in cylindrical waveguide. Negative effective permittivity and permeability are obtained. Moreover the impedances are extracted to show that this structure is operating in its dominant TE mode.

Actually the novelty of this work is the design of a single mode guided structure with multiple controllable metamaterial bands both for below and above the cutoff frequency.

1. Introduction

Negative refractive index materials basic theories and artificial realizations have already been introduced. Transmission line models have been proposed for these structures by periodic shunt inductance and series capacitance [1]. Recently, an intensive study of the propagation of electromagnetic waves in media with negative permittivity and permeability has been presented in the literature [2– 4]. Some unique properties such as a negative index of refraction, supporting backward waves, and so forth, have been shown. But the main goal in this field is to control the metamaterial bands [5]. In this paper we tried to achieve a formula that enables us to control and design a structure with metamaterial multipassbands.

In the second section we have supposed a magnetic anisotropic guided cylindrical medium with scalar permittivity and diagonal tensor permeability. Then we have analyzed the wave propagation inside of this structure to extract the characteristic equation for TE modes. By using this equation it is proved that by changing the signs of the components of the permeability tensor we can obtain different situations such as backward, forward an even evanescent at below and above the cutoff frequency. Then we focus on backward case and calculate the real and imaginary parts of effective permeability and permittivity to prove the left hand property. Actually in this section we propose a design formula to control the metamaterial passbands for below and above the cutoff frequency.

In the third section by obtaining the impedances we have proved that such a structure supports only the dominant TE_{11}.

2. Analysis of TE and extracting the constitutive parameters

At the first, we consider a magnetic anisotropic medium in cylindrical coordinate. The characteristics of such a medium is mentioned below

$$\bar{\bar{\mu}} = \begin{bmatrix} \mu_\rho & 0 & 0 \\ 0 & \mu_\Psi & 0 \\ 0 & 0 & \mu_z \end{bmatrix} \quad \& \quad \varepsilon \tag{1}$$

The permittivity of this structure is a scalar and the permeability is a diagonal tensor. By writing down the Faraday and Ampere equations and extending them into different directions and by considering $\boldsymbol{H_z} = H_{(\rho,\Psi)}e^{-j\beta z}$, we can derive an equation that describes wave propagation in cylindrical medium versus H_z for TE modes.

$$\nabla \times \boldsymbol{E} = -j\omega \begin{bmatrix} \mu_\rho & 0 & 0 \\ 0 & \mu_\Psi & 0 \\ 0 & 0 & \mu_z \end{bmatrix} \begin{bmatrix} \boldsymbol{H_\rho} \\ \boldsymbol{H_\Psi} \\ \boldsymbol{H_z} \end{bmatrix} \tag{2}$$

$$\nabla \times \boldsymbol{H} = j\omega\varepsilon\boldsymbol{E} \tag{3}$$

Then we have

$$\frac{\mu_\rho}{\mu_z(-\beta^2+\omega^2\mu_\rho\varepsilon)}\left[\frac{\partial^2 H_{(\rho,\Psi)}}{\partial\rho^2}+\frac{1}{\rho}\frac{\partial H_{(\rho,\Psi)}}{\partial\rho}\right]+ \frac{\mu_\Psi}{\mu_z(-\beta^2+\omega^2\mu_\Psi\varepsilon)}\frac{1}{\rho^2}\frac{\partial^2 H_{(\rho,\Psi)}}{\partial\Psi^2}+H_{(\rho,\Psi)}=0 \tag{4}$$

We shall use the method of separation to solve the Eq. 4 and finding the β for TE modes. If we suppose that $\boldsymbol{H_z} = f_{(\rho)}g_{(\Psi)}e^{-j\beta z}$ then we can derive some equations that describe $f_{(\rho)}$and $g_{(\Psi)}$. By some algebraic manipulation we have

$$\frac{\mu_\rho}{\mu_z(-\beta^2+\omega^2\mu_\rho\varepsilon)}\frac{1}{f}\left[\frac{d^2f}{d\rho^2}+\frac{1}{\rho}\frac{df}{df}\right]+$$
$$\frac{\mu_\Psi}{\mu_z(-\beta^2+\omega^2\mu_\Psi\varepsilon)}\frac{1}{\rho^2}\frac{1}{g}\frac{d^2g}{dg^2}+1=0 \quad (5)$$

We know that g should be periodic corresponding to Ψ. So, we should have

$$\frac{1}{g}\frac{d^2g}{d\Psi^2}=-m^2 \qquad m: integer \quad (6)$$
$$g=A\cos m\Psi+B\sin m\Psi \quad (7)$$

By defining the below parameters, we can extract a differential equation to describe the f.

$$\frac{1}{h^2}=\frac{\mu_\rho}{\mu_z(-\beta^2+\omega^2\mu_\rho\varepsilon)} \quad \nu^2=m^2\frac{\mu_\Psi(-\beta^2+\omega^2\mu_\rho\varepsilon)}{\mu_\rho(-\beta^2+\omega^2\mu_\Psi\varepsilon)} \quad (8)$$
$$\frac{d^2f}{d(\rho h)^2}+\frac{1}{\rho h}\frac{df}{d(\rho h)}+\left(1-\frac{\nu^2}{(\rho h)^2}\right)f=0 \quad (9)$$

Eq. 9 is the Lommel differential equation [6]. In this equation ν is not necessarily an integer, so this equation is the generalized form of Bessel equation. The answers of this equation are the Lommel functions. The Lommel functions are J_ν and Y_ν. Y_ν tends to infinity when the region of solution contains the origin of the coordinate and so, in our problem for $\rho < a$ we should omit this function. By these assumptions we have

$$f=CJ_\nu(\rho h) \quad C: an\ arbitrary\ Constant \quad (10)$$

Now, by calculating the different components of the electric and magnetic fields for TE mode and exerting the PEC boundary conditions at $\rho=a$ we can find that

$$h=\frac{\chi'_{\nu n}}{a} \quad (11)$$

Which $\chi'_{\nu n}$ is the n-th zero of the derivative of the ν-th order of Lommel function and a is the radius of the waveguide. Now by using the Eq. 8 and the h which is defined in Eq. 11 we can find an expression for propagation constant of TE modes.

$$\beta^2=\omega^2\mu_\rho\varepsilon-\frac{\mu_\rho}{\mu_z}\left(\frac{\chi'_{\nu n}}{a}\right)^2 \quad (12)$$

By considering the supposed anisotropic medium as a homogenous medium, we can obtain effective permeability and effective permittivity. If we define $\beta^2=\omega^2\mu_{eff}\varepsilon_{eff}$ then we can find some expressions for μ_{eff} and ε_{eff} as follow

$$\mu_{eff}=\frac{1}{\mu_z} \qquad \varepsilon_{eff}=\mu_\rho\mu_z\varepsilon-\mu_\rho\left(\frac{\chi'_{\nu n}}{a}\right)^2 \quad (13)$$

By looking carefully to Eq. 13 we can conclude that different situations of wave propagation (backward, forward or evanescent) can be achieved by changing the signs of μ_ρ and μ_z for TE modes. If we suppose $\mu_z<0$ and $\mu_\rho>0$, we have negative μ_{eff} and ε_{eff}, so we have LH passband. If we suppose $\mu_z<0$ and $\mu_\rho<0$ we have negative μ_{eff} and positive ε_{eff}, so we have evanescent mode and at last if we suppose $\mu_z>0$ and $\mu_\rho>0$, we have positive μ_{eff} and positive or negative ε_{eff} and as a result we have an evanescent or RH propagative mode. Here we focus on the case of $\mu_z<0$ and $\mu_\rho>0$ where from Eq. 13 one can obtain backward wave propagation. As it is reported in [5], when the magnetic field of the incident wave is parallel to the axis of MSRRs, they can produce negative permeability along the direction of their axis in their resonance frequencies. So, by locating MSRRs in the Z-direction of a cylindrical waveguide we can obtain negative μ_z because a cylindrical waveguide has a magnetic field component along the Z direction at its dominant TE_{11} mode and we can suppose $\mu_\rho=\mu_0$ because there is no MSRRs along the radius. MSRRs can resonate both below and above the cutoff of a cylindrical waveguide So if we consider the illumination of TE mode on MSRRs we can satisfy the condition of LH propagation ($\mu_z<0$ and $\mu_\rho>0$) at the resonance frequencies of MSRRs. We suppose a MSRR which comprises two copper rings placed back to back on Rogers RT6002 substrate (substrate thickness 0.7 mm) with slots oriented in opposite directions. The rings have an outer diameter of 4mm with track width of 1 mm and a slit width of 0.5 mm. Such a MSRR has two resonance frequencies one in 6.7 GHz and the other in 11.4 GHz. If we locate these MSRRs in the Z direction of a cylindrical waveguide with radius of 9 mm(cutoff frequency of 10 GHz), we can achieve negative μ_z both below and above the cutoff of the waveguide. As a result, below/above cutoff dual metamaterial passband will be realized. We have located 13 MSRRs along the Z direction of a cylindrical waveguide. Such a structure is shown in Fig. 1.

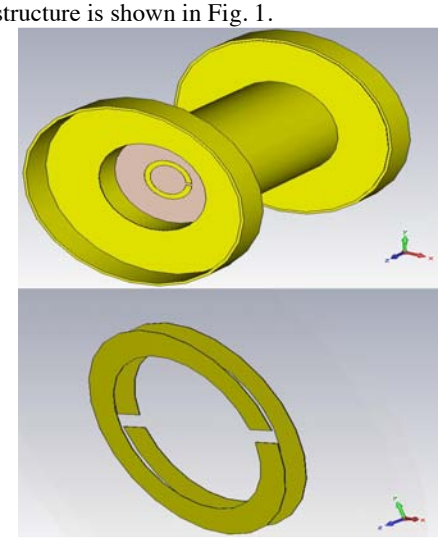

Fig. 1. Perspective view of a MSRR and the waveguide with MSRRs inside.

In Fig. 1, we have used two bigger waveguide at the ends to excite the smaller waveguide under its cutoff frequency 10 GHz.

The below and the above cutoff LH passbands are depicted in Fig. 2a and 2b. To be sure about the LH property of these passbands we have calculated the effective permeability and effective permittivity in these bands by the method introduced in [7]. Our extraction approach begins by introducing composite terms V_1 and V_2 with S-Parameter.

$$V_1 = S_{21}+S_{11} \qquad V_2 = S_{21}-S_{11} \tag{14}$$

$$X = {1 + V_1V_2}/{V_1 + V_2} = {1 + Z^2}/{2Z} \tag{15}$$

Where the transmission term

$$Z = \exp\left(j\omega k_0\sqrt{\varepsilon_{eff}\mu_{eff}}d\right) \tag{16}$$

Consequently from Eq. 13

$$Z = X \pm \sqrt{X^2 - 1} \tag{17}$$

Note that the expression for Z is a complex function with multiple branches. The ambiguity can be resolved using the condition $e\eta_{eff} > 0$. The combination of Eq. 13 and 14 yields

$$\sqrt{\varepsilon_{eff}\mu_{eff}} = j\frac{\ln(Z)}{\omega k_0 d} \tag{18}$$

And we have

$$\eta_{eff} = \eta_0\frac{1+Z}{1-Z}\frac{1-V_2}{1+V_2} = \eta_0\sqrt{\frac{\mu_{eff}}{\varepsilon_{eff}}} \tag{19}$$

$$\varepsilon_{eff} = j\frac{\ln(Z)}{\omega k_0 d}\frac{1+Z}{1-Z}\frac{1-V_2}{1+V_2} \tag{20}$$

$$\mu_{eff} = j\frac{\ln(Z)}{\omega k_0 d}\frac{1-Z}{1+Z}\frac{1+V_2}{1-V_2} \tag{21}$$

The resulted effective permittivity and permeability are shown in Fig. 3. As it is obvious in Fig. 3, the real parts of effective permeability and permittivity are negative for below and above cutoff passband. So we can conclude that by using the Eq. 12 and 13 and tuning the resonance frequency of a MSRR, we can achieve the below/above cutoff dual metamaterial passband. Actually we can introduce Eqs. 12 and 13 as designing equations because by using these equations and negation of μ_z by resonances of MSRRs we can control our LH bands. Now, there is a question. All the above analysis was for TE illumination, but how can we be sure about illumination of dominant TE on the MSRRs? In the next section of the paper we will answer this question.

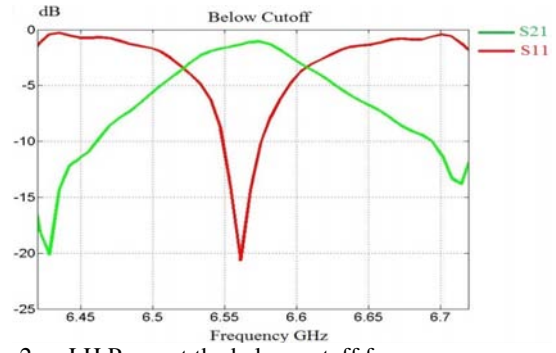

Fig. 2a. . LH Passe at the below cutoff frequency.

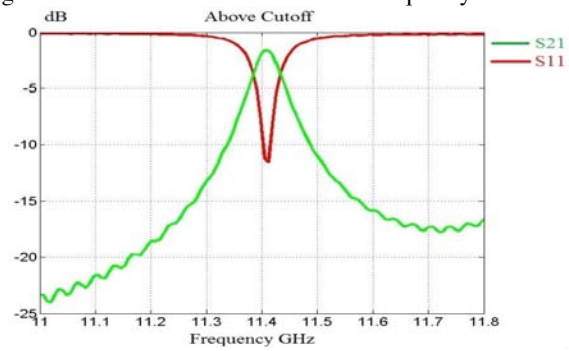

Fig. 2b. LH Pass at the above cutoff frequency.

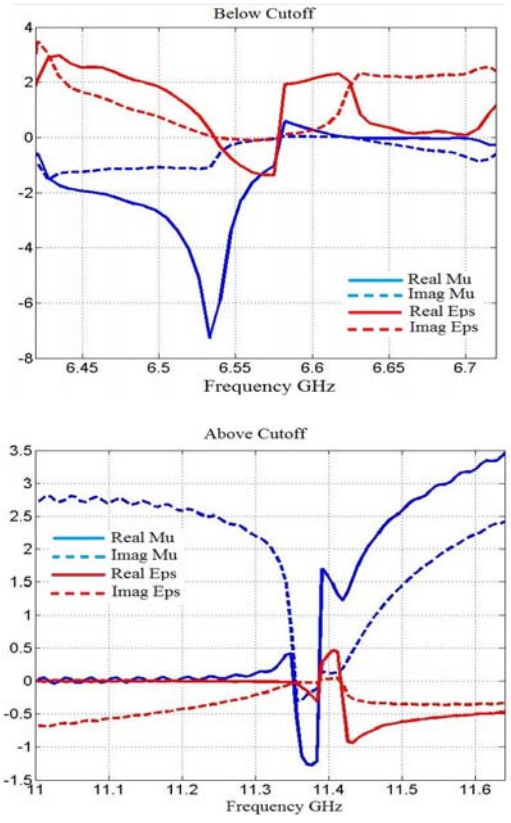

Fig. 3. Real and Imaginary parts of effective permeability and permittivity for above and below cutoff passbands.

3. Impedances of TM Modes and the Proof of Single Mode Operation

To answer this question we will extract the cutoff frequencies for TE and TM modes in such an anisotropic medium, then we will show that the dominant TE mode is TE11 and dominant TM mode is TM01 and at last by obtaining the impedances we will show that it is TE11 mode that illuminates the MSRRs.
At the first we will find the cutoff frequency for TE mode. By setting $\beta = 0$ in Eq. 12 we have :

$$Cutoff\ For\ TE\ Modes \xrightarrow{yields} f_c^2 = \frac{1}{4\pi^2\mu_z\varepsilon}(\frac{\chi'_{\nu n}}{a})^2 \quad (22)$$

When we suppose that $\beta = 0$, from Eq. 8 we have $\nu^2 = m^2$, so the Lommel equation becomes Bessel. Then $\chi'_{\nu n}$ will be n-th zero of the derivative of the ν-th order Bessel function. Among the values of $\chi'_{\nu n}$, the χ'_{11} has the smallest value. So, between the TE modes, TE_{11} is the dominant and the next TE mode is TE_{01}. By finding the transverse components of fields for TE_{11} and by using the Maxwell Equations, we can find the TE_{11} impedance. We shall note that by locating the MSRRs along the Z direction we can approximately set the μ_ρ and μ_ψ equal to μ_0. So we have

$$Z_{TE_{11}} = \frac{\omega\mu_\rho}{\beta_{TE_{11}}} \xrightarrow{\mu_\rho=\mu_0} \frac{\omega\mu_0}{\sqrt{\omega^2\mu_0\varepsilon - \frac{\mu_0}{\mu_z}(\frac{\chi'_{11}}{a})^2}} \quad (23)$$

By an analysis similar to section 1, we can extract the propagation constant for TM modes. We suppose that

$$\frac{1}{h^2} = \frac{1}{(-\beta^2 + \omega^2\mu_\psi\varepsilon)} \quad \nu^2 = m^2\frac{(-\beta^2 + \omega^2\mu_\psi\varepsilon)}{(-\beta^2 + \omega^2\mu_\rho\varepsilon)} \quad (24)$$

Then we have

$$For\ TM\ Modes \xrightarrow{yields} \beta^2 = \omega^2\mu_\psi\varepsilon - (\frac{\chi_{\nu n}}{a})^2 \quad (25)$$

Now, by setting $\beta = 0$ in Eq. 10 we have :

$$Cutoff\ For\ TM\ Modes \xrightarrow{yields} f_c^2 = \frac{1}{4\pi^2\mu_\psi\varepsilon}(\frac{\chi_{\nu n}}{a})^2 \quad (26)$$

When we suppose that $\beta = 0$, from Eq. 24 we have $\nu^2 = m^2$, so, again the Lommel equation becomes Bessel. Then $\chi_{\nu n}$ will be n-th zero of the of the ν-th order Bessel function. Among the values of $\chi_{\nu n}$, the χ_{01} has the smallest value. So, between the TM modes, TM_{01} is the dominant. By finding the transverse components of fields for TM_{01} and by using the Maxwell Equations, we can find the TM_{01} impedance. We shall note that by locating the MSRRs along the Z direction we can approximately set the μ_ρ and μ_ψ equal to μ_0. So we have

$$Z_{TM_{01}} = \frac{\beta_{TM_{01}}}{\omega\varepsilon}\left(\frac{-\beta^2+\omega^2\mu_\rho\varepsilon}{-\beta^2+\omega^2\mu_\psi\varepsilon}\right) \xrightarrow{\mu_\rho=\mu_\psi=\mu_0} \frac{\sqrt{\omega^2\mu_0\varepsilon-(\frac{\chi_{01}}{a})^2}}{\omega\varepsilon} \quad (27)$$

According to Eq. 27, we can calculate the impedance of TM01 mode at the frequencies of passbands in Fig. 2a and 2b. It is calculated and depicted in Fig. 4. As it is obvious the real part of impedances is zero, so we can conclude that the TM01 mode does not propagate and as a result non of the TM modes does not propagate in the LH passbands.

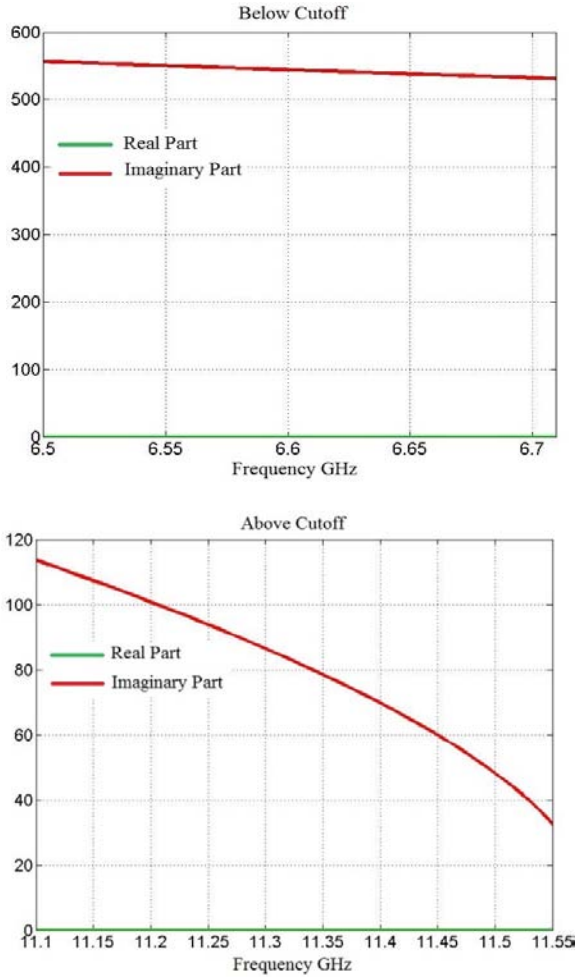

Fig. 4. Real and Imaginary Parts of impedance of dominant TM mode.

Now we shall prove that this structure supports just the dominant TE_{11} mode. As it proved from Eq. 22, the dominant mode is TE_{11} and the next mode is TE_{01}. The cutoff frequency of TE_{11} is 10 GHz and from Eq. 20 we can find that the ratio of the cutoff frequencies of TE_{11} and TE_{01} is

$$\frac{f_{cTE_{01}}}{f_{cTE_{11}}} = \frac{\chi'_{01}}{\chi'_{11}} = \frac{3.832}{1.841} = 2.08 \rightarrow f_{cTE_{01}} = 20.8\ GHz \quad (26)$$

As it is calculated above, the cutoff frequency of TE_{01} is 20.8 GHz but our operating frequency is 6.55GHz for below cutoff and 11.4 GHz for above cutoff, so, just TE_{11} propagates through the structure and the next TE mode definitely does not propagate.

4. Conclusions

In this paper, we have solved the problem of wave propagation in a magnetic anisotropic cylindrical waveguide. The characteristic equations for TE and TM modes have been extracted. It has been proved that such an anisotropic structure can support backward wave propagation both at below and above the cutoff frequency. To be sure about the backward property of these passbands, we have shown that the real parts of the effective permeability and permittivity are negative at the desired metamaterial bands. In the continuation by obtaining the impedances, we have proved that the propagated wave inside this supposed medium is actually a guided single mode wave.

References

[1] A. Lai, C. Caloz, and T. Itoh, Composite right/left-handed transmission line metamaterials, IEEE Microwave Magazine, vol. 5, no. 3, pp. 34–50, Sept. 2004.

[2] R.W. Ziolkowski and E. Heyman, Wave propagation in media having negative permittivity and permeability, Physical Rev E, 64 (2001), 056625.

[3] I.V. Lindell, S.A. Tretyakov, K.I. Nikoskinen, and S. Ilvonen, BW media: Media with negative parameters, capable of supporting backward waves, Microwave Opt Technol Lett 31 (2001), 129–133.

[4] Yansheng Xu, A Study Of Waveguides Filled With Anisotropic Metamaterials, MICROWAVE AND OPTICAL TECHNOLOGY LETTERS / Vol. 41, No. 5, June 5 2004

[5] Fan-Yi Meng, Qun Wu, Daniel Erni, Le-Wei Li. “Controllable Metamaterial-Loaded Waveguides Supporting Backward and Forward Waves”, IEEE Transaction on Antenna and Propagation, Vol. 59, NO. 9, September 2011.

[6] Zwillinger, D. Handbook of Differential Equations, 3rd ed. Boston, MA: Academic Press, p. 125, 1997.

[7] R. W. Ziolkowski, “Design, fabrication, and testing of double negative metamaterials,” IEEE Trans. Antennas Propag., vol. 51, pp. 1516–1529, 2003.

Reducing Radar Cross Section by investigation electromagnetic materials

Somayeh Komeylian[1] and Farrokh Hojjat-Kashani[2]
[1] Electrical and Engineering Department , Islamic Azad University South , Tehran, Iran
[2] Electrical and Engineering Department, University of Science and Technology, Tehran, Iran
Email: somayeh@komeylian.com
Email: kashani@iust.ac.ir

Abstract

Decreasing the Radar Cross Section (RCS) is investigated in electromagnetic materials, i.e. double-positive (DPS) , double-negative (DNG) , epsilon-negative (ENG) and mu-negative (MNG) materials. The interesting properties of these materials lead to a great flexibility in manufacturing structures with unusual electromagnetic characteristics. The valid conditions for achieving the transparency and gaining resonance for an electrically small cylinder are established, in this corresponding The effect of incidence direction on RCS inclusive of transparency and resonance conditions is also explored ,through computer simulations for an electrically small cylinder.

***INDEX TERMS*—RADAR CROSS SECTION, MATAMATERIALS, INUISIBILITY, RESONANCE, TRANSPARENCY**

I. INTRODUCTION

Recently, reducing the Radar Cross Section (RCS) of various structures for achieving transparency and obtaining resonant structures have received much attention. For instance, in [1-4], the transparency conditions for typical objects of cylindrical and spherical shapes were established. The resonance conditions of such objects were also considered in[8],[9]. Now, we aim to derive and elucidate these unusual particularizes of this group of electromagnetic materials, Figure.1, for electrically small cylindric object. [6],[7].

Invisibility means that an object doesn't obstruct what is behind it and its scattering cross section is significantly low, at least in a narrow frequency band. Therefore, by passing the light through these structures, under transparency phenomena scattering, distortion, or observation are dramatically decreased. In this paper, we are interested in extracting the transparency conditions for an electrically small cylinder for both polarizations, i.e. TE and TM.

An electrically small object generally shows a weak scattering for any incident (plane) wave. A peak in the scattering cross section of such an object which depends on its polarizations means that a resonance. We can use Metamaterials for gaining an unusual scattering, i.e.huge scattering resonance. Another task of this paper, is to derive resonance conditions for this electrically small cylinder and for both polarizations.

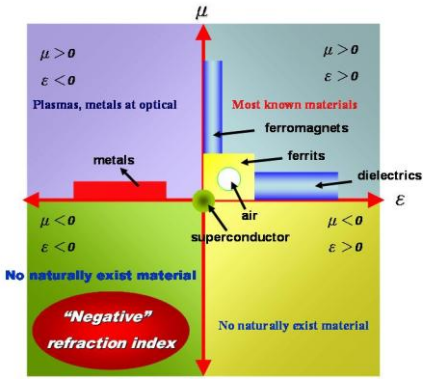

Figure .1. material classifications

In addition to above, RCS is related to not only transparency and resonance conditions, but also the direction of incidence. Therefore, we next illustrate the effect of direction incidence on RCS under transparency and resonance conditions. Numerical results are provided in the form of normalized bistatic echo widths.

II. THEORETICAL BACKGROUND FOR NORMALIZED BISTATIC ECHO WIDTH.

Consider a plane wave consider a plane wave obliquely incidence on an electrically small cylinder with the radius a and infinite length. Adopting similar procedure as in [5], the incident, transmitted and scattered electric fields can be represented respectively as follows,

$$E_z^i = E_o sin\theta_o e^{jk_o z cos\theta_o} \sum_{n=-\infty}^{+\infty} j^{-n} J_n(k_o \rho sin\theta_o) e^{jn(\varphi-\varphi_o)} \quad (1\text{-a})$$

$$E_z^t = E_o sin\theta_o e^{jk_o z cos\theta_o} \sum_{n=-\infty}^{+\infty} j^{-n} a_n{}^{TM} J_n(k_c \rho sin\theta_1) e^{jn(\varphi-\varphi_o)} \quad (1\text{-b})$$

$$E_z^s = E_o sin\theta_o e^{jk_o z cos\theta_o} \sum_{n=-\infty}^{+\infty} j^{-n} c_n^{TM} H_n^{(z)}(k_o \rho sin\theta_o) e^{jn(\varphi-\varphi_o)} \quad (1\text{-c})$$

where $k_c = \omega\sqrt{\mu_c \varepsilon_c}$ is the wave number in the Metamaterials of the cylinder. The unknown coefficients a_n^{TM},b_n^{TM} and c_n^{TM} are determined from applying boundary conditions. For far field zone, the scattered electric field is obtained using the large argument approximation of Hankels and Bessels functions. Normalized bistatic echo width is then realized by the following expressions,

$$\frac{\sigma^{TM}}{\lambda_o} = \lim_{\rho\to\infty}[2\pi\rho\frac{|E_z^S|^2}{|E_z^I|^2}]/\lambda_o = \frac{2}{\pi}\frac{1}{sin\theta_o}\{|\sum_{n=-\infty}^{+\infty} c_n^{TM} e^{jn(\varphi-\varphi_o)}|^2 + \frac{1}{\eta_o^2}|\sum_{n=-\infty}^{+\infty}\tilde{c}_n^{TM} e^{jn(\varphi-\varphi_0)}|^2\} \quad (2)$$

Likewise, the unknown coefficient, $\tilde{c}_n$, are obtained by applying BC. Under consideration at normally condition, : i.e, $\varphi = 0\ or\ \theta_o = 90$ the equation(1)to become changed into equation (2) as follows,

$$\frac{\sigma^{TM}}{\lambda_o} = \frac{2}{\pi}|\sum_{n=-\infty}^{+\infty} c_n^{TM} e^{jn(\varphi-\varphi_o)}|^2 \quad (3)$$

where c_n^{TM}, is:

$$c_n^{TM} = \frac{\zeta J_n(ka)\acute{J}_n(K_o a) - \acute{J}_n(Ka)J_n(K_o a)}{\acute{J}_n(ka)H_n^{(2)}(k_o a) - \zeta J_n(ka)H'^{(2)}_n(k_o a)} \quad (4)$$

where $\zeta = \sqrt{\frac{\mu_c\,\varepsilon_o}{\mu_o\,\varepsilon_c}}$

The procedure for TE^z polarization is the same as that of TM^z polarization, except for having electric fields replaced by magnetic fields and applying corresponding boundary conditions. Thus the formulations of RCS remain the same except for c_n^{TE} , which is found by the following form,

$$c_n^{TE} = \frac{J_n(ka)\acute{J}_n(k_o a) - \zeta \acute{J_n}(ka)J(k_o a)}{\zeta \acute{J}_n(ka)H_n^{(2)}(k_o a) - J_n(ka)H'^{(2)}_n(k_o a)} \quad (5)$$

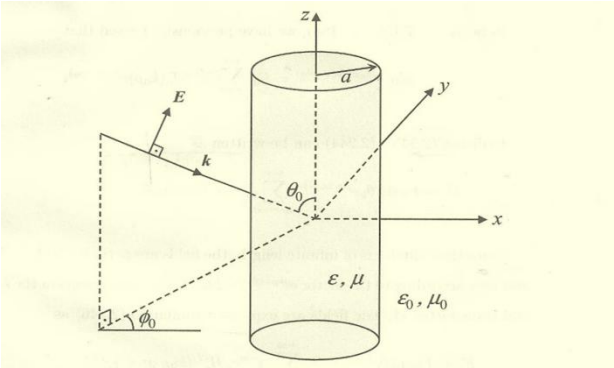

Figure .2. Uniform plane wave obliquely incident on a Metamaterials cylinder: TM^z Polarization

III. TRANSPARENCY FOR ELECTRICALLY SMALL CYLINDER

The transparency conditions for an electrically small cylindrical is derived, for both polarizations by setting the numerator of the scattering coefficients, given in the equations (4) , (5) , to zero. In the sub-wavelength limit, assuming |k|a<<1 and k_oa<<1 and utilizing the small argument forms of Bessel and Hankel functions, the following transparency conditions are obtained as follows,

$$c_n^{TM} = 0 \longrightarrow \zeta k = k_o \longrightarrow \mu_c = \mu_o \quad (6)$$

$$c_n^{TE} = 0 \longrightarrow \zeta k_o = k \longrightarrow \varepsilon_c = \varepsilon_o \quad (7)$$

Equations (5) and (6), obviously show the best conditions for the drastic scattering reduction. For TM polarization, in order to get results using of the DPS or MNG materials are concluded. Furtheremore, for TE polarization utilizing of the DPS or ENG materials are inferred as we have indicated that its derivation in appendix A and B.

IV. RESONANT ELECTRICALLY SMALL CYLINDER

The resonance condition for an electrically small cylindrical scattered is derived, for both polarizations, by setting the denominator of the scattering coefficients, given in equations (4) , (5) , to zero. This results in the maximum RCS and yields the following resonance conditions:

$$c_n^{TM} = \infty \longrightarrow -\zeta k = k_o \longrightarrow \mu_c = -\mu_o \quad (8)$$

$$c_n^{TE} = \infty \longrightarrow \zeta k_o = -k \longrightarrow \varepsilon_c = -\varepsilon_o \quad (9)$$

Equations (8) and (9) , explicitly denote the enormous scattering in comparison to length of the given objects. For TM polarization, for the best result employing the MNG and DNG materials are realized. In addition to, for TE polarization applying the ENG and DNG materials for the best results are understood as we have calculated in appendix C and D.

The major restrictions on using metallic structures are their conductivity loss and difficulties of fabrications. Moreover, most of the known such materials have inherent anisotropic peculiarities and narrow band width resonance.

The merits of employing mere dielectric Metamaterials in comparison with metallic materials are feasibility for fabrication, having no metallic loss, and designing by means of isotropic Metamaterials. In order to get results and high efficiency, the Metamaterials have received a majority of candidates.

V. NUMERICAL RESULTS

Due to gain further insights into these conditions, here some numerical results are fulfilled by matlab simulations. Our numerical computations rely on the analytical extractions shows that transparency conditions for TE polarization are achieved using of DPS and ENG materials. Moreover, the transparency conditions for TM polarization are gained using DPS and MNG materials. Figure.2.

a)

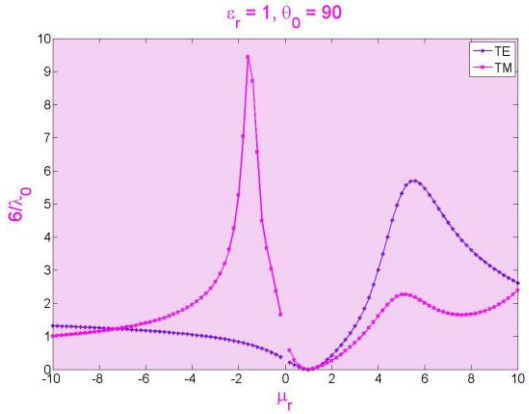

b)

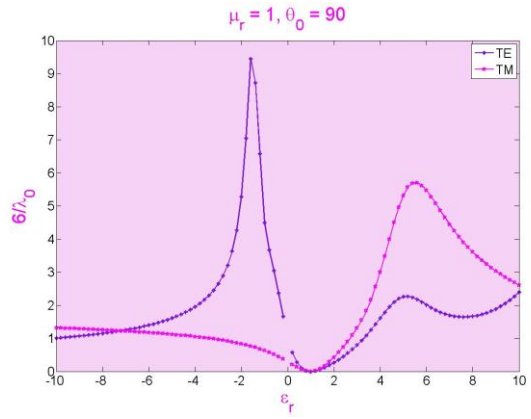

Figure .3. Normalized monostatic echo width of cylinder (a=5mm, f=1GHz) for transparency conditions or RCS minimization.

a)

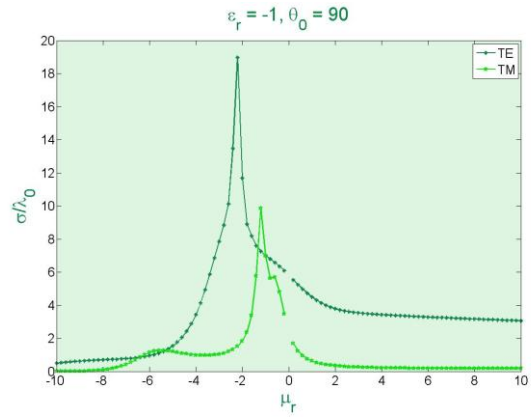

b)

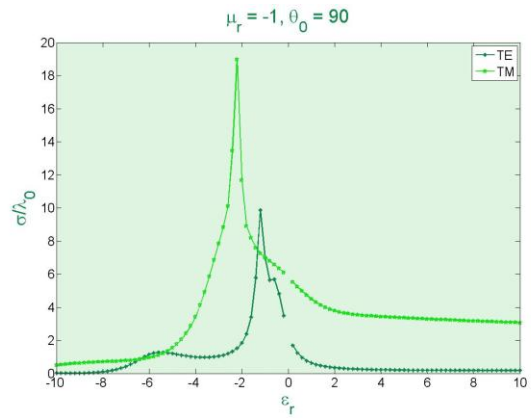

Figure .4. Normalized monostatic echo width of Metamaterial cylinder (a=5mm , f=1GHz) for resonance condition or RCS maximization.

Moreover, for TE polarization the resonance condition are gained by Metamaterials and ENG materials. Also, for TM polarization the resonance conditions are obtained by Metamaterials and MNG materials. Figure (3).

Furthermore, the monostatic echo widths are perfectly continuous when the medium changes to ENG or MNG from DPS or DNG, except in a very small interval where μ or ε are near to zero.

Figure .5 depicts the bistatic normalized echo widths inclusive of transparency and resonance conditions for TE polarization. Under transparency phenomena, Figure .5-a, the maximum RCS has occurred dramatically in the incidence direction, i.e. $\varphi=0^{\circ}$, after that in the backscattering direction, i.e. $\varphi=180^{\circ}$, However, under resonance condition, Figure .5-b, the minimum RCS has happened in the both directions and almost at $\varphi=90^{\circ}$. Therefore, the values of RCS is not only depend on the backscattering direction, but also on the incidence direction.

a)

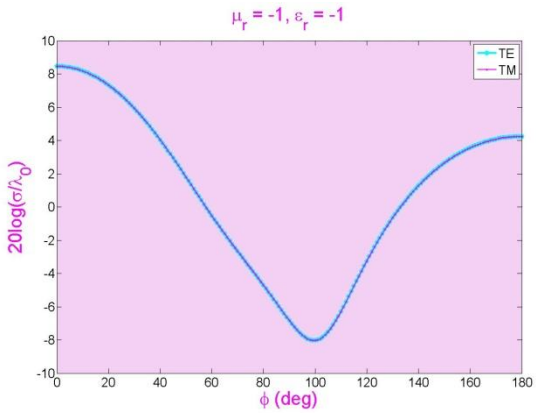

b)

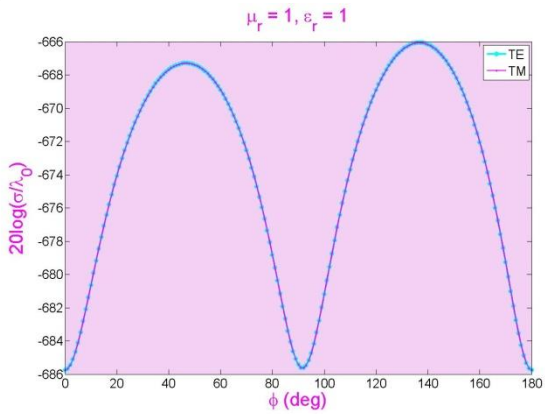

Figure. 5. Normalized bistatic echo widths for (a) DPS materials (b) Metamaterials.

VI. CONCLUSION

The goal of this paper, as we have elucidated, is to provide a comprehensive investigation of the given materials for an electrically small cylinder to achieve the best invisibility and resonance conditions. For the given object, $\mu_c = \mu_o$ has derived as the transparency condition for TM polarization which is yielded to utilize the MNG and DPS materials. Furthermore, $\varepsilon_c = \varepsilon_o$ has calculated for the best result of resonance condition of TE polarization which is achieved to use the ENG and DPS materials. On the other hand, $\mu_c = \mu_o$has extracted as the result of huge scattering for TM polarization which applying of the MNG and DNG materials is concluded. Besides, $\varepsilon_c = \varepsilon_o$has computed for resonance

condition of TE polarization which employing of ENG and DNG materials are inferred.

The bistatic echo widths is illustrated for TE polarization under transparency and resonance conditions through the computer simulation. The clear inference shows the dependency of maximum RCS on both incidence and backscattering directions.

VII. APPENDIX

A: The derivation of transparency condition for TE polarization is as follows,

$$c_n^{TE} = 0 \rightarrow J_n(ka)\acute{J}_n(k_o a) - \zeta \acute{J_n}(ka)J(k_o a) = 0 \quad (10)$$

Under consideration of |k|a<<1 and $k_o a$<<1 conditions we could use the approximation of Bessel functions as follows,

$$\frac{1}{n!}\left(\frac{ka}{2}\right)^n \times \frac{1}{2}\frac{1}{(n-1)!}\left(\frac{k_0 a}{2}\right)^{n-1} = \zeta \times \frac{1}{2}\frac{1}{(n-1)!}\left(\frac{ka}{2}\right)^{n-1} \times \frac{1}{n!}\left(\frac{k_0 a}{2}\right)^n \quad (11)$$

By simplifying the above equation we have the form,

$$\zeta K_0 = K \quad (12)$$

By substituting the values of K and K_0we can derivate the bellow form,

$$\varepsilon_c = \varepsilon_o. \quad (13)$$

B: The extraction of transparency condition for TM polarization is,

$$c_n^{TM} = 0 \rightarrow \zeta \acute{J}_n(\kappa a)J_n^{'}(k_o a) - J_n^{'}(ka)J_n(k_o a) = 0 \quad (14)$$

Under the similar assumption in appendix A and employing the approximation of Bessel functions we can writ the following equation,

$$\zeta \times \frac{1}{n!}\left(\frac{ka}{2}\right)^n \times \frac{1}{2}\frac{1}{(n-1)!}\frac{(k_0 a)^{n-1}}{2} = \frac{1}{2}\frac{1}{(n-1)!}\left(\frac{ka}{2}\right)^{n-1} \times \frac{1}{n!}\frac{(k_0 a)^n}{2} \quad (15)$$

By simplifying the last equation, the bellow equation would be found,

$$\zeta k = k_0 \quad (16)$$

By substituting the values of K and K_0, the following result would be concluded,

$$\mu_c = \mu_0 \quad (17)$$

C: The extraction of resonance condition for TE polarization is,

$$c_n^{TE} \rightarrow \infty \rightarrow \zeta \acute{J}_n(ka)H_n^{(2)}(k_o a) - J_n(ka)H'^{(2)}_n(k_o a) = 0 \quad (18)$$

Based on the assumption in appendix A we could apply the approximation of Hankel functions as follows,

$$\zeta \times \frac{1}{2}\frac{1}{(n-1)!}\left(\frac{ka}{2}\right)^{n-1} \times j\left(\frac{2}{k_0 a}\right)^n \frac{(n-1)!}{\pi} = \frac{1}{n!}\left(\frac{ka}{2}\right)^n \times (-j)\frac{2^n}{\pi}\frac{n!}{(k_0 a)^{n+1}} \quad (19)$$

By simplifying the above relationships we have the equations,

$$\zeta K_0 = -K \quad (20)$$

By substituting the values of K and K_0 we can extract the following equation,

$$\varepsilon_c = -\varepsilon_o. \quad (21)$$

D: The derivation of resonance condition for TM is as follow polarization,

$$c_n^{TM} \rightarrow \infty \rightarrow \acute{J}_n(ka)H_n^{(2)}(k_o a) - \zeta J_n(ka)H'^{(2)}_n(k_o a) = 0 \quad (22)$$

According to the supposition in Appendix A and applying the approximation of Bessel functions, the following equation would be written,

$$\frac{1}{2} \times \frac{1}{(n-1)!}\left(\frac{ka}{2}\right)^{n-1} \times j\left(\frac{2}{k_0 a}\right)^n \frac{(n-1)!}{\pi} = \zeta \frac{1}{n!}\left(\frac{ka}{2}\right)^n (-j)\frac{2^n}{\pi}\frac{n!}{(k_0 a)^{n+1}} \quad (23)$$

By the simplifying the last equation, the following expression could be realized,

$$K_0 = -\zeta K \quad (24)$$

By substituting the values of K and K_0 the bellow result could be concluded,

$$\mu_c = -\mu_0 \quad (25)$$

VIII. REFERENCES

[1] A. Alú and N. Engheta, "Achieving transparency with plasmonic ad coatings, " phys. Rev. E, vol.72, pp. 01662311-9, July 2005.

[2] A. Alú and N. Engheta, "Cloaking and transparency for collections of particles with Metamaterial and plasmonic," Optics Express 7578, vol,IS, No.12, 11 June 2007.

[3] E.Irci and Vakur B. Ertürk," Investigation of Metamaterials coated conducting cylinders for achieving transparency and maximizing Radar Cross Section," IEEE Xplore, 21 October 2008.

[4] Joshua A.Grodon and Richard W.Ziolkowski, "CNP optical Metamaterials, "OPTICS EXPRESS, vol.16,No.9, 28 April 2008.

[5] Grdinc Irci, "Wave propagation in Metamaterial structures and retrieval of homogenization parameters," A Thesis engineering and sciences of bilkend university in partial fulfill ent of the equirements for the degree of muster of science, " August 2007.

[6] Andrea Alú, Nader Engheta, A. Erentok and Richard W.Ziolkowski,"single-negative, double-negative, and Low – index Metamaterials and their electromagnetic applications,"IEEE Transactions on Antennas and Propagation Magazine, vol.49, page 23-36, February 2004.

[7] Akram Ahmadi,"Metamaterials demonstrating focusing and radiation characteristics applications, " Electrical Engineering Dissertations, 01 January 2010.

[8] ____, "Resonances in sub-wavelength cylindrical structures made of pairs of double-negative and double-negative or epsilon-negative and mu-negative coaxial shells," in Proc. Int. Conf. on Electromagnetics in Advanced Advanced Applications. Torino, Italy. Sep. 8-12 2003, pp. 435-438.

[9] ____,"Sub-wavelength resonant structures containing double-negative (DNG) or single-negative (SNG) media: Planar, cylindrical ad spherical cavities, waveguides, and open

scatteres," Progress in Electromagnetic Research Symp., Waikiki, Hi, Oct. 13-16 2003, p. 12.
[10] C. A. Balanis, Advanced Engineering Electromagnetics. New York: Wiley, 1989, ch. 11, pp. 595-596.
[11] C. Li and Z. Shen, "Electromagnetic scattering by a conducting cylinder coated with Metamaterials," Progress In Electromagnetics Research, vol. 42, pp. 91-105, 2003.

Moment Methods in Spectral Domain for Crossed-dipole Frequency Selective Surface

Somayeh Komeylian[1] and Farrokh Hojjat-Kashani[2]
[1] Electrical and Engineering Department , Islamic Azad University South , Tehran, Iran
[2] Electrical and Engineering Department, University of Science and Technology, Tehran, Iran
Email: somayeh@komeylian.com
Email: kashani@iust.ac.ir

Abstract

The Moment Method is a full-wave analysis with the superior validity in practice as well as simplicity in its analysis which it would be offered for analyzing Frequency Selective Surface. The main advantage of this method is that the reflection and transmission coefficient could be computed efficiently for any stratified structure.
In this paper, we aim to model crossed-dipole Frequency Selective Surface by the Method of Moments in the spectral domain.
To ascertain the process of the extraction of the total reflection coefficient, we exploit the stratified layers in a structure which is employed in an antenna reflector.
Moreover, to show a good estimate of the induced surface current density on the Frequency Selective Surface, we have expressed the basis functions which are relevant to the shape of the patches.

Introduction

To predict electromagnetic scattering of the periodic structures have been studying for over a century now. The Method of Moments (MoM) have received the great majority of the candidates for the planar periodic multilayer structures.
To elucidate the process of the derivation of the total reflection coefficient, here, it is supposed that a single layer frequency selective surface which is embedded in the stratification of the layers as is depicted in Figure. 1.

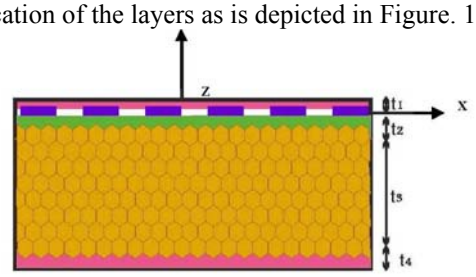

Name of material	Thickness (mm)	Relative permittivity	Usage
Kevlar	t_1=0.05	4.1-j0.024	Protective film
Kapton	t_2=0.18	3.2-j0.02	Dielectric substrate
Kevlar honeycomb	t_3=7.5	1.05	Dielectric honeycomb structure
Kevlar	t_4=0.18	4.1-j0.024	2th protective layers

Figure .1. The configuration of dielectric layers used in FSS.

The shape of patch element is based on controlling the frequency response of the surface. We interest in starting with the crossed–dipole Frequency Selective Surface which is considered to be periodic in the non-orthogonal

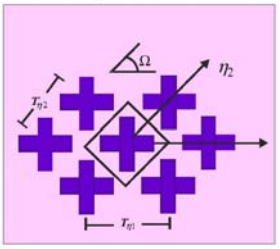

Figure.2. Based on the spectral-domain method of moments.

coordinate system, i.e. η_1 and η_2, with the periodicities $T_{\eta 1}$ and $T_{\eta 2}$ respectively. Therefore, this structure consists of the periodic, sub-section elements to generate the whole of the Frequency Selective Surface which each of them name "unit cell".

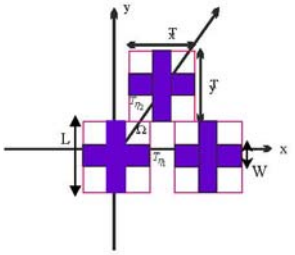

Figure.3. common geometry of two demintional unit cell.

Besides, many useful conclusions can be deduced from the transformation properties of various observables under rotations. Therefore it would be offered the rotation of the axes in considerable detail in this article.
On the other hand, the disadvantage of the MoM is the low speed in its convergence in both the basis functions and the spectral Green's functions.Hence, we have developed the asymptotic behavior of the of the Green's functions.
Moreover in order that one of the components of the scattered electric field is resulted from the reflected field which crossed-dipole elements have removed, it may interest you to know that the extraction of the reflection coefficient in this situation. Therefore we have maintained its derivation.
Furthermore the current density on the whole of the two-dimensional Frequency Selective Surface will be expanded by a series with a set of complex-valued weight coefficient, i.e. $\{c_j\}$.

Therefore we have exploited the spectral Galerkin equation to gain this set of complex-valued weight coefficient.

In this corresponding, we persevere in our efforts to ascertain how the modal of Frequency Selective Surface will be extracted by Method of Moment in spectral domain.

I. Extraction of the Green's functions

The approach of this stage relies on the transverse equivalent transmission line for a spectral wave.

It is necessary to rotate through angle ϕ, carrying ou into ox, due to following considerations: (1) in order to get the satisfaction of phase matching condition at every point on the boundary planes, (2) furthermore, in the new system, both **E** and **H** will maintain merely one tangential component at the boundary planes, regardless of polarization, (3) when the current sheet J_u or J_v is appeared at the coordinates, one of its components is on the rise to a field which TE-to–W, (H_w, E_y, H_x), and the other component is on the rise to a field which is TM-to-W, (E_w, E_x, H_y). In the other words, J_x current generates exactly the TM field and J_y current produces only the TE fields. Figure 4.

a)

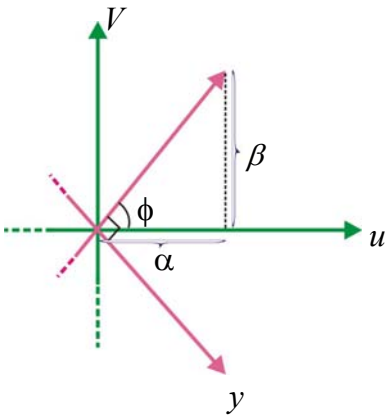

b)

$$\begin{bmatrix}\hat{x}\\ \hat{y}\end{bmatrix}=\begin{bmatrix}\cos\phi & \sin\phi\\ \sin\phi & -\cos\phi\end{bmatrix}\begin{bmatrix}\hat{u}\\ \hat{v}\end{bmatrix}$$

$$\begin{bmatrix}\hat{u}\\ \hat{v}\end{bmatrix}=\begin{bmatrix}\cos\phi & \sin\phi\\ \sin\phi & -\cos\phi\end{bmatrix}\begin{bmatrix}\hat{x}\\ \hat{y}\end{bmatrix}$$

$$\hat{z}=-\hat{w}$$

Figure .4.Coordinate transformation

According to the equivalent transmission lines, the characteristic impedances in the +Z direction in ith layer are determined as follows,

$$z_{oi}^{TE}\overset{\Delta}{=}\frac{-E_y}{H_x}=\frac{j\omega\mu_o}{\gamma_i} \quad (1)$$

$$z_{oi}^{TM}\overset{\Delta}{=}\frac{E_x}{H_y}=\frac{\gamma_i}{j\omega\varepsilon_{ri}\varepsilon_o} \qquad i=1,2,3,4 \quad (2)$$

where $\gamma_i=\sqrt{\alpha^2+\beta^2-\varepsilon_{ri}k_0^2}$ is the propagation constant in +Z direction in the ith layer, i.e. i=1,2,3,4.

On the other hand, the surface current density $J=(\hat{x}\cos\phi+\hat{y}\sin\phi)e^{j(\alpha u+\beta V)}$ could be utilized as satisfaction of the following boundary conditions,

(i) tangential electric field is continuous at z=0,

$$\hat{z}\times\left[\mathbf{E}(0^+)-\mathbf{E}(0^-)\right]=0 \quad (3)$$

(ii) In order that the presence of the surface current density, i.e.**J**, the tangential magnetic field is discontinuous at z=0,

$$\hat{z}\times\left[\mathbf{H}(0^+)-\mathbf{H}(0^-)\right]=\mathbf{J} \quad (4)$$

By expansion of the equation (4) in the Cartesian coordinate, the following expressions can be obtained,

$J_y=(H_x(0^+)-H_x(0^-))$ (5)

$J_x=-(H_y(0^+)-H_y(0^-))$ (6)

Moreover, a shunt current source which is applied in the equivalent transmission line models is owing to the discontinuity in tangential magnetic field. For TE polarization by applying equation and Kirchoff's current law at the place of the source will be gained by the following equations,

BC: $J_y=H_x(0^+)-H_x(0^-)$ (7)

KCL: $I_s=I(0^+)+I(0^-)$ (8)

By comparison the equations (7) and (8) with $\mathbf{J}, I_s=\sin\phi$ can be realized. On the one hand, v=I_s z_{in}^{TE} and $E_y^{TE}\leftrightarrow -V, E_y^{TE}$ could be obtained as follows,

$$E_y^{TE}=-z_{in}^{TE}\sin\phi e^{j(\alpha u+\beta V)}=E_{y_o}^{TE}e^{j(\alpha u+\beta V)} \quad (9)$$

The same as TE polarization, for TM polarization would be found as follows,

BC: $-J_x=H_y(0^+)-H_y(0^-)$ (10)

KCL: $I_s=I(0^+)+I(0^-)$ (11)

In the similar to the procedure of the TE polarization, $I_s=-\cos\phi$ can be gained by comparing the equations (10) and (11) with J. since V=$I_s\times z_{in}^{TM}$ and $E_x^{TM}\leftrightarrow +V, E_y^{TM}$ can be computed as follows,

$$E_y^{TM}=-z_{in}^{TM}\cos\phi e^{j(\alpha u+\beta V)} \quad (12)$$

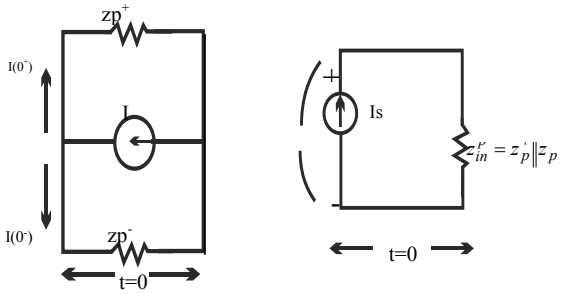

Figure.5. Equvalent transmission lines subscript 'p' signifies that the type of polaritations.

Now, the TE and TM components should be comprised to gained total electric field by the following equations,

$$E_u=(E_{y_o}^{TE}\sin\phi+E_{x_o}^{TM}\cos\phi)e^{j(\alpha u+\beta V)}$$

$$=-(z_{in}^{TE}\sin^2\phi+z_{in}^{TM}\cos^2\phi)e^{j(\alpha u+\beta V)} \quad (13\text{-a})$$

$$E_V=(-E_{y_o}^{TE}\cos\phi+E_{x_o}^{TM}\sin\phi)e^{j(\alpha u+\beta V)}$$

$$=+(z_{in}^{TE}-z_{in}^{TM})\sin\phi\cos\phi\ e^{j(\alpha u+\beta V)} \quad (13\text{-b})$$

On the one hand, transform relationship between the scattered field and the surface current is defined the form,

$$\begin{bmatrix}\tilde{E}_u(\alpha,\beta)\\ \tilde{E}_V(\alpha,\beta)\end{bmatrix}=\begin{bmatrix}\tilde{G}_{uu}(\alpha,\beta) & \tilde{G}_{uV}(\alpha,\beta)\\ \tilde{G}_{Vu}(\alpha,\beta) & \tilde{G}_{VV}(\alpha,\beta)\end{bmatrix}\begin{bmatrix}\tilde{J}_u(\alpha,\beta)\\ \tilde{J}_V(\alpha,\beta)\end{bmatrix} \quad (14)$$

By substituting the equations of the electric fields and surface current into the above definition would be computed the following equations,

$$\widetilde{G}_{uu} = \frac{\widetilde{E}_u}{\widetilde{J}_u} = -\left(z_{in}^{TE}\sin^2\phi + z_{in}^{TM}\cos^2\phi\right) \quad (15\text{-a})$$

$$\widetilde{G}_{Vu} = \frac{\widetilde{E}_v}{\widetilde{J}_u} = +\left(z_{in}^{TE} - z_{in}^{TM}\right)\sin\phi\cos\phi \quad (15\text{-b})$$

$$\widetilde{G}_{uV} = \frac{\widetilde{E}_u}{\widetilde{J}_V} = +\left(z_{in}^{TE} - z_{in}^{TM}\right)\sin\phi\cos\phi \quad (15\text{-c})$$

$$\widetilde{G}_{VV} = \frac{\widetilde{E}_V}{\widetilde{J}_V} = -\left(z_{in}^{TE}\cos^2\phi - z_{in}^{TM}\sin^2\phi\right) \quad (15\text{-d})$$

where: $z_{in}^{TE} = z_{oo}^{TE} \,||\, z_{oo}^{TE} = \dfrac{j\omega\mu}{2\gamma_o}$ (16-a)

$$z_{in}^{TE} = z_{oo}^{TM} \,||\, z_{oo}^{TM} = \frac{\gamma_o}{2j\omega\varepsilon_o} \quad (16\text{-b})$$

and z_{oo}^{TE} *and* z_{oo}^{TM} are the characteristic impedances for TE and TM polarizations of the plane wave fields in free space with propagation constant γ_o, i.e. $\varepsilon_r = 1$.

Note: the impedances z_P^+ and z_P^-, in Figure 5., could be determined with regarding to the Transmission Line theory by the following expressions,

$$z_P^+ = z_{01}^P \frac{z_{01}^P + z_{oo}^P \coth\gamma_1 t_1}{z_{oo}^P + z_{01}^P \coth\gamma_1 t_1} \quad (17\text{-a})$$

$$z_P^- = z_{02}^P \frac{z_{02}^P + z_{oo}^P \coth\gamma_2 t_2}{z_{oo}^P + z_{02}^P \coth\gamma_2 t_2} \quad (17\text{-b})$$

The total input impedance seen by source, in Figure. 5, could be obtained by combining the z_P^+ with z_P^-, parallely.

II. Gaining the asymptotic behavior of the Green's functions

The asymptotic expressions for characteristic impedances which are based on Transmission Line theory can be computed under the following considerations, i.e. $\gamma_p^2 >> |\varepsilon_{ri}|K_o^2$ and $\gamma_p t_i > \pi$ for each finite thickness of layer. These considerations result in the forms,

$$\gamma_i \to \gamma_p \quad (18)$$

$$\text{Coth } \gamma_i t_i \to 1 \quad (19)$$

Therefore,

$$z_{oi}^{TE} \to \frac{j\omega\mu}{\gamma_\rho} \quad (20)$$

$$z_{oi}^{TM} \to \frac{\gamma_p}{j\omega\varepsilon_{ri}\varepsilon_o} \quad (21)$$

The input impedances resulted from (20) and (21) as follows,

$$z_{in}^{TM} \to \frac{j\omega\mu}{2\gamma_\rho} \quad (22)$$

$$z_{in}^{TM} \to \frac{\gamma_\rho}{j\omega\varepsilon_o(\varepsilon_{r^+} + \varepsilon_{r^-})} \quad (23)$$

where ε_{r+} and ε_{r^-} are the relative permittivities of two layers.

By substituting the asymptotic expressions (22) and (23) into the equations (15) the asymptotic behavior of the Green's functions are obtained as follows,

$$\widetilde{G}_{uu} = \frac{1}{j\omega\varepsilon_o\sqrt{\alpha^2+\beta^2}}\left[\frac{-k_0^2\beta^2}{2(\alpha^2+\beta^2)} + \frac{\alpha^2}{(\varepsilon_{r^+}+\varepsilon_{r^-})}\right] \quad (24\text{-a})$$

$$\widetilde{G}_{uV} = \frac{-\alpha\beta}{j\omega\varepsilon_o\sqrt{\alpha^2+\beta^2}}\left[\frac{k_0^2}{2(\alpha^2+\beta^2)} + \frac{1}{(\varepsilon_{r^+}+\varepsilon_{r^-})}\right] \quad (24\text{-b})$$

$$\widetilde{G}_{VV} = \frac{-1}{j\omega\varepsilon_o\sqrt{\alpha^2+\beta^2}}\left[\frac{-k_0^2\alpha^2}{2(\alpha^2+\beta^2)} + \frac{\beta^2}{(\varepsilon_{r^+}+\varepsilon_{r^-})}\right] \quad (24\text{-C})$$

The asymptotic expansions of the Green's functions are necessary to ascertain the total reflection coefficient. The merits of the usage of the asymptotic behavior of the Green's functions, instead of $G(\alpha_n, \beta_{mn})$, are both accuracy and speed to its convergence.

III. Computations of the reflected field

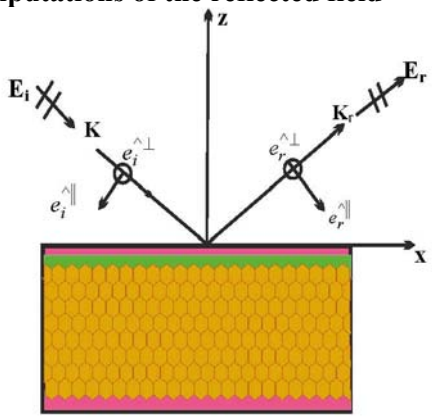

Figure.6. reflected fields from the surface whose the crossed dipoles are removed.

As the Figure. 6 shows the incident fields for both polarizations are exposed by the following expressions,

$$\mathbf{E}_i^{TE}(\mathbf{r}) = E_i\frac{\mathbf{k}\times\hat{z}}{|\mathbf{k}\times\hat{z}|}e^{j\mathbf{k}.\mathbf{r}} = E_i\hat{e}_i^{\perp}e^{j\mathbf{k}.\mathbf{r}} = E_o(\hat{x}\sin\phi_i - \hat{y}\cos\phi_i)e^{j\mathbf{k}.\mathbf{r}} \quad (25)$$

$$E_i^{TM}(r) = E_i\frac{k\times(k\times\hat{z})}{|k\times(k\times\hat{z})|}e^{jk.r} = E_o\hat{e}_i^{II}e^{jk.r}$$

$$= E_i(\hat{x}\cos\theta_i\cos\phi_i + \hat{y}\cos\theta_i\sin\theta_i - \hat{z}\sin\theta_i)e^{j\mathbf{k}.\mathbf{r}} \quad (26)$$

The unit vectors for both polarizations, TE and TM, are ascertained as follows:

$$e_r^{\perp} = -\hat{e}_i^{\perp} \quad (27)$$

$$\hat{e}_r = (2\hat{z}\hat{z} - \overline{\overline{I}}).\hat{e}_i^{\parallel} \quad (28)$$

Where $\overline{\overline{I}}$ is the three-dimensional unit dyadic,i.e. $\overline{\overline{I}} \overset{\Delta}{=} \hat{x}\hat{x} + \hat{y}\hat{y} + \hat{z}\hat{z}$, The reflected fields result from the equations (27) and (28) the forms,

$$\mathbf{E}_r^{TE}(\mathbf{r}) = E_o(-\hat{a}_x\sin\phi_i + \hat{a}_y\cos\phi_i)\Gamma^{TE}e^{j\mathbf{k}_r.\mathbf{r}} \quad (29)$$

$$\mathbf{E}_r^{TM}(\mathbf{r}) = E_o(-\hat{a}_x cin\theta_i cin\phi_i - \hat{a}_y\cos\theta_i\sin\phi_i - \hat{a}_z\sin\theta_i)\Gamma^{TM}e^{j\mathbf{k}_r.\mathbf{r}} \quad (30)$$

The wave propagation in the reflected direction is defined as follows,

$$\mathbf{k}_r \overset{\Delta}{=} (\overline{\overline{I}} - 2\hat{z}\hat{z}).\mathbf{k} \quad (31)$$

where **k** is the wave vector of the incident plane wave, $\mathbf{k} = K_o(\hat{x}\sin\theta\cos\phi + \hat{y}\sin\theta\sin\phi + \hat{z}\cos\theta)$ and $K_o = \omega\sqrt{\mu_o\varepsilon_o}$, and Γ^P is the reflection coefficient of the structure which is shown in Figure.6. It could be determined by the Theory Transmission Line.

IV. Fourier Transform of the current density surface

Based on Figure.7 the induced current density on the whole Frequency Selective Surface, i.e. J(x,y), would be written in the following expression,

where $\mathbf{J}_o(x,y)$ is the current density on a single patch of Frequency Selective Surface and ,

$$k_x = k_o \sin\theta_i \cos\phi_i \qquad (33\text{-a})$$

$$k_y = k_o \sin\theta_i \sin\phi_i \qquad (33\text{-b})$$

According to the definition of Fourier transform which is given by the following equation,

$$\tilde{\mathbf{f}}(\alpha,\beta) = \int_{-\infty}^{+\infty}\int_{-\infty}^{+\infty} \tilde{f}(x,y)\, e^{-j(\alpha x+\beta y)} dxdy \qquad (34)$$

The Fourier transform of J(x,y) is gained as follows,

$$\tilde{\mathbf{J}}(\alpha,\beta) = \tilde{\mathbf{J}}_o(\alpha,\beta)\frac{2\pi}{T_{\eta_1}}\frac{2\pi}{T_{\eta_2}\sin\Omega}\sum_{P=-\infty}^{+\infty}\sum_{q=-\infty}^{+\infty}\delta(\alpha-\alpha_p)(\beta-\beta_{pq}) \qquad (35)$$

where $$\alpha_P = \frac{2\pi P}{T\eta_1} + k_x \qquad (36)$$

$$\beta_{Pq} = \frac{2\pi q}{T_{\eta_2}\sin\Omega} - \frac{2\pi P}{T_{\eta_1}}\cot\Omega + k_y \qquad (37)$$

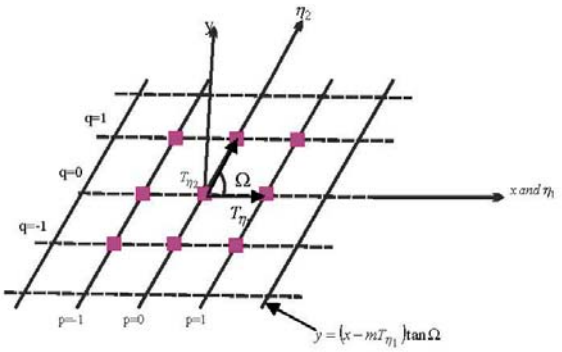

Figure.7. A two dimensional periodic FSS

Therefore, if a plane wave field is impinged on the Frequency Selective surface, the scattered field is including the infinite numbers of the discrete plane waves with the wave numbers α_ρ and β_{pq} which are transverse phase constants.

V. The spectral-Galerkin equation

The spectra domain Method of the Moments procedure have utilized as the solution in this stage.

First of all, $\mathbf{J}_o(\alpha,\beta)$ could be extended by choosing the proper series of linearly independent functions, i.e.$\{\mathbf{j}_j\}$, in the following expression:

$$\begin{bmatrix}\tilde{J}_{xo}\\ \tilde{J}_{yo}\end{bmatrix} = \sum_{j=1}^{I} c_j \begin{bmatrix}\tilde{J}_{xj}\\ \tilde{J}_{yj}\end{bmatrix} \qquad (38)$$

By substituting the equation (38) into the equation (14) the scattered electric field is determined as follows,

$$\begin{bmatrix}E_x^S\\ E_y^S\end{bmatrix} = \frac{1}{4\pi^2}\sum_{j=1}^{I} c_j \int_{-\infty}^{+\infty}\int_{-\infty}^{+\infty}\begin{bmatrix}\tilde{G}_{xx} & \tilde{G}_{xy}\\ \tilde{G}_{yx} & \tilde{G}_{yy}\end{bmatrix}\begin{bmatrix}\tilde{J}_{xj}\\ \tilde{J}_{yj}\end{bmatrix}\Pi(\alpha,\beta)\, e^{j(\alpha u+\beta V)} d\alpha\, d\beta \qquad (39)$$

In order that the frequency selective surface is finite in two dimensions, the value of $\Pi(\alpha,\beta)$ is equal to one.

Moreover, an inner product for two dimensional elements would defined in the form,

$$< f.g >= \int_{-\infty}^{+\infty}\int_{-\infty}^{+\infty} f^T(x,y) g(x,y) dxdy \qquad (40)$$

where the superscript "T" indicates that transpose. Now, we intend to employ the inner product on the scattered electric field in the equation (39), therefore,

$$< \mathbf{j}_i^*, \mathbf{E}^S >= \frac{1}{4\pi^2}\sum_{j=1}^{I} c_j \int\int \; \int\int j_i^\dagger(x,y) e^{j(\alpha x+\beta y)} dxdy\, \tilde{\mathbf{G}}(\alpha,\beta)\tilde{\mathbf{j}}_j(\alpha,\beta)\tilde{\mathbf{\Pi}}(\alpha,\beta) d\alpha\, d\beta \qquad (41)$$

where $\int j_i^\dagger(x,y) e^{j(\alpha x+\beta y)} dxdy$ is the Fourier transform of $j_i^\dagger(x,y)$, therefore, the equation (41) can be simplified to this form,

$$\frac{-1}{4\pi^2}\sum_{j=1}^{I} c_j \int_{-\infty}^{+\infty}\int_{-\infty}^{+\infty}\tilde{\mathbf{j}}_i^\dagger(\alpha,\beta)\tilde{\mathbf{G}}(\alpha,\beta)\tilde{\mathbf{j}}_j(\alpha,\beta)\tilde{\mathbf{\Pi}}(\alpha,\beta) d\alpha\, d\beta =< \mathbf{j}_i^*, \mathbf{E}_{inc} >$$

i=1,2,…,I (42)

In other words, the transform relationship between the scattered field and the surface current density has indicated in the equation (14) would be applied in the last equation.

The spectral-Galerkin equation results from this substitution as follows,

$$\frac{-1}{T_{\eta_1}T_{\eta_2}\sin\Omega}\sum_{j=1}^{M} c_j \int_{-\infty}^{+\infty}\int_{-\infty}^{+\infty}\tilde{\mathbf{j}}_i^\dagger(\alpha,\beta)\tilde{\mathbf{G}}(\alpha,\beta)\tilde{\mathbf{j}}_j(\alpha,\beta) d\alpha\, d\beta =$$

$$\int_{-\infty}^{+\infty}\int_{-\infty}^{+\infty}\mathbf{j}_i^\dagger \mathbf{E}_{inc}(x,y) dx\, dy \qquad i = 1,2,....,M \qquad (43)$$

where the superscript "†" signifies that complex conjugate transpose and M is the number of the crossed-dipole elements where are etched on the dielectric medium.

VI. Gaining the expression of the transverse electric field, i.e.x-y components

According to the spectral-domain of moment analysis relationship between the electric field at the surface $z=t_1$ and induced current at the surface z=0 is given by,

$$\begin{bmatrix}\tilde{E}_u(z=t_1)\\ \tilde{E}_V(z=t_1)\end{bmatrix} = \begin{bmatrix}\tilde{G}_{uu} & \tilde{G}_{uv}\\ \tilde{G}_{Vu} & G_{VV}\end{bmatrix}\begin{bmatrix}\tilde{J}_x(z=0)\\ \tilde{J}_y(z=0)\end{bmatrix} \qquad (44)$$

Under consideration the equations (44), (43) and (34), the expression (45) can be obtained as follows,

$$\sum_{p,q=-\infty}^{+\infty} E_{pqt} e^{-\gamma_{pqt1}} 4\pi^2\delta(\alpha-\alpha_{pq})\delta(\beta-\beta_{pq})$$

$$= \sum_{p,q=-\infty}^{+\infty} \tilde{G}(\alpha_{pq},\beta_{pq})\frac{2\pi}{T_{\eta 1}}\frac{2\pi}{T_{\eta 2}\, sin\Omega}\delta(\alpha-\alpha_{pq})\delta(\beta-\beta_{pq}) \qquad (45)$$

By comparing two sides of the equation (45) the transverse electric field, i.e. x-y components, would be realized in the form,

$$\mathbf{E}_{pqt} = \frac{e^{\gamma_{pq} t_1}}{T_{\eta_1} T_{\eta_2} \sin\Omega} \tilde{\mathbf{G}}(\alpha_{pq}, \beta_{pq}) \tilde{\mathbf{J}}_o(\alpha_{pq}, \beta_{pq}) \quad (46)$$

where subscript "t" , signifies that transverse component.

VII. Basis functions

Basis functions are employed to show the approximation of the induced surface current density on the Frequency Selective Surface. According to the crossed-dipole shape, Figure. 3, the basis functions can be realized in these forms,

$$\mathrm{j}_{xk}(x,y) = \sin\left[\frac{k\pi}{L}(x+\frac{L}{2})\right] P_x(-\frac{L}{2},\frac{L}{2}) P_y(-\frac{w}{2},\frac{w}{2})$$

k=1,2,…,M (47-a)

$$\mathrm{j}_{yk}(x,y) = \sin\left[\frac{k\pi}{L}(x+\frac{L}{2})\right] P_x(-\frac{w}{2},\frac{w}{2}) P_y(-\frac{L}{2},\frac{L}{2})$$

k=1,2,…,M (47-b)

$$\mathbf{j}_j(x,y) = \hat{x}\,\mathrm{sgn}(x)\cos(\frac{\pi x}{L}) P_x(-\frac{L}{2},\frac{L}{2}) P_y(-\frac{w}{2},\frac{w}{2}) - \hat{y}\,\mathrm{sgn}(y)\cos(\frac{\pi y}{L}) P_x(-\frac{w}{2},\frac{w}{2}) P_y(-\frac{L}{2},\frac{L}{2}) \quad (47-c)$$

Based on the Fourier transform, the currents equations would be found as follows,

$$\tilde{\mathbf{j}}_{xk}(\alpha,\beta) = \frac{-jLw}{2} e^{j(\frac{k\pi}{2})} \frac{\sin(\beta\frac{w}{2})}{\beta\frac{w}{2}} \left\{ \frac{\sin(\frac{k\pi}{2}-\frac{\alpha L}{2})}{\frac{k\pi}{2}-\frac{\alpha L}{2}} - (-1)^K \frac{\sin(\frac{k\pi}{2}+\frac{\alpha L}{2})}{\frac{k\pi}{2}+\frac{\alpha L}{2}} \right\}$$

i=1,2,…,M (48-a)

$$\tilde{\mathrm{j}}_{yk}(\alpha,\beta) = \frac{-jLw}{2} e^{j(\frac{k\pi}{2})} \frac{\sin(\alpha\frac{w}{2})}{\alpha\frac{w}{2}} \left\{ \frac{\sin(\frac{k\pi}{2}-\frac{\beta L}{2})}{\frac{k\pi}{2}-\frac{\beta L}{2}} - (-1)^K \frac{\sin(\frac{k\pi}{2}+\frac{\beta L}{2})}{\frac{k\pi}{2}+\frac{\beta L}{2}} \right\}$$

j=1,2,…,M (48-b)

$$\tilde{\mathrm{j}}_j(\alpha,\beta) = \frac{jLw}{2} \left\{ \hat{x} \frac{\sin(\beta\frac{w}{2})}{\beta\frac{w}{2}} \left[\frac{1-\cos(\frac{\pi}{2}-\frac{\alpha L}{2})}{\frac{\pi}{2}-\frac{\alpha L}{2}} - \frac{1-\cos(\frac{\pi}{2}+\frac{\alpha L}{2})}{\frac{\pi}{2}+\frac{\alpha L}{2}} \right] - \hat{y} \frac{\sin(\alpha\frac{w}{2})}{\alpha\frac{w}{2}} \left[\frac{1-\cos(\frac{\pi}{2}-\frac{\beta L}{2})}{\frac{\pi}{2}-\frac{\beta L}{2}} - \frac{1-\cos(\frac{\pi}{2}+\frac{\beta L}{2})}{\frac{\pi}{2}+\frac{\beta L}{2}} \right] \right\} \quad (48-c)$$

Therefore, the Fourier transform can be determined in the following form,

$$\mathbf{J}_o(\alpha,\beta) = \sum_{j=1}^{M} c_j \mathbf{j}_j(\alpha,\beta) \quad (49)$$

where $\{c_j\}$ is a set of a complex–valued weight coefficient.

VIII. Computation of the total reflection coefficient of the frequency selective surface

The goal of this stage is to derivate the reflection coefficient for the Frequency Selective Surface which for the Frequency Selective Surface has illustrated in figure.1. The magnetic and electric vector potential for this structure are defined by this form,

$$\begin{Bmatrix} \mathbf{A} \\ \mathbf{F} \end{Bmatrix} = \hat{z}\, e^{j(k_x x + k_y y) + \gamma_{oo} z} \quad (50)$$

Furthermore, the whole scattered electric field will be fund in a discrete spectrum form as follows,

$$\mathbf{E}_{\mathbf{S}}(z \geq t_1) = \sum_{p,q=-\infty}^{+\infty} (\mathbf{E}_{qp} + \mathbf{E}_{oo}^{ref} \delta_{op} \delta_{oq}) e^{j(\alpha_{pq} x + \beta_{pq} y) - \gamma_{qp} z} \quad (51)$$

Based on the equation (51) the scattered field consists of two parts: (1) E_{pq}, is relevanted to the scattered field which is resulted from the induced current on the etched screen in the presence of the dielectric medium, (2) E_{00}^{ref}, the scattered field component is arisen from the reflected field f dielectric medium whose crossed-dipole elements, have removed as has clarified in the third stage.

If the scattered field splits into the its TE and TM components, z-direction electric and magnetic vector potentials will define in these expressions,

$$\mathbf{A}^S(z \geq t_1) = \hat{z} \sum_{p,q=-\infty}^{+\infty} R_{pq}^{TM} \psi_{pq}^{ref} = \hat{z} \sum_{p,q=-\infty}^{+\infty} R_{pq}^{TM} e^{j(\alpha_{pq} x + \beta_{pq} y) - \gamma_{pq} z} \quad (52)$$

$$\mathbf{F}^S(z \geq t_1) = \hat{z} \sum_{p,q=-\infty}^{+\infty} R_{pq}^{TE} \psi_{pq}^{ref} = \hat{z} \sum_{p,q=-\infty}^{+\infty} R_{pq}^{TE} e^{j(\alpha_{pq} x + \beta_{pq} y) - \gamma_{pq} z} \quad (52)$$

On the other hand, an expression for the scattered field defines in the form,

$$\mathbf{E}^{\boldsymbol{S}} = -\overline{\nabla} \times \mathbf{F}^{\boldsymbol{S}} - \boldsymbol{j\omega\mu} \mathbf{A}^{\boldsymbol{S}} + \frac{1}{\boldsymbol{j\omega\varepsilon_o}} \overline{\nabla}(\overline{\nabla}.\mathbf{A}^{\boldsymbol{S}}) \quad (53)$$

By substituting equations (46) and (47) into equation (48) in Cartesian coordinates, we can maintain the following expressions,

$$E_x^S = \sum_{p,q} \left[-j\beta_{pq} R_{pq}^{TE} - \frac{j\alpha_{pq}\gamma_{pq}}{j\omega\varepsilon_o} R_{pq}^{TM} \right] \psi_{pq}^{ref} \quad (54\text{-a})$$

$$E_y^S = \sum_{p,q} \left[+j\alpha_{pq} R_{pq}^{TE} - \frac{j\beta_{pq}\gamma_{pq}}{j\omega\varepsilon_o} R_{pq}^{TM} \right] \psi_{pq}^{ref} \quad (54\text{-b})$$

$$E_z^S = \sum_{p,q} \left[\frac{\gamma_{pq}}{j\omega\varepsilon_o} - j\omega\mu \right] R_{pq}^{TM} \psi_{pq}^{ref} \quad (54\text{-c})$$

Therefore, the entire scattered field is the form:

$$\mathbf{E}^S(z \geq t_1) = E_x^S + E_y^S + E_z^S \quad (55)$$

Now, we must set two equations (50) and (45) equally and the expression of the reflection coefficients would be resulted as follows,

$$R_{pq}^{TE} = \frac{j\left[\beta_{pq}(E_{qpx} + E_{oox}^r \delta_{op}\delta_{op}) - \alpha_{pqy}(E_{pqy} + E_{ooy}^r \delta_{op}\delta_{oq})\right]}{(\alpha_{pq}^2 + \beta_{pq}^2)} \quad (56)$$

$$R_{pq}^{TM} = \frac{j\left[\alpha_{pq}(E_{qpx} + E_{oox}^r \delta_{op}\delta_{op}) - \beta_{pqy}(E_{pqy} + E_{ooy}^r \delta_{op}\delta_{oq})\right]}{(\alpha_{pq}^2 + \beta_{pq}^2)\frac{\gamma_{pq}}{j\omega\varepsilon_o}} \quad (57)$$

Conclusion

In conclusion, we have employed to the Method of Moment in spectral domain to model the crossed-dipole Frequency Selective Surface which is involve in the following stages: (1) extraction of the Green's functions, (2) gaining the asymptotic behavior of the green's functions, (3) computations of the reflected field, (4) applying Fourier transform of the current density surface, (5) using the spectral-Galerkin equation, (6) gaining the expression of the transverse electric field, (7) employing expressions of the basis current functions, (8) computation of the total reflection coefficient of the Frequency

Selective Surface. In order to get results we have fulfilled all these stages explicitly.

REFRENCE

[1] Sören poulsen, "scattering from frequency selective surfaces: A continuity condition for entire domain basis functions and an improved set of basis functions for crossed dipoles", lund Institute of Technology, Department of Applied Electronics, Electromagnetic Theory, P.O. Box 163, SE-341 23 lund, Sweden, October 28, 1999.

[2] S. Komylian, F. Hojat-Kashani, " Intense Scrutiny In Cross-dipole Frequency Selective Surface", under submission, antenna conference, iWAT2012, Arizona, USA.

Loss-Induced Omnidirectional Anti-Snell's Law Refraction in ϵ-near-Zero Metamaterials

Simin Feng

Michelson Lab, Physics Division,
Naval Air Warfare Center, China Lake, California, USA
*corresponding author, E-mail: simin.feng@navy.mil

Abstract

Contrary to popular belief, conventional wisdom states that light bends away from the normal when it passes from high to low refractive index media, here we demonstrate that the electromagnetic power can bend to the normal in nearly parallel for all angles of incidence when passing from arbitrary high refractive index medium (or air) to ϵ-near-zero (ENZ) metamaterial. This counterintuitive to conventional Snell's law refraction is resulted from the interplay between ENZ and material loss, which switches the transmission angle from the grazing to the normal. Moreover, the material loss can increase the transmission at the air-ENZ interface. For an ideal loss configuration, the collimated beam can travel indefinitely without decay in anisotropic ENZ media when the material loss approaches infinity.

1. Introduction

Metamaterials have gained a lot of attention due to their intriguing properties, such as negative refraction [1], electromagnetic cloaking [2, 3] and shielding [4], ultrathin waveguides [5, 6], beam shaping [7]–[10], and self-collimation [11]–[13]. Wave refraction at the interface, a fundamental phenomenon in optics, is described by Snell's law which dictates light bends towards the normal when passing from low to high refractive index media. As a manifestation of this effect, directive emission into air by a source placed inside the material with vanishingly small permittivity, known as epsilon-near-zero (ENZ) metamaterials, was demonstrated recently [14]. From the reciprocal theorem, for radiation from high refractive index medium to ENZ material, the transmitted beam should spread out into grazing angles. Contrary to this conventional behavior, we will show that the electromagnetic (EM) power can bend to the normal when light passes from arbitrary high ($\epsilon_1 \gg 1$) to low ($\epsilon_2 \approx 0$) refractive index media as shown in Fig. 1a – anti-Snell's law refraction. Moreover, the direction of the transmission is close to the normal for all incidence angles. Unlike negative refraction, this anti-Snell's law refraction is induced by material loss. The interplay between ENZ and loss leads to unusual wave behavior that switches the transmission angle from the grazing to the normal for all angles of incidence. In the lossless case, the air-ENZ interface, in the limit of $\epsilon \to 0$, acts as a mirror due to highly mismatched impedance. However, EM properties in lossy ENZ media are unconventional and counterintuitive. Material loss can switch a broadband reflection to a broadband transmission, meanwhile bend all spatial components to the normal. Moreover, the transmission at the air-ENZ interface can increase with the increase of loss. Furthermore, for a certain loss design, the propagation loss in anisotropic ENZ media decreases with increasing the material loss.

The refraction and propagation anomaly can be used to project EM power into one direction as shown in Fig. 1b, where the waves coming from all directions are bent to the normal upon entering the ENZ. A plasmonic coating is superimposed on the ENZ to enhance the transmission through structural resonances. Regardless of the incidence angles, the transmitted powers can impinge normally to the receptors or photocells embedded in the ENZ medium, increasing the acceptance angle and energy transfer.

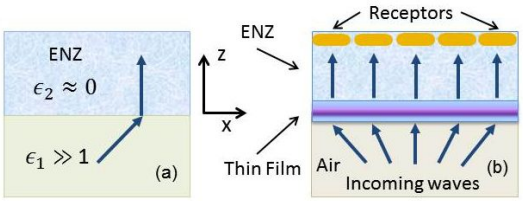

Figure 1: (a) A plane wave is incident from an arbitrary high permittivity ($\epsilon_1 \gg 1$) medium to ENZ ($\epsilon_2 \approx 0$) metamaterial. (b) Incoming waves from different directions in air are bent to the normal upon entering the ENZ medium. A plasmonic thin film is superimposed on the ENZ material to enhance the transmission. Receptors or photocells are embedded in the ENZ metamaterial.

2. Anti-Snell's law refraction

2.1. Angular switching

Our derivation is based on anisotropic media. Results can be applied to isotropic media. Assuming a harmonic time dependence $\exp(-i\omega t)$ for the EM field, from Maxwell's equations, we have

$$\begin{aligned} \nabla \times \left(\bar{\bar{\mu}}_n^{-1} \cdot \nabla \times \boldsymbol{E}\right) &= k_0^2 \left(\bar{\bar{\epsilon}}_n \cdot \boldsymbol{E}\right), \\ \nabla \times \left(\bar{\bar{\epsilon}}_n^{-1} \cdot \nabla \times \boldsymbol{H}\right) &= k_0^2 \left(\bar{\bar{\mu}}_n \cdot \boldsymbol{H}\right), \end{aligned} \tag{1}$$

where $k_0 = \omega/c$; and the $\bar{\bar{\epsilon}}_n$ and $\bar{\bar{\mu}}_n$ are, respectively, the permittivity and permeability tensors for each uniform area

$(n = 1, 2, \cdots)$, which in the principal coordinates can be described by

$$\begin{aligned} \bar{\bar{\epsilon}}_n &= \epsilon_{nx}\hat{\boldsymbol{x}}\hat{\boldsymbol{x}} + \epsilon_{ny}\hat{\boldsymbol{y}}\hat{\boldsymbol{y}} + \epsilon_{nz}\hat{\boldsymbol{z}}\hat{\boldsymbol{z}}\,, \\ \bar{\bar{\mu}}_n &= \mu_{nx}\hat{\boldsymbol{x}}\hat{\boldsymbol{x}} + \mu_{ny}\hat{\boldsymbol{y}}\hat{\boldsymbol{y}} + \mu_{nz}\hat{\boldsymbol{z}}\hat{\boldsymbol{z}}\,. \end{aligned} \tag{2}$$

Consider transverse magnetic (TM) modes, corresponding to non-zero field components H_y, E_x, and E_z. The magnetic field H_y satisfies the following wave equation:

$$\frac{1}{\epsilon_z}\frac{\partial^2 H_y}{\partial x^2} + \frac{1}{\epsilon_x}\frac{\partial^2 H_y}{\partial z^2} + k_0^2\mu_y H_y = 0\,, \tag{3}$$

which permits solutions of the form $\psi(z)\exp(i\beta x)$. Here the transverse wave number β is determined by the incident wave, and is conserved across the interface,

$$\beta^2 = k_0^2\epsilon_{nz}\mu_{ny} - \alpha_n^2\frac{\epsilon_{nz}}{\epsilon_{nx}}\,, \qquad (n = 1, 2, \cdots)\,, \tag{4}$$

where α_n is the wave number in the z direction. The functional form of $\psi(z)$ is either a simple exponential $\exp(i\alpha_n z)$ for the semi-infinite regions or a superposition of $\cos(\alpha_n z)$ and $\sin(\alpha_n z)$ terms for the bounded regions along the z direction. The other two components E_x and E_z can be solved from H_y using Maxwell's equations. By

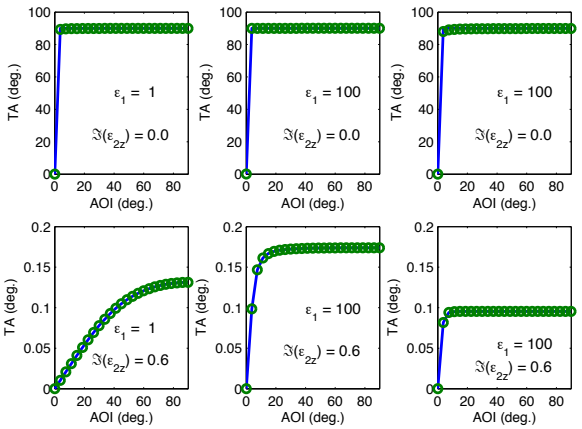

Figure 2: TA of the Poynting vector vs. AOI when $\epsilon_{2z} = 0.001 + i\epsilon_{2z}^i$. Left and middle panels: anisotropic ENZ with $\epsilon_{2x} = 1$. Right panels: isotropic ENZ with $\epsilon_{2x} = \epsilon_{2z}$. Top panels: $\epsilon_{2z}^i = 0$. Bottom panels: $\epsilon_{2z}^i = 0.6$. Left panels: $\epsilon_1 = 1$. Middle and right panels: $\epsilon_1 = 100$. A good agreement between the numerical (blue-solid) and analytical (green-circles) results. Material loss switches the TA from the grazing angle 90° (top panels) to the near-zero angle (bottom panels) for all AOI.

matching boundary conditions at the interfaces, i.e., the continuity of H_y and E_x, the EM field can be derived in each region; and then the Poynting vector $\boldsymbol{S}$ can be computed from $\boldsymbol{S} = \Re(\boldsymbol{E} \times \boldsymbol{H}^*)$. In anisotropic materials, the direction of the Poynting vector is different from that of the phase front of the field. Here, only the direction of the Poynting vector is considered since it is associated with the energy transport. The angle (θ_S) of the Poynting vector is measured from the Poynting vector to the surface normal, and is given by $\theta_S = \tan^{-1}(S_x/S_z)$. Assume non-magnetic materials $\mu_j = 1$ $(j = 1, 2)$. In Fig. 1a, the input side is isotropic material with permittivity ϵ_1; the output side is ENZ material ($\epsilon_2 \approx 0$). In the following, both anisotropic ($\epsilon_{2x} \neq \epsilon_{2z}$) and isotropic ($\epsilon_{2x} = \epsilon_{2z}$) ENZ media will be considered. Figure 2 illustrates the effect of ENZ-material loss on the transmission angle (TA) plotted against angle of incidence (AOI) with and without loss for different permittivity (ϵ_1) of the input medium. In the top panels, when the loss is zero $\big(\Im(\epsilon_{2z}) = 0\big)$, the TA is 90° (grazing angle) except for the normal incidence, which is complied with Snell's law. In the bottom panels, with a moderate loss $\Im(\epsilon_{2z}) = 0.6$, the TA switches to near zero (normal direction) for all AOI. This switching phenomenon persists even for the much higher permittivity ($\epsilon_1 = 100$) of the input medium (middle and right panels).

2.2. Analysis

To understand this loss-induced switching phenomenon, we analyze the transmission angle (θ_S), which is given by

$$\tan(\theta_S) = \frac{S_x}{S_z} = \frac{\Re\left(\dfrac{\bar{\beta}}{\epsilon_{2z}}\right)}{\Re\left[\sqrt{\dfrac{\mu_{2y}}{\epsilon_{2x}} - \dfrac{\big(\bar{\beta}\big)^2}{\epsilon_{2x}\epsilon_{2z}}}\right]}\,, \tag{5}$$

where $\bar{\beta} \equiv \beta/k_0$, and $\bar{\beta}$ (real) is given by incidence angle. The transmission angle of the Poynting vector depends only on the input and output media. In the case of $\epsilon_{2x} \to 0$ and ϵ_{2z} finite, Eq. (5) indicates $\theta_S \to 0^\circ$ (normal direction). For the case of $\epsilon_{2z} \to 0$ and ϵ_{2x} finite and the case of isotropic ENZ material with $\epsilon_{2x} = \epsilon_{2z} \to 0$, the analysis is more involved. The numerator of Eq. (5) can be written as

$$\Re\left(\frac{\bar{\beta}}{\epsilon_{2z}}\right) = \frac{\bar{\beta}\,\epsilon_{2z}^r}{|\epsilon_{2z}|^2}\,, \tag{6}$$

where $\epsilon_{2z}^r \equiv \Re(\epsilon_{2z})$. Assuming μ_{2y} is real, the denominator of Eq. (5) becomes

$$\Re\left[\sqrt{\frac{\mu_{2y}}{\epsilon_{2x}} - \frac{\big(\bar{\beta}\big)^2}{\epsilon_{2x}\epsilon_{2z}}}\right] = \frac{a\,\bar{\beta}}{|\epsilon_{2x}\epsilon_{2z}|}\,, \tag{7}$$

where

$$a^2 = \frac{1}{2}\left(A\epsilon_{2x}^r + B|\epsilon_{2x}| - \epsilon_{2x}^r\epsilon_{2z}^r + \epsilon_{2x}^i\epsilon_{2z}^i\right)\,, \tag{8}$$

where $\epsilon_{2z}^i \equiv \Im(\epsilon_{2z})$, $\epsilon_{2x}^r \equiv \Re(\epsilon_{2x})$, $\epsilon_{2x}^i \equiv \Im(\epsilon_{2x})$, and

$$A \equiv \frac{|\epsilon_{2z}|^2\mu_{2y}}{\big(\bar{\beta}\big)^2}\,, \quad B = \sqrt{|\epsilon_{2z}|^2 - 2A\epsilon_{2z}^r + A^2}\,. \tag{9}$$

Thus, the transmission angle (θ_S) becomes

$$\tan(\theta_S) = \frac{|\epsilon_{2x}|\epsilon_{2z}^r}{a\,|\epsilon_{2z}|}\,. \tag{10}$$

The loss-induced angular switch in Fig. 2 can be explained from Eq. (10). For the anisotropic medium $\epsilon_{2x} \neq \epsilon_{2z}$ and ϵ_{2x} is finite, if $\epsilon^i_{2z} = 0$, when $\epsilon^r_{2z} \to 0$, $\epsilon^r_{2z}/|\epsilon_{2z}| \to 1$ and $a \to 0$, thus $\theta_S \to 90°$. If $\epsilon^i_{2z} \neq 0$, when $\epsilon^r_{2z} \to 0$, $\epsilon^r_{2z}/|\epsilon_{2z}| \to 0$ and a is finite, thus $\theta_S \to 0°$. On the other hand, if ϵ_{2z} is finite, when $\epsilon_{2x} \to 0$, $a \to \sqrt{\epsilon_{2x}}$, and thus $\theta_S \to 0°$. For the isotropic case, let $\epsilon_{2x} = \epsilon_{2z} \equiv \epsilon^r_2 + i\epsilon^i_2$. If $\epsilon^i_2 = 0$, when $\epsilon^r_2 \to 0$, $\epsilon^r_{2z}/|\epsilon_{2z}| \to 1$ and $a \to (\epsilon^r_2)^{3/2}$, thus $\theta_S \to 90°$. If $\epsilon^i_2 \neq 0$, when $\epsilon^r_2 \to 0$, $\epsilon^r_{2z}/|\epsilon_{2z}| \to 0$ and a is finite, therefore $\theta_S \to 0°$. Equation (10) indicates when ϵ_{2z} is finite, both the real and imaginary of ϵ_{2x} should approach zero in order for $\theta_S \to 0°$. To validate Eq. (10), in Fig. 2 the TA calculated from Eq. (10) (green-circles) are compared to those computed numerically (blue-solid), showing a perfect agreement.

2.3. Angular width

To validate the loss-induced switching behavior is a robust feature, in Fig. 3 the transmission angle vs. AOI is plotted for different real parts of ϵ_{2z} and ϵ_{2x} and loss. In essence,

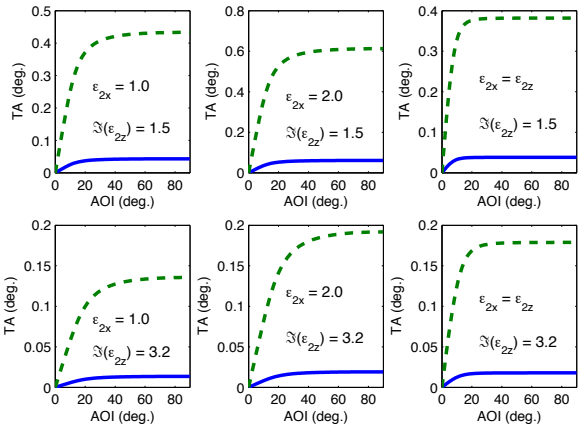

Figure 3: TA vs. AOI when $\Re(\epsilon_{2z}) = 0.001$ (blue-solid) and $\Re(\epsilon_{2z}) = 0.01$ (green-dashed). Top panels: $\Im(\epsilon_{2z}) = 1.5$. Bottom panels: $\Im(\epsilon_{2z}) = 3.2$. The ENZ material is anisotropic with $\epsilon_{2x} = 1.0$ (left panels) and $\epsilon_{2x} = 2.0$ (middle panels), and isotropic (right panels). The permittivity of the input medium $\epsilon_1 = 36$.

the transmission angle decreases with increasing the loss $\Im(\epsilon_{2z})$ and decreasing $\Re(\epsilon_{2z})$. When $\Re(\epsilon_{2z}) \to 0$, angular width of the transmission can be estimated from

$$\Delta\theta_S \approx \begin{cases} \dfrac{\sqrt{2}\,|\epsilon_x|\,\epsilon^r_z}{|\epsilon_z|^{3/2}\sqrt{|\epsilon_x| + \epsilon^i_x + \eta\,\epsilon^r_x}}\,, & \text{if } \eta \leq 1 \\ \dfrac{\sqrt{2}\,|\epsilon_x|\,\epsilon^r_z}{|\epsilon_z|^{3/2}\sqrt{\epsilon^i_x + \eta\big(|\epsilon_x| + \epsilon^r_x\big)}}\,, & \text{if } \eta \geq 1 \end{cases}, \quad (11)$$

where $\eta \equiv \dfrac{|\epsilon_z|\mu_y}{\epsilon_1\mu_1}$, and the subscript 2 in ϵ_x, ϵ_z, and μ_y was omitted in above equation. Figure 4 demonstrates how rapidly the transmission angle converges to zero as the loss

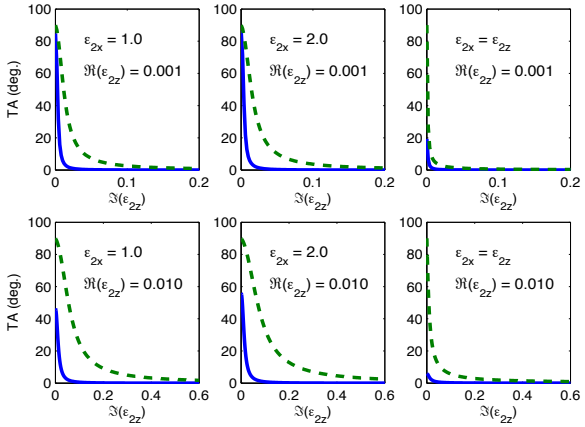

Figure 4: TA vs. $\Im(\epsilon_{2z})$ when AOI $= 0.1°$ (blue-solid) and AOI $= 89°$ (green-dashed). Top panels: $\Re(\epsilon_{2z}) = 0.001$. Bottom panels: $\Re(\epsilon_{2z}) = 0.01$. Left and middle panels: anisotropic ENZ material with $\epsilon_{2x} = 1.0$ (left) and $\epsilon_{2x} = 2.0$ (middle). Right panels: isotropic ENZ material. The permittivity of the input medium $\epsilon_1 = 36$. TA quickly converges to zero in all the scenarios.

$\Im(\epsilon_{2z})$ increases for different $\Re(\epsilon_{2z})$ and ϵ_{2x}. The blue-solid curves represent the transmission angles for the near-zero angle of incidence, while the green-dashed curves for the grazing angle of incidence. The difference of these two curves represents to the transmission angular width, which is narrower in the isotropic ENZ media (right panels) than that in the anisotropic media (left and middle panels). Hence, the omnidirectionally collimated transmission can occur when $\Im(\epsilon_{2z}) \gg \Re(\epsilon_{2z})$ and $\Re(\epsilon_{2z}) \to 0$.

3. Loss-assisted transmission

Not only can the loss switch the transmission angle from the grazing to the normal, but also it can increase the transmission amplitude. The transmission and reflection coefficients of the power at the interface can be calculated from

$$T = \frac{\Re(\mathcal{Z}_2)}{\Re(\mathcal{Z}_1)}\frac{4\left|\mathcal{Z}_1\right|^2}{\left|\mathcal{Z}_1 + \mathcal{Z}_2\right|^2}\,, \qquad R = \left|\frac{\mathcal{Z}_1 - \mathcal{Z}_2}{\mathcal{Z}_1 + \mathcal{Z}_2}\right|^2\,, \quad (12)$$

where $\mathcal{Z}_1$ and $\mathcal{Z}_2$ are, respectively, the input and output impedances generalized for oblique incidence, given by $\mathcal{Z}_j = \alpha_j/\epsilon_{jx}$ $(j = 1, 2)$. Without loss, the mismatched impedance prevents EM waves from entering the medium. With loss this picture changes dramatically. In fact, the loss can mitigate the mismatch and increases the transmission. Figure 5 shows the transmittance and reflectance (top and middle panels) of a plane wave incident from air to the ENZ material, as well as the TA (bottom panels). To confirm our results, the numerically computed transmittance (blue-solid) and reflectance (green-dashed) using scattering matrix method are compared to the analytical calculation (circles) using Eq. (12). The TA in the right bottom panel spreads out from $0°$ to $90°$ since both $\Re(\epsilon_{2z})$ and $|\epsilon_{2x}| \neq 0$ (see Eq. (10) and the analysis). The flat transmission and

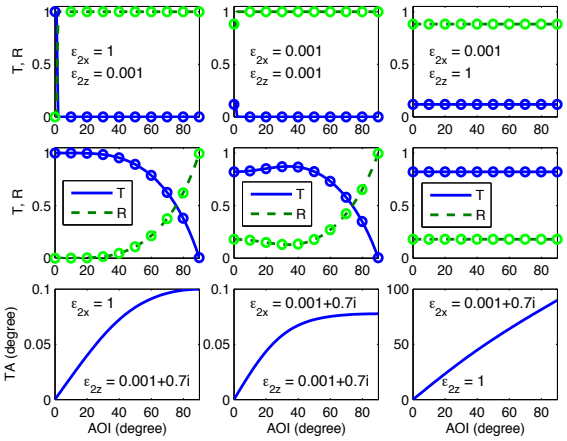

Figure 5: Transmittance (blue) and reflectance (green) vs. AOI without loss (top panels) and with loss (middle panels), showing perfect agreement between the numerical (solid & dashed curves) and analytical results (circles). Bottom panels: TA corresponding to the middle panels. The middle panels have the same permittivities as those in the corresponding bottom panels.

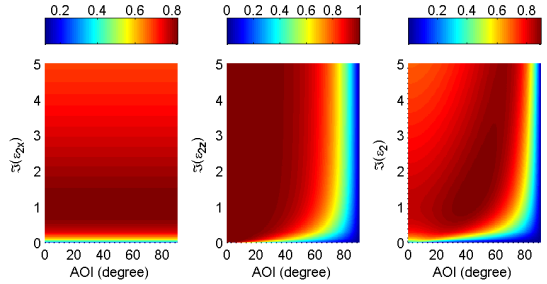

Figure 6: Transmittance vs. AOI and loss when incident from air to the ENZ medium. Left panel: $\Re(\epsilon_{2x}) = 0.001$ and $\epsilon_{2z} = 1$. Middle panel: $\epsilon_{2x} = 1$ and $\Re(\epsilon_{2z}) = 0.001$. Right panel: $\epsilon_{2x} = \epsilon_{2z} = \epsilon_2$ and $\Re(\epsilon_2) = 0.001$. Note the transmission is zero without loss.

reflection in the right panels is a special case where the angular dependent term in the denominator and numerator of Eq. (12) happens to cancel each other when $\epsilon_{2z} = 1$ and $\epsilon_1 = 1 \Rightarrow \mathcal{Z}_j = \cos\theta/\sqrt{\epsilon_j}$ $(j = 1, 2)$. Figure 6 presents the transmittance as a function of AOI and loss. The angular independence in the left panel is the special case. Clearly, material loss provides a mechanism for the EM power to enter the "door", and switches the broadband total reflection to the broadband transmission.

4. Loss-assisted propagation

Some material loss can increase the propagation distance in anisotropic ENZ materials. The propagation constant in the z-direction, from Eq. (4), is given by

$$k_z \equiv \alpha = \sqrt{k_0^2 \epsilon_x \mu_y - \frac{\epsilon_x}{\epsilon_z}\beta^2}\,. \tag{13}$$

For the fixed ϵ_x, a higher loss in ϵ_z means a smaller $\Im(k_z)$, and thus a longer propagation distance since waves inside the ENZ medium propagate in the z-direction according to above analysis. Thus, if the loss in ϵ_x can be kept small, the loss in ϵ_z is, in fact, favored for propagation. Assume $\mu_y = 1$, it is straight forward to derive the imaginary of k_z:

$$\begin{aligned}\Big(\Im(k_z)\Big)^2 &= \frac{1}{2}\Big[|\epsilon_x|\sqrt{1 - 2\gamma\epsilon_z^r + \gamma^2|\epsilon_z|^2} - \\ &\qquad \epsilon_x^r + \gamma\big(\epsilon_x^r\epsilon_z^r + \epsilon_x^i\epsilon_z^i\big)\Big] \\ &\to \frac{1}{2}\Big[|\epsilon_x| - \epsilon_x^r\Big]\,, \quad \text{as } \Im(\epsilon_z) \to \infty\,,\end{aligned} \tag{14}$$

where $\gamma \equiv \left(\dfrac{\beta}{k_0|\epsilon_z|}\right)^2$. Figure 7 demonstrates the effect of the loss on the propagation in the anisotropic ENZ medium. The left panels show the propagation loss $\Im(k_{2z})$ versus the material loss $\Im(\epsilon_{2z})$ at different AOI and ϵ_{2x}. When the loss $\Im(\epsilon_{2z}) \to \infty$, the propagation loss exponentially decays to the limit determined by the $\Im(\epsilon_{2x})$. The right panels present the normalized transmission versus AOI at different propagation distances inside the anisotropic ENZ medium with different loss $\Im(\epsilon_z)$. The right-bottom panel indicates the transmission increases with the increase of the loss $\Im(\epsilon_{2z})$ and is eventually saturated (the curves for $\Im(\epsilon_{2z}) = 3$ and $\Im(\epsilon_{2z}) = 20$ are on top of each other). A broadband spatial frequency can enter the ENZ medium with more than 90% transmission for the angular bandwidth up to 50 degree and more than 50% for up to 75 degree. As the wave propagates inside the ENZ medium, the power from the non-zero AOI is gradually absorbed except for the normal incidence (right-middle and right-top panels). This process is in fact quite opposite to what occurs in the lossless ENZ slab which, in the limit of $\epsilon \to 0$, only allow the normal incidence for a total transmission and reject non-zero spatial components by the mismatched interface [10]. Therefore, a lossless ENZ slab acts as a spatial filter [10], not a collimator. Whereas a lossy air-ENZ interface behaves as a collimator since a broadband spatial frequency can pass the interface in parallel. Ideally, the EM wave can propagate forever without decay if the loss $\Im(\epsilon_z) \to \infty$ and the loss $\Im(\epsilon_x) = 0$. Physically, it can be understood that ϵ_z is important for matching at the interface, but once the wave enters the material it propagates mostly along the normal, so the electric field 'feels' only the x-component of the permittivity. In essence, when the $|\epsilon_z|$ increases, the influence of the ϵ_z on wave propagation diminishes as the result of reducing transmission angle (see Fig. 4). Figure 8 shows the propagation of the normalized total power in the ENZ medium at different losses. When $\Im(\epsilon_{2z}) = 20$ (right panel), the power reduces to 60% after a propagation of 5λ. Note that the flat wavefront occurs only inside the ENZ medium. When the power comes out of the medium into air, the wavefront will return to the original form due to the conservation of the parallel wave vector β. This result is different from the lossless ENZ slab where the wavefront keeps flat in air [10] since in their case the tilted wavefronts

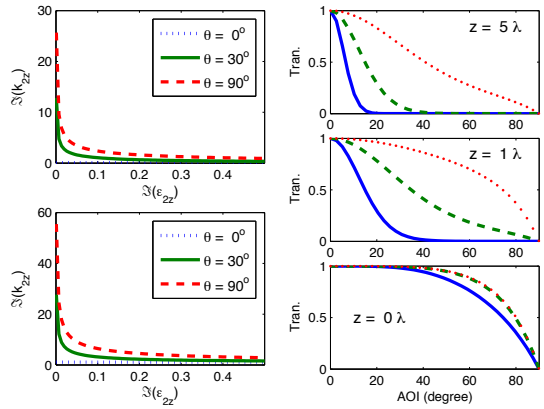

Figure 7: Left panels: $\Im(k_{2z})$ vs. $\Im(\epsilon_{2z})$ when $\epsilon_{2x} = 1 + 0.2i$ (top) and $\epsilon_{2x} = 2 + 4i$ (bottom) at the AOI $= 0°$ (blue-dots), $30°$ (green-solid), and $90°$ (red-dashed). Right panels: transmitted power (normalized by the input power at each AOI) in the ENZ medium vs. AOI at the air-ENZ interface ($z = 0$, bottom), at the propagation distance $z = \lambda$ (middle), and $z = 5\lambda$ (top). $\epsilon_{2x} = 1$. Blue-solid: $\Im(\epsilon_{2z}) = 0.6$. Green-dashed: $\Im(\epsilon_{2z}) = 3$. Red-dots: $\Im(\epsilon_{2z}) = 20$. No propagation decay for the normal beam since $\beta = 0$ in Eq. (13). $\Re(\epsilon_{2z}) = 0.001$ for all plots.

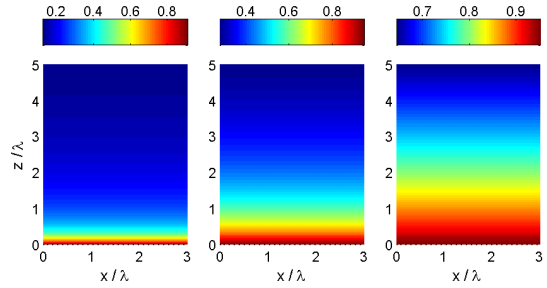

Figure 8: Normalized total transmitted power (integrated over AOI) inside the ENZ material. $\Re(\epsilon_{2z}) = 0.001$ and $\epsilon_{2x} = 1$. Left: $\Im(\epsilon_{2z}) = 0.6$. Middle: $\Im(\epsilon_{2z}) = 3$. Right: $\Im(\epsilon_{2z}) = 20$. Color bars represent the magnitude of the power. The higher the loss $\Im(\epsilon_{2z})$, the slower the propagation decay.

can never get into the material in the first place. It is well-known that many fascinating effects are diminished due to the high loss of metamaterials. However, the material loss here can play a positive role, which collimates the beam and increases the transmission and propagation inside the ENZ medium.

5. Applications

Above unconventional phenomena may have applications, such as directive antennas. Instead of radiation, here we explore them from a receiving perspective, i.e., redirect the EM power coming from different directions to the direction of the receivers to enhance the acquisition power, as shown in Fig. 1b, where a matching coating is deposited on the surface of the ENZ medium to make the effective impedance of the overall structure matched to that of air. For simplicity, we used a dielectric-metal-dielectric thin film as the coating. With proper thicknesses, this sandwich structure can possess nearly-flat dispersion curve [15, 16] due to coupled surface plasmon from closely spaced two dielectric-metal interfaces. By varying the thicknesses of the layers, the resonant frequency can be tuned. In our simulation, the dielectric and metallic layers are amorphous polycarbonate (APC) and silver (Ag), respectively. The refractive index of the APC is given by [17]

$$n_p = 1.5567 + 8.0797 \times 10^{-3}/\lambda^2 + 3.5971 \times 10^{-4}/\lambda^4,$$

where λ is the wavelength in μm. The loss of APC is very small and neglected. The Ag absorption is included via the complex permittivity from Palik [18].

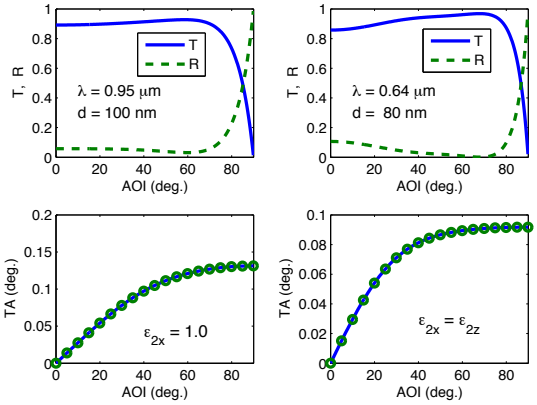

Figure 9: Top panels: Transmittance (blue-solid) and reflectance (green-dashed) of the APC-Ag-APC film vs. AOI when the back of the film is ENZ medium with $\epsilon_{2x} = 1$ (left panels) and $\epsilon_{2x} = \epsilon_{2z}$ (right panels). $\epsilon_{2z} = 0.001 + 0.6i$. Bottom panels: corresponding TA computed numerically (blue-solid) and analytically (green-circles), showing a perfect agreement. The thickness of the Ag layer is 10 nm.

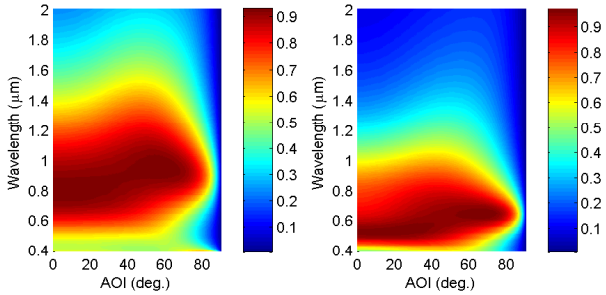

Figure 10: Transmittance of the APC-Ag-APC coating versus AOI and wavelength when the medium at the back of the coating is the anisotropic (left panel) and isotropic (right panel) ENZ materials. Color-bars represent the magnitude of the transmittance. Simulation parameters are the same as those in Fig. 9. In both cases, a wide-angle 90% transmission is observed.

Figure 9 shows the transmittance and reflectance (top

panels) of a plane wave incident from air to the APC-Ag-APC structure, as well as the corresponding TA (bottom panels). At the resonance, the thickness of the APC layer $d = 100\,\text{nm}$ and the resonant wavelength $\lambda = 0.95\,\mu\text{m}$ for the anisotropic ENZ (left panels), and $d = 80\,\text{nm}$ and $\lambda = 0.64\,\mu\text{m}$ for the isotropic ENZ (right panels) media. About 90% transmission is achieved for the AOI up to 70° with a nearly-collimated beam propagating in the normal direction. Compared with the one without the coating (see the right-bottom panel of Fig. 7), the angular bandwith is increased by 40%. A 2D view showing the transmittance of the APC-Ag-APC as a function of AOI and wavelength is presented in Fig. 10. Note the loss of the ENZ medium was not included in the transmission, which was computed right after the film, i.e., before traveling through the ENZ medium. If the receptors are embedded close to the back of the film, the propagation loss in the ENZ medium can be minimized. On the other hand, by designing the anisotropic loss, $\Im(\epsilon_x) \approx 0$ and $\Im(\epsilon_z) \gg 0$, the propagation distance can be increased. With the recent advances in fabrication, it seems plausible to precisely control the permittivity and permeability of metamaterials.

6. Conclusions

In conclusions, we have demonstrated the counterintuitive anti-Snell's law refraction and loss-improved transmission and propagation in the ENZ materials. These results are generally sensitive to polarization and narrow band due to frequency dispersion. Nevertheless, these unconventional phenomena may find applications in antennas, detectors, and sensors to increase the angular bandwidth and the EM power without using optical lenses and mechanical gimbals. The concept of designing the anisotropic loss to control the direction and transmission of EM power brings a positive perspective to material loss and may open up a new avenue for metamaterial designs.

Acknowledgement

The work was supported by NAVAIR's ILIR program.

References

[1] R. A. Shelby, D. R. Smith, and S. Schultz, Experimental Verification of a Negative Index of Refraction, *Science* 292: 77–79, 2001.

[2] J. B. Pendry, D. Schurig, D. R. Smith, Controlling Electromagnetic Fields, *Science* 312: 1780–1782, 2006.

[3] R. Liu, C. Ji, J. J. Mock, J. Y. Chin, T. J. Cui, and D. R. Smith, Broadband Ground-Plane Cloak, *Science* 323: 366–369, 2009.

[4] S. Feng and K. Halterman, Parametrically Shielding Electromagnetic Fields by Nonlinear Metamaterials, *Phys. Rev. Lett.* 100: 063901, 2008.

[5] M. G. Silveirinha and N. Engheta, Tunneling of Electromagnetic Energy through Subwavelength Channels and Bends using ϵ-Near-Zero Materials, *Phys. Rev. Lett.* 97: 157403, 2006.

[6] D. C. Adams, S. Inampudi, T. Ribaudo, D. Slocum, S. Vangala, N. A. Kuhta, W. D. Goodhue, V. A. Podolskiy, and D. Wasserman, Funneling Light through a Subwavelength Aperture with Epsilon-Near-Zero Materials, *Phys. Rev. Lett.* 107: 133901, 2011.

[7] R. W. Ziolkowski, Propagation in and scattering from a matched metamaterial having a zero index of refraction, *Phys. Rev. E* 70: 046608, 2004.

[8] K. Halterman, S. Feng, and V. C. Nguyen, Controlled leaky wave radiation from anisotropic epsilon near zero metamaterials, *Phys. Rev. B* 84: 075162, 2011.

[9] Y. Jin and S. He, Enhancing and suppressing radiation with some permeability-near-zero structures, *Opt. Express* 18: 16587–16593, 2010.

[10] A. Alù, M. G. Silveirinha, A. Salandrino, and N. Engheta, Epsilon-near-zero metamaterials and electromagnetic sources: Tailoring the radiation phase pattern, *Phys. Rev. B* 75: 155410, 2007.

[11] S. Feng and J. M. Elson, Diffraction-suppressed high-resolution imaging through metallodielectric nanofilms, *Opt. Express* 14: 216–221, 2006.

[12] V. Mocella, S. Cabrini, A. S. P. Chang, P. Dardano, L. Moretti, I. Rendina, D. Olynick, B. Harteneck, and S. Dhuey, Self-Collimation of Light over Millimeter-Scale Distance in a Quasi-Zero-Average-Index Metamaterial, *Phys. Rev. Lett.* 102: 133902, 2009.

[13] R. Pollès, E. Centeno, J. Arlandis, and A. Moreau, Self-collimation and focusing effects in zero-average index metamaterials, *Opt. Express* 19: 6149–6154, 2011.

[14] S. Enoch, G. Tayeb, P. Sabouroux, N. Gueŕin, and P. Vincent, A Metamaterial for Directive Emission, *Phys. Rev. Lett.* 89: 213902, 2002.

[15] H. Shin, M. F. Yanik, and S. Fan, Omnidirectional resonance in a metaldielectricmetal geometry, *Appl. Phys. Lett.* 84: 4421–4423, 2004.

[16] J. Zhang, H. Jiang, W. Shen, X. Liu, Y. Li, and P. Gu, Omnidirectional transmission bands of one dimensional metaldielectric periodic structures, *J. Opt. Soc. Am. B* 25: 1474–1478, 2008.

[17] M. J. Roberts, S. Feng, M. Moran, and L. Johnson, Effective permittivity near zero in nanolaminates of silver and amorphous polycarbonate, *J. Nanophoton.* 4: 043511, 2010.

[18] E. D. Palik, *Handbook of Optical Constants of Solids*, Academic, San Diego, 1998.

Localized surface Plasmon Bragg grating on SOI waveguide at telecom wavelengths

M. Fevrier[1,2], P. Gogol[1,2], A. Aassime[1,2], R. Mégy[1,2], D. Bouville[1,2], J. M. Lourtioz[1,2] and B. Dagens[1,2*]
1. Univ Paris-Sud, Laboratoire IEF, UMR 8622, Orsay, F-91405, France
2. CNRS, Orsay, F-91405, France
[*]corresponding author: beatrice.dagens@ief.u-psud.fr

Abstract

We show that metal nanoparticle chains supporting localized surface plasmon resonance can behave as transmission Bragg gratings on dielectric waveguide. An analytical model is developed to interpret experimental results.

1. Introduction

Metallic nanoparticles (MNP) supporting localized surface plasmon (LSPs) can confine light at sub-wavelength scales [1] with many potential applications to plasmonic nanolasers [2], SERS [3,4], bio-sensors [5], waveguiding [6] – [8]. To date, most of the studies conducted on the LSPs have been performed using free-space or near-field configurations, where MNP chains can incidentally behave as grating couplers. For instance, an increase of the LSP resonance lifetime was demonstrated by using a diffraction order of an MNP [9] – [11]. In 2004, Quidant et al. observed strong modulations in the near-field spectra of a composite device including MNPs with TiO_2 microguide at visible frequency [12]. Recently Zhou et al. reported polariton propagation in a 2D grating of gold NPs by coupling either to the transverse or longitudinal resonant LSP modes [13]. Yet, the excitation of LSP in a truly guided configuration remains a crucial step towards the implementation of plasmonic functions in photonics integrated circuits.

In this paper, we analyze both theoretically and experimentally the LSP Bragg grating (LSPBG) integrated in a guided wave SOI (silicon-on-insulator) configuration at telecom wavelengths. We show that different propagation regimes and transmission spectra at the waveguide output can be obtained depending on the positions of Bragg frequency orders with respect to the LSP resonance. To investigate theoretically the behavior of such LSPBGs, we propose an analytical model where the MNP is described as a periodic modulation of the waveguide refractive index. Prior to this, an equivalent index of the metallic film is derived from the coupled dipole approximation method in the quasi-static approximation. Our approach is similar to that recently used for modeling the optical properties of 2D gold NP grating excited in Kretshman-Raether configuration [14]. The propagation in the waveguide with LSP Bragg grating is then described by using the coupled mode theory (CMT) [15-16].

The paper is organized as follows. The analytical model of LSPBG is presented in the next section. The different LSPBG behaviors are then illustrated by varying the LSP resonance frequency (i.e., the size of nanoparticles) at a constant grating period. Next, Finite Difference Time Domain (FDTD) calculations are used to validate the main assumptions in the model. Experiments are then presented, and waveguide transmission measurements are compared to theoretical predictions.

2. Analytical model of LSP Bragg gratings

Fig. 1(a) show the basic scheme of a dielectric (SOI) waveguide with a LSP Bragg grating deposited on top. The inter-particle distance d is chosen to provide at least one grating order within the wavelength range of interest. The size of nanoparticles is chosen in such a way that the LSP resonance occur in the same wavelength range. One appropriate shape to excite the LSP resonance with a TE waveguide mode is the ellipsoidal nanorod with long axis perpendicular to propagation (fig. 1 (b)). In what follows, D1 and D2 will denote the long axis and small axis respectively. As gold is an absorbing material, MNPs can actually perturb the waveguide refractive index in two ways. They not only affect the real part of the refractive index, but also its imaginary part. As will be seen later, this can lead to different LSPBG regimes depending on the respective positions of Bragg and LSP resonances.

Coupled mode theory is commonly used to provide an analytical description of Bragg gratings [17]. However, LSPBG is not a standard case since both the LSP resonance and the Bragg resonance must be accounted for. Here, we make the assumption that an equivalent index of refraction $\tilde{n}_{eq}$ can be assigned to the MNP grating layer supporting LSP resonance. To calculate $\tilde{n}_{eq}$ each MNP is approximated by a point dipole, and its interaction with the underlying waveguide is accounted for via the image dipole formalism. The quasi-static approximation is then used since the inter-particle spacing (~ 500 nm) is sufficiently long to assume uncoupled particles. The same approach was made for 2D grating of MNPs excited in the Kretshman-Raether configuration [14] as well as for a Bragg grating in a free space configuration [18]. The originality of our approach stems from the use of a waveguide configuration. Once

$\tilde{n}_{eq}$ is obtained, it is injected in the CMT model to calculate the waveguide transmission (Figure1 (c)).

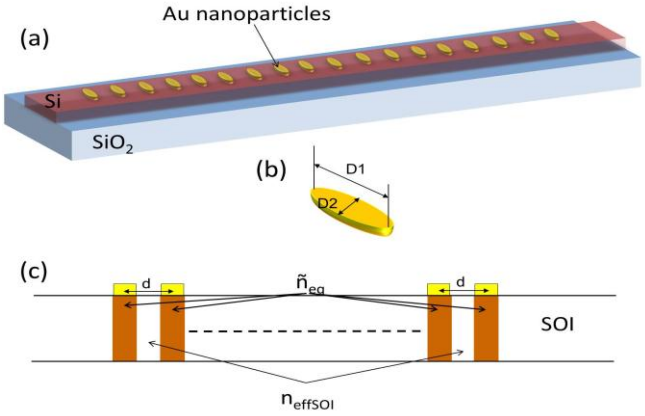

Figure 1: (a) Schematic view of a LSP Bragg grating on SOI waveguide. (b) Schematic view of a given nanoparticle. (c) Principle scheme for the analytical model. Nanoparticles are replaced by transverse waveguide slices with the equivalent index $\tilde{n}_{eq}$.

2.1. Determination of the equivalent index layer

We consider a MNP grating on a substrate permittivity ε_{sub} and immerged in a medium with permittivity ε_{ext}. The MNP grating layer is presently approximated by an equivalent medium with a dielectric function ε_{eq}. The term "equivalent" is preferred to "effective" not to be confused with the effective index of the waveguide. The macroscopic polarization $\vec{P}$ of this equivalent medium is then related to its permittivity and the macroscopic external field $\vec{E}_{ext}$ via [19]:

$$\vec{P} = \varepsilon_0(\varepsilon_{eq} - \varepsilon_{ext})\vec{E}_{ext}, \quad (1)$$

The polarization $\vec{P}$ is also written as the sum of the dipolar moments $\vec{P}$ of individual particles $\vec{P} = N\vec{P}$ where N is the number of particles per unit volume. This lead to:

$$\vec{P} = N\varepsilon_0 V\alpha(\omega)\varepsilon_{ext}\vec{E}_{loc}, \quad (2)$$

where V is the volume and α(ω) is the polarisability of an individual particle $\vec{E}_{loc}$ is the local field "seen" by this particle. In the quasi-static approximation, the polarisability of an ellipsoidal particle with permittivity ε_m and a depolarization factor L_s in a medium with permittivity ε_{ext} is defined by [20] :

$$\alpha(\omega) = \frac{\varepsilon_m - \varepsilon_{ext}}{\varepsilon_{ext} + L_s(\varepsilon_m - \varepsilon_{ext})}, \quad (3)$$

When the local field $\vec{E}_{loc}$ is known, it is possible to determine the equivalent permittivity ε_{eq} from equation (1) and (2):

$$\varepsilon_0(\varepsilon_{eq} - \varepsilon_{ext})\vec{E}_{ext} = N\varepsilon_0 V\alpha(\omega)\varepsilon_{ext}\vec{E}_{loc}. \quad (4)$$

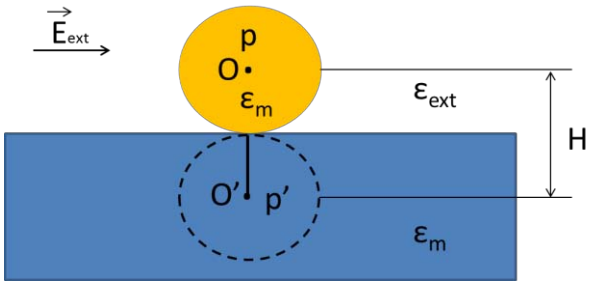

Figure 2: Schematic of a particle placed on a substrate and its image dipole.

Actually, $\vec{E}_{loc}$ can be calculated by considering the particle as a point dipole. The image dipole formalism is then used to account for the presence of a substrate that is presently assumed to be isotropic and non-magnetic (fig. 2). The image dipole $\vec{p}'$ associated to the dipole moment $\vec{p}$ carried by the particle at the interface between the substrate (ε_{sub}) and the external medium (ε_{ext}), is written [21]:

$$\vec{p}' = -\vec{p}\frac{\varepsilon_{sub} - \varepsilon_{ext}}{\varepsilon_{ext} + \varepsilon_{sub}}. \quad (5)$$

The local field in O then results from two contributions, the applied external field $\vec{E}_{ext}$ and the field created by the image dipole $\vec{E}_{img}$: $\vec{E}_{loc} = \vec{E}_{ext} + \vec{E}_{img}$. The electrostatic potential created at any point of space is the sum of the potentials created by dipole $\vec{p}$ and image dipole $\vec{p}'$, respectively. Using the quasi-static approximation, the general expression of the field crated by a dipole $\vec{p}$ at a distance r (point M) in a medium with a dielectric ε_{ext} is:

$$\vec{E}_{dip} = \frac{1}{4\pi\varepsilon_0\varepsilon_{ext}}\frac{3(\vec{p}.\vec{R})\vec{R} - \vec{p}}{r^3}, \quad (6)$$

where $\vec{R} = r.\vec{u}$ with $\vec{u}$ the unit vector born by $\overrightarrow{OM}$. Using the general expression (6), the field created by the image dipole $\vec{p}'$ located in O' at point O is given by:

$$\vec{E}_{dip} = \frac{1}{4\pi\varepsilon_0\varepsilon_{ext}}\frac{3(\vec{p}.\overrightarrow{O'O})\overrightarrow{O'O} - \vec{p}'}{\left|\overrightarrow{O'O}\right|^3}, \quad (7)$$

Since the image dipole $\vec{p}'$ is oriented perpendicularly to $\overrightarrow{O'O}$, then: $\vec{p}'.\overrightarrow{O'O} = 0$. By denoting $\left|\overrightarrow{O'O}\right| = H$ and using Eq. (5), the expression of field $\vec{E}_{img}$ can be re-written as:

$$\vec{E}_{img} = -\frac{1}{4\pi\varepsilon_0\varepsilon_{ext}}\frac{\vec{p}'}{r^3} = \frac{1}{4\pi\varepsilon_0\varepsilon_{ext}H^3}\frac{\varepsilon_{sub} - \varepsilon_{ext}}{\varepsilon_{ext} + \varepsilon_{sub}}\vec{p} \quad (8)$$

This leads to the following expression $\vec{E}_{loc}$:

$$\vec{E}_{loc} = \frac{1}{4\pi\varepsilon_0\varepsilon_{ext}}\left(\frac{\varepsilon_{sub}-\varepsilon_{ext}}{\varepsilon_{ext}+\varepsilon_{sub}}\frac{\vec{p}}{H^3}\right)+\vec{E}_{ext} \quad (9)$$

Where $\vec{P} = N\varepsilon_0 V\alpha(\omega)\varepsilon_{ext}\vec{E}_{loc}$. Let us define K as:

$$-K = \frac{1}{4\pi\varepsilon_0\varepsilon_{ext}}\left(\frac{\varepsilon_{sub}-\varepsilon_{ext}}{\varepsilon_{ext}+\varepsilon_{sub}}\frac{1}{H^3}\right). \quad (10)$$

The equivalent permittivity ε_{eq} is then determined by using the Eqs. (4), (9) and (10). After straightforward calculations, we obtain:

$$\varepsilon_{eq} = \varepsilon_{ext} + \frac{NV\alpha(\omega)\varepsilon_{ext}}{1+KV\varepsilon_0\varepsilon_{ext}\alpha(\omega)}. \quad (11)$$

The expression for ε_{eq} (or rather, that of $\tilde{n}_{eq} = \sqrt{\varepsilon_{eq}}$) is then used in the coupled mode theory to account for the LSP resonance in the Bragg grating. Here it is worthwhile recalling that the "one-particle" model used to derive ε_{eq} not only assumes uncoupled particles, but also neglects radiation losses in the system. As will be seen in Section 5, this leads to a non-symmetric plasmon absorption line whose width is narrower than in measurements. In turn, basic mechanisms of LSP Bragg grating are correctly described.

2.2. Coupled mode theory with LSP resonance

In order to adapt CMT [17] to LSP Bragg gratings, we use the simplified scheme of a periodically structured waveguide shown in fig. 1(c). In waveguide regions close to particles, the waveguide refractive index is taken to be equal to $\tilde{n}_{eq}$. In other regions, the effective index of the bare waveguide, $n_{eff_{SOI}}$ is kept. This implicitly assumes that in waveguide regions close to particles, the electromagnetic energy of the TE guided mode is almost totally transferred to the particles themselves. FDTD simulations reported in Section 4 supports this assumption.

The periodic modulation thus simulated along the waveguide simultaneously includes a "pure" refractive index modulation (real part of the index) and a loss modulation due to nanoparticles (imaginary part of the index). Using the general expression of the complex index of refraction for a material with gain (or loss), $\tilde{n}_{eq}$ is written:

$$\tilde{n}_{eq} = n_{eq} + i\frac{\gamma_{eq}}{k_0} \quad (12)$$

where $k_0=2\pi/\lambda$, λ is the wavelength, n_{eq} the refractive index and γ_{eq} the material gain (or losses if $\gamma < 0$) constant in intensity. For the sake of simplicity, we consider a sinusoidal modulation along the waveguide with real part oscillating between n_{effsoi} and n_{eq} and the imaginary part oscillating between 0 and γ_{eq}/k_0. For such a modulation, the spatial evolutions of the real and imaginary parts of the optical index in the propagation direction equal:

$$n(x) = n_0 + n_1\cos\left(\frac{2\pi x}{d}\right) \quad (13)$$
$$\gamma(x) = \gamma_0 + \gamma_1\cos\left(\frac{2\pi x}{d}\right)$$

were the value of n_0, n_1, γ_0 and γ_1 are determined from initial conditions. Setting the origin at the first particle, we obtain:

$$n_0 = \frac{n_{eq}-n_{eff_{SOI}}}{2}$$
$$n_1 = \frac{n_{eq}+n_{eff_{SOI}}}{2} \quad (14)$$
$$\frac{\gamma_0}{k_0} = \frac{\gamma_1}{k_0}$$
$$\frac{\gamma_1}{k_0} = \frac{\gamma_{eq}}{2k_0}$$

The CMT model then leads to the following coupled differential system [17]:

$$\frac{dA}{dx} = -i\kappa B(x)e^{i2\Delta\beta x} + i\gamma_0 A(x) \quad (15)$$
$$\frac{dB}{dx} = i\kappa A(x)e^{-i2\Delta\beta x} - i\gamma_0 B(x)$$

where A(x) and B(x) represent the propagative and contra-propagative modes, respectively. The coupling constant, κ, is given by:

$$\kappa = \frac{\pi}{\lambda_0}\left(\frac{n_{eq}+n_{eff_{SOI}}}{2}+i\frac{\gamma_{eq}}{2k_0}\right). \quad (16)$$

The phase mismatch 2β is given by:

$$2\Delta\beta = n_{eff_{SOI}}\frac{2\pi}{\lambda} - m\frac{2\pi}{d}. \quad (17)$$

The resolution of coupled differential equations (15) allows us to calculate the normalized transmission and reflection coefficients for the waveguide with LSP Bragg grating:

$$T = \left\|\frac{A(x)}{A_0}\right\|^2. \quad (18)$$
$$R = \left\|\frac{B(x)}{A_0}\right\|^2$$

Let us recall here that the specific parameters of nanoparticles are included in the model via Eq. (3). In what follows, the particle size is used as a variable parameter to investigate the different behaviors of LSP Bragg grating.

3. LSP Bragg grating behaviors

We consider a Bragg grating made of 50 particles with the Bragg resonance at λ=1500 nm. In principle, particles should be spaced by 300 nm to operate in the first Bragg order. However, this would lead in turn to strong coupling between particles with the consequences that MNP chain itself would behave as a waveguide [8] and the Bragg grating mechanism would be strongly perturbed. For this reason, a 600 nm spacing is fixed between particles corresponding to a second-order grating. Fig. 3 shows the calculated waveguide transmission and reflection for LSP Bragg gratings with different MNP sizes. Three situations are found depending on the spectral position of the LSP. When LSP resonance occurs at shorter wavelength than the Bragg resonance (fig. 3(a)), the waveguide transmission exhibits a minimum at the Bragg wavelength as expected. When the LSP resonance coincides with the Bragg resonance, the transmission dip is replaced by a small transmission peak. At the same time, the Bragg reflection is significantly attenuated (fig. 3(b)). When the plasmon resonance wavelength is longer than the Bragg wavelength λ_{Bragg}, a weak but quite detectable peak appears in the transmission spectrum (fig. 3(c)). Calculated curves showing the real (n_{eq}) and imaginary ($k_{eq}=\gamma_{eq}/k_0$) parts of the equivalent layer index (right column in fig. 3) help us to explain the different behaviors. For a plasmon resonance at short wavelength (fig. 3(a)), the real part of the refractive index dominates, and the device behaves as a standard Bragg grating. For a plasmon resonance at a longer wavelength than λ_{Bragg} (fig. 3(c)), the imaginary part of the refractive index dominates, and the transmission curve corresponds to a Bragg grating modulated by losses [17]. Fig. 3(b) represents an intermediate situation.

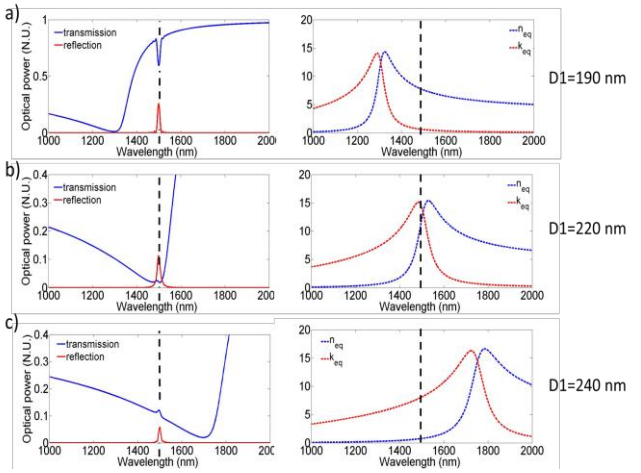

Figure 3: Left column: calculated transmission and reflection spectra of an SOI waveguide with LSP Bragg grating. Right column: real (n_{eq}) and imaginary (k_{eq}) parts of the equivalent layer refractive index. The vertical dashed line shows the spectral position of the Bragg resonance. The long axis of gold ellipsoids is D1 = 190, 210 and 240 nm in a), b) and c), respectively. Their short axis and height are identical in the three cases: D2 = 80 nm, h = 30 nm.

4. FDTD calculations

FDTD calculations were performed to validate the analytical model. A commercial software from Lumerical, FDTD Solutions was used for this purpose. Because a precise modeling of > 25 µm long structures (50 gold nanoparticles) with 3 nm accuracy needed time-consuming simulations, we therefore limited ourselves to structures comprised of only five nanoparticles, further referred to as "native" Bragg gratings. The spacing between particles was chosen to be 500 nm, close to that measured in fabricated structures (see Section 5). Correspondingly, the grating second order was calculated to occur near l =1325 nm. The short axis and height of gold ellipsoids were taken to be D2 = 80 nm and h = 30 nm in all calculations. The long ellipsoid axis (D1) was varied from 180 to 210 nm.

Figure 4 shows FDTD results for a "native" Bragg grating comprised of five particles with D1 = 180 nm. In this case, the plasmon resonance occurs at a wavelength shorter than the Bragg resonance. In agreement with theoretical predictions from the analytical model (fig. 3(a)), the waveguide transmission exhibits a minimum at the Bragg wavelength while a maximum is obtained for the waveguide reflection (fig. 4(a)). The field maps show that the propagation of the TE waveguide mode is strongly perturbed by particles. This perturbation is stronger at short wavelengths (fig. 4(b)) than at long wavelengths (fig. 4(d)). At 1326 nm, the clear evidence of two field maxima between neighboring particles (fig. 4(c)) confirms that the Bragg grating is operated on its second order. Interferences between the two counter-propagating waves are well resolved in the first part of the waveguide. A detailed inspection of the field distribution in the central part of the waveguide shows that the field intensity is weak below the particles while it is strong between particles. A very high intensity is also calculated in the very proximity of particles themselves (dotted squares in b), c) and d)). These results justify the approximations used to establish coupled mode equations in Section 3.

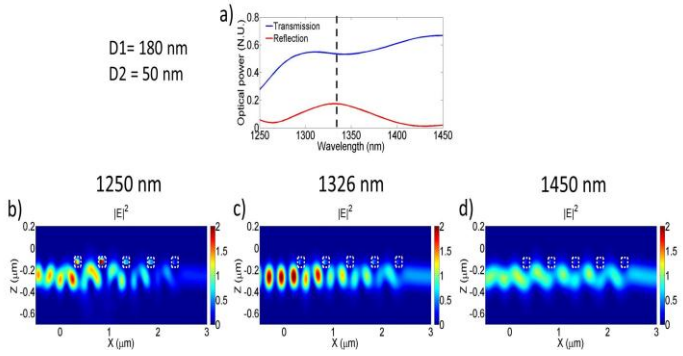

Figure 4: FDTD simulations of a "native" LSP Bragg grating consisting of 5 gold ellipsoids with D1=180 nm, D2 = 50 nm and h = 30 nm. a): waveguide transmission and reflection spectra calculated around the Bragg wavelength

(~1326 nm). b), c) and d): mapping of the field intensity $|E|^2$ along a longitudinal waveguide cross-section for $\lambda = 1250$, 1326 and 1450 nm, respectively. White dotted squares indicate the positions of the particles.

Figure 5 shows FDTD calculations for D1=190 nm. The plasmon resonance wavelength coincides with the Bragg wavelength in this case. In agreement with predictions from the analytical model (fig. 3(b)), a transmission peak is now observed at the Bragg resonance (fig. 5(a)). The calculated field maps (figs. 5(b, c, d)) are similar to those of fig. 4.

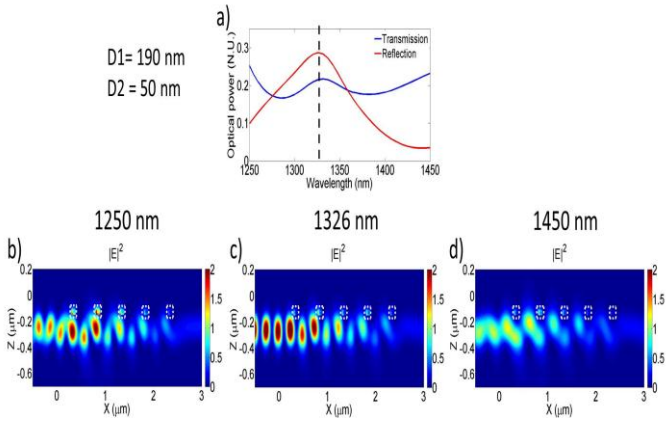

Figure 5: Same as fig. 4 except for D1 = 190 nm

For gold ellipsoids with a long axis D1 = 210 nm (fig. 6), the plasmon resonance is shifted to the long wavelength side of the Bragg resonance. Again in agreement with the results of the analytical model (fig. 3(c)), the waveguide transmission spectrum exhibits a small peak near the Bragg resonance. The exact location of this peak also depends on the shape of the plasmon absorption curve. The calculated field maps (figs. 6(b, c, d)) are similar to those of fig. 4.

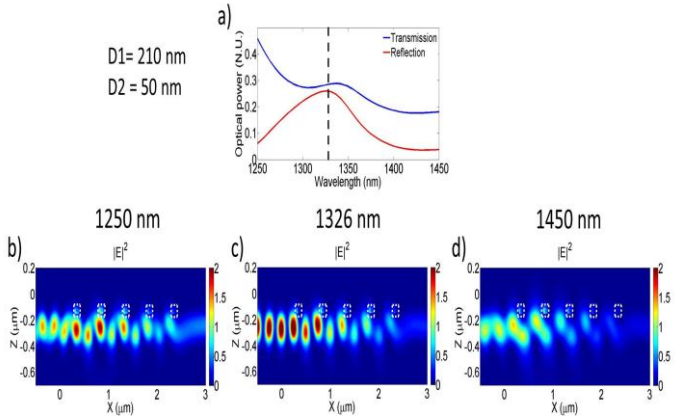

Figure 6: Same as fig. 4 except for D1 = 210 nm.

5. Experiments

Three series of LSP Bragg gratings as schematically shown in fig. 1 were fabricated on single-mode silicon (Si) ridge waveguides with 500 × 220 nm^2 cross-section. All gratings were composed of 50 gold ellipsoids periodically spaced by ~ 510 nm (fig. 7). The main difference between the three series of gratings was the size of ellipsoids. The long axis and short axis were respectively: D1 = 169 ± 5nm; D2 = 57 ± 5nm (fig. 7(a)), D1 = 181 ± 5nm; D2 = 50 ± 5nm (fig. 7(b)) and D1 = 211 ± 5nm; D2 = 59 ± 5nm (fig. 7(c)). Gold nanoparticles were fabricated on top of Si waveguides using electron-beam lithography followed by a lift-off process. A 30 nm gold layer was deposited by electron-beam evaporation. A 1 nm titanium (Ti) adhesion layer was deposited prior to the deposition of gold. A Drude model was used to fit the ellipsometric measurements of deposited gold layers. Accurate dispersion data of gold obtained in this way were further used in the analytical model as well as in FDTD simulations.

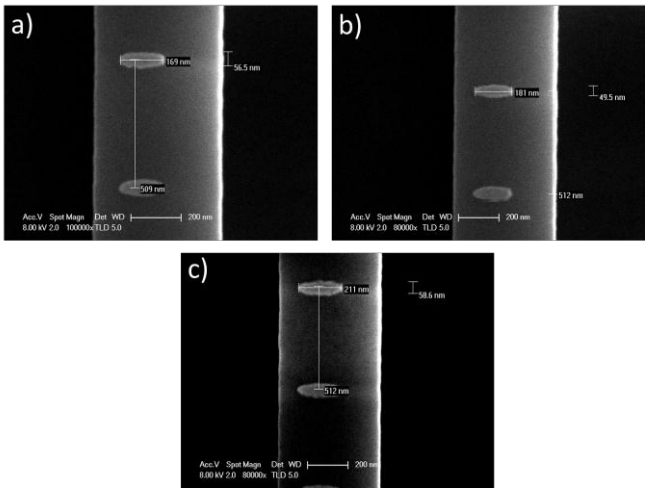

Figure 7: Scanning Electron Microscope (SEM) images of nanoparticles for the three series of fabricated LSP Bragg gratings. The particle sizes are different in the three cases.

The waveguide transmission spectra were measured by injecting a polarized light to the butt facet of the Si waveguide using a lensed polarization maintaining fiber. A cw tunable laser with polarization set to TE was used as the light source. A × 20 objective with 0.35 numerical aperture was used to collect the transmitted light at the waveguide output. The collected light was then detected with a power meter. Normalization of transmission measurements was achieved using a reference waveguide without MNP. The input light was scanned by steps of 1 nm over the 1260-1630 nm range. Figure 8 shows a comparison between experimental results and theoretical results from the analytical model. "Noise" on the experimental curves is due to Fabry-Perot oscillations caused by reflections at the waveguide ends. For structures a) and b), the LSP resonance occurs at a lower wavelength than the second-order Bragg

resonance near 1320 nm. Transmission dips are then experimentally observed at the Bragg resonance in agreement with the predictions of the analytical model (figs. 5(a) and (b)). For gold particles with larger size (fig. 8(c)), the LSP resonance occurs at a longer wavelength than the Bragg resonance. A weak transmission peak is observed in this case as in fig. 5(c). In the three cases a), b) and c), the plasmon linewidth is broader than predicted theoretically. This difference is mainly explained by the quasi-static approximation used in the analytical model. Indeed, radiative losses of metallic dipoles are neglected with the consequence that the calculated LSP resonance presents a better quality factor than the experimental one. On the other hand, fabrication imperfections and particle size dispersion tend to increase the measured LSP bandwidth. It is finally worthwhile noticing that Fabry-Perot oscillations can be used in conjunction with the Bragg grating resonance to produce narrow transmission peaks with relatively high (near 30dB) rejection ratio (fig. 8(c)).

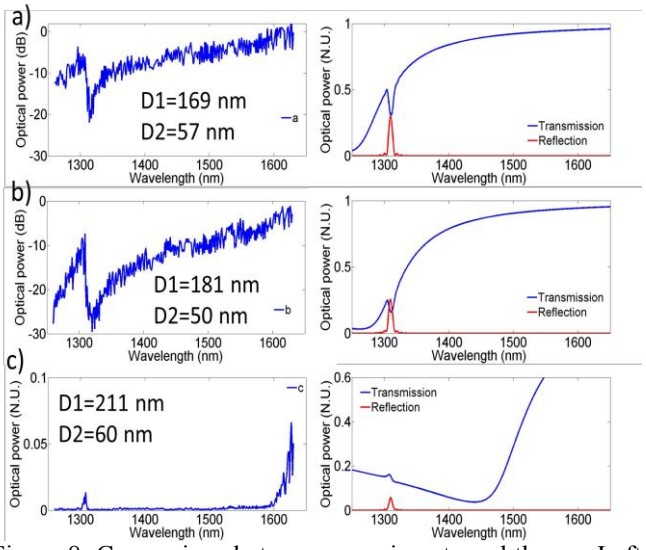

Figure 8: Comparison between experiments and theory. Left column: waveguide transmission spectra measured for fabricated LSP Bragg gratings a), b), and c). In figures a) and b) logarithmic scale is used for better visibility. Right column: theoretical calculations from the analytical model.

6. Conclusion

In this work we have developed the concept of localized surface plasmon Bragg gratings integrated on dielectric waveguide. We have demonstrated both theoretically and experimentally that different types of transmission responses could be obtained depending on the spectral position of the LSP resonance with respect to the Bragg resonance. As a major result, LSP gratings can be operated either in the refractive index modulation regime or in the loss modulation regime. For a given grating period, the operating regime can be controlled with the size of metallic particles. An analytical model has been developed to qualitatively predict the grating behavior. The model predictions have been verified from FDTD simulations of short gratings with a small number of particles. Although no attempt has been presently made to optimize the LSP Bragg grating performances, we believe that these gratings can find applications to optical filtering and chemical or bio-sensing. Metallic losses in guided optics can be partially compensated for with the use of amplifier waveguide sections.

Acknowledgements

The authors acknowledge R. Colombelli and D. Costantini for useful discussions. C. Delacour and A. Chelnokov for sample preparation. This work has been supported by the Agence Nationale de la Recherche under contract PLACIDO N° ANR-08-BLAN-0285-01. The M. Février grant has been funded by Region Ile-de-France.

References

[1] W. L. Barnes, A. Dereux and T. W. Ebbesen, Nature, 424, 824, (2003).
[2] M. A. Noginov et al., Nature, 460, 1110, (2009).
[3] D. K. Lim, K. S. Jeon, H. M. Kim, J. M. Nam and Y. D.Suh, Nature Mater. 9, 60, (2010).
[4] S. M. Nie and S. R. Emery, Science. 275, 1102, (1997).
[5] C. Huang et al., Biomed Microdevices. 11, 839, (2009).
[6] M. Quinten, A. Leitner, J. R Krenn and F. R. Aussenegg, Opt. Lett. 23, 1331, (1999).
[7] J. R Krenn et al., Phys. Rev. Lett. 82, 2890, (1999).
[8] M. Fevrier et al., Nano letters. 12, 1032, (2012).
[9] S. L. Zou, N. Janel and G. C. Schatz, J. Chem. Phys. 120, 10871, (2004).
[10] Y. Z. Chu, E. Schonbrun, T. Yang and K. B. Crozier, Appl. Phys. Lett. 93, 181108, (2008).
[11] V. G. Kravets, F. Schedin, and A. N. Grigorenko, Phys. Rev. Lett. 101, 087403, (2008).
[12] R. Quidant, C. Girard, J. C. Weeber, and A. Dereux, Phys. Rev. B. 69, 085407, (2004).
[13] W. Zhou and T. W. Odom, Nature Nanotech. 6, 423, (2011).
[14] Y. Uchio, M. Shimojo, K. Furuya and K. Kajikawa, J. Phys. Chem. C, 114, 4816, (2010).
[15] S. Zhang, D. A. Genov, Y. Wang, M. Liu, and X. Zhang, Phys. Rev. Lett. 101, 047401, (2008).
[16] R. D Kekapture, E. S. Barnard, W. Cai, and M. Brongersma, Phys. Rev. Lett. 104, 243902, (2010).
[17] A. Yariv and P. Yeh. Photonics optical electronics in modern communications, sixth edition, Oxford University press, 2005.
[18] E. Lidorikis, S. Egusa and J. D. Joannopoulos, J. A. P. 101, 054304, (2007).
[19] T. Yamaguchi, S. Yoshida, and A. Kinbara, Thin Solid Film. 21, 173, 1974.
[20] C. F. Bohren and D. R. Huffman, Wiley : New York, (1983).
[21] J. Jackson. Classical Electrodynamics. Wiley : New York, (1999).

Electromagnetic coupling in a planar periodic configuration of resonators

C. Jouvaud[*1], A. Ourir[2], and J. de Rosny[2]
[1]CEA, DAM, Gramat, F-46500 Gramat, France
[2]Institut Langevin, Université Denis Diderot Paris 7, UMRS CNRS 7587, ESPCI,
10 rue Vauquelin 75231 Paris cedex 05, France.
* camille.jouvaud@espci.fr

Abstract

We are studying arrays composed of a periodic arrangement of sub-wavelength resonators. An analytical model is developed inside an array of 4 by 4 multi-gap split ring resonators. To describe the frequency splitting of the single fundamental resonance, we propose a simple model based on the approximation of each resonator as an electrical dipole and a magnetic dipole that are driven by the same complex amplitude. We show that the relative strength of the two dipoles strongly depends on cell symmetry. With this approximation, the dispersion relation can be obtained for an infinite size array. A simple matrix diagonalization provides a powerful way to deduce the resonant frequencies for finite size array. These results are comforted by numerical simulations. Finally, an experimental demonstration of a tunable antenna based on this study is presented.

1. Introduction

Behavior of electromagnetic waves in periodic medium in which the lattice is much smaller than the wavelength is a challenging field. Metamaterials are such composite structures, which involves periodic arrays of sub wavelength inclusions. By designing the elementary cell and controlling some parameters like a given permittivity and/or permeability, metamaterials can make up global mediums with interesting properties, like a negative refractive index.[1]

Most of the time, the resonant cell of a metamaterial are designed to minimize the coupling between cells. Consequently, all the metamaterial resonates at the same frequency. This condition is required to apply theory of homogenization and assume the metamaterial as a continuous material. Nevertheless, coupling effect always occurs and its preponderance is only a question of relative weight with the self-resonance of the cell.

The coupling between an array of half wavelength long rods that are only spaced by less a tenth of a wavelength have been studied in ref.2. It has been shown that the coupling induces a strong splitting of the resonance frequencies. This phenomenon is analogous to Kronig-Penney potential wells in solid state physics [3].
In this paper, we investigate the behavior of a finite array of split ring resonators (SRR) popularized by Pendry et al.[4].. We develop a dipolar model based on near-field effects. We use this model to describe the nature and the origin of the coupling between the resonators. Finally, we study the far-field radiation of the finite structure.

Two types of array are studied. Both consist of 4 by 4 split ring resonators. For the first one, we use an asymmetric square SRR with 3 gaps at the center of 3 sides. For the second one, we use a symmetric square SRR with 4 gaps at the center of the 4 sides. In Fig.1, a small loop placed above one SRR of the first array provides a near field excitation of the structure. It shows the splitting of the main resonance. This splitting is the result of the coupling effect between the resonators. When the small loop antenna is placed above the second structure, the splitting phenomenon remains but fewer resonances are observed (Fig.2). We propose here to use a dipolar model to investigate these phenomena.

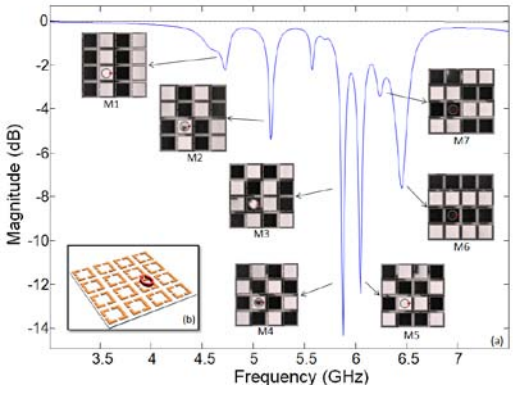

Figure 1: (a) Reflection coefficient of a small loop antenna. The M1 to M7 gray level maps show the normal magnetic field for 7 resonant frequencies. (b) the 4 by 4 array of 3-gaps SRR. In red, the small loop antenna.

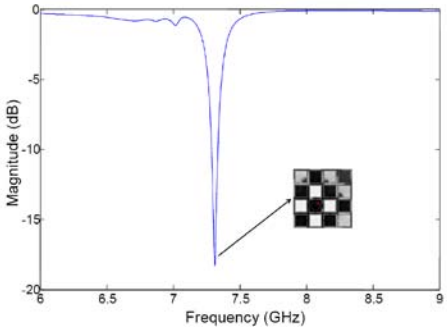

Figure 2 : Reflection coefficient of a small loop antenna of a 4 by 4 array of 4-gaps SRR

2. A dipolar model

We propose an original coupling model which is a generalization of the work published in Ref [5][6]. It is well known that the current distribution of the fundamental mode depends mainly on frequency. Moreover we assume that this current distribution can be approximated only by an electrical and a magnetic dipole. This approximation have been done with a Langrangian approach in [7].The expression of these dipoles are given by the geometry of the elementary cell:

$$\mathbf{P} = \frac{Id\mathbf{u}_d}{i\omega} \qquad (1)$$
$$\mathbf{M} = IS\mathbf{u}_m$$

where d and S are respectively a characteristic distance and an effective surface of the resonator.

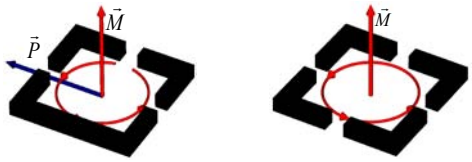

Figure 3: The dipolar model for a 3 gaps and an 4 gaps SRR

A 3 gaps SRR provides a magnetic and a electric dipoles disposed as shown in Fig.3 While, because of its geometrical symmetry, the 4 gaps SRR is only associated with a magnetic dipole.

Near-field radiations of the electric and magnetic dipoles at a distance r are given in Eq.2.

$$\mathbf{E} = \frac{1}{4\pi\varepsilon_0}\frac{(3(\mathbf{u}_d.\mathbf{P})\mathbf{u}_d - \mathbf{P})}{r^3} \qquad (2)$$
$$\mathbf{B} = \frac{\mu_0}{4\pi}\frac{(3(\mathbf{u}_m.\mathbf{M})\mathbf{u}_m - \mathbf{M})}{r^3}$$

With this approximation, an analytic expression of the coupling between two cells is obtained. We choose to describe the coupling in terms of electrical impedance, i.e., the FEM induced on a cell when a current flows through another one.

$$emf = -i\omega\iint \mathbf{B}_1.d\mathbf{S}_2 + \oint \mathbf{E}_1.d\mathbf{l}_2 \qquad (3)$$

To describe the interaction between all the cells of the array, we introduce the mutual coupling matrix Zm. Moreover, we have to introduce the diagonal self-impedance matrix Zs. Because, we deal with simple resonators, we assume that the electrical behavior of each resonator is well described by a simple RLC (resistance, inductance, capacitive) system.

3. Currents determination

From the self (Zs) and mutual impedance (Zm) matrices resulting from the near-field radiation of a magnetic and an electric dipole, we deduce a set of *N* equations, where *N* is the number of cells, between the complex amplitude of the currents on the cells and the excitation FEM on each cell.

$$(i\omega L_s + \frac{1}{i\omega C_s} + R_s)I(l,m) + \sum_{l'\neq l, m'\neq m} Z(l'-l, m'-m)I(l',m') = 0 \qquad (4)$$

An implicit dispersion relation is deduced from (4) when *N* is very large. Limiting the coupling to the closest neighbors, an explicit and simple can be worked out for a 3 gaps SRR (see Fig.4(a)) and 4 gaps structure (see Fig.4(b)). From this relation, we can derive the span of the frequency splitting of the fundamental resonance. Those two curves reflect the magnetic and electric coupling for the first structure and the magnetic coupling for a second one.

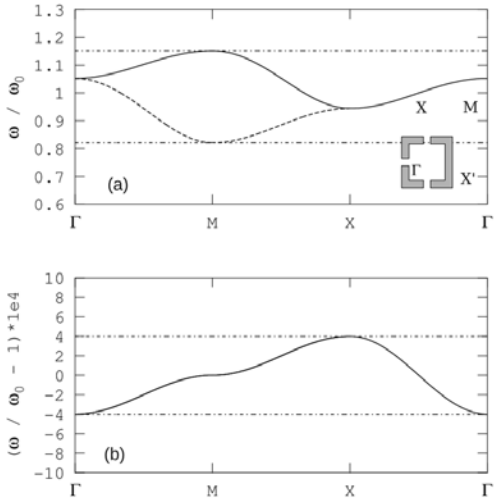

Figure 4: Dispersion relations for two arrays of 3-gap cells (a) and of 4-gap cells (b). The dispersion relation is plotted on the 4 major axis of the Brillouin zone. The dashed lines show the minimum and maximum values.

For finite size system, the complex amplitude on each resonator is deduced from the inversion of the mutual coupling matrix which is the sum of the self and mutual impedance matrices ($\mathbf{Z}=\mathbf{Z}_m+\mathbf{Z}_s$)

$$\mathbf{I} = (\mathbf{Z}_m + \mathbf{Z}_s)^{-1}\mathbf{S},$$

where **S** is the fem induces on each cell by the source.

We show that the resonances occurs when the imaginary part of the eigen-values of **Z** are equal to zero. Because $\mathbf{Z}_s$ is equal to the identity matrix time the self impedance for an individual cell, a resonance appears when the imaginary part of the self impedance is opposite in sign to the self impedance. Fig.5 shows the calculated resonant modes for the 3 gaps structure. As expected, we observe that frequency position and the amplitude of the modes depend on both the mutual and the self impedance of the resonators. For 4 gaps structure, we have shown theoretically that only one resonance is observed because the coupling effect is too weak to induce a mode splitting effect. Actually, as shown by [8], even with SRR, the electric coupling can completely dominate the magnetic one.

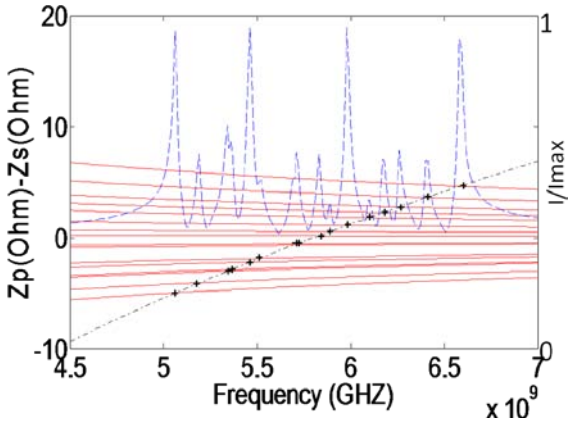

Figure 5: Frequency dependence of : the self impedance versus frequency (dash-dotted line), the imaginary part of the eigen-values of the mutual impedance times minus one (Continuous line shows) and the current of one particular cell. These results are obtained with an array of 4 by 4 3-gap cells.

4. A dynamic antenna tuning and beamforming

The eigen-modes of finite size arrays are poor radiators because the spatial oscillations of the mode patterns are smaller than a wavelength and sub-wavelength modes hardly couple to propagative waves. However the Purcell's effect can mitigate this limitation. Indeed, the strong resonance effect significantly enhances the radiated power and compensates for the low coupling.

The studied structure can thereby be used as an antenna radiating at these frequencies. With the impedance formalism, the antenna pattern is simply worked out from the current distribution of the array. On Fig. 6, instead of tuning the fundamental frequency of the single cells, we electrically tune the resonance frequency of the cells thanks to diodes which has a variable capacitance that is a function of the voltage applied on its terminals (varicaps). Fig. 7 shows the pattern of the radiated field for different voltages impressed to the diodes. The different patterns correspond to different splitted modes.

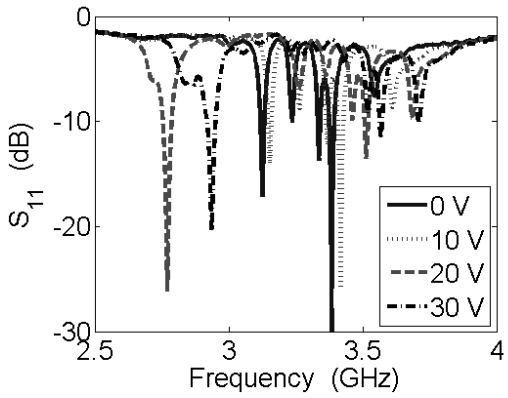

Figure 6: Measured reflection coefficient of a small loop antenna for different voltage applied.

Thus, a tunable directive antenna can be realized by adjusting the working frequency. This main advantages of this antenna is to show a small form factor, a tunable radiation directivity and a good matching.

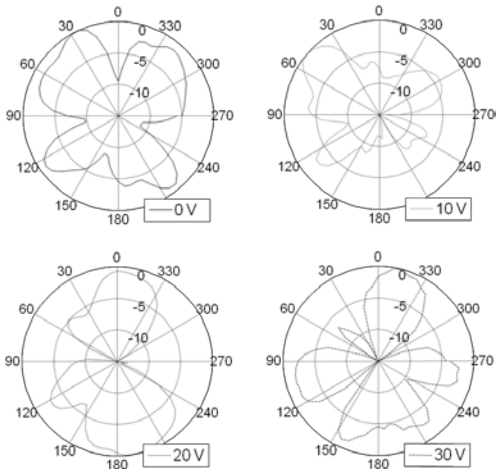

Figure 7: Measured radiation pattern of a small array of 3 gaps SRR for different applied voltage on the Varicaps for the same frequency.

5. Conclusions

We developed a model based on impedance formalism for infinite and finite size array of electric and magnetic resonators that are separated by less than fraction of a wavelength. Based on this approach, the electromagnetic behavior of such a structure is explained. The electromagnetic coupling induces a frequency splitting of the fundamental mode a single cell. The dispersion relation leads to estimate frequency span of the modes. Diagonalization of the mutual impedance matrix explains why the fundamental mode is splitted into *N* modes where *N* is the number of cells of the array. Finally an application to a tunable directive antenna is proposed. This small antenna shows good radiation efficiency.

6. Acknowledgments

This work has been partially supported by the French National Agency (ANR) for its financial support with the project OPTRANS (number 2010 BLAN 0124 04). We gratefully acknowledge the financial support of the French government-funded technological research organization CEA/DAM.

References

[1] D. R. Smith et al. " Composite Medium with Simultaneously Negative Permeability and Permittivity", Phys. Rev. Lett. 84 , 4184 (2000).

[2] Lemoult F., Lerosey,G., Rosny, J., and Fink, M., "Resonant Metalenses for Breaking the Diffraction Barrier", Phys. Rev. Lett. No.104, 20390,1 (2010).

[3] R. Kronig and W. G. Penney, Quantum mechanics of electrons in crystal lattices. Proc. R. Soc. London Ser. A, 130,499-512 (1931).

[4] J. B. Pendry, A. J. Holden, D. J. Robbins, and W. J. Stewart, “Magnetism from conductors and enhanced nonlinear phenomena”, IEEE Trans. Microwave Theory Tech. 47, 2075 (1999).

[5] Marques, M., and al,"Role of bianisotropy in negative permeability and left-handed metamaterials" , Phys Rev B. No. 65, 144440, (2002).

[6] E. Shamonina, V. A. Kalinin, K. H. Ringhofer, and L. Solymar, "Magnetoinductive waves in one, two, and three dimensions" J. Appl. Phys. 92, 6252, (2002).

[7] Sersic, I.; Frimmer, M.; Verhagen, E. & Koenderink, A. F."Electric and Magnetic Dipole Coupling in Near-Infrared Split-Ring Metamaterial Arrays" Physical Review Letters, 103, 213902, (2009).

[8] Katsarakis, N.; Koschny, T.; Kafesaki, M.; Economou, E.N .& Soukoulis,C.M."Electric coupling to the magnetic resonance of split ring resonators"Applied Physics Letters, AIP, 84, 2943-2945, (2004).

A Compact Slotted Coplanar-Waveguide (CPW) Fed Metamaterial Inspired Patch Antenna for the Wi-MAX 5.5 GHz Application

M. A. Wan Nordin[1,2], M. T. Islam[1], N. Misran[2]

[1]Institute of Space Science (ANGKASA), Universiti Kebangsaan Malaysia, Malaysia
[2]Department of Electrical, Electronic and Systems Engineering, Universiti Kebangsaan Malaysia, Malaysia

Abstract

A metamaterial-inspired compact patch antenna resonating at 5.5 GHz for the 5.5 GHz Wi-MAX range application is proposed. The antenna is fed using a coplanar-waveguide (CPW) feedline that has been designed to have a characteristic impedance of 50Ω. The compact antenna is also a wideband antenna with a bandwidth (below -10 dB) of 1.3 GHz in the said frequency range, with a gain of 2.2 dB. The size of the patch in terms of the free-space wavelength is $\lambda_0/15$ x $\lambda_0/9$ x $\lambda_0/29$. The wide bandwidth of the antenna is achieved through reactively loading the single patch through the incorporation of the slot.

1. Introduction

Lately, the electromagnetic metamaterial (MTM) has drawn considerable attention amongst engineers due to the potential applications arising from the newly proposed electromagnetic concepts. Electromagnetic MTM can be achieved through resonant structures such as the split-ring resonator-thin wire (SRR-TW) or non-resonant structures which are transmission line-based [1]. The transmission line (TL) approach towards a MTM structure has led towards the proposed general structure/ model known as the composite right/left-handed transmission line (CRLH-TL) [2]. The CRLH-TL MTM structure is achieved by incorporating series capacitances and shunt inductances into a transmission line. The incorporated elements are termed left-handed since they contribute towards the left-handedness characteristic of the propagation within the CRLH-TL. The series capacitance and shunt inductance can be achieved through discrete or distributed components. Amongst famous techniques by which the series capacitance and shunt inductance are achieved are through the metal-insulator-metal (MIM) capacitors and vias, respectively [3]. It is good to note that the loading of the capacitors and inductors into the planar structure, are in essence a reactive loading mechanism.

Most of the proposed MTM structures are bulk structures, which are structures that are achieved through array arrangement of MTM unit cells that would finally form an MTM. However, bulk MTM structures have several shortcomings such as cumulative unit cell losses and difficulty in the overall fabrication process [4]. Recently, structures known as metamaterial-inspired antennas were proposed [4]-[6]. Metamaterial-inspired antennas are designed using the MTM paradigm, understanding and parameters derived from MTM equivalent-circuit models in order to achieve new structures or improve the performance of existing structures [7]. Proposed metamaterial-inspired antennas have no more than a few unit-cells, which helps in circumventing the current limitations of bulk MTM structures.

Reactive loading is one form of using the MTM paradigm into antenna designs [5]. By reactively loading a planar antenna, the equivalent-circuit parameters of the antenna can be modified. This gives rise to different antenna design and performance measurement. In this paper, the reactive loading idea was used to improve the performance of a coplanar-waveguide (CPW) fed patch antenna working at the 5.5 GHz Wi-MAX frequency, while maintaining the compact structure of the initial antenna.

2. Antenna Design

The geometry and configuration of the proposed antenna is shown in Fig. 1. The antenna was designed on a substrate that has a dielectric permittivity, ε_r of 10.2 with a thickness of 1.905 mm. The antenna is in the form of a single patch which has a single T-like slot incorporated onto it, and is fed by a coplanar waveguide (CPW) transmission line that has 50Ω characteristic impedance. The proposed antenna structure has no ground plane on the bottom side. The length, L and width, W of the entire antenna structure are 25 mm and 32 mm respectively. The length of the patch, Lp, and its width, W_p are 5.7 mm and 6.2 mm respectively. This corresponds to $\lambda_0/15$ x $\lambda_0/9$ x $\lambda_0/29$ at the resonant frequency, where λ_0 is the free-space wavelength. The slots have width, Ws, and length, L_s, which are 0.5 mm and 4.2 mm respectively. The single patch antenna without the slots being incorporated is a single patch antenna that resonates at the Wi-MAX 5.5 GHz frequency.

At the resonant frequency, the surface currents throughout the surface of the radiating patch are in-phase as shown in Fig. 2a. The introduction of the slot onto the single patch antenna is inspired by the reactive loading of planar MTM structures. The slot introduced a series capacitive loading to the single patch antenna through the gaps within the slots. The introduction of the slot did not change the phase of the surface current distribution when compared to the single patch antenna's surface current shown in Fig. 2a. The path of the current was only slightly increased, corresponding to a slight increase in the series

inductance. The gaps produced by the slots provided for series capacitances. The surface current of the proposed slotted antenna is shown in Fig. 2b.

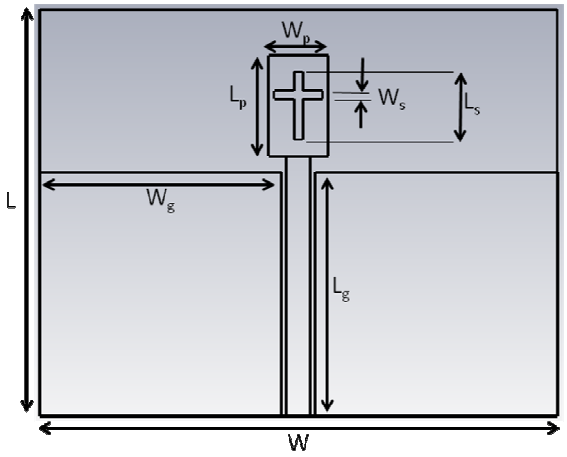

Figure 1: The geometry of the proposed antenna structure.

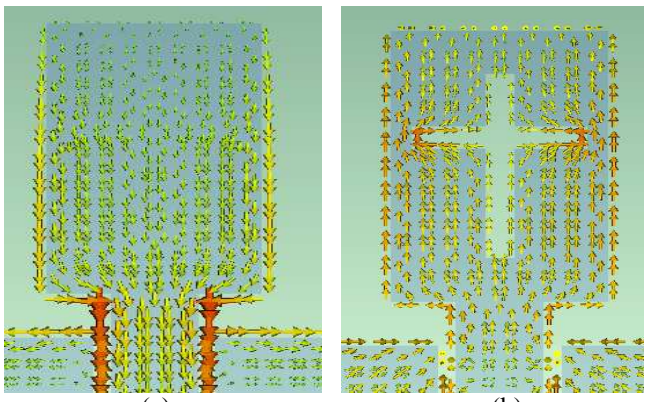

(a) (b)

Figure 2 (a) Surface current distribution of the monopole antenna at 5.5 GHz (b) Surface current distribution of the slotted monopole antenna at 5.5 GHz

3. Results and Discussion

The antenna structure was analyzed using the Finite Integration Technique (FIT) based software, CST. The return loss, S_{11} of both the single patch and the proposed slotted patch antenna is shown in Fig. 3. The series capacitance which was introduced by the slot was seen to have enhanced the bandwidth of the single patch at the resonant frequency of 5.5 GHz. Before the slots were incorporated, the antenna had a -10dB bandwidth of 23%. The slots were able to increase this bandwidth to 33% at the same resonant frequency, giving a bandwidth (at -10dB) of 1.8 GHz. This enables the antenna to be categorized as an ultra wideband (UWB) antenna.

The gain of the slotted antenna was also improved as compared to the single patch antenna. The gain of the slotted antenna is 2.2 dB, while the single patch antenna had a gain of 2.1 dB. The simulated radiation pattern of the proposed slotted antenna is shown in Fig. 4. Fig 4a shows the radiation pattern of the antenna of the E plane (xy-plane, $\theta=90^0$) and Fig 4b the H plane (yz-plane, $\varphi=90^0$).

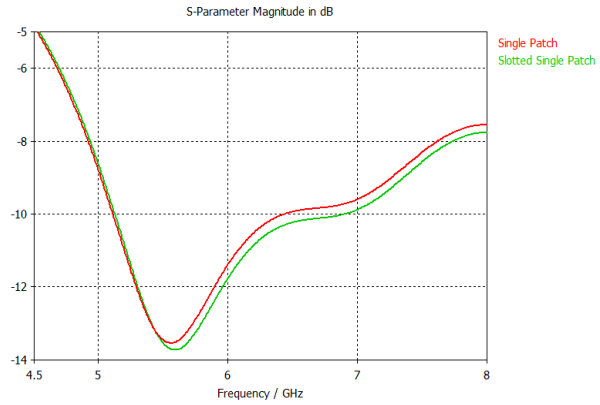

Figure 3 The return losses, S11 of the single patch antenna and the proposed slotted antenna

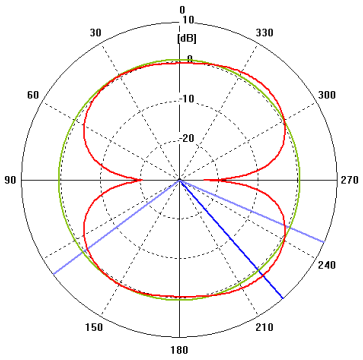

(a)

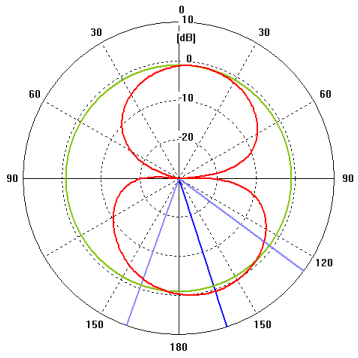

(b)

Figure 4 Simulated radiation patterns of the proposed slotted antenna at 5.5 GHz (a) E plane (xy-plane, $\theta=90^0$) and (b) H plane (yz-plane, $\varphi=90^0$)

4. Conclusions

A bandwidth and gain enhanced slotted patch antenna was designed for the 5.5 GHz Wi-MAX application. The slot

that was introduced onto the single patch configuration served as a capacitive loading for the antenna design, which was able to improve the bandwidth and gain of the initial antenna. The proposed slotted patch antenna has a -10dB bandwidth of 33% and gain of 2.2dB. The size of the antenna at resonant frequency, in terms of the free-space wavelength is $\lambda_0/15$ x $\lambda_0/9$ x $\lambda_0/29$.

References

[1] C. Caloz and T. Itoh, Electromagnetic Metamaterials: Transmission Line Theory and Microwave Applications, the Engineering Approach, John Wiley & Sons, Inc, 2006

[2] C. Caloz and T. Itoh, "Novel microwave devices and structures based on the transmission line approach of metamaterials", IEEE-MTT Int'l Symp., vol. 1, pp. 195-198, June 2003

[3] C. Caloz, A. Lai, T. Itoh, "Wave interactions in a left-handed mushroom structure", Ant. and Prop. Soc. Int. Symp. 2004

[4] R. W. Ziolkowski, P. Jin, C-C Lin, Metamaterial-inspired engineering of antennas, Proc. of the IEEE Vol. 99, No. 10, 1720- 1731, Oct. 2011

[5] J. Zhu and G. V. Eleftheriades, "Dual-band metamaterial-inspired monopole antenna for WiFi applications", Electronics Lett., Vol. 45, No. 22, Oct. 2009

[6] R. W. Ziolkowski, P. Jin, C-C Lin, Multi-functional, electrically small, metamaterial-inspired, near-field resonant parasitic antennas, Proc. of ICECom 2010

[7] R. W. Ziolkowski and A. Erentok, " Metamaterial-based efficient electrically small antennas", IEEE Trans. On Ant. And Prop. Vol. 54, No. 7, July 2006

Design and Simulation of Novel Compact and Reconfigurable Double Negative Metamaterial unit-cell

Behnam Zarghooni and Tayeb A. Denidni

Institut National de la Recherche Scientifique (INRS)
Uniersity of Quebec, Montreal, Quebec, Canada
E-mail: zarghooni@emt.inrs.ca, denidni@emt.inrs.ca

Abstract

In this paper, a novel reconfigurable unit-cell structure for planar Double Negative (DNG) metamaterials is presented. DNG metamaterials are materials having both μ and ε less than zero. The presented structure is first simulated with CST Microwave Studio and then, the results of CST are used in a parameter extraction algorithm using a MATLAB code and the constitutive parameters of the structure are extracted. According to the simulation results, this structure has a wider bandwidth and smaller size compared to other conventional structures.

1. Introduction

Double Negative (DNG) Metamaterials are amongst the most interesting subjects during the recent years, the first appearance of this concept was in the famous paper of Veselago in 1968 [1], where it has been proved that an electromagnetic wave can propagate in a material having both relative permeability and permittivity less than zero. According to Veselago, in DNG metamaterials, unlike the conventional materials, the direction of the Poynting vector is antiparallel to the direction of the phase velocity. He also showed that DNG materials have a negative index of refraction.

The first physical realization of negative permittivity was in 1990s. Pendry et al. used an array of thin wires to realize an epsilon-negative (ENG) media [2]. A structure with negative permeability by using periodical Split Ring Resonators (SRR) has been developed in [3]. Smith et al were the first group who developed a double negative media in 2000 [4]. They used an array of SRRs and thin metallic wires to realize a structure with negative permittivity and permeability at the same time. Since then, many different applications have been found for DNG metamaterials in the field of antennas and propagation. For example, DNG metamaterials can be used as a cover to improve the antenna performance [5] or to increase the antenna directivity [6] or in the substrate of patch antennas [7].

The idea of designing a spiral resonator was first introduced by J.D. Baena et al in 2004 [8]. They showed that spiral structures can have some advantages over the conventional split-ring resonators. According to Baena et al, spiral resonators can provide a reduction of size in a DNG unit-cell. Here, in order to propose a structure with a better bandwidth, we use the same technique used in broadband antennas that is gradually changing the dimensions of the structure [9]. In this paper, we combine these two key techniques to design a novel compact DNG unit-cell with an enhanced bandwidth. In addition, in order to obtain a reconfigurable structure, two PIN diodes are embedded in the proposed structure. When the diodes are on, the unit-cell is a modified shape three-turn spiral, but when the diodes are off, the unit-cell behaves like three open rings with gradually changing dimensions inside each other. Each of these structures has certain characteristics and we discuss them in the following sections.

2. The unit-cell layout

Fig. 1 shows the structure of the unit cell. This structure consists of a three-turn spiral resonator, printed on a slab of dielectric, but the line width of the rings of the spiral is not constant and is gradually changing from a maximum in center to zero in the edge.

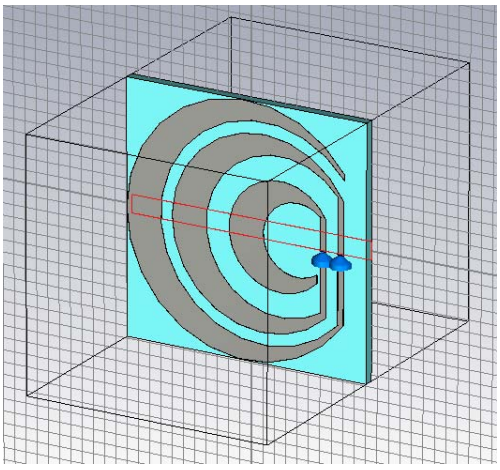

Figure 1- The unit-cell structure.

The two vertical lines in Fig. 1 are in fact a part of the modified spiral. These lines are used for connecting the rings of the spiral together and completing the structure of the spiral. Two PIN diodes are embedded in these lines, so when the diodes are on, the unit cell is in fact a modified

shape spiral, but when the diodes are off, the unit cell acts as a structure with three rings inside each other with gradually changing dimensions, so we can switch between these two different configurations by setting the diodes on or off. These two different structures i.e. *modified shape three-turn spiral* and *three rings inside each other* are shown in Fig. 2 (a) and (b) respectively.

(a)

(b)

Figure 2- Two different configurations of the unit-cell (a) when the diodes are on (b) when the diodes are off.

The structures are simulated as the unit-cells of a planar DNG metamaterials and the scattering parameters are obtained.

3. Simulation results

The simulation S parameters for Fig. 2 are shown in Fig. 3 (a) to (d). The simulation is done using CST Microwave Studio and the unit-cell boundary conditions are applied.

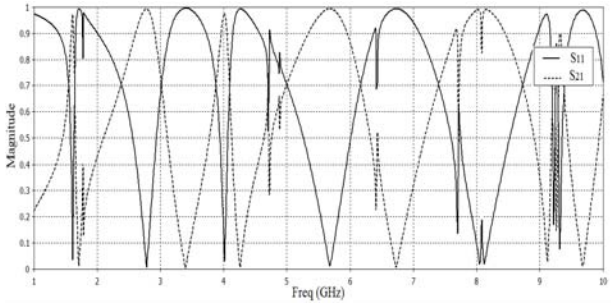

(a) Magnitude of S_{11} and S_{21} when the diodes are ON.

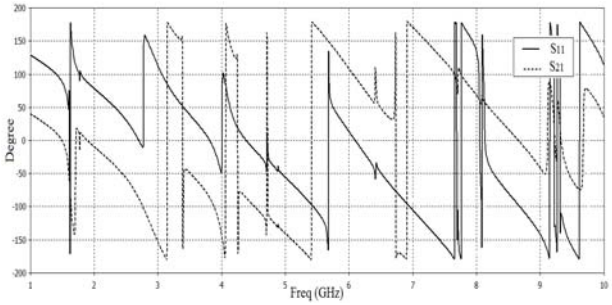

(b) Phase of S_{11} and S_{21} when the diodes are ON.

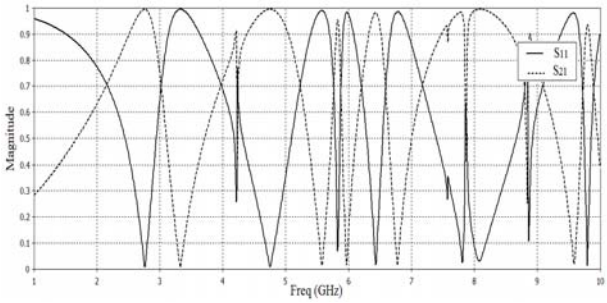

(c) Magnitude of S_{11} and S_{21} when the diodes are OFF.

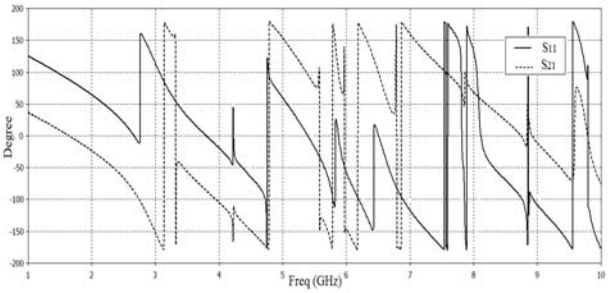

(d) Phase of S_{11} and S_{21} when the diodes are OFF.

Figure 3- The simulated S parameters for the unit-cell in two different configurations.

Comparing the results of the two different configurations in Fig. 3 shows that the structure is reconfigurable.

4. Parameter extraction

The constitutive parameters of the media can be related to the magnitude and phase of S_{11} and S_{21} using the method described in [10]. In this method, we consider the parameters of S_{11} and S_{21} as the reflection and transmission coefficients. Therefore, for the impedance Z and the refractive index n we have

$$z = \pm\sqrt{\frac{(1+S_{11})^2 - S_{21}^{\,2}}{(1-S_{11})^2 - S_{21}^{\,2}}} \qquad (1)$$

$$n = \frac{1}{k_0 d}\{[\mathrm{Im}[\ln(e^{jnk_0 d}) + 2m\pi] - j\,\mathrm{Re}[\ln(e^{jnk_0 d})]\} \qquad (2)$$

where k_0 and d are the wave number in free space and the unit-cell thickness, respectively, and *m* is an integer number which is related to the branch index of the logarithm function. The sign for Z in the equation (1) is chosen by this requirement that the real part of Z should be positive in order to have a passive medium. Permeability and permittivity can be calculated from

$$\mu = \frac{n}{Z} \tag{3}$$

$$\varepsilon = nZ \tag{4}$$

Applying the above algorithm to the S parameters of the unit-cell, we can extract μ and ε for this structure. The results are shown in Fig. 4.

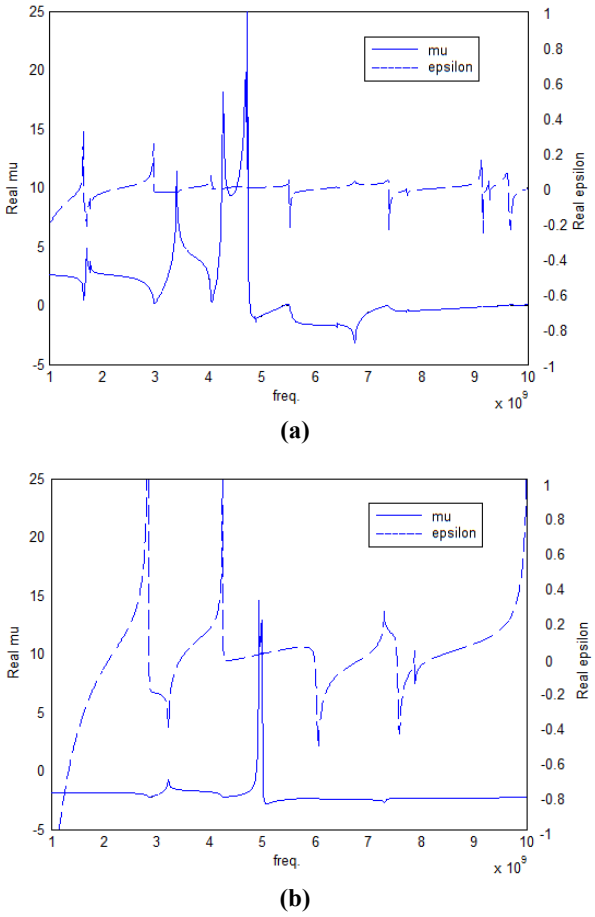

Figure 4- The extracted constitutive parameters of the unit-cell in two different configurations (a) when the diodes are on (b) when the diodes are off.

5. Modeling the structure

As shown in Fig. 5, a Double Split Ring Resonator (DSR), which is widely used as a unit-cell of conventional DNG metamaterials, can be modeled as an LC resonant circuit [8].

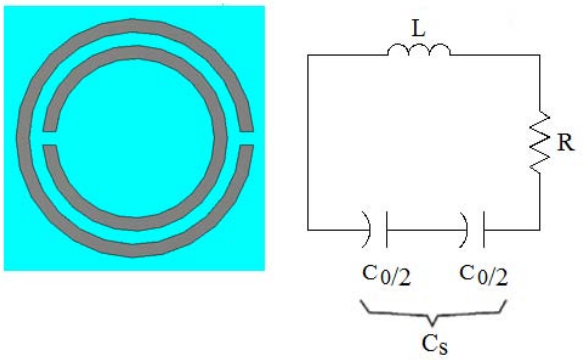

Figure 5- RLC model of a conventional DSR. C_0 is the capacitance between the half rings and C_S is the capacitance of the resonator.

According to this model, the resonance frequency of DSR can be calculated as below

$$f_0 = \frac{1}{2\pi\sqrt{LC_s}} \tag{5}$$

According to Baena et al, a 3 turn spiral resonator can be modeled as below [8].

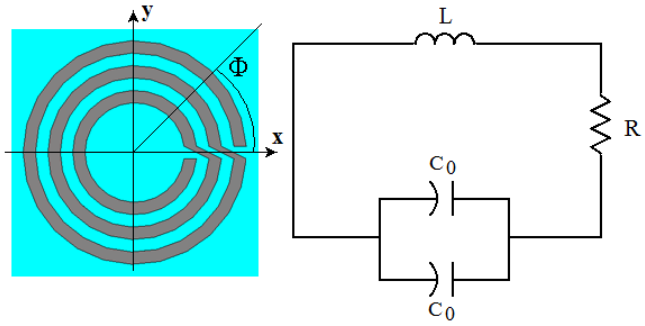

Figure 6- RLC model of a three-turn spiral.

Fig. 6 shows that the capacitance of the model is increased compared to Fig. 5. In the three-turn spiral, the current distribution is uniform in the middle ring but not uniform in the outer and inner rings [8]. For the outer ring, the current density starts from zero at Φ=0 and goes to a maximum at Φ=2π. For the inner ring, the current density is exactly reversed and starts from a maximum at Φ=0 and goes to zero at Φ=2π. So, the capacitance of the three turn spiral is larger than the conventional DSR. The difference between our three-turn resonator and the Banea's is the graduate change of the line width from zero at Φ=0, 2π to a maximum at Φ=π. Fig. 7 shows the geometry of the modified shape spiral. This new geometry causes some changes in the current distribution. Firstly, the current distribution is not anymore uniform in the middle ring. Since the width of the line is maximum at Φ=π, the current should be larger at center (Φ=π) than the edges (Φ=0, 2π), and there is a maximum in the current distribution of the middle ring at Φ=π. For the outer and inner rings, there is also a maximum at Φ=π, but for the outer the current is zero at Φ=0 while for the inner, the current is zero at Φ=2π.

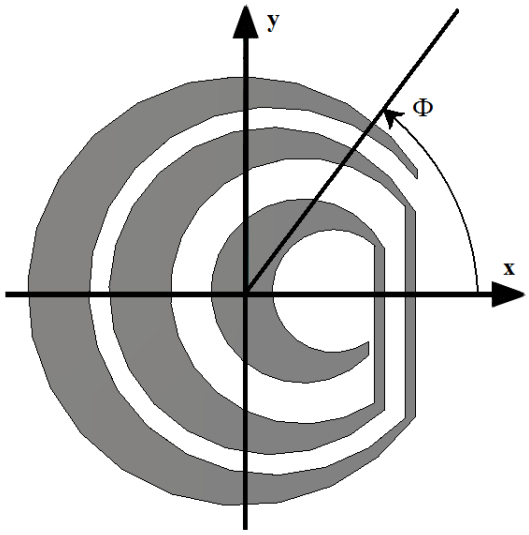

Figure 7- The modified shape three turn spiral.

Therefore, we can say that the capacitance of the modified shape spiral is larger than that of the Baena's spiral, while the inductances of both of the structures are roughly the same. So, having a larger capacitance and the same inductance, our spiral structure can presents smaller electrical size compared to Baena's.

6. Comparing with conventional SRRs

In order to show the advantages of the structure proposed in this paper over a conventional SRR and also over Baena's three-turn spiral structure, we compare the results of the proposed unit-cell with those two structures. Fig. 8 (a), (b) and (c) show the extracted relative permittivity and permeability for a conventional SRR, a three-turn spiral and our structure, respectively. In order to better understand the performance of each structure, horizontal lines showing zeros of ε and μ are plotted in each graph. Comparing these graphs reveals that the bandwidth of negativity for our structure for μ is roughly from 5 GHz to 10 GHz while for the three turn spiral the bandwidth is from 4.9 GHz to 6 GHz and for SRR the bandwidth is from 4.8 GHz to 5.3 GHz. It means that the bandwidth is at least 3 times better than the other structure. There is also a down frequency shift in the first resonance of permittivity and permeability of the structure. The vertical arrows in Fig. 8 (a), (b) and (c) show the place of the first resonance for μ and ε. The down frequency shift means that the electrical size of the structure is larger than that of the other structures while the physical dimensions are the same. Therefore, we can miniaturize the physical size of the structure while keeping the electrical dimensions smaller than the other structures. According to Fig. 8, the miniaturization factor is 0.66.

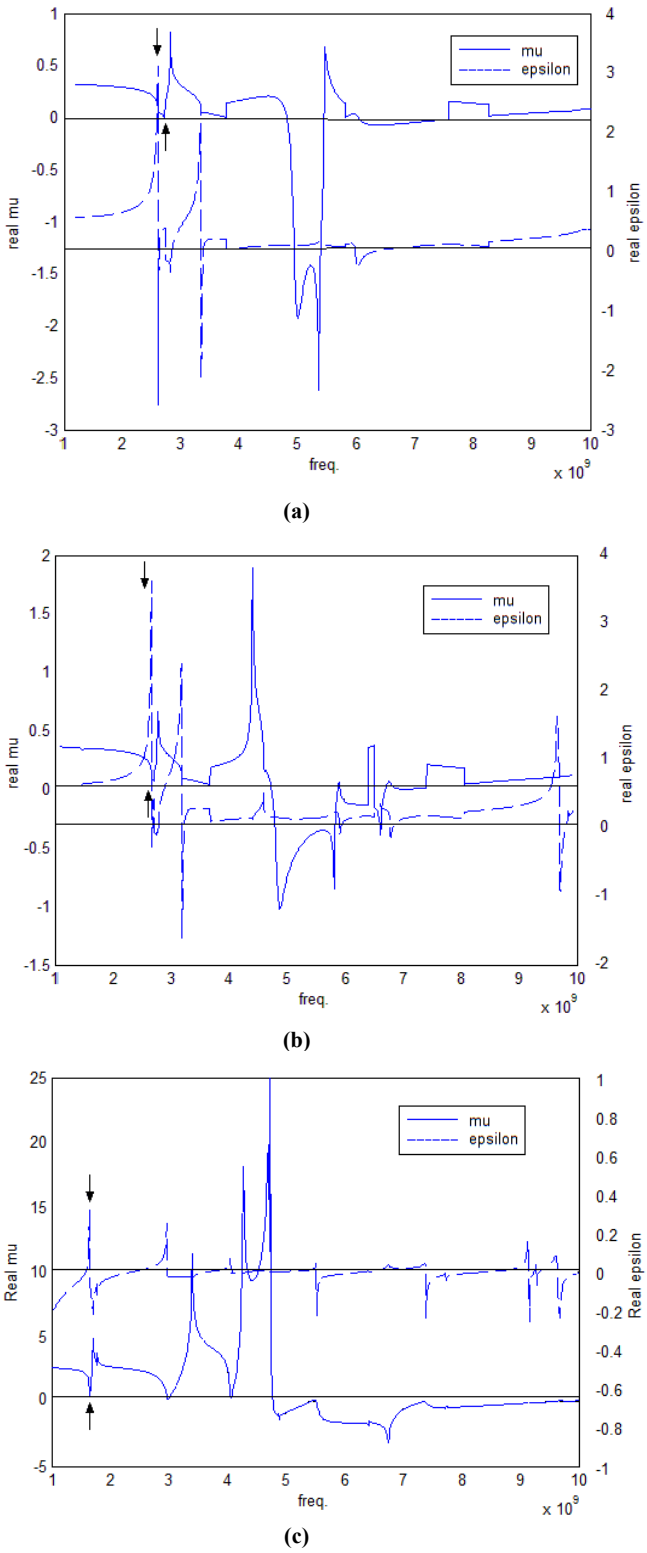

Figure 8- The relative permittivity and permeability for (a) conventional DSR, (b) three turn spiral with constant line width (c) the structure presented in this paper.

7. Conclusions

In this paper, a novel reconfigurable unit-cell structure for planar Double Negative (DNG) metamaterials has been presented. This unit-cell is based on the concepts of spiral resonators and gradually changing dimension structures. These two key features allow the unit-cell to have smaller electrical dimensions and a wider bandwidth compared to conventional unit-cell structures. Putting two diodes in this structure, the unit-cell can switch between a spiral configuration and three open rings, leading to change the parameters of the structure.

References

[1] A.-B. Zhang, C.-D. Kim, E. Yamada, F.G. Smith, The numerical investigation on the turbulent heat transfer, *Int. J. Heat Mass Transfer* 12: 345−365, 2010.

[2] S.V. Patankar, *Numerical Heat Transfer and Fluid Flow*, Hemisphere Publishers, New York, 1980.

[3] W.M. Kays, M.E. Crawford, *Heat transfer*, Wiley, New York, pp.256-258, 1990.

[4] Y. Kawaguchi, T. Tsukahara, M. Motozawa, Experimental and numerical investigations of turbulent drag reduction phenomena by additives, *Proc. ASCHT09*, Jeju, Korea, pp. 23−32, 2009.

[5] R. W. Ziolkowski and A. Kipple, "Application of double negative metamaterials to increase the power radiated by electrically small antennas," *IEEE Trans. Antennas Propagat.*, vol. 51, no. 10, pp. 2626–2640, Oct. 2003.

[6] B.-I. Wu, W. Wang, J. Pacheco, X. Chen, "T. Grzegorczyk, and J.A. Kong, A study of using metamaterials as antenna substrate to enhance gain, " *Prog Electromagn Res PIERS*, vol. 51 pp. 295–328, 2005.

[7] S. Enoch, G. Tayeb, P. Sabouroux, N. Gu´erin, and P. Vincent, "A metamaterial for directive emission," *Phys. Rev. Lett.*, vol. 89, pp. 213902, 2002.

[8] Baena, J. D., R. Marques and F. Medina, "Artificial magnetic metamaterial design by using spiral resonators," *Phys. Rev. Lett., B* 69, Vol. 69, pp. 014402 (1)-(5), 2004.

[9] Kraus, J. D. and R. J. Marhefka, *Antennas for All Applications,* McGraw-Hill, 2001.

[10] X. Chen, T. M. Grzegorczyk, B. Wu, J. Pacheco Jr. and J. A. Kong, "Robust method to retrieve the constitutive effective parameters of metamaterials," *Phys. Rev. Lett.,* E 70, 016608 (2004).

Bandpass Waveguide Filter with Multispurious Rejection

Saeed Fallahzadeh [1], Ali Molaei[2], Mina Nazari[3], Majid Tayarani[1]

[1]Department of Electrical Engineering, Iran University of Science and Technology (IUST), Tehran, Iran
[2]Department of Electrical and computer Engineering, University of Tehran (UT), Tehran, Iran
[3]Faculty of Engineering Department of Electrical Engineering, Tarbiat Modares University (TMU), Tehran, Iran
*Ali Molaei, E-mail: a.molaei@ut.ac.ir

Abstract

In this paper, spurious passband suppression in waveguide bandpass filter by means of split ring resonators (SRRs) is proposed. The bandpass waveguide filter is designed using complementary split ring resonators (CSRRs). Then, the split ring resonator (SRR) arrays are loaded in the waveguide to reject multiple spurious passbands.
Simulation results show that for a 3rd order bandpass filter, a rejection level exceeding 35dB is obtained in the first three spurious passbands, while the desired passband is maintained unaltered.

1. Introduction

Split Ring Resonators (SRRs) and Complementary Split-Ring Resonators (CSRRs) are widely used in electromagnetic applications [1-8]. SRRs and CSRRs can be used to design slow wave transmission lines, phase shifters, various kinds of microstrip filters, etc [9-11]. Considering each propagation mode of the waveguide as a transmission line, SRR and CSRR structures can be used as resonance elements to design waveguide filters [12-16].

The circuit model of the SRR elements in the waveguide is a parallel capacitance and inductance, placed in series in the transmission line, therefore, these elements can be used to design bandstop filters [12,13]. On the other hand, using the duality theorem and Babinet's principle, the CSRRs can be used to design bandpass filters [14-16].

In this paper, the CSRR array with a period equal to λ/4 (λ=λwaveguide@ f_0=8.5 GHz) is used to design a 3rd order bandpass waveguide filter. Then, multispurious passbands of filter are suppressed using the SRR array pairs.
The bandpass filter, considered here, is a 3rd order filter with 500MHz Bandwidth around operating frequency 8.5 GHz (5.88% bandwidth) implemented in a WR90 waveguide. RT/Duroid 5880 substrate is used to design the CSRR and SRR elements.
Simulation results show that for a 3rd order bandpass filter a rejection level exceeding 35 dB is obtained in the first three spurious passbands, while the desired passband is kept unaltered.
All the filter designs have been validated by simulation using the CST software.

2. Design of CSRR

The structure of a CSRR in waveguide as proposed by [15] is shown in Figure 1. The CSRR considered as an electric dipole that cab be excited by an axial electric field. By locating the CSRR transversally in the waveguide, good interaction with the electromagnetic fields can be achieved [14].

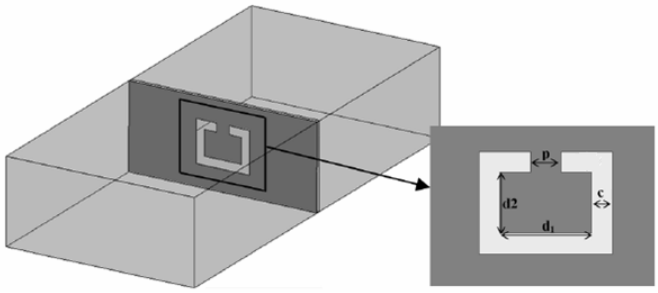

Figure 1: CSRR configuration in waveguide

The transmission responses for the presented unit cell are simulated by means of CST microwave studio software package. Figure 2 illustrates frequency response for a CSRR loaded waveguide with geometrical parameters d1=5.4mm, d2=2.4mm, c=0.8mm and p=2.5mm.

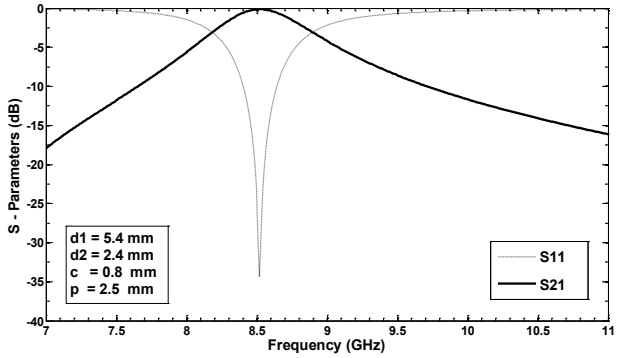

Figure 2: Frequency response for a CSRR loaded waveguide

The resonance frequency and bandwidth of CSRR are adjusted by properly choosing the geometrical parameters of CSRR. the various geometrical parameters and their effect on the resonance frequency (frequency in which the S_{12} is maximum) and the relative bandwidth of frequency response of CSRR, are shown in Table 1.

Table 1. Variation of resonance frequency (f_0) and relative bandwidth (BW) of CSRR structure versus geometrical parameters (↑ increase, ↓decrease).

parameter	f_0	BW
d_1 ↑	↓	↑
d_2 ↑	↓	↓
c ↑	↓	↑
p ↑	↑	↑

The CSRR element can be modeled by a parallel LC circuit placed in parallel form across the transmission line [14]. The values of the L and C components are related to the geometrical parameters of the CSRR and these elements can be used to design bandpass filters. The equivalent circuit model of a CSRR in the waveguide is depicted in Figure. 3.

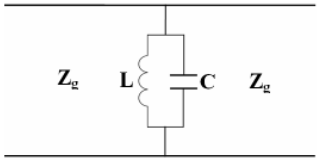

Figure 3: Circuit model of a CSRR in waveguide.

3. Design of SRR

SRRs behave as a resonant magnetic dipole so an external magnetic flux can excite it, exhibiting a strong diamagnetism above their first resonance. Figure 4 shows the topology of the SRR structure. The SRR is placed longitudinally in the waveguide.

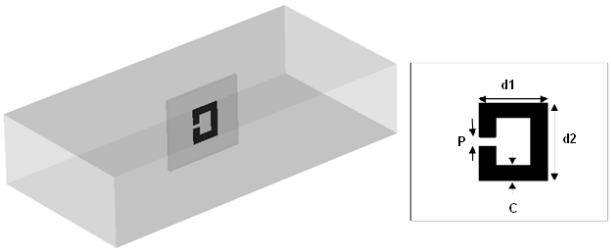

Figure 4: SRR configuration in waveguide.

The scattering parameters simulated in the SRR loaded waveguide is depicted in Figure 5.The waveguide is excited by its fundamental TE_{10} mode. The SRR were placed longitudinally in the waveguide and they were excited by the magnetic field perpendicular to the SRR element.

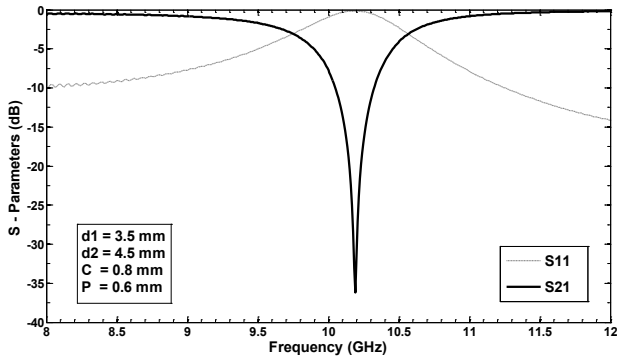

Figure 5: Scattering parameters of the SRR loaded waveguide.

Geometrical parameters such as ring length, gap and the metal width affect the resonant frequency and bandwidth. The effect of the geometrical parameters on frequency response of CSRR is shown in Table 2.

Table 2. Variation of resonance frequency (f_0) and relative bandwidth (BW) of SRR structure versus different parameters.

parameter	f_0	BW
d_2 ↑	↓	↓
d_1 ↑	↓	↓
c ↑	↓	↑
p ↑	↑	↑

The SRR element can be modeled by a parallel LC circuit placed in series form across a transmission line. The circuit model of SRR loaded waveguide is depicted in Figure 6.

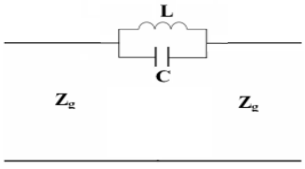

Figure 6: Circuit model of SRR loaded waveguide

The stopband attenuation and bandwidth depends on the number of SRRs. To achieve desired bandwidth and attenuation, the SRR array pairs are used. The triad array pairs of SRR and simulated results are shown in Figure 7.

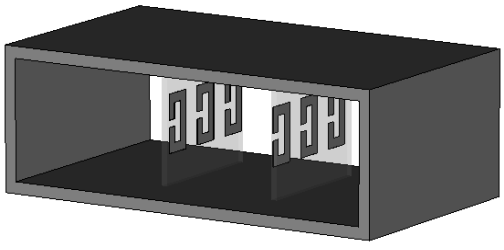

(a)

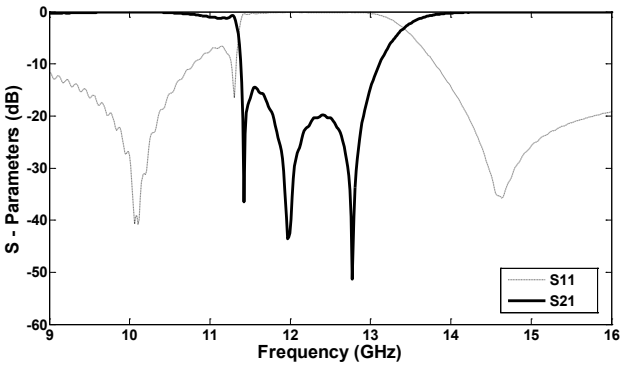

(b)

Figure 7: (a) SRR array pair configuration (b) simulated results

4. 3rd order Bandpass Filter using CSRR Array

Using the classic procedure of designing filter a 3rd order Chebyshev bandpass waveguide filter in the X-band, using three CSRRs placed with a period equal to λ/4 (λ=λwaveguide@ f_0=8.5 GHz), is designed. The center frequency of filter is 8.5GHz. The final waveguide filter is designed using the λ/4 transmission line as transformer. It is realized with CSRR structures and the simulated results of the filter are depicted in Figure. 8.

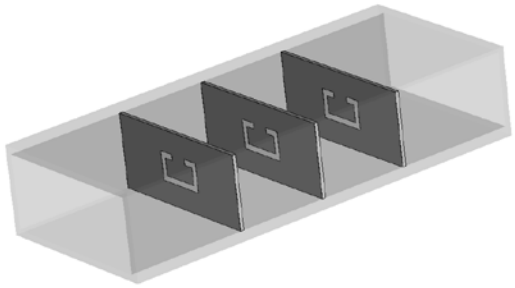

(a)

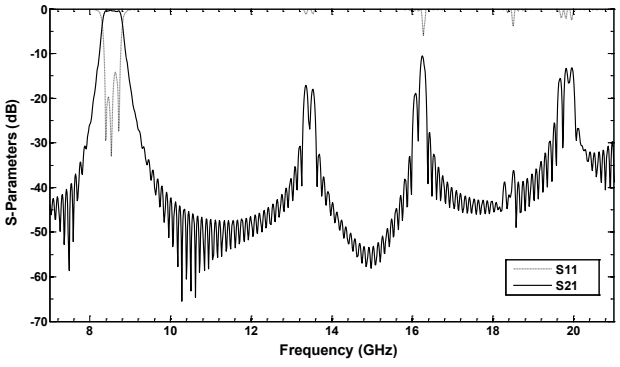

(b)

Figure 8: (a) 3rd order bandpass waveguide filter configuration (b) S-parameters simulation

5. Spurious Passbands Suppression

The common problem of the bandpass filters is spurious passbands. The elimination of harmonic bands by means of SRR arrays, will be applied to a third-order bandpass filter. Thus, by the use of two SRR array pairs the first three spurious passbands is suppressed. The structure must be designed so that it most affects the higher order response and least affects the fundamental response. By shifting longitudinal arrays of SRRs from the center of the waveguide to the side walls, the interaction between the arrays and the fundamental response becomes less.

The bandwidth and attenuation of stopband are specified by the geometrical parameters of the SRR in the array (summarized in Table 2), number of unit cells and offset of the arrays from center of the waveguide. It is found that the attenuation is increasing with the number of unit cells. From the simulation, more than 35dB suppression in the first three spurious passband has been obtained for this design while the desired passband is maintained unaltered.

The final designed filter and simulated results are depicted in Figure 9.

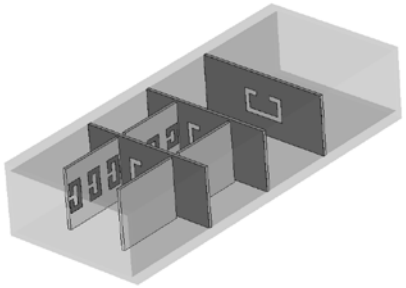

(a)

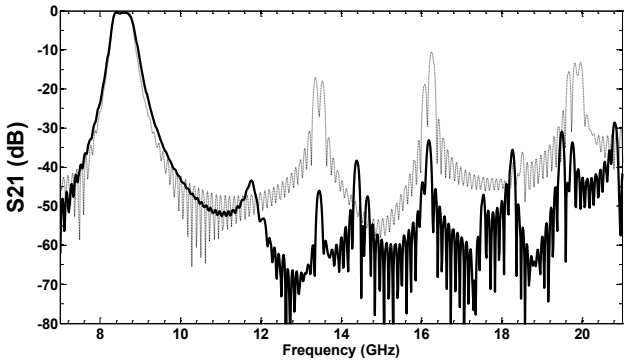

(b)

Figure 9: (a) Final filter structure (b) Simulated S21 parameter for the conventional (dotted line) and the multispurious rejection (solid line) bandpass filters.

6. Conclusions

A new approach for the rejection of undesired bands in waveguide filter, based on SRRs, has been proposed. We designed a 3rd order Chebyshev bandpass filter in the X-band using three CSRR located λ/4 away from each other,

then by placing longitudinal SRR arrays shifted from center, the spurious responses has been suppressed. We have shown a 35 dB rejection level for the first three spurious passbands leaving the passband of the structure unaltered.

References

[1] Li, D., Y. J. Xie, P. Wang, and R. Yang, "Applications of split ring resonances on multi-band frequency selective surfaces," J. of Electromagn. Waves and Appl., Vol. 21, No. 11, 1551 1563, 2007.

[2] Gurel, L., O. Ergul, and A. Unal, "Accurate analysis of metamaterials involving finite arrays of split-ring resonators and thin wires," Progress In Electromagnetics Research Symposium, PIERS 2007, Beijing, China, March 26-30, 2007.

[3] Zhao, Q., L. Kang, B. Du, B. Li, and J. Zhou, "Tunable metamaterials based on nematic liquid crystals," Progress In Electromagnetics Research Symposium, PIERS 2007, Beijing, China, March 26-30, 2007.

[4] Jelinek, L., J. Machac, and J. Zehentner, "A magnetic metamaterial composed of randomly oriented SRRs," PIERS Online, Vol. 2, No. 6, 624-627, 2006.

[5] Chang, K. and L. Hsieh, Microwave Ring Circuits and Related Structures, John Wiley & Sons, Inc, 2004.

[6] Xu, W., L.-W. Li, H.-Y. Yao, T.-S. Yeo, and Q. Wu, " Extraction of constitutive relation tensor parameters of SRR structures using transmission line theory," J. of Electromagn. Waves and Appl., Vol. 20, No. 1, 13-25, 2006.

[7] Wu, Q., M.-F. Wu, F.-Y. Meng, J. Wu, and L.-W. Li, " SRRs' artificial magnetic metamaterials modeling using transmission line theory," Progress In Electromagnetics Research Symposium, PIERS 2005, Hangzhou, China, August 22-26, 2005.

[8] Garcia-Garcia, J., F. Aznar, M. Gil, J. Bonache, and F. Martin, "Size reduction of SRRs for metamaterial and left handed media design," Progress In Electromagnetics Research Symposium, PIERS 2007, Beijing, China, March 26-30, 2007.

[9] H. Mosallaei, and K. Sarabandi, "A Compact Wide-band EBG Structure Utilizing Embedded Resonant Circuits," IEEE Antennas and Wireless Propagagation Letters, vol. 4, 2005.

[10] F. Falcone, F. Martin, J. Bonache, R. Marqués, and M. Sorolla,"Coplanar waveguide structures loaded with split ring resonators," Microwave and Optical Technology Letters, vol. 40, pp. 3–6, 2004.

[11] J. Bonache, F. Martin, J. Garcia-Garcia,I. Gil, R. Marques and M. Sorolla, "Ultra Wide Band Pass Filters (UWBPF) Based On Complementary Split Rings Resonators," Microwave and Optical Technology Letters , vol.46, no.3, August 5,2005.

[12] A. Shelkovnikov, and D. Budimir, "Left-Handed Rectangular Waveguide Bandstop Filters," Microwave and Optical Technology Letters , vol. 48, no. 5, May 2006.

[13] B. Jitha, C. S. Nimisha, C. K. Aanandan, P. Mohanan, and K.Vasudevan, "SRR Loaded Waveguide Band Rejection Filter With Adjustable BandWidth," Microwave and Optical Technology Letters, vol. 48, no. 7, July 2006.

[14] N. Ortiz, J. D. Baena, M. Beruete, F. Falcone,M. A. G. Laso, T. Lopetegi, R. Marque, F. Martın, J. Garcıa-Garcıa, and M. Sorolla, "Complementary Split-Ring Resonator For Compact Waveguide Filter Design," Microwave and Optical Technology Letters , vol.46, no. 1, July 5, 2005.

[15] H. Bahrami, M. Hakkak, and A. Pirhadi," Analysis and Design of Highly Compact Bandpass Waveguide Filter Utilizing Complementary Split Ring Resonators (CSRR)," Progress In Electromagnetics Research, PIER 80, 107–122, 2008.

[16] F. Falcone, T. Lopetegi, M. A. G. Laso, J. D. Baena, J. Bonache, M.Beruete, R. Marqués, F. Martín, and M. Sorolla, "Babinet principle applied to metasurface and metamaterial design," Physical Review Letters, vol. 93,pp. 197 401(1-4),
2004.

Bandwidth constraints for passive superluminal propagation through metamaterials

Mats Gustafsson

Department of Electrical and Information Technology,
Lund University, Lund, sweden
E-mail: mats.gustafsson@eit.lth.se

Abstract

Superluminal transmission of electromagnetic waves is usually observed in a narrow bandwidth range and the velocity outside this range is subluminal. In this paper, it is shown that the transmission coefficient for superluminal propagation though a periodic metamaterial structure satisfies a sum rule. The sum rule and its corresponding physical bound relate wavelength regions with a phase velocity above an arbitrary threshold with the thickness of the slab. The theoretical results are illustrated with numerical examples.

1. Introduction

Superluminal propagation of electromagnetic waves refers to propagation faster than the speed of light in free space [1–6]. It is common to distinguish between group and phase velocity. The phase velocity of electromagnetic waves in waveguides and periodic structures can exceed the speed of light in free space. Material that supports superluminal propagation are dispersive [4–6]. In this paper, superluminal propagation through arbitrary synthesized metamaterial slabs are analyzed by comparison with an idealized superluminal slab. It is shown that the bandwidth is inversely proportional to $1-n_{\mathrm{m}}$, where $n_{\mathrm{m}}<1$ is the refractive index of the desired ideal homogeneous superluminal slab.

The bounds are based on integral identities for Herglotz functions and follow the general approach introduced in [7]. Similar approaches have previously been successfully applied to derive bounds on lossless matching networks [8], radar absorbers [9], high impedance surfaces [10], scattering and absorption of electromagnetic waves [11–13], antennas [14], extra ordinary transmission [15, 16], and temporal dispersion of metamaterials [17].

This paper is organized as follows. Superluminal transmission through periodic slabs are analyzed in sec. 2. Numerical examples of a homogeneous Drude dispersive slab and a periodic wire medium are presented in Sec. 3. Two appendices follow the conclusions in Sec. 4. First, sum rules for Herglotz functions and the Herglotz pulse function are reviewed in Sec. A. Transmission coefficients are analyzed in Sec. B.

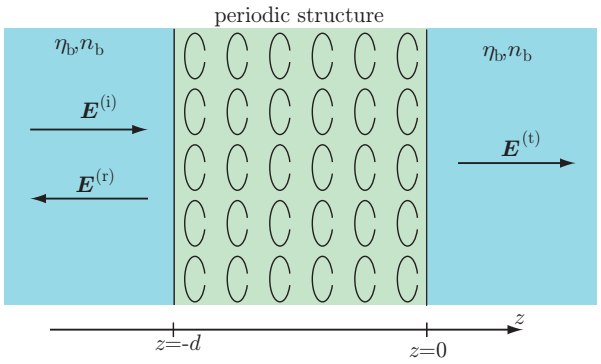

Figure 1: Transmission through a periodic structure in $z\in[-d,0]$ immersed between two half spaces with impedance η_{b} and refractive index n_{b}.

2. Superluminal transmission

Consider the synthesis of a periodic metamaterial with desired refractive index $n(k)\approx n_{\mathrm{m}}<1$ and impedance $\eta(k)\approx\eta_{\mathrm{m}}$ in the wavenumber range $k\in\mathcal{B}=[k_1,k_2]$. The metamaterial is placed between two slabs made from lossless non-dispersive materials with refractive index $n(k)=n_{\mathrm{b}}\geq 1$ and impedance $\eta(k)=\eta_{\mathrm{b}}=\eta_{\mathrm{m}}$. Here, we assume that these materials exist. Note that they can be synthesized from ordinary materials with $\epsilon_{\mathrm{r}}\geq 1$ and $\mu_{\mathrm{r}}\geq 1$ over a sufficiently large bandwidth.

The transmitted field $\boldsymbol{E}^{(\mathrm{t})}(k,\boldsymbol{r})$ is expanded in a Fourier series (Floquet modes) [18]. It is only the lowest order mode that propagates for low frequencies. Let T denote the co-polarized component of the lowest order mode of the transmission dyadic [13]. Use that the periodic structure is composed of ordinary materials where the wavefront velocity is limited by the speed of light c_0. This means that the transmitted field depends causally with respect to the incident field, *i.e.*, the transmitted field cannot precede the incident field. The transmission coefficient is hence a holomorphic function of k in $\operatorname{Im}k>0$. Moreover passivity imply that $|T(k)|\leq 1$ for $\operatorname{Im}k\geq 0$. This gives the representation $T(k)=B_{\mathrm{p}}(k)\mathrm{e}^{\mathrm{i}h(k)}$ where $h(k)$ is a Herglotz function with the high-frequency asymptotic $h(k)\sim\alpha kd$ as $k\hat{\to}\infty$ for some $\alpha\geq 0$, see App. A.

The transmission coefficient for the desired homoge-

neous superluminal slab is

$$T_{\rm m}(k) = \frac{(1-r_0^2){\rm e}^{{\rm i}(n_{\rm m}-1)kd}}{1-r_0^2{\rm e}^{2{\rm i}n_{\rm m}kd}} = {\rm e}^{{\rm i}(n_{\rm m}-1)kd} \qquad (1)$$

as the impedance mismatch, $r_0 = (\eta_{\rm b}-\eta_{\rm m})/(\eta_{\rm b}+\eta_{\rm m}) = 0$. Note that the transmission coefficient has a reversed phase, $n_{\rm m}-1<0$, compared to ordinary materials with refractive index $n \geq 1$.

It is desired to have $T(k) \approx T_{\rm m}(k)$ for $k \in \mathcal{B}$. Consider the quotient

$$T(k)/T_{\rm m}(k) = B_{\rm p}(k){\rm e}^{{\rm i}(h(k)+kd(1-n_{\rm m}))}, \qquad (2)$$

where the bandwidth with $T(k)/T_{\rm m}(k) \approx 1$ is determined from compositions with a pulse Herglotz function see App. A. The asymptotic low- and high-frequency expansions of the argument are

$$h(k)+kd(1-n_{\rm m}) \sim \begin{cases} \mathcal{O}(k^{-1}) & \text{as } k\hat{\to}0 \\ (\alpha+1-n_{\rm m})kd & \text{as } k\hat{\to}\infty \end{cases} \qquad (3)$$

giving the bound (30)

$$\max_{k\in\mathcal{B}}|T(k)-T_{\rm m}(k)| \geq \frac{(1-n_{\rm m})Bk_0d}{4}\begin{cases}1 & \text{lossy}\\ 2 & \text{lossless}\end{cases} \quad \text{for } B \ll 1 \qquad (4)$$

or equivalently a bound on the fractional bandwidth

$$B \leq B_{\rm bound} = 2\frac{\max_{k\in\mathcal{B}}|T(k)-T_{\rm m}(k)|}{(1-n_{\rm m})k_0d}\begin{cases}2 \text{ lossy}\\ 1 \text{ lossless.}\end{cases} \qquad (5)$$

It is illustrative to compare the bound (4) with the results in [17], where it is shown that the temporal dispersion of the refractive index satisfies

$$\max_{k\in\mathcal{B}}|k(n(k)-1)| \geq \frac{(1-n_{\rm m})Bk_0}{2}\begin{cases}1 & \text{lossy}\\ 2 & \text{lossless}\end{cases} \qquad (6)$$

for superluminal phase velocities. Using an arbitrary small impedance mismatch, $r_0 = 0$, and $|k(n-1)| \ll 1$ gives

$$\max_{k\in\mathcal{B}}|T(k)-T_{\rm m}(k)| \geq \frac{(1-n_{\rm m})Bk_0d}{2}\begin{cases}1 & \text{lossy}\\ 2 & \text{lossless}\end{cases} \qquad (7)$$

for $B \ll 1$. The results (4) and (7) differ by a factor of two. This is explained by the fact that the transmission coefficients of homogeneous slabs have no transmission zeros, *i.e.*, there are no Blaschke product in the representation $T(k) = {\rm e}^{{\rm i}h(k)}$. The bound is hence reduced to the analysis of $|h(k)| \leq \Delta$ over a bandwidth $\mathcal{B}$. This is the case analyzed in [17] using the pulse Herglotz function. Note that $|h(k)+n2\pi| < \Delta$ also adds a factor of two to the bound if $n \neq 0$.

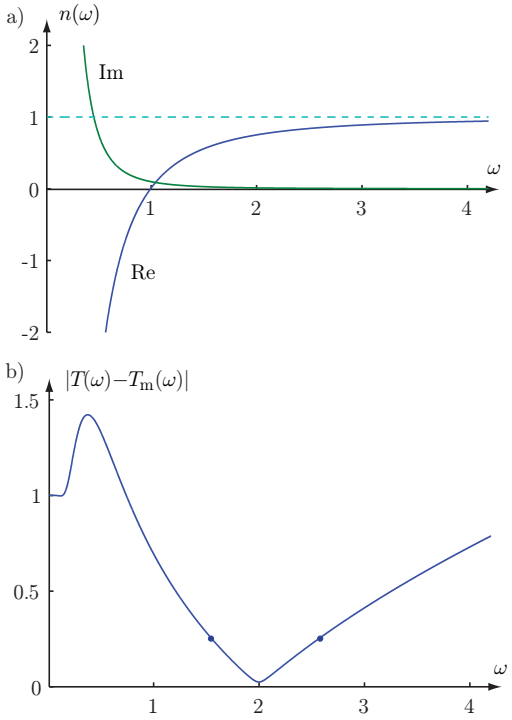

Figure 2: Drude dispersive model (8) with $\omega_{\rm p} = 1$ and $\omega_{\rm r} = 0.1$. b) difference $|T(k)-T_{\rm m}(k)|$ with $n_{\rm m} = 0.75$ giving $B \approx 0.49$ and $B/B_{\rm bound} \approx 0.50$ where the threshold $\max_{k\in\mathcal{B}}|T(k)-T_{\rm m}(k)| = 0.25$ is used.

3. Numerical examples

3.1. Drude dispersive slab

A homogeneous slab with Drude models for the permittivity and permeability is used to illustrate the bounds (4) and (7). Let

$$\epsilon(\omega) = \mu(\omega) = 1 + \frac{\omega_{\rm p}^2}{-{\rm i}\omega(-{\rm i}\omega+\omega_{\rm r})}, \qquad (8)$$

where dimensionless units are used for the thickness $d/{\rm c}_0 = 1$, plasma frequency $\omega_{\rm p} = 1$ and the resonance frequency $\omega_{\rm r} = 0.1$, see Fig. 2a. The difference $|T(\omega)-T_{\rm m}(\omega)|$ is depicted in Fig. 2b for the refractive index $n_{\rm m} = 0.75$. It is observed that $T(\omega) \approx T_{\rm m}(\omega)$ and $n(\omega) \approx n_{\rm m}$ for $\omega = \omega_0 \approx 2$. The fractional bandwidth is $B \approx 0.49$ that is comparable to the bound (7) and a factor of two below (4), where the lossless cases are used. Note, that the bound (4) overestimates the bandwidth for the homogeneous slab since is has no transmission zeros and that it is used for $|h| \ll 1$.

3.2. Periodic wire medium

The transmission is also illustrated with a periodic structure composed of a wire medium, *i.e.*, infinite strips in the y-direction, see Fig. 3a. This is a classical structure that emulate a plasma [20] with a low-frequency permittivity of the form (8). The strips are aligned with the y-direction

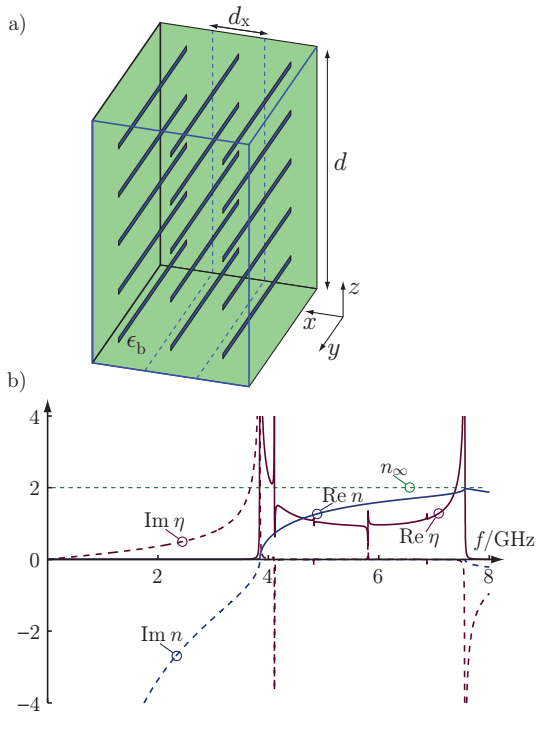

Figure 3: Transmission through a periodic wire medium. a) geometry. b) reconstructed refractive index, n, and relative impedance, η using an equivalent homogeneous slab [19].

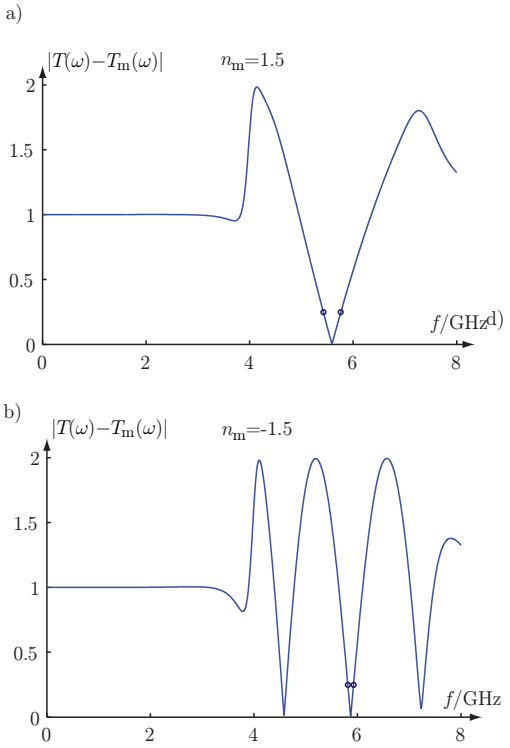

Figure 4: Transmission through a periodic wire medium. a) difference $|T(k) - T_{\rm m}(k)|$ with $n_{\rm m} = 1.5$, $B \approx 6\%$, and $B/B_{\rm bound} \approx 0.36$. b) difference $|T(k) - T_{\rm m}(k)|$ with $n_{\rm m} = -1.5$, $B \approx 2\%$, and $B/B_{\rm bound} \approx 0.81$.

and periodic in the x-direction with the unit cell length $d_{\rm x} = 10\,{\rm mm}$. Five strips with width $1\,{\rm mm}$ are placed in the z-direction at distances $10\,{\rm mm}$. The strips are embedded in a non-magnetic homogeneous slab with permittivity $\epsilon_{\rm b} = 4$ and thickness $d = 50\,{\rm mm}$. This means that the speed of the wave front is limited by ${\rm c}_0/n_\infty$, where $n_\infty = \sqrt{\epsilon_{\rm b}} = 2$ is the index if refraction for high frequencies.

The transmission and reflection coefficient are computed for $f \leq 8\,{\rm GHz}$ using the F-solver in CST Microwave studio. The relative impedance η and refractive index n of an equivalent homogeneous slab [19] are depicted in Fig. 3b. The low-frequency results resembles the permittivity from a non-magnetic Drude model (8). It is observed that $\eta \approx 1$ and ${\rm Im}\, n \approx 0$ for $4\,{\rm GHz} < f < 7.5\,{\rm GHz}$ giving a transmission $|T(\omega)| \approx 1$. The refractive index increases from 0 to $2 = n_\infty$ in this frequency range giving a phase velocity below ${\rm c}_0/n_\infty$. The difference $|T(\omega) - T_{\rm m}(\omega)|$ with $n_{\rm m} = 1.5 < n_\infty$ is depicted in Fig. 4a. Here, it is observed that $T(\omega) \approx T_{\rm m}(\omega)$ for $\omega/(2\pi) = f_0 = 5.5\,{\rm GHz}$ in agreement with the reconstruction in Fig. 3b, where $n(f_0) \approx 1.5$ and $\eta(f_0) \approx 1$. The bound (4) is determined for $\max|T - T_{\rm m}| = 0.25$ giving

$$B \leq B_{\rm bound} = \frac{2\max_{k\in\mathcal{B}}|T - T_{\rm m}|}{(n_\infty - n_{\rm m})k_0 d} = \frac{1}{2(n_\infty - n_{\rm m})k_0 d}. \quad (9)$$

The result is $B \approx 6\%$ and $B/B_{\rm bound} \approx 0.36$. This is close to the result for the homogeneous slab (7). Also the reconstructed refractive index in Fig. 3b satisfies the Kramers-Kronig relations with a high-frequency response $n(\omega) \to n_\infty = 2$ as $\omega \hat{\to} \infty$. The results are hence restricted by the sharper bound in (7).

The bound (4) does not rely on the existence of a refractive index and is valid for arbitrary periodic structures. As an example the difference from $T_{\rm m} = {\rm e}^{{\rm i}kd(n_{\rm m}-n_\infty)}$ with $n_{\rm m} = -1.5$ is depicted in Fig. 4b. It is observed that $T \approx T_{\rm m}$ for $f \approx$ GHz. The fractional bandwidth for $f \approx 5\,{\rm GHz}$ is $B \approx 1.8\%$ giving the performance $B/B_{\rm bound} \approx 0.81$ that is seen to be above the corresponding bound of material models in (7).

4. Conclusions

Bandwidth constraints on superluminal wave propagation through passive metamaterial slabs are analyzed in this paper. It is shown that the bandwidth is inversely proportional to $1 - n_{\rm m}$, where $n_{\rm m}$ is the refractive index of the desired superluminal slab. The derivation follows the approach in [7], where Herglotz functions are used to construct sum rules and physical bounds. Passivity is essential as it offers energy conservation used to bound the transmission coefficients by unity. It is also known that the temporal dispersion of causal but active material models is not very restrictive [21].

Acknowledgement

This work was supported by the Swedish research council.

A. Pulse Herglotz function

Herglotz functions, $h(z)$, are holomorphic in the upper half plane $\mathrm{Im}\, z > 0$ and map the upper half plane into itself, *i.e.*, $\mathrm{Im}\, h(z) \geq 0$, see [7, 22]. Here, we also restrict the analysis to symmetric Herglotz function $h(z) = -h^*(-z^*)$. They have at most linear growth as $z \hat{\to} \infty$ and at most a simple pole as $z \hat{\to} 0$, where $\hat{\to}$ denotes limits for $0 < \alpha \leq \arg(z) \leq \pi - \alpha$. Their asymptotic expansions are hence of the form

$$h(z) = \sum_{n=0}^{N_0} a_{2n-1} z^{2n-1} + o(z^{2N_0-1}) \quad \text{as } z \hat{\to} 0 \tag{10}$$

and

$$h(z) = \sum_{n=0}^{N_\infty} b_{1-2n} z^{1-2n} + o(z^{1-2N_\infty}) \quad \text{as } z \hat{\to} \infty \tag{11}$$

for some $N_0 \geq 0$ and $N_\infty \geq 0$, see [7]. The expansions (10) and (11) guarantees that $\mathrm{Im}(x)$ satisfy the integral identities

$$\frac{2}{\pi} \int_0^\infty \frac{\mathrm{Im}\{h(x)\}}{x^{2n}}\, \mathrm{d}x = \begin{cases} -b_{2n-1} & n < 0 \\ a_{-1} - b_{-1} & n = 0 \\ a_1 - b_1 & n = 1 \\ a_{2n-1} & n > 1, \end{cases} \tag{12}$$

where $n = 1 - N_\infty, ..., N_0$, see [7] for details. Note that a simplified notation is used in this paper where the limits in (12) are dropped, *i.e.*, the integrand is the limit $h(x + \mathrm{i}y)$ as $y \to 0$.

Composition of Herglotz functions is a powerful method to construct new Herglotz functions and integral identities (12). The pulse function

$$\begin{aligned} h_\Delta(z) &= \frac{1}{\pi} \int_{|\xi| \leq \Delta} \frac{1}{\xi - z}\, \mathrm{d}\xi \\ &= \frac{1}{\pi} \ln \frac{z - \Delta}{z + \Delta} \sim \begin{cases} \mathrm{i} & \text{as } z \to 0 \\ -\frac{2}{\pi} \frac{\Delta}{z} & \text{as } z \to \infty \end{cases} \end{aligned} \tag{13}$$

is used in [7, 17] to bound the amplitude of Herglotz functions. Here, the pulse function is generalized to bound the variation of Herglotz functions from a constant. Consider the Herglotz function generated by a constant $\mathrm{Im}\, h(x)$ in $|x \mp x_0| < \Delta$, *i.e.*,

$$\begin{aligned} h_{x_0,\Delta}(z) &= \frac{1}{\pi} \int_{|\xi \pm x_0| \leq \Delta} \frac{1}{\xi - z}\, \mathrm{d}\xi \\ &= \frac{1}{\pi} \ln \frac{z - x_0 - \Delta}{z - x_0 + \Delta} + \frac{1}{\pi} \ln \frac{z + x_0 - \Delta}{z + x_0 + \Delta} \\ &= \frac{1}{\pi} \ln \frac{(z-\Delta)^2 - x_0^2}{(z+\Delta)^2 - x_0^2} \sim \begin{cases} \frac{4}{\pi} \frac{\Delta}{x_0^2 - \Delta^2} z & \text{as } z \to 0 \\ -\frac{4}{\pi} \frac{\Delta}{z} & \text{as } z \to \infty, \end{cases} \end{aligned} \tag{14}$$

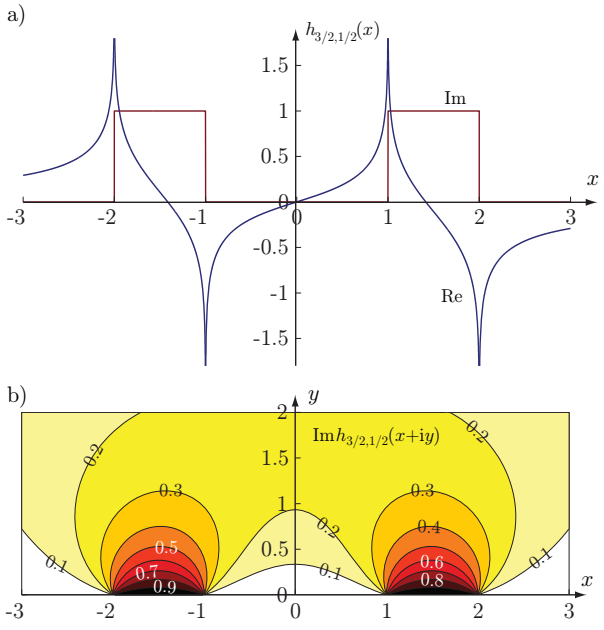

Figure 5: The generalized pulse Herglotz function $h_{3/2,1/2}$ with $x_0 = 3/2$ and $\Delta = 1/2$. a) real and imaginary parts of $h_{3/2,1/2}(x)$. b) contour plot of the imaginary part as function of $z = x + \mathrm{i}y$.

where $x_0 > \Delta$, see Fig. 5. The generalized pulse function has the properties

$$\begin{cases} \mathrm{Im}\, h_{x_0,\Delta}(z) \leq 1 \\ \mathrm{Im}\, h_{x_0,\Delta}(x) = 1 \quad \text{for } |x \mp x_0| < \Delta \\ \mathrm{Im}\, h_{x_0,\Delta}(x) = 0 \quad \text{for } |x \mp x_0| > \Delta \\ \mathrm{Im}\, h_{x_0,\Delta}(z) \geq 1/2 \quad \text{for } |z \mp x_0| < \Delta. \end{cases} \tag{15}$$

Note that the case $x_0 < \Delta$ reduces to the pulse Herglotz function (13) with $\Delta \to x_0 + \Delta$. It has similar properties as in (15) but the high-frequency asymptotic is smaller as seen in (13), *i.e.*, $2(x_0 + \Delta) < 4\Delta$.

B. Passive transmission and reflection coefficients

Passive transmission (and reflection) coefficients can be decomposed as

$$T(k) = B_\mathrm{p}(k) \mathrm{e}^{\mathrm{i}h(k)}, \tag{16}$$

where $B_\mathrm{p}(k)$ is a Blaschke product and $h(k)$ is a Herglotz function [7]. The symmetry $T(k) = T^*(-k^*)$ implies the symmetries $B_\mathrm{p}(k) = B_\mathrm{p}^*(-k^*)$ and $h(k) = -h^*(-k^*)$. Blaschke products have the amplitude $|B_\mathrm{p}(k)| = 1$ for $k \in \mathbb{R}$ and can be constructed from the zeros, k_n, of $T(k)$ in $\mathrm{Im}\, k > 0$, *i.e.*, $T(k_n) = 0$. They have the representation

$$B_\mathrm{p}(k) = \prod_n \frac{k - k_n}{k - k_n^*}, \quad \mathrm{Im}\, k_n > 0, \tag{17}$$

where the symmetry $B_\mathrm{p}^*(-k^*) = B_\mathrm{p}(k)$ implies that if k_n is a zero than so is $-k_n^*$.

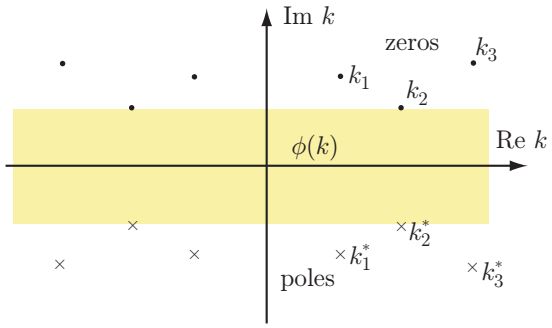

Figure 6: Zeros and poles of a Blaschke product (17) and the region of definition for the argument $\phi(k)$ (shaded region).

Blaschke products can also be written as functions $B_{\rm p}(k) = {\rm e}^{{\rm i}\phi(k)}$, where the argument $\phi(k) = \phi^*(k^*)$ is an odd function for $k \in \mathbb{R}$, *i.e.*, $\phi(-k) = -\phi(k)$. The argument is determined from

$$\phi(k) = -{\rm i}\int_0^k \frac{B_{\rm p}'(\kappa)}{B_{\rm p}(\kappa)}\,{\rm d}\kappa \tag{18}$$

that shows that the argument is monotone for $k \in \mathbb{R}$, *i.e.*,

$$\phi'(k) = -{\rm i}\frac{B_{\rm p}'(k)}{B_{\rm p}(k)} = \sum_n \frac{2\,{\rm Im}\,k_n}{(k-k_n^*)^2}\frac{k-k_n^*}{k-k_n} = \sum_n \frac{2\,{\rm Im}\,k_n}{(k-{\rm Re}\,k_n)^2+({\rm Im}\,k_n)^2} \geq 0. \tag{19}$$

The function $\phi(k)$ is not holomorphic in the entire upper half plane, ${\rm Im}\,k > 0$, but it is holomorphic in a region around $k \in \mathbb{R}$. Its Taylor series expansion around a point $k_0 \in \mathbb{R}$ is

$$\phi(k) = \sum_{n=0}^{\infty} \alpha_n (k-k_0)^n, \tag{20}$$

where the convergence radius is related to the distance $\min_n |k_n - {\rm e}^{{\rm i}\phi(k_0)}|$. The inequality (19) ensures that the linear term $\alpha_1 \geq 0$. This expresses the transmission coefficient $T(k) = B_{\rm p}(k){\rm e}^{{\rm i}h(k)}$ as

$$T(k) = {\rm e}^{{\rm i}(h(k)+\alpha_0+\alpha_1 k-\alpha_1 k_0)}{\rm e}^{{\rm i}\sum_{m=2}^{\infty}\alpha_m(k-k_0)^m} \tag{21}$$

for ${\rm Im}\,k > 0$ and $|k-k_0| < {\rm Im}\,k_n$. It has a similar expansion around $k = -k_0$.

The results in this paper rely on the analysis of transmission coefficients that have $T(k) \approx 1$ around $k = \pm k_0$ and are generated by Herglotz functions $h(k)$ having the high-frequency asymptotic $h(k) \sim b_1 k$ as $k \hat{\to} \infty$. Consider the difference $1 - T(k)$ around $k = k_0$. Use (21), to get

$$1-T(k) = \big(1-{\rm e}^{{\rm i}(h(k)+\alpha_1 k+\alpha_0-\alpha_1 k_0)}\big)\big(1+\mathcal{O}(B^2)\big) \tag{22}$$

as $B \to 0$. The difference is hence governed by the variation of $\psi(k) = h(k) + \alpha_1 k + \alpha_0 - \alpha_1 k_0$ around $k = k_0$, *i.e.*, one needs to have a function

$$h(k) + \alpha_1 k \approx \begin{cases} -\alpha_0 + \alpha_1 k_0 & \text{for } k \approx k_0 \\ +\alpha_0 - \alpha_1 k_0 & \text{for } k \approx -k_0. \end{cases} \tag{23}$$

This is a Herglotz function and its minimal variation can be determined by composition of $h(k) + \alpha_1 k$ with the pulse Herglotz function $h_{-\alpha_0+\alpha_1 k_0,\Delta}$. This new Herglotz function has the asymptotic expansions

$$h_{-\alpha_0+\alpha_1 k_0,\Delta}\big(h(k)+\alpha_1 k\big) \sim \begin{cases} \mathcal{O}(1) \text{ as } k\hat{\to}0 \\ -\frac{4\Delta}{\pi k(b_1+\alpha_1)} \text{ as } k\hat{\to}\infty \end{cases} \tag{24}$$

that follows from the expansion $h(k) + \alpha_1 k \sim (b_1 + \alpha_1)k$ as $k \hat{\to} \infty$. It satisfies the $n = 0$ sum rule (12)

$$\int_0^\infty {\rm Im}\{h_{-\alpha_0+\alpha_1 k_0,\Delta}\big(h(k)+\alpha_1 k\big)\}\,{\rm d}k = \frac{2\Delta}{b_1+\alpha_1}. \tag{25}$$

The integral is bounded from below by its minimum value over a bandwidth $\mathcal{B} = [k_1, k_2]$ times the bandwidth, *i.e.*,

$$Bk_0 \min_{k\in\mathcal{B}} {\rm Im}\{h_{-\alpha_0+\alpha_1 k_0,\Delta}\big(h(k)+\alpha_1 k\big)\} \leq \frac{2\Delta}{b_1+\alpha_1} \leq \frac{2\Delta}{b_1}, \tag{26}$$

where $B = (k_2 - k_1)/k_0$ is the fractional bandwidth and $k_0 = (k_1 + k_2)/2$ is the center wavenumber. Now, consider a bandwidth such that

$$\max_{k\in\mathcal{B}} |h(k) + \alpha_1 k + \alpha_0 - \alpha_1 k_0| = \Delta. \tag{27}$$

Use (26) and the properties (15) to get

$$\max_{k\in\mathcal{B}} |h(k)+\alpha_1 k+\alpha_0-\alpha_1 k_0| \geq \frac{b_1 B k_0}{2}\begin{cases} 1/2 \text{ lossy case} \\ 1 \text{ lossless case,} \end{cases} \tag{28}$$

where ${\rm Im}\,h(k) = 0$ in the lossless case.

For the superluminal case, we consider $|1 - T(k)|$. Set $\psi = \psi_{\rm r} + {\rm i}\psi_{\rm i} = h(k) + \alpha_1 k + \alpha_0 - \alpha_1 k_0$ and use

$$|1 - {\rm e}^{{\rm i}\psi}| \approx |\psi| + \mathcal{O}(|\psi|^2) \quad \text{as } |\psi| \to 0 \tag{29}$$

as $|\psi| \to 0$. This gives the final estimates

$$\begin{aligned} \max_{k\in\mathcal{B}} |1 - T(k)| &= \max_{k\in\mathcal{B}} |1 - {\rm e}^{{\rm i}(h(k)+\alpha_1 k+\alpha_0-\alpha_1 k_0)}|\big(1+\mathcal{O}(B^2)\big) \\ &\geq |h(k) + \alpha_1 k + \alpha_0 - \alpha_1 k_0|\big(1+\mathcal{O}(B^2)\big) \\ &\geq \frac{b_1 B k_0}{4} + \mathcal{O}(B^3) \end{aligned} \tag{30}$$

as $B \to 0$, where the lossy case in (28) is used in (30).

References

[1] R. Tomaschitz, "Refraction angles and transmission rates of polarized superluminal radiation," *Physica B: Condensed Matter*, vol. 404, no. 8-11, pp. 1383–1393, 2009.

[2] D. Sokolovski and R. Mayato, "superluminal transmission via entanglement, superoscillations, and quasi-dirac distributions," *Physical Review A*, vol. 81, no. 2, p. 022105, 2010.

[3] S. Ojha, K. Thapa, and S. Singh, "Superluminal propagation in plasma photonic band gap materials," *Optik-International Journal for Light and Electron Optics*, vol. 119, no. 2, pp. 81–85, 2008.

[4] L. J. Wang, A. Kuzmich, and A. Dogariu, "Gain-assisted superluminal light propagation," *Nature*, vol. 406, pp. 277–279, Jul. 2000.

[5] D. Mugnai, A. Ranfagni, and R. Ruggeri, "Observation of superluminal behaviors in wave propagation," *Phys. Rev. Lett.*, vol. 84, no. 21, pp. 4830–4833, 2000.

[6] R. W. Ziolkowski, "Superluminal transmission of information through an electromagnetic metamaterial," *Phys. Rev. E*, vol. 63, no. 4, p. 46604, 2001.

[7] A. Bernland, A. Luger, and M. Gustafsson, "Sum rules and constraints on passive systems," *J. Phys. A: Math. Theor.*, vol. 44, no. 14, p. 145205, 2011.

[8] R. M. Fano, "Theoretical limitations on the broadband matching of arbitrary impedances," *Journal of the Franklin Institute*, vol. 249, no. 1,2, pp. 57–83 and 139–154, 1950.

[9] K. N. Rozanov, "Ultimate thickness to bandwidth ratio of radar absorbers," *IEEE Trans. Antennas Propagat.*, vol. 48, no. 8, pp. 1230–1234, Aug. 2000.

[10] M. Gustafsson and D. Sjöberg, "Physical bounds and sum rules for high-impedance surfaces," *IEEE Trans. Antennas Propagat.*, vol. 59, no. 6, pp. 2196–2204, 2011.

[11] C. Sohl, M. Gustafsson, and G. Kristensson, "Physical limitations on broadband scattering by heterogeneous obstacles," *J. Phys. A: Math. Theor.*, vol. 40, pp. 11 165–11 182, 2007.

[12] M. Gustafsson, "Time-domain approach to the forward scattering sum rule," *Proc. R. Soc. A*, vol. 466, pp. 3579–3592, 2010.

[13] M. Gustafsson, I. Vakili, S. E. B. Keskin, D. Sjöberg, and C. Larsson, "Optical theorem and forward scattering sum rule for periodic structures," *IEEE Transactions on Antennas and Propagatation*, 2012, in press.

[14] M. Gustafsson, C. Sohl, and G. Kristensson, "Physical limitations on antennas of arbitrary shape," *Proc. R. Soc. A*, vol. 463, pp. 2589–2607, 2007.

[15] M. Gustafsson, "Sum rule for the transmission cross section of apertures in thin opaque screens," *Opt. Lett.*, vol. 34, no. 13, pp. 2003–2005, 2009.

[16] M. Gustafsson, D. Sjoberg, and I. Vakili, "On the extraordinary transmission through sub-wavelength apertures in perfectly conducting sheets," in *Electromagnetics in Advanced Applications (ICEAA), 2011 International Conference on*. IEEE, 2011, pp. 1233–1236.

[17] M. Gustafsson and D. Sjöberg, "Sum rules and physical bounds on passive metamaterials," *New Journal of Physics*, vol. 12, p. 043046, 2010.

[18] J. van Bladel, *Electromagnetic Fields*, 2nd ed. Piscataway, NJ: IEEE Press, 2007.

[19] A. M. Nicolson and G. F. Ross, "Measurement of the intrinsic properties of materials by time-domain techniques," *IEEE Trans. Instrumentation and Measurement*, vol. 19, pp. 377–382, 1970.

[20] F. Capolino, Ed., *Applications of Metamaterials*. CRC Press, 2009.

[21] B. Nistad and J. Skaar, "Causality and electromagnetic properties of active media," *Phys. Rev. E*, vol. 78, no. 3, 2008.

[22] H. M. Nussenzveig, *Causality and dispersion relations*. London: Academic Press, 1972.

Mutual Coupling Reduction for MIMO antennas using MNG metamaterial substrate

Belgacem AOUADI, Mondher LABIDI, and Jamel BELHADJ TAHAR

6'Tel Research Unit, Higher School of Communications of Tunis, Sup'Com University of Carthage, Tunisia
E-mail: b_aouadi@yahoo.fr

Abstract

In this paper, we design a μ-Negative metamaterial (MNG), to be inserted between two substrates, in order to efficiently suppress the electromagnetic coupling to achieve the full potential of using MIMO antenna array at about 13.4GHz.
The performance of a rectangular patch antenna array with MNG between two substrates was evaluated relative to a similar array constructed on an only Teflon substrate.

1. Introduction

The MIMO (Multi-Input Multi-Output) system has received a great attention in wireless communications. In fact, it can increase the capacity of a communication channel without requiring additional power or spectrum, unlike other systems [1]. Furthermore, MIMO techniques combine signals from multiple antennas to exploit the multipath in wireless channel and enable higher capacity, better coverage and increased reliability. However, High coupling coefficient between two antennas introduces higher correlation thus worse performance and the implementation of multi-antenna structures is challenging in the very limited space provided by the multi-system small terminal. Many researchers have investigated different methods to overcome these constraints. Metamaterials have been extensively applied for antenna applications recently to achieve mutual coupling reduction [2]. Indeed, Metamaterial structures have the property to significantly reduce the circuit size and improve the isolation between each antenna. On the other hand, negative permittivity materials usually can be obtained by using MNG which is composed by C-SRR. The resonance frequency is determined by the capacitance and inductance of its structure [3].Furthermore, in [4], the MNG is inserted between the two antennas (back to back) and it consists of Edge-Coupled Split Ring Resonator (EC-SRR) and a Broadside-Coupled Square Ring Resonator (BC-SRR).

In this paper, we use only C-SRR to design the MNG structure and it will be inserted between two substrates.
Details of the antenna design and experimental results are presented and discussed.
Ansoft HFSS simulator is used in this paper to simulate a 2x2 MIMO antennas system.

2. Antenna and MNG designs

Initially, The MIMO system consists of two rectangular patch antennas, the ground plane and the substrate. As shown in Fig.1, each rectangular patch element is assumed as a Finite conductivity and has a dimensions of Lp =7mm and Wp =6.5 mm. It was fed by a 50 Ω microstrip line which consists of two branches with values of wide =0.8 mm and 0.3 mm. The perfect conductor ground plane has a dimension of 30.94×27.5 mm^2.They are deposited on a 0.6mm thick Teflon substrate (εr = 2.2). The spacing between the two elements is λ/2 where λ is the free space wavelength.

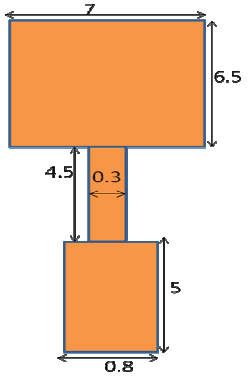

Figure 1: Dimensions of the antenna (in millimeter)

In order to reduce the size of each antenna and enhance the mutual coupling, we have used the MNG structure between two Teflon substrates with a 0.5 mm as thickness and have dimensions of 29.04* 19.17mm^2 for each. First, The MNG consists of a group of 4 sets of C-SRR. Each set consists of 8 unit cells. The separation distance between the slabs is 5.31mm.Moreover, the effective permeability characteristics of the C-SRR unit cell can be determined using the method described in [5] and it was -0.5 at 13.4 GHz as mentioned in Fig.2. Second, we have designed two rectangular patch antennas which assumed as a Finite conductivity with a dimension of Lp =6mm and Wp = 6mm. We have conserved the dimensions of the microstrip line. According this situation, we have achieved more than 47% reduction in size of each antenna. The dimensions of the used C-SRR are

shown in Fig. 3.The Perspective view of the two antennas with MNG and the same spacing (λ/2) is shown in Fig.4.

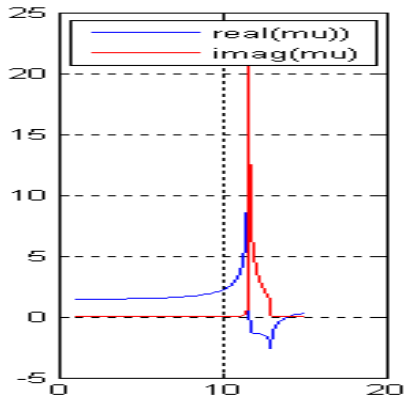

Figure 2: Simulated effective permeability

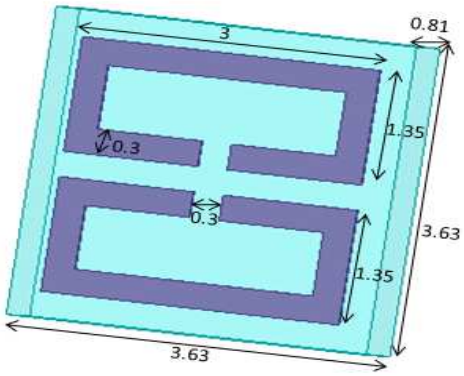

Figure 3: Dimensions (in millimeter) of the proposed C-SRR

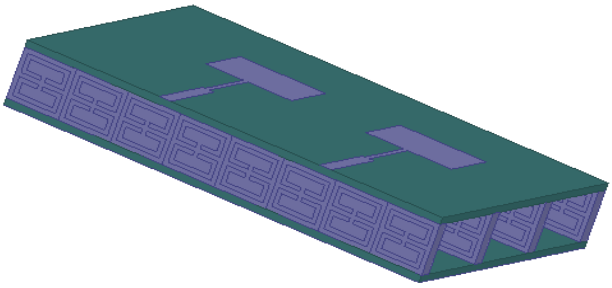

Figure 4: Perspective view of the two antennas with C-SRR

3. Analysis of Results

3.1. S-parameters

The simulated S-parameters with and without C-SRR structure are illustrated in Fig. 5.
When the two radiating elements were excited, we have a return loss of -12.65dB compared to -24.12 dB after the C-SRR structure was inserted as proposed above. On the other hand, a reduction in mutual coupling of 3 dB was achieved for the antenna system with C-SRR. Otherwise, the isolation measured in terms of S_{12} is -16dB compared to -19 dB thanks to MNG structure.

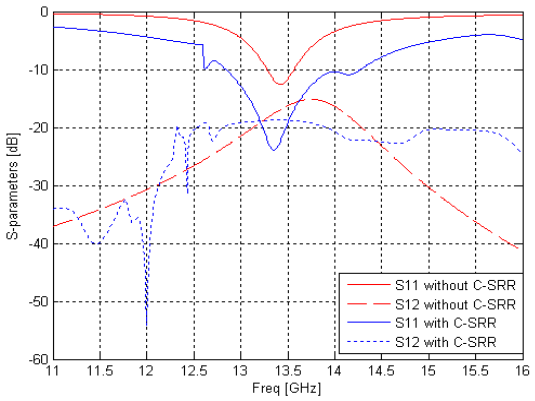

Figure 5: Measured S-parameters with and without C-SRR.

3.2. Bandwidth and gain

Fig .5 shows also that the 10 -dB bandwidth of the proposed 2*2 MIMO system without MNG is approximately 290MHz. This bandwidth is compared to that with MNG and it was 1.14 GHz. Therefore, we note a significant increase in bandwidth of 850MHZ.
The radiation pattern in Fig.6 shows a peak gain of 2.12dB (H-plane) and 2.03dB (E-plane) respectively compared to 1.22 dB and 1.06 dB for the design without C-SRR.
Thus, we also note that the gain was clearly fructified.

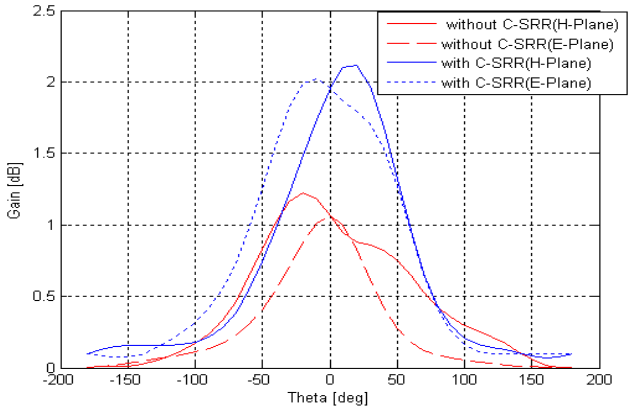

Figure 6: Measured gain with and without C-SRR (E-Plane and H-plane)

4. Conclusion

In this study, we have proposed and evaluated a method to enhance the isolation characteristic of 2*2 MIMO system using C-SRR. Indeed, The C-SRR array structure was inserted between two Teflon substrates. Besides, the miniaturization of the two antennas was successfully accomplished with a percentage of 47.25% as compared as the initial system without C-SRR. Additionally, we have improved the mutual coupling, the bandwidth and the gain. Thus, we can confirm that the MNG structure based on C-SRR can be used in MIMO antennas system to fructify its performances.

References

[1]R. D. Murch, K. B. Letaief, “Antenna systems for broadband wireless access”, IEEE Commun. Mag., vol. 40, pp. 76–83, Apr. 2002.

[2] M. M. Bait-Suwailam, M. S. Boybay, and O. M. Ramahi, “Electromagnetic Coupling Reduction in High-Profile Monopole Antennas Using Single-Negative Magnetic Metamaterials for MIMO Applications,” IEEE Trans. Antennas Propag.,vol. 58, no. 9, pp. 2894–2902, Sep., 2010.

[3]Ricardo Marqués, Ferran Martín and Mario Sorolla, Metamaterials with Negative Parameters: Theory, Design and Microwave Applications, Wiley Inter-Science, 2008

[4]Haider R. Khaleel, Hussain M. Al-Rizzo, Daniel G. Rucker , Yasir A. Rahmatallah, and Seshadri Mohan, “Mutual Coupling Reduction of Dual-band Printed Monopoles Using MNG Metamaterial”, IEEE AP-S/URSI 2011, 978-1-4244-9561-0/11/$26.00, 2011 .

[5]Rechard W. Ziolkowski, "Design, fabrication, and testing of double negative metamaterials," IEEE Transaction on Antennas Propagation., vo1.51, No. 7, pp.1516-1529, July 2003.

Mechanism of optoelectronic switch, operating on surface plasmon-polaritons in monolayer graphene

Yuliy V. Bludov*, Mikhail I. Vasilevskiy, Nuno M. R. Peres

Centro de Física, Universidade do Minho, Campus de Gualtar, Braga 4710-057, Portugal
*corresponding author, E-mail: bludov@fisica.uminho.pt

Abstract

It is shown that one can explore the optical conductivity of graphene, together with the ability of controlling its electronic density by an applied gate voltage, in order to achieve resonant coupling between an external electromagnetic radiation and surface plasmon-polaritons in the graphene layer. This phenomenon can be achieved either in the attenuated total reflection structure or in diffraction grating. This opens the possibility of electrical control of the intensity of light, reflected from the graphene, by switching between the regimes of total reflection and total absorption. The predicted effect can be used to build graphene-based optoelectronic switches.

1. Introduction

Coupling of light to the surface charges at metal-dielectric interface gives rise to the special kind of electromagnetic waves – surface plasmon-polaritons (SPPs) [1]. The specific properties of SPPs allow their using in variety of practical applications, like, e.g., plasmon sensors [2], or high-resolution image [3].

At the same time diffraction of light on periodical structures leads to the series of interesting phenomena. Thus, the spectrum of nanostructure *photonic crystal* is characterized by its band-gap structure [4]. The ability of light to propagate in such photonic crystal depends upon the fact, whether its wavelength belongs to the allowed band, or to the photonic band gap. From the other side, diffraction of p-polarized light on the metal surface with periodical surface grating is characterized by the presence of so-called Wood and Rayleigh anomalies [5], first one occurring due to the resonant excitation of the SPPs on the metal surface. Transmission gratings, operating on the same resonant light diffraction mechanism, are known to exhibit an unusual property: this kind of structures can be highly transmitting at certain frequencies. As an example, a transmittancy of light through a flat, optically thick metal film, perforated with the subwavelength hole 2D array can be much larger than that expected from the standard aperture theory [6].

Nowadays a two-dimensional carbon material graphene attracts strong attention of researches in different areas [7, 8, 9] due to its unique and unusual properties. In plasmonics interest to graphene arises from the fact, that mobility of electrons in graphene (due to their Dirac-cone spectrum shape) is much higher compared with that in conventional two-dimensional electron gas (for review see, e.g., [10]). At the same time the charge-carrier density (and, as a consequence, the spectrum of SPPs) in graphene can be easily controlled through electrostatic doping by applying external gate voltage to the graphene layer [11]. Latter gives an opportunity to elaborate graphene-based terahertz metamaterials and optoelectronic devices (like graphene-ribbon array [12] or attenuated total reflection (ATR) scheme [13]), where plasmon absorption peak frequency can be electrostatically tuned. One more interesting property of graphene is the existence of s-polarized SPP mode [14], this fact allows creation a broadband graphene polarizer [15].

The aim of the present paper is to demonstrate the possibility of the attenuation of the microwave range electromagnetic waves by partial transforming the incident wave energy into the energy of SPPs in graphene monolayer. We achieve this using either the ATR scheme, or diffraction grating. We show, that by applying the gate voltage to graphene layer it is possible to tune the attenuation coefficient in wide range - from almost total absorption till almost total reflectance of electromagnetic waves.

2. Excitation of surface plasmon-polaritons in attenuated total reflection scheme with graphene layer

In this section we consider the ATR structure for coupling SPPs to external electromagnetic wave in so called Otto geometry (Fig. 1). Thus, the p-polarized electromagnetic wave with frequency ω falls on the interface between the prism (with dielectric constant ε_3) and dielectric film characterized by the dielectric constant ε_2. This film is considered to be deposited on top of single graphene layer, which in its turn being deposited on the substrate with dielectric constant ε_1. Further in the paper we suppose, that all dielectric constants are real. If the angle of incidence Θ is bigger than the critical angle of total internal reflection Θ_c (determined as $\sin\Theta_c = \max(\varepsilon_1, \varepsilon_2)/\varepsilon_3$), then the electromagnetic wave in the gap between prism and graphene will be evanescent in the direction z. Further two scenarios of its interaction with graphene layer are possible, which can be described in the following simplified manner: (i) if the x-component of the incident wave wavevector

$$k_x = \kappa\sqrt{\varepsilon_3}\sin\Theta \qquad (1)$$

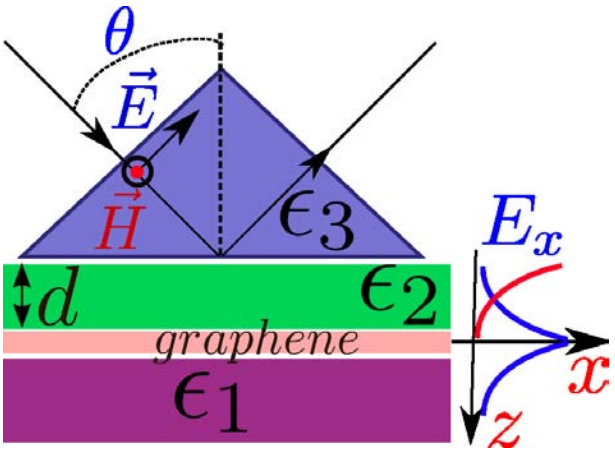

Figure 1: ATR scheme in Otto geometry, containing the graphene layer on the substrate, and dielectric prism separated from graphene by a dielectric film of thickness d.

(here $\kappa = \omega/c$) does not coincide with the eigen wavevector of SPPs in graphene $k_{SPP}(\omega)$ at frequency of incident wave, the interaction between external electromagnetic wave and SPPs is off-resonant and low efficient, and, hence, the incident wave is almost totally reflected at the prism-dielectric interface (the reflectivity of ATR structure is close to unity); (ii) in opposite situation, when $k_x = k_{SPP}(\omega)$[1], the incident electromagnetic wave–SPP resonant coupling is highly efficient, and energy of electromagnetic wave can be transformed into the energy of excited SPP in graphene. Latter results in drastic decrease of the ATR structure reflectivity in the vicinity of SPP resonance.

In order to describe the above-mentioned mechanism quantitatively, we solve Maxwell equations $\mathrm{rot}\mathbf{E}^{(m)} = i\kappa\mathbf{H}^{(m)}$, $\mathrm{rot}\mathbf{H}^{(m)} = -i\kappa\varepsilon_m\mathbf{E}^{(m)}$ separately in each of three media $m = 1, 2, 3$. Since our problem is uniform in direction y, components of p-polarized electromagnetic field $\mathbf{E}^{(m)} = \{E_x^{(m)}, 0, E_z^{(m)}\}$ and $\mathbf{H}^{(m)} = \{0, H_y^{(m)}, 0\}$ in the semi-infinite medium $m = 3$ (inside the prism, which occupies a half-space $z < -d$) will have form

$$H_y^{(3)}(x,z) = -\frac{\sqrt{\varepsilon_3}}{\sin\Theta}E_z^{(3)}(x,z) = \exp(ik_x x)\times \quad (2)$$
$$\{H_i\exp[ik_z(z+d)] + H_r\exp[-ik_z(z+d)]\},$$
$$E_x^{(3)}(x,z) = \exp(ik_x x)\frac{\cos\Theta}{\sqrt{\varepsilon_3}}\times \quad (3)$$
$$\{H_i\exp[ik_z(z+d)] - H_r\exp[-ik_z(z+d)]\},$$

where $k_z = \kappa\sqrt{\varepsilon_3}\cos\Theta$ is z-component of the wavevector. Eqs.(2)–(3) represent a superposition of incident wave (with magnetic field amplitude H_i), and the reflected wave, propagating in the positive and negative direction of axis z, respectively.

In the dielectric film between prism and graphene($-d < z < 0$, medium $m = 2$) solutions of Maxwell equations

$$H_y^{(2)}(x,z) = -\frac{\varepsilon_2}{\sqrt{\varepsilon_3}\sin\Theta}E_z^{(2)}(x,z) = \exp(ik_x x)\times \quad (4)$$
$$\left\{B_+^{(2)}\exp[p_2(z+d)] + B_-^{(2)}\exp[-p_2(z+d)]\right\},$$
$$E_x^{(2)}(x,z) = -i\frac{p_2}{\kappa\varepsilon_2}\exp(ik_x x)\times \quad (5)$$
$$\left\{B_+^{(2)}\exp[p_2(z+d)] - B_-^{(2)}\exp[-p_2(z+d)]\right\},$$

describe the superpositions of two evanescent waves, while in the graphene substrate ($z > 0$, medium $m = 1$)

$$H_y^{(1)}(x,z) = -\frac{\varepsilon_1}{\sqrt{\varepsilon_3}\sin\Theta}E_z^{(1)}(x,z) = \quad (6)$$
$$\exp(ik_x x)B_-^{(1)}\exp[-p_1 z],$$
$$E_x^{(1)}(x,z) = i\frac{p_1}{\kappa\varepsilon_1}\exp(ik_x x)B_-^{(1)}\exp[-p_1 z], \quad (7)$$

solutions represent one evanescent wave, which amplitude decreases in positive direction of axis z. In Eqs.(4)–(7) $p_m = \kappa\sqrt{\varepsilon_3\sin^2\Theta - \varepsilon_m} \geq 0$.

Boundary conditions at $z = -d$ and $z = 0$ are slightly different. So, at the interface $z = -d$ (between prism and dielectric film) boundary conditions imply the continuity of the tangential components of the electric and magnetic field, $E_x^{(3)}(x,-d) = E_x^{(2)}(x,-d)$, $H_y^{(3)}(x,-d) = H_y^{(2)}(x,-d)]$. Meanwhile, at the interface $z = 0$ situation is changed due to presence of graphene layer: the tangential component of the electric field is still continuous $E_x^{(1)}(x,0) = E_x^{(2)}(x,0)$, while the discontinuity of the tangential component of the magnetic field, $H_y^{(1)}(x,0) - H_y^{(2)}(x,0) = -(4\pi/c)j_x = -(4\pi/c)\sigma(\omega)E_x(x,0)$ stems from the presence of surface currents in the graphene layer. Matching these boundary conditions, we obtain an explicit expression for the amplitude of the reflected field, namely

$$H_r = -H_i\frac{\left\{\frac{\varepsilon_1}{p_1}+i\frac{4\pi}{c\kappa}\sigma(\omega)\right\}\overline{\chi_1}+\frac{\varepsilon_2}{p_2}\overline{\chi_2}}{\left\{\frac{\varepsilon_1}{p_1}+i\frac{4\pi}{c\kappa}\sigma(\omega)\right\}\chi_1+\frac{\varepsilon_2}{p_2}\chi_2}, \quad (8)$$

where

$$\chi_1 = \tanh[p_2 d] - \frac{i\kappa\varepsilon_2\cos\Theta}{p_2\sqrt{\varepsilon_3}},$$
$$\chi_2 = 1 - \frac{i\kappa\varepsilon_2\cos\Theta}{p_2\sqrt{\varepsilon_3}}\tanh[p_2 d],$$

and overbar stands for complex conjugation.

To analyze properties of Eq.(8) we notice, that in the limit of infinitely thick dielectric film $d \to \infty$ the equality of its denominator to zero gives

$$\frac{\varepsilon_1}{p_1} + \frac{\varepsilon_2}{p_2} + i\frac{4\pi}{c\kappa}\sigma(\omega) = 0. \quad (9)$$

Formal substitution of $k_{SPP} = \kappa\sqrt{\varepsilon_3}\sin\Theta$ into Eq.(9) transforms this equation into dispersion relations $\omega(k_{SPP}) = 0$ for the p–polarized SPPs in graphene surrounded by two semi-infinite media (ε_1 and ε_2). Here we

[1] below it will be shown, that this equality is valid only for infinite distance $d \to \infty$ between graphene and prism surface, in other case a certain correction to this condition should be introduced.

solve the dispersion relation Eq.(9) for the graphene on SiO_2 substrate (with $\varepsilon_1 = 3.9$), neglecting real part of conductivity $\mathrm{Real}(\sigma(\omega)) = 0$ (dispersion curves in the case of nonzero real part of conductivity can be seen, e.g., in Ref.[13]). From Fig.2(a) we can see that as eigen wavevector k_{SPP} increases the eigenfrequency ω of SPPs increases monotonically as well. Hence, SPPs possess a positive group velocity, which is smaller than speed of light in either of the surrounding dielectrics, that is $\partial\omega/\partial k_{SPP} < c/\sqrt{\max(\varepsilon_1, \varepsilon_2)}$. At the same time increasing of the chemical potential of graphene results in growing of the SPP group velocity [compare two dispersion curves for $V = 25\,\mathrm{V}$ and $V = 50\,\mathrm{V}$ in Fig.2(a)]. From other side, gate-controlled graphene conductivity originates another interesting phenomenon. Since in the ATR structure the excitation of SPP occurs, when the ATR scanline (1) crosses the SPP dispersion curve $\omega(k_{SPP})$, the resonance can be tuned by changing the gate voltage applied to the graphene layer. If the parameters of incident electromagnetic wave (frequency and angle of incidence) and gate voltage V are adjusted in order to excite SPPs at frequency $\omega = \Omega$ [crossing point in Fig.2(a)], the excitation of SPP will correspond to the minimum of reflectivity of ATR structure. Then, if the parameters of incident wave are kept unchanged, while gate voltage is varied to V' , the condition for the SPP excitation at frequency $\omega = \Omega$ is not met any more (these conditions will be met at frequency Ω'). Thus, the reflection coefficient, corresponding to frequency Ω will be increased, this opens a possibility to construct a microwave attenuator, where the power of reflected electromagnetic wave is tuned through the gate voltage.

The reflectivity $R = |H_r/H_i|^2$of ATR structure, calculated according to Eq.(8), is depicted in Fig.2(b), which shows the minimum value of R at particular values of incident wave parameters Θ and ω (that can be controlled independently). Comparison of Fig.2(a) and Fig.2(b) demonstrates good correspondence between exact calculation of position of reflectivity minimum and its estimation, which comes from crossing point of the dispersion relation and ATR scanline (in both cases $\Omega \approx 5.2\,\mathrm{meV}$). It is clear that the value of R can be made very small and even zero by an appropriate choice of Θ and ω. For the fixed Θ the value of ω at which reflectivity minimum occurs, and the value of this minimum R, can be read off from Figs.2(c) and 2(d). At the same time for any value of gate voltage it is possible to find such pair of (Θ, ω), at which reflectivity of ATR structure will be $R = 0$ (in a particular case, depicted in Figs.2(b)–(d), these parameters are $\Theta \approx 34.4°$and $\omega = 2.95\,\mathrm{meV}$). In other words, in this case the whole energy of incident wave is transformed into energy of excited SPPs in graphene. In Figs.2(e) the pair of these parameters (Θ, ω) at which total absorption of p-polarized incident wave is achieved is shown as function of gate voltage.

From Fig.2(f) we can see that indeed it is possible to tune externally the resonance absorption condition by changing the external gate voltage. Fig.2(f) demonstrates the possibility of changing the ATR structure's reflectivity

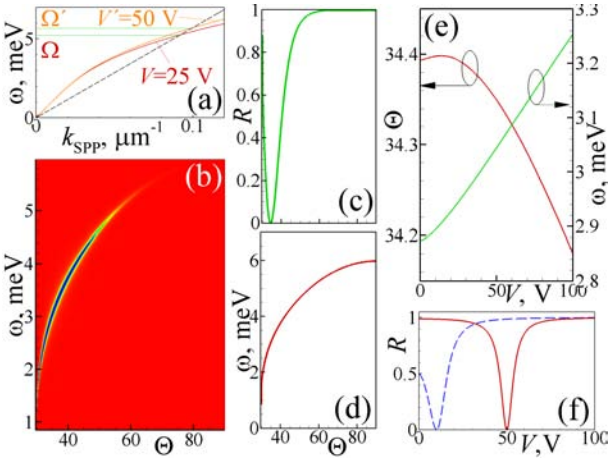

Figure 2: (a) SPP eigenfrequency ω versus eigen wavevector k_{SPP}, calculated for a single graphene layer with the following parameters: $\mu \simeq 0.16\,\mathrm{eV}$, $\mu \simeq 0.22\,\mathrm{eV}$, which can be achieved by applying the gate voltage $V = 25\,\mathrm{V}$ or $V = 50\,\mathrm{V}$ (indicated in panel), correspondingly, to graphene layer deposited on SiO_2 substrate with thickness 300 nm [11]; dispersion curves are combined with the ATR scanline (1) [dashed line] for angle of incidence $\Theta = 60°$. (b) Reflectivity R versus angle of incidence Θ and frequency ω for the ATR structure with $\mu \simeq 0.16\,\mathrm{eV}$ (corresponding to $V = 25\,\mathrm{V}$ of gate voltage), where blue and red colors correspond to low and high reflectivities, correspondingly. (c) Reflectivity R versus angle of incidence Θ, corresponding to the minimal value of $R(\omega, \Theta)$, depicted in panel (a). (d) Frequency ω at which for given Θ the minimum of R in panel (a) occurs. (e) Angle of incidence Θ, and frequency ω, corresponding to zero reflectivity of the ATR structure versus gate voltage V. (f) Reflectivity R versus gate voltage V for ATR structure with $\Theta = 34.40\,°, \omega = 2.894\,\mathrm{meV}$ [dashed line] or $\Theta = 34.35°$, $\omega = 3.044\,\mathrm{meV}$ [solid line]. In all panels other parameters are $\varepsilon_1 = 3.9$, $\varepsilon_2 = 1$, $\varepsilon_3 = 16$, $d = 40\,\mu\mathrm{m}$.

from zero to almost unity (full reflectance) by varying the gate voltage within a range of $\delta V \sim 10\,V$. As a result, the ATR structure with graphene layer can operate as *an attenuator of electromagnetic waves* operating in the *terahertz* range, where the intensity of the reflected electromagnetic wave can be tuned by the gate voltage, applied to graphene.

3. Excitation of surface plasmon–polaritons in graphene by incident wave diffraction on periodic grating

Another possibility to excite SPPs is to use some kind of periodic grating in the system (this can be either periodicity of substrate, or that of graphene conductivity). In this case SPPs can be excited by the incident propagating electromagnetic wave, falling directly on graphene; excitation of SPPs occurs as the result of diffraction of this wave on periodicity. To realize this phenomenon, we con-

sider the structure, similar to that depicted in Fig.1, but without using prism ($\varepsilon_3 = \varepsilon_2$), and the dielectric permeability of graphene substrate being periodically modulated along direction x with the modulation period D as $\varepsilon_1(x) = \varepsilon_1(x+D) = \varepsilon'[1 + a\cos(gx)]$. Here a is the modulation depth (which is considered to be small $a \ll 1$), $g = 2\pi/D$ is the periodicity constant, ε' is the average dielectric permeability of substrate.

In the case of coordinate-dependent dielectric permeability the magnetic field of the p-polarized wave is governed by the wave equation (which is obtained from the Maxwell equations)

$$-\frac{d\left[\log\varepsilon_m(x)\right]}{dx}\frac{\partial H_y^{(m)}(x,z)}{\partial x} + \frac{\partial^2 H_y^{(m)}(x,z)}{\partial x^2} + \frac{\partial^2 H_y^{(m)}(x,z)}{\partial z^2} + \kappa^2\varepsilon_m(x)H_y^{(m)}(x,z) = 0. \quad (10)$$

Here $m = 1, 2$ is the index of the medium (similar to that, introduced in Sec.2). Since the dielectric permeability is periodic, the solution of Eq.(10) can be given in the form of Fourier–Floquet series

$$H_y^{(m)} = \exp(ik_x x)\sum_{n=-\infty}^{\infty} h_n^{(m)}(z)\exp(ingx), \quad (11)$$

where $h_n^{(m)}(z)$ is the amplitudes of n-th spatial harmonics of magnetic field in medium m, and k_x is determined as Eq.(1). In medium $m = 2$ dielectric permeability is coordinate-independent, and, as a result, spatial harmonics are independent and can be represented as

$$h_n^{(2)}(z) = \delta_{n,0}H_i\exp(-p_n^{(2)}z) + H_n^{(r)}\exp(p_n^{(2)}z), \quad (12)$$

where $p_n^{(2)} = \left[(k_x+ng)^2 - \kappa^2\varepsilon_2\right]^{1/2}$, such that $\mathrm{Real}(p_n^{(2)}) \geq 0$, $\mathrm{Imag}(p_n^{(2)}) \leq 0$. Notice that for zeroth harmonic $p_0^{(2)} = -ik_z$, and it corresponds to the superposition of forward-propagating incident wave with amplitude H_i and backward-propagating reflected wave with amplitude $H_0^{(r)}$, while for $n \neq 0$ Eq.(12) describes either backward-propagating diffracted wave (if $\mathrm{Real}(p_n^{(2)}) = 0$) with amplitude $H_n^{(r)}$, or evanescent wave (if $\mathrm{Imag}(p_n^{(2)}) = 0$). In latter case $H_n^{(r)}$ corresponds to its amplitude at boundary $z = 0$.

In medium $m = 1$ situation is more complicated: here spatial harmonics of transmitted wave are coupled due to spatial periodicity. Namely, they are described by system of equations

$$\frac{d^2h_n^{(1)}(z)}{dz^2} - \left(p_n^{(1)}\right)^2 h_n^{(1)}(z) - \frac{a}{2}\left\{q_{n,n-1}h_{n-1}^{(1)}(z) + q_{n,n+1}h_{n+1}^{(1)}(z)\right\} = 0, \quad (13)$$

where $q_{n,n'} = (n'-n)\,g\,(k_x+ng) - \kappa^2\varepsilon'$, $p_n^{(1)} = \left[(k_x+ng)^2 - \kappa^2\varepsilon'\right]^{1/2}$. The system of Eqs.(13) possesses a solution (for details see, e.g., [16])

$$h_n^{(1)}(z) = \sum_{n'=-\infty}^{\infty} H_{n'}^{(t)}\exp\left(-\gamma_{n'}^{1/2}z\right)\varphi_{n,n'}.$$

Here $\gamma_{n'}$ are the eigenvalues of tridiagonal matrix $\hat{T}$ (which elements are $T_{n,n'} = (a/2)\left[\delta_{n,n'+1} + \delta_{n,n'-1}\right]q_{n,n'} + \delta_{n,n'}\left(p_n^{(1)}\right)^2$), and $\varphi_{n,n'}$ is the n-th element of matrix $\hat{T}$ eigenvector, corresponding to n' eigenvalue. The boundary conditions at $z = 0$, similar to that of Sec.2, imply

$$h_n^{(1)}(0) - h_n^{(2)}(0) + \frac{4\pi}{ic\kappa\varepsilon_2}\sigma(\omega)\frac{dh_n^{(2)}(0)}{dz} = 0,$$
$$\frac{1}{\varepsilon'}\left[\frac{dh_n^{(1)}(0)}{dz} - \frac{a}{2}\frac{dh_{n-1}^{(1)}(0)}{dz} - \frac{a}{2}\frac{dh_{n+1}^{(1)}(0)}{dz}\right] - \frac{1}{\varepsilon_2}\frac{dh_n^{(2)}(0)}{dz} = 0,$$

from which we obtain linear system of equations for amplitudes of reflected $H_n^{(r)}$ and transmitted $H_n^{(t)}$ harmonics

$$\sum_{n'=-\infty}^{\infty} H_{n'}^{(t)}\varphi_{n,n'} - H_n^{(r)}\left[1 - \frac{4\pi p_n^{(2)}}{ic\kappa\varepsilon_2}\sigma(\omega)\right] = \delta_{n,0}H_i\left[1 + \frac{4\pi p_n^{(2)}}{ic\kappa\varepsilon_2}\sigma(\omega)\right], \quad (14)$$

$$\frac{1}{\varepsilon'}\sum_{n'=-\infty}^{\infty}\gamma_{n'}^{1/2}H_{n'}^{(t)}\left[\varphi_{n,n'} - \frac{a}{2}\varphi_{n-1,n'} - \frac{a}{2}\varphi_{n+1,n'}\right] + \frac{p_n^{(2)}}{\varepsilon_2}H_n^{(r)} = -\delta_{n,0}H_i\frac{p_n^{(2)}}{\varepsilon_2}. \quad (15)$$

Qualitatively the process of SPP excitation in periodic structure can be described in the following manner. The incident wave falling on graphene, upon the diffraction on the periodical modulation of the substrate excites a series of spatial harmonics (here evanescent harmonics correspond to SPPs). The coupling between harmonics during the diffraction process can clearly be seen from (and mathematically described by) the coupled Eqs.(13). The excitation of n-th harmonic occurs with maximal efficiency, when parameters of incident wave (angle of incidence Θ and frequency ω) correspond to the crossing point between the SPP dispersion curve $\omega(k_{SPP})$ and line

$$k_x = \kappa\varepsilon_2^{1/2}\sin\Theta + ng \quad (16)$$

[similar to the ATR case (1)]. This situation is depicted in Fig.3(a) for $n = \pm 1$ (notice, that excitation of harmonics with higher numbers $|n| \geq 2$ is less effective), where for given parameters SPPs can be excited at frequencies $\Omega_{-1} \approx 9.5\,\mathrm{meV}$ and $\Omega_1 \approx 10\,\mathrm{meV}$. The excited SPP harmonic (through the above-mentioned coupling) makes an influence on the zeroth reflected harmonics, giving rise to some anomaly in the reflection spectrum. At the same time,

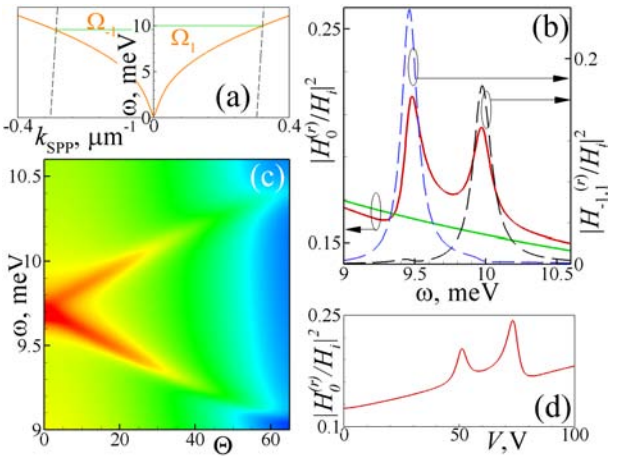

Figure 3: (a) SPP eigenfrequency ω versus eigen wavevector k_{SPP}, calculated for gate voltage $V = 50\,\mathrm{V}$ [same as in Fig.2(a)], but combined with lines (16) for $n = 1$ and $n = -1$ (right and left dashed line, respectively). (b) Reflection coefficient of zero harmonic $\left|H_0^{(r)}/H_i\right|^2$ (red solid line) and relative square amplitudes $\left|H_n^{(r)}/H_i\right|^2$ of $n = 1$ (black dashed lines) and $n = -1$ (blue dashed lines) harmonics *vs* frequency ω. For the comparison the reflectivity of the graphene, deposited on nonmodulated substrate is depicted by solid green line. (c) Reflection coefficient of zero harmonic $\left|H_0^{(r)}/H_i\right|^2$ versus frequency ω and angle of incidence Θ for direct excitation of SPPs in graphene by incident electromagnetic wave. (d) Reflection coefficient of zero harmonic $\left|H_0^{(r)}/H_i\right|^2$ *vs* gate voltage V at fixed frequency $\omega = 10\,\mathrm{meV}$. Other parameters are: gate voltage $V = 50\,\mathrm{V}$ (panels a,b,c), angle of incidence $\Theta = 20°$ (panels a,b,d), modulation depth $a = 0.2$ (panels b,c,d), $\varepsilon' = 3.9$, $\varepsilon_2 = 1$, $D = 20.67\,\mu\mathrm{m}$.

when SPP excitation conditions are not met, the reflectivity of the graphene on modulated substrate does not differ significantly from that of the graphene on nonmodulated one. This fact is confirmed by Fig.3(b), where reflection coefficient of zeroth harmonics (red solid line) possesses two maxima (which frequencies coincide with $\Omega_{\pm 1}$, predicted in Fig.3(a)], these maxima correspond to the excitation of SPPs on $n = \pm 1$ harmonics (dashed lines). Here reflection coefficients was obtained from Eqs.(14)–(15). Notice, that this situation is completely opposite to the ATR structure, where SPP excitation revealed in the reflectivity minima. The angular dependence demonstrates, that frequency splitting between two reflectivity maxima, being zero at normal incidence $\Theta = 0$, then monotonically increases with an increase of Θ. At the same time, similar to the ATR structure, in the graphene deposited on modulated substrate it is also possible to tune its reflectivity by changing the gate voltage V [see Fig.3(d)], this dependence exposes two maxima. Nevertheless variation range is not too wide (between $\left|H_0^{(r)}/H_i\right|^2 \approx 0.15$ and $\left|H_0^{(r)}/H_i\right|^2 \approx 0.25$), if compared to that of ATR structure (where it can be varied from total reflection to total absorption). In order to increase the reflectivity one should use gratings with larger modulation depth a.

4. Conclusions

To conclude, we have demonstrated that both the ATR structure and periodic grating incorporating a monolayer graphene sheet can operate as THz attenuator where the reflectance of an electromagnetic wave can be switched from nearly unity to nearly zero (in ATR structure) by applying an external gate voltage to the graphene layer. Since the typical frequencies are $\sim 5\,\mathrm{meV}$ (or $\sim 1.2\,\mathrm{THz}$), this structure can operate in the submillimeter range. The frequency of excited SPPs can be increased by using a prism material with a higher dielectric permeability ε_3 in ATR structure, or smaller grating period in periodic gratings. The proposed device can also be used for spectroscopy of the graphene optical conductivity through measuring the characteristics of the excited SPPs.

References

[1] A. A. Maradudin, *Surface Polaritons. Electromagnetic Waves at Surfaces and Interfaces*, Amsterdam, North-Holland, 1982.

[2] J. Homola, S. S. Yee, and G. Gauglitz, Surface plasmon resonance sensors: review, *Sensors and Actuators B* 54: 3–15, 1999.

[3] S. Kawata, Y. Inouye, and P. Verma, Plasmonics for near-field nano-imaging and superlensing, *Nature Photonics* 3: 388–394, 2009.

[4] D. W. Prather, A. Sharkawy, S. Shi, J. Murakowski, G. Schneider, *Photonic Crystals, Theory, Applications and Fabrication*, Wiley, New Jersey, 2009.

[5] R. W. Wood, Anomalous diffraction gratings, *Phys. Rev.* 48: 928–936, 1935.

[6] T. W. Ebbesen, H. J. Lezec, H. F. Ghaemi, T. Thio, and P. A. Wolff, Extraordinary optical transmission through sub-wavelength hole array, *Nature* 391: 667–669, 1998.

[7] A. K. Geim, and K. S. Novoselov, The rise of graphene, *Nature Materials* 6: 183–191, 2007.

[8] A. K. Geim, Graphene: status and prospects, *Science* 324: 1530–1534, 2009.

[9] M.J. Allen, V.C. Tung, and R.B. Kaner, Honeycomb carbon: a review of graphene, *Chemical Reviews* 110: 132–145, 2010.

[10] A. H. Castro Neto, F. Guinea, N. M. R. Peres, K. S. Novoselov, A. K. Geim, The electronic properties of graphene, *Rev. Mod. Phys.* 81: 109–162, 2009.

[11] Z. Q. Li, E. A. Henriksen, Z. Jiang, Zhao Hao, M. C. Martin, P. Kim, H. L. Stormer, and D. N. Basov, Dirac charge dynamics in graphene by infrared spectroscopy, *Nature Physics* 4: 532–535, 2008.

[12] Long Ju, B. Geng, J. Horng, C. Girit, M. C. Martin, Zhao Hao, H. A. Bechtel, Xiaogan Liang, A. Zettl, Y. Ron Shen, and F. Wang, Graphene plasmonics for tunable terahertz metamaterials, *Nature Nanotechnology* 6: 630–634, 2011.

[13] Yu. V. Bludov, M. I. Vasilevskiy, and N. M. R. Peres, Mechanism for graphene-based optoelectronic switches by tuning surface plasmon-polaritons in monolayer graphene, *Europhys. Lett.* 92: 68001, 2010.

[14] S. A. Mikhailov and K. Ziegler, New Electromagnetic Mode in Graphene, *Phys. Rev. Lett.* 99: 016803, 2007.

[15] Qiaoliang Bao, Han Zhang, Bing Wang, Zhenhua Ni, Candy Haley Yi Xuan Lim, Yu Wang, Ding Yuan Tang, and Kian Ping Loh, Broadband graphene polarizer, *Nature Photonics* 5: 411–415, 2011.

[16] A. V. Kats and Yu. V. Bludov, Investigation of the spectra of coupled polaritons on the periodically modulated metallic layer and the narrow regions of anomalous transparency, *Proceedings of SPIE* 5221: 207–217, 2003.

Functionally graded laminated phononic crystals with damages

Mikhail Golub[1,*], Sergey Fomenko[1], Chuanzeng Zhang[2], Tinh Quoc Bui[2]

[1]Institute for Mathematics, Mechanics and Informatics, Kuban State University, Krasnodar, Russian Federation
[2]Chair of Structural Mechanics, Department of Civil Engineering, University of Siegen, Siegen, Germany
*corresponding author, E-mail: m_golub@inbox.ru

Abstract

Elastic wave propagation in functionally graded periodically layered and damaged composites is investigated using the extended transfer matrix method and the boundary integral equation method. Two different models are developed to approximate the damaged layer, namely, a periodic array of cracks and continuously distributed springs in the layer. The focus of this analysis is on the wave transmission and reflection, band-gaps, localization and resonance phenomena due to the influences of functionally graded properties and crack-like damages.

1. Introduction

In recent years, an increasing research interest on a new class of functional composites, the so-called phononic crystals (PCs), arises in the research community from many different disciplines. PCs consist of two or more different constituent materials with a periodic arrangement, and many anomalous wave propagation phenomena may arise in such periodic structures. PCs may show some surprising effects, which have potential applications such as in the design and functional optimization of novel multi-functional composites, development of new acoustic and ultrasonic devices (wave detectors, wave filters, acoustic lenses, etc.), noise reduction and vibration isolation in high-precision mechanical systems and many others [1]. Usually the interface is assumed to be continuous in the stress and displacement components in the simulation, while an interface in a real situation is much more complicated. The reason could arise from micro level due to misfits at the grain boundaries, or on a macro scale where a thin interface layer connects the two solids. Various methods have been developed to model such imperfect interfaces [2, 3, 4]. Another possible approach to deal with this mismatch between two different materials is to impose a layer of a functionally graded material between the two homogeneous solids.

Elastic wave guides are susceptible to damages like cracks during the manufacturing or in service. In particular, the delamination at imperfect interfaces between the constituents and interior cracks in the individual layers can occur. Such interface or interior damages may change the dynamic properties of the periodic composites and correspondingly cause noticeable alterations in band-gaps and wave transmission spectra. To simplify the analysis, imperfect interfaces are usually approximated by a periodic/stochastic distribution of interface cracks or by spring boundary conditions [5], where the latter in a limiting case corresponds to a crack. Several analytical and numerical approaches have been developed so far for wave propagation analysis in periodic structures [6] including the transfer matrix method employed in the present work. Wave propagation and diffraction by a crack in multilayered composite structures can be efficiently investigated by using boundary integral representations and Green's functions in conjunction with the integral-transform technique [7].

The present study is a continuation of our previous research works [8, 9, 10]. Here a special type of PCs is considered, namely, the one-dimensional PCs consisting of unit-cells composed of two different elastic materials with a periodicity in the thickness direction, where functionally graded (FG) interlayers are placed between the two neighboring homogeneous layers with a single crack or a distribution of cracks.

2. Characterization of wave motion in phononic crystals

In order to investigate wave phenomena in periodic layered structures, several problems are studied (see Figures 1, 5). In the following sections, numerical results for the propagation characteristics of P- and SV-waves in a periodic composite with crack-like damages are presented. Numerical calculations are carried out for the same material parameters as in [10]. The structure is composed of N unit-cells with periodically spaced Alumina and Aluminium, which are denoted as Materials A and B correspondingly.

	Material	Density $[kg/m^3]$	Young's modulus $[GPa]$	Poisson's ratio
A	Alumina	4000	400	0.231
B	Aluminium	2700	70	0.33

Table 1: Elastic moduli and densities of materials A and B.

The two half-planes $i = 0$, $i = N + 1$ (the surrounding media) are assumed to have the same elastic properties as material A. The material parameters (density ρ_1, Young's modulus and Poisson's ratio) are given in Table 1.

2.1. Energy flow

The transport of the elastic wave energy corresponding to the time-harmonic displacement field $\mathbf{u}e^{-i\omega t}$ with the circular frequency ω can be visualized by the energy streamlines, which show the trajectories of the time-averaged energy fluxes [11]. At every point energy streamlines are tangential to the power density vector $\mathbf{e} = (e_x, e_z) = (e_1, e_2)$ introduced by Umov [12] for elastodynamic wave fields in the 19th century. Its components are expressed via the displacement and stress vectors $\mathbf{u}$ and $\boldsymbol{\tau}_n$: $e_n = -\frac{\omega}{2}\mathrm{Im}\,(\mathbf{u}, \boldsymbol{\tau}_n)$, where $\boldsymbol{\tau}_n$ is the amplitude of the stress vector on an elementary area orthogonal to the n-th coordinate axis.

2.2. Transmission and reflection coefficients

The displacement vector $\mathbf{u} = \{u_1, u_2\} = \{u_x, u_z\}$ in the elastic media is governed by the equations of motion

$$\sigma_{ij,j} + \rho\omega^2 u_i = 0, \quad i, j = 1, 2 \tag{1}$$

where the stress tensor σ_{ij} can be expressed in terms of the derivatives of the displacement components u_i by

$$\sigma_{ij} = \lambda(u_{1,1} + u_{2,2})\delta_{ij} + \mu(u_{i,j} + u_{j,i}). \tag{2}$$

Here δ_{ij} is the Kronecker symbol; λ and μ are the Lamé coefficients.

In the multilayered media the elastic constants λ and μ are piecewise continuous functions with jumps on the layer interfaces $z = z_n$. On the interfaces, the following continuity conditions for the displacement and the stress components should be satisfied

$$[u_i]_{z_n} = 0, \quad [\sigma_{2i}]_{z_n} = 0.$$

Here $[f]_{z_n}$ denotes the jump of the function $f(z)$ at $z = z_n$.

In order to demonstrate the scheme, the simplest case of plane SH wave propagation is considered. The displacement fields in both half-planes are plane waves and can be expressed in the following form

$$u_1(z) = e^{ik_A \sin\theta x} \begin{cases} e^{ik_A \cos\theta z} + A^- e^{-ik_A \cos\theta z}, & z \le 0 \\ A^+ e^{ik_A \cos\theta (z-d)}, & z \ge NH \end{cases}$$

while the component $u_2 = 0$. Here θ is the incidence angle, A^+ and A^- are the amplitudes of the transmitted and reflected plane waves, k_A is the wavenumber of the SH-waves in the lower and upper half-planes [13].

The generalized state vector $\mathbf{v}(z)$ composed of the displacement u_1 and the stress component σ_{12} can be expressed in terms of the propagator or transfer matrix (T-matrix) [14] by

$$\mathbf{v}(d) = \mathbf{T} \cdot \mathbf{v}(0).$$

The amplitudes A^+ and A^- of the transmitted and reflected plane waves should satisfy the energy conservation law. The total transfer matrix $\mathbf{T}$ is a multiplication of the transfer matrices $\mathbf{T}_i$ of all the sublayers, e.g. [10].

The amplitudes of the reflected and transmitted waves do not give sufficient information needed for the analysis, so the energy transmission coefficient κ^+ and the energy reflection coefficient κ^- are introduced. The energy transmission coefficient $\kappa^+ = E^+/E^0$ is defined as the ratio of the time-averaged energy flow transmitted through the layered stack E^+ to the energy transferable by the plane wave E^0, and analogously for the reflection coefficient $\kappa^- = E^-/E^0$. Obviously the energy conservation law must be satisfied, i.e. $\kappa^+ + \kappa^- = 1$.

2.3. Pass-bands and band-gaps

The transmission coefficient $\kappa^\pm$ is a suitable characteristic quantity to describe pass-bands and band-gaps, see [10]. Band-gaps are frequency ranges in which the transmission coefficient is zero, i.e., no wave propagation is possible in band-gaps. In general, band-gaps are dependent on the type and the incidence angle θ of the incoming waves. For the demonstration of the wave propagation phenomena related to a periodically layered composite structure, it is often sufficient to consider the first band-gap only, because similar wave propagation phenomena are also expected at medium and high frequencies.

3. Functionally graded phononic crystals

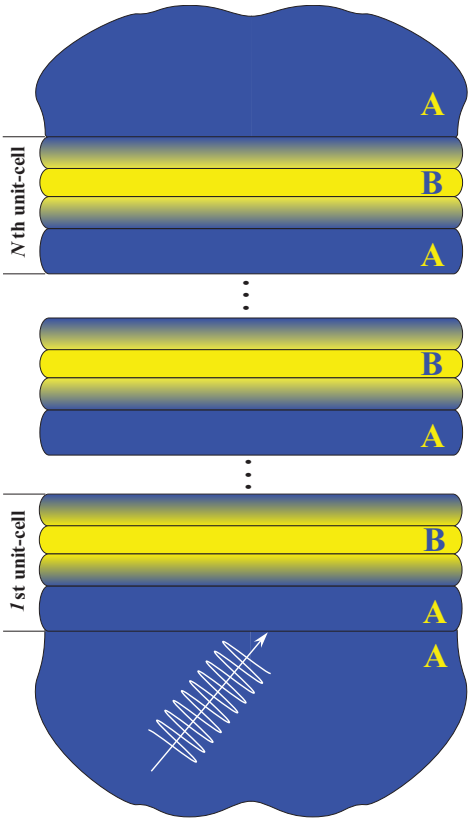

Figure 1: Geometry of the undamaged functionally graded periodic laminate.

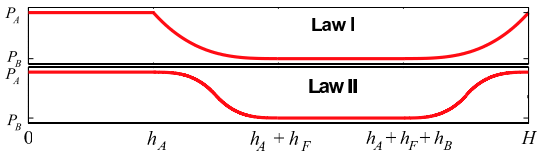

Figure 2: Variation of the material parameters.

The phononic crystals (PCs) under consideration are composed of finite periodically spaced unit-cells in the thickness direction made of both functionally graded (FG) and isotropic materials (Figure 1). The FG interlayers are composites consisting of two material phases with their composition varying in the thickness direction leading to continuous functions for the elastic constants $\lambda(z)$, $\mu(z)$ and the density $\rho(z)$.

Two models for the FG layers are developed. The first model is the so-called explicit FG model, in which the transfer matrix is derived by the numerical solution of the equations of motion with variable coefficients. The second model is the multilayer model, where a number of homogeneous isotropic sublayers of piecewise constant material properties is used to approximate the FG interlayers. In this case the transfer matrix $\mathbf{T}_F$ of the functionally graded layer is approximated by a multiplication of the transfer matrices of all the isotropic sublayers [10]. The correctness and the accuracy of both models are verified by comparing the computed wave transmission coefficient and band-gaps.

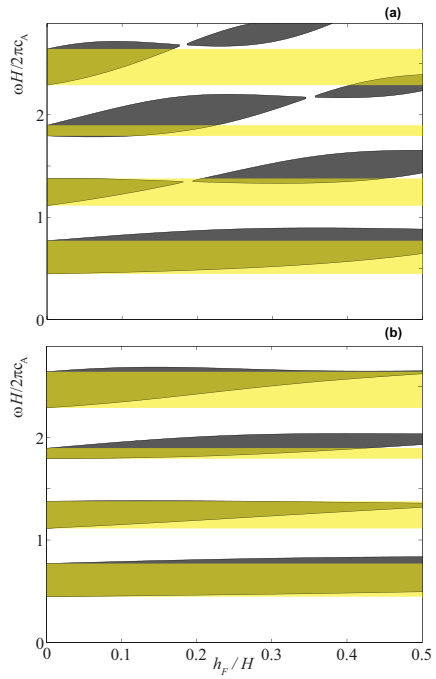

Figure 3: Influences of the interlayer thickness h_F/H on band-gaps for $h_A/h_B = 1$ and incident P-wave. (a) Law I; (b) Law II; (Darker and lighter domains denote band-gaps with and without FG interlayers respectively).

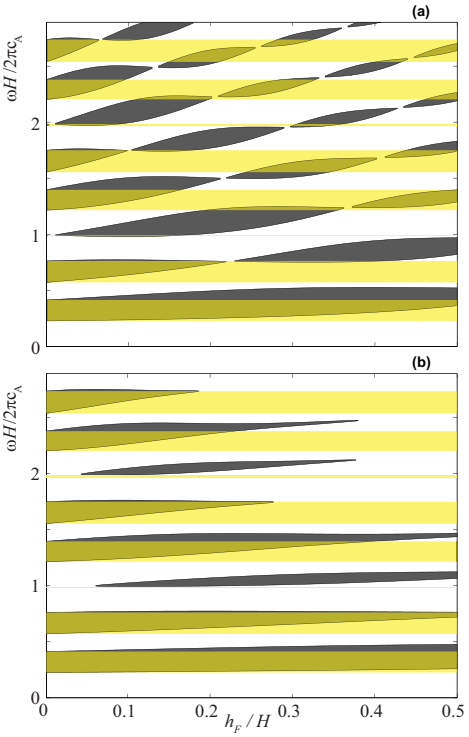

Figure 4: Influences of the interlayer thickness h_F/H on band-gaps for $h_A/h_B = 1$ and incident SV-wave. (a) Law I; (b) Law II; (Darker and lighter domains denote band-gaps with and without FG interlayers respectively).

The location and the width of the band-gaps are in general dependent on the material gradation law describing the FG interlayers and the geometrical parameters of the periodic laminates. Here, we first analyze the effects of the FG interlayers on the band-gaps for the power-law material gradation. An example for the variation of the material parameters in the power-law I and power-law II within the unit-cell is presented in Figure 2.

The band-gaps are presented in Figures 3 and 4, which show the influences of the relative thickness of the FG interlayers h_F/H on the band-gaps. Figure 3 presents the numerical results for the incident plane time-harmonic P-wave and different power-laws of the material gradation while Figure 4 stands for the plane time-harmonic SV-wave at the incidence angle $\theta = 0°$ for both case. The presence of the FG interlayers in a PC and the material gradation law have essential influences on the band-gaps (their form and location) in comparison with that without FG interlayers (case of $h_F = 0$) in the medium and high frequency ranges.

4. Damaged phononic crystals

Now we consider time-harmonic wave propagation in a PC with a damaged layer, see Figure 5. The damage is assumed to be in the M-th unit-cell at a distance d from the interface $z = a_{M-1}$. Different kinds of damages are considered, namely, a single crack, a distribution of cracks, and spring-like boundary conditions, see Figure 6. In order to

verify the analysis, the thickness of the FG interlayers for the damaged PC is assumed to be zero, i.e., $h_F = 0$ and only homogeneous sublayers are present.

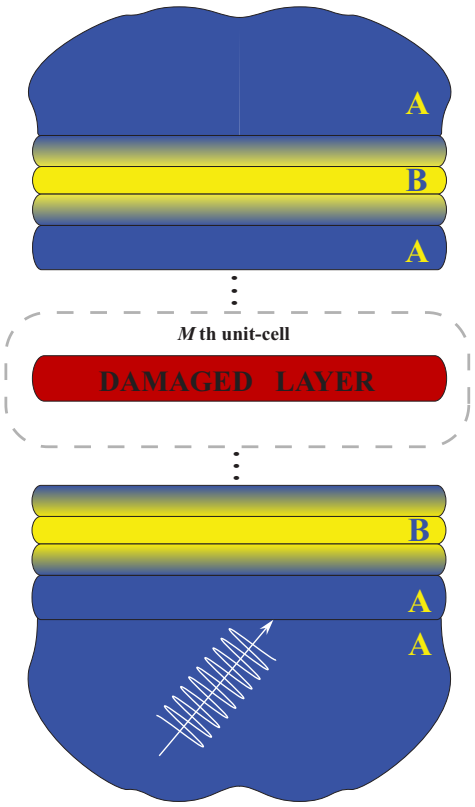

Figure 5: Geometry of the damaged functionally graded periodic laminate.

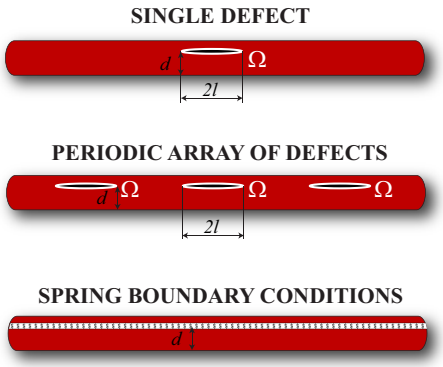

Figure 6: Three different types of the damages.

4.1. A single crack

The total displacement field $\mathbf{u} = \mathbf{u}^{\text{in}} + \boldsymbol{u}^{\text{sc}}$ in the periodic laminate with a strip-like crack of length $2l$ is continuous everywhere except on the crack-faces, where $\boldsymbol{\tau}(x,z) = \{\tau_{xz}(x,z), \tau_{zz}(x,z)\} = 0$. The scattered wave field in the composite media is considered separately for the two layered half-planes

$$\boldsymbol{u}^{\text{sc}}(x,z) = \begin{cases} \boldsymbol{u}^{-}(x,z), & z < 0, \\ \boldsymbol{u}^{+}(x,z), & z > 0, \end{cases} \tag{3}$$

and the corresponding integral representations for each half-plane are applied in a similar manner as in [8]. On the top surface of both half-planes an unknown load $\mathbf{p}(\mathbf{x})$ is introduced, and an integral representation for the scattered displacement field is then employed [7]. For a large number of layers the method is time consuming, thus the technique developed in [7] is applied. The explicit description of the numerical construction of the Fourier-transform of the Green's matrix for multilayered elastic half-planes can be found [15]. The load $\mathbf{p}(\mathbf{x})$ is determined from the solution of the integral equation for the crack-opening-displacements using a Galerkin method.

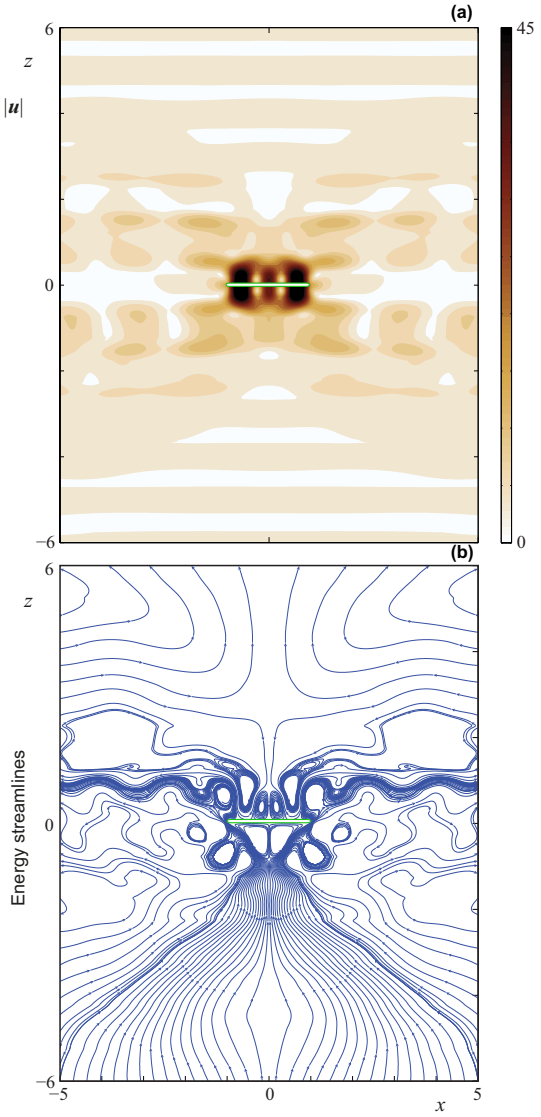

Figure 7: The displacement amplitude $|\mathbf{u}(x,z)|$ and related energy streamlines for P-wave propagation at an angle $\theta = 0°$; $h_A/h_B = 1$; $l/H = 1.0$; $d/H = 0.25$; $\omega = 2.713$.

The presence of a single crack does not change the band-gaps and the pass-bands. However, a single crack changes the local wave pattern in its surroundings. Thus, some localization and resonance phenomena can be observed, which are especially important to the failure of the material from the practical point of view. The presence of a crack may cause noticeably large amplitudes of the wave motion, i.e., wave localization, in the vicinity of the crack. In addition, very large stress and displacement amplitudes are observed at resonance frequencies, and the localization exhibits also in the occurrence of the energy vortices near the cracks, for more details see [16].

In order to demonstrate the wave localization effect, the parameters l, d and ω corresponding to the strongest resonances have been found after the analysis of the average CODs and the stress intensity factors (SIFs). The corresponding wave pattern is shown in Figure 7 via the displacement amplitudes $\boldsymbol{u}$ and the energy streamlines, where the crack is depicted by the green prolongated rounded rectangle. The wave pattern is symmetrical with respect to the $x = 0$ axis due to the normal wave incidence ($\theta = 0°$). The energy flow is sufficiently reflected by the crack and goes like a channel wave in the two layers over and below the damaged layer. Pairs of the energy vortices are observed near the crack, where in the centers of the energy vortices $|\mathbf{e}| = 0$. The maximum energy flow is concentrated near the crack seen as dark zones in Figure 7.

4.2. Distributed damages

Two different models are developed to approximate the damaged layer with a distribution of cracks, namely, a periodic array of cracks of length $2l$ and spacing s and continuously distributed springs in the layer. In the first model, the total wave field in the stack of elastic layers with cracks is described by a sum of incident wave field determined by the transfer matrix method and the scattered wave field governed by a boundary integral representation [7] in terms of the crack-opening-displacements (CODs) on the crack-faces. The problems for a single crack and for a periodic array of cracks are solved by using a boundary integral equation method in combination with a Galerkin method. In the second model, the damaged layer is approximated by the spring boundary conditions which allows us to use the T-matrix method with an approximate estimation of the spring stiffness [5]. To this end, the following spring boundary conditions are introduced

$$\sigma_{iz}^{+} = \sigma_{iz}^{-} = \left(\frac{\lambda^{+} + 2\mu^{+}}{(\lambda^{+} + \mu^{+})\mu^{+}} + \frac{\lambda^{-} + 2\mu^{-}}{(\lambda^{-} + \mu^{-})\mu^{-}} \right)^{-1} \times \\ \times \frac{4s}{\pi l^2} \times (u_i^{+} - u_i^{-}), \qquad (4)$$

which relate the stresses and the displacements above and below the line of the cracks denoted by the signs $\pm$. The constant in Equation (4) is given for distributed cracks of length $2l$ with a density $2l/s$, see [5] for more details.

The numerical results presented in Figures 8 and 9 illustrate the wave energy transmission through the periodically layered composite weakened by a damaged layer. The transmission coefficients $\kappa^{+}(\omega, l/H)$ calculated by the model of periodic collinear cracks and the spring model are shown in Figures 8 and 9 respectively for a normal incidence of a plane time P-wave ($\theta = 0°$). The energy transmission coefficients obtained by both models are in a good agreement in the low-frequency range. In the second and third pass-bands, obvious differences in the transmission coefficients from both models are observed. Since the spring model is based on an averaging technique [17] and the low-frequency assumption, the model is inadequate for medium and high frequencies, and for predicting the wave localization, resonance peaks of $\kappa^{+}(\omega, l/H)$ in the pass-bands and stress concentration phenomena near crack-tips.

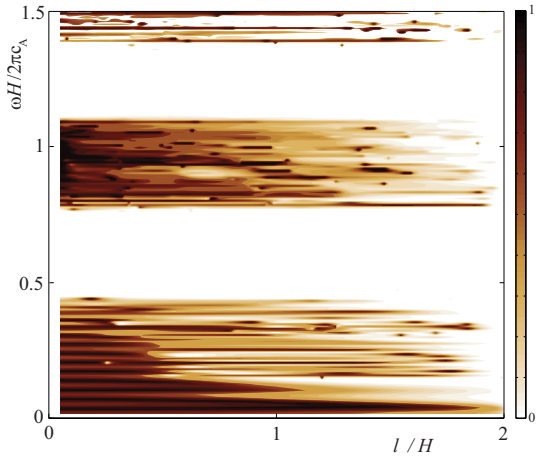

Figure 8: Transmission coefficient $\kappa^{+}(\omega, l/H)$ in the damaged PC modeled by a periodic array of cracks in the $M = 15$th layer. P-wave propagation at an angle $\theta = 0°$; $h_A/h_B = 1$; $d/H = 0.25$.

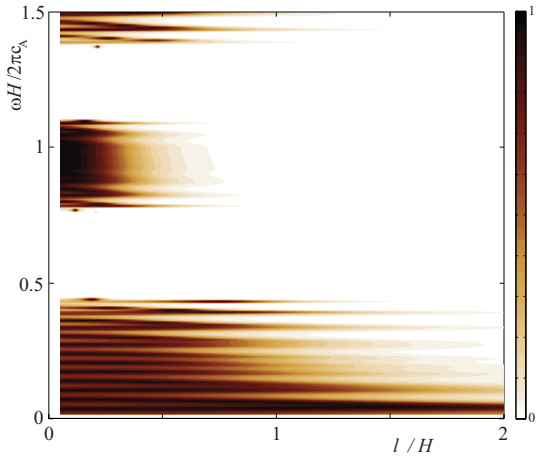

Figure 9: Transmission coefficient $\kappa^{+}(\omega, l/H)$ in the damaged PC modeled by the spring boundary conditions in the $M = 15$th layer. P-wave propagation at an angle $\theta = 0°$; $h_A/h_B = 1$; $d/H = 0.25$.

5. Conclusions

- The location and the width of the band-gaps are dependent on the law describing the material gradation, the thickness of the FG interlayers, the relative thickness of the homogeneous layers, and the incidence angle of plane time-harmonic waves.
- The size and the position of the band-gaps are not influenced by the position and the size of a single crack, while the presence of a single crack may lead to wave resonances in its vicinity.
- The band-gaps may be significantly affected by a distribution of cracks in a layer, and they are dependent on the crack-size, the crack-spacing, and crack-distance to the interface.
- The dynamic loading on a periodic composite structure with a crack may cause wave localization between the crack-faces and the closest interfaces, and it may become stronger when they are closer.
- The spring model is a simple and efficient model for predicting low-frequency band-gaps. However, it cannot predict the wave localization and resonance phenomena.
- Interface cracks do not exhibit strong resonances within the band-gaps and the corresponding dynamic stress intensity factors have small magnitudes in the band-gaps.

Acknowledgement

The work is supported by the Russian Foundation for Basic Research, the Ministry of Education and Science of the Russian Federation (1.1.2/10463) and the German Research Foundation (DFG, Project No. ZH 15/11-2), which are gratefully acknowledged.

References

[1] M. Maldovan and E. L. Thomas. *Periodic Materials and Interference Lithography for Photonics, Phononics and Mechanics*. Wiley-VCH Verlag GmbH & Co. KGaA, Weinheim, Germany, 2009.

[2] J. P. Jones and J. S. Whittier. Waves in a flexibly bonded interface. *Journal of Applied Mathematics andMechanics*, 34:905–909, 1967.

[3] S. I. Rokhlin and Y. J. Wang. Analysis of boundary conditions for elastic wave interaction with an interface between two solids. *Journal of the Acoustical Society of America*, 89:503–515, 1991.

[4] A. Boström, P. Bövik, and P. Olsson. A comparison of exact first order and spring boundary conditions for scattering by thin layers. *Journal of Nondestructive Evaluation*, 11:175–184, 1992.

[5] M. V. Golub and A. Boström. Interface damage modelled by spring boundary conditions for in-plane elastic waves. *Wave Motion*, 48(2):105–115, 2011.

[6] M. Sigalas, M. S. Kushwaha, E. N. Economou, M. Kafesaki, I. E. Psarobas, and W. Steurer. Classical vibrational modes in phononic lattices: theory and experiment. *Zeitschrift für Kristallographie*, 220:765–809, 2005.

[7] E. V. Glushkov and N. V. Glushkova. On the efficient implementation of the integral equation method in elastodynamics. *Journal of Computational Acoustics*, 9(3):889–898, 2001.

[8] M. V. Golub, Ch. Zhang, and Y.-S. Wang. SH-wave propagation and resonance phenomena in a periodically layered composite structure with a crack. *Journal of Sound and Vibration*, 330(13):3141–3154, 2011.

[9] M. V. Golub, Ch. Zhang, and Y.-S. Wang. SH-wave propagation and scattering in periodically layered composites with a damaged layer. *Journal of Sound and Vibration*, 331(8):18291843, 2012.

[10] M. V. Golub, S. I. Fomenko, T. Q. Bui, Ch. Zhang, and Y.-S. Wang. Transmission and band gaps of elastic SH waves in functionally graded periodic laminates. *International Journal of Solids and Structures*, 49(2):344–354, 2012.

[11] E. V. Glushkov and N. V. Glushkova. Blocking property of energy vortices in elastic waveguides. *Journal of Acoustical Society of America*, 102:1356–1360, 1997.

[12] N. A. Umov. Ableitung der bewegungsgleichungen der energie continuirlichen körpern. *Zeitschrift für Mathematik und Physik*, 19(5):1–22, 1874.

[13] L. M. Brekhovskikh and O. A. Godin. *Acoustics of layered media I. Plane and quasi-plane waves.* Springer Berlin / Heidelberg, 1998.

[14] W. Thomson. Transmission of elastic waves in stratified solid medium. *Journal of Applied Physics*, 21:89–94, 1950.

[15] V. A. Babeshko, E. V. Glushkov, and J. F. Zinchenko. *Dynamics of inhomogeneous linear-elastic media (in Russian)*. Nauka, Moscow, 1989.

[16] E. Glushkov, N. Glushkova, M. Golub, and A. Eremin. Resonance blocking and passing effects in two-dimensional elastic waveguides with obstacles. *Journal of the Acoustical Society of America*, 130(1):113–121, 2011.

[17] A. Boström and G. R. Wickham. On the boundary conditions for ultrasonic transmission by partially closed cracks. *Journal of Nondestructive Evaluation*, 10:139–149, 1991.

Control of sonic metamaterial stopband

A. R. J. Murray, J. S. Bell. E. Hendry, I. R. Summers, J. R. Sambles and A. P. Hibbins

School of Physics, University of Exeter, Stocker Road, Exeter, EX4 4QL, United Kingdom
*corresponding author, E-mail: a.r.j.murray@exeter.ac.uk

Abstract

The acoustic transmittance of two closely spaced rigid plates perforated with a square array of circular holes is studied both experimentally and numerically. The system exhibits a band of acoustic attenuation originating from hybridization between a two-dimensional resonance in the gap between the plates, and pipe modes in the holes. Misalignment of the holes in either one or both lateral dimensions shifts the centre frequency of the stop band to maintain the conditions required for zero transmission.

1. Introduction

The acoustic double fishnet (ADF) structure comprises two rigid plates, each perforated with a square array of circular holes, with the holes on one plate perfectly aligned with the holes on the other. Previous studies have shown how when the two plates are separated by a sub-wavelength gap, the system exhibits a band of near-perfect acoustic attenuation [1-3]. The present study investigates the influence of plate misalignment on the acoustic transmittance. Figure 1 shows a schematic of the misaligned ADF structure.

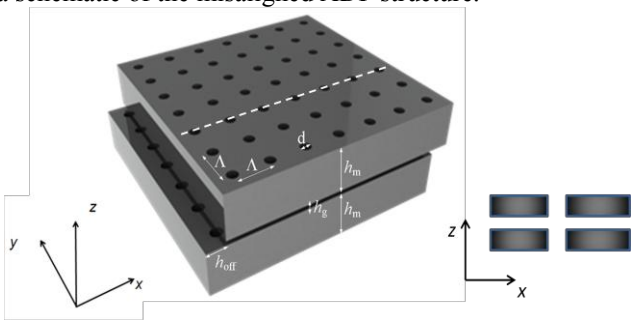

Figure 1: Schematic diagram of ADF structure, with plate thickness h_m, and gap size h_g. The circular holes, of diameter d, are arranged in a square array with pitch Λ. The lateral displacement between the plates is h_{off}. The right-side inset illustrates a cross section of a unit cell (shown with no lateral displacement) taken along the dashed white line.

The presence of a small gap between the two plates leads to the hybridisation of the two-dimensional resonance in the gap between the plates with the pipe modes in the holes leading to frequency shifts of the resulting transmission peaks. Moreover, the presence of the gap also leads to near-perfect suppression of sound transmission across a frequency band dictated by the pitch Λ.

When the holes in the two plates are aligned (i.e. each pair of aligned holes behave as a long pipe with a the gap at its mid-length), odd-order modes (exhibiting a pressure antinode in the region of the gap) are strongly perturbed in frequency, due to volume flow leakage into the gap, whereas even-order modes (exhibiting a pressure node in the region of the gap) are largely unaffected. The frequency at which sound blockage occurs corresponds with a resonance of the two-dimensional mode in the gap. Considering a symmetrical unit cell centred over one of the holes, the pressure must be maximal along the (square) boundary in the gap at the frequency of the "gap resonance". As the plates are misaligned, the condition for zero transmission changes. Using symmetry arguments, there must still be a pressure antinode at the boundary of a square unit cell located centrally over the input hole, however for no sound to be transmitted there must be a pressure node located at the output hole. In this case, there is no pressure variation at the output hole and therefore no coupling between the holes in the two plates, and thus no transmission of sound. When the pressure wave in the gap satisfies these conditions, the sound field is no longer a simple resonance of the gap. It follows that the frequency of sound blockage should increase with misalignment of the plates, as the pressure node in the gap at the output hole spatially approaches a pressure antinode at the unit cell boundary, effectively forcing a quarter-wave into a smaller distance. It is clear that the case when the holes are aligned is a special case that satisfies the conditions for zero transmission.

2. Modelling

Figure 2 (a) and (b) show theoretical transmission spectra modelled with a modal matching technique (described in Ref. 3) for the cases of lateral and diagonal misalignment respectively. The technique involves matching the acoustic pressure and velocity functions at the each of the interfaces through the structure. Both plots clearly show the increase in frequency of the stop band as the plates are misaligned. Preliminary results from an analytical model (to be described in a future article) also agree well with these findings.

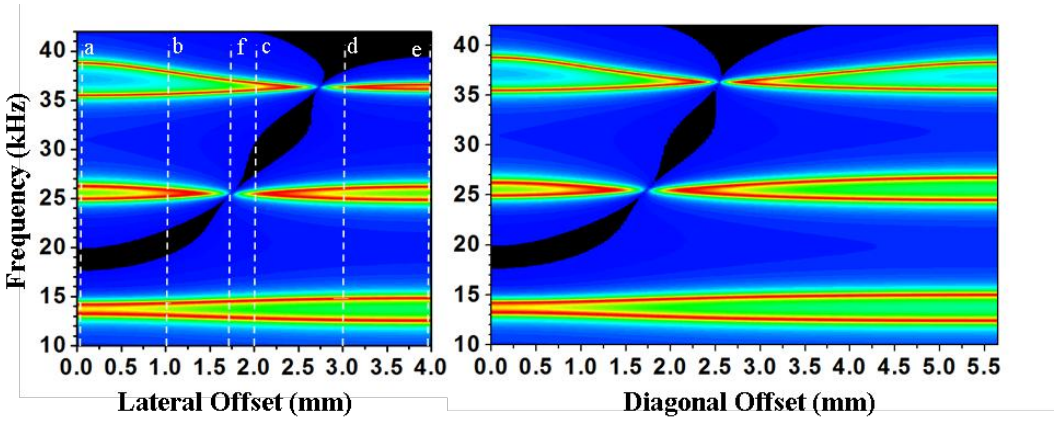

Figure 2: (a) Predicted transmission spectra using a modal matching technique [3], showing the resonant modes of two h_m = 12 mm thick perspex plates separated by h_g = 0.94 mm at increasing lateral plate offsets. Red shading indicates regions of strong transmission, and black indicates transmission amplitudes of less than 0.5%. (b) Similiar transmission spectra as (a) with plates offset diagonally.

3. Experiment

The experimental sample consists of two perspex (Lucite) plates, with thickness h_m = 12 mm and perforated with circular holes of diameter d = 2.4 mm in a square array of pitch Λ = 8 mm. The square plates have sides of length 200 mm (corresponding to a 25×25 array of holes), and are separated by an air-filled gap with h_g = 0.94 mm. A plane sound was normally incident in air on to the sample. The experiments were undertaken with frequencies ranging between 10 and 40 kHz. A series of sample geometries were studied with 1 mm incremental offsets of the plates and an additional data set obtained at an offset of 1.69 mm to demonstrate the strong suppression of a transmission resonance (Figure 3). The experiments utilised a pair of parabolic mirrors, one to produce the plane wave from point source and the other to focus the transmitted sound wave into the detector.

4. Discussion

The data presented (Fig. 3) shows generally good agreement with the theoretically predicted transmittance of the ADF structure. Note, that in comparison with the model, the experimental results exhibit non-unity transmittance on resonance, and imperfect sound blockage. It is proposed that this error is associated with the failure to fully account for viscous losses within the narrow pipes in the system. As shown in Bell *et al*. [3] the magnitude of sound suppression is significantly greater than that provided by a single holey plate of equivalent total thickness. Offsetting the plates provides a reasonably simple method of tuning the location of the stop band and as shown in Figure 3 (f), the stop band can be used to significantly reduce the strength of transmission resonances that are otherwise present, thus producing a broader frequency band with significant sound suppression.

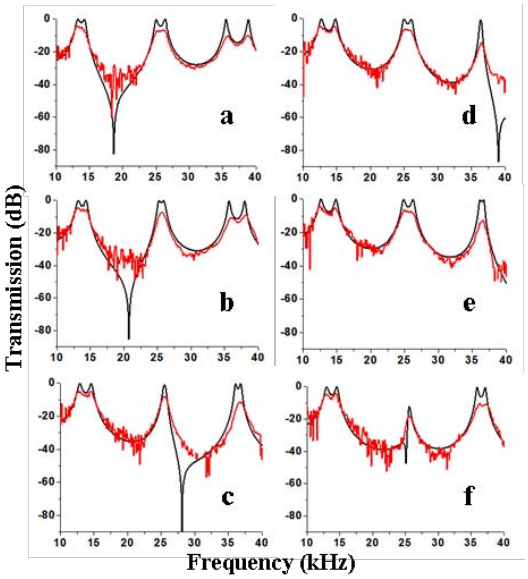

Figure 3: Experimental (red line) and theoretical modelled (black line) transmission results through the ADF structure in air. Graphs (a)-(e) show the transmission for h_{off} = 0 mm, 1 mm, 2 mm, 3 mm, and 4 mm respectively. Graph (f) shows the transmission for h_{off} = 1.69 mm.

Acknowledgements

The authors acknowledge funding by the EPSRC and Sonardyne International, and thank N. Cole, M. Wears and K. White for their technical support.

5. References

[1] F. Liu, F. Cai, Y. Ding and Z. Liu, Appl. Phys. Lett., **92**, 103504 (2008).

[2] J. Christensen, L. Martin-Moreno, and F. J. Garcia-Vidal, Appl. Phys. Lett., **97**, 134106 (2010).

[3] Bell *et al*. (under review)

Nano-Signature of Surface Charge Spatial Distribution of Metal Nanoparticles Irradiated Off-Resonance

Xuan Zhou[1], Claire Deeb[1,2], Davy Gérard[1], Alexandre Bouhelier[3], Prashant K. Jain[4], Jérôme Plain[1], Olivier Soppera[5], Lavinia Balan[5], Pascal. Royer[1], Gary P. Wiederrecht[2], and Renaud Bachelot[1]*

[1]Laboratoire de Nanotechnologie et d'instrumentation Optique, Université de Technologie de Troyes, France
[2]Center for Nanoscale Materials, Argonne National Laboratory, Argonne, Illinois 60439, USA
[3]Laboratoire Interdisciplinaire Carnot de Bourgogne, Dijon, France
[4]Department of Chemistry, 600S Mathews Ave, University of Illinois, Urbana, IL 61801, USA
[5]Institut de Science des Matériaux de Mulhouse IS2M-CNRS LCR 7228, Université de Haute-Alsace, France
*corresponding author, E-mail: renaud.bachelot@utt.fr

Abstract

We report on the imaging of localized electric field on a metal/dielectric interface of gold nanoparticles out of their plasmon resonance. The surface polarization charges caused by the discontinuity of the electric field at emtal/dielectric surface provide a tiny local field enhancement. At some precise positions on the surface of nanoparticles, the resulting effective local field intensity becomes high enough to overcome the threshold dose of a photo-sensitive formulation, and hence the polymerization process is initiated. We finally end up with a cross-linked 3D polymer structure that is actually molding the spatial distribution of the surface charges held on the metal/dielectric interface.

1. Introduction

The applications of surface plasmons in such fields as fluorescence enhancement [1, 2], surface enhanced Raman spectroscopy [3], near-field microscopy [4] and nanosensing [5, 6] are currently the focus of researches. Unlike numerous studies that have reported the on-resonance excitation of plasmons of a metallic nanoparticle (MNP), the off-resonance excitation is seldom stated except for the lightning rod effect [7]. This is mostly due to the fact that when excited out of its resonance, MNP generates a localized field that is extremely weak, and thus it can hardly be measured. In this article, we report on imaging, with an unprecedented resolution of 5nm the polarization surface charge distribution on gold nanorods (GNRs) and gold nanotriangles (GNTs) excited out of their resonance.

Our experiment is based on nanoscale photopolymerization induced by the local optical field intensity in the vicinity of MNPs [8-10]. At the interface of metal and dielectric, the behavior of electric field medium follows the boundary conditions of electromagnetic fields:

$$E_{1n} - E_{2n} = \frac{\sigma_s}{\varepsilon_0} = \chi \boldsymbol{n} \cdot \boldsymbol{E_0} \,, \qquad (1)$$

Where E_{1n} and E_{2n} are the normal complements of electric field inside and outside the nanoparticle, σ_s is the surface charge density, ε_0 is the vacuum permittivity, χ is the metal electric susceptibility, $\boldsymbol{n}$ is the normal vector at a given point on the surface of MNP, and $\boldsymbol{E_0}$ is the incident electric field. The local electric field at MNP surface is the sum of incident field $\boldsymbol{E_0}$ and the field $\chi \boldsymbol{n} \cdot \boldsymbol{E_0}$, which is generated from the excited surface charges that corresponding to the discontinuity of electric field at the metal/dielectric interface. A tiny enhancement of the electric field is therefore introduced in the vicinity of MNPs. By irradiating the nanoparticles, coated by a drop of photopolymerizable formulation[11], with a polarized plane wave whose dose is below the threshold, polymers formed only in the places where the local electric field is enhanced to overcome the threshold[10]. This finally imprints the distribution of surface charges at the vicinity of MNPs.

2. Experiments

The photopolymerizable formulation is constituted by pentaerythritol tri/tetraacrylate monomer (PETIA) 96%wt, methyldiethanolamine (MDEA) 4%wt, and Eosin Y 0.5%wt. When absorbing photons, the molecules of Eosin Y are excited to triplet state, which then interacts with amine to form the radical. Polymerization is initiated by radicals that react with monomer to end up with a 3D cross-linked polymer structure [10, 11].

As is shown in Figure 1, differently oriented GNRs were fabricated on a glass substrate using electron beam lithography. The orientation of a nanorod is defined by the angle (θ) of its major axis with respect to the incident laser polarization, which is along the Y axis (Figure 1a). The major and minor axes of GNRs were 235nm and 85nm respectively, which correspond to a plasmon resonance of 1313nm for the major axis, and 662nm for the minor axis (Figure 1b). The spectrum was calculated for a single GNR embedded in the photopolymerizable formulation of a 1.485 refractive index.

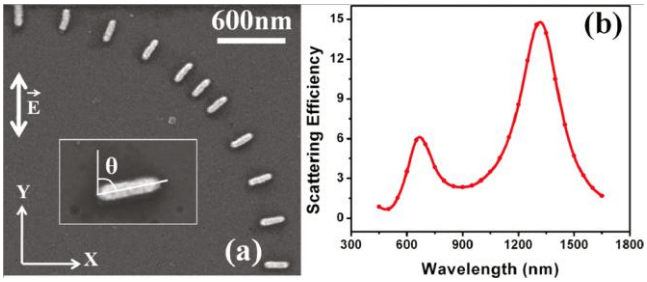

Figure 1: (a) SEM image of GNRs with different orientation from θ = 0° to = 90°. (b) Calculated far-field scattering spectrum for a single nanorod embedded in a 1.485 refractive index medium.

After AFM characterization, the sample was coated with a drop of polymerizable formulation and was irradiated "off-resonance" by a linearly polarized laser beam at λ = 530nm. The dose of incident laser was 65% of the threshold dose to prevent the formulation from polymerizing under far field exposure. Only near-field enhanced extra-intensity allows the threshold to be exceeded. After the rinsing procedure, AFM scan was carried on exactly the same GNRs. The differential image, which is the result of subtracting pixel to pixel the AFM image before polymerization from that taken after the procedure, indicates the polymer that was formed in the vicinity of GNRs, and hence it clearly reveals the zones where the threshold dose has been overcome (Figure 2).

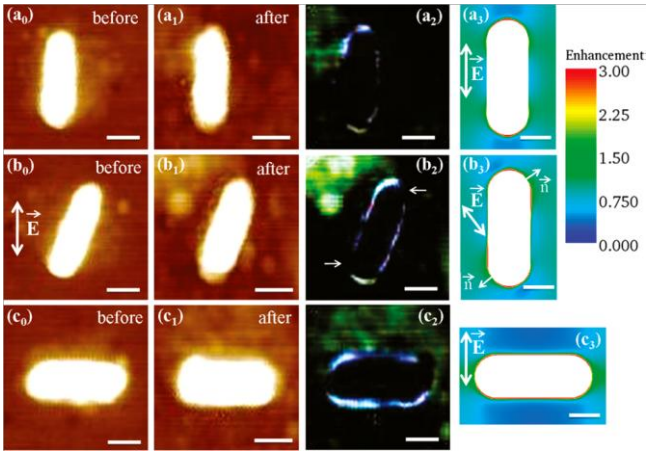

Figure 2: Characterizations of GNRs oriented (a) θ = 0° (b) θ = 22.5° and (c) θ = 90° with respect to the incident laser polarization: AFM images (a_0) (b_0) (c_0) before and (a_1) (b_1) (c_1) after polymerization, (a_2) (b_2) (c_2) corresponding differential images and (a_3) (b_3) (c_3) FDTD calculations of field enhancement around GNRs embedded in a medium with a refractive index of 1.485. Scale bars correspond to 90nm.

3. Results and Discussions

It turns out that when the unit normal vector ***n*** on the GNR surface is parallel to the polarization of incident light, the polymer extension reaches its maximum; Conversely, the elongation of GNR is minimum when ***n*** is perpendicular to the incident polarization, as pointed out by white arrows in Figure 2b_2. A 3D-FDTD calculation of the near field enhancement was performed for all the three different oriented particles (Figure2 a_3, b_3 and c_3). Experimental and calculated results match quite well.

To better learn about the behavior of the polarized surface charges at the vicinity of GNRs, a quantitative study has been carried out on 44 nanorods with 11 different orientations from 0° to 90°.

Figure 3 shows the dependence of GNRs extensions along major and minor axes on the orientation of nanoparticles. It turns out that the elongation along major axis is at its maximum when the GNR major axis is parallel to the laser polarization (θ = 0° in Figure 3a), then decreases with the inclination of the particle to finally reaches its minimum when the major axis is perpendicular to the incident laser polarization (θ = 90°). For the minor axis extension, maximum occurs when the GNR major axis is perpendicular to the incident polarization (θ = 90°), while no elongation exists when this axis is parallel to the polarization (θ = 0°).

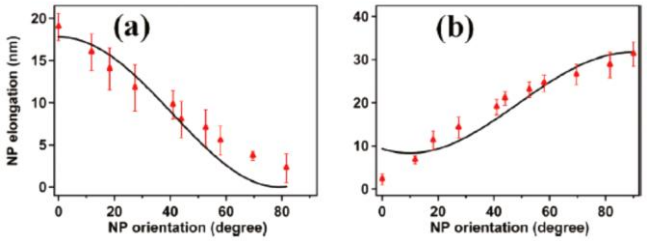

Figure 3: Elongations of GNRs along (a) major and (b) minor axes as a function of NP orientation (θ).

Once above the threshold dose, the polymer elongation (l) is assumed to be proportional to the local electric field intensity (I_{surf}):

$$l = \alpha I_{surf} \quad , \tag{2}$$

where α is a coefficient corresponding to the photo-physical properties of the polymer. As is stated above, the local electric field of a MNP is the sum of incident field and induced dipole field. On the surface of a GNR, the field intensity can therefore be induced:

$$I_{surf} = (\boldsymbol{E_0} + \chi \boldsymbol{n} \cdot \boldsymbol{E_0})^2 = I_0(1 + \chi \boldsymbol{n} \cdot \widehat{\boldsymbol{E}}_{\boldsymbol{0}})^2 \,, \tag{3}$$

where $\widehat{\boldsymbol{E}}_{\boldsymbol{0}}$ is the unit vector of incident electric field. Along major (M) and minor (m) axis, the local field intensity can be expressed respectively as

$$I_{surf}^{M} = I_0(1 + \chi^2 \cos^2\theta + 2\chi \cos\theta \cos\Phi) \,, \tag{4a}$$

$$I_{surf}^{m} = I_0(1 + \chi^2 \sin^2\theta + 2\chi \sin\theta \cos\Phi) \,, \tag{4b}$$

where Φ is the phase difference between the incident and the induced electronic fields. Assuming that the two fields are in same phase because of the quasistatic approximation, the polymer elongation on both axes can be written as

$$l_M = l_0(1 + \chi^2 \cos^2\theta + 2\chi \cos\theta) \,, \tag{5a}$$

$$l_m = l_0(1 + \chi^2 \sin^2\theta + 2\chi \sin\theta) \,, \tag{5b}$$

For the elongation along major axis, Equation 5a is used to fit the experimental results (black solid line in Figure 3a). We obtained $\chi = -5.2 \pm 0.1$. $l_0 = \alpha I_0$ is set to be 1nm, which corresponds to the resolution of measurement on AFM images. As to the minor axis, the measured elongations of GNRs were fitted with

$$l_m = l_0(1 + \chi^2 \sin^2\theta + 2\chi \sin\theta) + l_1 , \qquad (6)$$

where $l_1 = 8.3nm$ is an offset and $\chi = -5.8 \pm 0.3$.

It is worth noticing that the real part of dielectric constant for gold at $\lambda = 530$nm is $\varepsilon_r = -4.5$. The electric susceptibility $\chi = \varepsilon_r - 1 = -5.5$. This matches well with the average value of χ that is obtained from major and minor axes.

To confirm our method, the same procedures were performed on samples of triangular colloids. The nanotriangles were spin-coated onto an aminosilane-functionalized glass substrate. Again, the 530nm laser was used as incident beam for the off-resonance photopolymerization.

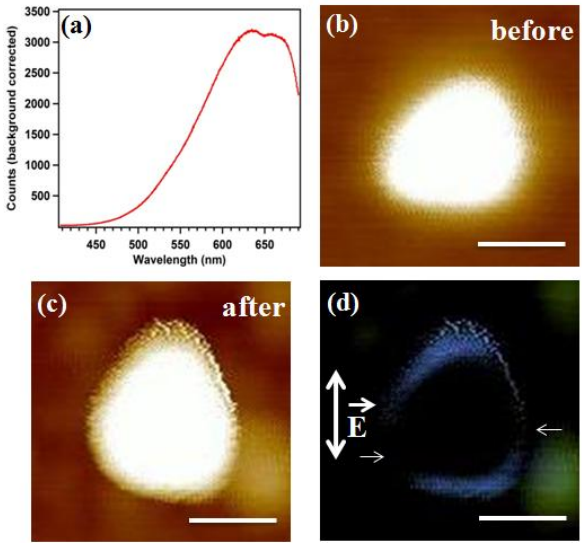

Figure 4: (a) Extinction spectrum of triangular nanoparticles. AFM images on a unique particle (b) before and (c) after polymerization procedures, (d) is the differential image. Scale bars represent for 40nm.

It is remarkable that the elongation of GNTs has a maximum value at the vertices and bottom side of the triangle, where the normal vector of the surface is parallel to the polarization axis, and a minimum value around the two bottom corners, as pointed out by the white arrows in Figure 4d, where the normal vector is perpendicular to the polarization direction.

4. Conclusions

We reported on the observation of spatial distribution of surface charges using nanoscale photopolymerization on the surface of MNPs. By irradiating off their resonances the MNPs that coated by the photopolymerizable formulation, polymer structures can be generated wherever the dose of localized electromagnetic field is sufficiently enhanced to exceed the threshold for polymerization. The field enhancement is caused by the optical electric field that associated with surface charges at metal/dielectric interface. Polymer formed in this way produced, on the AFM image, a measured elongation of nanoparticles with a resolution of sub 5nm.

Acknowledgements

This work is partly supported by the PUF program 2010.

References

[1] R. Bardhan, , N. K. Grady, J. R. Cole, A. Joshi, and N. J. Halas, Fluorescence Enhancement by Au Nanostructures: Nanoshells and Nanorods, *ACS nano*, 3: 744-752, 2009.

[2] F. Tam, G. P. Goodrich, B. R. Johnson, and N. J. Halas, Plasmonic Enhancement of Molecular Fluorescence, *Nano Lett*, 7: 469-501, 2007.

[3] J. M. McLellan, Z. Y. Li, A. R. Siekkinen, and Y. Xia, The SERS Activity of Supported Ag Nanocube Strongly Depends on Its orientation Relative to Laser Polarization, *Nano Lett*, 7: 1013-1017, 2007.

[4] G. P. Wiederrecht, Near-field Optial Imaging of Noble Metal Nanoparticles, *Eur. Phys. J. Appl. Phys.*, 28: 3-18, 2004.

[5] J. M. Bingham, J. N. Anker, L. E. Kreno, and R. Van Duyne, Gas Sensing with High-Resolution Localized Surface Plasmon Resonance Spectroscopy, *J. Am. Chem. Soc.*, 132: 17358-17359, 2010.

[6] C. Wu, and Q.-H. Xu, Stable and Functionable Mesoporous Silica-Coated Gold Nanorods as Sensitive Localized Surface Plasmon Resonance (LSPR) Nanosensors, *Langmuir* 25: 9441-9446, 2009.

[7] B. Lamprecht, J. R. Kerenn, A. Leitner, and F. R. Aussenegg, "Resonant and Off-Resonant Light-Driven Plasmons in Metal Nanoparticles Studied by Femtosecond-Resolution Third-Harmonic Generation," *Phys. Rev. Lett.*, Vol. 83: 4421, 1999.

[8] H. Ibn El Ahrach, R. Bachelot, A. Vial, G. Lerondel, J. Plain, P. Royer, O. Soppera, Degeneracy Breaking of the Plasmon Resonance of Single Metal Nanoparticles by Nanoscale Near-Field Photopolymerization, *Phys. Rev. Lett*, 98: 107402, 2007.

[9] C. Deeb, X. Zhou, D. Gérard, A. Bouhelier, P. K. Jain, J. Plain, O. Soppera, P. Royer and R. Bachelot, Off-Resonant Optical Excitation of Gold Nanorods: Nanoscale Imprint of Polarization Surface Charge Distribution, J. Phys. Chem. Lett., 2: 7-11, 2011.

[10] C. Deeb, R. Bachelot, J. Plain, A. L. Baudrion, S. Jradi, A. Bouhelier, O. Soppera, P. K. Jain, L. Huang, C. Ecoffet, et al., Quantitative Analysis of Localized Surface Plasmons Based on Molecular Probing, ACS Nano, 4: 4579-4586, 2010.

[11] Soppera, S. Jradi, D. J. Lougnot, Photopolymerization with microscale resolution: incluence of the physico-chemical and photonic parameters, J. Polym. Sci. Part A: Polym Chem 6: 3783–3794, 2008.

Single metafilm effective medium behavior in optical domain: Maxwell-Garnett approximation and beyond

Natalia Dubrovina[1], Loïc O. Le Cunff[3], N. Burokur[1], R. Ghasemi[1], A. Degiron[1,2], A. De Lustrac[1], A. Vial[3], G. Lerondel[3], and A. Lupu[1,2]

[1]Univ. Paris-Sud, Institut d'Electronique Fondamentale, UMR 8622, 91405 Orsay Cedex, France
[2]CNRS, Orsay, F-91405, France
[3]Laboratoire de Nanotechnologie et d'Instrumentation Optique, Institut Charles Delaunay, Université de Technologie de Troyes, 12 rue Marie Curie, BP 2060, 10010 Troyes Cedex, France
*corresponding author: anatole.lupu@u-psud.fr

Abstract

It is empirically shown by numerical modeling that a single metafilm formed by an array of cut wires on a Silicon substrate behaves like a homogeneous layer for normal or oblique incidence.

1. Introduction

Metamaterials (MMs) have generated a lot of interest during the last decade due to their ability to provide unusual electromagnetic behavior, not encountered in natural materials [1,2]. They are commonly obtained by an implementation of a periodical arrangement of resonant elements, called also meta-atoms. Both the periodicity and the size of resonant elements are typically much smaller than the wavelength. This feature makes it possible to model their properties using an approach similar to that used for continuous media in classical electrodynamics or optics.

In this approach, MMs are treated as bulk effective media with a certain thickness and associated dielectric permittivity ε and magnetic permeability μ that are anisotropic in the most general case.

This approach proved to be valid, but essentially in the microwave domain [3]. Difficulties arise in the optical domain, in particular for the most common case of a single metafilm on a dielectric substrate. As mentioned by several authors [3-7], it is not clear whether the effective medium approach is valid for describing single metafilm behavior and what thickness should be assigned to the MMs in this case.

A few attempts to provide an answer to this question were done in [8,9]. In [9] the behavior of a metafilm formed by gold nanowires and split ring resonators (SRRs) was investigated by Fourier transform infrared (FTIR) experiments in the mid IR domain. By exploiting the interferogram of the asymmetric cavity formed by the metafilm and the silicon substrate and the zero order of transmission of the silicon/metamaterial phase mask, it was shown that an effective index of refraction could be indeed assigned to the metafilm around the first plasmonic resonance of SRRs. However since this kind of interferometric measurements is sensitive to the optical length difference, the question of unambiguous determination of a metafilm effective index and thickness remains still open.

This paper aims at providing an answer to this question and to demonstrate that in the limit of Maxwell-Garnett (M-G) effective medium model, the behavior of a single metafilm on a substrate can be approximated by that of a homogeneous layer with a thickness equal to that of the deposited metal.

2. Single metafilm modeling and effective medium behavior validity criteria

For our study we consider the example of an array of gold cut wires (CWs) on a Silicon substrate. It represents probably the most elementary type of MMs used for building more complex geometry MMs. Its greatest advantage is the essentially non-magnetic behavior with $\mu \approx 1$ due to the absence of notable coupling between the electrical and magnetic resonances.

To prove that such a CW meta-surface can be indeed described as a homogeneous layer, it is necessary to verify that its behavior meets the following conditions:

- Effective magnetic permeability $\mu \approx 1$, except near the resonance region (non-magnetic behavior).
- Linearity of the dielectric permittivity variation with MMs surface filling factor ρ (validity of (M-G) approximation).
- Linearity of the optical length variation with respect to the deposited metal thickness).
- Invariance of the MMs layer dielectric permittivity with respect to the incidence angle variation

The phase and amplitude transmission and reflection modeling of an array of gold cut wires (CWs) on a Silicon substrate is performed by means of HFSS software from

Ansoft [10] and finite difference time domain (FDTD) modeling [11]. The dielectric permittivity of Au used for numerical modeling is that given by Palik [12]. For the sake of simplicity we consider a substrate with a refractive index of 3.45 that doesn't vary with the wavelength. This index value is that of the silicon at 1.5μm. To calculate the metafilm effective permittivity ε_{eff} and permeability μ_{eff} from the complex reflection and transmission coefficients ***r*** and ***t***, respectively, we use the retrieval method detailed in [13], derived in much the same way as in [6].

The refraction index of a metafilm of thickness ***h*** is:

$$n_{eff} = \sqrt{\left(\frac{\beta}{k_0 h}\right)^2 + n_1^2 \sin^2\theta_1} \qquad (1)$$

Here $\beta = \pm arc\cos(\cos\beta) + \frac{2\pi m}{k_0 h}$ (2)

where m is an integer. The explanation about the proper choice of the sign and value of the integer coefficient m can be found in [14].

In its turn:

$$\cos\beta = \frac{\sqrt{p_1 p_l}}{p_1(1-r) + p_l(1+r)} \frac{\left(1 - r^2 + t'^2\right)}{t'} \qquad (3)$$

where $p = \sqrt{\frac{\varepsilon}{\mu}}\cos\theta = \frac{1}{z}\cos\theta$ (4)

is the medium characteristic admittance, i.e. the inverse of the medium impedance z for polarization perpendicular to the incidence plane. The index 1 and l designate first and last semi-infinite media. The metafilm layer impedance z_{eff} is used for calculating $\varepsilon_{eff}=n_{eff}/z_{eff}$ and $\mu_{eff}=n_{eff}\cdot z_{eff}$:

$$z_{eff}^2 = \frac{1}{\cos^2(\theta_{eff})} \frac{\frac{1}{p_l}\cos\beta - \frac{1}{\sqrt{p_1 p_l}}\frac{1+r}{t'}}{p_l\cos\beta - \sqrt{p_1 p_l}\frac{1-r}{t'}} \qquad (5)$$

where $\cos\theta_{eff} = \sqrt{1 - \left(\frac{n_1}{n_{eff}}\right)\sin^2\theta_1}$ (6)

The obtained results were used to verify the introduced above effective medium validity criteria. For this the numerical modeling detailed below was performed.

2.1. Metafilm thickness determination

The first point of our analysis concerns the determination of the thickness to be assigned to the metafilm. As mentioned, outside the resonance region, the effective permeability obtained by the retrieval procedure must be consistent with the condition μ≈1 [14].

In the (M-G) approximation the MMs layer represents a mixture of CWs and air. Here we make the hypothesis that its thickness ***h*** equals that of the deposited metal. To verify this assertion, HFSS numerical modeling was performed for CWs with several metal thicknesses ranging from 20nm to 100nm. The length of the CWs is fixed to 200nm and its width to 50nm. The separation distance between adjacent CWs in transverse and longitudinal directions is 250nm and 100nm, respectively. The related filling factor ρ, defined as the fraction of the surface occupied by the MMs is 11% and corresponds to the case of a weak coupling interaction between the CWs.

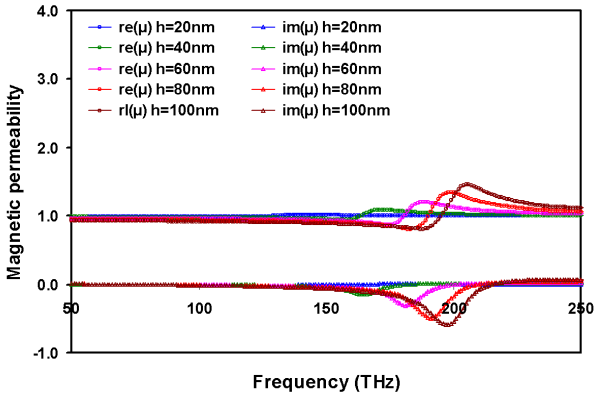

Figure 1: Real and imaginary parts of magnetic permeability μ obtained for different metal thickness CW array.

The results obtained for normal incidence with electric field orientation along the longitudinal CWs axis are displayed Fig. 1. It can be seen that outside the resonance region the condition μ≈1 is well satisfied in the whole range of metal thickness variation, thus validating our hypothesis about the thickness of the effective layer. The region where μ differs from unity corresponds to the well-known magnetic antiresonance that is always concomitant with the electric resonance [15].

The shift toward higher frequencies of the resonance when metal thickness is increased is likely to be related to the decrease of the asymmetric bound supermode effective index [16,17] for higher metal thickness. The gold material dispersion also brings contribution to the effective supermode index variation.

2.2. Dielectric permittivity variation with filling factor

The previous example has shown the validity of the (M-G) effective medium model for the case of a low filling factor MMs layer. Increasing the filling factor would obviously result in an adjacent CWs interaction enhancement that could alter the validity of M-G approximation. To verify the M-G approximation validity for higher filling factors, we vary the separation distance between CWs along both the longitudinal and transverse direction.

The results obtained at normal incidence for 200×50×10nm CWs with electric field orientation along the longitudinal axis are shown Fig. 2. In this example the filling factor variation is obtained by changing the transverse separation between adjacent CWs. For better viewing the displayed results represent the effective permittivity normalized by the filling factor: $\varepsilon_{norm}=\varepsilon_{eff}/\rho$.

As it can be seen, the normalized permittivity is little dependent on the filling factor. For both real and imaginary part the maximal variation of permittivity is less than 16%, while the filling factor variation attains 450%. The shift of the resonance toward higher frequencies with the increase of the filling factor is in agreement with similar MMs structures reported in [18]. This shift is due to the

enhancement of coupling between CWs by dipolar interaction. As it will be shown in the following, the variation of the normalized permittivity would be even lower without the frequency shift.

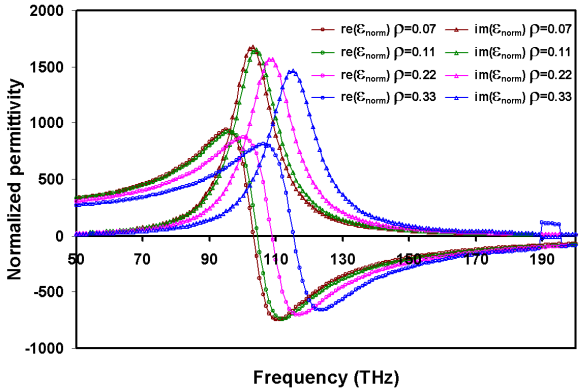

Figure 2: Real and imaginary parts of normalized MMs permittivity spectral characteristics for different filling factors. Metal thickness 10nm.

The relative independence of the normalized permittivity is conserved when the variation of the filling factor is performed in a different manner. This point was verified for filling factor variation obtained by changing the longitudinal separation distance or the width of the CWs, the rest of parameters being fixed. Similar behavior holds also for higher metafilm thicknesses. Note also the high values of normalized permittivity exceeding 1000. Even for a filling factor of 10% this means an effective index around 10 at resonance.

2.3. Single metafilm optical length study

Genuine MMs effective parameters have to be independent of the MMs thickness. For the microwave domain this condition is readily verified by varying the number of MMs layers. A convergence of the retrieved MMs effective parameters is expected with the increase of the number of layers. In the case of a single metafilm layer this means that effective parameters have to be independent of the metal thickness. The equivalent condition is to have a linear variation of the optical length with $\boldsymbol{h}$.

As for the previous examples CWs length is 200nm and width is 50nm while normal incident light electric field orientation is along the longitudinal axis. The refractive index used to calculate the optical length corresponds to the maximal value of the effective index at the resonance frequency. As for the permittivity, its value is also normalized by the filling factor.

The variation of the optical length (normalized by the filling factor) as a function of the thickness $\boldsymbol{h}$ for different CWs densities is shown Fig. 3a. The displayed results show that the variation of the optical length with metal thickness is approximately linear for a thin metal. Strong deviations from linearity occur for metal thicknesses above 50nm, especially for higher filling factors.

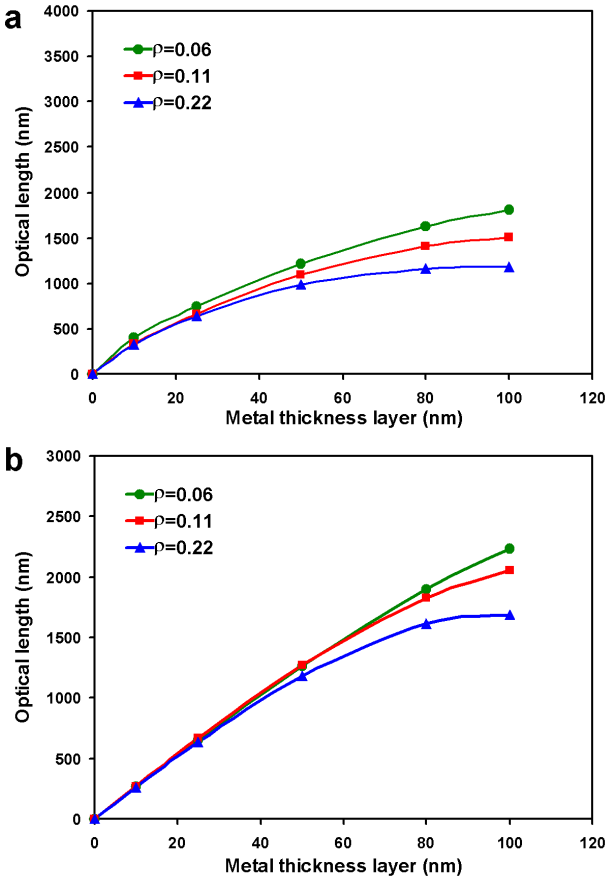

Figure 3: (a) Normalized by filling factor optical length for different CWs densities. b) Same as (a) for 148THz fixed resonance frequency using tuned CWs.

To understand the deviation from linear dependence we compare the spectral characteristics of the normalized permittivity for different MMs thickness. The results corresponding to 10, 25 and 50nm MMs thickness are represented Fig. 4a. The shift of the resonance frequency and permittivity variation are much more important as compared to the case of filling factor variation shown Fig. 3.

To separate thickness and frequency contributions, the length and width of 10 and 50nm thick CWs was tuned to shift the resonance to 148THz while keeping the same filling factor. For 10nm thick CWs this was achieved by changing the length to 138nm, the width to 72nm and having same unit cell size of 300×300nm. A similar procedure was applied to the 50nm thick MMs. For this case the CWs length and width are 245×41nm for a 300×300nm unit cell.

The normalized permittivities for CWs having a resonance at 148THz are represented Fig. 4b. The variation of the normalized permittivity is less than 12% in this case, while it attains 248% for the case corresponding to Fig. 4a. It thus appears that a frequency shift brings a significant contribution in the change of the metafim effective parameters.

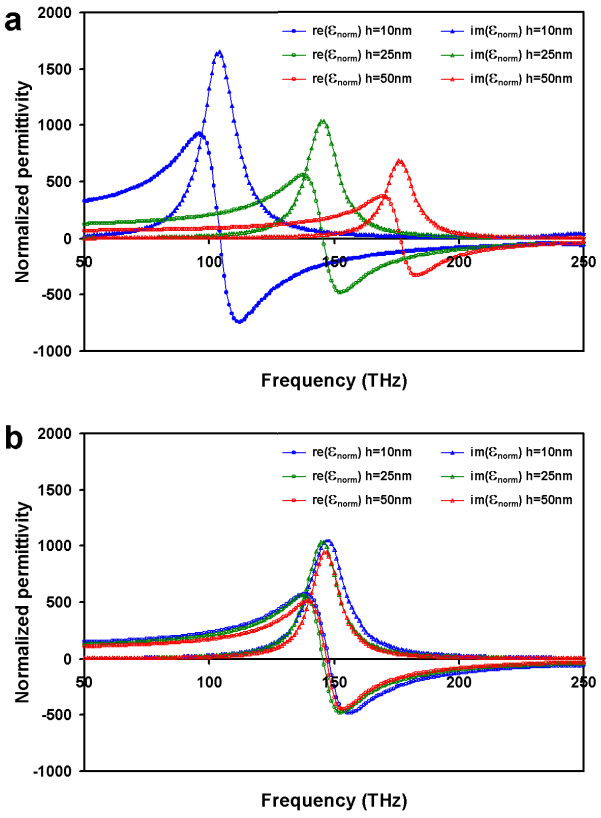

Figure 4: (a) Real and imaginary parts of normalized MMs permittivity spectral characteristics for different metafilm thickness. (b) Same as (a) for 148THz fixed resonance frequency using tuned CWs.

The optical length determined for the case of a resonance frequency fixed to 148THz using CWs tuning procedure is shown Fig. 4b. The dependence is much more linear in this case, especially when the filling factor is low. This result further proves the validity of the M-G effective medium model applied to a single metafilm layer.

2.4. Metafilm oblique incidence s polarization behavior

The last point of our analysis concerns the metafilm effective medium behavior under oblique incidence. For p polarization the homogeneous layer approximation is not valid because of the anisotropy of the CW properties with respect to the electric field orientation. For the time being there is no reliable analytical anisotropy retrieval procedure that would allow an appropriate treatment of this case. For this reason our analysis is mainly limited to the case of s polarization, while some discussion concerning the possible implementation of the retrieval procedure for p polarization is presented in the next section. For the s polarization the electric field orientation along the CWs longitudinal axis doesn't vary with the incidence angle. The configuration corresponding to this case is sketched Fig. 5.

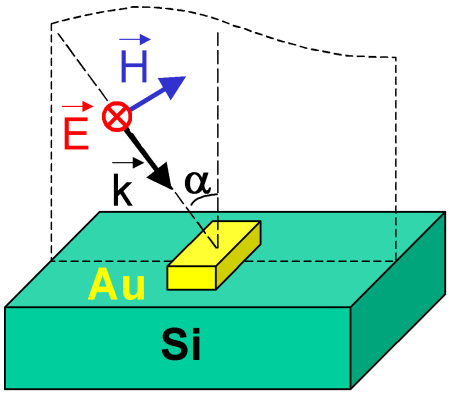

Figure 5: Sketch of s polarization oblique incidence configuration.

The reflection and transmission spectra computed for different angles of incidence are shown in Fig. 6a.

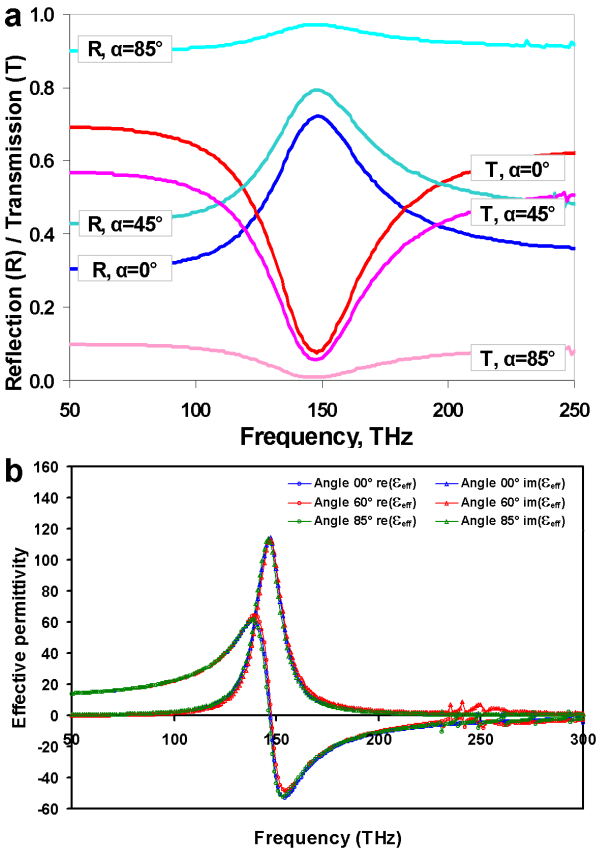

Figure 6: a) Reflection and transmission spectra of single metafilm layer for s polarization different incidence angles. b) Real and imaginary parts of effective MMs permittivity spectral characteristics for s polarization different incidence angles.

The plotted results correspond to 200×50×25nm CWs with 11% filling factor. It can be observed that in accordance with Fresnel reflection coefficients, the

reflectivity increases with the incidence angle. At the same time an apparent decrease of the resonance variation for high incidence angles is observed in transmission and reflection.

To extract the metafilm effective parameters we use the described retrieval procedure. The obtained results represented in Fig 6b show that permittivity and permeability are independent of the incidence angle. It should be noted also that outside the resonance region the effective permittivity and respectively the effective index are not too high for low filling factors. As it can be inferred from the Fig. 6b, at low frequency $n_{eff} \approx 3.8$, that is not too much higher as compared to Silicon. So at high incidence angles, as those showed in our example, the refraction angle inside the metafilm should substantially deviate from the normal axis. It follows from that the independence of the metafilm effective parameters of the incident angle can not be attributed to the near normal axis propagation as it was suggested in [19] were split ring resonators (SRRs) single metafilm was investigated for different incidence angles in the THz spectral domain.

The presented results show that for the particular investigated geometry, when the electric field is oriented along the main MMs symmetry axis, the metafilm behavior is fully analogous to that of a homogeneous layer. The thickness of this layer is that of the deposited metal.

2.5. Full anisotropic characterization

While there is no reliable analytical way to perform a retrieval of the anisotropic dielectric tensor in the case of the p polarization (Fig. 7), another approach can be followed, in which the full permittivity and permeability tensors are retrieved either through brute-force search or heuristic methods.

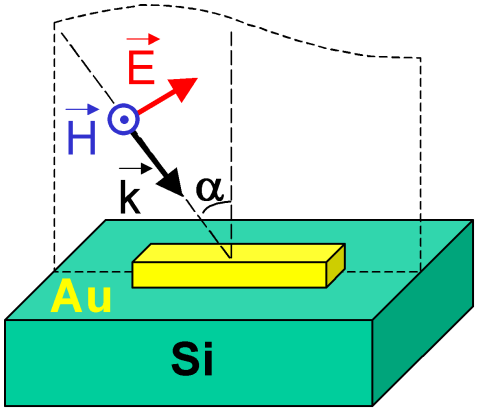

Figure 7: Sketch of p polarization oblique incidence configuration.

To do this, one only needs to know how to solve the direct problem, which is the optical response of an anisotropic slab [20] with known dielectric and permittivity tensors. The inverse problem – retrieving the tensors from known reflection and transmission coefficients – can be solved by trial and error, through the implementation of an evolutionary search algorithm.

If the tensors are assumed to be diagonal – which is reasonable given the geometry of the structure presented here – the retrieval can be done in two steps: first the components of the tensors which are parallel the substrate are retrieved from result computed for normal incidence, then the tensor components perpendicular to the substrate are retrieved from results computed for oblique incidence. It is one of the future directions of our work.

In the case where the tensors are not diagonal, a similar procedure can be applied, first by retrieving only the components related to the plane parallel to the substrate, and then by computing the remaining components using several different angles of incidence and several polarization. In this case, the retrieval of the optical parameters of the material can be seen as a constrained multi-objective optimization problem.

3. Summary and conclusions

The aim of the present work was to investigate the possibility to describe single metafilm layer behavior formed by an array of CWs as an effective medium. It has been shown that for the particular investigated geometry, when the electric field is oriented along the main MMs symmetry axis, the metafilm behavior is indeed analogous to that of a homogeneous layer. The thickness of this layer is that of the deposited metal. The validity of this conclusion was verified with respect to a number of criteria consistent with the Maxwell-Garnett effective medium model.

It was shown namely that outside the resonance region the magnetic permeability $\mu \approx 1$ and that in accordance with the M-G approximation the effective permittivity is proportional to the filling factor of the MMs. It was found that for small metal thickness and filling factors the metafilm optical length is proportional to the metal thickness. The linearity of the optical length with metal thickness turns to be greatly improved when considering tuned MMs having the same resonance frequency.

Finally, for the polarization perpendicular to the incidence plane the metafilm permittivity is independent of the incident angle.

The generalization of this approach to the case of in-plane polarization was considered, and a study of this case is soon to be submitted [21].

Acknowledgements

This work was supported by the French National Research Agency (ANR Metaphotonique, contract number 7452RA09) and the Champagne-Ardenne region.

References

[1] V. G. Veselago, "The electrodynamics of substances with simultaneously negative values of permittivity and permeability," *Sov. Phys. Usp*. 10, 504, 1968.

[2] J.B. Pendry, "Negative refraction makes a perfect lens," *Phys. Rev. Lett*. 85, 3966, 2000.

[3] X. Chen, T. M. Grzegorczyk, B. I. Wu, J. Pacheco, and J. A. Kong, "Robust method to retrieve the constitutive effective parameters of metamaterials," *Phys. Rev. E* 70, 016608, 2004.

[4] T. Driscoll, D. N. Basov, W. J. Padilla, J. J. Mock and D. R. Smith, "Electromagnetic characterization of planar metamaterials by oblique angle spectroscopic measurements," *Phys. Rev. B* 75, 115114, 2007.

[5] J. Zhou, T. Koschny, M. Kafesaki, and C. M. Soukoulis, "Negative refractive index response of weakly and strongly coupled optical metamaterials," *Phys. Rev. B* 80, 035109, 2009.

[6] C. Menzel, C. Rockstuhl, T. Paul, and F. Lederer, "Retrieving effective parameters for metamaterials at oblique incidence," *Phys. Rev. B* 77, 195328, 2008.

[7] C R Simovski, "On electromagnetic characterization and homogenization of nanostructured metamaterials," *J. Opt.* 13 013001 (2011).

[8] S. Zhang, W. Fan, N. C. Panoiu, K. J. Malloy, R. M. Osgood, and S. R. J. Brueck, *Phys. Rev. Lett*. 95, 137404, 2005.

[9] B. Kanté, A. de Lustrac, J.-M. Lourtioz , "Optical metafilms on a dielectric substrate," *Phys. Rev. B* 80, 205120 (2009).

[10] www.ansoft.com/products/hf/hfss/

[11] A. Taflove, S.C. Hagness. "*Computational electrodynamics: the finite-difference time domain method*". Artech House antennas and propagation library. Artech House, 2005.

[12] E. D. Palik, *Handbook of optical constants of solids* (Academic Press, New York, NY 1998).

[13] A. Lupu, N. Dubrovina, R. Ghasemi, A. Degiron, and A. de Lustrac, "Metal–dielectric metamaterials for guided wave silicon photonics," Opt. Express 19, 24746–24761, 2011.

[14] D. R. Smith, S. Schultz, P. Markos and C. M. Soukoulis, "Determination of effective permittivity and permeability of metamaterials from reflection and transmission coefficients," *Phys. Rev B 65*, 195104, 2002.

[15] T. Koschny, P. Markoš, D. R. Smith, and C. M. Soukoulis, "Resonant and antiresonant frequency dependence of the effective parameters of metamaterials," *Phys. Rev. E* 68, 065602(R), 2003.

[16] D. Sarid, "Long-range surface-plasma waves on very thin metal films," *Phys. Rev. Lett*. 47, 1927–1930, 1981.

[17] P. Berini, "Long-range surface plasmon-polaritons," *Adv. Opt. Photonics* 1, 484–588, 2009.

[18] D. Weber, P. Albella, P. Alonso-González, F. Neubrech, H. Gui, T. Nagao, R. Hillenbrand, J. Aizpurua, and A. Pucci, "Longitudinal and transverse coupling in infrared gold nanoantenna arrays: long range versus short range interaction regimes," *Opt. Express* 19, 15047-15061, 2011.

[19] C. Menzel, R. Singh, C. Rockstuhl, W. Zhang, and F. Lederer, "Effective properties of terahertz double split-ring resonators at oblique incidence," *J. Opt. Soc. Am. B* 26, B143-B147, 2009.

[20] D. W. Berreman. "Optics in stratified and anisotropic media: 4x4 – matrix formulation" *J. Opt. Soc. Am.* 62, 502-510, 1972.

[21] L. O. Le Cunff, N. Dubrovina, A. Vial, A. De Lustrac, A. Lupu, G. Lerondel, "3D modeling of metamaterials and anisotropic characterization" (to be submitted).

Surface polaritons at the interface between a metal and a layer of nanocrystal quantum dots

Yuliy V. Bludov*, Mikhail I. Vasilevskiy

Centro de Física, Universidade do Minho, Campus de Gualtar, Braga 4710-057, Portugal
*corresponding author, E-mail: bludov@fisica.uminho.pt

Abstract

Surface plasmon-polaritons (SPPs) in a multilayer structure consisting of a metallic film and one or more layers of nanocrystal (NC) quantum dots (QDs) are studied. It is shown that there is resonance coupling between the plasmon-polaritons propagating along the metal/NC-layer interface and excitons confined in the dots, which produces a considerable effect on the optical properties of the structure unless the dispersion of the QD size is too large. Using a transfer matrix formalism, multilayer structures consisting of NC composite and metallic films are considered and it is demonstrated that the coupling extends over several layers of different type. It can be explored in order to selectively excite QDs of different size by making a layer-by layer assembled NC planar structure and using an attenuated total reflection (ATR) configuration for the SPP-enhanced excitation of the dots. It opens the possibility to control the relative intensity of light of different color, emitted by the QDs of different size.

1. Introduction

Colloidal chemistry techniques have proved the ability to synthesize high quality nanocrystals (NCs) of II-VI semiconductors, possessing the properties of quantum dots (QDs). With these NCs, a broad variety of nanostructures can be prepared, including multilayer structures of QDs of different average size, deposited on different substrates [1]. Combining such structures with other materials, such as organic dielectrics [2] or graphene [3], can result in new interesting physics and applications related to the energy transfer from photoexcited NCs to these materials.

Recent experiments [4] demostrated the possibility of strong coupling between excitons confined in nanocrystal quantum dots (QDs) and surface plasmon-polaritons (SPPs) propagating along the interface of a silver film and the QD layer deposited on top of it. The observation was achieved by measuring attenuated total reflection (ATR) spectra of the structure. In this work we develop the theory of the observed effect taking into account the QD size dispersion. We will show that the resonance SPP coupling to excitons confined in QDs can be considerable unless the dispersion of the QD size is too large or the dots are too far from the metal/dielectric interface. The resonance coupling can be used for controllable pumping the dots in order to explore their uncomparable luminescence properties [1]. Based on the calculated results, we will discuss possible applications of ATR structures containing, beyond the silver film, several layers of NCs of different average size.

The paper is organized as follows. First, we introduce the complex dielectric function for a composite medium containing semiconductor NCs and exemplify it for the case of CdSe QDs embedded in PMMA. Next, we obtain and illustrate the SPP dispersion relations and, finally, present and discuss the calculated results for the reflectivity of ATR structures containing several QDs and metallic layers arranged in a number of different ways.

2. Dielectric function of a composite material containing quantum dots

A single QD can be described by a bare electronic susceptibility that takes into account inter-band transitions [1]:

$$\chi(\omega) = \frac{4\left|d_{cv}\right|^2}{3V}\sum_n\left[\frac{\left|\beta_n\right|^2}{E_n - i\Gamma - \hbar\omega} + \frac{\left|\beta_n\right|^2}{E_n - i\Gamma + \hbar\omega}\right], \tag{1}$$

where the sum runs over confined exciton states with energies E_i ($i = 0$ denotes exciton vacuum), d_{cv} is the transition dipole moment matrix element between valence and conduction bands of the underlying semiconductor material, V is the QD volume and

$$\beta_i = g_i \int_{QD} \Psi_{ex}^{(i)}\left(\mathbf{r},\mathbf{r}\right) d\mathbf{r}$$

with g_i and $\Psi_{ex}^{(i)}\left(\mathbf{r}_e,\mathbf{r}_h\right)$ denoting the degeneracy factor and the wavefunction of the corresponding exciton states.

The quantity

$$\epsilon_{QD}(\omega) = \epsilon_s^{\infty} + 4\pi\chi(\omega) \tag{2}$$

can be regarded as a QD dielectric function, where ϵ_s^{∞} is the high-frequency dielectric constant of the QD material. However, it can be more convenient to define the QD polarizability (assuming spherical shape of the dot),

$$\alpha(\omega) = \frac{\epsilon_{QD}(\omega) - \epsilon_h}{\epsilon_{QD}(\omega) + 2\epsilon_h} a^3\,, \tag{3}$$

where a is the QD radius and ϵ_h is the dielectric constant of the host material. Using these quantities (2), (3), one can

[1] It relates the QD polarization to the electric field inside the dot.

calculate an effective dielectric function, $\epsilon^\star$, of the composite material containing uniform size QDs embedded in the host matrix using one of the following schemes:

(i) Maxwell-Garnett approximation (MGA) valid in the low QD concentration limit [5],

$$\frac{\epsilon^\star - \epsilon_h}{\epsilon^\star + 2\epsilon_h} = \frac{4\pi}{3} N\alpha \,; \tag{4}$$

(ii) Bruggemann mean field approximation (BA) [6],

$$f\frac{\epsilon_{QD} - \epsilon^\star}{\epsilon_{QD} + 2\epsilon^\star} + (1-f)\frac{\epsilon_h - \epsilon^\star}{\epsilon_h + 2\epsilon^\star} = 0 \,, \tag{5}$$

where $f = \frac{4\pi}{3} N a^3$ is the volume fraction of QDs. BA is valid when $f \sim 0.5$. MGA can be extended up to $f \sim 0.1$ using a renormalized polarizability which takes into account dipole-dipole interactions between QDs as explained in Ref.[7].

The modified MGA (MMGA) proposed in Refs. [7, 8] allows for taking into account the QD radius dispersion. Let $F(a)$ denote the radius distribution function. The renormalized polarizability, $\alpha^\star$, can be calculated by the following equations,

$$\alpha^\star = \int \alpha(a') \frac{1 - \sqrt{1 - 4\Theta(a')}}{2\Theta(a')} F(a') da' \,; \tag{6}$$

$$\Theta(a') = \frac{8\pi}{3} N\alpha(a') \int \frac{\alpha(a)}{(a'+a)^3} F(a) da \tag{7}$$

where $\alpha(a)$ is the polarizability of a QD of radius a. For uniform-size QDs Eqs. (6) and (7) reduce to

$$\alpha^\star(a) = \frac{2a^3}{f\tilde{\alpha}} \left(1 - \sqrt{1 - f\tilde{\alpha}^2}\right)$$

where $\tilde{\alpha} = \alpha/a^3$. $\alpha^\star$ replaces α in Eq. (4) [notice that for small QD volume fraction f we get $\alpha^\star = \alpha$].

Using the mean-field idea of absence of scattering "'on average"' in a composite where its constituents are present in comparable fractions [9], we can generalize BA by taking into account the QD radius dispersion. Thus, we introduce the modified BA (MBA) for $\epsilon^\star$ through the following equation,

$$f \int \frac{\epsilon_{QD}(a',\omega) - \epsilon^\star}{\epsilon_{QD}(a',\omega) + 2\epsilon^\star} F(a') da' + (1-f)\frac{\epsilon_h - \epsilon^\star}{\epsilon_h + 2\epsilon^\star} = 0 \,. \tag{8}$$

3. The case of CdSe spherical QDs

Within the simplest model neglecting the Coulomb interaction between the electron and hole (strong confinement limit) and multiple sub-band structure of the valence band, the QD exciton spectrum is given by [10]

$$E_i = E_g + \frac{\hbar^2 \xi_i^2}{2\mu a^2} \tag{9}$$

where E_g is the band gap energy (=1.75 eV for CdSe), μ is the electron-hole reduced mass and $\xi_1 = \pi$, $\xi_2 \approx 4.49$, $\xi_3 \approx 5.76, \ldots$ are the roots of the spherical Bessel functions. Within this model, $\beta_i = 2$ for all $i \geq 1$. [2] The dipole moment matrix element can be expressed as

$$d_{cv} = \frac{e\hbar}{i m_0 E_g} p_{cv}$$

where m_0 is the free electron mass and $2p_{cv}^2/m_0 \approx$20 eV [12]. We take $\epsilon_h = 1.5$ for PMMA matrix and assume a Gaussian distribution of QD radius,

$$F(a) = \frac{1}{\sqrt{2\pi\Delta_a^2}} \exp\left[-\frac{(a-\bar{a})^2}{2\Delta_a^2}\right]$$

where the mean, $\bar{a}$, and the variance, Δ_a, describe QD's average radius and size dispersion, respectively. The real and imaginary parts of the effective dielectric function of the QD/PMMA composite calculated for $f = 0.1$ and 0.3 is shown in Fig. 1. A small imaginary part, $\Gamma = 1$ meV, was introduced in the denominators of Eq. (1).

As it can be seen from Fig. 1, the imaginary part of the effective dielectric function has a resonance at the exciton frequency, with the broadening depending on the QD concentration and size dispersion. The real part of $\epsilon^\star$ can reach negative values in the vicinity of the exciton frequency only for vanishing dispersion [Fig. 1(a)], while for larger dispersion it always remains positive [compare with Figs. 1(b) and 1(c)]. For higher f [Fig. 1(d)] the difference in the real part of $\varepsilon^\star$ in the vicinity of the resonance becomes more pronounced. At the same time, increasing the filling factor results in an increase and the proportional broadening of the peaks of the imaginary part of the effective dielectric function [compare Figs. 1(c) and 1(d)]. This is in qualitative agreement with the experimentally measured absorption spectra of dilute dispersions and close-packed films of nanocrystal QDs [13].

4. SPP's at metal/NC-layer interface

In order to demonstrate the involved physics, we shall first discuss the dispersion relation for surface plasmon-polaritons in a simplified structure. Let us consider an electromagneic wave in the vicinity of a plane interface between two semi-infinite media, a metal and a QD/dielectric composite, and assume that the wave is $p-$polarized. We choose x axis along the direction of propagation of the electromagnetic wave within the interface plane and z axis perpendicular to the interface. Assuming electromagnetic field's time and x-coordinate dependence to be of the form $\exp(ikx - i\omega t)$ (where k and ω are the wavenumber and frequency, respectively), we can write down the SPP dispersion relation in the form: [14]

$$\frac{\varepsilon_M(\omega)}{p_M} + \frac{\varepsilon^*(\omega)}{p^*} = 0, \tag{10}$$

[2] We use this model for the sake of simplicity. Generalization to the more realistic one [11, 12] taking into account complex valence band structure of the underlying material and fine structure of the confined hole states is straightforward.

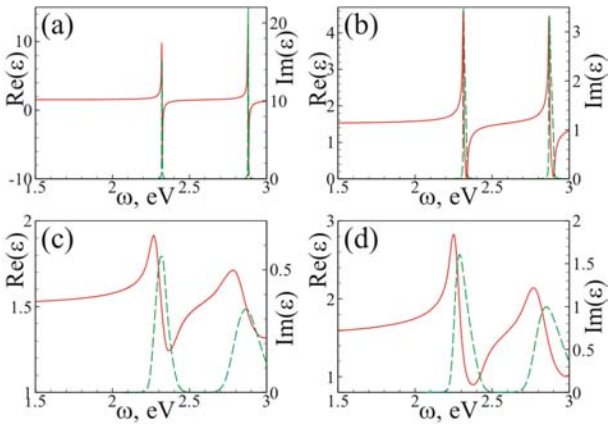

Figure 1: (color online) Real (solid lines) and imaginary (dashed lines) parts of the CdSe QD - PMMA composite dielectric function for average QD radius $\bar{a} = 3\,$nm, calculated using either MMGA with filling factor $f = 0.1$ and QD radius dispersion $\Delta_a = 0$ (panel a), $\Delta_a = 0.005\bar{a}$ (panel b), and $\Delta_a = 0.1\bar{a}$ (panel c), or MBA with filling factor $f = 0.3$ and QD radius dispersion $\Delta_a = 0.1\bar{a}$ (panel d).

where $p_M = \sqrt{k^2 - \kappa^2\varepsilon_M(\omega)}$, $p^* = \sqrt{k^2 - \kappa^2\varepsilon^*(\omega)}$, $\kappa = \omega/c$ and $\varepsilon_M(\omega)$ is the Drude-type dielectric function of the metal. Eq. (10) can be solved for the wavenumber k, yielding

$$k = \kappa \left(\frac{\varepsilon^*(\omega)\varepsilon_M(\omega)}{\varepsilon^*(\omega) + \varepsilon_M(\omega)} \right)^{1/2} . \qquad (11)$$

The amplitude of the electromagnetic wave decays exponentially at both sides of the interface, $\sim \exp(-p^* z)$ for $z > 0$ and $\sim \exp(p_M z)$ for $z < 0$.

The frequency dependence of the real and imaginary parts of k for an Ag/QD–PMMA interface is shown in Figs. 2(a), 2(c), 2(e) and 2(g). $\mathrm{Im}(k)$ increases drastically in the vicinity of QD exciton transition frequencies. It reflects the resonant coupling between SPPs and QD excitons. Again, the resonance peak broadens with the increase of the QD size dispersion [compare Figs.2(a), 2(c), 2(e)] because of the weaker coupling involving fewer QDs for each given ω. Notice that the strengthening and relative narrowing of the resonance peak can be achieved by increasing of filling factor f [compare Figs. 2(e) and 2(g)].

As known, SPPs can be probed in the ATR geometry schematically shown in Fig. 3. The system consists of a prism, an Ag film [3], and one or more layers of CdSe QD–PMMA composites. Qualitatively the mechanism of SPPs probing can be expressed in the following manner. The frequency and the x-projection of the wavevector of an external electromagnetic wave, connected by the relation known as "ATR scanline",

$$k_x = \frac{\omega}{c}\sqrt{\epsilon_g}\sin\theta\,. \qquad (12)$$

[3]For the dielectric function of silver we used the expression and parameters given in Ref. [15].

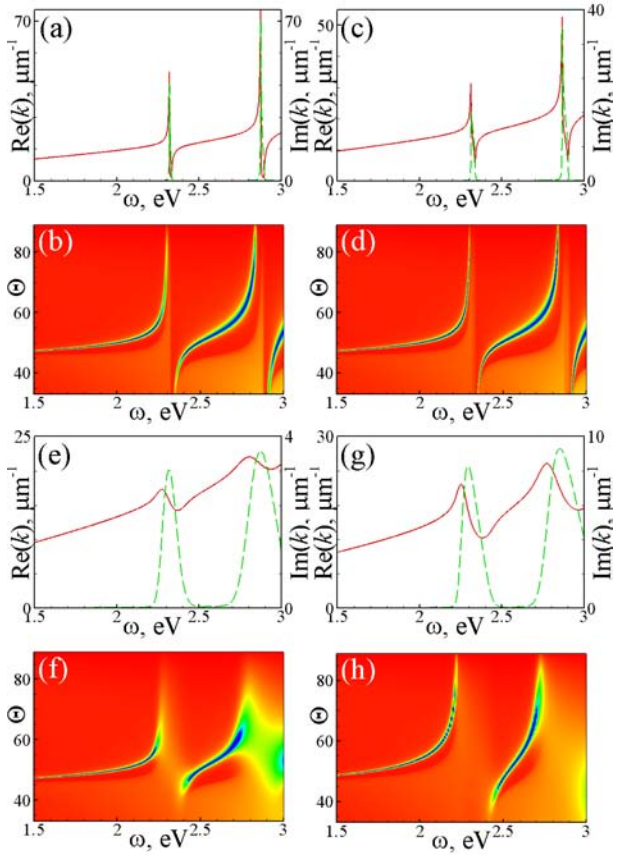

Figure 2: (color online) Panels **(a, c, e, g):** Real (solid lines) and imaginary (dashed lines) parts of the SPP wavevector versus frequency, calculated for the interface between semiinfinite CdSe QD - PMMA composite and silver; Panels **(b, d, f, h):** reflectivity R *versus* angle of incidence θ, and frequency ω for the ATR structure with a glass prism ($\varepsilon_g = 2.9584$), a silver film of thickness $d = 53.3\,$nm, and a semiinfinite composite medium. The composite dielectric function was calculated for average QD radius $\bar{a} = 3\,$nm using MMGA with filling factor $f = 0.1$, and $\Delta_a = 0$ (panels a, b), $\Delta_a = 0.005\bar{a}$ (panels c, d), and $\Delta_a = 0.1\bar{a}$ (panels e, f) or MBA with filling factor $f = 0.3$ and $\Delta_a = 0.1\bar{a}$ (panels g, h).

should match ω and $\mathrm{Re}(k)$ of the surface polaritons [**?**]. In Eq. (12) ϵ_g is the dielectric constant of the prism and θ is the angle of incidence. In other words, the ATR scanline should intersect the SPP dispersion curve given by Eq. (11) in the case of a single interface. The matching is achieved by adjusting ω and/or θ and is detected by measuring the reflectance, R, which shows characteristic dips corresponding to the resonance transfer of the electromagnetic energy into surface polaritons.

The reflectivity of the general structure consisting of N finite layers (each layer being characterized by a complex dielectric function $\varepsilon_n(\omega)$ and occupies the spatial domain $z_{n-1} < z < z_n$, $n = 1, 2, \ldots, N$), and cladded by two semiinfinte media (which occupy half-spaces $z <$

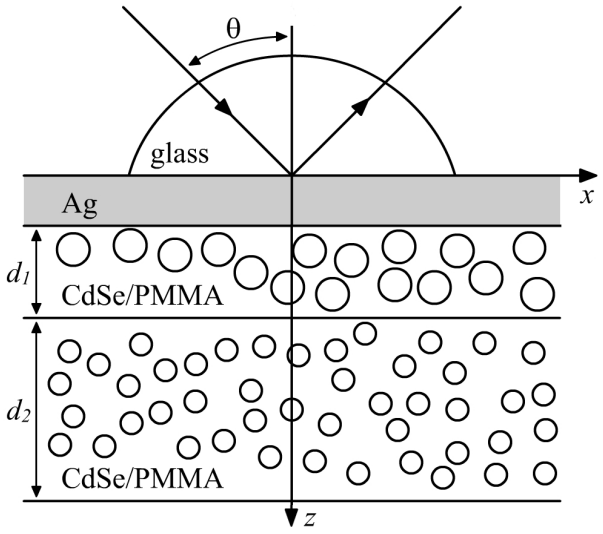

Figure 3: ATR structure composed of a glass prism, a silver plate, and two composite layers containing semiconductor NCs of different average size

$z_0 = 0$ and $z > z_N$ and have dielectric constants $\varepsilon_0(\omega)$ and $\varepsilon_{N+1}(\omega)$, respectively) can be obtained by transfer-matrix formalism and be represented as

$$r = -\frac{T_{12}}{T_{11}}, \tag{13}$$

where T_{11} and T_{12} are the elements of the transfer matrix $\hat{T} = \prod_{n=1}^{N} \hat{F}_n$. In its turn

$$\hat{F}_n = \begin{pmatrix} Q_n^{(+)} e^{\kappa q_n (z_n - z_{n-1})} & Q_n^{(-)} e^{-\kappa q_n (z_n - z_{n-1})} \\ Q_n^{(-)} e^{\kappa q_n (z_n - z_{n-1})} & Q_n^{(+)} e^{-\kappa q_n (z_n - z_{n-1})} \end{pmatrix} \tag{14}$$

is the transfer matrix of the n-th layer. In the relation (14)

$$Q_n^{(\pm)} = \frac{1}{2}\left[1 \pm \frac{\varepsilon_n(\omega) q_{n+1}}{\varepsilon_{n+1}(\omega) q_n}\right], \qquad q_n = \sqrt{(k_x/\kappa)^2 - \epsilon_n}.$$

The reflectivity $R = |r|^2$ of the structure depicted in Fig. 3 can be obtained from Eq.(13), putting $N = 4$, the interface coordinates are $z_0 = 0$, $z_1 = d$, $z_2 = d + d_1$, $z_3 = d + d_1 + d_2$, and the dielectric functions of the layers and cladding media are $\varepsilon_0 = \epsilon_g$, $\varepsilon_1 = \varepsilon_M$, $\varepsilon_2 = \varepsilon_1^*$, $\varepsilon_3 = \varepsilon_2^*$, and $\varepsilon_4 = 1$ ($\varepsilon_{1,2}^*$ denotes the dielectric function of the CdSe QD–PMMA composite with the QD mean size $a_{1,2}$).

The minima in the ATR spectra shown in Figs. 2(b), 2(d), 2(f), and 2(h) correspond to the intersections of the dispersion curves with the ATR scanline and resemble the structure of the corresponding $\mathrm{Re}(k)$ *versus* ω dependencies [Figs. 2(a), 2(c), 2(e), and 2(g)].

5. Results and discussion

Let us consider the structure of the SPP-exciton resonance in more detail. In the case of semiinfinite composite with

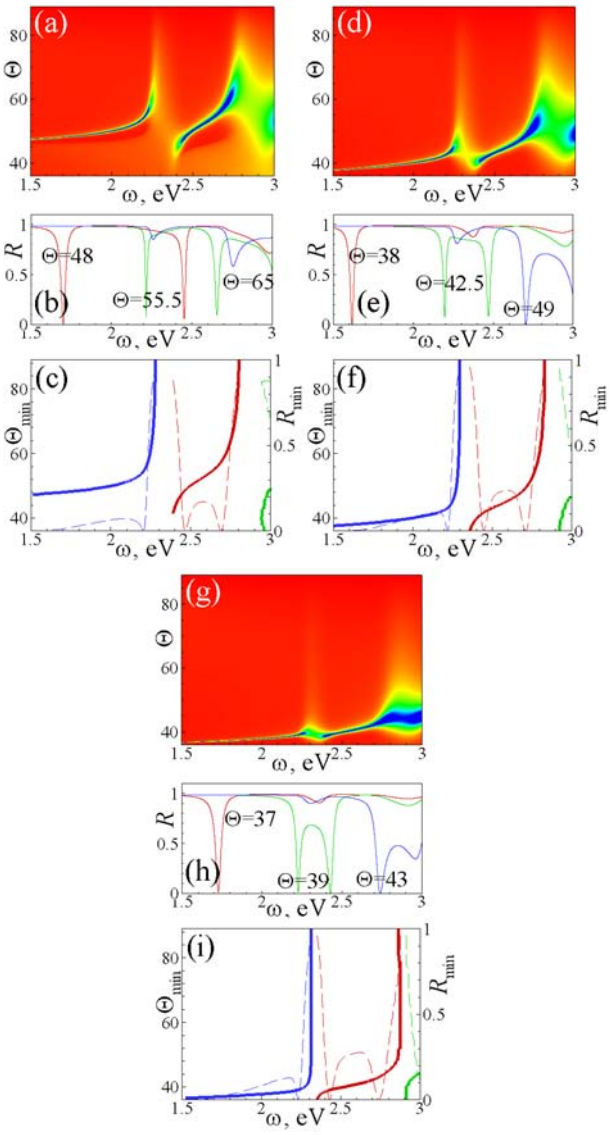

Figure 4: (color online) Reflectivity *versus* angle of incidence θ and frequency ω [panels **(a, d, g)**]; reflectivity *versus* frequency ω for a fixed θ [panels **(b, e, h)**]; minimal reflectivity R_{min} (dashed lines) and corresponding angle of incidence θ_{min} (solid lines) for a given ω [panels **(c, f, i)**] for the ATR structure with glass prism $\varepsilon_g = 2.9584$, silver film of thickness $d = 53.3$ nm, and CdSe QD–PMMA composite layer of different thickness: semiinfinite (a–c), $d_1 = 53.3$ nm (d–f) and $d_1 = 19.78$ nm (g–i). In the case of finite d_1, the medium at $z < -d_1$ is vacuum. The composite dielectric function was calculated using MMGA with $f = 0.1$, $\bar{a} = 3$ nm and $\Delta_a = 0.1\bar{a}$.

CdSe NCs [Figs. 4(a)–(c)] the resonant interaction of modes occurs at $\theta \approx 50^o$ for the chosen set of parameters. In the vicinity of this angle the dependence $R(\omega)$ exhibits *two* minima with approximately equal depth, while for other angles of incidence one of the minima is significantly deeper than the other [see Fig. 4(b)]. This is char-

acteristic of mode anticrossing and corresponds to the experimental observation of Ref. [4]. The positions of these minima (i.e., the angles of incidence, θ_{min}, at which the reflectance reaches its minimum, R_{min}, for a given frequency) are depicted in Fig. 4(c), where one can clearly see the resonant SPP-exciton interaction, or mode anticrossing. At the same time, the depth of the resonant minima of $R_{min}(\omega)$ at the corresponding angles θ_{min} demonstrates that there are at least three points ($\omega \approx 2.2\,$eV, $\omega \approx 2.47\,$eV, $\omega \approx 2.7\,$eV) where the reflectivity of the ATR structure reaches zero, $R_{min} = 0$.

How does the CdSe QD–PMMA layer thickness influence the ATR spectrum? First, the ATR resonance minima are shifted to lower angles of incidence [compare Figs. 4(a) and 4(d)]. Secondly, the anticrossing of modes becomes weaker as manifested by the smaller separation of the reflectance minima in Fig. 4(e) for $\theta \approx 42.5^o$, as well as in Fig. 4(f)]. Thirdly, the values of R_{min} far from the exciton resonance frequency are higher than in the case of semi-infinite composite medium. Further decrease of the CdSe QD–PMMA layer thickness [Figs. 4 (g)–(i)] leads to the damping of the SPP-exciton interaction. For example, in the case of Fig. 4(g) the resonance is hardly distinguishable (it is confirmed also by Fig. 4(i) where the positions of resonant minima are shown explicitly). The change in the reflectivity spectrum when the angle θ is tuned into resonance, shown in Fig. 4(i), can be compared to the experimental data of Ref. [4] showing a good agrement with Fig. 3 of that article.

Now let us turn to the structures with the same silver film and *two* composite layers, one of thickness d_1 containing QDs of average radius a_1 and the other (semi-infinite) with QDs of radius a_2 (Fig. 3 with $d_2 \to \infty$). In the ATR spectrum of this structure [Figs. 5(a), 5(d)], one can observe resonances corresponding to both a_1 [$\omega \approx 2.12\,$eV, $\omega \approx 2.5\,$eV and $\omega \approx 2.95\,$eV in Figs. 5(a), 5(d)] and a_2 QDs [$\omega \approx 2.3\,$eV and $\omega \approx 2.85\,$eV in Figs. 5 (a), 5(d)]. Increasing d_1 results in a stronger anticrossing between the SPP and the a_1 QD exciton modes, and in a weakening of the a_2 resonance [compare Figs. 5(a) and 5(d)]. Nevertheless, choosing an appropriate composite layer thickness, one can achieve SPP coupling to QD excitons localized in the composite layer which is not adjacent to the metallic film.

ATR minima correspond to some particular values of ω and θ for which the energy of the incident electromagnetic wave is most efficiently transferred to SPP and, consequently, to the QD excitons. This is shown in Figs. 5(b),(c),(e) and (f), where the squared average amplitude of the electric field is plotted for each of the CdSe QD–PMMA layers. It represents the intensity of excitation of QD luminescence, whose characteristic colour is determined by the QD size. Therefore one can adjust the relative intensity of light of different colours emitted by two or more composite layers containing QDs of different average radii. It opens the possibility of building a lighting device based on a planar strucrure of multiple NC layers, similar to that presented in Ref. [16], with colour characteristics which can be controlled either by the excitation frequency or by the ATR incidence angle.

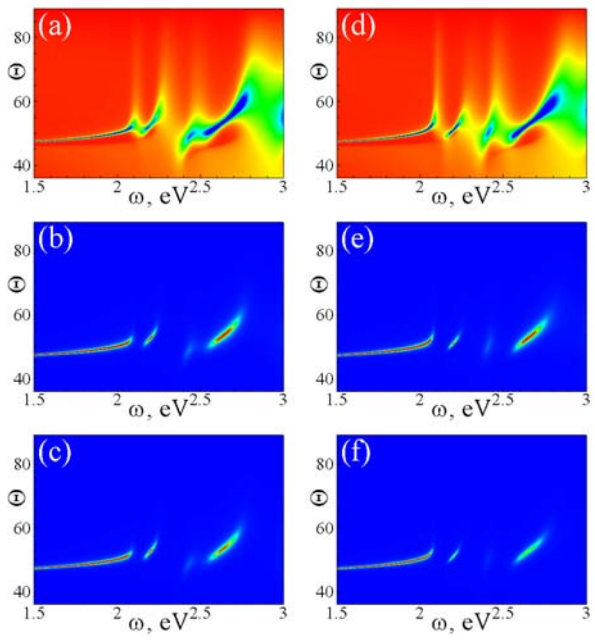

Figure 5: (color online) Reflectivity (a, d), and relative electric field square amplitude $|E_x(z)/E_i|^2$ at $z = d$ (b, e) and $z = d+d_1$ (c, f) *versus* angle of incidence and frequency for the ATR structure consisting of glass prism $\varepsilon_g = 2.9584$, Ag film of thickness $d = 53.3\,$nm and two CdSe QD–PMMA composite layers, one of thickness $d_1 = 19.78$ nm (a–c) or $d_1 = 53.3\,$nm (d–e) and average QD radius $a_1 = 3.7\,$nm, and the other semi-infinite, with average QD radius $a_2 = 3\,$nm. The dielectric functions for both composite layers were calculated using MMGA with $f = 0.1$ and QD radius dispersion $\Delta_a = 0.1\bar{a}$ in all cases.

Finally, we considered several other types of potentially interesting sandwich-type structures containing two [Fig. 6(a)], or three [Fig. 6(b)] interfaces between silver and CdSe QD–PMMA composite. For the structures of Fig. 6, the calculated reflectivity spectra contain two or three minima (at different θ for a given frequency), respectively. In these plots one can observe a rather sophisticated "bunching" of modes in the vicinity of the excitonic resonance.

6. Conclusion

In summary, we have shown that the resonance coupling between the plasmon-polaritons propagating along the metal/NC-layer interface and excitons confined in chemically synthesized semiconductor NCs, experimentally observed in Ref. [4], can be nicely described theoretically using the appropriate effective dielectric function for the NC composite layer and standard multilayer optics. The SPP-exciton interaction produces a considerable effect on the optical properties of the structure if the dispersion of the

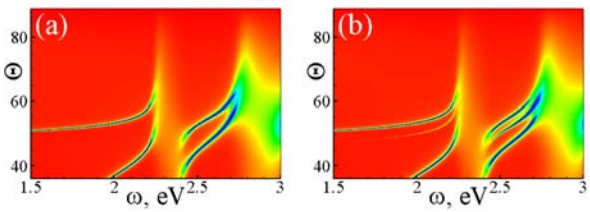

Figure 6: (color online) Panels (a, b): Reflectivity *versus* angle of incidence and frequency for the ATR structure consisting of glass prism, one silver film of thickness $d = 53.3$ nm, one CdSe QD–PMMA composite layer with average QD radius $a_1 = 3$ nm and thickness $d^* = 300$ nm, and a semiinfinite silver layer (a) or a second silver film of thickness $d_M = 69.23$ nm and a semi-infinite CdSe QD–PMMA composite with average QD radius a_1 (b).

NC size in the composite layer is not too large. In particular, it can be used for obtaining the metal-enhanced fluorescence of QDs[17]. Moreover, we have shown that combining several composite layers with appropriately sized quantum dots and/or more than one metallic films can result in interesting interactions between the various SPP and exciton modes. Owing to these interactions, the energy of an incident electromagnetic wave can be distributed, by means of surface plasmons, between the different QD species, as it has been suggested for molecules adsorbed on a metallic surface [18]. It can provide the possibility to control the relative intensity of light of different colors, emitted by the QDs of different sizes layer-by-layer assembled into a planar structure.

Acknowledgement

The work was supported by the FCT (Portugal) under the grant PTDC/FIS/113199/2009.

References

[1] A. L. Rogach (ed.), *Semiconductor Nanocrystal Quantum Dots*, Springer-Verlag, Wien, 2008.

[2] D. M. Basko, V. M. Agranovich, F. Bassani, G. C. La Rocca, Energy transfer from a semiconductor quantum dot to an organic matrix, *Eur. Phys. J. B* 13: 653–659, 2000.

[3] Zheyuan Chen, S. Berciaud, C. Nuckolls, T. F. Heinz, L. E. Brus, Energy Transfer from Individual Semiconductor Nanocrystals to Graphene, *ACS Nano* 4: 2964–2964, 2010.

[4] D. E. Gomez, R. C. Vernon, P. Mulvaney, T. J. Davis, Surface plasmon mediated strong exciton-photon coupling in semiconductor nanocrystals, *Nano Lett.* 10: 274–278, 2010.

[5] J. C. Maxwell–Garnett, Colours in Metal Glasses and in Metallic Films, *Philos. Trans. R. Soc. London* 203: 385–420, 1904.

[6] D. A. G. Bruggeman, Berechnung verschiedener physikalischer Konstanten von heterogenen Substanzen, *Ann. Physik (Leipzig)* 24: 636–679, 1935.

[7] M. I. Vasilevskiy and E. V. Anda, Effective dielectric response of semiconductor composites, *Phys. Rev. B* 54: 5844-5851, 1996.

[8] M. I. Vasilevskiy, Effective Dielectric Response of Composites Containing Uniaxial Inclusions, *phys. stat. sol. (b)* 219: 197–204, 2000.

[9] R. Landauer, Electrical Conductivity In Inhomogeneous Media, *AIP Proc.* 40: 2–45, 1978.

[10] L. E. Brus, Electronelectron and electron-hole interactions in small semiconductor crystallites: The size dependence of the lowest excited electronic state, *J. Chem. Phys.* 80: 4403–4409 (1984).

[11] P. C. Sercel and K. J. Vahala, Analytical formalism for determining quantum-wire and quantum-dot band structure in the multiband envelope-function approximation, *Phys. Rev. B* 42: 3690–3710 (1990).

[12] Al. L. Efros, Luminescence polarization of CdSe microcrystals, *Phys. Rev. B* 46: 7448–7458, 1992; Al. L. Efros, M. Rosen, M. Kuno, M. Nirmal, D. J. Norris, and M. Bawendi, Band-edge exciton in quantum dots of semiconductors with a degenerate valence band: Dark and bright exciton states, *Phys. Rev. B* 54: 4843–4856, 1996.

[13] C. A. Leatherdale and M. Bawendi, Observation of solvatochromism in CdSe colloidal quantum dots, *Phys. Rev. B* 63: 165315, 2001.

[14] H. Raether, *Surface Plasmons on Smooth and Rough Surfaces and on Gratings*, Springer-Verlag, Berlin, 1988.

[15] P. B. Johnson and R. W. Christy, Optical Constants of the Noble Metals, *Phys. Rev. B* 6: 4370–4379, 1972.

[16] T. Franzl, T. A. Klar, S. Scheitinger, A. L. Rogach, and J. Feldmann, Exciton Recycling in Graded Gap Nanocrystal Structures, *Nano Lett.* 4: 1599–1603, 2004.

[17] P. P. Pompa, L. Martiradonna, A. Della Torre, F. Della Sala, L. Manna, M. De Vittorio, F. Calabi, R. Cingolani, R. Rinaldi, Metal-enhanced fluorescence of colloidal nanocrystals with nanoscale control, *Nature Nanotechnology* 1: 126–130, 2006).

[18] G. P. Weiderrecht, J. E. Hall, and A. Boutheiler, Control of Molecular Energy Redistribution Pathways via Surface Plasmon Gating, *Phys. Rev. Lett.* 98: 083001, 2007.

Ultrasmall plasmonic cavity for refractive index sensor

Soon-Hong Kwon[1], Hong-Gyu Park[2]

[1] -A 1 -
[2]Department of Physics, Korea University, Seoul 136-701, Korea*corresponding author, E-mail: soonhong.kwon@gmail.com

Abstract

We propose an ultrasmall plasmonic cavity for refractive index sensor based on channel-waveguides of different widths. Plasmonic mode-gap due to cutoff frequency enables strong optical confinement in a subwavelength volume and also suppression of radiation loss. Because of strong field overlap of the SPP mode with environmental material and small cavity size, the proposed plasmonic cavity is an ideal building block for sensitive refractive index sensor. Large sensitivity (S = 1130 nm/RIU) and the figure of merit (FOM = 270) are achieved in the small cavity size (600 nm × 800 nm × 1400 nm). This open-type channel-waveguide plasmonic cavity can open up broad range of applications including biochemical sensing and strong light-matter interactions.

1. Introduction

In the biochemical sensors, the resonant frequency shift induced by the change of the index of refraction is used to analyze samples. Owing to the compactness of the microcavities, the sensors have been realized by using various structures such as photonic crystal cavities [1,2], microdisks [3], and microrings [4]. However, dielectric cavities such as photonic crystal cavities face a limit of sensitivity since part of electric field of cavity mode always exist in the dielectric material as well as in environmental material to be analyzed. Compared with such dielectric cavity, surface-plasmon polariton (SPP) has large amount of energy in the environmental material and can be sensitive to small refractive index change.

In this paper, we demonstrate a heterostructure plasmonic cavity consisting of two different width channel waveguides for an ultrasmall and sensitive refractive index sensor. SPP mode-gap mechanism [5-7] based on width-modulation and metallic wall mirrors suppresses the optical scattering loss and enables strong confinement of the cavity mode with resonant wavelength of 1495 nm in the tiny cavity region of 600 nm × 800 nm × 1400 nm. Owing to strong field overlapping with the environmental material, the large wavelength shift per refractive index unit, S, of 1130 nm/RIU is calculated over broad range of refractive index change. Relatively large Q factor (360) and S of the plasmonic cavity gives relatively large FOM of 270

2. Results and discussion

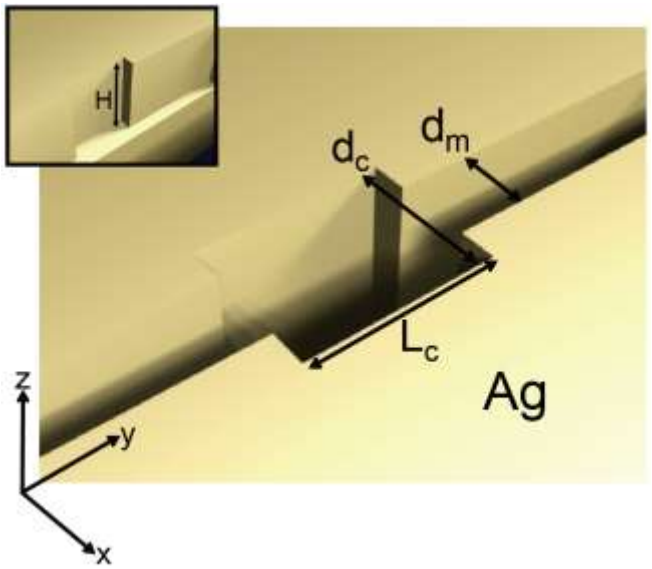

Figure 1: Schematic diagram of the proposed SPP heterostructure channel waveguide cavity. SPP mode is confined in the cavity region (width, d_c, length, L_c) sandwiched by two mirror waveguides with width of d_m. Inset shows the cross-section along the y-direction, indicating the depth of the channel waveguide as H

We propose the plasmonic cavity based on the channel waveguides of different widths where an air slot with a rectangular cross-section is formed in the metal layer [5-7]. The heterostructure cavity is consisting of the cavity region of the wide (width d_c) waveguide and two mirror regions of the narrow (width d_m) waveguides, as shown in Fig. 1. The narrow channel waveguides at both sides of the cavity region (length, L_c) prevent the propagation of SPP modes in the y-direction. The depth of both channel waveguides is indicated by H in the inset of Fig. 1. Here, silver is assumed because of low absorption loss.

In order to apply as refractive index sensor, the transmission signal of the cavity resonant mode can be measured using this cavity structure by connecting input/output waveguides into the mirror regions. Hence, broad band light source or tunable laser would efficiently excite SPPs from the input waveguide and deliver resonance information into the output waveguide. We

assume that the air slot is filled by the liquid to be analyzed. The propose plasmonic cavity can be easily fabricated by stripping technique using template structure [8,9]. Depositing metal carefully on the template structure with smooth surface and stripping off the deposited metal structure can guarantee the sub-nanometer roughness of the plasmonic cavity, which can be applied to construct the proposed cavity to minimize the scattering loss from the metal roughness.

To understand quantitatively how SPPs are confined in this structure, the dispersion curves of the SPP mode excited in the channel waveguides are calculated by the 3D finite-difference time-domain (FDTD) simulation. The waveguide is assumed as an infinitely long silver-air channel waveguide of width d (inset of Fig. 2). Two values of d (300 nm and 600 nm) were used, where 300 nm and 600 nm corresponds to the width of the mirror (d_m) and cavity (d_c) waveguides, respectively. The refractive index of the liquid filled inside air slot was set to 1.318, the index of the water at telecommunication wavelength. The silver is described by the Drude model: $\varepsilon(\omega) = \varepsilon_\infty - \omega_p^2 / (\omega^2 + i\gamma\omega)$. Here, the background dielectric constant, ε_∞; the plasma frequency, ω_p; and the collision frequency, γ, at room temperature were set to 3.1, 1.4×10^{16} s^{-1}, and 3.1×10^{13} s^{-1}, respectively, by fitting the experimentally determined dielectric function of silver [5-7,10].

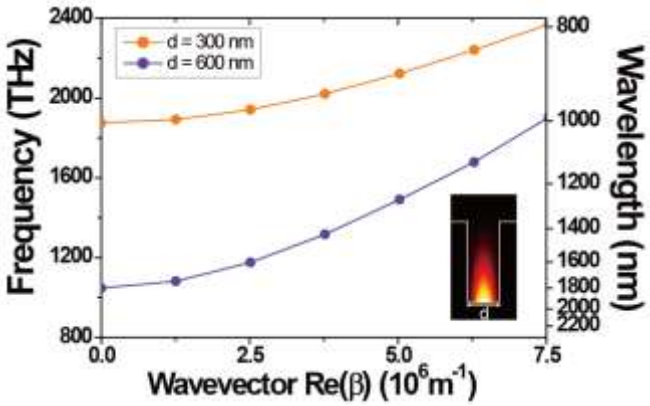

Figure 2: Dispersion curves of the SPP modes for waveguides of different widths, 600 nm (blue) and 300 nm (orange). The inset shows the electric field intensity profile of the SPP waveguide mode.

The SPP waveguide mode which is strongly confined at the bottom silver surface can be excited in the simulation, as shown in the inset of Fig. 2.) In the plasmonic waveguide with metallic wall localizing the SPP mode, the cutoff frequency at zero wavevector appears due to the finite waveguide width. The cutoff frequency decreases with increasing the waveguide width d as SPP mode with longer wavelength can be allowed [5-7]. For the waveguide with d = 600 nm, corresponding to the cavity region, the cutoff frequency is 1050 THz (1796 nm) smaller than that when d = 300 nm, 1881 THz (1005 nm). In this channel waveguide, it is possible that only SPP mode with higher frequency (shorter wavelength) than the cutoff frequency is transmitted through the waveguide. Therefore, varying waveguide width can allow or forbidden the transmission of the SPP mode with certain wavelength. For example, when the frequency of the mode is existing in the region from 1050 and 1881 THz, between the cutoff frequencies of two waveguides with d = 600 nm and d= 300 nm, the SPP mode excited in the wider waveguide cannot propagate into the narrower waveguide. Hence, the narrower waveguide can be considered as a mirror for the SPP waveguide mode with the frequency in the mode-gap, which corresponds to the range between the cutoff frequencies.

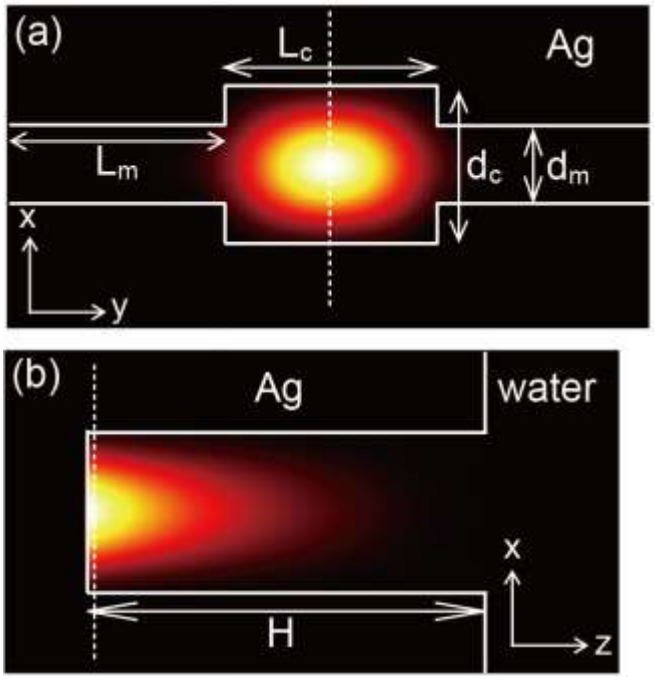

Figure 3: The electric field intensity mode profiles of the SPP cavity mode obtained at the (a) top and (b) side cross-sections. The top (side) view is obtained at the white dotted surface marked in the side (top) view.

Using this mode-gap mirror, a channel waveguide heterostructure SPP cavity can be constructed, comprising a wider waveguide with finite length between two narrower waveguides like the schematic diagram in Fig. 1 [6]. We investigated the confinement of the SPP cavity mode in such a cavity through 3D FDTD (see Fig. 3). The dimensions of the cavity region (wider waveguide) are assumed d_c = 600 nm and L_c = 800 nm. The mirror regions (narrower waveguide) are defined by d_m = 300 nm and L_m = 1000 nm. The depth, H, of the waveguide is set to 1400 nm. In order to maintain strong confinement of the SPP mode, Lm and H were set large enough.

In this plasmonic cavity, the SPP cavity mode with a 1495 nm (1261 THz) could be found inside the cavity region (600 nm × 800 nm). It is shown that the SPP mode excited in this cavity structure is strongly confined at the bottom surface (silver/water interface) of the channel waveguide through the electric field intensity profiles in Figs. 3(a) and (b). As expected in the property of the mode-gap in Fig. 2, the SPP cavity mode is confined between two mirror waveguide along the y-axis by the mode-gap (1050 – 1881THz). In addition, metallic walls also confine the

cavity mode along x-axis. It should be noted that the electric field of the proposed cavity mode is mostly placed in the water and hence it is expected that the change of the refractive index in the water can affect the properties of the cavity mode seriously.

Among two losses, metallic absorption loss and scattering loss, in the plasmonic cavity, scattering loss into the free space near the interfaces between cavity and mirror waveguides, which is dominant optical loss factor in two-dimensional photonic crystal cavities [11], is negligible in this cavity even though the cavity structure changes abruptly. Because the dominant electric field of the SPP modes is directed normal to the silver surface, the scattered lights tends to radiate through the surface which can be suppressed by the mode-gap mirrors and metallic wall mirrors. Indeed, the ultra-high optical Q factor of 2.3×10^5 was estimated by neglecting metallic absorption (the damping constant, γ, to zero) [5,8]. It means that the proposed plasmonic cavity is designed to minimize the optical loss which deteriorates the transmission signal of the cavity resonance. On the other hand, since the metallic absorption loss increases with increasing temperature and becomes dominant loss [5,8], the Q factor of the SPP cavity is obtained 360 at room temperature.

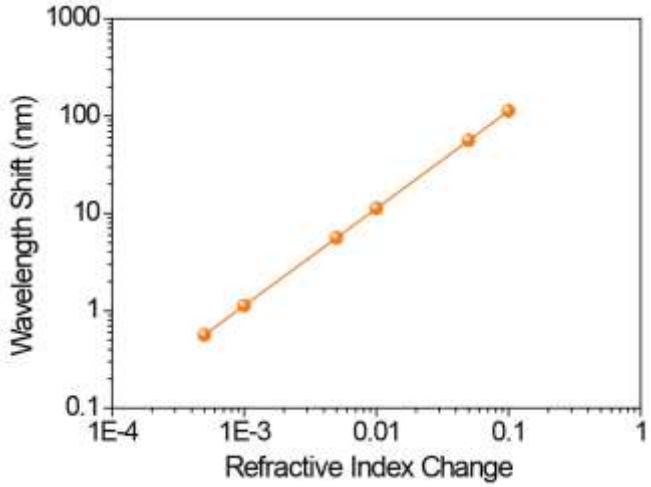

Figure 4: Resonant wavelength shift versus refractive index change of the environmental material. Sensitivity (slope of the graph) is estimated as 1130.

In order to investigate the sensitivity, S, of the proposed cavity to the refractive index change of the water, the resonant wavelength is calculated as the index increases from the index of the water (1.318). Here, S is defined as the wavelength shifts per the refractive index unit (RIU) [1,12]. The amount of the wavelength shift at different index change is shown in Fig. 4. The response of the resonant wavelength shift indicates excellent linearity over the broad range of index change from 5×10^{-4} to 1.0×10^{-1}. The estimated sensitivity is S = 1130 nm/RIU. This is 3 times larger than photonic crystal cavity made of low index material, and is about 6 times larger than ring resonator [12,13]. The figure of merit (FOM = SQ/λ = 270) is order of magnitude larger than pervious surface plasmon sensors [12,14]. The required volume of the sample material to be analyzed can be estimated by the dimension of the cavity region, 600 nm × 800 nm × 1400 nm, which is only 0.7 fL.

3. Conclusions

In this paper, we demonstrate an ultrasmall plasmonic channel waveguide cavity for refractive index sensor, where the cavity mode with telecommunication wavelength at 1495 nm can be confined in the smaller cavity waveguide sandwiched by two larger mirror waveguides. The mode-gap mechanism and metallic wall confines the cavity mode in a sub-micrometer cavity region. By suppressing scattering loss, the proposed cavity has high optical Q of 2.3×10^5, resulting that optical loss of the cavity becomes negligible. Only metallic absorption loss, which is inherently unavoidable, has to be considered and concludes the Q factor of the cavity as 360 at room temperature. The Q factor corresponding to the full-width half-maximum linewidth of 4.1 nm in the cavity resonance. The field profile of the cavity mode shows strong field overlapping in the environmental material. Therefore, the strong wavelength shift per refractive index unit, S, of 1130 nm/RIU is obtained and also relatively large FOM of 270 is estimated. This high sensitivity of the propose cavity and the small amount of the required sample (0.7 fL) would suggest one of best candidates for ultrasmall surface plasmonic index sensors.

On the other hand, the proposed simple mode-gap mechanism achieving strong 3D subwavelength optical confinement and good cavity feedback can be applied to the design of the plasmonic cavity for the strong light-matter interactions of very small physical size. Especially, the accessibility to the cavity surface in this open-type channel waveguide can open possibilities to manipulate the positioning the quantum emitters, e.g. NV centers or colloidal quantum dots, at the electric field maximum of the cavity region

Acknowledgements

This research was supported by the Basic Science Research Program through the National Research Foundation of Korea (NRF) funded by the Ministry of Education, Science and Technology (Grant No. 2011-0014026).

References

[1] S.-H. Kwon, T. Suenner, M. Kamp, and A. Forchel, Optimization of photonic crystal cavity for chemical sensing, *Opt. Express* 16: 11709-11717, 2008.

[2] T. Suenner, T. Stichel, S.-H. Kwon, T. W. Schlereth, S. Hoefling, M. Kamp, and A. Forchel, Photonic crystal cavity based gas sensor, *Appl. Phys. Lett*. 92: 261112-1-261112-3, 2008.

[3] A. M. Armani and K. J. Vahala, Heavy water detection using ultra-high-Q microcavities, *Opt. Lett*. 31: 1896-1898, 2006.

[4] J. T. Robinson, L. Chen, and M. Lipson, On-chip gas detection in silicon optical microcavities, *Opt. Express* 16: 4296-4301, 2008.

[5] M.-K. Seo, S.-H. Kwon, H.-S. Ee, and H.-G. Park, Full three-dimensional subwavelength high-Q surface-plasmon-polariton cavity, *Nano Lett*. 9: 4078-4082, 2009.

[6] J.-H. Kang, H.-G. Park, and S.-H. Kwon, Room-temperature high-Q channel-waveguide surface plasmon nanocavity, *Opt. Express* 19: 13892-13898, 2011.

[7] J.-H. Kang, Y.-S. No, S.-H. Kwon, H.-G. Park, Ultra-small subwavelength nanorod plasmonic cavity, *Opt. Lett.* 36: 2011-2013, 2011.

[8] S.-H. Kwon, J.-H. Kang, C. Seassal, S.-K. Kim, P. Regreny, Y.-H. Lee, C. M. Lieber, and H.-G. Park, Subwavelength plasmonic lasing from a semiconductor nanodisk with silver nanopan cavity, *Nano Lett*. 10: 3679-3683, 2010.

[9] P. Nagpal, N. C. Lindquist, S.-H. Oh, and D. J. Norris, Ultrasmooth patterned metals for plasmonics and metamaterials, *Science* 325: 594-597, 2009.

[10] P. B. Johnson and R. W. Christy, Optical-constants of noble-metals, *Phys. Rev. B* 6: 4370-4379, 1972.

[11] B. S. Song, S. Noda, T. Asano, and Y. Akahane, Ultra-high-Q photonic double-heterostructure nanocavity, *Nat. Mater*. 4: 207-210, 2005.

[12] Q. Quan, I. B. Burgess, S. K. Y. Tang, D. L. Floyd, and M. Loncar, High-Q, low index-contrast polymeric photonic crystal nanobeam cavities, *Opt. Express* 19: 22191-22197, 2011.

[13] I. M. White and X. Fan, On the performance quantification of resonant refractive index sensors, O*pt. Express* 16: 1020-1028, 2008.

[14] J. N. Anker, W. P. Hall, O. Lyandres, N. C. Shah, J. Zhao and R. P. Van Duyne, Biosensing with plasmonic nanosensors *Nat. Mater*. 7: 442-453, 2008.

Power flow in the interior and exterior of cylindrical coated nano-particles

Samel Arslanagić

Department of Electrical Engineering, Electromagnetic Systems,
Technical University of Denmark, Denmark
E-mail: sar@elektro.dtu.dk

Abstract

Electrically small configurations consisting of resonant active coated nano-particles of a circularly cylindrical shape are considered in the case of a magnetic line source excitation at optical frequencies. The active particles are comprised of a canonical gain-impregnated silica nano-core covered concentrically with a silver, gold, or copper nano-shell. Particular attention is devoted to both the direction and the magnitude of the power flow density inside and outside of such particles. The results for the active coated nano-particles are related to those of the corresponding passive designs at optical frequencies, and are further contrasted to the results for the electrically small structures based on epsilon-negative materials at radio frequencies.

1. Introduction

Numerous potential applications exploiting metamaterials (MTMs), as well as plasmonic materials, have been proposed [1, 2], with particular attention devoted to sub-wavelength MTM-based [3]-[5] and plasmonic-based [6]-[10] particles. The gain inclusion in the active designs was found to lead to the so-called super-resonant states, which for a plane wave incidence resulted in scattering cross-sections vastly surpassing values predicted by the geometrical size of the CNPs [6], [10]. Similarly, enormously large radiated powers were obtained in the case of localized excitation sources [8], [9]. These are all desirable features which make the plasmonic-based CNPs attractive candidates for nano-sensing, -lasing and -amplifying applications; see e.g., a recent review [11] and the works references therein for an excellent overview of applications and potentials of plasmonic-based devices.

To better understand the interaction between the localized sources and plasmonic-based particles, and their overall radiation process, the present work investigates the power flow associated with various types of circularly cylindrical active coated nano-particles (CNPs) excited by a magnetic line source (MLS) at optical frequencies. Specifically, the active particles are comprised of a gain-impregnated silica nano-core covered concentrically with a silver, gold, or copper nano-shell where the size-dependency of the permittivity of this nano-shell is taken into account. The gain model for the active CNPs is a canonical, constant frequency, gain model. The previously reported super-resonant states of the proposed active CNPs in [9], and the associated large levels of the radiated power, are correlated with the correspondingly large localizations of the power density near specific parts of the shell-interfaces and its corresponding large magnitude inside the gain region. The resulting interactions with the gain material lead to a strong and distinct dipolar power radiation in all of these electrically small, active super-resonant CNP designs. These active CNP power flow results are compared to those obtained for the corresponding passive structures at optical frequencies, and are further contrasted to epsilon-negative (ENG) sub-wavelength resonator designs at radio frequencies. The latter sheds further light on important differences between the optical and radio frequency cases. We note that interesting power flow results were reported in [5] for MTM-based cylindrical configurations for a finite radius line source excitation, as well as in [10] for active, and [11], [12] for passive nano-particles of spherical shape, against which the present findings for the cylindrical active CNPs will be displayed. Throughout the work, the time factor $\exp(j\omega t)$, with ω being the angular frequency, and t being the time, is assumed and suppressed.

2. Configuration and methods of analysis

We consider the CNP configuration depicted in Figure 1; it consists of an infinite circular cylindrical nano-core (Region 1) covered concentrically with an infinite cylindrical nano-shell (Region 2). The inner and outer radii of the nano-shell are denoted by ρ_1 and ρ_2, respectively, and the CNP is imbedded in free-space (region 3) with the permittivity, ε_0, permeability, μ_0, and wave number $k_0 = \omega\sqrt{\varepsilon_0\mu_0} = 2\pi/\lambda$, with λ being the free-space wavelength. The CNP is illuminated by the field provided by an arbitrarily located and infinitely long magnetic line source (MLS) possessing a constant magnetic current I_m [V/m]. The nano-core and nano-shell regions of the CNP may, in general, contain an arbitrary simple, lossy and dispersive material. However, for the present purposes, specific materials are chosen for these two regions, as explained later in Section 3 of this manuscript.

A circular cylindrical coordinate system (ρ,ϕ,z) and an associated rectangular coordinate system (x,y,z) are introduced such that their origins coincide with the cross-sectional center of the CNP, and such that the entire CNP-MLS configuration is infinite in the z-direction, with the MLS being parallel to the axis of the cylinders. The coordinates of the observation point are (ρ,ϕ), while those of the MLS are (ρ_s,ϕ_s).

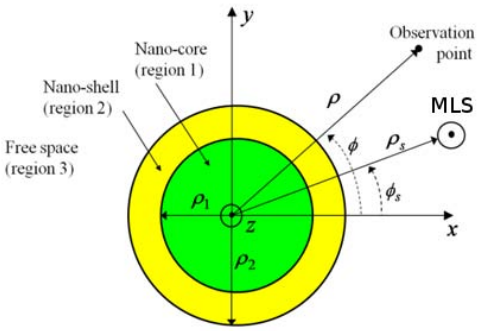

Figure 1: The MLS-excited CNP.

The analytical solution for the problem in Figure 1 has been derived in [4], and only its main features will be outlined in here. For the MLS excitation case, the magnetic field in all regions (incident and scattered fields in the region containing the MLS, and total fields in the remaining regions) contains only a z-component, i.e., $\boldsymbol{H}=\hat{z}H_z$, while the electric field in all regions has the form of $\boldsymbol{E}=\hat{\rho}E_\rho+\hat{\phi}E_\phi$, where E_ρ and E_ϕ are its ρ - and ϕ -components. The unknown field components are expanded in cylindrical wave functions, and thus contain a number of unknown expansion coefficients. The latter follow in a straightforward manner from the application of the electromagnetic boundary conditions at the two interfaces of the CNP. These field solutions were used in [4] to perform an extensive study of electrically small passive MTM-based particles of cylindrical shape. To account for the near- and far-field properties of a number of cylindrical active plasmonic-based CNP configurations, the necessary gain levels for the so-called super-resonant state were determined recently [9]. To further address the intriguing electromagnetic properties of these particles, the field solutions from [4] are presently used to explore the flow of electromagnetic power inside and outside the CNP. This is done in terms of the Poynting vector $\boldsymbol{S}$, which is given by

$$\boldsymbol{S}=(1/2)\,\mathrm{Re}\{\boldsymbol{E}\times\boldsymbol{H}^*\}=\hat{x}S_x+\hat{y}S_y$$

$$=\hat{x}\left[S_\rho\cos\phi-S_\phi\sin\phi\right]+\hat{y}\left[S_\rho\sin\phi+S_\phi\cos\phi\right], \qquad (1)$$

where S_x and S_y are the x- and y-components of $\boldsymbol{S}$, while $S_\rho=\mathrm{Re}\{E_\phi H_z^*\}/2$ and $S_\phi=-\mathrm{Re}\{E_\rho H_z^*\}/2$ are its ρ - and ϕ -components. The asterix * designates complex conjugation. In Section 3, attention will be devoted to both the amplitude and the direction of the Poynting vector determined with (1).

3. Results and discussions

As reported in [6], [8]-[10], highly resonant sub-wavelength CNPs can be designed by including gain in their interiors, e.g., their nano-cores. As to the cylindrical CNPs considered in [9], the nano-core was in all cases made of silica, had a radius of 24 nm, and was coated with a 6 nm thick plasmonic (silver, gold, or copper) nano-shell. The permittivity of the silica nano-core was expressed as $\varepsilon_1=(n^2-\kappa^2-2jn\kappa)\varepsilon_0$ and was comprised of two contributions: a contribution from its refractive index in the considered frequency region ($n=\sqrt{2.05}$) and a contribution from the canonical gain model. The parameter κ (termed the optical loss or gain constant) determines the nature of the nano-core: lossless (and passive) for $\kappa=0$, lossy and passive for $\kappa>0$ (optical loss constant) and active for $\kappa<0$ (optical gain constant). As to the plasmonic nano-shell permittivity, its empirical values, which account for its size-dependence and were used successfully in [6], were employed. In particular, for the silver-based CNP configuration excited by a MLS, the so-called super-resonant state, with a large total radiated power, was identified for $\kappa=-0.175$ and the free-space excitation wavelength $\lambda=577.70$ nm [9]. This total radiated power enhancement is shown in Figure 2 in terms of the normalized radiation resistance (NRR) as a function of the wavelength when the MLS is located at 12 nm along the positive x-axis and has the current amplitude: $I_m=1$ [V/m].

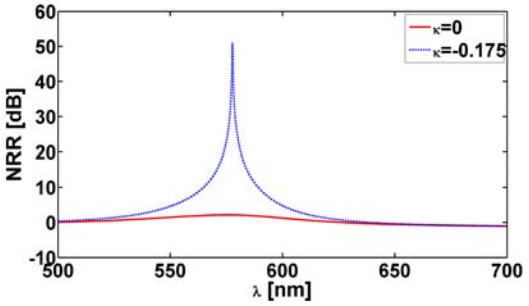

Figure 1: The NRR of a silver-based passive and super-resonant active CNP.

Note that the NRR equals the total power radiated by the MLS in the presence of the CNP normalized with the power radiated by the MLS alone in free-space. As can be seen in the figure, a peak value of the NRR ≈ 51dB is found for the super-resonant active CNP at 577.70 nm. This should be compared to a NRR of around 2 dB for the corresponding lossless and passive CNP ($\kappa=0$), which also is included in the figure. As explained in [9] in terms of the near-field distributions of the magnetic field, the super-resonance behavior reported in Figure 2 for the active silver-based CNP is due to a strong excitation of the resonant dipole

mode inside the CNP. The existence of the resonant dipole mode inside an electrically small CNP (diameter size of approximately $\lambda/10$) is a result of juxtaposing of two materials, one with positive permittivity (silica nano-core) and the other with a negative permittivity (silver nano-shell) [1]. The strong excitation of this dipole mode is heavily assisted by the gain-impregnation of the silica-nano core; its presence overcomes the plasmonic material losses [6].

The super-resonant state of the active Ag-based CNP is next illustrated in Figure 3a). The magnitude (color) and direction (arrows) of the Poynting vector (1) is shown when the MLS is located at 12 nm along the positive *x*-axis.

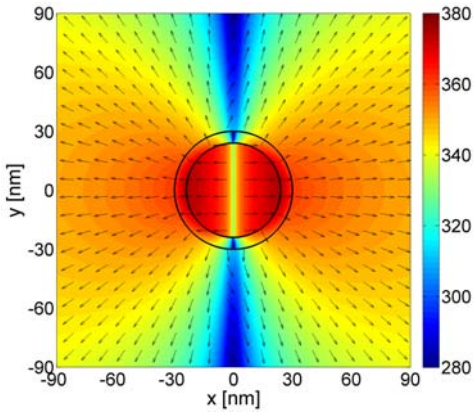

(a)

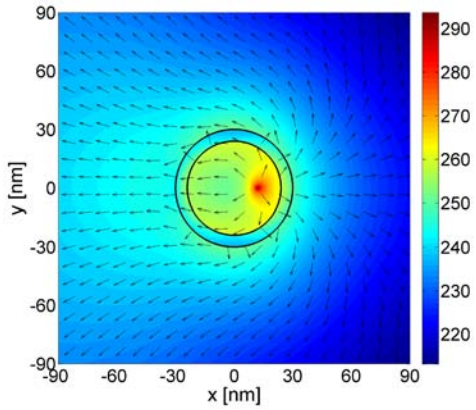

(b)

Figure 3: The magnitude (color) and direction (arrows) of the power flow density for the super-resonant active Ag-based CNP (a) and for the corresponding passive Ag-based CNP (b). In both cases, the radius of the silica nano-core is 24 nm, the thickness of the plasmonic nano-shell is 6 nm, and the MLS is located at 12 nm along the positive *x*-axis. Note that the dynamic range in (a) is larger than that in (b). The curves representing the cylindrical surfaces of the CNP are included in the figure.

A very clear and strong dipolar pattern, as though it is being produced by a dipolar source of radiation centered at the origin of the CNP, is observed in this figure. The power density is rather strong and homogeneous in strength and direction inside the CNP. It is mainly directed along the negative and positive *x*-direction in the left and right halves, respectively, of the nano-core. This is particularly true near the inner surface of the nano-shell, where one witnesses a profound localization of the power density within the CNP. The interaction of the large fields in the electrically small resonant CNP with the canonical gain inside the nano-core leads to a clear and strong dipolar radiated power pattern. This radiated power behavior is illustrated with by an outward-propagating Poynting vector from the surface of the CNP in Figure 3a). While the magnitude of the Poynting vector suggests the pattern is symmetric, its direction reveals a slight asymmetry which is attributed to the off-set MLS location in this case. In contrast to the super-resonant Ag-based CNP results, Figure 3b) shows the magnitude and the direction of the corresponding passive Ag-based CNP. No excitation of a resonant dipole mode is in evidence; this is consistent with the very low radiated power levels observed, e.g., in Figure 2.

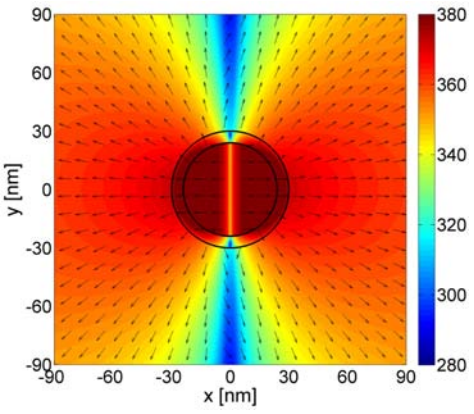

(a)

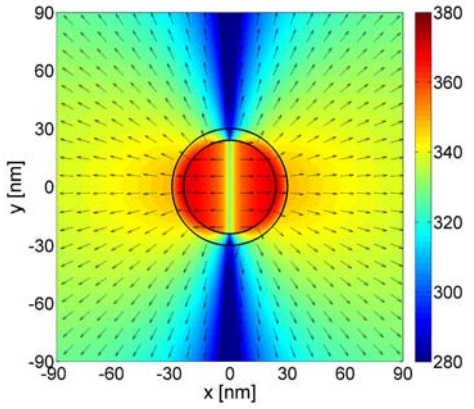

(b)

Figure 4: The magnitude (color) and direction (arrows) of the power flow density for the super-resonant active Au-based CNP (a) and Cu-based CNP (b). In both cases, the radius of the silica nano-core is 24 nm, the thickness of the plasmonic nano-shell is 6 nm, and the MLS is located at 12 nm along the positive *x*-axis. The curves representing the cylindrical surfaces of the CNP are included in the figure.

Besides the Ag-based CNP configuration considered above,

the corresponding super-resonant CNPs with their nano-shell composed of either gold or copper have also been studied [9]. For the Au-based CNP, the super-resonance was identified for $\kappa = -0.262$ and $\lambda = 669.39$ nm, with a resulting NRR ≈ 56dB. For the Cu-based CNP, it was identified for $\kappa = -0.310$ and $\lambda = 662.19$ nm, with a resulting NRR ≈ 46dB. The behavior of the latter two CNPs with the MLS located at 12 nm along the positive *x*-axis is illustrated further with the power flow density results reported for the Au-based CNP in Figure 4a) and for the Cu-based CNP in Figure 4b). Again, the power flow clearly has a dipolar form. However, its magnitude for the Au-based CNP surpasses the values for the other two CNPs given in Figures 3a) and 4b). Because it has the highest losses, the corresponding value for the super-resonant Cu-based CNP is the lowest of all of the super-resonant cases. The large levels of the power flow density for the Au-based CNP correspond to a strong localization of the power density within the CNP, which in turn leads to the largest NRR values of the three super-resonant CNP cases. The relatively low levels for the Cu-based CNP are perfectly in line with the correspondingly lowest NRR values.

We note that for all super-resonant CNPs cases considered above, the power flow has also been observed in an extended range up to 200 nm in both the *x*- and *y*-directions. Throughout such a range, a clear dipolar pattern, suggesting an outwardly propagating power flow density away from the CNP, was observed. Moreover, power flow results were obtained for super-resonant CNPs ($\kappa = -0.175$) for wavelengths shorter ($\lambda = 567.70$) and longer ($\lambda = 587.70$) than the super-resonant state wavelength ($\lambda = 577.70$). Although they are not included here, these results still show dipolar patterns with an outwardly propagating power flow density similar to those found in Figures 3a) and 4, but with a lower strength. Thus, contrary to power flows for active [10] and passive [13] nano-particles of spherical shape, which were found to exhibit specific vortices near their plasmon resonances, this is not the case for the (infinite and, hence, effectively two-dimensional) active *super-resonant* CNPs of cylindrical shape investigated here.

The above results for the electrically small super-resonant cylindrical CNPs, which employ the naturally occurring ENG-based metals at optical frequencies, are next contrasted to the analogous electrically small structures at radio frequencies which must utilize ENG metamaterials. To this end, Figure 5a) shows the NRR as a function of frequency, *f*, for a resonant sub-wavelength ENG shell with an inner radius of 6 mm and an outer radius of 10.03 mm. The ENG shell is modeled by a lossless Drude dispersion model [1] adjusted to select the relative permittivity of the shell to be -3.0 at the design frequency of 300 MHz (giving the diameter of the particle to be $\lambda/50$). The so-selected geometrical and electrical parameters of the shell are in compliance with the well-known resonance conditions in electrically small structures of cylindrical shape [3], [4]. Figure 5a), which was obtained when the MLS was located along the *x*-axis at 3mm, shows a resonance phenomenon with the NRR ≈ 17 dB at 300 MHz. The associated power flow density (magnitude and direction) is depicted in Figure 5b). It is found to differ significantly from any of the super-resonant active CNP cases. In this case, the power flow lines are seen to exhibit an interesting behavior, including vortices, at the three "deep-blue" spots – one to the left of the particle and two inside the shell-region. In fact, the power flow *outside* of the resonant ENG-based particle resembles the one for the lossless and passive CNP in Figure 3b), rather than that of the super-resonant active CNP. In the latter, the significantly smaller physical size of the particle, as well as the gain inclusion, are the driving factors behind the clear and strong outward power flow and the dipolar shape of the response.

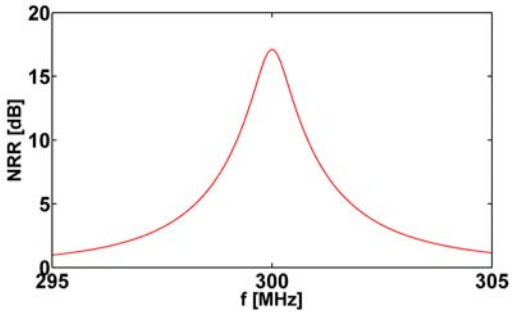

(a)

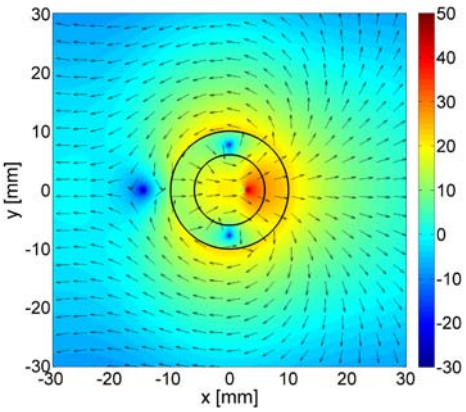

(b)

Figure 5: (a) The NRR as a function of frequency, *f*, for an ENG shell. (b) The magnitude (color) and direction (arrows) of the power flow density for the resonant ENG-shell at 300 MHz. In (a) and (b), the MLS is at 3 mm along the positive *x*-axis. Note that the curves representing the cylindrical surfaces of the ENG shell are also included in (b).

4. Summary and conclusions

The power flow density (magnitude and direction) in the interior and exterior of electrically small configurations consisting of resonant active coated nano-particles (CNPs) of a circularly cylindrical shape was examined. The source of excitation was taken to be an infinitely long magnetic line source (MLS) at optical frequencies. The active particles were comprised of a canonical gain-impregnated silica nano-

core covered concentrically with a silver, gold, or copper nano-shell. The previously reported super-resonant states, excited in silver-, gold-, and copper-based CNPs and leading to large powers extracted from the MLS for a given value of the current along it, were confirmed with the power flow density results. For all cases, the power density was found to be rather strong and homogeneous in strength and direction inside the CNP; this being particularly so near the inner surface of the nano-shell, where a profound localization of the power density within the CNP was observed. The interaction of such large fields with the canonical gain inside the nano-core was found to lead to a clear and strong dipolar power pattern, with an outwardly propagating power flow density. These effects were found to be most notable for the gold-based CNP, as it is the least lossy case of all at the resonance wavelength. Moreover, no peculiar behavior in terms of certain vortices was found for the cylindrical *active* and s*uper-resonant* active CNPs at specific wavelengths that are shorter or longer than the resonant wavelength, this appearing in contrast to the observations for spherical particles [10], [13]. The results for the active CNPs at optical frequencies were furthermore contrasted to those obtained at radio frequencies for the corresponding epsilon-negative based particles. The latter resulted in power flow behavior significantly different from any of the super-resonant active optical CNP cases. In fact, the power flow lines in the radio frequency case were found to exhibit an interesting behavior including vortices at specific locations in the interior and exterior of the particle.

References

[1] N. Engheta, and R. W. Ziolkowski, *Metamaterials-Physics and Engineering Applications*, John Wiley & Sons, New York, 2006.

[2] W. Cai, and V. Shalaev, *Optical Metamaterials*, Springer, Berlin, 2010.

[3] A. Alú, and N. Engheta, "Polarizabilities and effective parameters for collections of spherical nano-particles of concentric double-negative (DNG), single-negative (SNG) and/or double-positive (DPS) metamaterial layers," *J. Appl. Phys*., vol. 97, 094 310, May 2005.

[4] S. Arslanagić, R. W. Ziolkowski, and O. Breinbjerg, "Analytical and numerical investigation of the radiation and scattering from concentric metamaterial cylinders excited by an electric line source," *Radio Sci*., vol. 42, RS6S15, doi: 10.1029/2007RS 003644, Nov. 2007.

[5] S. Arslanagić, N. C. J. Clausen, R. R. Pedersen, and O. Breinbjerg, "Properties of sub-wavlength resonances in metamaterial cylinders," *NATO Advanced Research Workshop – Metamaterials for Secure Information and Communication Technologies*, Marokko, 2008.

[6] J. A. Gordon, and R. W. Ziolkowski, "The design and simulated performance of a coated nano-particle laser," *Opt. Exp*., vol. 15, issue 5, pp. 2622-2653, March 2007.

[7] A. Alú, and N. Engheta, "Plasmonic and metamaterial cloaking: physical mechanisms and potentials," *J. Opt. A: Pure Appl. Opt*., 10, 2008, doi: 10.1088/1464-4258/10/9/093002.

[8] S. Arslanagić, and R. W. Ziolkowski, "Active coated nano-particle excited by an arbitrarily located electric Hertzian dipole – resonance and transparency effects," *J. Opt.,* Vol. 12, 024014, 2010.

[9] S. Arslanagić, Liu, Y., Malureanu, R., and R. W. Ziolkowski, "Impact of the excitation source and plasmonic material on cylindrical active coated nano-particles," *Sensors*, Vol. 11, 9109-9120, 2011.

[10] S. D. Campbell, and R. W. Ziolkowski, "Impact of strong localization of the incident power flow density on the nano-amplifier characteristics of active coated nano-particles," *Opt. Commun.*, In Press, Available online 19 November 2011.

[11] N. J. Halas, "Plasmonics: an emerging field fostered by *Nano Letters*," *Nano Lett*., 10, pp. 3816-3822, doi: 10.1021/nl1032342, 2010.

[12] Z. B. Wang, B. S. Luk'yanchuk, M. H. Hong, Y. Lin, and T.C. Chong, "Energy flow around a small particle investigated by classical Mie theory," *Phys. Rev. B*, 70,035418, 2004.

[13] M. V. Bashevoy, V. A. Fedotov, and N. I. Zheludev, "Optical whirlpool on an absorbing metallic nanoparticle," *Opt. Exp*., vol. 13, no. 21, pp. 8372-8379.

Directive properties of active coated nano-particles

Samel Arslanagić[1*], and Richard W. Ziolkowski[2]

[1]Department of Electrical Engineering, Electromagnetic Systems,
Technical University of Denmark, Denmark
[2]Department of Electrical and Computer Engineering, University of Arizona, USA
*corresponding author, E-mail: sar@elektro.dtu.dk

Abstract

The directivities of the fields radiated by a variety of cylindrical and spherical active coated nano-particles, which are excited by their respective sources of illumination at optical frequencies, are investigated. Particular attention is devoted to the influence of the source location and optical gain constant on the directivities. While significant variations in the directivities are realized in the cylindrical cases for different source locations within and slightly outside the nano-particles and values of the optical gain constant, the corresponding spherical cases exhibit negligible differences.

1. Introduction

The performance of electrically small antennas (ESAs) is constrained by certain conventional limitations. For instance, if not matched properly, they are very inefficient radiators of electromagnetic energy, due to their intrinsic non-resonant nature, with accompanying low directivities [1]. While a variety of traditional matching techniques exist, the recent advent in metamaterial (MTM) research has, among other things, fostered truly novel means of matching ESAs [2]. In particular, the use of double-negative (DNG), epsilon-negative (ENG), and/or mu-negative (MNG) MTMs was found to lead to interesting and highly resonant properties in sub-wavelength configurations when properly combined with ordinary double-positive (DPS) materials [2]-[5]. These resonances were exploited in [6] and [7], where efficient MTM-based ESAs were proposed, and in [8] where MTM-inspired electrically small near-field parasitic resonators were used as impedance transformers to realize matching of the overall antenna system to its source and to the wave impedance of the medium in which it radiates. While the above works focused on radio and microwave frequencies, similar highly resonant properties, for potential use in nano-sensing, -amplifying and -antenna applications, were reported for passive plasmonic-based configurations at optical frequencies, see e.g., [9], [10] and the works referenced therein, as well as *active* plasmonic-based configurations, see e.g., [11] and the works referenced therein, as well as [12] and [13]. In particular, interesting enhancements of directivity patterns for higher order mode sub-wavelength radiators made of DPS materials in conjunction with passive MTMs or plasmonic materials, were reported in [10], this providing an alternate route towards sub-wavelength radiators with high directivities.

The present work examines the directivity properties of nano-antennas consisting of active coated nano-particles (CNPs) of cylindrical and spherical shape excited by their respective sources of illumination at optical frequencies. For spherical CNPs, the source of excitation is an electric Hertzian dipole, which is taken to be normal as well as tangential to surfaces of the CNP, while for cylindrical CNPs, the source of excitation is an infinitely long magnetic line source (MLS). The CNPs emphasized inhere are all made of a silica nano-core and are layered with a concentric silver nano-shell; however, other variations in the materials of the CNP can be easily accounted for. The gain is introduced inside the dielectric part of the CNP, i.e., the nano-core, via the so-called canonical, constant frequency, gain model. This work constitutes an extension of [12] and [13] where detailed near-field studies have revealed super-resonant properties of the examined active CNPs despite their very small electrical sizes. Particular attention is devoted to the influence of the source location and the optical gain constant on the resulting directivity patterns. In the cylindrical case, it is shown how the directivity of a super-resonant CNP can be re-shaped by either changing the location of the MLS or adjusting the value of the optical gain constant. As to the spherical CNPs, the resulting directivity patterns are shown to be unaffected by the presence of the CNP - even in its super-resonant state for which large amounts of the radiated power are extracted from the source – and they largely correspond to the pattern of an isolated dipole. Thus, as in the passive spherical case [10], the dipolar resonance excited inside the examined active spherical CNPs does not modify the directivity pattern of the exciting Hertzian dipole, but rather enhances its total radiated power.

This paper is organized as follows. Section 2 presents the configurations to be discussed, while the methods of their analysis and the associated analytical results are summarized in Section 3. The numerical results are presented in Section 4, and the entire work is summarized and concluded in Section 5. Throughout the work, the time factor $\exp(j\omega t)$, with ω being the angular frequency, and t being the time, is assumed and suppressed.

2. Configurations

We consider both cylindrical (Figure 1a)) and spherical (Figure 1b)) CNPs.

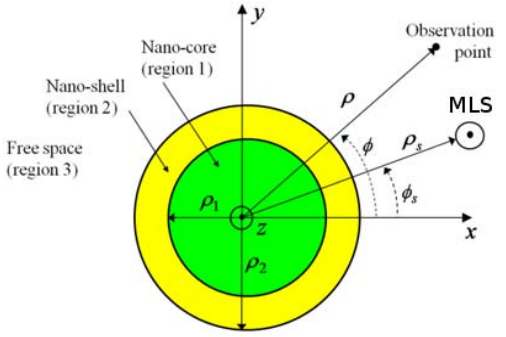

(a)

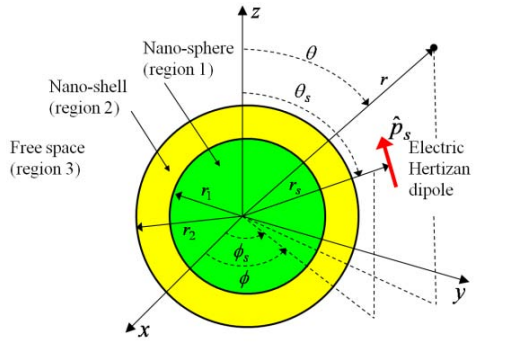

(b)

Figure 1: The cylindrical (a), and spherical (b) CNP configurations.

In both cases, they are comprised of a dielectric nano-core covered concentrically with a plasmonic nano-shell, and are immersed in free-space, which has the permittivity, ε_0, permeability, μ_0, and thus the intrinsic impedance $\eta_0 = \sqrt{\mu_0 / \varepsilon_0}$ and wave number $k_0 = \omega\sqrt{\varepsilon_0\mu_0} = 2\pi / \lambda$, where λ denotes the free-space wavelength.

For the cylindrical CNP, the inner and outer radii of the nano-shell are denoted by ρ_1 and ρ_2, respectively. The CNP is illuminated by the field generated by an arbitrarily located infinitely long magnetic line source (MLS) possessing a constant magnetic current I_m [V/m]. A circular cylindrical coordinate system, with the coordinates (ρ, ϕ, z) and an associated rectangular coordinate system (x, y, z) are introduced such that their origins coincide with the cross-sectional center of the CNP. Furthermore, the entire CNP-MLS configuration is infinite in the *z*-direction, with the MLS being parallel to the axis of the cylinders. The coordinates of the observation point are (ρ, ϕ), and those of the MLS are (ρ_s, ϕ_s).

For the spherical CNP, the inner and outer radii of the nano-shell are denoted by r_1 and r_2, respectively. The CNP is illuminated by the field generated by an arbitrarily oriented and located electric Hertzian dipole (EHD) with the dipole moment $\vec{p} = \hat{p}_s p_s$, where $\hat{p}_s$ is its orientation and p_s [Am] is its complex amplitude. A spherical coordinate system (r, θ, ϕ) and the associated rectangular coordinate system (x, y, z) are introduced such that the origin of these coincide with the center of the CNP. The coordinates of the observation point are (r, θ, ϕ), and those of the EHD are (r_s, θ_s, ϕ_s).

3. Analytical results

The analytical solutions for the problems shown in Figure 1 have been derived in [4] and [5], and are used here to study the directivity of these configurations.

For the cylindrical CNP configurations, the solution procedure is as follows. The field due to the MLS, which constitutes the known incident field, is expanded in terms of cylindrical wave functions. This is likewise the case with the unknown scattered fields due to the CNP in the three regions. The fields due to the CNP involve the unknown expansion coefficients $C_{i,n}$, where $i = 1$ for the field in region 1, $i = 2$ and 3 for the field in region 2, and $i = 4$ for the field in region 3, and where the symbol n is the mode number ($n = 0$ is the monopole mode in the expansion, $n = 1$ is the dipole mode, etc. for the other modes). The unknown expansion coefficients depend on the location of the MLS and are obtained by enforcing the boundary conditions at the two cylindrical interfaces, $\rho = \rho_1$ and $\rho = \rho_2$. With the exact field solutions at hand, the directivity, *D*, defined as the ratio of the radiation intensity to the total average power per unit angle, can be expressed as [4]

$$D(\phi) = \frac{2 \cdot \left| \sum_{n=0}^{N_{\max}} \tau_n j^n \alpha_n \cos[n(\phi - \phi_s)] \right|^2}{\sum_{n=0}^{N_{\max}} \tau_n^2 (3 - \tau_n) |\alpha_n|^2}, \qquad (1)$$

where $\alpha_n = C_{4,n}$ for the MLS inside the CNP, and $\alpha_n = J_n(k_0\rho_s) + C_{4,n}$ for the MLS outside the CNP. In these results, the function $J_n(\cdot)$ is the Bessel function of order n, τ_n is the Neumann number ($\tau_n = 1$ for the $n = 0$ mode and $\tau_n = 2$ otherwise), while $N_{\max}$ is the truncation limit in the implementation of the exact infinite summation chosen to ensure the convergence of the expansion in (1). The expression in (1) was used to study the directivity properties of sub-wavelength passive MTM-based particles in [4], and of super-resonant active CNPs in [13] for a variety of MLS locations.

For the spherical CNP configuration, the solution procedure is as follows. The field due to the EHD, which

constitutes the known incident field, is expanded in terms of transverse magnetic (TM) and transverse electric (TE) spherical waves with the known expansion coefficients $a_{nm}^{(c)}$ (TM coefficients), and $b_{nm}^{(c)}$, (TE coefficients), where the index c denotes the region in which the field is determined. The unknown scattered fields due to the CNP in the three regions are likewise expanded in terms of TM and TE spherical waves; these expansions involve the unknown TM and TE expansion coefficients denoted by $A_{i,nm}$ and $B_{i,nm}$, respectively, where $i=1$ for the field in region 1, $i=2$ and 3 for the field in region 2, and $i=4$ for the field in region 3. These expansion coefficients depend on the EHD location and orientation, and are easily obtained by enforcing the boundary conditions on the two spherical interfaces, $r=r_1$ and $r=r_2$. The general field solutions have been obtained in [5] and are specialized here for the far-field observation points in order to derive an expression for the directivity of the configuration in Figure 2b). In particular, the directivity takes on the form,

$$D(\theta,\phi)=\frac{2\pi}{\eta_0}\frac{1}{P_t}\left(\left|F_{t,\theta}\right|^2+\left|F_{t,\phi}\right|^2\right), \tag{2}$$

where

$$F_{t,\theta}= \sum_{n=1}^{N_{\max}}\sum_{m=-n}^{n} j^{n-1}e^{jm\phi}\times \left[\frac{1}{\omega\varepsilon_0}\alpha_{nm}\frac{d}{d\theta}P_n^{|m|}(\cos\theta)+\beta_{nm}\frac{1}{k_0}\frac{jm}{\sin\theta}P_n^{|m|}(\cos\theta)\right], \tag{3a}$$

and

$$F_{t,\phi}= \sum_{n=1}^{N_{\max}}\sum_{m=-n}^{n} j^{n-1}e^{jm\phi}\times \left[\frac{1}{\omega\varepsilon_0}\alpha_{nm}\frac{jm}{\sin\theta}P_n^{|m|}(\cos\theta)-\beta_{nm}\frac{1}{k_0}\frac{d}{d\theta}P_n^{|m|}(\cos\theta)\right], \tag{3b}$$

are, respectively, the θ- and ϕ- components of the total radiation vector, $\boldsymbol{F}_t(\theta,\phi)$, which is related to the total far-field term $\boldsymbol{E}_t(\theta,\phi)$ through the relation $\boldsymbol{E}_t(\theta,\varphi)\approx\boldsymbol{F}_t(\theta,\varphi)\exp(-jk_0r)/r$. Moreover, the quantity P_t is the total radiated power, and is expressed as [5]

$$P_t=\frac{\pi}{\omega k_0}\sum_{n=1}^{N_{\max}}\sum_{m=-n}^{n}2\frac{n(n+1)}{2n+1}\frac{(n+|m|)!}{(n-|m|)!}\left[\frac{|\alpha_{nm}|^2}{\varepsilon_0}+\frac{|\beta_{nm}|^2}{\mu_0}\right]. \tag{4}$$

In the above expressions, $\alpha_{nm}=A_{4,nm}$ and $\beta_{nm}=B_{4,nm}$, when the EHD is inside the two regions of the CNP, while $\alpha_{nm}=a_{nm}^{(4)}+A_{4,nm}$ and $\beta_{nm}=b_{nm}^{(4)}+B_{4,nm}$, when the EHD is outside the CNP [5]. Moreover, $P_n^{|m|}(\cdot)$ is the associated Legendre function of the first kind of degree n and order $|m|$, while the symbol $N_{\max}$ is the truncation limit in the implementation of the exact infinite summation chosen to ensure the convergence of the expansion in (2). While the expression for the total radiated power in (4) was used in [5] and [12], [14] to conduct a thorough analysis of sub-wavelength resonances in passive and active spherical CNPs, respectively, the directivity properties of such active particles on the basis of (2) have not been reported previously.

4. Numerical results and discussion

4.1. Background – sub-wavelength resonances in CNPs

Previous results [11]-[14] have demonstrated that highly resonant sub-wavelength CNPs can be designed by including gain, e.g., inside their nano-cores. This configuration was found to lead to scattering cross-sections that are orders of magnitude larger than the values predicted by their geometrical sizes, see e.g., [11] and the works referenced therein, as well as to the enormous radiated powers for localized excitation sources [12]-[14]. Significant attention in those works has been devoted to a CNP consisting of a silica nano-core of radius 24 nm, coated with a 6nm thick silver nano-shell for which the size-dependency of the permittivity was taken into account. The silica nano-core permittivity consisted of two contributions: one from its refractive index $n=\sqrt{2.05}$ in the frequency region of interest and another accounting for the canonical, constant frequency, gain model through which its permittivity reads $\varepsilon_1=(n^2-\kappa^2-2jn\kappa)\varepsilon_0$, where the parameter κ (optical loss or gain constant) determines the nature of the nano-core: lossless (and passive) for $\kappa=0$, lossy and passive for $\kappa>0$ (optical loss constant) and active for $\kappa<0$ (optical gain constant). For such CNPs, the so-called super-resonant states, with very large radiated powers, were identified for the cylindrical case for $\kappa=-0.175$ at the excitation wavelength of $\lambda=577.70$ nm, and for the spherical case for $\kappa=-0.245$ at the excitation wavelength of $\lambda=502.1$ nm. These super-resonances are illustrated in Figure 2 in terms of the normalized radiation resistance (NRR), i.e., the ratio of the total power radiated when the source and the CNP are present to the total power radiated by the source in the absence of the CNP, as a function of the source location, x_s. The sources are located along the positive x-axis for both the cylindrical and the spherical Ag-based CNPs. For the cylindrical CNP, the MLS possesses a current amplitude $I_m=1$ [V/m], while both x- as well as z- oriented EHDs have a dipole moment $p_s=5\cdot10^{-9}$ [Am]. In what follows, the directivity properties of these Ag-based CNPs of cylindrical and spherical shape are thoroughly examined.

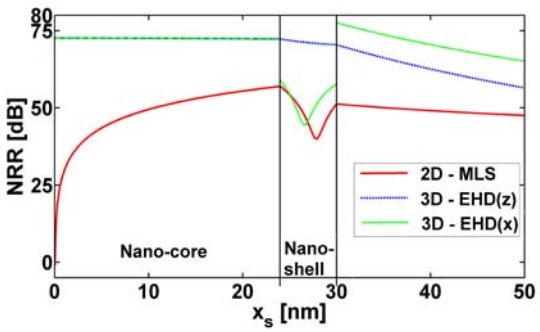

Figure 2: Normalized radiation resistance (NRR) as a function of the source location, x_s, along the positive x-axis for both the cylindrical (2D) and the spherical (3D) super-resonant Ag-based CNPs. In the latter case, the EHD is taken to be both x- and z-oriented. The nano-core and nano-shell regions are indicated in the figure.

4.2. Cylindrical CNPs

The large variations in the NRR shown in Figure 2, with the alternating MLS location in the cylindrical case were thoroughly explained in [13]. Here, it is of great interest to explore the directivity behavior of such configurations. As illustrated in Figure 3a), which shows the directivity (1) for the super-resonant ($\kappa = -0.175$; $\lambda = 577.70$ nm) Ag-based CNP for the indicated MLS locations along the positive x-axis within the nano-core, there are large variations in the resulting patterns. The directivity in the super-resonant state can be re-shaped from a perfectly monopolar pattern (attained at x_s = 0 nm) to a perfectly symmetric dipolar pattern (attained at x_s = 5nm) with small variations in the MLS location. The former case agrees well with the absence of any resonant phenomena observed in Figure 2 when the MLS is at or very near the center of the CNP (NRR around 0 dB). On the other hand, the latter case indicates a strong excitation (NRR around 45 dB for x_s = 5nm) of the dipolar mode necessary for the rapidly increasing NRR values in Figure 2 for MLS locations further away from the CNP center. These far-field results are in line with the near-field distributions reported for this Ag-based CNP configuration in [13]. The maximum directivity of 2 is found for the perfectly symmetric dipolar pattern in Figure 3a) along the $\phi = 0^o$ and $\phi = 180^o$ directions. However, larger values can be obtained for specific MLS locations (near the CNP center) for which the dominant mode is a mixture of a monopolar and dipolar modes, rather than the resonant dipolar mode alone. For instance, the result obtained for x_s = 0.1 nm given in Figure 3b) illustrates this point.

Apart from the pattern re-shaping possibilities with varying location of the MLS, it is interesting to note that adjustment of the optical gain constant κ for a given location of the source can likewise re-shape the overall directivity pattern. With reference to Figure 3b), which shows the directivity for the Ag-based CNP when the MLS is located at x_s = 5nm, the perfectly symmetric dipolar pattern attained in the super-resonant case can be re-shaped such that its main beam is along the $\phi = 0^o$ or $\phi = 180^o$ direction, depending on the value of κ. For the examined values of κ which are larger than the super-resonant value ($\kappa = -0.175$), the main beam (which is approaching a maximum directivity of 3) points in the $\phi = 180^o$ direction. In contrast, it points along the $\phi = 0^o$ direction for values of κ smaller than the super-resonant value.

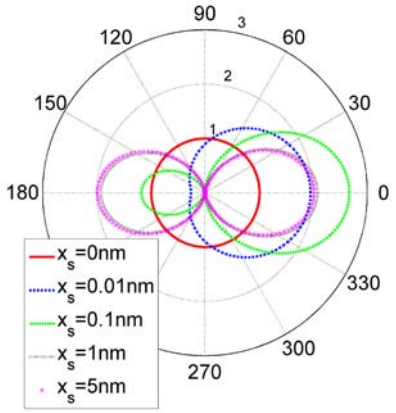

(a)

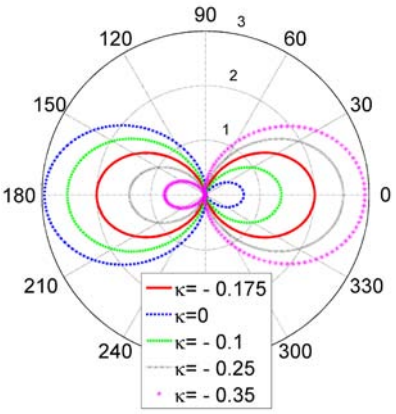

(b)

Figure 3: Directivity for the Ag-based CNP excited by a MLS. In (a), the CNP is super-resonant, and different MLS locations, x_s , inside the nano-core along the positive x-axis are considered. In (b), the MLS is located at x_s = 5nm and different values of the optical gain constant κ are considered.

Aside from these interesting results for the cylindrical Ag-based CNP, a few other remarks are in order. As explained in [13] using the near-field distribution results, the main reason for the peak amplitude changes of the NRR in Figure 2 is the difference in the coupling strength with the varying MLS location which determines the potency of the underlying resonant dipolar mode. As an example, the near-field of the resonant dipolar mode is significantly stronger for the MLS located near the nano-shell interface, e.g., at x_s = 23 nm, than inside the nano-shell at x_s = 28.74 nm, where the NRR experiences the dip shown in Figure 2. However,

once the MLS is sufficiently far away from the origin so that the perfectly symmetric dipolar pattern is obtained, as the one illustrated in Figure 3a) for x_s = 5 nm, the very same directivity pattern (of maximum directivity of 2) results also for other MLS locations inside the CNP, as well as outside of it at close distances. This is partly illustrated in Figure 4) which shows the directivity for three MLS locations inside the nano-shell of the super-resonant Ag-based CNP: near the first interface (x_s = 25 nm), at the location of minimum NRR inside the nano-shell (x_s = 27.84 nm), and near the second interface (x_s = 29 nm). In all cases, the same symmetric dipolar pattern is observed.

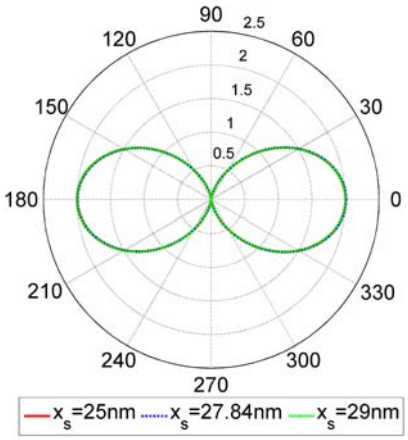

Figure 4: Directivity for the super-resonant Ag-based CNP excited by a MLS located at three different locations inside the nano-shell region of the particle.

Thus, once the MLS location is established away from the origin, the symmetric dipolar pattern is observed. Moreover, the explanation for the varying levels of the NRR found in Figure 2 cannot be revealed by inspecting the directivity patterns (*which are identical*), but rather the near-field distributions must be examined. Results essentially the same as those in Figure 4 are also obtained for MLS locations in the exterior of the CNP at sufficiently close distances to it.

It is furthermore interesting to parallel the above results with those of the corresponding sub-wavelength resonant MTM-based structures at radio frequencies [5]. In [5], an electric line source excitation of double-negative (DNG) or mu-negative (MNG) coated passive structures were examined. As remarked there, those results also apply, by duality, to epsilon-negative (ENG) coated passive structures excited by a MLS. The maximum NRR levels in [5] for the resonant cylindrical MTM-based structures are well below (with maximum NRR around 23 dB) those reported in Figure 2. Moreover, a complete symmetry in their dipolar directivity patterns was not obtained. In particular, for the source inside the ENG shell-region, asymmetric directivity patterns (which are each other's images with respect to *y*-axis) result for MLS locations near the first and the second shell interface. This is in sharp contrast to the results of Figure 4 where identical and completely symmetric patterns are obtained. In addition, since the NRR of the MTM-based structures in [5] drops to 0 dB for a particular source location inside the shell-region, the pattern re-shaping also occurs for altering source locations in this region. Specifically, for the minimum NRR location of the source inside the shell-region, a perfect monopolar pattern is obtained [5]. These findings for sub-wavelength resonant MTM-based ENG-coated passive structures, as those studied in [5], appear in sharp contrast to the above gain-enhanced results for the Ag-based active CNPs.

4.3. Spherical CNPs

Figure 2 reveals interesting differences between the *z*- and *x*-oriented EHD excitations of the super-resonant Ag-based spherical CNP, which were detailed through near-field investigations in [14].

Figure 5 shows the directivity of the Ag-based CNP for varying values of the parameter κ in the case of a *z*-oriented EHD excitation. The EHD has the dipole moment $p_s = 5 \cdot 10^{-9}$ [Am] and is located on the *x*-axis at +12 nm from the origin. Specifically, the E-plane (*xz*-plane) pattern results are shown in Figure 5a) and the H-plane (*xy*-plane) pattern results are shown in Figure 5b). Despite the large levels of the NRR, the directivity of the super-resonant state, which is clearly dipolar, is not enhanced relative to that of an isolated *z*-oriented EHD. In particular, its value remains around 1.5. Unlike the cylindrical case, there is a complete symmetry in the CNP and, consequently, no preferred axis. Moreover, the investigated values of κ are found, again because of the symmetry, to have only a negligible effect on the directivity. The directivity of the super-resonant Ag-based CNP is shown in Figure 5c) as a function of $\theta \in (0^o, 180^o)$ and $\phi \in (0^o, 360^o)$, clearly supporting the above observations.

For the *x*-oriented EHD excitation of the super-resonant Ag-based CNP, Figure 6 shows the resulting directivity. The E-plane (*xz*-plane) pattern is shown in Figure 6a); the H-plane (*yz*-plane) pattern is shown in Figure 6b). The directivity as a function of $\theta \in (0^o, 180^o)$ and $\phi \in (0^o, 360^o)$ is shown in Figure 6c). Except from the flipping of the E-plane pattern by 90° relative to the *z*-oriented EHD case in Figure 5a), the same over-all conclusions apply as with the *z*-oriented EHD case, i.e., the directivity is not enhanced by the presence of the super-resonant Ag-based CNP (for which large NRR values are obtained), its maximum value remains around 1.5 (which is that of an isolated EHD), and the H-plane (*xy*-plane) pattern is azimuthally symmetric. This behavior is again expected because of the spherical symmetry of the CNP. Thus, as in the passive spherical case [10], the dipolar resonance excited inside the examined active electrically small spherical CNPs does not modify the directivity pattern of the exciting Hertzian dipole, but rather reinforces it. Moreover, the varying NRR levels observed for the *x*-oriented EHD in Figure 2 cannot be revealed through the directivity pattern alone, but rather require studying the near-field distributions.

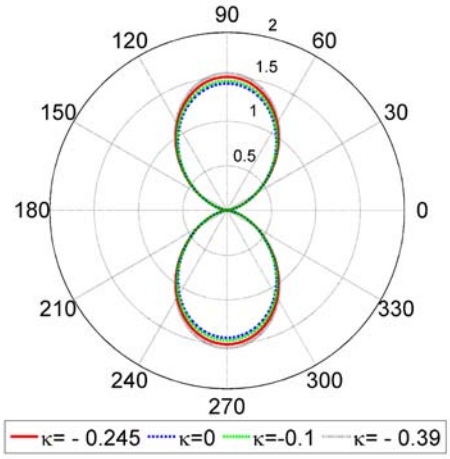

(a)

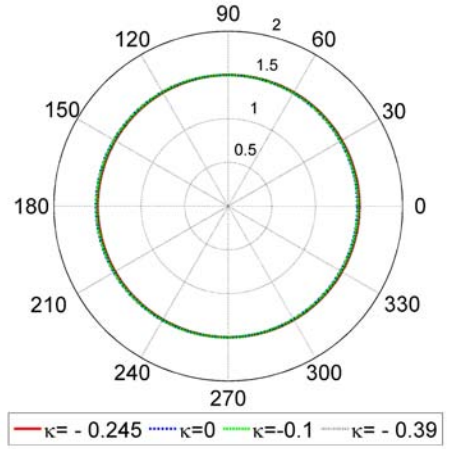

(b)

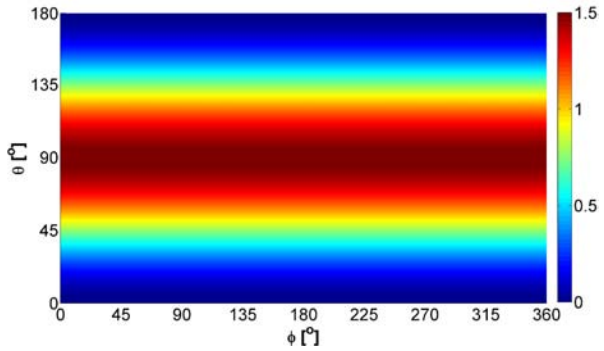

(c)

Figure 5: Directivity for the Ag-based CNP for a *z*-oriented EHD located along the *x*-axis at +12 nm for different values of the parameter κ. The E-plane (*xz*-plane) pattern results are shown in (a), and the H-plane pattern results (*xy*-plane) are shown in (b). In the case of the super-resonant Ag-based CNP, the directivity is shown in (c) for all values of θ and ϕ.

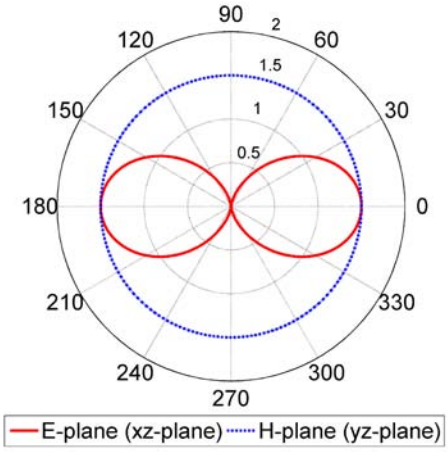

(a)

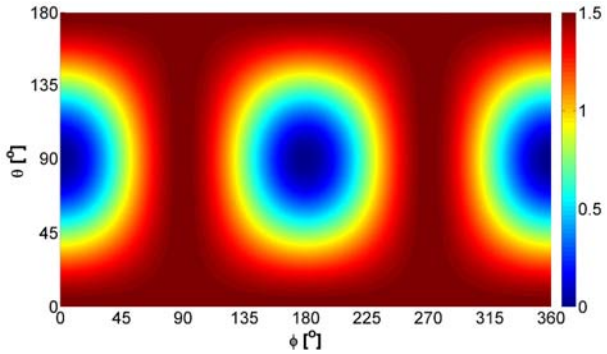

(b)

Figure 6: Directivity for the super-resonant Ag-based CNP for a *x*-oriented EHD located along the *x*-axis at 12 nm. The E-plane (*xz*-plane) results are shown in (a), the H-plane results (*yz*-plane) are shown in (b), while the results for all values of θ and ϕ are shown in (c).

5. Summary and conclusions

This work examined the directivity properties of nano-antennas made of active CNPs of cylindrical and spherical shapes; the CNPs were excited by a magnetic line source (MLS), in the cylindrical case, and an electric Hertzian dipole (EHD), in the spherical case. The nano-core of the particle consisted of silica, whereas silver was used for the nano-shell material. A canonical, constant frequency, gain model was incorporated inside the dielectric part of the particle. In our studies, particular attention was devoted to the influence of the source location and the optical gain constant on the resulting directivity patterns.

For cylindrical active CNPs, significant variation in the directivity was reported when either the MLS location or the value of the optical gain constant was varied. Specifically, pattern re-shaping from a perfectly monopolar form to a perfectly dipolar pattern (with maximum directivity of 2) was demonstrated for super-resonant CNPs upon the variation of the MLS location - the re-shaping being owed to the coupling strength with the varying MLS location which determines the potency of the underlying resonant dipolar

mode. Moreover, the perfectly symmetric dipolar patterns of the super-resonant CNPs were re-shaped by proper adjustments of the optical gain constant; their main beams pointed in either the $\phi = 0^o$ or $\phi = 180^o$ directions, with the corresponding directivities of almost 3. Moreover, it was found that, once the MLS location for a super-resonant CNP is sufficiently away from its center, the symmetric dipolar mode is excited, and it dominates the behavior of the directivity pattern. The pattern was found to remain unaltered for MLS locations inside the nano-core even at locations further away from the CNP center, as well as for those inside the nano-shell, and outside the CNP at close distances to it. These results are in sharp contrast to those reported for corresponding passive MTM-based configurations at radio frequencies.

The directivity patterns for the active spherical CNPs were shown to be unaffected by variations in the parameters specifying the configurations - even in its super-resonant state for which large amounts of the radiated power are generated by the source. In particular, it was demonstrated that they largely correspond to the pattern of an isolated dipole, i.e., their maximum value remained around 1.5. Unlike the cylindrical case, there is a complete symmetry in the CNP and, consequently, no preferred axis. Thus, as in the passive spherical case treated in [10], the dipolar resonance excited inside the active spherical CNPs does not modify the directivity pattern of the exciting Hertzian dipole. The potential excitation of higher order modes in other configurations of the active CNPs will be considered in a future report.

References

[1] R. E. Collin, *Antennas and Radiowave Propagation*, McGraw-Hill, Int. Ed., 1985.

[2] N. Engheta, and R. W. Ziolkowski, *Metamaterials-Physics and Engineering Applications*, John Wiley & Sons, New York, 2006.

[3] A. Alú, and N. Engheta, "Polarizabilities and effective parameters for collections of spherical nano-particles fromed by pairs of concentric double-negative (DNG), single-negative (SNG) and/or double-positive (DPS) metamaterial layers," *J. Appl. Phys*., Vol. 97, p. 094310, May 2005.

[4] S. Arslanagić, R. W. Ziolkowski, and O. Breinbjerg, "Analytical and numerical investigation of the radiation from concentric metamaterial spheres excited by an electric Hertzian dipole," *Radio Sci*., Vol. 42, 2007, doi:10.1029/2007RS003663.

[5] S. Arslanagić, R. W. Ziolkowski, and O. Breinbjerg, "Analytical and numerical investigation of the radiation and scattering from concentric metamaterial cylinders excited by an electric line source," *Radio Sci*., Vol. 42, 2007, doi:10.1029/2007RS003644.

[6] H. R. Stuart, and A. Pidwerbetsky, "Electrically small antenna elements using negative permittivity radiators," *IEEE Trans. Antennas Propag*., Vol. 54, No.6, pp. 1644-1653, June, 2006.

[7] R. W. Ziolkowski, and A. Erentok "Metamaterial-based efficient electrically small antennas," *IEEE Trans. Antennas Propag.,* Vol. 54, No. 7, pp.2113-2130, July 2006.

[8] A. Erentok, and R.W. Ziolkowski, "Metamaterial-inspired efficient electrically small antennas," *IEEE Ant. Propag.,* Vol. 56, No. 3, 691-707, 2008.

[9] S. J. Oldenburg, G. D. Hale, J. B. Jackson, and N. J. Halas, "Light scattering from dipole and quadrupole nanoshell antennas," *Appl. Phys. Lett*., Vol. 75, No. 8, pp. 1063-1065, Aug. 1999.

[10] A. Alú, and N. Engheta, "Enhanced directivity from sub-wavelength infrared/optical nano-antennas loaded with plasmonic materials or metamaterials," *IEEE Trans. Ant. Propag.*, Vol. 55, No. 11, 3027–3039, 2007.

[11] J. A. Gordon, and R. W. Ziolkowski, "The design and simulated performance of a coated nano-particle laser," *Opt. Express*, Vol. 15, No. 5, 2622-2651, 2007.

[12] S. Arslanagić, and R. W. Ziolkowski, "Active coated nano-particle excited by an arbitrarily located electric Hertzian dipole – resonance and transparency effects," *J. Opt.,* Vol. 12, 024014, 2010.

[13] S. Arslanagić, and R. W. Ziolkowski, "Impact of the excitation source and plasmonic material on cylindrical active coated nano-particles," *Sensors*, Vol. 11, 9109-9120, 2011.

[14] R. W. Ziolkowski, S. Arslanagić, and J. Geng, "Where high-frequency engineering advances opics: active nanoparticles as nanoantennas," to appear in *Optical Nanoantennas*, Eds. A. Alú and M. Agio, Cambridge University Press, London, 2012.

Quantum Surface plasmon resonance system based on electromagnetically -induced transparency

Chunguang Du

State Key Laboratory of Low-Dimensional Quantum Physics, Department of Physics,
Tsinghua University, Beijing, China
*corresponding author, E-mail: ducg@mail.tsinghua.edu.cn

Abstract

A scheme for a new kind of surface plasmon resonance system (SPR) is proposed. The system is composed of three layers: a prism, a thin metal film, and a hybrid dielectric consisting of EIT atoms and a background substance. It is found that due to the inherently quantum feature of EIT, the EIT-based SPR system exhibits some interesting quantum properties, which are absent in ordinary SPR systems and may be used for novel sensors which can detect very small variations of quantum properties of matters such as small shifts of atomic levels caused by external fields and have sub-wavelength spatial resolution.

1. Introduction

Electromagnetically induced transparency (EIT) is a fascinating effect in which an otherwise opaque medium becomes transparent to a resonant (probe) field by use of another (coupling) field [1]. The destructive quantum interference between two atomic transition pathways leads to null absorption and large dispersion within the induced transparency window. The phenomenon has attracted great attention on account of its potential applications in the coherent control of the optical properties of atomic media and solid systems, e.g. photonic crystals [2], or quantum metamaterials [3]. Recent theoretical investigation has also shown that EIT can be used for coherent control of the group velocity [4] of the polaritons at the surface of a negative-refractive- index metamaterial under the condition of near-zero loss of the polaritons. The key point of this investigation is that the near-zero loss can be realized at special frequencies where the double negative indexes occurs(i.e., the real part of the permittivity and the permeability are both negative). However, for a bulk metal, only the permittivity can have a negative real part in the visible spectrum. So a question arises: for surface-plasmon polaritons at a metal surface, will coherent control based on EIT be possible, or will some other coherent phenomena be observed? It will be shown in this paper that coherent control is indeed tolerant of metal loss, and some very interesting phenomena may be observed, even for an EIT material of very low atomic number density. It will be also shown that new phenomena can occur when surface plasmons are excited under EIT conditions. To my knowledge, an SPR system based on EIT has never been investigated before, and this kind of system may to be used for novel sensors for detecting not only the small variations of refractive index as ordinary SPR system[5], but also the quantum properties such as small shifts of energy-levels of matters with sub-wavelength spatial resolution.

2. EIT in an atomic medium

The EIT medium can be an atomic gas or doped solid medium composed of three-level atoms of Λ configuration. For a single atom, the wavefunction of the electronic state can be written as $|\psi(t)\rangle = c_0(t)|0\rangle + c_1(t)|1\rangle + c_2(t)|2\rangle$, where c_0, c_1, and c_2 are the probability amplitude of the ground state, the excited state, and the second ground state of the atom, respectively.

According to the Schrödinger equation in the interaction picture, the motion of the probability amplitudes can be obtained as follows (with the method similar to Ref. [1])

$$\begin{array}{l} i\frac{dc_0}{dt} = \frac{\Omega_p(x,y,z)}{2}c_1 \\ i\frac{dc_1}{dt} = -(\delta_p + i\frac{\gamma}{2})c_1 + \frac{\Omega_p(x,y,z)}{2}c_0 + \frac{\Omega_c(x,y,z)}{2}c_2 \\ i\frac{dc_2}{dt} = -(\delta_p - \delta_c + i\frac{\gamma'}{2})c_2 + \frac{\Omega_c(x,y,z)}{2}c_1 \end{array} . \quad (1)$$

Here δ_p is the probe detuning defined by $\delta_p = \omega_p - \omega_{10}$, and δ_c is the coupling detuning defined by $\delta_c = \omega_c - \omega_{12}$, where ω_p and ω_c are the angular frequencies of the probe and coupling fields, respectively, ω_{10} and ω_{12} are the atomic transition angular frequencies of $|1> -|0>$ and $|1> -|2>$ transitions, respectively, Ω_p and Ω_c are the Rabi-frequencies defined by $\Omega_p(x,y,z) = \frac{\overrightarrow{\mu}_{10}\cdot\mathbf{E}_p(x,y,z)}{\hbar}$ and $\Omega_c(x,y,z) = \frac{\overrightarrow{\mu}_{21}\cdot\mathbf{E}_c(x,y,z)}{\hbar}$, respectively, $\mathbf{E}_p(x,y,z)$ and $\mathbf{E}_c(x,y,z)$ are the electric field amplitudes of the probe and the coupling fields, respectively, and, $\overrightarrow{\mu}_{10}$ and $\overrightarrow{\mu}_{21}$ are the transition electronic dipole moments of $|1> -|0>$ and $|1> -|2>$ transitions, respectively. Also, γ and γ' are the decay rates of states $|1>$ and $|2>$, respectively. The quantum interference between $|0> -|1>$ and $|2> -|1>$ transitions can strongly modify the optical response of the system. All the laser fields in this paper are assumed to be monochromatic. In this case, the field amplitudes $\mathbf{E}_p$ and $\mathbf{E}_c$ are time independent. However, it should be noted that, in general cases $\mathbf{E}_p$ or $\mathbf{E}_c$ can be position dependent. For the sake of simplicity, we assume the EIT medium is composed of cold atoms where the Doppler effect can be neglected, and only consider the weak probe field case where

$\Omega_p << \gamma, \Omega_c$. According to Ref. [1], the susceptibility χ can be given by

$$\chi(x,y,z) = -\frac{|\overrightarrow{\mu}_{10}|^2 N}{\hbar\varepsilon_0}\frac{c_0^* c_1}{\Omega_p(x,y,z)}. \quad (2)$$

We consider the transitions of the sodium D2 line. According to Ref. [6], $|\overrightarrow{\mu}_{10}|$ can be evaluated by $|\overrightarrow{\mu}_{10}| = \sqrt{\frac{1}{3}}3.5247ea_0$ with a_0 being the Bohr radius and ε_0 the permittivity of vacuum, and $\gamma = 61.54$MHz. According to Ref. [7], $N = 3\times10^{18}/m^3$.

We assume that the atom is initially in the ground state, and probe field is assumed to be very weak so that $c_0(t) \approx 1$ is satisfied at all times. The steady-state solution of Eq.(1) can be easily obtained, and substituting the solution into Eq. (2) , it is easy to obtained that

$$\chi(x,y,z) = -\frac{|\overrightarrow{\mu}_{10}|^2 N}{\hbar\varepsilon_0}\frac{\frac{1}{2}(\delta_p-\delta_c+i\frac{\gamma'}{2})}{-\frac{1}{4}\Omega_c(x,y,z)^2+(\delta_p+i\frac{\gamma}{2})(\delta_p-\delta_c+i\frac{\gamma'}{2})}. \quad (3)$$

It should be noted that, according to Eq. (3), χ is independent on Ω_p , i.e. the atomic medium is a linear medium for the probe field under the weak-field approximation, and the function $\chi(x,y,z)$ depends on the function $\Omega_c(x,y,z)$.

We assume that the incident coupling beam (in the prism) is a traveling wave with planar wavefront. Under this condition, if we consider the coupling field in the EIT medium, however, we find there are two typical situations:

(1) The coupling field in the EIT medium is a freely-propagating field. In this situation, constant Ω_c lead to a spatially independent susceptibility χ. This result is applicable to all the cases where the probe field in the EIT medium is weak, even to the case where the probe field is a SPP but the coupling field is a freely-propagating field of planar-wave.

(2) The coupling field in the EIT medium a SPP field. In this situation, spatially dependent function $\Omega_c(x,y,z)$ leads to a spatially dependent susceptibility $\chi(x,y,z)$.

The two situations occur for different incident angles (θ_c) and have quite different frequency spectra of reflectivity, which will be discussed later.

3. Surface EIT with a freely-propagating coupling field

In this section we consider the case of freely-propagating coupling field. The scheme of EIT-based SPR is shown in Fig. 1, where the EIT medium can be atomic gases or doped solid medium which are composed of of three-level atoms of Λ configuration.

The coupling field in the dielectric can be a freely propagating field when $\mathrm{Im}(k_{\mathrm{dx}}) = 0$, or an evanescent field when $\mathrm{Im}(k_{\mathrm{dx}}) > 0$, depending on the incident angle θ_c. We can calculate θ_c according to Eqs.(8) and (10). If the

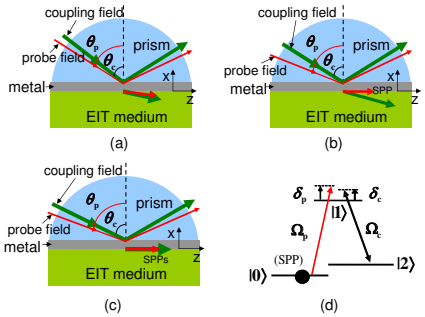

Figure 1: (Color online) Schematic of the system. The system is composed of an atomic EIT medium (green), a metal film(gray), and a cylindrical prism (blue).(a) The case that both of the probe field and the coupling field in the atomic medium are freely propagating fields (no SPR effect). (b) The case that the probe field is a SPP field but the coupling field is a freely propagating field in the atomic medium. (c) The case that both of the probe field and the coupling field are SPP fields. (d) Energy-level diagram of three-level atoms of Λ-configuration.

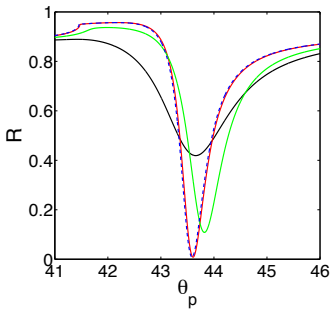

Figure 2: (Color online) Angle-dependence of the probe-field reflectivity (R) for different dielectric layers (Blue dashed: vacuum; Black: two-level atom ($\Omega_c = 0$) with $\delta_p = 0$; Red: EIT atom with $\delta_p = 0$ and $\Omega_c = 1.23\gamma$; Green: EIT atom with $\delta_p = 0.3\gamma$ and $\Omega_c = 1.23\gamma$. The atomic transitions are of sodium D2 line where $\lambda_0 = 589.1$ nm (probe-field wavelength); $\gamma = 61.54$ MHz, $\omega_{20} = 1.8$ GHz. Other parameters: $n_{\mathrm{p}} = 1.51$, $N = 3.3\times10^{18}/m^3$, $\varepsilon_{\mathrm{m}} = -13.3 + 0.883i$ [15] (which is approximated a constant within EIT frequency-band (about 100 MHz)), and $q = 50$ nm(thickness of the silver film).

imaginary parts of n_{p} and ε_d can be neglected, we can easily obtain the critical angle with the equation $k_{\mathrm{dx}}^2 = 0$, i.e. $n_{\mathrm{p}}\sin\theta = \sqrt{\varepsilon_{\mathrm{d}}}$, which gives the critical angle θ_{crt}. For $n_{\mathrm{p}} = 1.51$ and $\varepsilon_{\mathrm{d}} = 1$, we obtain $\theta_{crt} = 41.47^{\mathrm{o}}$.

In the case of $\theta_c < \theta_{crt}$, the coupling field in the dielectric is a freely propagating field (shown in Fig. 1(a) and (b)), and Ω_c is spatially independent. With effective-

medium theory and taking into account local-field effects for generality, the permittivity of the atomic medium can be given by [8, 9]

$$\varepsilon_d = \varepsilon_b + \frac{\chi}{1-\frac{1}{3}\chi}\frac{\varepsilon_b+2}{3}, \tag{4}$$

where ε_b is the background permittivity and χ is given by Eq.(3). The background is assumed to be an vacuum (ε_b=1) or a very dilute dielectric ($\varepsilon_b \approx 1$). Here N is the density of the atomic number. So ε_d can be easily obtained with above equationsin particular, for dilute vapors ($\frac{1}{3}\chi << 1$), ε_d can be given by $\varepsilon_d \approx \varepsilon_b + \chi$.

It should be noted that, because the coupling field only drives transition $|2> -|1>$ of the atoms and the population in state $|2>$ is near zero at all times, the effect of the atoms on the coupling field can be safely neglected. So we only consider the effect of the atomic medium on the probe field. We now calculate the reflectivity R of the probe beam defined by $R = |r_{\rm pmd}|^2$, where $r_{\rm pmd}$ is the three-layer amplitude reflection coefficient and is given by the Fresnel formula

$$r_{\rm pmd} = \frac{r_{\rm pm} + r_{\rm md}\exp(2ik_{\rm mx}q)}{1 + r_{\rm pm}r_{\rm md}\exp(2ik_{\rm mx}q)}, \tag{5}$$

where q is the thickness of the metal film, and the two-layer amplitude reflection coefficients $r_{\rm pm}$ and $r_{\rm md}$ at the prism/metal and metal/dielectric interfaces, respectively, are given by

$$r_{\rm pm} = \frac{\varepsilon_{\rm m}k_{px} - \varepsilon_{\rm p}k_{\rm mx}}{\varepsilon_{\rm m}k_{px} + \varepsilon_{\rm p}k_{\rm mx}} \tag{6}$$

and

$$r_{\rm md} = \frac{\varepsilon_{\rm d}k_{\rm mx} - \varepsilon_{\rm m}k_{\rm dx}}{\varepsilon_{\rm d}k_{\rm mx} + \varepsilon_{\rm m}k_{\rm dx}}. \tag{7}$$

Here k_z is parallel wave vector and can be given by

$$k_z = k_0 n_{\rm p}\sin\theta_p, \tag{8}$$

where

$$k_0 = \frac{\omega_p}{c}, \tag{9}$$

and k_{jx} are normal wave vectors and can be given by

$$k_{jx} = \sqrt{k_0^2\varepsilon_j - k_z^2} \tag{10}$$

with $j = {\rm p,m,d}$ denoting the prism, the metal, and the dielectric (EIT medium), respectively. The field enhancement due to surface plasmon is defined by [10] $T = |t_{\rm pmd}|^2$ with $t_{\rm pmd} = \frac{H_y(m/d)}{H_y(p/m)}$, where $H_y(m/d)$ and $H_y(p/m)$ are the magnetic field at metal/dielectric and prism/metal interfaces, respectively, and $t_{\rm pmd}$ can be calculated with the Fresnel formula

$$t_{\rm pmd} = \frac{t_{\rm pm}t_{\rm md}\exp(ik_{\rm mx}q))}{1 + r_{\rm pm}r_{\rm md}\exp(2ik_{\rm mx}q)}, \tag{11}$$

where $t_{ij} = 1 + r_{ij}$ being derived from the boundary conditions, and $i,j = {\rm p,m}$ or $i,j = {\rm m,d}$. Similarly, we can also calculate the field enhancement of the electric field T_e, which is defined by $T_e = \frac{|\mathbf{E}(m/d)|^2}{|\mathbf{E}(p/m)|^2}$, where $\mathbf{E}(m/d)$ and $\mathbf{E}(p/m)$ are the electric field at metal/dielectric and prism/metal interfaces, respectively. For TM polarization, according to Ref. [10], the relation between T_e and T is given by $T_e = \frac{\varepsilon_{\rm p}}{\varepsilon_{\rm d}}T$.

With Eqs.(3) and (4), we can calculate the permittivity of the atomic medium, and, in combination with Eqs. (5), (6), (7),(8), (9), and (10), we can calculate the reflectivity (R) of the probe-field laser beam. It is found that the probe-field reflectivity is strongly influenced by the coupling laser via the quantum interference effect in the EIT medium.

4. Surface EIT with a SPP coupling field

In this section we consider the case of SPP coupling field. The SPP coupling field is resonantly excited by the incident coupling beam when $\theta_c \approx \theta_{res}$ ($\theta_{res} > \theta_{crt}$), and can be numerically determined by the angle of minimum reflectivity of the coupling beam. For an evanescent-wave coupling field ($\theta_c > \theta_{crt}$), the Rabi-frequency (Ω_c) can be written as $\Omega_c(x) = \Omega_{c0}e^{-ik_{\rm vx}^{(c)}x}$, where $x < 0$ (i.e. in the atomic medium), and,

$${k_{\rm vx}}^{\rm (c)} = \sqrt{\frac{\omega_c^2}{c^2} - {k_z^{\rm (c)}}^2}, \tag{12}$$

$$k_z^{\rm (c)} = \frac{\omega_c}{c}n_{\rm p}\sin\theta_c. \tag{13}$$

In resonant case when SPP is excited, i.e. $\theta_c \approx \theta_{res}$, we obtain that ${k_{\rm vx}}^{\rm (c)} \approx i\kappa^{(c)}$ with $\kappa^{(c)}$ being a real number which represent the attenuation of the SPP in x-direction. In this case, to calculate the reflection coefficient at metal/dielectric interface ($r_{\rm md}$), we firstly consider the three-layer (metal/vacuum/dielectric) structure and then set the thickness of the vacuum layer ($q_{\rm v}$) to be zero.

The magnetic field $\mathbf{H}$ of the incident field is given by $\mathbf{H} = H_{Iy}\mathbf{e}_y$ with $H_{Iy}(x,z) = A_I e^{-ik_{\rm vx}x + ik_z z}$, where A_I is the field amplitude, and $k_{\rm vx}$ is the x-component of the wavevector in the vacuum layer being given by

$$k_{\rm vx} = \sqrt{\frac{\omega_p^2}{c^2} - k_z^2}, \tag{14}$$

and k_z is given by Eq. (8).

The three-layer (metal/vacuum/dielectric) amplitude reflectivity is given by

$$r_{\rm mvd} = \frac{r_{\rm mv} + r_{\rm vd}\exp(2ik_{\rm vx}q_{\rm v})}{1 + r_{\rm mv}r_{\rm vd}\exp(2ik_{\rm vx}q_{\rm v})}. \tag{15}$$

Set $q_{\rm v} = 0$, we obtain two-layer (metal/dielectric) amplitude reflectivity $r_{\rm md}$:

$$r_{\rm md} = \frac{r_{\rm mv} + r_{\rm vd}}{1 + r_{\rm mv}r_{\rm vd}}, \tag{16}$$

where

$$r_{\rm mv} = \frac{k_{\rm mx} - \varepsilon_{\rm m}k_{\rm vx}}{k_{\rm mx} + \varepsilon_{\rm m}k_{\rm vx}}. \tag{17}$$

We now calculate $r_{\rm vd}$. We consider a probe field propagating in vacuum is made incidence on the the dielectric

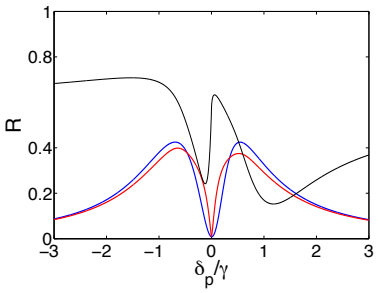

Figure 3: (Color online) Reflectivity of the probe laser beam R versus the probe-detuning δ_p for $\theta_p = 43.61^{\rm o}$. The blue curve is for freely-propagating coupling field ($\theta_c < \theta_{crt}$) and $\varepsilon_{\rm b} = 1$; The other (red and black) curves are for SPP coupling field in the case of $\theta_c \approx \theta_p$ (red for $\varepsilon_{\rm b} = 1$ and black for $\varepsilon_{\rm b} = 1.005$). Here $\Omega_c = \Omega_{c0} = 1.2A$, other parameters are same as that in Fig. 2

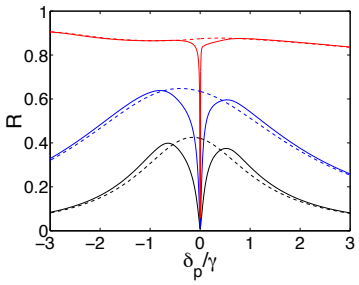

Figure 4: (Color online) Detuning spectra of the reflectivity R for $\theta_p = 43.61^{\rm o}$ but different atomic densities, where the coupling field is a SPP in the case of $\theta_c \approx \theta_p$. The solid curves are for $\Omega_{c0} = 1.2A$, while the dashed curves are for $\Omega_{c0} = 0$ (Black: $N = 3.3 \times 10^{18}/m^3$; blue: $N = 8 \times 10^{18}/m^3$; red: $N = 8 \times 10^{19}/m^3$.). Other parameters are the same as in Fig. 2.

surface. If $\varepsilon_{\rm d}(x) \approx 1$, with perturbation theory similar to that in Ref. [11], the reflection field can be written as

$$H_{Ry}(x,z) = A_I e^{ik_z z} k_0^2 \int_{-\infty}^{0} G(x-x') \left[\varepsilon_{\rm d}(x') - 1\right] e^{-ik_{\rm vx}x'} dx'. \tag{18}$$

The Green function $G(x-x')$ is given by

$$G(x-x') = \frac{i}{2k_{\rm vx}} e^{ik_{\rm vx}(x-x')} \tag{19}$$

The amplitude reflectivity $r_{\rm vd}$, which is defined by $\frac{H_{Ry}(0,z)}{H_{Iy}(0,z)}$, can be obtained by substituting Eq. (19) into (18) as follows

$$r_{\rm vd} = \frac{k_0^2}{k_{\rm vx}^2}\left[\varepsilon_{\rm b} - 1 - \frac{|\overrightarrow{\mu}_{10}|^2 N}{\hbar\varepsilon_0}\frac{1}{\delta_p + i\gamma/2} F(1,b;1+b;1/\beta)\right] \tag{20}$$

where F is the general hypergeometric function[12], and,

$$b = -ik_{\rm vx}/{\rm Im}[{k_{\rm vx}}^{(c)}], \tag{21}$$

$$\beta = \frac{4(\delta_p + i\gamma/2)(\delta_p - \delta_c + i\gamma'/2)}{\Omega_{c0}^2}. \tag{22}$$

In the typical case when $\omega_p \approx \omega_c$ (e.g. $\omega_p - \omega_c \approx 1.8$ GHz in the EIT experiment of Ref.[7]), if we take $\theta_p = \theta_c$, according to Eqs.(14), (12), (13), and (8), it is easy to see that $k_{\rm vx} \approx {k_{\rm vx}}^{(c)} = i{\rm Im}[{k_{\rm vx}}^{(c)}]$, and therefore it is obtained from Eq. (21) that $b \approx 1$. Substituting it into Eq. (20)), we obtain

$$r_{\rm vd} = \frac{k_0^2}{{k_{\rm vx}}^2}\left[\varepsilon_{\rm b} - 1 - \frac{|\overrightarrow{\mu}_{10}|^2 N}{\hbar\varepsilon_0}\frac{\beta}{\delta_p + i\gamma/2}\ln(1-1/\beta)\right], \tag{23}$$

Using Eqs. (15), (16), (17), (23), and (8), we can numerically calculate the reflectivity of the probe beam (R). The incident-angle-dependence of reflectivity is shown in Fig. 2. It obvious that the angle-dependence of reflectivity $R(\theta_p)$ will be strongly modified by the coupling field and the resonance angle (i.e. the dip in the Fig. 2) is very sensitive to the probe detunings (δ_p). When the dielectric is an EIT medium and $\delta_p = 0$, the $R(\theta_p)$ curve is very close to that when there is a vacuum. If the probe field is slightly detuned from resonance, e.g. $\delta = 0.5\gamma$, the resonance angle (i.e. the dip in the $R(\theta_p)$ curve) will be significantly shifted. For the two-level case, however, the minimum of R is much larger than in the EIT case. Similar phenomena can also occur on the field enhancement factors (T and T_e) . This kind of properties may be used for detecting the very small atomic-level shifts induced by external fields. In this sense this SPR system can be regarded as a quantum SPR system.

The probe-detuning dependence is shown in Fig. 3. Because of very steep dispersion of the atomic medium for the probe field, the reflectivity spectrum R is extremely sensitive to the probe detuning δ_p. If both the lasers are monochromatic, then the variations of δ_p and δ_c account for atomic level shifts induced by environmental fields, e.g. by DC magnetic fields via the Zeeman effect. It should be emphasized that a probe-field SPP strongly confined in the metal/EIT medium interface only responds to a DC magnetic field very near the interface. Consequently, it may be possible to apply this EIT-SPR system in novel magnetometers for highly localized measurements.

It is also found from Fig. 3 that the reflectivity spectrum R is sensitive to variation of the substrate permittivity $\varepsilon_{\rm b}$. For a dilute-gas EIT medium, a small increase in $\varepsilon_{\rm b}$ can be caused by another background dilute gas mixed with the EIT gas. It is shown that a variation of only 5/1000 of $\epsilon_{\rm b}$ can dramatically change the reflectivity spectrum (see Fig. 3, red curve for $\varepsilon_{\rm b} = 0$, while black curve for $\varepsilon_{\rm b} = 1.005$). Although $\varepsilon_{\rm b}$ depends on ω_p in general, it is frequency independent within the ultra-narrow EIT transparency window. The substrate sensitivity of the spectrum may possibly be used for chemical or biological sensors.

The detuning spectrum of the reflectivity R is also strongly dependent on the atomic number density of the EIT

medium , as shown in Fig. 4. In the two-level case there is a peak in the $R(\delta_p)$ spectrum, which becomes broader with the increase of the atomic number density N. In the EIT case, however, a very narrow dip appears at the center of the background peak. It is interesting that as N increases the dip becomes narrower but the background peak becomes broader.

5. Interpretation of the resonant excitation of the probe-field SPP

In order to understand the resonant phenomena we roughly evaluate the propagation constant of the probe field SPP ($k_{\rm SPP}$). We consider a weak probe field polariton [transverse magnetic (TM) mode] at the interface between a homogeneous dielectric and a metal of semi-infinite medium. From the surface boundary conditions for an SPP wave vector, its magnetic field can be given by [13, 14]

$$H_y = H_{y0} e^{ik_{\rm spp} z \pm \kappa_{\rm m,d} x} \tag{24}$$

where '+' is for $x < 0$, while '−' is for $x > 0$, and H_{y0} is field-amplitude. $k_{\rm spp}$ and $\kappa_{\rm m,d}$ are given by

$$k_{\rm spp} = k_0 \sqrt{\frac{\varepsilon_{\rm d}\varepsilon_{\rm m}}{\varepsilon_{\rm d}+\varepsilon_{\rm m}}} \tag{25}$$

and

$$\kappa_{\rm m,d} = \sqrt{k_{\rm spp}^2 - k_0^2 \varepsilon_{\rm m,d}}, \tag{26}$$

where $\varepsilon_{\rm d}$ and $\varepsilon_{\rm m}$ are the permittivities of the dielectric and the metal, respectively. For the EIT case, $\varepsilon_{\rm d}$ will be coherently controlled by the coupling field. Because the EIT 'transparency' range is very narrow (about 100 MHz)), the frequency dependence of $\varepsilon_{\rm m}$ can be safely neglected. The probe field wavelength is taken to be about 589.1 nm, where, according to experimental data [15], $\varepsilon_{\rm m} = -13.3 + 0.883i$, and the imaginary part accounts for metal loss.

It should be emphasized that the amplitude of the electric component of the coupling field $\mathbf{E}_c$ is spatially independent for freely propagating (traveling) fields, but decays exponentially with x for SPP. Only in the former case is $\varepsilon_{\rm d}$ spatially independent and Eqs. (25) and (26) are valid. For a coupling-field SPP, $\Omega_c(x) = \Omega_{c0} e^{{\rm Re}[\kappa_c]x}$, then $\varepsilon_{\rm d}$ will depend on x. If the variation of the refractivity satisfies $\delta n_{\rm d} << n_{\rm b} \approx 1$, then the SPP propagation constant $k_{\rm spp}$ can be calculated by perturbation theory [11]:

$$k_{\rm spp} = k_{\rm spp}^{(0)} + \delta k_{\rm spp} \tag{27}$$

where

$$\delta k_{\rm spp} = \frac{1}{2}\frac{k_0^2}{k_{\rm spp}^{(0)}} {\rm Re}\left[\kappa_p^{(0)}\right] \int_{-\infty}^{0} e^{2{\rm Re}\left[\kappa_p^{(0)}\right]x} \left[\varepsilon_{\rm d}(x) - 1\right] dx. \tag{28}$$

According to Eq. (26) the zeroth-order propagation constant and confinement are $k_{\rm spp}^{(0)}(\omega_i) = \frac{\omega_i}{c}\sqrt{\frac{\varepsilon_{\rm m}(\omega_i)}{1+\varepsilon_{\rm m}(\omega_i)}}$, and $\kappa_i^{(0)} = \frac{\omega_i}{c}\sqrt{\frac{1}{1+\varepsilon_{\rm m}(\omega_i)} - \varepsilon_b}$, respectively ($i = p, c$ denote 'probe' and 'coupling' ,respectively).

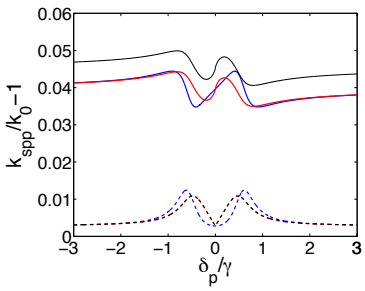

Figure 5: (Color online) Probe-detuning dependence of $k_{\rm spp}/k_0 - 1$, where $k_{\rm spp}$ is the propagation constant of the probe-field SPP (the solid and dashed curves denote its real and imaginary parts, respectively). Black curves are for SPP coupling field and $\varepsilon_{\rm b} = 1.005$; Blue curves are for freely-propagating coupling field and $\varepsilon_{\rm b} = 1$; Red curves are for SPP coupling field and $\varepsilon_{\rm b} = 1$. The parameters are the same as in Fig. 3.

If the difference of the two ground states is very small compared with the laser frequencies, e.g. 1.8GHz in the experiment of Ref.[7], then $\varepsilon_{\rm m}(\omega_p) \approx \varepsilon_{\rm m}(\omega_c)$, and then $\kappa_p^{(0)} \approx \kappa_c$, where the superscript 0 denotes 'zeroth order', i.e. the case when the dielectric is vacuum. Thus we obtain

$$\delta k_{\rm spp} = \frac{1}{2}\frac{k_0^2}{k_{\rm spp}^{(0)}}\left[\varepsilon_{\rm b} - 1 + \frac{|\overrightarrow{\mu}_{10}|^2 N}{\hbar\varepsilon_0}\frac{\beta}{\delta_p + i\gamma/2}\ln(1 - 1/\beta)\right]. \tag{29}$$

Within the EIT transparency window, ${\rm Im}(k_{\rm spp}) \approx 0$, i.e. the polaritons only suffer low losses. Fig. 5 shows the probe-detuning dependence of the propagation constant, $k_{\rm spp}(\delta_p)$. The ultra-narrow bandwidth of transparency and the steep dispersion of the bulk EIT-medium leads to a sharp dip in ${\rm Im}[k_{\rm spp}(\delta_p)]$ (blue dashed curve) and a large gradient of the function ${\rm Re}[k_{\rm spp}(\delta_p)]$ (blue solid curve), and therefore lead to a sharp resonant excitation of SPP. Although more accurate calculation for $k_{\rm spp}$ should consider the role of the thickness of the metal film (see eg. Ref. [10]), the rough evaluate here present a simple and qualitative explanation of the sharp dip in the reflectivity spectrum $R(\delta_p)$.

It is interesting that, comparing the two cases: the coupling field is a SPP and that it is a freely-propagating field, we find in the formal case the gradient of the ${\rm Re}[k_{\rm spp}(\delta_p)]$ curve is more steep(see red solid curve in Fig. 5.), and the dips in ${\rm Im}[k_{\rm spp}(\delta_p)]$ (see red dashed curve in Fig. 5) is pointed, which lead to pointed dip in $R(\delta_p)$ (see the red curve in Fig. 3). The pointed dips arises from the strong confinement of the coupling-field SPP which are absent in ordinary EIT systems, and are signatures of the surface EIT and should be observable experimentally.

6. Discussion

The coupling field will be an evanescent field if $\theta_c > \theta_c^{(crt)}$, but will be a freely propagating field if $\theta_c < \theta_c^{(crt)}$. In practice, the EIT-SPR system may be realized with three different schemes using different arrangements of the coupling field, as follows.

(1) With thin silver films (e.g. $q = 20 - 30$ nm) and a normally incident coupling beam.

(2) With thicker silver films (e.g. 50 nm) and a TM (p-polarized) coupling field with the incidence angle of $\theta_c \approx \theta_c^{(crt)}$. In this case $T_e \approx 0.47$.

(3) With an incidence angle of $\theta_c \approx \theta_{res}$. Similar to (2) but the field enhancement factor T_e is very large($T_e \approx 100$ for 50 nm silver film). Hence the EIT -based coherent control is effective even if the coupling-field at the input end of the system is very weak, which may be used for low-light-level optical switching. .

It should also be noted that although here both the coupling and the probe fields are assumed to be classical, we should consider the possibility of observing nonclassical phenomena arising from the quantum properties of EM fields. The large field-enhancement effect can lead to strong coupling between photon and atom. Further investigation should be made on the quantum state exchange between photon and atom in this SPR system, which may attract broad interest due to its potential applications in quantum information science.

7. Conclusions

In conclusion, a new kind of surface-plasmon-resonance system is proposed which is based on EIT effect of atomic medium. It is found that this system has remarkable quantum properties, i.e. can be extremely sensitive to the small variations of the quantum properties of the detected matters such as their energy-level shifts, and therefore may be used for novel sensors for detecting quantum state of matters, novel magnetometers with subwavelength resolution, and nano-optical devices for quantum information processing.

Acknowledgement

This work is supported by the National Natural Science Foundation of China (Grant No. 10504016) and partially supported by the 973 program (Grant No.2010CB922904) of the Ministry of Science and Technology (MOST), China.

References

[1] M. Fleischhauer, A. Imamoglu, J.P. Marangos, Electromagnetically induced transparency: Optics in coherent media, *Rev. Mod. Phys* 77: 633–673, 2005.

[2] C.H. Raymond Ooi, C.H. Kam, Controlling quantum resonances in photonic crystals and thin films with electromagnetically induced transparency, *Phys .Rev. B* 81: 195119, 2010.

[3] C.G. Du, H.Y. Chen, S.Q. Li, Quantum left-handed metamaterial from superconducting quantum-interference devices, *Phys. Rev. B* 74: 113105, 2006.

[4] A. Kamli, S.A. Moiseev, B.C. Sanders, Coherent Control of Low Loss Surface Polaritons, *Phys. Rev. Lett.* 101: 263601, 2008.

[5] I. Abdulhalim, M. Zourob, A. Lakhtakia, Surface Plasmon Resonance for Biosensing: A Mini-Review, *Electromagnetics* 28: 214–242, 2008.

[6] D. A. Steck, Sodium D Line Data, available online at http://steck.us/alkalidata (revision 2.1.4, 23 December 2010).

[7] L.V. Hau, S.E. Harris, Z.D. Dutton, C.H. Behroozi, Light speed reduction to 17 metres per second in an ultracold atomic gas, *NATURE* 397: 594–598, 1999.

[8] D.E. Aspnes, Local-field effects and effective-medium theory: A microscopic perspective, *American Journal of Physics* 50: 704–709, 1982.

[9] M.E. Crenshaw, C.M. Bowden, Local-field effects in a dense collection of two-level atoms embedded in a dielectric medium: Intrinsic optical bistability enhancement and local cooperative effects, *Phys. Rev A* 53: 1139–1142, 1996.

[10] H. Raether, *Surface plasmons on smooth and rough surfaces and on gratings*, Springer-Verlag Berlin, pp. 10–18, 118–123 Heidelberg 1988.

[11] A.W. Snyder, J.D. Love, *Optical waveguide theory*, Chap viii. Chapman, London 1983.

[12] I.S. Gradshteyn and I.M. Ryzhik, *Table of integrals, series, and products*, Academic Press, New York 1980.

[13] J. Homola, Electromagnetic Theory of Surface Plasmons, *Springer Ser Chem Sens Biosens* 4: 3–44 (2006).

[14] I.V. Shadrivov, A.A. Sukhorukov, Y.S. Kivshar, A.A. Zharov, A.D. Boardman, and P. Egan, Nonlinear surface waves in left-handed materials, *Phys. Rev. E* 69: 016617 (2004).

[15] E.D. Palik, *Handbook of optical constants of solids*, Academic Press, Orlando, pp.356, 1985.

Main and higher mode absorption dependencies of open semiconductor plasma waveguide on the percentage of heavy holes

A. Bubnelis[1,2], L. Nickelson[1,2]

[1]State Research Institute Center for Physical Sciences and Technology, Vilnius, Lithuania
[2]Vilnius Gediminas Technical University, Lithuania
*corresponding author, E-mail: lucynickelson@gmail.com

Abstract

Abstract—In this work are examined the phase and attenuation constants of open magnetoactive *p*-Ge rod waveguides in the wide frequency range. Our algorithm allows analyzing the very high waveguide losses. Dispersion characteristics of *p*-Ge with two component hole charge carriers waveguide are calculated when the ratio of heavy holes' concentration in the material is equal to 10 %, 40 % and 80 % of the total free carrier concentration. Dispersion characteristics of the main helicon and eight higher helicon modes are presented here. There are the degeneration and the transformation of higher hybrid modes at some heavy holes' concentrations. The waveguide broadbandwidth can be considerably extended due to the fact that the losses of the higher parasitic modes are considerably larger in the comparison to the main mode loss at the certain heavy holes' concentration.

1. Introduction

The solution of Maxwell equations for propagation of electromagnetic (EM) waves in the unbounded magnetoactive semiconductor plasma is carefully analyzed in many works [1, 2]. The EM wave propagation in the metal waveguide filled with magnetoactive semiconductor plasma is also investigated in details, e.g. [3]. On the base of magnetoactive semiconductor plasma waveguides are worked out controllable microwave devices, i.e. phase shifters, modulators, converters, switches, filters [4–6].

The electrodynamical analyze of the open (without a metal screen) magnetoactive semiconductor waveguides is relevant because these waveguides are used in nowadays technologies as various optoelectronic, plasmonic devices and laser system elements [7].

The dependencies of real part of longitudinal propagation constant on the frequency are given in [8] for magnetoactive *p*-Ge and *p*-Si plasma waveguides. In the last article the semiconductor losses were not taken accent.

As the magnetoactive semiconductor plasma usually possesses high losses for this reason the study of loss dependencies on the carrier concentration and frequency are the topic of special interest.

Here we present the dispersion characteristics of open lossy plasma germanium (Ge) cylindrical waveguide when the semiconductor material contains the different percentages of light and heavy holes' carriers. The solution of this boundary problem in the rigorous electrodynamical formulation was fulfilled by the partial area method with using of the Müller's method for the searching of complex propagation constants [9].

Here is presented dependencies of the complex longitudinal propagation constant $\underline{h} = h' - \mathrm{i}h''$, where h' is the phase constant and h'' is the waveguide attenuation constant (losses) on the percentage of light hole N_l and heavy hole N_h concentrations and the operating frequency *f*. The investigation was accomplished for the EM wave with the left-handed circular polarization (looking from EM source) when the azimuthal dependence is expressed by $e^{+i\varphi}$ in the wide frequency range from 5 GHz till 200 GHz. These kinds of EM waves are also called the helicon or the extraordinary waves. We have used our created computer software in the MATLAB language. Here is shown a number of important properties of two component hole *p*-Ge waveguides that can be useful to design controllable microwave devices.

2. Permittivity tensor of magnetoactive *p*-Ge with two component hole carriers

Electrodynamical properties of *p*-Ge semiconductor placed in a constant longitudinal magnetic field are characterized by the relative permittivity tensor $\underline{\ddot{\varepsilon}}_r^{p\text{-Ge}}$ [1, 5]:

$$\underline{\ddot{\varepsilon}}_r^{p\text{-Ge}} = \begin{vmatrix} \underline{\varepsilon}_{xx}^{p\text{-Ge}} & \mathrm{i}\underline{\varepsilon}_{xy}^{p\text{-Ge}} & 0 \\ -\mathrm{i}\underline{\varepsilon}_{xy}^{p\text{-Ge}} & \underline{\varepsilon}_{xx}^{p\text{-Ge}} & 0 \\ 0 & 0 & \underline{\varepsilon}_{zz}^{p\text{-Ge}} \end{vmatrix}, \tag{1}$$

where $\underline{\varepsilon}_{xx}^{p\text{-Ge}}$, $\underline{\varepsilon}_{xy}^{p\text{-Ge}}$, $\underline{\varepsilon}_{zz}^{p\text{-Ge}}$ are the complex permittivity tensor' components:

$$\underline{\varepsilon}_{xx}^{p\text{-Ge}} = \varepsilon_k^{p\text{-Ge}} \left(1 - \sum_{n=1}^{2} \left(\frac{\mathrm{i}\omega_{pn}^2}{\omega} \cdot \frac{(\nu_n + \mathrm{i}\omega)}{(\nu_n + \mathrm{i}\omega)^2 + \omega_{cn}^2} \right) \right), \tag{2}$$

$$\underline{\varepsilon}_{xy}^{p\text{-Ge}} = -\varepsilon_k^{p\text{-Ge}} \sum_{n=1}^{2} \left(\frac{\omega_{pn}^2}{\omega} \cdot \frac{\omega_{cn}}{(\nu_n + \mathrm{i}\omega)^2 + \omega_{cn}^2} \right), \tag{3}$$

$$\underline{\varepsilon}_{zz}^{p\text{-Ge}} = \varepsilon_k^{p\text{-Ge}} \left(1 - \sum_{n=1}^{2} \left(\frac{\mathrm{i}\omega_{pn}^2}{\omega} \cdot \frac{1}{(\nu_n + \mathrm{i}\omega)} \right) \right), \tag{4}$$

where $\omega_{pn}^2 = e^2 N_n / m_n^* \varepsilon_0 \varepsilon_k^{p\text{-Ge}}$ is the plasma angular frequency, $\omega_{cn} = eB_0 / m_n^*$ is the cyclotron resonance angular frequency, $\nu_n = e / \mu_n m_n^*$ is the free carriers average collision frequency, ω is the angular operating frequency. The index n indicates that the frequencies are calculated for the heavy holes ($n = 1$) or for the light holes ($n = 2$). The tensor components (2)–(4) depend on the germanium parameters such as the material lattice permittivity $\varepsilon_k^{p\text{-Ge}}$, the operating frequency f, the magnetic induction B_0 of external constant magnetic field strength and other notations are given in [5].

In the present article we give the results of our calculations for the *p*-Ge waveguide when the semiconductor material has two component charge carriers, i.e. heavy and light holes. The tensor components depend on the percentages of certain kind of holes in the comparison with the total concentration *N*. The total concentration *N* is the sum of the light hole N_l and heavy hole N_h concentrations. The altering of rate N_h / N allows us to change the electrical semiconductor parameters. This makes it possible to select the required waveguide electrodynamical characteristics as the broadbandwidth, the losses, the wavelength and the kind of operating mode.

3. Dependences of the complex propagation constant on the percentage of heavy holes' concentration

Dispersion characteristics of *p*-Ge waveguide are calculated when the ratio of heavy holes' concentration N_h is equal to 10 %, 40 % and 80 % of the total free carrier concentration $N = 4 \cdot 10^{19}\ \mathrm{m}^{-3}$. Calculations were fulfilled for the waveguide with the radius equal to 1 mm, $B_0 = 1$ T, $\varepsilon_k^{p\text{-Ge}} = 16$. The effective mass of *p*-Ge heavy holes is $m_h^* = 0.279 m_e$, the effective mobility is $\mu_h^* = 6.3\ \mathrm{m}^2/\mathrm{V \cdot s}$. The values for the light holes are: $m_l^* = 0.043 m_e$, $\mu_l^* = 40.9\ \mathrm{m}^2/\mathrm{V \cdot s}$.

In Figs 1–6 is given the complex propagation constant dependencies of the main helicon and eight higher helicon modes on frequencies. It is known that the main mode HE_{11} of cylindrical semiconductor waveguide without the external magnetic field B_0 is a hybrid mode with the first and second subscripts equal to 1. As it known the first subscript denotes the number of the EM field variations in the azimuthal direction and the second subscript shows the variations along the waveguide radius [5, 6].

Here are only analyzed modes with the first subscript equal to 1, i.e. the same azimuthal symmetry by φ as the main mode. We do not classify here the investigated hybrid modes of the dissipative gyrotropic waveguide because the mode kind can transform with the changing of frequency.

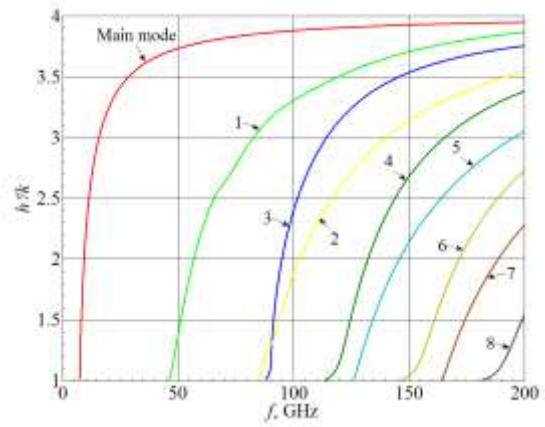

Figure 1: Dependences of waveguide normalized phase constant on the frequency when the heavy holes' concentration is 10 % of the total carrier concentration.

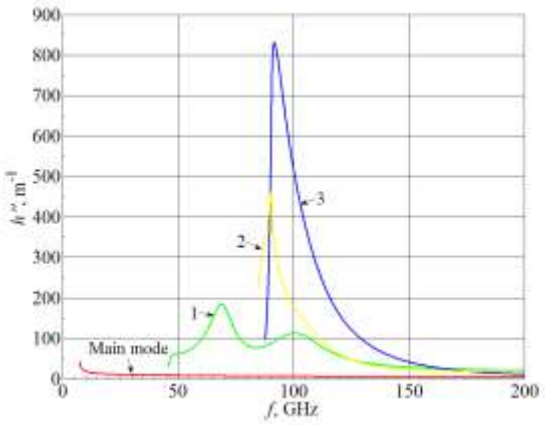

(a)

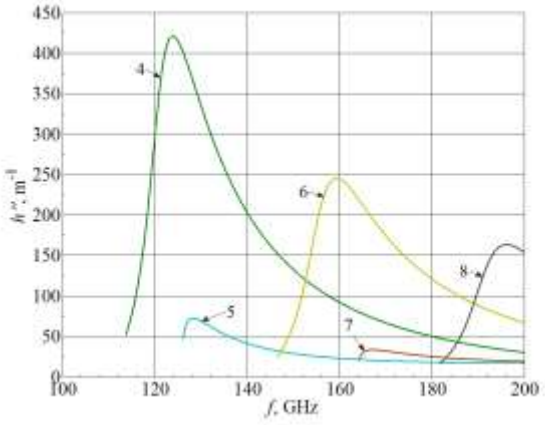

(b)

Figure 2: Dependences of waveguide losses on the frequency when the heavy holes' concentration is 10 % of total carrier concentration.

In Figs 1, 3, 5 we present the normalized real part h'/k of complex propagation constant $\underline{h}$, where k is the wave-number in a vacuum.

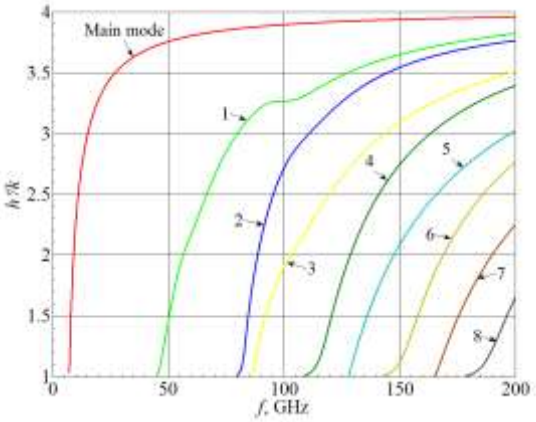

Figure 3: Dependences of waveguide normalized phase constant on the frequency when the heavy holes' concentration is 40 % of the total carrier concentration.

The cutoff frequency f_{cut} of the main mode is 7.5 GHz, 7.24 GHz and 6.74 GHz when the heavy holes' concentration is 10 %, 40 %, 80 % of N, respectively (Figs 1, 3, 5). The cutoff frequency of the main mode with increasing of rate N_h/N slowly moves to the lower frequencies. The broadbandwidth of the p-Ge waveguide is equal 128 % (Fig. 1), 129 % (Fig. 3), 135 % (Fig. 5), respectively.

We have examined the dispersion characteristics at the heavy holes' concentration from 0 till 100 % with the step equal to 5 %. On this risen we can note the general properties of the dispersion characteristics dependent on concentration N_h. We have observed the transformation of waves with a change of values N_h and f. As an example in Fig. 1 we can see the intersection of the second and third higher modes' curves at $f = 90.5$ GHz. This means that the degeneration of second and third modes is observed at this frequency. The transformation of these modes occurs at frequencies higher than 90.5 GHz because the second subscript values of these higher modes change by the places.

In Figs 2, 4 and 6 are presented the waveguide losses. Loss graphs are separated in two parts for the larger clarity. In Figs 2a, 4a and 6a are shown the main and three higher mode losses. These modes are denoted by numbers 1, 2, 3. In Figs. 2b, 4b and 6b are shown other five higher modes' losses. The fourth higher mode is denoted by a number 4 and so on. In Figs 2a, 4a, 6a we see that the loss of the main mode are much lower than losses of all higher modes in the entire frequency range. It is important to note that the first higher mode loss is higher than the main mode loss for all value N_h. Because the higher modes losses are significant this fact can be used to extend the broadbandwidth of the waveguide. Initially the first higher mode loss grows till the maximum and then this loss slowly diminish with the growth of frequency. The maximum of the first higher mode loss is $h''_{\max} = 184$ m^{-1} ($f = 69$ GHz) at the N_h equal to 10 %, 405 m^{-1} ($f = 99$ GHz) at the N_h equal to 40 %, 1305 m^{-1} ($f = 102.7$ GHz) at N_h equal to 80 % of N.

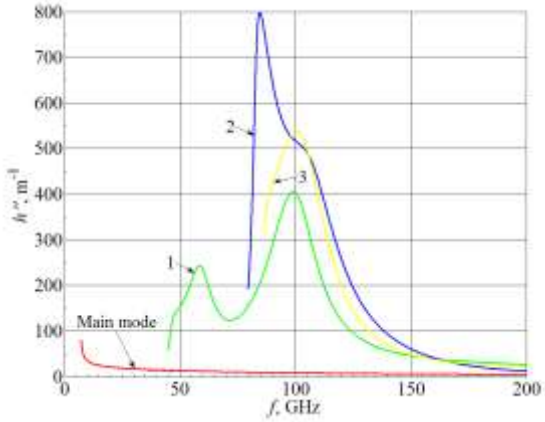

(a)

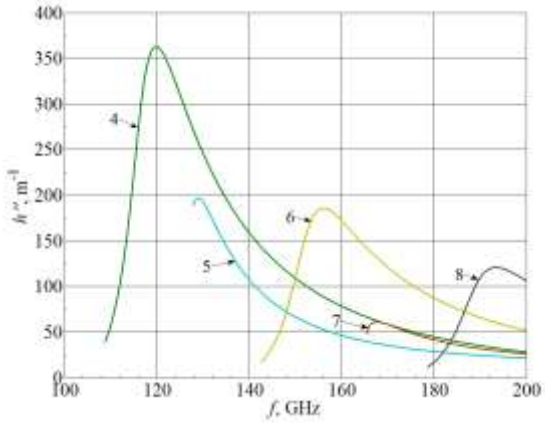

(b)

Figure 4: Dependences of waveguide loss on the frequency when heavy holes' concentration is 40 % of total carrier concentration.

The second and third higher modes' curves detach and degeneration is removed when the heavy holes' concentration is grown till 40 % and higher. The third higher mode' cutoff frequency changes noticeably (Fig. 3) in the comparison with the same mode f_{cut} of the previous case (Fig. 1).

We see that the first and second higher mode curves intersect at $f = 101.4$ GHz when the heavy holes' concentration is 80 % (Fig. 5). The transformation of these higher modes is happened at the frequencies higher than 101.4 GHz. We see that the maximum peak magnitude grows with the increasing of N_h. This behavior of the first higher mode loss points that this mode attenuates in the waveguide in a natural way. This means that the waveguide broadbandwidth additionally increases because of the sufficiently rapid attenuation of the first parasitic higher mode.

The relation of the main mode loss at the specified frequencies and the smallest loss of every higher parasitic mode is quite large.

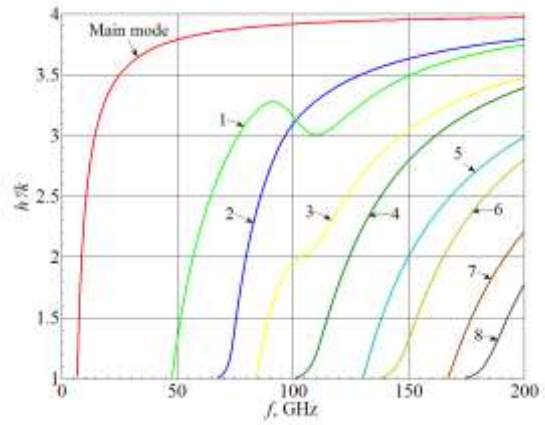

Figure 5: Dependences of waveguide normalized phase constant on the frequency when the heavy holes' concentration is 80 % of the total carrier concentration.

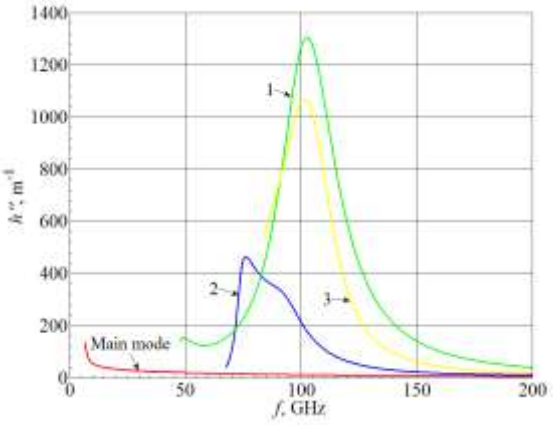

(a)

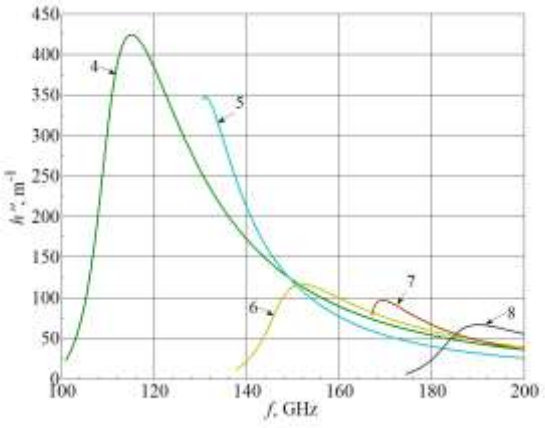

(b)

Figure 6: Dependences of waveguide loss on the frequency when heavy holes' concentration is 80 % of total carrier concentration.

The relation minimum at $N_h/N = 0.4$ is approximately equal to 4 (at $f = 46$ GHz and 200 GHz) and the relation maximum is 48 (at $f = 99$ GHz). Similar relationships of losses are also observed with other percentages of the heavy holes. The large difference loss of main and higher parasitic modes contributes to development of broadbandwidth devices.

Conclusions

1. The dispersion characteristics of open cylindrical semiconductor plasma *p*-Ge waveguides were investigated by using of our computer code that was written in MATLAB language. The computer code is based on the method of the partial area method. Our code allows analyzing the very high losses of waveguide (see Fig. 6a).

2. Here we present calculated dependencies of the phase and attenuation constants of the magnetoactive *p*-Ge waveguide with two component hole charge carriers on the percentage of the heavy holes' concentration in the wide frequency range 5–200 GHz (Figs 1–6).

3. Here is shown that can be the degeneration and the transformation of the higher hybrid helicon modes at same percentage of the heavy holes' concentration and frequencies (Figs 1 & 5).

4. We discovered that the main mode loss is very small and the maximum loss peak of the first higher mode grows with the increasing of the heavy holes' concentration (Figs 2a, 4a & 6a). It promotes the expansion of the waveguide broadbandwidth.

References

[1] E. D. Palik, J. K. Furdyna, Infrared and microwave magnetoplasma effects in semiconductors, *Reports Progress in Physics*, 33: 1193–1322, 1970.

[2] A. C. Baynham, Magnetoplasma wave propagation in the two-carrier system provided by p-type semiconductors: a study of the transport properties of *p*-type germanium using magnetoplasma waves, *J. Phys. C: Solid State Phys* 1: 1447–1454, 1968.

[3] S. Liu, L. W. Li, M. S. Leong, T. S. Yeo, Theory of gyroelectric waveguides, *Progress In Electromagnetics Research* 29: 231–259, 2000.

[4] N. Sujuki, S. Yokoshima, Plasma processing apparatus having circular waveguide and plasma processing method, *Patent No US 6,652,709 B1*, Nov. 25, 2003.

[5] L. Nickelson, S. Asmontas, V. Malisauskas, V. Shugurov, *The open cylindrical gyrotropic waveguides*, Technika, Vilnius (in Lithuanian), 2007.

[6] J. A. Kong, *Electromagnetic Wave Theory*, EMW publishing, Cambridge, Massachusetts, USA, 2008.

[7] J. Ballato, T. Hawkins, P. Foy, S. Morris, N. K. Hon, B. Jalali, R. Rice, Silica-clad crystalline germanium core optical fibers, *Optics Letters* 36: 687–688, 2011.

[8] L. Nickelson, S. Asmontas, V. Malisauskas, R. Martavicius, The dependence of open cylindrical magnetoactive *p*-Ge and *p*-Si plasma waveguide mode cutoff frequencies on hole concentrations, *Journal of Plasma Physics* 75: 35–51, 2009.

[9] S. Asmontas, L. Nickelson, A. Bubnelis, R. Martavicius, J. Skudutis, Hybrid Mode Dispersion Characteristic Dependencies of Cylindrical Dipolar Glass Waveguides on Temperatures, *Electronics and Electrical Engineering* 106: 83–86, 2010.

We want that our paper to be considered for publication in journal Advanced Electromagnetics (AEM)

Nanocomposite C-Pd thin films – a new material with specific spectral properties

Małgorzata Suchańska[1], Hovik Baghdasaryan[2], Justyna Kęczkowska[1*]

[1] Kielce University of Technology, al. 1000 –lecia P.P. 7, 25-314 Kielce, Poland
[2] State Engineering University of Armenia, 105 Terian str, Yerevan 0009, Armenia
[*]corresponding author: j.keczkowska@tu.kielce.pl

Abstract

In this paper, the results of optical investigations for thin films of carbon-palladium (C-Pd) nanocomposites are presented. This films were prepared using two steps method (PVD/ CVD). The optical and Raman spectroscopy has been used to characterize the material. The multinanolayer model was used to explain the specific spectral properties.

1. Introduction

Findings of novel materials with specific spectral properties are very interesting from both fundamental and technological points of view and will inspire designs of new photonic devices.

Nanocomposite C-Pd thin films are interesting objects of studies thanks to their electrical features [1,2]. However, there is much less information concerning the optical properties of such structures. For this reason, the preparation and studies of carbon-metallic nanocomposites are becoming vital for seeking materials with controllable band structure and optical properties. In recent years new nanocomposites containing palladium and carbon nanostructures have been prepared in Poland [3, 4]. Optical and electrical properties of these carbon-palladium samples (C-Pd samples) have been investigated first by our group [2, 5, 6].

In this paper the study of dependences between the nanocomposite structure and its spectral properties were performed using optical transmission spectroscopy (OS) and Raman Spectroscopy (RS). An attempt of theoretical approach to facilitate understanding of specific sprectral properties of nanocomposite C-Pd thin film in UV-NIR range is presented.

2. Experimental

The technology of obtaining C-Pd films using the two-step method was developed in the Tele & Radio Research Institute in Warsaw (Poland) [3, 4]. In the first step of the process (PVD –Physical Vapour Deposition method) the films constituting the matrix for structures obtained in the second step (CVD –Chemical Vapour Deposition method) are created. Depending on the technological parameter of each process we obtain films with various weight percentage content of Pd and various structure of carbonaceous matrix. The detailed information on the technological process are described in papers [3,4]. The films obtained in first step (PVD) are carbon-palladium nanocomposites where palladium nanograins are embedded in the carbonaceous matrix [7]. In second step (CVD) the porous structure is obtained [8].

The Raman spectra measurements were carried out using Jobin Yvon-Spex T64000 Raman spectrometer with triple-grid monochromator, equipped with confocal microscope and CCD detector (with the resolution of 1024 x 256 pixels) cooled with liquid nitrogen. For the measurements the single monochromatisation was applied, with Rayleigh dispersion used effectively by Notch-type filters. The measurements were carried out in ambient temperature for the excitation wavelength of 514,5 nm. Acquisition of spectra was performed for spectral range 150 do 3500 cm^{-1}.

The transmission spectra measurement were carried out by means of Cary 5000 dispersion spectrophotometer in the range from 200 – 3500 nm, with the resolution of 1nm.

3. Results and discussion

3.1. Raman study

The Raman spectroscopy investigations of PVD samples give us an information that carbonaceous matrix consists of different allotropic forms of carbon (Fig. 1).

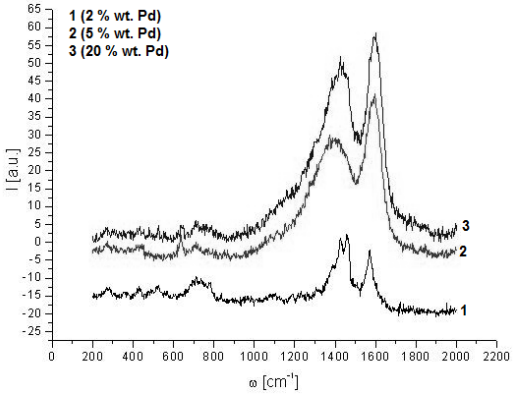

Figure 1. Raman spectra of C-Pd films with different contents Pd (%wt) obtained in PVD method.

In the measured range (from 150 to 2000 cm^{-1}) the bands characteristic of C_{60} fullerene, graphite and amorphous carbon (G and D bands) were observed.

In the Raman spectra for samples obtained using CVD method the D and G bands, as well as the additional bands in the range of 2000-3500 cm^{-1} were observed (Fig. 2).

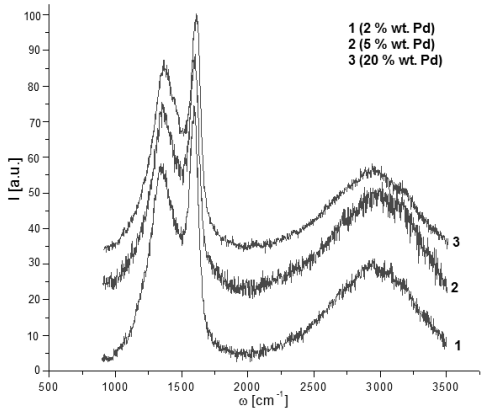

Figure 2. Raman spectra of C-Pd films with different contents Pd (%wt), obtained in CVD method.

To obtain information on the location and intensity of the bands originated of carbonaceous structures, the spectra decomposition was performed using Lorentz function. The spectrum decomposition into bands was carried out using Origin software. The analysis showed existence of two main separated bands, placed at 1336 - 1361 cm^{-1} (D–band) and at 1590 - 1595 cm^{-1} (G–band). To determine the level of graphitization, the intensity ratio I_D /I_G was found. Results of such analysis are presented in Table 1. The I_D/I_G ratio value may indicate the presence of amorphous carbon in the examined samples [9]. The other three bands isolated in the analysis in the range of 2000 - 3500 cm^{-1} may result from the carbon-hydrogen or oxygen-hydrogen interactions [10, 11].

Table 1. Band analysis of Raman spectra for C-Pd nanocomposite obtained in PVD/CVD process using Lorentz function

Sample	D -band		G-band		I_D/I_G
	ω [cm^{-1}]	$\Gamma_{1/2}$	ω [cm^{-1}]	$\Gamma_{1/2}$	
(1)	1357	141	1592	38	0.92
(2)	1361	144	1590	40	0.93
(3)	1364	142	1595	49	0.94

3.2. Optical study

In Fig. 3 the optical transmittance spectra for PVD (1) and CVD (2) samples are presented. A shape of dependence transmittance on wavelength is different for PVD (1) and CVD (2) samples. PVD samples are characterized with a very low absorption coefficient in IR range and a high value of this coefficient in the UV – VIS range. For CVD samples the absorption coefficient in IR range higher them for PVD samples.

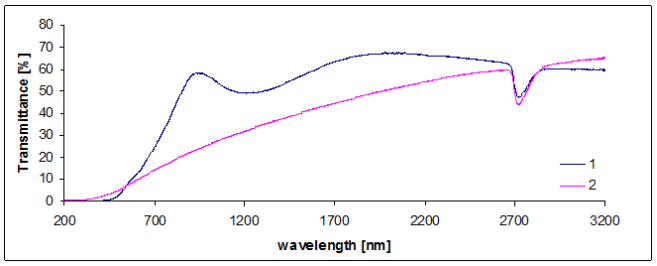

Figure 3. Transmittance spectra of PVD (1) and CVD (2) samples.

UV-VIS spectroscopy of fullerenes indicates the presence of strong absorption bands in the range from 200-400nm, related to the electron transition in C_{60} molecule structure [12]. In our opinion a strong absorption band observed near 2700 nm originate from the silica substrate.

In NIR region the transmittance coefficients are subject to the quasi-periodic modulation resulting from the interference on the boundaries of the carbon-palladium layer. The position of the local minimum and maximum varies for particular samples which may confirm the diversified sample thickness and/or various values of the layer refractive effective coefficient n_{eff}. The minimum optical transmittance coefficient value decreases for the wavelength values where the wave reflected from the layer-air boundary is phase-coincident with the wave reflected on the layer-substrate boundary.

To analyze spectral characteristics of C-Pd nanocomposite (of overall thickness ≈ 300 nm) deposited on SiO_2 substrate (≈1mm thickness) is suggested to exploit multinanolayers approach. For this analysis the method of single expression was used [13].

3.3. Theoretical model

For modelling metal-dielectric nanocomposites the well known approach of effective permittivity (so called Maxwell Garnet approach) has been used [14, 15]. This approach is applicable exclusively for spherical nanoparticles at low weight ratio [14, 15]. Microscopic analysis of C–Pd nanocomposites indicates, that the forms (shapes) of Pd nanograins in C–Pd nanocomposites are far to be spherical [8], what makes the Maxwell Garnet approach inadequate for C-Pd nanocomposites treatment.

In the present work as an alternative is suggested to model thin film C-Pd nanocomposite using an appropriate multinanolayer structure. The model of the nanocomposite nanolayers of C, Pd and air pores was established in arbitrary way and many possible nanolayers alternations have been considered. Average values of reflectance and transmittance coefficients were analyzed in context of consistency with the experimental results. An advantage of this model is the correct solution of boundary problem by taking into account the thickness of substrate and boundaries of all nanolayers.

It was observed, that application of known values for permittivity of the bulk palladium [16] brings to the strong discrepancy with experimental results. The difference in permittivity value of nanoparticles and bulk material is discussed in [13]. An influence of the shape of metallic

nanoparticles on its permittivity value was also discussed in [15, 17, 18].

In our model we consider the normal incidence of plane electromagnetic wave on a thin nanocomposite layer located on the SiO_2 substrate. The nanocomposite is represented as a multinanolayer structure with random alternation of C, Pd and air pore nanolayers. The thickness (L) of constituting nanolayers has been varied:

$$L_{C60} = 20 - 40 \text{ nm} \quad (1)$$

$$L_{Pd} = 10 - 30 \text{ nm} \quad (2)$$

$$L_{\text{air pores}} = 10 - 30 \text{ nm} \quad (3)$$

In Fig. 4 an example of the modeling for normal incidence of plane electromagnetic wave (from the left to right) on the multinanolayer structure (L> 300 nm) located on the substrate (L=500nm), is presented.

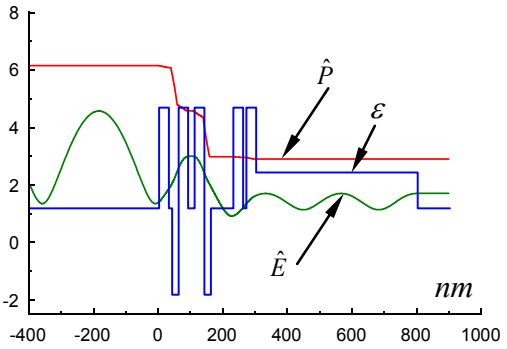

Figure 4. Distributions of values of permittivity ε, amplitude of electric field $\hat{E}$ and power flow density $\hat{P}$ within and out of the structure.

The wavelength of incident wave is:

$$\lambda_0 = 700 \text{ nm} \quad (4)$$

$$\varepsilon_{sub} = 2.25 \quad (5)$$

$$\varepsilon'_{C60} = 4.5 \quad (6)$$

$$\varepsilon''_{C60} = -0.1 \quad (7)$$

$$\varepsilon'_{Pd} = -2 \quad (8)$$

$$\varepsilon''_{Pd} = -1.5 \quad (9)$$

$$L_{C60} = 30 \text{ nm} \quad (10)$$

$$L_{Pd} = 20 \text{ nm} \quad (11)$$

$$L_{air-pores} = 10 \text{ nm}. \quad (12)$$

For the considered structure the reflectance and transmittance are $R = 0.2967$ and $T = 0.3305$ correspondingly. For the wavelengths near infrared the main loss takes place in Pd nanolayer, what is visible as the sharp decrease of power flow $\hat{P}$ in Fig. 4.

The modelling indicated conditions when an agreement with the experiment is possible:

- a value of complex permittivity for Pd nanograins should be lower than value of permittivity for bulk Pd [eg. 16];
- the values of complex permittivity of C_{60} fullerene, known from the literature [19], are satisfactory for modelling.

The outcome from the modelling:

- the nanograins Pd having an arbitrary shape cannot be modeled by using the permittivity value for bulk Pd;
- the main contribution in loss within the structure is stipulated by C_{60} fullerene presence what was observed as low transmittance in UV range (200- 400nm) and in increase of transmittance at IR range;
- the difference in transmittance for PVD and CVD structures is stipulated by the presence of air pores in CVD structures. Within the air pores the field amplitude is higher relatively to the other nanolayers of a structure. This brings to the increase of loss in neighbour layers of C_{60} fullerene and Pd nanograins;
- an observed in experiments sharp decrease of transmittance at 2700nm (in Fig. 3) is not stipulated by the structure and rather by the specific chemical composition of the substrate.

4. Conclusions

In conclusion, the suggested model of multinanolayer structure is pertinent for analysis thin films of metal-dielectric nanoporous materials and can be considered as an alternative to the well-known methods of modelling.

Based upon our experiments we can conclude that advantage of nanocomposite C-Pd thin films is a unique opportunity to monitoring optical properties by technological parameters. Theoretical analysis of the results and further research would be also useful for better understanding specific optical properties of nanocomposite carbon–metal composite thin films.

Acknowledgements

This research was performed in the framework of the EU COST Action MP0702 and financed by Polish Ministry of Science and Higher Education (577/N-COST/2009/0 research project).

References

[1] E. Czerwosz,P. Dłużewski, J. Kęczkowska, M. Kozłowski, M.. Suchańska and H. Wronka, Palladium nanocrystals and their properties, *Materials Science-Poland* 26: 119-125, 2008.

[2] E. Czerwosz, Badania zmian własności przewodnictwa elektrycznego warstw palladowo-węglowych pod wpływem gazów zawierających związki wodoru, *Przegląd Elektrotechniczny* 10: 61-64, 2010 (in Polish).

[3] M. Kozłowski, R. Diduszko, K. Olszewska, H. Wronka and E. Czerwosz, Nanostructural palladium films for sensor applications, *Vacuum* 82: 956-961, 2008.

[4] E. Kowalska, E. Czerwosz and J. Radomska, Metoda syntezy nanoporowatych materiałów węglowo-palladowych, *Elektronika* 1: 32-35, 2009 (in Polish).

[5] R. Belka, M. Suchańska, E. Czerwosz, A. Chiasera and M. Ferrari, The optical study of nanoporous C=Pd thin films, *Proceeding of SPIE* 7502: 750223, 2011

[6] E. Kowalska, E. Czerwosz, M. Kozłowski, W. Surga, J. Radomska, H. Wronka, Structural, thermal, and electrical properties of carbonaceous films containing palladium nanocrystals, *J. Therm. Anal Calorim.* 101:737–742, 2010.

[7] E. Czerwosz, R. Diduszko, P. Dłużewski, J. Kęczkowska, M. Kozłowski, J. Rymarczyk, M.Suchańska, Properties of Pd nanocrystals prepared by PVD metod, *Vacuum* 82: 372 -376, 2008.
[8] J. Rymarczyk, M. Kozłowski, E. Czerwosz, E. Kowalska, Badania mikroskopowe nanostrukturalnych warstw palladowo-węglowych otrzymywanych w dwu stopniowej metodzie PVD/CVD, *Elektronika* 6: 46-52, 2010 (in Polish).
[9] A. C. Ferrari, J. Robertson, Interpretation of Raman spectra of disordered and amorphous carbon; *Physical Review B* 61: 14095–14107, 2000.
[10] P. K. Chu, L. Li: Characterization of amorphous and nanocrystalline carbon films; *Materials Chemistry and Physics* 96: 253–277, 2006.
[11] M. Yoshikawa, G. Katagiri, H. Ishida, A. Ishitani, T. Akamatsu, Raman spectra of diamond like amorphous carbon films, *J. Appl. Phys*. 64: 6464–6468, 1988.
[12] G. Orlandi, F. Negri, Electronic states and transitions in C_{60} and C_{70} fullerenes*, Photochem. Photobiol. Sci*. 1: 289-308, 2002.
[13] H. V. Baghdasaryan, T.M. Knyazyan, Problem of Plane EM Wave Self-action in Multilayer Structure: an Exact Solution, *Optical and Quantum Electronics* 31: 1059-1072, 1999.
[14] J.C. Maxwell Garnet, *Phil. Trans*. 203: 385, 1904; ibid. 205: 237, 1906.
[15] O.S. Heavens, Optical properties of thin solid films, *Dover publ. Inc*., 1991.
[16] http://refractiveindex.info
[17] P.N. Prasad, *Nanophotonics*, Wiley-Interscience, 2004.
[18] S.V. Gaponenko, *Introduction to Nanophotonics*, Cambridge University Press, 2010.
[19] K.H. Hiromichi et.al, Dielectric constants of C_{60} and C_{70} – thin films, *J. Phys. Chem. Solids*, 58: 19-23, 1997.

Optimal structure for Resonant THz Detection of Plasmons-Polaritons in the 2D quantum wells

L. Cao, A.-S. Grimault-Jacquin*, and F. Aniel

[1]Institut d'Electronique Fondamentale, CNRS UMR 8622 Université Paris Sud 91405 Orsay cedex, France
*corresponding author: anne-sophie.grimault@u-psud.fr

Abstract

We investigate terahertz plasmon-polariton (PP) resonances for hetero-structures (AlGaN/GaN, SiGe/ Si/SiGe, AlGaAs/ GaAs and InAlGaN/ GaN) with grating coupler in order to find the overall optimal structure showing the strongest absorption. We show by a parametric study (influence of geometry, temperature…) that the resonances are tunable in frequency allowing to a control of the terahertz detection and GaN based heterostructures present the higher PP resonances at room temperature. The non uniform 2DEG distribution function in the gated and ungated regions is used for the structure AlGaAs/GaAs and its absorption spectrum is compared with that of homogeneous 2DEG. Moreover, the effect of the metallization biasing on the spectrum has also been studied, showing that the resonant frequency is tunable.

1. Introduction

Two dimensional electron gas (2DEG) presents a growing interest in the Terahertz (THz) frequency range for the development of compact, tunable, room temperature operating, cheap sources and detectors [1]. The high electron concentration and large electron mobility value are the main advantages of 2DEG confined in heterostructures. Such devices are based on plasmon–polariton (PP) properties. The coupling between the two dimensional plasmon and the electromagnetic (EM) field is the key issue to be solved. PP can be excited through a metal grating deposited above heterostructures. The existence of metal modifies the carrier concentration in the quantum well (QW) in a varying degree depending on the Fermi level pinning at the free semiconductor surface compared with the barrier height below the metallization. The non uniform 2DEG can change the properties of the resonant peaks in the absorption spectrum and influence the coupling efficiency.

This article deals with the coupling effect between incident EM wave and 2D plasmons in four typical hetero structures in order to find out the best material. Section 2 demonstrates the homogeneous 2DEG calculation model based on the Drude type conductivity. The absorption spectrum is compared by the commercial code ANSOFT HFSS [2] based on finite element method (FEM) and an indigenous program based on the coupled wave method (CWM) [3]. The results of the parametric study of the influences of structure, material and temperature properties on the PP excitation strength are shown with HFSS for the four materials. In section 3, the non uniform 2DEG distribution is considered for the structure AlGaAs/GaAs, and the effect of polarization on the absorption spectrum is evaluated using the CWM code. Section 4 gives the general conclusions and perspectives of this work.

2. Homogeneous 2DEG

2.1. Modeling of homogeneous 2DEG

The modeling of the 2DEG can be addressed through an anisotropic permittivity of the layers [4] or through a sheet Drude conductivity as in [5]. Both approaches were compared and provided the same results. For a typical hetero-structure, such as AlGaAs/GaAs shown in Figure 1, the 2DEG thickness is usually a dozen of nanometers. In order to couple the normally incident electromagnetic wave in THz frequency range, the periodic metal gratings are deposited at a distance of d from the 2DEG layer. The width of the metal strip is denoted as W and L is the period of gratings. The thickness of the grating metallization is 200 nm and the conductivity of gold is supposed to be $\sigma_{GOLD}=4.1\times10^7$ S/m. Electric field is polarized along the x axis, and the whole structure is assumed to be infinite in the y direction.

The electrons in the QWs can move freely in the x-y plane while their wavevector is quantified along the growth axis. Its anisotropic permittivity component ε_{xx} is modeled according to the Drude type conductivity σ_{3D} , while ε_{zz} is kept as the static permittivity of the background material where 2DEG lies. No absorption is considered in both the barrier and substrate layers.

$$\varepsilon_{xx}(x\,|\,\omega)=\varepsilon_{yy}(x\,|\,\omega)=\varepsilon_s+\frac{i\sigma_{3D}(x\,|\,\omega)}{\omega\varepsilon_0},\ \varepsilon_{zz}=\varepsilon_s \qquad (1)$$

and

$$\sigma_{3D}(x\,|\,\omega)=\frac{N_s(x)e^2\tau}{m^*d_{2DEG}(1-j\omega\tau)}$$

where ε_s is the relative permittivity of the substrate, ε_0 is the permittivity in vacuum, $N_s(x)$ is the sheet carriers density in function of the position x in the gas layer, d_{2DEG} is

the thickness of QW, $\tau = \mu_{2DEG} m^* / e$ is the momentum relaxation time, μ_{2DEG}, m^* and e are the mobility, effective mass and unit charge of an electron respectively.

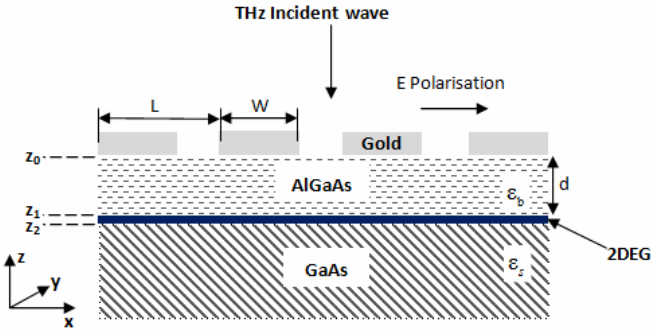

Figure 1: Calculation model for AlGaAs/GaAs nominal structure.

The PP resonances depend on the grating period (L), the aspect ratio (W/L where W is the finger length of the grating), the distance (d) between gratings and QWs, and the sheet carriers density (Ns). Besides AlGaAs/GaAs, the PP performances of other three hetero structures will be studied at room and cryogenic temperatures. The parameters of the standard structures including a 12 nm QW thickness are reported in Table 1. For the convenience of comparison, the first resonant peak position is fixed at 1 THz, and the different grating periods L are chosen according to the simulation results in the next section. L increases with carrier density N_S of the 2DEG when the barrier thickness d is fixed.

Table 1: Parameters of the four nominal structures

Material	Ns (m^{-2})	L (μm)	d (nm)	μ_{2DEG} @300K (m^2/Vs)	μ_{2DEG} @77K (m^2/Vs)
AlGaN/GaN	1.2×10^{17}	2.2	25	0.2	1.0
InAlN/GaN	1.2×10^{17}	1.55	10	0.11	0.33
SiGe/Si/SiGe	5×10^{16}	1.3	25	0.3	3.2
AlGaAs/GaAs	10^{16}	1.0	25	0.8	5

The dielectric function is not position-dependent $\varepsilon_{xx}(x|\omega)=\varepsilon(\omega)$, when substituting Ns(x)=Ns in the expression (1).Two methods are available for the spectrum calculation (Transmission, Reflection and Absorption) in the multilayer structure with periodic metal gratings:

- Commercial code ANSOFT HFSS based on FEM
- Indigenous program based on transfer matrix method

According to Maxwell equations, for a normal and TM polarized incident wave illustrated in Figure 1, the non zero field components are related in the thin 2DEG layer ($z_2<z<z_1$) by

$$E_x(x;z\,|\,\omega) = \frac{-j}{\omega\varepsilon_0\varepsilon_{xx}(\omega)}\frac{\partial H_y(x;z\,|\,\omega)}{\partial z}$$
$$E_z(x;z\,|\,\omega) = \frac{j}{\omega\varepsilon_0\varepsilon_{zz}}\frac{\partial H_y(x;z\,|\,\omega)}{\partial x} \quad (2)$$
$$H_y(x;z\,|\,\omega) = \frac{1}{j\omega\mu_0}\left(\frac{\partial E_x(x;z\,|\,\omega)}{\partial z} - \frac{\partial E_z(x;z\,|\,\omega)}{\partial x}\right)$$

where μ_0 is the vacuum permeability. Once H_y has been obtained, E_x and E_z could be calculated according to (2). Because of the periodicity of the grating, the EM field can be expressed as a quasi-periodic expansion,

$$H_y(x;z\,|\,\omega) = \sqrt{\frac{\varepsilon_0}{\mu_0}}\sum_{n=-\infty}^{+\infty}\exp(jk_{xn}x)H_{yn}(z\,|\,\omega) \quad (3)$$
$$= \sqrt{\frac{\varepsilon_0}{\mu_0}}\sum_{n=-\infty}^{+\infty}\exp(jk_{xn}x)\left[A_n\exp(-jk_{zn}(z-z_1)) + B_n\exp(jk_{zn}(z-z_1))\right]$$

where A_n and B_n are the incident (-z direction) and reflected (z direction) field amplitude, respectively. The in-plane wave vector are $k_{xn}=k_x+2\pi n/L$, n=0,±1,±2... following the scattering order of grating and the x component of incident wave vector $k_x=0$. The z component of wave vector

$$k_{zn} = \sqrt{\frac{\varepsilon_{xx}(\omega)}{\varepsilon_{zz}}\left(\varepsilon_{zz}\frac{\omega^2}{c^2} - k_{xn}^2\right)} \quad (4)$$

In the numerical realization, the maximum number of scattering waves is truncated. In our simulation, $n_{max} \geq 15$ is sufficient to achieve a good convergence criterion ($\max(\Delta T)<10^{-6}$). The field amplitudes A_n and B_n in each material layer are linked by the boundary conditions. By applying suitable initial conditions, the spectrum are given by the corresponding field amplitudes of the n=0 order wave in the semi-infinite superstrate ($z>z_0$) and substrate ($z<z_2$).

$$T = \frac{\left|A_{n=0}^{substrate}\right|}{\sqrt{\varepsilon_s}\left|A_{n=0}^{air}\right|}, R = \frac{\left|B_{n=0}^{air}\right|}{\left|A_{n=0}^{air}\right|}, A = 1 - T - R \quad (5)$$

The two approaches are in excellent agreement for the absorption spectrum of the nominal AlGaN/GaN structure from 0 to 5 THz shown in Figure 2.

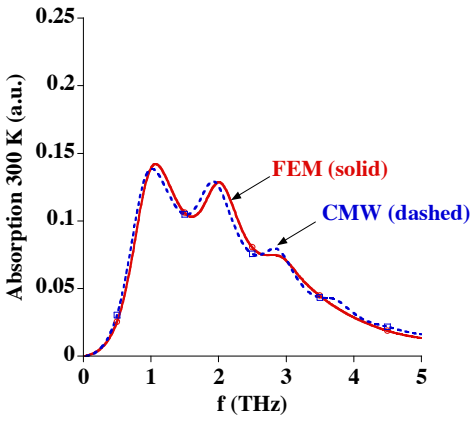

Figure 2 Comparison of the two numerical methods: Absorption spectrum of the nominal AlGaN/GaN structure at 300 K, where L=2.2μm, W/L=0.75 and $N_s=1.2\times10^{17}$ m^{-2} (solid line: HFSS(FEM), ΔS=0.005 broken line: CMW, n_{max}=25)

2.2. Absorption spectrum

In this section, we present the numerical results of the PP resonances at 300 K and 77 K for the four nominal hetero-structures with HFSS, where the electron concentration is uniform as listed in Table 1.

The main results are that, in order to have a strong PP excitation, we should have high Ns and a relatively small d. A large d distance allows a strong decrease of the evanescent waves at the vicinity of metal gratings, however,

a too small d distance will also reduce the coupling efficiency because of the screening effect of metals) and great W/L (0.25-0.9 in the simulation) [see also in Ref.8]. Here we find the optimal structure which has the maximum PP absorption amplitude among the four nominal materials at different temperatures.

Figure 3 (a) and (b) present the absorption spectra for each material at 300 K and 77 K. Each spectrum was normalized by the equivalent spectrum of the incident wave. The role played by the grating and the quantum well must be carefully separated to isolate the very intrinsic contribution of the PP on the absorption signal. The first peak is located at 1THz while the other resonances can shift slightly from 2 or 4 THz. The PP resonances are more pronounced and are narrower as the low field electron mobility, μ improves. Low temperature increases the resolution of PP resonance without modifying PP dispersion. This is because that, for resonant excitation, the quality factor $\omega\tau$ is improved (narrow peak) and the 2DEG dielectric function is nearly unchanged according to equation (1). Among the different studied hetero-structures, the optimal PP resonance in amplitude and width at half height at 1 THz is obtained for InAlN/GaN quantum well. However, the structure AlGaAs/GaAs and SiGe/Si/SiGe also show equivalent resonant amplitudes at 77 K because of the greater increase of carrier mobility.

The PP dispersion shows the frequency is proportional to the square root of the in-plan wave vector k_{xn}. Figure 4 shows the first resonant frequency position f_1 versus the grating period L, where the relation [9,10] $f_1 \sim \sqrt{k_{x1}} \sim \frac{1}{\sqrt{L}}$ holds. The frequency can be tuned in the 0.5~3 THz frequency range through the gratings period in the micron range. The different L values listed in Table 1 have been chosen in such way, that all the structures exhibit the same f1=1 THz first absorption resonance peak.

3. Non uniform 2DEG

In most publications dealing with the PP resonances with metal gratings, the carrier concentration is considered to be constant with the position in x direction. Strictly speaking, due to the different Fermi levels pinning at the interfaces metal/semiconductor and air/semiconductor, the electron density will vary within one period.

The electron density distribution in 2DEG layer with and without metals on top of the structure can be calculated numerically by a self consistent one dimensional Poisson-Schrödinger solver in the frame of the envelope approximation and of the effective mass [11,12].

The Au/Ti barrier height on the AlGaAs layer is 0.85 eV [13] will the surface potential is chosen equal to 0.65 eV in the ungated region. For the two hetero structures based on group III-nitride layers, the Fermi level pinning does not vary greatly in the two regions then the approximation of a homogeneous 2DEG distribution is reasonable. Concerning the surface Fermi level of the strained Si/SiO2 interface as far as we know no measurements data are available.

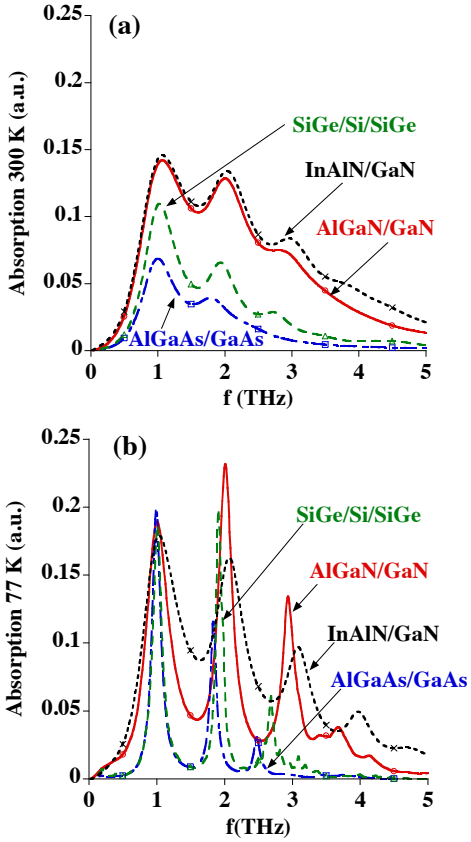

Figure 3: Absorption spectra for the four nominal materials at (a) 300 K and (b) 77 K.

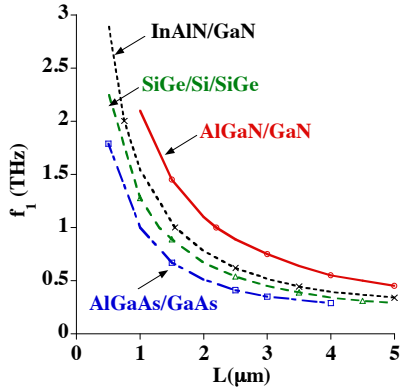

Figure 4: Tunability of grating period on the first resonant peak position for the four nominal materials at 300 K.

Then only the AlGaAs/GaAs heterostructure will be considered for the non homogeneous 2DEG modeling with the homemade program.

By applying a V_G bias on the meal and the density N_1 (see Figure 6) will be altered accordingly. The tunability of the resonance frequency in the absorption spectrum can be possibly realized by varying the applied bias, as it will be shown by the modeling.

The calculated wave function and energy bands are displayed in Figure 5 and sheet carrier concentration N_1 is

listed in Table 2 with varying voltage. V_G=0.2V gives a homogeneous 2DEG (N_1=N_2) and the values around 0.2V will alter slightly N_1. Large negative V_G can greatly reduce N_1. In the simulation, the doping level N_D=2×10^{19}cm^{-3} in a 2 nm thickness $Al_{0.3}Ga_{0.7}As$, which is separated by a 3 nm NID $Al_{0.3}Ga_{0.7}As$ layer from the NID GaAs surface. The total thickness of AlGaAs is 25 nm.

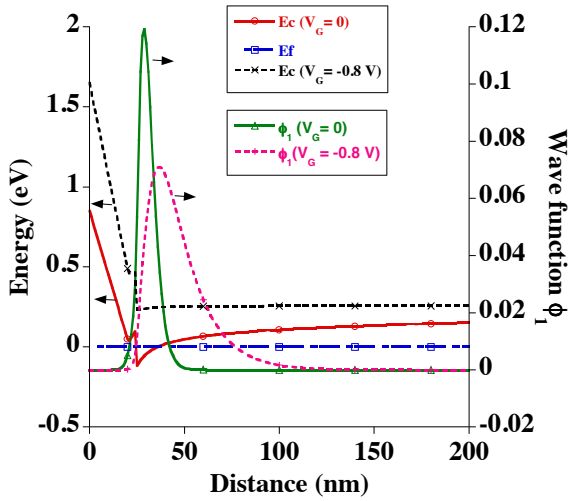

Figure 5 Calculated wave function and energy bands in AlGaAs/GaAs for the two cases: V_G=0 and V_G=-0.8V

Table 2: Electron sheet concentration N_1 in the gated region with applied voltage V_G (V) for AlGaAs/GaAs structure, where N_2=1.65×10^{16} m^{-2}.

V_G(V)	N_1 (m^{-2})
0.4	1.72×10^{16}
0.2	1.65×10^{16}
0	1.28×10^{16}
-0.5	0.71×10^{16}
-0.8	0.12×10^{16}

3.1. Modeling of PP with a non uniform 2DEG

Three types of 2DEG concentration profiles functions (piecewise constant, linear and parabolic) have been used to calculate the absorption spectrum of AlGaAs/GaAs structure, which is shown in Figure 6.

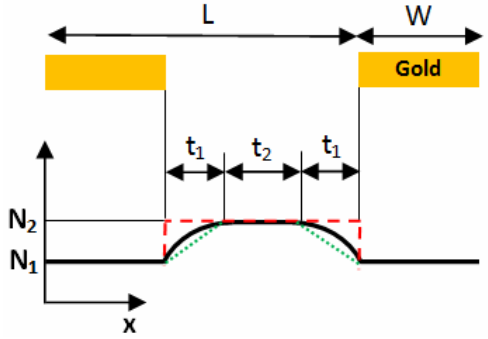

Figure 6 (color online) Parabolic (solid), linear (dotted) and piecewise constant (broken) one dimensional distribution profile of electron concentration in 2DEG layer

When Ns varies with x, the 2DEG permittivity ε_{xx} will become position dependent within a period. The coupled wave method (CMW) [3,6] is employed to find the wave vector and electromagnetic field in the 12 nm thick 2DEG layer. Because of the periodic metal on top of the structure, the carrier distribution function is supposed to be periodic with the same periodicity L. The Fourier expansion of the dielectric function ε_{xx} in this layer is:

$$\varepsilon_{xx}(x\,|\,\omega) = \sum_{n=-\infty}^{+\infty} \varepsilon_n(\omega)\exp(j\frac{2\pi n}{L}x) \qquad (6)$$
$$\varepsilon_n(\omega) = \frac{1}{L}\int_0^L \varepsilon_{xx}(x\,|\,\omega)\exp(-j\frac{2\pi n}{L}x)dx$$

The wave vector dependent permittivity ε_n is given by the integral of the position dependent permittivity ε_{xx} in one period of the gratings. After substituting (6) into (2) and doing the Fourier expansion described in Ref.6 to get better numerical convergence, we arrive at an eigenvalue problem in matrix form for solving the z-component of the wave vector in the 2DEG region. Once the wave vector and EM distributions are calculated in the 2DEG layer, the spectrum can be obtained based on the standard procedures as in the above case with homogeneous 2DEG.

For piecewise constant distribution, the sheet concentrations of 2DEG in the gated and non gated portion of one grating period are constant and assigned as N_1 and N_2 respectively.

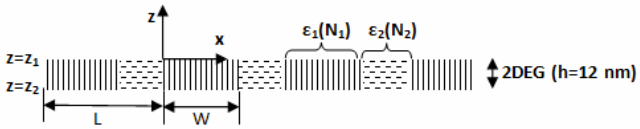

Figure 7 Piecewise constant periodic permittivity in 2DEG layer

As illustrated in the Figure 7, the periodic permittivity ε_{xx} is expressed as

$$\varepsilon_{xx}(x\,|\,\omega) = \begin{cases} \varepsilon_1(\omega), mL < x < mL + W \\ \varepsilon_2(\omega), mL + W < x < (m+1)L \end{cases}, \qquad (7)$$

Where $\varepsilon_1(\omega)$ and $\varepsilon_2(\omega)$ are calculated by substituting N_1 and N_2 into equation (1) accordingly, m is an integer.
And the Fourier component ε_n is given by equation (6)

$$\varepsilon_n(\omega) = \begin{cases} \frac{W}{L}\varepsilon_1(\omega) + \frac{L-W}{L}\varepsilon_2(\omega) & n = 0 \\ \left(\varepsilon_1(\omega) - \varepsilon_2(\omega)\right)\frac{1-\exp(-j\frac{2\pi n}{L}W)}{j2\pi n} & n \neq 0 \end{cases}, \qquad (8)$$

For the linear and parabolic 2DEG distribution function, the integral in equation (6) should be solved numerically to find the values ε_n. The present modeling approach remains local further investigations require a non local model based on Green functions.

3.2. Results and discussions

In Figure 8, the three types of 2DEG profile functions are compared for the AlGaAs/GaAs structure at room temperature. The sheet density $N_1=1.28\times10^{16}$ m^{-2} with $V_G=0$. The spatial extension of the transition zone has been calculated: t_1 =20 nm (Figure 6), connecting the two adjacent regions with constant 2DEG concentrations. The absorption at low frequencies is attributed to the Drude absorption background, where the metal gratings do not exist. The three models show exactly the same spectrum, and this is due to the connection region width t_1 (20 nm) is very small comparing with the gap width L-W (250 nm in minimum). For the easiness of calculation, only the piecewise constant model is utilized for the structure AlGaAs/GaAs.

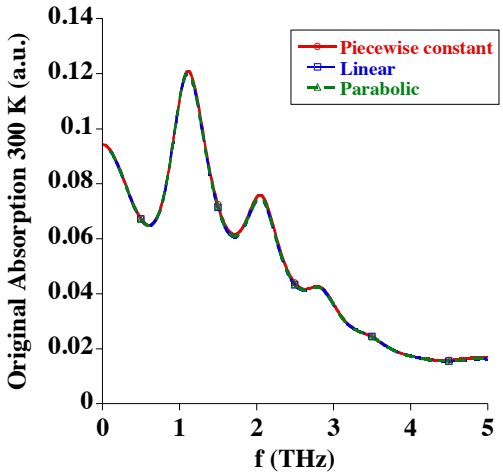

Figure 8 Comparison of the absorption spectrum with the three types of 2DEG density distribution functions (parabolic, linear and piecewise constant) for AlGaAs/GaAs at 300 K, where $N_1=1.28\times10^{16}$ m^{-2}, $N_2=1.65\times10^{16}$ m^{-2}, t_1= 20nm, L=1 μm and W=0.75 μm

Now we turn to the influence of "gate" biasing on the absorption spectrum. The electron concentration N_2 in the ungated region is kept constant and N_1 in the gated region is varied between 0.12×10^{16} m^{-2} and 1.65×10^{16} m^{-2}. The influence of N1 on the absorption spectrum of the AlGaAs/GaAs structure is shown in Figure 9 with two typical metal filling factors W/L.

Several observations can be made:

(1) In comparison with the concentration N_2, a slightly higher (lower) N_1 will shifts the resonant peaks to high (low) frequencies. This is because the gated plasmon frequency increases monotonically with the carrier density. The piecewise constant 2DEG is not equivalent to a homogeneous 2DEG with an average concentration $N_{avg}=N_1*W/L+N_2*(L-W)/L$, because the gated and ungated plasmon follow different dispersions [14] and absorption mechanisms.

(2) When the 2DEG is mostly gated as in Figure 9(a), the absorption amplitudes decrease a little and if the gated 2DEG concentration is nearly zero, a resonance peak appears at a higher frequency (2.3 THz) with an important amplitude. We attribute this phenomenon as the onset of microcavities in the region L-W and the ungated plasmon begins to dominate in the absorption spectrum. As the metal strip width W decreases shown in Figure 9(b), two resonance peaks appear (the second peak exists at 5.02 THz but not shown in Figure 9(a)) and the first peak shifts to low frequency (1.2 THz) due to the increase of ungated plasmon wavelength proportional to the gap width L-W. The resonant amplitude has a higher value than that with the homogeneous 2DEG concentration $N_1=N_2=1.65\times10^{16}$ m^{-2}, showing the ungated plasmon is more efficient to coupler with the incident THz signal [15]. This effect will be further studied in a future work.

(3) As the metal width W decreases, all the absorption amplitudes decrease and the resonant peaks of the gated plasmon move to a slightly larger values predicted in Ref.5, while the shift of the ungated plasmon resonant position is in an inverse direction.

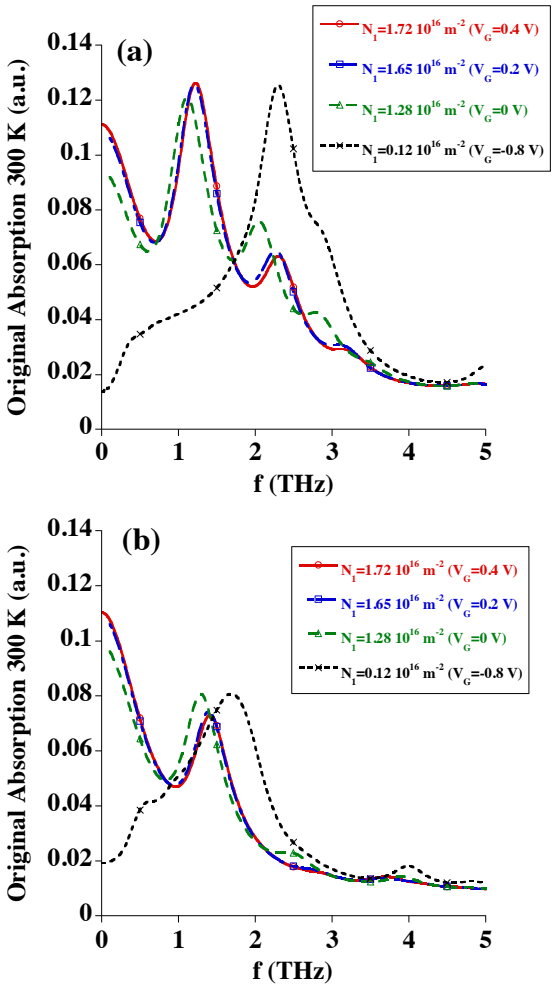

Figure 9 Absorption spectrum of the AlGaAs/GaAs structure with different 2DEG concentration N_1 at 300 K, where the metal width (a) W=0.75μm and (b) W=0.5μm. The piecewise constant model is used with the parameters $N_2=1.65\times10^{16}$ m^{-2} and L=1μm.

4. Conclusions

In conclusion, the effectiveness of the coupling between 2D plasmon and THz waves for several hetero structures such as

AlGaN/GaN, InAlN/GaN, SiGe/Si/SiGe, AlGaAs/ GaAs has been calculated using HFSS software and home made model. The overall optimal hetero structure which has the maximum absorption due to the excitation of plasmon polariton has been proved to be the nitride based material. A large carrier concentration could be formed by the high spontaneous and piezoelectric polarizations without any doping layer. The other types of structures also have interesting performances at cryogenic temperatures because of the dramatic increase of the momentum relaxation time. Then the incidence of a non uniform 2DEG concentration in the QW has been investigated. Three non uniform 2DEG profile models (piecewise constant, linear and parabolic) have been compared by the coupled wave method for the structure AlGaAs/GaAs. They are equivalent in this case because of the calculated small width t_1 of the transition region. The effect of the metallization voltage on the absorption spectrum reveals that the excitation of the ungated plasmon polariton shows considerable absorptions, following a way different from the gated plasmon polariton. Further investigations are still needed. Moreover, the tunability of the resonant frequency by the polarization on metals is also possible.

The perspectives of this work are to take into account the non locality of the dielectric permittivity in the QW.

References

[1] W.Knap et al., "Field effect transistors for terahertz detection: physics and first imaging applications", J. Infrared Milli Terahz Waves, Vol.30, 2009, 1319-1337.

[2] http://www.ansys.com/

[3] L.Wendler, N.Finger and E.Gornik,"Grating-coupler assisted infrared spectroscopy on anisotropic multilayer systems: A comparative study", Infrared Physics & Technology, 2005, Vol.46, 291-307.

[4] L. Wendler, T. Kraft, “Theory of grating-coupler-assisted infrared spectroscopy of lower dimensional electron systems: Local optics of anisotropic multilayer systems with grating”, Physica B, 1999, Vol. 271 33-98.

[5] A. Muravjov *et al*., “Temperature dependence of plasmonic Terahertz absorption in grating gate gallium nitride transistor structure”, Appl. Phys. Lett. , 2010, Vol. 96, 042105.

[6] Lifeng Li, "Use of Fourier series in the analysis of discontinuous periodic structures", J.Opt.Soc.Am.A, 1996, Vol.13,1870-1876.

[7] S.A.Mikhailov, "Plasma instability and amplification of electromagnetic waves in low-dimensional electron systems", Physical Review B, Vol.58, No.3, 1998, 1517-1532.

[8] Noriyuki Okisu et al., “Far-infrared emission from two dimensional plasmons in AlGaAs/GaAs heterointerfaces”, Appl. Phys. Lett. , 1986, Vol. 48, No.12.

[9] K.Hirakawa et al., "Far-infrared emission spectroscopy of hot two-dimensional plasmons in AlGaAs/GaAs heterojunctions", Appl. Phys. Lett.,Vol.67, 1995, 2326-2328.

[10] G.L.Snider, I.-H.Tan, and E.L.Hu, "Electron states in mesa-etched one-dimensional quantum well wires", J. of Applied Physics, Vol.68, 1990, 2849-2853.

[11] I.-H. Tan, G.L. Snider, and E.L. Hu, “A self-consistent solution of Schrödinger-Poisson equations using a nonuniform mesh”, J. of Applied Physics, Vol. 68, 1990, 4071-4076.

[12] D.H.Zhang, "Metal contacts to n-type AlGaAs grown by molecular beam epitaxy", Materials Science and Engineering, Vol.B60, 1999, 189-193.

[13] M. Nakayama, "Theory of surface waves coupled to surface carriers", J. of the Physical Society of Japan, Vol.36, No.2, 1974, 393-398.

[14] V.V.Popov, A.N.Koudymov, M.Shur and O.V.Polischuk, "Tuning of ungated plasmons by a gate in the field-effect transistor with two-dimensional electron channel", J. of Applied physics, Vol.104, 2008, 024508.

Molecular detection with multi-functional plasmonic metamaterial

Cheng Kuang Chen[1], Shun Wang[2], Ta Jen Yen[*],

[1]Department of Material Science and Engineering, National Tsing Hua University, HsinChu, Taiwan
*corresponding author, E-mail: Tjyen@mx.nthu.edu.tw

Abstract

A sensitive molecule detector is realized by strong plasmon-vibration coupling effects between functional groups and plasmonic meta-surfaces. Various plasmonic meta-surfaces are fabricated by a series of asymmetric spilt ring resonators arrays (asy-SRRA). The ASRRA inherent strong localized plasmonic infrared field enhances the spectral signature of molecular vibrations. The fabricated ASRRs structures exhibit multiple reflectance peaks, whose spectral positions are designable by our standing-wave plasmonic resonance model, providing a design rule for this multi-mode plasmon-vibration sensor (MPVS). By employing unpolarized light, our experiment results perform significant plasmon-vibration resonances in the bands respective at subradiant mode and superradiant mode resonances. We further manifest that the superradiant modes possess greater sensitivity associated with stronger localized electromagnetic field than the subradiant mode. These unique merits enable the ASRR-based sensor a multi-functional biosensor and a potential label-free imaging device.

1. Introduction

The plasmonic effects currently attract lot of interesting, these nano-scale metallic structures displaying many fascinating applications in optical frequency, including biomedical and chemical sensing [1], surface enhanced and near field microscopy [2]. Like a focusing antenna [3], plasmonic structures can collect the incident light and be localized on the surfaces, therefore, such light-matter interaction processes and resonance, are called localized surface Plasmon resonance (LSPR), which strongly depended on the shape, size and environment refractive index [4]. Based on these concepts, scientists theoretically and excrementally manifest some of refractive index sensors, which structured from nanorods [5], nanoparticles [6], nano pillars [7], and more complex geometry: nanoscale split ring resonators (SRRs) [8]. A common approach to SRR based index sensing is to measure the localized surface plamon resonance (LSPR) wavelength shift with small index changes in local environment. However, these sensors can only detect the refractive index change, quite impotent to identify dilute molecular compound. To determine molecule composition, the surface enhanced vibrational spectroscopy is an efficiency technique, which owing ability to amplify function groups oscillation through localized surface plasmon resonance.

Complementary to refractive index sensors are surface enhanced characteristics, including surface enhanced Raman scattering (SERS) [9] and surface enhanced infrared absorption (SEIRA) [10]. Both techniques are widely applied on chemical and biological sensing since the high electric field intensities of nano-structures leading significant signal enhancement, for instance, the signal enhancement factors in SERS and SEIRA are respectively on the order 10^8 and 10^4-10^5. Clearly, the enhancement factor of SEIRA is much weaker than SERS, because the SEIRA enhancement factor only depends on $|E^2|$ versus $|E^4|$ for SERS. Such weak response in SEIRA obstructs the sensing development, therefore, in this study, we design a coupler free, labeler free, and tunable spectrum range molecule detection platform based on various asymmetrical split ring resonators (asy-SRR) array. Our asy-SRRs under the electric field excitation, perform strong eigenfriquencies resonance [11]. At the multi-modes resonances, the Asy-SRRs efficiently confine electromagnetic fields and enhance the SEIRA effects.

2. Asymmetry split ring resonators (asy-SRR) array fabrication

As a consequence, the design of the asy-SRR unit cell was specified by side length d, bottom side length s, line width w and total length $L = 2d+s-w$, respectively, as shown in Fig. 1(a). To reveal the influence of total length L on the resonance response, four different aspect ratio asy-SRR square arrays were fabricated by 50 nm thick gold layers on double published silicon substrates with an area of $200\times200\mu m^2$ through E-beam lithographic and lift-off processes. The details of the measured geometric parameters of each sample can be found in Table 1. Next, the fabricated SRRs were characterized by a micro-Fourier transform infrared spectroscopic system (μ-FTIR) in reflectance measurements directly under normal incidence without using optical couplers (please see the Fig. 1(b)). For analyst layer, we deposit a thin polymethylmethacrylate (PMMA) film, whose two major function groups, carbonyl (C=O) and C-O stretching are respectively to of 1730 cm^{-1} and 1150 cm^{-1} resonant frequencies [12].

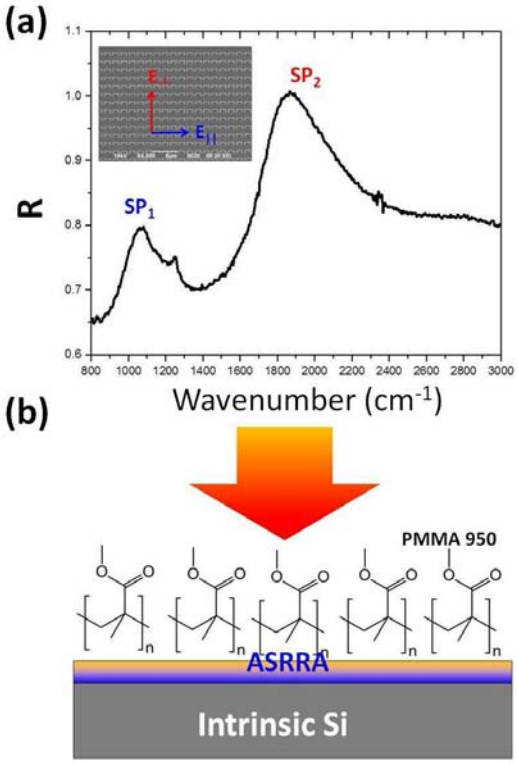

Figure 1: (a) Upleft: Scanning electron microscopic (SEM) picture displays the asy-SRR array template, whose linewidth is 80 nm and 2 um for periodicity. Besides, the asy-SRR array reflects two plamonic modes, respectively indicated to SP_1 and SP_2. (b) Sketch of measurement setup, the PMMA was deposited on the asy-SRR array; and the IR incident light is normal to ASRRA surface.

Table 1. Measured geometrical parameters of the fabricated planar asy-SRRs.

Design (nm)	Side length (d, nm)	Bottom length (s, nm)	Line width (w, nm)	Aspect ratio (d/s)
Asy-800	350	1200	102	0.29
Asy-700	450	750	106	0.6
Asy-600	500	600	98	0.83
Asy-500	600	510	80	1.166

3. Strong plasmon-vibration coupling between ASRRA and molecular function group

There are two resonant band positions of Asy-SRR designed to match to the carbonyl (C=O) and C-H stretch vibration frequency, and that could be numerically verified by using a commercial finite integral time domain (CST Microwave Studio). The measured spectra are shown in Fig. 1(a), presenting multiple reflectance peaks (SP_1 and SP_2) under a normal incident unpolarized light, located at 1950^{-1} and 3100 cm^{-1}. Both plasmonic modes also could be excited by polarized light, corresponding to E-field polarization directions (defined as E∥ and E⊥), respectively [8]. Their resonance wavelengths can be interpreted by the standing-wave plasmonic resonance (SWPR) model:

$$L = \frac{m(\lambda_m + \lambda_0)}{2n_{eff}} \quad (1)$$

, where L denotes the total length of SRR, λ_m is the resonance wavelength, m is the resonance mode, n_{eff} is the effective refractive index of the dielectric environment and λ_0 depends on the geometric structure. Therefore, by controlling various geometric aspect ratio of asy-SRR, the plasmonic modes resonant frequencies should locate at fixed positions, easing the design rules.

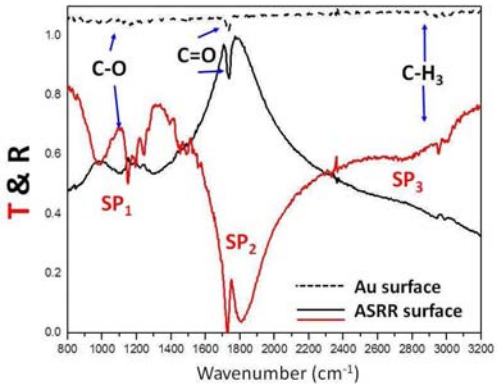

Figure 2: Measured transmission (red) and reflection (black) spectra, the solid spectra present as the PMMA deposited on the asy-500 SRR array. The dash spectrum shows the reflection spectrum of PMMA deposited on 50 nm gold thin film.

By applying an analyte layer (PMMA, 50nm), a series of significant plasmon induced vibration resonances can be observed on the asy-SRRA template. First, the PMMA is deposited on the bare gold smooth film. Its measured spectra is shown in Fig. 2, exhibiting a noise but flat reflection spectra, whose reflection is only changed 0.05 by carbonyl vibration and 0.008 by C-O stretching. Then, the same thickness of PMMA is coated on the ays-SRRA template, the measured reflection spectrum exhibits a frequency dependent enhancement, in which, the carbonyl and C-O vibration signals are amplified near to 0.14 and 0.1. Notably, based on theatrical and experimental work, the enhanced area main within 10 nm from the particle structure [13], thus, the values of enhancement factors can reach up to 2×10^3 of magnitude. Particularly, the PMMA could not bond to the gold surface, therefore, it is very large enhancement factor compared to the conversional coupler free chemical sensor.

The enhancement factor is also strong dependent on the resonant frequency, as shown in the Fig. 3(a). For conventional chemical compound, different function groups are vibrating at their specific frequencies, call chemical fingerprint. Here, we emulate the effect of various molecules coupled to an asy-SRRA template by employing a Lorentz oscillator model (for analyte) and Drude model (for gold) media. The Lorentz model is chosen for that they can analog to molecular vibration, and reproduce a similar absorption

profile associated to measured spectra of the function group vibration. Our simulation results indicate that with very close frequency (small $\Delta\omega$) between vibration and asy-SRRA's stranding wave plasmonic (SP) resonance, the reflection spectra changing 0.08 and 0.14 for first (1st SP mode) and second SP modes (2nd SP mode), respectively. Their relative enhancement factors are near to 10^4, however, with more difference resonance frequencies between vibration and SP modes (large $\Delta\omega$), the enhanced factor exhibits continue decay tendency as the rate of $1/\Delta\omega$, finally, the enhancement factors are left over 10^1 to 10^2 for 1st SP mode and 2nd SP mode, respectively. Based on above results, we summary that our ASRRA template can support multi-bands sensing range and large enhancement factors (EF), differed from previous plasmonic sensing schemes that rely on index change [14].

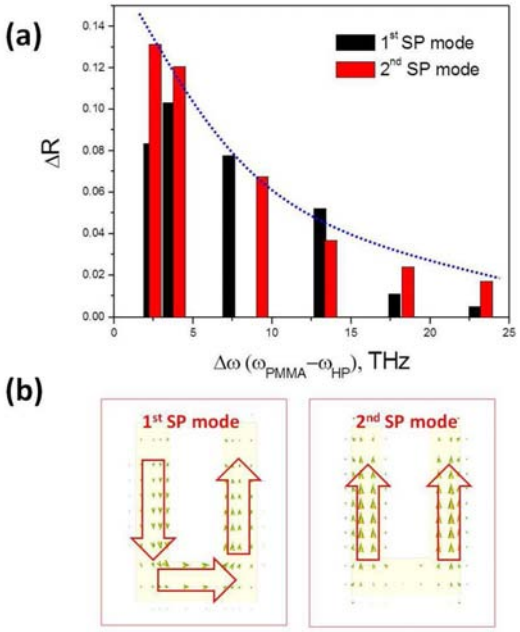

Figure 3: (a) A bar chart shows the reflection change with frequency difference ($\Delta\omega=|\omega_{PMMA}-\omega_{SP}|$) between molecular vibration mode and plasmonic mode. (b) The current density of 1st SP and 2nd mode, whose dipole modes are shown as arrows.

4. Achieved sensitive sensor by enhanced localized field

To further discuss the nature of the enhancement phenomena at both SP modes resonances, we apply three dimensional field analyses, which can detail display the local electric field energy density and current distribution on the surface of nano structures. In the far-field detection, the enhanced factors (EF) are the ratio of surface fields (E_{sur}) to the far field illumination (E_{in}) [15], in other words, the energy is focused by SRR-type antenna and absorbed by PMMA molecules with near field coupling, then, the vibration energy reradiated to far field by SRR-type antenna. Based on this concept, the antenna type will directly influence the coupling efficiency, for instance, the first SP mode (1st SP mode) revealing double-out phase-dipoles type resonance (subradiant mode) on sidebars of the asy-SRR structure, but second SP mode (2nd SP mode) exhibiting double-inphase-dipoles mode (superradiant mode) on sidebar (as shown in Fig. 3(b)). The inphase-dipoles mode induced by 2nd SP mode will be more efficiency coupled to the molecular vibration since the energy absorption obeyed:

$$A \propto \left| \partial u / \partial Q \bullet \vec{E} \right|^2 \quad (2)$$

, where the u and Q respective are molecular polarizability and induced current. Clearly, the second mode (2nd SP mode) is oscillating paralleled to incident fields, perfectly coupled to far-field and molecule, leading more sensitivity than 1st SP mode, as show in Fig. 4(a).

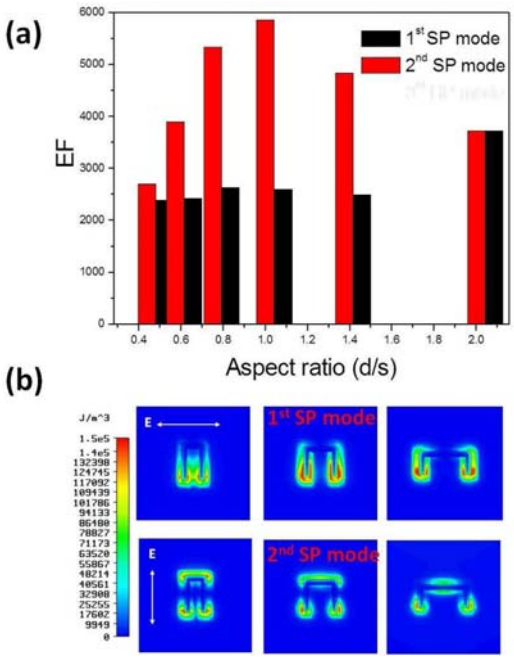

Figure 4: (a) A bar chart of enhancement factor (EF) versus to aspect ratio of asy-SRR. (b) Electric energy distribution of various aspect ratio of asy-SRR, (left, aspect ratio=2; middle, aspect ratio=1; and right, aspect ratio=0.33).

Figure 4(a) also shows the relationship between various aspect ratio of asy-SRR and its enhanced sensitivity (EF). The EF of 2nd SP mode strongly depends on the aspect ratio, but 1st SP not. At the 2nd SP mode resonance, the most symmetric shape (the aspect ratio is equal to one) of SRR will enhanced more significant than other shapes asy-SRRs. Such different EF attributes are referred to their shapes, which could be explained by their field distribution. As shown in Fig. 4(b), at the 1st SP mode resonances, the localized electric energy density maintain on the magnitude of 10^5 J/m^3, unaffected with the aspect ratio of asy-SRR shape. For 2nd SP mode, as Fig. 4(b) shown, the localized field of sidebar is strongly excited in the narrow shape of asy-SRR but its localized area is not enough to enhance more PMMA molecules. Thus, as Fig. 4(b) shown, with wider shape, the localized field suffered small loss, but

wider shape could increase the effective area, amplifying EF value. However, as Fig. 4(b) shown, a too wide shape will weaken its localized fields to reduce the EF value, because short excited sidebars cannot contribute enough energy to entire structure.

5. Conclusion

In this study, we successfully demonstrate asy-SRR based molecular detector, which can experimentally enhance least three order of vibration signal in multi-bands. The unit asy-SRR also demonstrates strong enhanced local fields, whose electric energy densities are five orders larger than that of incident electromagnetic fields, such simulation results are agree well to measured profiles. These enhanced near fields interact with molecules vibration, leading a Fano-type resonance mode and allowing far-field detection. We also make a summary of that the enhancement factor of 2nd SP mode dependent on the aspect ratio of asy-SRR since the trade-off between localized field intensity and its effective area. Base on our simulation and experiment results, the asy-SRR could be optimized to a sensitive biosensor or a potential label-free imaging device.

Acknowledgements

The authors would like to gratefully acknowledge the financial support from the National Science Council (NSC98-2112-M-007-002-MY3, NSC100-2120-M-010-001, and NSC100-2120-M-002-008), and from the Ministry of Education (“Aim for the Top University Plan” for National Tsing Hua University.

References

[1] S. Lal, S. Link, and N. J. Halas, "Nano-optics from sensing to waveguiding," Nat Photonics 1, 641-648 (2007).
[2] M. Moskovits, "Surface-Enhanced Spectroscopy," Rev Mod Phys 57, 783-826 (1985).
[3] T. Kosako, Y. Kadoya, and H. F. Hofmann, "Directional control of light by a nano-optical Yagi-Uda antenna," Nat Photonics 4, 312-315 (2010).
[4] M. E. Stewart, C. R. Anderton, L. B. Thompson, J. Maria, S. K. Gray, J. A. Rogers, and R. G. Nuzzo, "Nanostructured plasmonic sensors," Chem Rev 108, 494-521 (2008).
[5] W. S. Chang, J. W. Ha, L. S. Slaughter, and S. Link, "Plasmonic nanorod absorbers as orientation sensors," P Natl Acad Sci USA 107, 2781-2786 (2010).
[6] S. Malynych and G. Chumanov, "Coupled planar silver nanoparticle arrays as refractive index sensors," J Opt a-Pure Appl Op 8, S144-S147 (2006).
[7] T. Xu, N. Zhu, M. Y. C. Xu, L. Wosinski, J. S. Aitchison, and H. E. Ruda, "Pillar-array based optical sensor," Opt Express 18, 5420-5425 (2010).
[8] Y. T. Chang, Y. C. Lai, C. T. Li, C. K. Chen, and T. J. Yen, "A multi-functional plasmonic biosensor," Opt Express 18, 9561-9569 (2010).
[9] S. M. Nie and S. R. Emery, "Probing single molecules and single nanoparticles by surface-enhanced Raman scattering," Science 275, 1102-1106 (1997).
[10] F. Le, D. W. Brandl, Y. A. Urzhumov, H. Wang, J. Kundu, N. J. Halas, J. Aizpurua, and P. Nordlander, "Metallic nanoparticle arrays: A common substrate for both surface-enhanced Raman scattering and surface-enhanced infrared absorption," Acs Nano 2, 707-718 (2008).
[11] C. Y. Chen, S. C. Wu, and T. J. Yen, "Experimental verification of standing-wave plasmonic resonances in split-ring resonators," Appl Phys Lett 93(2008).
[12] M. S. Anderson, "Surface enhanced infrared absorption by coupling phonon and plasma resonance," Appl Phys Lett 87(2005).
[13] R. Hillenbrand, T. Taubner, and F. Keilmann, "Phonon-enhanced light-matter interaction at the nanometre scale," Nature 418, 159-162 (2002).
[14] B. Lahiri, A. Z. Khokhar, R. M. De La Rue, S. G. McMeekin, and N. P. Johnson, "Asymmetric split ring resonators for optical sensing of organic materials," Opt Express 17, 1107-1115 (2009).
[15] D. J. Shelton, I. Brener, J. C. Ginn, M. B. Sinclair, D. W. Peters, K. R. Coffey, and G. D. Boreman, "Strong Coupling between Nanoscale Metamaterials and Phonons," Nano Lett 11, 2104-2108 (2011).

Plasmon beams interaction at the surface of photorefractive crystals

Daria O. Ignatyeva, Anatoly P. Sukhorukov

Lomonosov Moscow State University, Moscow, Russia
*corresponding author, E-mail: ignatyeva@physics.msu.ru

Abstract

We present a novel theory of surface plasmon polariton interaction on the surface of photorefractive crystal. The effect of the total internal reflection of a weak signal plasmon beam from a high-power reference beam is discussed. Both ray and wave theories are used to describe signal propagation. The effect of the signal tunneling through the narrow inhomogeneity induced by the reference beam is considered.

1. Introduction

Surface plasmon polariton (SPP) is electromagnetic wave propagating along the interface of media with different signs of permittivity or permeability values. Recently besides widely known SPP on metal–dielectric interfaces [1, 2] also SPP on left-handed [3, 4] and exotic metamaterial interfaces [5] are studied.

Optical SPP is localized in a very thin layer of less than 1 μm and exponentially decays in the direction transverse to the interface. This unique feature can be used both in nonlinear photonics due to very high energy concentration and in compact plasmonic devices. Therefore the methods of SPP control are of prime interest. Nowadays several methods of SPP management by nanoparticles or heterostructure design are proposed [6, 7].

We focus our attention on the possibility of light-by-light control that has a great importance for nonlinear optics and photonics [8, 9]. The properties or direction of a signal laser beam are controlled by a reference beam. A very perspective approach is to combine methods of nonlinear photonics with the recent success of plasmonics [10, 11] in order to engineer high-speed and compact devices [12]. In this work the possibility of signal surface plasmon propagation direction management with the high-power reference plasmon via the phenomenon of total internal reflection is demonstrated.

The total internal reflection is a well-known optical phenomenon that takes place if the light falls on a boundary of a less dense medium. However the inhomogeneity of the refractive index induced in the nonlinear media by a high-power laser beam can act like such boundary, too, causing the opacity of the reference beam region and the total reflection of the signal beam. The phenomenon of the nonlinear total internal reflection of the bulk laser beams was considered in Ref. [13, 14]. This work is devoted to the plasmon interaction with the inhomogeneity of the dielectric permittivity induced by the high-power reference plasmon in the photorefractive crystal.

2. Theory of SPP beam propagation on photorefractive surface

We consider an interaction of two plasmon beams at the interface between the photorefractive crystal (i.e. lithium niobate) and the noble metal (i.e. silver or gold). The following differential equation describes the monochromatic reference plasmon propagation along the interface:

$$\Delta\vec{E} - \text{grad div}\vec{E} + \varepsilon_j k_0^2 \vec{E} = 0, \tag{1}$$

where index $j = d, m$ corresponds to metal or dielectric, $k_0 = \omega/c$ is the wave number in vacuum. The geometry of the problem is selected to be as follows: Oz axis is perpendicular to the interface, the dielectric and metal occupy half-spaces $z > 0$ and $z < 0$ correspondingly. The pump plasmon beam propagates along Ox axis, the signal beam propagates at a small angle φ to it.

Under the influence of strong electromagnetic field due to the photorefractive effect dielectric permittivity ε_d changes:

$$\varepsilon_d\left(|\vec{E}|^2\right) = \varepsilon_L + \varepsilon_{NL}\left(|\vec{E}|^2\right) = \varepsilon_L + \chi\frac{|\vec{E}|^2}{\alpha + |\vec{E}|^2}, \tag{2}$$

where ε_L is the linear part of dielectric permittivity, and nonlinear part ε_{NL} is determined by the field intensity with the coefficients χ describing nonlinearity and α corresponding to saturation intensity value.

For the solution of the Eq. (1) we use the slowly varying amplitude method adapted for the paraxial plasmonic beams that was described in Ref. [15] in detail. We seek the solution of Eq. (1) in the following form:

$$\vec{E} = \left[A(x,y)E_{x0}(z)\vec{e}_x - iB(x,y)E_{z0}(z)\vec{e}_z\right]e^{-i\beta x} \tag{3}$$

where A, B are the slowly varying amplitudes and

$$\vec{E_0} = \{E_{x0}, 0, E_{z0}\} \tag{4}$$

is the transversal profile obtained as a solution of linear equation (1):

$$E_{x0} = e^{\gamma_j|z|}, \tag{5}$$

$$E_{z0} = \frac{\beta}{\gamma_j}sgn(z)e^{\gamma_j|z|}. \tag{6}$$

The propagation constant β and the localization coefficients γ_j are determined as:

$$\beta = k_0\sqrt{\frac{\varepsilon_m\varepsilon_L}{\varepsilon_m+\varepsilon_L}}, \tag{7}$$

$$\gamma_j = k_0\sqrt{-\frac{\varepsilon_j^2}{\varepsilon_m+\varepsilon_L}}. \tag{8}$$

Note that in the more complicated case (e.g. on gyrotropic interface [16]) SPP has another profile and dispersion.

We assume that the plasmon profile and polarization remains nearly the same as in the linear problem ($A \approx B$, $\frac{\partial A}{\partial z} = 0$) and the beams are rather wide so that $|\frac{\partial A}{\partial x}| \ll \beta|A|$. Substituting (3) in Eq. (1), multiplying the equation projections onto Ox and Oz axis by E_{x0} and E_{z0} correspondingly, and integrating over transverse coordinate z the sum of the obtained equations we finally get

$$\frac{\partial^2 A}{\partial y^2} - 2i\beta\theta_1\frac{\partial A}{\partial x} + \chi\theta_2 k_0^2 A\left[1 - \frac{\alpha\theta_3}{|A|^2}\ln\left(1+\frac{|A|^2}{\alpha\theta_3}\right)\right] = 0. \tag{9}$$

The coefficients $\theta_{j=1,2,3}$ appear due to the integration that physically means averaging over transversal direction. These coefficients equal:

$$\theta_1 = 1 - \frac{\kappa}{1+\kappa^2}, \tag{10}$$

$$\theta_2 = \frac{1}{1+\kappa^2}, \tag{11}$$

$$\theta_3 = \frac{\kappa}{1+\kappa}, \tag{12}$$

where $\kappa = -\varepsilon_2/\varepsilon_1$. Notice that usually $|\varepsilon_1| \gg \varepsilon_2$ and $\kappa \ll 1$ so that the coefficient $\theta_1 \approx 1$ leading to the linear parabolic diffraction equation that was obtained in the linear case in our previous work [17]. The photorefractive nonlinearity coefficient χ is multiplied by $\theta_2 \approx 1$ (in the extreme case of $\kappa \ll 1$) since the electromagnetic field is mainly concentrated in photorefractive dielectric. The saturation value α is re-normalized to θ_3 for convenience. The coefficient θ_3 actually accounts for field amplitude $|A(x,y)\vec{E}(0)|$ normalization.

3. SPP beam propagation in the presence of SPP-induced inhomogeneity

We consider two SPP beams propagating at a small angle to each other. One of the SPP beams is high-power reference beam and another is weak signal beam. Therefore the influence of signal beam on the reference beam propagation can be neglected and only self-action and diffraction phenomena taken into account:

$$\frac{\partial A_r(x,y)}{\partial x} + iD_r\frac{\partial^2 A_r(x,y)}{\partial y^2} + i\frac{\chi k_0^2}{2\beta_r\theta_{1r}}A\left[1 - \frac{\alpha\theta_{3r}}{|A_r|^2}\ln\left(1+\frac{|A_r|^2}{\alpha\theta_{3r}}\right)\right] = 0. \tag{13}$$

In this equation index r refers to the reference beam, $D_r = \frac{1}{2\beta_r\theta_{1r}}$ is the diffraction coefficient.

The equation describing signal SPP (index s) propagation can be obtained in a quite similar way. We assume that self-action of the signal plasmon is weak and can be neglected while diffraction and the dielectric permittivity inhomogeneity induced by the pump should be taken into account:

$$\frac{\partial A_s(x,y)}{\partial x} + iD_s\frac{\partial^2 A_s(x,y)}{\partial y^2} + i\frac{\sigma(x,y)}{2\beta_s\theta_{1s}}A_s(x,y) = 0, \tag{14}$$

where the induced inhomogeneity:

$$\sigma(x,y) = \int_0^{+\infty}\frac{\kappa_s k_{0s}^3\chi}{2\gamma_{2s}^2\theta_s^2\varepsilon_2}\frac{|A_r(x,y)|^2|\vec{E}_{0r}(z)|^2|\vec{E}_{0s}(z)|^2}{\alpha+|A_r(x,y)|^2|\vec{E}_{0r}(z)|^2}dz. \tag{15}$$

is determined both by pump and signal plasmon transversal profiles. The sign of inhomogeneity coincides with the nonlinearity sign χ. The profile of the inhomogeneity due to the saturation of photorefractive nonlinearity does not exactly repeat the shape of the pump plasmon beam. As far as $\partial\sigma/\partial|A_r|^2 > 0$ the regions with higher plasmon intensity correspond to the larger inhomogeneity values.

Although the value of inhomogeneity σ can not be derived analytically it can be numerically calculated almost for every possible pump field distribution and pump and signal frequency ratios. For the intensities of the reference beam much smaller than the saturation intensity the induced inhomogeneity can be analytically derived as:

$$\sigma(x,y) = \theta_4\chi\frac{|A_r(x,y)|^2}{\alpha}, \tag{16}$$

where the coefficient θ_4

$$\theta_4 = \frac{(1+\kappa_r)\gamma_{2s}k_0^2}{2\kappa_r\beta_s^2\theta_{1s}(\gamma_{2s}+\gamma_{2r})}. \tag{17}$$

In this case the inhomogeneity profile repeats the profile of the reference beam.

4. Ray theory of signal SPP propagation

Now we assume that the induced efficient inhomogeneity $\sigma(x,y)$ is known and focus our attention on the possible regimes of signal plasmon beam propagation. For the simplification of our analysis we derive the equation for the signal plasmon trajectory. We use the eikonal method of ray theory that was described in [13] in a detail. The equation for the signal plasmon beam trajectory is:

$$\frac{d^2y}{dx^2} = \frac{\partial\sigma(x,y)}{\partial y}. \tag{18}$$

If we consider a rather small interaction region so that its sizes do not exceed the pump diffraction and nonlinear lengths we can assume that the reference plasmon amplitude does not change significantly in this region so that

$A_r(x,y) \approx A_r(y)$. Therefore the inhomogeneity $\sigma = \sigma(y)$ and the solution of the Eq. (18) have the following form:

$$x = x_0 \pm \sqrt{(2)} \int_{y_0}^{y} \frac{d\xi}{\sqrt{\sigma(\xi) - \sigma(y_0) + \varphi^2/2}}. \qquad (19)$$

For the different parts of the trajectory the sign before the integral is different. Notice that the solution in defocusing media ($\sigma < 0$) can have a turning point y_t at which the trajectory is parallel to the x axis ($dy/dx = 0$) if

$$\sigma(y_t) - \sigma(y_0) = -\varphi^2/2. \qquad (20)$$

The direction of signal plasmon beam propagation sufficiently depends both on the induced inhomogeneity and on the initial tilt angle φ. For the fixed inhomogeneity the turning point exists only if the initial tilt angle is less than the critical value φ_{cr} determined as:

$$\max(-\sigma) = \varphi_{cr}^2/2. \qquad (21)$$

Here we neglected the permittivity change at the initial point y_0 (that is considered to be at a rather large distance from a pump plasmon).

Depending on the ratio between initial tilt signal angle and maximum effective inhomogeneity induces by pump three possible regimes of signal plasmon propagation can be distinguished (see Fig. 1). Notice that although the trajectory itself sufficiently depends on the reference beam profile the regime of propagation does not depend on it.

The first regime is the analogous of ordinary refraction of a beam in the inhomogeneous media and takes place if $\varphi > \varphi_{cr}$. The trajectory of the signal beam is curved though it keeps propagating at the initial angle after passing the inhomogeneity.

The second regime takes place if $\varphi < \varphi_{cr}$ and is analogous to the total internal reflection phenomenon on the interface of two dielectric media. The signal plasmon beam is reflected from the inhomogeneity.

The third regime corresponds to the strict fulfillment of the condition $\varphi = \varphi_{cr}$. It can be shown (see Eq. (18)) that all the derivatives $d^m y/dx^m$ tend to zero near the turning point so that the signal ray asymptotically approaches inhomogeneity maximum.

The trajectories of the signal plasmon corresponding to these three regimes were calculated by solving the Eq. (18) and are shown in Fig. 1.

5. Spectral approach to the signal SPP propagation description

We confirmed the theoretical results presented here by the numerical simulation of signal SPP beam propagation in the presence of the pump SPP. We neglected the self-action and diffraction of the pump beam and considered its profile unchanged. Such simplification allowed us to solve the Eq. (14) for a signal plasmon beam numerically with a fixed inhomogeneity induced by the pump beam. Hereafter the specification signal of a plasmon beam will be omitted.

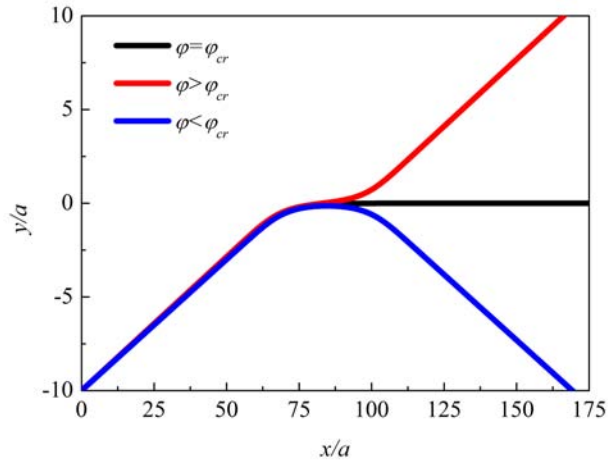

Figure 1: The trajectories of the signal plasmon beam corresponding to the same initial tilt and the different reference plasmon intensities: green curve – below, red curve - equal, blue curve - above the critical value.

The maximum of the initial spatial SPP spectrum $S(x=0,k_y)$:

$$S(x=0,k_y) = \int_{-\infty}^{+\infty} A(x=0,k_y) e^{-ik_y y} dy \qquad (22)$$

at certain k_{yi} can be associated with the initial angle φ:

$$\varphi = \frac{k_{yi}}{\beta}. \qquad (23)$$

For the definiteness we assume that $k_{yi} > 0$ that means that the plasmon beam is initially located in the region $y < 0$. The paraxial approximation used above is valid only if the tilt angles are small $\varphi \ll 1$, or $k_{yi} \ll \beta$.

If all components of the spatial plasmon spectrum correspond to the initial angles of total internal reflection or to the refraction angles the ray theory describes the plasmon propagation with a very good accuracy (see Fig. (2).

However near critical angle due to the finite spatial spectrum width part of the spectral components get in the reflection region while the others occur to be refracted. This two spectral parts are bounded by the critical value k_{y0}. The transmission coefficient can be calculated:

$$T = \frac{\int_{k_{y0}}^{+\infty} S^2(x=0,k_y) dk_y}{\int_{-\infty}^{+\infty} S^2(x=0,k_y) dk_y}. \qquad (24)$$

Note that Fresnel reflection is neglected in our examination since the inhomogeneity is very small $\sigma \ll 1$ and the phenomenon discussed above appear only due to the finite width of the spatial spectrum.

The amount of energy corresponding to the propagation parallel to the inhomogeneity exactly equals to zero since it

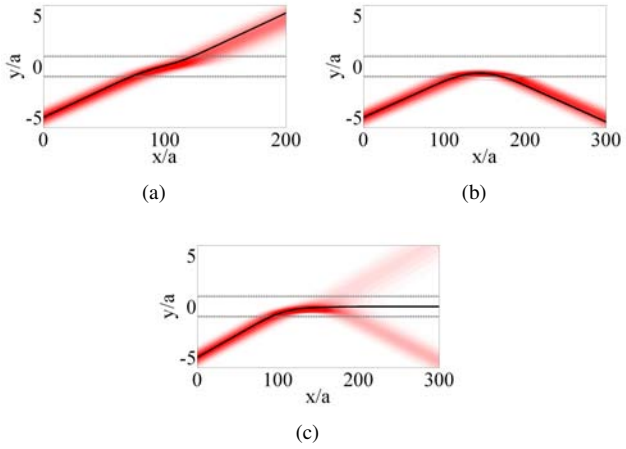

Figure 2: (a) The refraction ($\varphi = 1.25\varphi_{cr}$) and (b) reflection ($\varphi = 0.8\varphi_{cr}$) of SPP on the induced inhomogeneity (shown by gray dash lines). (c) SPP partial reflection and partial refraction near the critical initial angle $\varphi = \varphi_{cr}$. Black line illustrates the results of the ray theory.

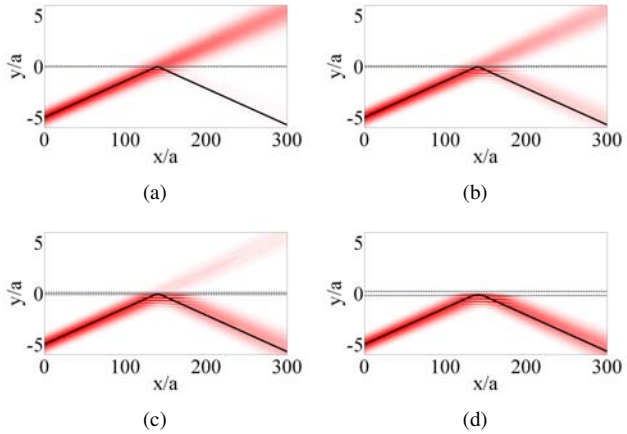

Figure 3: SPP tunneling through the induced inhomogeneity shown by gray lines. Reference beam width equals $a_r = 0.02a_s, 0.05a_s, 0.1a_s, 0.2a_s$ for (a)-(d) figures correspondingly. Black lines illustrate the results of the ray theory.

can be defined as: $\int_{k_{y0}}^{k_{y0}} S^2(x=0,k_y)dk_y = 0$. This approach explains why the beam tilted at near-critical angle is divided by inhomogeneity into two but not three parts (in contrast to the mentioned above three regimes of ray propagation).

Therefore the plasmon beam is partially reflected and partially transmitted through the inhomogeneity if its central spectral component is close to the critical value as it is illustrated by the Fig. 2 (c).

In our numerical calculations the amplitude of the induced inhomogeneity was $\sigma_0 = 10^{-3}$ and its profile had Gaussian form $\sigma(y) = \sigma_0 e^{-y^2/a^2}$ with the width $a = 50\beta/2\pi$ equal to the signal beam width. The value of critical angle was $\varphi_{cr} = 2.6^o$.

6. SPP beam tunneling through the induced inhomogeneity

According to the developed ray theory of signal SPP propagation in the presence of the induced inhomogeneity the regime of the SPP propagation (reflection or refraction) is determined only by the magnitude of the inhomogeneity and not by its shape or width. However if the inhomogeneity width is rather small the effect of tunneling that is similar to the same effect in quantum mechanics can be observed.

In analogy with quantum mechanics (see, for example, [18]) we can determine the turning points $y_{t_{1,2}}$ (see Eq. (20)):

$$\sigma(y_{t_{1,2}}) = -\frac{\varphi^2}{2} \tag{25}$$

and the tunneling coefficient can be written as:

$$\tilde{T} = \frac{e^{-2\psi}}{\left(1 + \frac{1}{4}e^{-2\psi}\right)^2}, \tag{26}$$

where

$$\psi = \int_{y_{t_1}}^{y_{t_2}} \beta\theta_1 \sqrt{-(\sigma(y) + \frac{\varphi^2}{2})}dy. \tag{27}$$

It is important to mention that this expression for tunneling coefficient is different from the transmission coefficient (24). In both cases of tunneling and partial transmission the incident beam is partially reflected and partially refracted nevertheless this phenomenon occurs due to two different mechanisms. Tunneling of the beam through the inhomogeneity is possible due to the leakage of the waves that are evanescent between the turning points and sufficiently depends on the width and profile of the inhomogeneity as is follows from Eq. (26). Partial transmission described by Eq. (24) occurs due to the wide spatial plasmon beam spectrum and depends only on the signal beam shape and the magnitude of the inhomogeneity (that determines k_{y0}).

Fig. 3 illustrates the tunneling of the signal plasmon beam through the inhomogeneities of different width.

In order to determine accurately the transmission and reflection coefficients one should take into account both finite spatial spectrum width and tunneling effect. The resulting transmission coefficient can be found as:

$$T = \int_{-\infty}^{+\infty} \tilde{T}(k_y)S^2(k_y)dk_y. \tag{28}$$

In order to induce higher inhomogeneities the pump beam can be focused and the signal plasmon can be reflected from its waist. Although we considered the reference beam profile to remain unchanged the results obtained above can be also applicable for this case if the interaction region is rather small. Anyway the tunneling effect certainly will take place for a narrow reference beam waists.

7. Conclusion

Theory of surface plasmon polariton interaction on the surfaces of photorefractive crystals was developed. The equation for the self-influence of the reference plasmon beam was derived using the slowly varying amplitude method and averaging over the transversal coordinate. Similar equation was obtained for the weak signal beam propagation in the presence of the inhomogeneity induced by the pump beam. Due to the nonlinearity saturation the profile of the inhomogeneity can differ from the profile of the pump surface plasmon beam.

Using the ray theory we found three regimes of possible signal plasmon propagation: refraction, total internal reflection and degenerate regime of signal trapping. Due to the finite spatial spectrum width signal beam can be almost entirely or partially reflected or refracted. The effect of tunneling of a signal plasmon beam through a narrow inhomogeneity is demonstrated.

Therefore depending on the initial tilt and the inhomogeneity value controlled by the reference plasmon intensity the signal plasmon can be reflected of transmitted through the inhomogeneity. This allows us to manage the signal plasmon direction by modulating the reference plasmon intensity.

Acknowledgement

We appreciate fruitful discussions with V.E. Lobanov. This work is supported by RFBR, Russian Federation Presidential Grant No. MK-3123.2011.2, the FTP Scientific and scientific-pedagogical personnel of the innovative Russia (contract No. 16.740.11.0577) and Dynasty Foundation.

References

[1] S.A. Maier, *Plasmonics: Fundamentals and Applications,* Springer, New York, 2006.

[2] H. Raether, *Surface Plasmons,* Springer, Berlin, 1988.

[3] I.V. Shadrivov, A.A. Sukhorukov, Yu.S. Kivshar, A.A. Zharov, A.D. Boardman, P. Egan, Nonlinear surface waves in left-handed materials, *Phys. Rev. E.* 69: 016617, 2004.

[4] R. Ruppin, Surface plasmon-polaritons of a left-handed medium, *Phys. Lett. A* 277: 61–64, 2000.

[5] A.V. Kats, S. Savel'ev, V.A. Yampol'skii, F. Nori, Left-handed interfaces for electromagnetic surface waves *Phys. Rev. Lett.* 98: 073901, 2007.

[6] A.L. Stepanov, J.R. Krenn, H. Ditlbacher, A. Hohenau, A. Drezet, B. Steinberger, A. Leitner, F.R. Aussenegg, Quantitative analysis of surface plasmon interaction with silver nanoparticles, *Opt. Lett.* 30: 1524-1526, 2005.

[7] V.I. Belotelov, D.A. Bykov, L.L. Doskolovich, A.K. Zvezdin, On surface plasmon polariton wavepacket dynamics in metal-dielectric heterostructures, *J. Phys.: Condens. Matter.* 22: 395301, 2010.

[8] *Soliton Driven Photonics*, eds. A.D. Boardman, A.P. Sukhorukov, Kluwer, Dordrecht, 2001.

[9] H.M. Gibbs, *Optical Bistability: Controlling Light with Light*, Academic, New York, 1985.

[10] T. Utikal, M.I. Stockman, A.P. Heberle, M. Lippitz, H. Giessen, All-optical control of the ultrafast dynamics of a hybrid plasmonic system, *Phys. Rev. Lett.* 104: 11, 113903, 2010.

[11] G.A. Wurtz, R. Pollard, A.V. Zayats, Optical bistability in nonlinear surface-plasmon polaritonic crystals, *Phys. Rev. Lett.* 97: 057402, 2006.

[12] K.F. MacDonald, Z.L. Samson, M.I. Stockman and N.I. Zheludev, Ultrafast active plasmonics, *Nat. Photon.* 3: 55–58, 2009.

[13] V.E. Lobanov, A.P. Sukhorukov, Repulsion and total reflection with mismatched three-wave interaction of noncollinear optical beams in quadratic media, *Phys. Rev. A*, 84: 023821, 2011.

[14] A.P. Sukhorukov, V.E. Lobanov, A.A. Kalinovich, Nonlinear diffraction and total internal reflection in optical-beam interaction in defocusing media, *J. Russ. Laser Res.*, 31(1): 1–11, 2010.

[15] A.R. Davoyan, I.V. Shadrivov, Yu.S. Kivshar, Self-focusing and spatial plasmon-polariton solitons, *Opt. Express.* 17:21732, 2009.

[16] D.O. Ignatyeva, A.N. Kalish, G.Yu. Levkina, A.P. Sukhorukov, Surface plasmon polaritons at gyrotropic interfaces, *Phys. Rev. A*, 2012 (accepted).

[17] D.O. Saparina, A.P. Sukhorukov, Diffraction of surface waves in metals and metamaterials, *BRAS: Physics*, 73: 12, 1594–1597, 2009.

[18] M. Razavy, *Quantum Theory of Tunneling,* World Scientific, Singapore, 2003

THz surface plasmon waves on planar Goubau lines

Djamal Gacemi[1], Juliette Mangeney[1,*], Karine Blary[2], Jean-Francois Lampin[2], Thibault Laurent[1], Tahsin Akalin[2], Paul Crozat[1] and Fanqi Meng[1]

[1]Institut d'Electronique Fondamentale, UMR CNRS 8622, Univ. Paris Sud-XI, France
[2] Institut d'Electronique de Microélectronique et de Nanotechnologie, UMR CNRS 8520, France
*corresponding author, E-mail: Juliette.mangeney@u-psud.fr

Abstract

We investigate surface plasmon waves propagating on planar Goubau lines, so-called Goubau mode, using a guided-wave terahertz spectroscopy system based on a freely positionable electro-optic probe. We show the radial nature of the Goubau mode and its confinement around the Goubau line over few tenths of microns (λ/10).

1. Introduction

Significant progress on waveguides that captures and confines THz radiation generated in free-space have been reported in the past few years [1,2,3]. For instance, studies have shown that parallel-plate metal waveguides show low loss and low group velocity dispersion in the THz frequency range. In return, only few works have been focused on integrated waveguides in which the THz radiation is confined near a surface. Theses on-chip waveguides are very promising candidates for broadband THz near field sensing and imaging, spectroscopy of microfluidic systems and ultra-wide bandwidth circuits. Here we report the experimental investigation of the THz surface waves propagating on planar Goubau lines (G-line) made of a single metal wire formed on a low-permittivity dielectric substrate.

2. Experiment

The G-line used in this work is formed by a 2-mm-long single rectangular-shaped conducting wire lying on a flat quartz substrate. The width of the cross-section signal conductor is 5 µm, made from Ti/Au 20/250 nm deposited on a 250 µm-thick quartz substrate. At each extremity, the G-line is linked to a tapered coplanar waveguide. The tapered coplanar waveguides role is the preshaping of the Goubau mode [4]. Our guided-wave THz time domain spectroscopy system uses an erbium-doped fiber laser that delivers 1.55 µm wavelength femtosecond pulses. The generation of single cycle THz pulses is achieved by the illumination of an ultrafast photoconductive switch made by a bonding lifted-off film of ion-irradiated $In_{0.53}Ga_{0.47}As$ material deposited onto the coplanar waveguide section (see Fig1). The detection of the THz pulses propagating along the G-line is achieved using a fiber-coupled ZnTe electro-optic probe.

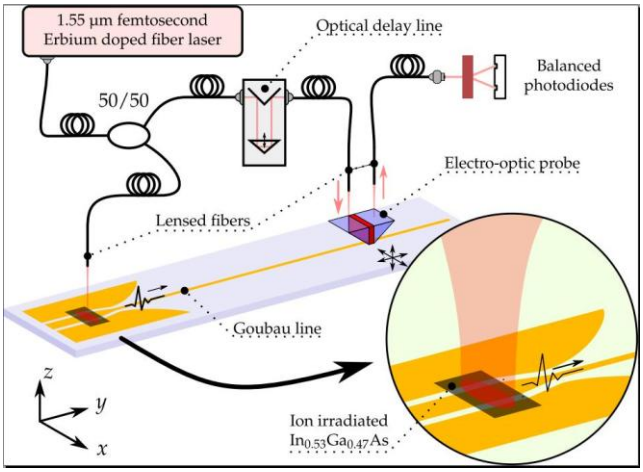

Figure 1: THz guided-wave time domain spectroscopy set-up.

The ZnTe crystal can be oriented to detect either the horizontally polarized component or the vertically polarized component of the THz electric field. The fiber-coupled electro-optic probe, attached to a supporting motorized three-axis translation stage, can be independently positioned from the other optical components. The whole system is fiber integrated [5].

3. Results

Figure 2a displays the transient electrical waveforms, generated by the ion-irradiated $In_{0.53}Ga_{0.47}As$ photoconductive switch and measured by the electro-optic probe at the entrance of the G-line, and after 1mm of propagation along the G-line. After 1 mm propagation distance, the pulse is distorted due to dispersion effects and its amplitude is decreased by a factor 1.75 due to metal skin-effect losses, dielectric losses in the substrate and radiative losses. The amplitude of the spectra of these transient waveforms, obtained by fast Fourier transform, are shown in Fig.2b. After 1 mm of propagation distance, the spectrum extends up to 0.9 THz with a dynamic of ~35 dB (Fig.2b).

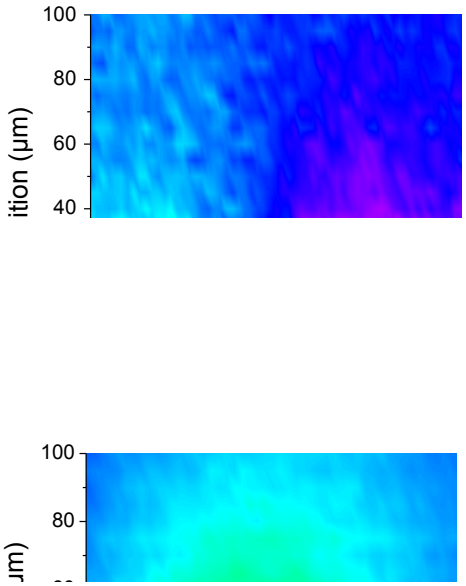

Figure 2: (a) THz waveforms measured at the entrance of the G-line (0 mm) and after a propagation distance of 1 mm. (b) Spectra in amplitude of the temporal waveforms.

The spatial profile of the mode is measured by scanning the electro-optic detector in a plane perpendicular to the G-line axis, with a time delay fixed at the peak of the THz pulse. Figure 3a and b show the spatial distribution of the projection of the electric field onto the vertical and the horizontal direction respectively, measured using electro-optic probes with distinct orientations of the ZnTe crystal. The polarity reversal of the horizontal component of the electric field as the electro-optic probe scans across the G-line clearly shows the radial nature of the Goubau mode. The amplitude of the vertical component of the electric field above the G-line (in the z direction) falls to 1/e of its maxima value at 64.5 µm, demonstrating the confinement of the Goubau mode around the wire. This value represents the broadband surface plasmon decay length weighted over the broad spectrum of the THz pulse used.

Figure 3: The spatial distribution of the projection of the electric field onto the vertical direction (a) and onto the horizontal direction (b).

4. Conclusion

In conclusion, we demonstrated that the THz electric field of the surface plasmon waves propagating on planar G-lines is confined near a surface around the wire over few tenths of microns (λ/10) making waveguides based on G-lines very promising for many applications such as high resolution imaging and spectroscopy.

References

[1] L.Dazhang, J. Cunningham, M.B. Byrne,S. Khanna, C.D.Wood, A.D. Burnett, S.M. Ershad, E.H. Linfield, and A.G. Davies, On-chip terahertz Goubau-line waveguides with integrated photoconfuctive emitters and mode-discriminating detector, *App.Phys.Lett*, Vol. **95**, 092903, 2009.

[2] K. Wang and and D. M. Mittleman, Metal wires for terahertz wave guiding, *Nature*, Vol. 432, pp. 376–379, 2004.

[3] N. Laman, S. S. Harsha, D. Grischkowsky, and J. S. Melinger, 7 GHz resolution waveguide THz spectroscopy of explosives related solids showing new features, *Opt. Express,* Vol. **16**, 4094-4105, 2008.

[4] T. Akalin et al., Single-Wire Transmission Lines at Terahertz Frequencies*,* *IEEE MTT*, Vol. **54**, 2762, 2006.

[5] L. Meignien, J. Mangeney, P. Crozat, L. Duvillaret, and M. Hanna, Two-port vectorial terahertz electro-optic sampling system, *App.Phys.Lett*, Vol. **92**, 131103-131105, 2008.

Tunable coherent perfect absorption using a composite film

Shourya Dutta-Gupta[1,*], Olivier J. F. Martin[1] and S. Dutta Gupta[2]

[1]Nanophotonics and Metrology Laboratory, Swiss Federal Insitute of Technology Lausanne, Switzerland
[2]School of Physics, University of Hyderabad, India
*corresponding author, Email: shourya.duttagupta@epfl.ch

Abstract

Coherent perfect absorption (CPA) using a colloidal gold film is studied when the structure is illuminated using either plane waves or gaussian beams from opposite sides at oblique incidence. Using standard tranfer matrix approach, we show that the CPA frequency can be tuned over the visible range of the spectrum by appropriately tuning the system parameters. We also show that it is possible to achieve CPA at two distinct frequencies for oblique incidence. Furthermore, we demonstrate that CPA can be achieved when the composite film is illuminated by two gaussian beams with a beam waist of $50\,\mu$m from either side.

1. Introduction

Perfect absorption by micro and nano structures has been extensively studied for their possible applications in enhancing solar cell efficiency, light storage and development of ultrasensitive biosensors. Geometries that have been used to achive critical coupling or perfect absorption of light by a structure include gratings, fiber–disc systems and planar dielectric structures with a few nanometer thick absorbing layer [1, 2, 3, 4]. It was shown by Cai *et al.* that it is possible to slow down light and eventually store it in the structure by using the fiber–disc system [2]. A different approach using a nano absorbing layer placed on a dielectric Bragg reflector (DBR) separated by a spacer, was investigated by Tischler *et al.* and Dutta Gupta [3, 4]. The spacer between the DBR and the absorbing layer controlled the amplitudes and phases of the different reflected waves comming from different interfaces. Thus by tuning the thickness of the spacer, it was possible to ensure zero reflection due to destructive interference of the the reflected waves from different interfaces. Moreover, by choosing parameters of the DBR such that the working wavelength was in a stop band ensured zero transmission from the structure. Therefore, the structure neither transmitted nor reflected, implying that the entire incident light was "perfectly" absorbed by the few–nanometer thick lossy layer.

Usually a single incident beam is used for illuminating the sample when studying the critical coupling of light by a structure. Recently, it was shown by Cao *et al.* that the use of two incident beams from opposite sides leads to the so called coherent perfect absorption (CPA), which has the added flexibility that the two beams can be controlled independently [5, 6]. A silicon slab of thickness $100\,\mu$m was illuminated from either side at normal incidence and by tuning the phase of one incident beam with respect to the other it was possible to achieve coherent perfect absorption of light. A limitation of using such a silicon slab as the absorber in CPA is tunability of the CPA frequency. In a recent paper we showed that it is possible to achieve CPA using a metal-dielectric composite slab when it is illuminated with plane waves at normal incidence from either side [7]. The tunability of the CPA frequency was demonstrated by modifying the properties of the composite film. Furthermore, it was shown that it is possible to achieve CPA at two distinct frequencies.

In this paper, we first study coherent perfect absorption of light when a metal-dielectric composite slab is illuminated by two plane waves incident at oblique angles from either side. We show that it is possible to achieve CPA at two distinct frequencies for oblique incidence as well. Finally, we study how the CPA of light is modified when the structure is illuminated by two gaussian beams from either sides as opposed to two plane waves.

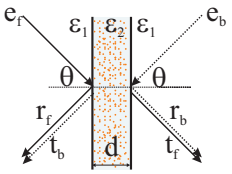

Figure 1: Schematics of the CPA setup.

2. Formulation

Consider the geometry shown in Fig. 1, where a metal–dielectric ($\mathrm{Au}-\mathrm{SiO_2}$) composite layer of thickness d is illuminated by two coherent monochromatic planewaves with unit amplitude incident from either side at an angle θ. For future reference we label the wave propagating forward and incident from left (right) and resulting reflected and transmitted waves with subscript f (b). Symmetry (incident and emmergent media are the same) ensures that the total scattered amplitudes in the medium of incidence and emergence are the same since the reflected and transmitted amplitudes individually are the same ($r_f = r_b = r$, $t_f = t_b = t$). The nature of scattering in both directions is governed by the interference between r and t. It will be destructive and leading to CPA if the magnitudes of these waves are the same with a phase difference of π, i.e., $|r| = |t|$ and $|\Delta\phi| = |\phi_r - \phi_t| = \pi$, where ϕ_r and ϕ_t refer

to the phases of r and t, respectively. Inherent symmetry ensures that when destructive interference occurs in the incidence medium, the same would happen in the emergence medium, leading to CPA.

The complex reflection and transmission amplitudes for plane wave illumination were calculated using the transfer matrix approach [8]. The contributions for left and right incidences were calculated separately and then superposed to obtain the total scattered amplitudes on both the sides. In all the calculations presented in this paper the following parameters were kept constant: $\varepsilon_1 = 1.0$ and $\varepsilon_d = 2.25$ (SiO_2). The dielectric function of gold was taken from the data provided by Johnson and Christy [9]. The optical properties of this metal–dielectric composite ($Au - SiO_2$), with a metal volume fraction of f_m, were modelled using the Bruggeman effective medium theory. Space frequency decomposition technique was used to decompose the gaussian beam into various plane waves and the response of each plane wave was calculated using the transfer matrix approach.

3. Results and discussions

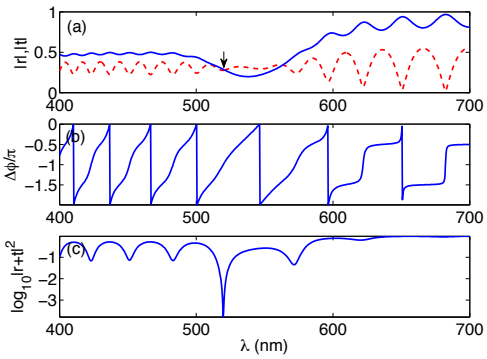

Figure 2: Absolute values of reflected (dashed line) and transmitted (solid line) amplitudes $|r|$ and $|t|$ (arrow shows the point where conditions for CPA are satisfied), (b) phase difference $\Delta\phi$ between the forward reflected and backward transmitted plane waves and (c) $log_{10}|r+t|^2$, as a function of λ for $f_m = 0.0035$, $\theta = 45^\circ$ and $d = 5.1\,\mu$m.

3.1. Plane wave illumination

Let the structure shown in Fig. 1 be illuminated by plane waves from either side at an angle of $\theta = 45^\circ$. The dependence of $|r|$, $|t|$, $\Delta\phi$ and $log_{10}|r+t|^2$ as functions of λ for a composite layer with $f_m = 0.0035$ and $d = 5.1\,\mu$m is shown in Fig. 2. It can be seen that the necessary conditions for CPA, i.e., destructive interference between r and t, is satisfied at 520 nm. Moreover, we observe dual crossings of $|r|$ and $|t|$ curves in Fig. 2(a), implying amplitude matching at two different wavelengths. While the phase difference condition for CPA is satisfied at one of these crossings (the left one at $\lambda = 520\,$nm), it is slightly off for the other one. Similar to the case of CPA occuring at dual frequencies for normal incidence, it should be possible to achieve CPA at two distinct frequencies for oblique incidence [7]. This is shown in Fig. 3, where by choosing $f_m = 0.0045$ and $d = 5\,\mu m$, we see two distinct wavelengths where the CPA condition is satisfied.

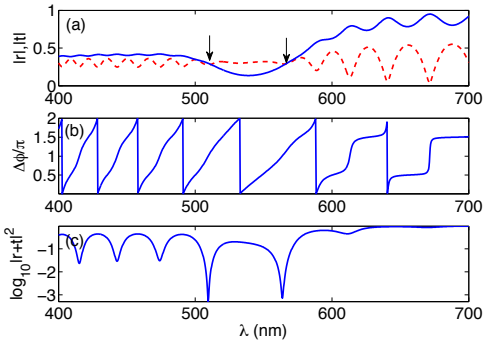

Figure 3: Absolute values of reflected (dashed line) and transmitted (solid line) amplitudes $|r|$ and $|t|$ (arrow shows the point where conditions for CPA are satisfied), (b) phase difference $\Delta\phi$ between the forward reflected and backward transmitted plane waves and (c) $log_{10}|r+t|^2$, as a function of λ for $f_m = 0.0045$, $\theta = 45^\circ$ and $d = 5\,\mu$m.

Figure 4 shows the variation of $|r|$,$|t|$, $\Delta\phi$ and $log_{10}|r+t|^2$ as a function of θ for a composite layer with $f_m = 0.0024$ and $d = 5.0\,\mu$m when it is illuminated with plane waves with $\lambda = 532\,$nm. It can be seen that the CPA condition is fulfilled at $\theta = 52.65^\circ$, i.e, $|r| = |t|$ and $\Delta\phi = \pi$.

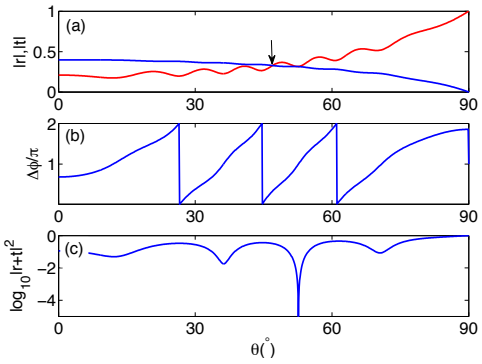

Figure 4: Absolute values of reflected (dashed line) and transmitted (solid line) amplitudes $|r|$ and $|t|$ (arrow shows the point where conditions for CPA are satisfied), (b) phase difference $\Delta\phi$ between the forward reflected and backward transmitted plane waves and (c) $log_{10}|r+t|^2$, as a function of θ for $f_m = 0.0024$, $\lambda = 532\,$nm and $d = 5\,\mu$m.

Looking at the dispersion diagram of the system (see Fig. 5), i.e., the log of the total scattered intensity as a function of θ and λ, we observe multiple parameter combinations of θ and λ for which the CPA conditions are fulfilled. The position of the CPA dips can be tuned by varying the volume fraction of the composite (see Fig. 5 (a) and (b)). Further control of the CPA frequency can be achieved by

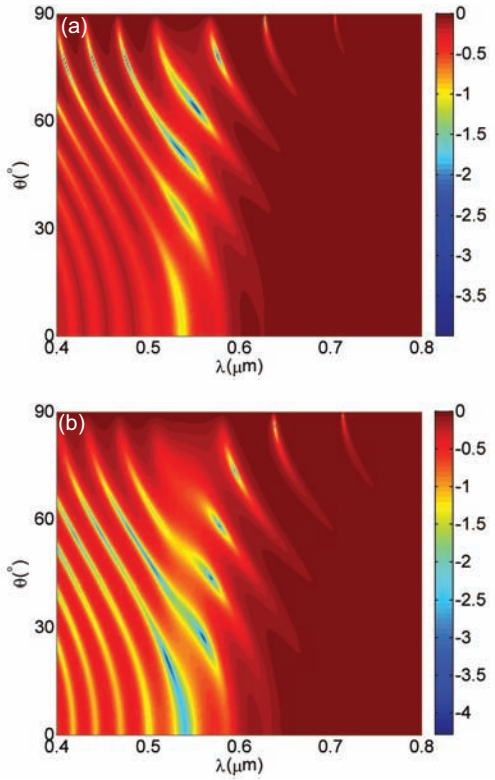

Figure 5: Log of the total scattered intensity ($log_{10}|r+t|^2$) as a function of θ and λ for (a) $f_m = 0.002$ and (b) $f_m = 0.005$. The thickness of the slab was taken to be $5\,\mu$m.

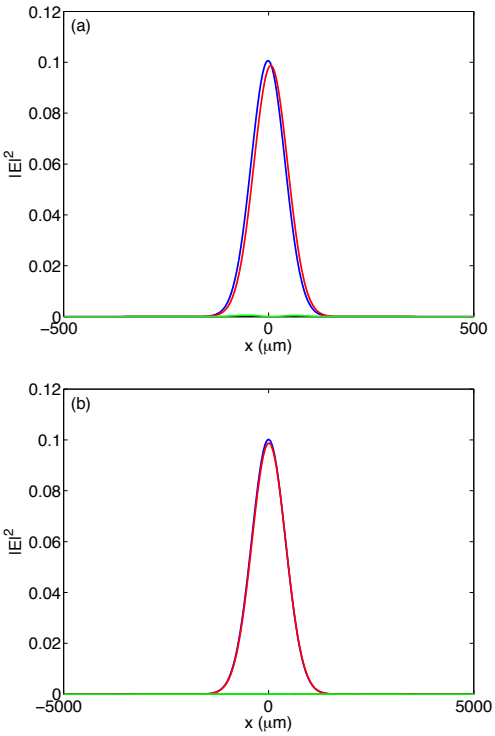

Figure 6: $|E_r|^2$ (blue), $|E_t|^2$ (red) and $|E_r + E_t|^2$ (green) as a function of the cross-section of the beam for gaussian beams incident at an angle of $52.65°$ with a waist of (a) $w_0 = 50\,\mu$m and (b)$w_0 = 500\,\mu$m. The other parameters were the same as in Fig. 4.

varying the thickness of the composite as well as its constituents.

3.2. Gaussian beam illumination

We now study how coherent perfect absorption is modified when two gaussian beams are used to illuminate the sample from either side as opposed to two plane waves. Let the structure shown in Fig. 1 be illuminated by two gaussian beams, each with a beam waist of w_0 and $\lambda = 532\,$nm, at an angle of $\theta = 52.65°$ from either side. The aforementioned parameters were chosen such that coherent perfect absorption was ensured for plane wave illumination (see Fig. 4). Figure 6 shows the intensity of the electric field (at the composite-air interface) for both single and dual gaussian beam incidences for two different beam waists ($w_0 = 50\,\mu$m and $w_0 = 500\,\mu$m). It can be clearly seen for both the beam waists considered here, the total electric field intensity ($|E_r + E_t|^2$) due to dual beam incidence is negligible compared to single beam incidence ($|E_r|^2$ or $|E_t|^2$). Therefore, a tightly focussed gaussian beams with beam waist of $50\,\mu$m can be absorbed by such a composite film.

4. Conclusion

In conclusion, we have shown coherent perfect abasorption using a metal-dielectric composite illuminated either by plane waves or by gaussian beams from either side. Moreover, the flexibility of using such a composite was demonstrated by showing the tunability of the CPA frequency by appropriately choosing the system parameters. We also demonstrated that it is possible to achieve CPA at two distinct frequencies even for oblique plane wave incidences. Finally, we showed that when the composite film was illuminated by two gaussian beams simultaneously, with a waist of $w_0 = 50\,\mu$m, it was possible to achieve CPA. We have also studied plasmon mediated CPA and the role of long and short range modes in such perfect absorption. These results will be reported else where.

References

[1] E. Popov, L. Tsonev, and D. Maystre, Lamellar metallic grating anomalies, *Applied Optics*, 33: 5214-5219, 1994.

[2] M. Cai, O. Painter and K. J. Vahala, Observation of Critical Coupling in a Fiber Taper to a Silica-Microsphere Whispering-Gallery Mode System, *PRL*, 85: 74–77, 2000.

[3] J. R. Tischler, M. S. Bradley and V. Bulovic, Critically coupled resonators in vertical geometry using a planar mirror and a 5 nm thick absorbing film, *Opt. Lett.*, 31: 2045–2047, 2006.

[4] S. Dutta Gupta, Strong interaction mediated critical coupling at two distinct frequencies, *Opt. Lett.*, 32: 1483-1485, 2007.

[5] Y. D. Chong, L. Ge, H. Cao, and A. D. Stone, Coherent Perfect Absorbers: Time-Reversed Lasers, *PRL*, 105: 053901, 2010.

[6] W. Wan, Y. D. Chong, L. Ge, H. Noh, A. D. Stone and H. Cao, Time-Reversed Lasing and Interferometric Control of Absorption, *Science ,* 331: 889–892, 2011.

[7] S. Dutta-Gupta, O. J. F. Martin, S. Dutta Gupta and G. S. Agarwal, Controllable coherent perfect absorption in a composite film, *Opt. Exp. ,* 20: 1330–1336, 2011.

[8] M. Born and E. Wolf, *Principles of Optics*, Cambridge University Press, New York, 1999.

[9] P. B. Johnson, and R. W. Christy, Optical constants of the noble metals, *Phys. Rev. B,* 6: 4370-4379, 1972

Optical properties of single silver triangular nanoprism.

F. K. GUEDJE[a,b,c] , M. POTARA[b], S. ASTILEAN[b] and M. N. HOUNKONNOU[a]

[a] *International Chair of Mathematical Physics and Applications*
ICMPA-UNESCO Chair
University of Abomey-Calavi, 072 B.P. 50 Cotonou, Republic of Benin

[b] *Institute for Interdisciplinary Experimental Research, Nanobiophotonics Center*
Babes-Bolyai University, Treboniu Laurian 42, 400271 Cluj-Napoca, Romania

[c] *Ecole des Sciences et Techniques du Bâtiment et de la Route (ESTBR)*
Université d'Abomey-Calavi, 072 B.P. 50 Cotonou, Republique du Bénin

Abstract

The ability to provide large electric field enhancements make the triangular nanoprisms and branched nanoparticles very attractive for applications in surface-enhanced Raman scattering ($SERS$). Theoretical studies on the optical properties of triangular prisms in water solution are presented in this paper to determine how structural modifications and the incident field polarization affect the extinction spectrum and the enhanced local electric-fields (E-field) around particles in the wavelength range $300 - 1000$ nm. The near-field properties such as the E-field close to the particle determine the electromagnetic enhancements in SERS. The full orientation could be approximated using three orientations, but orientations where the polarization vector is parallel to the triangular cross section are most important to the overall extinction than those where the polarization vector is perpendicular to the plane. The extinction spectrum presents three distinct localized surface plasmon resonances ($LSPR$) for silver triangular nanoprism. These are assigned as in-plane dipolar and quadrupolar plasmon excitations using electrodynamic modeling based on the finite difference time domain ($FDTD$). The dipole resonance is found to be very intense, and its peak wavelength is extremely sensitive to the thickness and edge length of the nanoprism. In contrast, the intensity of the quadrupole resonance is much weaker relative to the dipole resonance. The distribution of the local field around the particle at specified wavelengths, showing values of the peak field is presented. All of the localized surface plasmon resonances are clearly resolved in the visible. The experimental data are used for comparison. These new spectral features could be very promising in nano-optics and for bio-sensing applications.

1 Introduction

Recent interest in nanoparticles is propelled by both the advances in scientific understanding of their synthesis and physical properties [1–6] as well as the possibility of using them for applications in chemical and biological sensing [7–11], cancer treatment [4, 12, 13], catalysis [14, 15], as markers for transmission electron microscopy (TEM) and scanning electron microscopy (SEM) [16, 17] and various specialized photonic and electronic applications [18–20]. These applications are based on the unique optical properties of metal nanoparticles [21, 22].

When the incident electromagnetic wave interacts with a nanoparticle, localized surface plasmon resonance (LSPR), which is a collective oscillation of conduction electrons, is excited. This phenomenon has two key consequences: first, selective photon absorption allows the optical properties

of the nanoparticles to be monitored. Second, enhancement of the electromagnetic fields surrounding the nanoparticles lead to surface-enhanced spectroscopic techniques including surface enhanced Raman spectroscopy [23].

LSPR of a nanoparticle is very sensitive to its components [24], shape [21, 25], size [26], and dielectric environment [27, 28]. Nanoparticles of different sizes have been studied for their optical spectra and surface-enhanced Raman scattering (SERS) properties. Anisotropic metal nanoparticles like nanoprisms or branched nanostructures may be attractive for applications that use surface enhanced Raman spectroscopy as they provide large electric enhancements.

This article is organized as follows. In section II, we briefly introduce the FDTD method. In section III, our main results are provided. Silver triangular nanoprism is given as an example to study the influence of orientation and size on LSPR properties. The modulation on the dipole and quadrupole surface plasmon resonance peak and the corresponding local field enhancement characteristics are investigated and discussed. Theoretical and experimental spectra are compared. The section IV is devoted to the conclusion.

2 Numerical Methodology

The optical properties of nanoparticles can be calculated exactly only for simple shape like sphere [29–31]. This justifies why various numerical methods and techniques have been applied to solve Maxwell equations for non-spherical particles. In case of metal nanoparticles, these tools allow us to compute the plasmon resonance as well as local electric fields, and hence the local enhancement of fields and effects resulting from them. The most commonly used numerically accurate methods are discrete dipole approximation (DDA) and T-matrix methods, though multiple multipole methods (MMP) and finite difference time domain (FDTD) methods have been utilized as well [32]. Of all, the finite difference time domain technique of Taflove [33–36] and Sullivan [37] has proved to be a powerful tool to calculate the spectra as well as the near field properties of metal colloids. This method solves the time-dependent Maxwell equations by discretizing space and time and involves a relativity simple time-stepping algorithm. The electric flux dependent form of Maxwell equations is given by:

$$\frac{\partial \vec{D}}{\partial t} = \nabla \times \vec{H} \tag{1}$$

$$\vec{D}(\omega) = \epsilon(\omega)\vec{E}(\omega) \tag{2}$$

$$\frac{\partial \vec{H}}{\partial t} = -\frac{1}{\mu_0}\nabla \times \vec{E} \tag{3}$$

where $\vec{H}$, $\vec{E}$ and $\vec{D}$ are the magnetic, electric and displacement field, respectively. μ_0 is the permeability of free space and $\epsilon(\omega)$ the complex dielectric constant. The technique consists of solving these equations on a discrete grid, replacing all derivatives by finite differences. To indicate time, Yee's superscript [38] is used. The superscript n is related to time t by the following equation. The variable $\triangle t$ is referred to as the time-step size,

$$t = n\triangle t \tag{4}$$

In the FDTD method, electric field values are only defined at whole number time steps, while magnetic field values are defined only at half time steps. Thus relative to time step n, two arbitrary electric field values can be expressed as,

$$E^n[i,j,k] \qquad \text{and} \qquad E^{n+1}[i,j,k] \tag{5}$$

Likewise, relative to time step n, two magnetic field values can be written as,

$$H^{n+\frac{1}{2}}[i,j,k] \qquad \text{and} \qquad H^{n-\frac{1}{2}}[i,j,k] \tag{6}$$

The benefit of defining electric and magnetic field components in this way in regard to time is that it allows electric and magnetic field component updates in a FDTD analysis to be interlaced in time. Electric field values are first calculated at each time step, then the magnetic field values are computed at half time steps. Note that in updating a field component, only past electric and magnetic field components are required. In cases where an electric field value is needed at a half time step, a value can be approximated by averaging electric field values between whole time steps. According to Taflove and Brodwin [33], for a FDTD analysis based on central differencing to remain stable the following mathematical statement must be true:

$$v_{max}.\triangle t \leq ((\triangle x)^{-2} + (\triangle y)^{-2} + (\triangle z)^{-2})^{-\frac{1}{2}} \tag{7}$$

where v_{max} is the maximum wave phase velocity expected in the model, $\triangle t$ is the time step size, $\triangle x$, $\triangle y$ and $\triangle z$ refer to the mesh discretization size along each coordinate axis. The choice of the mesh density and the time step size is motivated by the need for analysis stability and accuracy. The stability criterion sets a minimum limit in the relationship between the time step size, mesh cell size, and propagation speed. Likewise the need for accuracy sets a limiting relationship between the quality of results and the overall mesh size. The simulation is computationally intensive when high spatial precision is required; the latter generates the problem of computer memory allocation.

3 Results and discussion

All calculations here refer to water as the external dielectric medium. The FDTD calculations use a cubic grid with a grid spacing of 1.0 nm. This grid spacing leads to high-quality simulations of extinction spectra which are converged with respect to grid spacing.

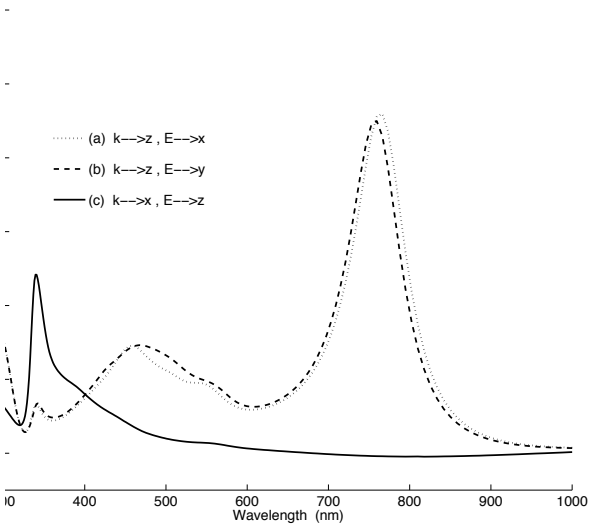

Figure 1: *Absorption spectrum of silver triangular nanoprism (edge length 100 nm, thickness 15 nm) in water solution n=1.33, FDTD simulations with grid=1.0 nm, with different $\vec{E}$ orientations.*

In Figure 1, there are three dominant peaks in the absorption spectrum corresponding to different modes of plasmon excitation. The spectrum of the Ag triangular prism with side length 100 nm and thickness 15 nm shows a strong in-plane dipole plasmon resonance at 766 nm (curve a) and 760 nm (curve b) , an in-plane quadrupole resonance at 458 nm (curve a) and 468 nm (curve b), and an out-of-plane quadrupole resonance at 341 nm refers to the bluest resonance. This third plasmon resonance, due to out-of-plane quadrupole excitation, is accessible in our calculations; it appears with great intensity when $\vec{E}$ is perpendicular to the large face of the prism (curve c).

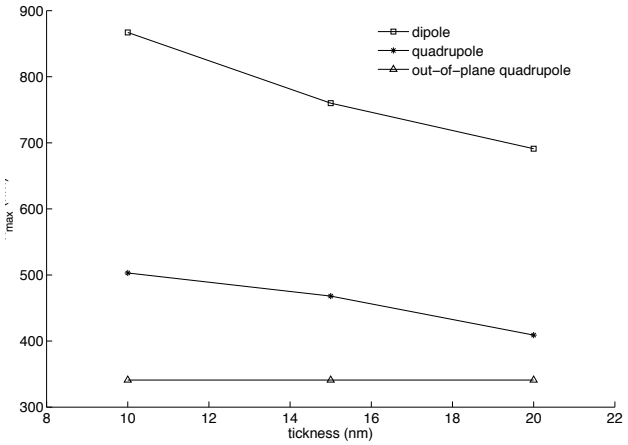

Figure 2: *Plot of the relationship between the prism thickness and the LSPR response. The silver triangular nanoprism (edge length 100 nm with different thickness) in water solution n=1.33.*

Figure 2 shows that the long wavelength dipole resonance shifts to red as the thickness decreases. Increasing the prism aspect ratio for fixed edge length, we note a red shift of the resonance corresponding to the dipole mode from 691 to 867 nm and quadrupole mode from 409 to 506 nm. It is important to notice that the out-of-plane quadrupole resonance is invariable and its value 341 nm does not change, despite the variation of the length and thickness of the triangular prism (Figure 1 and 2).The extinction spectrum of the nanoprisms is also sensitive to the thickness of the particles.

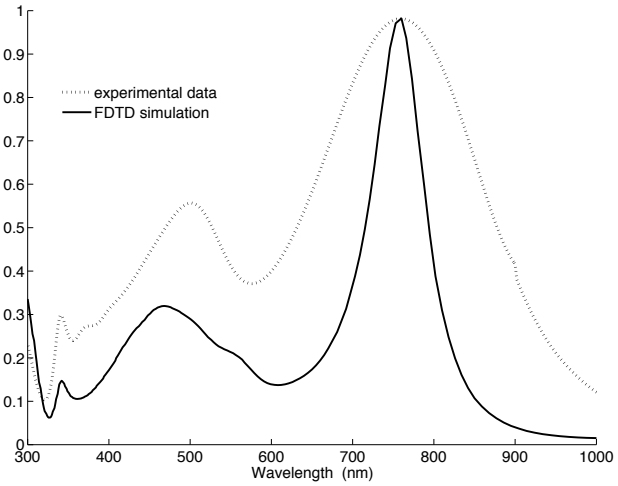

Figure 3: *Experimental ensemble extinction spectrum (....) vs theoretical modeling (black curve) of a single triangular nanoprism using the FDTD method. The theoretical spectrum is calculated for a nanoprism with edge length 100 nm and height 15 nm. FDTD simulations with grid=1.0nm*

Figure 3 compares ensemble averaged results with those provided by the theory for single triangular nanoparticles. This comparison gives significant information about the triangular nanoprism properties, including the assignment of the modes of plasmon excitation which are responsible for each of the three experimentally observed plasmon peaks at 760, 500 and 342 nm in the case of nano triangular prism of length 100 nm and thickness 15 nm.

SERS has been the subject of extensive studies, and it is generally agreed that an important contribution to the SERS enhancement comes from the electromagnetic field enhancements that occur near the particle surface as a result of plasmon excitation [39]. This E-field enhancement in turn leads to enhanced Raman scattering intensities.
The E-field contours show that the maximum enhancement for the dipole resonances occurs at the prism tips. The largest fields ($|E|^2$) for the dipole resonance is $3,7.10^4$ times the applied field for the triangular prism (Figure 4). The fields for in-plane quadrupole resonance is less than for the dipole resonance (Figure 5). The shorter wavelength resonances have smaller E-fields as represented in Figure 6. The calculations reveal that the electric field intensity on the metal monomer decays significantly with distance. One can see that the intensity of the near field is sensible to the prism aspect ratio.

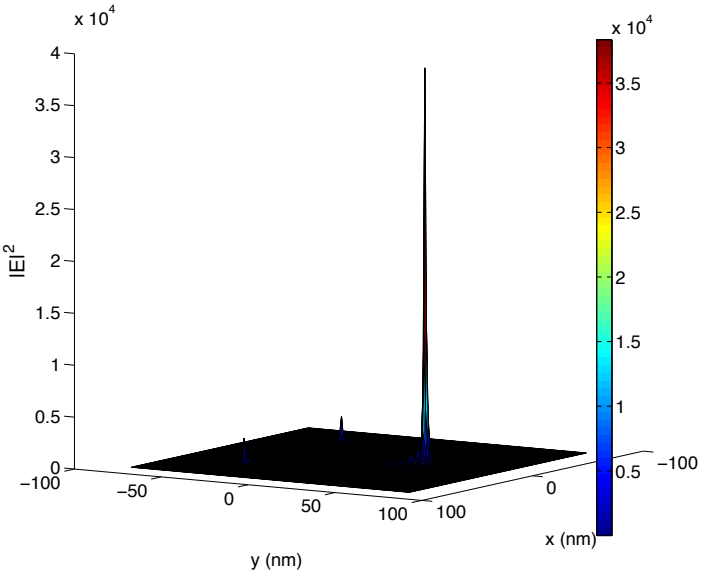

Figure 4: *3D plots of the E-field enhancement contours external to Ag nanoprism at* $\lambda = 760nm$. *The axis perpendicular to the selected plane represents the amount of E-field enhancement around the nanoprism. The incident field* $\vec{E}$ *is polarized in the y direction and propagating in the z direction. FDTD simulations with grid=1.0nm.*

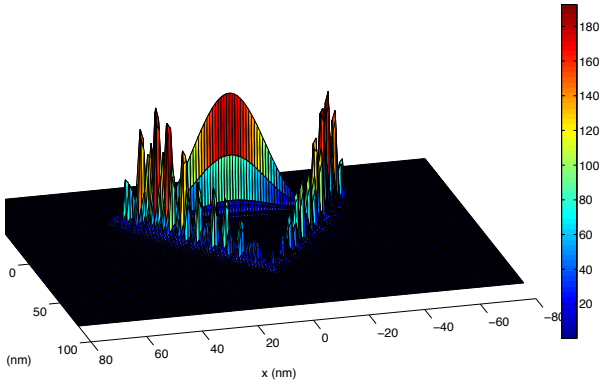

Figure 5: *3D plots of the E-field enhancement contours external to Ag nanoprism at* $\lambda = 468nm$. *The axis perpendicular to the selected plane represents the amount of E-field enhancement around the nanoprism. The incident field* $\vec{E}$ *is polarized in the y direction and propagating in the z direction. FDTD simulations with grid=1.0nm.*

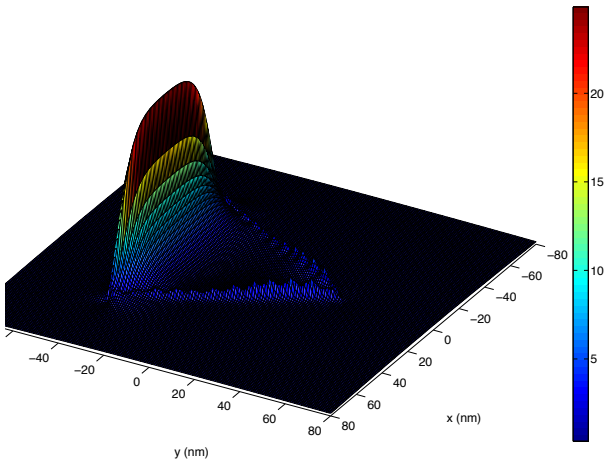

Figure 6: *3D plots of the E-field enhancement contours external to Ag nanoprism at* $\lambda = 341nm$*. The axis perpendicular to the selected plane represents the amount of E-field enhancement around the nanoprism. The incident field* $\vec{E}$ *is polarized in the y direction and propagating in the z direction. FDTD simulations with grid=1.0nm.*

4 Conclusion

We use the finite difference time domain method to study the optical properties of isolated silver triangular nanoprism. It is noted that the full orientation could be approximated using three orientations [40], but orientations where the polarization vector $\vec{E}$ is parallel to the triangular cross section are most important to the overall extinction than orientations where the polarization vector is perpendicular to the plane. The positions of plasmon resonances depend, among other parameters, on particle size, or more specifically on the ratio between the edge length and thickness. These particles exhibit distinct dipole and quadrupole plasmon resonances; the excitations of these resonances create an E-field external to the particles that is important in determining normal and single molecule SERS intensities. The anisotropic nanoparticles, particularly nanoparticles with sharp points such as triangular nanoprisms, produce much stronger electric fields than the simplest structures like nanospheres, nanorods [41]. The peak enhancement is associated with peak extinction for all structures studied.

acknowledgements

This work is partially supported by the Abdus Salam International Centre for Theoretical Physics (ICTP, Trieste, Italy) through the Office of External Activities (OEA) - Prj-15. The ICMPA is in partnership with the Daniel Iagolnitzer Foundation (DIF), France.

References

[1] M. A. El-Sayed, *Some interesting properties of metals confined in time and nanometer space of different shapes*,Accounts of Chemical Research 34,pp. 257-264, 2001.

[2] L. A. Dykman and V. A. Bogatyrev, *Gold nanoparticles: synthesis, functionalization, the use in biochemistry and immunochemistry*, Uspekhi Khimii, vol. 76, no. 2,199213, 2007.

[3] M. C. Daniel and D. Astruc, *Gold nanoparticles: assembly, supramolecular chemistry, quantum-size-related properties, and applications toward biology, catalysis, and nanotechnology*, Chemical Reviews, vol. 104, no. 1, pp. 293346, 2004.

[4] X. Huang, P. K. Jain, I. H. El-Sayed, M. A. El-Sayed, *Gold nanoparticles and nanorods in medicine: From cancer diagnostics to photothermal therapy*, Invited Review, Nanomedicine, 2(5), pp. 681-693,2007.

[5] X. Lin, A. Samia, Synthesis, *assembly and physical properties of magnetic nanoparticles*, Journal of Magnetism and Magnetic Materials, Vol.305, Issue: 1,Elsevier, pp. 100-109, 2006.

[6] C. Burda, X. Chen, R. Narayanan, and M. A. El-Sayed, *Chemistry and properties of nanocrystals of different shapes*, Chemical Reviews, vol. 105, no. 4, pp. 10251102, 2005.

[7] K. A. Willets and R. P. Van Duyne, *Localized Surface Plasmon Resonance Spectroscopy and Sensing*,Annual Review of Physical Chemistry,Vol. 58, pp267-297,2007.

[8] De M., Ghosh P. S. and Rotello V. M., *Applications of Nanoparticles in Biology. Advanced Materials*, 20,pp. 42254241, 2008.

[9] A. J. Haes, C. L. Haynes, A. D. McFarland, G. C. Schatz, R. P. Van Duyne and S. Zou, *Plasmonic Materials for Surface-Enhanced Sensing and Spectroscopy*. MRS Bulletin, 30, pp 368-375,2005.

[10] C. J. Murphy, A. M. Gole, S. E. Hunyadi, J. W. Stone, Sisco, P. Alkilany, A. Hankins, P. L. Kinard, B., *Chemical Sensing and Imaging with Metallic Nanorods*, Chem. Comm., pp. 544-557, 2008.

[11] M. Baia, S. Astilean, T. Iliescu, *Raman and SERS investigations of pharmaceuticals*, Ed. Springer, 2009.

[12] W. Chen, J. Zhang, *Using Nanoparticles to Enable Simultaneous Radiation and Photodynamic Therapies for Cancer Treatment,Journal of Nanoscience and Nanotechnology*, Vol. 6, no. 4,pp. 1159-1166(8), 2006.

[13] Y. V. Maksym, G. Xiaohu, X. Yun, and al. *Emerging use of nanoparticles in diagnosis and treatment of breast cancer*, The Lancet Oncology, Vol. 7, Issue 8,pp. 657-667, 2006.

[14] R. Narayanan and M. A. El-Sayed,*Catalysis with Transition Metal Nanoparticles in Colloidal Solution:Nanoparticle Shape Dependence and Stability*,J. Phys. Chem. B, 109 (26), pp. 1266312676, 2005.

[15] C. R. Henry , *Catalysis by Nanoparticles,Nanocatalysis, NanoScience and Technology*,pp. 245-268,DOI: $10.1007/978-3-540-32646-5-3$, 2007.

[16] K.Safarova, A.Dvorak, R. Kubinek, M.Vujtek, A. Rek, *Usage of AFM, SEM and TEM for the research of carbon nanotubes*, Modern Research and Educational Topics in Microscopy, A. Mndez-Vilas and J. Daz (Eds.), 2007.

[17] S. Thiberge, A. Nechushtan, D. Sprinzak, O. Gileadi and V Behar, *Scanning electron microscopy of cells and tissues under fully hydrated conditions*, Proceedings of the National Academy of Sciences, Vol. 101, Issue: 10, pp. 3346-3351, 2004.

[18] S. A. Maiera and H. A. Atwater, *Plasmonics: Localization and guiding of electromagnetic energy in metal/dielectric structures*,J. of Appl. Physics, Vol 98,DOI:10.1063/1.1951057, 2005.

[19] D. Astruc, E. Boisselier and C. Ornelas, *Dendrimers Designed for Functions: From Physical, Photophysical, and Supramolecular Properties to Applications in Sensing, Catalysis, Molecular Electronics, Photonics, and Nanomedicine*,Chem. Rev., vol.110 (4), pp 18571959, 2010.

[20] M. Dragoman, D. Dragoman, *Plasmonics: Applications to nanoscale terahertz and optical devices,Progress in Quantum Electronics*, Vol. 32, Issue 1, pp. 1-41, 2008.

[21] C. M. Cobley, S. E. Skrabalak, D. J. Campbell and Y. Xia, *Shape-Controlled Synthesis of Silver Nanoparticles for Plasmonic and Sensing Applications*, Plasmonics, Vol. 4, n0. 2, 171-179, DOI:10.1007/s11468-009-9088-0

[22] B. Wiley, Y. G. Sun, J. Y. Chen, H. Cang, Z. Y. Li, X. D. Li, Y. N. Xia, *Shape-controlled synthesis of silver and gold nanostructures*, MRS Bull., 30, 356-361, 2005.

[23] E. Hao, G. C. Schatz, *Electromagnetic fields around silver nanoparticles and dimers*, J. Chem. Phys. 120(1), pp.357-66, 2004.

[24] S. Link, Z.L. Wang, M.A. El-Sayed, *Alloy Formation of Gold-Silver Nanoparticles and the Dependence of the Plasmon Absorption on Their Composition*, J. Phys. Chem. B, 1999, 103 (18), pp. 3529-3533, 1999.

[25] K. L. Kelly,E. Coronado,L. L. Zhao,G. C. Schatz,*The optical properties of metal nanoparticles: the influence of size, shape and dielectric environment* , J. Phys. Chem. B,107(3),668-677 , 2003.

[26] C. L. Haynes, R.P. Van Duyne, *Nanosphere Lithography: A Versatile Nanofabrication Tool for Studies of Size-Dependent Nanoparticle Optics*, J. Phys. Chem. B,105, pp. 5599-5611, 2001.

[27] J. J. Mock, D.R. Smith, Schultz, *Local Refractive Index Dependence of Plasmon Resonance Spectra from Individual Nanoparticles*,Nano Letters, 2003, 3 (4), pp 485491

[28] R. Jin, Y. Cao, C.A. Mirkin, K. L. Kelly, G. C. Schatz, Zheng, *Photoinduced Conversion of Silver Nanospheres to Nanoprisms*, Science, Vol. 294 no. 5548 pp. 1901-1903, 2001.

[29] G. Mie, *Contribution to the optics of turbid media, especially colloidal metal suspensions.* Ann. Phys. 25, 377-445,1908.

[30] H. C. Van de Hulst, *Light Scattering by Small Particles*, Wiley, New York, 1957

[31] C. F. Bohren, and D.R. Huffman, *Absorption and Scattering of Light by Small Particles*, Wiley, New York, 1983

[32] K.L. Kelly, A.A. Lazarides, G.C. Schatz, Computing in Science and Engineering 3, pp.67-73, 2001.

[33] A. Taflove and M. E. Brodwin, *Numerical Solution of Steady-State Electromagnetic Scattering Problems Using the Time-Dependent Maxwells Equations*,IEEE Transactions on Microwave Theory and Techniques, vol. 23, no. 8, pp. 623 - 630, 1975.

[34] Taflove and Umashankar, *Review of FD-TD Numerical Modeling of Electromagnetic Wave Scattering and Radar Cross Section*, Proceedings of the IEEE, vol. 77, no. 5, pp. 682 - 699, 1989.

[35] Taflove and Umashankar,*The Finite-Difference Time-Domain Method for Numerical Modeling of Electromagnetic Wave Interactions with Arbitrary Structures*, PIER2 Progress In Electromagnetics Research, Finite Element and Finite Difference Methods in Electromagnetics Scattering, Elsevier, 1990.

[36] A. Taflove,S. C. Hagness, *Computational Electrodynamics:The finite-difference time domain method*, Artech. House, Inc., Norwood, MA, 2000.

[37] D. M. Sullivan, *Electromagnetic Simulation Using the FDTD Method*, IEEE Press, Piscataway, NJ, 2000.

[38] K. S. Yee, *Numerical solution of initial boundary value problems involving Maxwell's equations in isotropic media*, IEEE Trans. Antennas Propag., 14, pp.302-307, 1966.

[39] G. C. Schatz, *Electrodynamics of nonspherical noble metal nanoparticles and nanoparticle aggregates*, J. Mol. Struct., THEOCHEM 573, 7380, 2001.

[40] R. Jin, Y. Cao and al.,*Photoinduced Conversion of Silver Nanospheres to Nanoprisms*, Science, Vol.294, no. 5548, pp.1901-1903, 2001.

[41] F.K. Guedje, S. Boca, M. Potara, A. Modrea and S.Astilean, *Finite Difference Time Domain (FDTD) calculations of surface Plasmon resonance of different size and shape metallic nanoparticles*, Studia, Physica, pp.39-48, 2009.

Focusing surface plasmons on Er^{3+} ions through gold planar plasmonic lenses

V.A.G. Rivera, F.A. Ferri, L.A.O. Nunes, A.R. Zanatta and E. Marega Jr.

Instituto de Física de São Carlos - INOF, USP, Caixa Postal 369, 13560-970, São Carlos – SP, Brazil
*corresponding author, E-mail: garcia@ursa.ifsc.usp.br

Abstract

Gold plasmonic lenses consisting of planar concentric rings with different periods were milled with a Focused gallium Ion Beam on a gold thin film deposited onto an Er^{3+}-doped tellurite glass. The plasmonic lenses were vertically illuminated with an argon ion laser (488 nm) highly focused by means of a 20x objective lens. The focusing mechanism of the plasmonic lenses is explained by using a simple coherent interference model of surface plasmon-polariton (SPP) generation on the circular grating as a result of the incident field. As a result, phase modulation can be accomplished by the groove gap, similar to a nano-slit array with different widths. This focusing allows a high confinement of SPPs which excited the Er^{3+} ions of the substrate. The Er^{3+} luminescence spectra were measured in the far-field (500−750 nm wavelength range), where we could verify the excitation yield of the plasmonic lens on the Er^{3+} ions. We analyze the influence of physical and geometrical parameters on the luminescence spectra. The variation of these parameters resulted in considerable changes of the luminescence spectra.

1. Introduction

Surface plasmons (SP) enable the localization of light in nanoscale and provide an effective way to control the excitation and emission properties of quantum systems. The confinement of electromagnetic fields in regions as small as possible is important for technological applications such as sub-waveguides and optical sensors. Particularly, periodic ring structures around a nano-aperture are of great interest because the optical transmittance through these systems can be improved with respect to that of an isolated aperture [1]. A variety of nano-aperture structures have been designed and studied, e.g., the first experimental demonstration of such effects was carried out using a silver bull's eye (BE) structure, where a high increase in the efficiency was achieved owing to the enhanced and localized transmittance [2]. In this sense, we are focusing on the so-called BE, consisting of a nano-aperture surrounded by annular grooves. In this structure, the transmitted light through the nano-aperture can be strongly confinement due to the excitation of SP improved in the course of the periodic corrugations [3, 4, 5]. Such a periodic structure at the interface behaves like an antenna which collects and couples the incident light into SPs at a given wavelength λ, resulting in very high fields above the aperture and therefore in high transmission efficiencies under appropriate conditions [6]. This enables great potential applications of BE as device elements are well documented, being implemented, for instance, within photodetector architectures where it enhances the signal to noise ratio [7], and within vertical-cavity surface-emitting lasers (VCSELs) and quantum cascade lasers (QCLs) [8] to control polarization and mode definition, as genuine sub-wavelength optical wave plates [9]. Nevertheless, in BE with periodic concentric rings the maximum transmission is achieved when the SPPs interferes constructively above the aperture, i.e., the coupling between the groove and aperture modes is essential for strengthening the field at the aperture [10], allowing an improvement of the confinement of SPPs.

Tellurite glasses are possible candidates as substrates in plasmonics due to the exhibition of low optical absorption at visible and infrared wavelengths, and represents a compromise between the desire for a low phonon energy host coupled with the need to retain mechanical strength [11]. Low phonon energy generally provides high fluorescence quantum efficiency [12]. Then, when tellurite glasses are doped with rare-earths such properties allow high radiative emission rates, favorable to much higher quantum efficiencies [13, 14]. Furthermore, plasmonic structures can also enhance nonlinear effects of these rare-earths by concentrating light into nonlinear media placed directly within a field enhancement region [15, 16]. Hence, BEs can locally excited quantum systems such as Er^{3+} ions, incrementing the emission intensity.

We report our experimental results of the emission of the Er^{3+} ions through the BEs, where the periodic rings around to nano-aperture has a planar lens structure. These structures excite the Er^{3+} ions embedded in the substrate (tellurite glass) via SPPs, then the radiative emission of Er^{3+} forms SPPs in the interface of the metallic film with the substrate, which propagates by means of the nano-hole, emitting the luminescence of the Er^{3+} ions outside the BEs.

2. Sample preparation and experimental setup

In order to investigate the luminescence of the Er^{3+} ions through the BEs in these concentric rings, as well as its dependence with the ring separation, a tellurite glass substrate with 1.0 wt % of Er_2O_3, submitted to 2.5 hours of

annealing time was prepared [17]. The sample was cut in a square piece of approximately 6.0×3.0×0.5 mm^3 and polished until obtaining a good surface quality. Then, a gold thin film with 240 nm of thickness was deposited on the substrate. When the film thickness is near half- or full-integer wavelengths of the guided mode within the nano-hole, or, in other words, the "nano-cavity", an optimal transmission is achieved, which implies a field enhancement inside the nano-aperture [18]. Finally, the nanostructures were fabricated by focused gallium ion beam (FIB) milling (Dual Beam FEI Quanta 3D 200i (Ga^+ ions, 30 keV), as illustrated in Figs. 1(a) - (c). The ring elements have about 100 nm of separation (see Fig. 1(a)). It is valuable to point out that the optical properties of the metallic nanostructures are strongly dependent of their shape, gap and depth [16].

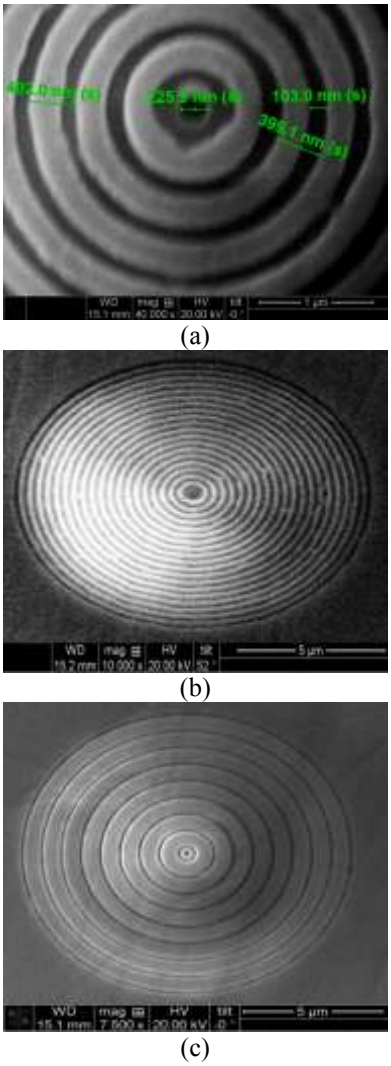

(a) (b) (c)

Figure 1. SEM images of BEs with rings forming planar plasmonic lens, milled in the 240 nm thick Au film deposited onto the tellurite glass substrate with a gap of: (a) 300 nm and 15 groove-rings, (b) 200 nm and 20 groove-rings, (c) 600 nm and 9 groove-rings.

In this gold film a circle hole was milled with diameter of 240 nm. Additionally, rings (i.e., groove depth h = 80 nm) were added, forming planar lenses with periodic gaps (separation between the rings). These groove-rings have widths (g, in Fig. 2) of approximately 100 nm. In total, five planar lenses were fabricated with 20, 15, 12, 10 and 9 groove-rings for gaps g = 200, 300, 400, 500 and 600 nm, respectively, as measured by a Talystep profilometer.

We carried out a series of measurements of the optical emission through the BE structures. The intensity luminescence (I_{out}) measurement set-up consists of a 488.0 nm wavelength light beam from an Ar ion laser, with a power of about 40 μW, aligned to the optical axis of a microscope. The beam is focused at normal incidence onto the sample surface by a 20× microscope objective (with a numerical aperture of 0.4). The emission intensity from the Er^{3+} emission through each BE structure is then detected with a charged-coupled device (CCD) array detector. Light intensity is obtained by integrating the signal over the entire region of interest in the CCD image and subtracting the background originating from electronic noise. The luminescence intensity of every structure was recorded in the far-field by the CCD as the sample was stepped using an X-Y translation stage. Figure 2 shows the schematic of the measurement setup. The luminescence light was collected with the same objective lens.

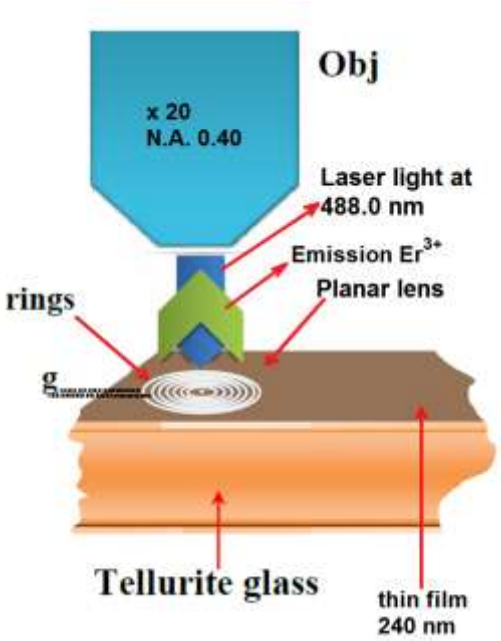

Figure 2. Schematic of the luminescence experiment. An Ar ion laser light source at 488.0 nm is normally focused onto the sample surface by a 20× microscope objective lens. The detector, a charge-coupled device (CCD) camera, records the emission intensity through the BE structures as the sample surface was stepped.

The λ_{spp} was calculated from the usual formula for the guided wave on a flat metal surface [19], $n_{spp} = \sqrt{\frac{\varepsilon_d \varepsilon_m}{\varepsilon_d + \varepsilon_m}}$ and $\lambda_{spp} = \lambda_{exc} / n_{spp}$, where λ_{exc} is the incident wavelength, ε_m

and ε_d are the dielectric constant of the metal and adjacent dielectric (here, air), respectively.

3. Results and discussion

Firstly, for a wavelength λ_{exc} at 488.0 nm, the absorption coefficient α is equal to 76.3 μm^{-1}, with a transmittance $T = 2.7\times10^{-8}$, for an Au film of 240 nnm of thickness. Thus, we can neglect the immediate excitation of the host matrix by λ_{exc} via the transmission T (Figure 3 (a) shows the background measured without the BE structure). The central nano-aperture (240 nm of diameter) was illuminated by the incident λ_{exc} with intensity I_0 and re-illuminated by light coming from the ring array via SPPs, with a λ_{spp} = 468.2 nm in the metallic surface with intensity I^i_{spp}. Here, I^i_{spp} is the intensity of diffractive wavelet at ith groove-ring. The SPPs propagate along the surface of the metal film, and can have a phase modulation (Φ) due to the concentric groove-rings. Therefore, a constructive interference of such diffracted beams leads to the focusing effect at a certain point on the beam axis [20]. Adjusting the parameters of the groove-rings (such as width, depth, period, and number), the diffracted beams can be manipulated resulting in an enhancement of I^i_{spp} in plasmonic planar lens [15]. The spacing between the rings determines the phase mismatch between the waves generated from the inner and outer rings. By tuning to the λ_{spp}, the periodicity provides momentum matching along the groove-ring, ensuring resonant SPPs excitation at the foci. Here, the circular grating effectively becomes active coupling elements, depending on the groove-ring gap, Figure 3 (a). Therefore, this focusing allows a high confinement in the BE structure which excited the Er^{3+} ions of the substrate, i.e., we have an extraordinary optical transmission in the nano-hole [1], incremented through the the grooves-rings. Thus, the total transmittance intensity through the hole can be expressed as [21]:

$$I_{total} = \sum_{i=1}^{N} C I^i_{spp} I_0 \frac{4r_i}{\lambda_{spp}} \exp\left(\frac{-|r-r_i|}{l_{spp}}\right) \qquad (1)$$

Where r is the radius of central hole, r_i is the radius of each zone, i is the ith number of the groove-ring, l_{spp} $(=\lambda_{exc}\,\mathrm{Im}[n_{spp}]^{-1}/4\pi)$ is the propagation length for the SPP wave, C is the coupling efficiency of the groove [22], and N is the number of groove-rings of the planar lens. C is a complex function $C = C(h, |r-r_i|, g, \Phi, \lambda_{spp})$. Also, we can write $|r-r_i| = Ng$. Furthermore, when SPP waves propagate across a single slit, the transmitted intensity will be modified by the wave that will gain a phase Φ [23]. Therefore, each groove-ring of plasmonic lens re-illuminates the BE via SPP.

The BE structure transmitted light into the substrate excites the Er^{3+} ions with intensity I_{total}, generating a SPP in the metallic film/substrate interface. Radiative transition of the Er^{3+} depends of the pumped population density n_f, which is small compared to the total population. For that reason, the ground state population density n_0 can be considered constant, and the pumped population density n_f is proportional to the pump radiation intensity, i.e., I_{total}: $n_f / n_0 \propto I_{total}\tau_f$, where τ_f is the n_f lifetime.

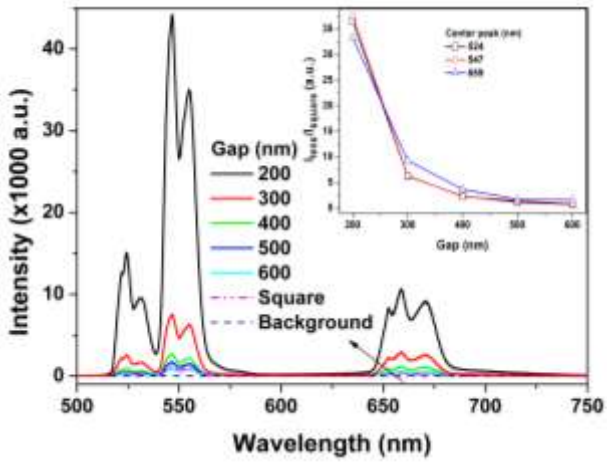

(a)

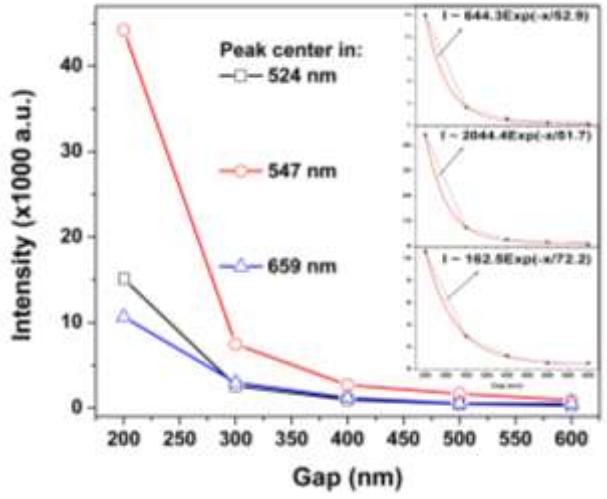

(b)

Figure 3. (a) Emission spectra of Er^{3+} ions through the nano-aperture with 240 nm of diameter, for the different plasmonic lens. We can see that the background line is practically neglected. Also, it is shown the emission spectra of a square of 500×500 nm^2 milled with a thickness of 240 nm (short-dot dashed line). Inset shows the behavior of this increment for the different normalized Er^{3+} ion transitions. (b) Intensity of the central peaks in 524 nm ($^2H_{11/2}\rightarrow{}^4I_{15/2}$ electronic transition), 547 nm ($^4S_{3/2}\rightarrow{}^4I_{15/2}$ electronic transition) and 659 nm ($^4F_{9/2}\rightarrow{}^4I_{15/2}$ electronic transition). The insets show fittings from equation (2) for these transitions. Here, the dashed straight lines are the experimental points.

The emission intensity of the Er^{3+} ion is proportional to the pump radiation intensity, i.e., $I_{out} \propto n_f(I_{total})$, which is a function of the plasmonic lens, inset of Figure 3 (a). Then, the radiative transitions of the Er^{3+} ions can propagate in the interface via SPP, e.g., λ_{SPP} = 210 nm for λ = 547 nm from the $^2H_{11/2}\rightarrow{}^4I_{13/2}$ Er^{3+} transition, and emit through the BE. In other words, the nano-aperture receives and transmits the

Er^{3+} emission, Figs. 3 (a) and (b). The measured micro-luminescence clearly confirms that planar plasmonic lenses can confine with great efficiency, and when *g* decreases the intensity increases. This indicates that planar lenses are efficient for confining SPPs at the nano-aperture, i.e., BEs nanostructures obtains an efficient structure with a high I_{total}. Figure 3 (a) shows the luminescence spectra of a square of 500×500 nm^2 milled with a thickness of 240 nm (short-dot dashed line). The intensity of this square is lower in comparison with the BEs structures, Figure 3 (a), where the effective square area of the substrate that was excited directly by the beam light (λ_{exc}) is greater in comparison with the nano-hole of 240 nm of diameter, $A_{square}\left(=25.0\times10^4\,nm^2\right) > A_{nano-hole}\left(=4.5\times10^4\,nm^2\right)$. The inset of Figure 3 (a) shows the intensity of the peaks from different planar lens normalized with the intensity of the peaks obtained from square milled, $I_{lens\_peak}/I_{square\_peak}$ for the center peaks in 524 nm ($^2H_{11/2}\rightarrow{}^4I_{15/2}$ electronic transition), 547 nm ($^4S_{3/2}\rightarrow{}^4I_{15/2}$ electronic transition) and 659 nm ($^4F_{9/2}\rightarrow{}^4I_{15/2}$ electronic transition). We can see the improvement obtained increases exponentially with the decrease the gap, which behavior is approximately the same for the other transitions, Figure 3 (b). These experimental results indicate that the groove-rings array response can be understood as the response of an isolated groove-ring. In fact, let us now consider an isolated groove in equation (1), where we can obtain the following approximation:

$$I_{out} \approx I_{total} \approx CI_{spp}I_0\frac{4Ng}{\lambda_{spp}}\exp\left(\frac{-Ng}{l_{spp}}\right) \qquad (2)$$

Values of fitting are shown in the inset of Figure 3 (b) for the three Er^{3+} ion transitions. From the obtained numeric values, we can say that for 547 nm the term $4CI_{spp}I_0Ng/\lambda_{spp}$ is higher than the other terms, resulting in an improvement in this transition in comparison with the other transitions. This is due the dependency of *C* with g, Φ, and λ_{spp}, i.e., the observed increasing is attributed to a constructive interference of such diffracted beams, allowing a strong focusing in the nano-hole. Also, we can verify the dependency of the term $\exp\left(-Ng/l_{spp}\right)$ with λ_{exc}.

4. Conclusions

Plasmonic lenses forming bull's eye structure with different gaps, milled in a gold thin film on the top of an Er^{3+}-doped tellurite glass can be excited via a surface plasmon, where the intensity of transmission of these structures depends of g, Φ, and λ_{spp}. The transmittance presents a maxima for given values of gap and phase, and, therefore, a constructive interference of the light reemitted by the groove-rings (in this case, behaving almost independently), occurs into the central hole. This reemitted light, in the form of surface plasmons into the substrate, excites the Er^{3+} ions. The luminescence spectra of the Er^{3+} ions passing through the sub-wavelength apertures in the visible region were detected in the far-field radiation, and clearly show their dependence with the pumped radiation intensity I_{total}, which depends of the plasmonic planar lens. These bull's eye structures have tunable surface plasmon resonances, and the coupling of the Er^{3+} ions to such structures can lead the discovering of interesting optical and electronic properties. This might also lead to applications in optical telecommunications, and, of course, in nanophotonics.

Acknowledgements

This work was financially supported by the Brazilian agencies FAPESP and CNPq under CEPOF/INOF (Instituto Nacional de Óptica e Fotônica).

References

[1] T.W. Ebbesen, H. L. Lezec, H. F. Ghaemi, T. Thio, and P.A. Wolff, Extraordinary optical transmission through subwavelength hole arrays, Nature 391:667-669, 1998.

[2] A. Nahata, R.A. Linke, T. Ishi, and K. Ohashi, Enhanced nonlinear optical conversion from a periodically nanostructured metal film, Opt. Lett. 28:423–425, 2003.

[3] F.I. Baida, D. V. Labeke, and B. Guizal, Enhanced Confined Light Transmission by Single Subwavelength Apertures in Metallic Films, Appl. Opt. 42:68116815, 2003.

[4] A. Degiron and T. Ebbesen, Analysis of the transmission process through single apertures surrounded by periodic corrugations, Opt. Express 12:3694-3700, 2004.

[5] O. Mahboub, S. C. Palacios, C. Genet, F. J. Garcia-Vidal, S. G. Rodrigo, L. Martin-Moreno, and T. W. Ebbesen, Optimization of bull's eye structures for transmission enhancement, Opt. Express 18:11292-11299, 2010.

[6] T. Thio, H. J. Lezec, T. W. Ebbesen, K. M. Pellerin, G. D. Lewen, A. Nahata, and R. A. Linke, Giant optical transmission of sub-wavelength apertures: physics and applications, Nanotechnology 13(3):429–432, 2002.

[7] T. Ishi, J. Fujikata, K. Makita, T. Baba, and K. Ohashi, Si Nano-Photodiode with a Surface Plasmon Antenna, Jpn. J. Appl. Phys. 44(12):L364–L366, 2005.

[8] N. Yu, Q. J. Wang, C. Pflügl, L. Diehl, F. Capasso, T. Edamura, S. Furuta, M. Yamanishi, and H. Kan, Semiconductor lasers with integrated plasmonic polarizers, Appl. Phys. Lett. 94(15):151101, 2009.

[9] A. Drezet, C. Genet, and T. W. Ebbesen, Miniature plasmonic wave plates, Phys. Rev. Lett. 101(4):043902, 2008.

[10] N. Bonod, E. Popov, D. Gérard, J. Wenger, and H. Rigneault, Field enhancement in a circular aperture surrounded by a single channel groove, Opt. Express 16(3):2276–2287, 2008.

[11] J.S. Wang, E. M. Vogel and E. Snitzer, Tellurite glass: A new candidate for fiber devices, Opt. Mater. 3:187, 1994.

[12] J. S. Wang, E. Snitzer, E. M. Vogel and J. G. H. Sigel, 1.47, 1.88 and 2.8 μm emission of Tm^{3+} and Tm^{3+}-Ho^{3+} -codoped tellurite glasses, J. Lumin. 61:145, 1994.

[13] S.F. Collins, G.W. Baxter, S.A. Wade, T. Sun, K.T.V. Grattan, Z.Y. Zhang and A.M. Palmer, Comparison of fluorescence-based temperature sensor schemes: Theoretical analysis and experimental validation, J. Appl. Phys. 84:4649, 1998.

[14] V.A.G. Rivera, Y. Ledemi, S.P.A. Osorio, D. Manzani, Y. Messaddeq, L.A.O. Nunes, E. Marega Jr., Efficient plasmonic coupling between Er^{3+}:(Ag/Au) in tellurite glasses; J. Non-Crys. Sol. 358:399-405, 2011.

[15] V.A.G. Rivera, F. A. Ferri, S. P. A. Osorio, L. A. O. Nunez, A. R. Zanatta, Sr. and E. Marega, Jr., Focusing surface plasmons on Er^{3+} ions with convex/concave plasmonic lenses, Proc. SPIE 8269:82692I, 2012; http://dx.doi.org/10.1117/12.909346.

[16] V.A.G. Rivera, F. A. Ferri, S. P. A. Osorio, L. A. O. Nunez, A.R. Zanatta and E. Marega, Jr., Luminescence enhancement of Er^{3+} ions from electric multipole nanostructure arrays, Proc. SPIE 8269:82692H, 2012; http://dx.doi.org/10.1117/12.909323.

[17] V.A.G. Rivera, S.P.A. Osorio, Y. Ledemi, D. Manzani, Y. Messaddeq, L.A.O. Nunes, E. Marega Jr., Localized surface plasmon resonance interaction with Er^{3+}-doped tellurite glass, Opt. Exp. 18 (24):25321-25328, 2010.

[18] F.A. Ferri, V.A.G. Rivera, S.P.A. Osorio, O. B. Silva, A.R. Zanatta, B.V. Ben-Hur, J. Weiner, E. Marega, Jr., Influence of film thickness on the optical transmission through subwavelength single slits in metallic thin films, App. Opt. Tech. 50:G11, 2011.

[19] D. Pacifici, H.J. Lezec, A. Atwater Harry, J. Weiner, Quantitative determination of optical transmission through subwavelength slit arrays in Ag films: Role of surface wave interference and local coupling between adjacent slits, Phys. Rev. B 77:115411, 2008.

[20] B. Ung and Y. Sheng, Optical surface waves over metallo-dielectric nanostructures: Sommerfeld integrals revisited, Opt Express 16 (12):9073–9086, 2008.

[21] S. Carretero-Palacios, O. Mahboub, F. J. Garcia-Vidal, L. Martin-Moreno,1 Sergio G. Rodrigo,1 C. Genet and T. W. Ebbesen, Mechanisms for extraordinary optical transmission through bull's eye structures, Opt. Exp. 19(11):10429-10442, 2011.

[22] Yongqi Fu and Xiuli Zhou, Plasmonic Lenses: A Review, Plasmonics 5:287–310, 2010.

[23] Jennifer M. Steele, Zhaowei Liu, Yuan Wang, and Xiang Zhang, Resonant and non-resonant generation and focusing of surface plasmons with circular gratings, Opt. Exp. 14(12):5664, 2006.

Tunable plasmon resonance modes on gold nanoparticles Er3+-doped germanium-tellurite glass

V.A.G. Rivera[1*], Y. Ledemi[2], S.P.A. Osorio[1], D. Manzani[3], F.A. Ferri[1], Sidney J.L. Ribeiro[3], L.A.O. Nunes[1] and E. Marega Jr.[1]

[1] Instituto de Física de São Carlos - INOF, USP, Caixa Postal 369, 13560-970, São Carlos – SP, Brasil
[2] Centre d'optique, photonique et laser, 2375 rue de la Terrasse, Université Laval, Quebec (Qc), Canada
[3] Institute of Chemistry – São Paulo State University- UNESP, P.O. Box 355, 14801-970, Araraquara – SP, Brasil
*corresponding author, E-mail: Garcia@ursa.ifsc.usp.br

Abstract

The plasmon resonance modes of gold nanoparticles embedded in an erbium doped germanium-tellurite glass are activated using laser lines at 808 and 480 nm in resonance with radiative transitions of Er^{3+} ions. The gold nanoparticles were grown within the host glass by thermal annealing at several times, leading to diameters lower than 1.6 nm. The resonance wavelengths determined theoretically and experimentally are 770 and 800 nm, respectively. The absorption wavelength of nanoparticles was determined by using the Frohlich condition. Gold nanoparticles provide tunable emission resulting in a large enhancement for the $^2H_{11/2} \rightarrow {}^4I_{13/2}$ (emission at 805 nm) and $^4S_{3/2} \rightarrow {}^4I_{13/2}$ (emission at 840 nm) electronic transitions of Er^{3+} ions, this is associate with the quantum yield of the energy transfer transition. The excitation pathways, up-conversion and luminescence spectra of Er^{3+} ions are described through simplified energy levels diagrams. We observed that up-conversion is favored by the excited-state absorption due to the presence of the gold nanoparticles coupled with the Er^{3+} ions within the glass matrix.

1. Introduction

The wavelength and intensity of the Localized surface plasmon resonance (LSPR) in a nanoparticle (NP) is strongly affected by the refractive index in its immediate vicinity. When the NP is embedded in a dielectric, e.g., a glassy system, the field around the particle becomes inhomogeneous [1-3]. Nanoparticles within a transparent dielectric (glass) have extraordinary size-dependent optical properties that have recently been the subject of extensive studies due to their potential application as nonlinear optical materials for photonic devices [2]. Regarding the process of production of the NPs, new materials with unique properties may be obtained. Indeed, some of these properties can be even improved, e.g., the utilization of plasmonic effects into a host matrix with photonic applications of current interest [3-5]. Several preparation methods have been reported in the literature such as the use of electron beam, femtosecond lasers, ultra-violet irradiation, and heat-treatment [4, 5]. Concerning the host matrix, germanium-tellurite glasses are very good candidates for such investigations because they exhibit a large transmittance window (visible and infrared region), low cutoff phonon energy, high refractive index, and high chemical stability [5, 6]. As previously reported in the literature [7], Ag^+ ions in germanium-tellurite glass are very mobile and tend to aggregate. So, NPs of various sizes can coexist, depending on the time and temperature of annealing. On the other hand, Au^{3+} ions display lower mobility into the same glassy network.

Unfortunately, the characteristic size of a NP is strongly dependent of the fabrication process that usually gives rise to a mixture of different NPs diameters, making it difficult to correlate certain properties that define the NPs sizes. Inasmuch as the absorption cross section depends on the NP size [5, 8], the frequency of incident radiation can be chosen such that only particles whose size lies in a narrow range within the NPs size distribution, absorb light efficiently [9]. It must be kept in mind that during decay of the electronic excitation, the absorbed photon energy rapidly dissipates for a temperature increment into surrounding media (Joule effect) [10].

The LSPR will have the effect of considerably enhance the electric field strength around the nanoparticle. This can, in principle, lead to enhanced emission from Er^{3+} ions located within the region of enhanced field [7, 9], provided that the frequency of the enhanced electric field corresponds with the excitation frequency of the emission Er^{3+}. However, if the light-emitting structure is too close to the metal portion, its excited state may be quenched by energy transfer to the metal, which causes the decay nonradiatively. These effects (enhancement or quenching) depends strongly on the distance between the two components (Er^{3+} ions and Au-NPs), the spatial range of the electric field, the spatial charge distribution and other factors [11, 12].

The goal of the work presented here is to investigate the best way to achieve an efficient coupling between gold nanoparticles (Au-NPs) and Er^{3+} ions, considering: (i) the incident radiation and (ii) the energy transfer between Er^{3+} ions and Au-NPs in order to enhance (or not) the luminescence intensity in these germanium-tellurite glass

samples. Additionally, it is presented the effects of the system glass on the nucleation and formation of NPs.

2. Coupling between plasmonic and Er^{3+} ions

An emerging topic in plasmonics is the study of the interaction of plasmonic and electronic transitions systems. Although the proper description of this phenomenon would require a quantum mechanical approach, the qualitative aspects of this interaction can be modeled using classical EM methods [13]. Recently, Enriquez *et al.* [14] reported the enhanced resonance light scattering properties of Au-NPs due to interaction with Eu3+ ions. In spite of several studies, the mechanism of the interaction between rare-earth ions and metal particles is not fully understood yet.

We can have a scattering: $Q_{scatt} = Q_{scatt}^{(Ray)}\left(\omega, \omega_p, d\right)$, where: $Q_{scatt}^{(Ray)} = \frac{8}{3}\frac{\omega_p{}^4 q^4}{\left(\omega^2 - \omega_p{}^2\right)^2 + \frac{4}{9}q^6\omega_p{}^4}$ is the Rayleigh scattering [13] , ω the frequency of excitation, ω_p the plasmon frequency of the Au-NPs, d the diameter of the NPs and $q = \omega d/c$, with c the speed of light. This scattering not only depends on the NP size, but also on the incident radiation and the plasmon modes resonance. Regarding this effect, Localized Surface Plasmons (LSPs) are collective oscillations of the conduction electrons in noble metals. The movement of the conduction electrons upon excitation with incident light leads to a buildup of polarization charges on the particle surface. This acts as a restoring force, allowing a resonance with a particular frequency (resonance mode), which is termed dipole surface plasmon resonance frequency. These induced dipoles (higher multipoles) are proportional to $(d/2r)2l+1$, where r is the interparticle distance, and l is the multipole order (l=1 for dipole, l=2 for quadrupole, etc) [15].

3. Samples preparation and setupCoupling between plasmonic and Er^{3+} ions

In our work, we use a tellurite glasses, prepared according to the composition $75TeO_2$ + $15Na_2O$ +7ZnO + $2GeO_2$ + $1Er_2O_3$ (mol %), by the classical melt-casting technique. The glasses were doped with 0.25% of $AuCl_3$ (wt %). The precursors TeO_2, Na_2CO_3, ZnO GeO_2, Er_2O_3 and $AuCl_3$ were weighed in appropriate amounts to obtain a 10 g. The melting was carried out in a platinum crucible at 750 ^{0}C for 2.0 hours and the homogenized glass melt was then poured onto a pre-heated brass mold. The annealing treatments aiming to reduce the Au^{3+} ions to Au^0 atoms and to nucleate the Au-NPs were performed at 300 °C for 2.5, 5.0, 7.5 and 10.0 hours and subsequently cooled down to room temperature inside the same electrical furnace to minimize internal stresses. The glasses samples of 45×20×2 mm^3 were finally polished for the optical characterizations.

The glass transition temperature value (T_g) was determined by Differential Scanning Calorimetry (DSC) with heating rates of 10 ^{0}C/min. The measured onset values of T_g is 287 ± 2 ^{0}C. The X-ray diffraction (XRD) patterns were obtained from a Rigaku-Rota Flex model RU200B diffractometer. Transmission electron microscopy (TEM) images were acquired with a Philips-CM120 equipment.

Optical absorption spectra were recorded with a Lambda 900 Perkin-Elmer spectrophotometer, and the luminescence measurements were performed by exciting the samples with a continuous wave (cw) Argon ion laser at 488 nm, and a cw diode laser at 808 nm in resonance with the Er^{3+} ions electronic transitions $^4I_{15/2}\rightarrow{}^4I_{11/2}$, $^4I_{15/2}\rightarrow{}^4F_{7/2}$ and $^4I_{15/2}\rightarrow{}^4I_{9/2}$ respectively, and analyzed using a Lock-in amplifier equipped with an InGaAs detector. To measure the $^4I_{13/2}$ lifetime, the samples were irradiated with an Optical Parametric Oscillator (OPO) centered at 480 nm with a pulse train of 5 ns. The data are fitted using $I(t) = I_0 + I_1\exp[-t/\tau_1] + I_2\exp[-t/\tau_2]$, where I_0, I_1 and I_2 are the intensities at zero time. The average lifetime was calculated by the following expression [9]: $\tau = \frac{I_1\tau_1^2 + I_2\tau_1^2}{I_1\tau_1 + I_2\tau_2}$. The emission signal was recorded on the oscilloscope. Refractive index of the samples was measured by using a M-Lines Metricon equipment, at three wavelengths: 532, 633 and 1550 nm.

4. Results and discussion

The Figure 1 presents the TEM images of the samples heat treated at 300 ^{0}C during 2.5 hours (a), 5.0 h (c) and 7.5 h (e) with their corresponding NPs size distribution (b), (d) and (f), respectively. We can notice the irregular circular shape on the TEM images, aspect ratio [0.8 – 1.3]. The picture (c), whose magnification is lower, show the deformation caused by elastic stress generated into the glass by the migration and nucleation of Au-NPs [5]. Moreover, the distribution of the NPs on the TEM images is quite inhomogeneous, confirmed by the rather broad size distribution presented in Figure 1 (b), (d) and (f). Figure 1 also shows the X-ray diffraction patterns (g) of the glass with the annealing time as a parameter. Two diffraction peaks are observed in Figure 1 (g) on the patterns of the samples containing Au-NPs at 2θ = 38.3 ± 0.4° and 2θ = 44.6 ± 0.3°, that were attributed to the Au crystals (111) and (200) diffraction planes, respectively [16]. The average sizes of the Au crystals, calculated from the Scherrer's relation, are reported in the Table 1. In the melting process, the Au^{3+} ions and Au^0 atoms are formed by thermal reduction of Au^{3+} ions (Au^{3+}+3e$^-$ →Au^0).

Our process is initiated through by the precursors that are raw materials of high purity, mixed and melted in a platinum crucible, into an electric furnace at 750 ^{o}C for two hours. The thermal reduction pathway proposal is: $2AuCl_3 \rightarrow 2Au^{3+} + 3Cl_{2(g)}^0$. The precursor oxides involved during the melting are transfer of electrons. Therefore, we can have formation of atom gold (Au^0). In other words: Au^{3+}+3e$^-$→Au^0 (standard reduction potential), i.e., the reduction is thermodynamically favored due to high redox potential. Considering the redox reactions we have:

$$AuCl_3 \xrightarrow[254\ ^oC]{heat} AuCl + Cl_{2(g)}^0$$

That is, by thermal decomposition. Then, when heated at 290 ^{0}C, gold (I) chloride decomposes to gold and chlorine gas:

$$2AuCl \xrightarrow{heat,\ 290\ ^\circ C} 2Au + Cl^0_{2(g)}$$

Finally we have:

$$AuCl_3 + AuCl \xrightarrow{heat} 2Au^0{}_{(s)} + 2Cl^0_{2(g)}$$

For $Au_{(s)}$:

$$\Delta_f H = 0\frac{KJ}{mol}, \Delta_f G^0 = 0\frac{KJ}{mol} \text{ and } S^0 = 47.5\frac{J}{molK}.$$

For AuCl:

$$\Delta_f H = -34.8\frac{KJ}{mol}, \Delta_f G^0 = -17.43\frac{KJ}{mol} \text{ and } S^0 = 99.6\frac{J}{molK}.$$

For $AuCl_3$:

$$\Delta_f H = -117.6\frac{KJ}{mol}, \Delta_f G^0 = -55.2\frac{KJ}{mol} \text{ and } S^0 = 147.3\frac{J}{molK}.$$

Finally, for $Cl_{2(g)}$:

$$\Delta_f H = 0\frac{KJ}{mol}, \Delta_f G^0 = 0\frac{KJ}{mol} \text{ and } S^0 = 233\frac{J}{molK}$$

The Gibbs free energy of each reaction is (T = 298.15 K): ΔG_1~27.55 KJ/mol and ΔG_1~31.21 KJ/mol [17]. Thus, the Gibbs free energy of the resultant reaction is: ΔG~58.76 KJ/mol.

The growth of Au-NPs occurs in the thermal treated, where the viscosity is sufficient to simultaneously promote the diffusion of the Au^{3+} (low concentration) and Au^0 (high concentration) entities within the glassy network. Due to the kinetics of nucleation, the size distribution becomes non-homogeneous, as it can be observed in Figure 1 (b), (d) and (f). We found that the required size of the Au-NP to overcome the thermodynamic barrier [5] is $2r^* \approx 1.6$ nm, (Figure 1 (d)) for 5 h annealing. This shows that when the NPs achieve this size, the nucleation stopped. As the particle nucleation process (coalescence) has to overcome the glass elastic stress, microscopic cracks may be formed (Figure 1 (c)). Moreover, the diffusion-controlled growth promotes the formation of non-uniform NPs. The graph presenting the NPs size versus annealing time (Figure 1 (h)), a diameter decrease can be observed with the annealing time. When the NPs reach approximately 1.6 nm of diameter (limit size $2r^*$), Au^0 atoms may be released from NP surface to reduce the total Gibbs free energy, decreasing the Au-NPs size, and form (probably) a new nucleation center, see Figure 1 (h) for 7.5 h. Additionally, a noticeable color change of all samples is observed with the naked eye.

We can observe from Figure 1 (h) that the Au-NPs size formed in our glass samples range from ~ 0.8 to 1.6 nm. The optical properties discussed hereafter take into account those particle sizes. The concentration N (atoms/cm^3) of Au atoms and Er^{3+} ions and the average distance between Er^{3+} ions and Au-NPs (mean inter-ionic distance r_m [17]) are reported in the Table 1. The density of the glass samples $\rho_{Au\text{-}NPs\text{-}x}$ = 5.34±0.12 was measured by the Archimedes method using distilled water as immersion medium. The LSPR dependence on the matrix refractive index can be calculated by [7]: $\omega_p = \sqrt{4\pi n' e^2 / \varepsilon_0 \varepsilon_d(\omega) m^*}$, where n' is the electrons density, e the electron charge, $\left(\varepsilon_d(\omega) = n_\lambda{}^2\right)$ the dielectric permittivity, ω the excitation frequency and m^* the electron mass.

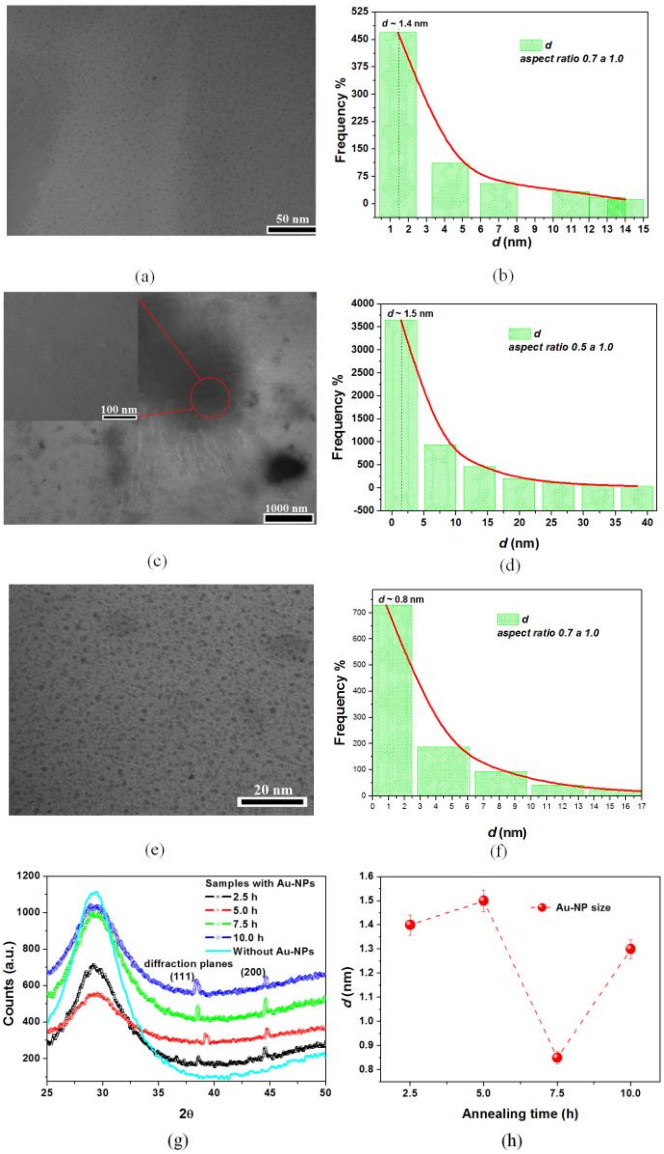

Figure 1. TEM images of the glass samples (a) 2.5 h, (c) 5.0 and (e) 7.5 of annealing at 300 ^{0}C with their respective NP size distribution (b), (d) e (f), where the aspect ratio change significantly with the increase of annealing time. The picture (c) shows the effects of the elastic stress. (g) X-ray diffraction patterns of the glass samples as a function of annealing time and (h) estimated Au-NPs' diameter d versus annealing time. Error bars to 3%.

The measured mean values for the refractive index of samples containing Au-NPs are: $n_{\lambda=533}$ = 2.014±0.003, $n_{\lambda=633}$ = 1.992±0.002 and $n_{\lambda=1530}$ = 1.940±0.003. The measured mean values for the samples without Au-NPs are: $n_{\lambda=533}$ = 2.293±0.002, $n_{\lambda=633}$ = 2.007±0.002 and $n_{\lambda=1530}$ = 1.951±0.003. It appears that NPs modify the medium polarizability and the dielectric function (Table 1). By using the measured refractive index values and the Sellmeier's

equation [18], we have calculated that the wavelength of surface plasmon resonance λ_p is 749 and 773 nm for excitation wavelengths of 488 and 808 nm respectively, $\omega_p(\varepsilon_d(\omega))$.

No absorption band related to the LSPR is observed in the absorption spectra presented in Figure 2 (a), probably due to the low quantity of Au into the samples and the existence of an Er^{3+} absorption band in that region, which may hide the plasmon band. That's why glass samples without Er^{3+} ions were also prepared. Their optical absorption spectra, shown in Figure 2 (b), clearly exhibit the LSPR absorption band in the 702 - 860 nm range approximately.

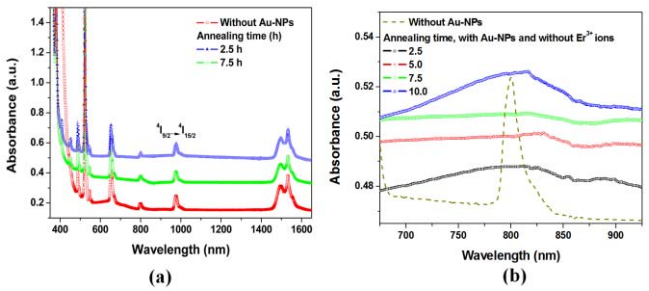

Figure 2: (a) Absorption spectra of glass samples as function of annealing time and of the glass without Au-NPs. The Plasmon band is not observed because the amount of the Au-NPs is not sufficient to originate a modification in the plasmon band. (b) Absorption spectra of the Er^{3+} ions without samples containing Au-NPs only annealed for the same time of all samples in study; line black is the without metallic NPs glass doped with Er^{3+} ions.

In the Gans theory, the LSPR is only a function of the aspect ratio and refractive index. Thus, in certain conditions, a linear relationship between them can be resulted [19]. Nevertheless, numerical results suggest that, even when the aspect ratio is fixed and the retardation effect is weak, the position of longitudinal resonance can still depend strongly with the aspect ratio [20, 21] . Using the model of Cheng - ping Huang et al [22], we can write: $\lambda_p = \pi n\sqrt{10\kappa(2\delta^2 + r^2 ln[\kappa])}$, where κ is the aspect ratio of the Au-NPs, and δ is the skin depth of gold (~21.9 nm) [22]. This means a breakdown of the linear behavior presenting oscillations electrons originating from the amorphous geometry of the Au-NPs associated with the inertia of electrons.

To carry out simulations, we have used the measured values of refractive index ($n_{\lambda=488}$ = 2.21 and $n_{\lambda=808}$ = 1.98 by means of a fitting using the Sellmeier equation [18]), and aspect ratio from 0.8 up to 1.3 nm. The results are shown in the Figure 3.

One can see that both analytical calculations are in agreement with the experiments; concerning the spectral position of λ_p as well as its dependence on the aspect ratio (a deviation is present when the aspect ratio becomes very small).

An incident field induces a dipole moment inside the NPs proportional to $\vec{E}_{in} = \frac{3\varepsilon_d}{\varepsilon(\omega)+2\varepsilon_d}\vec{E}_0$ [23], where $\varepsilon(\omega) = \varepsilon' + i\varepsilon''$, is the complex and frequency dependent dielectric constant of the NPs. In this scenario, the absorption coefficient α of the plasmon band is expressed by [24]: $\alpha = p\omega|f|^2\varepsilon''/nc$ with: $f = 3\varepsilon_d/(\varepsilon(\omega)+2\varepsilon_d)$, p is the volume fraction occupied by NPs and f the local field factor.

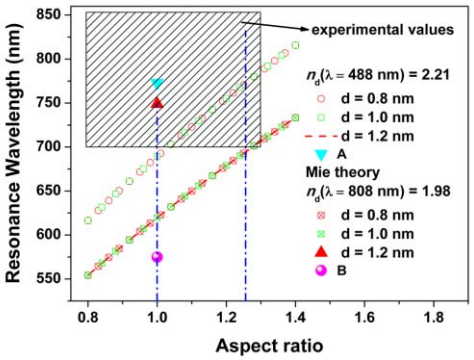

Figure 3. Dependence of the resonance wavelength on the aspect ratio for the samples with Au-NPs, where d is the size of the Au-NPs. A and B, the wavelengths λ_p of the LSPR, are 749 and 773 nm. The circle is the value obtained from Mie theory assuming a spherical nanoparticle for n_d (λ=488 nm) = 2.21. The box with spaced lines is a representation of the values from optical absorption data (see Fig. 2 (b)).

From the latter equation, for $\varepsilon(\omega) \approx -2\varepsilon_d$, the Au-NP absorption presents a maximum. The case: $\mathrm{Re}[\varepsilon(\omega)] = -2\varepsilon_d$, the so-called the Frohlich condition is associated with dipole mode [23].

Table 1: Some calculated physical properties as: concentration N, distance between Er^{3+}:Au-NP, average size of Au-NPs.

Physical parameter	Average for all samples
N(atom/cm^3)	
Er^{3+}	2.17×10^{20}
r_m (Å)	25.5 ± 1.2
Diffraction plane (111), size (nm)	0.91 ± 0.21
Diffraction plane (200), size (nm)	1.25 ± 0.38

Thus NPs can be excited by a predefined incident radiation through a direct coupling between the excited states of the both Er^{3+} ions and NPs, resulting in: (i) a local field increase (Frohlich condition), at ω_p, (ii) a nonradiatively decay (heat generation by Joule effect) or (iii) a radiative energy release which depends on the albedo of the NPs. Thereby, the exact response of LSPR will depend on the details of the physical system (e.g., ε_d, arrangement), and usually not strictly symmetric about the resonant frequency.

The dielectric constants $\varepsilon(\lambda)$ and $-2\varepsilon_d(\lambda)$ reported in the Table 2 were determined from the refractive index measurements of the host matrix and from the data of Palik [25] for gold. The bold values indicate that the Frohlich

condition is < 0.8, i.e., absorption by NPs is quasi-effective. In other words, the Er^{3+}:Au-NP system exhibits a good local field factor *f*. Consequently, a luminescence intensity enhancement is expected for the corresponding Er^{3+} transitions, presented in Table 2 – text in bold.

Table 2: Frohlich condition of Er^{3+} radiative transitions and Rayleigh scattering $Q_{scatt}^{(Ray)}$, and $\omega_p = \frac{2\pi c}{\lambda_p (=800\ nm)}$.

Electronic Transitions of Er^{3+} ion (λ(nm))	Re[ε(λ)] (F/m)	-2ε$_d$(λ) (F/m)	$Q_{scatt}^{(Ray)}(\lambda)$
$^4F_{7/2}\rightarrow{}^4I_{15/2}$ (488)	-1.83	-8.30	--
$^4S_{3/2}\rightarrow{}^4I_{15/2}$ (550)	**-7.11**	-8.86	--
$^4F_{9/2}\rightarrow{}^4I_{15/2}$ (650)	-10.75	**-7.88**	<<< 1
$^4I_{9/2}\rightarrow{}^4I_{15/2}$ (800)	-25.12	**-7.74**	**80387.11**
$^4I_{11/2}\rightarrow{}^4I_{15/2}$ (980)	-44.69	**-7.65**	<<< 1
$^4I_{13/2}\rightarrow{}^4I_{15/2}$ (1550)	-131.95	**-7.54**	<<< 1

A schematic representation of the interaction process within the Er^{3+}:Au-NP system is depicted in Figure 4. The calculated Rayleigh scattering values for different wavelength are reported in the Table 2, evidencing a more prominent scattering at λ = 800 nm.

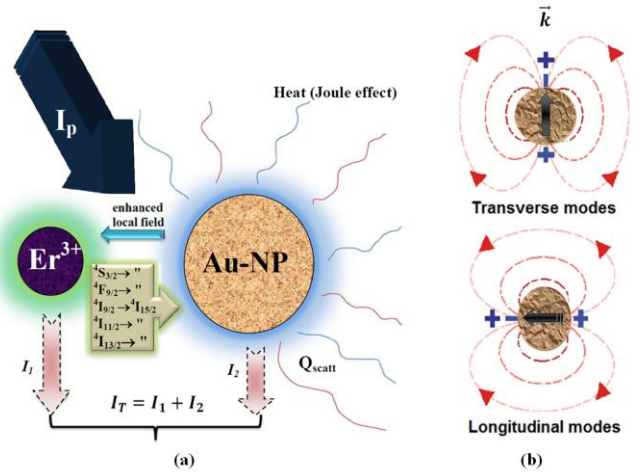

Figure 4: (a) Schematic representation of the Er^{3+}:Au-NP system, (i) absorption of the incident radiation I_p by the Er^{3+} ion while the Au-NP absorbs the excitation frequency resonant with λ_p; (ii) activation of the Au-NPs by energy transfer from the Er^{3+}:Au-NP coupling; (iii) by assuming that: $|\varepsilon(\omega)+2\varepsilon_d| < 0.8$, a quasi-effective absorption occurs, enhancing the local field; (iv) the NPs oscillate with ω_p and can decay nonradiatively by heat generation (Joule effect) or radiatively releasing energy that depends on the albedo of the NPs (Q_{scatt}). (v) Au-NP transmitter, via electric dipole. Such coupling depends on the distance between the Au-NPs and Er^{3+} ions. Finally, the emission intensity is: $I_T = I_1+I_2$. (b) Representation of metallic Au-NP for two different polarizations that depend $\vec{k}$.

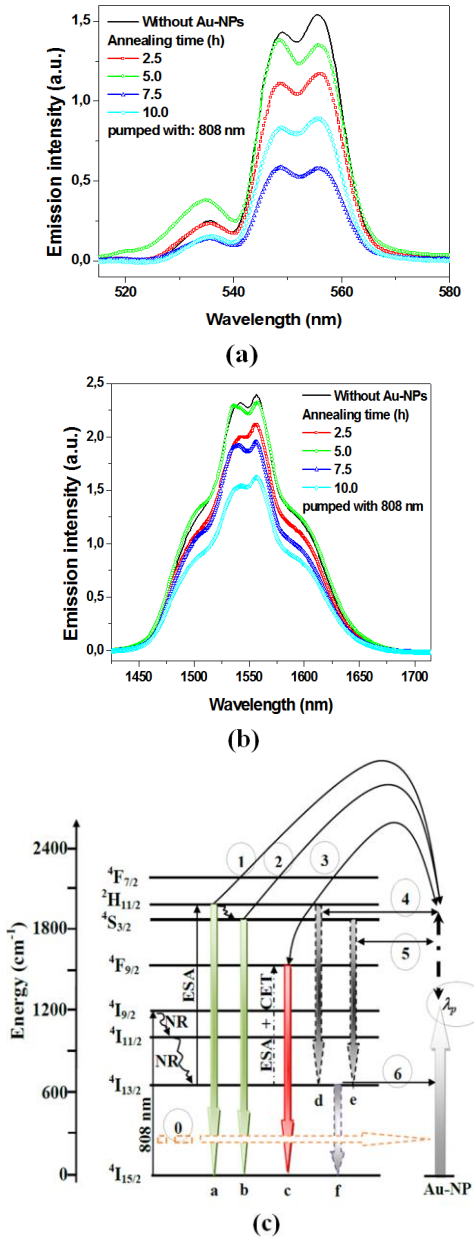

Figure 5: (a) Quenching is observed for all samples. However, enhancement of the $^2H_{11/2}\rightarrow{}^4I_{15/2}$ transition is observed for the sample heat treated for 5.0 h (b) Luminescence spectra at the telecommunication window. Quenching is observed for all samples. (c) Er^{3+} energy levels diagram. Pumping at 808 nm: (0) Absorption of Au-NPs (1) energy transfer from Er^{3+} ($^2H_{11/2}\rightarrow{}^4I_{15/2}$ transition) to Au-NPs. (2) energy transfer from Er^{3+} to Au-NPs. Quenching of the $^4S_{3/2}\rightarrow{}^4I_{15/2}$ transition. (3), (4) and (5) $^4F_{9/2}\rightarrow{}^4I_{15/2}$, $^2H_{11/2}\rightarrow{}^4I_{13/2}$ and $^4S_{3/2}\rightarrow{}^4I_{13/2}$ transitions. Energy transfer from Au-NPs to Er^{3+} with an enhancement in local field due to proximity with λ_p (6) Luminescence quenching for $^2H_{11/2}\rightarrow{}^4I_{13/2}$ (805 nm) and $^4S_{3/2}\rightarrow{}^4I_{13/2}$ (840 nm) transitions electronic. Pumping at 808 nm. Center peak: a – 530, b – 556, c – 675, d – 805, e – 830 and f – 1555 nm. NR: non-radiative transition, ESA: Excited State Absorption and CET: Cooperative Energy Transfer.

One might expect that the most favored transitions are: $^4I_{9/2}\rightarrow{}^4I_{15/2}$ (direct emission, with low probability) or $^2H_{11/2}\rightarrow{}^4I_{13/2}$ and $^4S_{3/2}\rightarrow{}^4I_{13/2}$ (thermal population levels, 4-levels transitions). In order to check these hypotheses, different excitation wavelengths were used to determine what process or transitions are favored into this tellurite glass. Energy transfer processes could have either a negative or a positive impact for a specific excited state depending on the efficiency coupling between Er^{3+}:Au-NP, i.e., the size and shape of the Au-NP and their environment with the Er^{3+} ions.

Figure 5 (a) shows the up-conversion (UC) emission spectra in the region from 510 up to 580 nm of the Er^{3+}:Au-NPs doped glass samples pumped at 808 nm ($^4I_{15/2}\rightarrow{}^4I_{9/2}$ transition). Quenching is observed for all samples. Ground state absorption is followed by non-radiative transition and excited-state absorption (ESA) from the $^4I_{13/2}$ level to $^2H_{11/2}$ level. In parallel, the Au-NPs partly absorb the excitation beam due to its nearby wavelength with λ_p, resulting in both UC and luminescence quenching (Figures 4 (a) and 4 (b)). Although it was no possible to record emission spectra in the 600-900 nm range, we assumed that a large enhancement of the luminescence occurs in this region in comparison with the emission upon excitation at 488 nm (Figure 6 (a) and (b)). Once again, the results suggest that the observed excited state absorption (ESA) is favored by the presence of the Au-NPs. Figure 6 (d) presents a basic energy level diagram of Er^{3+} ions and describes the emission and excitation pathways related to the emission spectra presented in Figures 4 (a) and (b), as well as the Au-NP interaction with the Er^{3+} ions.

Figure 6 shows the UC emission when the samples are pumped at 488 nm ($^4I_{15/2}\rightarrow{}^4F_{7/2}$ transition). In the 520-580 nm region (Figure 6 (a)), the luminescence quenching observed can be explained considering an energy transfer from Er^{3+} to Au-NPs, leading to $^2H_{11/2}\rightarrow{}^4I_{15/2}$ and $^4S_{3/2}\rightarrow{}^4I_{15/2}$ transitions. Figure 6 (b) shows a large enhancement for the $^4F_{9/2}\rightarrow{}^4I_{15/2}$, $^2H_{11/2}\rightarrow{}^4I_{15/2}$ and $^4S_{3/2}\rightarrow{}^4I_{15/2}$ transitions, for all samples except the one for 2.5 h. The enhancement observed for the $^4F_{9/2}\rightarrow{}^4I_{15/2}$ transition is own to the plasmon resonance at Frohlich condition (see Table 2), and not ESA as in previous cases. Additionally, in the region from 780 to 860 nm the Er^{3+} emission is close to λ_p, i.e., an enhancement of both Er^{3+} ions and Au-NPs emission intensity is obtained.

A particular behavior observed in the Figure 6 (c), in the telecommunication range, is that the sample heated for 7.5 h exhibits a large enhancement (~80% intensity increment) and a blue-shift for the $^4I_{13/2}\rightarrow{}^4I_{15/2}$ transition. Such feature can be related to the size of the Au-NPs, which is the smallest in comparison with the other samples (0.9 ± 0.1 nm of diameter), and therefore, the electric dipole is favored [7]. As for the luminescence studies at 808 nm excitation described above, a simplified energy level diagram for Er^{3+} ions is presented in Figure 6 (d) and describes the excitation pathways and the luminescence emission shown in Figure 6 (a) to (c) and also the Au-NP:Er^{3+} interaction.

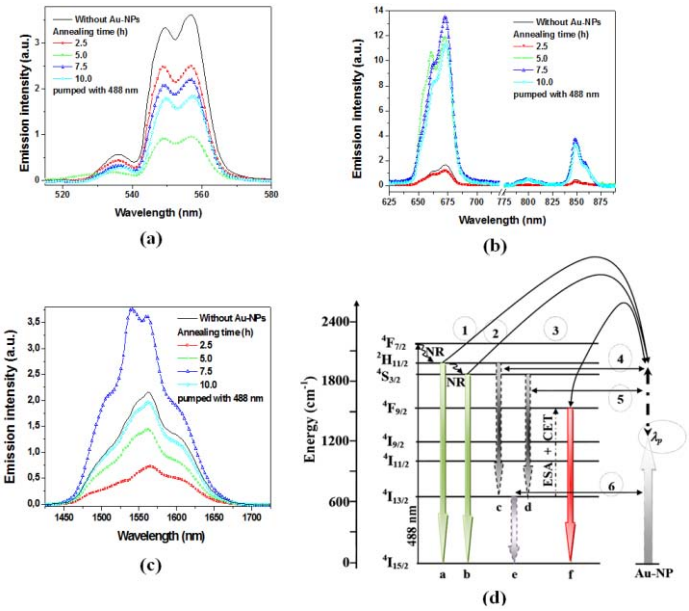

Figure 6: (a) Luminescence spectra in the 520 up to 580 nm region. Quenching is observed for all samples (b) Enhancement in the 625 up to 900 nm region are observed for all samples, except the sample with annealing of 2.5 h. The ESA process is benefited because the presence of the Au-NPs. (c) Particular case of 80% enhancement and a blue-shift for the $^4I_{13/2}\rightarrow{}^4I_{15/2}$ observed for the sample heat treated for 7.5 h. (c) Basic energy levels diagram of Er^{3+} ions pumped with 480 nm: (1) energy transfer from Er^{3+} ($^2H_{11/2}\rightarrow{}^4I_{15/2}$ transition) to Au-NPs. (2) The same of (1) but in the $^4S_{3/2}\rightarrow{}^4I_{15/2}$ transition. (3), (4) and (5) $^4F_{9/2}\rightarrow{}^4I_{15/2}$, $^2H_{11/2}\rightarrow{}^4I_{13/2}$ and $^4S_{3/2}\rightarrow{}^4I_{13/2}$ transitions are favored for the process of energy transfer from Au-NPs to Er^{3+} together with an enhancement of the local field due to cover λ_p in this region, with the exception of the sample heat treated for 2.5 h (6) Luminescence quenching for $^4F_{9/2}\rightarrow{}^4I_{15/2}$ (660 nm), $^2H_{11/2}\rightarrow{}^4I_{13/2}$ (805 nm) and $^4S_{3/2}\rightarrow{}^4I_{13/2}$ (840 nm) transitions. Nevertheless, the sample with 7.5 and 10.0 h of annealing time. show an increment of the intensity of emission. All the processes are pumped with a cw diode laser at 480 nm. Center peak: a – 536, b – 559, c – 675, d – 800, e – 850 and f – 1555 nm.

Depending on the polarization direction of the incident radiation on the Au-NP, a blue-shift of the plasmon resonance band is observed for transverse modes, and a red-shift for longitudinal modes [23], Figure 4 (b). From the results presented in Figures 4 and 5, a blue shift is observed in most spectra. One possible cause for this result is that a randomly Au-NPs distribution, produced a randomly polarization distribution (TE/TM), thus, in the addition of the modes intensity, some terms may canceled each other but the rest is sufficient for shows blue shift.

Figure 7 shows the lifetimes as a function on annealing time for the Er^{3+} ions, of the levels $^2H_{11/2}$ and $^4S_{3/2}$, pumped at λ_{pump} = 488 nm and 100 mW. Measurements were performed with a 10 nm bandwidth filter centered at 800 and 850 nm, respectively. Decay times obtained for Au-NPs without samples are also shown for comparison.

Luminescence enhancement is possible for the $^2H_{11/2} \rightarrow {}^4I_{13/2}$ (805 nm) and $^2S_{4/2} \rightarrow {}^4I_{13/2}$ (840 nm) transitions, which can be explained by the increased excitation transition rate of the Er^{+3} ions due to the proximity between the λ_p and the excitation wavelength. This increased excitation rate is responsible for the $^2H_{11/2}$ and $^4S_{3/2}$ lifetime lowering, in agreement with the results reported in references [7, 9].

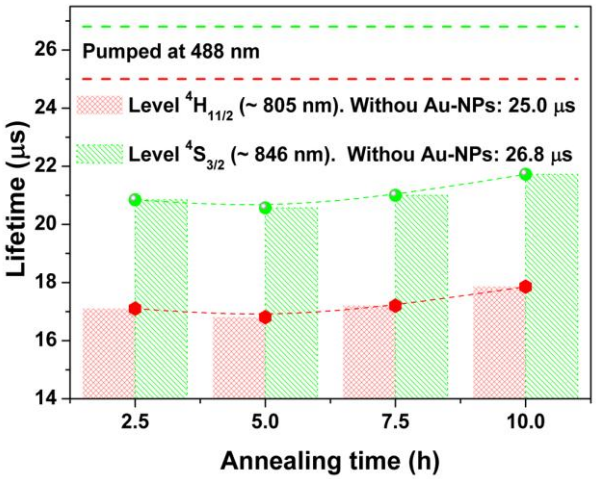

Figure 7: Decay times values for the levels $^2H_{11/2}$ (805 nm) and $^4S_{3/2}$ (850 nm), pumped with an OPO center in 488 nm, 100 mW. Luminescence enhancement occurred in the samples with Au-NP (solids bar) as indicated by the lowering of lifetime as compared with the respective samples without Au-NP (dashed lines).

The lifetime is given by the inverse of the total decay rate, $\tau = \left(-\Gamma + k_{nr}\right)^{-1}$, where Γ is the emissive rate and k_{nr} is the nonradiative decay rate. This k_{nr} is associate with the quantum yield of the energy transfer transition (from Er^{3+} ions), i.e., the fraction of energy transfer in the Er3+ ion excitation event [26]: $E = 1 - \tau_{Au-NPs}/\tau_{Er^{3+}}$, where $\tau_{Er^{3+}}$ and τ_{Au-NPs} represent the lifetimes in the absence of Au-NPs and presence of Au-NPs respectively (assuming that the separation distance Er^{3+}:Au-NPs is fixed for the present calculation). Table 3 shows the transfer efficiency (E) in our samples.

Table 3. Calculated transfer efficiencies in the samples with different annealing times.

Electronic Transitions	Annealing time (h)			
	2.5	5.0	7.5	10.0
$^4H_{11/2}$ (~805 nm)	31.6	32.8	31.2	28.6
$^4S_{3/2}$ (~846 nm)	22.2	23.3	21.6	18.9

The values of $\tau_{Er^{3+}}$ are shown in the Figure 7. Therefore, this fraction of energy transfer from Er^{3+} ions for Au-NPs is responsible for the lifetime lowering of electronic transitions.

5. Conclusions

In summary, we verified that the Au-NPs form electric dipoles with the emitters, the Er^{3+} ions. These are activated by the $^4F_{9/2} \rightarrow {}^4I_{15/2}$, $^4I_{9/2} \rightarrow {}^4I_{15/2}$, $^4I_{11/2} \rightarrow {}^4I_{15/2}$ and $^4I_{13/2} \rightarrow {}^4I_{15/2}$ transitions of the Er^{3+} ions, forming a LSPR. For a plasmon wavelength of about 800 nm an enhancement of the Er^{3+} ions luminescence is observed for the band ranging from 800 up to 840 nm upon excitation at 488 nm. Both effects are obtained for UC luminescence since the presence of Au-NPs favors the ESA process. An enhancement of the luminescence spectrum is also observed in the region 640 up to 720 nm, excepted for the glass heated for 2.5 h. Furthermore, a luminescence quenching is observed in the telecommunication window. However, a large enhancement is observed in this window for the sample annealed for 7.5 h when excited at 488 nm. In this case, the formation of electric dipoles is found to be dependent with the NP size. These dipoles produce an enhanced local field and consequently an increment of the luminescence intensity. The decrease lifetime indicates that energy transfer occurs between the Er^{3+} ions and the Au-NPs, leading to an increase in the radiative transition rate from these levels, this is verified through quantum yield of the energy transfer transition about 19 % to up 33 %. Nevertheless, the formation and diffusion of Au-NPs in the TeO_2-Na_2O-ZnO-GeO_2-Er_2O_3 germanium-tellurite glass matrix is not favorable because of the small NPs size produced in the matrix and the induced mechanical stress resulting in microscopic cracks into the glass.

Acknowledgements

This work was financially supported by the Brazilian agencies FAPESP, CNPq and under CEPOF/INOF (Instituto Nacional de Óptica e Fotônica).

References

[1] M.A. Garcia, Surface plasmons in metallic nanoparticles: fundamentals and applications, J. Phys. D: Appl. Phys. 44:283001, 2011.

[2] Ertugrul Cubukcu, Nanfang Yu, Elizabeth J. Smythe, Laurent Diehl, Kenneth B. Crozier, Federico Capasso, Plasmonic Laser Antennas and Related Devices, *IEEE J. Selec. Toop. In Q. ELE.* 14(6):1448-1461, 2008.

[3] Lue Juh-Tzeng, A review of characterization and physical properties studies of metallic nanoparticles, J. Phys. Chem. Solids 62(201):1599-1612, 2001.

[4] T.A.A. de Assumpção, D.M. da Silva, L.R.P. Kassab, J.R. Martinelli, C.B. de Araújo, Influence of the temperature on the nucleation of silver nanoparticles in Tm^{3+}/Yb^{3+} codoped $PbOGeO_2$ glasses, J. Non-Crys. Solid 356:2465-2467, 2010.

[5] V. A. G. Rivera, S.P.A. Osorio, D. Manzani, Y. Messaddeq, L. A. O. Nunes, E. Marega Jr., Growth of silver nano-particle embedded in tellurite glass: Interaction between localized surface plasmon resonance and Er^{3+} ions, Opt. Mat. 33:888-892, 2011.

[6] V.A.G. Rivera, E.F. Chillcce, E. Rodriguez, C.L. Cesar and L.C. Barbosa, Planar waveguides by ion exchange in Er^{3+}-doped tellurite glass, J. Non-Crys. Solids 352:363-367, 2006.

[7] V.A.G. Rivera, S.P.A. Osorio, Y. Ledemi, D. Manzani, Y. Messaddeq, L. A. O. Nunes, E. Marega Jr., Localized surface plasmon resonance interaction with Er^{3+}-doped tellurite glass, Opt. Exp. 18(24):25321-25328, 2010.

[8] U. Kreibig, M. Vollmer, Optical Properties of Metal Clusters, Springer Series of Material Science 25, Springer, Berlin, 1995.

[9] S.P.A. Osorio, V.A.G. Rivera, L.A.O Nunes, D. Manzani, Y. Messaddeq, E. Marega Jr, Plasmonic coupling in Er3+:Au tellurite glass, Plasmonic (DOI) 10.1007/s11468-011-9275-7, 2011.

[10] Nagaraj, A.A. Krokhin, Long-range surface plasmons in dielectric structure with highly anisotropic substrates, Phys. Rev. B 81:085426, 2010.

[11] A.O. Govorov , G.W. Bryant, W. Zhang, T. Skeini, J. Lee, N.A. Kotov, J.M. Slocik, R.R. Naik, Exciton-plasmon interaction and hybrid excitons in semiconductor-metal nanoparticle assemblies, Nano Lett. 6:984, 2006.

[12] M.B. Cortie and A.M. McDonagh, Optical properties of hybrid and alloy plasmonic nanoparticles. Chem. Rev. 111:3713, 2011.

[13] Luciana R.P. Kassab, Diego S. da Silva, Ricardo de Almeida, Cid B. de Araújo, Photoluminescence enhancement by gold nanoparticles in Eu^{3+} doped GeO_2–Bi_2O_3 glasses, Appl. Phys. Lett. 94:101912, 2009.

[14] A. Cruz Enriquez, I. A. Rivero Espejel, E.A. Garcia, M. E. Diaz-Garcia, Enhanced resonance light scattering properties of gold nanoparticles due to cooperative binding, Anal. Bioanal. Chem. 391:807, 2008.

[15] Zhengxin Liu, Honghong Wang, Hao Li, Xuemei Wang, Red shift of plasmon resonance frequency due to interacting Ag nanoparticles embedded in single crystal TEXSi02TEX by implantation, App. Phys. Lett. 72(15):1823-1825, 1998.

[16] JCPDS Card File No. 4-0784.

[17] Tirtha Som, Basudeb Karmakar, Nanosilver enhanced upconversion fluorescence of erbium ions in Er^{3+}: Ag-antimony glass nanocomposites, J. Appl. Phys. 105:013102, 2009.

[18] W. Sellmeier, Zur Erklärung der abnormen Farbenfolge im Spectrum einiger Substanzen, Ann. Phys. Chem. 143:271, 1871.

[19] S. Link, M. B. Mohamed, M. A. El-Sayed, Simulation of the optical absorption spectra of gold nanorods as a function of their aspect ratio and the effect of the medium dielectric constant, J. Phys. Chem. B 103:3073, 1999.

[20] H. Kuwata, H. Tamaru, K. Esumi, K. Miyano, Resonant light scattering from metal nanoparticles: Practical analysis beyond Rayleigh approximation, Appl. Phys. Lett. 83:4625, 2003.

[21] S. W. Prescott and P. Mulvaney, Gold nanorod extinction spectra, J.Appl.Phys. 99:123504, 2006.

[22] Cheng-ping Huang, Xiao-gang Yin, Huang Huang, Yong-yuan Zhu, Study of plasmon resonance in a gold nanorod with an LC circuit model, Opt. Exp. 17(8):6407, 2009.

[23] S.A. Maier, Plasmonics: Fundamental and applications, Springer, New York, 2007.

[24] F. Hache, D. Ricard, C. Flytzanis, U. Kreibig, The optical Kerr effect in small metal particles and metal colloids: the case gold, Appl. Phys. A 47:347-357, 1988.

[25] E. D. Palik, Handbook of Optical Constants of Solids Academic. Orlando, FL, 1985.

[26] Lakowicz J, Principles of Fluorescence Spectroscopy. New York: Plenum, 2006.

Analysis of Plasmonic-Photonic Resonances in Hybrid Metallo-Dielecric Quasicrystals

Armando Ricciardi[1], Alessio Crescitelli[1], Marco Consales[1], Alberto Micco[1], Vincenzo Galdi[2], Emanuela Esposito[3], Andrea Cusano[1*]

[1]Optoelectronic Division, Engineering Department, University of Sannio,Benevento, Italy
[2]Waves Group, Dept. of Engineering, University of Sannio, Benevento, Italy
[3]Istituto di Cibernetica C.N.R., Arco Felice, Pozzuoli, Italy
*corresponding author, E-mail: a.cusano@unisannio.it

Abstract

We report the evidence of plasmonic-photonic resonances in hybrid metallo-dielectric quasi-crystal nanostructures composed of aperiodically-patterned low-contrast dielectric slabs backed on a metal layer. Via both experimental and numerical studies, with specific reference to the Ammann-Beenker octagonal tiling geometry, we analyze the resonant phenomena and investigate the underlying physics. We show that, by comparison with standard periodic structures with the same filling factor, a richer spectrum of resonant modes may be excited, characterized by a distinctive plasmonic or photonic behavior. Concerning the possible applications, we explore the structure functionalization via high refractive index overlays, as well as its surface sensitivity to deposition of nanolayers of materials mimicking bio-molecular binding. Finally, in connection with the energy-harvesting field, we also present a comparative study on the application of 1-D periodic- and quasiperiodic-based nanostructures as backreflectors for thin-film solar-cell photovoltaics.

1. Introduction

Currently, there is a great deal of interest in the study of out-of-plane resonances occurring in nanostructured metallic and dielectric films, stimulated by applications to highly strategic fields such as chemical and biological sensing. It is well known that flat metallic films can support surface plasmon polaritons (SPPs), which are due to coherent oscillations of the surface charge density bound at the metal surface[1]. Moreover, nanostructured metallic films may also give rise to local surface plasmon resonances which, in contrast with propagating SPPs, are confined around the nanostructure, and exhibit higher local field intensity [2]. Furthermore, dielectric photonic crystals (PCs) slabs [3] can support guided resonances (GRs) due to the coupling of leaky modes with the continuum of radiative modes of the surrounding environment [4]. Both types of resonant phenomena (henceforth, simply referred to as "plasmonic" and "photonic," respectively) are characterized by peculiar spectral features and selectivity. In particular, they exhibit strong sensitivity in terms of wavelength shift to changes in the refractive properties of the surrounding environment. While well-established chemical/bio-sensing schemes are either plasmonic- (see, e.g., Refs. 5-7) or photonic-based (see, e.g., Refs. 8-9), some recent studies [10-12] have demonstrated the very promising potentials of hybrid plasmonic-photonic platforms based on metallo-dielectric nanostructures. The potential interplay between plasmonic and photonic resonances can maintain the advantages offered by the single constituents, while overcoming their respective limitations such as the lossy character of plasmonic resonances. 2-D nanostructured metallo-dielectric plasmonic-photonic crystals have been successfully fabricated [10-12] via self-assembly of a dielectric PC structure constituted by a mono-layer of colloidal spheres on a metallic film. Such hybrid structures may exhibit very high-quality-factor plasmonic and photonic resonant modes, with a high degree of tunability and a strong sensitivity to external materials deposited on the dielectric PC surface. The inherent richness of interplaying resonant phenomena renders these structures extremely promising candidates for a variety of other applications (besides sensing [13]), e.g., to tunable light-emitting and active filtering devices.

The above plasmonic-photonic structures are inherently based on periodic nanostructuring, which can be easily achieved via self-assembly. However, recent studies on either plasmonic (e.g., arrays of sub-wavelength holes in metallic screens, [14] and arrays of plasmonic nanoparticles [15-16]) or photonic (holey dielectric slabs [17-20]) structures, have demonstrated the possible advantages of using aperiodically-ordered lattice geometries. Such geometries, inspired by the concept of "quasi-crystal" (QC) in solid-state physics, [21-22] retain the essential characteristics of periodic-like light scattering (and, hence, the possibility of exciting plasmonic/photonic resonances) while introducing additional geometric degrees of freedom (e.g., higher-order non-crystallographic rotational symmetries, richer spatial spectra and defect states, etc.) that can be judiciously exploited for tuning/optimizing the response. Here we present a numerical and experimental study of hybrid plasmonic and photonic resonances in nanostructured low-contrast metallo-dielectric QCs. In particular, the metallo-dielectric nanostructure considered in this study is schematically represented in Fig. 1a. It essentially consists of a patterned (holey) dielectric layer backed by an unpatterned nanosized metallic (aluminum)

film laid on a sapphire substrate. The pattern is based on the octagonal (Ammann-Beenker) quasi-periodic square-rhombus tiling [22] shown in Fig. 1b. We design and fabricate this structure and characterize its out-of-plane optical response in terms of plasmonic and photonic resonances, studying their dependence on nanosized deposited overlays. We also compare the results with those pertaining to a standard periodic (square) geometry with same filling factor, highlighting similarities and differences.

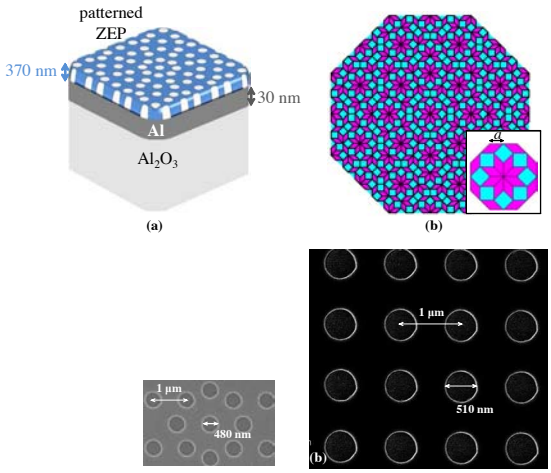

Figure 1: (a) 3-D schematic (not in scale) of the hybrid metallo-dielectric structure with indication of the layer thickness values. (b) Ammann-Beenker tiling (third stage), with a zoom of the central region and the lattice constant a (square/rhombus tile sidelength) shown in the inset. SEM images of the QC (c) and square (d) lattices patterned onto the ZEP layer. The inset in (a) shows a magnified detail. The measured values of lattice constant a = 1 μm and hole diameter (480 nm in (c), and 510 nm in (d)) are also indicated.

2. Fabrication and Characterization

The nanometer-size patterns were defined in an electron-beam positive resist by standard electron beam lithography (EBL). A 30 nm film of aluminum was first deposited on a sapphire substrate by direct-current magnetron sputtering in an ultra-high vacuum system at a base pressure of 8×10^{-8} Torr. The sample was then spin-coated with ~ 370 nm of electron-beam positive resist (ZEP 520A, Zeon Chemicals) and baked on an hot plate for 2 min at 180°C. Subsequently, a 400×400 μm^2 matrix of circular holes (placed at the tiling vertices) was patterned on the same substrate by using a Raith 150 EBL system with a voltage of 20kV and a dose of 55 $\mu C/cm^2$. In this process, the metallic film also acts as charge dissipation layer to avoid deflection of the electron-beam during the writing process. After the electron-beam exposure, the sample was developed in a ZED N50 solution (Zeon Chemicals) for 45 sec, and subsequently rinsed in isopropanol. The scanning electron microscope (SEM) image of the fabricated structure is shown in Fig. 1(c). In order to highlight similarities and differences with the standard (periodic) case, we also fabricated a square crystal (shown in Fig. 1d), with same lattice constant and slightly different hole radius, to equalize the filling fraction (~21%). With the SEM metrology tools, the hole diameter was found to be 480 nm for the QC case, and 510 nm for the periodic case, while the lattice constant a was found to be 1 μm in both cases.

In order to characterize the hybrid photonic-plasmonic resonant behavior of the fabricated samples, we performed out-of-plane spectral reflectance measurements at normal incidence, via a standard reflection setup. We utilized a broad-band white light source directly coupled into a standard fiber-based reflection probe acting simultaneously as light launcher and collector. The reflection probe illuminates the entire patterned area via an optical fiber bundle with six outside fibers in ring-shaped configuration. The light reflected by the sample (placed on a motorized XYZ positioning stage enabling a 10 μm absolute on-axis accuracy) is collected by a central fiber (with a collection spot diameter ~350 μm) directly connected to an optical spectrum analyzer operating with a resolution of 0.4 nm. As a tradeoff between the fulfilling of paraxial (normal incidence) conditions and an adequate signal-to-noise ratio, we selected a distance of 7 mm between the sample and the reflection probe.

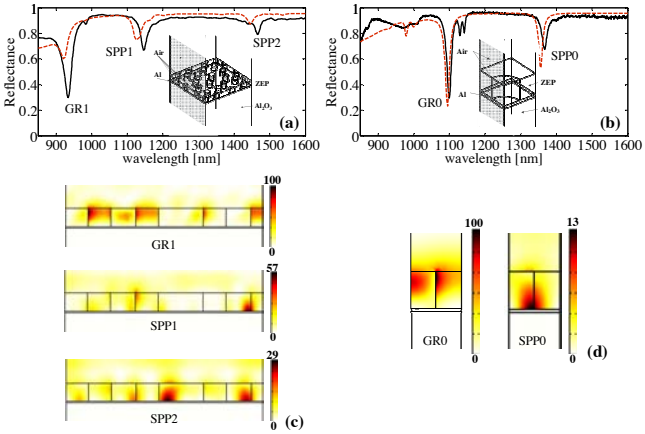

Figure 2: (a), (b) Experimental (black solid) and numerical (red dashed) reflectance spectra of the hybrid metallo-dielectric QC and periodic samples shown Fig. 1(c) and 2(d), respectively. The insets show the (quarter of) supercell (a) and unit-cell (b) used in the simulations. (c), (d) Electric field intensity maps (normalized with respect to the maximum value observed) at the reflectance minima in a section of the structure (shaded wall in the inset) for the QC and periodic case, respectively.

The measured reflectance spectra were finally normalized with respect the (known) reference response of an aluminum mirror. The measured reflectance spectra for normally-incident un-polarized light are shown as black-solid lines in Figs. 2a and 2b for the QC and periodic structures, respectively. For the QC case (Fig. 2a), three sharp resonant dips appear at 934 nm (with quality factor Q~41), 1146.5 nm (Q~51) and 1466 nm (Q~89). For the periodic case, two dips are observed at 1100 nm (Q~74) and 1367 nm (Q~84).

We also carried out numerical studies (via the finite-element-based commercial software package COMSOL

Multiphysics [23]) aimed at assessing the predictability of the resonant phenomena and understanding their physical nature. For the simpler periodic case, also in view of the mirror symmetries involved, the computational domain was reduced to one-quarter of the unit-cell (shown as an inset in Fig. 2b) with perfectly-electric-conducting (PEC) and perfectly-magnetic-conducting (PMC) in-plane terminations compatible with normal-incidence illumination. In the more complex QC case, where the use of the unit-cell concept is prevented by the lack of translational symmetry, we relied on a periodic approximant based on a suitably large square "supercell" of sidelength $L = (4 + 3\sqrt{2}) \cdot a$, [17-19] whose mirror symmetry also allowed its reduction to a single quarter (see the inset in Fig. 2(a)). The numerically computed reflectance spectra, also shown (as red-dashed curves) in Figs. 2(a) and 2(b), are in very good agreement with the experimental results. While this was somehow expectable for the periodic case, it was not to be taken for granted for the QC case. In fact, the actual applicability and effectiveness of periodic-approximant-based numerical modeling as a computationally affordable design tool for hybrid QC constitutes one of the key results of the present study.

3. Resonances Classification

The resonant dips in Figs. 2a and 2b are attributable to the excitation of plasmonic (SPP) and photonic (GR) modes. In the hybrid structure considered here, the patterned dielectric layer plays a two-fold role, acting both as a diffraction grating for the excitation of SPPs and, at the same time, as a guiding layer supporting photonic GRs. Both types of resonant phenomena arise from phase-matching conditions between modes supported by the structure and Bragg peaks in the spatial spectrum of the holey structure (reciprocal lattice). In view of their inherently richer spatial spectra, and the consequent easier achievement of phase-matching conditions, it is not surprising that the QC structure may exhibit a higher number of resonances (by comparison with the periodic counterpart) and offer extra degrees of freedom for their design.

In order to identify the physical nature of the resonances, we studied the corresponding field distributions, which are expected to be mostly localized in the dielectric region for the GR case, and essentially bound at the metal-dielectric interface for the SPP case. As it can be observed from Fig. 2c, for the QC case, the lowest-wavelength resonance exhibits a field distribution mostly concentrated in the dielectric region, and may accordingly be classified as photonic (henceforth labeled as GR1). Conversely, both the dips at 1146.5 nm and 1466 nm are attributable to plasmonic resonances (SPP1 and SPP2, respectively), since their field distributions turn out to be mostly bound at the metal-film interface. Likewise, for the periodic case shown in Fig. 2d, the resonance occurring at 1100 nm can be classified as photonic (GR0), whereas the one located at 1367 nm as plasmonic (SPP0).

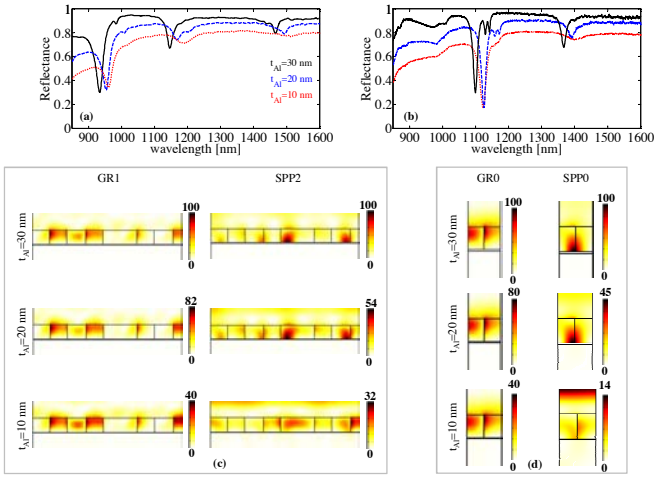

Figure 3: (a), (b) (a), (b) Experimental reflectance of the QC and periodic structures, respectively, for different values of the aluminum film thickness. (c), (d) Electric field intensity for the QC and periodic structures, respectively, at the reflectance minima for photonic (first column) plasmonic (second column), and different values of the aluminum film thickness.

A further validation of our resonance classification may be derived investigating the effect of the metal film thickness on the observed resonances. Intuitively, a significant influence of the metal thickness on the plasmonic resonances excitation and modal field distribution is expected in view of the active role of the metal in supporting SPPs. Conversely, in the photonic case, a weaker influence is expected, since the metal film essentially plays the passive role of a mere reflective mirror. In this framework, we fabricated and characterized two additional samples with different values of aluminum thickness t_{Al} (10 nm and 20 nm), with the other geometrical parameters kept constant. Closer to the resonances, two markedly different trends are observed. While the photonic resonance remains essentially stable, as expected, the plasmonic resonances become sharper and more pronounced. In particular, for both the QC and periodic cases, the higher-wavelength plasmonic resonances practically disappear for t_{Al} =10 nm. As a further indication, Figs. 3c and 4d show the corresponding field distributions for the QC and periodic case, respectively. Differently from the photonic case, the plasmonic resonances are excited when t_{Al} approaches 20 nm. Moreover, for increasing aluminum thickness, it can be observed that the resonant field distributions tend to become more concentrated (in the dielectric layer, for the photonic case; at the metal-film interface, for the plasmonic case). This may justify the blue-shift observed in Figs. 3(a) and 3(b), which, in agreement with the numerical predictions in Ref. 24, is much stronger in the plasmonic case. However, small differences in the hole radii among the different samples (due to fabrication tolerances) may also contribute to such blue-shift.

We point out that, although no specific parameter optimization was performed, the Q-factors exhibited by our hybrid metallo-dielectric structures are significantly larger

than those observed in typical plasmonic crystal configurations (see, e.g., Ref. 25). To summarize, in our parameter configuration, the highest Q-factor was observed for a plasmonic resonance in the QC case. Moreover, the QC structure was found to exhibit a richer resonant spectrum, with a resonance dip amplitude comparable with the periodic counterpart.

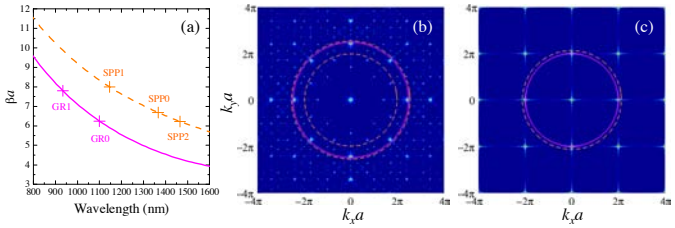

Figure 4: (a) Dispersion curves of the lowest-order anti-symmetrical TE bound mode supported by a homogenized grounded dielectric slab waveguide (magenta-solid), and the SPP mode supported at the interface between the aluminum and homogenized-dielectric media (orange-dashed). (b), (c) Spatial spectra of the QC and periodic PC, respectively, with overlayed the circles of radii βa pertaining to the resonant wavelengths (marked with crosses and labeled in the dispersion curves).

4. Mode Coupling Mechanism

From the physical viewpoint, the observed resonant phenomena may be understood via approximate semi-analytical models based on phase-matching conditions between Bragg-type peaks in the lattice spatial spectrum (reciprocal lattice) and the photonic and plasmonic bound modes supported by an effective homogenized structure. For instance, Figure 4a shows the dispersion curves for i) the lowest-order anti-symmetric transverse-electric (TE1) photonic bound mode supported by a homogenized (assuming a filling-factor of 21%) dielectric slab waveguide backed by a perfectly conducting metallic wall[33] (magenta-solid), and ii) the SPP mode supported at the interface between the aluminum and homogenized-dielectric media [1] (orange-dashed). From these curves, it is possible to extract the (real part of) in-plane propagation constant (normalized to the lattice constant a) pertaining to the resonant wavelengths in Figure 2 (marked with crosses and labeled in Figure 4a), and therefore assess the phase-matching conditions $\beta a = |k_n| a$ (with k_n denoting a Bragg wave-vector in the reciprocal space) by drawing circles of radii βa overlayed on the spatial spectra of the QC and periodic PC, as shown in Figures 4b and 4c, respectively. It can be observed that, for both the QC and periodic PC case, all the circles fall rather close to certain orders of spectral peaks, and may therefore be associated to the corresponding phase-matching conditions. As a further illustration of the inherent richness of resonant phenomena in these hybrid structures, it is also observed that the same order of spectral peaks can yield resonances at different wavelengths by interacting with both a photonic and plasmonic mode (e.g., GR1 and SPP1, or GR0 and SPP0).

Moreover, by comparing Figures 4a and 4b, it clearly emerges the inherently denser character of the QC spatial spectrum, and the consequent easier achievement of phase-matching conditions. It is therefore not surprising that the QC structure may exhibit a higher number of resonances and offer extra degrees of freedom for their design.
The intrinsic difference of the nature and spacing of the resonances in a QC can be exploited in a number of applications, such as solar cells or nonlinear phase matching, as well as chemical and biological sensing. For instance, in thin-film solar cells, the resonance spacing and coupling strength may be adjusted so as to match the spectral profile of the absorbing layer, whereas in nonlinear phase matching, non-evenly-spaced resonances may be useful in order to compensate for material dispersion. An additional feature of these structures is their potential ability to tailor the resonant optical field distribution so as to enhance the spectral sensitivity to local environmental changes, which plays a fundamental role in label-free sensors for chemical and biological detection.

5. Resonance Tuning

Tuning and re-configurability of resonant modes represent key features for components and devices to be incorporated in modern optical systems. In this framework, the use of nanosized HRI coatings represents an effective approach typically exploited to modify the modal distributions, and particularly suited to tailor the final spectral characteristics of optical components. In addition, the exploitation of suitable active HRI materials may open up promising perspectives for actively (e.g., electronically, magnetically, thermally) tuning the resonances of the functionalized device. In order to assess the applicability of this approach to our hybrid metallo-dielectric QCs, we deposited a 15nm-thick layer of SiO (refractive index ~1.95) on the surface of a sample. For comparison, we also fabricated a periodic counterpart using the same procedure.

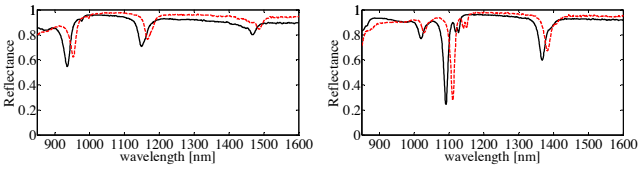

Figure 5: (a), (b) Reflectance spectra for uncoated (black solid) and 15nm SiO-coated (red dashed) QC and periodic structures, respectively.

The reflectance spectra of the SiO-coated QC and periodic structures are compared in Fig. 5 with those pertaining to the uncoated samples. As it can be observed, the HRI functionalization produces three main effects: i) a red shift of all resonant modes, ii) the improvement of the quality factor of both photonic and plasmonic resonances, and iii) an increase of the reflectance baseline, also accompanied by a decrease of resonance visibility. Specifically, for the QC case, photonic and plasmonic resonances shift towards longer wavelengths (consistent with an increase of the effective refractive index of the

resonant modes due to the higher refractive index of the overlay with respect to the patterned dielectric), also exhibiting a dip amplitude reduction of ~18%. This clearly reveals that the SiO deposition, as expected, occurs either on the top surface of the structure or inside its holes, thereby enabling the electric field associated to both photonic and plasmonic modes to be modified by the HRI material. In particular, the red-shift exhibited by the plasmonic resonances SPP1 and SPP2 ($\Delta\lambda_{SPP1}$=17.6 nm and $\Delta\lambda_{SPP2}$ =18.0 nm) is more pronounced than that observed in the photonic case ($\Delta\lambda_{GR1}$=17.2 nm). A qualitatively similar behavior is obtained in the periodic case, where red-shifts of the same order are also observed for both the GR0 and SPP0 resonances. Here, however, the shift associated to the photonic resonance ($\Delta\lambda_{GR0}$= 19.2 nm) turns out to be larger than the plasmonic one ($\Delta\lambda_{SPP0}$= 15.2 nm).

Another important advantage of the HRI functionalization is the Q-factor enhancement. Indeed, the reflectance spectra reported in Fig. 5 clearly show that the resonance dips become sharper after the SiO deposition. In particular, with reference to the QC case in Fig. 5a, a 27% Q-factor enhancement was calculated for the photonic resonance GR1, as well as of nearly 12% and 8% for the plasmonic resonances SPP1 and SPP2, respectively. This effect is also observed for the periodic structure (cf. Fig. 5b), but with a weaker Q-factor enhancement, namely ~9% for the photonic resonance GR0, and no sensible variation for the plasmonic resonance SPP0. Further optimization margins may be expected by exploiting the geometrical degrees of freedom in the aperiodic tiling, so as to favor a stronger modal overlap with the HRI overlay.

6. Resonance Surface Sensitivity

Due to the high surface sensitivity of the resonant modes demonstrated in the case of HRI functionalization, we performed a different experiment, using suitable nanosized overlays with refractive index similar to those exhibited by most of the biological species of practical interest. Specifically, we carried out the deposition of nanoscale (15 nm thick) overlays of SiO_2 (refractive index ~1.45), which well resembles the binding typical of biomolecular interactions [26].

Figure 6a compares the reflectance spectra of the QC structure before and after the deposition. Also in this case, a red-shift of both resonance types occurs, but less evident than the SiO case, mainly due to the lower refractive index of SiO_2. In particular, the photonic resonance GR1 exhibits a slightly larger shift ($\Delta\lambda_{GR1}$=6.4 nm) than the plasmonic ones SPP1 and SPP2 ($\Delta\lambda_{SPP1}$=$\Delta\lambda_{SPP2}$=6.0 nm). For comparison, we show in Fig. 6e the reflectance spectra of the uncoated and SiO_2-coated periodic samples. Also in this case, the wavelength shift observed for the photonic resonance GR0 ($\Delta\lambda_{GR0}$= 6.4 nm) is slightly larger than that associated to the plasmonic one SPP0 ($\Delta\lambda_{SPP0}$=4.0 nm). Interestingly, while the wavelength shifts of the photonic resonances observed in the QC and periodic cases turn out to be comparable, the plasmonic resonances in the QC case exhibit a sensitivity enhancement up to 50% with respect to the periodic counterpart. The above results reveal promising molecular sensitivity at monolayer scale, namely, surface sensitivities (in terms of resonance shift per nanometer of deposited overlay) as high as 0.40 nm and 0.43 nm for the plasmonic and photonic resonances, respectively. Considering the typical sizes of biological molecules (3.8-5.2 nm), it can be inferred that the binding of a single biological monolayer to the sample surface is able to generate a resonance shift of approximately 1.5-2 nm, which may be easily detected via low-cost commercial spectrophotometer, thereby opening up new perspectives in label-free biochemical sensing. Moreover, for the QC case, further optimization margins exist by acting on the tiling geometry, so as to tailor the field distribution of the resonant modes for improving their surface sensitivity.

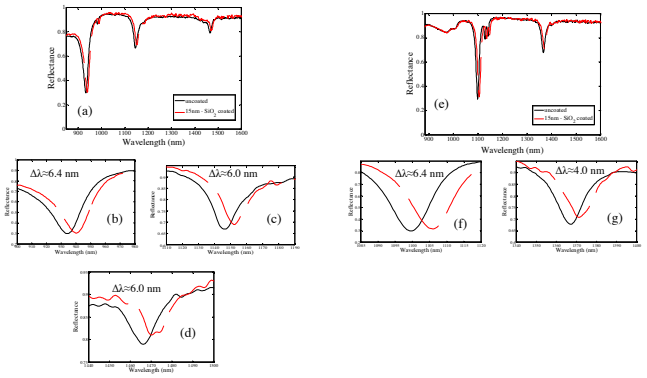

Figure 6: (a), (b) Reflectivity spectra for uncoated (black solid) and 15nm-SiO_2 coated (red dashed) metallo-dielectric PQC (a) and PC (e) structures. The insets (b-d) and (f,g) show magnified details around the resonance dips for the PQC and PC case, respectively.

7. Absorption Enhancement in Thin Film Solar Cells with Quasi-Periodic Backreflectors

Due The ability to engineer the plasmonic and photonic resonances (e.g., number and spectral locations) may provide new solutions in a variety of highly strategic fields, such as thin-film solar cells. In this context, it is well known that a serious limitation to the overall efficiency stems from the poor light absorption, especially at longer wavelengths of the solar spectrum, which is in turn attributable to the limited thickness of the semiconductor (active) region with respect to the absorption length of near infrared photons[28] Accordingly, over the last few years, light-trapping techniques have been proposed in order to increase the optical thickness of the absorbing layer. A particularly promising approach relies on the use of metallic nanogratings on the back surface, which can couple the incoming radiation into both plasmonic (excited at the metal/semiconductor interface) and photonic modes (guided directly in the semiconductor layer).[28] In such configurations, the patterned metallic backreflector is capable of efficiently coupling the incoming light into photonic and plasmonic modes whose field distributions are mainly localized in the active region of the solar cell.[29] In this framework, QC backreflectors may be exploited to

judiciously tailor the number and location of photonic/plasmonic modes within the near-infrared wavelength range, so as to enhance the overall performance.

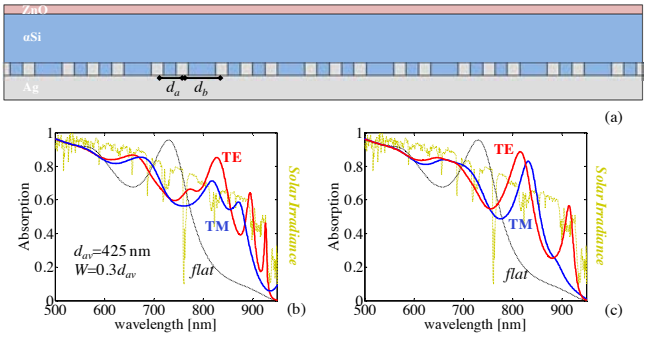

Figure 7: (a) Schematic (supercell for numerical simulation) of the solar cell with a Fibonacci-like nanograting as backreflector. (b) AM 1.5 solar spectrum (golden-dotted); absorption spectra for the TE polarization (red-solid) and TM polarization (blue-solid) of the structure in (a); absorption spectrum of the solar cell with a silver mirror as backreflector (black-dotted). (c) Same as (b), but with a periodic grating as backreflector. Details in the text.

As a representative example, we evaluate the performance of a 1-D nanograting based on the generalized- Fibonacci deterministic aperiodic sequence. The proposed solar-cell structure is shown in Figure 7a. It essentially consists of a 50 nm thick top layer of ZnO acting as a transparent electrode, a light-absorbing amorphous silicon middle layer (active region) with a thickness of 200 nm, and a silver nanograting which also serves as the bottom electrode. The grating is constituted of ridges of thickness 50 nm, placed according to the generalized-Fibonacci geometry with the scale-ratio parameter $\nu = d_b / d_a = \tau$ (where d_a and $d_b = \nu\, d_a$ denote the two scales of the model and $\tau = (1+\sqrt{5})/2$ the Golden mean) and width $W = 0.3\, d_{av}$, with $d_{av} = (d_a + \tau\, d_b)/(1+\tau) = 425$ nm denoting the average spacing. The grating grooves are filled with amorphous silicon.

The light absorption is calculated [29] as the flux of the Poynting vector (real part) through the surface of the amorphous-silicon layer (including the grooves) when the structure is illuminated by a normally incident plane wave. Similar considerations as for the previously studied (octagonal) structure hold, with the periodic approximant shown in Figure 7a (21-element supercell). The ZnO refractive index was extracted directly from measurements (1.96 @ λ=500 nm, and 1.77 @ λ=950 nm).

Figure 7b shows the absorption spectra in the wavelength range 500-950 nm for both the transverse-electric (TE) and transverse-magnetic (TM) polarizations ($A_{TE}(\lambda)$ and $A_{TM}(\lambda)$, respectively), overlayed on the AM 1.5 normalized solar spectrum $S(\lambda)$. Several absorption peaks can be observed, each of which may attributable to the excitation of i) cavity resonances due to the Fabry-Peròt effect, ii) guided photonic modes in the amorphous-silicon planar waveguide, or iii) plasmonic modes at the semiconductor-metal interface (only for the TM case).[29]

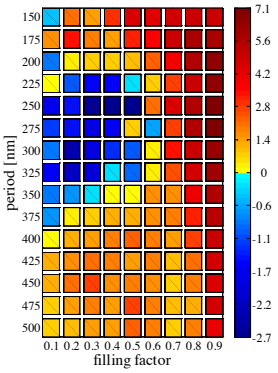

Figure 8: Total-absorption excess enhancement factor E' in (4), pertaining to a Fibonacci-like grating with respect to a periodic one, as function of the (average) period and filling factor.

A detailed discussion and classification of these three effects is beyond the scope of the present work. Also shown in Figure 7b is the absorption spectrum $A_{flat}(\lambda)$ of the same solar cell with a flat silver mirror in place of the grating. The total-absorption excess enhancement factor E with respect to this reference configuration, defined as

$$E = 100\left(\frac{\eta_{Fibonacci}}{\eta_{flat}} - 1\right) \tag{1}$$

with

$$\eta_{Fibonacci} = \frac{1}{2}\left[\int A_{TE}(\lambda)\cdot S(\lambda)\cdot d\lambda + \int A_{TM}(\lambda)\cdot S(\lambda)\cdot d\lambda\right] \tag{2}$$

$$\eta_{flat} = \int A_{flat}(\lambda)\cdot S(\lambda)\cdot d\lambda \tag{3}$$

was found to be 14.7 %. As a comparison, Figure 7c shows the absorption spectra pertaining to a periodic nanograting ($\nu = 1$) with same average spacing and filling factor. In this case, fewer absorption peaks (for both polarizations) can be observed, likely attributable to the lower number of photonic and plasmonic modes excited in the structure, resulting in a 2.2 % lower enhancement factor. In order to facilitate direct comparison between periodic and aperiodic nanogratings, as a figure of merit, we evaluated the total-absorption excess enhancement factor

$$E' = 100\left(\frac{\eta_{Fibonacci}}{\eta_{periodic}} - 1\right) \tag{4}$$

(with $\eta_{periodic}$ defined as in (3) but for a periodic grating) for different combinations of the average period (within the range 150 - 500 nm) and filling factor (within 10% to 90%), with the results summarized as a false-color-scale plot in Figure 8. It can be observed that, although not fully optimized, the Fibonacci geometry may yield up to 7%

higher enhancements (against a maximum 2.7% loss) for given average spacings and filling factors.

8. Conclusions

In conclusion, we have reported here the first evidence of out-of-plane resonances in hybrid metallo-dielectric QC nanostructures. Via measurements and full-wave numerical simulations on structures characterized by octagonal (Amman-Beenker) geometry, we have observed the presence of sharp resonant dips in the reflectance spectrum, attributable to the excitation of plasmonic and photonic resonant modes, and verified the actual applicability of periodic-approximant-based computationally-affordable design tools.

By comparison with a reference periodic (square) structure with same filling fraction, the proposed QC structure exhibits a richer resonant spectrum, which is attributable to the easier achievement of phase-matching conditions endowed by its denser Bragg spectrum. Moreover, the measured Q-factors, in the QC and periodic cases, turn out to be comparable and higher than those observed in periodic patterned fully metallic nanostructures.[28-31] We have also assessed the surface sensitivity with respect to nanosized deposition of SiO overlays (for response tuning/optimization), and SiO2 overlays (with refractive index resembling that of biological molecules). The proposed metallo-dielectric QC nanostructures exhibit remarkably high surface sensitivity, namely, □0.4 nm wavelength shift per nanometer of deposited SiO2 overlay, with an enhancement of 50% with respect to the plasmonic resonances in the periodic counterpart. By acting on the extra degrees of freedom typical of QCs, there exist further margin of optimization for the surface sensitivity, and therefore concrete perspectives to outperform PC-based chemical and biological sensors based on periodic nanostructures currently available on the market.

Finally, we have shown that the resonance-engineering capabilities of QC nanostructures, in terms of tailoring the number and spectral positions of plasmonic and photonic resonances, may be effectively exploited in order to enhance the efficiency of thin film solar cells.

Overall, the results and examples illustrated here pave the way to the development of novel nanodevices, with possible applications to a variety of highly strategic fields, ranging from chemical and biological sensing to energy harvesting.

References

[1] Maier, S. A. *Plasmonics: Fundamentals and applications*; Springer: Berlin, 2007.

[2] Hutter, E.; Fendler, J. Exploitation of localized surface plasmon resonance. *Advanced Materials* 2004, 16, 1685.

[3] Joannopoulos, J. D.; Johnson S. G.; Meade R. D.; Winn J. N. *Photonic crystals: Molding the flow of light, second edition*; Princeton University Press: New Jersey, 2008.

[4] Fan, S.; Joannopoulos, J. D. Analysis of guided resonances in photonic crystal slabs. *Phys. Rev.* B 2002, 65, 235112.

[5] Ostuni, E.; Chapman, R. G.; Holmlin, R. E.; Takayama, S.; Whitesides, G. M. A survey of structure–property relationships of surfaces that resist the adsorption of protein, *Langmuir* 2001, 17, 5605.

[6] Zhao, J.; Zhang, X.; Yonzon, C. R.; Haes, A. J.; Van Duyne, R. P. Localized surface plasmon resonance biosensors. *Nanomedicine* 2006, 1, 219.

[7] Lassiter, J. B.; Sobhani, H.; Fan, J. A.; Kundu, J.; Capasso, F.; Nordlander, P.; Halas, N. J. Fano resonances in plasmonic nanoclusters: Geometrical and chemical tunability. *Nano Lett. 2010*, 10, 3184.

[8] Ganesh, N.; Zhang, W.; Mathias, P. C.; Chow, E.; Sooares, J. A. N. T.; Malyarchuk, V.; Smith, A. D.; Cunningham, B. T. Enhanced fluorescence emission from quantum dots on a photonic crystal surface. *Nature Nanotechnology* 2007, 2, 515.

[9] El Beheiry, M.; V, L.; Fan, S.; Levi, O. Sensitivity enhancement in photonic crystal slab biosensors. *Opt. Express* 2010, 18, 22702.

[10] Yu, X.; Shi, L.; Han, D.; Zi, J.; Paul V. Braun, P. V. High quality factor metallo dielectric hybrid plasmonic–photonic crystals. *Adv. Funct. Mater.* 2010, 20, 1910.

[11] López-García, M.; Galisteo-López, J. F.; Blanco, A.; Sánchez-Marcos, J.; López, C.; García-Martín, A. Enhancement and directionality of spontaneous emission in hybrid self-assembled photonic–plasmonic crystals. *Small* 2010, 6, 757.

[12] Shi, L.; Liu, X.; Yina, H.; Zi, J. Optical response of a flat metallic surface coated with a monolayer array of latex spheres. *Phys. Lett. A* 2010, 374, 1059.

[13] De Angelis, F.; Patrini, M.; Das, G.; Maksymov, I.; Galli, M.; Businaro, L:, Andreani, L. C.; Di Fabrizio, E. A hybrid plasmonic–photonic nanodevice for label-free detection of a few molecules. *Nano Lett.* 2008, 8, 2321.

[14] Matsui, T.; Agrawal, A.; Nahata, A.; Vardeny, Z. V. Transmission resonances through aperiodic arrays of subwavelength apertures. *Nature* 2007, 446, 517.

[15] Gopinath, A.; Boriskina, S. V.; Feng, N.-N.; Reinhard, B. M.; Dal Negro, L. Photonic-plasmonic scattering resonances in deterministic aperiodic structures. *Nano Lett. 2008*, 8, 2423.

[16] Forestiere, C.; Miano, G.; Boriskina, S. V.; Dal Negro, L. The role of nanoparticle shapes and deterministic aperiodicity for the design of nanoplasmonic arrays. *Opt. Express* 2009, 17, 9648.

[17] Ricciardi, A.; Gallina, I.; Campopiano, S.; Castaldi, G.; Pisco, M.; Galdi, V.; Cusano, A. Guided resonances in photonic quasicrystals. *Opt. Express* 2009, 17, 6335.

[18] Gallina, I.; Pisco, M.; Ricciardi, A.; Campopiano, S.; Castaldi, G.; Cusano, A.; Galdi, V. Guided resonances in photonic crystals with point-defected aperiodically-ordered supercells. *Opt. Express* 2009, 17, 19586.

[19] Pisco, M.; Ricciardi, A.; Gallina, I.; Castaldi, G.; Campopiano, S.; Cutolo, A.; Cusano, A.; Galdi, V. Tuning efficiency and sensitivity of guided resonances in photonic crystals and quasi-crystals: A comparative study. *Opt. Express* 2010, 18, 17280.

[20] Ricciardi, A.; Pisco, M.; Gallina, I.; Campopiano, S.; Galdi, V.; O' Faolain, L.; Krauss, T. F.; Cusano, A. Experimental evidence of guided resonances in photonic crystals with aperiodically-ordered supercells. *Opt. Lett.* 2010, 35, 3946.

[21] Levine, D.; Steinhardt, P. J. Quasicrystals: A new class of ordered structures. *Phys. Rev. Lett.* 1984, 53, 2477.

[22] Senechal, M. *Quasicrystals and geometry*; Cambridge University Press: Cambridge, UK, 1995.

[23] http://www.comsol.com/

[24] Nemova G.; Kashyap R. Theoretical model of a planar integrated refractive index sensor based on surface plasmon-polariton excitation. *Opt. Commun.* 2007, 275, 76.

[25] Ebbesen, T. W.; Lezec, H. J.; Ghaemi, H. F.; Thio, T.; Wolff, P. A.; Extraordinary optical transmission through sub-wavelength hole arrays. *Nature* 1998, 391, 667.

[26] Tsargorodskaya, A.; Nabok, A. V.; Ray, A. K. Ellipsometric study of the adsorption of bovine serum albumin into porous silicon, Nanotechnology 2004, 15, 703.

[27] Lifshitz, R.; Arie, A.; Bahabad, A. Photonic quasicrystals for nonlinear optical frequency conversion. *Phys. Rev. Lett.* 2005, 95, 133901 (2005).

[28] Atwater A.; Polman A. Plasmonics for improved photovoltaic devices. Nature Materials 2010, 9, 205.

[29] . W. Wang, S. Wu, K. Reinhardt, Y. Lu, S. Chen, *Nano Lett.* 2010, 10, 2012

Lab on Fiber Technology enables Nanophotonics within optical fibers

A. Crescitelli[1], A. Ricciardi[1], M. Consales[1], E. Esposito[2], A. Cutolo[1], A. Cusano[1*]
[1] Optoelectronic Division, Engineering Department, University of Sannio, Benevento, Italy
[2] Istituto di Cibernetica C.N.R., Arco Felice, Italy
[*]corresponding author: a.cusano@unisannio.it

Abstract

We report the design, fabrication and characterization of a 2D hybrid metallo-dielectric nanostructure supporting localized surface plasmon resonances (LSPR), directly realized by innovatively applying the electron beam lithography technique on the cleaved end face of a standard single mode optical fiber (SMF). In our configuration, the structure is illuminated in the out-of-plane direction and plasmonic-photonic resonances are excited due to the phase matching condition between the scattered waves and the modes supported by the hybrid nanostructure. The resonances can be easily tuned by acting on the physical and geometrical parameters of the structure. Moreover, with a view towards possible applications, we present some preliminary results demonstrating how the proposed device can work effectively as an optical probe for label free chemical and biological sensing as well as a microphone for acoustic wave detection.

1. Introduction

The "Lab on Fiber" concept essentially envisages the integration of highly functionalized materials at nano and micro scale within a single optical fiber and aims to develop a novel generation of miniaturized and advanced "all-in-fiber" technological platforms (namely "Labs") for both communication and sensing applications.
The "Lab on Fiber" Technology would thus represent the cornerstone of a photonics technological revolution enabling the implementation of fiber-based multifunction sensing and actuating micro- and nano-systems, showing unique advantages in terms of miniaturization, light weight, cost effectiveness, robustness, power consumption and information control. Multifunctional labs integrated in a single optical fiber, exchanging information and combining sensorial data, could provide effective auto-diagnostic features as well as new photonic and electro-optic functionalities useful in many strategic sectors such as optical processing, environment, life science, safety and security. The labs design deals with all those phenomena that provide light manipulation and control at nanoscale, such as trapping and guiding effects in photonic crystals [1-3] and quasicrystals [4, 5] as well as plasmonic nanostructures [6-9], eventually combined all together in hybrid metallo-dielectric devices [10-13].
However, the realization of highly integrated optical fiber devices requires that several micro and nanostructures be fabricated, embedded and connected all together in order to achieve the necessary light-matter interaction and physical connection. As a consequence, a critical issue to be addressed consists in the definition of a reliable fabrication procedure able to integrate and process, at micro- and nano-scale, several materials with the desired physical, mechanical, magnetic, chemical and biological properties onto unconventional substrates such as the optical fiber tip.
Promising approaches in this direction were recently introduced by Capasso's group [14,15]. The proposed methodology relies on the preventive fabrication of metallic nanostructures on planar silicon wafers by means of electron-beam lithography (EBL), and their successive transfer to small and/or non conventional substrates (i.e. the fiber tip) [14].
A further method in this direction was also recently demonstrated by the same group through the use of soft lithography and mechanical sectioning, using an ultramicrotome equipped with a diamond knife. Dip coating technique was finally adopted to transfer onto the optical fiber facet composite nano-slices containing gold nanostructures with complex shapes [15] opening the way to the development of competitive all-fiber localized surface plasmon resonances (LSPRs)- and surface-enhanced raman spectroscopy-based sensing devices.
Following the transferring approach, a monolithic silicon photonic crystal (PC) fiber tip sensor (for both refractive index and temperature sensing) was also recently proposed by Jung et al. [17] employing a complex combination of EBL and reactive ion etching (RIE) for the structure fabrication and focused ion beam (FIB) milling for the transferring step. A simpler and low cost method based on UV nano imprint and transfer lithography (NITL) technique was introduced by Scheerlinck et al. [18]. This procedure was applied for the fabrication of optical probes for photonic integrated circuits based on a waveguide-to-fiber gold grating coupler [18].
Although these methods rely on well-assessed fabrication processes on planar substrates, the final transferring step plays a fundamental role in determining both the fabrication yield and the performance of the final device. This aspect is crucial since it poses severe limitations in the ability to control the transferring procedure at nanoscale, as well as in the adhesive strength of the nanostructures.

To overcome these limitations, alternative approaches based on direct-write patterning of the fiber tip have been explored. The key aspect of these methodologies is to adapt all the standard fabrication processes and tools in terms of material deposition (spin coating, dip coating, sputtering, evaporation, etc..), sub-wavelength patterning and post-processing (FIB, EBL, RIE, etc..) to operate on the optical fiber tip. This approach is not straightforward, however, since spin coating and etching procedures are very challenging when operating on such a substrate [14,15].
Thus far, only few direct-writing attempts have been performed [19-20] in particular for creating metallic nanostructures, giving rise to LSPR effects exploited for chemical and biological sensing. In particular, FIB milling of gold-coated fiber tips has been used to fabricate ordered arrays of apertures with sub-wavelength dimensions and submicron periodicity [19]. Moreover, by using EBL and RIE, ordered arrays of gold nanodots have been fabricated on the fiber tip for biosensing demonstration [20].

In this work we report on a reliable fabrication process that enables the realization of both dielectric and metallic nanostructures directly on the fiber facet, involving conventional nanotechnology techniques.

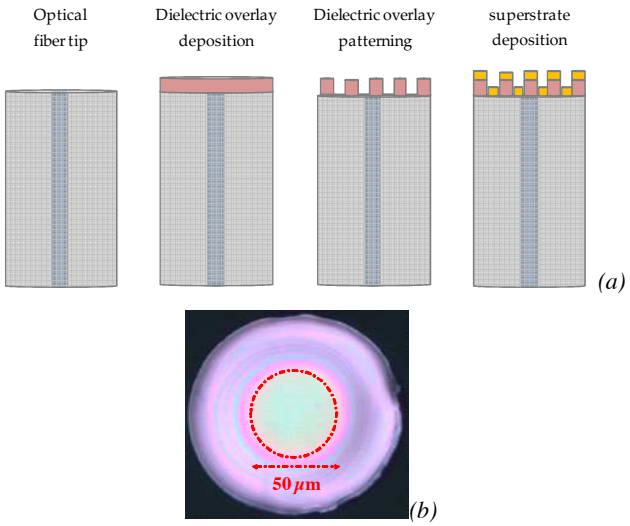

Figure 1: a) Schematics of the main technological steps for the fabrication of the hybrid metallo-dielectric PC based fiber tip device, (b) microscope image of the ZEP overlay deposited by spin coated on the fiber facet.

2. Structure Fabrication

The hybrid structure was realized by means of conventional nano-scale deposition and fabrication/patterning tools typically exploited for planar devices and here properly adapted to enable direct in-fiber operations. In particular, the fabrication steps (reproduced in Fig. 1a), are: 1) dielectric overlay deposition with flat surface over the fiber core, 2) dielectric overlay nano-patterning and 3) metallic superstrate deposition. A positive tone electron beam resist (ZEP 520A, Zeon Chemicals, refractive index n~1.54) and gold have been selected as dielectric and metallic materials, respectively. One of the main innovations of this approach relies on the capability to deposit ZEP layers onto the fiber facet with controlled and uniform thickness over the fiber core by using a modified spin coating technique. Specifically, the modified spin coating technique enables the direct deposition of ZEP overlays onto the cleaved end of SMF, with controllable thickness ranging from 100 to 400 nm and flat surface areas nearly 50 μm in diameter large. With reference to Fig. 1a, the fiber facet of a SMF (core and cladding diameters of 9 μm and 125 μm, respectively) was firstly coated with a 200 nm-thick layer of ZEP by means of the modified spin coating technique.

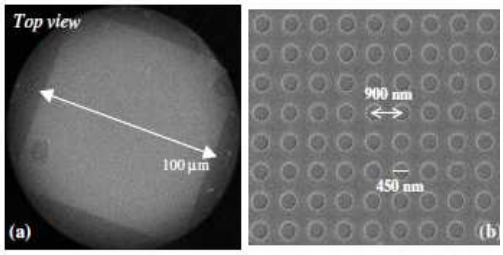

Figura 2: (a) SEM image of the patterned fiber and (b) zoomed detail.

The microscope top view of the spinned fiber is shown in Fig. 1b: the concentric circles of different colors are attributable to the ZEP film thickness variation due to edge bead. However a uniform thickness area of approximately 50 μm in diameter around the center of the optical fiber has been estimated to be sufficient to cover the active optical area. With the purpose of estimating the obtained layer thickness, an hole was drilled onto the coated fiber tip by an excimer laser, operating at 248 nm; then the layer thickness was measured via an optical profilometer (Veeco, Wyko 9100 NT) and was found to be around 200 nm ± 10 nm. The square lattice, consisting of a 100×100 μm^2 matrix of circular holes (holes radius r=225 nm, period a=900 nm), was written on the covered fiber tip, by using a Raith 150 e-beam lithography system. Finally, a 40 nm gold layer was sputtered on the fiber tip to realize the photonic-plasmonic device. The SEM image (top view) of the fabricated device is shown in Fig 2a together with a zoomed-in image of the holey structure (Fig. 2b). The fabrication process follows almost ordinary lithographic techniques, allows rapid prototyping with a 90% yield and is able to produce robust and reusable devices.

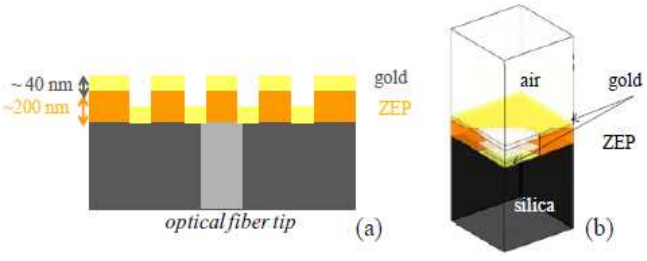

Figure 3: (a) schematic of the hybrid metallo-dielectric PC

structure integrated on the optical fiber tip. (b) 3D view of ¼ of unit cell (computational domain).

3. Numerical and Experimental Analysis

When the realized hybrid structure is illuminated in out-of-plane configuration, as the case of single mode fiber illumination in the paraxial propagation regime, hybrid plasmonic-photonic resonances are expected to be excited due to the phase matching condition between the scattered waves and the modes supported by the hybrid nanostructure [21]. A numerical analysis of the structure (schematically represented in Fig. 3a) has been carried out by the commercial software COMSOL Multiphysics (RF module) based on the finite element method. Following the same approach of [22], by exploiting the crystal translational and mirror symmetries, the computational domain can be reduced to one quarter of unit cell. The resulting structure (Fig. 3b) supports a transverse electromagnetic wave emulating the normally-incident plane-wave. The Lorentz–Drude model was used for modeling gold in the IR wavelengths. Fig. 4 shows the numerically retrieved reflectance spectrum for the structure exhibiting period a=900 nm and holes radius r=225 nm, corresponding to a filling factor (radius to period ratio, r/a) of about 0.25.

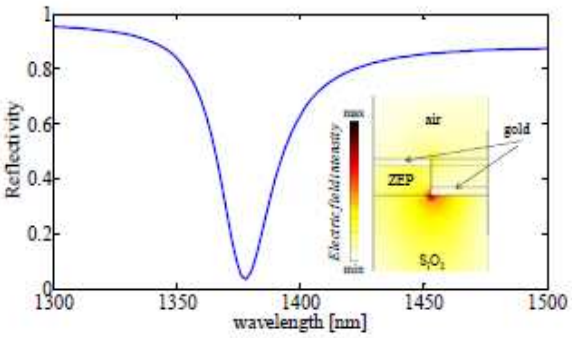

Figura 4: Simulated reflectivity of the hybrid metallo-dilectric structure of Fig. 3a. The PC period is a=900nm and the holes radius is 450 nm. (inset) Electric field intensity distribution at the reflectivity minimum.

The high reflectivity (>85%) base line is interrupted by a resonance dip centered at 1378 nm with a Q-factor of 53. In the inset of Fig. 4, the cross section of the electric field distribution corresponding to the resonant mode evaluated at the resonance wavelength is shown.

According to PC theory, the resonant wavelength can be tailored for the specific application by a proper choice of the device parameters (lattice period, filling factor, dielectric and gold thickness). In order to experimental characterize the realized structure, the optical reflectance spectrum has been measured using as reference mirror a second optical fiber terminated with a 160 nm-thick gold film. The measured reflectance is shown in Fig. 5 (solid black curve).

A resonance dip centered at 1311 nm was found with a Q-factor of about 23. Comparing the experimental reflectivity with the numerical counterpart it is possible to notice a considerable blue shift (67 nm), together with a reduction of both the visibility and the Q-factor. These discrepancies can be attributed to the fabrication tolerances and mainly to the numerical analysis carried out in the hypothesis of plane wave excitation assuming an infinite structure in the periodicity plane. In order to demonstrate the tunability of our device via a proper crystal design, we also fabricated other two samples with different periods (850 nm and 1000 nm) and same filling factor (r=213 nm and r=250 nm). Since the resonant wavelengths are directly related to the lattice period, a red shift is expected in the case of higher lattice period while a blue shift should occur in the opposite case. Indeed, we experimentally observed a red shift of about 100 nm for a=1000 nm and a blue shift of approx. 70 nm for a=850 nm (see Fig. 5).

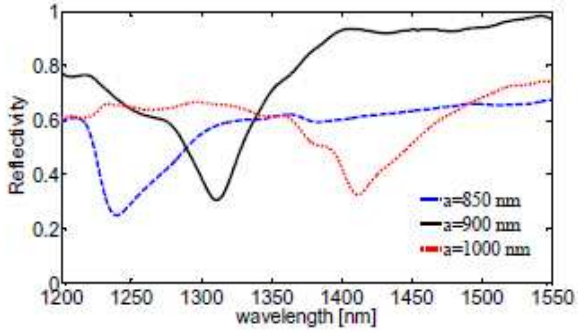

Figura 5: Measured reflectivity of hybrid metallo-dilectric PC-based structures characterized by a period a=850 (dashed blue curve), a=900nm (solid black curve) and a=1000nm (dotted red curve).

4. Refractive Index Measurements

The metallo-dielectric nanostructure fabricated onto the fiber tip supports LSPRs, whose excitation wavelengths are very sensitive to variations of the surrounding refractive index. Therefore, a change in the local or bulk refractive index around the fiber tip device gives rise to a wavelength shift of the resonant peak due to a change of the phase matching condition. Actually, a 40 nm thick gold layer deposited on fiber tip strongly shields the external environment from the plasmonic mode excited within the hybrid crystal, resulting in a very weak sensitivity. In order to enhance the surface sensitivity of the final device, it is necessary to increase the light matter interaction with the external environment by properly tailoring the resonant mode field distribution. To this aim, we can exploit all the degrees of freedom exhibited by the hybrid nanostructures, *e.g.* the lattice design and layer thickness. On this basis, we fabricated and tested a different sample with a gold layer thickness of only 20 nm (keeping constant the other geometrical parameters *i.e.* a=900 nm, r=225 nm and t_{ZEP}=200 nm).

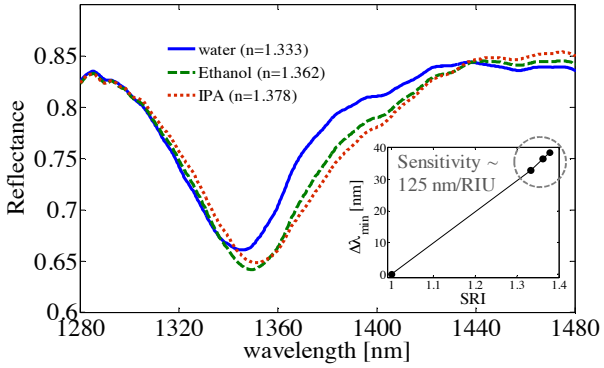

Figura 6: Reflectance spectra of a sample with a 20 nm thick gold thickness, immersed in water (solid blue), ethanol (dashed green) and isopropyl alcohol (dotted red); (inset) relative wavelength shifts of the reflection dips as a function of the SRI.

The new sample was then immersed in different liquid solutions such as water (n=1.333), ethanol (n=1.362) and isopropyl alcohol (n=1.378) and the reflectance spectra were measured. The experimental results are shown in Fig. 6, in which is evident the typical red-shift of the curves with increasing values of the surrounding refractive index (SRI). In particular, in the inset of Fig. 6 we plot the relative wavelength shifts of the reflection dips as a function of the SRI. The graph demonstrates a sensitivity of ~125 nm/RIU for detecting changes in the bulk refractive indices of different chemicals surrounding the fiber tip device.
We point out that no attempts at this stage have been made to optimize the platform performances. However, by exploiting the degrees of freedom offered when dealing with composite metallo-dielectric nanostructures, some optimization strategies for performance improvement are presently under investigation.

5. Acoustic Detection

As a further application, we also investigated the capability of our LSPR-based fiber tip device to detect acoustic waves. Indeed, by taking advantage from the typical low Young's modulus of the patterned ZEP, significant variations in the geometrical characteristics of the patterned dielectric slab are expected in response to an applied acoustic pressure wave, hence promoting a consequent shift of the resonant wavelength. It is important to stress, in this case, the fundamental and active role played by the dielectric structure to determine the acoustic performance of the final device.

As proof of principle, preliminary acoustic experiments have been carried out by testing the sample characterized by a period a=900 nm (whose reflectance spectrum is shown in Fig. 5). A schematic representation of the exploited setup is shown in Fig. 7. An acoustic tone of frequency f was generated by an audio speaker and then launched onto the fiber facet. The sample was interrogated by means of a tunable laser (Thotlabs – INTUN TL1300-B) locked at the wavelength corresponding to the steepest slope of the resonance right edge. The optical power reflected by the fiber tip is modulated as a consequence of the resonance shift induced by the applied acoustic wave, depending on the effective strain acting on the hybrid structure. The modulated reflected power is delivered through a circulator to a photo-detector whose electrical response is proportional to the intensity of the applied wave. Finally the electric signals are amplified and stored via a PC. Furthermore, in order to gather information about the actual incident acoustic pressure, a reference microphone was placed in close proximity of the fiber sensor.

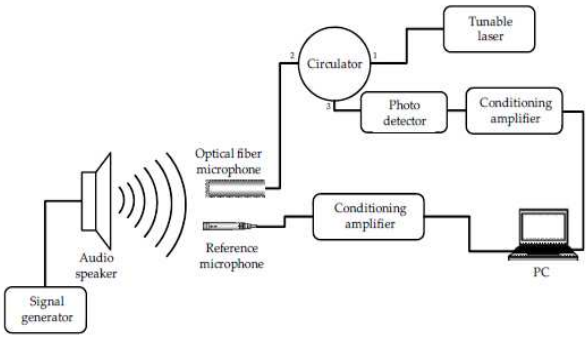

Figura 7: Experimental setup exploited for the acoustic measurements.

In Fig.8.a (upper curve) it is reported the typical time response of the hybrid crystal-based device to a 4kHz acoustic tone with duration of about 250ms. For comparison, the response of the reference microphone is also reported in Fig. 8.a (lower curve).

Data clearly reveal the capability of the fiber sensor to detect the incident acoustic wave along with the good agreement with the reference device. As evident, the electrical signal is delayed in respect with the optical counterpart, the delay being due to the slightly longer distance at which the reference microphone is located from the acoustic source. In addition it is worth noting that, although a relatively high noise level is visible in Fig. 8.a (the standard deviation of the sensor signal - σ_{noise} - in absence of acoustic wave is nearly 0.1V), that can be attributable to the instability of the utilized tunable laser, the response of the metallo-dielectric fiber facet device was found to be more than an order of magnitude higher than the noise level. In Fig. 8.b the FFT spectra obtained by the same optical fiber microphone in response to three acoustic tone with different frequencies (4, 4.5 and 5 kHz) are also shown.

The ability of the optical device to discriminate among them is clearly evident. The different amplitude of the sample response to the three tones is due to the different amplification the optical signal undergoes during the electronic processing. Once again, we emphasize that the above results are only preliminary and no efforts have been made to optimize the performance of the final device. Hence, also in this case, further optimization margins exist through varying the crystal design and metallic layer thickness in order to maximize the dependence of the resonant wavelength on the geometric features of the patterned polymer.

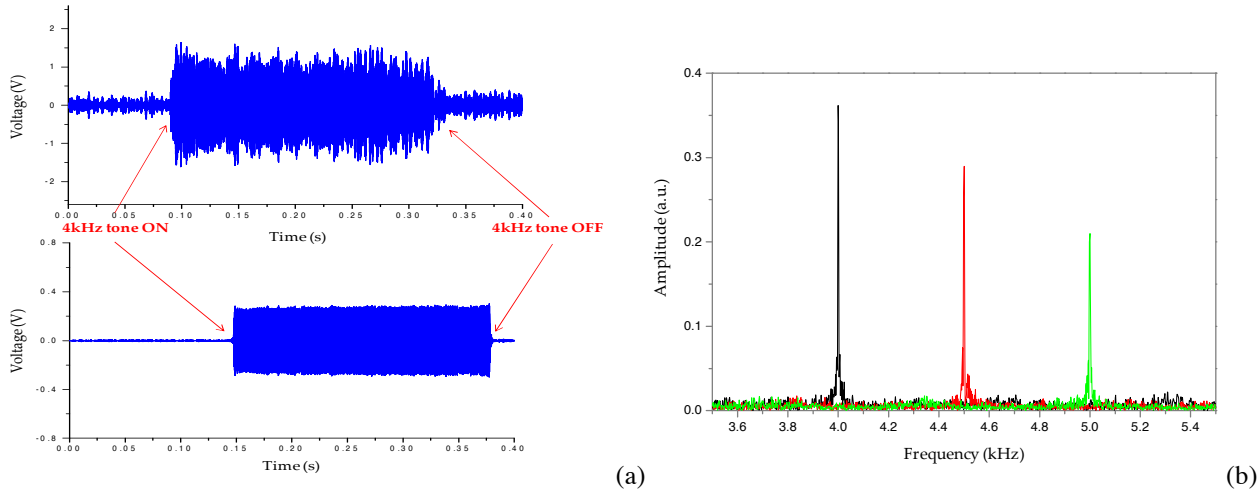

(a) (b)

Figure 8: (a)Typical time responses of the hybrid metallo-dielectric fiber tip device (top) and reference microphone (bottom) to a 4KHz acoustic pressure pulse with duration 250 ms. (b) FFT spectra obtained by the optical fiber sensor in response to three acoustic tones with increasing frequency (4, 4.5 and 5 kHz)

6. Conclusions

To summarize, we report the design, fabrication and characterization of a 2D hybrid metallo-dielectric nanostructure supporting LSPR, directly realized on the end face of a SMF. In particular, using a customization of the standard spin coating method, we were able to deposit ZEP overlays onto the cleaved end of SMF, with controllable thickness and flat surface areas nearly 50 μm around the fiber core. Moreover, via measurements and numerical simulations, we observed the presence of a resonant dip in the reflectance spectrum due to the phase matching condition between the scattered waves and the modes supported by the hybrid metallo-dielectric PC structure. As reported, the resonance dip can be easily tuned by acting also on the geometrical parameters of the lattice. Moreover, with a view towards possible applications, we first present some preliminary results demonstrating the capability of our platform to be used for label free chemical and biological applications with a bulk sensitivity of about 125 nm/RIU. Finally, we also show the surprising capability of the proposed platform to detect acoustic waves taking advantage from the low elastic modulus of the patterned polymer. Overall, our results demonstrate how the definition of viable "Lab on Fiber" technologies would open up the realization of technological worlds completely integrated in a single optical fiber to be exploited in many application fields.

References

[1] Joannopoulos, J. D.; Johnson S. G.; Meade R. D.; Winn J. N. Photonic Crystals: Molding the Flow of Light, second edition; Princeton University Press: New Jersey, 2008.

[2] Fan, S.; Joannopoulos, J. D. Analysis of Guided Resonances in Photonic Crystal Slabs. Phys. Rev. B 2002, 65, 235112, 1-8.

[3] Fujita, M.; Takahashi, S.; Tanaka, Y.; Asano, T.; Noda, S. Simultaneous Inhibition and Redistribution of Spontaneous Light Emission in Photonic Crystals. Science 2005, 308, 1296-1298.

[4] Ricciardi, A.; Pisco, M.; Gallina, I.; Campopiano, S.; Galdi, V.; O'Faolain, L.; Krauss, T. F.; Cusano, A. Experimental evidence of guided resonances in photonic crystals with aperiodically-ordered supercells. Opt. Lett. 2010, 35, 3946-3948.

[5] Ricciardi, A.; Pisco, M; Cutolo, A.; Cusano, A; O'Faolain, L.; Krauss, T. F.; Castaldi, G.; Galdi, V. Evidence of Guided Resonances in Photonic Quasicrystal slabs. Phys. Rev. B 2011, 84, 085135 (4 pages).

[6] Halas, N. J. Plasmonics: An Emerging Field Fostered by Nano Letters. Nano Lett. 2010, 10, 3816-3822.

[7] Lassiter, J. B.; Sobhani, H.; Fan, J. A.; Kundu, J.; Capasso, F.; Nordlander, P.; Halas, N. J. Fano Resonances in Plasmonic Nanoclusters: Geometrical and Chemical Tunability. Nano Lett. 2010, 10, 3184-3189.

[8] Schuller, J.A.; Barnard, E. S.; Cai, W.; Jun, Y.C.; White, J.S.; Brongersma M.L. Plasmonics for extreme light concentration and manipulation. Nature Materials 2010, 9, 193-204.

[9] Gopinath, A.; Boriskina, S. V.; Feng, N.-N.; Reinhard, B. M.; Dal Negro, L. Photonic-plasmonic scattering resonances in deterministic aperiodic structures. Nano Lett. 2008, 8, 2423-2431.

[10] Maier, S. A; Atwater, H. A. Plasmonics: Localization and Guiding of Electromagnetic Energy in Metal/Dielectric Structures. J. Appl. Phys. 2005, 98, 011101 (10 pages).

[11] Yao, J.; Le, A.-P.; Gray, S. K.; Moore, J. S.; Rogers, J. A.; Nuzzo, R. G. Functional Nanostructured Plasmonic Materials. Advanced Materials 2010, 22, 1102-1110.

[12] Yu, X.; Shi, L.; Han, D.; Zi, J.; Paul V. Braun, P. V. High quality factor metallo dielectric hybrid plasmonic–photonic crystals. Adv. Funct. Mater. 2010, 20, 1910-1916.

[13] Romanov, S. G.; Korovin, A. V.; Regensburger, A.; Peschel, U. Hybrid Colloidal Plasmonic-Photonic Crystals. Adv. Mater. 2011, 23, 2515-2533.

[14] Smythe, E. J.; Dickey, M. D.; Whitesides, G.M.; Capasso, F. A Technique to Transfer Metallic Nanoscale Patterns to Small and Nonplanar Surfaces. ACS Nano 2009, 3, 59-65.

[15] Lipomi, D. J.; Martinez, R. V.; Kats, M. A.; Kang, S. H.; Kim, P.; Aizenberg, J; Capasso, F.; Whitesides, G. M. Patterning the Tips of Optical Fibers with Metallic Nanostructures Using Nanoskiving. Nano Lett. 2011, 11(2), 632-636.

[16] Di Falco, A.; Ploschner, M.; Krauss, T.F. Flexible Metamaterials at Visible Wavelengths. New J. Phys. 2010, 12, 113006 (7 pages).

[17] Jung, I. W.; Park, B.; Provine, J.; Howe, R. T.; Solgaard, O. Highly Sensitive Monolithic Silicon Photonic Crystal Fiber Tip Sensor for Simultaneous Measurement of Refractive Index and Temperature. J. Light. Technol. 2011, 29, 1367-1374.

[18] Scheerlinck, S.; Dubruel, P.; Bienstman, P.; Schacht, E.; Van Thourhout, D.; Baets, R. Metal Grating Patterning on Fiber Facets by UV-Based Nano Imprint and Transfer Lithography Using Optical Alignment. J. Light. Technol. 2009, 27, 1415-1420.

[19] Dhawan, A.; Gerhold, M.; Muth, J. Plasmonic Structures based on Subwavelength Apertures for Chemical and Biological Sensing Applications. IEEE Sens. J. 2008, 8, 942-950.

[20] Lin Y.; Zou Y.; Lindquist R. G. A Reflection-based Localized Surface Plasmon Resonance Fiber-Optic Probe for Biochemical Sensing. Biomed Opt Exp. 2011, 2, 478-484.

[21] Rosenblatt, D.; Sharon, A.; Friesem, A. A. Resonant Grating Waveguide Structures. IEEE J. Quantum Electron. 1997, 33, 2038-2059.

[22] Ricciardi A. et al., “Guided resonances in photonic quasicrystals”, Optics Express, vol. 17, pp. 6335-6346, 2009.

Dispersion engineering for photonic crystal based nanophotonic devices

Maxence Hofman[1], Xavier Mélique[1], Didier Lippens[1], Olivier Vanbésien[1*], Geoffroy Scherrer[2], Benoit Cluzel[2], Frédérique de Fornel[2], Muamer Kadic[3], Wojciech Śmigaj[3-4], Sébastien Guenneau[3], and Boris Gralak[3]

[1]IEMN, UMR CNRS 8520, Université Lille 1, BP 60069, 59652 Villeneuve d'Ascq Cedex, France
[2] OCP-ICB, UMR CNRS 6303, 9 Avenue A. Savary, BP 47870, 21078 Dijon, France
[3] Institut Fresnel, CNRS Université Aix-Marseille, Campus de St Jérôme, 13397 Marseille Cedex 20, France
[4]currently at Dpt. of Mathematics, UCL, London, UK, and Faculty of Physics, Adam Mickiewicz University, Poznań, Poland
*corresponding author, E-mail: Olivier.Vanbesien@iemn.univ-lille1.fr

Abstract

In this paper, we report the design, the fabrication and the near field optical microscopy of Negative Index Material (NIM) flat lenses. They were fabricated on the basis of an InP-based photonic crystal technological platform and show the possibility of subwavelength focusing by NIM. Particular attention is paid to the analysis of SNOM images using three-dimensional simulations. Finally, preliminary results for a GRadient INdex (GRIN) slab and for a two-dimensional cloaking device are presented.

1. Introduction

All-dielectric artificial propagation media – including photonic crystals (PCs), metamaterials and transformation optics based devices – appear as potential candidates to achieve advanced functionalities in the field of integrated nanophotonics at infrared and visible wavelengths [1-5]. The common feature of all these approaches is their dispersion engineering – and resulting ultrarefraction phenomena – which occur at various wavelength scales depending on the targeted applications. In this paper, three paths to control light propagation and focusing at infrared (1.55 μm) are explored. They result from a close collaboration between Institut Fresnel/Marseille and IEMN/Lille for design (home-made code for device design and commercial FDTD software for two and three-dimensional virtual prototyping), IEMN/Lille for fabrication (single mask original process using a negative resist) and ICB/Dijon for characterization (scanning near field optical microscopy – SNOM – set-up).

First, an optimized PC-based flat lens optimized in resolution (~ 0.8λ) and transmission efficiency (~ 30 %) is presented. It operates in the negative refraction regime (n = -1) [6-8] with a patterning scale (a/λ) of 0.3 (a denotes the crystal period). The double focusing of a quasi-point source was unambiguously experimentally assessed and validated by three dimensional (3D) simulations. Second, the focusing of a plane wave was studied by means of so-called GRIN (gradient index) lenses [9]. Square lattices of hole and pillar arrays were designed, operating for complementary optical field polarization, in the long wavelength regime (a/λ < 0.1). Index variation in the direction transverse to the direction of propagation is obtained by varying the hole or pillar diameters while the lattice period is kept constant. Here again, the focusing is clearly evidenced by means of SNOM measurements. Then, in a prospective manner, partial invisibility was searched by means of two dimensional (2D) transformation optics concepts to go beyond initial proposals based on mixed pass- and stop- band photonic crystals [10]. Here, the idea consists in decreasing the scattering by an object deposited on a reflector [11]. A preliminary feasibility study of such a device will be initiated.

The plan of the paper is as follows: Section 2 is devoted to fundamental physical principles which allow us to exploit ultra-refraction phenomena using local and bulk dispersion engineering in patterned dielectrics. In section 3, the InP-based technological platform used to fabricate hole and pillar arrays at nanometer scale are presented. In Section 4, experimental results by means of near field optical microscopy are shown and analyzed notably by means of 3D FDTD simulations. Section 4 contains concluding remarks and prospects towards cloaking devices or integration of flat photonic lenses in imaging systems are evoked.

2. Dispersion engineering in all-dielectric propagation media

To perform dispersion engineering in all-dielectric artificial materials, two main research axes are privileged, depending on the structuring scale of the matter (a) versus operating wavelength (λ). For a/λ ratios above 0.3, we face the domain of PCs, intrinsically periodic, and whose ultra-refraction phenomena are extracted from band-structure calculations. Generally, it consists in a "bulk" dispersion engineering to reach one particular operating mode. One of the most well-known examples of this class of devices is undoubtedly the "flat lens", detailed in section 2.1. For

lower a/λ ratios, typically around 0.1, we reach the "metamaterial" regime with no requisite of periodicity and, using the tools of transformation optics, localized dispersion engineering becomes possible to develop GRIN (gradient index) lenses, for example (see section 2.2) or more complex devices towards the goal of invisibility.

2.1. Photonic crystal based flat lens

Figure 1 summarizes the main characteristics of the 2D PC-based flat lens we designed. In brief, we use a 2D PC of air holes etched in a semiconductor matrix. The refractive index of the latter is set to 3.26 and corresponds to the one of the first propagating mode in an InP/InGaAsP/InP heterostructure aimed to operate in monomode regime around 1.5 μm. Lattice period and air filling factor are adjusted to reach an n = -1 regime (crossing between the light line and a pass-band with negative slope) in the second pass-band of the PC for a/λ = 0.31. The triangular arrangement of air holes is used to promote isotropic behavior in terms of refraction.

2D Photonic Crystal:		
Hole diameter	347 nm	
Lattice period	476 nm	
Filling factor	48 %	
Effective index (n_{eff})	3.26	
Anti-reflecting coatings (ARC):		
Triangle height (h)	329 nm	
Triangle base (b)	238 nm	
Semiconductor thickness in front of a hole (t)	33 nm	
Flat lens:		
Number of rows	13	
Thickness :		
- Without ARC	5.36 µm	
- With ARC	6 µm	
Resolution at 1.55 µm	640 nm (0.41λ)	
Focusing lengths		
- d_1	2.24 µm	
- d_2	2.35 µm	

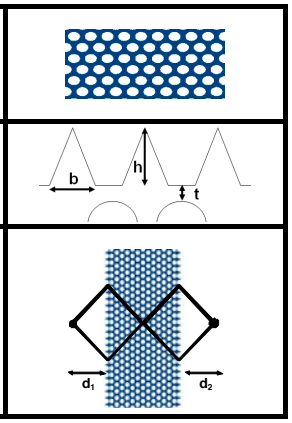

Figure 1: Dimensioning and expected performances of the 2D PC based flat lens at 1.55 μm.

As it is commonly admitted in the field of PCs, an n = -1 index value is not sufficient to guarantee the fabrication of a performing flat lens. Indeed, in terms of surface impedance, such an n value is not synonymous of z = 1, the necessary condition to match that of the adjacent air. Moreover, extraction of effective permittivity (ε) and permeability (μ) which can be performed (with caution for such a/λ values) on such crystals shows that not only ε and μ are far from unity but they also vary strongly with the incidence angle of the wave impinging on the crystal. To overcome this limitation and to obtain high light transmission efficiency through the lens, anti-reflection coatings (ARCs) have been superimposed on both sides of the lens. The main concern was to ensure matching for the largest incidence angle range possible. 2D simulations of PCs covered by ARCs composed of triangles situated between two successive holes of the PC (see Figure 1, middle row) yielded transmission levels higher than 80% for incidence angle as high as 60°.

As shown in Figure 2, which illustrates the double focusing obtained for an incident point source with a flat lens, promising performances are obtained with a very low level of reflection at the input of the lens and a well-defined and bright spot on the right hand side whose position fits merely the expected value using geometrical optics. A slight difference between d_1 and d_2 (theoretically perfectly equal) that is observed is probably due to the presence of the ARCs whose thicknesses are not negligible compared to the lens thickness (10 %). The estimated resolution reaches 0.41λ, which is lower than the Rayleigh limit, bringing this lens in the field of "superlenses" but it remains higher than the structuring scale as it can be expected (far from the concept of "perfect lens" that only uses effective constitutive parameters but ignores the real patterning scale).

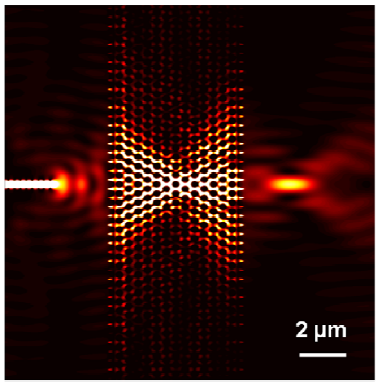

Figure 2: 2D FDTD simulation of the PC based flat lens described in Figure 1.

2.2. GRIN lenses

The double focusing of a point source using a flat lens obtained by negative refraction is not the sole operating mode which could be interesting to reach using flat lenses in the field of nanophotonics. Even if the previous lens possesses interesting properties in terms of applications, notably the fact that it behaves very differently versus the nature of the incident wave (fully transparent in theory for a plane wave and focusing for a point source), the opposite behavior could also be of interest: the focusing of a plane wave. GRIN lenses, for GRadient INdex lenses, have been discovered a long time ago but very few have been engineered up to now for integrated nanophotonics. In this area, our ability to engineer dispersion using periodic or pseudo-periodic PCs or metamaterials can be helpful to design original and efficient lenses?

Figure 3 illustrates an approach that can be developed based by changing some of the parameters of a PC lattice to modify locally its effective refractive index. Let us mention here that what matters to control precisely the propagation of light in the device is the index difference between two regions of space. The origin of this gradient, i.e. whether it arises from a domain with positive or negative index values, is not fundamental. This explains why such gradients can be obtained for low a/λ values by exploiting for example the

slope of the first band of an all-dielectric PC, slope whose amplitude depends mainly on two coupled parameters: the lattice period and the filling factor. Moreover, as a local engineering is needed and has to operate for a particular incidence angle, most of the constraints developed in the previous paragraph concerning isotropy for impedance matching are here relaxed. Additional degrees of freedom will exist for the design of GRIN lens, such as the use of hole or pillar arrays, as shown in the following.

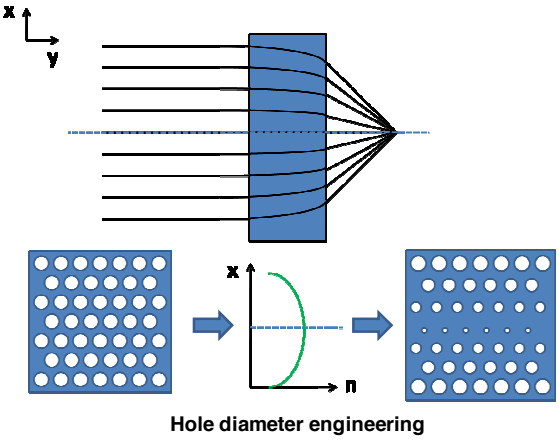

Figure 3: GRIN lens design by local hole diameter engineering of a 2D photonic crystal

Since, the effective index in the first band of a PC is a direct consequence of the filling factor, it appears natural, for a fixed lattice period, to diminish the air hole diameter (Figure 3) or to increase the semiconducting pillar diameter if one wants to increase the local index. Also, it can be shown that a parabolic variation of the index in the direction normal to the direction of the propagation makes optical rays bend towards a specific point of the real space.

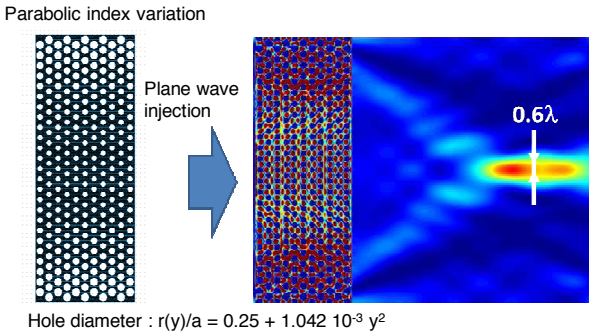

Figure 4: 2D FDTD simulation of the focusing of a plane wave by a PC based GRIN lens at 1.55 μm.

Figure 4 shows a 2D FDTD simulation of a GRIN lens based on a hole diameter engineering at 1.55 μm starting from a PC equivalent to the one described for the flat lens. A 0.6λ spot size is obtained. Here, given that geometrical changes are required, a crucial issue is to estimate the range of particle, hole or pillar, diameters within reach of our technological platform.

3. Technological platform

The all-dielectric prototypes developed in the following make use of a common one-mask technological process. It allows us to create the different building blocks including the devices and their environment: optical waveguide for injecting and/or collecting light as well as hole or pillar arrays for the active zones.

To build the 2D ½ photonic devices, we start from an InP-based heterostructure grown by molecular beam epitaxy: Superstrate InP (0.2 μm) / Core InGaAsP (0.5 μm) / InP (1.3 μm) / InP Substrate. Based on such a heterostructure, it is possible to confine light in a plane (in the direction of growth) and to use a unique propagation mode. This propagation can then be modulated in the other two spatial directions by a 2D-PC. The transverse propagation mode is characterized by an effective index which is found to be 3.26.

Fabrication of PCs for near-field and infrared operation, or even towards the visible range, relies on exploiting the most advanced micro- and nanotechnologies. These are electron lithography and deep etching, respectively. The first allows us to define the pattern and geometry according to the nanometric scale, while the second allows us to make holes as well as define pillars with a high aspect ratio and anisotropy. The technological process that we will describe briefly draws its originality from its simplicity, that is to say a unique mask allowing us to define large plots and/or guides (several dozen or hundreds of µm long) and the lattice of submicronic holes in a single step. This same mask is used also for etching. Figure 5(a) details the process developed while Figure 5(b) illustrates some results obtained at different stages of the process.

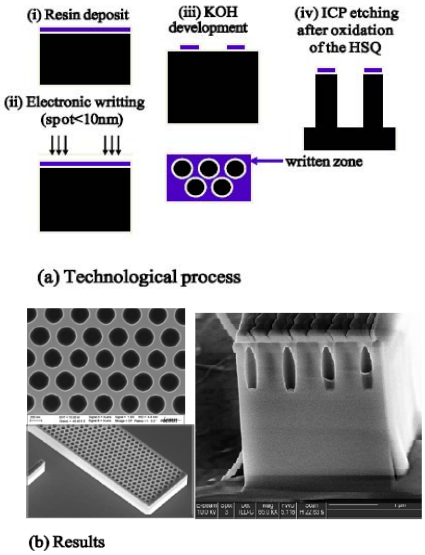

Figure 5: (a) One-mask technological process and (b) SEM view of fabricated devices.

The technological process relies on the use of a negative electronic resist, hydrogen silsesquioxane (HSQ), which is

well known for its resolution (~3–8 nm) and its capacity to resist plasma attacks after oxidation. Moreover, its negativity implies that only written zones will remain in place after development. This represents an undeniable advantage for our structures, insofar as the optical wave guides (narrow at 0.4–0.6 µm, but long at some mm) and the PC (with hole filling factor approaching 50%) can be simultaneously defined.

In short, a resist thickness of approximately 500 nm is deposited on the epitaxial layer. After looking for an optimal dose and fine correction of the proximity effects, a stage of electronic lithography allows us to describe the pattern to be created in the resist. This pattern integrates rectangular structures with a high length/width aspect ratio and discs that are submicronic in size but high in density. Non-exposed resist is dissolved with a KOH developer. The remaining resist is then oxidized and acquires a hardness that is sufficient to withstand etching of the semiconductor epitaxial layer. Etching is done by inductive coupled plasma, with a gas of the type $Cl_2/H_2/CH_4$, allowing us to obtain the desired anisotropic etching with the high aspect ratio after optimization. Width/diameter ratios for the holes of approximately five to 10 can be obtained, allowing us to reach the 2D½ regime we are looking for. Figure 5(b) illustrates some results obtained showing the large regularity obtained for the lattice associated with the perfectly defined etching flank for the lens. The same approach is used to fabricate the ARCs on both sides of the lens or for the fabrication of pillar arrays. In this last case, special attention is paid to the deep etching since its dynamic differs (species evacuation) compared to the hole formation.

4. Experiments and Analysis

4.1. SNOM measurements

Figure 6 shows SNOM (scanning near filed optical microscope) measurements which illustrates the double focusing effect with an n = -1 PC based flat lenses at λ = 1.55 μm. In the first case (1), which corresponds to a bare 21-rows lens, a focused spot with a low intensity, approximately $1/100^e$ of the incident power, is registered at the expected position behind the lens (about 4.3 μm / half the lens thickness for an equivalent source-lens distance). The associated resolution, taking into account the finite dimension of the probe is estimated to 0.8λ. The second set of experiments (2) tests the behavior of 13-row lenses covered by ARCs. Several different ARC designs were used to test the robustness of our theoretical approach to technological constraints. In all cases, the transmission light efficiency is significantly increased compared to the bare lens to reach a maximum estimated about 30 %. In this last case, resolution is close to λ, probably due to a set of PCs with higher propagation losses due to less deep holes obtained during the etching process.

Such a result is however extremely encouraging, even if from the 2D design process to the 3D prototype reality, many parameters can cause a slight shift of the optimal operating wavelength around the targeted value (around a few per cent). Moreover, the ARC design which tolerates a large range of incidence angles remains resonant in wavelength and is also designed for a precise wavelength. Here also, small deviations from the initial mask design to the fabricated lens interface can be obtained. This quite general issue of 3D reality versus 2D design will be addressed in the next paragraph.

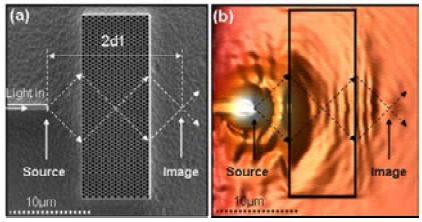

(1) 21-row n = -1 flat lens without ARCs / λ = 1.55 μm

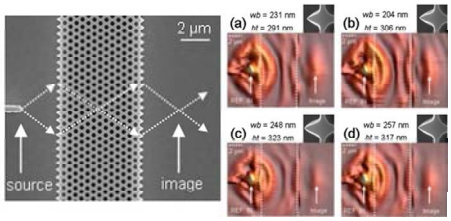

(2) 13-row n = -1 flat lens with ARCs / λ = 1.55 μm

Figure 6: Double focusing experiments (using SNOM set-up) using PC based n = -1 flat lenses at 1.55 μm

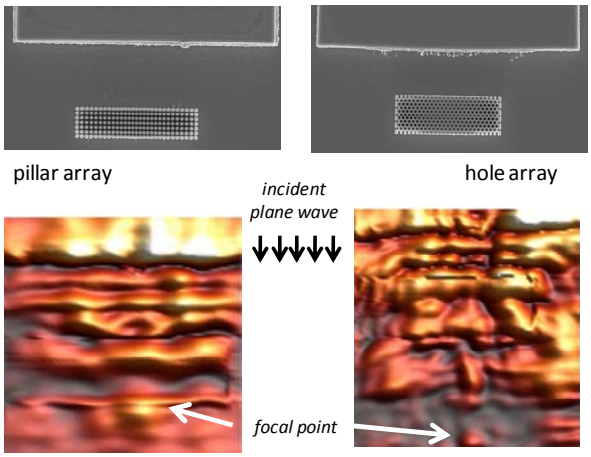

Figure 7: Focusing of a plane wave by a pillar-based (left side) or hole-based (right side) GRIN lens at 1.55 μm

Figure 7 illustrates the preliminary results obtained in the case of hole-based or pillar-based GRIN lenses also at 1.55 μm. As a major difference compared to flat focusing lenses, one can observe the injection region which consists of a large (three times the lens dimension) aperture cut waveguide to generate a quasi-plane wave. In practice we

start from a classical optical waveguide, as before, but instead of keeping it at a subwavelength dimension up to the vicinity of the lens, this "horn" waveguide is progressively widened, over a distance much longer than the guided wavelength to avoid extra losses. As seen on the SNOM images, it allows us to define a planar wavefront as expected. For the two lenses, a focus spot is obtained at the output of the lens at the position anticipated by the FDTD calculations (0.7λ). In the hole case, the width of this spot is about 0.8λ (taking into account the probe finite dimension), close to the expected theoretical value. In the pillar case, a larger spot is unexpectedly obtained which remains to be fully interpreted.

4.2. Three dimensional analysis

In the field of nanophotonics making use of PCs and/or metamaterials to exploit abnormal refraction properties, most of the designing procedures are carried on 2D models. By essence, reality is intrinsically 3D and so are the fabricated prototypes. The analysis of measurements becomes thus sometimes difficult when exclusively compared to 2D simulations. Erroneous conclusions can even be drawn from a careful study of experimental images.

To avoid such misguided interpretations, 3D calculations are required even if they may be impractical for optimization purposes due to the calculation time and memory space requirements needed to obtain sufficient precision. However, for reverse engineering, a post-2D numerical image reconstruction is particularly information-rich. Figure 8 illustrates such an approach dedicated to the double focusing experiment by an n = -1 flat lens evaluated using SNOM images.

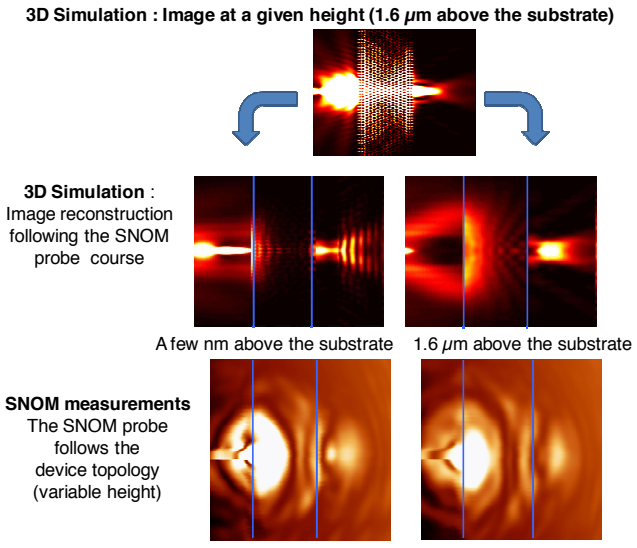

Figure 8: Analysis of SNOM images using 3D FDTD simulation of the double focusing experiment by a flat lens

In practice, a SNOM image is formed by recording the optical power coupled to a probe which follows the device topology at a given distance, and thus at a variable absolute altitude. Looking at Figure 5(b), this means that the reconstructed image is composed of information collected at different heights and does not correspond to the case of a 2D simulation which presupposes invariance in the transverse direction. To obtain simulated images as close as possible to the experimental ones, shown at the bottom of Figure 8, we start from a full 3D FDTD device simulation (taking into account the epitaxial sequence in the vertical direction, the input waveguide, the real lens height and finite depth of holes, ARCs, …) and extract the calculated optical field using the topology map given by the SNOM. Such a procedure has been applied for two distinct SNOM probe courses: a few nanometers (left side of figure 8) and 1.6 μm (right side of figure 8) above the surface. Behind the lens this latter distance corresponds to the longitudinal plane of the quantum well of the confining heterostructure and thus to the plane where maximum optical power is expected.

Strong similarities between SNOM and such reconstructed images can be evidenced. One of the main added values of the approach concerns the spot size estimation. It is very tempting using SNOM images to claim a subwavelength resolution using the image corresponding to a probe course close to the substrate (left side of Figure 8). However in this case, the spot position is too close from the output interface of the lens compared to the targeted operating regime, and do not respect Snell's law of refraction for n = -1. On the contrary, the right hand side images, calculated in the quantum well plane of the confining heterostructure, give larger spots, not subwavelength (between 0.8λ and λ), but correctly positioned. This shows the extreme difficulty of interpreting SNOM images directly, especially when devices have rough surfaces and a probe which follows their topology at a fixed distance.

Despite these necessary precautions, our 3D analysis has unambiguously confirmed that the measured phenomena were those expected and optimized using a 2D approach. Excellent performances have been obtained both for flat lenses and GRIN lenses at optical wavelengths. However, the 2D picture of a double focusing using a PC based flat lens or plane wave focusing using a GRIN lens is often too simple to evaluate resolutions and a fully 3D approach is required to predict the real performance of such devices for applications in future integrated photonic circuits.

5. Concluding remarks and prospects

At this stage, we have shown the ability of full dielectric periodic or pseudo-periodic 2D½ crystals to reach interesting performances as focusing lenses (for point sources or plane waves) using bulk or localized dispersion engineering. We have also seen that, on a practical side, both hole and pillar based approaches for patterning a semiconducting heterostructure can be employed.

If it is commonly accepted now that PC based devices will not reach outstanding performances in terms of subwavelength resolution for example due to their

structuring scale compared to the promises of metamaterials, they are undoubtedly the most mature systems for applications at optical wavelengths. To deepen our knowledge, the next development stages of such devices can be envisaged in two main directions.

First, can the field of transformation optics rich of proposals for manipulating light at ultra-short scale be explored using all-dielectric structures [12-13]? One possible avenue would be to design geometries mixing holes and pillars. As shown in Figure 9, our technological "single mask" process can fully meet these objectives. In this case, the main practical challenge is to evaluate the ultimate limits in dimensions for pillar or hole diameters and heights we are able to fabricate to fulfill the stringent precision of dispersion required by the theory of transformation optics to perform cloaking or routing functions at optical wavelengths.

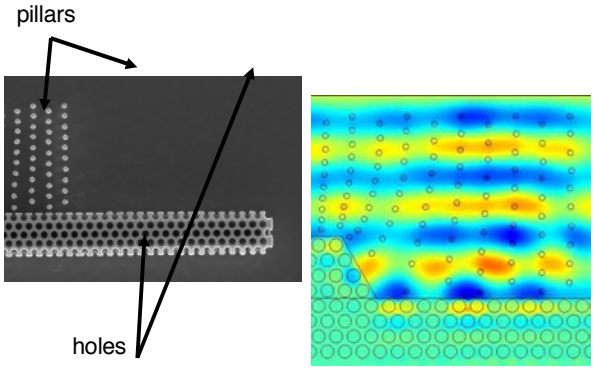

Figure 9: Towards transformation optics based devices: combination of holes and pillars in a single technological process for a metamaterial which mimics a flat mirror.

The second research axis consists in understanding how the fabricated lenses could be of use for more complex applications for detection and/or imaging [14]. Preliminary results for infrared detection and imaging, inspired by tomography in reflection, including an n = - 1 flat lens have been proposed [15]. These works are currently pursued with GRIN lenses in a transmissive approach.

In all cases, it is believed that the performances reached by all-dielectric devices at optical wavelengths open right now the way for future innovative applications for integrated nanophotonics.

Acknowledgements

This work was founded by Agence Nationale de la Recherche under contract PNANO - FANI.

References

[1] J.B. Pendry, Negative refraction makes a perfect lens, *Phys Rev Lett*; 85: 3966-3969, 2000

[2] J.B. Pendry, D. Schurig D, D.R. Smith, Controlling electromagnetic fields, *Science*, 312: 1780-82, 2006

[3] V.M. Shalaev, W. Cai, U.K. Chettiar, H.K.Yuan, A.K. Sarychev, V.P. Drachev, A.V. Kildishev, Negative index of refraction in optical metamaterials, *Optics Letters,* 30: 3356-58, 2005

[4] H. Kosaka, T. Kawashima, A. Tomita, M. Notomi, T. Tamamura, T. Sato, S. Kawakami, Superprism phenomena in photonic crystals, *Physical Review B* 58 :10096, 1998

[5] N. Engheta, R.W. Ziolkowski, A positive future for double negative metamaterials, *IEEE Transactions on MTT* 53: 1535-56, 2005

[6] N. Fabre, L. Lalouat, B. Cluzel, X. Mélique, D. Lippens, F. de Fornel, O. Vanbésien, Optical near-field microscopy of light focusing through a photonic crystal flat lens, *Phys. Rev. Lett.*, 101: 073901, 2008.

[7] W. Smigaj, B. Gralak, R. Pierre, G. Tayeb, Antireflection gratings for a photonic crystal flat lens, *Optics Letters*, 34: 3532–3534, 2009.

[8] G. Scherrer, M. Hofman, W. Smigaj, B. Gralak, X. Mélique, O. Vanbésien, D. Lippens, C. Dumas, B. Cluzel, F. de Fornel, Interface engineering for improved light transmission through photonic crystal lenses, *Appl. Phys. Lett.*, 97: 071119, 2010

[9] Q. Wu, J.M. Gibbons, W. Park, Graded negative index lens by photonic crystals, *Optics express,* 16: 16941, 2008

[10] O. Vanbésien, N. Fabre, X. Mélique, D. Lippens, Photonic crystal based cloaking device at optical wavelengths, *Applied Optics*, 47:1358-1362, 2008.

[11] J. Renger, M. Kadic, G. Dupont, S.S. Acimovic, S. Guenneau, R. Quidant, S. Enoch, Hidden progress: broadband plasmonic invisibility, *Optics Express*, 18: 15757-15768, 2010

[12] D. Schurig, J.J. Mock, B.J. Justice, S.A. Cummer, J.B. Pendry, A.F. Starr, D.R. Smith, Metamaterial electromagnetic cloak at microwave frequencies. *Science,* 314: 977-80, 2006

[13] E. Centeno, D. Cassagne, Graded Photonic crystals. *Optics Letters,* 30: 2278-81, 2005

[14] G. Wang, J. Fang, X.T. Dong, Refocusing of backscattered microwaves in target detection by using LHM flat lens, *Optics Express*, 15: 3312, 2007

[15] M. Hofman, D. Lippens, O. Vanbésien, Image reconstruction using a photonic crystal based flat lens operating at 1.55 μm, *Applied Optics*, 49:5806-5813, 2010

Rigorous Analysis of Line Source Radiation in Photonic Crystals

Vakhtang Jandieri1[1]*, Kiyotoshi Yasumoto[2]

[1]School of Electronics and Computer Science, Kyungpook National University, Republic of Korea
[2]College of Information Science and Technology, Nanjing Forestry University, China
Professor Emeritus of Kyushu University, Fukuoka, Japan
*corresponding author, E-mail: jandieri@ee.knu.ac.kr

Abstract

A novel formulation of radiation from a localized line source placed in two-dimensional photonic crystals consisting of layered periodic arrays of parallel circular cylinders is presented. The method employs the spectral domain approach. The spectral response of the photonic crystals to the line source excitation is calculated using the lattice sums, the T-matrix of a circular cylinder and the generalized reflection and transmission matrices of the layered system. The far-zone radiated field is obtained using the conventional asymptotic method to the spectral response. The radiation patterns of the localized line source sandwiched by two photonic crystals are numerically studied. It is shown that the directivity is uniquely characterized by the transmission windows of the photonic crystals in the frequency and angular spectral domains and the Fabry-Perot resonance condition for the radiated field in the space surrounding the source.

1. Introduction

Photonic crystals are periodic dielectric or metallic structures [1], in which the propagation of electromagnetic waves in particular direction is prohibited or allowed within a certain frequency range. Because of these distinct features, the photonic crystals have received a growing attention for their applications to antennas and waveguide components in microwave and millimetre wave regions. For the antenna applications, the electromagnetic crystals have been used as substrates [2] and superstrates [3] for the radiating elements. The electromagnetic radiation from antennas coupled to photonic crystals has been extensively investigated using the array scanning method [4] combined with the method of moments, the phased array method [5] combined with the plane-wave expansion method, the finite difference time domain method [6]. These studies have reported that the radiation patterns of antennas are remarkably improved through the interaction with photonic crystals.

In this paper, we propose a novel approach to formulate the radiation from a line source placed in photonic crystals consisting of layered periodic arrays of parallel circular cylinders. The method employs the spectral domain approach. The line source is transformed into an infinite periodic array of linearly phased line sources in the spectral domain. For each of spectral components, the periodic line sources excite a set of weighted space-harmonic fields. The spectral response of the photonic crystal to the line source excitation is calculated using the lattice sums [7], the T-matrix of a circular cylinder, and the generalized reflection and transmission matrices of the layered system [8]. The radiated field is obtained by the finite integral of the spectral response. The directivity and beam shaping of radiation related to the far-zone fields can be calculated by the conventional asymptotic method without performing the integration.

In this manuscript, we give the physical insight into why the radiation patterns are modified in the presence of the photonic crystals. For this purpose, the lattice sums and generalized reflection matrix technique in the spectral domain is useful because the radiated far field is obtained in closed-form using the generalized reflection and transmission matrices of photonic crystals. It is shown that the directivity of radiation is uniquely determined by the location of transmission windows of the photonic crystal in the frequency and angular spectral domains and the Fabry-Perot resonance condition for the radiated field in the space surrounding the source. Numerical examples demonstrate the validity of the theoretical analysis.

2. Formulation of the Problem

We consider a two-dimensional model of a localized source coupled to a photonic crystal as shown in Fig. 1. An impressed electric line source with $\boldsymbol{J}(x,y) = \delta(x)\delta(y)\hat{\boldsymbol{z}}$ is located at the origin of x-y coordinate system. The line source is sandwiched in between a photonic crystal and a dielectric slab backed by a perfect conductor with separation distances t_1 and t_2, respectively. The background medium is a free space. The crystal consists of N-layered periodic arrays of circular cylinders, which are infinitely long in the z direction and periodically spaced with a common distance h in the x direction. The cylindrical elements should be same along each layer of the arrays but those in different layers need not be necessarily the same in material properties and dimensions. Figure 1 shows a typical configuration of the square lattice, where the identical arrays of cylinders with the same radius a and relative permittivity ε are layered

with an equal spacing in the y direction. The relative permittivity and thickness of the dielectric slab are ε_s and d, respectively.

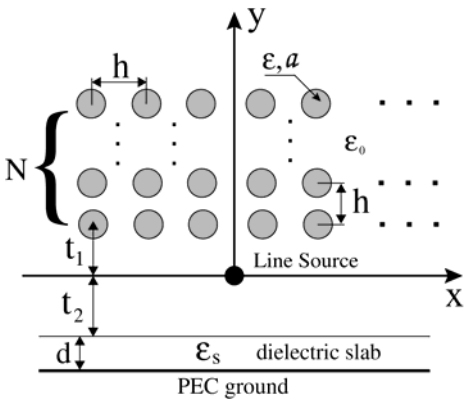

Fig.1. A line source sandwiched in between 2D photonic crystal and a dielectric slab backed by a perfect conductor.

Since the system concerned is not periodic, the conventional Floquet mode expansion method cannot be directly used. Instead, let us consider the expression of the localized line source in terms of an infinite periodic array of linearly phased line sources in the spectral domain. Using the identities:

$$\delta(x)=\frac{1}{2\pi}\int_{-\infty}^{\infty} e^{i\xi x}\,d\xi=\frac{1}{2\pi}\sum_{\ell=-\infty}^{\infty} e^{i2\ell\pi x/h}\int_{-\pi/h}^{\pi/h} e^{i\xi x}\,d\xi \tag{1}$$

$$\sum_{\ell=-\infty}^{\infty}\delta(x-\ell h)=\frac{1}{h}\sum_{\ell=-\infty}^{\infty} e^{i2\ell\pi x/h}, \tag{2}$$

we have the following expression:

$$\delta(x)=\frac{h}{2\pi}\int_{-\pi/h}^{\pi/h}\left[\sum_{\ell=-\infty}^{\infty}\delta(x-\ell h)e^{i\ell h\xi}\right]d\xi. \tag{3}$$

It follows that if $E_{z,P}(x,y,\xi)$ is the electric field radiated from a periodic array of line sources defined as:

$$J_P(x,y,\xi)=\sum_{\ell=-\infty}^{\infty}\delta(y)\delta(x-\ell h)e^{i\ell h\xi}, \tag{4}$$

the radiated field $E_z(x,y)$ from a localized line source:

$$J_0(x,y)=\delta(x)\delta(y) \tag{5}$$

is given by:

$$E_z(x,y)=\frac{h}{2\pi}\int_{-\pi/h}^{\pi/h}E_{z,P}(x,y,\xi)\,d\xi. \tag{6}$$

Thus the problem is reduced to calculate the electric field $E_{z,P}(x,y,\xi)$ radiated from the infinite periodic array of linearly phased line sources $J_P(x,y,\xi)$.

Using the Fourier integral representation of the Hankel function, the primary field $E_z^i(x,y,\xi)$ radiated from the periodic line sources $J_P(x,y,\xi)$ defined by (4) is expressed as follows:

$$E_z^i(x,y,\xi)=\sum_{\ell=-\infty}^{\infty}e^{i\ell h\xi}H_0^{(1)}(k_0\rho_\ell)$$

$$=\frac{2}{h}\begin{cases}\displaystyle\sum_{\ell=-\infty}^{\infty}\frac{e^{i[\xi_\ell x+\kappa_\ell(\xi)y]}}{\kappa_\ell(\xi)} & (y>0)\\ \displaystyle\sum_{\ell=-\infty}^{\infty}\frac{e^{i[\xi_\ell x-\kappa_\ell(\xi)y]}}{\kappa_\ell(\xi)} & (y<0)\end{cases} \tag{7}$$

with

$$\xi_\ell=\xi+\frac{2\ell\pi}{h},\quad \kappa_\ell(\xi)=\sqrt{k_0^2-\xi_\ell^2} \tag{8}$$

where $k_0=2\pi/\lambda_0$, $H_0^{(1)}$ is the zero-th order Hankel function of the first kind and ρ_ℓ is the local coordinate with the origin at the ℓ-th line source. Since the primary field is expressed as a superposition of the Floquet mode, the scattered fields can be calculated using the technique of the reflection and transmission matrices of layered periodic arrays for the incidence of plane waves. The periodic line sources located on the plane $y=0$ excite a set of space harmonic fields up-going in the region $y>0$ and down-going in the region $y<0$. Employing $e^{i[\xi_\ell x\pm\kappa_\ell(\xi)y]}$ $(\ell=0,\pm1,\pm2,\cdots)$ as the basis for the field representation, the up-going and down-going space harmonics given by (7) are expressed in terms of the amplitude vector $\mathbf{s}(\xi)$ defined as follows:

$$\mathbf{s}(\xi)=\left[\frac{2}{h\kappa_\ell(\xi)}\right]. \tag{9}$$

Using the lattice sums and generalized reflection matrix technique, radiation problem is reduced to a reflection and transmission problem of electromagnetic crystal for space harmonic fields $\{e^{i[\xi_\ell x+\kappa_\ell(\xi)y]}\}$, where $\xi_l=\xi+2l\pi/h$ $(l=0,\pm1,\pm2,\cdots)$. ***The details of the calculation procedure***

are presented in [9,10]. Following the proposed analysis by the authors, the amplitude vector $\mathbf{c}(\xi)$ of space harmonic fields characterizing the transmitted field into the upper half-space is obtained as follows [9,10]:

$$\begin{aligned}\mathbf{c}(\xi) &= \overline{\overline{\mathbf{T}}}(\xi)\cdot\mathbf{s}(\xi) \\ &= \overline{\mathbf{F}}_1(\xi)\Big\{\mathbf{\Lambda}_1(\xi)+\mathbf{\Lambda}(\xi)\mathbf{D}^{-1}(\xi)\overline{\mathbf{R}}_2(\xi)\mathbf{\Lambda}_2(\xi)\times \\ &\quad [\mathbf{I}+\mathbf{\Lambda}_1(\xi)\overline{\mathbf{R}}_1(\xi)\mathbf{\Lambda}_1(\xi)]\Big\}\cdot\mathbf{s}(\xi)\end{aligned} \tag{10}$$

with

$$\mathbf{D}(\xi) = \mathbf{I} - \overline{\mathbf{R}}_2(\xi)\mathbf{\Lambda}(\xi)\overline{\mathbf{R}}_1(\xi)\mathbf{\Lambda}(\xi) \tag{11}$$

$$\mathbf{\Lambda}_1(\xi) = [\mathrm{e}^{i\kappa_l(\xi)t_1}\,\delta_{ll'}] \tag{12}$$

$$\mathbf{\Lambda}_2(\xi) = [\mathrm{e}^{i\kappa_l(\xi)t_2}\,\delta_{ll'}] \tag{13}$$

$$\mathbf{\Lambda}(\xi) = [\mathrm{e}^{i\kappa_l(\xi)t}\,\delta_{ll'}] \quad (t = t_1 + t_2), \tag{14}$$

where $\overline{\mathbf{R}}_1(\xi)$ and $\overline{\mathbf{F}}_1(\xi)$ are the generalized reflection and transmission matrices of the upper crystal, $\overline{\mathbf{R}}_2(\xi)$ is the reflection matrix of the dielectric slab backed by a perfect conductor, $\mathbf{s}(\xi)$ denotes the vector of the spectral amplitude of the line source excitation and $\delta_{ll'}$ is the Kronecker's delta. Applying the steepest-decent method to the transmitted field in the spectral domain expressed in terms of $\mathbf{c}(\xi)$, the far field of radiation is obtained as follows:

$$E_z(\rho,\varphi) = \frac{h}{\lambda_0}\sqrt{2\pi}\,\sin\varphi\exp\left(-i\frac{\pi}{4}\right)\frac{\exp(ik_0\rho)}{\sqrt{k_0\rho}}\times \sum_{l=-\infty}^{\infty}\overline{\overline{T}}_{0l}(\xi)s_l(\xi)\Big|_{\xi=k_0\cos\varphi}, \tag{15}$$

where $\overline{\overline{T}}_{0l}(\xi)$ represents the $(0, l)$-element of the matrix $\overline{\overline{\mathbf{T}}}$ defined in Eq.(10), $\rho = \sqrt{x^2+y^2}$ and φ is the observation angle measured from the x-axis. In what follows, we shall focus the present analysis on the case of $h/\lambda_0 < 1.0$, which is usually assumed in the antenna applications of photonic crystals. In this case, the principal nature of the far field given by Eq.(15) is governed by the fundamental space-harmonic component with $l = 0$ because all other harmonic components contained in $\overline{\overline{T}}_{0l}(\xi)$ become the non-propagating evanescent waves in the y direction. Approximating $\overline{\overline{T}}_{00}(k_0\cos\varphi)$ by the principal terms, we have:

$$\overline{\overline{T}}_{00}(k_0\cos\varphi) \approx \frac{\overline{F}_{1,00}(k_0,\varphi)}{D(k_0,\varphi)}K(k_0,\varphi)\,\mathrm{e}^{ik_0t_1\sin\varphi} \tag{16}$$

where

$$\begin{aligned}K(k_0,\varphi) &= D(k_0,\varphi) + \mathrm{e}^{i2k_0t_2\sin\varphi}\,\overline{R}_{2,00}(k_0,\varphi)\times \\ &\quad [1+\mathrm{e}^{i2k_0t_1\sin\varphi}\,\overline{R}_{1,00}(k_0,\varphi)]\end{aligned} \tag{17}$$

$$D(k_0,\varphi) = 1-\mathrm{e}^{i2k_0t\sin\varphi}\,\overline{R}_{1,00}(k_0,\varphi)\overline{R}_{2,00}(k_0,\varphi). \tag{18}$$

Since $s_0(k_0\cos\varphi)$ in Eq.(9) is proportional to $1/\sin\varphi$, it follows that the directivity of radiation is proportional to $|\overline{\overline{T}}_{00}(k_0,\varphi)|^2$. In (16)-(18), $\overline{R}_{1,00}(k_0,\varphi)$ and $\overline{F}_{1,00}(k_0,\varphi)$ have unique features distinct from those of conventional dielectrics and magnetic materials. For photonic crystals, there exist stopbands or transmission bands in which the propagation of electromagnetic waves in particular direction is prohibited or allowed within a certain frequency range. The locations of the stopbands and transmission bands and their strengths depend on the lattice parameters and sizes of the crystal. $\left|\overline{R}_{1,00}(k_0,\varphi)\right| = 1$ and $\left|\overline{F}_{1,00}(k_0,\varphi)\right| = 0$ in stopbands, $0 \le \left|\overline{R}_{1,00}(k_0,\varphi)\right| < 1$ and $0 < \left|\overline{F}_{1,00}(k_0,\varphi)\right| \le 1$ in the transmission bands. On the other hand, $\left|\overline{R}_{2,00}(k_0,\varphi)\right| = 1$ over $0 < \varphi < 180°$ because the lower dielectric slab is backed by a perfect conductor.

3. Design Principle of Directivity of the Line Source Coupled to Photonic Crystals

Equations (16)-(18) indicates that the directivity depends on three functions $\overline{F}_{1,00}(k_0,\varphi)$, $D(k_0,\varphi)$ and $K(k_0,\varphi)$. Since $K(k_0,\varphi)$ is a smooth function of φ for a fixed wave-number k_0, the directivity is governed by the frequency and angular-spectral response of $\overline{F}_{1,00}(k_0,\varphi)$ and $D(k_0,\varphi)$. Bearing this in mind, the directivity is categorized into three cases as follows:

Case [1]: $\left|\overline{F}_{1,00}(k_0,\varphi)\right| = 0$ and $\left|\overline{R}_{1,00}(k_0,\varphi)\right| = 1$ for $0 \le \varphi \le 180°$;

In this case, the transmission of electromagnetic waves through the electromagnetic crystal is prohibited for a given frequency and hence there is no radiation into the upper half-space for $0 \le \varphi \le 180°$.

Case [2]: $\left|\overline{R}_{1,00}(k_0,\varphi)\right| \approx 1$ and $\left|D(k_0,\varphi)\right| \approx 0$;

In this case, the space sandwiched by the grounded dielectric slab and the upper crystal behaves as a Fabry-Perot resonator to the line source. The primary field radiated from the line source resonates when $\left|D(k_0,\varphi)\right| = 0$ is satisfied and the radiation is enhanced in the particular direction φ which satisfies $\left|D(k_0,\varphi)\right| \approx 0$ for the given frequency.

Taking into account $\left|\overline{R}_{1,00}(k_0,\varphi)\right| \approx 1$ and $\left|\overline{R}_{2,00}(k_0,\varphi)\right| = 1$, we may express $\overline{R}_{1,00}(k_0,\varphi)$ and $\overline{R}_{2,00}(k_0,\varphi)$ as follows:

$$\overline{R}_{1,00}(k_0,\varphi) \approx e^{i\theta_1(k_0,\varphi)} \tag{19}$$

$$\overline{R}_{2,00}(k_0,\varphi) = e^{i\theta_2(k_0,\varphi)} \tag{20}$$

where θ_1 and θ_2 represent the phase angles of the reflection coefficients. Then the resonance condition $\left|D(k_0,\varphi)\right| = 0$ for the Fabry-Perot resonator is expressed as follows:

$$P(k_0,\varphi) = 2k_0 t\sin\varphi + (\theta_1+\theta_2) = 2n\pi \quad (n = 1,2,3,\cdots) \tag{21}$$

where $P(k_0,\varphi)$ defines the phase function in the transverse direction and $t = t_1 + t_2$. It should be noted that even if the resonance condition (21) is satisfied for a particular direction φ, the radiation into the upper half-space does not occur so long as the transmission window with $\left|\overline{F}_{1,00}(k_0,\varphi)\right| \neq 0$ is not opened in that direction.

Case [3]: $0 < \left|\overline{F}_{1,00}(k_0,\varphi)\right| \leq 1$ and $\left|D(k_0,\varphi)\right| \neq 0$;
In this case, the resonance condition is not satisfied and hence the primary field from the line source is directly radiated into the upper half space through the transmission windows of the upper crystal. Then the directivity strongly depends on the intrinsic electromagnetic nature of the crystal.

4. Numerical Validation of the Theory

To validate the proposed principle for designing the directivity, we have simulated the radiation pattern of the line source shown in Fig. 1 for several different resonator size $t = t_1 + t_2$. The photonic crystal consists of a square lattice formed by the parallel circular cylinders having radius $a/h = 0.13$ and relative permittivity $\varepsilon = 9.8$. The relative permittivity and thickness of the lower dielectric slab are $\varepsilon_s = 3.5$ and $d/h = 1.0$. The line source is excited at the frequency $h/\lambda_0 = 0.49$ where $\lambda_0 = 2\pi/k_0$. At this normalized frequency only the 0-th order space harmonic becomes the propagation wave. All of these parameters are fixed throughout the numerical examples.
Firstly, we calculated the generalized reflection $\left|\overline{R}_{1,00}\right|$ and transmission $\left|\overline{F}_{1,00}\right|$ coefficients of the upper crystal with $N = 12$ and the phase function $P(k_0,\varphi)$. Figure 2 shows $\left|\overline{R}_{1,00}\right|$ and $\left|\overline{F}_{1,00}\right|$ as functions of the observation angle φ.

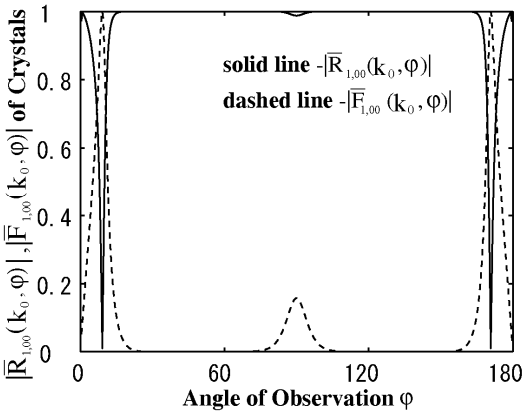

Fig.2. Generalized reflection $\left|\overline{R}_{1,00}(k_0,\varphi)\right|$ and transmission $\left|\overline{F}_{1,00}(k_0,\varphi)\right|$ coefficients of the electromagnetic crystal with $N = 12$ as functions of the angle φ of observation.

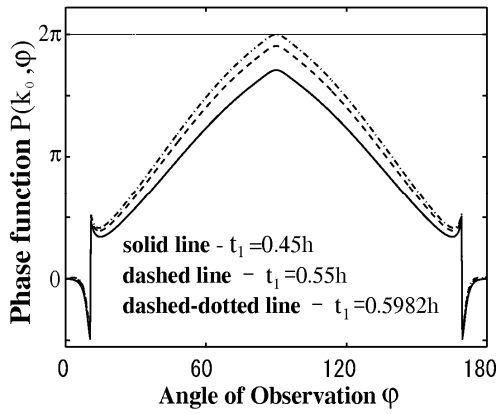

Fig.3. Phase function $P(k_0,\varphi)$ versus the angle φ of observation for different values of the distance t_1 between the line source and the electromagnetic crystal, where $t_2/h = 0.5$ and $N = 12$.

For the given frequency $h/\lambda_0 = 0.49$, there exist wide stop-bands in the directions of $25^\circ < \varphi < 82^\circ$ and $98^\circ < \varphi < 155^\circ$. Within the stop-bands, the crystal behaves as a perfectly reflecting superstrate with $\left|\overline{R}_{1,00}\right| = 1$, which does not allow the transmission of electromagnetic waves radiated from the line source. We can see that the reflection coefficient is almost zero at $\varphi \approx 10^\circ$ and $\varphi \approx 170^\circ$ and narrow transmission bands are formed around these two directions. It could be seen also that the transmission coefficient is $\left|\overline{F}_{1,00}\right| \approx 0.18$ at $\varphi = 90^\circ$ and the reflection coefficient $\left|\overline{R}_{1,00}\right|$ is very close to 1.0 in this direction. On the other hand, $\left|\overline{R}_{2,00}\right| = 1$ for $0^\circ < \varphi < 180^\circ$, because the

dielectric slab is backed by a perfect conductor. Figure 3 shows the phase function $P(k_0,\varphi)$ defined by Eq.(21) as functions of φ for $t_2/h = 0.5$ and three different values of t_1: $t_1/h = 0.45,\ 0.55$ and 0.5982. Note that the size of the resonator $(t = t_1 + t_2)$ increases with t_1. We can see that the phase function $P(k_0,\varphi)$ at around $\varphi = 90^\circ$ approaches to the resonance as t_1 increases. When $t_1/h = 0.5982$, a complete resonance, which satisfies Eq. (21) with $n = 1$ is obtained at $\varphi = 90^\circ$.

The characteristics of $\left|\overline{R}_{1,00}(k_0,\varphi)\right|$, $\left|\overline{F}_{1,00}(k_0,\varphi)\right|$ and $P(k_0,\varphi)$ shown in Figs. 2 and 3 are used to analyze the directivity of radiation under the prescribed parameters. The results are compared with those numerically calculated using Eq. (15). Figure 3 shows that when $t_1/h = 0.45$, the phase function $P(k_0,\varphi)$ is far from the resonance condition Eq.(21) over $0^\circ < \varphi < 180^\circ$. Then the energy radiated from the line source is transmitted in the three directions of $\varphi \approx 10^\circ$, 90° and 170° through the transmission windows of the upper crystal as shown in Fig. 2. When $t_1/h = 0.55$, the phase function $P(k_0,\varphi)$ approaches to the resonance for $\varphi = 90^\circ$ and hence, the radiation in this direction is increased, whereas the radiation in $\varphi \approx 10^\circ$ and 170° is decreased because these directions are far from the resonance. When $t_1/h = 0.5982$, the phase function satisfies the resonance condition for $\varphi = 90^\circ$ and hence the resonant radiation in this direction will occur with a suppression of the directional side lobes in the directions of $\varphi \approx 10^\circ$ and 170°. The directivity of radiation calculated using Eq. (15) is shown in Fig. 4 for three different values of t_1. We can confirm that the directivity predicted from the analysis on $\left|\overline{R}_{1,00}(k_0,\varphi)\right|$, $\left|\overline{F}_{1,00}(k_0,\varphi)\right|$ and $P(k_0,\varphi)$ agrees well with those obtained from the rigorous field analysis.

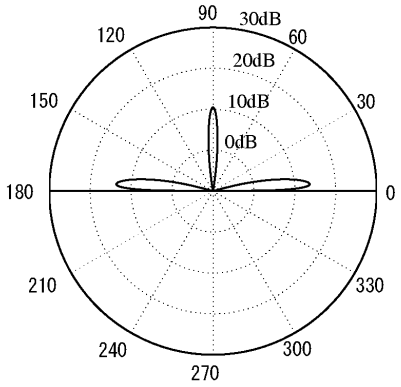

(*a*) $t_1/h = 0.45$

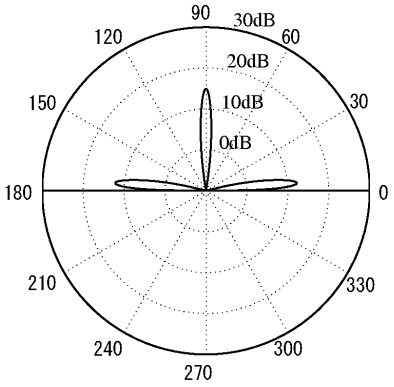

(*b*) $t_1/h = 0.55$

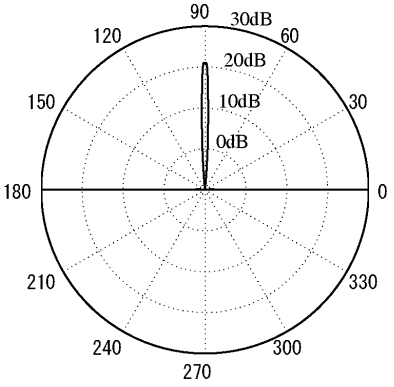

(*c*) $t_1/h = 0.5982$

Fig.4. Radiation patterns of the line source placed with (a) $t_1/h = 0.45$, (b) $t_1/h = 0.55$ and (c) $t_1/h = 0.5982$, where $t_2/h = 0.5$ and $N = 12$.

Figure 5 shows the phase function $P(k_0,\varphi)$ when t_1 is further increased to $t_1/h = 1.20$ and 1.618. The phase function for $t_1/h = 1.20$ satisfies the resonance condition (21) with $n = 1$ at $\varphi \approx 45^\circ$ and 135°. However, we note that there occurs no resonant radiation because $\left|\overline{F}_{1,00}(k_0,\varphi)\right| = 0$ in these directions as shown in Fig. 2. In this case, the radiated energy is transmitted through the transmission windows at $\varphi \approx 10^\circ, 90^\circ$ and 170° of the upper crystal. We also note that $P(k_0, 90^\circ) \approx 3\pi$ when $t_1/h = 1.20$. This means that the transmission into the direction of $\varphi \approx 90^\circ$ is in anti-resonance and hence the radiation in this direction is significantly decreased. When $t_1/h = 1.20$, therefore, we can expect a directivity with enhanced directional lobes in the directions of $\varphi \approx 10^\circ$ and 170°. When $t_1/h = 1.618$, on the other hand, the phase function $P(k_0,\varphi)$ satisfies the resonance condition (13) at $\varphi \approx 35^\circ, 90^\circ$ and 145°. For this case, there is no radiation in the direction of $\varphi \approx 35^\circ$ and

145° because $\left|\overline{F}_{1,00}(k_0,\varphi)\right|=0$ in these directions, whereas we can expect a strong resonant radiation in the direction of $\varphi \approx 90^\circ$ through the transmission window as shown in Fig.2. The directivity calculated using Eq.(15) is illustrated in Fig. 6.

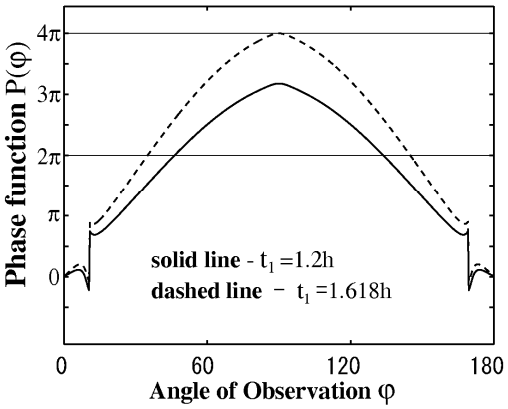

Fig.5. Phase function $P(k_0,\varphi)$ versus the angle φ of observation for $t_1/h=1.20$ and $t_1/h=1.618$, where $t_2/h=0.5$ and $N=12$.

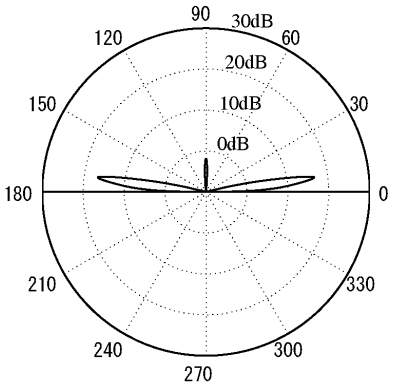

$(a)\ t_1/h=1.20$

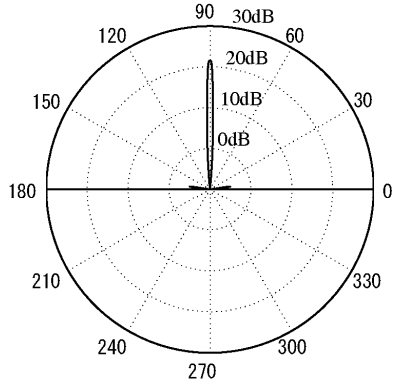

$(b)\ t_1/h=1.618$

Fig.6. Radiation pattern of the line source placed with (a) $t_1/h=1.2$ and (b) $t_1/h=1.618$, where $t_2/h=0.5$ and $N=12$.

We can confirm again that directivity predicted from the analysis on $\left|\overline{R}_{1,00}(k_0,\varphi)\right|$, $\left|\overline{F}_{1,00}(k_0,\varphi)\right|$ and $P(k_0,\varphi)$ agrees well with those obtained from the rigorous field analysis.

5. Conclusions

A novel formulation of radiation from a localized line source embedded in photonic crystals consisting of layered periodic arrays of parallel circular cylinders is proposed. The method employs the spectral domain approach. The line source is transformed into an infinite periodic array of linearly phased line sources in spectral domain. In the spectral domain the radiation problem is reduced to the problem of reflection and transmission of the space harmonic waves by the finite photonic crystals. The spectral response of the photonic crystal to the line source excitation has been calculated using the lattice sums, T-matrix of a circular cylinder, and the generalized reflection and transmission matrices of the layered system. The directivity of radiation from a localized source coupled to photonic crystals has been investigated theoretically using a two-dimensional model. The closed form expression for the far field of radiation has been derived and used to analyze the directivity. We have shown that the directivity is uniquely determined by the characteristics of the transmission windows of the crystals and the Fabry-Perot resonance condition for the radiated field in the space surrounding the source. This peculiar feature could be used to design and control the radiation pattern of photonic-crystal-based antennas.

References

[1] E. Yablonovitch, Photonic band-gap structures, *J. Opt. Soc. Am.B,* 10(2), 283-295, 1993.

[2] G. Tayeb and D. Maystre, "Rigorous theoretical study of finite-size two-dimensional photonic crystals doped by microcavities," *J. Opt. Soc. Am. A*, vol. 14, no.12, p.3323-3332, 1997.

[3] Y.J. Lee, J. Yeo, K.D. Ko, R. Mittra, Y.Lee, and W.S. Park, "A novel design technique for control of defect frequencies of an electromagnetic bandgap (EBG) superstrate for dual-band directivity enhancement," *Microwave and Opt. Tech. Lett*., vol. 42, no.1, p. 25-31, 2004.

[4] H. Y. D. Yang, "Theory of antenna radiation from photonic-bandgap materials," *Electromagnetics*, vol. 19, no. 3, p. 255-276, May/June 1999.

[5] C. Caloz, A. K. Skrivervik, and F. E. Gardiol, "An efficient method to determine green's functions of a two-dimensional photonic crystal excited by a line source –The phased-array method," *IEEE Trans. on Microwave Theory and Techniques*, vol. 50, no. 5, p. 1380-1391, May 2002.

[6] M. Thevenot, C. Cheype, A. Reineix, and B. Jecko, "Directive Photonic-Bandgap Antennas," *IEEE Trans. on Microwave Theory and Techniques*, vol. 47, no. 11, pp. 2115-2122, Nov. 1999.

[7] K. Yasumoto and K. Yoshitomi: "Efficient Calculation of Lattice Sums for Free-Space Periodic Green's Function," *IEEE Transactions on Antennas and Propagation,* vol. 47, no.6, pp.1050-1055, June 1999.

[8] K. Yasumoto and H. Jia, "Modeling of Photonic Crystals by Layered Periodic Arrays of Cylinders," in *Electromagnetic Theory and Applications for Photonic Crystals,* K. Yasumoto, ed., CRC Press, Chapter 3, pp.123-190, 2005.

[9] V. Jandieri, K. Yasumoto and H. Toyama, "Radiation from a line source placed in two-dimensional photonic crystals," *International Journal of Infrared and Millimeter Waves*, vol.28, no.12, p.1161-1173, 2007.

[10] V. Jandieri, K. Yasumoto and B. Gupta, "Directivity of Radiation from a Localized Source Coupled to Electromagnetic Crystals", *International Journal of Infrared, Millimetre and Terahertz Waves*, vol. 30, no. 10, 1102-1112, 2009.

Dispersion engineered slot photonic crystal waveguides for slow light operation

Charles Caer[1], Xavier Le Roux[1], Laurent Vivien[1], Eric Cassan[1]

[1]Institut d'Electronique Fondamentale, Univ. Paris-Sud, CNRS, Bât. 220, F91405 Orsay, France
*corresponding author, E-mail: charles.caer@u-psud.fr

Abstract

We introduce a novel design of wide Slot Photonic Crystal Waveguides (SPCW) by structuring the slot as a comb. This allows performing dispersion engineering in order to achieve very low group velocities over a few nanometers bandwidth. This kind of SPCW offers opportunities to realize devices requiring strong interactions between light and an optically non-linear low index material by providing an ultra-high optical density while easing the filling of the slot due to its width. We will present dispersion engineering results by Plane Wave Expansion method and Finite Difference Time Domain analysis, followed by experimental realization.

1. Introduction

Photonic Crystals Waveguides (PCW) operating in slow light regime are promising devices for all-optical signal processing and enhanced light-matter interactions [1]. However, the issue of propagation losses at low group velocities is still challenging their generalization, whereas it has partially addressed by dispersion engineering [2]. The strong dependence of the nonlinear phase shift on the group velocity gives rise to strong benefits of slow light for nonlinear operations [3]. This gain can be further enhanced with the introduction of a slot, allowing the use of nonlinear polymers with higher figures of merit than silicon [4]. Indeed, for $\chi^{(2)}$ nonlinear polymers, efficient electrooptic modulation has already been successfully reported [5-6].

Opening a slot along the line defect of PCW pulls the fundamental mode of the slot within the photonic bandgap [7]. This slope is positive in the First Brillouin Zone (FBZ), unlike the standard defect mode. Depending on the slot width, these two guided modes with the same even symmetry can coexist [8], but the W1 defect mode exits the photonic bandgap in case of large slots. The latter has received more interest than the slot one, because of the stronger optical confinement in narrow slots and an easier coupling from/to a photonic nanowire. Due to a stronger confinement in narrower slots and an easier coupling, the W1 defect band has received more interest [5-6,8-9]. But wider slots improve the poling efficiency of $\chi^{(2)}$ polymers and are more easily filled [6].

We report here a method to obtain a SPCW with wide slot, i.e. > 150 nm, operating in a flat band slow light regime. We realize this dispersion engineering by adding corrugations to the slot, similar to Bragg gratings. This provides three additional degrees of freedom and allows tailoring the guided mode in order to obtain a flat band group index curve. It is shown that these corrugations improve the localization of the electric field along the waveguide direction.

We engineer the dispersion curves of the two modes, because the W1 defect mode presents an easier coupling from a strip waveguide due its mode profile and this mode is guiding light when the slot is narrow, whereas the "slot" mode is relevant when the slot is very large, which can be required in applications such as sensing despite a lower coupling efficiency, as explained in [10].

2. Dispersion engineering of the slot

2.1. Introduction of a slot mode

The SPCW is optimized through calculations performed by Plane Wave Expansion method using the MPB software [11] for a quasi-TE polarization. Eigenmodes are calculated in the unit cell depicted in fig. 1, consisting in a Silicon On Insulator (SOI) slab with a lower silica layer and an upper cladding layer (e.g. polymer), with indices $n_{Silicon}$=3.48, n_{Silica}=1.44 and $n_{Polymer}$=1.6, respectively. The slab thickness h is fixed to 260 nm, the lattice constant a=400 nm, and the hole radius r is 120 nm to ensure a wide TE bandgap. As explained in our previous work [12], the optimization process begins with the choice of the desired slot width W_{slot}. For technological reasons, it is preferable to work with large slots, at least larger than 150 nm. This requires an enlargement of the line defect in order to keep the guided mode within the photonic bandgap. Therefore, we change the W1 defect to W1.25, i.e. a width of $1.25\sqrt{3}a$.

2.2. Tuning the slot mode

The W1.25 photonic crystal waveguide is taken as a starting point. We then calculate the dispersion diagram for increasing values of W_{slot}, in order to evaluate the suitable W_{slot} value giving a flat dispersion curve under the light line to the "slot" mode. The dispersion curve is progressively flattened for increasing W_{slot} values, as the frequency values increase near the edge of the FBZ at k=0.5. The optimum is found around W_{slot}=0.4a because for larger values, the dispersion curve slope becomes positive. In the same time, the increasing values of W_{slot} reject the W1 defect

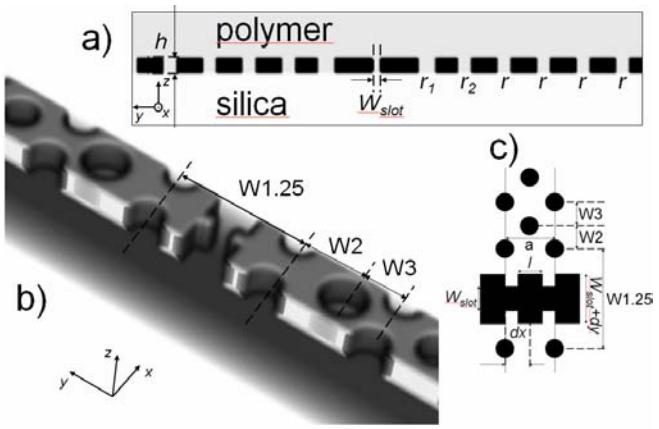

Figure 1: Schematic draw of the unit cell with all relevant parameters in the *yz* plane.

mode outside the photonic bandgap when it reaches W_{slot}=0.4*a*. Next, it is here necessary to pre-compensate the slope of the guided mode before introducing corrugations to the slot by shifting the W2 and W3 hole rows. Forecoming simulations indeed show that decreasing the two values of W2 and W3 (which are nominally equal to $0.5\sqrt{3}a$) makes the slope negative under the light line.

We then introduce corrugations on the slot as described in fig. 1. The comb possesses three parameters: the duty cycle *l*, the depth *dy* of the gratings, and the displacement *dx* of the comb grating regards to the center of the first hole row. It is crucial to keep the periodicity of the comb exactly the same as that of the photonic crystal. Therefore, the bandgap remains controlled by the hole lattice, and the comb provides the three additional degrees of freedom previously mentioned for dispersion engineering. Results about the obtained group index values by considering W1.25, W2=W3=$0.4\sqrt{3}a$, W_{slot}=0.4*a*, dx=0, *l*=0.8, *dy*=0.35*a*, respectively, are reported on fig.2. By referring to the definition of the group index bandwidth product (GBP):

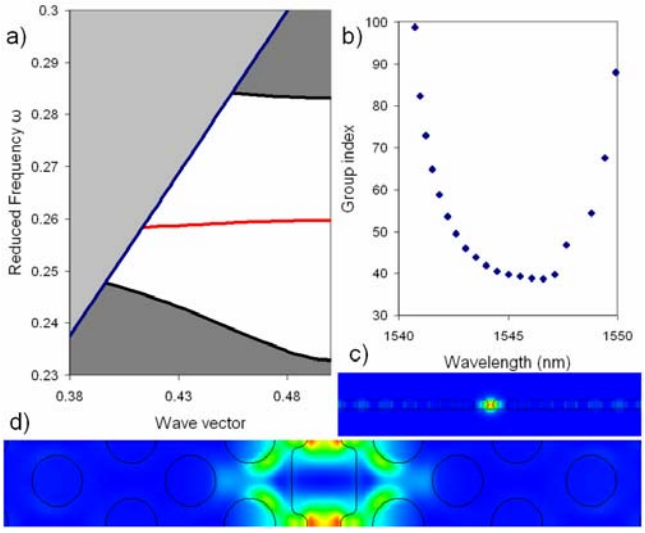

Figure 2: a) Band diagram of the dispersion engineered slot mode. b) Corresponding group index. c) Cross-section of the $\varepsilon|\mathbf{E}|^2$ pattern at *k*=0.45 in the *yz* plane. d) Same pattern viewed in the *xy* plane.

$$GBP = \langle n_g \rangle \frac{\Delta\omega}{\omega_0}, \qquad (1)$$

where $\langle n_g \rangle$ stands for the average group index over a bandwidth $\Delta\omega$ and ω_0 the central wavelength, we obtain a GBP of 0.139. It has to be kept in mind that this GBP is not as large as in some previous studies [2] because of the cladding layer index considered here ($n_{Polymer}$=1.6) which enlarges the light cone compared to air cladding, thus reducing the available bandwidth.

We express the optical confinement [12] by defining the ratio of optical power within the slot over the total power, and the optical intensity *I* as divided by the cross-section of section of the slot, i.e. $h*W_{slot}$ with *h* the height of the silicon slab. We include the effect of electromagnetic density enhancement due to slow light propagation by setting this confinement as the product of the previous optical intensity and the group index n_g for the m-th mode:

$$\eta_m = \frac{n_{g,m}}{hW_s} \frac{\int_{comb} \left(\varepsilon(r)|E_m(r)|^2\right) d^3r}{\int_{cell} \left(\varepsilon(r)|E_m(r)|^2\right) d^3r} \qquad (2)$$

We find here for our structure a confinement factor of 144 μm^{-2}, for an in-slot confinement of 15% of the total power. We recall for comparison that in the case of total internal reflection slot waveguide with the same slot width, the confinement factor is only around 10 μm^{-2}, representing a fifteen-fold enhancement of the confinement. Interestingly, compared to SPCW without any structuration of the slot, the narrowing of the slot provides a stronger confinement of the mode along the waveguide direction, as seen on fig. 2 d). Despite an expectable increase of the scattering losses, it still remains interesting since the modal volume becomes strongly reduced by this structuration, and the same goes for the nonlinear effective area of the guided mode.

2.3. Tuning the W1 mode

Similar dispersion engineering to the one presented in the previous section can be applied to tune the W1 defect mode. The origin of this mode being different, it is less sensitive to the structuration of the comb, when the mode is far from the air band. Nevertheless, we can apply the same procedure. We start with the choice of an adequate slot width, the slope is adjusted by changing the values of W2 and W3, and finally, we tailor the comb. If we want to engineer the dispersion of a SPCW with a wider slot, it is better to work with an enlarged PCW channel, e.g. W1.4, but we lose the benefit of a stronger localization of light at the narrowing, and it is harder to tailor the W1 defect mode which is more sensitive to the modification of the hole array. Moreover, a W1.25 defect still strongly reduces the overlap between the mode and the holes, and leaves the slot as the main source of scattering, then reducing the losses if compared to W1 SPCWs. After structuring the slot, we can see that the parameter *dx* affects the mode profile. An optimum confinement is found when *dx*=0.5*a,* as depicted on fig. 3. This means that where the mode is naturally localized in the slot, adding a corrugation there will strongly enhance the local intensity in the slot, even more if the comb duty cycle

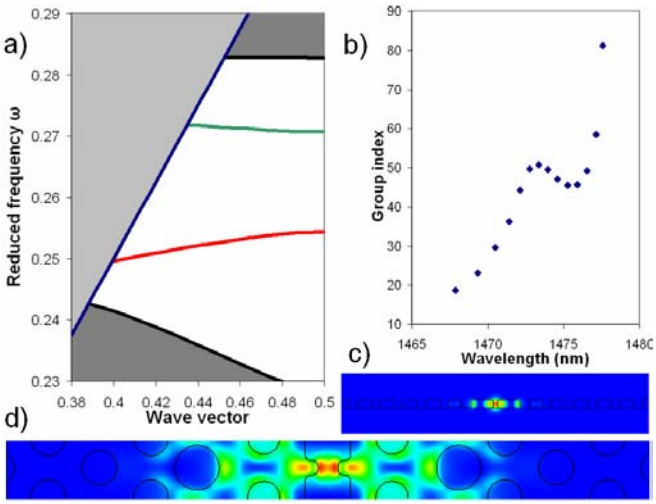

Figure 3: a) Band diagram of the dispersion engineered W1 defect mode (green curve). b) Corresponding group index. c) Cross-section of the $\varepsilon|\mathbf{E}|^2$ pattern at k=0.45 in the yz plane. d) Same pattern viewed in the xy plane.

l is increased, leading to very sharp corrugations. We finally tune the mode to obtain a flat band group index curve by reducing the radius r_1 of the first hole row to 0.28a and by increasing the radius r_2 of the second hole row to 0.38a, similarly to [9]. In this case, with the following parameters: W1.4, W2=0.65, W3=0.45, W_{slot}= 0.35a, dx=0.5a, dy=0.4a, l=0.75, r_1=0.28a, r_2=0.38a, we obtain a mean group index of 48 over a bandwidth of 4.5 nm, giving a GBP of 0.147. This configuration gives a field concentration of 13% in the slot, and a confinement factor of 177 μm^{-2}. We do not exploit the "slot" mode in this case, although present in the photonic bandgap, since the shape of the comb decreases the confinement of the mode in the slot, thus reducing its interest.

3. FDTD Analysis

After optimization of the guided mode in the SPCW, it is a necessity to compute the transmission of a complete device for the evaluation of the propagation losses. The transmission spectrum of the photonic crystal waveguide is calculated by Finite Difference Time Domain simulation using the MEEP software [13]. The implemented structure is shown on fig. 4. It consists of a SPCW with input and output waveguides. The strip waveguides are converted by a 15 µm long taper into slot waveguides with a high coupling efficiency [14] in order to convert adiabatically the mode within the slot, at the input and output of the SPCW. Then, the slot waveguide mode can be coupled to the SPCW one using two transitions regions to adapt the fast light propagation to a slow light regime by slightly stretching the PC lattice in the longitudinal direction [15]. In the injection zone, and next to the reflection zone, the lattice constants a_{inj} and a_{refl} are stretched to 420 nm and 410 nm, respectively, while the lattice constant a remains 400 nm in the central part of the SPCW. As a whole, the length of the photonic crystal crystal waveguide is 88.7µm, which keeps the device footprint to an acceptable value, and the length of the

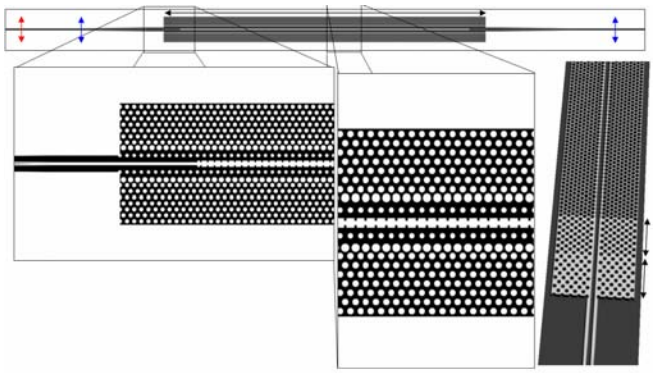

Figure 4: Representation of the FDTD computational cell with different detailed views. The source and the sensors are highlighted in red and blue, respectively.

complete structure with all sub-regions is 177.5 µm. The computational cell is wide enough to avoid coupling with the Perfectly Matched Layers. We perform here 2D FDTD calculations with slab effective index approximation for two reasons: 3D FDTD is excessively time consuming for long devices and out-of-plane losses are not a drawback, since we work exclusively under the light line and backscattering is the main source of losses. The effective index of the silicon in the present case is evaluated to 2.83 by slab optical mode solver. The simulation time range is 70 ps (i.e. 50,000 c/a time units) and the source is a broadband gaussian pulse centered at 1,550 nm with a spectral width of 500 nm. The sensors have a resolution of 50 pm. The grid resolution is 20 nm per pixel. This represents a computation time of 50 hours on 16 CPU. The parameters of the photonic crystal are W1.4, $W2$=0.65, $W3$=0.45, $r1$=0.25a, $r2$=0.38a, r=0.3a, and those of the comb are W_{slot}=0.4a, dy=0.5a, dx=0.5a, and l=0.75. The engineered SPCW has a "W1" mode with group index *plateau* of 45 over 5 nm as shown in fig. 5 and calculated by PWE method. The group index dependence with respect to the bandwidth is extracted from the Fabry-Perot fringes as described in [16]. The transmission is around -12dB, even close to the band edge, confirming the efficiency of the mode conversion and a low level of intrinsic losses and coupling losses. However, we find a mismatch between the group index curves calculated by

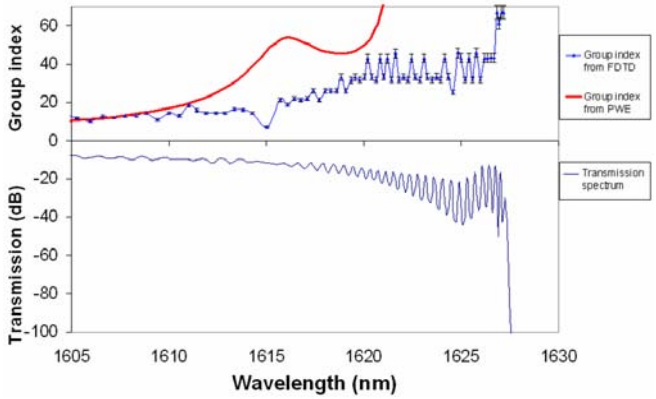

Figure 5: Up: group indices obtained by PWE calculation (red curve) and FDTD calculation (blue dotted curve). Down: corresponding FDTD transmission spectrum.

PWE and FDTD methods due to a difference of the definition of the computation grid, making hard to retieve the same flat band group index curve with the same parameters obtained by PWE. Moreover, the band edge is shifted of approximately 5 nm. However, we retrieve a flat band group index curve by FDTD calculation, confirming the operation in slow light regime with a mean group index of 35 on a 6 nm bandwidth. We underline here that the running time is a critical parameter for the observation of the interference fringes: indeed, physically, the slow pulse needs to reach the output in order to be detected by the sensor. Therefore, group indices above 70 are not consistent. However, this computation gives a good estimation of the level of coupling and intrinsic losses in the SPCW and shows that it is possible to manipulate slow light by FDTD method by directly linking it to the transmission spectrum.

4. Conclusions

We have demonstrated that a comb photonic crystal waveguide is a suitable structure for strongly confining light in a low index material. We have shown that a proper dispersion engineering of the slot itself ensures a flat band group index curve, enabling a slow light operation over a a few nanometers bandwidth. Two structures relying on two different guided modes have been presented. They are operating in slow light regime with group indices of 40 and 48 over bandwidths of 5 nm and 4.5nm, respectively, with slot widths above 140 nm at the narrowest parts. In-slot optical confinements of 15% and 13 % are reported. The slot enlargement is not realized at the expense of a low optical intensity, and the narrowing of the slot into the comb presents a high localization of the electric field, which is of interest for configurations requiring small modal volume and nonlinear effective area.

Finally, FDTD calculations showed an efficient mode conversion from the photonic wire to the SPCW and a high transmission near the band edge. The simulated structure shows slow light operation with a flat band group index of 35 over a bandwidth of 6 nm and a transmission of -12 dB at the band edge. The high localization of the electric field will offer a good opportunity for sensing devices and nonlinear optical effects.

The next task is to work towards the experimental achievement of slow light propagation in a dispersion engineered comb photonic crystal waveguide by analyzing the interference fringes in a Mach-Zehnder Interferometer.

Acknowledgements

Charles Caer acknowledges a scholarship from the French Ministry of Education and Research.

References

[1] T.F. Krauss, Slow light in photonic crystal waveguides, *J. Phys. D: Appl. Phys.* 40: 2666–2670, 2007.

[2] S.A. Schulz, L. O'Faolain, D.M. Beggs, T.P. White, A. Melloni, T.F. Krauss, Dispersion engineered slow light in photonic crystals: a comparison, *J. Opt.* 12: 104004-1-10, 2010.

[3] C. Monat, B. Corcoran, D. Pudo, M. Ebnali-Heidari, C. Grillet, M.D. Pelusi, D.J. Moss, B.J. Eggleton, T.P. White, L. O'Faolain, T.F. Krauss, Slow Light Enhanced Nonlinear Optics in Silicon Photonic Crystal Waveguides, *IEEE J. Sel. Top. Quantum Electron.* 16: 344-356, 2010.

[4] J. Leuthold, W. Freude, J.-M. Brosi, R. Baets, P. Dumon, I. Biaggio, M.L. Scimeca, F. Diederich, B. Frank, C. Koos, Silicon Organic Hybrid Technology - A Platform for Practical Nonlinear Optics, *Proc. of the IEEE*, 97:1304-1316, 2009.

[5] J.-H. Wülbern, S. Prorok, J. Hampe, A. Petrov, M. Eich, J. Luo, A.K.-Y. Jen, M. Jenett, A. Jacob, 40 GHz electro-optic modulation in hybrid silicon–organic slotted photonic crystal waveguides, *Opt. Lett.* 35: 2753-2755, 2010.

[6] X. Wang, C.-Y. Lin, S. Chakravarty, J. Luo, A.K.-Y. Jen, R.T. Chen, Effective in-device r33 of 735 pm/V on electro-optic polymer infiltrated silicon photonic crystal slot waveguides, *Opt. Lett.* 36: 882-884, 2011.

[7] A. Di Falco, L. O'Faolain, T.F. Krauss, Dispersion control and slow light in slotted photonic crystal waveguides, *Appl. Phys. Lett.* 92: 083501-1-3, 2008.

[8] J. Gao, J.F. McMillan, M.-C. Wu, J. Zheng, S. Assefa, C.W. Wong, Demonstration of an air-slot mode-gap confined photonic crystal slab nanocavity with ultrasmall mode volumes, *Appl. Phys Lett.* 96: 051123-1-3, 2010.

[9] J.-M. Brosi, C. Koos, L.C. Andreani, M. Waldow, J. Leuthold, W. Freude, High-speed-low voltage electro-optic modulator with a polymer infiltrated silicon photonic crystal waveguide, *Opt. Express* 16: 4177-4191, 2008.

[10] M. Scullion, A. Di Falco, T. F. Krauss, High Efficiency Interface for Coupling Into Slotted Photonic Crystal Waveguides, *IEEE J. Photon.*3: 203-208, 2011.

[11] S.G. Johnson, J.D. Joannopoulos, Block-iterative frequency-domain methods for Maxwell's equations in a planewave basis, Opt. *Express* 8: 173-190, 2000.

[12] C. Caer, X. Le Roux, V.K. Do, D. Marris-Morini, N. Izard, L. Vivien, D. Gao, E. Cassan, Dispersion Engineering of Wide Slot Photonic Crystal Waveguides by Bragg-like Corrugation of the Slot, *IEEE Photon. Technol. Lett.* 23: 1298-1300, 2011.

[13] A. F. Oskooi, D. Roundy, M. Ibanescu, P. Bermel, J. D. Joannopoulos, S. G. Johnson, A flexible free-software package for electromagnetic simulations by the FDTD method, *Comput. Phys. Commun.* 181: 687-702, 2010.

[14] Z. Wang, N. Zhu, Y. Tang, L. Wosinski, D. Dai, S. He, Ultracompact low-loss coupler between strip and slot waveguides, *Opt. Lett.* 34: 1498-1500, 2009.

[15] J.-P. Hugonin, P. Lalanne, T.P. White, T.F. Krauss, Coupling into slow-mode photonic crystal Waveguides, *Opt. Lett.* 32: 2638-2640, 2007.

[16] Y.A. Vlasov, S.J. McNab, Coupling into the slow light mode in slab-type photonic crystal waveguides, *Opt. Lett.* 31: 50-52, 2006.

Resonant and slow light self-collimation in photonic band gap metamaterials

Emmanuel Centeno*, Julien Arlandis, Rémi Pollès, Antoine Moreau

Institut Pascal,
Université Blaise Pascal, UMR CNRS 6602, 63177 Aubière, France
*corresponding author, E-mail: Emmanuel.Centeno@univ-bpclermont.fr

Abstract

Self-collimation of light is explored in novel photonic crystals structures that combine either positive and negative index layers or homogeneous and etched dielectric materials. These novel photonic crystals are demonstrated to present resonant or slow light self-collimation effects. In metamaterials of zero-average optical index, diffraction-free beams are in addition propelled with a cancelled total phase delay. In all dielectric structures based on 2D photonic crystal properties, self-collimation is shown to arise for almost non-etched structures and in a slow light regime. A beam propagation model is developed and gives a comprehensive interpretation of these beam shaping properties.

1. Introduction

Beating light diffraction with linear optical devices has attracted much attention the last decade because of potential applications for telecommunications, biophotonics or imaging systems. Using photonic crystals (PhCs) and more recently metamaterials, it has been shown that diffraction-free beams can be generated without the help of any nonlinear process such as Kerr effect. This linear property known as self-collimation effect has firstly been introduced by H. Kosaka in his pioneering works on PhCs[1]. In this approach, self-collimation stems from the use of "flat dispersion curves" that present parallel group velocities for all the Bloch waves constituting the beam. An other route to stop diffraction relies on the unusual properties of metamaterials. This alternative has been recently explored in some theoretical studies [2], [3], [4] and in an experiment involving dielectric PhC superlattices [5]. These structures are based on 1D PhCs with a unit cell consisting of layers with complementaries electric and magnetic permittivities have led to the concept of zero-average index metamaterials [6],[7], [8]. Such metamaterials, presenting a null average index over a lattice period, are known to present a forbidden band named zero-$\bar{n}$ gap that is insensitive to the period scaling, to disorder or to the light polarization [7]. These properties have been experimentally demonstrated with metamaterials layers presenting double negative electric and magnetic permittivities alternated with air layers at GHz frequencies [9]. These experimental demonstrations have been transposed in the near-infrared spectrum of light with photonic crystal superlattices [10], [5]. Kocaman and co-authors have in addition proven that the phase delay of a signal propagating through an average index material is cancelled when its frequency lies in the zero-$\bar{n}$ gap. Although the transmission efficiency is very low in that case, these experimental results show the ability of zero average index material to control the light phase [11].

In recent works, we have shown that the self-collimation effect can be made resonant or be combined with slow light regime in layered media [4], [12]. Here, we first present a beam propagation theory in layered media that provides the key parameters for getting the mesoscopic self-collimation or the phase compensation mechanism. Then we consider zero-average index metamaterials and demonstrate that resonant self-collimated beams lying in zero-$\bar{n}$ gap allow to cancel the phase delay of the signal while maintaining a high transmission efficiency - conversely to the recent results of Kocaman and co-authors [11]. The role of material dispersion and its impact on the resonance conditions in the zero-$\bar{n}$ gap will be discussed. In the third part, we will demonstrate that zero-average index materials are not necessary to get self-collimation. Photonic crystal superlattices of all-positive optical index materials will be shown to propel diffraction-free beams. Guided by the theoretical model, we will demonstrate that mesoscopic self-collimation of light is governed by a scale-invariant law. This theory leads to the design of original devices with very low filling factors in air and presenting slow light and self-collimation effects.

2. Theory of mescocopic self-collimation

Let us consider a layered media whose unit cell consists in two slabs of thicknesses d_1 and d_2 (of lattice constant $D = d_1 + d_2$), characterized by their dispersion relations of the form $k_y(\omega, k_x)$. These photonic dispersions represent either the effective optical properties of a metamaterial slab or the photonic band diagram of a PhC layer. A Gaussian beam $U(x,0) = \exp(-x^2/W_0^2)$, of initial waist W_0, impinges the structures at $y = 0$. Assuming that reflections at the layer interfaces are neglected, the electromagnetic field is obtained with the following Fourier transform :

$$U(x,y) = \int_{-\infty}^{\infty} dk_x U(k_x,0) e^{ik_x x} e^{ik_y(\omega,k_x)y} \qquad (1)$$

where $U(k_x,0) = W_0/(2\sqrt{\pi})\exp(-(k_x W_0/2)^2)$. In the paraxial approximation, the propagation constant in each

layer takes the quadratic form:

$$k_y(\omega, k_x) = k_y(\omega, 0) + \frac{k_x^2}{2} \left. \frac{\partial^2 k_y}{\partial k_x^2} \right|_{k_x=0} \quad (2)$$

For a given direction propagation, a dispersion curve $k_y(\omega, k_x)$ is characterized by its curvature index n_c which is related to the local curvature: $\frac{1}{k_0 n_c} = -\left. \frac{\partial^2 k_y}{\partial k_x^2} \right|_{k_x=0}$. In the case of a homogeneous medium, n_c simply equal to the optical index, but it can take positive or negative values for metamaterial or 2D PhC media. Plugging Eq.(2) into Eq.(1), one can derive the expression of the beam propagating through a lattice period D:

$$U(x, D) = e^{i\langle k_y(\omega,0)\rangle D} \int_{-\infty}^{\infty} dk_x U(k_x, 0) e^{-iD\frac{k_x^2}{2k_0}\left\langle \frac{1}{n_c} \right\rangle} \quad (3)$$

This expression shows that to important parameters control the phase and shape of the beam. It appears that the wave accumulates the mean phase $\langle k_y(\omega, 0)\rangle D = k_1 d_1 + k_2 d_2$ and that the initial Gaussian beam can be retrieved when the average curvature is null: $\left\langle \frac{1}{n_c} \right\rangle = 0$. By introducing the ratio in thickness layers $\alpha = d_2/d_1$, this condition writes:

$$1/n_{c1} + \alpha/n_{c2} = 0 \quad (4)$$

This result demonstrates that beams self-collimated at the mesoscopic scale obey to a scale-invariant law since it not depends on the period D. In the following sections, we will see that those parameters have a direct impact on the phase compensation and self-collimation effects.

3. Self-collimation in zero-average index metamaterials

Before demonstrating resonant and slow light self-collimation in zero-average index metamaterials, let us recall the necessary conditions to open a zero-$\bar{n}$ and resonant modes. For a 1D PhC consisting of a set of periodic layers of thickness d_1 and d_2, optical indices n_1 and n_2 and impedances η_1 and η_2 respectively, the dispersion relation reads:

$$\cos(\kappa D) = \cos(\langle k \rangle D) + \tau \sin(n_1 k d_1) \sin(|n_2| k d_2), \quad (5)$$

where $\tau = \frac{(\eta_1 - \eta_2)^2}{2\eta_1\eta_2}$ and $k = 2\pi/\lambda$ is the wave number in vacuum and κ the Bloch wave vector. For mismatched impedances, the zero-$\bar{n}$ gap appears when the average phase over a lattice period is null i.e $\langle k \rangle D = 0$. In the case of homogeneous layers this leads to the zero-average index condition $n_1 d_1 + n_2 d_2 = 0$ [7]. Singular resonances can however exist when the Fabry-Perot (FP) condition, $k n_1 d_1 = m\pi$ is satisfied (m being an integer). As discussed in [4], for dispersive materials the opening of the zero-$\bar{n}$ gap and the obtention of the FP resonance can occur for different frequencies. The offset between both conditions dramatically disturbs the band diagram since the resonance broadening reduces the extend of the zero-$\bar{n}$ gap.

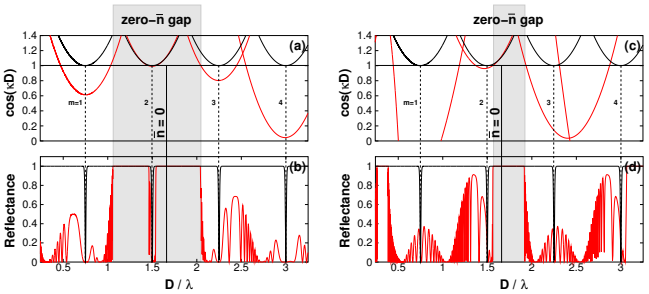

Figure 1: (a) and (c): dispersion relation. (b) and (d): Reflection coefficient for the structure composed of $N = 50$ periods. Black and red curves correspond to the non-dispersive and dispersive cases respectively. The parameters are $n_1 = 1$, $n_2^0 = -2$, $\eta_1 = 1$, $\eta_2 = 0.5$, $d_1 = 2D/3$, $d_2 = D/3$ and $D/\lambda_0 = 13/8$. In (a) and (b) the dispersion parameter is $C = 0.5/\lambda_0$ and in (c) and (d) the dispersion increases to $C = 1/\lambda_0$.

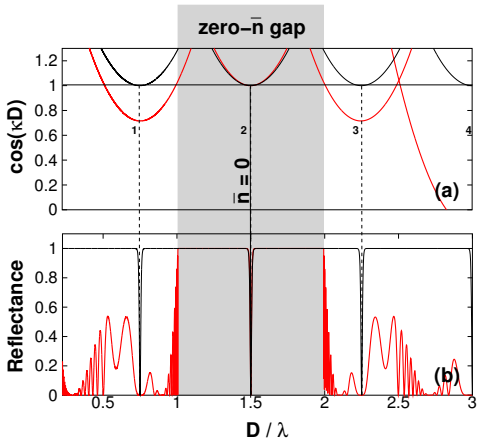

Figure 2: (a) dispersion relation, (b) reflection coefficient where black and red curves correspond to the non-dispersive and dispersive cases respectively. Same parameters as in Fig. 1 but $D/\lambda_0 = 1.5$.

The impact of dispersion is studied by considering that $n_2(\lambda) = n_2^0 + \Delta n_2(\lambda)$, where $\Delta n_2(\lambda) = C(\lambda - \lambda_0)$ is assumed in first approximation to be a linear function vanishing at the wavelength λ_0. Figures 1 and 2 show that the FP peak broaden when the dispersion parameter C increases.

However, when the FP and the zero-average index conditions are simultaneously satisfied for the same frequency, a sharp resonance appears whatever the material dispersion, Fig. 2. These results indicate that a high control of the material parameters is needed to create the right electromagnetic environment for the excitation of FP modes in the zero-$\bar{n}$ gap. Conversely to common defect modes localized in microcavities embedded in Bragg mirrors, FP modes in zero-average index materials are obtained without breaking the lattice period and propagate throughout the whole structure without an exponential decay. This unique property allows us to envisage resonant beam shaping opera-

tions such as self-collimation. Since a FP mode is characterized by singulars wavevector and frequency, its dispersive properties cannot been deduced from a band diagram analysis. However, the previous theory shows that mesoscopic self-collimation is obtained when the dispersion curvature are compensated for. In the case of homogeneous slabs this condition writes $d_1/n_1 + d_2/n_2 = 0$. Combining the zero-average index condition with the latter mesoscopic self-collimation leads to $d_1 = d_2$ and $n_1 = -n_2$, which are the parameters settled in V. Mocella's experiment [5]. Figure 4 shows the propagation of a self-collimated beam through 200λ zero-average index metamaterial for the reduce frequency $D/\lambda = 1.5$ corresponding to the resonant FP mode of Fig. 2.

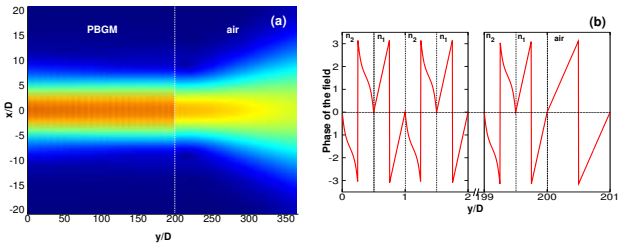

Figure 3: (a) Modulus of the electromagnetic field for a self-collimated FP mode. (b) Phase of the signal inside the zero-average index metamaterial.

Beyond the resonant behavior of this diffraction-free mechanism, one can see that the phase of the signal is exactly compensated over one lattice period. This zero-phase delay is in agreement with Eq.(3) where the accumulate phase is null when the zero-average index condition is satisfied i.e. $\langle k_y(\omega, 0)\rangle\, D = 0$. This property as recently been experimentally observed but in a devices that not support FP modes leading to a very low transmission efficiency smaller than 20dB [11]. Here, this zero-phase delay can be combined with a resonant self-collimated beam carrying a high amount of energy. The simulation of Fig. 3 shows that the transmission coefficient is larger than 90% and finally the incident beam seems to be translated over hundred of wavelengths without any change in its phase or shape. This result also proves that beam shaping operation can be dissociated from the value of the optical index but rather depends on the local dispersion curvature. This property can be used to tune the mesoscopic self-collimation frequency at the desired frequency in the photonic band diagram. The operating frequency can in particular be shifted near a photonic band gap edge where the speed of light is known to dramatically decrease. Figure 4 gives the dispersion curve and group index ($n_g = c/v_g$) for a zero-average index metamaterial presenting a self-collimated condition at the boundary of a zero-$\bar{n}$ gap. High group index of 40 can be expected in this configuration, showing the versatility of layered positive and negative index structures.

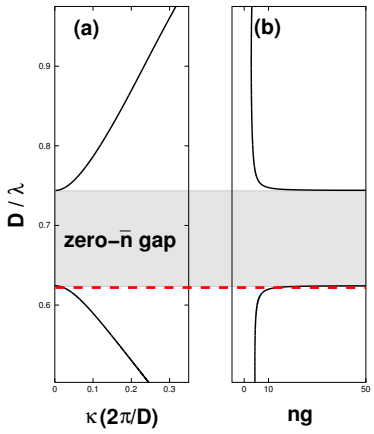

Figure 4: Band diagram and group index of a structure whose parameters are $n_1 = 1$, $n_2^0 = -1.25$, $\eta_1 = 1$, $\eta_2 = 0.5$, $d_1 = 5D/9$, $d_2 = 4D/9$, $D/\lambda_0 = 39/55$ and $C = 1/\lambda_0$. The red dashed line indicates the self-collimation frequency $D/\lambda = 0.612$.

4. Self-collimation in photonic crystal superlattices

Photonic crystals superlattices have firstly been introduced to mimic zero-average index metamaterials but in the near-infrared spectrum of light. This approach has successfully proven that negative index slab of metamaterials can be replaced by 2D PhC layers of -1 effective index leading thus to open a zero-$\bar{n}$ gap [5], [11]. However, we have recently demonstrated that these complex nanophotonic structures can also been used to generate self-collimated beams without the need of zero-average index devices. Our approach relaxes the numerous optical conditions introduced in the previous section and enables to go further in the control of light [12]. We start with the first dispersion band of a 2D PhC consisting of a square lattice of air holes etched in a dielectric material of optical index n_2. In TM polarization, one recognizes a frequency domain presenting flat iso-frequency curves used for guiding self-collimated beams [13], Fig. 5. As shown Eq.(3), the local curvature of the dispersion curve drives the divergence of the beam during its propagation through the PhC. In our case, flat iso-frequency curves are associated to a null curvature in the ΓM direction at the reduce frequency $a/\lambda = 0.235$, Fig.6a. The curvature changes sign either side of this frequency with a 2D PhC passing from a dispersive to a focalizing regime for higher frequencies. Let us stress that here, the focalization is related to the curvature of dispersion relation and not to a specific value of the effective phase index.

Mesoscopic self-collimation stems from the focalization power of 2D PhCs to compensate diffraction in homogeneous layers. Consider now a photonic crystal superlattice alternating periodically the previous 2D PhC sized in a layer of thickness d_1 and a homogeneous slab of thickness d_2 and optical index n_2. The null average curvature con-

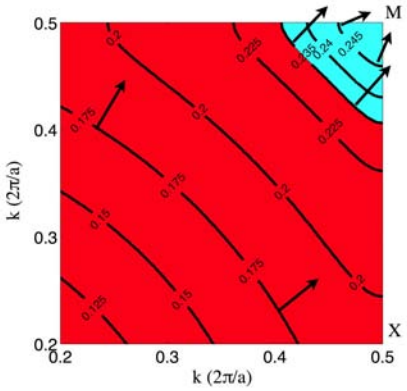

Figure 5: Iso-frequency curves of the first band and for TE polarization. The PhC parameters are $r/a = 0.2$ and $n_2 = 2.9$. The arrows indicate the direction of the group velocity and the red and blue areas correspond respectively to IFCs of positive and negative curvatures.

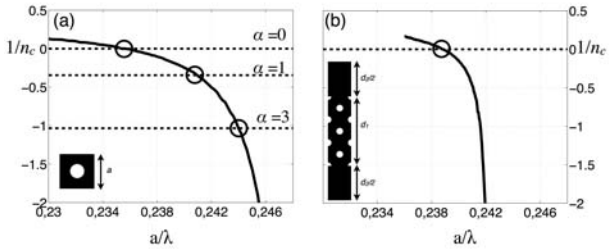

Figure 6: Curvature function $1/n_c$ computed in ΓM direction versus the reduce frequency. (a) For the infinite 2D PhC of unit cell depicted in the inset. The intersection points between $1/n_c$ and the straight dashed-lines for $\alpha = 0$, 1 and 3 correspond respectively to the self-collimation frequencies for the unbounded 2D PhC and for PhC superlattices of two filling ratios in PhC layers. (b) Graph of $1/n_c$ computed for the supercell corresponding to a PhC superlattice with $\alpha = 1$ and $d_1 = 3a\sqrt{2}$ shown in the inset.

dition over a macro period D writes $1/n_c = -\alpha/n_2$ with $\alpha = d_2/d_1$ showing that a continuous set of operating frequency can be chosen providing that $1/n_c$ is negative. Self-collimation is then expected to appears at the reduced frequencies 0.241 and 0.244 for $\alpha = 1$ and $\alpha = 3$ respectively. These frequencies agree within an error of 1% to the exact values extracted from superlattices band structures. For instance with $\alpha = 1$, the dispersion diagram obtained for the unit cell depicted in the inset of Fig.6.b gives a null curvature at 0.239. These results are also confirmed by FDTD simulations of beam propagation through superlattices presenting two ratios $\alpha = 1$ and $\alpha = 3$, Fig.7. Notice that the filling factor in air is dramatically reduced since it attains only 3% for $\alpha = 3$. This demonstrates that self-collimation is achievable in almost non-etched devices.
Similarly to zero-average index metamaterials, a smart engineering of the dispersion relation allows us to push the

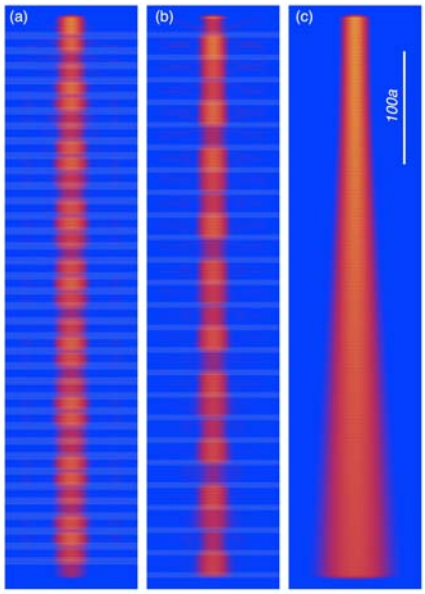

Figure 7: Map of the magnetic field modulus for a Gaussian beam of waist $W_0 = 8a$ (a) At the reduce frequency $a/\lambda = 0.239$ for a PhC superlattice for $d_1 = 4a\sqrt{2}$ and $\alpha = 1$. (b) At the reduce frequency 0.243 for $d_1 = 3a\sqrt{2}$ and $\alpha = 3$. (c) The same Gaussian beam propagating in a homogeneous medium of optical index $n_2 = 2.9$ and for $a/\lambda = 0.239$.

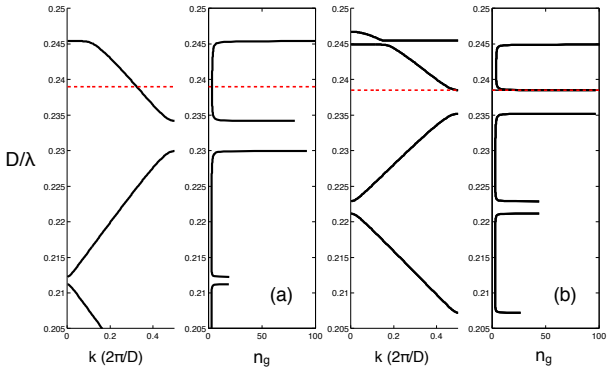

Figure 8: Band diagram in the ΓM direction and group index of the PhC superlattice for $\alpha = 1$. The red dashed lines indicate the self-collimation frequency $a/\lambda = 0.239$. (a) The macro period is $D = 6a\sqrt{2}$. (b) The macro period is $D = 8a\sqrt{2}$. In that case the self-collimation effect appears in the slow light regime.

mesoscopic self-collimation frequency around a band gap edge by tuning the size of the macro period D. Figure 8 shows dispersion band diagrams and their associated group index for superlattices having a fixed $\alpha = 1$ but with two

distinct macro periods. New photonic band gaps originating from Bragg interferences open now in the frequency rang corresponding to the transparent window of the unbounded 2D PhC. It is seen that an additional forbidden band appears at the vicinity of the mesoscopic self-collimation frequency for $D = 8a\sqrt{2}$. In that case high group index of 30 to 50 can be found, enabling a slow light regime [12]. These results show that self-collimation can be combined with slow light in superlattices, a property unattainable with other PhC based devices.

5. Conclusions

Layered metamaterials provide a new way for beating light diffraction. We have shown that a mesoscopic self-collimation effect takes place at the scale of the macro period of the layered media thanks to a periodic focusing property that exactly balances diffraction. The dispersion curvatures seen by light during its propagation through consecutive layers plays a fundamental role in the self-collimation effect. This property being scale invariant, it is possible to play with the dispersive properties of metamaterials to render self-collimation resonant or to combine it with slow light. In the case of all-dielectric devices, 2D PhCs slab are shown to present negative curvature - allowing us to propose almost non etched superlattices presenting slow self-collimated light. These unique properties pave attractive perspectives to increase light-matter interaction in the diffraction-free regime.

Acknowledgement

This work is supported by the Agence Nationale pour la Recherche of France ($NT09\_517025$). The authors thank the Centre Informatique National de l'Enseignement Supérieur for its computing support.

References

[1] H. Kosaka, T. Kawashima, A. Tomita, M. Notomi, T. Tamamura, T. Sato, and S. Kawakami,
Self-collimating phenomena in photonic crystals,
Appl. Phys. Lett. 74: 1212-1214, 1999.

[2] I. Shadrivov, A. Sukhorukov, and Y. Kivshar,
Beam shaping by a periodic structure with negative refraction,
App. Phys. Lett. 82: 3820-3822, 2003.

[3] Z. Wang, H. Jiang, Y. Li, and H. Chen,
Enhancement of self-collimated fields in photonic crystals consisting of two kinds of single-negative materials,
Opt Express 18: 14311-14318, 2010.

[4] R. Pollés, E. Centeno, J. Arlandis, and A. Moreau,
Self-collimation and focusing effects in zero-average index metamaterials,
Opt Express 19: 6149-6154, 2011.

[5] V. Mocella, S. Cabrini, A. Chang, P. Dardano, L. Moretti, I. Rendina, D. Olynick, B. Harteneck, and S. Dhuey,
Self-Collimation of Light over Millimeter-Scale Distance in a Quasi-Zero-Average-Index Metamaterial
Phys Rev Lett 102: 133902-4, 2009.

[6] I. Nefedov and S. Tretyakov,
Photonic band gap structure containing metamaterial with negative permittivity and permeability,
Phys. Rev. E 66: 036611-4, 2002.

[7] J. Li, L. Zhou, C. Chan, and P. Sheng,
Photonic band gap from a stack of positive and negative index materials,
Phys. Rev. Lett. 90: 83901-4, 2003.

[8] D. Bria, B. Djafari-Rouhani, A. Akjouj, L. Dobrzynski, J. Vigneron, E. El Boudouti, and A. Nougaoui,
Band structure and omnidirectional photonic band gap in lamellar structures with left-handed materials,
Phys. Rev. E 69: 066613-10, 2004.

[9] Y. Yuan, L. Ran, J. Huangfu, H. Chen, L. Shen, and J. Kong,
Experimental verification of zero order bandgap in a layered stack of left-handed and right-handed materials,
Opt Express 14: 22202227, 2006.

[10] S. Kocaman, R. Chatterjee, N. Panoiu, J. Mcmillan, M. Yu, R. Osgood, D. Kwong, and C. Wong,
Observation of Zeroth-Order Band Gaps in Negative-Refraction Photonic Crystal Superlattices at Near-Infrared Frequencies,
Phys Rev Lett, 102: 203905-4, 2009.

[11] S. Kocaman, M. S. Aras, P. Hsieh, J. F. Mcmillan, C. G. Biris, N. C. Panoiu, M. B. Yu, D. L. Kwong, A. Stein, and C. W. Wong,
Zero phase delay in negative-refractive-index photonic crystal superlattices,
Nat Photonics 5: 17, 2011.

[12] J. Arlandis, E. Centeno, A. Moreau, J. Campos, O. Gauthier-Lafaye, and A. Monmayrant Mesoscopic self-collimation and slow light in all-positive index layered photonic crystals,
Phys. Rev. Lett 108: 037401-4, 2012.

[13] K. Vynck, E. Centeno, M. Le Vassor d'Yerville, and D. Cassagne,
Efficient light coupling from integrated single-mode waveguides to supercollimating photonic crystals on silicon-on-insulator platforms,
Appl. Phys. Lett. 92: 103128-3, 2008.

All-dielectric photonic metamaterials operating beyond the homogenization regime

K. V. Do[1], X. Le Roux[1], C. Caer[1], D. Morini[1], and L. Vivien[1], E. Cassan[1,*]

[1]Institut d'Electronique Fondamentale, Université Paris Sud –CNRS, bât. 220, 91405 Orsay, France
*eric.cassan.u-psud.fr

Abstract

Photonic metamaterials made of graded photonic crystals operating near the bandgap frequency region are proposed for field manipulation around λ=1.5µm. Proof-of-concept structures have been studied using Hamiltonian optics and FDTD simulation, fabricated, and characterized using far-field optical measurements. Experimental results are in good agreement with predictions, showing the interest of graded photonic crystals as an (ultra-low loss) alternative solution to the use of metamaterials combining dielectric and metallic materials with sub-wavelength unit cells.

1. Introduction

Controlling light trajectories and beam cross-sections of waves in slab optical structures has received a strong interest for some years. The main proposed approach is based on the use of metamaterials [1-4]. With the formalism of coordinate transformations, this method has led to several results showing the possibility to control the flow of electromagnetic fields in almost arbitrary shape waveguiding structures [5-10]. However, strongly anisotropic metamaterials with complicated permittivities and permeabilities are needed at optical wavelengths, while strong losses often appear due to the use of metals. This is why experimental results have been mostly obtained by reducing the goals to the use of all-dielectric structures, i.e. by using sub-wavelength dielectric structures to control the local average optical index of planar waveguides [11,12].

We present here another approach for the control of optical beams, which relies on strong index contrast (silicon on insulator: SOI) photonic crystals operating near the photonic bandgap and allows to: i) remove the use of metals, ii) operate with dielectric corrugation with periods around 400nm to lead to easier clean room fabrication.

Proof-of-concept structures made of one or several 90°-bends have been theoretically studied, designed, fabricated using e-beam lithography and ICP etching techniques, and optically characterized in the near infra-red around λ=1.5µm.

2. Design

To address light manipulation properties in the diffraction regime, it was decided to design a 90°-bending structure relying on a graded photonic crystal (GPhC) area. The considered structure is made of a two dimensional gradient of air hole filling factor in a square lattice photonic crystal with lattice constant a=390nm on the 260nm thick silicon film of SOI wafer. Hole radius of GPhC area varies in x-y coordinate by a function of $r/a(\rho)=0.35.\exp(-\rho^2/2R^2)$, where $\rho=\sqrt{(x^2+y^2)}$ is distance from the bottom left corner (0,0) point of GPhC area (zero point), as shown in Fig. 1, with R=62µm. The PhC lattice in considered configuration was rotated by 45° to minimize the incident angle around zero. Practically, in the GPhC area, the maximum value of holes radius is 136nm at zero point and hole radius is limited to 85nm for lattice points located above the distance 0.96R from the origin.

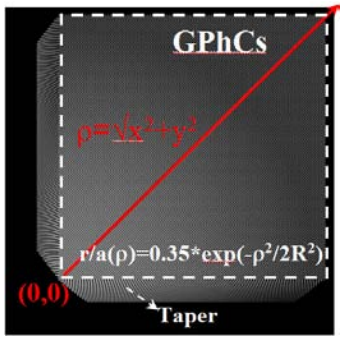

Figure 1: Graded photonic crystal (GPhCs) structure with two-dimensional chirp of air hole filling factor

The chosen configuration also includes two additional input and output tapering regions which are made of a two-dimensional chirp of the air hole radius and a one-dimensional chirp of the lattice period. The purpose of using these two tapers is to minimize the impedance mismatch for electromagnetic waves at the slab waveguides/GPhC interfaces and thus minimize the power reflection. Input light beam is chosen to be injected to the GPhCs area at the (x=0,y=R/2) incident point.

Within the proposed configuration, the photonic bandstructure (PBS) locally varies with in space due to the two-dimensional chirp of the structure. Fig. 2a shows the calculated PBS of a 2D PhC made of r/a=0.31 normalized radius (value of the air hole radius at the incident point) in a 2.95 index host material, and performed using the MIT Photonic Band (MBP) software. This index value was chosen as it corresponds to the effective index obtained for a

260nm thick silicon on insulator (SOI) slab waveguide at λ=1550nm for the TE light polarization. Fig. 2b presents the equi-frequency surfaces (EFSs) exploited in reciprocal space for the first band and obtained by considering again the photonic lattice at the incident point. Due to the strong periodic corrugation, EFSs departs for circles above the homogenization regime and turns into square shapes around the M points for a/λ approaching 0.20-0.22. The operating frequencies designed for the considered configuration are in the first TE band with normalized frequency a/λ around 0.25, near the bandgap between the first and second band where EFSs have circle-like shape, close to M point as seen in Fig. 2b.

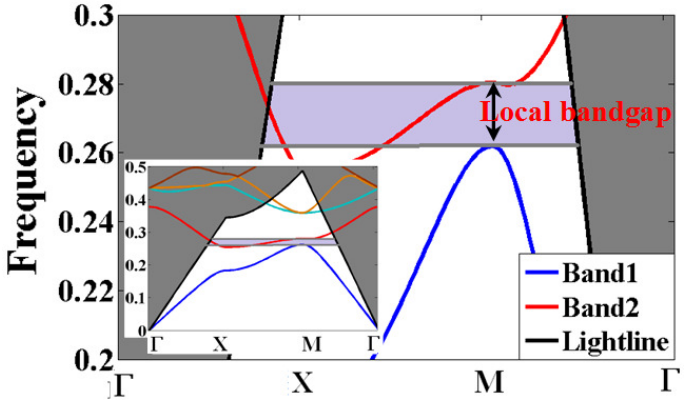

(a)

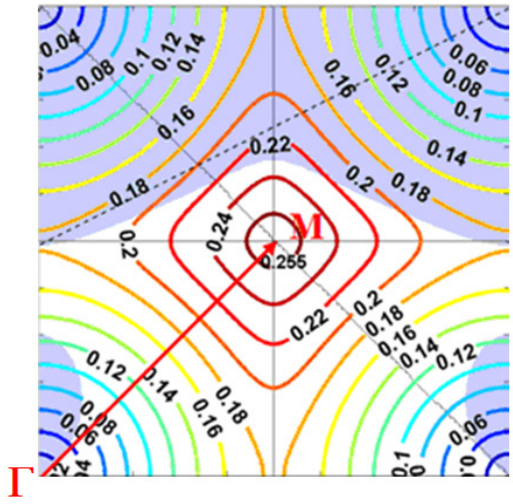

(b)

Figure 2: (a) Photonic bandstructure of the first band of a square lattice photonic crystal made of air holes with *r/a*=0.31 normalized radius (value to be considered at the incident light point) in TE light polarization, in a 2.95 effective index slab waveguide, and (b) Equi-Frequency Surfaces in a quarter of the first Brillouin area for the same band, with values of the normalized frequency a/λ..

Fig. 3(a) shows the simulated light path within the considered GPhC configuration using two-dimensional Finite-Difference Time-Domain (FDTD) method. In this simulation, a Gaussian beam waist of 7a (2.6μm) was used to excite the electric field in transverse electric (TE) polarization [13].

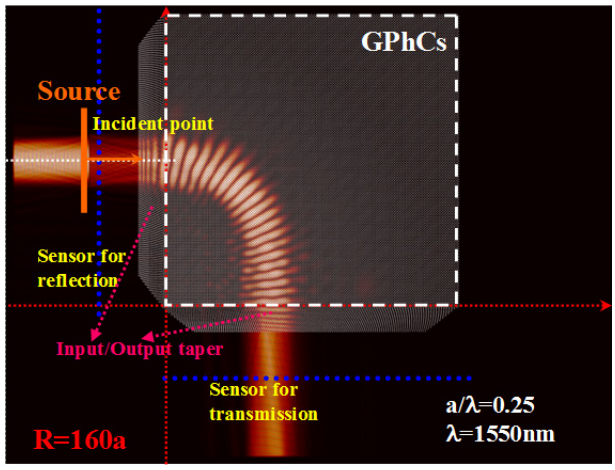

(a)

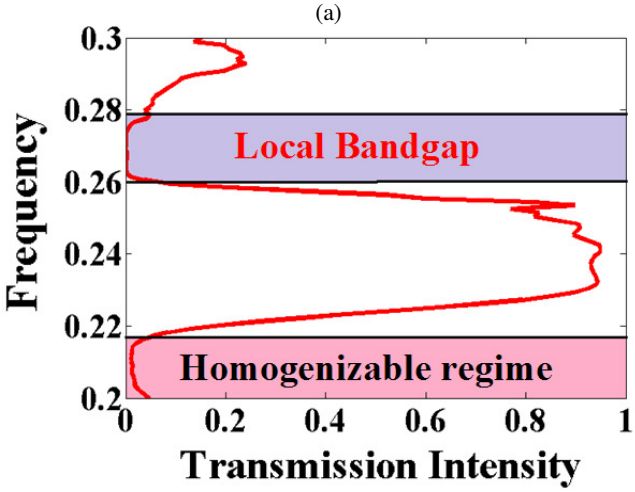

(b)

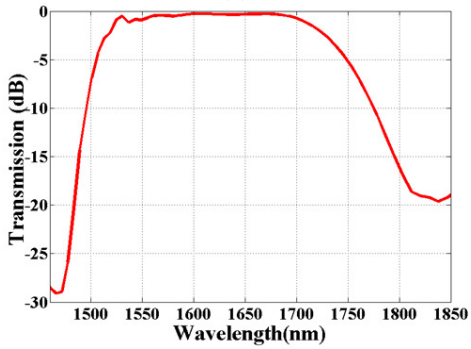

(c)

Figure 3: (a) Distribution of electric field at normalized frequency a/λ=0.25 inside the GPhC structure with input/output tapers, (b) and (c) Overall transmission spectrum of the studied configuration calculated using FDTD simulation as a function of frequency and wavelength, respectively.

As can be seen, after penetrating into the GPhC region, light path is bended to the right, i.e. towards the region of large radius air holes. Such a property could not be observed with a sub-wavelength corrugation of the photonic crystal area. The structure was designed to frequencies close to the bandgap between band 1 and band 2 but below the light line to minimize the out-off-plane losses. As can be seen in Fig. 3b, the calculated transmission is around 90% for the targeted operating frequencies (0.23-0.25). This transmission power was collected by the sensor for

transmission. A good agreement between the calculated transmission spectra in Fig. 3b and the band structure in Fig. 2a is obtained. For frequencies lower than 0.2, transmission power is almost zero, as at this frequency light tends to goes straight, whereas in the range of 0.26-0.28, frequency is inside the photonic bandgap between the first and second band, thus making the transmission power negligible.

Pursuing similar ideas, a for 4-channel demultiplexer configuration was designed by combining three 90°-bending structures, as shown in Fig. 4a. Fig. 4b presents the field steady-state maps obtained for four frequencies: 0.255, 0.25, 0.245 and 0.24, respectively. It clearly shows a left to right shift of the beam for decreasing frequencies. Within this configuration, the overall insertion loss is around -2dB for each of four channels and the crosstalk is around -10dB as seen in Fig. 4c.

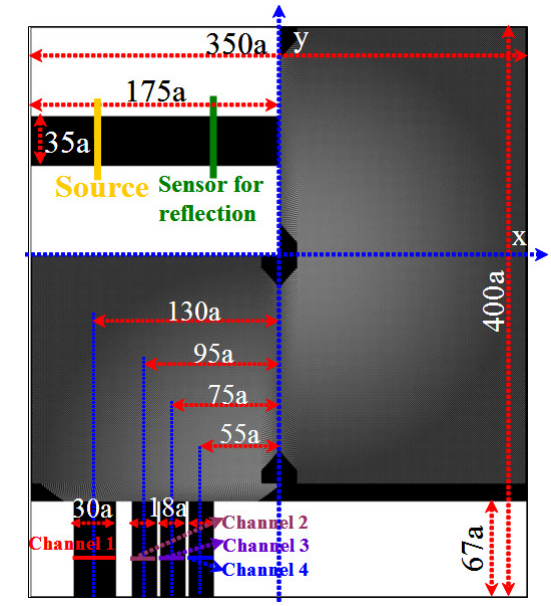

(a)

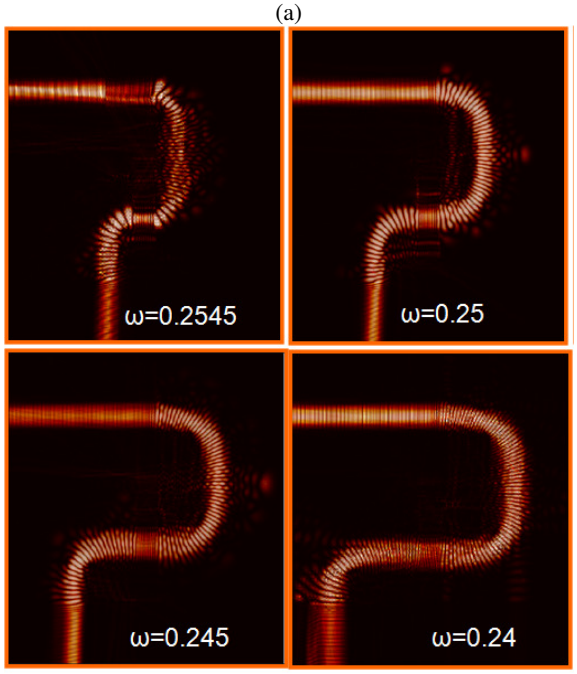

(b)

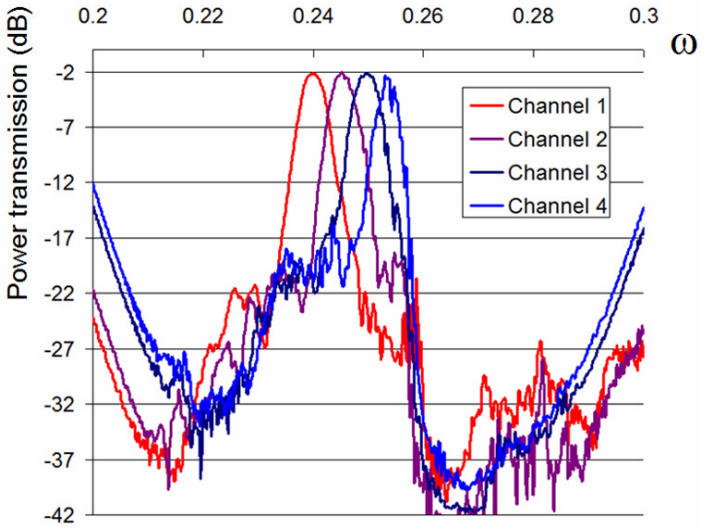

(c)

Figure 4: FDTD simulation of 270°-bending structure that allow the four-channel demultiplexers (a) Overview of the structure dielectric permittivity, (b) Steady-state Hz fields obtained for four frequencies ω=0.2545; 0.25; 0.245 and 0.24, respectively and (c) Calculated transmission at each output channel

3. Fabrication and experimental results

For fabrication, we turned back to simpler structures. Their processing contained two stages. Strip waveguides were first defined using a RAITH150 electron beam lithography process using negative resist. The GPhC structure was then separately insolated by mean of a lithography process with positive resist. The photoresist patterns were transferred to the 150nm thick top silica cladding layer using a reactive ion etching system, This layer served as mask to etch the silicon film through a SF_6/O_2 anisotropic etching process.

To give a better picture of the fabricated GPhCs devices, three SEM images are shown in Fig. 5a, 5b and 5c for the 90° bending structure, 90°-bending structure for 2-channel demultiplexer, and 270°-bending for 4-channel demultiplexer.

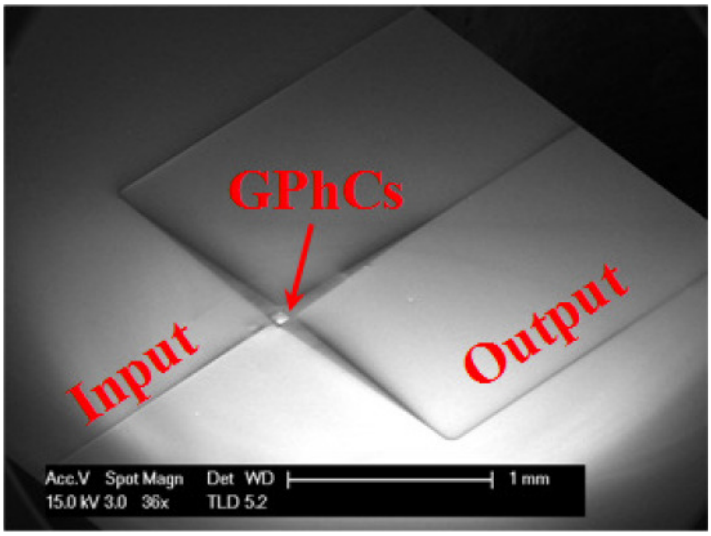

(a)

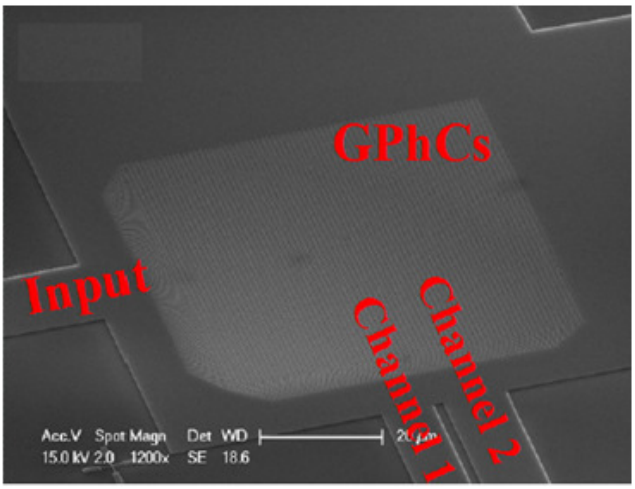

(b)

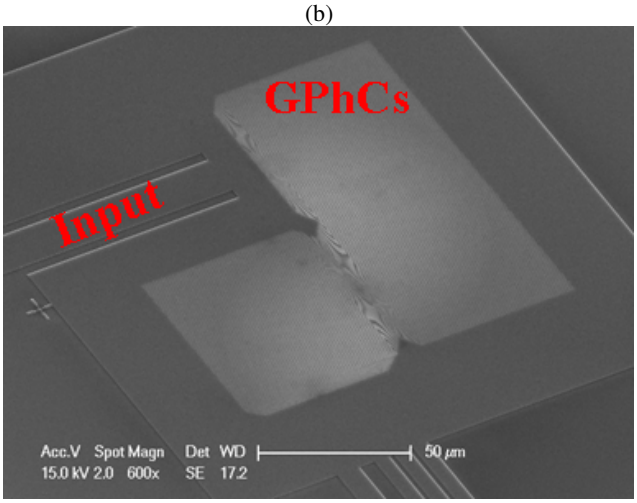

(c)

Figure 5: Scanning electron microscope images: (a) Overall view of studied GPhCs structure with input/output waveguides, (b) GPhCs with two output waveguides for two-channel demultiplexer, and (c) a 270°-bending configuration.

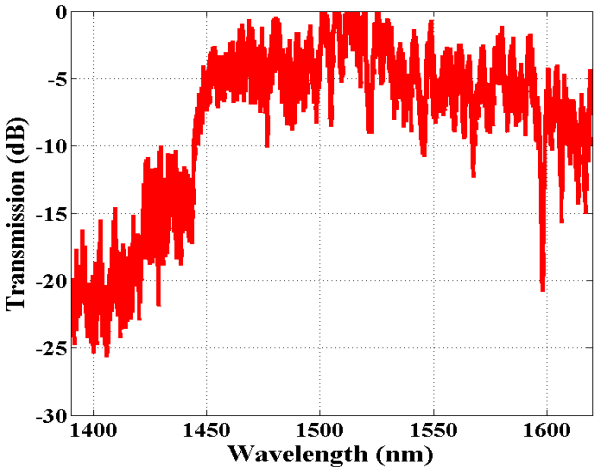

(a)

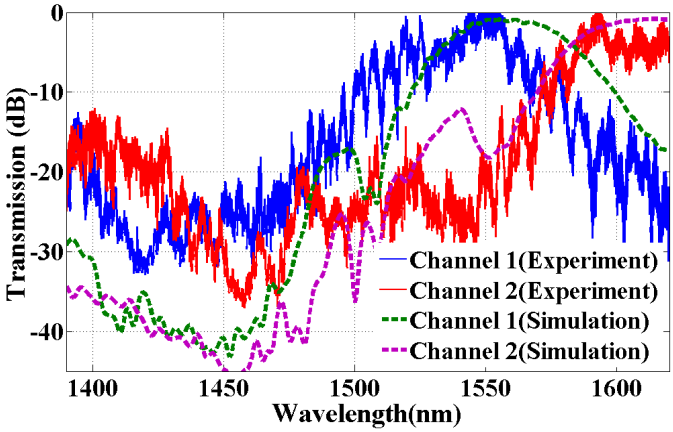

(b)

Figure 6: (a) Experimental overall transmission of studied GPhCs showing the 90°-bending effect at optical wavelength and (b) Operation of two-channel demultiplexer based on GPhCs channel 1: λ_1 = 1552nm and channel 2: λ_2 = 1616nm.

The fabricated devices have been characterized by using a tunable laser which gives a wide spectra band from 1390nm to 1620nm. Light was set to a polarization controller to provide TE polarization, then through an optical fiber at the entrance facet of structure, and coupled into the input a strip waveguide of 3µm width. The first output waveguide has a width of 90µm to cover all the GPhC area width, i.e. to collect the whole light power after the 90°-turn inside the PhC area. This output waveguide is then slowly reduced to 3µm width with a 1 mm transition length. A microscope objective was used to collect the output transmission power, and the signal was then used to measure the optical transfer function a MT9820A using optical component tester. To estimate the optical losses in fabricated GPhCs device, the measured results were normalized by the signal obtained in the normalization samples that has exactly the same dimensions and input/output beam conditions.

The normalized 90°-turn light transmission powers through the one and two output waveguides configurations, respectively, are shown in Figs. 6a and 6b . The observed ripples are due to Fabry-Perot resonances at the two edges of the sample. Fig. 6a shows that light is bended and transmitted through the GPhC area with low loss. It can be also seen that light bending occurs at slightly shorter wavelengths that predicted using FDTD simulation, and that the band width is smaller in comparison with the simulation result (see Fig. 3c). This wavelength shift and the bandwidth constrain can be understood by the fact that 2D simulation was done with the effective index approximation [15].

Results of Fig. 6b show a correct agreement between experiments and simulation, with again a slight wavelength blue-shift, just like already pointed out. Two centered wavelengths of the demultiplexer are well separated and then collected at two output channels with low loss (<2dB) and low crosstalk (less than -20dB).

4. Conclusions

In order to explore the possibility of light manipulation by photonic metamaterials, a graded photonic crystal relying on an all-dielectric structure to minimize the optical losses has been chosen and studied. The structure was designed to work in the diffraction regime, thus enabling the reconfiguration of the light paths by wavelength tuning and facilitating the technological fabrication if compared with sub-wavelength structures.

The obtained experimental results are in good agreement with the predictions performed using the equations of Hamiltonian optics and Finite-Difference Time-Domain simulations [13,14,15]. They show the low level of optical loss in the fabricated graded photonic crystal structure (~2dB). As a whole, the reported results open opportunities for light manipulation and applications in photonic circuits using a combination of unusual dispersive phenomena in PhCs and additional degrees of freedom brought by a generalized two-dimensional chirp of PhCs lattice parameters. This is also an alternative solution to the use of photonic metamaterials combining dielectric and metallic materials with sub-wavelength unit cells.

Acknowledgements

The authors thank the French National Research Agency (ANR).

References

[1] D. R. Smith, J. B. Pendry and M. C. K Wiltshire, Metamaterials and negative refactive index, *Science*, Vol. 305, pp.788-792, 2004.

[2] J. B. Pendry, D. Schurig and D. R. Smith, Controlling electromagnetic field, *Science*, Vol. 312, 1780-1782, 2006.

[3] Nader Engheta, Richard W. Ziolkowski, Metamaterials: Physics and engineering explorations, *Science*, John Wiley and Sons, 211-221 (2006).

[4] Zouhdi, Saïd; Ari Sihvola, Alexey P. Vinogradov, Metamaterials and Plasmonics: Fundamentals, Modelling, Applications. *New York: Springer-Verlag*. 3-10, Chap. 3, 106, 2008.

[5] Alexander V. Kildishev and Vladimir M. Shalaev, Engineering space for light via transformation optics, *Optics Letters*, Vol. 33, N°1, 43-45, 2008.

[6] Marco Rahm, Steven A. Cummer, David Schurig, John B. Pendry and David R. Smith, Optical design of reflectionless complex media by finite embedded coordinate transformations, *Physical Review Letters*, Vol. 100, 063903-063906, 2008.

[7] M. Rahm, D. A. Robert, J. B. Pendry and D/ R. Smith, Transformation-optical design of adaptive beam bends and beam expanders, *Optics Express*, Vol. 16, N°15, 11555-11567, 2008.

[8] Zhong Lei Mei and Tie Jun Cui, Arbitrary bending of electromagnetic waves using isotropic materials, *Journal of Applied Physics*, Vol. 105, 104913-104917, 2009.

[9] Nathan I. Landy and Willie J. Padilla, Guiding light with conformal transformations, *Optics Express* Vol. 17, N°17, 14872-14879, 2009.

[10] Weiqiang Dign, Donghua Tang, Yan Liu, Lixue Chen and Xiudong Sun, Arbitrary waveguide bends using isotropic and homogeneous metamaterial, *Applied Phys. Lett.*, Vol. 96, 041102-041104, 2010.

[11] Jason Valentine, Jensen Li, Thomas Zentgraf, Guy Bartal and Xiang Zhang, An optical cloak made of dielectrics, *Nature Materials*, Vol. 8, 568-571, 2009.

[12] Lucas H. Gabrielli, Jaime Cardenas, Carl B. Poitras and Michal Lipson, Silicon nanostructure cloak operating at optical frequencies, *Nature Photonics*, Vol. 3, 461-463, 2009.

[13] E. Cassan, K. V. Do, C. Caer, D. Marris-Morini and L. Vivien, Short-Wavelength Light Propagation in Graded Photonic Crystals, *Journal of Lightwave Technology*, Vol. 29, N°13, 1937-1943, 2011.

[14] K. V. Do, X. Le Roux, C. Caer, D. Marris-Morini, N. Izard, L. Vivien and E. Cassan, Wavelength Demultiplexer Based on a Two-Dimensional Graded Photonic Crystal, *Photonics Technology Letters*, Vol. 23, N°15, 1094-1096, 2011.

[15] Khanh-Van Do, Xavier Le Roux, Delphine Marris-Morini, Laurent Vivien, and Eric Cassan, Experimental demonstration of light bending at optical frequencies usisng a non-homongenizable graded photonic crystal, *Optics Express*, Vol 20, Issue 4, 4776-4783, 2012.

Asymmetric transmission without breaking time reversal symmetry: anomalous diffraction vs polarization conversion

Andriy E. Serebryannikov[1]

[1]Hamburg University of Technology, E-3, D-21071 Hamburg, Germany
E-mail: serebryannikov@tu-harburg.de

Abstract

The diffraction inspired and polarization conversion based mechanisms of the strongly asymmetric reciprocal transmission are compared and attempted to be seen from the point of view of the unified multichannel (multiport) theory. The corresponding performances can be based on either photonic crystals or (quasi) planar arrays of meta-atoms that are made of linear isotropic materials. Realizable transmission regimes, conditions of existence, and peculiarities of design are discussed.

1. Introduction

Diodes and isolators belong to the most important components that are required in various microwave and optical circuits. Searching for the possibility of the obtaining of a diode-like unidirectional transmission without breaking time reversal symmetry, i.e., without using anisotropic or nonlinear materials, has been the focus of interest for many years. Formally, nonreciprocal transmission could also be considered as the asymmetric one, if forward and backward transmittances are distinguished. In this paper, we follow the terminology, according to which the term *asymmetric transmission* means a type of reciprocal transmission with different forward and backward transmittances, at the same excitation applied to the both sides of the structure. It is distinguished from the nonreciprocal transmission that is associated with the effect of anisotropic and nonlinear constituents. Today, at least two mechanisms of the asymmetric transmission are known in the structures that contain isotropic and linear constituents only. In fact, they need either anomalous redistribution of the incident-wave energy in favor of higher diffraction orders [1,2], or rather strong polarization conversion [3,4]. In this paper, similarities and differences of these two mechanisms are discussed. The emphasis will be put on the operation regimes with transmittance being high in one direction and nearly zero in the opposite direction.

As known, the spatial inversion symmetry breaking, e.g., structural asymmetry of the slab with respect to the midplane, is a necessary condition for obtaining asymmetric transmission. Slabs of photonic crystals (PC) with one-side corrugations known as the nonsymmetric PC gratings [1] and gratings that are made of ultralow-index materials (ULIM) [2] are the perfect candidates for the obtaining of the diffraction inspired asymmetric transmission. In these structures, unidirectional transmission, i.e., a significant transmission at the corrugated-side illumination and a vanishing transmission at the opposite-side illumination can be obtained due to that the coupling conditions for higher orders are different at the two sides. Double-layer arrays that contain metallic elements designed to show chirality are associated with the polarization conversion based mechanism of asymmetric transmission. Indeed, the cross-polarized components of transmission can appear for a linearly polarized incident wave, which are seen as asymmetric ones, provided that the incident wave has the same polarization at the front-side and the back-side illumination. It will be shown that these two mechanisms can be considered as the counterparts of the unified mechanism of asymmetric transmission. Clearly, each of them has its own advantages and disadvantages, depending on the application. The common problem that often remains unsolved is obtaining of (nearly) total transmission in one direction. Thus, numerical results will be presented for the structures that fulfill this requirement in the best way.

2. Diffraction Inspired Asymmetry

First, let us discuss the basic features of the diffraction inspired mechanism of asymmetric transmission. If the incident wave is linearly polarized, all the waves involved into diffraction keep the same polarization. For this mechanism, zero order must be not coupled to Floquet-

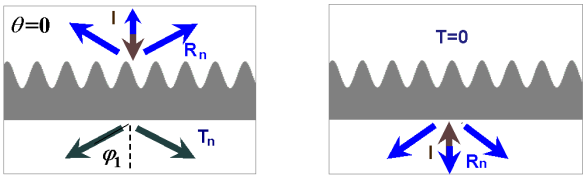

Figure 1: Beam diagrams illustrating the diffraction inspired unidirectionality at normal incidence, θ=0, when two higher orders are coupled to a Floquet-Bloch wave at the corrugated interface; left – corrugated-side illumination, right – noncorrugated-side illumination; brown arrows – incident beam (I), navy arrows – transmitted beams (Tn), and dark-blue arrows - reflected beams (Rn).

Bloch wave(s) in the PC, while the conditions of coupling for higher orders must be different at the two interfaces due to the different periods.

Figure 1 presents the beam diagram that is associated with the unidirectional splitting regime [1]. It may correspond to any shape of the equifrequency dispersion contours (EFCs), for which there is no coupling when the tangential wave vector k_x=0, in contrast to a certain range of variation of $|k_x|>kb$. This regime can be realized, for example, in one-dimensional PCs with hyperbolic dispersion, or two-dimensional square-lattice PCs with EFCs located around M or X points. Then, some higher orders may be coupled to a Floquet-Bloch wave of the PC in a one-way manner, while zero order is uncoupled regardless of the illumination side, provided that the corrugation periods at

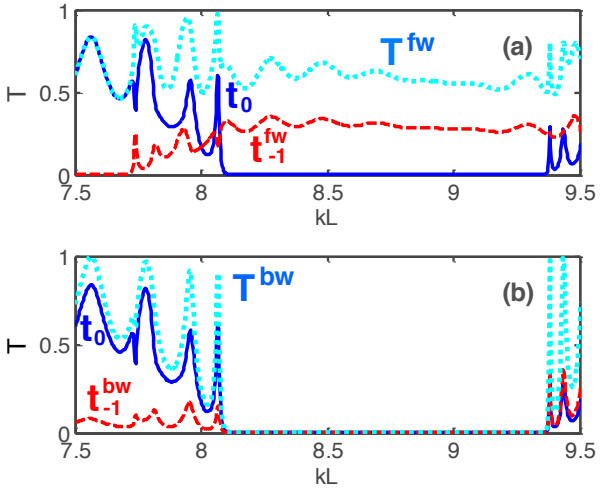

Figure 2: Transmission for PC grating with one-side corrugations obtained by removing every second rod from one of the interface layers of a square-lattice PC composed of twelve layers of dielectric rods with permittivity ε=5.8 and rod-diameter-to-lattice-constant ratio d/a=0.4 at θ=0: plot (a) – corrugated-side illumination, plot (b) – noncorrugated-side illumination.

the two sides are different. Choosing a proper period at one of the interfaces and remaining the other one without additional corrugations, one can obtain the situation when the first-order transmission appears in the forward case, i.e., at the corrugated-side illumination ($t_{-1}^{fw}=t_{+1}^{fw}>0$, $t_0^{fw}=0$), while transmission is blocked in the backward case, i.e., at the noncorrugated-side illumination ($t_{-1}^{bw}=t_{+1}^{bw}=t_0^{bw}=0$). An example is presented in Fig. 2 at the TE-polarized plane incident wave. The range of unidirectional transmission extends here from kL=8.1 to kL=9.37 (grating period $L=2a$, a is lattice constant), where $T^{fw}>0.57$ while $T^{bw}\approx 0$.

Figure 3 shows the beam diagram for the single-beam unidirectional deflection regime [1]. It needs rather arbitrary EFC shapes, among which narrow circular EFCs around Γ point are simplest. The lattice and corrugation parameters can be chosen so that the forward transmission can be significant thanks to the coupling of the first negative order ($t_{-1}^{fw}>0$), while there is no backward transmission ($t_{-1}^{bw}=t_0^{bw}=t_0^{fw}=0$). Figure 4 presents an example of the transmission spectrum in TE-case. The range of unidirectional transmission extends here from kL=7.12 to kL=7.44, where $T^{fw}>0.6$ at the Fabry-Perot type maxima, while $T^{bw}\approx 0$. It is worth noting that the circular EFCs can be obtained by using an ULIM instead of a PC. Hence, unidirectional transmission that is similar to Fig. 4 can be obtained in an ULIM grating [2].

The known performances of the PC and ULIM gratings for unidirectional transmission suffer of a rather large thickness, which is typically no less than three free-space wavelengths. Very recently, the new design has been proposed, which is based on the stacked hole array that shows extraordinary transmission and is assembled with a grating at one of the interfaces, so that the thickness is less than one wavelength [5]. In the general case, design of the structures for the diffraction inspired unidirectional transmission should be based on a compromise between thickness, transmission efficiency, and bandwidth.

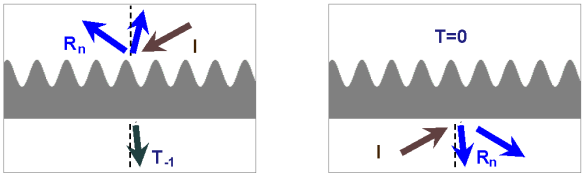

Figure 3: Same as Fig. 1, but at θ>0, in case when a single higher order is only coupled to a Floquet-Bloch wave at the corrugated interface.

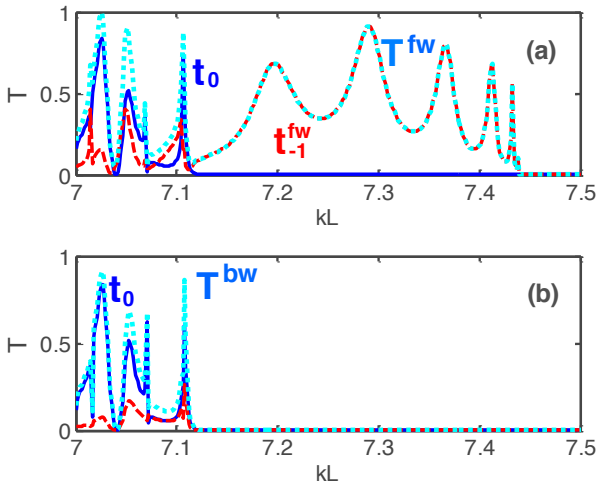

Figure 4: Same as Fig. 2, but at θ=30 degrees.

3. Asymmetry Based on Polarization Conversion

In contrast to PC and ULIM gratings, where asymmetric transmission is necessarily connected with the effect of higher diffraction orders, (quasi)planar arrays of the specially designed meta-atoms allow a desired polarization

manipulation, which can also result in strong asymmetry in transmission. If such an array is illuminated by a TE-polarized wave from the front side, one can obtain a transmitted wave with the dominant contribution of the TM-polarized (cross-polarized) component. However, if it is illuminated with the plane wave of the same polarization from the back side, transmission can be zero, that does not contradict with the reciprocity principle [4].

In line with the Jones matrix approach, in the forward transmission case, the electric field amplitudes of the incident wave (I_x^{fw} , I_y^{fw}) and transmitted wave (T_x^{fw} , T_y^{fw}) are connected to each other for the considered type of symmetry as follows [4]:

$$\begin{pmatrix} T_x^{fw} \\ T_y^{fw} \end{pmatrix} = \begin{pmatrix} \alpha & \beta \\ \gamma & \alpha \end{pmatrix} \begin{pmatrix} I_x^{fw} \\ I_y^{fw} \end{pmatrix}, \qquad (1)$$

where $\alpha = T_{xx}^{fw} = T_{yy}^{fw}$, $\beta = T_{xy}^{fw}$, and $\gamma = T_{yx}^{fw}$. In turn, in the backward case, one obtains

$$\begin{pmatrix} T_x^{bw} \\ T_y^{bw} \end{pmatrix} = \begin{pmatrix} \alpha & -\gamma \\ -\beta & \alpha \end{pmatrix} \begin{pmatrix} I_x^{bw} \\ I_y^{bw} \end{pmatrix}. \qquad (2)$$

According to (1) and (2), if $I_x^{fw} = I_x^{bw} = 0$, $I_y^{fw} = I_y^{bw} \neq 0$, and $\alpha = 0$, transmission is possible only due to the cross-polarized terms, i.e., $\beta \neq 0$ and $\gamma \neq 0$. This can lead to strong asymmetry in transmission, provided that β and γ are strongly distinguished. Thus, the design strategy should be based on suppression of the co-polarized transmission and making the difference between the cross-polarized terms as strong as possible.

Figure 5 presents an example, in which the relative sizes of L and I elements are close to those in Figs. 1, 2 in Ref. 4, but the physical sizes are rescaled to use at THz frequencies. For the sake of definiteness, we refer to the case when illumination is from the side of I elements as the forward transmission. In turn, when illumination is from the side of L elements, it is referred to as the backward transmission. The structure is illuminated with a TE-polarized plane wave (E field vector is along y axis), which corresponds to $I_y^{fw} = I_y^{bw} = 1$ and $I_x^{fw} = I_x^{bw} = 0$ in (1) and (2). In the vicinity of f=0.9THz, $T_{yy}^{fw} = T_{yy}^{bw}$ and T_{yx}^{fw} show the dips. However, T_{yx}^{bw} remains rather large, leading to that the backward transmission is substantially larger than the forward one. The transmitted wave shows elliptical polarization with a big difference between the axes, making this case rather close to that of linear polarization. In turn, the co-polarized terms dominate at f=0.6THz and f=1.15THz.

Figure 6 presents one more example. The main structural and symmetry features are similar to the design used in [6] as starting point, but sizes are chosen now to be consistent with those in Fig. 5. In other words, the array that consists of the meta-atoms shown in Fig. 5 can be obtained from that in Fig. 6 by transforming the U-shaped resonators (USRs) into L elements and rotated USRs into I elements. In Fig. 6, T_{yx}^{fw} is substantially larger than $T_{yy}^{fw} = T_{yy}^{bw}$ in the vicinity of two frequencies, f=0.95THz and f=1.05THz. Furthermore, since T_{yx}^{bw} is well suppressed, at least if f is varied from 0.96THz to 1.1THz, asymmetry manifests itself also in that the polarization at the backward

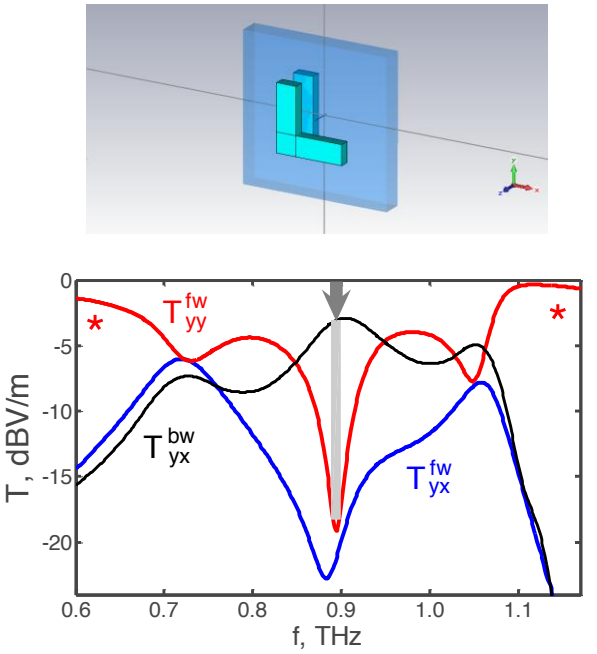

Figure 5: Transmission vs frequency for an infinite array of L-I type metaatoms; forward – illumination from the side of I-interface, backward – illumination from the side of L-interface; arrow and asterisk denote regimes of asymmetric and symmetric transmission, respectively.

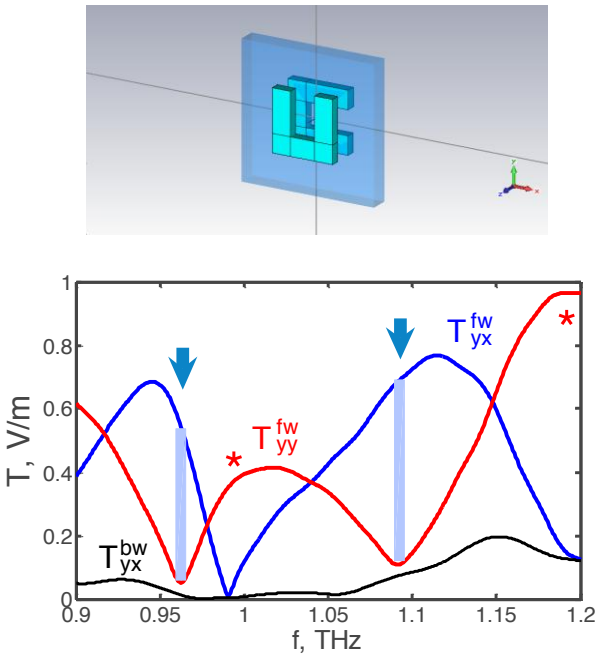

Figure 6: Same as Fig. 5, but for meta-atoms representing an USR – rotated USR pair.

transmission remains nearly linear within a wide range of variation in f, while that at the forward transmission is elliptical being close to a linear one at certain frequencies only. Note that the diffraction-free transmission can be achieved in very thin chiral structures. For example, the total thickness of the structure in Fig. 6 at 1THz is $\lambda/5$. A proper choice of topology of a unit cell and symmetry properties is very important for this mechanism.

4. Unified Multichannel Theory

The unified theory of asymmetric transmission in reciprocal structures can be built based on the multi- channel (multiport) transmission concept. Figure 7 presents three examples that illustrate possible scenarios of asymmetric transmission. The incident, transmitted, and reflected waves are shown in the forward transmission case in the same color. The same remains true in the backward transmission case. Plots (a) and (b) correspond to the diffraction inspired

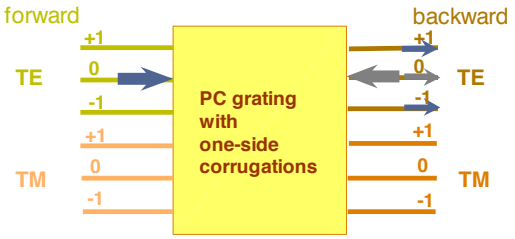

(a)

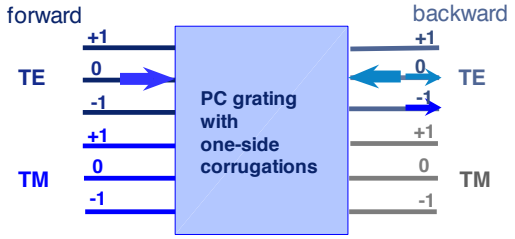

(b)

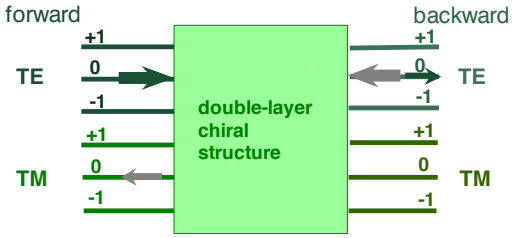

(c)

Figure 7: On the multichannel (multiport) interpretation of asymmetric transmission: (a) case of PC grating in Figs. 1,2; (b) case of PC grating in Figs. 3,4; (c) case of meta-atom arrays in Figs. 5.6.

asymmetric transmission. The difference between these two scenarios is that the latter can be realized using PCs/media with EFCs that are narrower than in air, at nonzero angles of incidence [1,2], like in Figs. 3,4, while the former can be obtained at normal incidence if EFCs are absent in the vicinity of zero tangential wavenumber [1], like in Figs. 1,2. Plot (c) corresponds to a diffraction-free scenario (all higher orders are evanescent) that is relevant to polarization conversion. It is similar to that demonstrated for the two chiral structures in Sec. 3. Indeed, the ideal case is assumed in Fig. 7(c), i.e., when the co-polarized transmission terms are zero, while all the incident-wave energy is transformed to the cross-polarized term in a one-way manner. This case is partially similar to that observed in the vicinity of 0.9 THz in Fig. 5. Note that polarization being closer to linear one than that in Figs. 5,6 might be obtained by using optimization. Combination of the polarization and diffraction relevant scenarios is also possible (not presented).

5. Conclusions

The diffraction inspired and polarization conversion based mechanisms of asymmetric reciprocal transmission have been compared. Their common feature is, in fact, that at least one additional transmission channel is required to compensate for the lack of anisotropic or/and nonlinear components. For the former mechanism, such a channel can occur due to a higher diffraction order. In this case, all the waves keep the same linear polarization. For the latter mechanism, such a channel is connected with the appearance of strong cross-polarized terms in transmission. In this case, ultrathin designs are possible. Strong asymmetry appears in transmission as a result of extreme redistribution of the incident-wave energy in favor of these new transmission channels.

Acknowledgements

This work has been supported by Deutsche Forschungsgemeinschaft under Project Nos., SE1409/2-1 and SE1409/2-2; the author thanks Prof. E. Ozbay and M. Mutlu, Bilkent University, Ankara for fruitful discussions.

References

[1] A.E. Serebryannikov, One-way diffraction effects in photonic crystal gratings made of isotropic materials, *Phys. Rev. B* 80: 155117, 2009.

[2] A.E. Serebryannikov and E. Ozbay, Unidirectional transmission in non-symmetric gratings containing metallic layers, *Opt. Express* 17: 13335-13345, 2009.

[3] V.A. Fedotov, P. L. Mladyonov, S. L. Prosvirnin, et al., Asymmetric propagation of electromagnetic waves through a planar chiral structure, *Phys. Rev. Lett.* 97: 167401, 2006.

[4] C. Menzel, C. Helgert, C. Rockstuhl, et al., Asymmetric transmission of linearly polarized light at optical metamaterilas, *Phys. Rev. Lett.* 104: 253902, 2009.

[5] M. Beruete, M., V. Torres, M. Navarro-Cia, A. E. Serebryannikov, and M. Sorolla, Using extraordinary transmission metamaterial in compact diode-like unidirectional device, submitted to *META'12*.

[6] X. Xiong, W.-H. Sun, Y.-J. Bao, et al., Construction of a chiral metamaterial with a U-shaped resonator assembly, *Phys. Rev. B* 81: 075119, 2010.

Hydrothermal Synthesis of ZnO nanorods and its application to photosensor

L.S. Chuah[1*], Y. Sivalingam[2], C. D. Natale[2], C. Falconi[2]

[1]Physics Section, School of Distance Education, Universiti Sains Malaysia, 11800 Minden, Penang, Malaysia.
[2]Department of Electronic Engineering, University of Rome Tor Vergata, Via del Politecnico 1, 00133 Roma, Italy.
Email: chuahleesiang@yahoo.com

Abstract

ZnO nanostructures furnish a track to a modern creation of devices. In this work, vertically zinc oxide (ZnO) nanorods have been strongly synthesized through an uncomplicated hydrothermal process on silicon substrates without the aid of a catalyst. Silicon substrate with seed layer was then vertically inserted into the aqueous precursor solution. The as-synthesized ZnO nanowires have diameters between 100-140 nm and lengths around 1 μm. It exhibits a stable UV emission at around 382 nm. The current-voltage (I-V) characteristics of platinum (Pt) ZnO nanorods photosensor under dark and illumination conditions was studied. The ideality factor (*n*) and Schottky barrier height (*SBH*) were ascertained by the I-V method. Well-defined response to UV illumination in the forward-biased state because of the photogeneration of further electron–hole pairs.

1. Introduction

During the past few years, there has been a growing attention in aligned one-dimensional (1-D) ZnO nanomaterials (nanobelts, nanotubes, nanorods and nanowires) for their dormant uses in fabricating nanoelectronic, nanophotonics, self-powdered nanosystems, optoelectronic devices, ultraviolet (UV) laser, new generation solar cells energy conversion, LEDs, high efficient chemical sensor, piezoelectric field effect transistors and nanogenerators [1-4].

Until the present time, many ZnO nanostructures have been fabricated with wires, rods, tubes, and walls. As the large surface to volume ratio of nanowires, surface plays vital function to ascertain its properties. The nanowires strengthen the novel electrical properties and optical characteristics of materials [5-7]. Quantum confinement effect because of the switch in nanoscale, shape and structure of semiconductor nanoparticles can alter the energy bands of the semiconductors and insulating oxide materials.

In recent years, ZnO nanostructures have been growth by many methods, for example thermal evaporation, vapor-phase transport process, hydrothermal, electrochemical deposition, alumina templates, metal organic chemical vapor deposition, etc [8-10]. Hydrothermal method is necessary due to its easy, simplicity, low synthesis temperature, low cost, uncomplicated routes and good prospect for large scale production [11,12]. In the hydrothermal preparation, where the water is utilized as the reaction solvent. Pressed down by hydrothermal circumstances, numerous starting materials can go through truly unpredicted reactions that are always followed by the synthesis of nanomaterial morphologies that are not approachable by classical techniques [13-15].

In view of silicon is low-cost and potential for integration with Si-based microelectronics devices, it is desirable to fabricate high quality ZnO nanoscale material on Si substrates. In this study, we study an uncomplicated route to fabricate ZnO nanorods on silicon substrate under hydrothermal conditions. The morphology and optical property of the ZnO nanorods are distinguished and its application as photosensor is discussed.

2. Experimental

ZnO nanowires were synthesized using a hydrothermal method on silicon (Si) substrate [1]. The ZnO seed layer solution was prepared using 0.005 M zinc acetate dehydrates dissolved in 50 ml absolute ethanol. For the purpose of enhance the wetting of the seed layer on silicon substrates, the substrates were illuminated by UV lamp for 20 min. The formation of the seed layer on silicon substrate was conducted via drop coating technique.

A seed layer is vital in the synthesis of aligned vertical nanorods as the seed will perform to lower the nucleation barrier. After ZnO seed layer coating on the silicon substrates, the substrates were post annealed in air at 400 ^{o}C for 30 min. Silicon substrates with seed layer were then vertically inserted into the aqueous precursor solution.

Then ZnO nanorods were grown on the seed layer using hydrothermal method in 0.025M aqueous precursor solution of zinc acetate dehydrate ($Zn(Ac)_2.2H_2O$, Sigma-Aldrich, 99%) and hexamethyltetramine (HMTA, Sigma-Aldrich, 99%) dissolved in 200 ml deionized water at low temperature (90^{o}C) for 4 hours. After nanorod growth, the substrate was separated from the chemical dissolvent, accompanied by rinsing with DI water, and followed by dried in air. The length of ZnO nanowires can be self restrained by the number of repetitive chemical reaction and time parameters.

The morphologies and nanostructures of the as-synthesized ZnO nanowires were studied by field emission scanning electron microscopy (FE-SEM). At room temperature, the dependent photoluminescence (PL) spectra are acquired using the 325 nm line of a He–Cd laser.

For the wafer wet leaning process previous to metallization of the contact metal layer, the ZnO nanorods samples were immersed in a 1:20 $NH_4OH:H_2O$ solution for 5 s followed by dip in a 1:50 $HF:H_2O$ solution [16]. Afterthat, it was cleaned with distilled water and blown dry with a nitrogen gas blower. The (Pt) Schottky contacts were coated by sputtering system with a metal mask in patterning of the contact structure. Pt is utilized as the Schottky contact metal for all the fabricated devices because of its high metal work function.

MSM photodiode is a plane designs correspond to two fork-shaped interdigitated contacts oppositely laying on the semiconductor exterior surface. These contacts functions as back to back Schottky contacts with fingers width of 230 μm, finger spacing of 400 μm, and the length of each electrode was about 3.3 mm. It consists of 4 fingers at each electrode [17].

Photocurrent and dark current of the fabricated photodiodes were then measured by Keithley high-voltage-source-measure-unit model 237-semiconductor parameter analyzer [18]. The ideality factors (n) and effective Schottky barrier heights (SBHs) are deduced from I-V measurement assuming the results can be described by the standard thermionic-emission equation [19].

3. Results and Discussion

The morphology of the hydrothermal sample was observed by field emission scanning electron microscope (FE-SEM). They exhibits a tendency to grow perpendicular to the silicon surface. ZnO nanorods with diameters of 100-140 nm with a narrow wire-wire distance can be seen in Figure 1. No other nanostructures are obtained except for the ZnO nanorods, it exhibiting the high purity. The SEM images perceptibly exhibit that uninterrupted nanorods can be grown on the silicon substrate surfaces with high density.

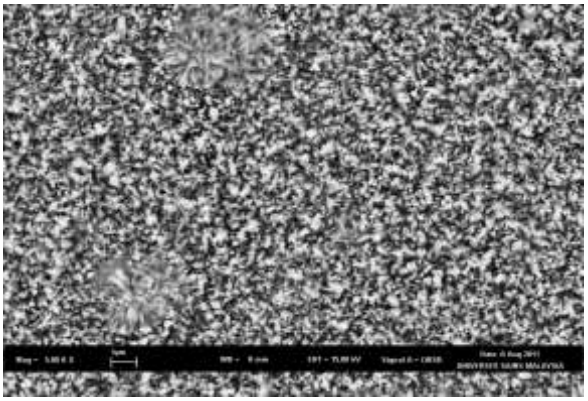

Figure 1: ZnO nanowires grown on a silicon surface.

The sharp crystallographic planes of the hexagonal shaped nanowires can be obviously identified, providing firm evidence that the ZnO nanowire orientate parallel with the *c*-axis. One of the most satisfactory features of SEM analysis is energy dispersive X-rays analysis (EDX). Figure 2 is the EDX spectrum compiled from the nanorods. The observed peaks similar to Zn and O, displaying that the nanorods are consisting of Zn and O only.

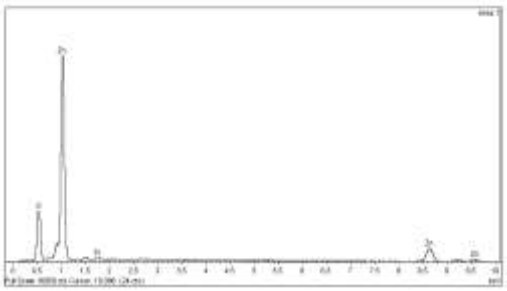

Figure 2: The corresponding EDX spectrum of the ZnO nanorods.

A Photoluminescence (PL) spectrum of the as-synthesized ZnO nanorods is shown in Figure 3 was derived at room temperature. The results show that an intense ultraviolet emission at 382 nm and a small blue-green band. The low blue emission presumably outcomes from the deep-level imperfection [20].

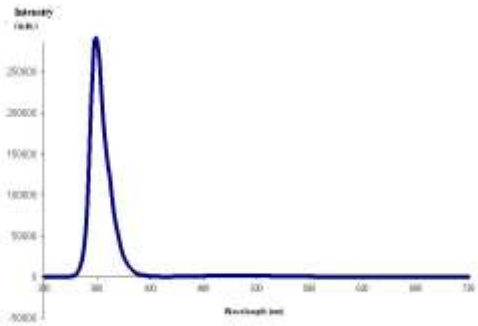

Figure 3: The near band edge PL spectra of ZnO nanorods.

Platinum (Pt) is an attractive metal that has been applied as stable Schottky contact of wide bandgap ZnO with superior thermal and chemical stabilities. A Schottky contact behaviour can be more strictly elucidated by the formal statement of equivalence which attains into account the barrier height lowering because of the electric field, tunneling effects, interfacial layer, and carrier recombination in the space charge region of the metal-semiconductor contact as contributed by [21-23]

$$I = I_0 \exp(eV / nkT)[1 - \exp(-eV / kT)] \quad (1)$$

where I is the current, V is the bias voltage, k is the Boltzmann constant, T is the absolute temperature, and n is the ideality factor. The expression for the saturation current, I_0 is

$$I_0 = SA^*T^2 \exp(-e\Phi_b / kT) \qquad (2)$$

where S is the contact area, A^* is the effective Richardson constant, and Φ_b is the Schottky barrier height. Equation (1) can also be written in the form of

$$\frac{I\exp(eV/kT)}{\exp(eV/kT)-1} = I_0 \exp(eV/nkT) \qquad (3)$$

At $T \leq 370$ K and when $V \leq -0.5$ V, equation (3) can be simplified to

$$I\exp(eV/kT) = I_0 \exp(eV/nkT) \qquad (4)$$

$$\ln [\, I\exp(eV/kT)\,] = \ln I_0 + eV/nkT \qquad (5)$$

The plot of $ln\ [\, I\exp(eV/kT)\,]$ vs V should give a straight line with the slope = e/nkT and y-intercept at $\ln I_0$. Using equation (2), the ideality factor (n) and Schottky barrier height (*SBH*) were determined by the *I-V* method. Using equation (2) and the theoretical value of A*, under dark condition, the Schottky barrier height derived by the I-V method is 0.49 eV. According to Bardeen at. al., the barrier height did not consistent with the difference in the work function value, but was frequently controlled by the surface states in ZnO itself [24].

Figures 4 show the difference current-voltage (*I-V)* characteristics of fabricated ZnO MSM photosensor with Pt electrodes measured under dark and illumination situations. The applied bias voltage ranged from 0 V to + 20 V. Upon the light illumination the current increases in forward bias conditions, which is the characteristic of a photodiode.

It was found that the dark current and photocurrent of the fabricated photosensor biased at 20 V were 5.5 x 10^{-3} A and 2.5 x 10^{-3}A, respectively. Furthermore, it was found that, we achieved a photocurrent to dark current contrast ratio of only 2. We conceive Pt should also form good Schottky contacts on our ZnO so that we should be able to effectively suppress the dark current. According to Young et. al., they believe that the annealing process should also form good Schottky contacts on their n-ZnO epitaxial layers so that to effectively suppress the dark current [25,26].

In Figure 4, different response to UV illumination can be seen in the forward-biased condition due to the photogeneration of extra electron–hole pairs. The significance of photocurrent raises with the increase of applied reverse bias because of the enhanced carrier collection [27,28]. When the UV light was imposed on ZnO nanorods, photo-generated excitons were separated by the built-in field. Under forward bias, the separation efficiency of photogeneration carriers (i.e. excitons) reduced due to the weakened built-in field. This characteristic shows that ZnO nanorods photosensor can easy detect UV light to produce the measurable photocurrent response. The *I–V* curve in the dark showed a turn-on voltage of 12 V for the forward bias.

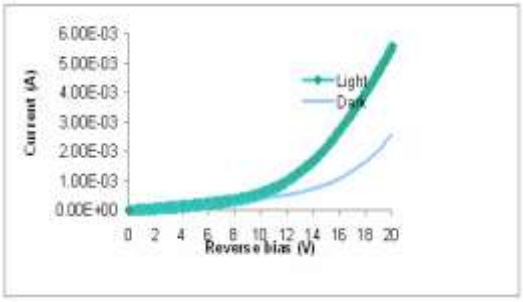

Fig. 3. The I-V characteristics of ZnO nanorods photosensor.

When the device was under illumination situation, the change of current was vital. Nevertheless, important difference in dark current was perceived. High dark current in the device could be associated to the low barrier height of the metal contact with the ZnO nanorods thin film. From the results, the value of the ideality factor is 1.05, consequently, it showing the high quality Schottky contact under investigation and the absence of a thick interfacial layer. Nevertheless, the presence of a thin interfacial layer cannot be ruled out except the semiconductor is cleaved in an ultra high vacuum (UHV) situation [29].

Conclusion

High quality and well aligned ZnO nanowires an array was synthesized on silicon substrates by hydrothermal method. The as-synthesized ZnO nanowires have diameters of 100-140 nm and lengths around 1 μm. It shows a strong UV emission at around 382 nm. From the results, the value of the ideality factor is 1.05, thus indicating the high quality Schottky contact under investigation and the absence of a thick interfacial layer. Besides that, under dark condition, the Schottky barrier height derived by the I-V method is 0.49 eV. The devices show high photosensivity in ultraviolet detection. The results propose that the ZnO nanorods-based devices have potential utilizations in ultraviolet photodetection.

Acknowledgements

The authors would like to acknowledge Universiti Sains Malaysia(302/JPNP/312001),FRGS (203/PJJAUH/6711159) and "API NANE" project for financial support. "API NANE" project (€580,000 funded by the Italian Institute of Technology, duration 3 years, started 1st February 2010, project leader is Christian Falconi).

References

[1] L. E. Greene, M. Law, D. H. Tan, M. Montano, J. Goldberger, G. Somorjai, P. Yang, *Nano Lett.*, *5*, 1231, 2005.

[2] S. Chu, D. Li, P.C. Chang, J. G. Lu, Flexible dye-sensitized solar cell based on vertical ZnO nanowire arrays, *Nano Res Lett.* 6, 38, 2010.

[3] J. Y. Park, S. W. Choi, S. S. Kim, Fabrication of a highly sensitive chemical sensor based on ZnO nanorod arrays. *Nano Res Lett*, 5, 353-359, 2009.

[4] K.S. Leschkies, R. Divakar, J. Basu, E. Enache-Pommer, J. E. Boercker, B. Carter, U. R. Kortshagen, D. J. Norris, E. S. Aydil, Photosensitization of ZnO nanowires with CdSe quantum dots for photovoltaic devices. *Nano Lett,* 7:1793-1798, 2007.

[5] J. J. Wu and S. C. Liu, Low-temperature growth of well-aligned ZnO nanorods by chemical vapor deposition, *Advanced Materials*, vol. 14, no. 3, pp. 215–218, 2002.

[6] B. Xiang, P. Wang, X. Zhang et al., "Rational synthesis of p-type zinc oxide nanowire arrays using simple chemical vapor deposition," *Nano Letters*, vol. 7, no. 2, pp. 323–328, (2007).

[7] W. I. Park, G. C. Yi, M. Kim, and S. J. Pennycook, "ZnO nanoneedles grown vertically on Si substrates by non-catalytic vapor-phase epitaxy," *Advanced Materials*, vol. 14, no. 24, pp. 1841–1843, 2002.

[8] J. Zhang, W.Y. Yu, L.D. Zhang, Phys. Lett. A 299, 276, 2002.

[9] J.S. Lee, K.S. Park, M.I. Kang, I.W. Park, J. Cryst. Growth, 254, 423, 2003.

[10] M.J. Zheng, L.D. Zhang, G.H. Li, W.Z. Shen, Chem. Phys. Lett. 363, 123, 2002.

[11] L. Tang, X.B. Bao, H. Zhou, A.H. Yuan, Physica E 40, 924, 2008.

[12] K.H. Tam, C.K. Cheung, Y.H. Leung, A.B. Djuri˘sic, C.C. Ling, C.D. Beling, S. Fung, W.M. Kwok, W.K. Chan, D.L. Phillips, L. Ding, W.K. Ge, J. Phys. Chem. B 110, 20865, 2006.

[13] L.E. Greene, M. Law, D.H. Tan, M. Montano, J. Goldberger, G. Somorjai, P. Yang, Nano Lett. 5, 1231, 2005.

[14] X.C. Song, Y.F. Zheng, E. Yang, Y. Wang, Mater. Lett. 61, 3904, 2007.

[15] Y.H. Tang, L.Z. Pei, Y.W. Chen, C. Guo, Phys. Rev. Lett. 95, 116102, 2005.

[16] L.S. Chuah, Z. Hassan, H. Abu Hassan, N.M. Ahmed, "GaN Schottky barrier photodiode on Si(111) with low-temperature-grown cap layer", Journal of Alloys and Compounds 481, L15-L19, 2009.

[17] L.S. Chuah, Z. Hassan, H. Abu Hassan, F.K. Yam, C.W. Chin, N.M. Ahmed, "Growth of III-nitrides on Si(111) by RF-MBE and its application to MSM photodiodes", Journal of Optoelectronics and Advanced Materials (JOAM), Vol. 10, No. 3, 569-572, 2008.

[18] L.S. Chuah, Z. Hassan, H. Abu Hassan, "The effects of annealing treatment in oxygen ambient on Ni/$Al_{0.09}Ga_{0.91}N$ UV photodetectors", Journal of Optoelectronics and Advanced Materials (JOAM), Vol. 11, No. 1, 76-82, 2009.

[19] L.S. Chuah, Z. Hassan, H. Abu Hassan, "Dark current characteristics of Ni contacts on porous AlGaN-based UV photodetector", Journal of Optoelectronics and Advanced Materials (JOAM), Vol. 9, No. 9, 2886-2890, 2007.

[20] X.D. Meng, B.X. Lin, B. J. Gu, J. J. Zhu, Z. Fu, A simple growth towards ZnO thin films and nanorods, Solid State Communications, vol. 135, 411-415, 2005.

[21] K. Sarpatwari, S. E. Mohney, O. O. Awadelkarim, Effects of barrier height inhomogeneities on the determination of the Richardson constant, J. Appl. Phys. 109, 014510, 2011.

[22] S. M. Sze, K. K. Ng, Physics of Semiconductor devices, John Wiley and Sons, 2007.

[23] E.H. Rhoderick and R.H. Williams, Metal-Semiconductor Contacts, 2nd Ed. Oxford: Clarendon Press, 1988.

[24] J. Bardeen, Surface states and rectification at a metal semiconductor contact, Physical Review, vol. 71, 717-727, 1974.

[25] S. J. Young, L. W. Ji, T. H. Fang, S. J. Chang, Y. K. Su, X. L. Du, ZnO ultraviolet photodiodes with Pd contact electrodes, Acta Materialia 55, 329-333, 2007.

[26] S. J. Young, Ir/n-ZnO Schottky barrier ultraviolet photodiodes, IEEE Sensors Journal, vol. 11, 1129-1133, 2011.

[27] J. P. Kar, M. Kumar, J. H. Choi, S. N. Das, S. Y. Choi, J. M. Myoung, Fabrication of ZnO thin film nanowires hybrid homojunction on silicon substrate, Solid State Communications, vol. 149, 1337-1341, 2009.

[28] H. Ohta, M. Kamiya, T. Kamiya, M. Hirano, H. Hosono, UV-detector based on pn-heterojunction diode composed of transparent oxide semiconductors, p-NiO/n-ZnO, Thin Solid Films, 445, 317-321, 2003.

[29] N. Newman, T. Kendelewicz, D. Thomson, S. H. Pan, S. J. Eglash, W. E. Spicer, Schottky barriers on atomically clean cleaved GaAs, Solid-State Electronics, 28, 307-312, 1985.

TiO_2 microspheres-based metamaterials exhibiting effective magnetic response in the terahertz regime

Riad Yahiaoui[1*], H. Němec[2], C. Kadlec[2], F. Kadlec[2], P. Kužel[2], U-C. Chung[3,4], C. Elissalde[3], M. Maglione[3] and P. Mounaix[1]

[1]LOMA, Univ. Bordeaux1, CNRS, UMR 5798, F-33400 Talence, France
[2] Institute of Physics, Academy of Sciences of the Czech Republic, Na Slovance 2, 182 21 Prague 8, Czech Republic
[3] ICMCB, Univ Bordeaux, CNRS – UPR 9048, 87 Avenue du Docteur Albert Schweitzer, 33608 Pessac cedex, France
[4]CRPP, CNRS – UPR 8641, 115 Avenue du Docteur Albert Schweitzer, 33600 Pessac cedex, France
*corresponding author: r.yahiaoui@loma.u-bordeaux1.fr

Abstract

Thin layers of all-dielectric metamaterials based on TiO_2 spherical particle resonators are investigated. A new method based on spray-drying of dissolved nanoparticles is used in the fabrication process. Spectral footprints of electric and magnetic dipoles are reported numerically and through experimental tests. It is a promising step for the construction of novel three-dimensional isotropic metamaterials exhibiting desired electromagnetic properties for terahertz applications.

1. Introduction

Since their advent, metamaterials have been explored for their potential use in sub-diffraction-limited imaging [1], medical imaging [2], sensing applications [3], cloaking [4] and so on. We focus in this paper on the study of All Dielectric (AD) metamaterials based on layers of Titanium Dioxide (TiO_2) microspheres. Their effective electric and magnetic responses are related to Mie resonances in each single particle. For high-enough dielectric permittivity of the particles, it is then possible to achieve e.g. negative effective magnetic permeability [5]. Although AD metamaterials have raised broad interests [6], only few of them have been experimentally shown to present a magnetic resonance in the THz spectral range. For example, laser micromachining was employed to fabricate a tunable THz metamaterial made of $SrTiO_3$ rods [7]. Majority of other works focused on the microwave region. For instance, Zhao *et al*. demonstrated experimentally a negative magnetic permeability at microwave frequencies in a three-dimensional dielectric composite metamaterial based on high dielectric permittivity cubic particles of $Ba_{0.5}Sr_{0.5}TiO_3$ (BST) coated with Teflon [8]. Vendik *et al*. [9] in their works investigated theoretically and numerically a periodic composite medium consisting of two lattices of dielectric spherical particles with different diameters or dielectric constants at microwave frequencies. The authors showed that effective isotropic double negative media (DNG) can be realized in the frequency region where the resonance of the TM mode in one kind of particles and of the TE mode in the other kind of particles are achieved simultaneously. Moreover, Peng *et al*., [10] observed experimentally a left-handed behaviour at gigahertz frequencies in an array of standard dielectric resonators. Lepetit *et al*. [11] have measured a negative refractive index in all-dielectric metamaterial in the microwave frequency range. Shibuya *et al*. [12] predicted theoretically a left-handed behaviour in a lattice combining two sets of TiO_2 cubes with two different sizes.

2. Our investigated metamaterials

In this work, inexpensive methods were used to fabricate monodisperse micron-sized spheres. First, we mixed commercial TiO_2-nanoparticles with ethanol to obtain a liquid suspension, which was suddenly dried upon spraying through a flame. This resulted in assembling TiO_2-nanoparticles into fragile mostly spherical dense clusters . These microspheres were then sintered in a tube furnace at 1200°C for 2 hours, in order to solidify them and to minimize their porosity. A scanning-electron-microscope image of these particles is shown in Fig. 1b.

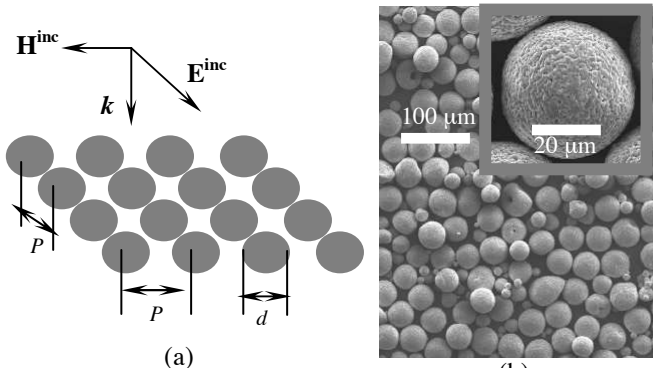

Figure 1: (a) Schematic view of the simulated microspheres-based metamaterial, with the relevant geometrical dimensions: diameter d = 45 μm, period P = 103 μm, and the appropriate electric and magnetic field polarizations. (b) Scanning electron microscope images of our TiO_2 microspheres before the sorting procedure.

The microspheres were finally sieved and sorted along their diameters d. We investigated powders with the following diameters: (i) $MS_{<38}$, $d < 38\,\mu$m, (ii) $MS_{38\text{-}40}$, $38\,\mu\text{m} < d < 40\,\mu$m, and (iii) $MS_{40\text{-}50}$, $40\,\mu\text{m} < d < 50\,\mu$m.

3. Result of numerical and experimental characterization

We measured the complex transmission and reflection of the samples by terahertz time domain spectroscopy (THz-TDS) to retrieve the effective electromagnetic response of the metamaterial structures. Thin layer of TiO_2 microparticles has been spread randomly between two thick blocks of sapphire separated by a $70\,\mu$m thick teflon (PTFE) o-ring. This fixes and controls the thickness of the film which is then essentially composed of a single layer of the microparticles.

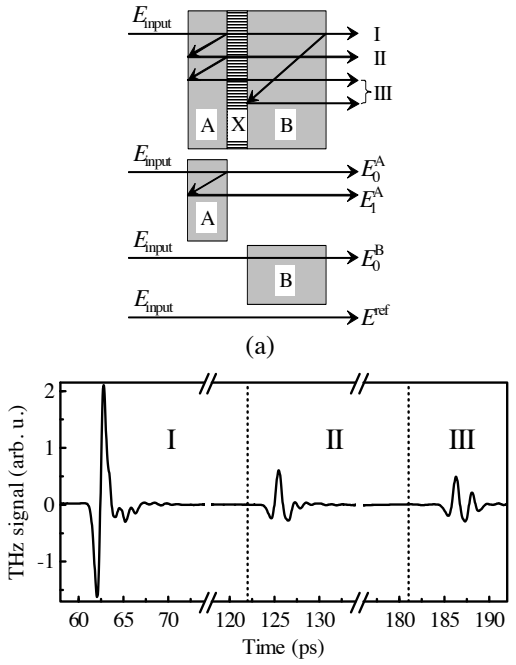

Figure 2: (a) Scheme of the pulse propagation through the structure AXB (sapphire – powder – sapphire) and within the three associated reference measurements. The reflected beams are shifted vertically for graphical clarity. (b) Example of the time-domain signal transmitted through the structure AXB. Dotted lines delimit the intervals containing: I – main pulse ($E_{0\text{-AXB}}$); II – 1st echo in A ($E_{1\text{-AXB}}$); III – superposition of 1st echo in B and 2nd echo in A.

THz pulses passing through the structure directly carry information about the complex transmittance of the powder while THz pulses coming from internal reflections in the blocks and from the partial reflection on the sapphire/powder interface carry information also about the complex reflectance of the powder (Fig. 2a). These pulses are resolved as a sequence of echoes in the time-domain signal transmitted through the entire structure [13] (see Fig. 2b). The sapphire block B is about 2 times thicker than the block A which ensures that the first internal reflection in the block A does not mix with the internal reflections from the block B. The measurement has to be supplemented by three reference measurements: (i) waveform transmitted through the block A (including the first echo), (ii) waveform transmitted through the block B and (iii) waveform transmitted through an empty space. The complex transmittance and reflectance spectra of the metamaterial are then calculated from

$$t = \frac{E_0^{\mathrm{AXB}} E^{\mathrm{ref}}}{E_0^{\mathrm{A}} E_0^{\mathrm{B}}} \cdot \frac{4 z_{\mathrm{B}}}{(1+z_{\mathrm{A}})(1+z_{\mathrm{B}})}, \qquad (1)$$

$$r = \frac{E_1^{\mathrm{AXB}} E_0^{\mathrm{A}}}{E_1^{\mathrm{A}} E_0^{\mathrm{AXB}}} \cdot \frac{1-z_{\mathrm{A}}}{1+z_{\mathrm{A}}}, \qquad (2)$$

where z_A and z_B are the relative wave impedances of the blocks A and B, respectively, and E denotes the Fourier transformations (spectra) of the time-domain signals defined in Fig. 2a. The use of the same blocks in the reference measurements ensures that the transmittance and reflectance phase is not corrupted by a possible uncertainty in the determination of the thickness of these blocks. We used thick sapphire blocks (3 and 6 mm). The internally reflected pulses (echoes) are thus separated by more than 60 ps (see dotted lines in Fig. 2b) which enables a good spectral resolution [$1/(60\ \text{ps}) \approx 0.03$ THz]. The transmission and reflection spectra are then extracted numerically as shown in Fig. 3. In the related numerical simulations, we considered a periodic array of monodisperse spheres (d = 45μm, filling factor = 10%), as illustrated in Fig. 1(a). We found that TiO_2 microparticles have a relative dielectric permittivity of about 92 and a moderate loss-level of about 5% ($\tan\delta \sim 0.05$) at terahertz frequencies. The overall agreement between simulation and experiment is rather good, keeping in mind that a regular structure is simulated while the measured sample is necessarily irregular and the microspheres may touch each other. We notice minor differences in the simulated phases compared to the measured ones (c.f. Fig. 3(b) and 3(d)) above the first Mie mode around 0.75 THz, which is probably due to the polydispersity of microspheres.

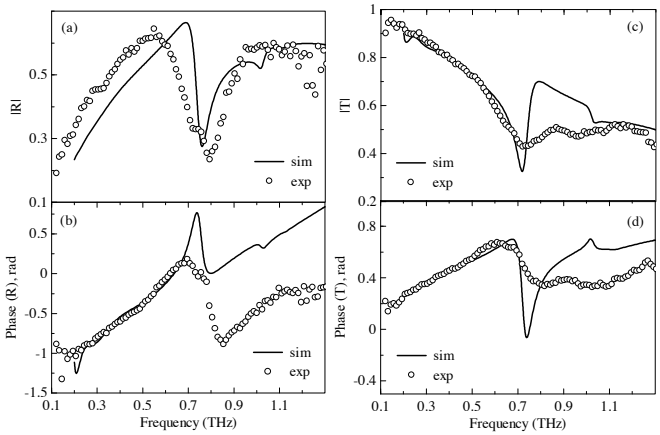

Figure 3: Spectra of the sample $MS_{40\text{-}50}$: simulated (solid lines) and measured (hollow circles) magnitude of the reflection (a), phase of the reflection (b), magnitude of the transmission (c), phase of the transmission (d).

4. Retrieval of the effective electromagnetic parameters

Using the retrieval method based on the inversion of Fresnel equations [14], we determined the effective permittivity and permeability. The result of the extraction procedure is given in Fig. 4. There is a good agreement between the simulated and the measured effective magnetic response (Fig. 4b). We believe that magnetic resonances are excited individually within each particle forming the metamaterial and it is only weakly influenced by the mutual coupling between particles [7,16,17]. Both measured and calculated effective dielectric permittivities are rather low (Fig. 4a), which is due to the low filling factor (about 10%) and low percolation degree which is controlled by the actual structure of the film [15].

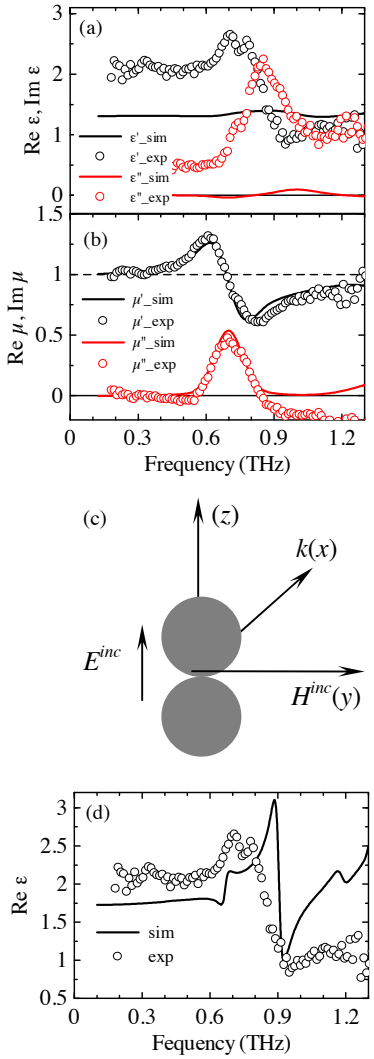

Figure 4: Dielectric permittivity (a), and magnetic permeability (b) of the sample $MS_{40\text{-}50}$. Circles: measured data, lines: simulations incorporating inhomogenous broadening. (c) Configuration of the dimer, with the probing electric field parallel to its axis. (d) Real part of the dielectric permittivity of the dimer (sphere diameters 50 μm, filling factor 15%) compared to the experimental permittivity from figure (a).

Furthermore, the calculated permittivity at low frequencies is significantly lower than the measured one and the resonance observed here is not as strong as the measured one. This difference between simulation and experiment can be partly explained by the complex topology of our samples [note that a simple square lattice of microspheres was considered in the simulations represented in Fig. 1(a)]. In order to attempt reproducing the resonant behavior of the electric response, we performed further numerical calculations taking into account pairs of microspheres in contact (dimers) arranged in a rectangular lattice, as illustrated in Fig. 4(c). The resonant behavior, similar to the experimental one shown in Fig. 4(d) is then observed in the permittivity spectra for probing electric field parallel to the dimer axis.

On the one hand, polydispersity of the spheres in samples broadens the resonance and prevents μ from reaching negative values. On the other hand, numerical simulations show that using much larger filling fraction (e.g. 50%) provides a metamaterial with $\mu < 0$ in spite of the inhomogeneous broadening. This implies that the microparticles fabricated by our method can induce a negative-permeability metamaterial for large filling fractions. Unfortunately, the high absorption for filling fractions exceeding ~15% precluded an accurate experimental determination of the permeability in such structures.

5. Conclusions

In conclusion, TiO_2 microparticles based metamaterials were fabricated using inexpensive spray-drying method. Numerical calculations and experimental characterizations have been conducted, demonstrating effective electric and magnetic response at terahertz frequencies, due to Mie resonances. It is a promising step for implementing improved electromagnetic functionalities, involving cheap and easy made metamaterials.

Acknowledgements

The work at the University of Bordeaux 1 was supported by the project "GIS-AMA-SAMM". The financial support by the Czech Science Foundation (Project No. P204/12/0232) is also acknowledged.

References

[1] N. Fang, H. Lee, C. Sun, and X. Zhang, Sub-diffraction-limited optical imaging with a silver superlens, *Science*, 308, pp. 534-537, 2005.

[2] M. J. Freire, R. Marques, and L. Jelinek, Experimental demonstration of a $\mu = -1$ metamaterial lens for magnetic resonance imaging, *Appl. Phys. Lett.* 93, 231108 (2008)

[3] K. Kneipp, H. Kneipp, I. Itzkan, R. R Dasari and M. S. Feld, Surface-enhanced raman scattering and biophysics, *J. Phys.: Condens. Matter* 14, pp. 597-624 (2002).

[4] D. Schurig, J. J. Mock, B. J. Justice, S. A. Cummer, J. B. Pendry, A. F. Starr and D. R. Smith,

Metamaterials electromagnetic cloak at microwave frequencies, *Science*, 314, pp. 977-980 (2006).

[5] S. O'Brien and J. B. Pendry, Photonic band-gap effects and magnetic activity in dielectric composites, *J. Phys.: Condens. Matter*. 14, pp. 4035-4044 (2002).

[6] Q. Zhao, J. Zhou, F. Zhang, and D. Lippens, Mie resonance-based dielectric metamaterials, *Mater. Today* 12, pp. 60-69 (2009).

[7] H. Němec, P. Kužel, F. Kadlec, C. Kadlec, R. Yahiaoui, and P. Mounaix, Tunable terahertz metamaterials with negative permeability, *Phys. Rev. B* 79, 241108 (2009).

[8] Q. Zhao, L. Kang, B. Du, H. Zhao, Q. Xie, X. Huang, B. Li, J. Zhou, and L. Li, Experimental demonstration of isotropic negative permeability in a three-dimensional dielectric composite, *Phys. Rev. Lett.* 101, 027402 (2008).

[9] O. G. Vendik, M. S. Gashinova, Artificial double negative (DNG) media composed by two different dielectric spheres lattices embedded in a dielectric matrix, *Proc. 34th European Microwave Conference*, Amsterdam, pp. 1209-1212 (2004).

[10] L. Peng, L. Ran, H. Chen, H. Zhang, H., J. A. Kong, and M. T. Grzegorczyk, Experimental observation of left-handed behavior in an array of standard dielectric resonators, *Phys. Rev. Lett.* 98, 157403 (2007).

[11] T. Lepetit, E. Akmonsoy, and J-P. Ganne, Experimental measurement of negative index in an all-dielectric metamaterial, *Appl. Phys. Lett.* 95, 121101 (2009).

[12] K. Shibuya, K. Takano, N. Matsumoto, K. Izumi, H. Miyazaki, Y. Jimba, and M. Hangyo, Terahertz metamaterials composed of TiO2 cube arrays, *Proc. Metamaterials*, Pamplona, pp. 777-779 (2008).

[13] L. Duvillaret, F. Garet, and J.-L. Coutaz, Highly precise determination of optical constants and sample thickness in terahertz time-domain spectroscopy, *Appl. Opt.* 38, pp. 409–415 (1999).

[14] D. R. Smith, S. Schultz, P. Markoš, and C. M. Soukoulis, Determination of effective permittivity and permeability of metamaterials from reflection and transmission coefficients, *Phys. Rev. B* 65, 195104 (2002).

[15] H. Němec, Z. Mics, M. Kempa, P. Kužel, O. Hayden, Y. Liu, T. Bein, and D. Fattakhova-Rohlfing, Tuning the conduction mechanism in niobium-doped titania nanoparticle network, *J. Phys. Chem. C*, 115, pp. 6968–6974 (2011).

[16] H. Němec, C. Kadlec, F. Kadlec, P. Kužel, R. Yahiaoui, U-C. Chung, C. Elissalde, M. Maglione and P. Mounaix, Resonant magnetic response of TiO2 microspheres at terahertz frequencies, *Appl. Phys. Lett.* 100, 061117 (2012).

[17] R.Yahiaoui, H. Němec, P. Kužel, F. Kadlec, C. Kadlec, and P. Mounaix, Broadband dielectric terahertz metamaterials with negative permeability, *Opt. Lett.* 34, pp. 3541-3543 (2009).

A Study on Natural Coral Stone – a Fractal Solid

Arnab Gangopadhyay, Aditi Sarkar, Aloke Sarkar*

Dept. of Physics, Bijoy Krishna Girls' College, 5/3 M.G. Road, Howrah 711101, W.B., India
*corresponding author, E-mail: alokesarkar@vsnl.net

Abstract

This present research work contains the study of Natural fractal material, coral stone. X-ray diffraction, FTIR, optical, dc and ac electrical characteristics are studied. The study includes Arrhenius like plots for both wafer and powder form of the material. Measurements show a possible partially irreversible phase transition occurs when coral is heated for a long time at an about 115 ^{o}C. From XRD data it has been also established that coral stone contains nano sized clusters which is supported by dc electrical measurement. The variation of ac conductivity of coral with thickness of the sample is studied and found exhibit an interesting feature of fractal solid. A scaling relation between ac conductivity and thickness has also been proposed here. Over all behavior of the specimen is that like that of a fractal system.

1. Introduction

The scaling behaviors of transport properties are very important for understanding the transport mechanisms of the fractal-like networks in fractal solid. Such studies have received extensive attention recently. Attempts have been made to analyze the transport properties including electrical conductivity, heat conduction, convective heat transfer, laminar flow, and turbulent flow in the networks and also derive the scaling exponents of the transport properties in the networks. It has been analyzed [1] that the scaling laws are different for different transport processes and the scaling exponents are sensitive to microstructures of the networks.
Coral stone is composed of mainly $CaCO_3$, Silica and have a trace of rare earth elements along with organic matter. It has a fractal structure. Studies of fractal solid are of considerable scientific and technological interest. Fractal solids may show some interesting characteristics functional properties [2]. It is also important in the field of electronics and telecommunication [3]. In a recent study [4] it has been demonstrated that a morphometrical method to quantify and characterize coral or corallites using Richardson Plots and Kaye's description of fractal dimensions was possible. A Jurassic coral species (*Aplosmilia spinosa*) and five recent coral species were analyzed using the Box-Counting Method. The method depicts the characterization of their morphologies at calicular and septal levels by their fractal dimensions (structural and textural). It is possible to establish the differences between species of *Montastraea* and to tackle the high phenotypic plasticity of *Montastraea annularis*. Application of fractal dimensions versus conventional methods (e.g., measurements of linear dimensions with a calliper, landmarks, Fourier analyses) to explore a rugged boundary object was analyzed. It appears that fractal techniquies have the potential to considerably simplify the morphometrical and statistical approaches, and be an important addition to methods based on Euclidian geometry.
In this present work, X-ray diffraction (XRD), Fourier transformed infrared spectroscopy (FTIR), optical spectroscopy (UV-VIS) and electrical measurements are carried out over natural coral specimen. A.c. and d.c. electrical properties of coral wafer are also investigated. The objective of this work is to investigate the fractal nature and scaling effect on ac/dc electrical characteristics. The overall results are discussed and analyzed in the following sections.

2. Material and experimental instruments

The specimen, coral wafer (Fig.1.) was cut from a coral branch that collected form Chennai. Two different cuts used as specimens for electrical experiment were transverse and longitudinal section of coral tree stone.

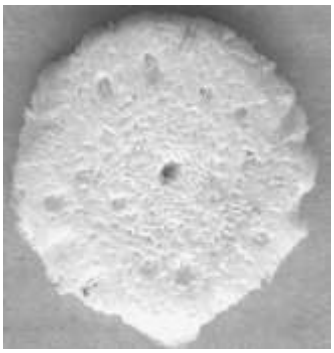

Figure 1: Transverse cross-section of Coral branch.

Crushed coral powder specimen was made by grinding coral with a grinder. The powdered specimen was used in Foruier Transformed Infra Red (FTIR) spectroscopy. The FTIR spectroscopic analysis has been found to be an effective probe in composition analysis of biomaterial. The FTIR spectroscopy was carried using Shimadzu (Japan)

model IR Affinity 1, in KBr window. UV-VIS absorption spectra of the sample were studied with 2450 UV-VIS spectrophotometer, Shimadzu, Japan in the range between 225 to 900 nm with sampling interval 0.5 nm and slit width 5 nm. The XRD of coral wafer was done to investigate its micro-structure and carried out with Cu K_α (λ = 1.541 nm) lines (PW 1836 (PHILLIPS), at 35kV, 25mA). The dc electrical properties were measured with KEITHLEY 2400 Source Meter. Ac measurement was done with HIOKI 3522-50 LCR HiTESTER, (JAPAN). Temperature was recorded with Tektronix DTM 900(USA). All the measurements were carried out at room temperature 25 C.

3. Results

In Fig.2 the XRD of coral stone is shown. This shows a clear manifestation by indicating the numerous peaks in XRD corresponding to possible fractal structure in the specimen.

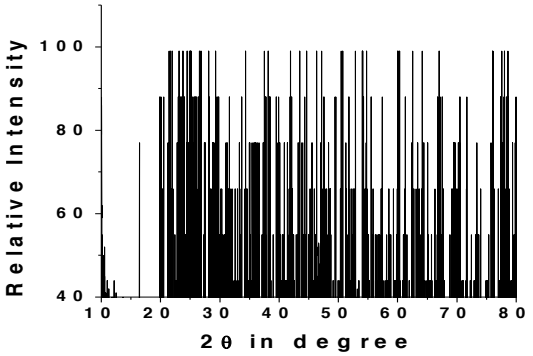

Figure 2: XRD of coral wafer.

Using Scherrer formula [4] it is found that the average particle size is of the order of 26.1nm. The occurrence of complicated and huge number of peaks in XRD pattern is the hall mark of fractal structure of natural coral stone. The presences of nano sized particles are also reflected in dc CVC [5]. The relevant intensity peaks are also compared with that of coralline hydroxyapatite [6].

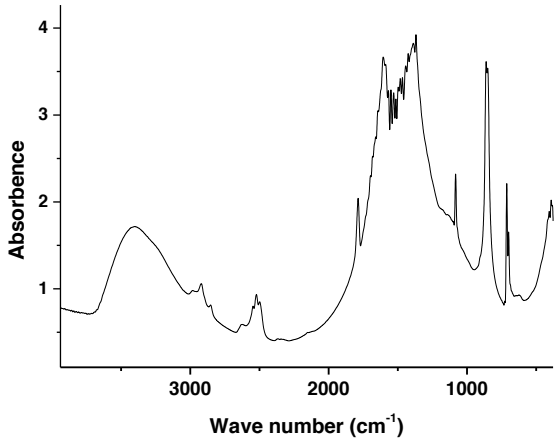

Figure 3: FTIR absorption spectra of coral.

The FTIR absorption spectrum is shown in Fig 3. Presence of primary amines and free secondary amines (3691 to 2997 cm^{-1}band) and amino acid (3390 cm^{-1}) confirms the structure rich in protein. Strong absorption peaks due to amide I, ketones, nitro urea, aromatic nitro compounds, sulfoxides, sufonic acids are also present. Such compounds are relevant because coral is produced by living micro organisms.

Fig.4 shows the UV-VIS absorption spectrum of coral specimen. The inset of the graph shows the nature of absorption over entire region. It shows almost uniform absorption in VIS region saving from strong absorption, in UV region, characteristics of bio-material. The graph shows some absorption peak between 600-900 nm due to presence of natural impurity in it.

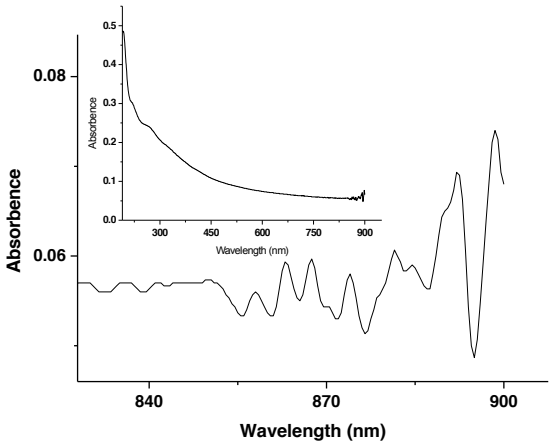

Figure 4: UV-VIS absorption spectrum.

The dc CVC of coral wafer is shown in Fig 5. This noise like oscillation is due to the structural complexity of the specimen. This is the feature of electronic conduction in porous fractal solid at room temperature (RT). The zigzag pattern is due to nano sized cluster and not due to noisy or bad data points [5]. It has been established that there is definite relation between separation of consecutive peaks of CVC and cluster size [7].

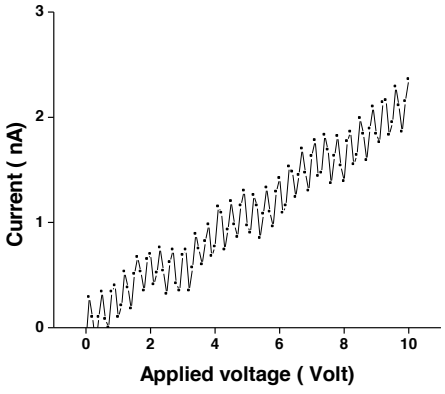

Figure 5: The dc CVC of coral wafer line.

Fig.6 shows the variation of electronic conductivity σ of powdered sample as the function of temperature by Arrhenius like plot. The result exhibits non-Arrhenius nature. This clearly indicates coral powder suffers a phase transition (at point 1) where slope of the curve changes from 38.151 to 2.134. It has been found that the nature of variation can be fitted by the expression, $\sigma T^n = \sigma_0 \exp(-\phi_0/KT)$ and using plateau region, value of 'n' is estimated as -0.8. Here, ϕ_0 is the activation energy.

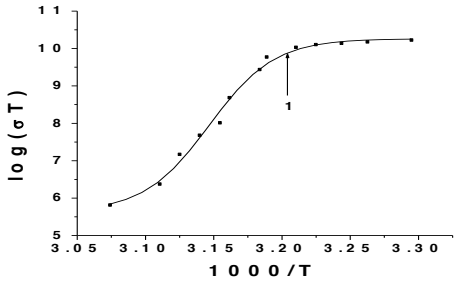

Figure 6: Arrhenius plot for Coral powder.

Fig. 7 summarizes the plot of measured ac current vs. impressed ac electric field at 60 kHz for eight samples with different thickness, ranging from 2.24mm to 4.3 mm.

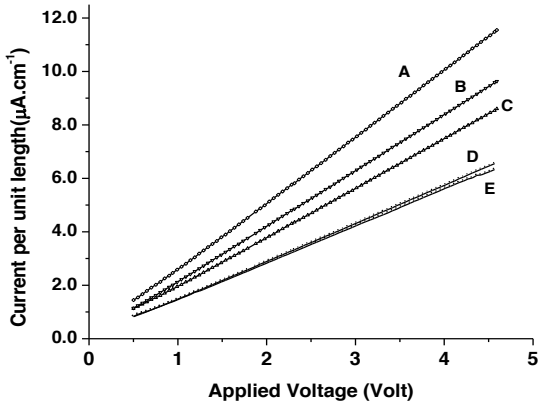

Figure 7: Variation of measured current vs. applied voltage at 60 KHz with varying thickness. Sample thickness are 4.3mm (A), 3.9mm (B), 3.4mm (C), 3.2mm (D), 2.87mm (D).

In vertical axes current per unit length is plotted. The curves become more and more stepper as thickness increases. It is clear that ac conductivity depends on thickness and nonlinearity (second order) is also present. The dependence of conductivity on thickness is shown in Fig. 8 with frequency of impressed field as a parameter. Frequency of ac field ranging from 5 kHz to 60 kHz is used for the measurement. The dependence of conductivity on thickness is exponential. On the physical ground the conductivity never be very large for long coral samples. We proposed that ac conductivity σ (d), being a function of thickness d, is given by

$$\sigma(d) = \sigma_0[3 - \exp(1 - (d/d_0)^{\gamma+1})] \quad (1)$$

where γ , σ_0 and d_0 are positive constants. Here d_0=3.8, γ=2.0, and σ_0 = 0.92 are used in equation (1) to fit the experimental data of Fig. 10.

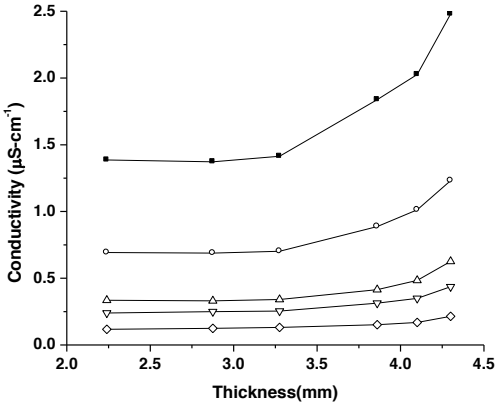

Figure 8: Conductivity vs. thickness at different frequency. (from bottom to top 5,10,15,30,60KHz respectively)

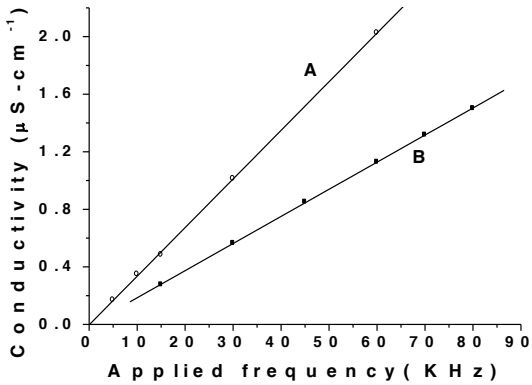

Figure 9: Conductivity vs. frequency plot of longitudinal (A) and transverse (B) cross-section of coral sample with same thickness.

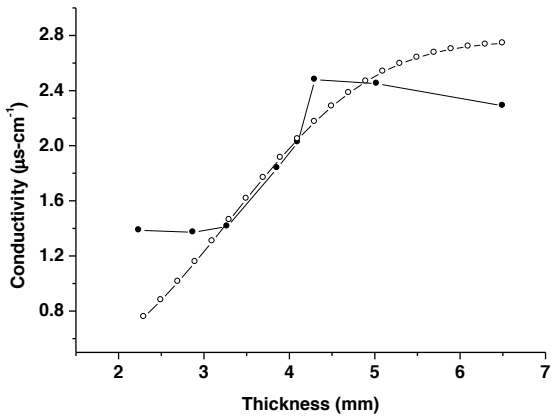

Figure 10: Variation of conductivity of coral with thickness at 60 kHz. Dot represents experimental data and circle

represents fitted data.

4. Discussion

Figure 9 shows the variation of a.c. conductivity of coral specimen with frequency of a.c. field. It also compares the results of longitudinal and transverse section of coral specimen. In both the cases the variation is found to be linear and hence the conductivity does not exhibit any power law variation with frequency of the impressed a.c. field. The figure however clearly indicates the anisotropy in electrical conduction which is again an indicator of fractal nature of the coral specimen. The feature is unusual in poor conducting material. It follows that imaginary part of dielectric constant of the coral stone is dispersion less.

The variation of electrical conductivity σ with the thickness of coral specimen is shown in Fig 10. Conductivity increases with increasing thickness of the specimen upto a value of d=4.8 mm and then it follows a slow declining trend upto d=6.2 mm. The observed nature of variation is a general feature of critical phenomenon. The variation of σ with d over the measured range has been fitted to a mathematical formula given by equation (1). In the three parameter formula given by equation (1), d_0 represents a critical length for onset percolation. The peak or saturated value corresponding to $d > d_0$ is the limiting bulk conduction in coral specimen.

Results of simulation studies showed that porosity of a fractal solid varies with its size. However constant porosity indicates a homogenous structure without any fractal characteristics. The said results may be summarized by the fact that porosity stabilizes to an almost constant value for definite cell dimension depending dimension of the fractal. But for still larger sizes there is a slow but definite decrease in porosity. This shows that though the structure is homogenous for small sizes a fractality appears above a certain cutoff scale. This effect is more prominent for low porosities. The porosity of fractals is directly related to percolation density and later is related to bulk electrical conductivity in the solid. The result of this work provides a direct evidence of the mentioned phenomenon.

Following quantum mechanical theory the finite electrical conductivity of an otherwise crystalline solid may explained in terms of electron-phonon interaction. Phonons are quasi-particle corresponding to dynamical excitation of the solid. The introduction of the notion of fractal index associated with the universal class quasiparticles, termed fractons [9], which obey specific fractal statistics. In a fractal solid in general quasi-particles are neither phonons nor fractons but have an inter-mixed nature. For a dimension- length of solid less than a characteristics length (L_0), fractons are excited however for length $L > L_0$, the phonons are excited. At intermediate length scale the quasi-particle are generalized as fracnons. Electron –fracton interaction was found [10] to be important in explaining formation of electron pair in some disorder system. Recently [11] it has been reported that the interaction may explain the origin of conductivity maxima in metallic system.

The results obtained from the variation of ac conductivity with specimen thickness (transverse) is a clear indication of fracton excitation and subsequent phonon excitation with a probable fracton phonon cross over that exhibit conductivity maxima. In fact the observed electrical conductivity variation can be explained by scaling behavior in fractal solid. In the fitted scaling law the value of the exponent γ=2.0 may be compared that of fractal dimension of coral [4] γ=1.92.

5. Conclusions

The overall results provide a clear indication for a possible porous fractal structure of the coral stone along with its functional properties. This material is appears to be a natural fractal solid containing nano structured unit which finds various novel properties important in material science. The scaling behaviour of electrical conductivity in fractal solid like coral is established.

Acknowledgments

Author A.G. and A.S. are thankful to U.G.C., New Delhi for JRF and CPE grants respectively. Author Aditi Sarkar acknowledges C.S.I.R. New Delhi, for providing J.R.F. A.S. is also thankful to U.G.C., New Delhi for Travel support.

References

[1] Peng Xu and Boming Yu , *J. Appl. Phys*. 100 : 104906-13, 2006

[2] K.Tsujii, *Polymer Journal*, 40 : 785-799, 2008.

[3] H.Isshiki, ECTS Trans. *On Electrical Engg and Telecomunication* , 4: 56AA 2006.

[4] B. Martin-Garin , B. Lathuilière , E. P. Verrecchia , J. Geister *Coral Reefs* 26: 3, 541-550, 2007

[5] B.D.Cullity, Elements of X-Ray Diffraction, Addison-Wesley Pub. Co. Reading, USA, pp. 78-99, 1956.

[6] A.Gangopadhyay and A.Sarkar , *Adv. in App. Res.,* 2 (1), 149-152, 2011

[7] E.C Shorrs and R.E. Holmes, Introduction to Bioceramics, eds. L.L Hench and J. Wilson, World Scientific, Singapore, p185, Ch 10, 1999.

[8] A.Gangopadhyay, A.sarkar and A.Sarkar, *Asian. J. Chem* 23:5581-5583, 2011.

[9] W. Cruz and R. de Oliveira, *Mod.Phys.Lett*. A15: 1931-1940, 2000.

[10] L. Yi, K.L Yao, *Physica B, condensed matter*, 194-196: 1439-1440, 1994.

[11] D.C Tian, J.X. Li and Z.H Zhang *Phys. Rev. B*, 45: 8116–8119 (1992).

Transformation-based Metamaterials for Enhancing the Ability of Computational Methods in Electromagnetics

Ozlem Ozgun[1*], and Mustafa Kuzuoglu[2]

[1]TED University, Dept. of Electrical Engineering, Ankara, Turkey
[2]Middle East Technical University, Dept. of Electrical Engineering, Ankara, Turkey
*corresponding author, E-mail: ozlem.ozgun@tedu.edu.tr

1. Introduction

It is a well-known fact that Maxwell's equations are form-invariant under coordinate transformations [1]. In other words, under a coordinate transformation Maxwell's equations preserve their mathematical form, but the constitutive parameters (i.e. the permittivity, permeability and conductivity) are modified. In order to account for the resulting change in the field behavior after the coordinate transformation, the original material parameters are replaced by *anisotropic* and *spatially-varying* constitutive parameters, yielding a duality relationship between geometry and constitutive relations. The concept of form invariance of Maxwell's equations under coordinate transformations is not new, but dates back to early twentieth century and has been first investigated by the mathematical physicist H. Bateman [2]. However, the idea became popular after almost a century, when it was demonstrated that it is possible to build an "invisibility cloak" by using a specific coordinate transformation [3]. The anisotropic material which is dictated by this transformation bends electromagnetic waves around the object in such a way that the object becomes invisible to an observer. This exciting discovery has been followed by other applications of *transformation media* (i.e., material media whose constitutive parameters are obtained by means of coordinate transformations), such as electromagnetic reshaping, lenses, rotators, etc [4-11]).

The main aim of this paper is the utilization of *virtual reality* transformation media in computational electromagnetics for the effective and efficient numerical modeling and solution of certain electromagnetic wave propagation problems in time or frequency domains. In other words, the concept of coordinate transformations is utilized only in the numerical models and the accompanying software (and therefore, they are named as *software metamaterials*, in order to distinguish them from the metamaterials constructed and used in the physical world), which implies that the spatial and/or temporal complexity of their constitutive parameters do not pose any challenge, since they only reside in *virtual reality*. Although there are several possible usages of software metamaterials in computational electromagnetics, three important applications of this approach will be discussed in this paper as explained below.

2. Applications of Software Metamaterials

(i) A coordinate transformation is introduced in order to handle *curved* geometries by using a Cartesian grid or mesh in finite methods such as the Finite Element Method (FEM) or the Finite Difference Time Domain (FDTD) method. The transformation is depicted in Fig. 1, where an object (e.g. a scatterer in the case of a scattering problem) with a curved boundary is illustrated. The object is placed within a hypothetical metamaterial layer and the region inside the software metamaterial layer Ω_{M} is mapped to the region $\tilde{\Omega} = \Omega \cup \Omega_{\mathrm{M}}$ by using the transformation given below:

$$\vec{r} \to \tilde{\vec{r}} = \mathrm{T}\left(\vec{r}\right) = K\left(\vec{r} - \vec{r}_{\mathrm{b}}\right) + \vec{r}_{\mathrm{c}} \qquad (1)$$

where $K = \left\|\vec{r}_{\mathrm{a}} - \vec{r}_{\mathrm{c}}\right\| / \left\|\vec{r}_{\mathrm{a}} - \vec{r}_{\mathrm{b}}\right\|$. The vectors $\vec{r}$ and $\tilde{\vec{r}}$ are the position vectors of the points P and $\tilde{\mathrm{P}}$ in the original and transformed coordinate systems, respectively. Also, $\vec{r}_{\mathrm{a}}$, $\vec{r}_{\mathrm{b}}$ and $\vec{r}_{\mathrm{c}}$ are the position vectors of the corresponding points. By means of this transformation, a one-to-one correspondence is achieved between the boundary of the object and the inner boundary of the virtual reality material layer which is conformal to a Cartesian grid. As a result, the curved geometry of the original object (which needs a discretization in terms of a non-uniform triangular mesh) can be handled by means of a software metamaterial layer whose boundary is conformal to a Cartesian coordinate system, which implies that a simpler uniform mesh with rectangular elements can be used in the numerical solution.

(ii) The second application is devised for the efficient solution of electromagnetic boundary value problems involving electrically-small geometric features. In FEM modeling, the difficulty associated with this problem can be resolved by means of local mesh refinement in the vicinity of fine geometric features. However, this is not an easy task in FEM, and it is formidable in finite difference schemes. Therefore, the coordinate transformation approach may be utilized in order to handle small-scale geometric subdomains efficiently. As an example of such a case, an object coated with an electrically-thin dielectric layer is

shown in Fig. 2. By means of a coordinate transformation, it is possible to use FEM without mesh refinement, with an easy-to-generate mesh by introducing a software metamaterial layer into the computational domain. In the design of the metamaterial, the region $\Omega_M = \Omega \cup \Omega_d$ is mapped to the region $\tilde{\Omega} = \Omega_d$, by using (1). This transformation *expands* the fields inside the thin dielectric layer to the metamaterial region.

(iii) Another application area of the coordinate transformation technique is the numerical modeling of electromagnetic boundary value problems involving non-convex objects. It is well-known that a non-convex object introduces an excessive *white space* region in FEM or FDTD models. This is a result of the fact that finite element or finite difference discretizations are approximations of boundary value problems governed by partial differential equations and in the case of a non-convex object, mutual coupling and/or multiple reflections from different parts must be handled. By means of a software metamaterial region, it is possible to *compress* the excessive space and guide the electromagnetic interactions through this region without causing any distortion in the electromagnetic field distribution. The utilization of transformation media in *spatial compression* is shown in Fig. 3. The coordinate transformation is designed by mapping Ω_M to the region $\tilde{\Omega} = \Omega \cup \Omega_M$, by using (1).

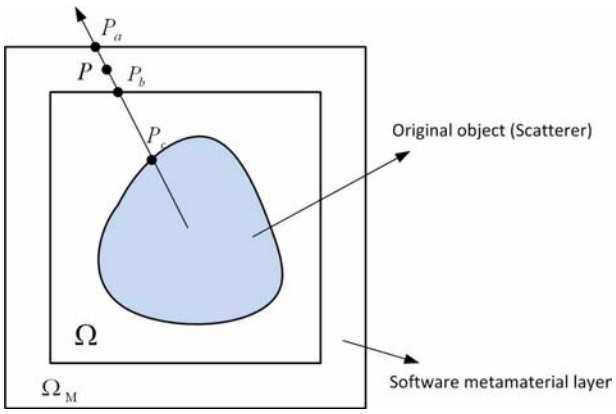

Fig. 1. Coordinate transformation for handling a curved geometry by means of a Cartesian grid.

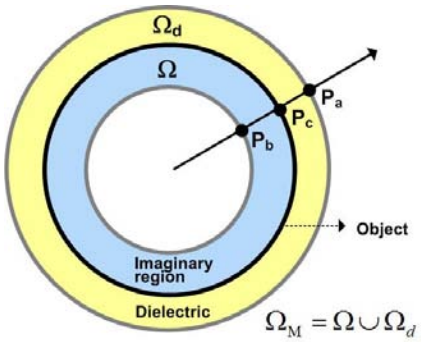

Fig. 2. Modeling an object coated by an electrically-thin dielectric layer.

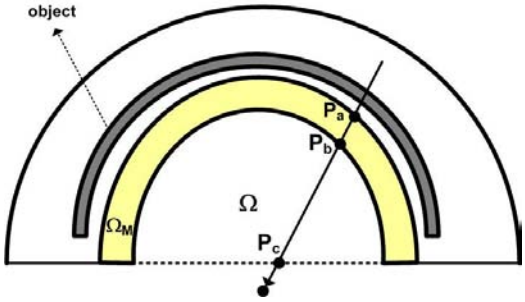

Fig. 3. Compression of excessive space.

3. Computation of Metamaterial Parameters using Form Invariance of Maxwell's Equations Under Coordinate Transformations

A general coordinate transformation ($T:\Omega \to \tilde{\Omega}$, $\vec{r} \to \tilde{\vec{r}} = T(\vec{r})$) maps any point $\vec{r} = (x, y, z)$ within the original space Ω to the point $\tilde{\vec{r}} = (\tilde{x}, \tilde{y}, \tilde{z})$ in the new space $\tilde{\Omega}$. Under this transformation, the electromagnetic field is also modified. It is possible to change the direction of propagation of an electromagnetic wave by means of this transformation. The role of a software metamaterial designed via a coordinate transformation is to obtain the required modification in the electromagnetic field for a simpler and more efficient numerical modeling.

The effect of a coordinate transformation on the electromagnetic field ($\vec{E}$, $\vec{H}$) is to transform the original material medium to a new anisotropic medium with constitutive parameters depending on the nature of the coordinate transformation. In this way, the mathematical expressions of Maxwell's equations remain invariant, with a proper modification of the constitutive parameters. As a specific example, assume that the original medium is free space with the permittivity and permeability parameters (ε_0, μ_0). In this case, Maxwell's equations are expressed as:

$$\nabla \times \vec{E}(\vec{r}) = -j\omega\mu_0 \vec{H}(\vec{r}) \tag{2}$$

$$\nabla \times \vec{H}(\vec{r}) = j\omega\varepsilon_0 \vec{E}(\vec{r}) \tag{3}$$

The coordinate transformation yields a new anisotropic medium with the tensor permittivity and permeability parameters given by ($\bar{\bar{\varepsilon}}, \bar{\bar{\mu}}$), and Maxwell's equations become:

$$\nabla \times \tilde{\vec{E}}(\vec{r}) = -j\omega\bar{\bar{\mu}} \cdot \tilde{\vec{H}}(\vec{r}) \tag{4}$$

$$\nabla \times \tilde{\vec{H}}(\vec{r}) = j\omega\bar{\bar{\varepsilon}} \cdot \tilde{\vec{E}}(\vec{r}) \tag{5}$$

The Jacobian matrix of the transformation plays an important role in the determination of the new field variables and constitutive parameters:

$$\bar{\bar{J}} = \frac{\partial(\tilde{x}, \tilde{y}, \tilde{z})}{\partial(x, y, z)} = \begin{bmatrix} \partial\tilde{x}/\partial x & \partial\tilde{x}/\partial y & \partial\tilde{x}/\partial z \\ \partial\tilde{y}/\partial x & \partial\tilde{y}/\partial y & \partial\tilde{y}/\partial z \\ \partial\tilde{z}/\partial x & \partial\tilde{z}/\partial y & \partial\tilde{z}/\partial z \end{bmatrix} \tag{6}$$

The relationship between the original and transformed field variables is given as [1]:

$$\tilde{\vec{E}}(\tilde{\vec{r}}) = \bar{\bar{J}}^{T} \cdot \vec{E}(\vec{r}) \tag{7}$$

$$\tilde{\vec{H}}(\tilde{\vec{r}}) = \bar{\bar{J}}^{T} \cdot \vec{H}(\vec{r}) \tag{8}$$

The constitutive parameters of the transformation medium are obtained as follows [1]:

$$\bar{\bar{\varepsilon}} = \varepsilon_0 \bar{\bar{\Lambda}} \tag{9}$$

$$\bar{\bar{\mu}} = \mu_0 \bar{\bar{\Lambda}} \tag{10}$$

$$\bar{\bar{\Lambda}} = (\det \bar{\bar{J}}) \left(\bar{\bar{J}}^{T} \cdot \bar{\bar{J}} \right)^{-1} \tag{11}$$

4. Numerical Results

The performance of each application in Sec. 2 is tested with various simulations performed by our finite element code or finite difference time domain code in the context of TM_z electromagnetic scattering problems.

(i) First, we consider the technique designed to handle *curved* geometries by using a Cartesian grid or mesh. In Fig. 4, we consider the scattering by a circular object whose radius is 1.8λ [λ=1 m is wavelength]. In the solution of this canonical problem by means of finite methods, the mesh must be fitted to the curved boundary of the object to get reliable results. Fig. 4(a) shows the standard finite element solution by using a triangular mesh that is conformal to the boundary. However, if a Cartesian mesh is employed, staircased modeling of the boundary will obviously cause errors due to non-conformal mesh. Fig. 4(b) shows the solution of the proposed approach which employs a matematerial layer of thickness 1.2λ fitted to the Cartesian grid. The metamaterial layer creates a virtual reality in the sense that Fig. 4(a) and 4(b) must be equivalent and must yield identical field values inside the free-space region (Ω). To confirm this claim, we measure the mean-square percentage difference between the field values of these two simulations as 0.0970%.

The second simulation is performed by the finite difference time domain method for the trapezoidal geometry shown in Fig. 5 and excited by a sine wave at 3 GHz. We measure the performance of the equivalent problem employing a metamaterial region in Fig. 5(b) over the original problem Fig. 5(a) at different time instants. The original problem is staircased on a "fine" Cartesian grid such that the staircasing error is reduced to a certain value by adjusting the grid size sufficiently small. The mean-square percentage difference between the field values of these two cases is 4.68e-5% (at n=800), 5.41e-4% (at n=1000), and 7.92e-4% (at n=1200).

The results demonstrate that the proposed approach can reliably be used without the need for changing simple Cartesian grids.

(ii) Second, we consider the approach for handling electrically-small geometric features. In Fig. 6, we assume that a circular object of diameter 2λ is coated by a thin dielectric layer of thickness λ/20 and dielectric constant 4. The thickness of the metamaterial layer is 0.5λ. In Fig. 6(a), a non-uniform mesh is created with element size λ/200 within the dielectric layer and λ/40 outside. However, in Fig. 6(b), a uniform mesh is used with element size λ/40 everywhere. The mean-square percentage difference between these two simulations is 8.20e-4%.

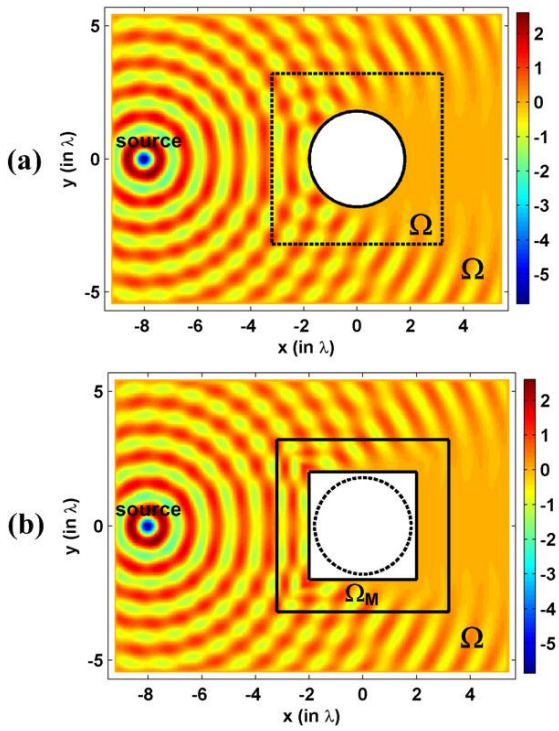

Fig. 4. Electric field distribution for scattering by a circular object [finite element method]: (a) Solution with a non-uniform mesh conformal to the curved boundary of the object, (b) Solution with a matematerial layer fitted to a uniform Cartesian grid.

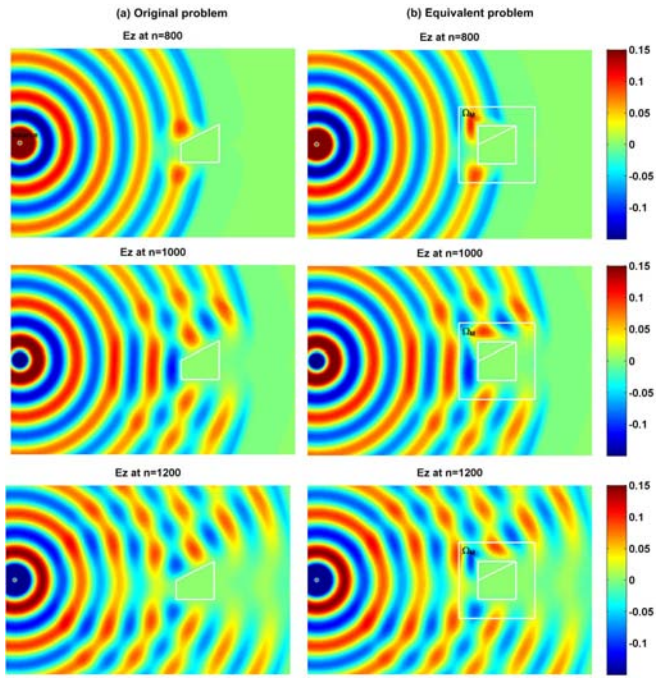

Fig. 5. Electric field distribution for scattering by a trapezoidal object at different time instants [finite difference time domain method]: (a) Solution with fine Cartesian grid, (b) Solution with a matematerial layer.

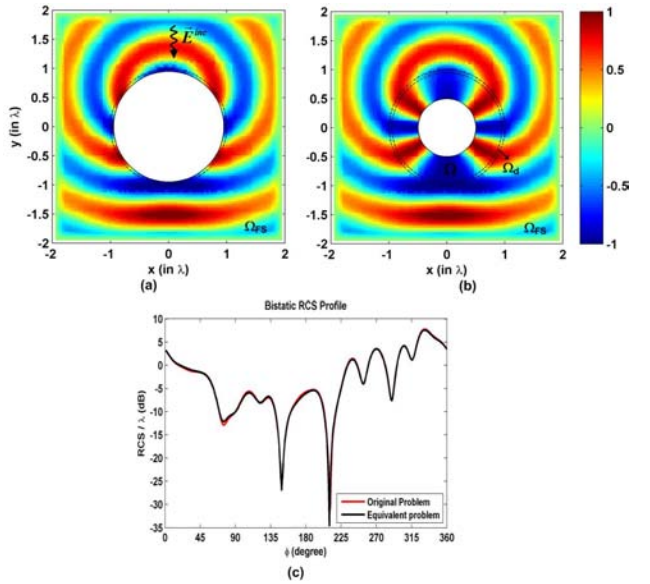

Fig. 6. Scattered electric field distribution from a circular object coated by a dielectric layer [finite element method]: (a) Original problem with refined mesh within the dielectric layer, (b) Equivalent problem with metamaterial layer, (c) Radar Cross Section (RCS) profiles.

(iii) Finally, we consider the transformation medium acting as a spatial space compressor. Fig. 7 illustrates a scattering problem, where a plane wave is incident to a thin half-circular inlet-like object whose diameter is 4λ. In this figure, we plot the scattered field distribution and the RCS profiles corresponding to the original and equivalent problems. In the equivalent problem, we design the metamaterial layer by using unit vectors directed along the center (P_c) shown by the 'black dot'. Note that the equivalent problem achieves 40% reduction in unknowns, in comparison to the original problem.

5. Conclusions

We have proposed new techniques for computational electromagnetics by placing anisotropic metamaterial regions, whose parameters are obtained by the coordinate transformation, within the computational domain in order to alleviate certain numerical difficulties. We have observed, through numerical results, that theoretical predictions are in good agreement with the numerical simulations.

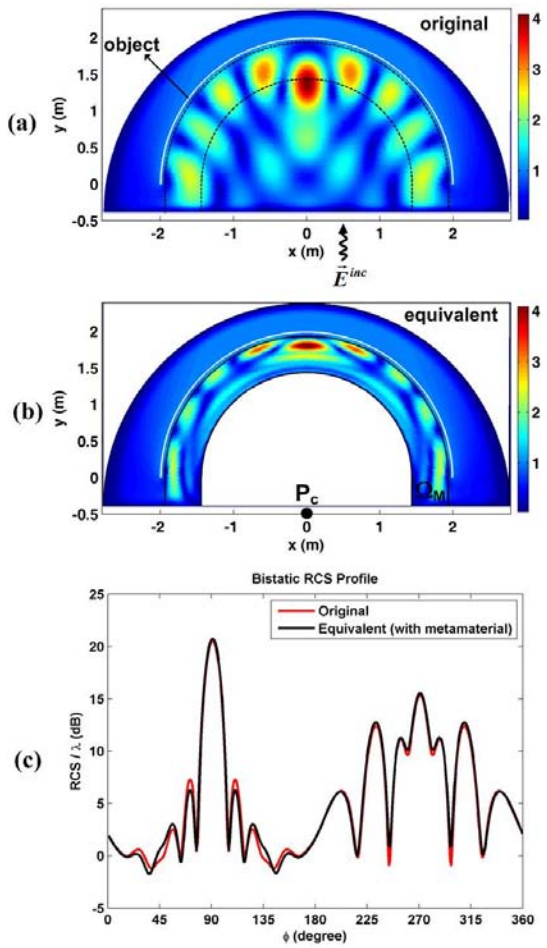

Fig. 7. Scattered electric field distribution for half-circular object by using a spatial domain compressor: (a) Original problem, (b) Equivalent problem with metamaterial layer, (c) Radar Cross Section (RCS) profiles.

References

[1] I.V. Lindell, *Methods for Electromagnetic Field Analysis*, Oxford Univ. Press, 1992.

[2] H. Bateman, The transformation of the electrodynamical equations, *Proc. London Math. Soc*., 8: 223-264, 1910.

[3] J.B. Pendry, D. Schurig, and D.R. Smith, Controlling electromagnetic fields, *Science*, 312: 1780-1782, 2006.

[4] O. Ozgun, and M. Kuzuoglu, Electromagnetic metamorphosis: Reshaping scatterers via conformal anisotropic metamaterial coatings, *Microwave Opt. Technol. Lett*., 49: 2386-2392, 2007.

[5] O. Ozgun, and M. Kuzuoglu, Utilization of anisotropic metamaterial layers in waveguide miniaturization and transitions, *IEEE Microwave and Wireless Components Letters*, 17: 754-756, 2007.

[6] O. Ozgun, and M. Kuzuoglu, Form-invariance of Maxwell's Equations in Coordinate Transformations: Metamaterials and Numerical Models, *Chapter 3 in Metamaterials: Classes, Properties and Applications*, Nova Science, 2010.

[7] B. Donderici, and F.L. Teixeria, Metamaterial blueprints for reflectionless waveguide bends, *IEEE Microwave and Wireless Components Letters*, 18: 233-235, 2008.

[8] I. Gallina, G. Castaldi, and V. Galdi, Transformation Media for Thin Planar Retrodirective Reflectors, *IEEE Antennas and Wireless Propagation Letters*, 7:603-605, 2008.

[9] G.X. Yu, W.X. Jiang, X.Y. Zhou, and T.J. Cui, Non-rotationally invariant invisibility cloaks and concentrators of EM Waves, *Eur. Phys. J. Appl. Phys*, 44: 181-185, 2008.

[10] B. Vasic, G. Isic, R. Gajic and K. Hingerl, Coordinate transformation based design of confined metamaterial structures, *Physical Review B*, 79: 085103, 2009.

[11] P.H. Tichit, S.N. Burokur, and A. Lustrac, Ultradirective antenna via transformation optics, *Journal of Applied Physics*, 105: 104912, 2009.

Nonlocal Transformation-Optics Metamaterials

Giuseppe Castaldi[1], Vincenzo Galdi[1*], Andrea Alù[2], Nader Engheta[3]

[1]CNR-SPIN and Waves Group, Department of Engineering, University of Sannio, Benevento, Italy
[2]Department of Electrical and Computer Engineering, The University of Texas at Austin, Austin, TX 78712, USA
[3]Department of Electrical and Systems Engineering, University of Pennsylvania, Philadelphia, PA 19104, USA
*corresponding author, E-mail: vgaldi@unisannio.it

Abstract

We review our recent results on a new framework for transformation optics based on nonlocal coordinate transformations in the spectral (wavenumber) domain, rather than in the conventional spatial domain. Our proposed approach supports a physically-incisive and powerful geometrical interpretation in terms of deformation of the equi-frequency contours, and it may open intriguing venues in dispersion engineering of electromagnetic metamaterials.

1. Introduction

Spatial dispersion [1, 2] in electromagnetic (EM) metamaterials is currently eliciting growing attention, in view of its relevance in many homogenized (effective-medium) models [3, 4] and anomalous wave interactions [5]–[7], as well as for the novel degrees of freedom that its proper tailoring may endow [8].

During recent years, the *transformation optics* (TO) paradigm, based on the form-invariant properties of coordinate-transformed Helmholtz [9] and Maxwell's equations [10], has become a very powerful and versatile framework for designing metamaterials with prescribed field-manipulation capabilities (see, e.g., [11] for a recent review). In spite of the several extensions and generalizations (see, e.g., [12]–[14]) proposed in order to enlarge the class of "transformation media" that may be obtained, attention and applications have been hitherto focused on *local* effects.

In a recent study [15], we have introduced a spectral-domain-based TO framework to engineer spatially-dispersive transformation media capable of yielding given *nonlocal* field manipulation effects. In what follows, we review the basic theory underlying this approach as we have given in [15], as well as some application-oriented aspects.

2. Nonlocal TO framework

2.1. Basic theory

As we have expressed in [15], our proposed framework relies on coordinate transformations in the spectral domain, where nonlocal constitutive relationships can easily be dealt with in terms of wavenumber-dependent constitutive operators.

Following our work in [15], for illustration, we start considering the (algebrized) Maxwell's curl equations in the time-harmonic $[\exp(-i\omega t)]$ spectral wavenumber domain $\mathbf{k}'$

$$i\mathbf{k}' \times \tilde{\mathbf{E}}'(\mathbf{k}') = i\omega\mu_0 \tilde{\mathbf{H}}'(\mathbf{k}') - \tilde{\mathbf{M}}'(\mathbf{k}'), \tag{1a}$$

$$i\mathbf{k}' \times \tilde{\mathbf{H}}'(\mathbf{k}') = -i\omega\varepsilon_0 \tilde{\mathbf{E}}'(\mathbf{k}') + \tilde{\mathbf{J}}'(\mathbf{k}'), \tag{1b}$$

which describe the radiation of assigned electric and magnetic source distributions ($\mathbf{J}'$ and $\mathbf{M}'$, respectively) in an auxiliary (primed coordinate) vacuum space. Here and henceforth, boldface symbols identify vector quantities, and the tilde $\sim$ identifies spectral-domain quantities. Next, we apply a real-valued coordinate transformation to a new spectral domain $\mathbf{k}$,

$$\mathbf{k}' = \underline{\underline{\tilde{\Lambda}}}^{T}(\mathbf{k}) \cdot \mathbf{k} = \tilde{\mathbf{F}}(\mathbf{k}), \tag{2}$$

where the double underline identifies a second-rank tensor operator, and the superscript ^{T} indicates the transpose. Similar to the standard (spatial-domain) TO approach [10], the form-invariant properties of Maxwells equations in the mapped spectral domain $\mathbf{k}$ can be exploited to relate the corresponding fields, sources, and constitutive relationships to those in the original vacuum domain, viz.,

$$\left\{\tilde{\mathbf{E}}, \tilde{\mathbf{H}}\right\}(\mathbf{k}) = \underline{\underline{\tilde{\Lambda}}}^{-T} \cdot \left\{\tilde{\mathbf{E}}', \tilde{\mathbf{H}}'\right\}\left[\tilde{\mathbf{F}}(\mathbf{k})\right], \tag{3a}$$

$$\left\{\tilde{\mathbf{J}}, \tilde{\mathbf{M}}\right\}(\mathbf{k}) = \det{}^{-1}\left(\underline{\underline{\tilde{\Lambda}}}\right)\underline{\underline{\tilde{\Lambda}}} \cdot \left\{\tilde{\mathbf{J}}', \tilde{\mathbf{M}}'\right\}\left[\tilde{\mathbf{F}}(\mathbf{k})\right], \tag{3b}$$

$$\left\{\underline{\underline{\tilde{\varepsilon}}}, \underline{\underline{\tilde{\mu}}}\right\}(\mathbf{k}) = \det{}^{-1}\left[\underline{\underline{\tilde{\Lambda}}}(\mathbf{k})\right]\underline{\underline{\tilde{\Lambda}}}(\mathbf{k}) \cdot \underline{\underline{\tilde{\Lambda}}}^{T}(\mathbf{k}), \tag{3c}$$

where $\det(\cdot)$ denotes the determinant, the superscript $^{-T}$ the inverse transpose, and $\underline{\underline{\tilde{\varepsilon}}}, \underline{\underline{\tilde{\mu}}}$ the relative permittivity and permeability tensors, respectively. The relationships in (3) in principle resemble those encountered in the standard (spatial-domain) TO approach [10], and trivially reduce to them in the case of *linear* spectral mapping [i.e., $\mathbf{k}$-independent $\underline{\underline{\tilde{\Lambda}}}$ in (2)], which corresponds to the *local* coordinate mapping

$$\mathbf{r}' = \underline{\underline{\tilde{\Lambda}}}^{-1} \cdot \mathbf{r}. \tag{4}$$

However, as we mentioned in [15], a general *nonlinear* spectral mapping in (2) would yield $\mathbf{k}$-dependent constitutive tensors in (3c), i.e., *nonlocal* constitutive relationships.

Moreover, specific physical properties may be directly enforced via suitable restrictions in the coordinate mapping. For instance, the Hermitian condition

$$\underline{\underline{\tilde{\Lambda}}}^{T}(\mathbf{k}) = \underline{\underline{\tilde{\Lambda}}}^{*}(\mathbf{k}) \tag{5}$$

yields *lossless* media, whereas the center-symmetry condition

$$\underline{\underline{\tilde{\Lambda}}}(\mathbf{k}) = \underline{\underline{\tilde{\Lambda}}}(-\mathbf{k}) \tag{6}$$

yields *reciprocal* media.

The above spectral field/source transformations can be used to systematically design a desired response in a fictitious curved-coordinate spectral domain, which may be equivalently obtained in an actual physical space filled up by a spatially-dispersive transformation medium whose constitutive "blueprints" are explicitly given in (3c).

2.2. Geometrical interpretation

Our nonlocal TO approach admits a geometrical interpretation in terms of direct manipulation of the dispersion characteristics via deformation of the *equi-frequency contours* (EFCs). Figure 1 exemplifies this interpretation with specific reference to an (x, z) two-dimensional (2-D) scenario, by showing the deformation of the circular EFC pertaining to the vacuum space [Fig. 1(a)]

$$k'^{2}_{x} + k'^{2}_{z} = k_0^2, \tag{7}$$

as an effect of the spectral mapping

$$\tilde{F}_x^2(k_x, k_z) + \tilde{F}_z^2(k_x, k_z) = k_0^2, \tag{8}$$

with $k_0 = \omega/c_0$ denoting the vacuum wavenumber, and $c_0 = 1/\sqrt{\varepsilon_0\mu_0}$ the corresponding speed of light. As we stated in [15], depending on the *single-* or *double-*valuedness of the mapping, this may result in a moderate deformation [Fig. 1(b)] or the appearance of an extra branch [Fig. 1(c)], respectively.

2.3. Possible applications

The geometrical interpretation above enables for direct manipulation of the kinematical (wavevector and velocity) properties of the wave propagation and reflection/refraction [16], and establishes a straightforward connection between the multi-valuedness of the mapping and the presence of additional extraordinary waves.

Moreover, considering the the same 2-D scenario as above with a single-valued coordinate mapping, and looking at the relationship between the 1-D spatial spectra of two (x-dependent) aperture transverse field distributions at two planes [say, $\tilde{\Phi}_0$ at $z = 0$, and $\tilde{\Phi}_d$ at $z = d$],

$$\tilde{\Phi}_d(k_x) = \exp(ik_z d)\, \tilde{\Phi}_0(k_x) \equiv \tilde{T}(k_x)\tilde{\Phi}_0(k_x), \tag{9}$$

we note that a desired *modulation transfer function* $\tilde{T}(k_x)$ may be in principle engineered via the mapping

$$k_z = -\frac{i}{d}\log\left[\tilde{T}(k_x)\right], \tag{10}$$

which defines in *explicit* form the EFC shape that is required. Within our framework, this shape may be obtained, for instance, via the spectral mapping [15]

$$\tilde{F}_x(k_x) = \sqrt{k_0^2 + \frac{1}{d^2}\log^2\left[\tilde{T}(k_x)\right]}, \quad \tilde{F}_z(k_z) = k_z. \tag{11}$$

It is evident that the applicability of our approach relies on the possibility to approximate the constitutive blueprints in (3c) within given frequency and wavenumber ranges. While this is significantly more challenging than what encountered in standard spatial-domain TO, we have shown in [15] that it is still possible to engineer interesting nonlocal effects based on simple artificial materials that can be described by nonlocal homogenized models. Here, we review the example [15].

3. Example of application

3.1. Problem statement

As an example of application, in what follows, we illustrate the design of a nonlocal transformation-medium half-space capable of splitting a transversely-magnetic (TM) polarized (i.e., y-directed magnetic field) plane wave with assigned wavevector $\mathbf{k}' = \mathbf{k}_i$ [with angle θ_i from the z-axis and associated group velocity $\mathbf{v}'_g(\mathbf{k}_i) = c_0\mathbf{k}_i/|\mathbf{k}_i|$, cf. Fig. 1(a)] impinging from vacuum into *two* transmitted waves with prescribed directions, i.e., group velocities forming angles θ_{t1} and θ_{t2}, respectively, with the z-axis.

3.2. Synthesis procedure

First, we note that a transmitted-wave wavevector $\mathbf{k}_t$ is the image of the incident wavevector $\mathbf{k}_i$ in the deformed ECF(s) (8), subject to the tangential-wavevector continuity $k_{tx} = k_{ix}$ and to the radiation condition $\mathrm{Re}(k_{tz}) > 0$ (see Fig. 1 for illustration), with corresponding group velocity (normal to the deformed EFC) via

$$\mathbf{v}_g(\mathbf{k}_t) \equiv \left.\frac{\partial\omega}{\partial\mathbf{k}}\right|_{\mathbf{k}_i} = \pm\frac{c_0\underline{\underline{\tilde{J}}}^{T}(\mathbf{k}_t)\cdot\tilde{\mathbf{F}}(\mathbf{k}_t)}{|\tilde{\mathbf{F}}(\mathbf{k}_t)|}, \tag{12}$$

where $\underline{\underline{\tilde{J}}}(\mathbf{k}) \equiv \partial\mathbf{k}'/\partial\mathbf{k}$ denotes the Jacobian matrix of the transformation in (2), and the $\pm$ sign is dictated by the radiation condition $\mathrm{Re}(v_{gz}) > 0$.

Our problem can be posed as finding a *double-valued* spectral-domain transformation (2) which maps [via (8)] the incident wavevector $\mathbf{k}_i$ into two transmitted wavevectors $\mathbf{k}_{t1}$ and $\mathbf{k}_{t2}$ with conserved tangential (i.e., x-) components and desired group-velocity directions, viz.,

$$k_{t1x} = k_{t2x} = k_{ix} = k_0\sin\theta_i, \tag{13a}$$

$$\frac{v_{gx}(\mathbf{k}_{t1,2})}{v_{gz}(\mathbf{k}_{t1,2})} = \tan\theta_{t1,2}, \tag{13b}$$

with $\mathbf{v}_g$ given by (12). For simplicity, as we have done in [15], we assume a variable-separated algebraic mapping

$$\tilde{F}_x(k_x) = k_x\sqrt{a_0 + a_2k_x^2}, \tag{14a}$$

$$\tilde{F}_z(k_z) = k_z\sqrt{b_0 + b_2k_z^2}, \tag{14b}$$

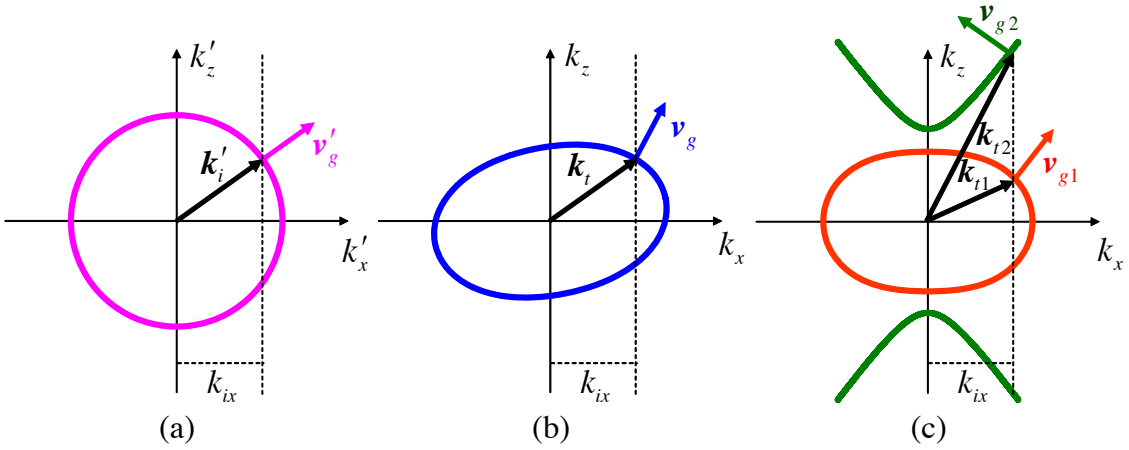

Figure 1: (From [15]) Schematic of EFCs pertaining to the auxiliary vacuum space (a) and the deformed versions obtained via a single-valued (b) and double-valued (c) spectral coordinate mapping. Also shown are the wavevectors and group velocities pertaining to a refraction scenario (details in the text).

which, substituted in (8) [with (13a)], yields $\mathbf{k}_{t1}$ and $\mathbf{k}_{t2}$ in analytical closed-form (see [15] for details). Then, analytical solution of the algebraic system of equations arising from (13b) [with (12) and (14)], yields two unknowns coefficients (say b_0 and b_2) in (14). This identifies a family of (infinite) coordinate transformations which, for the given incidence conditions, ensures the desired directions θ_{t1} and θ_{t2} of the transmitted waves (see [15] for details). For instance, assuming $\theta_i = 40^o$, and $\theta_{t1} = 70^o$ (i.e., positive refraction) and $\theta_{t2} = -45^o$ (i.e., negative refraction), a candidate double-valued EFC is shown [blue (solid) curves] in Fig. 2(a), with transformation parameters given in the caption. The degrees of freedom a_0 and a_2 in the transformation can be exploited so as to facilitate the engineering of the transformation medium. Additional degrees of freedom are available in the choice of the tensor operator $\underline{\underline{\tilde{\Lambda}}}$, whose association [via (2)] to the vector mapping $\tilde{\mathbf{F}}$ in (14) is not unique, reflecting the fact that different materials may exhibit identical EFCs. We consider a simple *diagonal* form

$$\underline{\underline{\tilde{\Lambda}}} = \begin{bmatrix} \tilde{F}_x/k_x & 0 & 0 \\ 0 & \tilde{\Lambda}_{yy} & 0 \\ 0 & 0 & \tilde{F}_z/k_z \end{bmatrix}, \tag{15}$$

where, for the assumed TM-polarization, the component $\tilde{\Lambda}_{yy}$ is a free parameter. Similar to the spatial-TO approach [17], it may be desirable to chose this parameter so as to ensure $\tilde{\mu}_{yy} = 1$, i.e., an *effectively non-magnetic* material, which may be more easily scalable towards optical frequencies. From (3c), it is readily understood that this condition may be obtained by choosing

$$\tilde{\Lambda}_{yy} = \frac{\tilde{F}_x \tilde{F}_z}{k_x k_z}, \tag{16}$$

which yields a uniaxial anisotropic medium with relevant permittivity components

$$\tilde{\varepsilon}_{xx}(k_z) = \frac{1}{b_0 + b_2 k_z^2}, \tag{17a}$$

$$\tilde{\varepsilon}_{zz}(k_x) = \frac{1}{a_0 + a_2 k_x^2}, \tag{17b}$$

shown [blue (solid) curves] in Figs. 2(b) and 2(c) for the same parameters as above.

The variable-separated *rational* form of the permittivity components in (17) closely resembles the nonlocal homogenized model derived in [18] for a 1-D multi-layered photonic crystal (PC). This suggests that, at a given frequency and within limited spectral-wavenumber ranges, such a simple artificial material may be exploited to approximate our TO-based constitutive blueprints. Within this framework, we consider a 1-D PC made of alternating layers of homogeneous, isotropic materials (with relative permittivity ε_a and ε_b, and thickness d_a and d_b, respectively) periodically stacked along the x-axis, as illustrated in the inset of Fig. 2(b). In order to derive the homogenized model, we developed a modified version of the procedure in [18], likewise based on matching the arising dispersion law with the McLaurin expansion of the exact Bloch-type dispersion law of the PC (see [15] for details). Finally, as shown in [15], via a semi-analytical procedure based on the matching between the above nonlocal homogenized model and the TO-based blueprints in (17) (see [15] for details), we were able to determine the parameters of a PC approximant, which, for the example considered, resulted in $\varepsilon_a = 2.752$, $d_a = 0.0668\lambda_0$, $\varepsilon_b = -2.082$, $d_b = 0.0332\lambda_0$ (with $\lambda_0 = 2\pi/k_0$ denoting the vacuum wavelength).

The corresponding exact (i.e., Bloch) EFCs and (nonlocal homogenized) constitutive parameters are also displayed [red (dashed) curves] in Fig. 2, showing a satisfactory agreement with the TO-based blueprints, especially in those regions of direct relevance to the refraction scenario of interest, i.e., nearby the transmitted wavevectors $\mathbf{k}_{t1}$ and

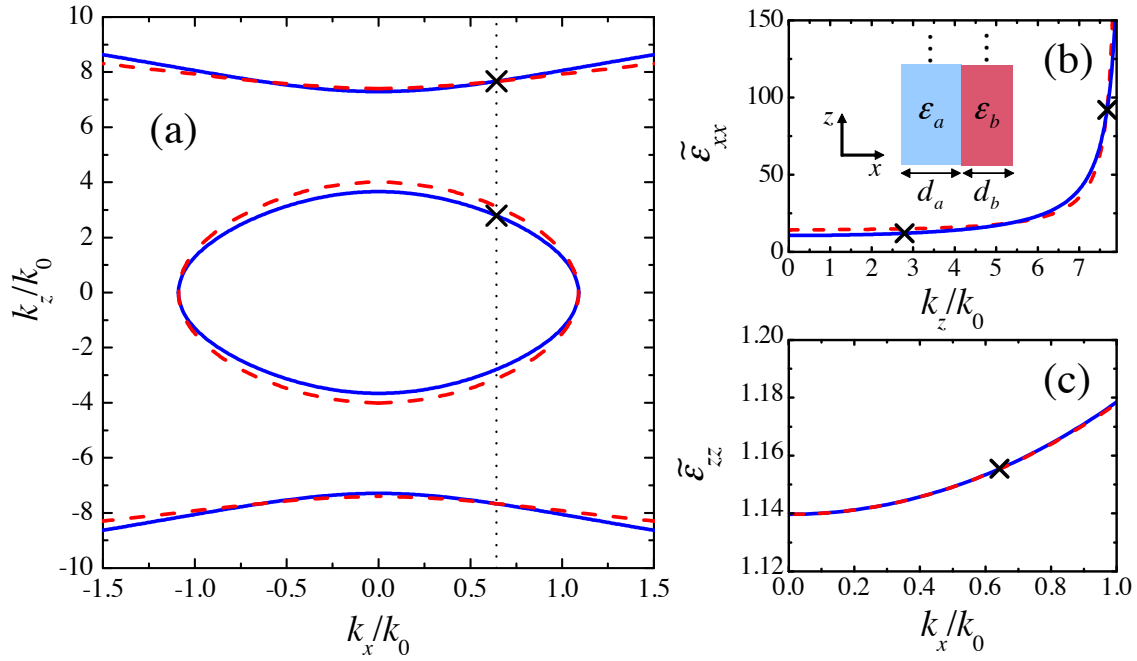

Figure 2: (From [15]) Examples of EFCs (a) and constitutive parameters (b,c) pertaining to a refraction scenario featuring the splitting of a plane wave with incidence angle $\theta_i = 40^o$ into two transmitted waves with angles $\theta_{t1} = 70^o$ and $\theta_{t2} = -45^o$. Blue (solid) curves represent the TO-based blueprints, obtained from (14) and (17) with $a_0 = 0.877$, $a_2 = -0.0289 k_0^{-2}$, $b_0 = 0.0934$, $b_2 = -0.0014 k_0^{-2}$. Red (dashed) curves pertain to the synthesized 1-D PC (unit-cell shown in the inset) with $\varepsilon_a = 2.752$, $d_a = 0.0668\lambda_0$, $\varepsilon_b = -2.082$, $d_b = 0.0332\lambda_0$ (see [15] for details). The vertical dotted line in (a) defines the incident wavenumber k_{ix}, from which the transmitted wavevectors (marked with crosses) are determined.

$\mathbf{k}_{t2}$ (marked with crosses).

3.3. Validation

In order to validate the above results, in [15] we carried out a finite-difference-time-domain (FDTD) simulation [19] involving a finite-size PC slab consisting of 890 unit cells [geometry and parameters as in Fig. 2(b)] with a total size of $89\lambda_0$ (along x) $\times$ $15\lambda_0$ (along z). The PC slab is illuminated by a collimated Gaussian beam with waist of size $15\lambda_0$, impinging from a vacuum region vacuum ($z < 0$) with an angle $\theta_i = 40^o$ with respect to the z-axis. We used a uniform spatial discretization of step $\Delta_x = \Delta_z = \lambda_0/120$, with time sampling $\Delta_t = \Delta_x/(5\sqrt{2}c_0)$ (i.e., five-time below the Courant numerical stability limit), and second-order Mur-type absorbing boundary conditions for terminating the computational domain. At this stage, we neglected material losses so as to better highlight the wave-splitting phenomenon of interest. In particular, for the negative-permittivity layers, we implemented (via the auxiliary differential equation method [19]) a plasma-type model

$$\varepsilon_b(\omega) = 1 - \frac{\omega_p^2}{\omega^2}, \tag{18}$$

with $\omega_p = 1.756\omega$.

From the field map shown in Fig. 3, it can be observed the splitting of an incident wide-waisted Gaussian beam into two transmitted beams, as well as the good agreement between the actual and prescribed transmitted directions.

We point out that, while the positively-refracted beam arises from *local* effects and may accordingly be predicted by standard effective-medium modeling, the negatively-refracted beam stems from the excitation and coupling of surface-plasmon-polaritons propagating along the interfaces between the negative-permittivity and dielectric layers of the PC, which are clearly visible in Fig. 3. This additional extraordinary wave can therefore be predicted (and controlled) only via *nonlocal* modeling.

The above results validate the synthesis procedure outlined in Sec. 3.2, and demonstrate that its outcomes are robust with respect to spatial truncation of the structure and illumination. More details can be found in [15].

4. Conclusions

In this review talk, we have summarized our recent results on a spectral-domain-based TO framework for the systematic synthesis of spatially-dispersive metamaterials embedding prescribed nonlocal field-transformation effects.

Our approach admits a physically-incisive and powerful geometrical interpretation in terms of EFC deformation, and relies on nonlocal homogenized models which are becoming increasingly available within the current research trends in materials engineering. Therefore, its relevance and practical applicability to a growing number of scenarios in spatial dispersion engineering may be envisaged within

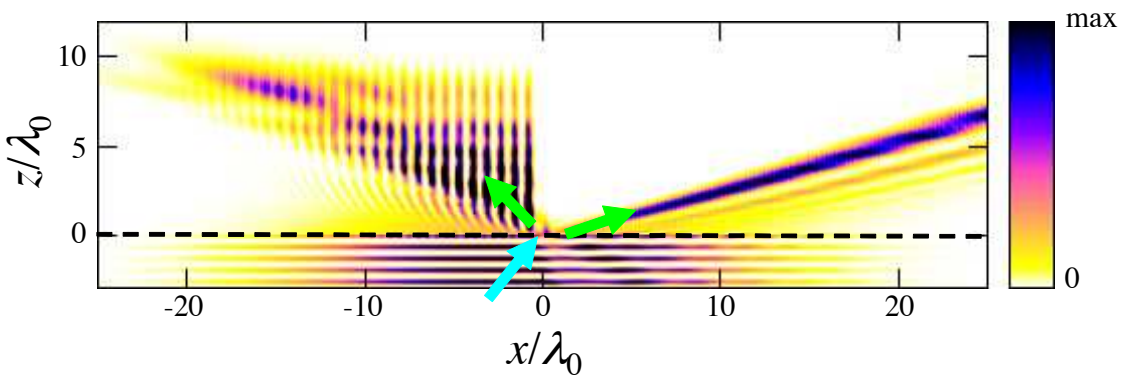

Figure 3: (From [15]) FDTD-computed magnetic-field intensity ($|H_y|^2$) map illustrating the transmission of a collimated Gaussian beam in a finite-size PC with parameters as in Fig. 2. The dashed line indicates the vacuum-PC interface, whereas the cyan and green thick arrows indicate the incident-beam and (prescribed) transmitted-beam directions, respectively.

the near future.

Also worth of interest is the exploration of non center-symmetric coordinate transformations for the engineering of *nonreciprocal* effects.

References

[1] P. Halevi, Ed., *Spatial Dispersion in Solids and Plasmas*, North-Holland, Amsterdam, 1992.

[2] V. M. Agranovich, V. Ginzburg, *Spatial Dispersion in Crystal Optics and the Theory of Excitons*, Wiley-Interscience, New York, 1966.

[3] M. G. Silveirinha, M. G., Generalized Lorentz-Lorenz formulas for microstructured materials, *Phys. Rev. B*, 76: 245117, 2007.

[4] A. Alù, Restoring the physical meaning of metamaterial constitutive parameters, *Phys. Rev. B*, 83: 081102R, 2011.

[5] A. Alù, First-principles homogenization theory for periodic metamaterials, *Phys. Rev. B*, 84: 075153, 2011.

[6] A. A. Orlov, P. M. Voroshilov, P. A. Belov, Y. S. Kivshar, Engineered optical nonlocality in nanostructured metamaterials, *Phys. Rev. B*, 84: 045424, 2011.

[7] G. A. Wurtz, R. Pollard, W. Hendren, G. P. Wiederrecht, D. J. Gosztola, V. A. Podolskiy, A. V. Zayats, Designed ultrafast optical nonlinearity in a plasmonic nanorod metamaterial enhanced by nonlocality, *Nature Nanotechnology*, 6, 107–111, 2011.

[8] M. Notomi, Manipulating light with strongly modulated photonic crystals, *Rep. Progr. Phys.*, 73: 096501, 2010.

[9] U. Leonhardt, Optical conformal mapping, *Science*, 312: 1777–1780, 2006.

[10] J. B. Pendry, D. Schurig, D. R. Smith, Controlling electromagnetic fields, *Science*, 312, 1780–1782, 2006.

[11] H. Chen, C. T. Chan, P. Sheng, Transformation optics and metamaterials, *Nature Materials*, 9: 387–396, 2010.

[12] S. A. Tretyakov, I. S. Nefedov, P. Alitalo, Generalized field-transforming metamaterials, *New J. Phys.*, 10: 115028, 2008.

[13] L. Bergamin, Generalized transformation optics from triple spacetime metamaterials, *Phys. Rev. A*, 78: 043825, 2008.

[14] G. Castaldi, I. Gallina, V. Galdi, A. Alù, N. Engheta, Transformation-optics generalization of tunnelling effects in bi-layers made of paired pseudo-epsilon-negative/mu-negative media, *J. Opt.*, 13: 024011, 2011.

[15] G. Castaldi, V. Galdi, A. Alù, N. Engheta, Nonlocal transformation optics, *Phys. Rev. Lett.*, 108: 063902, 2012.

[16] E. H. Lock, The properties of isofrequency dependences and the laws of geometrical optics, *Phys.-Usp.*, 51: 375–393, 2008.

[17] W. Cai, U. K. Chettiar, A. V. Kildishev, V. M. Shalaev, G. W. Milton, Nonmagnetic cloak with minimized scattering, *Appl. Phys. Lett.*, 91: 111105, 2007.

[18] J. Elser, V. A. Podolskiy, I. Salakhutdinov, I. Avrutsky, Nonlocal effects in effective-medium response of nanolayered metamaterials, *Appl. Phys. Lett.*, 90: 191109, 2007.

[19] A. Taflove, S. C. Hagness, *Computational Electrodynamics: The Finite-Difference Time-Domain Method*, 3rd Ed., Artech House, Norwood, MA, 2005.

Design of broadband microwave absorber utilizing FSS screen constructed with coupling configurations

Sun Liangkui, Zhang Chaoyang

National Key Laboratory of Science and Technology on Advanced Ceramic Fibers and Composites,College of Aerospace and Materials Engineering, National University of Defense Technology,Changsha,410073,China
*corresponding author, E-mail: slk_0_1999@yahoo.com.cn

Abstract

The design of a frequency selective surface (FSS) screen constructed using a coupling configuration to implement a broadband microwave absorber is presented in this paper. The reflectivity representation recognizes the characterization of the absorber. Simulation and measurement results are presented and analyzed. A coupling FSS screen is introduced in order to obtain a better bandwidth and absorption. The bandwidth with the reflectivity below -10dB could get 5.45-18GHz, compared with the 6.28-18GHz of the absorber with square patches FSS, provided that the thickness of the absorber is 4mm.

1. Introduction

Microwave absorber is a kind of function material that can be used in stealth technology. The applications in areocraft such as battleplan and missile determine that the absorber must have broadband wave absorbing performance to reduce the probability of being explored. As a potential candidate of high performance wave absorber, the researches of the metamaterial absorber are mostly concentrating on the perfect and multi-bands absorption [1-5]. Usually the Jaumann screen and lossy frequency selective surface (FSS) could realize broadband radar absorber [6-9]. Because of the egregious thickness of the Jaumann screen [6], lossy FSS absorber, which is consist of resistive FSS and dielectric substrate, is the best choice of the broadband absorber [9].

The main means of study the FSS absorber are numeric method and equivalent circuit method [9-10], also some optimization method is necessary due to the parameters determining the wave absorbing performance [11-12]. As to the single layer lossy FSS absorber, broadband wave absorbing performance can be realized through any FSS patterns [8-9]. But the optimal bandwidths of the familiar FSS absorbers have not been reported up to now. On the other hand, unlike the numerous FSS patterns designed in the HIP (high impedance surface) field [13-16], the FSS patterns reported in the lossy FSS absorber by far are simple, such as square patch, crisscross, and ring, whose impedance are represented by series RLC circuit [9]. In this letter, based on the optimized results of the conventional absorber, we report a broadband lossy FSS absorber using crisscross and fractal square patch to form a compact single particle. The reflectivity of the absorber exhibits three apexes in the frequency range of 2-18GHz. Moreover, owing to symmetry geometry, the absorber is independent on the polarization of an incident wave.

2. Design

On the basis of the conventional square patches shape, a complex and coupling FSS structure is presented, as shown in Figure 1 (b).

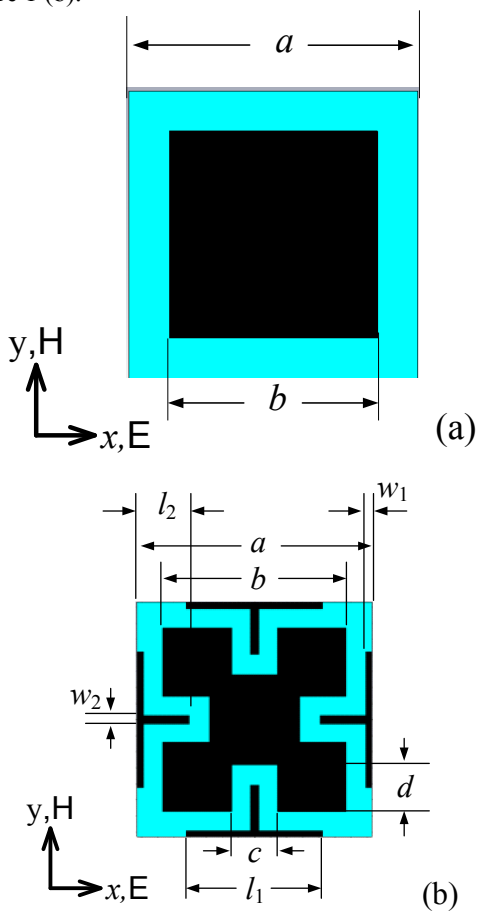

Figure.1 FSS screen of the absorber. The black represents the FSS and the blue indicates the dielectric substrate.

Compared with the square patches, the coupling structure has more optimizing parameters. The reflectivity properties, optimized by GA, are proposed for the coupling FSS absorbers and those of the square patches FSS absorber are also proposed for comparison, as shown in Figure 2. The results shown in Figure 2 indicate that the bandwidth is improved by using coupling FSS structure and there are three reflectivity nulls in the considerable frequency range.

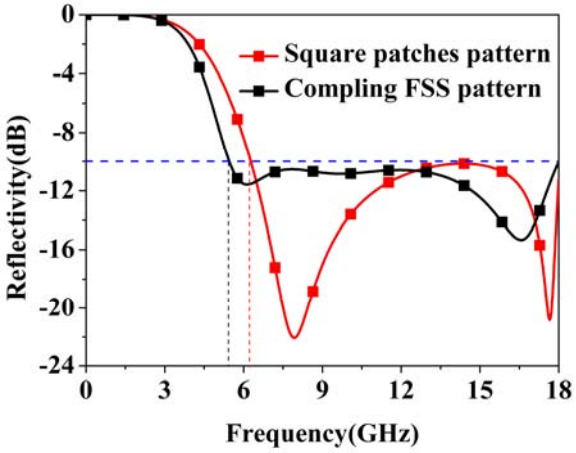

Figure 2: Modeled reflectivity of the absorber with different FSS pattern.

To get an insight into the origin of the bandwidth broadening, we monitor the surface current densities on the coupling FSS at resonance frequencies as shown in Figure 3.

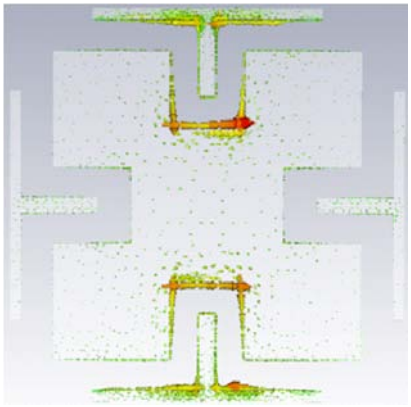

(a)

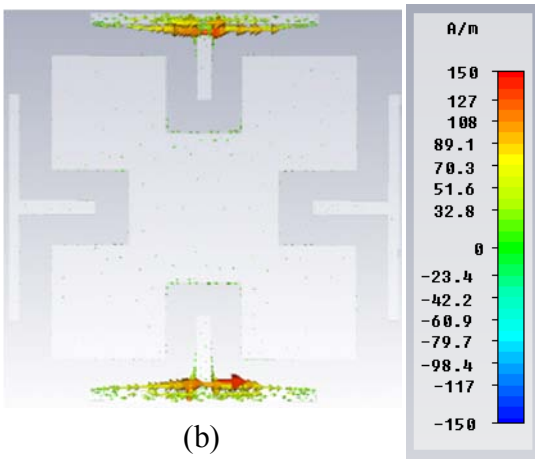

(b)

Figure 3: Distribution of the surface currents on the FSS at the resonance frequencies

The current distribution shown in Figure 3 indicates that there are two resonances in the coupling FSS, one of which is due to the coupling between the crisscross and the fractal square patch along the magnetic field direction. The other occurs between the adjacent unit cells along the electric field direction. We can predict that the double resonances are the main factors bringing the broadening of the bandwidth.

The optimized parameters of the absorbers are list in Table.1.

Table.1 Optimized parameters of the designed absorber

FSS shape	a (mm)	b (mm)	c (mm)	d (mm)	l_1 (mm)	l_2 (mm)	w_1 (mm)	w_2 (mm)	ε_r	Rs (Ω/□)
Square patches	13.7	10.3	/	/	/	/	/	/	1.8	99.8
Coupling FSS	17.8	13.9	3.6	3.8	11.4	4.8	0.45	1	1	29.7

3. Experiment and Result

The feasibility of the broadband absorber was demonstrated by experimental prototype. The resistive patterns representing the lossy FSS have been manufactured by the silk printing technique through a photo etched frame. The commercial rigid polyurethane foam was used as the dielectric substrate. The pictures of 180mm×180mm broadband sample is shown in Figure 4

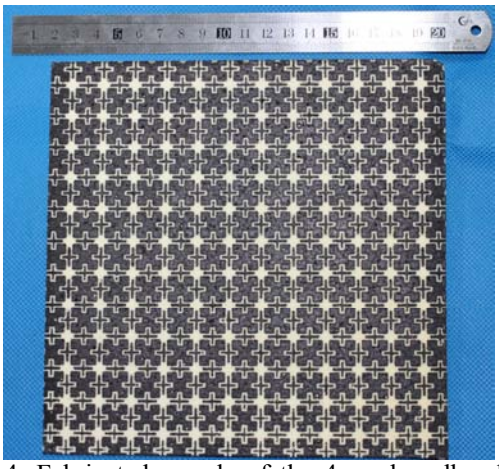

Figure 4: Fabricated sample of the 4mm broadband lossy FSS absorber

We verified the absorption performance of the broadband absorber in a microwave anechoic chamber. An Agilent 8720ET vector analyzer and two broadband double-ridged horn antennas are used to emit and receive the EM wave. Owing to the metal ground plane, the transmission is zero and the reflectivity represents the absorption. The measured reflectivity, compared with simulated result, is plotted in Figure 5

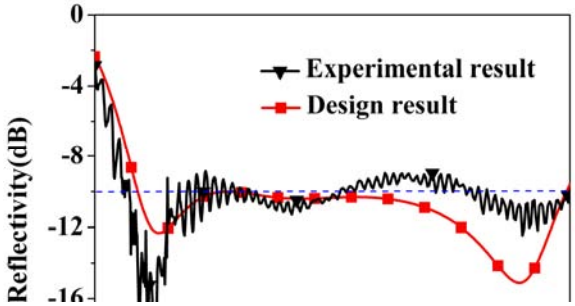

Figure 5: Comparison of the reflectivity of the broadband absorber between experimental (black curve) and simulated (red curve) results

Three absorption nulls exist in the considerable frequency range, which is consistent with the design result. The difference of the absorption intensity between the experiment and design is reasonably ascribed to the fabrication tolerances, such as the square resistance deviation of the lossy FSS. Both the simulation and experimental results indicate that the coupling in the FSS unit cell induces the absorption null in the low frequency, and lead to the enhancement of the bandwidth of the absorber.

In conclusion, a broadband metamaterial absorber with coupling FSS was design and fabricated. The design and experimental results show that the bandwidth with the reflectivity below -10dB of the 4mm thick absorber can get 5.27-18GHz, which is broader than 6.28-18GHz of the corresponding absorber with square FSS pattern.

References

[1] Xiaopeng Shen, Tie Jun Cui, Junming Zhao, Hui Feng Ma,Wei Xiang Jiang, and Hui Li, "Polarization-independent wide-angle triple-band metamaterial absorber", *OPTICS EXPRESS*.19, 9401-9407 (2011)

[2] N. I. Landy, S. Sajuyigbe, J. J. Mock, D. R. Smith, and W. J. Padilla, "Perfect metamaterial absorber", *Phys.Rev.Lett*. 100, 207402 (2008)

[3] Ruey-Lin Chern and Wei-Ting Hong, "Nearly perfect absorption in intrinsically low-loss grating structures" *OPTICS EXPRESS*.19, 8962-8972 (2011)

[4] Yongzhi Cheng, Helin Yang, Zhengze Cheng, NanWu, "Perfect metamaterial absorber based on a split-ring-cross resonator", *Appl Phys A*. 102, 99-103 (2011)

[5] By L. Huang and H. Chen, "Multi-band and polarization insensitive metamaterial absorber" Progress In Electromagnetics Research. 113, 103-110 (2011)

[6] Munk,B.A, Munk.P, Pryor.J, "On Designing Jaumann and Circuit Analog Absorber (CA Absorber) for Oblique Angel of Incidence", *IEEE Transactions on Antennas and Propagation*. 55, 186-193 (2007)

[7] Costa, F, Monorchio, A, Manara, G, "Ultra-thin absorbers by using high impedance surfaces with resistive frequency selective surfaces", International Symposium Antennas and Propagation Society. 2007

[8] Hai-Tao Liu , Hai-Feng Cheng, Zeng-Yong Chu, De-Yong Zhang, "Absorbing properties of frequency selective surface absorbers with cross-shaped resistive patches".*Material & Design* 28, 2166-2171 (2007)

[9] Filippo Costa, Agostino Monorchio, and Giuliano Manara, "Analysis and Design of Ultra Thin Electromagnetic Absorbers Comprising Resistively Loaded High Impedance Surfaces", *IEEE TRANSACTIONS ON ANTENNAS AND PROPAGATION*. 58, 1551-1558(2010)

[10] Yuri N. Kazantsev, Alexander V. Lopatin, Natalia E. Kazantseva, Alexander D. Shatrov, Valeri P. Mal'tsev, Jarmila Vilˇ cáková, and Petr Sáha, "Broadening of Operating Frequency Band of Magnetic-Type Radio Absorbers by FSS Incorporation". *IEEE TRANSACTIONS ON ANTENNAS AND PROPAGATION*, 58, 1227-1235 (2010)

[11] Dazhi Piao, Yanfei Li, Guizhen Lu, "Broadband electromagnetic absorber designs using genetic algorithm", Automation Congress, 2008

[12] Suomin Cui, Weile, D.S, Volakis, J.L, "Novel planar absorber designs using genetic algorithms", International Symposium Antennas and Propagation Society, 2009.

[13] Amr M. E. Safwat, "High impedance wire composite right/left-handed transmission lines", *Microwave and Optical Technology Letters*. 52, 1390-1393 (2010)

[14] M. E. de Cos, Y. Alvarez and F. Las-Heras, “A NOVEL APPROACH FOR RCS REDUCTION USING A COMBINATION OF ARTIFICIAL MAGNETIC CONDUCTORS”, *Progress In Electromagnetics Research*, 107, 147-159 (2010)

[15] Juan D. Baena, Ricardo Marque ´s and Francisco Medina, “Artificial magnetic metamaterial design by using spiral resonators”, *PHYSICAL REVIEW B*. 69, 014402 (2004)

[16] Junho Yeo, Ji-Fu Ma, and Raj Mittra, “GA-BASED DESIGN OF ARTIFICIAL MAGNETIC GROUND PLANES (AMGS) UTILIZING FREQUENCY-SELECTIVE SURFACES FOR BANDWIDTH ENHANCEMENT OF MICROSTRIP ANTENNAS”, *MICROWAVE AND OPTICAL TECHNOLOGY LETTERS*. 44, 6-12 (2005)

Metasurfaces: characterization and application as Partially Reflecting Surfaces for directivity enhancement of patch antennas

R. Yahiaoui[1,3], S. N. Burokur[2], V. Vigneras[3], A. de Lustrac[4], and P. Mounaix[1]

[1]Laboratoire Ondes et Matière d'Aquitaine, Université Bordeaux 1, CNRS, UMR 5798
351 Cours de la Libération, 33405 Talence Cedex, France
[2]LEME - Univ. Paris-Ouest, EA 4416, 92410 Ville d'Avray, France
[3]Laboratoire de L'intégration du Matériau au Système, Université Bordeaux 1, CNRS, UMR 5218
16 avenue Pey Berland 33607 Pessac Cedex, France
[4]IEF, Univ. Paris-Sud, CNRS, UMR 8622, 91405 Orsay cedex, France
*corresponding author: r.yahiaoui@loma.u-bordeaux1.fr

Abstract

In this paper we propose to investigate a metasurface designed, fabricated and characterized for an operation at microwave frequencies. A good quantitative agreement has been observed between simulations performed using finite element method-based commercial code HFSS and experiments made using a free space setup, based on vector network analyzer and horn antennas. Our proposed metasurface has further been validated as a Partially Reflecting Surface in a Fabry-Pérot cavity, with the aim to enhance the directivity of conventional microstrip patch antennas.

1. Introduction

Frequency Selective Surfaces (FSSs) are considered as spatial filters, which are generally realized using planar periodic structures [1-4]. Once exposed to an electromagnetic radiation, the FSS acts as a spatial filter, causing some wavelengths to be transmitted and others to be reflected. The response of a FSS is entirely determined by the size and geometry of the unit element, periodicity, and also by electrical properties of the dielectric substrate. FSSs have been initially used in military applications for stealth technology so as to reduce the Radar Cross Section (RCS) of an antenna system outside its frequency band of operation. In the last few years, many research groups have contributed to their development and integration in modern telecommunications systems. Considered as a subclass of metamaterial surfaces also known as metasurfaces, FSSs with their remarkable properties in controlling the propagation of electromagnetic waves have found many applications, which make them promising solutions to antennas and microwaves circuit's problems. Some examples are reflector antennas, radome design, polarizers, beam splitters and planar radar absorbers.

In this present work, we propose to investigate a Frequency Selective Surface. The sample is illuminated by a plane wave with TM polarization (i.e. *E*//*z*, *H*//*y* and *k*//*x*), at normal incidence with only one layer along the direction of propagation *k*. The dependency of the FSS on the incidence angle of the electromagnetic exciting wave is evaluated. The response of our FSS remains relatively unchanged for incidence angles between ± 45°. An enhancement of the selectivity of our FSS is validated by stacking several layers of our prototype sample along the direction of propagation *k*, and regularly spaced by an air gap. We also propose theoretically an original way to tune the response of our FSS. The basic idea consists in stacking two layers of our FSS (double-layered FSS) spaced by an air gap, and to apply a lateral displacement d to only one layer with regard to the other. Almost 22% tunability is observed using this method.

This FSS is then proposed as a metasurface acting as a Partially Reflecting Surface (PRS) in a Fabry-Pérot (FP) cavity with the main goal to enhance the directivity of a printed patch antenna inserted in this cavity. Numerical calculations, prototypes fabrication and experimental characterizations are performed in the microwave regime at around 9 GHz. Simulations and measurements agree very well, demonstrating a high directivity of the device.

2. Spectral response of the FSS

The proposed FSS is shown in Fig. 1(a). It consists of 35 μm thick metallic (copper) patterns printed on a single face of 0.5 mm thick dielectric substrate (Epoxy, $\varepsilon_r = 4.4$, $\tan(\delta) = 0.02$). The relevant geometrical dimensions of the FSS unit cell are as follows: a = 4 mm, b = 3 mm, c = 1 mm and d = 3 mm. Using the full wave electromagnetic simulator HFSS based on finite element method, we performed simulations in order to predict the spectral response of the structure. The sample is illuminated by a plane wave with TM polarization (i.e. *E*//*z*, *H*//*y* and *k*//*x*), at normal incidence with only one layer along the direction of propagation *k*. Microwave measurements have been done on a fabricated prototype composed of 23×25 cells. The reflection and transmission measurements have been performed applying an ABMillimetre™ network vector analyzer and horn antennas in a quasi-optical configuration.

In the transmission measurements, the incident plane waves are normal to the sample surface and the transmitted intensity is normalized with respect to transmission in free space between the two horn antennas. Similarly, the reflection coefficient, measured with a directional coupler in the reflection geometry, is normalized using a sheet of copper as reflecting mirror. Fig. 1(b) shows the simulated and measured transmission responses of the FSS. A pass band frequency behavior centered around 40 GHz with a bandwidth at -3 dB estimated at 6 GHz is observed. The bandwidth is rather wide, which indicates the poor selectivity of the spatial filter. The transmission peak reaches a maximum value of about -1 dB at 40 GHz and a good agreement is reported between simulations and experiments. The dip in the measured transmission around 38 GHz near the resonant frequency is due to the finite nature of the fabricated prototype, since we simulated an infinite 2D structure, which is fully illuminated by plane wave. Further numerical calculations that have been performed, but not shown here, demonstrated the critical influence of a more realistic and finite prototype on the spectral response.

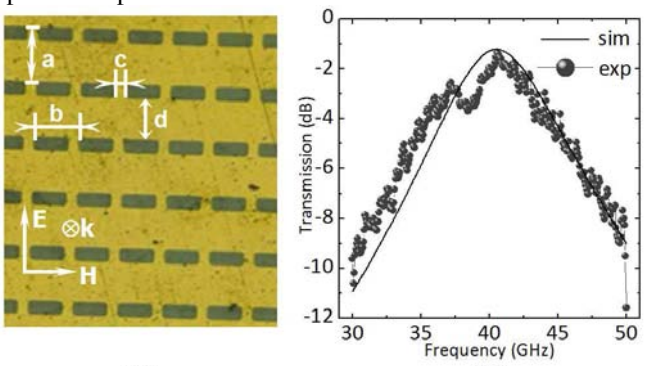

Figure 1: (a) Experimental prototype of our investigated Frequency Selective Surface with relevant geometrical dimensions a = 4 mm, b = 3 mm, c = 1 mm, d = 3 mm and t = 0.5 mm. The appropriate polarization of the electric and magnetic fields is also shown. (b) Magnitude of the simulated (solid line) and measured (line and symbols) transmission coefficient.

Depending on the targeted application, the selectivity of a spatial filter can be a very important and critical characteristic in its functionality, which should be taken into account during the design procedure. We propose here to enhance the selectivity of our FSS by stacking several layers of our prototype along the direction of propagation k, and regularly spaced by an air gap g_{air} = 1 mm. Indeed, the selectivity of the spatial filter is significantly increased as shown in Fig. 2(a) and a fairly good quantitative agreement between the simulated (solid lines) and measured (lines and symbols) transmission coefficient for 1, 2, 3 and 4 FSS layers is observed. The bandwidth of the filter at -3 dB goes from 6 GHz to 3 GHz for 4 FSS staked layers. We also notice a decrease in the level of transmission at the 40 GHz resonant frequency, with a minor shift towards lower frequencies in the measured responses, in the case of 3 and 4 staked layers, compared to the simulated responses. This shift may be due to the physical displacement that can occur between the metallic patterns when the layers are stacked.

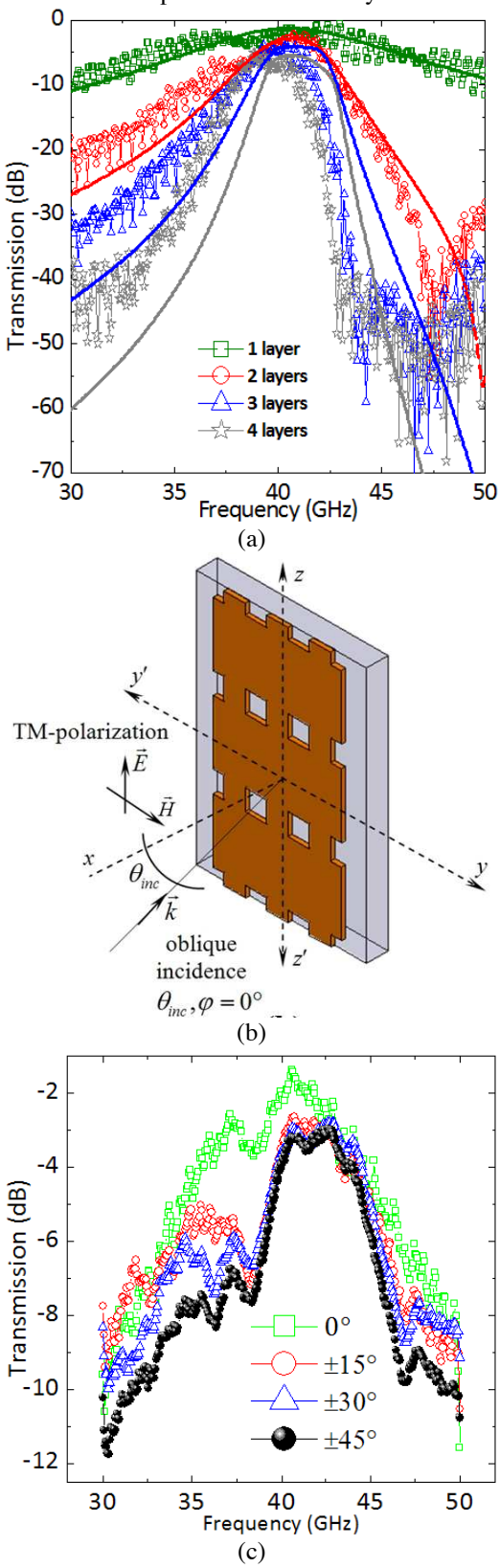

Figure 2: (a) Magnitude of the calculated (solid lines) and measured (lines and symbols) transmission coefficient for 1, 2, 3 and 4 stacked layers respectively along the direction of propagation k, (b) Our FSS under investigation, for the

angular study, (c) magnitude of the transmission coefficient of the FSS, measured for different incidence angles θ_{inc} between -45° and +45°.

The dependency of the FSS on the incidence angle of the electromagnetic exciting wave has also been evaluated. Fig. 2(b) shows the typical scenario used for the oblique incidence study of a single metasurface. The transmitting and receiving antennas remain fixed, while the sample under investigation is rotated. The response of our FSS remains relatively unchanged for incidence angles between ± 45° as depicted in Fig. 2(c), which is potentially very interesting and useful for oblique incidence applications. The dip appearing near the resonant frequency, which has been previously mentioned, is much more pronounced beyond ±15° incidence since the number of unit cells illuminated by the incident wave-fronts is reduced. However, measurements performed on a larger prototype should give better results.

3. Tunability of the spectral response of the FSS

Frequency tunable responses of electronic and electromagnetic devices are highly desired since they offer the possibility to operate at different frequencies. The most common method to obtain tunability is to change the effective electric length or the effective permittivity of the structure, and the techniques used to reach this goal are various and widely discussed in scientific literature. Here, we propose theoretically an original way to tune the response of our FSS. The basic idea consists in stacking two layers of our FSS (double-layered FSS) spaced by an air gap g_{air} = 1 mm, and to apply a lateral displacement d to only one layer with regard to the other, as illustrated in Fig. 3(a).

3.1. Double-layered FSS

The horizontal displacement d introduce additional peaks around 42.5 GHz, 45.9 GHz and 62.7 GHz respectively, as illustrated by the reflexion coefficient (black-solid-line) of Fig. 3(b) in the case d = 100 μm. For a better understanding of the origin of these peaks, we have performed a series of numerical simulations on our investigated double-layered FSS. Our investigations reveal that each peak is in fact a contribution of different sub-elements constituting the unit cell of the double-layered FSS, thus the resulting response is the superposition of each sub-element's response. Indeed, the unit cell of our investigated double-layered FSS can be regarded as a combination of an array of shifted metallic continuous-wire pairs in the direction of the electric field and an array of double-plate pairs. The first and the second higher order modes that appear around 42.5 GHz and 46 GHz, comes from the shifted metallic continuous-wire pairs and the third higher order mode that occurs at about 62.7 GHz corresponds to the contribution of the double-plate pairs, as it can be clearly observed in Fig. 3(b). Similar effect has been previously observed for multiple-frequency band applications in terahertz regime [5-7]. At this stage, it is important to note that when the air gap g_{air} and the horizontal shift d are set to 0, the double-layered FSS can be assimilated to the previously reported fishnet structure [8-9], presenting a negative effective index. However, due to the air gap of 1 mm used in our study, negative index will not be observed.

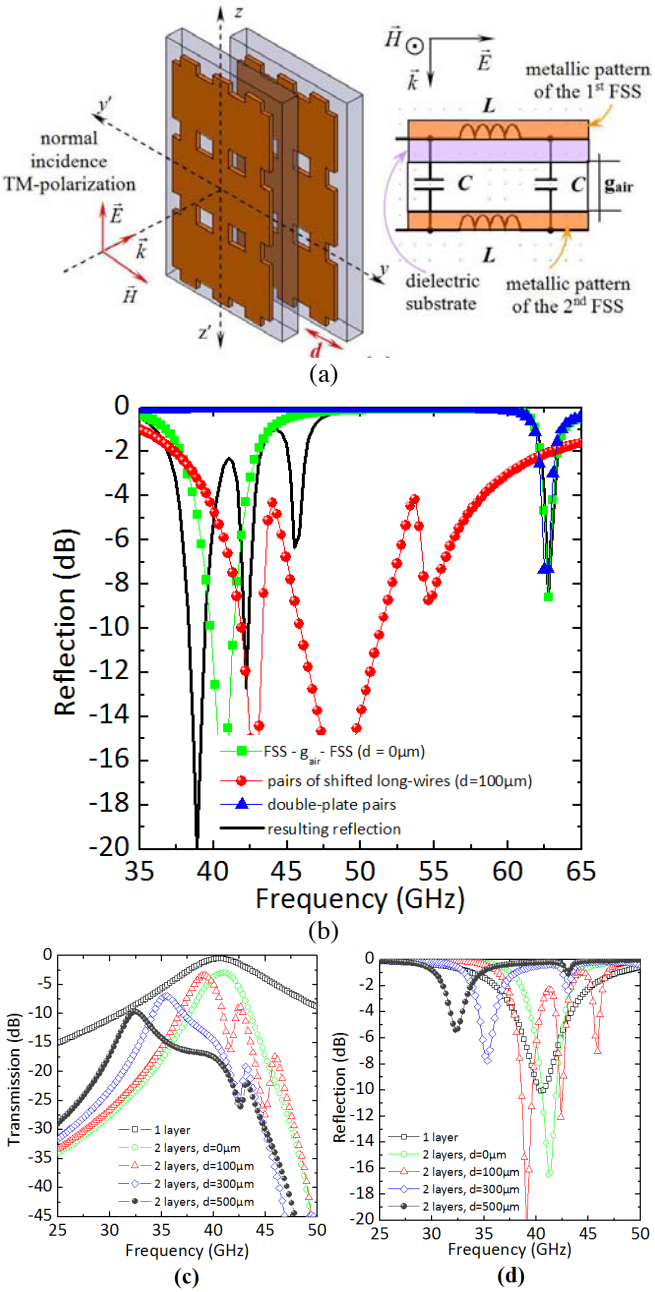

Figure 3: (a) Configuration of our system which leads the tunability of the spectral response of the double-FSS, one layer of the double-FSS is translated horizontally along the yy′ axis, while the second layer remains fixed, (b) illustration of the origin of additional peaks that appear on the reflection coefficient during the lateral displacement d. Tunability of the transmission (c) and the reflection (d) coefficients, for different values of the displacement d along yy' axis from 0 μm to 500 μm.

3.2. Tunable FSS

The tunability effect can be explained as follows: the total structure can be regarded as an electric equivalent *LC* circuit having a resonant frequency f_r. The resonant frequency strongly depends of the electric properties of the material used and the geometrical dimensions of the unit cell of the sample. As detailed in Ref. 8 for the fishnet structure, the FSS is composed of a slab (plate) and a neck (continuous wire). The resonant frequency of our investigated FSS is given by the following approximate expression [9]: $f_r = 1/2\pi\sqrt{LC}$, where L corresponds to the inductance of the metallic patterns of the unit cell along the direction of the electric field $\vec{E}$ and C corresponds to the capacitance created between the two metallic patterns separated by the dielectric substrate and the air-gap. The capacitance C takes into account both the capacitance C_n of the neck pair and the capacitance C_s of the slab pair. The lateral displacement along the *yy'* axis of one layer in the double-layered FSS causes a misalignment of the metal patterns, changing C_n and thus modifying the resonant frequency of the structure. In this case, C_s is unchanged. Figs. 3(c) and 3(d) show the tunability effect on the transmission and reflection spectra, respectively for different values of parameter d. The resonant frequency decreases from its nominal value 41 GHz to 32.5 GHz, when d goes from 0 μm to 500 μm (about 22% of tunability). From our calculations, we have also noticed that the translation of one layer along the electric field $\vec{E}$ direction (polarized along zz' axis) does not affect significantly the response of the FSS, creating only a minor level of tunability. In this type of translation, we will be in presence of two possible situations; either one neck faces another neck or one neck faces a slab. In both cases, C_n will be similar. However, C_s will be modified, but only slightly, explaining the minor level of tunability. The main transmission peak centered at about 41 GHz splits into new peaks which move in opposite directions. The fundamental mode decreases in intensity and moves towards low frequencies from 41 GHz to 32.5 GHz when d increases from 0 μm to 500 μm. As pointed out in the beginning of this section, higher order modes are observed in both transmission and reflection coefficients at the aforementioned frequencies.

4. Directivity enhancement of microstrip patch antennas

Following our investigations on the FSS in the above sections, we now propose a potential and interesting application of this metasurface. Indeed, the FSS can be very useful as a metasurface reflector in Fabry-Pérot (FP) cavities. Since the pioneering works of G. V. Trentini in the 50's [10], these cavities have been studied as reflex-cavity antennas for their directive emissions. Consequently, we propose to evaluate the studied FSS as a Partially Reflecting Surface (PRS) in a FP cavity so as to enhance the directivity of antennas based on the use of a single feeding source. This class of antennas has received renewed interest, particularly with the development of metallo-dielectric periodic structures [11-16].

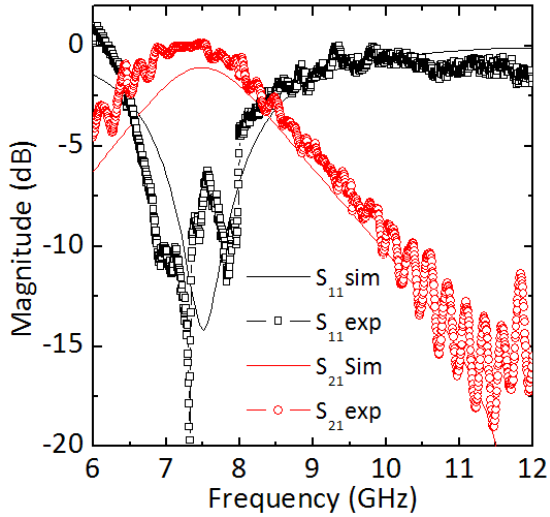

(a)

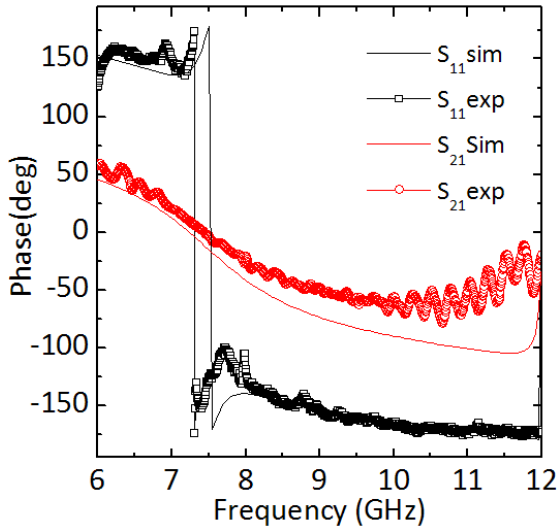

(b)

Figure 4: (a) Calculated (solid lines) and measured (lines and symbols) magnitudes (a) and phases (b) of transmission and reflection coefficients.

For antenna experimental measurement setup availability, we carry out this application investigation in the X band at around 9 GHz. Here we design our FSS in order to act as the PRS in such a reflex-cavity antenna. Using a standard printed circuit board and optical lithography, a planar prototype composed of 9×9 cells having optimized geometrical dimensions: a = 18 mm, b = 12 mm, c = 3.5 mm and d = 12 mm, has been fabricated on the epoxy substrate of thickness 1.6 mm in order to validate simulation results. Measurements have been carried out in an anechoic chamber using a network vector analyzer, and two broadband horn lens-antennas working in the [2 GHz - 18 GHz] frequency band are used as emitter and receiver. Fig. 4(a) shows the calculated (solid lines) and measured (lines and symbols) spectral responses of the structure. We observe a good quantitative agreement between theory and experiment. Our

proposed structure can be regarded as a pass-band spatial filter, with a first resonant mode localized at about 7.5 GHz. The reflection phase shown in Fig. 4(b) varies from +180° to -180° and passes through zero at resonance. The reflection phase values are used to calculate the thickness h versus frequency at which maximum boresight directivity (θ = 0°) can be obtained (Fig. 5(a)). This resonance thickness is determined by the following equation:

$$h_r + t\sqrt{\varepsilon_r} = (\varphi_{PRS} + \varphi_r)\frac{\lambda}{4\pi} \pm N\frac{\lambda}{2}, \qquad (1)$$

where φ_{PRS} represents the reflection phase of the partially reflecting surface, φ_r is the reflection phase of the reflector screen near the antenna, λ is the operating wavelength and N is an integer corresponding to the order of the cavity's electromagnetic mode. t and ε_r are the thickness and the relative dielectric permittivity dielectric substrate supporting the feeding source, respectively. At 9 GHz, a reflection phase close -180° is observed, suggesting a cavity thickness close to λ/2. We shall note that the reflection at this frequency is quite high (about -1 dB), which is necessary for confining electromagnetic waves in the cavity. This confinement allows achieving high directivity since directivity is given by D = (1+R)/(1-R) [11]. To illustrate the directivity enhancement, we performed numerical simulations and measurements on the cavity using the FSS reflector.

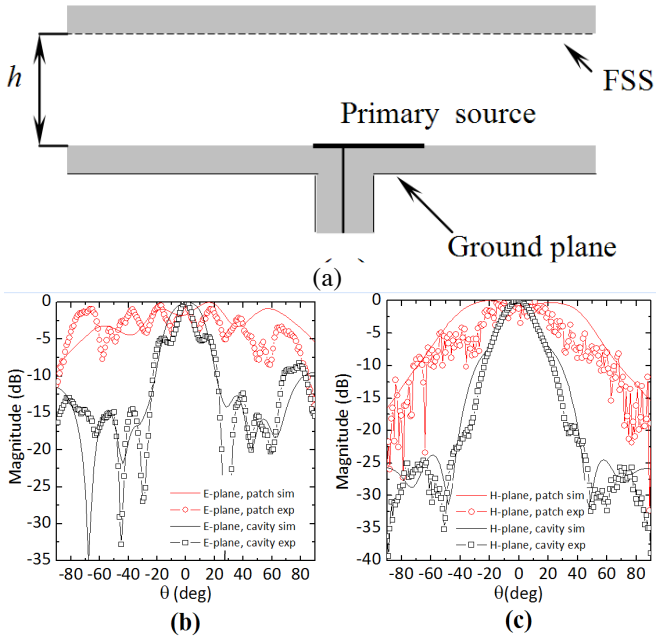

Figure 5: (a) Schematic view of Fabry-Pérot cavity antenna with the FSS as a partially reflecting surface. Calculated (solid lines) and measured (lines and symbols) radiation patterns for E-plane (b) and H-plane (c) for both patch antenna (red color) and Fabry-Pérot cavity (black color), respectively.

The cavity is fed by a microstrip patch antenna patterned also on an epoxy substrate. Figs. 5(b) and 5(c) show the calculated and the measured radiation patterns in E- and H-planes for the patch feed source and for the 15 mm thick resonant FP cavity, respectively. The performances obtained from measurements (lines with symbols) carried out on the fabricated prototypes agree very well with the numerical calculations (solid lines). The directivity of our investigated system is considerably enhanced and goes from 8 dB for the patch antenna to 20 dB for the cavity and the parasitic side lobes level of the cavity remains below -10 dB. These results show the potential application of our proposed FSS in a FP cavity for highly directive emissions. Moreover, the study performed on the frequency tunability of the double-layered FSS suggests the possibility of a frequency reconfigurable cavity using such type of FSS as reflector.

5. Conclusions

To summarize, we have theoretically and experimentally investigated a planar FSS that has been designed, fabricated and characterized for an operation frequency in the microwave regime. The selectivity of the studied FSS is considerably enhanced when stacking several layers. The angular robustness of the transmission response was demonstrated, and an original technique has been proposed in order to obtain a tunability of the spectral response. The FSS has been used as a Partially Reflecting Surface in a Fabry-Pérot cavity where the radiation patterns have shown a highly directive emission.

Acknowledgements

This work has been performed at the University of Bordeaux1, within the project "GIS AMA-SAMM". The authors would like to thank Philippe Maire for the fabrication of experimental prototypes and for fruitful discussions.

References

[1] E. A. Parker, S. B. Savia, Active frequency selective surfaces with ferroelectric substrates, *Proc. Inst. Elect. Eng. Microwaves Antennas* and *Propagation* 148(2): 103-108, 2001.

[2] J. Romeu, Y. Rahmat-Samii, Fractal FSS: a novel dual-band frequency selective surface, *IEEE Trans. Antennas Propag.* 48(7): 1097-1105, 2000.

[3] B. Schoenlinner, A. Abbaspour-Tamijani, L.C. Kempel, G. M. Rebeiz, Switchable low-loss RF MEMS Ka-band frequency-selective surface, *IEEE Trans. Antennas Propag.* 52(11): 2474-2481, 2004.

[4] K. Sarabandi, N. Behdad, A frequency selective surface with miniaturized elements, *IEEE Trans. Antennas Propag.* 55(5): 1239-1245, 2007.

[5] Y. Yuan, C. Bingham, T. Tyler, S. Palit, T. H. Hand, W. J. Padilla, N. M. Jokerst, S. A. Cummer, A dual-resonant terahertz metamaterial based on single particle electric-field-coupled resonators, *Appl. Phys. Lett.* 93: 191110, 2008.

[6] R.Yahiaoui, H. Němec, P. Kužel, F. Kadlec, C. Kadlec, P. Mounaix, Broadband dielectric terahertz

metamaterials with negative permeability, *Opt. Lett.* 34(22): 3541-3543, 2009.

[7] R. Yahiaoui, H. Němec, P. Kužel, F. Kadlec, C. Kadlec, P. Mounaix, Broadband dielectric terahertz metamaterials with negative permeability, *Appl. Phys. A*. 103(3): 689-692, 2011.

[8] M. Kafesaki, I. Tsiapa, N. Katsarakis, Th. Koschny, C. M. Soukoulis, E. N. Economou, Left-handed metamaterials: The fishnet structure and its variations, *Phys. Rev. B*. 75: 235114, 2007.

[9] C. Yan, Y. Cui, Q. Wang, S. Zhuo, Negative refractive indices of a confined discrete fishnet metamaterial at visible wavelengthselective surface with miniaturized elements, JOSA B 25(11): 1815-1819, 2008.

[10] G. V. Trentini, Partially reflecting sheet arrays, *IRE Trans. Antennas Propag*. AP-4(4): 666-671, 1956.

[11] A. P. Feresidis, G. Goussetis, S. Wang, J. C. Vardaxoglou, Artificial Magnetic Conductor Surfaces and their application to low-profile high-gain planar antennas, *IEEE Trans. Antennas Propag*. 53(1): 209-215, 2005.

[12] L. Zhou, H. Li, Y. Qin, Z. Wei, C. T. Chan, Directive emissions from subwavelength metamaterial-based cavities, *Appl. Phys. Lett*. 86: 101101, 2005.

[13] Ourir, A. de Lustrac, J.-M. Lourtioz, All-metamaterial-based sub-wavelength cavities ($\lambda/60$) for ultrathin directive antennas, *Appl. Phys. Lett*. 88: 084103, 2006.

[14] R. Yahiaoui, S. N. Burokur, A. de Lustrac, Enhanced directivity of ultra-thin metamaterial-based cavity antenna fed by multisource, *Electron. Lett*. 45(16): 814-816, 2009.

[15] S. N. Burokur, R. Yahiaoui, A. de Lustrac, Subwavelength metamaterial-based resonant cavities fed by multiple sources for high directivity, *Microwave Opt. Technol. Lett*. 51(8): 1883-1888, 2009.

[16] S. N. Burokur, J.-P. Daniel, P. Ratajczak, A. de Lustrac, Tunable bilayered metasurface for frequency reconfigurable directive emissions, *Appl. Phys. Lett*. 97: 064101, 2010.

Thick metallic slabs with axially inhomogeneous holes in the hybrid transmission regime

A. E. Serebryannikov[1]

[1]Hamburg University of Technology, E-3, D-21071 Hamburg, Germany
E-mail: serebryannikov@tu-harburg.de

Abstract

Transmission through thick metallic slabs that contain arrays of the holes, whose cross section is piecewise-constant in the axial direction, is studied. The cross section of an individual hole is assumed to be variable so that the evanescent-wave and propagating-wave regimes may co-exist at the neighboring sections of deep holes that create waveguide channels connecting the front-side and the back-side interface. It is shown that high-efficiency transmission can be obtained in such a tunneling regime, even if the evanescent-wave sections occupy rather a big part of the channel length.

1. Introduction

Arrays of the subwavelength annular holes in metallic slabs have been extensively studied for more than ten years [1]. As entry point for the present study, our recent results on transmission through thick metallic slabs with the annular hole arrays have been used [2]. High transmittance becomes possible due to squeezing of the normally incident plane wave into the annular waveguide channel. This invokes an efficient coupling to the mode TE_{11} of the coaxial waveguide, which is the lowest mode that may appear in the propagating-wave regime at normal incidence, while the tilting is needed to excite the TEM mode [3]. Termination of this waveguide at the slab interfaces leads to the interferences creates an open resonator and, thus, enables the Fabry-Perot type axial resonances, which manifest themselves as the well-pronounced transmission peaks.

In this paper, the emphasis is put on the structures, in which the waveguides that connect the slab interfaces contain both the propagating-wave sections (coaxial in our case) and the evanescent-wave sections (circular in our case). As a result, a hybrid transmission regime can be realized, when the propagating waves in the coaxial sections are coupled to the evanescent waves in their circular neighbors. The main goal here is to demonstrate that high transmission can occur despite a significant total length of the evanescent-wave sections. Special attention has been paid to the detecting of the possibilities of total transmission, when all the higher diffraction orders are evanescent. Extensive numerical simulations have been performed using CST Microwave Studio, a commercial solver, and a code based on modal analysis. The structures considered here have been designed to operate at the microwave frequencies. Thus, the PEC approximation is adopted for the metallic constituents. Each waveguide channel is assumed to contain several coaxial sections, which may be located periodically or aperiodically in the axial direction. The obtained results will be discussed in the context of the role of tunneling, axial Fabry-Perot type resonances, and lateral surface waves in the achieving of high-efficiency transmission through the structures, which are at least one free-space wavelength thick.

2. Results and Discussion

Let us consider the basic features of the typical transmission spectra. An example is shown in Fig. 1 in case when five rather thick disks are periodically placed inside a circular waveguide that is created by a deep hole. In fact, we have in this case an array of the holes with the axially inhomogeneous cross sections. The space between the disks and the outer wall is occupied with dielectric (ε=2.1). One

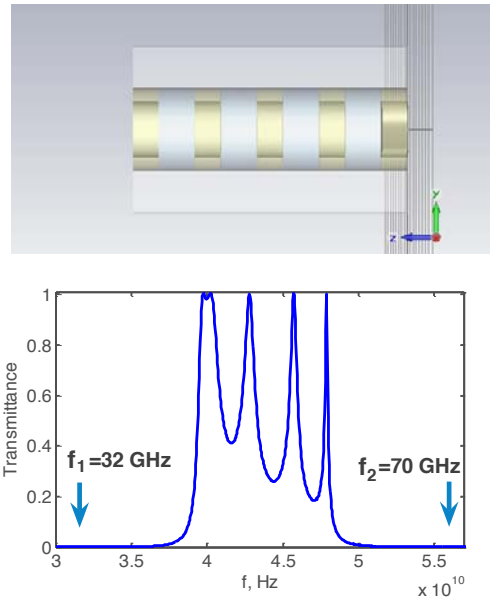

Figure 1: Unit cell of the array of circular holes with the thick disks that are inserted into the hole periodically in the axial direction.

can see that the resulting structure within an array period (unit cell) presents a finite piece of the composite waveguide in the solid metallic slab that contains short alternating pieces of the coaxial and the circular waveguide. The sections of these two types have different cutoffs, so that the propagating waves may appear in the coaxial sections only. The structure is illuminated with a linearly polarized, normally incident plane wave. The array period has been chosen so that the benefit of high transmittance, which is borrowed from the similar structures with the axially homogeneous coaxial waveguide channel [2], still remains.

The transmission spectrum in Fig. 1 shows the features that are typical for the open Fabry-Perot type resonators created by finite slabs of a dispersive lossless material. In other words, the observed peaks of T=1 have different width and, thus, are expected to correspond to different values of the equivalent group velocity and group index, and Q-factor. For example, the fourth peak, which is the narrowest one, corresponds to Q=210, while the second peak does to Q=39. In Fig. 1, the total thickness of the slab, D, is connected to the incident wave length as D/λ=1.07 and D/λ =1.28, at the lower and upper edges of the shown passband. The two arrows schematically show location of the cutoffs for the coaxial (f_1) and circular (f_2) sections, of which the waveguides do consist (in fact, f_2 should be located beyond the plot area). Below them, there is no transmission through the slabs with arrays of the holes showing either coaxial or circular cross section, which is not varied in the axial direction. Thus, our expectation concerning that the stacking of the alternating propagating-wave and evanescent-wave sections can lead to the propagating-wave regime in a composite structure is valid. Increase of D at fixed other parameters leads to the densening of the peaks (not shown) within the transmission band that is a quite predictable feature, being typical for the conventional Fabry-Perot resonances.

According to the classical waveguide theory, the phase and the group velocity of a certain waveguide mode are given by $v_{ph}=ck/\Gamma$ and $v_g=d\omega/d\Gamma=c\Gamma/k$, where propagation constant $\Gamma=k\left[1-(f_c/f)^2\right]^{1/2}$ and f_c is cutoff frequency, below which this mode is evanescent. Then, the equivalent phase and group indices of refraction can be introduced as $n_{ph}=\Gamma/k$ and $n_g=k/\Gamma$, respectively. Hence, both n_{ph} and n_g are real-valued at $f>f_c$ and imaginary-valued at $f<f_c$. Correspondingly, the propagating-wave and evanescent-wave sections are associated with the real and imaginary values of the equivalent indices. The presence of the evanescent-wave sections indicate some analogies with the tunneling mechanism in the periodic multilayer stacks, which requires that at least multilayers of one type would show single-negative parameters, i.e., either $\varepsilon<0$ or $\mu<0$ [4]. Thus, the transmission regime in Fig. 1 might be consistent with that arising in multilayer stacks of double-positive/-negative and single-negative materials.

Clearly, total transmission at a rather large extent of metallization of the interfaces would be impossible without strong lateral field components that allow one harvesting the incident-wave energy from a rather large area. They are often associated with surface waves, although discussion concerning the necessity of using this concept remains open, while the classical diffraction theory might give adequate tools to analyze these structures.

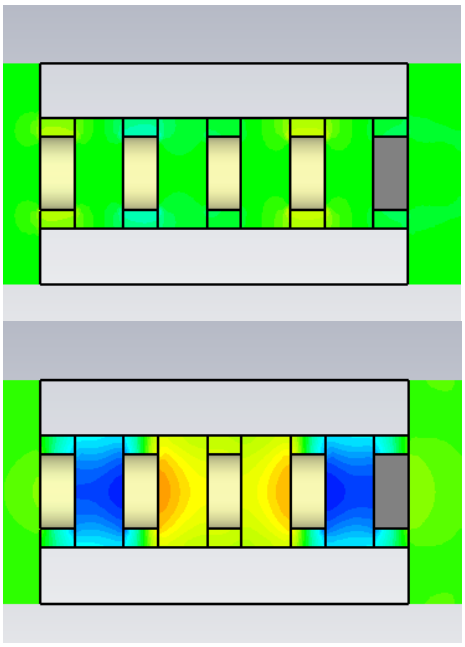

Figure 2: Electric (upper plot) and magnetic (lower plot) field distribution at the third peak in Fig. 1.

Figure 2 presents an example of the field distribution at one of the transmission maxima. Multifold enhancement of both electric and magnetic fields can occur as compared to the incident wave. In particular, strong magnetic field is observed within the evanescent-wave sections. In turn, electric field is strong inside and near the supporting dielectric rings, i.e., in the propagating-wave sections. It is worth noting that the passband occupies the same frequency range as in the periodic case in Fig. 1.

In order to check our initial guess concerning the role of periodicity in obtaining high-efficiency transmission due to the axial Fabry-Perot resonances, we distorted the periodicity of the structure in Fig. 1 by removing one of the disks within each hole, as shown in Fig. 3. Hence, one of the evanescent-wave sections is now longer than others. Although the signatures of the Fabry-Perot type resonances are still seen in the transmission spectrum, total (unity) transmission cannot be achieved.

Next, we changed the out-coupling, so that an evanescent-wave section is adjacent to the exit half-space, while a propagating-wave section is adjacent to the input half-space similarly to Fig. 1. Geometry of the structure and transmission spectrum are shown in Fig. 4. Despite of this modification, there is no significant difference between Figs. 3 and 4 in that concerns the maximum achievable transmittance. The only difference is that the peaks are well pronounced in Fig. 4. This occurs due to that the regular

(undistorted) waveguide section contains here more of the same periods. Thus, it is not important whether the outgoing wave is coupled out to an evanescent or a propagating wave. The same is related to the coupling of the incident wave. Presently, the structures with the evanescent-wave

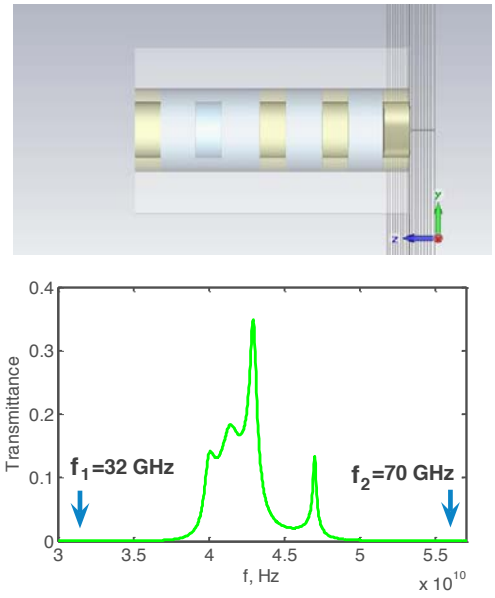

Figure 3: Unit cell of the array of circular holes with the broken axial periodicity and propagating-wave sections that are adjacent to the both interfaces.

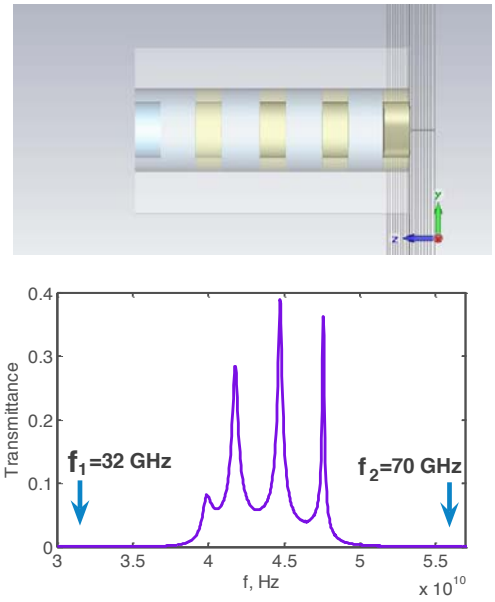

Figure 4: Same as Fig. 3, but the evanescent-wave section is adjacent to the exit interface.

coupling at the both interfaces are under study. Finally, the obtained transmission results have been compared with those for similar structures having the axially homogeneous circular holes from the point of view of transmission enhancement [2].

3. Conclusions

Resonance transmission through the thick metallic slabs with periodic arrays of the circular holes with the embedded disks that are located in the axial direction either periodically or aperiodically has been studied in detail. The principal possibility of obtaining high-efficiency transmission in these structures is connected, first of all, with tunneling through the evanescent-wave sections of the waveguide channels created by holes, and a proper choice of the array period that enables an efficient harvesting and in- and out-coupling. The axial Fabry-Perot type resonances are especially important for the obtaining of total transmission. The studied transmission regimes can also be obtained at higher, e.g., THz frequencies by re-scaling the structure.

Acknowledgements

This work has been supported by DFG under Project Nos., SE1409/2-1 and SE1409/2-2.

References

[1] S. M. Osborn and A. Roberts, Resonance and extraordinary transmission in annular aperture arrays, *Opt. Express* 14: 12623-12628, 2006.

[2] A. E. Serebryannikov, Transmission through thick metallic structures with subwavelength annular holes from the enhancement and slow-wave perspectives, *Proc. of 5th Int. Congress on Adv. Electromag. Mat. in Microwaves and Optics*, Barcelona, Spain, Oct 10-15, 2011.

[3] V. Lomakin, S. Li, and E. Michielssen, Transmission through and wave guidance on metal plates perforated by periodic arrays of through-holes with subwavelength coaxial cross-section. *Microwave Opt. Technol. Lett.* 49: 1554-1558, 2007.

[4] A. Alu and N. Engheta, Pairing an epsilon-negative slab with a mu-negative slab: resonance, tunneling and transparency, *IEEE Trans. Ant. Propag.* 51: 2558-2571, 2003.

Novel uniplanar flexible Artificial Magnetic Conductor

M. E. de Cos[1], and F. Las Heras[1]

[1]Area de Teoría de la Señal y Comunicaciones. Dpt. Ingeniería Eléctrica, Universidad de Oviedo.
Edificio Polivalente, Mod. 8. E-33203 Gijón, Asturias, Spain
*M. E. de Cos, E-mail: medecos@tsc.uniovi.es

Abstract

A novel flexible uniplanar Artificial Magnetic Conductor (AMC) design is presented. A prototype is manufactured and characterized under flat and bent conditions in anechoic chamber. The designed prototype shows broad AMC operation bandwidth, polarization angle independency and high angular stability margin when operating under oblique incidence.

1. Introduction

Metamaterials exhibit unique properties in controlling the propagation of electromagnetic waves which make them very attractive as potential solution for some microwaves circuits and antennas problems.

At microwave frequencies, uniplanar Frequency Selective Surfaces (FSSs) over a metallic ground plane can be used as Electromagnetic Band-Gaps (EBGs) (exhibiting one or several frequency bands in which no mode propagation is allowed) or as Artificial Magnetic Conductors (AMCs) (exhibiting in-phase reflection). In the absent of via holes, both EBG frequency band and AMC frequency band do not necessarily coincide [1]. At the resonance frequency, both EBGs and AMC structures, exhibit high impedance surface and so they are also called High Impedance Surfaces (HIS) [2]-[6].

AMCs are electromagnetically dual to Perfect Electric Conductors (PEC) and behave as Perfect Magnetic Conductors (PMCs) over a certain frequency band (as PMCs do not exist in Nature), the so-called AMC frequency band. AMCs can be used as reflectors, in the design of low-profile and highly efficient antennas and to reduce the antenna radiation to the body in wearable applications.

The interest in flexible AMCs is growing since it would be desirable to have AMC being object-shape-adapted for many applications as RFID tags over metallic objects [7], wearable antennas [8]-[11] and RCS reduction [12]-[13]. This would require the AMC to be flexible but without losing its functionality. In addition, the AMC performance for different polarization of the electrical incident field (under normal incidence) and under oblique incidence is very important. AMC designs with as higher angular stability as possible are desirable [14].

In this contribution a novel flexible AMC design is presented in section 2. It has several additional advantages as being uniplanar, compact and without via holes which makes it cost-reduced. A prototype of the flexible AMC is manufactured using a bendable dielectric substrate. Section 3 describes the AMC prototype characterization process and results, showing that in addition, the novel design exhibits broad AMC operation bandwidth together with high angular stability in both flat and bent conditions. Finally, some conclusions are given in section 4.

2. AMC design

Each unit-cell of an AMC structure implements a distributed LC network with one or more resonance frequencies at $1/\left(2\pi\sqrt{LC}\right)$ where the structure exhibits high surface impedance meanwhile the in-phase reflection bandwidth is proportional to $\sqrt{L/C}$. At frequencies below the resonance frequency the surface impedance of the periodic structure is inductive and supports TM waves whereas at frequencies higher than the resonance frequency, the surface impedance is capacitive and supports TE waves.

The unit-cell geometry together with the substrate relative permittivity and thickness mainly determine the AMC resonant frequency and AMC frequency bandwidth. So those are the elements modified by a designer in order to obtain an AMC at a specific frequency and with a given bandwidth. To increase the AMC bandwidth a thicker dielectric substrate is needed, as it increases the equivalent L, meanwhile it decreases the resonance frequency. Another way of increasing the equivalent L and so the AMC bandwidth, is including narrow strips in the geometry design. In addition, by reducing the substrate's relative dielectric permittivity ε_r and increasing the gap between adjacent unit-cells the equivalent C can be reduced and the AMC bandwidth will be also increased. Finally, it has to be taken into account that higher ε_r reduces the resonance frequency and the AMC bandwidth. In sum, to obtain both compact size and broad AMC operation bandwidth a trade-off solution has to be taken considering substrate thickness and ε_r.

Taking all these facts into account a uniplanar AMC [15]-[16] at 6GHz has been designed using ROGER3003 substrate with a thickness h=0.762 mm, relative dielectric permittivity ε_r = 3.0 and loss tangent tgδ=0.0013. The geometry of the AMC unit-cell is shown in Fig. 1 and the

final optimized dimensions for operation at 6GHz using Ansoft HFSS [17] are detailed in table I.

HFSS simulation set-up used to obtain the reflection coefficient phase based on Finite Element Method (FEM) and Bloch-Floquet theory is shown in Fig.2. It models a single unit-cell of the structure with periodic boundary conditions (PBCs) on its sides, to resemble the modelling of an infinite structure [2],[15]. To illuminate the periodic surface normal plane waves are launched using a waveport positioned a half-wavelength above it. The phase reference plane is taken on the periodic surface and the phase of the reflection coefficient for the AMC structure is compared to that of a PEC plane taken as reference, placed at exactly the same position as the AMC, in the same way as in [2].

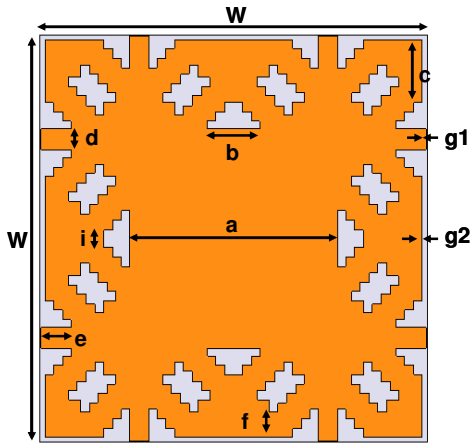

Figure 1: AMC unit-cell geometry top view.

Table 1: Unit-cell dimensions.

Dimensions (mm)				
W	**a**	**b**	**c**	**d**
12.000	6.456	1.646	1.827	0.609
e	**f**	**g1**	**g2**	**i**
0.945	0.730	0.032	0.154	0.522

Fig. 4 shows the reflection coefficient phase simulation [15] results for the designed AMC. As it could be expected, at low frequencies compared to the resonance frequency, the reflection coefficient phase is 180º, and the periodic structure behaves like a PEC. The reflection phase crosses through zero at the resonance frequency and returns to -180º above it. When the surface impedance exceeds the free space impedance the reflection phase falls in -90º, 90º. Image currents are in-phase rather than out of phase within this range, as in a PMC, and for this reason it is generally considered the AMC operation bandwidth. The inherent in-phase reflection property of AMCs makes possible antenna elements lay directly on the periodic surface without being short-circuited or malfunctioning.

From the reflection coefficient phase simulation results (see Fig.4) an AMC operation bandwidth of 500 MHz (8.33%) is obtained under normal incidence. It is a broad bandwidth for a very thin AMC (λ_0/65.6 at 6GHz).

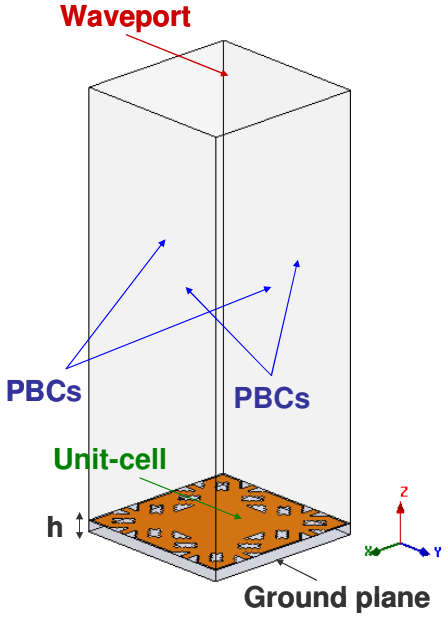

Figure 2: Simulation set-up for determining the reflection properties of the AMC.

At the resonance frequency an AMC behaves as a PMC exhibiting high surface impedance due to a very low value (ideally null) of the tangential magnetic field. To verify this fact, simulations have been carried out for a normal incident plane wave using the setup of Fig 2 (with PBCs so that the structure mimics an infinite AMC). Fig 3. shows the magnetic field variation along a plane at three different positions of the AMC unit-cell for different frequencies. As it could be expected, at the resonance frequency (6GHz) the magnetic field (H) on the periodic surface considerably decreases compared to its value at the other frequencies out of the AMC frequency band.

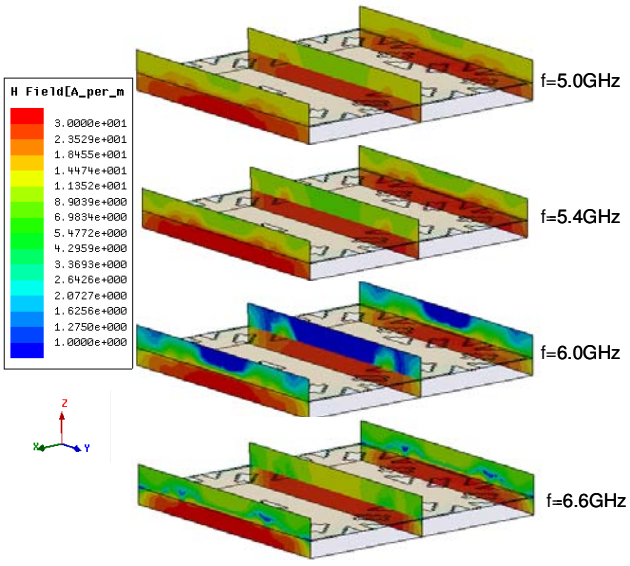

Figure 3: Magnetic field distribution on an AMC unit-cell with periodic boundary conditions at different frequencies.

Angular stability [14] is a key fact in AMC design and even more in flexible ones as in may of the intended applications, such as RFID tags or wearable antennas, it has a direct impact on their performance. For example, when combining and AMC with an antenna for an RFID tag, the AMC angular stability influences the antenna radiation performance and so the reading range. In sum, it is desirable an AMC with as higher angular stability as possible.

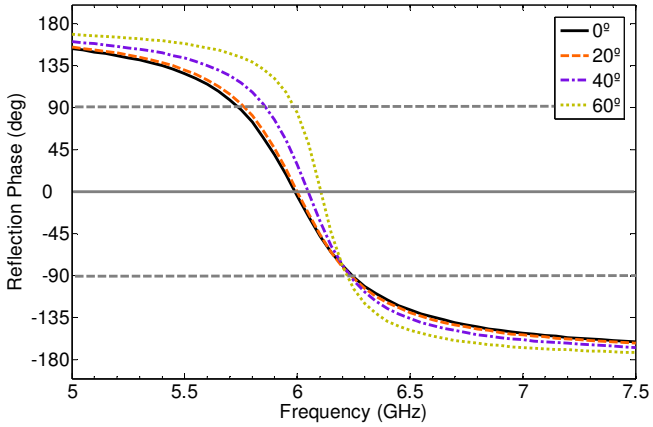

Figure 4: Simulation results of AMC reflection coefficient phase for TE polarization under different incidence angles θ_{inc}=0º, 20º, 40º and 60º .

Concerning AMC stability for different polarizations of the incident electric field, this can be ensured by using a symmetric design as the one presented in this contribution which exhibits four symmetry planes.

The reflection coefficient phase versus frequency for different incident angles θ_{inc} between 0º and 60º has been simulated for transverse electric (TE) polarized waves aiming to study the angular stability margin [14] of the presented structure. From Fig. 4 it can be obtained the absolute and relative deviations of the resonant frequency which are respectively 96MHz and 1.6%. So, it can be concluded that the presented AMC design is highly stable as it exhibits an angular margin of θ_{inc}=±60º.

3. AMC prototype characterization

A 12x12 cells AMC prototype has been manufactured using laser micromachining. The prototype physical size is 14.4cm x 14.4cm

Fig. 5 shows the reflection coefficient measurement setup in anechoic chamber (similar to the one used in [15]). Two horn antenna probes working in the band 5-7 GHz have been chosen as Tx and Rx, being 3m the separation between each probe and the object-under-test. The followed methodology [2],[15] is based on the utilization of a reference measurement (a metallic plate considered as PEC) to calculate the reflection coefficient of the AMC and is in fact the same used for the full-wave simulation. Taking into account the measured prototypes physical size (PEC and AMC have the same size), for the upper frequency (f = 7 GHz), the far field distance (RFF = $2D^2$ / λ) is $RFF_{,7GHz}$ ~ 0.97m, whereas for the lower frequency (f = 5 GHz) it decreases until $RFF_{,5GHz}$ ~ 0.69m. So the prototypes have been measured in far field conditions.

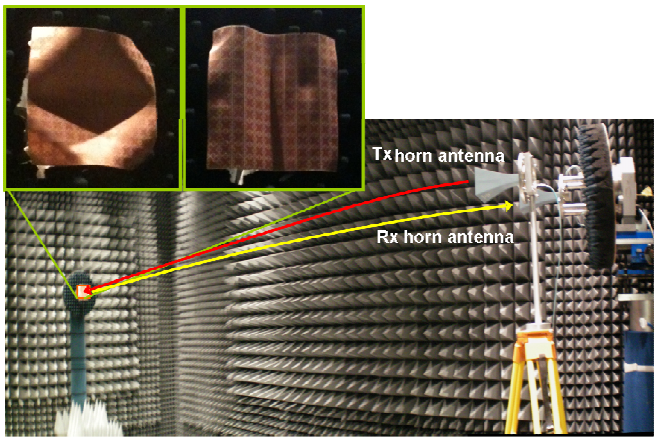

Figure 5: Reflection coefficient measurement set-up in anechoic camber.

There are many possible ways of bending an AMC. Two typical different bending patterns for the AMC have been selected and tested (see Fig.6) a “creeping” pattern which can be caused in textile AMC integrated in the garment for example when the arm is bent at the elbow, and a “smooth” pattern which can be caused in the torso or in the shoulder.

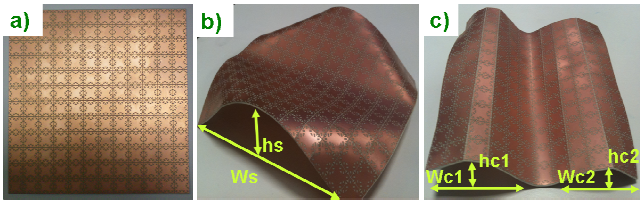

Figure 6: AMC manufactured prototype and bending patterns: a) Flat manufactured prototype b) smooth prototype with Ws=125mm, and hs=30mm; c) creeping prototype with Wc1=60mm, Wc2=52mm, hc1=18mm, and hc2=15mm

The measured reflection phase of the flat and bent manufactured prototypes for normal incidence conditions are shown in Fig. 7. The flat prototype has the resonance at 6.178GHz which means a 2.9% deviation with respect to the simulation (6.0GHz) due to under-etching in the laser micromachining. There is no frequency shift for the creeping bent prototype with respect to the flat prototype resonance, whereas the smooth bent prototype has its resonance at 6.208GHz, which means just a 1.69% deviation with respect to the flat prototype.

The flat prototype shows a 430MHz (6.96%) AMC operation bandwidth in good agreement with simulated value (8.33%) whereas the creeping bent prototype exhibits 625MHz (10.07%) and the smooth bent AMC shows 487MHz (8.02%), even slightly wider than that of the flat prototype.

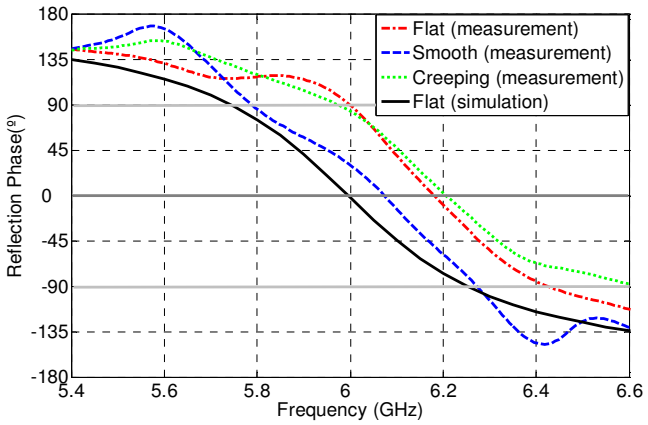

Figure 7: AMC reflection coefficient phase under flat and bent conditions.

Under normal incidence (θ_{inc} = 0º) the flat prototype presents the same reflection phase for any polarization due to the unit cell symmetry. In the case of the bent prototype, this invariance with respect to the polarization angle is also present.

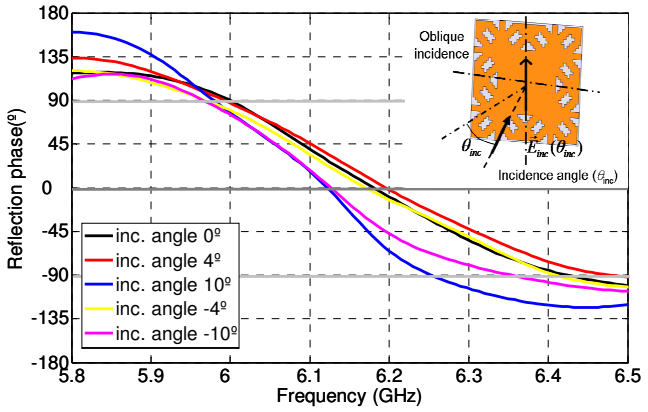

Figure 8: Reflection coefficient phase of the manufactured flat prototype for different incident angles (θ_{inc}).

The reflection coefficient phase versus frequency, for different incident angles θ_{inc} has been measured. As it was explained in the previous section, simulation results (see Fig.4) show an angular margin of θ_{inc}=±60º for transverse electric (TE) polarized waves with 1.6% relative deviation of the resonant frequency. In measurement this angular margin decreased due to finite size of prototypes. For the flat prototype resonance conditions are met within an angular margin of θ_{inc}=±10º (see Fig.8) whereas for the smooth and creeping bent prototypes (see Fig.9 and Fig.10) the obtained angular margin is θ_{inc}=±8º.

These results show that it is possible to obtain a flexible AMC without reducing the bandwidth of AMC performance with respect to a rigid AMC that uses the same unit cell design and preserving its angular stability under oblique incidence.

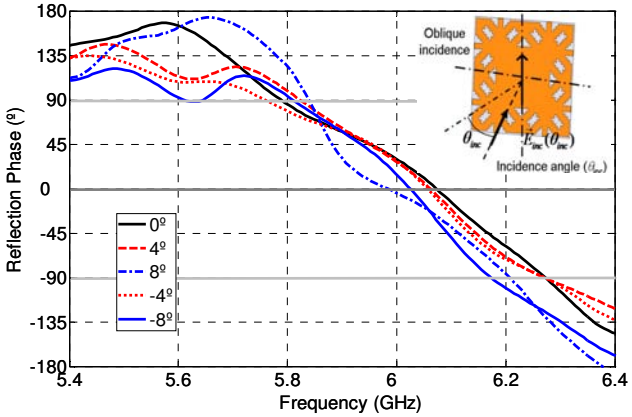

Figure 9: Reflection coefficient phase of the manufactured smooth prototype for different incident angles (θ_{inc}).

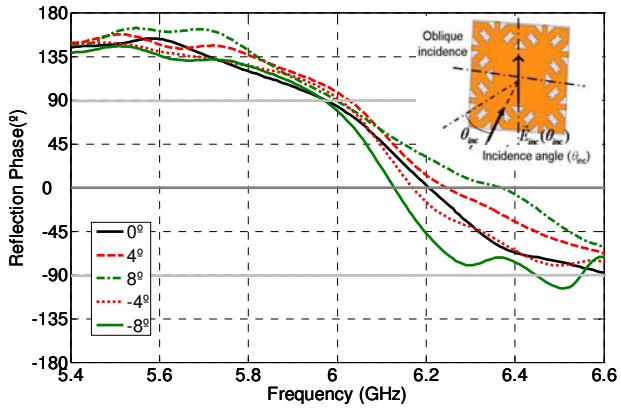

Figure 10: Reflection coefficient phase of the manufactured creeping prototype for different incident angles (θ_{inc}).

4. Conclusions

The presented novel uniplanar low-profile flexible AMC design without via holes exhibits broad AMC operation bandwidth, polarization angle independency under normal incidence and high angular stability under oblique incidence. Its low cost, simple fabrication and integration make it very attractive for applications involving antennas in RFID tags, wearable systems, and RCS reduction.

Acknowledgements

Work supported by the Ministerio de Ciencia e Innovación of Spain /FEDER under projects TEC2008-01638/TEC (INVEMTA) and CONSOLIDER-INGENIO CSD2008-00068 (TERASENSE), by the Gobierno del Principado de Asturias (PCTI)/FEDER-FSE under project PC10-06 (FLEXANT).

References

[1] G. Goussetis, A. P. Feresidis, and J.C.Vardaxoglou "Tailoring the AMC and EBG Characteristics of Periodic Metallic Arrays Printed on Grounded Dielectric Substrate", IEEE Trans. Antennas Propag., Vol.54, no.1, pp. 82-89, Jan 2006.

[2] D. Sievenpiper, L. Zhang, R. F. Jimenez Broas, N. G. Alexópolous and E. Yablonovithc, "High-impedance electromagnetic surfaces with a forbidden frequency band", IEEE Trans. Microwave Theory Tech., vol.47, no. 11, pp.2059-2074, Nov.1999

[3] F. R. Yang, K. P. Ma, Y. Qian, and T. Itoh, "A uniplanar compact photonic-bandgap (UC-PBG) structure and its applications for microwave circuit", IEEE Trans. Microwave Theory Tech., vol 47, no.8, 1509-1514, 1999

[4] D. J. Kern, D. H. Werner, A. Monorchio, L. Lanuza, and M. J. Wilhelm, "The design synthesis of multiband artificial magnetic conductors using high impedance frequency selective surfaces", IEEE Trans. on Antennas and Propag., Vol.53, No. 1, Jan. 2005.

[5] Y. Zhu, A. Bossavit and S. Zouhdi, "Surface impedance models for high impedance surfaces", Applied Physics A: Materials Science & Processing, Volume 103, Number 3, pp 677-683, 2011.

[6] M. Grelier, F. Linot, A.C. Lepage, X. Begaud, J.M. Le Mener and M. Soiron: "Analytical methods for AMC and EBG characterisations", Applied Physics A: Materials Science & Processing, Vol. 102, N.2, feb. 2011.

[7] R. C. Hadarig, M. E. de Cos, Y. Álvarez, and F. Las-Heras "Novel Bow-tie–AMC Combination for 5.8-GHz RFID Tags Usable with Metallic Objects" IEEE AWPL, Vol 9, pp 1217-1220, 2010.

[8] M. Mantash, A-C. Tarot, S. Collardey and K. Mabjoubi "Dual-band antenna for W-LAN applications with EBG", Proceedings of Metamaterials'2011, Barcelona, pp. 456 – 458, 10-15 October 2011, Spain.

[9] M. Mantash, A.C. Tarot, S. Collardey, K. Mahdjoubi, "Dual-band CPW-fed G-antenna using an EBG structure," Antennas and Propagation Conference (LAPC), Loughborough, pp. 453–456, 2010.

[10] S. Zhu and R. Langley, "Dual-Band Wearable Textile Antenna on an EBG Substrate", IEEE Trans. on Antennas and Propag., Vol.57, No. 4, April 2009.

[11] P. Salonen and Y. Rahmat-Samii, "WEBGA-wearable electromagnetic band-gap antenna", IEEE APS Int. Symp. Dig., vol.1, 451-4, Monterrey, CA, June 2004.

[12] María Elena de Cos, Yuri Álvarez, Fernando Las-Heras, "A novel approach for RCS reduction using a combination of Artificial Magnetic Conductors," Progress In Electromagnetics Research PIER 107, 147-159, 2010

[13] M. Paquay J-C. Iriarte, I. Ederra, R. Gonzalo and P. de Maagt "Thin AMC Structure for Radar Cross Section Reduction," IEEE Trans. on Antennas and Propag., vol. 55, No. 12, pp. 3630-3638, Dec 2007

[14] C. R. Simovski, P. de Maagt, S.A. Tretyakov, M. Paquay and A.A. Sochava, "Angular stabilisation of resonant frequency of artificial magnetic conductors for TE-incidence," Electron. Lett., vol. 40, no. 2, pp.92–93, Jan. 2004.

[15] M. E. de Cos, Y. Álvarez and F. Las-Heras, "Planar Artificial Magnetic Conductor: Design and Characterization setup in the RFID SHF Band", JEMWA, Vol 23, 1467-1478, 2009.

[16] A. P. Feresidis, G. Goussetis, S. Wang, and J. C. Vardaxoglou, "Artificial magnetic conductor surfaces and their application to low profile highgain planar antennas," IEEE T.A.P. vol. 53 no. 1 pp. 209–215, Jan. 2005.

[17] Ansoft HFSS, from Ansoft Corporation, Four Station Square Suite 200, Pittsburgh, PA 15219.

A Polarization-/Angle-Insensitive, Bandwidth-Optimized, Metamaterial Absorber in the Microwave Regime

Alexandros I. Dimitriadis, Nikolaos V. Kantartzis, and Theodoros D. Tsiboukis

Department of Electrical and Computer Engineering,
Aristotle University of Thessaloniki, Thessaloniki GR-54124, Greece
*corresponding author, E-mail: aldimitr@auth.gr

Abstract

An enhanced metamaterial absorber based on the circumscribed-cross resonator is introduced in this paper. The new structure is polarization-independent, due to the symmetry of its unit cell, and is proven efficient for the attenuation of obliquely incident waves. The absorption mechanism is thoroughly investigated and is found to be mainly related to the losses of the dielectric substrate. Furthermore, by exploiting the scalability property of metamaterials, the operational bandwidth of our design can be drastically improved by placing unit cells with properly scaled resonators adjacent to each other. In this context, various combinations of three, four, and nine unit cells, that can increase the full width at half maximum up to as much as 11.18%, are developed. The overall performance of the proposed configurations is deemed promising for the realization of microwave metamaterial absorbers for several practical applications.

1. Introduction

Metamaterial absorbers have, recently, triggered a notable scientific investigation with an escalating impact on modern microwave systems. To this objective, the combination of an electric-LC (ELC) resonator with a split-wire has been proposed for the construction of an almost perfect arrangement, which, in its initial design, has been very sub-wavelength (around $\lambda_0/35$) [1]. Although quite narrowband and basically effective only for normally incident waves, this device inspired several researchers to probe its absorption mechanism [2], [3]. In the meanwhile, a considerable variety of instructive ideas have been launched in order to produce efficient metamaterial absorbers in the microwave, terahertz, and infrared frequency regions [4]-[10].

However, contemporary real-world applications, like RCS minimization from airplanes, steamboats and other vehicles or protection from electromagnetic interference due to mobile phones and local area networks, require more sophisticated features, while preserving the ultra-thin size of the original approach. Amid them, one can discern the larger bandwidth or multiple bands of operation as well as the wide-angle and polarization-independent absorption rates [11]-[17]. Essentially, most of the structures reported in the literature focus on the improvement of just one of the prior characteristics, thus turning the construction of an overall optimized device into a challenging design problem.

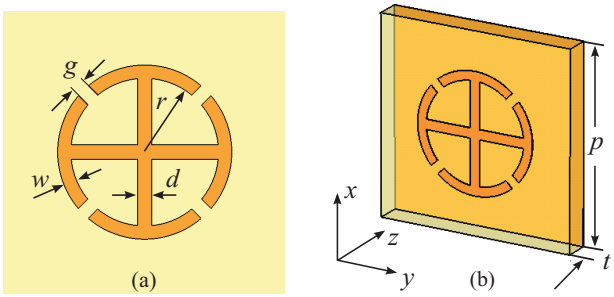

Figure 1: (a) Front and (b) perspective view of the CCR absorber. Dimensions: $r = 2.06\,\text{mm}$, $d = 0.40\,\text{mm}$, $g = 0.39\,\text{mm}$, $w = 0.37\,\text{mm}$, $p = 8\,\text{mm}$, and $t = 1\,\text{mm}$.

In this paper, a novel metamaterial absorber with improved bandwidth performance that operates around the middle of the microwave X-band ($8.0 - 12.0\,\text{GHz}$), is presented. The proposed design, implemented by means of the circumscribed-cross resonator (CCR), exhibits remarkable wide-angle absorption and independence on the polarization of the incident radiation. Moreover, taking avail of metamaterial scalability, the operational bandwidth of the structure is significantly enhanced by combining appropriately tailored unit cells in certain periodic arrangements. In this way, the demanding obliquely incident waves are efficiently absorbed, without any other non-physical conventions. The merits of the optimized absorber are thoroughly validated via different metal and dielectric material setups, while some possible future extensions are finally discussed.

2. Theory and design of the CCR absorber

The primary design concept of the proposed device is based on the CCR, depicted in Fig. 1a, which belongs to the class of ELC resonators [18] and its first resonance is usually excited by an electric field component parallel to one of its crossed wires. The CCR is imprinted on a standard 1 mm-thick FR-4 substrate ($\varepsilon_r = 4.3$, $\tan\delta = 0.022$), whereas the opposite face of the dielectric spacer is covered with a copper layer (Fig. 1b), so as to ensure zero transmission throughout the structure. Additionally, periodic boundary conditions are applied along the x- and y-axis in order to model an infinite array of unit cells. For our analysis, all simulations are carried out through the frequency domain solver of CST MWS$^{\text{TM}}$ computational package [19].

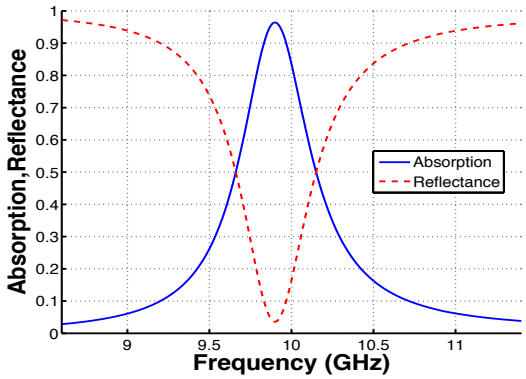

Figure 2: Absorption and reflectance of the proposed structure. The absorption peak of 96.41% occurs at the frequency of 9.90 GHz and the FWHM is 4.96%.

Starting with arbitrary dimensions and considering a normally incident plane wave propagating along the z-direction with its electric-field component polarized along the x-axis, a genetic algorithm is employed to reach the optimal unit cell parameters for maximum absorption near the middle of the X-band. The absorption of the structure is calculated from the values of the simulated scattering parameters through its definition as $A(\omega) = 1 - R(\omega) - T(\omega)$, with $R(\omega) = |S_{11}|^2$ and $T(\omega) = |S_{21}|^2$ being the reflectance and transmittance, respectively. Since $T(\omega) = 0$ due to the copper plane, Fig. 2 illustrates the reflectance and absorption of the device, revealing an absorption peak of 96.41% at 9.90 GHz and a full width at half maximum (FWHM) of 4.96% around this center frequency. Note, also, that the complete symmetry of the unit cell along the x- and y-direction ensures the accomplishment of similar absorptive behavior for arbitrary polarizations of the incident wave.

3. Angle-independent absorption characteristics of the CCR absorber

In this section, the response of our device to obliquely incident radiation is examined. To this end, angles θ and ϕ are defined, as those formed between the propagation vector of the incident wave and the z-axis over the yz- and xz-plane, respectively (see Fig. 1b for axes definition). Initially, angle θ is varied, while keeping $\phi = 0°$. The corresponding absorption curves are illustrated in Fig 3, indicating an almost angle-independent performance up to $\theta = 70°$. On the other hand, by setting $\theta = 0°$ and varying angle ϕ, Fig 4 is obtained. Again, the absorption spectrum remains almost unchanged, except for a slight downshift of the maximum absorption frequency for $\phi = 40°$.

Although the above results constitute a strong indication for the angle-insensitive performance of the proposed absorber, it is crucial to explore the most general case of obliquely incident radiation. For this goal, angles θ and ϕ are varied simultaneously (with a step of $10°$ each). The peak absorption values for all possible angle combinations, are given in the surface plot of Fig. 5. Very efficient absorption for any angle ϕ and for θ values up to $70°$ can be

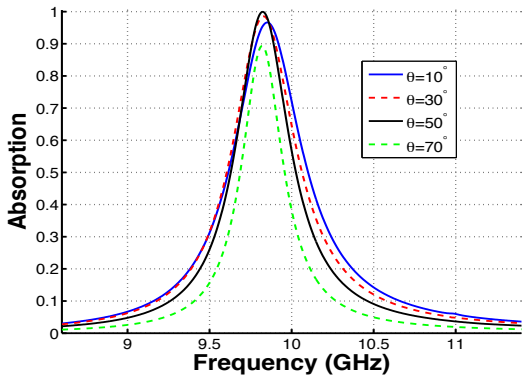

Figure 3: Absorption for various θ angles and $\phi = 0°$.

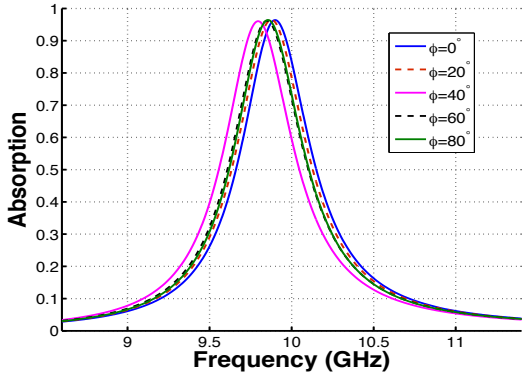

Figure 4: Absorption for various ϕ angles and $\theta = 0°$.

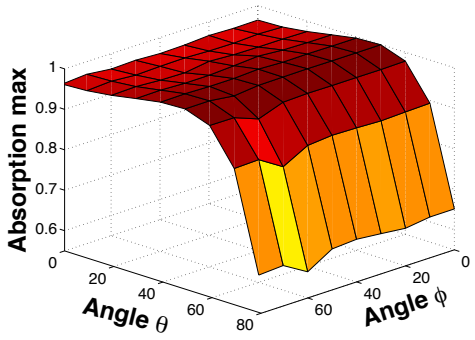

Figure 5: Absorption maximum for various combinations of obliquely incident waves (variations of θ and ϕ angles from $0°$ to $80°$, with a $10°$ increment for both of them).

promptly observed. However, slight variations in the center frequency of the maximum absorption occur, especially for angles larger than $60°$, as provided in Table 1. These findings are indeed very promising and seem to even transcend other similar results available in the literature [15].

4. Investigation of the loss mechanism

The absorption mechanism should be an issue of systematic investigation, since it can offer valuable physical interpretations. Actually, there are two generally accepted loss mechanisms; dielectric losses arising from the imaginary part of

Table 1: Maximum absorption frequency $f_{\max}$ (GHz) for various oblique incidence angles θ and ϕ.

Angle ϕ	Angle θ				
	0°	20°	40°	60°	80°
0°	9.90	9.84	9.81	9.83	9.80
20°	9.88	9.86	9.85	9.82	9.72
40°	9.80	9.79	9.76	9.61	9.67
60°	9.85	9.83	9.83	9.62	9.61
80°	9.85	9.88	9.85	9.83	9.71

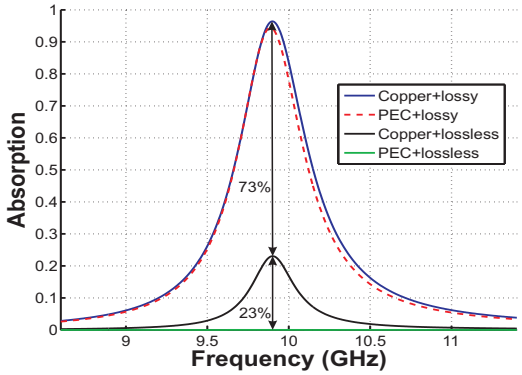

Figure 6: Absorption performance for different dielectrics (lossless or lossy) and metal properties (copper or PEC).

the substrate's dielectric constant and ohmic losses due to the finite conductivity of the structure's metallic parts.

Herein, we perform additional simulations for all possible combinations of dielectric (lossless or lossy) and metal (copper with finite conductivity or perfectly electric conductor (PEC)) types to reveal their actual contribution to the absorption performance, presented in Fig. 6. As expected, the PEC-lossless dielectric case exhibits zero absorbance over the whole frequency range. Moreover, in the copper-lossless substrate scenario, $A(\omega)$ reaches a peak value of 23% at 9.90 GHz. Such an outcome could lead to the assumption that both absorption mechanisms are involved in the CCR structure with additive effects. Nonetheless, in the case of a lossy dielectric, the absorbance plot remains almost unchanged when replacing copper with a PEC material, substantiating that practically only dielectric losses affect the optimized absorber's overall performance.

5. Bandwidth-enhanced variants

To further enhance the absorption bandwidth of the novel design, the scalability property of metamaterials is utilized. In particular, by multiplying the dimensions of the original CCR along the x- and y-axis with a scaling factor s, the center frequency can be downshifted ($s > 1$) or upshifted ($s < 1$), while the absorption curve retains its original shape and fractional bandwidth. This property may be used for the synthesis of multiband absorbers, as in [15]. It is mentioned that unit cells with different absorbing frequencies, owing to their scaled CCRs, can be alternately placed to form a multiband absorbing metasurface.

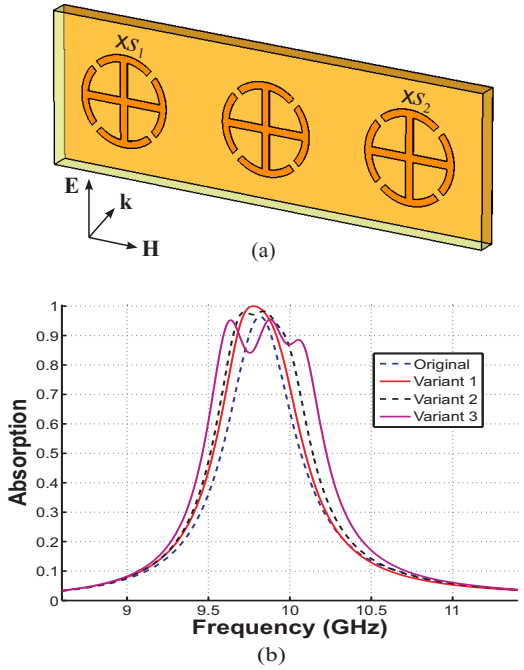

Figure 7: (a) Combined structure with three unit cells and (b) absorption performance of variants with different scaling factors, as explained in Table 2.

Table 2: Scaling factors and FWHM for the different variants of Fig. 7b.

	Orig.	Var. 1	Var. 2	Var. 3
s_1	1.000	0.990	0.985	0.980
s_2	1.000	1.010	1.015	1.020
FWHM	4.96%	5.66%	6.36%	7.68%

In this framework, we employ a similar idea to the original unit cell of Section 2, which can be considered as the borderline case of a multiband design. Specifically, by arranging unit cells with scaling factors very close to unity, adjacent to each other, a new, larger unit cell is formed with multiple overlapping absorptive regions. In the following subsections, diverse implementations with three, four, and nine unit cells are suggested and studied in order to improve the FWHM of the initially introduced CCR absorber.

5.1. Three unit-cells

First, our approach is applied to a set of three unit cells (Fig. 7a). As observed, two scaled unit cells, with scaling factors s_1 and s_2, respectively, are combined with the original one. Three different variants with enhanced FWHM values are illustrated in Fig. 7b, for the scaling factors summarized in Table 2. It becomes apparent that for scaling factors gradually departing from unity, the absorption spectrum of each individual unit cell starts to discriminate from the whole, leading to decreased overlapping and lower absorption peaks. However, it is stressed that in all variants of Fig. 7b, the FWHM is significantly increased from 4.96% of the original unit cell up to 7.68% for variant 3.

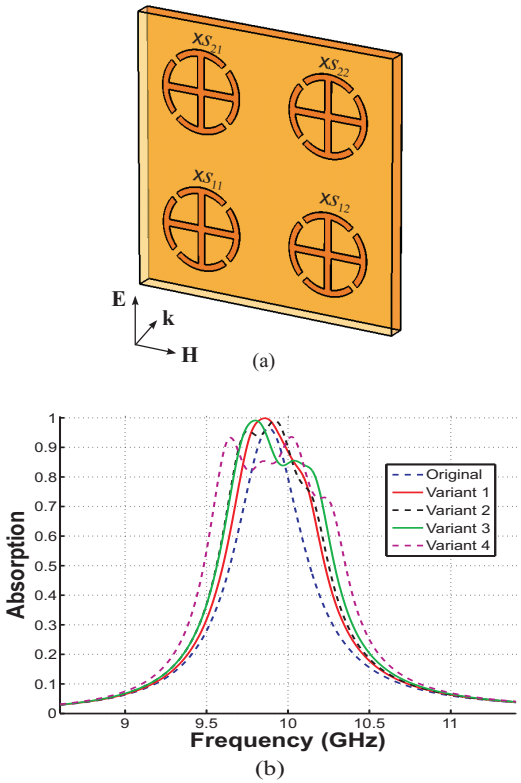

Figure 8: (a) Combined structure with four unit cells and (b) absorption performance of variants with different scaling factors, as explained in Table 3.

Table 3: Scaling factors and FWHM for the different variants of Fig. 8b.

	Orig.	Var. 1	Var. 2	Var. 3	Var. 4
s_{11}	1.000	0.985	1.000	0.980	0.970
s_{12}	1.000	1.005	0.980	1.010	0.990
s_{21}	1.000	1.015	1.020	1.020	1.010
s_{22}	1.000	0.995	1.000	0.990	1.030
FWHM	4.96%	6.36%	6.97%	7.37%	8.79%

5.2. Four unit-cells

Next, the same concept is utilized in a set of four unit cells, as in Fig. 8a. Various possibilities arise by properly controlling scaling factors s_{ij}, for $(i, j) = 1, 2$. Specifically, four different variants with improved FWHM values are demonstrated in Fig. 8b, for the scaling factors listed in Table 3. Again, we can readily detect the considerable bandwidth enhancement that is achieved through the pertinent selection of s_{ij}. For instance, in variant 4 of Fig. 8b, the FWHM is increased from 4.96% of the original unit cell to 8.79%.

5.3. Nine unit-cells

As our final configuration, we investigate the combined device of Fig. 9a, comprising nine unit cells, which offers additional design perspectives via the appropriate choice of scaling factors s_{ij}, for $(i, j) = 1, 2, 3$. In a similar fashion with the scenario of the previous subsection, four different variants with enhanced values of FWHM are considered and their performance is shown in Fig. 9b, for the scaling factors of Table 4. From the results, one can deduce that in all variants the FWHM is significantly raised; from 4.96% of the original unit cell up to 11.18% for variant 4.

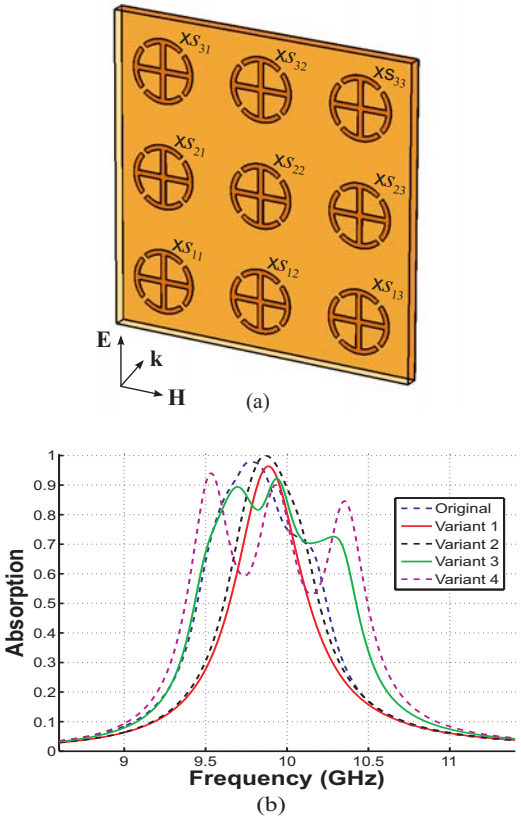

Figure 9: (a) Combined structure with nine unit cells and (b) absorption performance of variants with different scaling factors, as explained in Table 4.

Table 4: Scaling factors and FWHM for the different variants of Fig. 9b.

	Orig.	Var. 1	Var. 2	Var. 3	Var. 4
s_{11}	1.000	1.000	1.000	1.000	1.000
s_{12}	1.000	0.985	0.980	0.980	0.960
s_{13}	1.000	1.005	1.010	1.020	1.040
s_{21}	1.000	1.010	1.015	1.020	1.040
s_{22}	1.000	1.000	1.000	1.000	1.000
s_{23}	1.000	0.990	0.985	0.980	0.960
s_{31}	1.000	0.995	0.990	0.980	0.960
s_{32}	1.000	1.015	1.020	1.020	1.040
s_{33}	1.000	1.000	1.000	1.000	1.000
FWHM	4.96%	5.98%	8.08%	9.96%	11.18%

6. Discussion and conclusions

A class of robust metamaterial absorbers based on the CCR geometry has been presented in this paper. The proposed devices have been shown to exhibit several attractive characteristics, such as wide-angle and polarization-insensitive

absorption, by implementing an electrically thin ($\lambda_0/30$ at the resonance frequency), low-cost FR-4 dielectric substrate. In essence, analysis has proven that their performance is principally related to the dielectric losses of the substrate. Additionally, the possibility to attain bandwidth-enhanced structures has been extensively discussed and the FWHM of the original unit cell has been increased from 4.96% to 11.18%. Possible extensions of the new absorber can be envisaged in terms of tunable metamaterials, as an alternative path to performance-enhanced components. For example, by loading the CCRs with varactor elements, a fully controllable surface may be attained, as in [20], providing supplementary degrees of freedom to the design procedure presented herein. Hence, the aforementioned assets can render this structure a potential candidate for diverse real-world applications in the microwave spectrum.

Acknowledgement

This research has been co-financed by the EU (European Social Fund − ESF) and Greek national funds through the Operational Program "Education and Lifelong Learning" of the National Strategic Reference Framework (NSRF) − Research Funding Program: Heracleitus II. Investing in knowledge society through the European Social Fund.

References

[1] F.M. Landy, S. Sajuyigbe, J.J. Mock, D.R. Smith, W.J. Padilla, Perfect metamaterial absorber, *Phys. Rev. Lett*. 100: pp. 207402(1–3), 2008.

[2] C.G. Hu, X. Li, Q. Feng, X.N. Chen, X.G. Luo, Investigation on the role of the dielectric loss in metamaterial absorber, *Opt. Express* 18: pp. 6598–6603, 2010.

[3] T. Wang, L. Wang, Y. Nie, R. Gong, Relation between dielectric spacer thickness and absorption feature in metamaterials absorber, *Proc. Int. Symp. Sign. Syst. and Electron*., Nanjing, China, pp. 1–4, 2010.

[4] H. Tao, C.M. Bingham, A.C. Strikwerda, D. Pilon, D. Shrekenhamer, N.I. Landy, K. Fan, X. Zhang, W.J. Padilla, R.D. Averitt, Highly flexible wide angle of incidence terahertz metamaterial absorber: Design, fabrication and characterization, *Phys. Rev. B* 78: pp. 241103R(1–4), 2008.

[5] Q.Y. Wen, H.W. Zhang, Y.S. Xie, Q.H. Yang, Y.L. Liu, Dual band terahertz metamaterial absorber: Design, fabrication, and characterization, *Appl. Phys. Lett*. 95: pp. 241111(1–3), 2009.

[6] Y. Avitzour, Y.A. Urzhumov, G. Shvets, Wide-angle infrared absorber based on a negative-index plasmonic metamaterial, *Phys. Rev. B* 79: pp. 045131(1–5), 2009.

[7] F. Bilotti, A. Toscano, K.B. Alici, E. Ozbay Hu, L. Vegni, Design of miniaturized narrowband absorbers based on resonant-magnetic inclusions, *IEEE Trans. Electomagn. Compat*. 53: pp. 63–72, 2011.

[8] J. Sun, L. Liu, G. Dong, J. Zhou, An extremely broad band metamaterial absorber based on destructive interference, *Opt. Express* 19: pp. 21155–21162, 2011.

[9] W. Zhu, X. Zhao, B. Gong, L. Liu, B. Su, Optical metamaterial absorber based on leaf-shaped cells, *Appl. Phys. A - Mater.* 102: pp. 147–151, 2011.

[10] M. Pu, Q. Feng, M. Wang, C. Hu, C. Huang, X. Ma, Z. Zhao, C. Wang, X. Luo, Ultrathin broadband nearly perfect absorber with symmetrical coherent illumination, *Opt. Express* 20: pp. 2246–2254, 2012.

[11] J. Lee, S. Lim, Bandwidth-enhanced and polarisation-insensitive metamaterial absorber using double resonance, *Electron. Lett*. 47: pp. 8–9, 2011.

[12] Y. Cheng, H. Yang, Z. Cheng, N. Wu, Perfect metamaterial absorber based on a split-ring-cross resonator, *Appl. Phys. A - Mater.* 102: pp. 99–103, 2011.

[13] H. Li, L.H. Yuan, B. Zhou, X.P. Shen, Q. Cheng, T.J. Cui, Ultrathin multiband gigahertz metamaterial absorbers, *J. Appl. Phys*. 110: pp. 014909(1–8), 2011.

[14] L.K. Sun, H.F. Cheng, Y.J. Zhou, J. Wang, Low-frequency and broad band metamaterial absorber: Design, fabrication, and characterization, *Appl. Phys. A - Mater.* 105: pp. 49–53, 2011.

[15] L. Li, Y. Yang, C. Liang, A wide-angle polarization-insensitive ultra-thin metamaterial absorber with three resonant modes, *J. Appl. Phys*. 110: pp. 063702(1–5), 2011.

[16] Q. Ye, Y. Liu, H. Lin, M. Li, H. Yang, Multi-band metamaterial absorber made of multi-gap SRRs structure, *Appl. Phys. A - Mater.*, pp. 1–6, 2012.

[17] Y.Z. Cheng, Y. Wang, Y. Nie, R.Z. Gong, X. Xiong, X. Wang, Design, fabrication and measurement of a broadband polarization-insensitive metamaterial absorber based on lumped elements, *J. Appl. Phys*. 111: pp. 044902(1–4), 2012.

[18] H.T. Chen, J.F. O'Hara, A.J. Taylor, R.D. Averitt, C. Highstrete, M. Lee, W.J. Padilla, Complementary planar terahertz metamaterials, *Opt. Express* 11: pp. 1127–1130, 2011.

[19] Computer Simulation Technology, *CST MWS™: Computer Simulation Technology: Microwave Studio*, 2011.

[20] W. Withayachumnankul, C. Fumeaux, D. Abbott, Planar array of electric-LC resonators with broadband tunability, *IEEE Antennas Wireless Propag. Lett*. 10: pp. 577–580, 2011.

Design methodology to enhance high impedance surfaces performances

M. Grelier[1,2,*], A.C. Lepage[1], X. Begaud[1], M. Jousset[2] and S. Mallégol[2]

[1]Institut Telecom, Telecom ParisTech - LTCI CNRS UMR 5141,
46 rue Barrault 75634 Paris Cedex 13, France
[2]THALES Systèmes Aéroportés, 10 avenue de la 1ère DFL 29238 Brest Cedex 3, France
*corresponding author, E-mail: grelier@ieee.org

Abstract

A methodology is introduced for designing wideband, compact and ultra-thin high impedance surfaces (HIS). A parametric study is carried out to examine the effect of the periodicity on the electromagnetic properties of an HIS. This approach allows designers to reach the best trade-off for HIS performances.

1. Introduction

In recent years, artificial surfaces have been widely studied and used in microwave applications [1]. Within a limited frequency bandwidth, these periodic structures can exhibit an electromagnetic band gap (EBG) in which surface wave propagation is forbidden along the structure but also an high impedance surface (HIS) allowing incident electric field to be reflected without any phase shift. This last property makes them suitable as reflector for reducing the overall antenna thickness [2]. In addition of low profile requirement, some applications need supplementary specifications such as wideband characteristics, compact properties when the allocated area is limited.

All these features may not be satisfied at a time due to intrinsic limitations since the reflection phase feature of an HIS is directly related to its different physical and geometrical parameters: the substrate thickness, its relative dielectric constant, the patch width and the gap width [3]. Furthermore, these parameters are also subject to constraints imposed by the available materials and manufacturing processes. Parametric studies can be useful to quickly reach a solution [4], but most of the time, these studies only focus on one specification like the bandwidth without providing a global view. Moreover, the HIS periodicity is not completely taken into account in these analyses because the effect of each parameter is investigated separately.

In this paper, we propose a design procedure that gathers all needed information for designing low profile, broadband and compact HIS structures as best as possible when compromises must be done.

2. Design considerations

The concept of high impedance surface was first introduced by Sievenpiper [2]. In this study, the considered HIS is presented on Fig. 1. It's composed of a planar array of metallic square patches with no via printed on a grounded dielectric slab with a thickness h and a relative dielectric constant ε_r. The width of each square patch is w, the gap between neighbouring patches is g and the lattice period P=w+g.

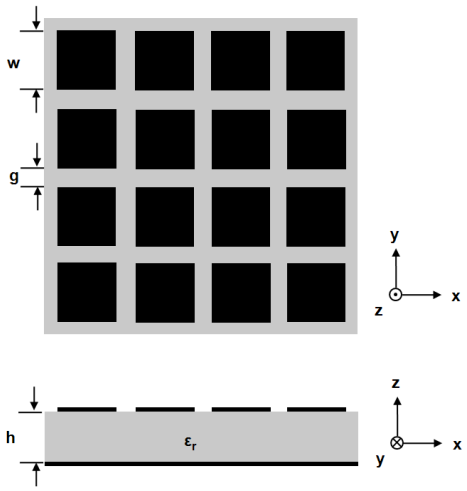

Figure 1: Configuration of the studied HIS

All these physical and geometrical parameters define the electromagnetic properties of the HIS that are commonly obtained by the reflection phase method [4]. This procedure consists in illuminating a unit cell with periodic boundary conditions by an incident plane wave under a normal incidence. Then the phase difference between the reflected and incident electric field at the surface is plotted as function of frequency. Fig. 2 displays the reflection phase diagram with the following parameter set: h=2mm, ε_r=2, w=4mm and g=2mm. Simulations have been performed with CST Microwave Studio® which results have already been verified by measurements [5]. The reflection phase is equal to zero for the resonant frequency f_0=15GHz. Here the HIS bandwidth (Δf) is defined as the frequency range over which the reflection coefficient phase varies from +90° to –90°. Within this band, when an antenna is placed above the HIS, the reflected backward radiation interferes constructively with the forward radiation. Here, the frequency band ranges from 11.3GHz to 19GHz. The HIS compactness, defined by the lattice period, is equal to 6mm.

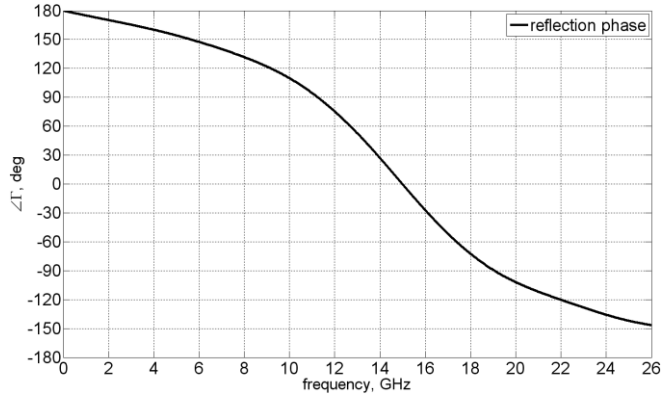

Figure 2: Reflection phase diagram

3. Design methodology

Unlike conventional parametric studies where each parameter is examined one by one while the others are kept constant, we propose to investigate the effects of w and g at the same time. That's why we don't express the period P by a sum but by a product as follows P=w+g=g(1+r) where r is the ratio w/g. Indeed, different combinations of w and g can yield the same value for P without producing the same results on the reflection phase. This decomposition enables to study the influence of P but also to focus on the ratio w/g which has rarely been done. For the sake of clarity, we only study the following cases where the parameters g and r vary by a factor 10: g=0.5mm, 1mm, 2mm, 3mm, 4mm, 5mm and r=1, 2, 5, 10. We extract for each couple (g, r) the resonant frequency, the HIS bandwidth and the HIS compactness from the reflection phase diagram. All these information are then reported in Fig. 3 and Fig. 4.

Fig. 3 illustrates the evolution of the HIS relative bandwidth $\Delta f/f_0$ with frequency. Reflection phase feature typically occurs from 2GHz to 26GHz. The relative bandwidth grows when r decreases for a constant g but also when g decreases for a constant r. We notice that several couples (g, r) having the same resonant frequency lead to a different relative bandwidth. For example, the couples (0.5, 5), (2, 2) and (5, 1) exhibit a resonant frequency at 15GHz and present a relative bandwidth $\Delta f/f_0$ respectively of 58%, 52% and 36%. This result can be used to maximize the bandwidth by only modifying the geometrical parameters.

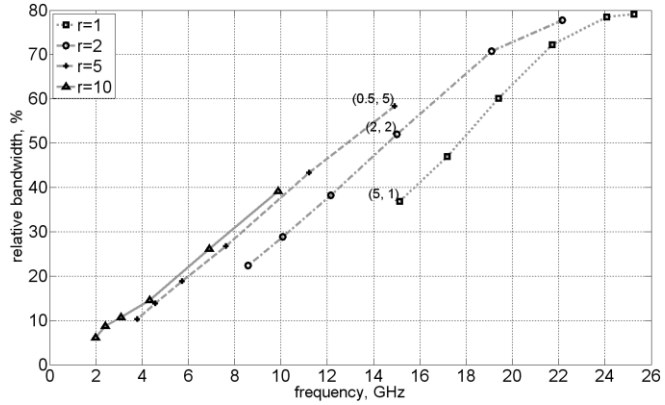

Figure 3: Evolution of the relative bandwidth $\Delta f/f_0$ for h=2mm and ε_r=2

Fig. 4 deals with the relative compactness by representing the evolution of the ratio λ_m/P versus frequency where λ_m is the wavelength in the medium [6]. We observe that for the same resonant frequency, the relative compactness gets better when g decreases and r increases. At f_0=15GHz, the couples (0.5, 5), (2, 2) and (5, 1) present a relative compactness λ_m/P respectively of 5.5, 2.5 and 1.7. These results help to converge more rapidly to the values of w and g in order to optimize the HIS compactness.

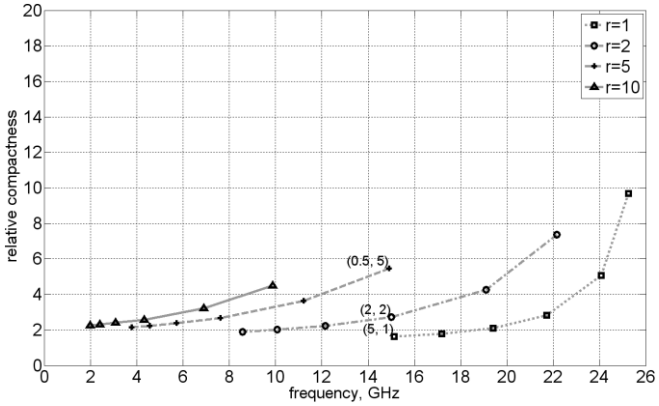

Figure 4: Evolution of the relative compactness λ_m/P for h=2mm and ε_r=2

These two previous graphs allow HIS designers to identify solutions that fulfill their requirements. In addition, they also point out some limitations. For instance, it's difficult to build an HIS whose characteristics are f_0=11.5GHz, λ_m/P=8 and $\Delta f/f_0$>70%. The only way to overcome this physical restriction is to increase either the relative permittivity or the substrate thickness. That is why the methodology is then applied to two other parameter sets: h=2mm and ε_r=8 (Fig. 5 and Fig. 6), h=4mm and ε_r=2 (Fig. 7 and Fig. 8).

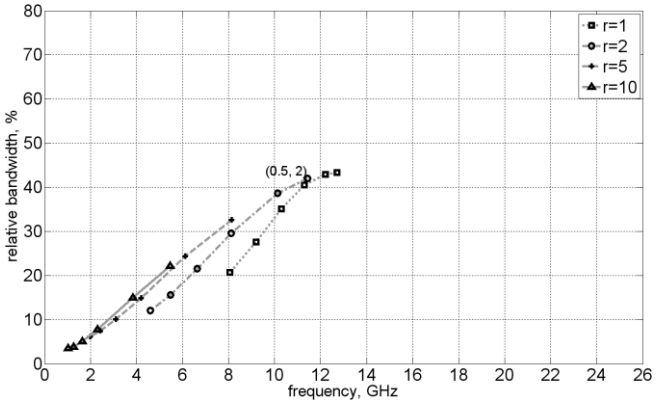

Figure 5: Evolution of the relative bandwidth $\Delta f/f_0$ for h=2mm and ε_r=8

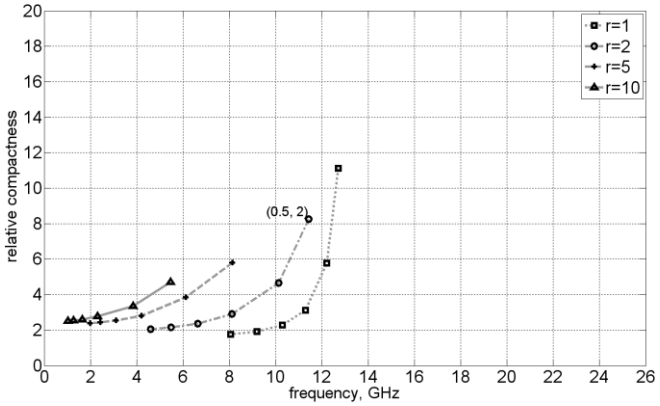

Figure 6: Evolution of the relative compactness λ_m/P for h=2mm and ε_r=8

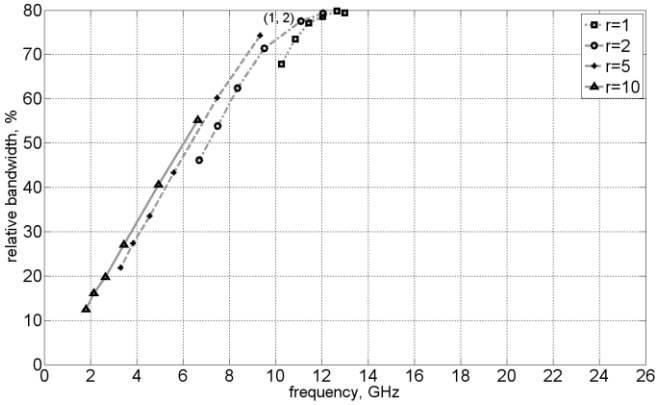

Figure 7: Evolution of the relative bandwidth $\Delta f/f_0$ for h=4mm and ε_r=2

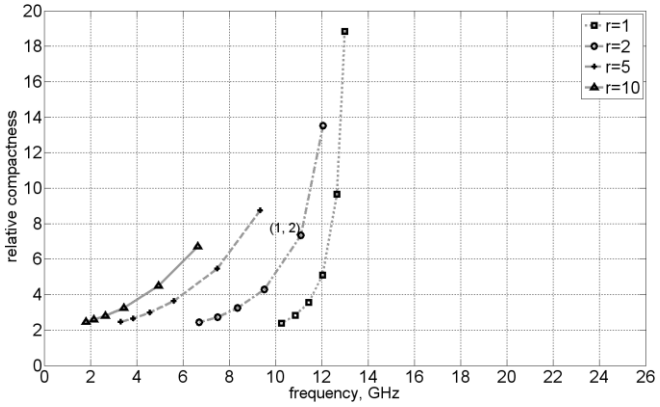

Figure 8: Evolution of the relative compactness λ_m/P for h=4mm and ε_r=2

Curves follow the same behaviour with a change of scale from a substrate configuration to another one. We can find a couple to satisfy the previous condition on the relative compactness with (0.5, 2) on Fig. 6 and with (1, 2) on Fig. 8. However, Fig. 5 and Fig. 7 demonstrate that the relative bandwidth condition is only achieved with the couple (1, 2) of the last parameter set. On the one hand increasing the relative permittivity reduces significantly the relative bandwidth. On the other hand increasing the HIS height runs counter to low profile requirement since h is doubled. This example illustrates the trade-offs that are involved in HIS design and highlights the advantages of the proposed methodology. Thanks to this procedure, it is possible to quickly know if the whole specification is achievable with the chosen material. Otherwise, it enables to determine which parameters have to be modified to obtain the best compromises.

4. Conclusions

A design procedure has been proposed for HIS relative bandwidth and relative compactness considerations. The adopted methodology provides guidelines for HIS designers and gives them an overview of which performances can be reached for a certain parameter set. Moreover the results of such analysis are reusable for further studies since the parameter set is entirely characterized. This principle can be extended for any HIS shape or any other characteristics such as relative thickness or EBG properties.

References

[1] P.S. Kildal, A.A. Kishk, and S. Maci, Special Issue on Artificial Magnetic Conductors, Soft/Hard Surfaces, and Other Complex Surfaces, *Antennas and Propagation, IEEE Transactions on* , vol.53, no.1, pp. 2- 7, Jan. 2005.

[2] D. Sievenpiper, L. Zhang, R.F.J. Broas, N.G. Alexopolous, and E. Yablonovitch, High-impedance electromagnetic surfaces with a forbidden frequency band, *Microwave Theory and Techniques, IEEE Transactions on* , vol.47, no.11, pp.2059-2074, Nov 1999.

[3] D.J. Kern, M.J. Wilhelm, D.H. Werner, and P.L. Werner, A novel design technique for ultra-thin tunable EBG AMC surfaces, *Antennas and Propagation Society International Symposium, 2004. IEEE* , vol.2, pp. 1167-1170 Vol.2, 20-25 June 2004.

[4] F. Yang and Y. Rahmat-Samii, Reflection phase characterizations of the EBG ground plane for low profile wire antenna applications, *Antennas and Propagation, IEEE Transactions on* , vol.51, no.10, pp. 2691- 2703, Oct. 2003.

[5] F. Linot, R. Cousin, X. Begaud, and M. Soiron, Design and measurement of high impedance surface, *Antennas and Propagation (EuCAP), 2010 Proceedings of the Fourth European Conference on*, Barcelona, 12-16 April 2010.

[6] E.O. Hammerstad, Equations for microstrip circuit design, *Proc. European Microwave Conf.*, pp. 268-272, September 1975.

Dual-band Artificial Magnetic Conductor

Julien Sarrazin*, Anne Claire Lepage, and Xavier Begaud

Institut Telecom, Telecom ParisTech - LTCI CNRS UMR 5141, Paris, France
*corresponding author, E-mail: julien.sarrazin@telecom-paristech.fr

Abstract

A dual-band Artificial Magnetic Conductor (AMC) is presented in this paper. The proposed metasurface is based on a spiral geometry in which an additional resonance has been introduced thanks to a physical understanding of the structure's behavior. The design is compact and the two frequency bands can be adjusted independently. Furthermore, an analytical model is developed which can predict both the frequencies at which the metasurface reflects incident waves in-phase.

1. Introduction

Metasurfaces such as High Impedance Surfaces (HIS) have a great potential regarding antenna applications [1]. These surfaces can exhibit two interesting properties. One is an Electromagnetic Band Gap (EBG) which forbids the propagation of surface waves. This property can help in reducing the mutual coupling between different antennas of an array for example. The second one is the in-phase reflection of incident waves that makes the metasurface behaving like an Artificial Magnetic Conductor (AMC). This second property allows locating such a metasurface close to an antenna in order to enhance its directivity by acting as a reflector.

AMC metasurfaces are resonant surfaces composed of printed unit-cells over a grounded dielectric slab. So the in-phase reflection of incident waves is achieved only about their resonance frequency. However, antennas are frequently operating at different frequencies simultaneously. Consequently, multi-band AMC are required.

Dual-band behavior can be obtained using two or more layers of metallic printed patterns [2, 3], or using lumped components [4, 5]. However, both these approaches increase the cost of the AMC. Thus, several uni-planar designs have been proposed in order to achieve either dual-band [6-11] or multi-band characteristics [12]. However, these surfaces are not easy to design because their frequency bands cannot be adjusted independently. In [13], a simple dual-band design based on a square patch and a slot is proposed for which two frequency bands can be adjusted independently. However, the unit-cell is relatively large and comparable to the size of a wideband monopole antenna [13]. This may be a problem especially if the surface available for the AMC is not large. A compact unit-cell design insures that a sufficient number of unit-cells can be located over a limited size surface in order to produce an in-phase reflection.

In this paper, a new dual-band AMC based on a spiral pattern is introduced. The proposed design is uni-planar and does not contain any vias in order to obtain an inexpensive and easy-to-fabricate structure. Each band can be tuned independently and to facilitate the design, an analytical model is given which can predict the resonance frequency of both the bands. Section 2 presents the spiral-based single-band AMC along with analytic formulae. In section 3, an additional resonance is introduced to achieve the dual-band behavior and the related analytical model is given. In section 4, a dual-band GPS application is considered and related designing issues are discussed. Finally, a conclusion is drawn in section 5.

2. Single-band AMC

2.1. Design

The proposed structure is based on a spiral unit-cell introduced in [14] which presents the advantage to be compact while exhibiting a bandwidth similar to other bigger patterns [15]. However, unlike in [14], the spiral used here does not contain any metallic vias and the structure is consequently similar to the one found in [16]. A quarter of the unit-cell is presented in figure 1. To obtain the complete unit-cell, the spiral has to be mirror duplicated along *x*- and *y*-axis. The metallic pattern is constructed with the geometrical parameters l_{spir} and g. g is the gap between spiral's arms and l_{spir} is related to the gap g and the width of spiral's arms w_{CPW} with:

$$l_{spir} = w_{CPW} + g \tag{1}$$

So the length of this quarter unit-cell is $8l_{spir}$. The spiral is printed on a grounded dielectric slab. In figure 1, the grounded dielectric slab is actually composed of two dielectric layers of thickness h_1, h_2 and relative permittivity ε_{r1}, ε_{r2}, respectively. Only the lower layer (h_1, ε_{r1}) has a ground plane. Two layers are taken into account in order to consider the following scenario. The upper layer is a dielectric substrate, necessary for the spiral to be printed, whereas the lower layer is only vacuum (which in practice can be foam or honeycomb structure). This vacuum layer is useful in order to increase the thickness of the structure, and so the AMC bandwidth, without increasing significantly neither the weight nor the losses.

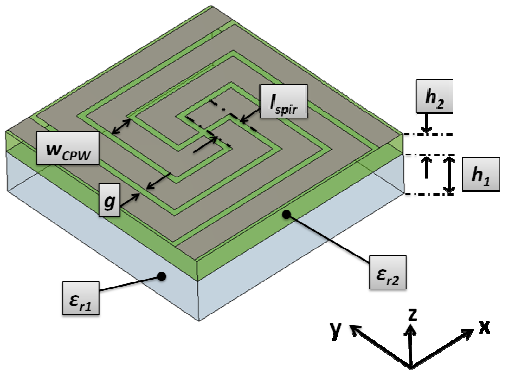

Figure 1: Single-band spiral AMC quarter unit-cell.

2.2. Analytical Modeling

In order to obtain a dual-band AMC, it is necessary to add a second resonance to the metasurface. To do so, we firstly analyze the resonance phenomenon involved in the spiral. The figure 2 presents the full spiral unit-cell. At the frequency for which the surface behaves like an AMC (i.e. when the reflected phase is null), a resonance occurs. A stationary wave is established in the split strip presented in blue color in figure 2 (the incident electric field is considered polarized along *x*-axis). This strip supports a coplanar waveguide (CPW)-like quasi-TEM mode of propagation with grey lines being its ground plane. Yellow lines are parts of the neighbor resonating strips. Note that when the electric field is polarized along *y*-axis, resonating strips become the ground plane and vice versa. So the structure is equivalent to a CPW stepped-impedance dipole. Consequently, its resonance frequency can be analytically determined.

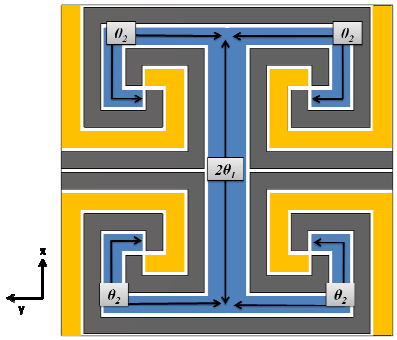

Figure 2: CPW stepped-impedance dipole identification.

By considering the first mode of a stepped-impedance resonator, resonance conditions are satisfied when [17]:

$$\tan(\theta_1)\tan(\theta_2) = R_z \tag{2}$$

where θ_1 et θ_2 are the electrical lengths showed in figure 2 and equal to:

$$\theta_1 = \beta_1 l_1 = \frac{\omega}{c}\sqrt{\varepsilon_{reff1}}\,l_1 \tag{3}$$

$$\theta_2 = \beta_2 l_2 = \frac{\omega}{c}\sqrt{\varepsilon_{reff2}}\,l_2 \tag{4}$$

with ω the angular frequency, c the light velocity, $l_1 = 6.5 l_{spir}$ and $l_2 = 9.5 l_{spir} - g/2$. R_z is the ratio between the characteristic impedance Z_2 of the dipole's part whose line length is θ_2 and width $W_{CPW2} = l_{spir}$-g and the characteristic impedance Z_1 of the part of length θ_1 and line width $W_{CPW1} = 2l_{spir}$-g. So the impedance ratio is equal to:

$$R_z = \frac{Z_2}{2Z_1} \tag{5}$$

Consequently, by determining R_z and the effective permittivity of each part of the dipole, the resonance frequency can be found by solving equation (2).

Characteristics of a multilayered substrate conductor-backed CPW can be determined with conformal mapping [18, 19] by assuming a propagating quasi-static TEM mode. Thus, the effective permittivity can be calculated using the following set of equations:

$$\varepsilon_{reff} = 1 + q_1\varepsilon_{r1} + q_2(\varepsilon_{r2} - \varepsilon_{r1}) \tag{6}$$

$$q_i = \frac{1}{2}\frac{K(k_i)}{K(k_i')}\frac{K(k_0')}{K(k_0)} \tag{7}$$

where K is the complete elliptic integral of the first kind and:

$$k_0 = \frac{a}{b} \tag{8}$$

$$k_1 = \frac{\tanh\left(\frac{\pi a}{2(h_1+h_2)}\right)}{\tanh\left(\frac{\pi b}{2(h_1+h_2)}\right)} \tag{9}$$

$$k_2 = \frac{\sinh\left(\frac{\pi a}{2h_2}\right)}{\sinh\left(\frac{\pi b}{2h_2}\right)} \tag{10}$$

$$k_i' = \sqrt{1-k_i^2} \tag{11}$$

$$a = \frac{w_{CPW}}{2} \tag{12}$$

$$b = \frac{w_{CPW}}{2} + g \tag{13}$$

To obtain the value of R_z from equation (5), impedances Z_1 and Z_2 are determined with:

$$Z = \frac{1}{c\sqrt{\varepsilon_{reff}}\,C_0} \tag{14}$$

$$C_0 = 2\varepsilon_0\left(\frac{K(k_0)}{K(k_0')} + \frac{K(k_1)}{K(k_1')}\right) \tag{15}$$

2.3. Numerical validation

To validate the proposed model, an example of spiral using no substrate but vacuum is firstly considered (so $\varepsilon_{r1} = \varepsilon_{r2} = 1$). Dimensions are $(h_1 + h_2) = 4.73$ mm and $g = 0.4$ mm. l_{spir} value ranges from 1.1 mm up to 4.7 mm.

The AMC behavior occurs when the CPW stepped-impedance dipole resonates. This resonance frequency is determined analytically by solving equation (5) and results are compared with those obtained from a full-wave-analysis with the frequency domain solver of CST Microwave Studio. From full-wave-analysis, the frequency at which the reflected phase is null in the AMC's plane is determined following the procedure described in [20]. Results are shown in figure 3. As expected, it is observed that when the size of the spiral increases (i.e. when l_{spir} increases), the null phase frequency decreases. Also, analytical and full-wave results are in good agreement, except when l_{spir} is small and so the null phase frequency is high. This can be explained by the fact that the analytical model supposes a quasi-static TEM mode of propagation. This assumption is valid as long as the substrate thickness is small compared to the wavelength. When the operating frequency increases, the thickness $h_1 + h_2$ becomes larger with respect to the wavelength. Nevertheless, for the given example, the model gives quite accurate results for frequencies below 2 GHz, even though the finite ground plane size, bends, open-end discontinuities and the coupling between the neighbor dipoles are not taken into account.

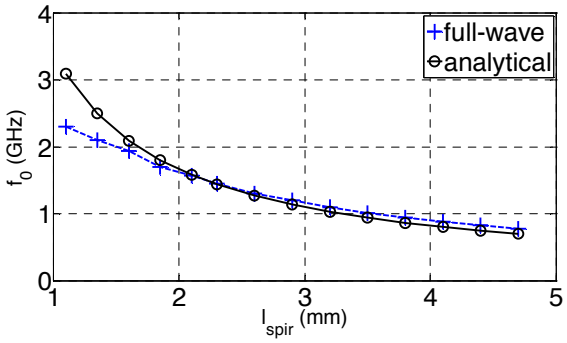

Figure 3: Influence of the spiral size (through parameter l_{spir}) on the null phase frequency ($\varepsilon_{r1} = \varepsilon_{r2} = 1$, $(h_1 + h_2) = 4.73$ mm, $g = 0.4$ mm).

As a second example, the presence of a dielectric layer is now considered. Dimensions are the same as previously except that l_{spir} is kept constant at 2.1 mm, h_1= 3.15 mm and h_2 = 1.58 mm. The effect of the relative permittivity ε_{r2} is investigated and its value ranges from 1 up to 9. Analytical and full-wave results are shown in figure 4. One can notice that the null phase frequency decreases from 1.57 GHz down to 0.75 GHz (from full-wave results) as the permittivity increases from 1 up to 9. When $\varepsilon_{r2} = 1$, analytical and full-wave results are in good agreement. However, the error increases as the permittivity increases, reaching about 11% when $\varepsilon_{r2} = 9$. It appears that, in the given example, the analytical model is more accurate for lower permittivity values. This may be explained by the fact that the higher the permittivity, the more the field is concentrated in the dielectric, thereby inducing more dispersion which is not taken into account in the analytical model.

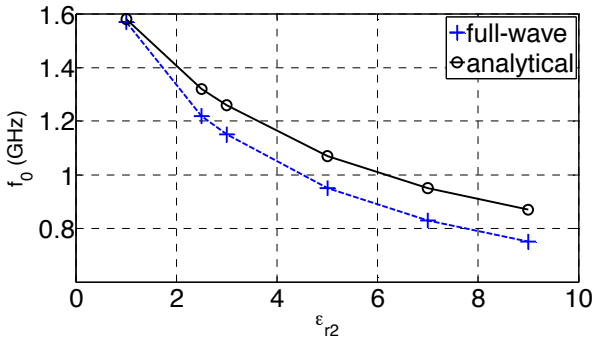

Figure 4: Influence of the relative permittivity ε_{r2} on the null phase frequency ($\varepsilon_{r1} = 1$, $h_1 = 3.15$ mm, $h_2 = 1.58$ mm, $g = 0.4$ mm, $l_{spir} = 2.1$ mm).

3. Dual-Band AMC

3.1. Design and concept

The proposed dual-band geometry is presented in figure 5. Because of its symmetry, only a quarter of the structure is shown. Knowing that the current circulating along a CPW is mainly concentrated along line edges, a slot can be etched in the middle of the CPW without disturbing too much the propagation along it. By doing so, the slot creates an additional propagation structure: a Coplanar Strip Line (CPS) of gap value w_{CPS}. This structure, being short-circuited at one end and open-circuited at the other end, introduces an additional resonance when its equivalent length (l_{CPS}) is equal to a quarter of guided wavelength. So by adjusting the length of the slot, it is possible to adjust the resonance frequency of the CPS while keeping unchanged the resonance frequency of the CPW.

To validate the concept, full-wave simulations are performed with CST Microwave Studio using the following properties: $\varepsilon_{r1} = \varepsilon_{r2} = 1$, $(h_1+h_2) = 4.73$ mm, $g = 0.4$ mm, $w_{CPS} = 0.2$ mm, $l_{spir} = 2.1$ mm and l_{CPS} varies from 26.75 mm up to 33.4 mm, which is the longest possible CPS length. At this value, the physical CPS length is equal to the physical CPW length ($l_{CPS} = l_1 + l_2$). Reflection phase results are shown in Figure 6. One can observe that the reflection becomes null twice over the frequency band of interest. At the lower frequency, the resonance is due to the CPW stepped-impedance dipole. At the upper frequency, the resonance is due to the CPS and so the frequency changes significantly for different values of l_{CPS}. Thus, two different null reflected phase frequencies can be adjusted independently which is highly suitable for dual-band designing.

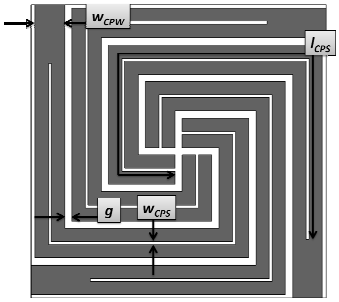

Figure 5: Dual-band spiral AMC quarter unit-cell.

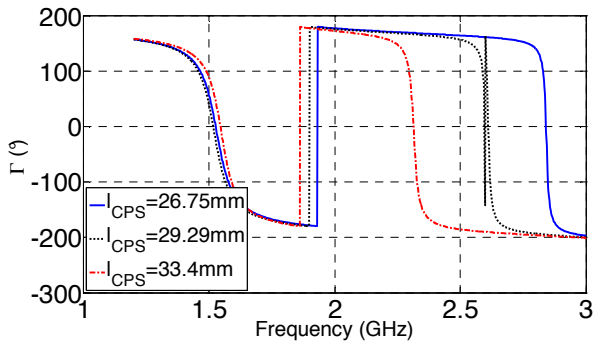

Figure 6: Reflection phase full-wave simulation results: influence of l_{CPS} ($\varepsilon_{r1} = \varepsilon_{r2} = 1$, $(h_1+h_2) = 4.73$ mm, $g = 0.4$ mm, $w_{CPS} = 0.2$ mm, $l_{spir} = 2.1$ mm).

3.2. Analytical Modeling

Considering the quarter-wavelength resonance of the CPS, the resonance frequency is thereby given by:

$$f_0^{CPS} = \frac{c}{4 l_{CPS} \sqrt{\varepsilon_{reff}}} \tag{16}$$

By again performing a conformal mapping based on a quasi-static TEM mode assumption and by neglecting the presence of the lower ground plane, the effective permittivity of the CPS can be determined by [18]:

$$\varepsilon_{reff} = 1 + \frac{(\varepsilon_{r2} - 1)}{2} \frac{K(k_0)}{K(k_0')} \frac{K(k_2')}{K(k_2)} \tag{17}$$

using same parameters than previously except that:

$$a = \frac{w_{CPS}}{2} \tag{18}$$

$$b = \frac{W_{CPW}}{2} = \frac{l_{spir} - g}{2} \tag{19}$$

3.3. Numerical validation

The accuracy of the proposed CPS model is studied by taking an example similar to the previous one with a vacuum substrate ($\varepsilon_{r1} = \varepsilon_{r2} = 1$) and the following dimensions are: $(h_1+h_2) = 4.73$ mm, $l_{spir} = 2.1$ mm, $g = 0.4$ mm and $w_{CPS} = 0.2$ mm. l_{CPS} varies from 25.75 mm up to 33.4 mm, which is the longest possible CPS length. Analytical results obtained from equation (16) are compared with a full-wave analysis in figure 7. The model and the full-wave analysis results are in good agreement although the lower ground plane is not taken into account. The gap w_{CPS} being narrow, the electromagnetic field is largely concentrated in its proximity and so the lower ground plane has little influence on the propagating mode.

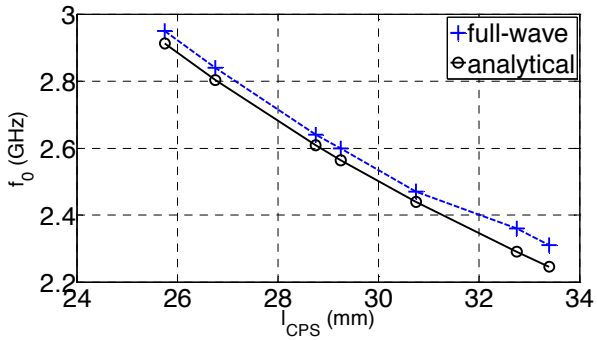

Figure 7: Influence of the CPS length (through parameter l_{CPS}) on the CPS null phase frequency ($\varepsilon_{r1} = \varepsilon_{r2} = 1$, $(h_1+h_2) = 4.73$ mm, $g = 0.4$ mm, $w_{CPS} = 0.2$ mm, $l_{spir} = 2.1$ mm).

The second example considers the presence of a dielectric layer. Dimensions are the same than previously except that l_{CPS} is now equal to 26.75 mm, $h_1 = 3.15$ mm and $h_2 = 1.58$ mm. The effect of the relative permittivity ε_{r2} is investigated and its value ranges from 1 up to 9. Analytical model is compared to full-wave analysis in figure 8. The null phase frequency decreases from 2.84 GHz down to 1.3 GHz as the permittivity increases from 1 up to 9. Results are in very good agreement. Since the CPS's gap w_{CPS} is small with respect to the wavelength, the quasi-static TEM mode assumption is largely satisfied.

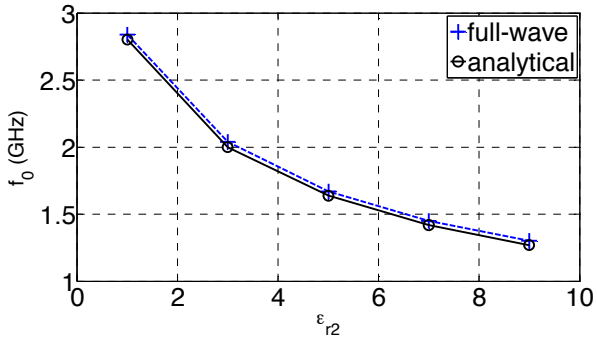

Figure 8: Influence of the relative permittivity ε_{r2} on the CPS null phase frequency ($\varepsilon_{r1} = 1$, $h_1 = 3.15$ mm, $h_2 = 1.58$ mm, $g = 0.4$ mm, $w_{CPS} = 0.2$ mm, $l_{spir} = 2.1$ mm, $l_{CPS} = 26.75$ mm).

4. Design Considerations

In some dual-band applications, the two operating frequencies are relatively close to each other. For instance, GPS operating bands L_1 and L_2 are centered on 1.57 GHz and 1.22 GHz, respectively. Designing a wideband AMC able to cover the upper and the lower bands simultaneously is challenging [4] and may lead to very thick metasurfaces. Thus, dual-band AMCs appear to be a possible solution. However, regarding this application, a ratio $f_u/f_l = 1.28$ between upper and lower frequencies is required. Such a low ratio is not easy to obtain with conventional dual-band AMC. Even with our proposed design where two distinct propagating structures can resonate, it can be observed, from previous sections, that this ratio may be difficult to obtain. For instance, by comparing the CPW resonance frequency obtained for $l_{spir} = 2.1$ mm in figure 3 (i.e. 1.57 GHz) and the CPS one obtained in figure 7 for the maximum slot length (i.e. 2.31 GHz), the ratio f_u/f_l reaches a value of 1.47. That is why an additional degree of freedom available within the structure is now investigated: the gap g. Its influence on the effective permittivity of each line can be simply and efficiently investigated with analytical models previously developed.

According to figure 1, a vacuum layer with a thickness $h_1 = 3.15$ mm and a substrate of permittivity $\varepsilon_{r2} = 2.5$ with a thickness $h_2 = 1.58$ mm is considered. Design parameters have following values: $l_{spir} = 2.3$ mm, $l_{CPS} = 35.3$ mm (this is the maximum possible value for which $l_{CPS} = l_1 + l_2$) and $w_{CPS} = 2.3$ mm. Results regarding the resonance frequencies of CPW and CPS lines are shown in figure 9. The gap g has no significant influence on the CPS's resonance. However, when g increases, the CPW's resonance frequency increases too and so the ratio f_u/f_l decreases. Consequently, the parameter g can be used to adjust the CPW resonance frequency, within the limit of the structure (the CPW width W_{CPW} and gap g are related through equation (1): when g increases, W_{CPW} decreases). For $g = 1$ mm, the upper frequency (CPS) is 1.625 GHz and the lower one (CPW) is 1.265 GHz. So a ratio $f_u/f_l = 1.28$ is achieved.

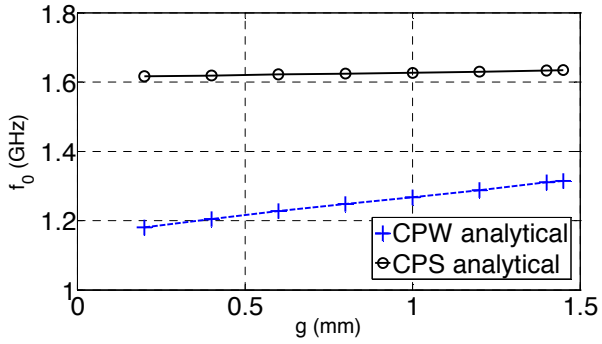

Figure 9: Influence of the gap g on the CPW and CPS null phase frequency ($\varepsilon_{r1} = \varepsilon_{r2} = 1$, $(h_1+h_2) = 4.73$ mm, $l_{spir} = 2.3$ mm, $l_{CPS} = 35.3$ mm).

Finally, taking into account previous comments, a final AMC is designed and simulated in CST Microwave Studio. After optimization, the following parameter values are found: $\varepsilon_{r1} = 1$, $\varepsilon_{r2} = 2.5$, $h_1 = 3.15$ mm, $h_2 = 1.58$ mm, $l_{spir} = 2.3$ mm, $l_{CPS} = 35.3$ mm, $g = 1.45$ mm, $w_{CPS} = 0.2$ mm. The obtained reflected phase is shown in figure 10. Null phase frequencies occur at 1.26 GHz and 1.61 GHz and so exhibit a ratio $f_u/f_l = 1.28$. The bandwidth defined with the +/-90° criteria on the reflected phase [1] are:

- lower-band: $\Delta_f = 4.3$ MHz (3.4%)
- upper-band: $\Delta_f = 1.13$ MHz (0.7%)

The lower band can cover the L_2 bandwidth (1.7 %); however the upper band cannot cover the L_1 bandwidth (1.5 %). Consequently further efforts should be done in order to increase this bandwidth.

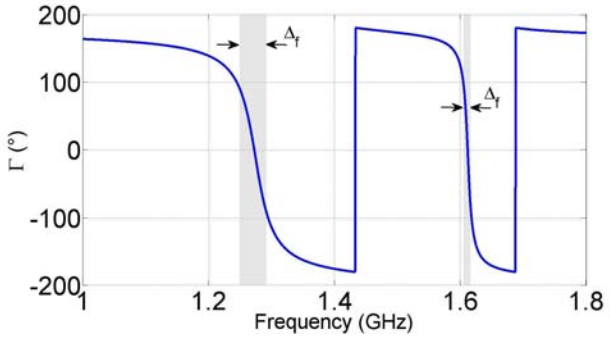

Figure 10: Dual-band AMC: reflection phase full-wave simulation results ($\varepsilon_{r1} = 1$, $\varepsilon_{r2} = 2.5$, $h_1 = 3.15$ mm, $h_2 = 1.58$ mm, $l_{spir} = 2.3$ mm, $l_{CPS} = 35.3$ mm, $g = 1.45$ mm, $w_{CPS} = 0.2$ mm).

5. Conclusions

In this paper, a new dual-band Artificial Magnetic Conductor (AMC) has been introduced. It has been shown that the two operating frequencies at which this AMC reflects incident waves in-phase can be set independently, which largely facilitates the designing process.

Based on a compact modified spiral pattern, the proposed AMC takes benefit of two different resonances involved within the structure. We have identified that one resonance takes place in a coplanar waveguide (CPW)-like structure whereas the other one occurs in a coplanar stripline (CPS)-like structure. Thanks to this identification, an analytical model based on conformal mapping has been developed. The model is able to predict with accuracy the null phase frequency of both bands under quasi-static assumption. Results obtained by the model have been validated with a commercial full-wave analysis software. Finally, it has been proved that the proposed design is capable of working on two bands close to each other, with a ratio $f_u/f_l = 1.28$ between upper and lower frequencies. These

results along with the analytical expressions make the proposed AMC an easy-to-design and versatile metasurface.

Acknowledgements

The research leading to these results has received funding from the European Defence Agency (EDA) under grant agreement MIMiCRA (*Metamaterial Inspired Microwave Conformal Radar Antennas*).

References

[1] D. Sievenpiper, *et Al*., "High-Impedance Electromagnetic Surfaces with a Forbidden Frequency Band", *IEEE Trans. on Microwave Theory and Tech*., vol. 47, no. 11, pp. 2059–2074, 1999.

[2] H.J. Lee, K.L. Ford, and R.J. Langley, "Dual band tunable EBG", *Electronics Letters* , vol. 44, no. 6, pp. 392-393, March 2008.

[3] J.H. Yoon, E.Y. Kim, Y. Lim, and Y.J. Yoon, "Equivalent circuit model and reflection phase control methods for dual-band AMC", *EUCAP Conference*, pp. 1222-1226, April 2011.

[4] M. Pigeon, C. Morlaas, and H. Aubert, "A Dual-band High Impedance Surface mounted with a spiral antenna for GNSS applications", *IEEE APWC Conference* pp. 994-997, Sept. 2011.

[5] M.G. Bray and D.H. Werner, "A novel design approach for an independently tunable dual-band EBG AMC surface", IEEE APS Symposium, vol. 1, pp. 289-292, June 2004.

[6] W. Wang, X.Y. Cao, R. Wang, and J.J. Ma, "A Small Dual-band EBG Structure for Microwave", *ICMMT Conference*, pp. 1637-1639, April 2008.

[7] N. Chahat, M. Zhadobov, R. Sauleau, and K. Mahdjoubi, "Improvement of the on-body performance of a dual-band textile antenna using an EBG structure", *LAPC Conference,* pp. 465-468, Nov. 2010.

[8] X. Chen, C.H. Liang, L. Liang, and Z.J. Su, "A low profile dual-band inverted L antenna with slotted electromagnetic band-gap (EBG) structures", *Int. Work. on Metamaterials,* pp. 341-343, Nov. 2008.

[9] L. Qi, H.M. Salgado, A.M. Moura, and J.R. Pereira, "Dual-band antenna design using an EBG Artificial Magnetic Conductor ground plane", *LAPC Conference*, pp. 217-220, March 2008.

[10] O. Folayan and R. Langley, "Compact EBG antenna", *EuCAP Conference*, pp. 1-4, Nov. 2006.

[11] H.H. Xie, Y.C. Jiao, K. Song, and Z. Zhang, "A Novel Multi-Band Electromagnetic Band-Gap Structure", *PIERS*, vol. 9, pp. 67-74, 2009.

[12] D.J. Kern, D.H. Werner, A. Monorchio, L. Lanuzza, and M.J. Wilhelm, "The design synthesis of multiband artificial magnetic conductors using high impedance frequency selective surfaces*", IEEE Trans. on Ant. and Propa*., vol. 53, no. 1, pp. 8- 17, Jan. 2005.

[13] N.A. Abbasi and R. Langley, "A wideband printed monopole antenna over dual-band AMC", *LAPC conference*, pp. 221-224, Nov. 2010.

[14] Q. R. Zheng, Y. Q. Fu, and N. C. Yuan, "A Novel Compact Spiral Electromagnetic Band-Gap (EBG) Structure", *IEEE Trans. on Ant. and Propag*., vol. 56, no. 6, pp. 1656–1660, 2006.

[15] F. Costa, S. Genovesi, and A. Monorchio, "On the bandwidth of printed frequency selective surfaces for designing high impedance surfaces", *IEEE Ant. Propag. Symp. 2009*, pp. 1-4, June 2009.

[16] L. Mouffok, *et Al*. "Mutual coupling reduction between dual polarized microstrip patch antennas using compact spiral artificial magnetic conductor", *EUCAP conference*, 902-912, 2011.

[17] M. Makimoto, and S. Yamashita, "Bandpass Filters Using Parallel Coupled Stripline Stepped Imepdance Resonators", *IEEE Trans. on Microwave Theory and Tech*., vol. 28, no. 12, pp. 1413–1417, 1980.

[18] R.N. Simons, "Coplanar Waveguide Circuits, Components, and Systems", *John Wiley & Sons*, 2001

[19] E. Carlsson, and S. Gevorgian, "Conformal Mapping of the Field and Charge Distributions in Multilayered Substrate CPW's", *IEEE Trans. on Microwave Theory and Tech*., vol. 47, no. 8, pp. 1544–1552, Aug. 1999.

[20] Y. Zhang, J. von Hagen, M.Younis, C. Fischer, and W. Wiesbeck "Planar Artificial Magnetic Conductors and Patch Antennas", *IEEE Trans. on Ant. and Propag*., vol. 51, no. 10, pp. 2704-2712, Oct. 2003.

Holographic metasurfaces for terahertz focusing: design, fabrication and experiment

Sergey Kuznetsov[1,2,*], Mikhail Astafyev[1,2], Miguel Navarro-Cia[3], Alexander Gelfand[4], Andrey Arzhannikov[1,2], and Manfred Thumm[1,5]

[1]Analytical and Technological Innovation Center "High Technologies and Novel Materials," Novosibirsk State University, Novosibirsk, Russia
[2]Budker Institute of Nuclear Physics SB RAS, Novosibirsk, Russia
[3]Experimental Solid State Group, Department of Physics, Imperial College London, London, UK
[4]Institute of Semiconductor Physics SB RAS, "TDIAM", Novosibirsk, Russia
[5]Karlsruhe Institute of Technology, Karlsruhe, Germany
*corresponding author, E-mail: SAKuznetsov@nsm.nsu.ru

Abstract

In this contribution we exploit the controlled reflection provided by metasurfaces together with holographic techniques to design non-profiled diffractive optical elements working at 334 GHz. The required metasurfaces are synthesized via an iterative algorithm, fabricated by photolithography and experimentally validated using a submillimeter-wave BWO spectrometer.

1. Introduction

Cosmetics have come a long way from the days of thick creams and pancakes powders. Using optically complex pigments and particles that scatter light, today's cosmetic industry has engineered sophisticated new products that enhance people's features rather than cover up their skin. Likewise, metamaterials, whose underlying physics relies as well in engineering the building block of the structure, hold promise to improve electromagnetic as well as acoustic devices [1]. However, great deal of research has done in microwaves and truly useful devices at higher frequencies are scarce. This lack of devices is even more dramatic at the terahertz spectrum (0.3 to 10 THz) because of its inherent underdevelopment compared to microwaves and optics arisen from historical reasons (founded on natural and technological limitations) [2].

2. Design

Within this framework, we aim to make the leap from theory to real application by designing, numerically analyzing, fabricating and measuring diffractive terahertz elements. The design's rule relies in the classical concept of holography. However, the practical implementation is based on metamaterial resonators given their great flexibility to map the continuous ideal spatial-dependent reflection with an accurate staircase approximation.

The schematic of our approach can be seen in Fig. 1. It relies on an artificial impedance surface [3] with spatial-dependent impedance. The required reflection was realized by geometrical morphing of the U-shape resonators from patches to split-rings along the metasurface. For an accurate performance, the reference beam, i.e. the beam incident to the metasurface, was characterized experimentally and its profile was included in the Gerchberg-Saxton iterative algorithm [4]. Subsequently, the designed patterns with overall dimensions 70 mm × 70 mm were then fabricated by photolithography on grounded polypropylene slabs. For the experimental characterization, a pyroelectric detector mounted on 2D raster scanning system combined with a subterahertz BWO spectrometer was used.

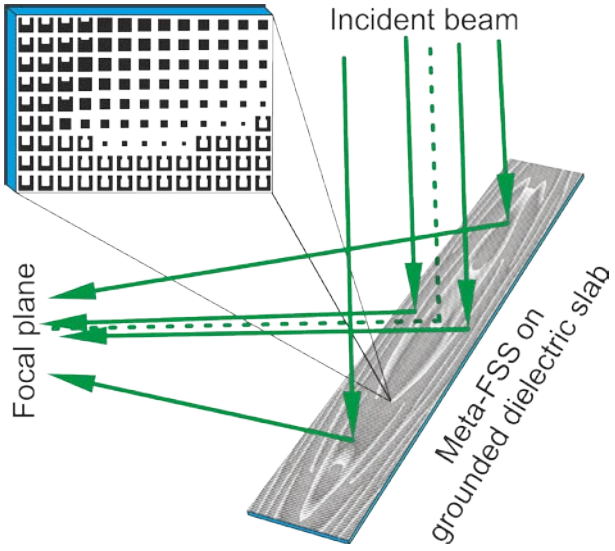

Figure 1: Schematic of the diffractive terahertz element based on the holographic metasurface.

3. Results

In this work, we developed and studied several holographic metasurfaces for reflective terahertz focusing designed for the frequency of 334 GHz. The devices included ones for focusing radiation into a single spot and four spaced spots. Fig. 2 and Fig. 3 illustrates examples of the experimentally measured intensity on the focal plane for both cases. The intensity is normalized to that of the incident beam. The obtained results demonstrate the operability of the proposed approach for creating flat (non-profiled) diffractive elements for the terahertz band.

Acknowledgements

This work is supported by the grant 11.G34.31.0033 of the Russian Federation Government.

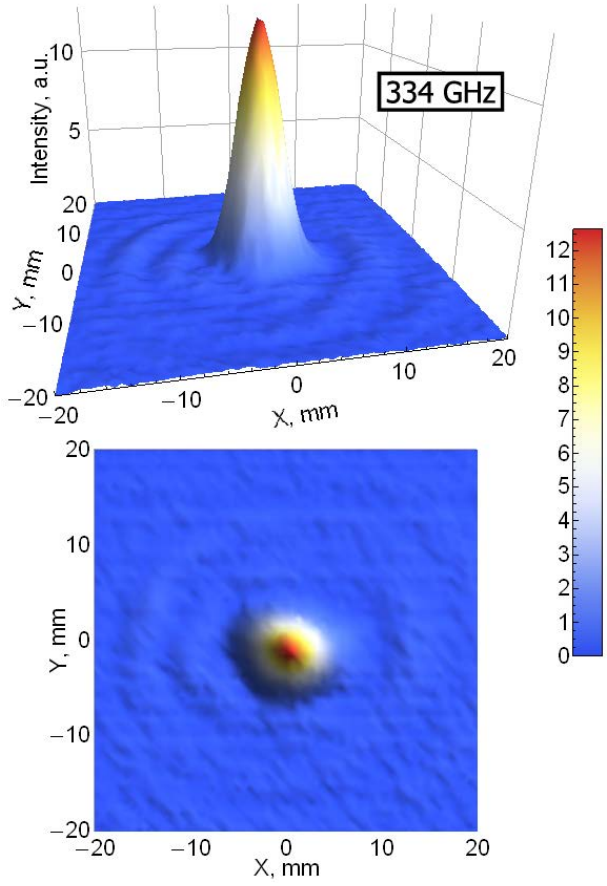

Figure 2: Experimental results on radiation focusing into a single spot at frequency 334 GHz.

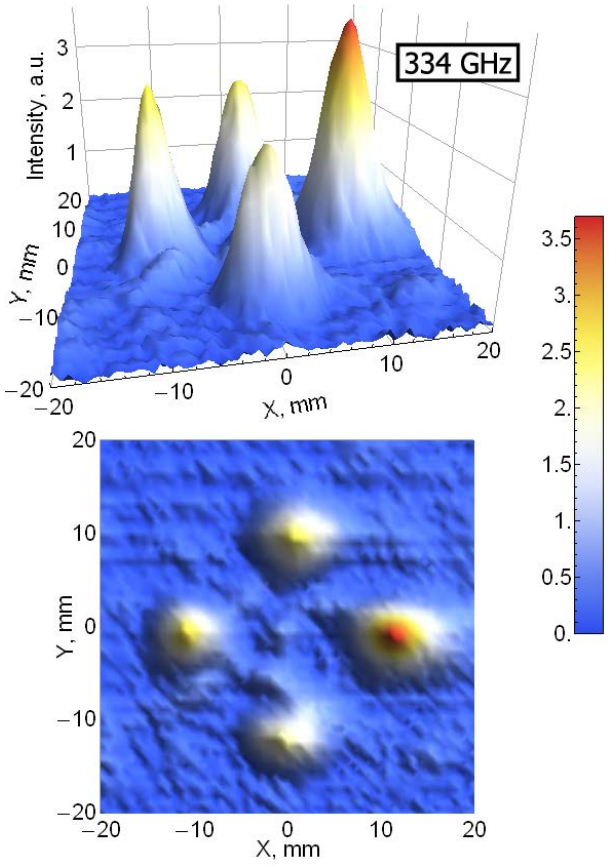

Figure 3: Experimental results on radiation focusing into four spaced spots at frequency 334 GHz.

References

[1] Solymar, L., and E. Shamonina, *Waves in Metamaterials*, Oxford University Press, New York, 2009.

[2] Siegel, P.H., "Terahertz Technology," *IEEE Trans. Microw. Theory Tech.*, Vol. 50, No. 3, 910-928, 2002.

[3] Balanis, C.A., *Modern Antenna Handbook*, Wiley Interscience, Hoboken, NJ, 2008.

[4] Soifer, V. A., ed., *Methods for Computer Design of Diffractive Optical Elements*, Wiley Interscience, New York, 2002.

Study of a microstrip antenna on anisotropic metamaterials

C. F. L. Vasconcelos[1*], M. R. M. L. Albuquerque[1], A. G. D'Assunção[1], and G. M. F. Freitas[2]
[1]Universidade Federal do Rio Grande do Norte, 59072-970, Natal, RN, Brazil
[2]Institut National des Sciences Appliquées de Lyon, 69621, Lyon, France
[*]corresponding author: cflinvas@yahoo.com.br

Abstract- In this work, annular ring microstrip antennas (ARMSA) on metamaterial substrates are modeled and analyzed using full-wave analysis in conjunction with Ansoft HFSS. The influence of the permeability tensor of the split ring resonator (SRR) medium on the resonant characteristics of the antenna is considered. Numerical results for typical resonant frequency behavior and return loss are presented as function of the metamaterial properties and antenna structural parameters.

In recent years, artificially structured metamaterials have received widespread attention in high frequency applications because of their ability to offer electromagnetic responses unavailable in conventional materials [1]-[2]. It has been considered a great potential substrate for a new generation of low-profile antennas and components for modern microwave technology [3]-[5]. Microstrip antennas are used in a broad range of applications such as mobile radio, wireless communications, aircraft, missile and satellite applications, due to their attractive features. In this work, annular ring antennas printed on metamaterial substrates are under consideration. From the modeling used in [5], it is possible to obtain the propagation characteristics of the ARMSA as a function of some geometrical dimensions and metamaterial properties. We consider enhanced positive electric permittivity and magnetic permeability for microwave applications [4].

The cross section view of the proposed antenna employing a metamaterial as substrate is depicted in Fig. 1. The annular ring patch is taken as perfectly conducting and has inner radius r_1 and outer radius r_2. The ground plane is assumed to be infinitely long and perfectly conducting. Dielectric region (1) is air-filled, with ε_0 and μ_0 denoting the free-space values of the permittivity and permeability, respectively.

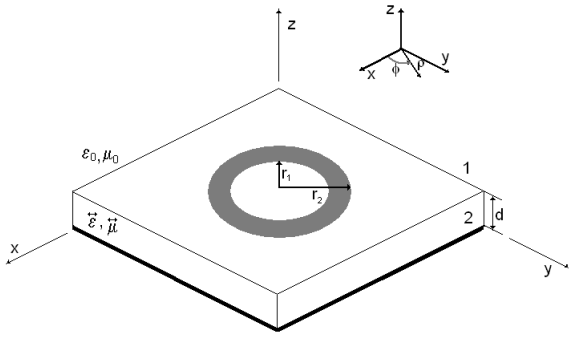

Fig. 1 – Geometry of an annular ring microstrip antenna.

For the ARMSA supported by metamaterial substrate (Fig. 1, region 2), the permittivity tensor and the permeability tensor are, respectively, given as [5]:

$$\vec{\varepsilon} = \varepsilon_0 \begin{bmatrix} \varepsilon_{\rho\rho} & 0 & 0 \\ 0 & \varepsilon_{\rho\rho} & 0 \\ 0 & 0 & \varepsilon_{zz} \end{bmatrix}; \qquad \vec{\mu} = \mu_0 \begin{bmatrix} \mu_{\rho\rho} & 0 & 0 \\ 0 & \mu_{\rho\rho} & 0 \\ 0 & 0 & \mu_{zz} \end{bmatrix} \tag{1}$$

Results are obtained taking into account two possible configurations of the metamaterial tensors by considering the variations of the effective permeability. In this paper, we consider that the components of the permittivity assume values $\varepsilon_{zz} = \varepsilon_{\rho\rho} = \varepsilon_r$. On the other hand, only z-component of the permeability assume effective values therefore $\mu_{\rho\rho} = 1$ and $\mu_{zz} = \mu_{eff}$ for the CASE 1. In the CASE 2, the only z-component of the permeability assume relative value therefore $\mu_{\rho\rho} = \mu_{eff}$ and $\mu_{zz} = 1$.

The analysis considers that the periodic arrangement of metallic elements is embedded in a dielectric with permittivity $\varepsilon_r = 4.4$ and permeability $\mu_r = 1$, composed of arrays of resonant cells each of which contains the split ring resonator (SRR), as shown in Fig. 2. The resonant frequency of this structure can be controlled by tuning the SRR dimensions. The component of the permeability tensor in the direction perpendicular to the plane of the SRR is given by [3]:

$$\mu_{eff} = 1 - \frac{F\omega^2}{\omega^2 - \omega_{0m}^2 + j\omega\zeta_m} \tag{2}$$

The effective permeability response to frequency variation of a periodic array of SRRs is depicted in Fig. 2, which exhibits the resonant behavior predicted by Eq. (2). The SRR unit cell was designed on FR4 substrate with $\varepsilon_r = 4.4$. The effect of the radius variations on the effective permeability is shown. For r = 15 mm, we choose that μ_{eff} is approximately 3.21 at 2.45 GHz. Also, it can be shown that the resonant frequency of the SRR structure shifts to a higher frequency when the radius r decreases.

Fig. 2 – Effective permeability as a function of resonant frequency.

In Fig. 3, numerical simulations using the Ansoft HFSS are carried out for an ARMSA supporting metamaterial substrate (CASE 1) with d = 4 mm, $\varepsilon_r = 4.4$, and $\mu_{eff} = 3.21$. The ARMSA is designed to resonate at 2.45 GHz, with outer radius $r_2 = 13.5$ mm. The results show that the resonant frequency of the proposed antenna on metamaterial substrate shifts to 2.48 GHz with a return loss of -14.6 dB and 2.28 GHz through full-wave analysis as described in [5], for the mode TM_{11}, showing a good agreement and validating the technique

developed in this work. If the antenna is printed on isotropic substrate (ε_r = 4.4), the resonant frequency approaches 2.55 GHz with a return loss of -15.8 dB. It can be seen that for the same resonant frequency, 2.48 GHz, the antenna on metamaterial substrate has better performance and a compression factor of the resonant frequency.

The input return losses for the metamaterial patch antenna (ε_r = 4.4, μ_{eff} = 3.21) and for the conventional patch antenna (ε_r = 4.4, μ_r = 1) are shown in Fig. 4. The resonant frequency of the metamaterial antenna (μ_{eff} = 3.21, $r_1 = r_2/2$, r_2 = 13.5 cm) is chosen at 2.48 GHz. The resonant frequency of the conventional antenna (μ_r = 1, $r_1 = r_2/2$, r_2 = 13.9 cm) is chosen at 2.48 GHz. It is also verified that the return losses are equal to -14.64 dB and -18.42 dB for the antenna printed on metamaterial and isotropic layer, respectively. The curves show that for the CASE 1 tensor configurations, the results of the resonant frequency and dimensions are very close to those obtained for the antenna on isotropic substrate.

Fig. 3 – Return loss as a function of resonant frequency.

Fig. 4 – Return loss as a function of resonant frequency.

Fig. 5 shows the variation of the return losses with the frequency for two different configuration of tensors, CASE 1 and CASE 2. Numerical simulations using the Ansoft HFSS are carried out for a patch antenna supporting metamaterial. From the results, it can be seen that for a given value of r_2, other resonant frequency appears for the CASE 2. The results give a return loss of -20.50 dB at 1.66 GHz. For the same antenna design, through full-wave analysis as described in [5], the resonant frequency is 1.28 GHz in the mode TM_{11}.

Fig. 5 – Return loss as a function of resonant frequency.

Conclusions - In this work, theoretical and numerical investigations have been carried out to study the effect of the metamaterial substrates on the resonance behavior of the annular ring microstrip patch antennas. It can be seen that the use of metamaterials, as antenna substrates, yields to the miniaturization of these structures. The results show the influence of the tensor of the metamaterial in the behavior of the ARMSA.

Acknowledgements - This work was supported by CNPq under covenant 573939/2008-0 (INCT-CSF) and covenant 620230/2008-8, CAPES, and Universidade Federal do Rio Grande do Norte (UFRN).

REFERENCES

1. Veselago, V. G. “The electrodynamics of substances with simultaneously negative values of ε and μ,” *Soviet Physics Uspekhi*, Vol.10, 509-514, 1968.
2. Smith, D. R., Padilla, W. J., Vier, D. C., Nemat-Nasser, S. C. and Schultz, S., “Composite medium with simultaneously negative permeability and permittivity,” *Phys. Rev. Letters*, Vol. 84, 4184-4187, 2000.
3. Itoh, T. and Caloz, C., *Electromagnetic Metamaterials: Transmission Line Theory and Microwave Applications*. New Jersey, USA: John Wiley&Sons, Inc., 2006.
4. Buell, K., Mosallaei, H. and Sarabandi, K., “A substrate for small patch antennas providing tunable miniaturization factors,” *IEEE Trans. Microwave Theory Tech*., Vol. 54, 135-146, 2006.
5. Vasconcelos, C. F. L., Albuquerque, M. R. M. L., Silva, S. G., Oliveira, J. R. S. and d’Assunção, A. G., “Full wave analysis of annular ring microstrip antenna on metamaterial,” *IEEE Trans. on Magnetics*, Vol. 47, 1110-1113, 2010.

Propagation Constant of a Rectangular Waveguides Partially Filled With Metamaterial Slab

Hedi SAKLI[1*], **Wissem FATHALLA**[1], **and Taoufik AGUILI**[1]
[1]Ecole Nationale d'Ingénieurs de Tunis (Labo SYS'COM), B.P :37, Le Belvédère, 1002 Tunis, Tunisia
[*]corresponding author: saklihedi@yahoo.fr

Abstract-In this paper, the propagation constant of a rectangular metallic waveguides partially and symmetrically filled with single negative metamaterial slab is studied. A rigorous study of the transverse operator method (TOM) is described to study the propagation in this waveguides followed by an application of the Galerkin's method. The results are compared to those previously published and they show a good agreement.

Introduction

Many researches have been interested in the propagation in guides of metamaterial [1-3]. H. Cory [4], Y. Xu [5] and D. Zhang [6] have studied the wave propagation in a rectangular metallic waveguide loaded with metamaterial slab.
In this paper, we have developed the TOM [7,8] followed by Galerkin's method to study a rectangular metallic waveguide partially filled with metamaterial slab. The TOM takes into account the discontinuities of these mediums applied in the transverse fields. We present a comparison with the literature.

Analysis

In a system of rectangular coordinates in an orthonormous reference mark of space $(\vec{u}_x, \vec{u}_y, \vec{u}_z)$, one may consider the structure of figure 1 comprising the media characterized by their scalar permittivity and permeability with i the order of the media ($i = 1, 2, 3$). In other words, let us consider the propagation of an electromagnetic wave in this structure according to Oz. E_z and H_z which will respectively be the longitudinal components of the electric and magnetic fields. Accordingly, E_t and H_t will respectively be the transverse components of the fields E and H.

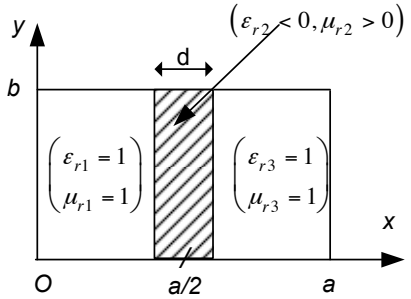

Fig. 1 The rectangular waveguide partially filled with metamaterial slab

The Maxwell equations describing the propagation of the electromagnetic field in an isotropic medium number i are written as

$$\vec{\nabla} \times \vec{E} = -j\omega\mu_i \vec{H} \tag{1}$$

$$\vec{\nabla} \times \vec{H} = j\omega\varepsilon_i \vec{E} \tag{2}$$

By setting :

$$\vec{H'} = j\sqrt{\frac{\mu_0}{\varepsilon_0}}.\vec{H} \tag{3}$$

we may get

$$\vec{\nabla} \times \vec{E} + k_0 \mu_{ri} \overrightarrow{H'} = \vec{0} \tag{4}$$

$$\vec{\nabla} \times \overrightarrow{H'} + k_0 \varepsilon_{ri} \vec{E} = \vec{0} \tag{5}$$

with $$k_0^2 = \omega^2 \mu_0 \varepsilon_0 \tag{6}$$

and $\vec{\nabla}\times$ is the rotational operator.

TOM consists in eliminating the longitudinal components E_z and H_z from the propagation equations (1) and (2). Thus, we ontain the following system of eauations

$$\begin{pmatrix} L_{11} & 0 \\ 0 & L_{22} \end{pmatrix} \begin{pmatrix} E_t \\ H_t' \end{pmatrix} = j\eta \partial_z \begin{pmatrix} E_t \\ H_t' \end{pmatrix} \tag{7}$$

$\hat{L}$ is called the transverse operator which is expressed by [7,8]

$$\hat{L} = \begin{pmatrix} L_{11} & 0 \\ 0 & L_{22} \end{pmatrix} = \begin{pmatrix} k_0 \varepsilon_{ri} - \frac{1}{k_0} \partial_t \frac{1}{\mu_{ri}} \partial_t^+ & 0 \\ 0 & k_0 \mu_{ri} - \frac{1}{k_0} \partial_t \frac{1}{\varepsilon_{ri}} \partial_t^+ \end{pmatrix} \tag{8}$$

with

$$\partial_t = \begin{pmatrix} \partial_y \\ -\partial_x \end{pmatrix},\ \partial_t^+ = (-\partial_y, \partial_x),\ \eta = \begin{pmatrix} 0 & \eta_0 \\ \eta_0 & 0 \end{pmatrix},\ \eta_0 = \begin{pmatrix} 0 & -j \\ j & 0 \end{pmatrix} \tag{9}$$

By realising an algebraic calculation, we obtain a system of propagation equations in E_t according to

$$\hat{L}' \vec{E_t} = k_z^2 \vec{E_t} \tag{10}$$

with k_z is the propagation constant according to z.

$$\hat{L}' = k_0^2 \mu_r \varepsilon_r - \mu_r \partial_t \left(\frac{1}{\mu_r} \partial_t^+ \right) - \eta_0 \partial_t \left(\frac{1}{\varepsilon_r} \partial_t^+ \right) \eta_0 \varepsilon_r \tag{11}$$

For the structure of figure 1, the expressions of the transverse electric field checking the boundary conditions ($E_t = 0$, for $x = 0$ or a, $y = 0$ or b), can be broken up in the following form

$$E_x = \sum_{m,n=0}^{\infty} E_{x,mn} \cos \frac{m\pi}{a} x . \sin \frac{n\pi}{b} y \tag{12}$$

$$E_y = \sum_{m,n=0}^{\infty} E_{y,mn} \sin \frac{m\pi}{a} x . \cos \frac{n\pi}{b} y \tag{13}$$

By applying the Galerkin method [8], we obtain the system with the eigenvalues according to

$$TE_t = k_z^2 E_t \tag{14}$$

T is a square matrix of order 2N with N the number of modes ; m and n are natural entireties such as $(m,n) \neq (0,0)$. The values and the proper vectors of T are respectiveley the propagation constants and the coefficients of the developpement of the real guide fields.

Simulation Results

Let us consider a rectangular guide of waves of width $a = 25\ mm$ as schown in fig. 1, partially and symmetrically filled with single negative metamaterial slab of relative permittivity $\varepsilon_{r2} = -2$ and relative permeability $\mu_{r2} = 1$ of thickness $d = 5\ mm$. We compare our results of the constant of propagation of the higher order mode with those of ref. [5].

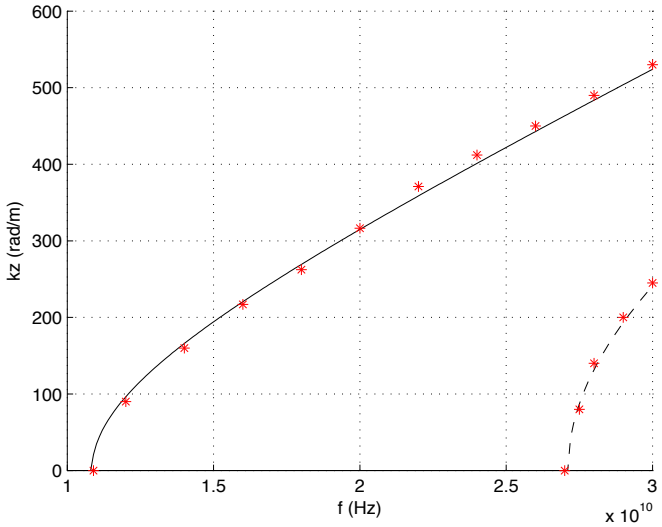

Fig. 2 The curves of the propagation constant according to the frequency
_____ : mode of order 1 (our results with TOM)
- - - - - - - - - - - : mode of order 2 (our results with TOM)
* * * * * * * * * * : Results of the ref. [5].

The obtained curves with the TOM of the propagation constant according to the frequency, are compared in fig. 2 with the curves schown with asterisks which are obtained in ref. [5]. From this figure, the cutoff frequencies increase with the thickness of the slab for all curves. It is found that the agreement between two methods is very good. We can say that the present method is effective for this problem.

Conclusion

We have studied the propagation of the rectangular metallic waveguide partially filled with metamaterial by the method called TOM which is rapidly and satisfying for this problem. Propagation constants and cutoff frequencies are calculated and increase with frequency.

REFERENCES

1. Eleftheriades, G. V., A. K. Iyer, and P. C. Kremer, "Planar negative refractive index media using periodically L-C loaded transmission lines," *IEEE Trans. Microwave Theory and Tech.,* No. 50, 2702-2712, 2002.
2. Wu, B. L., et all, "Guided waves with imaginary transverse wave number in a slab waveguide with negative permittivity and permeability," *J. Appl. Phys.,* 2003, 93, pp. 9386-9388.
3. Krowne, C . M., and M. Daniel, "Electronic aspects of propagation in left-handed guided wave structures, » Electromagnetic media interactions," *IEEE MTT-S Int. Symp.,* 309-312. Philadelphia, PA, 2003.
4. Cory, H. and A. Shtrom, "Wave propagation along a rectangular metallic waveguide longitudinally loaded with a metamaterial slab," *Microwave and Optical Technology Letters,* Vol. 41, No. 2, 123-127, 2004.
5. Xu, Y. "Wave propagation in rectangular waveguide filled with single negative metamaterial slab," *Electronics Letters IEE,* Vol. 39, No. 25, DOI: 10.1049/el:20031177, 2003.
6. Shu, W. and J. M. Songhang, "Wave propagation in grounded dielectric slabs with double negative metamaterials, "*PIERS Cambridge, USA,* pp. 246-250, March 26-29, 2006.
7. Tao J. W., R. Andriamanjato and H. Baudrand, "General waveguide problems studies by transverse operator method," *IEEE -Transactions on magnetics,* Vol. 31, No. 3, pp. 1626-1629, May 1995.
8. Sakli H., H. Benzina, T. Aguili and J. W. Tao, "Propagation constant of a rectangular

waveguides completely full of ferrite magnetized longitudinally," *International Journal of Infrared and Millimeter Waves*, (2009) 30:877-883. DOI: 10. 1007/s10762-009-9505-7.

Modeling of the crystal structure growth process of GaAs

Kulpash Iskakova[1], Rif Akhmaltdinov

[1]Kazakh National Pedagogical University, Almaty, Kazakhstan
E-mail: ahmanovakulpash@yahoo.com

Abstract

The current industry needs for new results require current capabilities of computer technology can solve problems on a whole new level. This article briefly describes the algorithms for obtaining the structures and the appearance of discontinuities in the growth of crystals.

1. Introduction

Solution of some technological issues requires study the internal structure of electron shells. There is a problem of explaining the phenomenon of increasing orders of the electronic resistivity silicon with the introduction of a probe by the diffusion of electrons. To elucidate the structure of the outer electron shells of the 18 copper is an essential knowledge of the inner radius of these shells that is the outer radius of the lower shells. Reference data on X-ray spectra have become an important and reliable source of information on the geometrical dimensions of the inner electron shells of atoms of any chemical element.

2. Computer simulation of Cu structure

For example, for copper Z = 29, R = 0,004915 nm. Computer simulation was carried out in the cluster approximation, which consists in the fact that the volume of the crystal was cut limited selection, the initial positions of the atoms which correspond to their positions in the nodes of the real crystal lattice. For copper in figure 1 is shown the sphere-rod model third sphere of the fcc lattice with 24 atoms, but the model is rotated 45є around the axis z.
In figure 2 is shown the sphere-rod model seventh sphere fcc lattice with 48 atoms. The model is rotated 45є about the axis of x. Atoms and bond rods are shown in different colors.

The modeling of properties shows that the crystal structure within a certain distance a gap of uniform growth occurs in the distances from the central atom. For copper, a spatial gap occurs after 321-th atomic node in the cluster. Further, these discontinuities are repeated periodically. And this is a defect associated with impaired growth are not in real crystals and the properties of the ideal lattice. The instability of the first cluster and the introduction of a defect in the corresponding crystal structure is the very first principle on which to conduct a fairly accurate analysis of the growth process of a real crystal and the resulting defects in it.

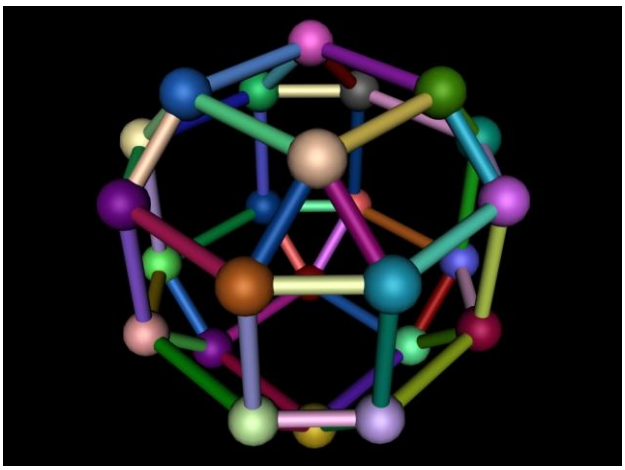

Figure 1: The sphere-rod model third sphere model of the fcc lattice with 24 atoms. The model is rotated 45є around the axis z. Atoms and bond rods are shown in different colors.

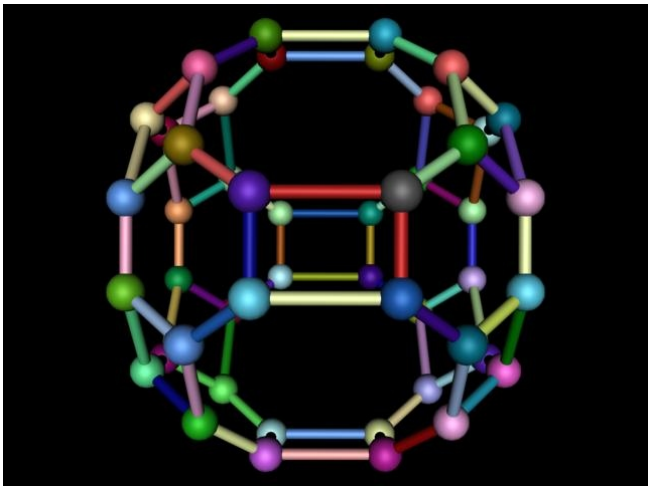

Figure 2: The sphere-rod model seventh sphere model of the fcc lattice with 48 atoms. The model is rotated 45є about the axis of x. Atoms and bond rods are shown in different colors.

Copper is a metal, but also for semiconductors, computer simulation provides essential information for subsequent analysis of the process of their growth and

ultimate properties. For example, computer simulation was conducted for the AsGa in the cluster approximation, which consists in the fact that the volume of the crystal was cut limited selection, the initial positions of the atoms of which comply with their provisions at the nodes of the real crystal lattice.

The lattice with a radius of 6 in her coverage of the atomic cores is considered. Calculation of the AsGa parameters were performed using the package we have created programs. As a cluster model was chosen 918-atom fragment of the crystal lattice of quantum dots based on GaAs. The properties of clusters depend on their size. Electron spectroscopy gives information averaged over the ensemble non isometric clusters on the surface and in the bulk solid. Therefore, to improve the accuracy and reliability of the information is necessary to create ensembles of clusters with a low dimensional variance.

Consider the finite crystal with unbroken intervals (except for the crystal boundary violation). For simplicity, we take a large number of cores, when there is a nearly ideal periodicity of the crystal. In this case, the parameters obtained from the mathematical formalism for the analysis of the band spectrum are periodic functions, except for the boundary of the crystal. The crystal potential and wave functions have a period equal to the distance between the cores, depending on the chosen direction. The energies have multiple frequency modulus of the wave vector in the quasi-momentum space [1]-[3]. Now turn to the crystal with a very small number of cores. In such a crystal frequency is not as ideal as in the previous case. The simulation of such a crystal is insurmountable difficulties for traditional methods, but this is the case is taken by us as a basic demonstration version. The object in question is distant from a perfect crystal due to its limited size. And despite this, the technique presented by us showed the periodicity of the above parameters. Thus in our problems are not used the condition of periodicity and Bloch's theorem as the necessary initial conditions. The figure 3 shows it on the example of GaAs.

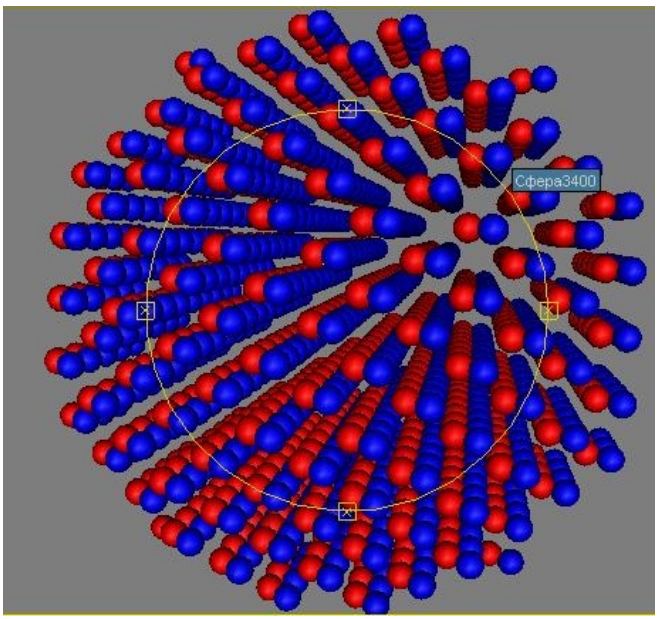

Figure 3: The As atoms and Ga for the radius of coverage 6. Red marked atoms As, in blue denote atoms Ga. Central atom is As.

2.1. Computer modeling of the crystal structure of GaAs

In computer modeling of the crystal structure of GaAs, combined with three-and five-valent elements are observed the following regularities (see Table I). When the radius of coverage is two in this range there are 38 cores. As the first atomic core in the center of origin, the four Ga atoms are located at a distance of 3 next 12 As atoms at a distance of 8. Nine Ga atoms at a distance there are 11. Six As atoms at a distance of 16, three Ga at a distance of 19 and three Ga at a distance of 27.

Table 1: The Combined lattice GaAs.

№	*x*	*y*	*z*	d^2	*Ion*	
0	0	0	0	0	As	
1	−1	−1	1	3	Ga	breaking
2	−1	1	−1	3	Ga	
3	1	−1	−1	3	Ga	
4	1	1	1	3	Ga	
5	0	2	−2	8	As	breaking
6	0	2	2	8	As	
7	0	−2	−2	8	As	
8	0	−2	2	8	As	
9	−2	2	0	8	As	
10	−2	−2	0	8	As	
11	2	2	0	8	As	
12	2	−2	0	8	As	
13	−2	0	2	8	As	
14	−2	0	−2	8	As	
15	2	0	2	8	As	
16	2	0	−2	8	As	
17	1	3	−1	11	Ga	breaking
18	1	−1	3	11	Ga	
19	−3	1	1	11	Ga	
20	−1	3	1	11	Ga	
21	3	1	−1	11	Ga	
22	1	−3	1	11	Ga	

23	−1	1	3	11	Ga	
24	3	−1	1	11	Ga	
25	1	1	−3	11	Ga	
26	0	4	0	16	As	breaking
27	−4	0	0	16	As	
28	4	0	0	16	As	
29	0	0	−4	16	As	
30	0	0	4	16	As	
31	0	−4	0	16	As	
32	3	3	1	19	Ga	breaking
33	1	3	3	19	Ga	
34	3	1	3	19	Ga	
35	1	5	1	27	Ga	breaking
36	5	1	1	27	Ga	
37	1	1	5	27	Ga	

Total number of cores with zero: 38

From this calculation, the differences in distance between the various groups are as (1):

$$\left.\begin{aligned} \Delta r_1 &= r_2 - r_1 = 3 \\ \Delta r_2 &= r_3 - r_2 = 5, \\ \Delta r_3 &= r_4 - r_3 = 3, \\ \Delta r_4 &= r_5 - r_4 = 5, \\ \Delta r_5 &= r_6 - r_5 = 3, \\ \Delta r_6 &= r_7 - r_6 = 8. \end{aligned}\right\} \quad (1)$$

We observe quasiperiodic change in the difference. At the border radius of coverage this periodicity is broken. When increasing the radius of coverage this periodicity is restored to the previous radius, but is broken on the new range. Thus, the boundary conditions lead to a violation of the periodicity. Simulated lattice shown in the following figures. The first figure shows the four first neighbors As in the lattice. Neighbors' ions Ga (blue) form a tetrahedron with the center of As (red).

The boundary atoms can approximately account for modeling the interface of the quantum dot with the matrix. The figure 4 shows the grid with a radius of coverage 1. There are 5 atomic cores in it. There is a periodic step structure. The structure of the central ion and its neighbors on the tetrahedron is stored and located in the center of this lattice.

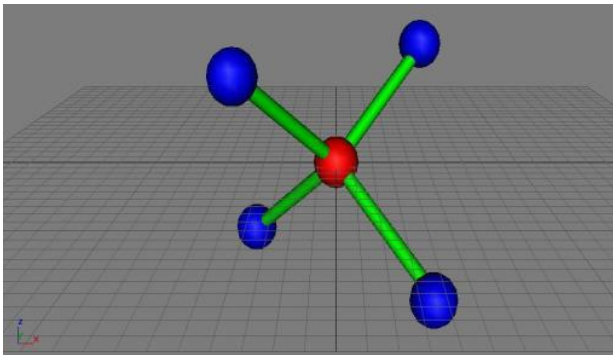

Figure 4: The grid with a radius of coverage where there are 5 atomic cores.

The figure 5 shows the grid with a radius of coverage 2. There are 38 atomic cores in it. There is a periodic step structure. The structure of the central ion and its neighbors on the tetrahedron is stored and located in the center of this lattice. The figure 6 shows the grid with a radius of coverage 3. There are 110 atomic cores in it. There is again a periodic step structure. The structure of the previous lattice is preserved. And while the structure of the central ion and its neighbors on the tetrahedron is stored and located in the center of this lattice. The figure 7 shows the grid with a radius of coverage 4. There are 282 atomic cores in it. Again, there is a periodic step structure. The structure of the previous lattice is preserved. Again, the structure of the central ion and its neighbors on the tetrahedron is stored and located in the center of this lattice. The figure 8 shows the grid with a radius of coverage 5. There are 498 atomic cores in it. There is a periodic step structure. The structure of the previous lattice is preserved. And the structure of the central ion and its neighbors on the tetrahedron is stored and located in the center of this lattice.

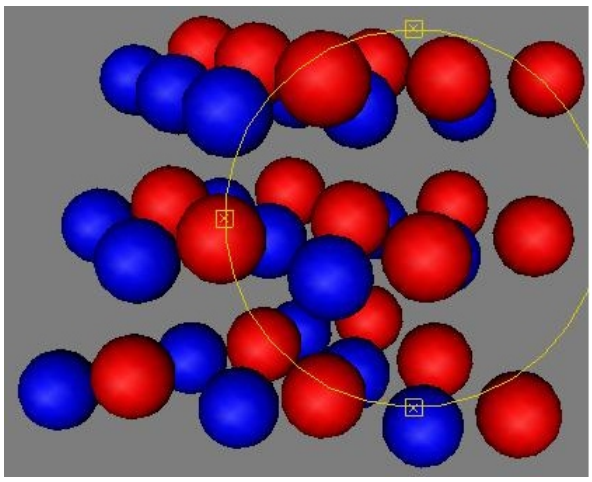

Figure 5: The grid with a radius of coverage 2 where there are 38 atomic cores.

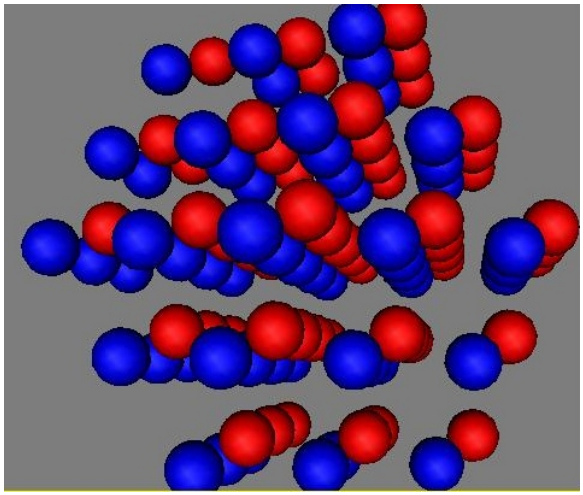

Figure 6: The grid with a radius of coverage 3. where there are 110 atomic cores.

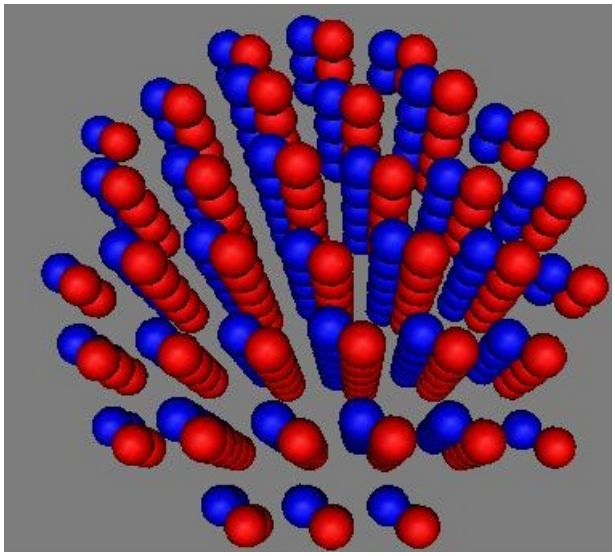

Figure 7: The grid with a radius of coverage 4. where there are 282 atomic cores.

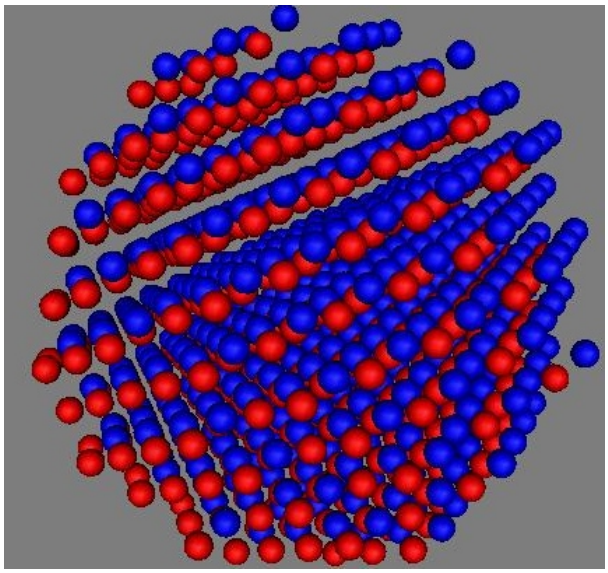

Figure 8: The grid with a radius of coverage 5. where there are 498 atomic cores.

The figure 1 shows the grid with a radius of coverage 6. There are 918 atomic cores in it. There is a periodic step structure. The structure of the previous lattice is preserved. And the structure of the central ion and its neighbors on the tetrahedron is stored and located in the center of this lattice.
It can be seen as an increase in the radius of coverage is restored periodicity in the lattice covered by the previous radius and there is a new violation of the periodicity on the boundary spanning lattice. The depth of violation increases with the radius of coverage. This is well observed in the tables you demonstrated for different cores.
On the basis of the direct lattice can construct the reciprocal lattice and define the properties of the Fermi surface. And the radius of coverage can be taken arbitrary (millions of skeletons).
The calculated structure allows to reach a real-time implementation and to take into account of defects and of real devices based on GaAs, because these are high-speed computing now by our proposed method.
On the basis of the direct lattice we can also construct the reciprocal lattice and define the properties of the Fermi surface. And the radius of coverage can be taken arbitrary (millions of skeletons). High-speed computing enables a dynamic computer simulation of the properties of real crystals of the GaAs.
Since the GaAs lattice is identical to the lattice of Si, sphalerite and diamond, we can apply the technology provided by and for these substances.
In calculating of coordination spheres cells of FCC- and BCC-lattices are presented as superlattice structure to fill own nodes by atoms of cells and additional nodes of the simple cubic lattices (SCL) — interstitial atoms [2]. The completing of coordination spheres with atoms is

determined on the basis of a small SC-lattice, taking into account octahedral, tetrahedral internodes.
If atoms in the lattice arrange with the dense packing, P-nodes are centers of the inter-body lattices in the methods of presentment of the spatial distribution of atoms and internodes along the coordination spheres in the crystals. Tetrahedral and octahedral internodes in the ion-interionic terminology mean inter-body lattice space surrounded by the atoms in the crystal lattice nodes.
The Table 1 contains the number of atoms and the distance from the central atom of the diamond-like structure. The distance is given in units of the lattice constant a. Let us choose the maximum distance based on these conditions, forming a set of atoms contributions on which the calculation of the potential are taken into account.

3. The crystal potential for crystals with the diamond structure

In this work we consider the crystal potential for crystals with the diamond structure. The Coulomb potential is the sum of the capacity building of the nucleus and the electrons occupied levels:

$$U_c = U_n + U_0, \tag{2}$$

where $U_n = -2Z/r$. Here, Z — number of the element, r — distance from the atom to the specified point.
Potential U_o is a solution of the Poisson equation:

$$\nabla^2 U_o = -8\pi\rho_o(r), \tag{3}$$

where $\rho_o(r)$ — the density of the electrons of the occupied levels at the distance r from the center of the atom. The density is calculated as follows:

$$\rho_0(r) = \sum_{n,l} r^2 R_{nl}^2(r). \tag{4}$$

Function $R_{nl}(r)$ — the radial part of the electron wave function for a hydrogen atom [4], [5]. Using the principle of superposition of the electronic densities and the additivity of the integral equation (3) can solve as follows:

$$U_0(r) = \sum_{i=0}^{I} u(r_i), \tag{5}$$

$$u(r_i) = \sum_{n,l} u_{nl}(r_i), \tag{6}$$

where I — the set of the number of atoms minus one, r_i — the distance from the center of the i-th atom to the specified point

$$\vec{r}_i = \vec{r} - \vec{a}_i. \tag{7}$$

Here a_i — the radius-vector of the i-th atom with respect to the center of origin. Let us obtain the Poisson equation for an electron of i-th atom:

$$\nabla^2 u_{nl}(\vec{r}_i) = -8\pi r_i^2 R_{nl}^2(\vec{r}_i). \tag{8}$$

Solving (8), we obtain

$$u(\vec{r}_i) = -8\pi \sum_{n,l} \iint u_{nl}(\vec{r}_i)\, d\vec{r}_i^{\,2}. \tag{9}$$

Directly using the functions (5, 6, 7, 8, 9) we find the potential U_0(r). This approach allows us to calculate effectively and accurately the electronic potential. We rewrite the expression (2) accounted for the entire set of atoms:

$$U_c(\vec{r}) = \sum_i U_n(\vec{r}_i) + U_0(\vec{r}). \tag{10}$$

Thus, the Coulomb potential is calculated from all the surrounding atoms [1], [6].
This approach allows us to select any line capacity in any direction from the lattice points, and may be any length of line. Moreover, we can specify a curved line capacity.
The cell potential near the nucleus has a singularity, and the distance from the nucleus is close to zero in hyperbole. For a single atom inside the Wigner-Seitz sphere the main contribution comes from the nucleus of an atom [6], [7].
Consider the cell potential obtained at the line potential. In this case, clearly seen the potential frequency, which is created by all the atoms are now set. In passing through the core potential becomes singular. The potential between the atoms is identical and negligible in the magnitude. There is a little effect of the atoms located at the centers of the faces of the two face-centered cubic lattices [8].
The obtained simulation results show the crystal potential, the crystal can be modeled with all its features. In contrast to known methods of calculating of the crystal potential as described in the engineering calculations of the crystal potential is universal. It gives the results without making any correction factors, does not require the use of logarithmic scales, and other non-uniform, allows you to quickly calculate the crystalline potential for all elements of the given crystal structure. There are facilities for the further developments of such technology in the direction of accounting for various disturbances. It will allow a calculating the electronic potential even more precisely. However, even without taking into account the properties of an ideal crystal, this calculation provides sufficiently accurate results. To illustrate the power and versatility of the described technique for the calculating of the potential capabilities it is shown an interaction potential on line drawn along the main diagonals of the two face-centered cubic lattices in figure 9.

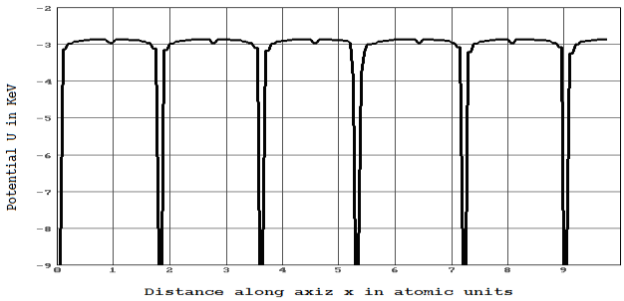

Figure 9: An interaction potential on line drawn along the main diagonals of the two face-centered cubic lattice.

In determining the energy spectra of quantum-mechanical problems for periodic structures, it often uses methods of the broadcast. In particular, semiconductors have a periodic structure. The crystal potential, having the grating period, usually modeled by the expression [1], [9]:

$$V(\vec{r}) = \left[\sum_{i=0}^{N} V_{\mathrm{n}}(\vec{r}_i) \right] + U_0(\vec{r}) + V_{\mathrm{exh}}(\vec{r}). \quad (11)$$

where $V_n(r_i)$ — the potential created by the i-th nucleus at the point r; $U_0(r)$ — the electronic potential, formed by the electrons of the core at some point r and is determined from the Poisson equation

$$\nabla^2 U_0(\vec{r}) = -8\pi\rho_0(\vec{r}). \quad (12)$$

Here $\rho_0(\mathbf{r})$ — the electronic density of the occupied levels at a distance r from the center of the atom; $V_{exh}(\mathbf{r})$ —the exchange potential at point $\mathbf{r}$; $\mathbf{r}_i = |\mathbf{r}-\mathbf{a}_i|$ — the distance from the i-th node to the point $\mathbf{r}$; $\mathbf{a}_i$ — the node location; N — the number of neighbors taken into account relatively to the cores. The solution of Schrцdinger equation based on the potential (11) is carried out by the Hartree-Fock-Slater [10].

The specificity of a solid compared to other bodies, is the decisive role of spatial-structural properties: a lattice type, a location and an interaction of the defects, a structure of core lattices and inter-ionic space. The period of the inter-ionic lattice coincides with the period of the core lattice. Spatially periodic structure of two weakly coupled and oppositely charged objects is the cause of the stability of rigid body — in this case the semiconductor GaAs — because between these objects appear spatially periodic Coulomb forces. In the geometric structure of each inter-ionic space surrounded on six sides by positive ion cores, and the ionic core in turn — intervals. For a uniform distribution of electrons in the space of interaction between them becomes energetically unfavorable. There is the possibility of an orderly arrangement of electrons in space, the emergence of the so-called Wigner or "electron crystal". The geometrical structure of the crystal consists not only of the atomic cores, but inter-ionic space intervals. The valence electrons in inter-ionic space intervals are also elements of the crystal, along with the atomic cores. The inter-ionic space is gap, i.e. the most probable location of the valence electrons. In addition, inter-ionic space intervals are also still a kind of “elements” of the crystal. But then the conclusion is that in the crystal lattice there are two — the well-known lattice consisting of the atomic cores, and another, equally important for the existence of the crystal lattice of the valence electrons are concentrated between the cores. The lattice periodicity of the atomic cores immediately implies the lattice periodicity of the inter-ionic space. Even more natural in such a conclusion, if you do not forget that the atomic cores of the crystal lattice — not a point in space, but the figures, which occupy a significant part of the whole space of the crystal, and inter-ionic space also has a periodic structure, as well as skeletons. The period of this lattice coincides with the usual of the core of the lattice. Figure 10 shows a two-dimensional lattice with the lattice constant a_0. The coordinate origin of the system Oxy is at the center of one of the cores, and the origin of the coordinate system $O'x'y'$ is located in the center of one of the inter-ionic cells. The coordinate system $O'x'y'$ is formed by the translation of the coordinate system Oxy in $a_0n/2$, where $n = \{0, 1, 2, ...\}$. We assume inter-ionic intervals are the inter-ionic elements of the lattice, which is shifted with respect to a core of the lattice by half a lattice constant in all coordinate axes.

Figure 10: A two-dimensional lattice with the lattice constant a_0. Cores and inter-ionic space two-dimensional lattice include 1) frame, 2) inter-ionic space.

The determining the location of the centers of the location of the centers of the inter-ionic intervals can be easily receive from the definition of the basis vector for the nodes of the crystal (the core) of the lattice with any structure. But it should be noted that by increasing the radius of inter-ionic volumes (not just their centers) there is a change the number under the consideration inter-ionic space compared to the amount covered by the cores. Since you want to cover all inter-ionic space surrounding covered the skeletons, the radius of coverage inter-ionic space few more skeletons examined. Crystal is in a stable condition thanks to the orderly arrangement of opposite charges. Most of the properties of crystals (eg, electrical conductivity, magnetic susceptibility), are caused not only property of the host lattice, but also the existence of inter-ionic lattice. This inter-ion lattice in addition to the core determines the physical properties of the crystal. Specificity of a solid compared to other bodies is that in them play crucial role spatial structural properties: the lattice type, location and interaction of defects, the structure of the nucleus and inter-

ion lattice. The period of the inter-ion lattice coincides with the period of the core lattice. Spatially periodic structure of two weakly coupled and oppositely charged objects is the cause of the stability of rigid body — in this case the GaAs — because between these objects appear spatially periodic Coulomb forces. In the geometric structure of each inter-ionic cell surrounded on six sides by positive ion cores, and the ionic core in turn — the inter-ionic gaps.

4. Discussion

Computer simulation of the properties of the crystal lattice gives to use up to 1010 ч 1012 atoms. Using the described technique can be obtained from any of these atomic systems, as well as changes in the radii of coordination spheres at various distances. Simultaneously, you can get a number of nearby neighbors, the location of atoms on the coordination sphere.

Thus, algorithms are developed for the FCC, BCC and diamond-like structures for determining the orderly and semiregular Archimedean and Platonic figures, as well as their complexes.

We can develop an algorithm for constructing the structure of compound semiconductor-type A3B5, based on this principle. For example, to the type of A3B5 of semiconductor compounds it is used compound GaAs. It is crystal lattice of two face-centered cubic lattices shifted relative to each other at j spatial diagonal. Each Ga atom has four nearest neighbors located at the tops of a tetrahedron. Each ion is surrounded by four nearest neighboring ions of opposite sign. There are four ions with qi qj= –1 at a distance a02S/2, eight ions of opposite sign of qi qj = +1 at the 2 distance a02S. The system of links of the GaAs structure establishes the order of the atomic body along tetrahedral combinations [2], [3]. For such compounds of the tetrahedral group of atoms is one-eighth of the basic lattice, so it is convenient to consider as a superstructure. The cell of the GaAs lattice consists of four tetrahedral sublattices.

One of the advantages of the described technique is its application to systems with short-range order, which does not use Bloch's theorem as the initial conditions. This was possible due to the fact that translational invariance follows as a consequence of the calculations, and not postulated initially. Thus, translational invariance in real space and in the quasi-momentum space is not a prerequisite for the determination of the crystal potential, wave functions and energies in wave vector space.

This, in turn, allows you to define these parameters not only for infinite crystals, but also for the real limits on the size of the crystals. Therefore, it is possible to determine the properties of crystals with impaired structure of a single scheme, with no additional idealizations. Individual interest is a violation of the periodicity on the boundary of the crystal. In fact, it is inherent in all real crystals violation of the ideal (i.e. infinite) crystal structure.

The violation of a perfect crystal at the border no doubt affects the theoretical study of the band spectrum. Boundary effects appear in the form of decay phase portraits of the main parameters (the crystal potential, the wave functions and energies in wave vector space) in all directions of the crystal boundaries (in our case spherical).

5. Conclusions

In the study of solid-state we considered two sites within the crystal, virtually connected to each other. A theoretical study of solid-state is easily accomplished with the use of these facilities both qualitative and quantitative methods. But the most effective way of investigating solids is to use a direct computer simulation, and that we have done for simple structures.

Thus, the use of techniques discussed in the article allows the calculation of real properties of GaAs crystals with defects and other constraints.

References

[1] T. Loucks, Augmented plane wave method. New York, W. A. Bendjamin Inc., 1967, p. 12-62.

[2] Iskakova K.A., Ahmaltdinov R.F., Possibilities of the modifications of the method of calculation of wave function and zonal spectrum of crystal structure, PCI-2010 «12th International Conference on the Physics and Chemistry of Ice». Sapporo, Japan.

[3] Iskakova K.A., Ahmaltdinov R.F., Modelling and calculation of FCC structures and principles of the algorithm structure Si, 88th annual meeting of the German Mineralogical Society, 19–22. September 2010 Munster, Germany.

[4] Bugaev V.N., Chepulski R. V. 1. Basic theory. The symmetry of interatomic lattice potentials in general crystal structures. – Acta crystallogr. 1995, v. 51,No 4, p. 456–462.

[5] Sowa E.C., Gonis A. A multisite interaction expansion of the total energy in metals. Instrum. and Meth. Phys. Res. B. 1995, v. 102, No 1–4, p. 1–2.

[6] Korhonen T., Puska M. I., Nieminen R. M. Vacancy formation energies for fcc and bcc transition metals. Phys. Rev. B. 1995, v. 51, No 15, p. 9526–9532.

[7] Mirabella D.A., Aldao C.M. Effects of orbital nonorthogonality on band structure within the hight binding scheme. Phys. Rev. B. 1994, v. 50, No 16,p. 12152–12155.

[8] Andrews Lawrence C., Bernstein Herbert I. Bravais lattice invariants. Acta Crystallogr. A. 1995, v. 51,No 3, p. 413–416.

[9] Krimmel H.G., Ehmann I., Elsasser C. Calculation of atomic forces using the lineorized – augmented – plane wave method. Phys. Rev. B. 1994, v. 50, No 12,p. 8846–8848.

[10] Bodralexe E., Marksteiner P., Oh Y., Freeman A. J. Coupled channel equation for potential with a Coulomb singularity. Comput. Phys. Commun. 1994, N. 82,p. 120–128.

Phase constant peculiarities of cylindrical zero-index anisotropic metamaterial waveguide.

L. Nickelson[1,2], A. Bubnelis[1,2], S. Asmontas[1]

[1]State Research Institute Center for Physical Sciences and Technology, Vilnius, Lithuania
[2]Vilnius Gediminas Technical University, Lithuania
*corresponding author, E-mail: lucynickelson@gmail.com

Abstract

Here we present the phase constant dependencies of propagating eigenmodes of open cylindrical anisotropic metamaterial waveguide when the metamaterial permittivity and permeability tensor components may accept values close or equal to zero. Dispersion characteristics of rod and hollow-core waveguides with the radii 0.5, 2.5 and 5 mm at the left handed polarization of microwave are shown here. There are unusual shape of eigenmode dispersion characteristics and anomalous sectors of the characteristics at certain frequencies. The first eigenmode of rod waveguide with the lowest cutoff frequency is a particularly important mode because it is a single one in the frequency range 1.0–1.9 GHz and some small variations on the frequency produce large changes in the phase constant. We can observe packages of dispersion characteristic branches when their cutoff frequencies closed to the metamaterial electric and magnetic plasma frequencies between 1.9 and 3.5 GHz. There are only three modes in the hollow core anisotropic metamaterial waveguide at the frequency range 1.4–2.8 GHz.

1. Introduction

In the last decade many specialist focused on the experimental and theoretical investigations of the zero-refractive index (or zero-index) metamaterials. The metamaterials attractive to researches due to their unconventional constitutive parameters and different anomalous effects too. Zero-index metamaterials may have the epsilon-near-zero (ENZ) and mu-near-zero (MNZ) properties simultaneously or one after another at different frequencies. These metamaterials are used in different devices as a transformer to achieve the perfect impedance match between two waveguides with a negligible reflection or to improve the electromagnetic (EM) wave transmission through a waveguide bend, for the matching of waveguide structure impedance with the free space impedance and etc. The metamaterials provides manipulating of the antenna phase fronts and enhancing the antenna radiation directivity. In a Zero-index metamaterial waveguide can be observed a super-tunneling effect. ENZ metamaterials may allow reducing of waveguide sizes and can be used as a frequency selective surface [1–5].

The controllable devices as modulators, phaseshifters, shields and etc. can be created on the base of anisotropic materials [6].

Zero-index metamaterials are dispersive media. The constitutive parameters of anisotropic metamaterials can be described by expressions that involve the plasma frequencies. A waveguide that has a boundary of anisotropic metamaterial-dielectric (air) can be assigned to plasmonic waveguides. Here we present dispersion characteristics of two open plasmonic waveguides Fig. 1.

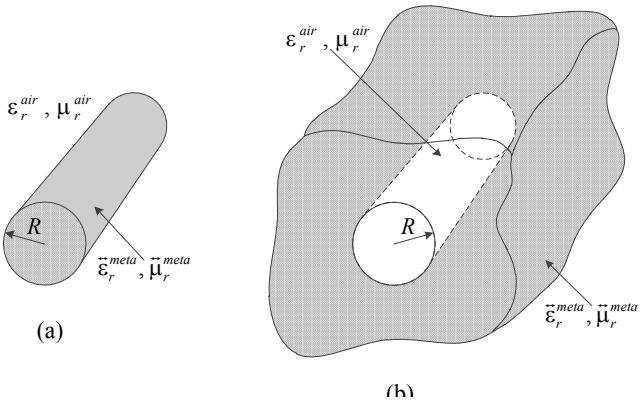

Figure 1: Cylindrical zero-index anisotropic metamaterial waveguide model (a) – open waveguide; (b) – hollow-core waveguide.

2. Permittivity and permeability tensors of zero-index anisotropic metamaterial

Electrodynamical parameters of the uniaxial electrically and magnetically anisotropic metamaterial, characterized by relative permittivity $\ddot{\varepsilon}_r^{meta}$ and permeability $\ddot{\mu}_r^{meta}$ tensors (1), were taken from the article [7]. In the mentioned article was considered an anisotropic dispersive lossless metamaterial slab. For this reason there were given only the real parts of the relative permittivity (ε_{xx}, ε_{zz}) and relative permeability (μ_{xx}, μ_{zz}) tensor components:

$$\ddot{\varepsilon}_r^{meta} = \begin{vmatrix} \varepsilon_{xx} & 0 & 0 \\ 0 & \varepsilon_{xx} & 0 \\ 0 & 0 & \varepsilon_{zz} \end{vmatrix}, \quad \ddot{\mu}_r^{meta} = \begin{vmatrix} \mu_{xx} & 0 & 0 \\ 0 & \mu_{xx} & 0 \\ 0 & 0 & \mu_{zz} \end{vmatrix}. \qquad (1)$$

The tensor components of the relative permittivity and the relative permeability are described by following formulas:

$$\varepsilon_{xx} = 1 - \omega_{epxx}^2 / \omega^2; \qquad \varepsilon_{zz} = 1 - \omega_{epzz}^2 / \omega^2;$$
$$\mu_{xx} = 1 - \omega_{epxx}^2 / \omega^2; \qquad \mu_{zz} = 1 - \omega_{epzz}^2 / \omega^2, \tag{2}$$

where $\omega = 2\pi f$ – angular frequency of EM oscillation; metamaterial electric $f_{epxx} = 3.46$ GHz, $f_{epzz} = 2.5$ GHz and magnetic $f_{mpxx} = 2.45$ GHz, $f_{mpzz} = 2$ GHz plasma frequencies, taken from [7].

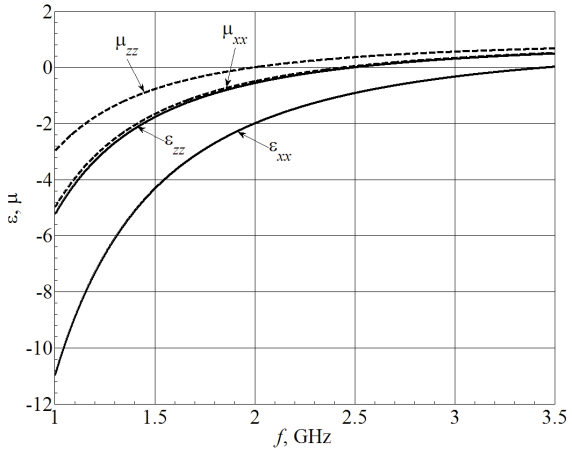

Figure 2: Dependences of the relative permittivity and permeability tensor components of the metamaterial on the frequency.

In Fig. 2 are presented dependencies of tensor components of the relative permittivity ε_{xx}, ε_{zz} and the relative permeability μ_{xx}, μ_{zz}.

The permittivity components ε_{xx} and ε_{zz} have negative values from 1.0 to ~3.5 GHz and from 1.0 to ~2.5 GHz, respectively. The permeability components μ_{xx} and μ_{zz} have negative values from 1.0 to ~2.5 GHz and from 1.0 to ~2 GHz, respectively. All tensor components are negative at the frequency range from 1.0 GHz to ~2 GHz. Absolute values of tensor components are less than 1 at the frequency range from ~2.5 GHz to 4 GHz. The values of tensor components become equal to zero at the operating frequency f equal to the metamaterial electric or magnetic plasma frequencies. This metamaterial is a plasmonic one.

3. Dispersion characteristics of open cylindrical zero-index anisotropic metamaterial waveguide.

The solution of Maxwell's equations for the circular anisotropic metamaterial waveguide was carried out by the partial area method [8–10]. The computer program for the dispersion characteristic calculations has created in MATLAB language. Our computer program allows take into account a very large material attenuation as well as the values of non-diagonal tensor components [9, 10].

We present here how the radius value of plasmonic waveguides affects on the propagating eigenmodes' dispersion characteristics, including dependencies of the eigenmode quantity and mode cutoff frequencies.

In Figs. 3, 4 and 5 are shown dispersion characteristics (phase constants) of open cylindrical waveguide (Fig. 1a) made of the uniaxial electrically and magnetically anisotropic metamaterial in the frequency range 1–3.5 GHz.

The calculations are performed for EM waves with left-handed circular polarization ($e^{+im\varphi}$), where m = 1 is azimuthal symmetry index, φ is the azimuthal coordinate.

Here are shown the phase constant h′ (the real part of longitudinal propagation constant) dependencies of plasmonic metamaterial waveguides with radii R equal to 0.5 mm, 2.5 mm, and 5 mm. The phase constant h′ is equal to $2\pi/\lambda_w$, where λ_w is the wavelength of certain mode. The analysis of Figs 3–5 shows that there are three main frequency areas where localize dispersion curves. A shape of all dispersion characteristics are unusual in the comparison with traditional dispersion characteristics of open cylindrical waveguides made of dielectrics, semiconductors or gyroelectric plasma [8–10]. Because the dispersion characteristic branches of analyzed here waveguides are quite vertical.

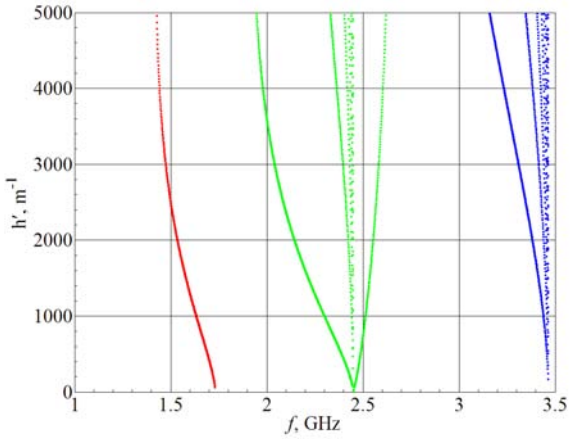

Figure 3: Phase constant dependencies of propagating eigenmodes of the anisotropic metamaterial waveguide with $R = 0.5$ mm.

We see that there is a single mode with the cutoff frequency 1.73 GHz, 1.71 GHz and 1.63 GHz, when waveguide radius is accordingly 0.5 mm, 2.5 mm and 5 mm (Figs. 3–5, red curves). The cutoff frequency of this mode shifted in the direction of lower frequencies with increasing of the waveguide radius. This first single mode is special one because the mode does not match any of plasma f_{epxx}, f_{epzz}, f_{mpxx}, f_{mpzz} frequencies. We can observe how a shape of the dispersion characteristic changes in the vicinity of the cutoff frequency.

We would like to draw your attention to the fact that the anisotropic metamaterial is described by the negative tensor components ε_{xx}, ε_{zz}, μ_{xx}, μ_{zz} in the frequencies less than 2 GHz (see Fig. 2). It is mean that the first mode propagates in the waveguide when the metamaterial is double negative (DN). This single mode (red curve in Figs 3–5) is particularly important because small changes in frequency produce large changes in the phase constant. The mode can be used for worked out a sensitive narrowband phaseshifter at frequencies between 1.4 and 1.65 GHz (Fig. 3) or other potential microwave devices.

We can watch a package with dispersion branches closed to cutoff frequency 2.5 GHz (Figs 3–5, green curves). We see that the left lateral dispersion branch of the package is a special eigenmode, i.e. this one is separated by a larger distance from other eigenmodes. The vertical

branch of the left lateral mode is located on the magnetic plasma f_{mpzz} frequency equal to 2 GHz. We can distinguish also the right lateral dispersion branch of the package.

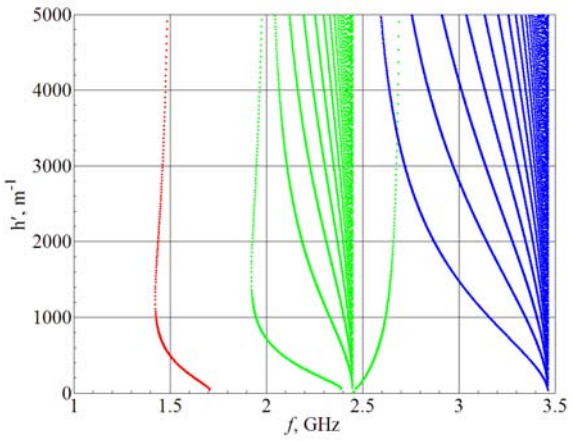

Figure 4: Phase constant dependencies of propagating eigenmodes of the anisotropic metamaterial waveguide with R = 2.5 mm.

The mode with this dispersion characteristic is also more specific one. i.e. this mode is separated by a larger distance from other modes. The vertical branch of this mode is located about 2.7 GHz and shifted at the higher frequencies with increasing of a radius.

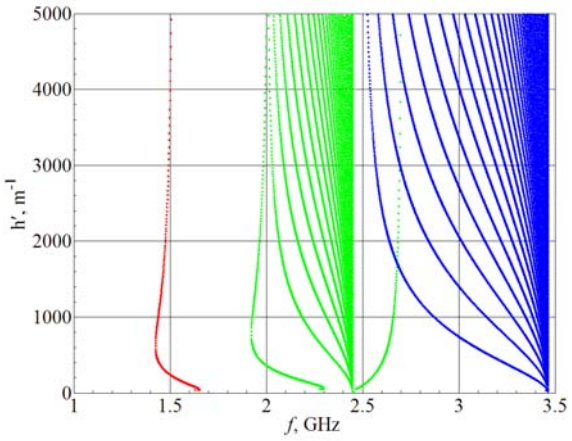

Figure 5: Phase constant dependencies of propagating eigenmodes of the anisotropic metamaterial waveguide with R = 5 mm.

A dense bunch of dispersion curves located between the extreme left and right curves that were described before. The number of curves increases rapidly at increasing of waveguide radius. It is interesting to note that all dispersion branches of the dense bunch are within the frequency band of 2–2.5 GHz. Apparently the dense bunch of dispersion characteristics related to plasma f_{epzz}, f_{mpxx} frequencies. The cutoff frequencies of dispersion characteristics of the dense bunch are the same and equal to $f \sim 2.46$ GHz. The dispersion curves fan out from a single point f_{mpxx}.

Second dense bunch of dispersion curves is at the electric plasma frequency $f_{epxx} \sim 3.46$ GHz (Figs. 3–5, blue curves). The number of curves increases rapidly at increasing of waveguide radius. All dispersion characteristics are within the frequency band of 2.5 GHz and 3.46 GHz.

The greatest number of modes can be excited at the electric plasma frequency $f_{epxx} \sim 3.46$ GHz in the comparison with other plasma frequencies. The cutoff frequencies of dispersion characteristics of this dense bunch are the same and equal to $f \sim 3.46$ GHz.

We did not find the plasmonic metamaterial waveguide eigenmodes in the frequency range from 3.5 GHz till 2000 GHz. The mode absence at higher frequencies is possible to explain by a fact that the metamaterial relative permittivity and permeability values at higher frequencies are close to the ones of air.

4. Dispersion characteristics of hollow-core cylindrical zero-index anisotropic metamaterial waveguide.

In Figs. 6–8 are shown dispersion characteristics (phase constants) of hollow-core cylindrical waveguide (Fig. 1b) made of the uniaxial electrically and magnetically anisotropic metamaterial in the frequency range 1.4–2.8 GHz.

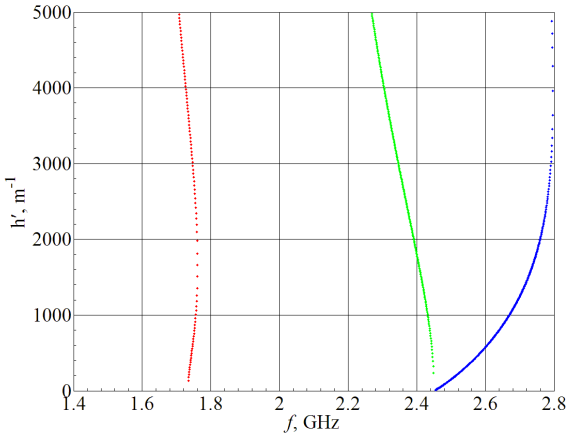

Figure 6: Phase constant dependencies of propagating eigenmodes of the hollow-core anisotropic metamaterial waveguide with R = 0.5 mm.

As in the case of an open waveguide there is a single mode that does not match any of plasma frequencies and propagates in the waveguide when the metamaterial is double negative (Figs 6–8, red curves).

The cutoff frequencies of this mode are 1.73 GHz, 1.75 GHz and 1.79 GHz, when waveguide radius accordingly equal to 0.5 mm, 2.5 mm and 5 mm.

We see, that in case of hollow-core waveguide, there are propagating only three modes in frequency range 1.4–2.8 GHz. The branch of second and third modes (Figs. 6–8, green and blue curves) has the same cutoff frequency equal to magnetic plasma frequency f_{mpxx} = 2.45 GHz. This cutoff frequency is independent on the waveguide radius. We can observe changes in a shape of dispersion curves with changing of waveguide radius. The dispersion characteristics are more vertical with low values of waveguide radius.

We did not find the plasmonic hollow-core metamaterial waveguide eigenmodes in the any other frequency range. The number of modes propagating in the hollow-core metamaterial waveguide is independent on waveguide radii.

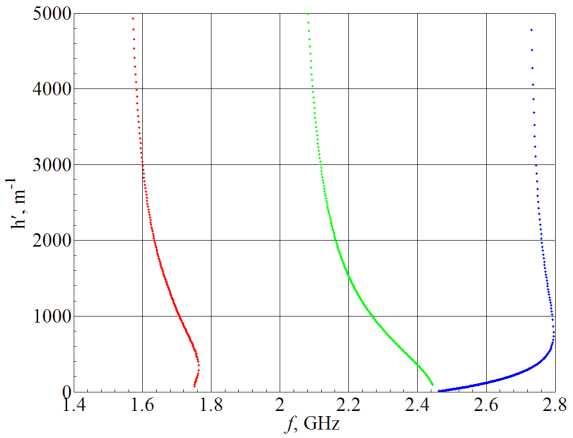

Figure 7: Phase constant dependencies of propagating eigenmodes of the hollow-core anisotropic metamaterial waveguide with $R = 2.5$ mm.

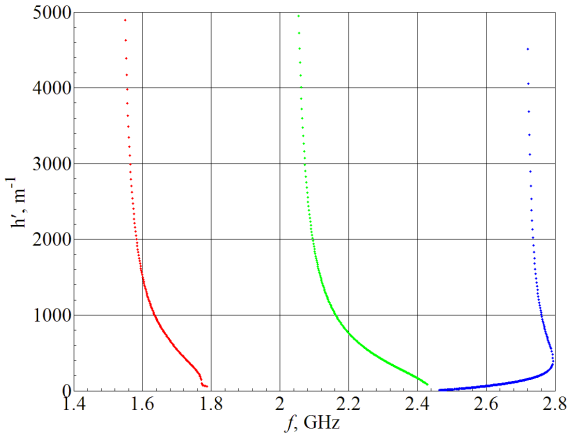

Figure. 8: phase constant dependencies of propagating eigenmodes of the hollow-core anisotropic metamaterial waveguide with $R = 5$ mm.

The specific dispersion characteristic features of hollow anisotropic waveguides can be used for a transmission of laser radiations or to working out plasma wakefield accelerators [11].

Conclusions

1. The open rod and hollow-core cylindrical anisotropic metamaterial waveguides were investigated by using of our MATLAB computer programs based on the partial area method.

2. The anomalous dispersion dependencies are observed for eigenmodes of the waveguides at the metamaterial plasma frequency range between 1 and 3.5 GHz. There are dispersion curve segments for considered waveguides when an increase of frequency accompanied by a decrease of phase constant.

3. We find a single eigenmode of rod waveguide with the cutoff frequency f_{cut} close to 1.7 GHz. The mode has a quite vertical dispersion characteristic when some small variations of f produces the very large changes in the phase constant.

4. There are two dispersion characteristic packages of rod waveguide at the frequency range 1.9–3.5 GHz.

5. There are only three modes in hollow-core waveguides: single mode with $f_{cut} \sim 1.75$ GHz and two modes with f_{cut} equal to the magnetic metamaterial plasma frequency $f_{mpxx} = 2.45$ GHz.

References

[1] B. Lopez-Garcia, D. V. B. Murthy, A. Corona-Chavez, Half mode microwave filters based on epsilon near zero and mu near zero concepts, *Progress In Electromagnetics Research* 113: 379-393, 2011.

[2] J. Luo, H. Chen, Y. Lai, P. Xu, L. Gao, Anomalous transmission properties of epsilon-near-zero metamaterials, *PIERS Proceedings*, Suzhou, China, pp. 1299-1302, 2011.

[3] J. Bai, S. Shi, D. W. Prather, Analysis of epsilon-near-zero metamaterial super-tunneling using cascaded ultra-narrow waveguide channels, *Progress In Electromagnetics Research M* 14: 113-121, 2010.

[4] B. Wang, K.-M. Huang, Shaping the radiation pattern with mu and epsilon-near-zero metamaterials, *Progress In Electromagnetics Research* 106: 107-119, 2010.

[5] H. Oraizi, A. Abdolali, Some aspects of radio wave propagation indouble zero metamaterials having the real parts of epsilon and mu equal to zero, *J. of Electromagn. Waves and Appl.* 23: 1957–1968, 2009.

[6] H. Liu, L. Li, M. Leong, S. Zouhdi, Transparent uniaxial, anisotropic spherical particles designed using radial anisotropy, Phys. Rev. E 84: 016605, 2011.

[7] S.-H. Liu, C.-H. Liang, W. Ding, L. Chen, W.-T. Pan, Electromagnetic wave propagation through a slab waveguide of uniaxially anisotropic dispersive metamaterial, *Progress In Electromagn. Research* 76: 467–475, 2007.

[8] L. Nickelson, S. Asmontas, V. Malisauskas, R. Martavicius, The dependence of open cylindrical magnetoactive *p*-Ge and *p*-Si plasma waveguide mode cutoff frequencies on hole concentrations, *Journal of Plasma Physic* 75: 35–51, 2009.

[9] S. Asmontas, L. Nickelson, A. Bubnelis, R. Martavicius, J. Skudutis, Hybrid Mode Dispersion Characteristic Dependencies of Cylindrical Dipolar Glass Waveguides on Temperatures, *Electronics and Electrical Engineering* 106: 83–86, 2010.

[10] L. Nickelson, A. Bubnelis, A. Baskys, R. Navickas, The magnetoactive *p*-Ge rod waveguide loss analysis on the concentration of two component hole charge carriers, *Electronics and Electrical Engineering* 110: 53–56, 2011.

[11] C. B. Schroeder, D. H. Whittum, J. S. Wurtele, Multimode Analysis of the Hollow Plasma Channel Wakefield Accelerator. Physical review letters 82: 1177-1180, 1999.

Couplonics Of Cyclic Ternary Systems: From Coupled Periodic Waveguides To Discrete Photonic Crystals

Yann G. Boucher[1,2]

[1] Université Européenne de Bretagne, ENIB, France
[2] CNRS, UMR 6082 FOTON, ENSSAT, 6 rue de Kerampont, BP 80518, F-22305 Lannion, France
E-mail: boucher@enib.fr

Abstract

In the context of coupled periodic waveguides, "couplonics" refers to the rigorous equivalence between continuous wave coupling and localized interactions. We extend it here to a cyclic ternary system, looked upon as the simplest discrete photonic crystal with actual periodic boundary conditions. A linear decomposition on a supermode basis enables one to reduce the original six-wave problem to three independent two-wave distributed Bragg reflectors (or 1D PC).

1. Introduction

Whatever the frequency range, a system made of coupled periodic waveguides (CPW) ensures simultaneously filtering and addressing functions. When dealing with CPW, "couplonics" [1-2] stems from the formal identification between the continuous configuration, represented by an invariant evolution operator, and the discrete one, seen as multiple-port networks interconnected by segments of transmission lines [3]. In a symmetric system limited to only two CPW, a linear decomposition on the even/odd eigenbasis (that of the "supermodes") enables one to express any scattering parameter as a linear superposition of S-parameters of the underlying even/odd two-port networks. On the other hand, for each supermode, the system can be thought of as an instance of Distributed Bragg Reflector (DBR), well described in terms of Coupled-Mode Theory (CMT) [4].

The ternary configuration is a bit more complicated. Even if the periodic waveguides are identical, the symmetries of the system depend on the distribution of the mutual coupling. In what follows, we consider a system made of three identical single-mode Λ-periodic waveguides, of propagation constant β along the z-axis, symmetrically coupled in a *cyclic* way [Fig. 1]. Such a configuration could be achieved, for instance, in a three-core optical fibre with a photo-induced index grating. For the sake of clarity, the unit cell of each waveguide is assumed symmetrical and lossless. Time dependence is taken as $\exp(+i\,\omega t)$.

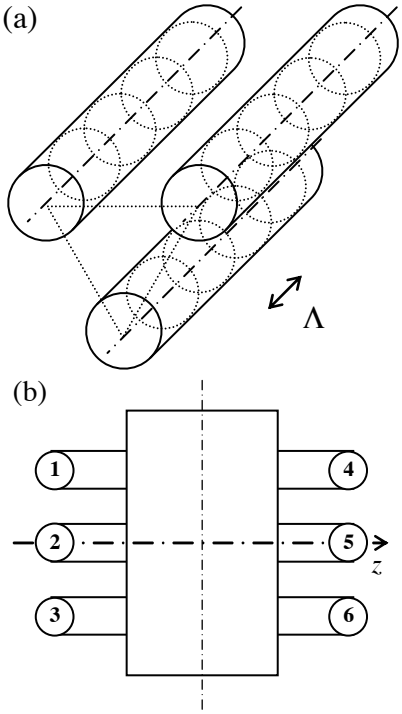

Figure 1: Cyclic ternary system made of single-mode Λ-periodic waveguides: (a) schematic representation; (b) unit cell seen as a symmetrical six-port network.

2. Evolution operator

2.1. Supermodes of the non-periodic structure

When only co-directional coupling occurs, with coupling constant χ (real and positive without loss of generality), slowly varying envelopes A_n of fields $F_n = A_n \exp(-i\,\beta z)$ should obey:

$$i\frac{\partial}{\partial z}\begin{pmatrix} A_1 \\ A_2 \\ A_3 \end{pmatrix} = [\mathrm{K}]\begin{pmatrix} A_1 \\ A_2 \\ A_3 \end{pmatrix} = \begin{pmatrix} 0 & \chi & \chi \\ \chi & 0 & \chi \\ \chi & \chi & 0 \end{pmatrix}\begin{pmatrix} A_1 \\ A_2 \\ A_3 \end{pmatrix}. \qquad (1)$$

Eigenvalues of operator [K] are $\lambda_a = +2\,\chi$, $\lambda_b = \lambda_c = -\chi$. We establish an orthogonal eigenmode basis such as:

$$\begin{pmatrix} A_1 \\ A_2 \\ A_3 \end{pmatrix} = [\mathrm{P}] \begin{pmatrix} A_a \\ A_b \\ A_c \end{pmatrix}, \qquad (2a)$$

$$[\mathrm{P}] = \frac{1}{\sqrt{6}} \begin{pmatrix} \sqrt{2} & -\sqrt{3} & 1 \\ \sqrt{2} & 0 & -2 \\ \sqrt{2} & \sqrt{3} & 1 \end{pmatrix}. \qquad (2b)$$

In that basis, the evolution operator is obviously diagonal. Note that in this cyclic case, the degeneracy is not completely lifted ($\lambda_b = \lambda_c$).

Matrix [P] is unitary. The inverse matrix reads:

$$[\mathrm{P}]^{-1} = \frac{1}{\sqrt{6}} \begin{pmatrix} \sqrt{2} & \sqrt{2} & \sqrt{2} \\ -\sqrt{3} & 0 & \sqrt{3} \\ 1 & -2 & 1 \end{pmatrix}. \qquad (2c)$$

2.2. Cyclic ternary periodic structure

The (6×6) evolution operator [K] connecting the envelopes (C_n^+, C_n^-) of co- and contra-propagating fields $F_n^+ = C_n^+ \exp(-i\,\beta_B\, z)$ and $F_n^- = C_n^- \exp(+i\,\beta_B\, z)$ reads:

$$i\frac{\partial}{\partial z} \begin{pmatrix} C_1^+ \\ C_1^- \\ C_2^+ \\ C_2^- \\ C_3^+ \\ C_3^- \end{pmatrix} = [\mathrm{K}] \begin{pmatrix} C_1^+ \\ C_1^- \\ C_2^+ \\ C_2^- \\ C_3^+ \\ C_3^- \end{pmatrix}, \qquad (3a)$$

with

$$[\mathrm{K}] = \begin{pmatrix} \delta & \kappa & \chi & \xi & \chi & \xi \\ -\kappa & -\delta & -\xi & -\chi & -\xi & -\chi \\ \chi & \xi & \delta & \kappa & \chi & \xi \\ -\xi & -\chi & -\kappa & -\delta & -\xi & -\chi \\ \chi & \xi & \chi & \xi & \delta & \kappa \\ -\xi & -\chi & -\xi & -\chi & -\kappa & -\delta \end{pmatrix} \qquad (3b)$$

where $\beta_B = \pi/\Lambda$ denotes the *Bragg wavevector*, $\delta = \beta - \beta_B$ the *detuning*, κ and ξ the (real positive) constants for *direct* and *crossed* contra-directional coupling.

A straightforward calculation shows that, in the eigenmode basis:

$$i\frac{\partial}{\partial z} \begin{pmatrix} C_x^+ \\ C_x^- \end{pmatrix} = \begin{pmatrix} \delta_x & \kappa_x \\ -\kappa_x & -\delta_x \end{pmatrix} \begin{pmatrix} C_x^+ \\ C_x^- \end{pmatrix}, \qquad (4a)$$

for $x \in \{a, b, c\}$, with

$$\delta_a = \delta + 2\,\chi, \quad \delta_b = \delta_c = \delta - \chi, \qquad (4b)$$

$$\kappa_a = \kappa + 2\,\xi, \quad \kappa_b = \kappa_c = \kappa - \xi. \qquad (4c)$$

We recognize the typical equation for contra-directional mode coupling in a Distributed Bragg Reflector (DBR), each "eigen-DBR" being characterized by a forbidden band of bandwidth $2\,\kappa_x$, centred on $\delta_x = 0$ [5]. This result can be thought of as a partial lift of degeneracy. Taken separately, each waveguide is characterised by a forbidden band of width $2\,\kappa$ centred on $\delta = 0$. In terms of supermodes, coupling constant χ is responsible for a shift of the band centres, whereas coupling constant ξ affects both the rejection rate and the bandwidth.

The transfer matrix [m_x] for a unit cell is such as:

$$\begin{pmatrix} C_x^+(0) \\ C_x^-(0) \end{pmatrix} = [\mathrm{m}_x] \begin{pmatrix} C_x^+(\Lambda) \\ C_x^-(\Lambda) \end{pmatrix}. \qquad (5a)$$

With $\gamma_x = [\,|\kappa_x|^2 - \delta_x^2\,]^{1/2}$, its elements are:

$$m_{x11} = -\left[\cosh(\gamma_x\Lambda) + i\left(\frac{\delta_x\Lambda}{\gamma_x\Lambda}\right)\sinh(\gamma_x\Lambda)\right], \qquad (5b)$$

$$m_{x12} = i\left(\frac{\kappa_x\Lambda}{\gamma_x\Lambda}\right)\sinh(\gamma_x\Lambda) = -m_{x21}, \qquad (5c)$$

$$m_{x22} = -\left[\cosh(\gamma_x\Lambda) - i\left(\frac{\delta_x\Lambda}{\gamma_x\Lambda}\right)\sinh(\gamma_x\Lambda)\right]. \qquad (5d)$$

For a structure made of N unit cells, the reflectance and transmittance read:

$$r_x = \frac{M_{x21}}{M_{x11}} = \frac{-i\,\kappa_x \sinh(\gamma_x L)}{\gamma_x \cosh(\gamma_x L) + i\,\delta_x \sinh(\gamma_x L)}, \qquad (6a)$$

$$t_x = \frac{(-1)^N\,\gamma_x}{\gamma_x \cosh(\gamma_x L) + i\,\delta_x \sinh(\gamma_x L)}, \qquad (6b)$$

with $L = N\,\Lambda$.

2.3. Scattering parameters

The system is therefore totally determined by four coefficients only:

$$r_a, \qquad r_b = r_c, \qquad (7a)$$

$$t_a, \qquad t_b = t_c. \qquad (7b)$$

It is not difficult to establish that:

$$S_{11} = S_{22} = S_{33} = (r_a + 2\,r_b)/3 = r_{//}, \qquad (8a)$$

$$S_{41} = S_{52} = S_{63} = (t_a + 2\,t_b)/3 = t_{//}, \qquad (8b)$$

$$S_{21} = S_{32} = S_{13} = (r_a - r_b)/3 = r_{\perp}, \qquad (8c)$$

$$S_{51} = S_{62} = S_{43} = (t_a - t_b)/3 = t_{\perp}. \qquad (8d)$$

The system is both *symmetrical* and *reciprocal*: $\forall\ (p, q)$, $S_{pq} = S_{qp}$. The *S*-parameters can take only one out of 4 values: direct transmission $t_{//}$ (S_{41} and the like), direct reflection $r_{//}$ (S_{pp}), crossed transmission $t_{\perp}$ (S_{51} and the like), crossed reflection $r_{\perp}$ (S_{21} and the like).

3. Discrete configuration

3.1. Transmittance and reflectance

Let us now consider the discrete configuration. The whole system is totally determined by four coefficients only: ($r_{//}$, $r_\perp$, $t_{//}$, $t_\perp$). Symmetries being the same as in the continuous case, eigenmodes of the former are also eigenmodes of the latter. We get:

$$r_a = r_{//} + 2\,r_\perp, \qquad r_b = r_c = r_{//} - r_\perp, \tag{9a}$$

$$t_a = t_{//} + 2\,t_\perp, \qquad t_b = t_c = t_{//} - t_\perp. \tag{9b}$$

Once again, the six-port network can be decomposed as a linear superposition of two-port networks.

3.2. Couplonic identification

For any eigenmode, the corresponding two-port network can always be expressed in terms of coupled-mode theory. This stems from the symmetry properties of the unitary transfer matrix of one unit cell, as elegantly established in 1997 by Matuschek *et al.* in the case of an arbitrary multilayer Distributed Bragg Reflector [6]. For a long time, it has been believed that CMT holds only in a perturbative way (for small index modulations), and only if the interaction length L is much greater than period Λ, but we would like to emphasise that, as shown in [6], the equivalence remains mathematically exact at the scale of Λ only, whatever the precise content of the unit cell.

This enables one to define without ambiguity, for any eigenmode $x \in \{a, b, c\}$, an equivalent coupling constant κ_x and an equivalent detuning δ_x.

Or, to be more specific, since we work at the scale of one unit cell, we can establish dimensionless parameters ($\kappa_a\Lambda$, $\delta_a\Lambda$) and ($\kappa_b\Lambda$, $\delta_b\Lambda$), which in turn lead to four dimensionless parameters ($\delta\Lambda$, $\kappa\Lambda$, $\chi\Lambda$, $\xi\Lambda$) that completely describe the whole system:

$$\delta\Lambda = \frac{\delta_a\Lambda + 2\delta_b\Lambda}{3}, \tag{10a}$$

$$\chi\Lambda = \frac{\delta_a\Lambda - \delta_b\Lambda}{3}, \tag{10b}$$

$$\kappa\Lambda = \frac{\kappa_a\Lambda + 2\kappa_b\Lambda}{3}, \tag{10c}$$

$$\xi\Lambda = \frac{\kappa_a\Lambda - \kappa_b\Lambda}{3}. \tag{10d}$$

We call *couplons* these parameters, which should be interpreted as *elementary quanta of detuning or coupling* that take place at the scale of one unit cell. As a matter of fact, as can be seen from Eqns.(5-6), the responses of the system made of N cells involves only multiple quantities such as $\delta L = N\,\delta\Lambda$, $\kappa L = N\,\kappa\Lambda$, $\chi L = N\,\chi\Lambda$, $\xi L = N\,\xi\Lambda$.

3.3. Normalised spectral responses

Whatever the configuration – continuous or discrete –, the spectral responses take the same form. For instance, we draw in Figure 2 the spectral transmittance of a cyclic ternary CPW system for $\kappa L = 2$, $\chi L = 1$, $\xi L = 0.25$, as compared to the spectral response of a single (uncoupled) periodic waveguide. The coupling is obviously responsible for a partial lift of degeneracy: taken separately, each periodic waveguide is characterised by a *forbidden band* centred on $\delta L = 0$, of bandwidth $2\,|\kappa L|$. In terms of supermodes, codirectional coupling constant χ is responsible for a shift of the stop-band, whereas crossed contradirectional coupling constant ξ modifies both its rejection rate and bandwidth.

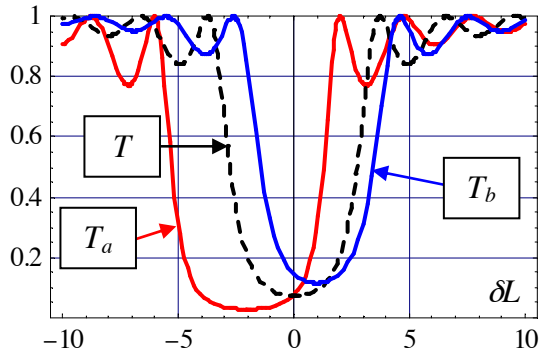

Figure 2: Normalised spectral transmittance T_a and T_b of the supermodes ($T_x = |t_x|^2$), as compared to transmittance T of a single (uncoupled) periodic waveguide ($\kappa L = 2$, $\chi L = 1$, $\xi L = 0.25$)

As a matter of fact, the maximum reflectance and minimum transmittance are given by [5]:

$$R_{x\max} = \tanh^2\left(|\kappa_x L|\right), \tag{11a}$$

$$T_{x\min} = 1 - \tanh^2\left(|\kappa_x L|\right). \tag{11b}$$

The reflectance is reported in Figure 3 for the same set of reduced parameters:

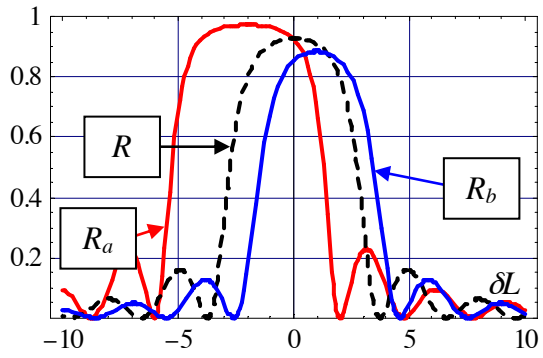

Figure 3: Normalised spectral reflectance R_a and R_b of the supermodes ($R_x = |r_x|^2$), as compared to transmittance R of a single (uncoupled) periodic waveguide ($\kappa L = 2$, $\chi L = 1$, $\xi L = 0.25$)

3.4. Universal Bragg reflector

The spectral response of a standard DBR is the key to that of the whole system, whatever the precise values of the "couplonic" parameters. Moreover, any actual lossless DBR can be reduced to one instance of a "universal" lossless Bragg reflector, as schematically depicted in Figure 4. As a matter of fact, only two parameters (κL, δL) govern its behaviour.

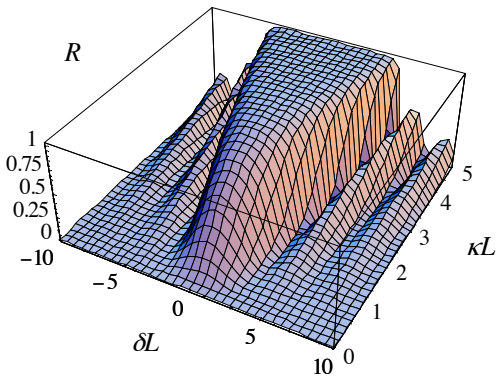

Figure 4: Normalised reflectance $R = |M_{21}/M_{11}|^2$ of a "universal" DBR.

Each spectrum of Figure 3 can be recovered by following a specific path over the universal relief of Figure 4. By an obvious topographic analogy [7], we can speak of "couplonic alpinism".

4. Conclusions

We have established analytically, in terms of reduced dimensionless parameters, the spectral responses of a cyclic ternary system made of symmetrically coupled periodic waveguides. In the supermode basis, the method stems from a rigorous mathematical identification between the continuous and discrete configurations.

Taking losses into account would not cause any special difficulty: it would be enough to add two new reduced parameters, corresponding respectively to average losses and to loss-modulation (loss coupling). Optical amplification would appear just as straightforward, the structure becoming a cyclic array of coupled Distributed Feedback (DFB) emitters [8].

The so-called "couplonic" approach is an elegant as well as powerful theoretical tool, not only for studying spectrally selective splitters, but also for the analysis or synthesis of discrete electromagnetic crystals of finite size [3]. Moreover, it comes well within the framework of current research on *discrete photonics* based on coupled waveguides [9-10].

5. Acknowledgements

The author would like to thank Nadia Belabas and her coworkers from Laboratoire de Photonique et de Nanostructures (LPN, CNRS UPR 20), Marcoussis, France, for inspiring discussions.

References

[1] Y.G. Boucher, Fundamentals of Couplonics, *Proc. SPIE Photonics Europe*, Strasbourg, France, Vol. 6182, 61821E, 2006.

[2] Y.G. Boucher, A.V. Lavrinenko, D.N. Chigrin, Out-of-phase Coupled Periodic Waveguides: a "couplonic" approach, *Optical Quantum Electron.*, Vol. 39, No. 10-11, 837-847, 2007.

[3] L. Le Floc'h, V. Quintard, J.-F. Favennec, Y. Boucher, Spectral Properties of a Periodic N×N Network of Interconnected Transmission Lines, *Microwave Optical Technol. Lett.*, Vol. 37, No. 4, 255-259, 2003.

[4] A.A. Barybin and V.A. Dmitriev, *Modern Electrodynamics and Coupled-Mode Theory: Application to Guided-Wave Optics*, Rinton Press, 2002.

[5] A. Yariv and P. Yeh, *Optical Waves in Crystals*, Wiley, New York, 1984.

[6] N. Matuschek, F.X. Kärtner, U.Keller, Exact Coupled-Mode Theories for Multilayer Interference Coatings with Arbitrary Strong Index Modulations, *IEEE J. Quantum Electron.*, Vol. 33 (3), 295-302, 1997.

[7] Y.G. Boucher, L. Le Floc'h, V. Quintard, J.-F. Favennec, "Canonical alpinism" and "canonical surf-riding": a universal tool for normalised parametric analysis of one-dimensional periodic structures, *Optical and Quantum Electronics*, Vol. 38 (1-3), 203-207, 2006.

[8] H. Kogelnik, C.V. Shank, Coupled-Wave Theory of Distributed Feedback Lasers, *J. Appl. Phys.*, Vol. 43, 2327-2335, 1972.

[9] N. Belabas, S. Bouchoule, I. Sagnes, J.A. Levenson, C. Minot, J.-M. Moison, Confining light flow in weakly coupled waveguide arrays by structuring the coupling constant: towards discrete diffractive optics, *Opt. Expr.*, Vol. 17 (5), 3148-3156, 2009.

[10] E. Feigenbaum, H.A. Atwater, Resonant Guided Wave Networks, *Phys. Rev. Lett.* Vol. 104, 147402, 2010.

Binary Programming Techniques for Linear Metamaterial Design Optimization

J. Saa-Seoane*, N.-C. Nguyen, H. Men, R. Freund, J. Peraire

Aerospace Computational Design Laboratory
Department of Aeronautics and Astronautics
and Sloan School of Management
Massachusetts Institute of Technology
*corresponding author, E-mail: jsaa@mit.edu

Abstract

The design of metamaterials is currently a fertile research domain. However, most of the metamaterial designs described in the literature arise from physical intuition, and often assume infinite periodicity. There is therefore a need for a design methodology capable of computing patterns and designs involving two different materials where the underlying design variables correspond to a finite set of pixels in a 2-dimensional mesh, and where the goal is a design with prescribed metamaterial properties. This naturally leads to the consideration of binary optimization models in contrast to classical (continuous) gradient-based methods which generically provide continuous solutions that then need to be "rounded" to binary values. While the potential drawback of binary optimization is that its computational complexity is usually NP-hard and hence theoretically unattractive, we show herein that binary optimization combined with a reduced basis approach can relatively efficiently produce very good solutions to metamaterial design problems of interest.

1. Introduction

Wave phenomena in acoustics, elastodynamics and electromagnetics have been widely studied in the last two decades. These phenomena have found numerous applications in many domains of engineering, and therefore accurate, efficient, and reliable numerical simulation is extremely important. For the problems in our scope of concern, a Finite Element Method is required since it provides geometric flexibility and well-known error bounds. In particular, the hybrid discontinuous Galerkin method, or just HDG, introduced in [**?**] for acoustics and elastodynamics as well as in [**?**] for Maxwell's equations and thus electromagnetics, has been proven to be a robust, accurate and efficient simulation tool for these sort of problems. Indeed, these methods were devised to guarantee that only the degrees of freedom of the approximation of the scalar variable on the interelement boundaries are globally coupled, see [**?**]. In addition to that, this method will provide particular properties that will become essential later on for the work presented in this paper.

The family of problems related to wave phenomena has lately increased due to the growing interest in metamaterial design. Metamaterials are materials that have very particular properties due only to their structure, not their composition. There is often a microscopic pattern of existing materials that, when extended periodically, will provide a particularly effective macroscopic property that is otherwise unobtainable. Potential applications of metamaterials in acoustics involve sound bullets and acoustic filters [**?**], negative Poisson's ratio materials in elastodynamics [**?**], and regarding electromagnetism, cloaking devices [**?**] and photonic bandgap phenomena [**?**] among others. Some of the examples above will be further analyzed in this paper as well as a similar extension to the heat equation.

The design of metamaterials usually is difficult because modeling and computing effective design patterns is fraught with computational challenges. Especially when trying to design manufacturable and realizable materials, physical and mathematical intuition are insufficient by themselves. One is therefore led to consider optimization-based approaches to design. However, the optimization problems that arise in metamaterial design are of discrete nature, leading to binary or mixed-integer optimization models that are theoretically hard problems. Indeed, in considering design variables that correspond to a finite set of pixels, the optimization problem is to choose between two given materials for each pixel, hence the typical application problem results in the need to solve a binary optimization model. Algorithms to solve binary optimization problems exactly are not efficient, i.e., they cannot be exactly solved in polynomial-time (with respect to the natural dimensions of the problem). In this paper we present a binary optimization model approach that combines local search approximation with a reduced basis approximation, that produces good local solutions with good relative efficiency. Our approach utilizes a reduced basis projected problem [**?**] and the use of binary generalized gradients to ensure feasibility of all solutions.

This paper will provide a capability for the simulation and design optimization of metamaterials. Section **??** explains the suitability of the HDG method used as well as derives the particular formulation for the Helmholtz equation case. Section **??** derives the reduced basis algorithm used for the binary optimization local search method that

is used for the design optimization. Results for the Poisson's equation as well as for the one dimensional bandgap problem are further analyzed in section **??**.

2. HDG method for Helmholtz equation

In this section we want to describe a Hybridizable Discontinuous Galerkin Method for a model Helmholtz equation. The extension of these results to the linear second order wave equation is trivial and can be found in [**?**]. Let us begin justifying the choice of this method for the simulations, which is actually a key point. Firstly, given the interest in high order methods, it is quite clear that a Finite Element Method -FEM- needs to be chosen. Furthermore, we need more geometric flexibility than the one offered by a Finite Differences or a Finite Volumes scheme. Nevertheless, classic continuous FEM would not work properly for the type of problems we are going to be dealing with due to the inherent discontinuities of the material and potential discontinuities of the solution. Therefore, Discontinuous Galerkin (DG) methods need to be considered. These methods have been proven to be quite successful for a variety hyperbolic problems, even nonlinear, but their extension to diffusion problems was criticized for providing suboptimal convergent approximations as well as producing a substantially larger amount of globally-coupled degrees of freedom. The HDG methods were introduced in [**?**] to address these issues.

In particular, the HDG methods provide a smaller global system of equations, especially for high orders of accuracy. The methods are highly parallelizable and superconvergence has also been proven [**?**, **?**]. On top of that, section **??** shows how the actual definition of the HDG method will allow the design parameters to be pulled out linearly for every single element of the discretization. Since the material properties are variables in metamaterial design problems, such capability allows for an overall crucial speed up when solving the system of equations as well as a dramatic reduction on the memory needed. All these reasons make the HDG method not only the most suitable but also unique for the metamaterial simulations that we are about to carry out.

2.1. HDG derivation

In this section we want to show how the hybridizable Discontinuous Galerkin method applies to a model Helmholtz equation. The extension from these derivations to a different domain or to Poisson's equation will be later discussed. To that end, let us firstly consider the Helmholtz problem as follows:

$$\begin{aligned} -\nabla\cdot\varepsilon\nabla u - k^2 u &= f \quad \text{in } \Omega\subset\mathbb{R}^d \\ \varepsilon\nabla u\cdot\vec{n} + iku &= g \quad \text{on } \partial\Omega_a \end{aligned} \tag{1}$$

where u is a scalar variable, ε is the square of the propagation speed, k is the wavenumber, f is a given source term and g determines the absorbing boundary condition. Moreover, Ω is a Lipschitz polyhedral domain in $\mathbb{R}^{d\geq 1}$. Note that the boundary condition considered in the description is first-order absorbing and it is taken solely for the purposes of illustration. Such boundary condition could be easily replaced by higher-order local or exact global conditions as well as by suitable perfectly matched layers.

The HDG method firstly writes the partial differential equation (PDE) as a first-order system of partial differential equations and thus, after introducing the gradient as $\mathbf{q} = \nabla u$ for convenience, the following system can be written:

$$\begin{aligned} \mathbf{q} - \nabla u &= 0 \quad \text{in } \Omega \\ -\nabla\cdot\varepsilon\mathbf{q} - k^2 u &= f \quad \text{in } \Omega \\ \varepsilon\mathbf{q}\cdot\mathbf{n} + iku &= g \quad \text{on } \partial\Omega_a \end{aligned} \tag{2}$$

Later on and for convenience, the term iku will be pushed into the righthandside modifying f and becoming a function of u. The second equation will therefore become $-\nabla\cdot\varepsilon\mathbf{q} = f_u$, where $f_u = f - iku$.

Let $\mathcal{T}_h$ form a triangulation of the domain Ω into elements K and $\partial\mathcal{T}_h = \{\partial K, K\in\mathcal{T}_h\}$ be the set of faces F of each element K of the triangulation, also known as $\mathcal{F}_h$. Then the method seeks a scalar approximation u_h to u, a vector approximation $\mathbf{q}_h$ to $\mathbf{q}$ and a scalar approximation $\hat{u}_h$ to the traces $\hat{u}_h$ minimizing the representation error in -or distance to- some approximation spaces defined as:

$$\begin{aligned} W_h &= \{w\in L^2(\mathcal{T}_h), w|_K \in W(K), \forall K\in\mathcal{T}_h\} \\ \mathbf{V}_h &= \{\mathbf{v}\in [L^2(\mathcal{T}_h)]^d, \mathbf{v}|_K \in \mathbf{V}(K), \forall K\in\mathcal{T}_h\} \\ M_h &= \{\mu\in L^2(\mathcal{F}_h), \mu|_F \in M(F), \forall F\in\mathcal{F}_h\} \end{aligned} \tag{3}$$

where $W(K)$, $\mathbf{V}(K)$ and $M(F)$ are suitably chosen finite dimensional spaces. Furthermore, let us define the contractions involved within this HDG method. For functions $\mathbf{v},\mathbf{w}\in[L^2(D)]^d$ we denote $(\mathbf{v},\mathbf{w})_D = \int_D \mathbf{v}\cdot\overline{\mathbf{w}}$; for functions $v,w\in L^2(D)$ we write $(v,w)_D = \int_D v\overline{w}$ if D is a domain in $\mathbb{R}^d$ and $\langle v,w\rangle_D = \int_D v\overline{w}$ if D is a domain in $\mathbb{R}^{d-1}$. We finally introduce

$$\begin{aligned} (v,w)_{\mathcal{T}_h} &= \sum_{K\in\mathcal{T}_h} (v,w)_K \\ (\mu,\eta)_{\partial\mathcal{T}_h} &= \sum_{K\in\mathcal{T}_h} (\mu,\eta)_{\partial K} \end{aligned} \tag{4}$$

for v,w defined in $\mathcal{T}_h$ and μ,η defined on $\partial\mathcal{T}_h$ respectively. The HDG approximations $u_h\in W_h$, $\mathbf{q}_h\in\mathbf{V}_h$ and $\widehat{u}_h\in M_h$ are now determined by requiring that the following finite discrete system of equations holds $\forall(s,\mathbf{r},\mu)\in W_h\times\mathbf{V}_h\times M_h$.

$$\begin{aligned} (\mathbf{q}_h,\mathbf{r})_{\mathcal{T}_h} + (u_h,\nabla\cdot\mathbf{r})_{\mathcal{T}_h} - \langle\widehat{u}_h,\mathbf{r}\cdot\mathbf{n}\rangle_{\partial\mathcal{T}_h} &= 0, \\ (\varepsilon\mathbf{q}_h,\nabla w)_{\mathcal{T}_h} - \langle\widehat{\varepsilon\mathbf{q}}_h\cdot\mathbf{n}, w\rangle_{\partial\mathcal{T}_h} - k^2(u_h,w)_{\mathcal{T}_h} &= (f,w)_{\mathcal{T}_h}, \\ -\langle\widehat{\varepsilon\mathbf{q}}_h\cdot\mathbf{n},\mu\rangle_{\partial\mathcal{T}_h\setminus\partial\Omega_a} + \langle\widehat{\varepsilon\mathbf{q}}_h\cdot\mathbf{n} + ik\widehat{u}_h,\mu\rangle_{\partial\Omega_a} &= \langle g,\mu\rangle_{\partial\Omega}. \end{aligned} \tag{5}$$

Note that the HDG method uses the extra stabilization condition for the flux traces through the definition of the numerical fluxes as

$$\widehat{\varepsilon\mathbf{q}}_h = \varepsilon\mathbf{q}_h + \tau(u_h - \widehat{u}_h)\mathbf{n} \tag{6}$$

on $\partial\mathcal{T}_h$. Here, τ is the so-called *stabilization* function. The actual definition of the numerical traces $\widehat{\mathbf{q}}_h$ is the key feature of the HDG method. The last equation in (**??**), which is defined over the degrees of freedom on the edges, can be solved for $\widehat{u}_h$ in a global sense and, after that, the rest of the equations will locally recover u_h and $\mathbf{q}_h$. Such local systems of equations can be totally parallelized and thus solved very efficiently for the degrees of freedom inside each element. Moreover, it has been shown in [**?**] that this Helmholtz problem actually achieves an optimal superconvergence order for both u_h and $\mathbf{q}_h$ after a postprocessing of the solution.

2.2. Implementation

Let us first of all define as U the variables related to the displacement u_h of the degrees of freedom inside each element, Q the variables related to their fluxes $\mathbf{q}_h$ and Λ the variables related to the traces $\widehat{u}_h$ for every degree of freedom along the edges of the triangulation. Now if equation (**??**) is plugged into the system of equations (**??**) we eliminate the $\widehat{\mathbf{q}}_h$ variables and thus the following system of equations is obtained.

$$\begin{aligned}(\mathbf{q}_h,\mathbf{r})_{\mathcal{T}_h}+(u_h,\nabla\cdot\mathbf{r})_{\mathcal{T}_h}-\langle\widehat{u}_h,\mathbf{r}\cdot\mathbf{n}\rangle_{\partial\mathcal{T}_h}=&\\ 0,&\\ -(\varepsilon\nabla\cdot\mathbf{q}_h,w)_{\mathcal{T}_h}-\tau\langle(u_h-\widehat{u}_h),w\rangle_{\partial\mathcal{T}_h}-&\\ k^2(u_h,w)_{\mathcal{T}_h}=&\\ (f,w)_{\mathcal{T}_h},&\\ -\langle\varepsilon\mathbf{q}_h\cdot\mathbf{n}-\tau(u_h-\widehat{u}_h),\mu\rangle_{\partial\mathcal{T}_h\setminus\partial\Omega_a}+&\\ \langle\varepsilon\mathbf{q}_h\cdot\mathbf{n}-\tau u_h-(\tau+ik)\widehat{u}_h,\mu\rangle_{\partial\Omega_a}=&\\ \langle g,\mu\rangle_{\partial\Omega}.&\end{aligned} \tag{7}$$

Now this system of equations gives rise to a matrix equation that can be written as follows:

$$\begin{bmatrix}\mathbb{A}&-\mathbb{B}^t&-\mathbb{C}^t\\ \mathbb{B}(\varepsilon)&\mathbb{D}^t&\mathbb{E}^t\\ \mathbb{C}(\varepsilon)&\mathbb{E}&\mathbb{M}\end{bmatrix}\begin{bmatrix}Q\\U\\\Lambda\end{bmatrix}=\begin{bmatrix}0\\F\\G\end{bmatrix} \tag{8}$$

where the submatrices $\mathbb{A},\mathbb{B},\mathbb{C},\mathbb{D},\mathbb{E}$ and $\mathbb{M}$ correspond to the discretization of the dot products above. One very interesting property of the HDG method shows up at this point: the matrices $\mathbb{A},\mathbb{B},\mathbb{C}$ and $\mathbb{D}$ are block diagonal, i.e. they are very sparse and every single element only contributes with nonzero entries to the degrees of freedom of that element. This fact will actually allow us to write equation (**??**) as a system of equations for Λ and then back solve for the inner element degrees of freedom, through the Schur complement. Moreover, there is another key property at this point: ε can be pulled out from the terms where it shows up. We will therefore be able to write the system (**??**) as follows:

$$\left(\mathbb{K}_0+\sum_{q=1}^{N_{el}}\varepsilon^q\mathbb{K}_q\right)\mathbf{u}=\mathbf{f} \tag{9}$$

for N_{el} number of elements. After writing Q from the first row in equation (**??**) as $Q=\mathbb{A}^{-1}(\mathbb{B}^tU+\mathbb{C}^t\Lambda)$ and considering $\mathbf{u}=[U\ \Lambda]^t$ and $\mathbf{f}=[F\ G]^t$ equation (**??**) holds for the following values of the matrices $\mathbb{K}_q,\forall q=0..N_{el}$.

$$\begin{aligned}\mathbb{K}_0&=\begin{bmatrix}\mathbb{D}&\mathbb{E}^t\\ \mathbb{E}&\mathbb{M}\end{bmatrix},\\ \mathbb{K}_q&=\begin{bmatrix}\mathbb{B}\mathbb{A}^{-1}\mathbb{B}^t&\mathbb{B}\mathbb{A}^{-1}\mathbb{C}^t\\ \mathbb{C}\mathbb{A}^{-1}\mathbb{B}^t&\mathbb{C}\mathbb{A}^{-1}\mathbb{C}^t\end{bmatrix},\forall q=1..N_{el}.\end{aligned} \tag{10}$$

Moreover, note how the terms $\mathbb{D}$ and $\mathbb{B}\mathbb{A}^{-1}\mathbb{B}^t$ are block diagonal (since both $\mathbb{A}$ and $\mathbb{B}$ are) and thus the system in (**??**) can be efficiently solved as any HDG method, i.e. solve only for the unknowns on the edges.

Being able to pull out ε elementwise will actually be the key feature for this method. We will no longer need to compute and store the HDG system matrices for every single pattern distribution but only once and store the elemental matrices. To solve for a particular distribution of material we will just need to assemble and solve the precomputed elemental matrices.

2.3. First-order absorbing boundary conditions

The first order absorbing boundary conditions have been introduced in [**?**] for the time dependent wave equation as

$$\frac{\partial u}{\partial t}+\nabla u\cdot\mathbf{n}=0. \tag{11}$$

Here, we are dealing with the Helmholtz equation which is the steady version of the second order time dependent wave equation derived through separation of variables. If we thus assume $u(x,t)=u(x)e^{i\omega t}$ and plug it in equation (**??**) we obtain the following expression:

$$\nabla u(x)\cdot\mathbf{n}=-i\omega u(x) \tag{12}$$

Furthermore, we are actually interested in applying the absorbing boundary conditions to the scattered field instead of the total field. We can thus write $u^s=u-u^0$, where u^s represents the scattered field, u the total solution and u^0 the original solution, i.e. initial condition in the time dependent problem. If we finally write (**??**) in terms of the scattered field we obtain the following expression:

$$\begin{aligned}\nabla u^s\cdot\mathbf{n}&=-i\omega u^s\\ &\Updownarrow\\ \nabla u\cdot\mathbf{n}&=-i\omega u+\nabla u^0\cdot\mathbf{n}+i\omega u^0\end{aligned} \tag{13}$$

yet to be applied to each of the boundaries in the actual domain Ω. Moreover, if there are extra boundary conditions which are Neumann we can just use $\nabla\cdot\mathbf{u}=h$ and proceed identically for any h; if there are any Dirichlet boundary conditions we may just change the approximation spaces introduced above to fit the values on such boundaries.

3. Binary Optimization

For a given wave phenomenon problem, let us consider $\boldsymbol{\varepsilon}$ to be the property defining each material. Since the problem will be governed by a Partial Differential Equation of the

form $F(\mathbf{u}(\boldsymbol{\varepsilon}), \boldsymbol{\varepsilon}) = 0$, the discretized PDE (with N_{el} discretized elements) can be expressed as a system of the form $A(\boldsymbol{\varepsilon})\mathbf{u} = \mathbf{f}$ in the linear case. Moreover, using the HDG discretization introduced in section **??**, the system matrix can be written as $A(\boldsymbol{\varepsilon}) = \mathbb{K}_0 + \sum_{q=1}^{N_{el}} \varepsilon^q \mathbb{K}_q$ as in equation (**??**). Let $J(\mathbf{u}(\boldsymbol{\varepsilon}), \boldsymbol{\varepsilon})$ be the objective function measuring the deviation to a desired and known solution −often just $J(\mathbf{u}(\boldsymbol{\varepsilon}), \boldsymbol{\varepsilon}) = ||\mathbf{u}(\boldsymbol{\varepsilon}) - \mathbf{u_0}||_2^2$ and denoted by $J(\mathbf{u}(\boldsymbol{\varepsilon}))$−, then the metamaterial design optimization problem can be written in the following general form:

$$\begin{aligned} \min_{\boldsymbol{\varepsilon}, \mathbf{u}} \quad & J(\mathbf{u}(\boldsymbol{\varepsilon}), \boldsymbol{\varepsilon}) \\ \text{s.t.} \quad & \left(\tau \mathbb{K}_0 + \sum_{q=1}^{N_{el}} \varepsilon^q \mathbb{K}_q\right) \mathbf{u} = \mathbf{f} \\ & \boldsymbol{\varepsilon} \in \{\varepsilon_{min}, \varepsilon_{max}\}^{N_{el}} \end{aligned} \tag{14}$$

Problem (**??**) arises in many areas of applied engineering such as inverse problems, shape optimization, topology optimization, optimal design and optimal control. However, the PDE constraints and the nature of the design variables often pose several significant challenges for contemporary optimization methods. First, the problem is in general nonlinear and non-convex due to an implicit dependence of the objective function on the design variables through the underlying PDEs. Second, the problem is large-scale since the discretization of the PDEs leads to a very large system of equations. And third, if some (or all) design variables can only take on integer or discrete values then problem (**??**) becomes a mixed-integer nonlinear optimization problem. Unfortunately, while discrete variables are common in practice, their presence causes the optimization problem to be NP-hard in general. It is therefore necessary to develop a suitable approximation of the problem in order to achieve computational tractability in practice.

In developing an approximation to the problem (**??**), we want to be able to efficiently compute the true objective function value. That is, for a given value of the design variables $\boldsymbol{\varepsilon}$, we want to compute $\mathbf{u}(\boldsymbol{\varepsilon})$ inexpensively and then compute $J(\mathbf{u})$. To that end, we will solve the PDE through a reduced basis approach. Subsection **??** derives the particular optimization problem after the reduced basis procedure is applied.

Also in the context of developing an approximation to the problem (**??**), in order to solve the optimization problem stated in (**??**) assuming we can now efficiently compute the objective function value, we still need to devise an optimization method that ensures the binary constraints $\boldsymbol{\varepsilon} \in \{\varepsilon_{\min}\varepsilon_{\max}\}^{N_{el}}$ are satisfied. To that end we introduce the binary gradients in Subsection **??**.

3.1. Reduced Basis

The reduced basis method (RB) method can be used to provide an accurate, reliable and efficient solution of parametrized PDEs, see [**?**, **?**] and further references therein. Material design or optimal control problems involve large numbers of parameters, and thus computing sensitivities or just solutions for the entire family of parameters is seldom achievable.

Let $n \leq N_{el}$ be the number of regions where a material parameter needs to be chosen and $k < n$ be a certain positive integer corresponding to the reduced basis size. For a given feasible pattern $\boldsymbol{\varepsilon} \in \{\varepsilon_{\min}, \varepsilon_{\max}\}^n$, let $\overline{\mathbf{u}}_1 = \mathbf{u}(\boldsymbol{\varepsilon})$, and define $k-1$ neighbors by just perturbing a small number of pixels from either $\varepsilon_{\min}$ to $\varepsilon_{\max}$ or *vice versa*, and then computing their corresponding solutions $\overline{\mathbf{u}}_j = \mathbf{u}(\boldsymbol{\varepsilon}^j)$ for $j = 2, \ldots, k$. We now define the reduced basis as $\overline{\Phi} = span[\overline{\mathbf{u}}_1, \overline{\mathbf{u}}_2, \ldots, \overline{\mathbf{u}}_k] \in \mathbb{R}^{N_{el} \times k}$, and we can then define an approximate version of any given $\mathbf{u}(\boldsymbol{\varepsilon})$ as $\tilde{\mathbf{u}}(\boldsymbol{\varepsilon}) = \sum_{j=1}^{k} \alpha_j(\boldsymbol{\varepsilon})\overline{\mathbf{u}}^k = \overline{\Phi}\boldsymbol{\alpha}(\boldsymbol{\varepsilon})$. Note that now the discretized system can be approximately solved as $\overline{\Phi}^t A(\boldsymbol{\varepsilon})\overline{\Phi}\boldsymbol{\alpha}(\boldsymbol{\varepsilon}) = \overline{\Phi}^t \mathbf{f}$. Finally, if we define $\tilde{A}^q = \overline{\Phi}^t A^q \overline{\Phi} \in \mathbb{R}^{k \times k}$, for $1 \leq q \leq n$ and also $\tilde{\mathbf{f}} = \overline{\Phi}^t \mathbf{f} \in \mathbb{R}^k$, we will be able to solve the governing system as:

$$\left(\sum_{q=1}^{n} \tilde{A}^q(\boldsymbol{\varepsilon})\right) \boldsymbol{\alpha}(\boldsymbol{\varepsilon}) = \tilde{\mathbf{f}} \tag{15}$$

which is a $k \times k$ system in contrast to the original $N_{el} \times N_{el}$ system. We then recover $\tilde{\mathbf{u}}(\boldsymbol{\varepsilon}) = \overline{\Phi}\boldsymbol{\alpha}(\boldsymbol{\varepsilon})$. Note, furthermore, that $\tilde{A}^q(\boldsymbol{\varepsilon})$ can be derived from A^q as in (**??**) and therefore still retains the property of being able to work with $\boldsymbol{\varepsilon}$ as needed.

3.2. Binary Gradient

Since we want to maintain binary solutions throughout the optimization process, we will only allow directional changes that leave a current pixel as is, or that flips $\varepsilon_{\min}$ to $\varepsilon_{\max}$ or *vice versa*. This can be done by defining the sensitivities of our objective function according to unitary changes instead of differential changes. To accomplish this we introduce the following binary generalized gradient:

$$G_m(\boldsymbol{\varepsilon}) = \frac{\Delta J(\mathbf{u}(\boldsymbol{\varepsilon}))}{\Delta \varepsilon} = \frac{J(\mathbf{u}(\boldsymbol{\chi}^m)) - J(\mathbf{u}(\boldsymbol{\varepsilon}))}{\varepsilon_{\max} - \varepsilon_{\min}}, \tag{16}$$

for $m = 1, \ldots, N_{el}$, where $\boldsymbol{\chi}^m$ just changes the m^{th} component of $\boldsymbol{\varepsilon}$ from $\varepsilon_{\min}$ to $\varepsilon_{\max}$ or *vice versa*. We then choose the descent direction that provides the smallest value of $G_m(\boldsymbol{\varepsilon})$ and advance in that descent direction iteratively, as in any steepest descent algorithm for continuous optimization.

3.3. Optimization Algorithm

Table **??** summarizes the optimization algorithm based on the ideas described above. Let $l \leq k$ be the size of the initial basis computed around an initial guess $\boldsymbol{\varepsilon}(0)$ and let the subindex of $\boldsymbol{\varepsilon}$ denote the vector position in the basis Φ.

Note that this algorithm is actually a local search approach to the binary optimization problem (**??**). The complexity of binary optimization problems is NP-hard, which implies that whenever the variable set is large, the problem is generically intractable. In our case, the parameter space

Table 1: Binary Optimization algorithm

1-	Start with an initial guess $\boldsymbol{\varepsilon}(0)$,
2-	Obtain the objective function value $J(\mathbf{u}(\boldsymbol{\varepsilon}(0)))$,
3-	Compute the solutions $\mathbf{u}_1 \cdots \mathbf{u}_l$ for $\boldsymbol{\varepsilon}_1 \cdots \boldsymbol{\varepsilon}_l$ exactly,
4-	Form $\Phi(\boldsymbol{\varepsilon}(0)) = [\mathbf{u}(\boldsymbol{\varepsilon}_1) \cdots \mathbf{u}(\boldsymbol{\varepsilon}_l))]$,
5-	Compute binary sensitivities G_m using (**??**) and (**??**),
6-	If $G_m \geq 0, \forall m$, end. Else, pick $\bar{m} = \arg\min_m G_m$ and set $\boldsymbol{\varepsilon}(0) \leftarrow \boldsymbol{\chi}^{\bar{m}}$,
7-	Compute l_0 random neighbors and update $\Phi(\boldsymbol{\varepsilon}(0)) \leftarrow [\Phi(\boldsymbol{\varepsilon}(0)) \; \mathbf{u}(\boldsymbol{\varepsilon}_1) \cdots \mathbf{u}(\boldsymbol{\varepsilon}_{l_0}))]$,
8-	If $size\{\Phi(\boldsymbol{\varepsilon}(0))\} = p > k$, remove the $p - k$ elements m with smallest values of $\alpha_m(\boldsymbol{\varepsilon}(0))$ in (**??**),
9-	Go to 2,

is very large, typically on the order of $\mathcal{O}(10^{2d})$ where d is the spatial dimension considered. Local search algorithms are a good approach to solve these problems. However, they are only able to guarantee local minima and the quality of the computed local minima really depends on the quality of the neighborhoods considered (often only very large neighborhoods work well). Metamaterial design optimization is yet harder, since unless the local search neighborhoods are very small, the computational burden of the local search methodology itself is excessive. By joining together the HDG properties and the reduced basis theory, we seek a balance wherein the approximate local search algorithm will find local optima of good quality with relatively good computation time. Several starting guesses, as well as further clever enhancements - like letting the solution worsen slightly to avoid getting stuck at a bad local optima - might be required for some applications.

4. Results

We have successfully applied the methodology described herein to one-dimensional photonic bandgap problems. In particular, we have succeeded in designing a binary material that is able to totally reflect a given frequency considering the finiteness of the domain. This phenomena is well-known if the pattern is considered periodic and therefore infinite (and hence is not realizable) but is not so well-known for finite structures. Section **??** below analyzes this problem, comparing the binary solution computed herein with the continuous optimum. In Section **??**, we apply the same optimization procedure to a 2-dimensional problem governed by the heat transfer equation.

4.1. The 1-dimensional Bandgap problem

Photonic crystals are periodic structures created from the arrangement of low and high index materials. They are designed to affect the motion of light by prohibiting the propagation of electromagnetic waves in all directions within certain frequency ranges. They have been of crucial use for the design of important novel devices and applications such as frequency filters, waveguides, switches and optical buffers, see for instance [**?**]. However, the results reported in a large fraction of the literature so far have been obtained without imposing integer constraints on the design variables.

Luckily, in the photonic bandgap problem, optimal solutions assuming infinite periodicity turn out to be binary, as observed by Lord Rayleigh as early as 1888, [**?**]. Nevertheless, if we are interested in extending the conceptual ideas introduced by the photonic bandgap to other wave phenomena, we need to mitigate the non-binary nature of the continuously relaxed optimal solution. Consequently, if we want to obtain satisfactory solutions −most notably fabricability−, we must effectively constrain solutions to be binary.

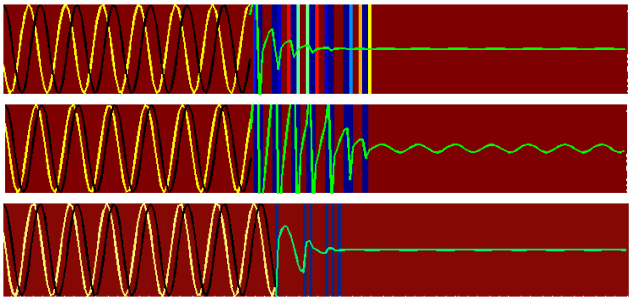

Figure 1: 1-dimensional Photonic Bandgap with yellow incident wave, black reflected wave and green transmitted wave. Top: continuous optimum; Middle: Discrete projection; Bottom: binary optimum.

Figure **??** shows the 1d photonic bandgap application. The governing equation for the frequency domain problem is exactly the Helmholtz equation analyzed in the first section where $\boldsymbol{\varepsilon}$ is the permittivity of the material. The incident frequency corresponds to $\omega \simeq 0.33$ after it has been normalized over the geometry. Here the photonic crystal is made up of two different materials: air ($\varepsilon = 1$, color coded as dark red) and silicon ($\varepsilon = 13$, color coded as blue).

Figure **??** shows the optimized structures obtained with (Top) the standard adjoint method with relaxation of the integer constraints, see [**?**] for the full derivations regarding the adjoint method for this particular example, (Middle) the adjoint method with enforcement of the integer constraints via projection into the closest binary value, and (Bottom) our proposed method. Our method produces exactly (up to machine precision error) an optimal binary solution within only six iterations, whereas the standard adjoint method computes an optimal solution which is not binary (and thus not fabricable nor acceptable) and the projected adjoint method produces a binary solution which is not optimal (and thus an inferior design).

This computational result is especially encouraging since the basis need not contain more than 10 solution vectors to guarantee a very good approximation of the exact solutions and therefore the systems of equations (**??**) used to compute the binary gradient never exceeded a 10×10 system. Furthermore the binary gradient computation (**??**) which is of order $\mathcal{O}(n)$ (recall n is the number of pixels

or more generally the parameter space size) took less time than one single HDG computation takes. It is also encouraging that the binary gradient computations are extremely accurate, with errors of $\mathcal{O}(10^{-8})$.

4.2. Poisson's Equation

In a similar setting but in a 2-dimensional context we consider the heat transfer problem. For this problem the governing equation will be the Poisson equation instead of Helmholtz equation, however, we can just adapt our derivations in the first section by removing the term $-k^2u$ that was actually included in the source term f_u for this purpose. The problem we want to solve now will be governed by the following partial differential equation:

$$\begin{aligned} -\nabla \cdot \varepsilon \nabla u &= f \quad \text{in } \Omega = [0,1]^2 \\ u &= 0 \quad \text{on } \partial\Omega \end{aligned} \tag{17}$$

where the source term has been chosen to be $f = 2\pi^2 \sin(\pi x)\sin(\pi y)$. We seek a 2-dimensional pattern maximizing the heat transferred from the Dirichlet boundaries of a square plate into the center point. Note that if we do not include an extra volume constraint, the optimum will be obtained when the material used everywhere corresponds to the one holding a larger thermal conductivity. Therefore the overall setting of the optimization problem for this case will be slightly modified by the volume constraint. If we choose $0 \leq \beta \leq 1$ as the volume fraction that we are allowed to change, the problem can be written as:

$$\begin{aligned} \min_{\boldsymbol{\varepsilon},\mathbf{u}} \quad & J(\mathbf{u}(\boldsymbol{\varepsilon}),\boldsymbol{\varepsilon}) \\ \text{s.t.} \quad & \left(\tau\mathbb{K}_0 + \sum_{q=1}^{N_{el}} \varepsilon^q \mathbb{K}_q\right)\mathbf{u} = \mathbf{f} \\ & \frac{1}{N_{el}} \sum_{q=1}^{N_{el}} \frac{\varepsilon^q - \varepsilon_{\min}}{\varepsilon_{\max} - \varepsilon_{\min}} \leq \beta \\ & \boldsymbol{\varepsilon} \in \{\varepsilon_{min}, \varepsilon_{max}\}^n \end{aligned} \tag{18}$$

A square domain with a 20 by 20 parametric grid has been considered with $\varepsilon_{\min} = 1$ and $\varepsilon_{\max} = 2$. Firstly, the problem has been solved considering the continuous relaxation $\boldsymbol{\varepsilon} \in [\varepsilon_{\min}, \varepsilon_{\max}]^{N_{el}}$ through the Adjoint method. In a very similar way to the bandgap problem and analogously derived to that case as in [**?**], the Adjoint method provides us with the sensitivities or gradient and thus the direction to take at each iterate. We can then pick a small enough step size, take the step, and iterate until we reach the final optimal and feasible solution determined by the volume constraint. Such a constraint can also be dualized into the objective function and one can instead solve the new optimization problem with the modified objective:

$$J(\mathbf{u}(\boldsymbol{\varepsilon}),\boldsymbol{\varepsilon}) = ||\mathbf{u}(\boldsymbol{\varepsilon})||_2^2 + \lambda\left(\sum_{q=1}^{N_{el}} \frac{\varepsilon^q - \varepsilon_{\min}}{\varepsilon_{\max} - \varepsilon_{\min}} - \beta N_{el}\right) \tag{19}$$

and the original set of constraints. Both strategies lead to the same solutions.

Note that for the homogeneous case with $\boldsymbol{\varepsilon} = \mathbf{1}$ the analytical solution $\mathbf{u} = \sin(\pi x)\sin(\pi y)$ to (**??**) provides a squared volume of $J(\mathbf{u}(\mathbf{1})) = 0.5$, whereas if we pick the homogeneous material with $\boldsymbol{\varepsilon} = 2$ the objective drops down to the value $J(\mathbf{u}(\mathbf{2})) = 0.0625$, which would be the optimal solution had not we considered the volume constraints.

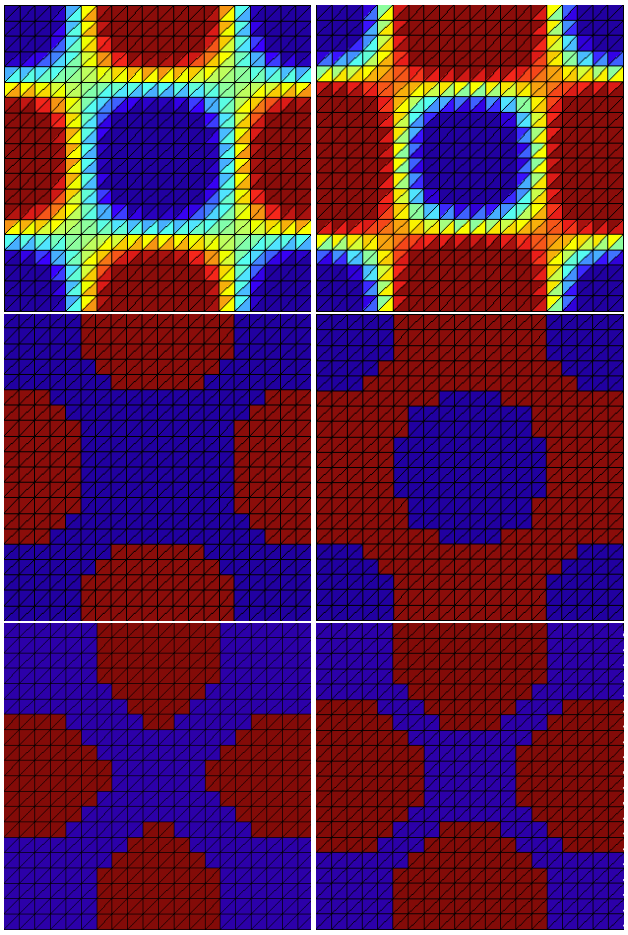

Figure 2: 2-dimensional heat transfer problem. Left figures correspond to $\beta = 0.44$ and right figures to $\beta = 0.58$. Top figures show the continuous solutions obtained through the Adjoint method, middle figures the projected binary solutions and bottom the the binary solutions after using our proposed method.

Results have been computed for $\beta = 0.44$ and $\beta = 0.58$ and are shown in Figure **??**. We can observe how the continuous optimal solutions provide a non-binary solution that after projection into $\boldsymbol{\varepsilon} = \{1,2\}^{N_{el}}$ and respecting the volume constraint, the resulting solution is suboptimal. In fact, for the case $\beta = 0.44$ the optimal objective value is $J(\mathbf{u}(\boldsymbol{\varepsilon}_{cont})) = ||\mathbf{u}||_2^2 = 0.0973$ in the continuous case, and once projected it increases to $J(\mathbf{u}(\varepsilon_{proj})) = 0.1020$. We can do better, as our binary optimum demonstrates, obtaining $J(\mathbf{u}(\boldsymbol{\varepsilon}_{bin})) = 0.0991$. Table **??** summarizes the different values obtained for each case.

Note how the binary optimum is more than 2.5 times closer to the continuous optima than the projected naive solution for $\beta = 0.44$ and more than 5.5 times closer for

Table 2: Results for the Heat transfer problem

β	J_{cont}	J_{proj}	J_{bin}
0%	0.5	0.5	0.5
44%	0.0973	0.1020	0.0991
58%	0.0825	0.0875	0.0834
100%	0.0625	0.0625	0.0625

$\beta = 0.58$. With a given material allowance we have thus been able to provide a binary pattern, easily fabricable, which is very close to the non-fabricable continuous optimum for the same volume of material.

5. Conclusions

The Adjoint method leads to continuous optimal solutions that provide an objective function value J_{cont} that is less than or equal to the value J_{bin}, where J_{cont} and J_{bin} denote the optimal objective values for the continuous relaxation of the problem and our binary optimization method, respectively. Clearly the binary solution is feasible to the continuously relaxed problem and therefore the inequality above follows. However, continuous solutions are not binary and thus not fabricable and hence not practical. If we just project the continuous solution we may easily produce inferior solutions, unless the continuous optimum is very robust. Both examples analyzed in this paper show that the projected binary optimum is indeed inferior in practice. Our proposed method is thus able to compute efficiently and accurately good local binary optima.

This paper presents a very different approach to the design of metamaterials. As we have seen so far, the HDG method allows us not only to obtain high order solutions efficiently but also provides us with a couple of properties that make a binary optimization approach possible. The reduced basis method lets us compute efficiently and accurately solutions of neighbors and demonstrates the practicality of our concept of a binary generalized gradient. This extension of the gradient concept lets us move only within feasible binary solutions while improving the objective function value. There is no guarantee that we will reach a global optimum, but that is something that can just not be expected in discrete optimization if we seek efficient algorithms (unless P=NP).

Acknowledgement

We would like to thank the 'LaCaixa' fellowship program for funding one of the authors of this publication. This research has been supported through AFOSR Grant No. FA9550-08-1-0350 and AFOSR Grant No. FA9550-11-1-0141.

References

[1] Nguyen, N. C., Peraire, J. and Cockburn, B. "High-order implicit hybridizable DG methods for acoustics and elastodynamics," *J. C. Phys.*, Vol. 230, No. 10, 3695–3718, 2011.

[2] Nguyen, N. C., Peraire, J. and Cockburn, B. "Hybridizable discontinuous Galerkin methods for the time-harmonic Maxwells equations," *J. C. Phys.*, Vol. 230, No. 19, 7151–7175, 2011.

[3] Schurig, D., Mock, J.J., Justice, B.J., Cummer, S.A., Pendry, J.B., Starr, A.F. and Smith, D.R "Metamaterial Electromagnetic Cloak at Microwave Frequencies," *Science.*, Vol. 314, No. 5801, 977–980, 2006.

[4] Men, H., Nguyen, N.C., Freund, R.M., Parrilo, P. and Peraire, J."Bandgap optimization of two-dimensional photonic crystals using semidefinite programming and subspace methods," *J. Comp. Phys.*, Vol. 229, No. 10, 3706–3725, 2010.

[5] Barrault, M., Maday, Y., Nguyen, N.C., Patera, A.T. "An 'empirical interpolation' method: application to efficient reduced-basis discretization of partial differential equations," *J. Comp. Phys.*, Vol. 229, No. 10, 3706–3725, 2010.

[6] Daraio, C., Ngo, D., Nesterenko, V.F., Fraternali, F. "Highly nonlinear pulse splitting and recombination in a two dimensional granular network," *P. Rev. E* , Vol. 82, No. 036603, 2010.

[7] Cockburn, B., Gopalakrishnan, J., Lazarov, R. "Unified hybridization of discontinuous Galerkin, mixed and continuous Galerkin methods for second order elliptic problems.," *SIAM J. Numeri. Anal.*, Vol. 47, 1319-1365, 2009.

[8] Lakes, R. "Foam structures with a negative Poisson's ratio." *Science.* Vol. 235,1038-1040, 1987.

[9] Saa-Seoane, J. "Simulation and Design Optimization for Linear Wave Phenomena on Metamaterials." *MIT Masters Thesis*, 2010.

[10] Antil, H., Heinkenschloss, M., Hoppe, R. H. W. and Sorensen, D. C. "Domain decomposition and model reduction for the numerical solution of pde constrained optimization problems with localized optimization variables." *Comput. Vis. Sci.* Vol. 13, 249-264, 2010.

[11] Boyaval, S., Le Bris, C., Lelivre, T., Maday, Y., Nguyen, N. C. and Patera, A. "Reduced basis techniques for stochastic problems." *Arch. Comput. Method. E.*. Vol. 17,435-454, 2010.

[12] Rayleigh, J. W. S. "On the remarkable phenomenon of crystalline reflexion described by Prof. Stokes", *Phil. Mag* Vol. 26: 256265, 1888.

A Microwave Engineering Perspective of the Superlens

Ravi S. Hegde, Yew Li Hor, and Wolfgang J. R. Hoefer*

Institute of High Performance Computing, A-Star, Singapore
*corresponding author, E-mail: hoeferwjr@ihpc.a-star.edu.sg

Abstract

Super-resolution imaging involves the interaction of electromagnetic waves with objects that have dimensions similar to, or smaller than the wavelength. That is precisely the hallmark of microwave technology. It suggests that microwave concepts and design approaches may not only be helpful in the description and modeling of the superlens behavior, but also provide useful tools for designing and realizing the superlens, notably the metamaterial itself. In this paper we present some interesting results and insights yielded by the microwave perspective, including waveguide, circuit and filter representations of the superlens.

1. Introduction

The goal of modeling devices or physical processes is to capture their essential characteristics. Reduction to the simplest possible representation not only facilitates their theoretical and numerical treatment but also can provide insights that are helpful in relating new observations to known phenomena. In the case of superresolution imaging with the Veselago/Pendry superlens [1][2] consisting of double-negative metamaterial, the use of waveguide and lumped element circuit models can considerably simplify both its theoretical and its numerical analysis at various levels of abstraction[3]. Given the long time required for the lens to reach the steady-state [4][5][6][7], such simplified models facilitate exploration of resolution limits, allow easy quantification of its imaging performance, and provide a link to microwave engineering and filter design. In this paper we highlight some interesting results and insights yielded by the microwave and filter perspective [6].

2. Waveguide model of sub-wavelength imaging

The imaging of a sub-wavelength sized object is typically based on a spatial Fourier transform of the field emanating from the object, either directly or by scattering of an incident field. The resulting continuous spatial spectrum is then transferred in the frequency domain through the superlens, and the image is recovered by inverse Fourier transform. In the general case this is a three-dimensional electromagnetic problem that must be solved in a semi-infinite half-space. Clearly, the treatment of this problem with space- and time-discrete numerical methods such as FDTD or TLM [8], will require large computational resources and long simulation times.

2.1. Discretization of the spatial spectrum

The first major simplification of the problem is achieved by discretizing the spatial spectrum of the object field into a series of harmonically related samples. This yields a spatial Fourier series; its inverse Fourier transform corresponds to the field produced not by a single object, but by an infinite array of such objects. Fig. 1 illustrates this concept for an object field that has the form of a half-cosine (approximating the field in a narrow slot illuminated by a plane wave polarized parallel to the slot (Fig. 1a)). The spatial Fourier transform perpendicular to the slot is given by:

$$F(k) = \frac{2w/\pi}{1-k^2(w/\pi)^2}\cos(kw/2) \quad , \qquad (1)$$

where w is the width of the slot, and $k=2\pi/\lambda_t$ is the transverse wavenumber or spatial angular frequency. (1) represents the continuous spatial spectrum shown in normalized form in Fig. 1b. If we sample this spectrum at intervals $n=k/\Delta k$ we obtain a Fourier series which represents the discrete spectrum of an infinite array of identical slots separated by a distance $s=2\pi/\Delta k$ (the red curve in Fig. 1a).

The latter curve has been obtained by adding only the first six Fourier terms together. Again, the functions are normalized for better comparison. This example shows that the image of a single slot is very well approximated by an image of periodic slots over the base w. However, the discrete Fourier series approximation considerably simplifies the mathematical formulation of image transmission by the superlens. It naturally leads to the spectral waveguide model of the superlens reported in [6]. This model not only yields existing steady-state formulations of superlens behavior in well-known waveguide terminology, but it also dramatically reduces the computational burden of numerical solutions when studying the dynamics of the lens. Note that this waveguide model describes the transfer of the object field to the image plane in terms of propagating and evanescent waveguide modes and is not a representation of the metamaterial of the lens. It is especially helpful in the transient numerical analysis of superlens behavior that requires millions of time steps [6].

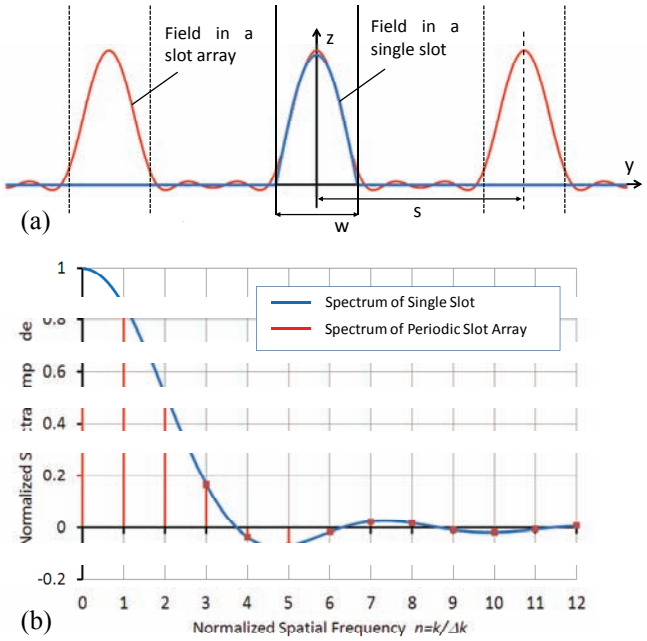

Fig. 1 (a) Electric field in a single slot and in periodic slots in a perfect conductor. (b) Normalized spatial spectrum of the single slot (continuous) and of periodic slots (discrete). *w=40 nm, s=100 nm.* Note that the term at *n=0* has only one-half the amplitude of the continuous spectrum since the spectral terms for negative *n* are not included in the discrete spectrum.

2.2. Waveguide model of coupled plasmonic resonances

The spectral waveguide model is well suited for the investigation of the dynamic field response of the superlens. As discussed in [4][5][9][10][11] the evanescent part of the object field (transmitted in the form of evanescent waveguide modes) excites surface resonances on the two faces of the superlens, thus forming a system of two weakly coupled resonators. In fact, the lens can support an even and an odd mode of coupled resonances. Their resonance frequencies are the roots of a transcendental transmission line equation formulated in terms of waveguide impedances and propagation constants. The equivalent transmission line models are shown in Fig. 2. When we simulate the transient response of the waveguide model including the lens, it is very realistic because the metamaterial can be modeled as a dispersive medium with properties that evolve during the transient build-up of electromagnetic energy in the metamaterial [6]. For the TE mode excitation illustrated in Fig. 1a, the classical waveguide expressions for the characteristic impedance and propagation constant naturally yield an inductive behavior of the air-filled sections of the waveguide model, while the metamaterial-filled sections behave capacitively. This indicates that the resonant response of the lens can be predicted by an extremely simple lumped element network consisting of two resonant LC circuits that are loosely coupled through a small reactive series element. This opens the way to the application of circuit and filter theory to superresolution imaging.

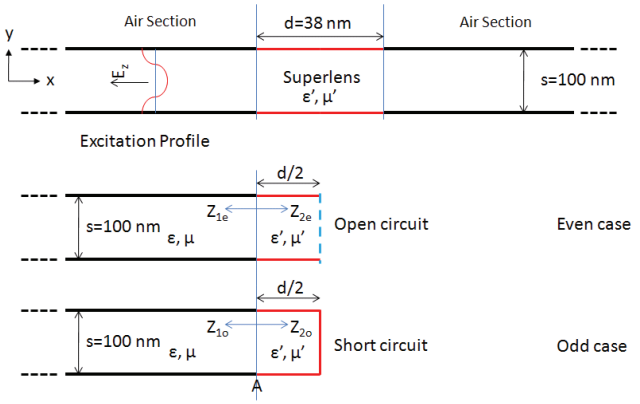

Fig. 2 Odd and even resonance conditions of the metamaterial superlens, modeled by the equivalent waveguide model. Even and odd eigenfrequencies are those frequencies at which the sum of the two impedances Z_{1e} and Z_{1o} in the plane *A* becomes zero in the even and odd cases, respectively (after [6]).

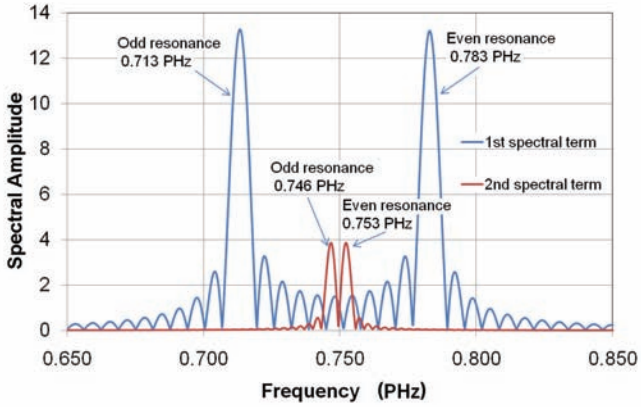

Fig. 3 Even and odd eigenfrequencies of the superlens for transverse wavelengths of *100 nm* (first spectral term) and *50 nm* (second spectral term), obtained with MEFiSTo-3D Pro simulation. Simulation data and theoretical values predicted by the model in Fig. 2 agree within *0.1%* (see [6]).

3. Lumped equivalent circuit of the superlens

The equivalent circuit of the lens and its even and odd variants that emulate the responses of the lens at the operating frequency and at the even and odd frequencies are shown in Fig. 4 a-c. The waveguide formalism yields simple expressions for the elements of that equivalent circuit in terms of the wave properties of the metamaterial [6]. However, the circuit model is not as good as the waveguide representation since the values of the lumped elements would have to be dependent on frequency to be accurate. Nevertheless, the model improves when the coupling between the resonators becomes weaker and the two characteristic frequencies degenerate into a single resonance.

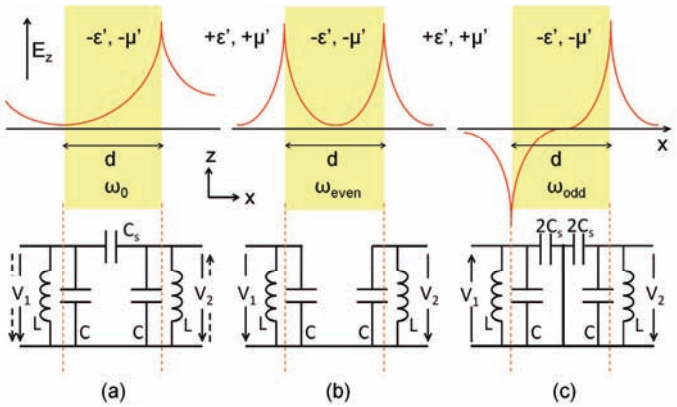

Fig. 4 Electric field distribution and equivalent lumped element circuit of the superlens (a) at the operating frequency, (b) at the even resonance frequency, and (c) at the odd resonance frequency.

Note that the models in Figs. 2 and 4 are valid for all evanescent spectral terms, but the values of the their circuit elements are different for different spectral terms.

The final step is now to create an equivalent network representation of an entire superresolution system based on a perfect Veselago/Pendry lens. Such a network would include the evanescent waveguide sections that separate the object and image planes form the lens. Knowing that at the operating frequency the field decays exponentially in positive *x*-direction, each section can be represented by an ideal transformer of turn ratio $n_1 / n_2 = e^{k_{xn} d/2}$ where k_{nx} is the longitudinal decay constant of the *n-th* spectral term. This value is based on the assumption that the object and image planes are both located at a distance *d/2* on each side of the lens. The equivalent circuit of the imaging system thus consists of a set of modal equivalent networks shown in Fig. 5.

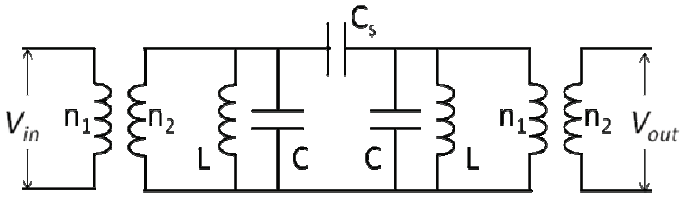

Fig. 5 Equivalent lumped element network of a superresolution imaging system containing a superlens. The complete system comprises one such circuit for every term of the discrete spatial spectrum. $n_1 / n_2 = e^{k_{xn} d/2}$.

The steps involved in the modeling of image transmission are as follows:

a. Perform a spatial Fourier transform of the field produced by the sub-wavelength object;
b. Discretize the spectrum into a Fourier series;
c. Determine the parameters of the equivalent circuit in Fig. 5 for each evanescent Fourier term;
d. Compute the output voltage of each circuit in response to the excitation by the appropriate Fourier term (Voltage proportional to the Fourier coefficient);
e. Compose the image by adding all transmitted Fourier terms together.

One might ask what the benefit of such an equivalent circuit would be when there exists already a well-known analytical transfer function in the literature that will give the same result. The main advantage of the circuit model is the physical interpretation of the lens as two coupled resonators [6] [7] which could be realized in many different ways [12][13], thus suggesting that there exist possible alternative realizations of superresolution devices. Indeed, the fishnet concept is such an alternative, and we can find circuit models of the fishnet elements [14] that are very similar to our coupled resonator model in Fig. 5. Further research is underway to explore other alternative structures that exhibit similar behavior and can be realized with sufficiently low loss to achieve significant large spatial spectral bandwidth suitable for superresolution imaging.

4. Conclusions

We have shown that the field emitted or scattered by a sub-wavelength object can be closely approximated by a Fourier series through sampling of its continuous spectrum. The discrete spectral terms can be interpreted as the eigenmodes of a spectral waveguide model that allows us to describe the superlens imaging of the object using waveguide formalism. The waveguide model is especially useful for numerical modeling of superlens imaging because it provides a compact computational domain truncated by boundary conditions that are numerically robust (perfect electric and magnetic walls), and allows fine discretization and large numbers of time steps that are required to handle the long settling times of the higher evanescent spectral terms. The waveguide model naturally leads to an even simpler coupled resonator model of the Veselago-Pendry superlens which provides deeper physical insight into the physics of the superlens, connects it with the theory of filters and resonant surfaces, and may facilitate the search for alternative ways to realize superresolution devices.

Acknowledgements

This work was supported by the Government of Singapore's Science and Engineering Research Council through A*Star SERC Grant No. 092 154 099 titled "Metamaterials Programme: Superlens".

References

[1] Veselago, V.G., "The electrodynamics of substances with simultaneously negative values of ε and μ," Sov. Phys. Usp., vol. 10, no. 4, pp. 509–514, Jan.-Feb. 1968.

[2] Pendry, J. B. “Negative refraction makes a perfect lens” *Phys. Rev. Lett*., vol. 85, no. 18, pp. 3966–3969, Oct. 2000.

[3] L. Solymar and E. Shamonina, *Waves in Metamaterials,* New York: Oxford University Press, 2009, pp. 157-159.

[4] G. Gomez-Santos, “Universal features of the time evolution of evanescent modes in a left-handed perfect lens” *Phys. Rev. Lett.,* vol. 90, no.7, pp. 077401-1 – 077401-4, Feb. 2003.

[5] X. S. Rao and C. K. Ong, “Subwavelength imaging by a left-handed material superlens”, Phys. Rev. E, vol. 68, pp. 067601-1 – 067601-3, Dec. 2003.

[6] Hegde, R.S., Zs. Szabó, Y.L. Hor, Y. Kiasat, E.P. Li and W.J.R. Hoefer, “The Dynamics of Nanoscale Superresolution Imaging with the Superlens” IEEE Trans. Microw. Theory Tech., vol. 59, no. 10, pp. 2612-2623, Oct. 2011.

[7] W. H. Wee, J. B. Pendry, “Universal Evolution of Perfect Lenses,” Phys. Rev. Lett. 106, 165503 (2011).

[8] P. P. M. So, H. Du and W. J. R. Hoefer, “Modeling of metamaterials with negative refractive index using 2-D shunt and 3-D SCN TLM networks”, *IEEE Trans. Microw. Theory Tech*., vol. 53, no. 4, pp. 1496–1505, Apr. 2005.

[9] R. Ruppin, “Surface polariton of the left-handed medium,” *Phys. Lett. A*, vol. 277, pp. 61-64, 2000.

[10] F. D. M. Haldane, “Electromagnetic surface modes at interface with negative refractive index make a ‘not-quite-perfect’ lens,” *Cond. Matt.,* 0206420, 2002.

[11] D. L. Sounas, N. V. Kantartzis, and T. D. Tsiboukis, "Temporal characteristics of resonant surface polaritons in superlensing planar double-negative slabs: Development of analytical schemes and numerical models," *Phys. Rev.* E 76, 046606-1-046606-12, 2007.

[12] A. Alu, N. Engheta, “Pairing an epsilon-negative slab with a mu-negative slab: resonance, tunneling and transparency,” *IEEE Transactions on Antennas and Propagation*, vol. 51, issue 10, pp. 2558-2571, 2003.

[13] A. Alu, N. Engheta, “Distributed-circuit-element description of guided-wave structures and cavities involving double-negative or single-negative media,” in *Proc. SPIE* 5218, 145 (2003).

[14] R. Marquès, L. Jelinek, F. Mesa, and F. Medina, “Analytical theory of wave propagation through stacked fishnet metamaterials,” *Optics Express*, vol. 17, no. 14 /, 11582, 2009.

Polarizability Matrix Extraction of a Bianisotropic Metamaterial from the Scattering Parameters of Normally Incident Plane Waves

Theodosios D. Karamanos, Alexandros I. Dimitriadis, and Nikolaos V. Kantartzis

Department of Electrical and Computer Engineering,
Aristotle University of Thessaloniki, Thessaloniki GR-54124, Greece
*corresponding author, E-mail: kant@auth.gr

Abstract

In this paper, a polarizability matrix retrieval method for bianisotropic metamaterials is presented. Assuming that scatterers can be modeled by electric and magnetic point-dipoles located at their centers, the induced dipole moments are analytically related to the normally incident fields, while the scattered fields are also analytically obtained for two individual cases of normal wave incidence. The latter can be combined with the incident fields, to express the desired polarizabilities, with regard to the measured or simulated scattering parameters. In this way, the polarizability matrix can be extracted by solving the resulting non-linear system of equations. The proposed technique is applied to two different split-ring resonator structures and reveals very good agreement with previously reported techniques.

1. Introduction

Over the past years, the problem of homogenization in metamaterials, i.e. their modeling via appropriate sets of effective parameters, has risen as a crucial subject for the sound comprehension of their properties as well as for design purposes. Two basic techniques for the calculation of effective parameters exist. The former extracts the effective constitutive parameters from the *S*-parameters of plane waves normally incident on bulk metamaterial structures, via the analytical inversion of the Fresnel-Airy equations [1], [2]. This approach has gained significant popularity due to its simplicity and adequate accuracy. However, it has also been questioned, since it completely ignores the microscopic structure of the metamaterial. Furthermore, several issues have occurred concerning the correct branch selection for the real part of the refraction index, as elaborately discussed in [3], while recently it has been proven that the constitutive parameters, so obtained, do not always represent meaningful material parameters [4]. The second approach, originating from the quasi-static Maxwell-Garnett mixing theory, employs the polarizabilities of individual scatterers in order to extract sets of effective metamaterial parameters [5–7]. For these techniques, the knowledge of the polarizability matrix of the scatterer under study is a crucial and relatively unexplored topic.

Recently, a dynamic approach has been presented for the extraction of electric and magnetic polarizabilities of simple uniaxial scatterers [8]. The scattereres are replaced by electric and magnetic dipole moments, assuming only their electrically small size. In this manner, an infinite array is considered to form a 2-D metasurface. Closed form expressions for the desired polarizabilities are obtained, as a function of the scattering parameters of normally incident plane waves and the interaction coefficients matrix [**C**], whose elements have previously been calculated in the form of rapidly convergent series [9].

To the best of our knowledge, such a procedure has not been yet applied to bianisotropic scatterers, which constitute an important part of practical metamaterials. In this paper, we implement an algorithm for the extraction of the polarizability matrix, bearing in mind its common form for the most popular bianisotropic metamaterials, namely the split-ring resonators (SRRs).

2. Polarizability extraction methodology

In this section, our polarizability matrix extraction technique is systematically described, starting from its typical form for a well-known bianisotropic particle; the edge-coupled split-ring resonator (EC-SRR). This structure can generally be modeled by three dipole moments, which can be directly estimated from the incident field and the polarizability matrix. Next, the scattered field of particle arrays is analytically treated, by substituting the discrete distribution of scatterers with equivalent electric and magnetic currents, induced on the array plane. The scattering parameters, derived from those surfaces, can then be written through their definition as a function of the particle dipole moments. The final objective is to construct and solve a system of equations in order to determine the polarizabilities through the simulated or measured scattering parameters of the structure.

2.1. Dipole moments calculation from the incident field

Let us consider the EC-SRR of Fig. 1 as the basis of our analysis, since it is a bianisotropic particle of great importance in the literature of metamaterials. Our analysis is based on the point-dipole approximation, which requires that the dimensions of the scatterer are small enough compared to the radiation wavelength in the surrounding space (typically smaller than $\lambda/2$). Under this assumption, the EC-SRR may be appropriately modeled by two electric dipole moments p_x, p_y and a magnetic dipole moment m_z [10], which can be related to the local electric and magnetic fields at its center, $\mathbf{E}_{loc}$ and $\mathbf{H}_{loc}$, respectively, through

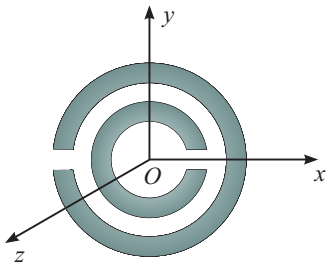

Figure 1: Geometry and axes definition of the EC-SRR.

$$\boldsymbol{\mu} = [\boldsymbol{\alpha}]\mathbf{f}^{loc} \Rightarrow \begin{bmatrix} p_x \\ p_y \\ c^{-1}m_z \end{bmatrix} = \begin{bmatrix} \alpha_{ee}^{xx} & 0 & 0 \\ 0 & \alpha_{ee}^{yy} & \alpha_{em}^{yz} \\ 0 & -\alpha_{em}^{yz} & \alpha_{mm}^{zz} \end{bmatrix} \begin{bmatrix} \varepsilon_0 E_x^{loc} \\ \varepsilon_0 E_y^{loc} \\ c^{-1}H_z^{loc} \end{bmatrix}, \quad (1)$$

where α_{ee}^{xx}, α_{ee}^{yy}, α_{em}^{yz}, and α_{mm}^{zz} are the electric-electric, electric-magnetic, and magnetic-magnetic polarizabilities of the scatterer, correspondingly. As the polarizability matrix [**α**] in (1) contains four unknown quantities, an equal number of linearly independent equations is required to uniquely define them. Considering an infinite array of particles and a plane wave normally incident on their plane, the local field at the center of any resonator is given by

$$\mathbf{f}^{loc} = \mathbf{f}^{inc} + \mathbf{f}^{scat} = \begin{bmatrix} \varepsilon_0 E_x^{inc} \\ \varepsilon_0 E_y^{inc} \\ c^{-1}H_z^{inc} \end{bmatrix} + \begin{bmatrix} \varepsilon_0 E_x^{scat} \\ \varepsilon_0 E_y^{scat} \\ c^{-1}H_z^{scat} \end{bmatrix}, \quad (2)$$

where $\mathbf{f}^{inc}$ is the incident field and $\mathbf{f}^{scat}$ stands for the scattered field vector induced at the center of an arbitrary scatterer from its neighboring ones, defined by

$$\mathbf{f}^{scat} = [\mathbf{C}]\boldsymbol{\mu} \Rightarrow \begin{bmatrix} \varepsilon_0 E_x^{scat} \\ \varepsilon_0 E_y^{scat} \\ c^{-1}H_z^{scat} \end{bmatrix} = \begin{bmatrix} C_{ee}^{xx} & 0 & 0 \\ 0 & C_{ee}^{yy} & C_{em}^{yz} \\ 0 & C_{em}^{yz} & C_{mm}^{zz} \end{bmatrix} \begin{bmatrix} p_x \\ p_y \\ c^{-1}m_z \end{bmatrix}. \quad (3)$$

The components of the interaction coefficient matrix [**C**] are computed via the dyadic Green's function method [11]. By substituting (2) and (3) into (1), the dipole moments of an arbitrary scatterer can be expressed as

$$\boldsymbol{\mu} = \left([\boldsymbol{\alpha}]^{-1} - [\mathbf{C}]\right)^{-1} \mathbf{f}^{inc}. \quad (4)$$

Let us, now, consider two different cases of normal incidence to an infinite array of EC-SRRs (in the following, we will refer to these arrays with the term "metasurface"). The first metasurface is depicted in Fig. 2. For this case, the components of the incident plane wave are

$$\mathbf{f}_A^{inc} = \left[\varepsilon_0 E_{x,A}^{inc} \;\; \varepsilon_0 E_{y,A}^{inc} \;\; c^{-1}H_{z,A}^{inc}\right]^T = \left[0 \;\; \varepsilon_0 E_{y,A}^{inc} \;\; \varepsilon_0 E_{y,A}^{inc}\right]^T \quad (5a)$$

or, by normalizing the incident electric field amplitude,

$$\mathbf{f}_A^{inc} = \left[0 \;\; \varepsilon_0 \;\; \varepsilon_0\right]^T. \quad (5b)$$

Substituting (5b) into (4), we acquire a set of dipole moments, denoted as

$$\boldsymbol{\mu}_A = \left[p_{x,A} \;\; p_{y,A} \;\; c^{-1}m_{z,A}\right]^T, \quad (5c)$$

as a function of the polarizability matrix [**α**].

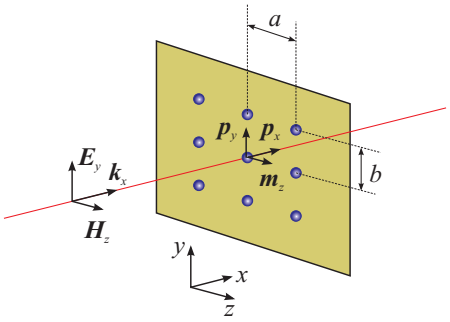

Figure 2: The first metasurface of bianisotropic scatterers at the $x = 0$ plane. The periods of the lattice along the y and z direction, are b and a, respectively. A TEM wave propagating along the x-axis impinges normally on the metasurface.

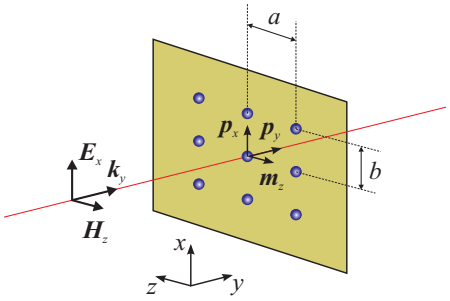

Figure 3: The second metasurface of bianisotropic scatterers at the $y = 0$ plane. The periods of the lattice along the x and z, direction are b and a, respectively. A TEM wave propagating along the y-axis impinges normally on the metasurface.

On the other hand, the second metasurface is given in Fig. 3. The components of the incident plane wave are

$$\mathbf{f}_B^{inc} = \left[\varepsilon_0 E_{x,B}^{inc} \;\; \varepsilon_0 E_{y,B}^{inc} \;\; c^{-1}H_{z,B}^{inc}\right]^T = \left[\varepsilon_0 E_{x,B}^{inc} \;\; 0 \;\; -\varepsilon_0 E_{x,B}^{inc}\right]^T \quad (6a)$$

or by normalizing the incident electric field amplitude,

$$\mathbf{f}_B^{inc} = \left[\varepsilon_0 \;\; 0 \;\; -\varepsilon_0\right]^T. \quad (6b)$$

Plugging (6b) into (4), a second set of dipoles with respect to the polarizabilities of (1) is obtained, which is defined by

$$\boldsymbol{\mu}_B = \left[p_{x,B} \;\; p_{y,B} \;\; c^{-1}m_{z,B}\right]^T. \quad (6c).$$

2.2. Dipole moments relation to the S-parameters

Having obtained the dipole moments of the scatterers from the incident field, we can, now, express them as a function of the simulated or measured scattering parameters of an equivalent homogenized surface.

Let us recall the two metasurfaces of Figs 2 and 3. For the first incidence case, the discrete array of electric and magnetic dipoles can be substituted with equivalent homogeneous electric and magnetic polarizations, given by

$$P_{sx,A} = p_{x,A} \sum_{m=-\infty}^{\infty} \sum_{n=-\infty}^{\infty} \delta(y - ma)\delta(z - nb). \quad (7)$$

Utilizing the Poisson summation formula, (7) transforms to

$$P_{sx,A} = \frac{p_{x,A}}{ab} \sum_{m=-\infty}^{\infty} \sum_{n=-\infty}^{\infty} e^{j\left(\frac{2\pi m}{a}y + \frac{2\pi n}{b}z\right)}. \quad (8)$$

In a similar fashion, electric polarization $P_{sy,A}$ and magnetic polarization $M_{sz,A}$ are found equal to

$$P_{sy,A} = \frac{p_{y,A}}{ab} \sum_{m=-\infty}^{\infty} \sum_{n=-\infty}^{\infty} e^{j\left(\frac{2\pi m}{a} y + \frac{2\pi n}{b} z\right)}, \quad (9)$$

$$M_{sz,A} = \frac{m_{z,A}}{ab} \sum_{m=-\infty}^{\infty} \sum_{n=-\infty}^{\infty} e^{j\left(\frac{2\pi m}{a} y + \frac{2\pi n}{b} z\right)}, \quad (10)$$

where $p_{x,A}$, $p_{y,A}$, and $m_{z,A}$, are the dipole moments of an arbitrary resonator, as described in subsection 2.1.

For a wave propagation toward the x-axis, (8)-(10) represent a sum of waves with a propagation constant of

$$\mathbf{k}_{mn} = k_x^{mn}\hat{\mathbf{x}} + k_y^{m}\hat{\mathbf{y}} + k_z^{n}\hat{\mathbf{z}} = k_x^{mn}\hat{\mathbf{x}} + \left(\frac{2\pi m}{a}\right)\hat{\mathbf{y}} + \left(\frac{2\pi n}{b}\right)\hat{\mathbf{z}}, \quad (11)$$

where caped quantities correspond to the unitary vectors of the Cartesian coordinate system, shown in Fig. 1. Hence, the propagation constant toward the x-direction is given by

$$k_x^{mn} = \sqrt{\left(k_0^2 - k_y^2 - k_z^2\right)} = \sqrt{\left(\omega\mu_0\varepsilon_0\right)^2 - \left(\frac{2\pi m}{a}\right)^2 - \left(\frac{2\pi n}{b}\right)^2}. \quad (12)$$

Note that for a propagating wave, we required $k_x^{mn} \in \mathbb{R}$. From (12) and the definition of $k_0 = \omega\mu_0\varepsilon_0$ as the free-space wavenumber, it follows that

$$\left(\frac{2\pi}{\lambda_0}\right)^2 > \left(\frac{2\pi m}{a}\right)^2 + \left(\frac{2\pi n}{b}\right)^2 \Rightarrow \left(\frac{1}{\lambda_0}\right)^2 > \left(\frac{m}{a}\right)^2 + \left(\frac{n}{b}\right)^2 \quad (13)$$

Moreover, if $a,b < \lambda_0/2$, which implies an electrically small unit cell, as already assumed, one gets

$$\left(\frac{1}{\lambda_0}\right)^2 > \left(\frac{2m}{\lambda_0}\right)^2 + \left(\frac{2n}{\lambda_0}\right)^2 = \frac{4}{\lambda_0^2}\left(m^2 + n^2\right). \quad (14)$$

As observed, the only solution of (14) is $m = n = 0$. This indicates that only the first (zeroth-order) term of the sum in (8)-(10) represents a propagating wave, while all higher-order terms correspond to evanescent waves. Therefore, the polarizations that contribute in that propagating wave are

$$P_{sx,A} = \frac{p_{x,A}}{ab}, \quad P_{sy,A} = \frac{p_{y,A}}{ab}, \quad M_{sz,A} = \frac{m_{z,A}}{ab}. \quad (15)$$

Likewise, the homogeneous electric and magnetic polarizations for the second metasurface are given by

$$P_{sx,B} = \frac{p_{x,B}}{ab} \sum_{m=-\infty}^{\infty} \sum_{n=-\infty}^{\infty} e^{j\left(\frac{2\pi m}{a} x + \frac{2\pi n}{b} z\right)}, \quad (16a)$$

$$P_{sy,B} = \frac{p_{y,B}}{ab} \sum_{m=-\infty}^{\infty} \sum_{n=-\infty}^{\infty} e^{j\left(\frac{2\pi m}{a} x + \frac{2\pi n}{b} z\right)}, \quad (16b)$$

$$M_{sz,B} = \frac{m_{z,B}}{ab} \sum_{m=-\infty}^{\infty} \sum_{n=-\infty}^{\infty} e^{j\left(\frac{2\pi m}{a} x + \frac{2\pi n}{b} z\right)}, \quad (16c)$$

and, finally, the polarizations' terms that contribute in a propagating wave are similar to those in (15), namely

$$P_{sx,B} = \frac{p_{x,B}}{ab}, \quad P_{sy,B} = \frac{p_{y,B}}{ab}, \quad M_{sz,B} = \frac{m_{z,B}}{ab}. \quad (17)$$

The scattered field from a metasurface can be evaluated through boundary conditions [12]

$$\hat{\mathbf{n}} \times \left(\mathbf{H}\big|_{z=0^+} - \mathbf{H}\big|_{z=0^-}\right) = \partial_t \mathbf{P}_s + \nabla \times \mathbf{M}_s = \mathbf{J}_s, \quad (18)$$

$$\hat{\mathbf{n}} \times \left(\mathbf{E}\big|_{z=0^+} - \mathbf{E}\big|_{z=0^-}\right) = \partial_t \mathbf{M}_s + \nabla \times \mathbf{P}_s = -\mathbf{K}_s. \quad (19)$$

Applying the right parts of (18) and (19), for the polarizations of (15), we acquire the equivalent electric, $\mathbf{J}_s$, and magnetic, $\mathbf{K}_s$, surface currents

$$\mathbf{J}_s = j\omega\frac{p_x}{ab}\hat{\mathbf{x}} + j\omega\frac{p_y}{ab}\hat{\mathbf{y}}, \quad (20)$$

$$\mathbf{K}_s = j\omega\mu_0\frac{m_z}{ab}\hat{\mathbf{z}}. \quad (21)$$

Furthermore, equating these results to the left-hand sides of (18) and (19), the scattering field from the equivalent homogenized metasurface is derived. For the first case, the scattered fields are obtained as

$$\hat{\mathbf{x}} \times \left(\mathbf{H}\big|_{x=0^+} - \mathbf{H}\big|_{x=0^-}\right) = \mathbf{J}_s \Rightarrow -\left(H_z\big|_{x=0^+} - H_z\big|_{x=0^-}\right) = J_{sy}. \quad (22)$$

As expected, surface current components normal to the surface do not produce any scattered field. Considering also that

$$H_z\big|_{x=0^+}^{scat,A} = -H_z\big|_{x=0^-}^{scat,A} \quad \text{and} \quad E_y\big|_{x=0^+}^{scat,A} = Z_0 H_z\big|_{x=0^+}^{scat,A},$$

equation (22) results in

$$\mathbf{E}_{J_s,A}^{scat} = -j\omega\frac{Z_0 p_{y,A}}{2ab} e^{-jk_0|x|}\hat{\mathbf{y}}, \quad (23)$$

where Z_0 is the characteristic impedance in vacuum. Analogously, from (19) and (21), the scattered electric field component due to the magnetic surface current, is given by

$$\mathbf{E}_{K_s,A}^{scat} = -\mathrm{sgn}(x)\frac{j\omega\mu_0 m_{z,A}}{2ab} e^{-jk_0|x|}\hat{\mathbf{y}}. \quad (24)$$

Summation of (23) and (24) leads to the scattered field expression of the first case, i.e.

$$\mathbf{E}_A^{scat} = -\frac{j\omega}{2ab}\left(Z_0 p_{y,A} - \mathrm{sgn}(x) j\omega\mu_0 m_{z,A}\right) e^{-jk_0|x|}\hat{\mathbf{y}}, \quad (25)$$

whereas the scattered field for the second case is derived by

$$\mathbf{E}_B^{scat} = -\frac{j\omega}{2ab}\left(Z_0 p_{x,B} + \mathrm{sgn}(y)\mu_0 m_{z,B}\right) e^{-jk_0|y|}\hat{\mathbf{x}}. \quad (26)$$

Through (25) and (26), we may find the S-parameters for each metasurface, owing to their relation with the reflected and transmitted wave at the reference planes ± l, as presented in Fig. 4. Distance l is sufficiently large so that higher order terms of (8)-(10) and (16) are adequately attenuated.

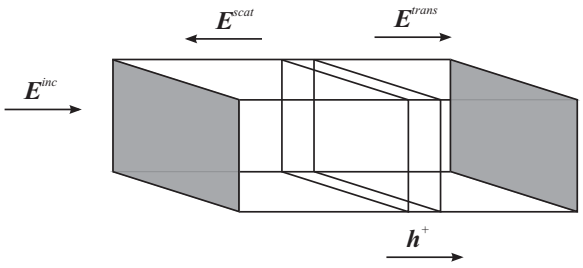

Figure 4: The simulation/measurement configuration. Propagation occurs along the positive h-direction, which corresponds to x- and y-axis (first and second case, respectively). The central rectangle depicts the metasurface and gray areas the reference planes, at a distance of ± l for the metasurface.

Subsequently, considering the fields on the reference planes, we calculate *S*-parameters by means of

$$S_{11} = \frac{E^{scat}(h=-l)}{E^{inc}(h=-l)} = \frac{E^{scat}}{E^{inc}} e^{-j2k_0 l}, \tag{27}$$

$$S_{21} = \frac{E^{trans}(h=+l)}{E^{inc}(h=-l)} = \frac{E^{inc}+E^{scat}}{E^{inc}} e^{-j2k_0 l}. \tag{28}$$

Substitution of (25) and (26) in (27) and (28), finally, yields the dipole moments parallel to each equivalent surface as a function of the *S*-parameters,

$$p_{y,A} = \frac{jab}{\omega Z_0}\left(S_{11,A}e^{j2k_0 l} + S_{21,A}e^{j2k_0 l} - 1\right), \tag{29a}$$

$$m_{z,A} = -\frac{jab}{\omega \mu_0}\left(S_{11,A}e^{j2k_0 l} - S_{21,A}e^{j2k_0 l} + 1\right), \tag{29b}$$

$$p_{x,B} = \frac{jab}{\omega Z_0}\left(S_{11,B}e^{j2k_0 l} + S_{21,B}e^{j2k_0 l} - 1\right), \tag{29c}$$

$$m_{z,B} = -\frac{jab}{\omega \mu_0}\left(S_{11,B}e^{j2k_0 l} - S_{21,B}e^{j2k_0 l} + 1\right). \tag{29d}$$

If we plug the dipole moments, evaluated from (4), for both incidence cases, into (29), a system of four linearly independent equations is obtained, containing polarizabilities α_{ee}^{xx}, α_{ee}^{yy}, α_{em}^{yz}, and α_{mm}^{zz}. Moreover, due to (1), equation (29c) contains only the a_{ee}^{xx} term and hence it can be solved directly, thus reducing the final system to three equations for the unknown polarizabilities α_{ee}^{yy}, α_{em}^{yz}, and α_{mm}^{zz}. Such system is non-linear and a closed solution, although very instructive, is not generally feasible. In the special case where $\alpha_{em}^{yz} = 0$, the closed-form solution of (29) is viable and the result coincides with the method presented in [8], as verified in Section 3. In the following section, we apply the Newton-Raphson method (see Appendix I) to numerically solve (29).

3. Results and Discussion

The new polarizability extraction methodology is, herein, applied to two SRR structures. All simulations are conducted via the frequency domain solver of the CST MWS™ computational package [13]. The first structure is the bianisotropic EC-SRR of Fig. 5, which is known to produce a strong magnetic field, opposite to the incident and perpendicular to its plane, on its first resonance frequency. The transmission coefficient of EC-SRR for *x*- and *y*-incidence is displayed in Fig. 6, indicating the first two resonances. The polarizabilitites, extracted by our technique are given in Fig. 7. It is straightforward to detect that both polarizabilities α_{ee}^{yy} and α_{mm}^{zz} become resonant approximately at the same frequency. This outcome is in agreement with the assumptions of [10]. Next, polarizabilities α_{ee}^{xx}, α_{ee}^{yy}, and α_{mm}^{zz} are further validated by comparing them with the Sipe-Kranendonk condition [14] for lossless scatterers, which reads (for $i = x,y,z$ and $j = e,m$)

$$\mathrm{Im}\left\{\frac{1}{\alpha_{jj}^{ii}}\right\} = \frac{k_0^3}{6\pi}. \tag{30}$$

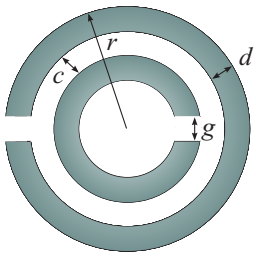

Figure 5: Geometry of the simulated EC-SRR, with r = 3.2 mm, c = 0.5 mm, d = 0.5 mm, and g = 0.5 mm. The periods of the lattice, as depicted in Figs 2 and 3, are $a = b$ = 10 mm, and the distance from the reference planes is $l = \pm 3a$.

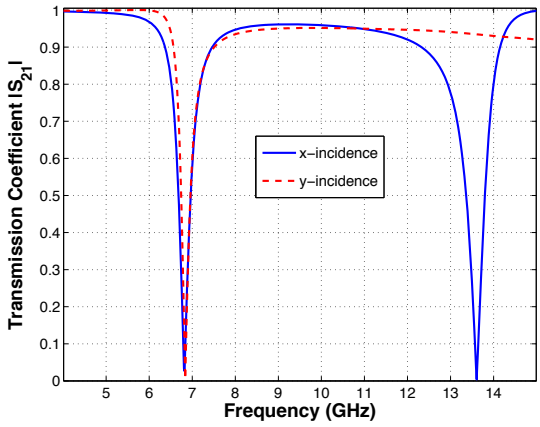

Figure 6: Transmission coefficient for the EC-SRR of Fig. 6, for the *x*- and *y*-incidence, respectively. The axes convention is the same as that established in Fig. 1.

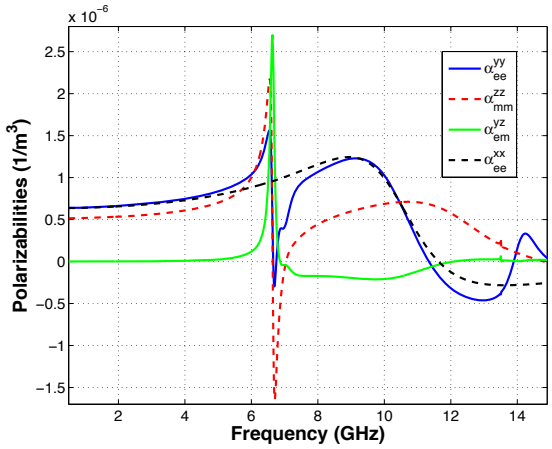

Figure 7: Polarizabilities of the EC-SRR, extracted via the proposed method.

As presented in Fig. 8, outside the resonance bands, where the lossless condition is not valid, the Sipe-Kranendonk condition is satisfied by the polarizabilities of Fig. 7.

Next, let us focus on the non-bianisotropic SRR (NB-SRR) of Fig. 9. Despite its designation, bianisotropic effects are not totally absent in that structure, as our analysis will reveal. The transmission coefficient for the two first resonances is illustrated in Fig. 10 for both *x*- and *y*-incidence, while the corresponding polarizabilities are presented in Fig.

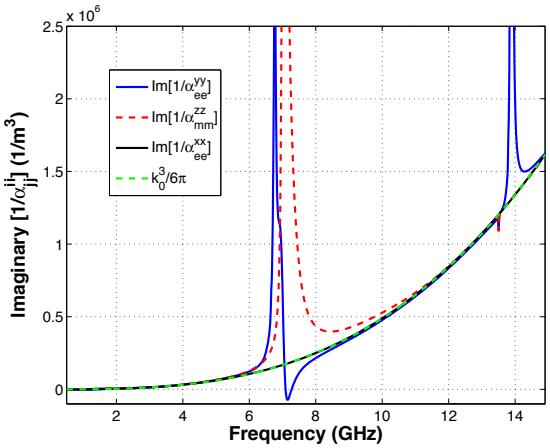

Figure 8: Comparison of the Sipe-Kranendonk criterion for lossless scatterers with the polarizabilities of the EC-SRR extracted in Fig. 7. The criterion is not satisfied on resonance bands, where the lossless assumption is not valid.

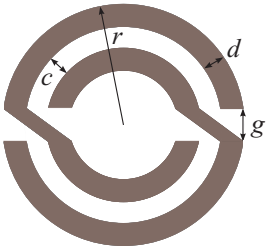

Figure 9: Geometry of the simulated NB-SRR, with r = 3.7 mm, c = 0.5 mm, d = 0.5 mm, and g = 0.5 mm. The periods of the lattice, as depicted in Figs 2 and 3, are $a = b$ = 15 mm, and the distance from the reference planes is $l = \pm 3a$.

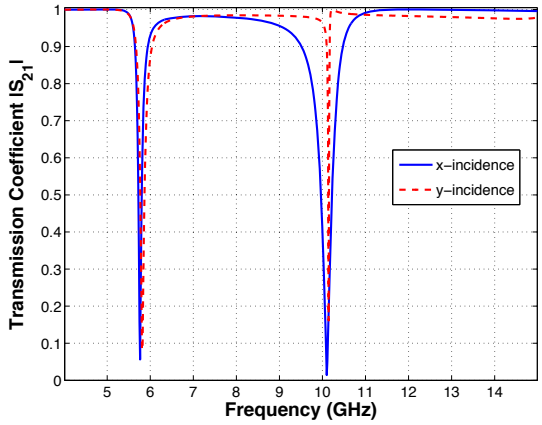

Figure 10: Transmission coefficient for the NB-SRR of Fig. 9, for the x- and y-incidence, respectively. The axes convention is the same as that established in Fig. 1.

11. Figure 12 presents a comparison of our results with those of [8], valid for uniaxially anisotropic scatterers, where a very good agreement can be promptly detected. Deviations are significant only in the resonance bands, where a considerable electric-magnetic polarizability has been is found in our simulations and has not been taken into account in [8]. These deductions suggest that the proposed

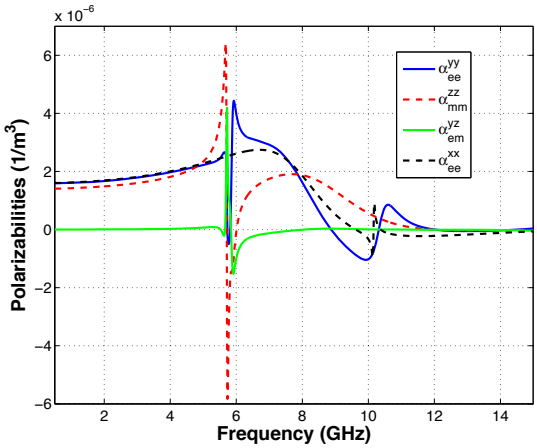

Figure 11: Polarizabilities of the NB-SRR, extracted via the proposed method.

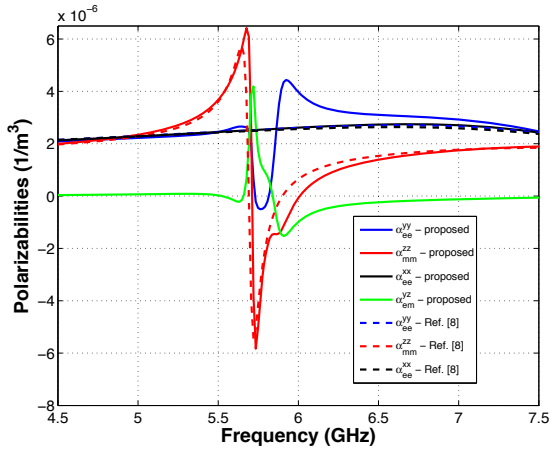

Figure 12: Detail of Fig. 11, including comparison of the results with those of [8].

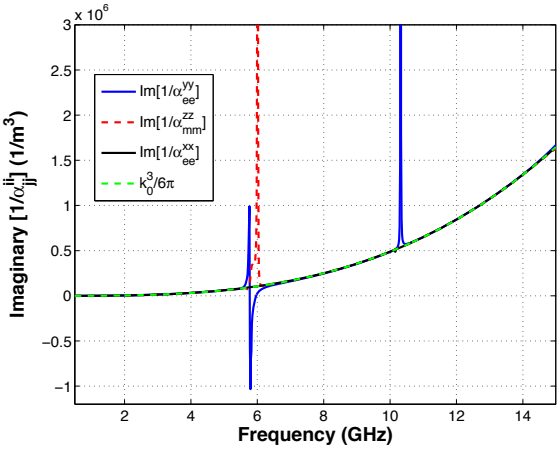

Figure 13: Comparison of the Sipe-Kranendonk criterion for lossless scatterers with the polarizabilities of the NB-SRR extracted in Fig. 11. The criterion is not satisfied on resonance bands, where the lossless assumption is not valid.

technique can be regarded as a generalization of [8], as already mentioned before. Finally in Fig. 13, by applying the

Sipe-Kranendonk criterion (30) on α_{ee}^{xx}, α_{ee}^{yy}, and α_{mm}^{zz}, we attain additional verification on the efficiency of our method.

4. Conclusions

A novel methodology for extracting polarizabilities from bianisotropic scatterers has been introduced in this paper. Its formulation is based on the use of the point-dipole approximation for both the microscopic and macroscopic description of an equivalent metasurface. Initially, the dipole moments are acquired as a function of the polarizabilities of the scatterers. Assuming, additionally, that infinite rectangular arrays of scatterers constitute equivalent homogenized metasurfaces, the equivalent surface currents generated by a normally incident wave are analytically obtained and dipole moments are expressed as a function of the simulated/ measured *S*-parameters. Furthermore, equating the polarizabilities, acquired from the microscopic and macroscopic approach, a non-linear system of equations for the unknown polarizabilities is derived, which can be numerically solved.

Concerning the certification of our algorithm, two of the most popular SRR structures, namely the EC-SRR and NB-SRR, have been investigated. The results are in very good agreement with those reported already in the relevant literature and have been further validated by means of the Sipe-Kranendonk criterion. Moreover, for the case of the NB-SRR, outcomes have been compared with those of an existing method, developed for uniaxially anisotropic scatterers. Again, our results coincidence is very satisfactory, while some differences between the two schemes is attributed to the existence of a non-vanishing electric-magnetic polarizability inside the resonance band, which is *a priori* ignored in [8].

Future work is going to address the expansion of the reported methodology to a broader set of scatterers, with an even larger number of unknown polarizabilites, on condition that an equal number of different and independent measurements can be carried out. Finally, polarizabilities extracted through the method could be utilized in rigorous homogenization techniques that are currently being developed, such as the one developed in [4].

Appendix I
The Newton-Raphson method for non-linear systems

Assume a non-linear system

$$\left[\mathbf{A}(u)\right]\{\mathbf{u}\} = \{\mathbf{b}\}, \tag{31a}$$

or in full form

$$\begin{aligned} &a_{11}u_1 + a_{12}u_2 + \ldots + a_{1n}u_n = b_1 \\ &a_{21}u_1 + a_{22}u_2 + \ldots + a_{2n}u_n = b_2 \\ &\ldots\ldots\ldots\ldots\ldots\ldots\ldots\ldots\ldots \\ &a_{n1}u_1 + a_{n2}u_2 + \ldots + a_{nn}u_n = b_n \end{aligned} \tag{31b}$$

where coefficients a_{ij}, are not constant, but functions of variables u_i. Vector $\{\mathbf{u}\}^T = \{u_1, u_2, ..., u_n\}$ contains the unknown parameters and $\{\mathbf{b}\}^T = \{b_1, b_2, ..., b_n\}$ contains constant components. Moreover, system (31) can be written as

$$\mathbf{f} = \begin{bmatrix} f_1 \\ f_2 \\ \ldots \\ f_n \end{bmatrix} = \begin{bmatrix} 0 \\ 0 \\ \ldots \\ 0 \end{bmatrix}, \tag{32}$$

where $f_i = a_{i1}u_1 + a_{i2}u_2 + \cdots + a_{in}u_n - b_i = 0$ for $i = (1, 2, ..., n)$.

According to the Newton-Raphson method, the approximate solutions $u^{(k+1)}$, $u^{(k+1)}$ on the (k+1)-th and k-th step respectively, are given by

$$\mathbf{u}^{(k+1)} = \mathbf{u}^{(k)} + \delta\mathbf{u}^{(k)}, \tag{33}$$

where vector $\delta\mathbf{u}^{(k)}$ represents the components' modification, while advancing from the k-th to the (k+1)-th step.

Let us consider the following Taylor expansion, where second order terms are forfeit

$$\begin{aligned} f_i\left(u_1^{(k+1)}, u_2^{(k+1)}, ..., u_n^{(k+1)}\right) &= f_i\left(u_1^{(k)}, u_2^{(k)}, ..., u_n^{(k)}\right) \\ &+ \cdots + \frac{\partial f_i}{\partial u_1}\delta u_1^{(k)} + \frac{\partial f_i}{\partial u_2}\delta u_2^{(k)} + \cdots + \frac{\partial f_i}{\partial u_n}\delta u_n^{(k)}, \end{aligned} \tag{34}$$

for $i = (1, 2, ..., n)$. Setting $f_i(u_1^{(k+1)}, u_2^{(k+1)}, ..., u_n^{(k+1)}) = 0$, we extract the following system of equations

$$\begin{aligned} &\frac{\partial f_1}{\partial u_1}\delta u_1^{(k)} + \frac{\partial f_1}{\partial u_2}\delta u_2^{(k)} + \cdots + \frac{\partial f_1}{\partial u_n}\delta u_n^{(k)} = -f_1\left(u_1^{(k)}, u_2^{(k)}, ..., u_n^{(k)}\right) \\ &\frac{\partial f_2}{\partial u_1}\delta u_1^{(k)} + \frac{\partial f_2}{\partial u_2}\delta u_2^{(k)} + \cdots + \frac{\partial f_2}{\partial u_n}\delta u_n^{(k)} = -f_2\left(u_1^{(k)}, u_2^{(k)}, ..., u_n^{(k)}\right) \\ &\ldots\ldots\ldots\ldots\ldots\ldots\ldots\ldots\ldots\ldots\ldots\ldots\ldots\ldots\ldots\ldots\ldots\ldots\ldots\ldots \\ &\frac{\partial f_n}{\partial u_1}\delta u_1^{(k)} + \frac{\partial f_n}{\partial u_2}\delta u_2^{(k)} + \cdots + \frac{\partial f_n}{\partial u_n}\delta u_n^{(k)} = -f_n\left(u_1^{(k)}, u_2^{(k)}, ..., u_n^{(k)}\right) \end{aligned} \tag{35}$$

Using the subsequent Jacobian matrix

$$\mathbf{J} = \begin{bmatrix} \frac{\partial f_1}{\partial u_1} & \frac{\partial f_1}{\partial u_2} & \ldots & \frac{\partial f_1}{\partial u_n} \\ \frac{\partial f_2}{\partial u_1} & \frac{\partial f_2}{\partial u_2} & \ldots & \frac{\partial f_2}{\partial u_n} \\ \ldots & \ldots & \ldots & \ldots \\ \frac{\partial f_n}{\partial u_1} & \frac{\partial f_n}{\partial u_2} & \ldots & \frac{\partial f_n}{\partial u_n} \end{bmatrix}, \tag{36}$$

equations (34) are rewritten as

$$\mathbf{J}\delta\mathbf{u}^{(k)} = -\mathbf{f}(\mathbf{u}^{(k)}). \tag{37}$$

Substituting (37) in (33) and taking into account (32), we derive

$$\mathbf{u}^{(k+1)} = \mathbf{u}^{(k)} - \mathbf{J}^{-1}\left[\mathbf{A}\left(\mathbf{u}^{(k)}\right)\mathbf{u}^{(k)} - \mathbf{b}\right], \tag{38}$$

where the elements of **J** are calculated via

$$J_{ij} = \frac{\partial f_i}{\partial u_i} = a_{ij} + \sum_{k=1}^{n}\frac{\partial a_{ik}}{\partial u_i}u_k. \tag{39}$$

Acknowledgements

This research has been co-financed by the EU (European Social Fund – ESF) and Greek national funds through the

Operational Program “Education and Lifelong Learning” of the National Strategic Reference Framework (NSRF) – Research Funding Program: Heracleitus II. Investing in knowledge society through the European Social Fund.

References

[1] D.R. Smith, S. Schultz, P. Markoš, C.M. Soukoulis, Determination of effective permittivity and permeability of metamaterials from reflection and transmission coefficients, *Phys. Rev. B* 65: pp. 195104(1–5), 2002.

[2] X. Chen, T.M. Grzegorczyk, B.-I. Wu, J. Pacheco, J.A. Kong, Robust method to retrieve the constitutive effective parameters of metamaterials, *Phys. Rev. E* 70: pp. 016608(1–7), 2004.

[3] V.V. Varadan, R. Ruyen, Unique retrieval of complex permittivity and permeability of dispersive materials from reflection and transmitted fields by enforcing causality, *IEEE Trans. Microw. Theory and Tech.* 55: pp. 2224–2230, 2007.

[4] A. Alù, First-principles homogenization theory for periodic metamaterials, *Phys. Rev. B*. 84: pp. 075153(1–18), 2011.

[5] A.H Sihvola, *Electromagnetic Mixing Formulas and Applications*, IEEE Electromagnetic Wave Series, Piscataway, New Jersey, 2000.

[6] D. Morits, C.R. Simovski, Electromagnetic characterization of planar and bulk metamaterials: A theoretical study, *Phys. Rev. B* 82: pp. 165114(1–10), 2010.

[7] A.I. Dimitriadis, N.V. Kantartzis, I.T. Rekanos, T.D. Tsiboukis, Efficient metafilm/metasurface characterization for obliquely incident TE waves via surface susceptibility models, *IEEE Trans. Magn.* 48: pp. 367–370, 2012.

[8] A.D. Scher, E.F. Kuester, Extracting the bulk effective parameters of a metamaterial via the scattering from a single planar array of particles, *Metamaterials* 3: pp. 44–55, 2009.

[9] P.A. Belov, C.R. Simovski, Homogenization of electromagnetic crystals formed by uniaxial resonant scatterers, *Phys. Rev. E* 72: pp. 026615(1–15), 2005.

[10] R. Marqués, F. Martín, M. Sorolla, *Metamaterials with Negative Parameters: Theory, Design and Microwave Applications*, John Wiley & Sons, New York, 2008.

[11] R.E. Collin, *Field Theory of Guided Waves*, IEEE Press, New Jersey, 1990.

[12] C.L. Holloway, M.A. Mohamed, E.F. Kuester, A. Dienstfrey, Reflection and transmission properties of a metafilm: with an application to a controllable surface composed of resonant particles, *IEEE Trans. Electromagn. Compat.* 47: pp. 853–865, 2005.

[13] *CST MWS™: Computer Simulation Technology: Microwave Studio*, Computer Simulation Technology Std., 2011.

[14] S.A. Tretyakov, *Analytical Modeling in Applied Electromagnetics*, Arthech House Publishers, Boston, pp. 96–98, 2003.

BIANISOTROPIC SUPERSTRATE EFFECT ON RECTANGULAR MICROSTRIP PATCH ANTENNA PARAMETERS

Chemseddine Zebiri [1], Fatiha Benabdelaziz [2], and Mohamed Lashab[2]
[1] *Electronics Department, Ferhat abbas University*
Route de bejaia, 19000 Setif, Algeria
[1]zebiri@ymail.com
[2]*Electronics Department, Constantine University*
Route Ain El bey, 25000 Constantine, Algeria

ABSTRACT
In this paper, the effects of the superstrate chirality on the resonant frequency and bandwidth of rectangular microstrip patch in a substrate-superstrate configuration are investigated. The problem is rigorously formulated via integral equation. This equation is solved using Galerkin's moment method; the complex resonance frequencies for TM_{01} mode are studied with sinusoidal basis functions. The obtained theoretical results show that the decrease is more important for high permittivity loading and negative chirality element.

Keywords: bi-anisotropic, rectangular microstrip, patch antenna, resonant frequency, bandwidth.

I. Introduction

Structures with substrate-superstrate are employed, in general, to improve parameters such as: profit, effectiveness and polarization of the antenna [1], where the superstrate is used as protection structure of the aerial elements against bad climatic conditions, such as: rain, fog, and snow etc….[2]. These are formed accidentally, and they affects the performances of the printed antennas [3] [4] [5]. Therefore for butter characterization and precise design, these effects must be taken into account.

The materials so called complex, such as biaxial, bi-anisotropic, or the use of an anisotropic superstrate, can have more interesting effects [6] [7].

The effects of the uniaxial anisotropy on the resonant frequency and the band-width of a monolayer rectangular microstrip antenna, were studied in several works [8] [9] and [10], where the two types of positive and negative uniaxial anisotropy were considered. In the other hand the effect of dielectric superstrate on the frequency and the band-width of radiating rectangular patch microstrip was evaluated in experiments by Bahl [11], and theoretically by Bouttout [5] and Zebiri [12]. They deduced that the bandwidth decreases for a high permittivity of the superstrate which has low thickness.

After having studied the effect of the magnetic uniaxial anisotropy and the chirality for a monolayer structure [7]. In this work, the effects of a bi-anisotropic superstrate on the resonant frequency and the band-width of the rectangular microstrip are considered in details. The problem of the complex resonant frequency considered here is formulated in terms of an integral equation; by using the Victor Fourier transform [13].

The idea to use chiral materials as substrate and superstrate in printed antenna circuit has been tried the first time by Engheta [14]. In the literature it has been shown that the power of surface wave can be generally stepped down when a chiral substrate is employed for printed microstrip circuit [15].

II. THEORY

The geometry under consideration is shown in Figure I. A rectangular patch with dimensions (a, b) along the two axes (ox, oy) respectively is printed on a grounded dielectric slab of thickness d_1. Above the radiating patch is the superstrate layer of thickness d_2. All the dielectric materials are assumed to be bi-anisotropic.

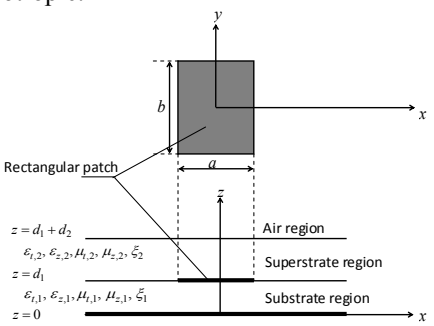

Figure 1: Geometrical structure of a superstrate loaded rectangular patch on a uniaxial substrate.

The composite bi-anisotropic chiral materials which exhibit the effect of chirality at microwave frequencies have been fabricated and characterized in many studies [16], [17]. The chiral mediums considered here can be described by a set of constitutive relations [18].

$$\vec{B} = \bar{\bar{\mu}}\vec{H} + \frac{1}{c_0}\bar{\bar{\xi}}\vec{E} \qquad (1)$$

$$\vec{D} = \bar{\bar{\varepsilon}}_i \vec{E} + \frac{1}{c_0} \bar{\bar{\eta}} \vec{H} \tag{2}$$

Where the permittivity, permeability and magneto-electric tensors are expressed as:

$$\varepsilon = \varepsilon_0 \varepsilon_r \tag{3}$$

$$\mu = \mu_0 \tag{4}$$

$$\bar{\bar{\xi}} = -\bar{\bar{\eta}} = j \begin{bmatrix} 0 & \xi & 0 \\ -\xi & 0 & 0 \\ 0 & 0 & 0 \end{bmatrix} \tag{5}$$

Assuming an ($e^{-i\omega t}$) time variation and starting from Maxwell's equations in the Fourier transform domain, we can show that the transverse magnetic (TM or E) and transverse electric (TE or H) counterparts of the tangential electric and magnetic fields in the Fourier domain for an anisotropic bounded region having anisotropy tensor of type (3)-(5) can be expressed in compact matrix form.

For an electric and non magnetic medium having biaxial anisotropy with regard to the permittivity the expressions are well detailed in [5] [12].

The proposed structure is studied and the boundary conditions have been applied after then the dyadic Green's function is obtained.

The surface current **J** on the patch can be expanded into a finite series of basis functions:

$$\mathbf{J}(r_s) = \sum_{n=1}^{N} a_n \begin{bmatrix} J_{xn}(r_s) \\ 0 \end{bmatrix} + \sum_{m=1}^{M} b_m \begin{bmatrix} 0 \\ J_{ym}(r_s) \end{bmatrix} \tag{6}$$

where a_n and b_m are the mode expansion coefficients to be sought. The integral equation describing the electric field on the patch is [19]:

$$\int_{-\infty}^{\infty} \int d\kappa_s \overline{\mathbf{F}}(\kappa_s, r_s) \cdot \overline{\mathbf{G}}(\kappa_s) \cdot \widetilde{\mathbf{J}}(\kappa_s) = 0 \tag{7}$$

Using the well-known Galerkin procedure of the moment method, the integral equation in (7) is discretized into the following matrix equation:

$$\begin{bmatrix} (\overline{\mathbf{B}}_1)_{N\times N} & (\overline{\mathbf{B}}_2)_{N\times M} \\ (\overline{\mathbf{B}}_3)_{M\times N} & (\overline{\mathbf{B}}_4)_{M\times M} \end{bmatrix} \cdot \begin{bmatrix} (\mathbf{a})_{N\times 1} \\ (\mathbf{b})_{M\times 1} \end{bmatrix} = \mathbf{0} \tag{8}$$

Where $\overline{\mathbf{G}}(\kappa_s)$ is given in Green function and the other parameters appeared in (6), (7) and (8) are defined in the same reference. A nontrivial solution of (8) is derived by seeking a complex frequency $f = f_r + if_i$, where f_r is the resonant frequency and $2f_i/f_r$ is the half-power bandwidth of the antenna.

III. RESULT

III.1. Real resonant frequency:

The effect of the chirality on the resonant frequency does not have the same effects as the other electromagnetic components [12], in this case (Figure 2), the effect of the chirality makes so that the real resonant frequency undergoes an autonomous increase for a positive magneto-electric element while raising the thickness of the layer of the superstrate (for negative element there is more accentuated reduction).

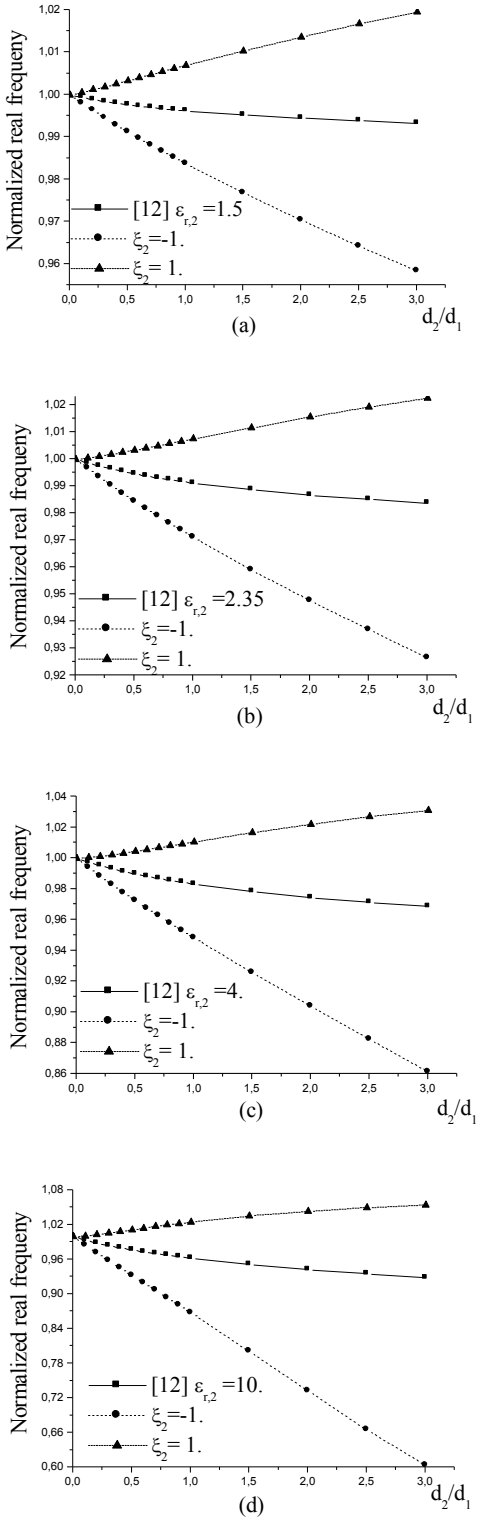

Figure 2: The chirality effect of a superstrate on the normalized real resonant frequency; a=6 cm, b=5 cm, d_1=0.1 cm, $\varepsilon_{r,1}$=2.35, (a) $\varepsilon_{r,2}$=1.5, (b) $\varepsilon_{r,2}$=2.35, (c) $\varepsilon_{r,2}$=4, (d) $\varepsilon_{r,2}$=10.

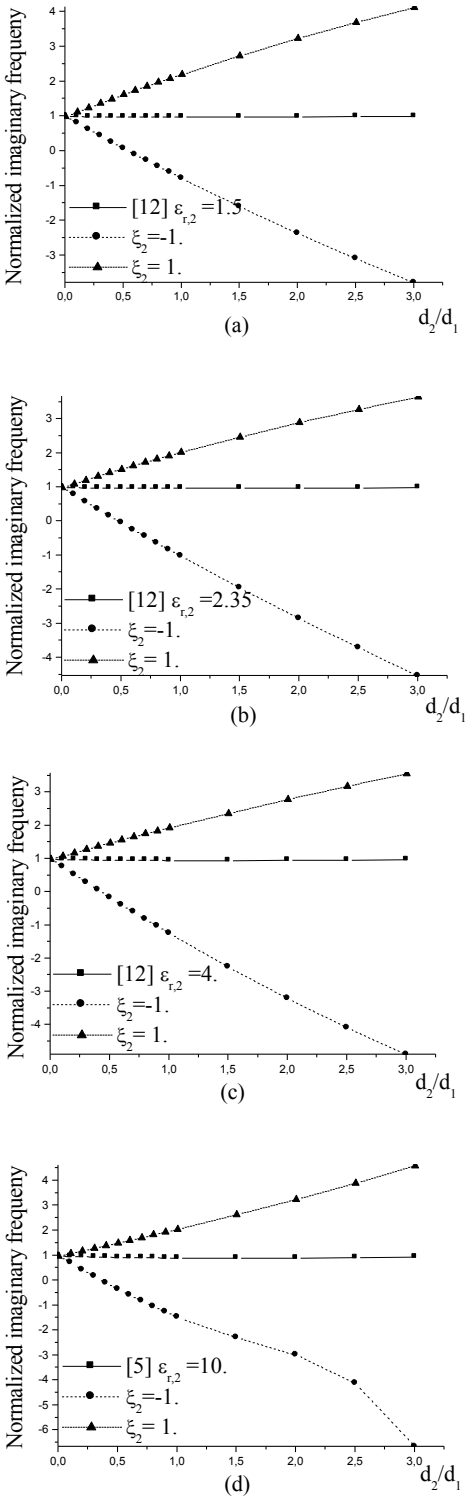

Figure 3: The chirality effect of a superstrate on the normalized imaginary resonant frequency; a=6 cm, b=5 cm, d_1=0.1 cm, $\varepsilon_{r,1}$=2.35, (a) $\varepsilon_{r,2}$=1.5, (b) $\varepsilon_{r,2}$=2.35, (c) $\varepsilon_{r,2}$=4, (d) $\varepsilon_{r,2}$=10.

In addition by raising the constant of permittivity, the real resonant frequency increase furthermore. We notice that the increase and decrease of the real resonant frequency are close to some percent to scores forty percent according to the value permittivity, which is a very important effect.

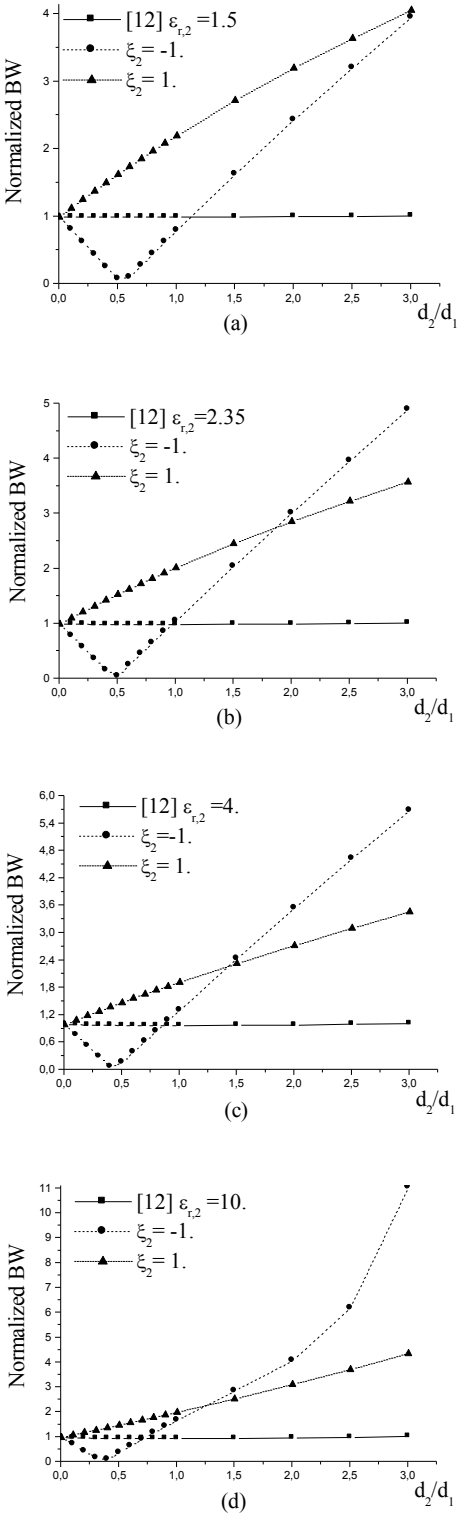

Figure 4: The chirality effect of a superstrate on the normalized bandwidth; a=6 cm, b=5 cm, d_1=0.1 cm, $\varepsilon_{r,1}$=2.35, (a) $\varepsilon_{r,2}$=1.5, (b) $\varepsilon_{r,2}$=2.35, (c) $\varepsilon_{r,2}$=4, (d) $\varepsilon_{r,2}$=10.

III.2. imaginary resonant frequency:

The chirality effect on the imaginary resonant frequency remains always the same for the real resonant frequency, except that it is more

important than on the real frequency, the normalized frequency multiple by 3 for a positive and multiple chirality by 6 in some case.

III.3. bandwidth:

The effect of the negative chirality element is more important on the band-width, because of its increase the 600% reach, and the value also cancelled the band-width, makes chiral medium adequate for the realization of resonator to conceive the antennas or the filters.

IV. CONCLUSION

The effect of the superstrate chirality on the resonance frequency and bandwidth has been studied using the integral equation formulation. Fast numerical convergence is obtained using sinusoidal basis functions to expand the current on the patch. Theoretical results for the resonant frequency and bandwidth have been presented for various constitutive parameters configurations.

V. REFERENCE

[1] N. G. Alexopoulos and D. R. Jackson, "Fundamental superstrate cover effects on printed circuit antennas," IEEE Trans. Antennas Propagat., vol. AP-32, pp. 807-816, Aug. 1984.

[2] V. Losada, R. R. Boix, and M. Horno, "Full-Wave Analysis of Circular Microstrip Resonators in Multilayered Media Containing Uniaxial Anisotropic Dielectrics Magnetized Ferrites, and Chiral Materials, Trans.On Microwave Theory And Techniques, VOL. 48, NO. 6, June 2000, pp 1057-1164

[3] J. T. Bernhard and C. J. Tousignant, "Resonant frequencies of rectangular microstrip antennas with flush and spaced dielectric superstrates", IEEE Trans. Antennas Propagat., vol. 47, pp. 302-308, Feb.1999.

[4] V. Losada, R. R. Boix, and M. Horno, "Resonant modes of circular microstrip patches in multilayered substrates", IEEE Trans. Microwave Theory Tech., vol. 47, pp. 488-498, Apr. 1999.

[5] F. Bouttout, F. Benabdelaziz, T. Fortaki and D. Khedrouche, "Resonant frequency and bandwidth of a superstrate-loaded rectangular patch on a uniaxial anisotropic substrate", Communications in Numerical Methods in Engineering, vol. 16, issue : 7, pp. 459-473, July 2000.

[6] D. Pozar, "Radiation and Scattering from a Microstrip Patch on a Uniaxial Substrate", IEEE Trans. Antennas Propagat., vol AP-35, NO. 6, pp. 613-617, June 1987

[7] C. Zebiri, M. Lashab, and F. Benabdelaziz, "Effect of anisotropic magneto-chirality on the characteristics of a microstrip resonator", IET Microwaves, Antennas & Propagation, 2010 , 4, (4), pp. 446-452.

[8] R. M. Nelson, D. Rogers, and A. G. D'Assuncao, "Resonant frequency of a rectangular microstrip patch on several uniaxial substrates", IEEE Trans. Antennas Propagat., vol. 38, pp. 973-981, July 1990.

[9] F. Bouttout, F. Benabdelaziz, A. Benghalia, D. Khedrouche and T. Fortaki, "Uniaxially anisotropic substrate effects on resonance of rectangular microstrip patch antenna", Electronics Letters, vol. 35, No. 4, pp. 255-256, 18 Feb. 1999.

[10] K. L. Wong, J. S. Row, C. W. Kuo, and K. C. Huang, "Resonance of a rectangular microstrip patch on a uniaxial substrate", IEEE Trans. Microwave Theory Tech., vol MTT-41, pp. 698-701, April 1993.

[11] I. J. Bahl, P. Bhartia, and S. S. Stuchly, "Design of microstrip antennas covered with a dielectric layer", IEEE Trans. Antennas Propagat., vol. AP-30, pp. 314-318, Mar. 1982.

[12] C. Zebiri, M. Lashab and F. Benabdelaziz, "Resonant frequency of a Microstrip Antenna on a Uniaxial Electric Superstrate", Mediterranean Microwave Symposium, MMS2009, November 15-17, 2009 - Tangiers, Morocco.

[13] W. C. Chew and T. M. Habashy, "The use of vector transforms in solving some electromagnetic scattering problems", IEEE Trans. Antennas Propagat., vol. AP-34, pp. 871-879.

[14] N. Engheta: The theory of chirostrip antennas'. Proceedings of the 1988 URSI International Radio Science Symposium, June 1988, Syracuse, New York, p. 213.

[15] N. Engheta, p. Pelet, reduction of surface waves in chlrostrlp antennas, indexing terms. Microstrip, antennas, 10th october 1990.

[16] K. W. Whites C. and Y. Chsu g," Composite Uniaxial Bianisotropic Chiral Materials Characterization," *J. Elaclromogn. Appl.,* flight. 11, pp. 311-394, 1997.

[17] Filiberto Bilotti and Lucio Vegni,"Radiation and Scattering Features of Patch antennas With bianisotropic Substrates", *IEEE trans. antennas propagat.*, Vol. 51, No. 3, pp. 449-456, March 2003.

[18] V. Dmitriev, "Tables of the Second Rank Constitutive Tensors for Linear Homogeneous media described by the point magnetic groups of symmetry", *Progress In Electromagnetics Research*, *PIER 28, 43–95, 2000.*

[19] E. H. Newman and D. Forrai, 'Scattering from a microstrip patch,' *IEEE Trans. Antennas Propagat.,* AP-35(3), 245-251, March 1987.

Analytical approach for CRLH based antennas design

Aïta Thior[1,2], Anne-Claire Lepage[1], Xavier Begaud[1], Olivier Maas[2]

[1]Institut Telecom, Telecom ParisTech - LTCI CNRS UMR 5141
46 rue Barrault 75634 Paris Cedex 13, France
[2]THALES Air Systems Business Line Surface Radar
Hameau de Roussigny 91470 Limours, France
*aita.thior@telecom-paristech.fr

Abstract

This paper presents an analytical model for CRLH (Composite Right-Left Handed) antennas preliminary design. The objective of this work is to develop a tool to estimate quickly the scattering and radiating characteristics of these CRLH based structures. The analytical model provides thus a set of parameters which roughly fulfill desired requirements. Afterwards, the antenna designer can refine the CRLH based antenna performances with full 3D electromagnetic simulation software.

1. Introduction

Composite Right-Left Handed (CRLH) radiating structures are very attractive antennas because of their scanning capability and wideband performances. These structures are generally periodic and present multiple resonances. In addition, when interdigital capacitors are used in the unit cell implementation, the small gap between digits requires fine meshing in the electromagnetic simulation. This could lead to very long simulation duration. In order to obtain a first design very quickly, an analytical model describing the electromagnetic behavior of these structures would be useful. The model can be used to realize antennas composed by CRLH unit cells by exploiting their radiation properties. Only based on the electromagnetic properties of the CRLH radiating structure, this model can estimate S-parameters and radiation performances of the whole antenna. To validate the analytical model, a meander antenna is designed with two branches composed by CRLH radiating structures. First of all S-parameters and radiations patterns of a linear CRLH radiating structure are presented. Afterwards the analytical model is detailed. And finally this model is used to predict S-parameters and radiations patterns of the CRLH based meander antenna.

2. Linear CRLH radiating structure

A CRLH structure is an artificial periodic transmission line structure. The CRLH unit cell used in this paper is a microstrip structure composed by an interdigital capacitor and a via-shorted stub [1] (figure 1).

The CRLH unit cell is printed on a Rogers Duroid RT5880 substrate (ε_r=2.2, tanδ=0.0009). Geometrical parameters of the cell are given in Table I.

Table 1: CRLH unit cell parameters

Variables	Length (mm)
Interdigital finger length	10.2
Interdigital finger width	0.3
Gap between fingers	0.3
Stub length	10.9
Stub width	1
Via radius	0.25
Substrate thickness	1.57

The CRLH unit cell has an infinitesimal length$(p \ll \lambda_g)$, where λg is the guided wavelength. Thus the CRLH unit cell can be characterized by an equivalent circuit model based on LC parameters of a transmission line (figure 2). For the ideal case, the interdigital capacitor of CRLH unit cell is synthesized by series capacitance C_L and series inductance L_R, while the stub inductor is a shunt inductor L_L and a capacitance C_R.

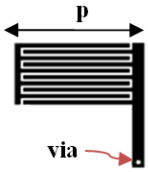

Figure 1: CRLH unit cell

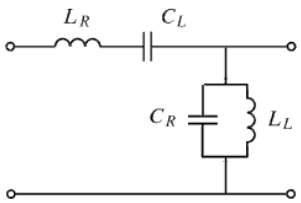

Figure2: Equivalent circuit model of a CRLH unit cell

Open waveguides or transmission lines act as a leaky-wave antenna if their dispersion diagram crosses the radiation cone. Radiation cone is the region delimited by the condition $-k_0 < \beta < k_0$, (k_0 is the free space propagation constant). The propagation constant β and the attenuation constant α of a CRLH structure, of a total length l, can be calculated from its transmission coefficient.

$$S_{21} = |S_{21}|e^{j.arg(S_{21})} = e^{-\alpha l}e^{-j\beta l} \quad (1)$$

The scan angle θ_0 of a CRLH leaky-wave antenna can be determined by the propagation constant β [2]:

$$\theta_0 = \sin^{-1}\left[\frac{\beta_{CRLH}(f)}{k_0(f)}\right] \quad (2)$$

Interdigital capacitors used in the CRLH unit cell implementation require fine meshing in the electromagnetic simulation and then very long simulation duration. In order to describe the leaky-wave behavior of the CRLH structure, an analytical model can be advantageously used.

2.1. Analytical approach for 1D CRLH leaky-wave antenna

To describe radiation patterns of the CRLH based antenna, an estimation of the electromagnetic properties of the linear CRLH radiating structure is needed. Different analytical approaches have been proposed to predict radiation patterns of CRLH leaky-wave antenna [3], [4]. The first one, applied here, uses an array factor approach. Because the CRLH leaky-wave antenna is a 1D periodic structure so it can be described as an antenna array where each antenna is represented by a CRLH unit cell. The spacing between antennas of the array is the length of the CRLH unit cell.

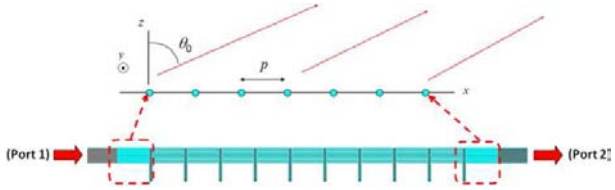

Figure 3: Array approach of a CRLH leaky-wave antenna

Due to its small length, the radiation pattern of the CRLH unit cell seems to be quasi isotropic. Nevertheless, electromagnetic simulations show that radiation patterns of the CRLH unit cell R_{UC} exhibit a maximum in broadside and minima at θ=±90°. This electromagnetic behavior looks like cos (θ). In order to improve the evaluation of the minima of the radiation patterns, a 0.5 factor is added in the description of the CRLH unit cell radiation patterns:

$$R_{UC}(\theta,\varphi) = \cos(0.5 * \theta) \quad (3)$$

Each CRLH unit cell is fed with an amplitude function $\mathbf{I_m}$ and a phase function $\boldsymbol{\chi_m}$.

$$I_m = I_0 e^{-\alpha m p} \quad (4)$$

$$\chi_m = -mk_0 p \sin\theta_0 = -m\beta_{CRLH}p \quad (5)$$

p is the CRLH unit cell length
α is the leakage factor of the CRLH structure
β is the propagation constant of the CRLH structure
m is the location of each CRLH unit cell in the linear CRLH radiating structure
M is the total number of CRLH unit cells of the linear CRLH radiating structure

The array factor of the CRLH radiating structure is:

$$AF(\theta,\varphi) = \sum_{m=0}^{M-1} I_m e^{jm(k_0 p \sin\theta\cos\varphi+\chi)} \quad (6)$$

$$AF(\theta,\varphi) = \sum_{m=0}^{M-1} I_m e^{jm(k_0 p \sin\theta\cos\varphi-k_0 p\sin\theta_0)} \quad (7)$$

The radiation pattern of the CRLH leaky-wave antenna can then be estimated by this analytical expression:

$$R(\theta,\varphi) = R_{UC}(\theta,\varphi) * AF(\theta,\varphi) \quad (8)$$

$$R(\theta,\varphi) = \cos(0.5*\theta) * \sum_{m=0}^{M-1} I_m e^{jm(k_0 p\sin\theta\cos\varphi-k_0 p\sin\theta_0)} \quad (9)$$

2.2. Validation of the 1D analytical approach

A CRLH leaky-wave antenna composed by 16 cells (Fig.4) is simulated with the TLM (Transmission Line Matrix) solver of CST Microwave Studio®. The CRLH unit cell has identical geometrical parameters than those presented on Table 1. However via shorted stubs are alternated in order to reduce cross-polarization level in radiation patterns [5].

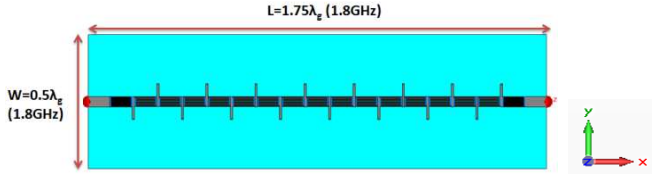

Figure 4: CRLH leaky-wave antenna with 16 cells

Full-wave simulation gives S-parameters of the CRLH antenna. Dispersion diagram is obtained from the phase of the transmission coefficient (Eq.1).

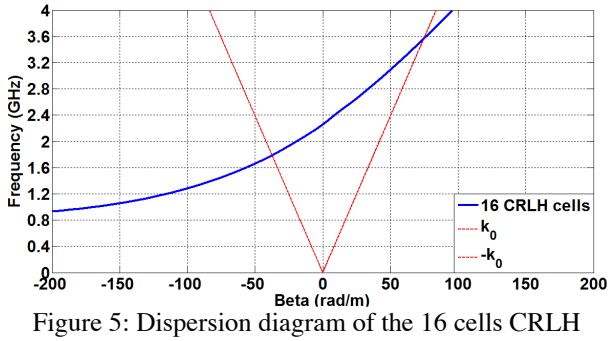

Figure 5: Dispersion diagram of the 16 cells CRLH leaky-wave antenna

Figure 5 shows that the CRLH leaky-wave bandwidth appears to be from 1.75 GHz to 3.6 GHz, with a zeroth order resonance (β=0) at 2.3 GHz.

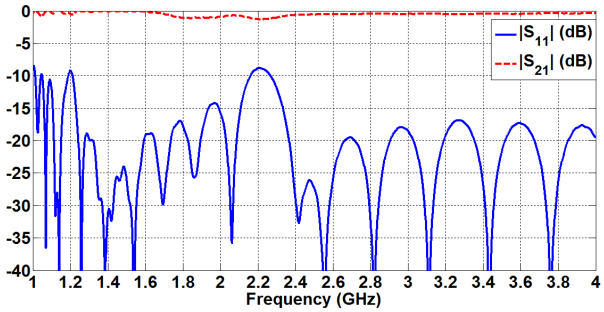

Figure 6: Simulated reflection and transmission coefficients of the 16 cells CRLH leaky-wave antenna

The return loss and the transmission coefficient of the CRLH antenna are presented in figure 6. The return loss of the CRLH antenna is less than -15dB from 1GHz to 4 GHz. However, close to the zeroth order resonance (2.3 GHz) from 2.2 GHz to 2.4 GHz, it goes around -7dB. This mismatching is due to the high variation of the input impedance around the zeroth order resonance. The transmission coefficient varies from -1 dB to -0.6 dB in the leaky-wave band (1.75-3.6 GHz). The radiation efficiency of the CRLH antenna can be calculated from S-parameters:

$$Radiation\ efficiency(\%) = 1 - |S_{11}|^2 - |S_{21}|^2 \quad (10)$$

Then S-parameters show that the radiation efficiency of the 16 cells CRLH leaky-wave antenna is approximately 20%.
In figure 7and figure 8, simulated radiation patterns are compared to those obtained with the 1D analytical model described above.
Radiation patterns synthesized by the analytical model illustrate well the scanning capability of the CRLH leaky-wave antenna. The direction of the main lobe and the HPBW are well estimated by the analytical model for the three frequencies presented in figure 7.Simulations exhibit in the (xOz) plane at least a difference of -13dB between co-polarization and cross-polarization. The HPBW is also well approximated in the (yOz) plane, but there are some level differences. Indeed the analytical model supposes that the CRLH leaky-wave antenna accepted power is all radiated on the polarization plane (xOz).

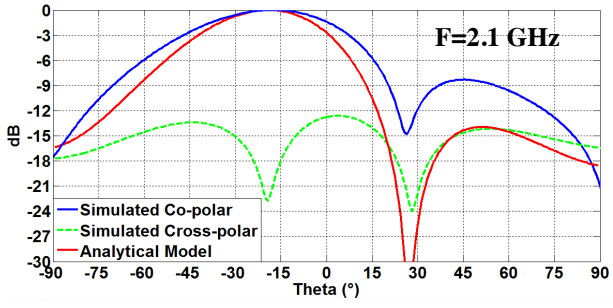

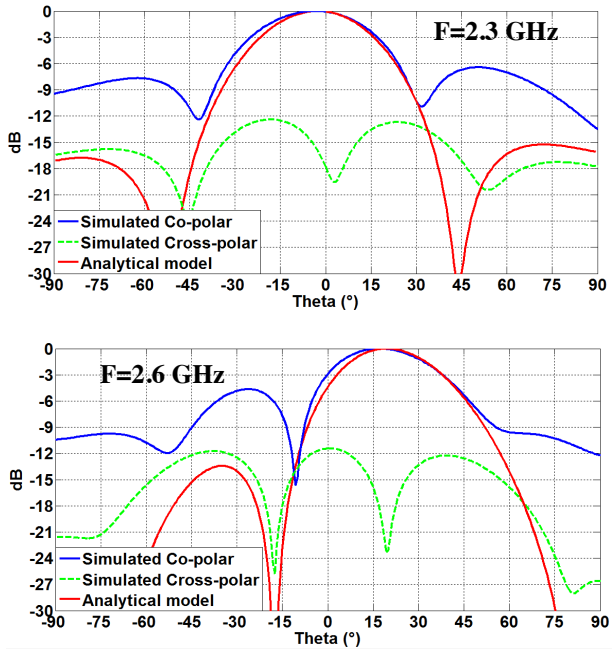

Figure 7: Radiation patterns of the 16 cells CRLH leaky-wave antenna in (xOz) plane (φ=0°)

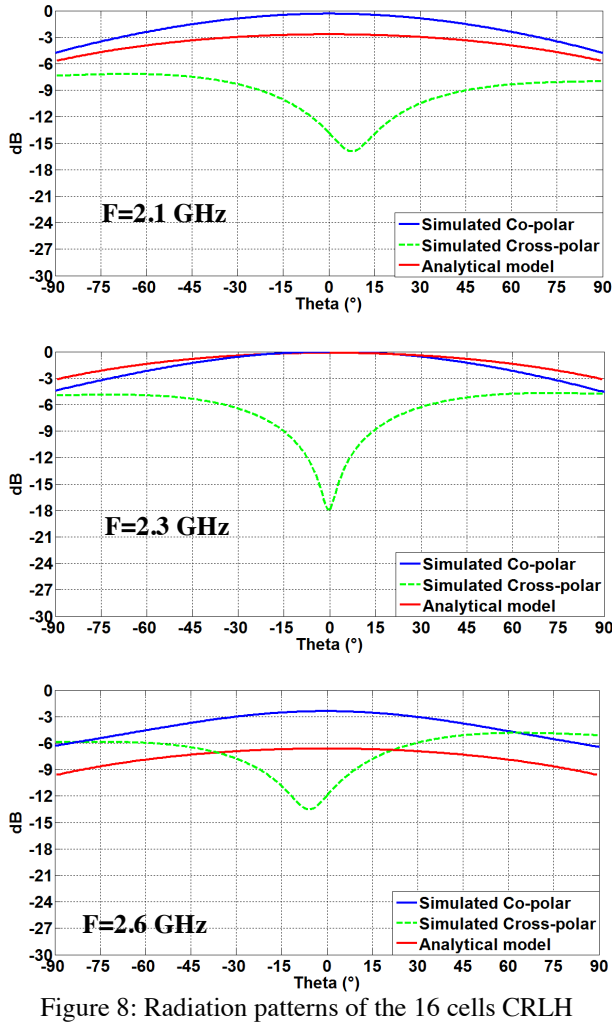

Figure 8: Radiation patterns of the 16 cells CRLH leaky-wave antenna in (yOz) plane (φ=90°)

3. CRLH based antennas

CRLH radiating structures can be used to design innovate antennas. The objective is to use the model based on electromagnetic properties of CRLH radiating structures to predict radiation patterns of the whole antenna.
The proposed CRLH based antenna has a shape of a meander line in which two CRLH structures are horizontal branches connected with microstrip bends as shown in figure 9. The linear CRLH leaky-wave antenna, composed of M cells, presented above is used to construct this CRLH based antenna. For this antenna, a 2D analytical model is developed.

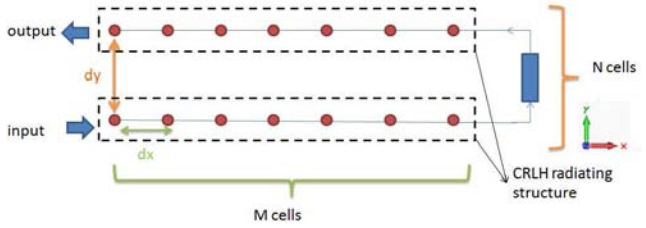

Figure 9: Array approach of the CRLH based meander antenna

3.1. Prediction of the S-parameters of the CRLH based meander antenna

The ABCD matrix of the complete antenna is calculated by cascading ABCD matrix of each branch of the meander antenna.

$$\begin{bmatrix} A & B \\ C & D \end{bmatrix}_{\substack{meander \\ antenna}} = \begin{bmatrix} A & B \\ C & D \end{bmatrix}_{CRLH_1} * \begin{bmatrix} A & B \\ C & D \end{bmatrix}_{\mu strip} * \begin{bmatrix} A & B \\ C & D \end{bmatrix}_{CRLH_2} \quad (11)$$

S-parameters of the meander antenna are then obtained from the ABCD matrix [6] by using equations (11) to (14), where Z_0 is the characteristic impedance of the CRLH structure.

$$A = \frac{(1+S_{11})(1-S_{22})+(S_{12}S_{21})}{2*S_{21}} \quad (12)$$

$$B = Z_0.\frac{(1+S_{11})(1+S_{22})-(S_{12}S_{21})}{2*S_{21}} \quad (13)$$

$$C = \frac{1}{Z_0}.\frac{(1-S_{11})(1-S_{22})-(S_{12}S_{21})}{2*S_{21}} \quad (14)$$

$$D = \frac{(1-S_{11})(1+S_{22})+(S_{12}S_{21})}{2*S_{21}} \quad (15)$$

The meander antenna is made of two identical CRLH radiating structures, so only S-parameters of the CRLH radiating structure and microstrip bends length are needed to calculate S-parameters of the whole antenna.

3.2. Prediction of radiation patterns of the CRLH based meander antenna with an analytical model

The CRLH based meander antenna is considered as a 2D array antenna, where each antenna is a CRLH unit cell. Each unit cell is identified by its location on (Ox) and (Oy) axis respectively by *dx* and *dy*.

For the 1st CRLH radiating structure, each *m* CRLH unit cell is fed with an amplitude function I_m^1 and phase amplitudeχ_m^1. χ_m^1 is, for each CRLH unit cell of the 1st line, the phase delay introduced by previous CRLH unit cells.

$$I_m^1 = I_0 e^{-\alpha m dx} \quad \text{and} \quad \chi_m^1 = -(\beta * m * dx) \quad (16)$$

So the array factor of the first CRLH radiating structure is:

$$AF_{CRLH1}(\theta,\varphi) = \sum_{m=0}^{M-1} I_m^1 e^{j\left((k_0*m*dx*sin\,\theta*cos\,\varphi)+\chi_m^1\right)} \quad (17)$$

For the 2nd CRLH line, each *m* CRLH unit cell is fed with an amplitude function I_m^2 and a phase function χ_m^2. χ_m^2 is the sum of the total phase delay introduced by the 1st CRLH line, the phase delay set by CRLH unit cells preceding this considered cell and the phase delay introduced by microstrip bends connecting the 1st and 2nd CRLH lines.

$$I_m^2 = I_0 e^{-\alpha*\left((M-1)*dx)+m*dx\right)} \quad (18)$$

$$\chi_m^2 = -\left((\beta*(M-1)*dx)+(\beta*(M-1-m)*dx)\right)+\delta \quad (19)$$

δ is the phase delay introduced by microstrip bends connecting the two CRLH radiating structures.
Then the array factor of the 2nd CRLH radiating structure is:

$$AF_{CRLH2}(\theta,\varphi) = \sum_{m=0}^{M-1} I_m^2 e^{j\left((k_0*(m*dx*sin\,\theta*cos\,\varphi)+(dy*\sin\theta*\sin\varphi))+\chi_m^2\right)} \quad (20)$$

The radiation pattern R(θ,φ) of the meander antenna is then obtained by a summation of radiation patterns of each CRLH radiating structure which are determined by the product of the single CRLH unit cell $R_{UC}(\theta,\varphi)$ and its array factor $AF_{CRLH1,2}$ (Equ.21). CRLH unit cells that are in the same CRLH radiating structure have the same polarization vector (p_1=1). However CRLH unit cells of the 2nd CRLH structure are polarized oppositely to those of the 1st one.

$$R(\theta,\varphi) = R_{UC}(\theta,\varphi) * p_1 * \left(AF_{CRLH1}(\theta,\varphi) - AF_{CRLH2}(\theta,\varphi)\right) \quad (21)$$

3.3. Validation of the analytical model

To validate prediction of the radiation patterns obtained with the analytical model presented above, a CRLH based meander antenna is simulated. The meander antenna is realized with two linear CRLH radiating structures. Each CRLH structure has 15 cells.

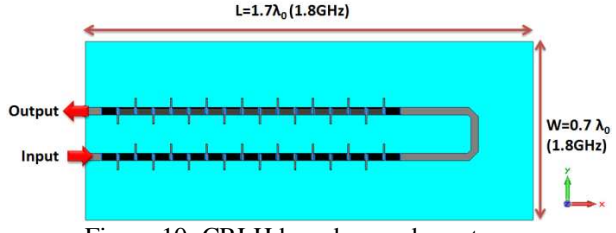

Figure 10: CRLH based meander antenna

Full-wave simulation of the CRLH based meander antenna is performed with the TLM (Transmission Line Matrix) solver of CST Microwave Studio®.
S-parameters obtained with the model by cascading chain matrixes of each element of the meander antenna (Eq.11) are compared with simulated S-parameters in figure 11.

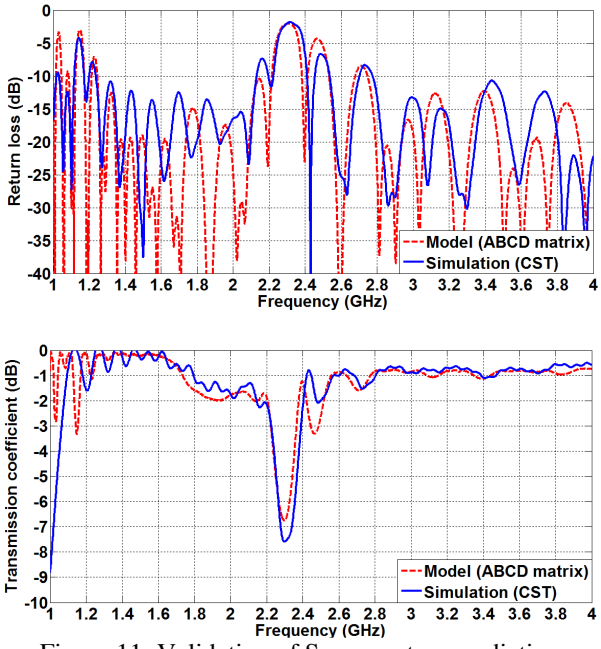

Figure 11: Validation of S-parameters prediction

Fig.11 exhibits a frequency shift of about 80MHz between simulation and model. The maximum difference between simulated and analytic transmission coefficients is about 0.7dB, while it is 5dB between simulated and analytic reflection coefficients. These dissimilarities can be explained by the cascade of the chain matrix of the different CRLH unit cells (in the analytical model), which does not take into account the coupling between CRLH unit cells.
The CRLH based meander antenna exhibits a good impedance matching ($|S_{11}|$<-10dB) from 1.5 GHz to 4 GHz, except around the zeroth order resonance like for the CRLH linear 16 cells presented above.
The radiation efficiency of the CRLH based antenna is calculated from S-parameters (Eq.10). Simulated and analytical S-parameters show that the maximum radiation efficiency of the CRLH based meander antenna is 25% at f=1.9 GHz. This radiation efficiency can be improved with a higher number of CRLH radiating structures.
Radiation patterns obtained with the analytical model are compared to the simulated results (Fig.12 and Fig.13). To validate the results obtained with the analytical model, three frequencies are chosen: f=1.9GHz (β<0), f=2.4GHz (β=0) and f=2.6 GHz (β>0). HPBW of the different radiation patterns are well estimated by the analytical model. We note a good agreement between simulation and analytical model especially in the (xOz) plane (φ=0°). Indeed in the model it is supposed that the antenna accepted power is all radiated in the (xOz) plane. That is why there are some discrepancies between simulation and model in the (yOz) plane.

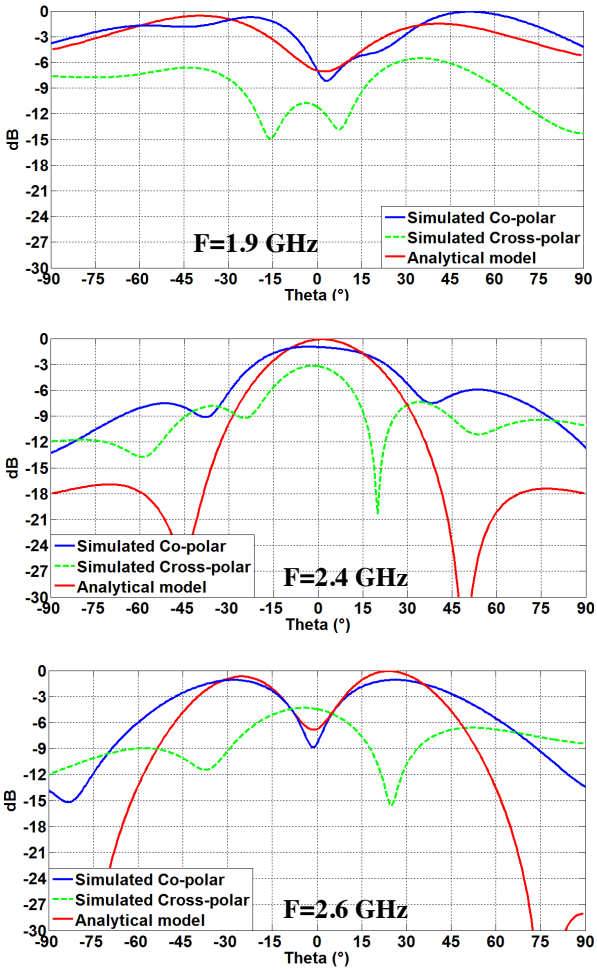

Figure 12: Radiation patterns of the CRLH based meander antenna in (xOz) plane (φ=0°)

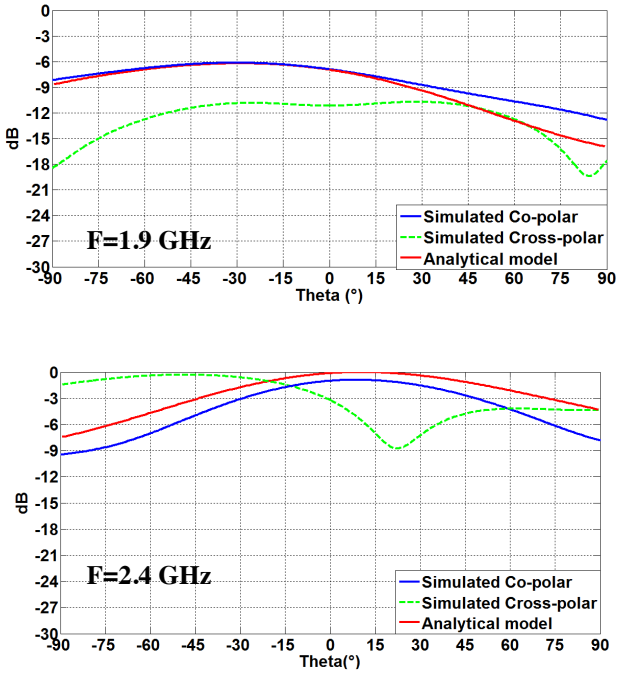

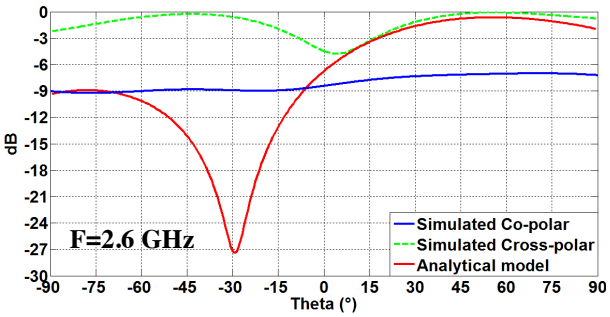

Figure 13: Radiation patterns of the CRLH based meander antenna in (yOz) plane (φ=90°)

The CRLH based meander antenna exhibits interesting behaviors. It has radiation patterns with large HPBW at the limit frequencies of the leaky wave bandwidth and when we approach the zeroth order resonance the HPBW of the main lobe is reduced. By adjusting appropriately the microstrip bends connecting the CRLH radiating structures of the meander antenna, radiation patterns of the whole antenna can be altered. We can obtain a main lobe more or less directive in broadside or another direction. In the other hand we can obtain radiation patterns with a high HPBW >±60°, and a maximum level at broadside more than -3dB. This last case would be very interesting compared to classical antenna arrays which provide a maximal HPBW of ±60°.

4. Conclusions

CRLH based antennas are designed by connecting CRLH radiating structures. An analytical model has been proposed to predict quickly their performance whatever the geometry of the complete antenna is. This model uses electromagnetic properties of the single CRLH radiating structure. Results obtained with full 3D electromagnetic simulation software prove the validity of the analytical model. This model is very useful because it provides rapidly performances of the CRLH based antenna while full 3D simulation software take long simulation duration (more than 3 days for a CRLH based meander antenna of 15 cells instead of 1 minute with the model). Thus the model can now be used to find the adequate geometry of the CRLH based antenna in order to have a desired radiation pattern.

References

[1] L. Liu,C. Caloz, T. Itoh, "Dominant mode leaky-wave antenna with backfire-toendfire scanning capability," *Electronics Letters,* vol. 38, 2002.

[2] A.Oliner, "Leaky-wave antennas" in *Antenna Engineering Handbook*, Third Edition, edited by R.C. Johnson, McGraw Hill, 1993.

[3] C. Caloz and T. Itoh, "Array Factor Approach of Leaky-Wave Antennas and Application to 1-D/2-D Composite Right/Left-Handed (CRLH) Structures", *IEEE Microwave and Wireless Components Letters*, Vol. 14, No. 6, June 2004.

[4] Z. Li, J. Wang, F. Li, "Prediction of radiation patterns of the CRLH leaky-wave antennas by different approaches", *IEEE International Conference on Microwave Technology & Computational Electromagnetics (ICMTCE),* Juin 2011.

[5] Francisco P. Casares-Miranda, Carlos Camacho-Peñalosa, and Christophe Caloz, "Active composite right/left-handed leaky-wave antennas", *IEEE Antennas and Propagation Society* , 2006.

[6] C. A. Balanis, Antenna Theory, 2nd edition, New York, Wiley 1997.

Periodic anti-Reflective Layer Design for the Thin Film Solar Cell using the Topology Optimization Procedure

Hyun-Jun Soh[1] and Jeonghoon Yoo[2*]

[1]Graduate School of Mechanical Engineering, Yonsei University, Seoul, Korea
[2] School of Mechanical Engineering, Yonsei University, Seoul, Korea
*corresponding author, E-mail: yoojh@yonsei.ac.kr

Abstract

The random textured surface or the patterned surface such as the pyramid or wedge shaped texture is commonly applied on the layer boundary between the silicon layer and the transparent conducting oxide (TCO) layer for the purpose of enhancing the sunlight absorbing efficiency of thin film solar cell. In order to obtain the high sunlight absorbing efficiency for the thin film solar cell, this study will suggest the design study to obtain the modified shape of the surface texture having the improved wave absorbing efficiency and topology optimization design method with time dependent finite element analysis is employed. The wave propagation is represented as the Maxwell's equation and is solved in time domain. The triangle patterned textured surface is considered as the initial shape of two-dimensional (2D) wave analysis and the periodic boundary condition is applied to save the computing time. The design objective is set to maximize the energy flux in time period at wave absorbing boundary and the objective function is calculated as the time integration of Poynting vector formulation. The design sensitivity for optimization is computed using the adjoint variable method and is also performed in time integrated calculation. Multiple layered design of silicon and TCO layers is obtained as the optimal shape of wave absorbing boundary pattern.

1. Introduction

Thin film solar cell is multi layered system and wave reflection losses are occurred at the layer boundaries such as interface of TCO and silicon layer. In order to obtain the high efficiency solar cell, the surface textures are employed [1-4]. Pyramid shaped texture, and groove patterned grating is generally used in absorbing layer boundary [5-7]. Haase *et al* considered the pyramid shaped front TCO and back TCO, and responses according to the open angle of the pyramid are compared. [6] Dewan *et al* showed the efficiency comparison according to the groove height and periodic size [7]. They supposed the specific texture pattern as the high efficiency absorbing boundary and the design study is restricted in initial design. This research shows design study suggestion having the design freedom for the surface texture of the thin film solar cell. Peculiarities of this study are using the finite element analysis of time dependent wave propagation and topology optimization design method.

Topology optimization is the material layout design method and it can be applied various physical field, such as elastic, thermal, acoustic, and electromagnetic field [8, 9]. It can be applied on not only just stationary problem but also dynamic field or time varying field problem [10-14]. Jensen *et al* obtained optimal topology in the wave field [10], and Matzen *et al* applied on the photonic crystal design problem [14]. This study aims to design of the wave absorbing structure for the thin film solar cell, and the wavelength of 700nm is considered as the incident wave condition. Maxwell's equation in time varying field is solved using finite element analysis program COMSOL and periodic boundary condition is applied to save the computation time due to the time integration calculation [11-13].

This study proposes absorbing layer boundary design in time dependent wave analysis condition for the purpose of reflection wave reduction and penetration wave enhancement. Numerical calculation is performed with 2D finite element models and the model used for analysis and design is illustrated in Fig. 1. Periodic boundary condition is applied at the left and right side [15]. The design domain set on the TCO layer and triangle shape is considered as the initial TCO shape. The measuring domain for objective function calculation and design sensitivity calculation is located under the design domain and the objective function is defined as the translated energy flux efficiency. The time integration calculation is applied on the objective function and design sensitivity analysis. The solid isotropic material and penalization method is used in design variable definition of topology optimization.

2. Analysis Model

2.1. Finite element model

The analysis model of thin film solar cell is illustrated in Fig. 1 and it is a multi-layered system of air, TCO layer and silicon layer. Since the periodic condition is applied, the periodic width of the initial surface texture is modeled and 600nm of periodic width is considered. The thickness of the silicon layer and the TCO layer are set to 1000nm and 900nm, respectively. The design domain is set on the TCO

layer and the width and the height of the design domain are 600nm and 900nm, respectively. The number of design domain elements is set to 300×450. The initial surface texture of absorbing layer is shaped as a triangle and 600nm of the periodic texture width and 300 nm of the triangle height are considered.

The measuring domain for objective function is set on the location under the TCO layer and the wave penetrated into the TCO layer and absorbed in the silicon layer is calculated in the domain.

2.2. Wave analysis

In the time-varying field, the optical wave propagation can be represented by the electric and magnetic wave formulation. In this wave analysis, the TM polarized electromagnetic wave mode is considered and it can be expressed using Maxwell's equation.

$$\nabla \cdot \frac{1}{\varepsilon_r} \nabla \mathbf{H} = \frac{1}{c_0^2} \frac{\partial^2}{\partial t^2} \mathbf{H} \tag{1}$$

where ε_r is the material property of optical media and it is the relative value of electric permittivity. It can be also expressed as n^2 and n means the refractive index. With 700nm wavelength, which is the specified value in this study, the refractive index values of Si and TCO are 3.7412+j0.0131 and 1.9736, respectively and Zinc-Oxide (ZnO) is selected as TCO material. **H** is the magnetic field vector and c_0 represents the wave speed of light in the vacuum.

In this study, 2D x and y plane wave propagation is considered and only z-directional field strength H_z is expressed. In the 2D system, the propagation wave can be written as follows.

$$\frac{\partial}{\partial x}\left(\frac{1}{\varepsilon_r}\frac{\partial}{\partial x}H_z\right) + \frac{\partial}{\partial y}\left(\frac{1}{\varepsilon_r}\frac{\partial}{\partial y}H_z\right) = \frac{1}{c^2}\frac{\partial^2}{\partial t^2}H_z \tag{2}$$

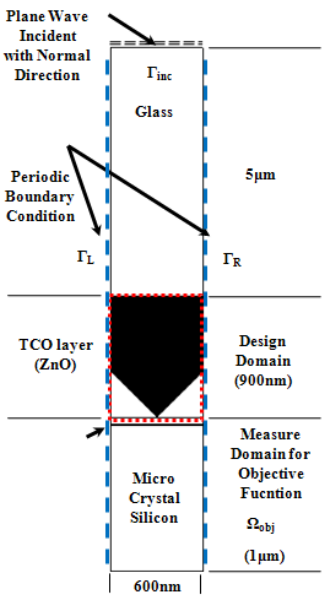

Figure 1: Schematic diagram of the analysis model.

2.3. Load and boundary Condition

In the incident wave boundary, the Sommerfeld radiation condition is applied. The incident wave is excited at the air boundary end and a single wave frequency is considered in this analysis. The load condition of incident wave can be written as follows.

$$\frac{1}{\varepsilon_r}\frac{\partial H_z}{\partial_x} + \frac{1}{\varepsilon_r}\frac{\partial H_z}{\partial_y} = j\frac{\omega}{c}(H_z - jH_z^{inc}) \tag{3}$$

where H_z^{inc} is the field strength amplitude of incident wave and the imaginary symbol of j is employed to match the phase of wave.

In the boundary condition of this analysis model, the periodic boundary condition is applied to reduce the model size and to save the computation time during the iterative analysis. The periodic boundary condition is employed in the left and right side of the analysis model and it can be written as follows.

$$H_z\left(x|\Gamma_L, y\right) = H_z\left(x|\Gamma_R, y\right) \tag{4}$$

In the electromagnetic wave field and the optical field, the energy flux which can be expressed by the Poynting vector formulation is generally used. Since the wave flows to the y-direction only, the Poynting vector formulation can be written as follows.

$$S = \mathrm{Re}\left[\frac{1}{j\omega\varepsilon_0\varepsilon_r}\left(\frac{\partial H_z}{\partial x}H_z^*\right) + \frac{1}{j\omega\varepsilon_0\varepsilon_r}\left(\frac{\partial H_z}{\partial y}H_z^*\right)\right] \tag{5}$$

3. Optimization

3.1. Topology optimization

Topology optimization is the structural design method to obtain the optimal layout of material distribution. The optimal layout is originally represented by void or solid filled condition of the material in each element in the design domain and it can be expressed to define the value of design variable to 0 or 1 in the numerical optimization problem. In cased of the two phase material problem, the problem can be changed to find out the material distribution of two materials χ_0 and χ_1 and the definition of material condition can be expressed as follows

$$\rho = \begin{cases} 0 \text{ in the media } \chi_0 \\ 1 \text{ in the media } \chi_1 \end{cases} \tag{6}$$

However, the virtual property of material, which represents the intermediate media condition, is necessary in order to avoid the discontinuity of χ_0 and χ_1 and in this case the design variable has the value between 0 and 1. The property in design domain is expressed as the proportional function of density parameter and it can be written as follows.

$$\chi(\rho) = \rho^P \chi_0 + \left(1 - \rho^P\right)\chi_1 \tag{7}$$

The density parameter ρ is the design variable in the topology optimization design problem and penalization parameter p is used for good convergence of density parameter to void or filled condition.

In the optical wave problem, the refractive index n is used for the design material. Since the design layout of surface texture or absorbing layer is on the TCO and Si, the design material can be written as follows.

$$n(\rho) = \rho^P n_{TCO}^{'} + (1-\rho^P) n_{Si}^{'} + i(\rho^P n_{TCO}^{''} + (1-\rho^P) n_{Si}^{''}) \quad (8)$$

3.2. Design Objective

The goal of the optimization problem is to obtain layout design of the absorbing layer in order to maximize the wave flux to penetrate into the TCO layer. The Poynting vector formulation is written in equation (5). In the time harmonic wave field, the Poynting vector is calculated as the time average form such as $<S>=0.5S$. However, the time integrated Poynting vector is calculated in this study, since Poynting vector history in time domain is considered. Thus, the time integrating formulations of the Poynting vector in measuring domain and in incident boundary are expressed as follows.

$$\Phi_{obj} = \int_{t_0}^{t_1}\int_{\Omega} S d\Omega d\tau \Big/ A \text{ in measuring domain} \quad (9)$$

$$\Phi_{inc} = \int_{t_0}^{t_1}\int_{\Gamma} S d\Gamma d\tau \Big/ L \text{ in incident boundary} \quad (10)$$

where Ω and Γ are the measuring domain and the incident boundary, respectively, and t_0, and t_1 are the time start and time end for time integration. A and L are the area of the measuring domain and the width of the incident boundary, respectively.

The objective function is defined as the energy flux efficiency η.

$$Maximize\ \eta = \frac{\Phi_{obj}}{\Phi_{inc}}, \quad (11)$$

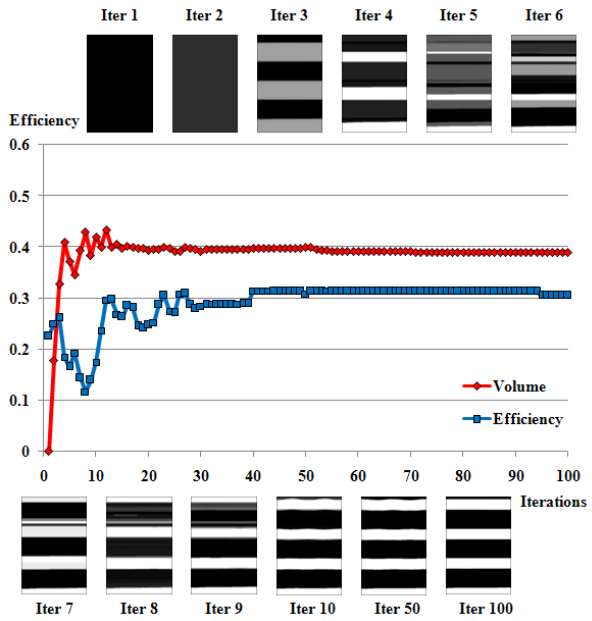

(a)

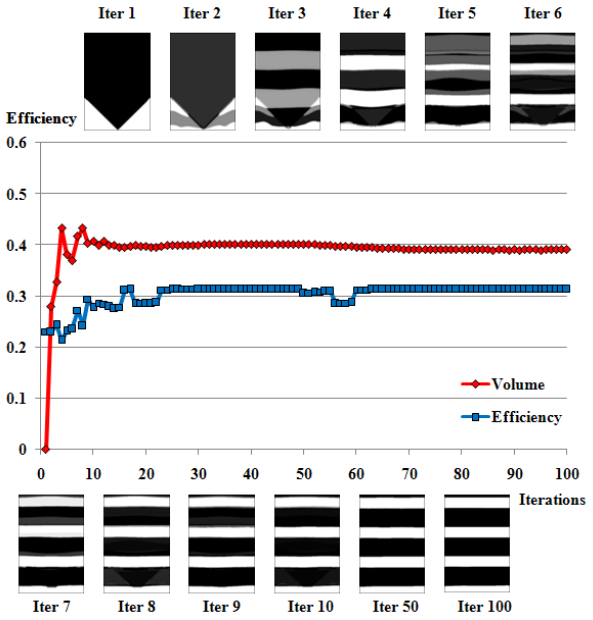

(b)

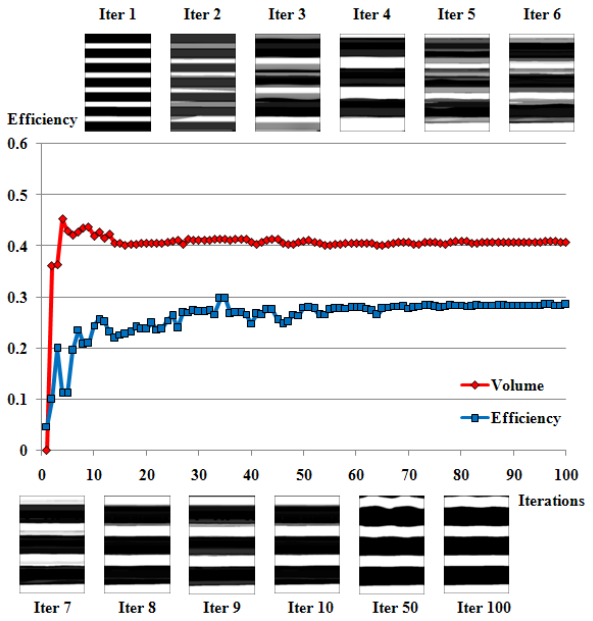

(c)

Figure 2: Convergence history of volume and objective function and its layer shape changes according to various initial conditions as (a) full TCO (b) wedge (c) multi layer.

4. Numerical Result

4.1. Topology Optimization Result

Topology optimization results are dependent on the initial condition of material distribution in general because the local optimum is found after the topology optimization design process. Three cases of initial conditions are considered in this study. First case is the full-TCO case and the whole design domain is filled with the TCO materials.

Second one is the wedge shaped texture generally considered as the anti-reflection boundary shape. The last case is the multi-layered shape and the thickness of each initial layers are determined from the anti-reflection coating thickness as $nd = \lambda/4$.

The volume and objective function convergence history and the layer shape history of the TCO/Si boundary layer resulted from the optimization process are displayed in Fig. 2 according to various initial conditions. The black domain represents the TCO layer and the white domain displays the Si layer. On the proceeding of optimization, it can be confirmed that the shape of TCO/Si boundary layer is converged to stacked layers of flat surface regardless of the initial conditions.

The average thickness of TCO layer ranges from 174 to 174.7nm and the range of Si is 96.7nm. It can be confirmed that the values converged to *1/n(λ/2)* values of TCO and Si, which are 177nm and 94nm, respectively. Thickness values are listed in Table 1 and the obtained shapes of result by topology optimization are compared in Fig.3. As can be confirmed in absorbing efficiency histories displayed in Fig. 2, every case shows improved performance compared with that of the wedge shaped initial model.

Table 1: Thickness values of the layered structure.

Thickness	Full TCO	Wedge	Multi Layer	1/n(λ/2)
d0	26	26	10	
d1	96	96	98	
d2	176	176	170	
d3	96	96	96	
d4	172	172	176	
d5	98	98	96	
d6	176	174	178	
Average TCO	174.7	174.0	174.7	177
Average Si	96.7	96.7	96.7	94

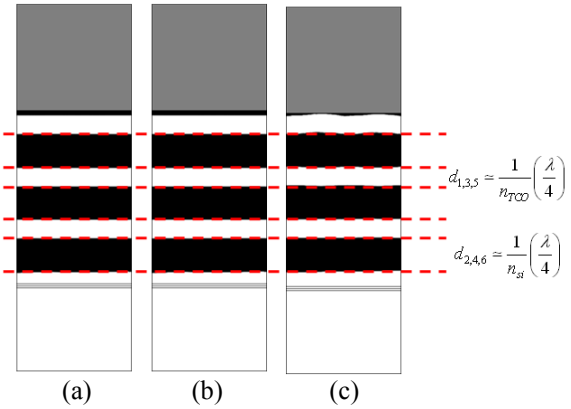

Figure 3: Layer thickness comparison of optimal results according to various initial conditions as (a) full TCO (b) wedge (c) multi layer.

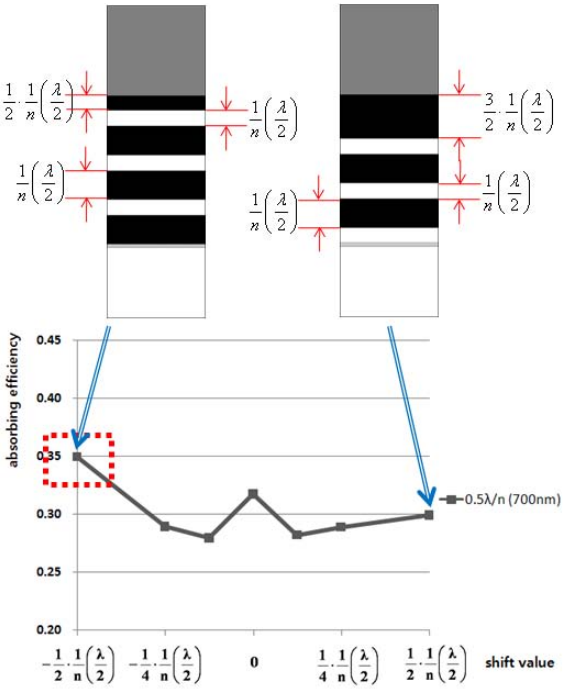

Figure 4: Wave absorbing efficiency comparison according to the design parameter variation.

4.2. Parameter study

In every case of the optimization procedure, the stacked layer is obtained as a result of topology optimization and the layer thickness is converged to the value of *1/n(λ/2)* except the first layer of TCO material. In order to find out the optimal thickness of the first TCO layer, a parameter study is performed. The default value of the first TCO layer is set to *1/n(λ/2)* and the parameter variation is defined to the 0.5~1.5 ratio of the default thickness.

The comparison plot of the wave absorbing efficiency is listed in Fig 4 and the *1/n(λ/4)* thickness case shows the maximum value of wave absorbing efficiency of 0.349. Therefore, the *1/n(λ/2)* thickness multi layered model with *1/n(λ/4)* thickness first TCO layered case can be optimal design for the purpose of maximizing the wave absorbing efficiency.

5. Conclusion

This study suggest a half wavelength thickness stacked layer model with quarter wavelength thickness TCO top layer on the TCO/Si boundary layer, to obtain highly efficient thin film solar cells. For layer structure design, it is confirmed that topology optimization combined with the time dependent finite element analysis and the time integrated design objective is effective. Regardless of the initial condition, a similar layered structure is obtained.

The important outcome of this study is to suggest a systematic design process for the structure which shows the improved wave absorbing performance for the specific wavelength of 700nm. For the future study, a design process for a specified wavelength range needs to be supplemented.

Acknowledgements

This work was supported by the National Research Foundation of Korea (NRF) grant funded by the Korea government (MEST) (No. 2011-0017512).

References

1. J. Müller, B. Rech, J. Springer and M. Vanecek, "TCO and light trapping in silicon thin film solar cells", *Sol. Energy*, 77 : 917–930, 2004.
2. J. Selvan, A.Delahoy, S. Guo and Y. Li, "A new light trapping TCO for nc-Si:H solar cells", *Solar Energy Mater. Sol. Cells*, 90 : 3371–3376, 2006.
3. J. Springer, A. Poruba, L. Müllerova and M. Vanecek, "Absorption loss at nanorough silver back reflector of thin-film silicon solar cells", *J. Appl. Phys.*, 95: 1427-1429, 2004.
4. J. Springer, B. Rech, W. Reetz, J. Müller and M. Vanecek, "Light trapping and optical losses in microcrystalline silicon pin solar cells deposited on surface-textured glass/ZnO substrates", *Sol. Energy Mater. Sol. Cells*, 85: 1–11, 2005.
5. P. Campbell and M. Green, "Light trapping properties of pyramidally textured surfaces", *J. Appl. Phys.*, 62: 243-249, 1987.
6. C. Haase and H. Stiebig, "Thin-film silicon solar cells with efficient periodic light trapping texture", *Appl. Phys. Lett.*, 91 : 061116, 2007.
7. R. Dewan and D. Knipp, "Light trapping in thin-film silicon solar cells with integrated diffraction grating", *J. Appl. Phys.* 106 : 74901,2009.
8. M. P. Bendsøe and N. Kikuchi, "Generating optimal topologies in optimal design using a homogenization method", *Comput. Method Appl. Mech. Engrg.*, 71: 197–224, 1988.
9. M. P. Bendsøe and O. Sigmund, "Material interpolation schemes in topology optimization", *Arch. Appl. Mech.*, 69 : 635-654, 1999.
10. J. S. Jensen and O. Sigmund, "Systematic design of photonic crystal structures using topology optimization: Low-loss waveguide bends", *Appl. Phys. Lett.*, 84: 2022–2024, 2004.
11. J. Dahl, J. S. Jensen and O. Sigmund, "Topology optimization for transient wave propagation problems in one dimension", *Struct. Multidisc. Optim.*, 36 : 585–595, 2008.
12. J. S. Jensen, "Space–time topology optimization for one-dimensional wave propagation", *Comput. Methods Appl. Mech. Engrg.*, 198 : 705-715, 2009.
13. J. S. Jensen, "Optimization of space-time material layout for 1D wave propagation with varying mass and stiffness parameters", *Control and Cybernetics*, 39: 599-614, 2010.
14. R. Matzen, J. S. Jensen and O. Sigmund, "Topology optimization for transient response of photonic crystal structures", *J. Opt. Soc. Am. B*, 27 : 2040-2050, 2010.
15. T. Nomura, S. Nishiwaki, K. Sato and K. Hirayama, "Topology optimization for the design of periodic microstructures composed of electromagnetic materials", *Finite Elements in Analysis and Design*, 45: 210-226, 2009.

Design of low loss meta-material coplanar waveguides on silicon for millimetre frequency applications.

Daniel Decle Colin [1] **and Zhirun Hu** [2]

Microwaves and Communication System Group,
University of Manchester, Manchester, United Kingdom
daniel.declecolin@postgrad.manchester.ac.uk [1] z.hu@manchester.ac.uk [2]

Abstract

The performance of monolithic microwave and millimeter wave integrated circuits (MMIC) built on silicon substrates is highly deteriorated for the losses due to the low resistivity of the modern Si-CMOS process. Furthermore, at the millimetre range of frequencies, the conductor losses due to the skin effect in the metal interconnections (which are enhanced due to the comparable dimensions of the metal layers of modern submicrometer Si-CMOS technology and the skin depth), reduce even more the overall performance of the Si-MMIC in terms of losses.

In this paper a new shielded coplanar waveguide designed in a 90nm Si-CMOS technology is presented, the design and optimization procedure are shown. The novelty of this new structure is its ability to reduce the losses caused not only for the substrate losses, but also the conductor losses. The shield of the coplanar waveguide is built using the metallization layers available for the technology. The analysis and design of the new structures is performed using the 3D EM finite element simulations. The results achieved show a loss reduction up to 40% compared to the normal coplanar waveguides.

1. Introduction

The design of current microwave and millimeter wave wireless communication systems has been largely dominated by the III-V compounds. The reason behind the domain of the III-V technologies is due to their better raw performance compared to other technologies. However the III-V compounds have important disadvantages in terms of cost, integration level and power consumption. As consequence of that, important limitations are imposed in the design wireless communication systems making them expensive, complex and with high power consumption.

On the other side, the recent advances of the submicrometer Si-CMOS process, has allowed the MOS transistor to reach maximum oscillation frequencies f_{max} in the order of hundred of GHz making the Si-CMOS process an interesting option for the development of low cost, high integrated and low power communication systems. However, some crucial issues must be addressed before to think in the Si-CMOS as the best option for the development of high frequency wireless communication systems. In this sense, the losses due to the low resistivity of the silicon substrates and the conductor losses due to the skin effect at high frequencies, has been recognized as the main limitation of the technology.

Many approaches has been proposed to reduce the losses of transmission lines built on Silicon substrates. In [1] [2] new materials are introduced to the Si-CMOS process in order to reduce the losses, however the insertion of different materials to the Si-CMOS technology, alter the manufacturing process making the new substrate more complex and with lower integration level. Another important approach is the development of shields using the metallization layers provided by the Si-CMOS technology [3] [5] [6] [7]. However most of them are focused in the reduction of the losses introduced by the substrate letting aside the metallization losses caused by the skin effect at high frequencies.

In this paper, is developed a new structure aimed to reduce the losses caused by the low resistivity of the substrate and the limited conductivity of the metal interconnections due to the skin effect. The new full floating shield avoids the interaction of the electromagnetic fields with the substrate reducing in this way the losses caused by the low resistivity of the silicon. Moreover, the new structure induces a better current distribution in the transmission line, maximizing the conductive capabilities of the line which in turns reduce the conductor losses. The paper is composed as follows: Section II provides a brief introduction of the main loss mechanisms and describe the development of the new shield structure, section III explain the characterization criteria used to evaluate the new structure, in section, in section IV are presented the final results finally in section V a conclusion is provided.

2. Development of low loss CPW structures.

The way in which a electromagnetic wave propagates is dependent of the characteristics of the propagation media. In this sense, the best way to describe the propagation characteristics of a wave is using the complex propagation constant described in Equation (1).

$$\gamma = \sqrt{\alpha + j\beta} \tag{1}$$

Where α describes the losses of the electromagnetic wave. The main source of losses in coplanar waveguides are the losses caused by the limited conductivity of the met-

allization layers and the losses caused by the low resistivity substrate, thus the losses can be described as Equation (2).

$$\alpha = \alpha_{cond} + \alpha_{subs} \tag{2}$$

Both loss mechanisms are frequency dependent, however, they behave in a totally different way, the approach followed to reduce their effects must take into consideration that behaviour, the loss mechanisms of the structure are described next.

2.1. Substrate losses.

The substrate losses are caused by the interaction of the electromagnetic fields to the substrate. This kind of losses can be divided as the losses due to the conductivity of the substrate, and the losses caused by the polarization of the substrate. The losses due to the conductivity of the substrate are not dependent on the frequency, however the losses caused by the polarization of the substrate has a strong frequency dependence as explained in [8]. Different approaches can be found to reduce the interaction between the electromagnetic fields of the transmission lines and the substrate as shown in [3] [5] [6] [7]. One approach followed to use a ground plane placed at the bottom of the substrate [9]. Another approach is to build a shield using the interconnection layers provide by the technology. The shield built can be grounded as shown in [6] or floating as depicted in [5] being this approach the most suitable for high frequency applications due to the advantages that a floating shield provide.

2.2. Conductive losses.

At high frequencies the losses due to the limited conductivity of the metallization layers are increased due to the reduction of the skin depth. The skin depth can be described as Equation (3):

$$\delta = \frac{1}{\sqrt{\pi \cdot \sigma \cdot \mu \cdot f}} \tag{3}$$

Added to the skin effect, the improper distribution of the current density reduces the conductive capabilities of the transmission line. In [4] a new approach aimed to produce a better distribution of the current density of the CPW is proposed. The structure proposed by [4] a grounded shield is built using the interconnection layers of the technology which is aimed to produce a better distribution of the current density increasing the capabilities of the transmission line. Taking the main advantages of the structures proposed by [4] and [5] new structure proposed and is shown in Figure 1. One important characteristic of this structure is that is fully floating structure.

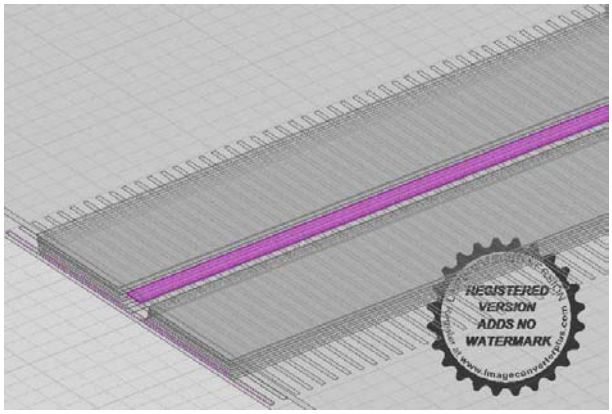

Figure 1: Structure Proposed.

The structure is designed to have a periodic shield that avoids the interaction of the electromagnetic field and the substrate, added to this, a second shield is designed above the periodic shield that reduces even more the interaction of the electromagnetic fields and the substrate as can be seen in Figure 2.

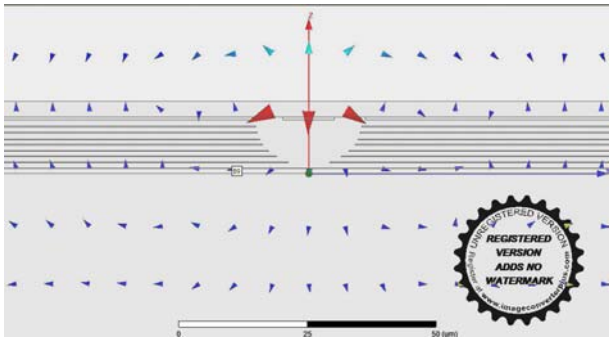

Figure 2: Field distribution of the structure proposed.

The second shield improves the current distribution of the transmission line maximizing the conductive properties of the transmission line. An map of the electromagnetic fields distribution of the conventional CPW is shown in Figure 3

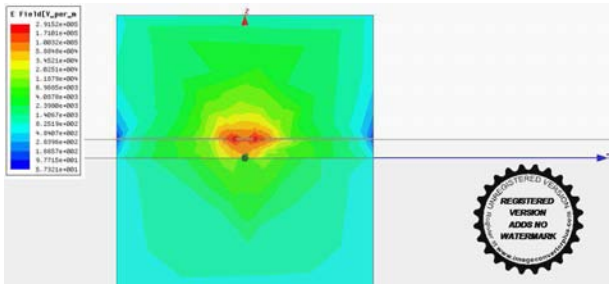

Figure 3: Electromagnetic fields of the CPW.

The electromagnetic fields of the structure proposed are shown in the Figure 4

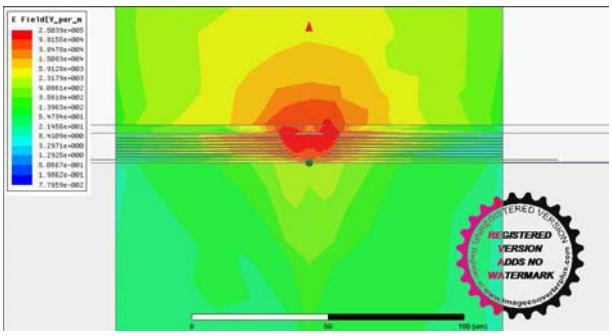

Figure 4: Electromagnetic fields of the structure proposed.

From the results shown, is clear the increased performance of the structure proposed compared to the conventional CPW.

3. Characterization of the new structure.

The characterization of the structures is performed following the approach of [10] where a methodology for extracting the components of transmission lines from the S-parameters, is developed. The relevance of this approach is the link between the physics of the wave characteristics and the S-parameters Equation (4).

$$\gamma = \frac{\ln\left(\frac{1-S_{11}^2+S_{21}^2}{2S_{21}} \pm K\right)}{l} \tag{4}$$

where K is described by Equation (5)

$$K = \sqrt{\frac{(S_{11}^2 - S_{21}^2 + 1)^2 - (2S_{11})^2}{(2S_{21})^2}} \tag{5}$$

Even though in [10] this methodology is demonstrated up to 20 GHz, in [12] and in [13] this methodology is used up to 120GHz. A second approach to characterize the losses in CPW is presented by [11] as Equation (6)

$$Dissipation = 10\log_{10}\frac{1-|S_{11}|^2}{|S_{21}|^2} \tag{6}$$

4. Results.

The performance in terms of losses of the transmission line proposed compared to the conventional CPW [14], finite grounded CPW [9] floating shield CPW [5] and stacked CPW [4] are shown in Figure 5. All the structures were built using the same dimensions.

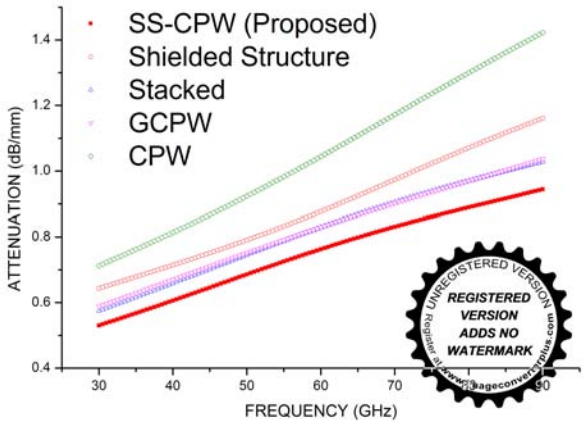

Figure 5: Attenuation Comparision.

The matching characteristics are shown in Figure 6

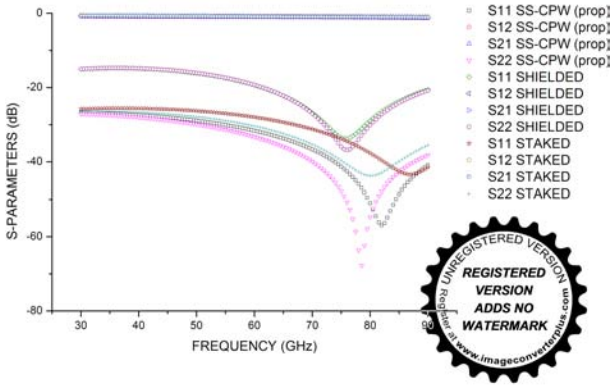

Figure 6: S parameters comparision.

As can be seen, the structure proposed reaches a loss reduction in the order of 40% and an increased performance in terms of matching.

5. Conclusions

A new full floating structure is proposed which effectively reduce the substrate losses and the conductive losses. The new structure uses the metallization layers provided by the modern Si-CMOS technology. The main advantage of this approach is that the process is not affected allowing to keep the advantages in terms of integration level and low cost. An improvement around of 40% in terms of losses is achieved in comparison to conventional coplanar waveguide CPW.

References

[1] Ponchak, George E.; RF Transmission Lines on Silicon Substrates, Microwave Conference, 1999. 29th European , vol.1, no., pp.158-161,Oct. 1999

[2] Wu, Y.H.; Chin, A.; Shih, K.H.; Wu, C.C.; Liao, C.P.; Pai, S.C.; Chi, C.C.; , RF loss and crosstalk on extremely high resistivity (10 k-1 MOcm) Si fabricated

by ion implantation, Microwave Symposium Digest. 2000 IEEE MTT-S International , vol.1, no., pp.221-224 vol.1, 2000

[3] Cheung, T.S.D.; Long, J.R.; , Shielded passive devices for silicon-based monolithic microwave and millimeter-wave integrated circuits, Solid- State Circuits, IEEE Journal of , vol.41, no.5, pp. 1183- 1200, May 2006

[4] Jaewon Kim; Byunghoo Jung; Cheung, P.; Harjani, R.; , Novel CMOS low-loss transmission line structure, Radio and Wireless Conference, 2004 IEEE , vol., no., pp. 235- 238, 19-22 Sept. 2004

[5] Hsiu-Ying Cho; Tzu-Jin Yeh; Liu, S.; Chung-Yu Wu; , High- Performance Slow-Wave Transmission Lines With Optimized Slot-Type Floating Shields, Electron Devices, IEEE Transactions on , vol.56, no.8, pp.1705-1711, Aug. 2009

[6] Sayag, A.; Ritter, D.; Goren, D.; , Compact Modeling and Comparative Analysis of Silicon-Chip Slow-Wave Transmission Lines With Slotted Bottom Metal Ground Planes, Microwave Theory and Techniques, IEEE Transactions on , vol.57, no.4, pp.840-847, April 2009

[7] Varonen, M.; Karkkainen, M.; Kantanen, M.; Halonen, K.; , Millimeter- Wave Integrated Circuits in 65-nm CMOS, Solid-State Circuits, IEEE Journal of , vol.43, no.9, pp.1991-2002, Sept. 2008

[8] C. J. F. Bottcher and P. Bordewijk; , Theory of electric polarization, Elsevier scientific publishing company, vol.2, 1978.

[9] Ching-Cheng Tien; Tzuang, C.-K.C.; Peng, S.T.; Chung-Chi Chang; , Transmission characteristics of finite-width conductor-backed coplanar waveguide, Microwave Theory and Techniques, IEEE Transactions on , vol.41, no.9, pp.1616-1624, Sep 1993

[10] Eisenstadt, W.R.; Eo, Y.; , S-parameter-based IC interconnect transmission line characterization, Components, Hybrids, and Manufacturing Technology, IEEE Transactions on , vol.15, no.4, pp.483-490, Aug 1992

[11] Fusco, V F; Hu, Z R; Wu, Y; Gamble, H G; Armstrong, B M; Stewart, J A C; , Silicon interconnects for millimetre wave circuits, Microwave Conference, 1995. 25th European , vol.1, no., pp.467-469, 4-4 Sept. 1995

[12] Jinglin Shi; Kai Kang; Yong Zhong Xiong; Fujiang Lin; , Investigation of CMOS on-chip transmission lines CPW, SCPW and CPWG up to 110GHz, Radio-Frequency Integration Technology, 2009. RFIT 2009. IEEE International Symposium on , vol., no., pp.269-272, Jan. 9 2009- Dec. 11 2009

[13] Kai Kang; Brinkhoff, J.; Jinglin Shi; Fujiang Lin; , On-Chip Coupled Transmission Line Modeling for Millimeter-Wave Applications Using Four-Port Measurements, Advanced Packaging, IEEE Transactions on , vol.33, no.1, pp.153-159, Feb. 2010

[14] Wen, C.P.; , Coplanar Waveguide: A Surface Strip Transmission Line Suitable for Nonreciprocal Gyromagnetic Device Applications, Microwave Theory and Techniques, IEEE Transactions on , vol.17, no.12, pp. 1087- 1090, Dec 1969

Different configurations of metamaterials coupled with an RF coil for MRI Applications

M. S. KHENNOUCHE[1] *, F. GADOT[1], B. BELIER[1] and A. de LUSTRAC[1]

[1]IEF – University of Paris Sud, 91405 Orsay cedex, FRANCE
* corresponding author: mohand-said.khennouche@u-psud.fr

Abstract

In this paper the effect of coupling two kinds of metamaterial cells with a coil to achieve Magnetic Resonance Imaging (MRI) is investigated. Both an array of four spirals and a single spiral-shaped metamaterial are associated to the coil antenna. The goal is to increase the sensitivity of the whole system and to improve the homogeneity of the RF magnetic field pattern. The spiral-shaped metamaterials associated to the antenna give very promising numerical results. We are fabricating both structures using microfabrication techniques because of the small size of the structures.

1. Introduction

In Magnetic Resonance Imaging (MRI), the use of a small sized radio frequency surface coil allows to perform high resolution images with sufficient signal to noise ratio (SNR) [1]. However, the magnetic field generated decreases as it goes deeper in the human body. Moreover, the presence of samples with high permittivity and conductivity detunes the RF coil and decreases its quality factor. Nevertheless, associating a new material usually called metamaterial is becoming a rather interesting solution to improve the overall performance of the system. Indeed, the effective parameters of metamaterials are tunable and they could be either positive or negative [2]-[7]. The idea of placing a swiss-roll over an RF coil to act as a magnetic flux guide was successfully tested [8]-[9]. This metamaterial allowed receiving images from more distant samples. Furthermore, the resolution of the metamaterial based structure was higher. In our design, the metamaterials will be used to increase the sensitivity of small surface coil by both improving the RF magnetic field pattern and reducing losses and frequency shift resulting from dielectric coupling with the sample.

2. The design of the RF coil

The RF coil consists of two transmission lines (see figure 1) on both sides of a 0.5 μm thick LaAlO3 substrate with a permittivity of 23.6. The two parts of the antenna are diametrically opposite to one other. These transmission lines are equivalent to an inductance and the substrate placed between the copper strips behaves like a distributed capacitance. The space between every two adjacent turns is 150 μm and the copper strips are 150 μm wide either. The external diameter of each side of the antenna is 13.6mm. This coil (both sides together), which was designed on HFSS, is operating at the VHF band for high resolution MRI at 1.5 Tesla.

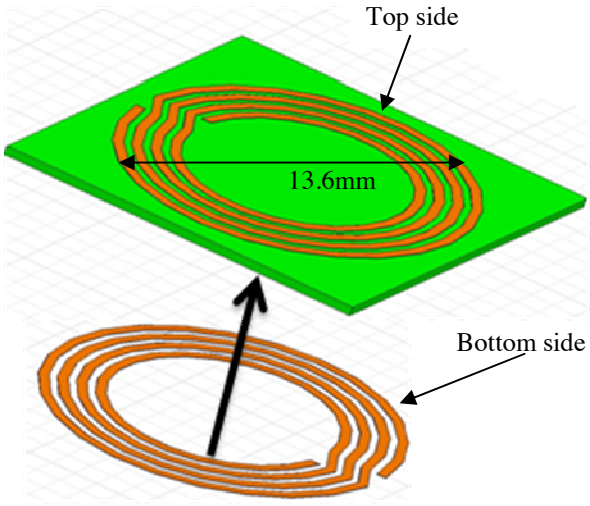

Figure 1: Detailed view of both sides of the coil antenna

Both sides of this antenna work together to maximize the magnitude of the magnetic field. The difference of 180° in the orientation of either coil makes that possible. The current in each coil generates constructive magnetic fields making it the best configuration.

This coil antenna generates a quite high magnetic field in its vicinity. However, the performance of this coil antenna needs to be improved for MRI technology. The magnetic field tends to weaken by a factor 9 or more, depending on the region of reference taken into consideration. Furthermore, one can notice on figure 2 that the magnetic field is not homogeneous near the RF coil.

One way to improve this RF coil antenna for MRI is the use of metamaterials. This periodic resonant material would

strengthen the magnetic field and would make it more homogeneous.

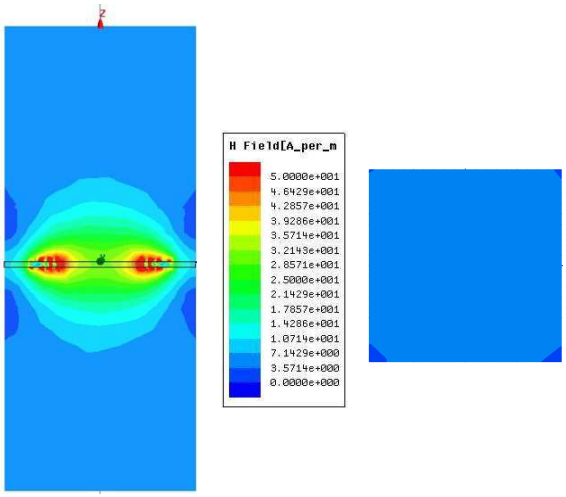

Figure 2: Side and bottom views (at 10 mm distance) of the magnitude of the magnetic field of the RF coil.

3. Metamaterials used with the RF coil

Metamaterial structures were associated to the coil antenna in order to form a new structure with a better performance. Indeed, the presence of metamaterials acts on the electromagnetic fields. In our case, we have chosen magnetic metamaterials in order to tailor the magnetic field generated by the coil antenna.

The coil antenna being $\lambda/100$ small, we need to use metamaterials with a comparable size. To obtain metamaterial structures as small as $\lambda/100$, we used metallic spiral resonators instead of the usual C-shaped resonators because the latter structure resonates at a frequency corresponding to just $\lambda/10$. Here, we present two different unit cells of metamaterials: two layers of a four-spiral array in which each spiral has 15 turns and two layers of a 25-turn spiral. The first unit cell is 18.6 mm wide and the latter is 15.3mm wide. Figure 3 and figure 4 show both types of metamaterials. The two layer metamaterials shown below are put on the top side of the coil antenna shown on figure 1.

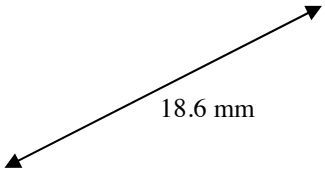

Figure 3: Two layers of four-spiral metamaterials with 15 turns in each spiral

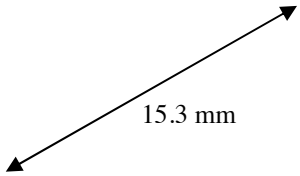

Figure 4: Two layers of 25-turn spirals forming the metamaterial

In the metamaterial structure on figure 3, the two layers are not identical as it is explicitly shown on figure 5. The two layers are actually symmetrical. In addition to that, in the same layer, the four spirals are not identically oriented either. They are arranged in such a way that the two spirals on the left are symmetrical to the two other spirals on the right. This symmetry in the same layer in combination with the symmetry between the two layers ensures the best interaction between each particle. In other words, by using this configuration we have the strongest magnetic field emanating from the whole structure.

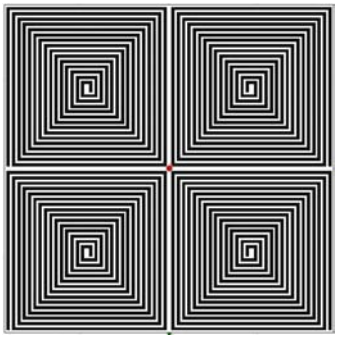

a)

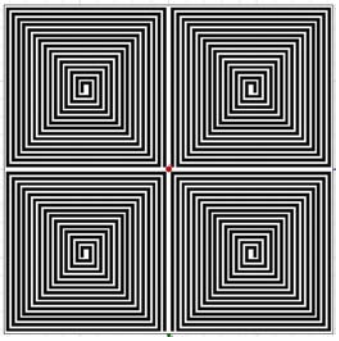

b)

Figure 5: First layer (a) and second layer (b) of a four-spiral metamaterial with15 turns in each spiral

The same statement holds for the metamaterial structure shown on figure 4: the two layers are not identical either. The two layers are symmetrical again. In other words, the second layer is rotated 180° around the axis that is orthogonal to the whole structure. This difference between the two layers is, just like what was mentioned in the last paragraph, aiming at making the magnetic field strongest.

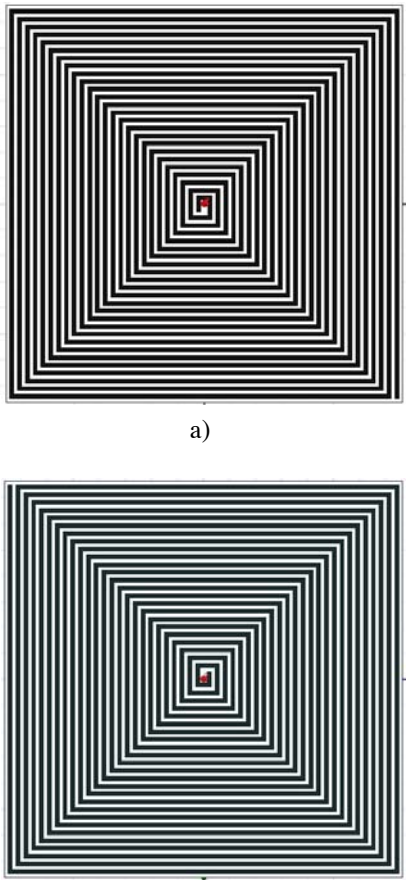

a)

b)

Figure 6: First layer (a) and second layer (b) of a 25 turn-spiral-shaped metamaterial

4. Numerical results

- **Case 1 : coil antenna associated to the first kind of metamaterials**

The next figure compares between the magnetic field calculated for the antenna alone (on the left) and the antenna associated to the two layer metamaterial previously shown on figure 3 (detailed views were given in figure 5). The difference can be easily seen because the calculations were made by considering exactly the same conditions.

Each value of the magnitude of the magnetic field is represented by a color. This color scale spans from dark blue to red. This represents magnitudes of the magnetic field going from 0.0000 A/m up to 50 A/m. Dark blue is assigned to smallest possible value and red is assigned to the highest value : 50A/m.

The bottom view of the magnetic field was picked up at a distance of 10 mm away from the bottom side of the antenna for having a reference. This allows us to see how the magnitude of the magnetic field decreases as the distance increases between the antenna and the sample. Moreover, it gives an overview of the homogeneity of the magnetic field at the considered distance.

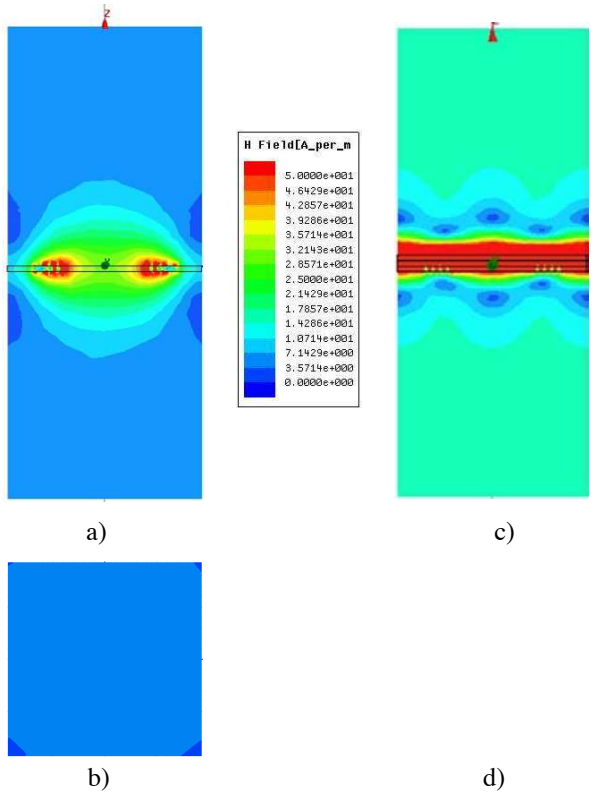

a) c)

b) d)

Figure 7: Side view (a) and bottom view (b) of the RF coil antenna without metamaterials versus side view (c) and bottom view (d) of the antenna with the first kind of metamaterials

If we refer to the scale given in middle, one can notice that both the bottom views and the side views of the magnetic field show that the metamaterial based structure give the best results. In the side view on the right (with metamaterials), the region exhibiting a maximum magnetic field (in red) is larger. Even in the farthest regions from the antenna the magnetic field is still increased by a factor of 4 at least.

The second feature we are interested in is field homogeneity. Both the side view and the bottom view (on the right) show that the magnetic field becomes more homogeneous when first kind of metamaterials is added to the RF coil antenna.

- **Case 2 : coil antenna associated to the second kind of metamaterials**

Similarly to figure 7, figure 8 summarizes the results of magnetic field magnitude calculations for the antenna alone (figure1) versus those obtained by adding the metamaterial structure introduced in figure 4. The figures on the left hand side represent the magnitude of the magnetic field of the coil antenna without metamaterials. The figures on the right hand side represent the magnitude of the magnetic field of the antenna after adding the second kind of metamaterial on the top of the coil antenna. The bottom views were picked up 10 mm away from the bottom side of the antenna for having the same reference as in previously calculated structures. Moreover, we use the same color scale and we consider exactly the same hypotheses to carry out the calculations. This allowed us to easily compare the results.

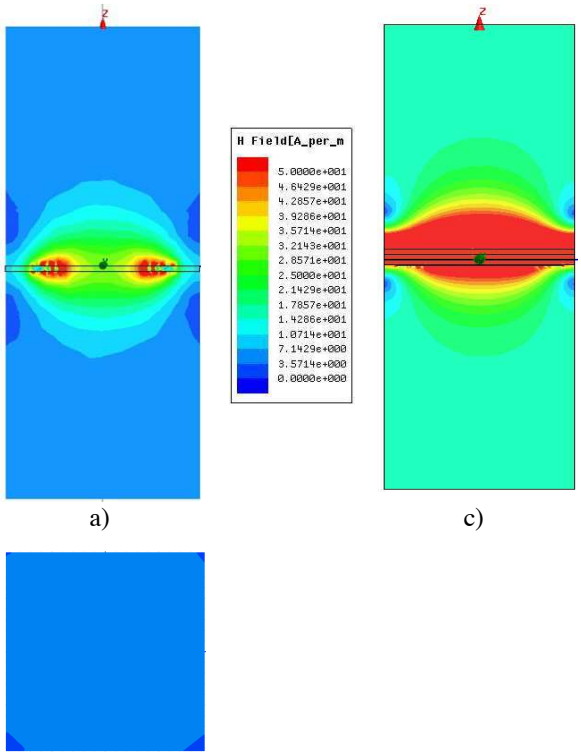

Figure 8: Side view (a) and bottom view (b) of the RF coil antenna without metamaterials versus side view (c) and bottom view (d) of the antenna with the second kind of metamaterials

The side view on the right has a larger area in red than in the side view on the left. This means the magnetic field reaches its maximum value in a larger area thanks to the second type of metamaterials added to the RF coil antenna. Furthermore, one can easily notice that the magnitude of the magnetic field of the coil antenna alone (in blue) is much weaker than that of the metamaterial based structure (in green). Actually, if we refer to the given the scale, one can see that the magnitude of the magnitude field was increased by a factor of 6.

As for the homogeneity criterion, it can be evaluated through the presence of the same value of the magnetic field around the considered structures. The side views give an overview of the evolution of the magnetic field as we move away from the structure of interest. However, it's easier to analyze the homogeneity of the magnetic field by considering just the bottom views. It can easily be seen that we obtain the same color on the whole plane-surface when metamaterials are added to the coil antenna. This means the metamaterials not only increase the value of the magnitude of the magnetic field, but they make it more homogeneous.

After having proven the benefits of adding the metamaterial structures (figures 3 and 4) to the coil antenna, practical results are needed to complete the study. We are fabricating all the structures presented in this paper. The fabrication process involves the use of microfabrication techniques due to the small size of the structures. This will be possible thanks to CTU IEF-MINERVE clean rooms and equipments.

In order to get as much data as possible, the structures will be fabricated by using the electrolytic deposition upon three different substrates: LaAlO3, Si and glass.

5. Conclusion

In this paper, an RF coil antenna was associated to two different kinds of metamaterials. The new structures give very interesting results for MRI because the magnetic fields become more homogeneous and 4 to 6 times stronger and even more in some regions. These successful results pave the way to the next step: fabrication and measurements. We are currently fabricating both particles on three different substrates: LaAlO3, Si and glass. This would give further proofs of the usefulness of using such structures in MRI technology.

References

[1] L. Darrasse L, J.-C. Ginefri, Perspectives with cryogenic RF probes in biomedical MRI, *Biochimie,* vol. 85, pp 915-937, 2003.

[2] V. G. Veselago, The electrodynamics of substances with simultaneously negative values of ε and μ , *Soviet Physics Uspekhi* ,vol. 10, pp 509-514,1968.

[3] D. R. Smith and Norman Kroll, Negative Refractive Index in Left-Handed Materials, *Physical Review Letters*, vol. 85, pp 2933-2936

[4] R. A. Shelby, D. R. Smith, S. Schultz, Experimental Verification of a Negative Index of Refraction, *Science*, vol. 292, pp 77-79, 2001.

[5] J.B. Pendry, A.J. Holden, W.J. Stewart, I. Youngs, Extremely Low Frequency Plasmons in Metallic Meso Structures, *Physical Review Letters,* vol. 76, pp 4773-4776, 1996.

[6] J.B. Pendry, A.J. Holden, D.J. Robbins, W.J. Stewart, Magnetism from Conductors and Enhanced Non-Linear Phenomena, *Microwave Theory and Techniques, IEEE Transactions*, vol. 47, pp 2075-2084, 1999.

[7] D. R. Smith, Willie J. Padilla, D. C. Vier, S. C. Nemat-Nasser and S. Schultz, Composite Medium with Simultaneously Negative Permeability and Permittivity, *Physical Review Letters*, vol. 84, pp 4184–4187, 2000.

[8] M. C. K. Wiltshire, J. B. Pendry, I. R. Young, D. J. Larkman, D. J. Gilderdale and J. V. Hajnal, Microstructured magnetic materials for RF flux guides in Magnetic Resonance Imaging, *Science*, vol. 291, pp 849-851, 2001.

[9] M. C. K. Wiltshire, J. V. Hajnal, J. B. Pendry, D. J. Edwards, and C. J. Stevens, Metamaterial endoscope for magnetic field transfer: near field imaging with magnetic wires, *Optics Express*, vol. 11, pp 709-715, 2003.

Proposal and Analysis of Artificial Dielectric Lens with Metallic Corrugated Structures for Terahertz Wave Band

Takuya Konno[1], Takahiro Suzuki[1], John C. Young[2], Mikio Saigusa[1]
Keisuke Takano[3], Hideaki Kitahara[3], Masanori Hangyo[3], and Takehito Suzuki[1*]

[1]Department of Electrical and Electronic Engineering,
Ibaraki University, 4-12-1 Nakanarusawa, Hitachi, Ibaraki 316-8511, Japan
[2]Electrical and Computer Engineering, University of Kentucky, Lexington, Kentucky 40506-0046, USA
[3]Institute of Laser Engineering, Osaka University, 2-6 Yamadaoka, Suita, Osaka 565-0871, Japan
*corresponding author, E-mail: takehito@mx.ibaraki.ac.jp

Abstract

Optical devices for the terahertz wave band are being developed now and require better designs. This paper proposes an artificial dielectric lens with metallic corrugated structures for the terahertz wave band. A periodic analysis model extracted from the full model by assuming periodicity confirms the phase delay, which produces the focusing effect. Full model analysis also confirms the focusing effect. The full model analysis also confirms that the focusing length is longer with the wider spacing of corrugated baffles, the wider metallic groove width, and the shallower groove depth. The lens shape without grooves does not produce the focusing effect. The results of the full model analysis are qualitatively consistent with those of the periodic model ones. This implies that the design for an exact size lens is possible by using the periodic model.

1. Introduction

Optical devices for the terahertz wave band ranging from 0.1 to 10 THz are now being developed and require better designs. It is not easy to arbitrarily realize a desired refractive index n using naturally-occurring materials. When materials are directly used for optical devices, the material properties themselves determine the optical characteristics. Typical lenses for the terahertz wave band are made of high density polymer, Tsurupica, and silicon with refractive indices of 1.52, 1.56, and 3.41, respectively. It is significant that the unit cell of the electromagnetic metamaterial controls the refractive index with respect to design flexibility and cost performance. Lenses composed of electromagnetic metamaterials, sphere arrays, disk arrays, square plate arrays, and strip arrays, have been proposed for microwave frequency band in [1]-[5]. These lenses produce focusing action due to the phase delay, slow wave effect. Lenses that make use of high phase velocity of propagation mode in a parallel plate have been proposed in [6]. The works in [7]-[10] present a metamaterial absorber, that in [11] presents an antireflection coating, that in [12] presents a metamaterial with an unnaturally high refractive index, and those in [13] and [14] present a three-dimensional metamaterial in the terahertz wave band. The effective permittivity and permeability of a metal slit array are derived and the proper refractive index is estimated as 1 in [15]. The work in [16] reports anomalies in a double-layered metallic slit. It is relatively easy to fabricate the terahertz electromagnetic metamaterial by metallic processing and chemical reduction on a film with thin metal [13], [14] when compared with a metamaterial in optical range because the dimensions of the unit element are on the order of tens of microns.

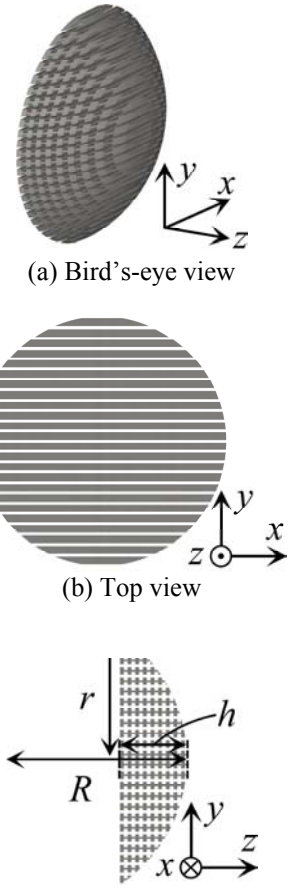

(a) Bird's-eye view

(b) Top view

(c) Side View

Figure 1: Lens with metal corrugated structure for terahertz wave band

This paper proposes an artificial dielectric lens with

metallic corrugated structures [17] and studies the focusing effect in the terahertz wave band. A periodic analysis model, extracted from the full model by assuming periodicity, confirms the phase delay used to estimate the focusing effect in the full model. Commercial EM simulators are now quite powerful but are still too heavy especially for the design optimization of a whole array. A lens with a large but finite and complicated unit cell array is generally cumbersome and challenging to design. The analysis and design using the periodic model is fast and effective for the iterative design procedure [18]. Results from the periodic model imply the possibility of efficient design for an exact size lens. The dimensions of the full analysis model are small compared with those of the actual lens to reduce analysis time. An HFSS simulation of the full model confirms that the focusing length is longer with the wider spacing of corrugated baffles, the wider metallic groove and the shallower groove. Section 2 explains the structure and dimensions of the artificial dielectric lens with metallic corrugation. Section 3 shows the analysis results of the periodic model and Section 4 shows those of the full model.

2. Structure and dimensions of artificial dielectric lens with metallic corrugation

Figure 1 shows the artificial dielectric lens with corrugated structures composed of baffles with a few 10 μm grooves. A $+z$ traveling TEM wave with a $+y$-polarized electric field propagates through the lens and converges at a focal point. The phase of electromagnetic wave in the dielectric material is delayed by the slow-wave effect. This effect is caused by the molecules and atoms which microscopically act as electrical dipoles to the electromagnetic wave. Thus, the lens shape focuses the electromagnetic wave. The corrugated structure is a slow-wave circuit. A lens composed of only baffles does not produce a slow wave effect and the beam does not converge since the refractive index is 1. An electromagnetic wave with an x-polarized electric field and y-polarized magnetic field does not converge due to cut-off.

The lens dimensions, r =1.32 mm (2.21λ), R =1.60 mm (2.67λ) and h =0.70 mm (1.17λ), are used for the full model analysis. Figure 2 shows the unit cell models. Pattern A is used to study the characteristics of the baffle spacing with corrugated grooves and the number of baffles N. The full model dimension is fixed. Pattern B is used to study the characteristics of the metallic groove width. Pattern C is used to study the characteristics of the metallic grooves depth. Table 1 shows the parameters of the reference model in Fig. 2. The design frequency is 0.5 THz.

3. Phase delay analysis by periodic model

Figure 3 shows the periodic analysis model extracted from the full model. The phase delay is computed from the analysis of the periodic model in Fig. 3. Figure 4 shows the phase delay results by Ansys HFSS (Ver. 13).

The dimensions of the baffle spacing d in Pattern A are d=30 μm (0.050λ), 50 μm (0.083λ), 70 μm (0.12λ). The delayed phase at the 9th groove is -148.9, -88.8 and -66.1 degrees with d=30 μm, 50 μm and 70 μm, respectively, as shown in Fig. 4 (a). The phase delay decreases as the

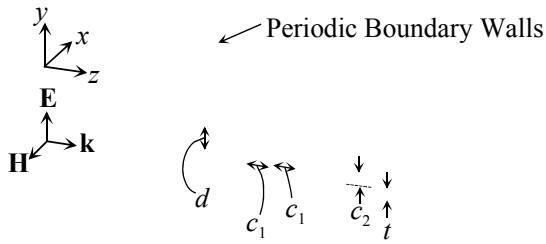

Figure 3: Analysis model with periodic boundary walls for estimation of phase delay.

Reference Model	Pattern A	Pattern B	Pattern C
Parameters	Distance d Number N	Width c_1	Depth c_2 Distance d
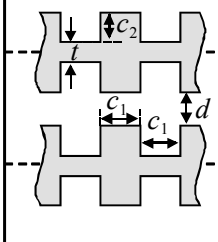 The number of corrugated plates is N.	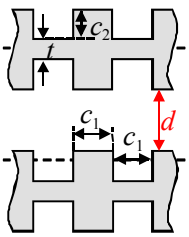 The number of corrugated plates is N.	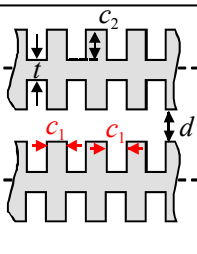 The number of corrugated plates is N.	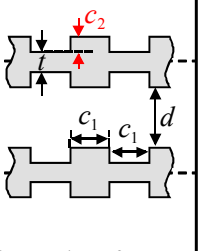 The number of corrugated plates is N.
Table 1	A-1 d = 50 μm, N = 20 A-2 d = 70 μm, N = 18	B-1 c_1 = 20 μm B-2 c_1 = 60 μm	C-1 c_2 = 15 μm, d = 60 μm C-2 c_2 = 0 μm, d = 90 μm

Figure 2: Unit cell models

Table 1: Lens parameters for reference model.

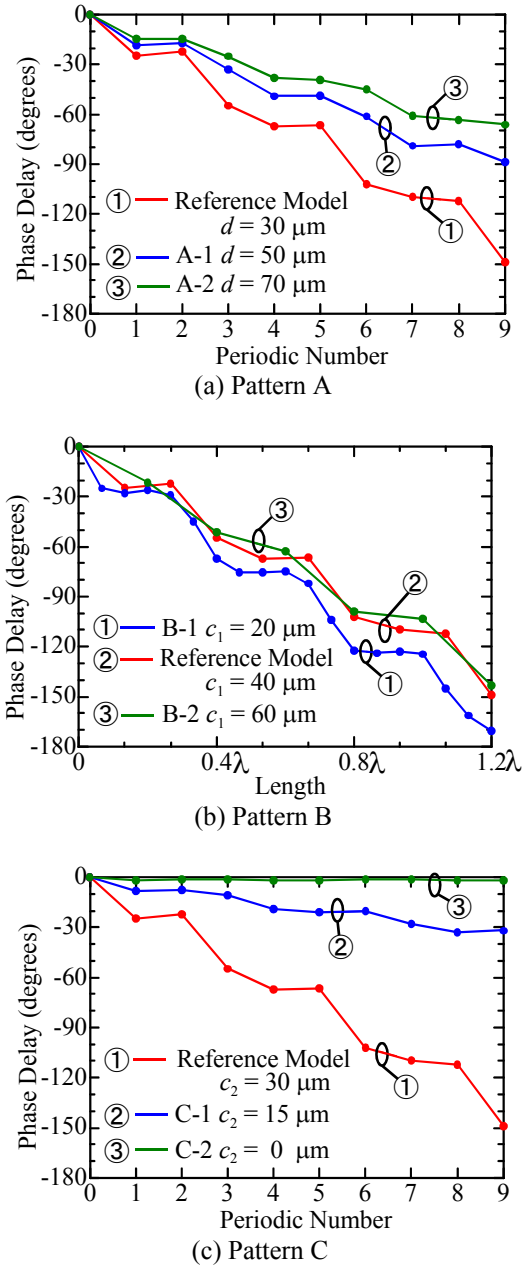

Figure 4: Phase delay for analysis model with periodic boundary walls.

baffle spacing d increases.

The dimensions of groove width c_1 in Pattern B are c_1 =20 μm (0.033λ), c_1=40 μm (0.067λ) and c_1=60 μm (0.10λ). The delayed phases are -170.7, -148.9 and -143.4 degrees with c_1 =20 μm, c_1=40 μm and c_1=60 μm, respectively, for 1.2λ pass length, as shown in Fig. 4 (b). The phase delay decreases as the groove width c_1 increases, but that for c_1=40 and c_1=60 μm are almost same.

The dimensions of groove depth c_2 in Pattern C are c_2=30 μm (0.050λ), c_2=15 μm (0.025λ), c_2=0 μm. The delayed phases at the 9th groove are -148.9, -31.9 and -1.6 degrees with c_2=30 μm, 15 μm and 0 μm, respectively, as shown in Fig. 4 (c). The phase delay decreases as the groove depth c_2 decreases.

The decreasing phase delays imply a decreasing of refractive index, which results in an increasing of the focusing length.

4. Lens full model analysis

Only one quarter of the analysis model is analyzed using image theory [19] in order to reduce the problem size. The full wave analysis results are obtained by Ansys HFSS (Ver. 13). The workstation CPU is an Intel Xeon 5690 (3.46 GHz 6 Core) x 2 and applied memory is 82.4 GB. It took 26 hours 9 minutes to analyze the reference model. The incident electric field with 1 V/m is shown in Figure 5 for the reference model. It is verified that the lens with corrugated structures produces a focusing effect. The local maximum value of the electric field magnitude is 2.5 times that of the incident wave at 2.31 mm (3.85λ) from the top of lens sphere.

4.1. Pattern A

Figure 6 (a) shows the full model analysis result for Pattern A-1, d =50 μm (0.083λ) and N =20. For Pattern A-1, the local maximum value of the electric field magnitude is 2.1 times that of the incident wave at 2.36 mm (3.93λ) from the top of the lens sphere, as shown in Figure 9 (a). Fig. 6 (b) shows the full model analysis result for Pattern A-2, d =70 μm (0.12λ), N =18. For Pattern A-2 the local maximum value of the electric field magnitude is 1.9 times that of the incident wave at 2.69 mm (4.49λ) from the top of the lens sphere, as shown in Fig. 9 (a). The results of periodic model in Fig. 4 (a) are qualitatively consistent with those of full model because the focusing length increases as the baffle spacing increases. The equivalent refractive index decreases as the baffle spacing increases.

4.2. Pattern B

Figure 7 (a) shows the full model analysis result for Pattern B-1, c_1=20 μm (0.033λ). The local maximum value of the electric field magnitude is 2.7 times that of the incident wave at 1.97 mm (3.29λ) from the top of the lens sphere, as shown in Fig. 9 (b). Fig. 7 (b) shows the full model analysis result for Pattern B-2, c_1=60 μm (0.10λ). The local maximum value of the electric field magnitude is 2.4 times that of the incident wave at 2.32 mm (3.86λ) from the top of the lens sphere, as shown in Fig. 9 (b). The focusing length for Pattern B-1 is shorter compared to that of the reference model. The focusing length for Pattern B-2 is almost the same compared to the reference model. The results of the full model are qualitatively consistent with those of the periodic model, as shown in Fig. 4 (b).The equivalent refractive index decreases as the metallic groove width c_1 increases.

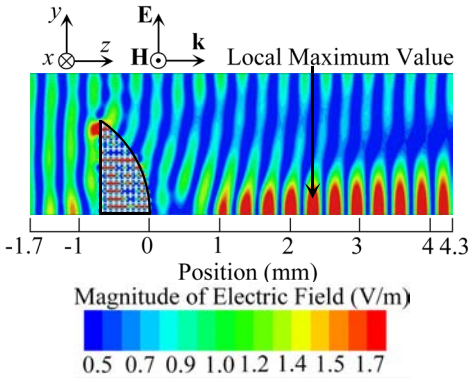

Figure 5: Full wave analysis results for criterion model.

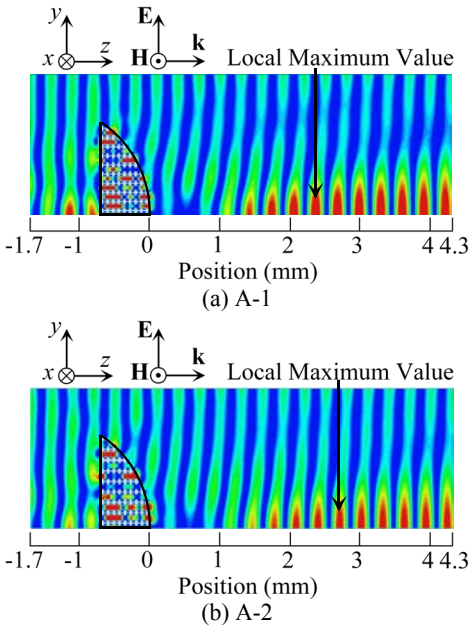

Figure 6: Full wave analysis results for model pattern A.

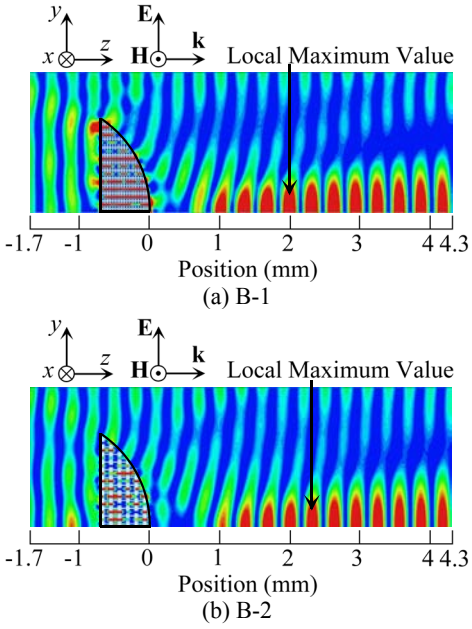

Figure 7: Full wave analysis results for model pattern B.

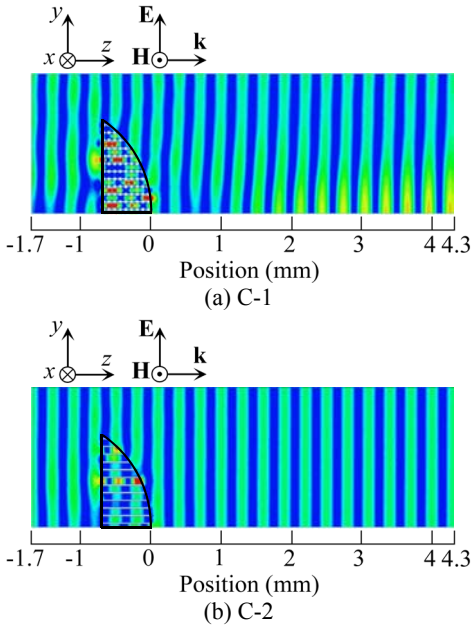

Figure 8: Full wave analysis results for model pattern C.

4.3. Pattern C

Figure 8 (a) shows the full model analysis result for Pattern C-1, c_2 =15 μm (0.025λ), d =60 μm (0.10λ). The focusing length is longer than the focusing length of the analysis model, 4.30 mm (7.17λ) for Pattern C-1, as shown in Fig. 9 (c). Fig. 8 (b) shows the full model analysis result without metallic grooves for Pattern C-2, d = 90 μm (0.15λ). A lens composed of only baffles does not converge as seen in Fig. 8 (b). The focusing length increases as the metallic groove depth c_2 decreases as seen by comparison between the reference model and Pattern C-1. The results of the full model are qualitatively consistent with those of the periodic model as shown in Fig. 4 (c). The equivalent refractive index decreases as the metallic groove depth c_2 decreases.

Thus, the full model analysis confirms that the focusing length is longer with the wider spacing of corrugated baffles, the wider metallic groove width, and the shallower groove depth. The results of the periodic model analysis imply the possibility of estimating the refractive index of artificial dielectric lens with metallic corrugated structures. The analysis and design of the actual-size lens is not easy and estimation by the periodic model is much more effective for an iterative design procedure.

5. Conclusions

This paper proposes an artificial dielectric lens that consists of metallic corrugated structures. The analyses of the periodic model confirm the phase delay and those of the full model confirm the focus effect. The full model analysis confirms that the focusing length is longer with the wider spacing of corrugated baffles, the wider metallic groove width, and the shallower groove depth. The lens shape with baffles only and no corrugation does not produce a focusing effect. The analysis using the periodic model can estimate the refractive index of an artificial dielectric lens with

metallic corrugated structures. We plan to fabricate the lenses and to measure the focusing effect and the equivalent refractive index.

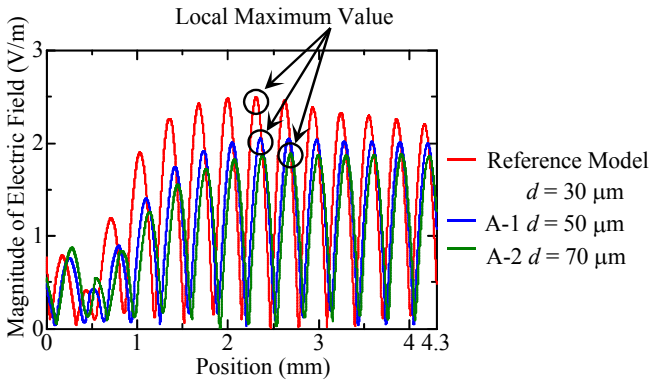

(a) Pattern A

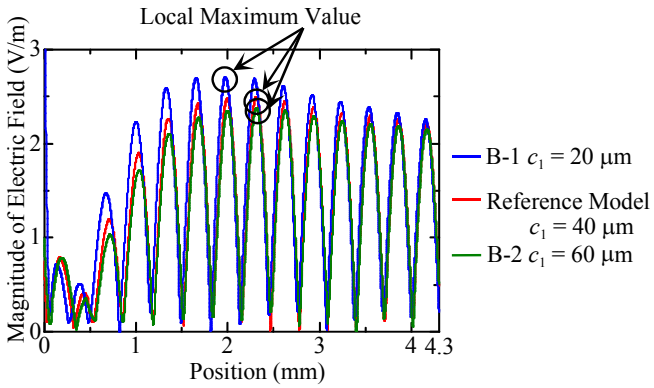

(b) Pattern B

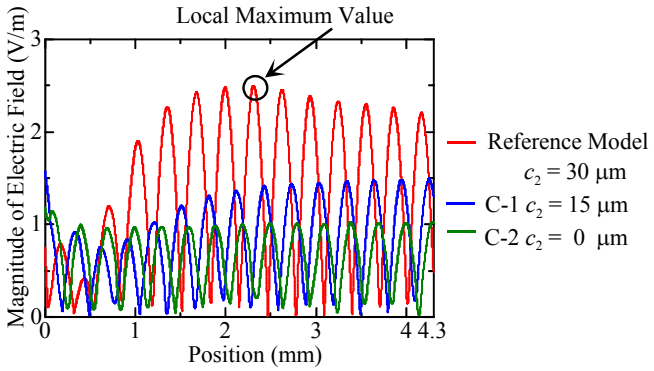

(c) Pattern C

Figure 9: Electric field.

Acknowledgements

This research was supported by the Ministry of Education, Science, Sports and Culture, Grant-in-Aid for Scientific Research on Innovative Areas under Grant No. 23109505, Adaptable and Seamless Technology Transfer Program through Target-driven R&D, Japan Science and Technology Agency No. AS231Z04696B, and aid for scientific research from Takayanagi Memorial Foundation.

References

[1] W. E. Kock, "Metallic delay lenses," Bell Syst. Tech. J., vol. 27, no. 1, pp. 58-82, Jan. 1948.

[2] S. S. D. Jones, and J. Brown, "Metallic delay lenses," Nature, vol. 163, pp. 324-325, Feb. 1949.

[3] J. Brown, "The design of metallic delay dielectrics," Proceedings of the IEE - Part III: Radio and Communication Engineering, vol. 97, no. 45, pp. 45-48, Jan. 1950.

[4] S. B. Cohn, "Microwave measurements on metallic delay media," Proceedings of the IRE, vol. 41, no. 9, pp. 1177-1183, Sep. 1953.

[5] J. Brown, W. Jackson, "The relative permittivity of tetragonal arrays of perfectly conducting thin discs," vol. 102, no. 1, pp. 37-42, Jan. 1955.

[6] W. E. Kock, "Metal-lens Antennas," Proceedings of the I. R. E. and Waves and Electrons, vol. 34, no. 11, pp. 828-836, Nov. 1946.

[7] N. I. Landy, S. Sajuyigbe, J. J. Mock, D. R. Smith, and W. J. Padilla, "Perfect metamaterial absorber," Phys. Rev. Lett., vol. 100, pp. 207402-1-207402-4, May 2008.

[8] H. Tao, N. I. Landy, C. M. Bingham, X. Zhang, R. D. Averitt, W. J. Padilla, "A metamaterial absorber for the terahertz regime: design, fabrication and characterization," Opt. Express, vol. 16, no. 10, pp. 7181-7188, May 2008.

[9] H. Tao, C. M. Bingham, A. C. Strikwerda, D. Pilon, D. Shrekenhamer, N. I. Landy, K. Fan, X. Zhang, W. J. Padilla, and R. D. Averitt, "Highly flexible wide angle of incidence terahertz metamaterial absorber: Design, fabrication, and characterization," Phys. Rev. B, vol. 78, pp. 241103-1-241103-4, Dec. 2008.

[10] N. I. Landy, C. M. Bingham, T. Tyler, N. Jokerst, D. R. Smith, and W. J. Padilla, "Design, theory, and measurement of a polarization-insensitive absorber for terahertz imaging," Phys. Rev. B, vol. 79, pp. 125104-1-125104-6, Mar. 2009.

[11] H.-T. Chen, J. Zhou, J. F. O'Hara, F. Chen, A. K. Azad, and A. J. Taylor, "Antireflection coating using metamaterials and identification of its mechanism," Phys. Rev. Lett., vol. 105, pp. 073901-1-073901-4, Aug. 2010.

[12] M. Choi, S. H. Lee, Y. Kim, S. B. Kang, J. Shin, M. H. Kwak, K.-Y. Kang, Y.-H. Lee, N. Park and B. Min, "A terahertz metamaterial with unnaturally high refractive index," Nature, vol. 470, pp. 369-374, Feb. 2011.

[13] F. Miyamaru, M. W. Takeda, and K. Taima, "Characterization of terahertz metamaterials fabricated on flexible plastic films: toward fabrication of bulk metamaterials in terahertz region," Appl. Phys. Express, vol. 2, pp. 042001-1-042001-3, Mar. 2009.

[14] F. Miyamaru, S. Kubota, K. Taima, K. Takano, M. Hangyo, and M. W. Takeda, "Three-dimensional bulk metamaterials operating in the terahertz range", Appl. Phys. Lett., vol. 96, pp. 081105-1-081105-3, Feb. 2010.

[15] J. Shin, J.-T. Shen, P. B. Catrysse, S. Fan, "Cut-through metal slit array as an anisotropic metamaterial film," IEEE J .Select. Top. Quant. Electron., Vol. 12, No.6, pp. 1116-1122, Nov. 2006.

[16] K. Akiyama, K. Takano, Y. Abe, Y. Tokuda, and M. Hangyo, "Optical transmission anomalies in a double-

layered metallic slit array," Opt. Express, vol. 18, no. 17, pp. 17876-17882, Aug. 2010.
[17] K. Sato, K. Sudo, J. Hirokawa and M. Ando, "Analysis of slot coupling in a corrugated radial waveguide," 2005 International Symposium on Antennas and Propagation (ISAP 2005), WB1-3, Vol.1, pp. 85-88, Aug. 3-5, 2005.
[18] K. Sakakibara, J. Hirokawa, M. Ando, and N. Goto, "Periodic Boundary Condition for Evaluation of External Mutual Couplings in a Slotted Waveguide Array," IEICE Trans. Commun., vol.E79-B, no.8, pp.1156-1164, Aug. 1996..
[19] C. A. Balanis, *Antenna Theory*: *Analysis and Design* (3rd edition), John Wiley & Sons, 2005, sec. 4. 7. 1.

Analysis of Artificial Dielectric Lens with Metallic Rectangular Chips for Terahertz Wave Band and Physical Explanation by Periodic Model

Takehito Suzuki[1*], Tomonari Suzuki[1], John C. Young[2], Keisuke Takano[3], Hideaki Kitahara[3], Masanori Hangyo[3]

[1]Department of Electrical & Electronic Engineering,
Ibaraki University, 4-12-1 Nakanarusawa, Hitachi, Ibaraki 316-8511, Japan
[2]Electrical and Computer Engineering, University of Kentucky, Lexington, Kentucky 40506-0046, USA
[3]Institute of Laser Engineering, Osaka University, 2-6 Yamadaoka, Suita, Osaka 565-0871, Japan
*corresponding author, E-mail: takehito@hcs.ibaraki.ac.jp

Abstract

Optical devices for the terahertz wave band are being developed now and require better designs. This paper analyzes an artificial dielectric lens with metallic rectangular chips for the terahertz wave band. This paper also provides an explanation of the phenomena by use of a periodic model. The periodic analysis model, extracted from the full one by assuming periodicity, confirms the phase delay as the mechanism that produces the focusing effect. Furthermore, the results of full model confirm the focusing length is longer with the larger periodicity of rectangular metal chips along the direction transverse to the propagation direction. It also indicates a nonuniform change for the periodicity along the propagation direction and the longer focusing length with narrower rectangular chips. The results of the full model analysis are qualitatively consistent with those of the periodic model one. This implies that the design for an exact size lens is possible through use of the periodic model.

1. Introduction

Optical devices for the terahertz wave band ranging from 0.1 to 10 THz are currently being developed and require improved designs. It is not easy to realize an arbitrary refractive index n using naturally-occurring materials. When materials are directly used for optical devices, the material properties themselves determine the optical characteristics. Typical lenses for the terahertz wave band are made of high density polymer, Tsurupica, and silicon with refractive indices of 1.52, 1.56, and 3.41, respectively. It is significant that the unit cell of the electromagnetic metamaterial controls the refractive index with respect to design flexibility and cost performance. Lenses composed of electromagnetic metamaterials, sphere arrays, disk arrays, square plate arrays, and strip arrays, have been proposed for microwave frequency band in [1]-[5]. These lenses produce focusing action due to the phase delay, slow wave effect. Lenses that use the high phase velocity of the propagation mode in a parallel plate waveguide structure have been proposed in [6]. The works in [7]-[10] present a metamaterial absorber, that in [11] presents an antireflection coating, that in [12] presents a metamaterial with an unnaturally high refractive index, and that in [13] and [14] present a three-dimensional metamaterial in the terahertz wave band. The effective permittivity and permeability of a metal slit array are derived and the proper refractive index is estimated as 1 in [15]. The work in [16] reports anomalies in a double-layered metallic slit. It is relatively easy to fabricate a terahertz-band metamaterial by metallic processing and chemical reduction on a film with thin metal [13], [14] compared to a metamaterial in optical range because the

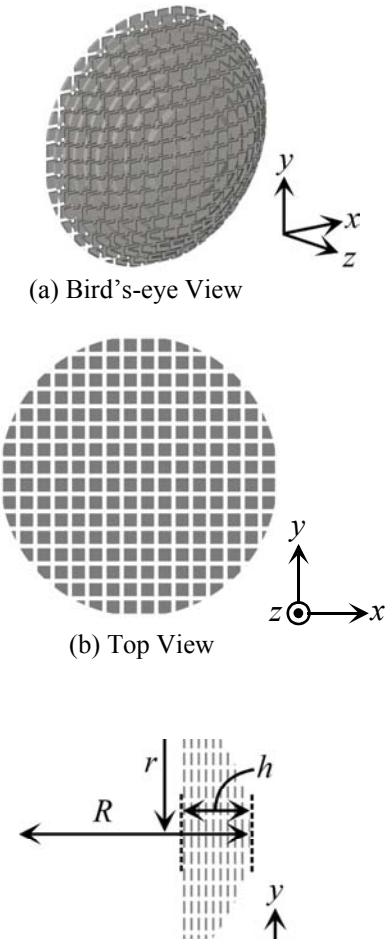

(a) Bird's-eye View

(b) Top View

(c) Side View

Figure 1: Lens of rectangular metallic chips for terahertz wave band

dimensions of the unit element are on the order of tens of microns.

This paper presents the focusing effect of an artificial dielectric lens with metallic rectangular chips in the terahertz wave band and operational explanation of the focusing length through use of a periodic analysis model. The periodic analysis model, which is extracted from the full model by assuming periodicity, confirms the phase delay used to estimate the focusing effect in the full model. Commercial EM simulators are now quite powerful but are still computationally heavy for the design and optimization of a whole array. A lens with a large but finite and complicated unit cell array is generally cumbersome and challenging to design. The work in [2] comments the necessity of further publication for an explanation of the lens operation. The analysis and design using the periodic model is fast and effective and can be used in an iterative design procedure [15]. An HFSS simulation of the full model confirms that the focusing length is longer with the larger periodicity of rectangular metal chips along the direction transverse to the propagation direction. It also confirms a nonuniform change for the periodicity along the propagation direction and the longer focusing length with narrower rectangular chips. These phenomena are demonstrated by the periodic analysis model. Results from the periodic model imply the possibility of efficient design for a full size lens. The dimensions of the full model in the analysis are small compared with those of the actual lens to reduce analysis time. Section 2 explains the structure and dimensions of artificial dielectric lens with metallic chips. Section 3 shows the analysis results of the periodic model and Section 4 shows those of full model.

2. Artificial dielectric lens with metallic rectangular chips

Figure 1 shows the artificial dielectric lens with metallic rectangular chips. A $+z$ traveling TEM wave with a x-polarized electric field propagates through the lens. For a true dielectric material, the phase of electromagnetic wave in the dielectric material is delayed by the slow-wave effect. This effect is caused by the molecules and atoms in the dielectric material acting as electrical dipoles to the electromagnetic wave. Thus, the lens shape focuses the electromagnetic wave. In the metallic lens, each of the rectangular metallic chips macroscopically acts as an electrical dipole and the behavior is similar to a dielectric material. The lens dimensions, r=1.32 mm (2.21λ), R=1.60 mm (2.67λ) and h=0.70 mm (1.17λ), are used for the full model analysis. Figure 2 shows the unit cell models. Pattern A focuses on the characteristics for periodicity of rectangular metal chips along the direction transverse to the propagation direction. Pattern B focuses on the characteristics for the periodicity along the propagation direction. Pattern C focuses on the characteristics for the rectangular chip size. The spacing of adjacent rectangular chips is fixed with 40 μm (0.067λ) in Pattern C. Table 1 shows the parameters of the reference model in Fig. 2. The design frequency is 0.5 THz.

3. Phase delay analysis by periodic model

Figure 3 shows the periodic analysis model extracted from the full model. The phase delay is derived from the analysis of the periodic model in Fig. 3. Figure 4 shows the phase delay results by Ansys HFSS (Ver. 13).

The dimensions of periodicity p_x and p_y in Pattern A are p_x=p_y=160 μm (0.27λ), 200 μm (0.33λ), 240 μm (0.40λ). The delayed phases at the 10th chip are -255.3, -159.4 and -108.3 degrees with p_x=p_y=160 μm, 200 μm and 240 μm, respectively, as shown in Fig. 4 (a). The phase delay decreases as the periodicity p_x and p_y increase.

The dimensions of p_z in Pattern B are p_z=30 μm (0.050λ), 70 μm (0.12λ), 110 μm (0.18λ). The delayed phases at the output edge are -209.9, -255.3 and -191.4 degrees with p_z=30 μm, 70 μm and 110 μm, respectively, as

Reference Model	Pattern A	Pattern B	Pattern C
Parameters	Length p_x Length p_y	Width p_z	Length a Length b
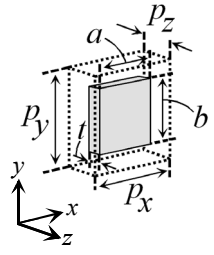	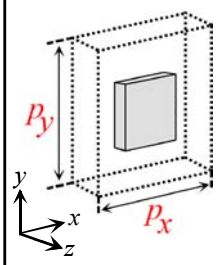	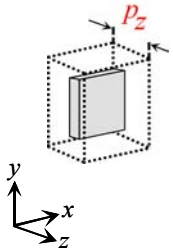	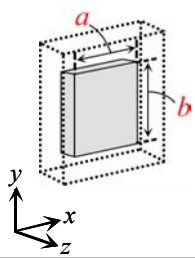
Table 1	A-1 p_x=200 μm, p_y=200 μm	B-1 p_z =30 μm	C-1 a =80 μm, b =80 μm
	A-2 p_x=240 μm, p_y=240 μm	B-2 p_z =110 μm	C-2 a =160 μm, b =160 μm

Figure 2: Unit cell models

shown in Fig. 4 (b). The length of horizontal axis in Fig. 4 (b) is normalized by wavelength. The phase delay changes nonuniformly with the periodicity p_x and p_y. These phenomena may be caused by the standing wave between the metal chips. The phase delay from p_z=30 μm to p_z=190 μm changes with periodicity, even though that from p_z=190 μm to p_z=230 μm does not change with periodicity. The dimensions of periodicity a and b in Pattern C are a=b=80 μm (0.13λ), 120 μm (0.20λ), 160 μm (0.27λ). The delayed phase at the 10th chip are -155.3, -255.3 and -391.1 degrees with a=80 μm, 120 μm and 160 μm, respectively, as shown in Fig. 4 (c). The phase delay increases as the chip size a and b increase.

The decreasing phase delays imply a decreasing of refractive index, which results in an increasing of the focusing length.

4. Lens full model analysis

Only one quarter of the analysis model is analyzed using image theory [16] in order to reduce the problem size. The full wave analysis results are obtained by Ansys HFSS (Ver. 13). The workstation CPU is an Intel Xeon 5690 (3.46 GHz 6 Core) x 2 and applied memory is 129 GB. It took 26 hours 23 minutes to analyze the reference model. The incident electric field is shown in Figure 5 for the reference model. It is verified that the lens with rectangular metallic chips produces a focusing effect. The local maximum value of the electric field magnitude is 3.6 times that of the incident wave at 1.12 mm (3.03λ) from the top of lens sphere.

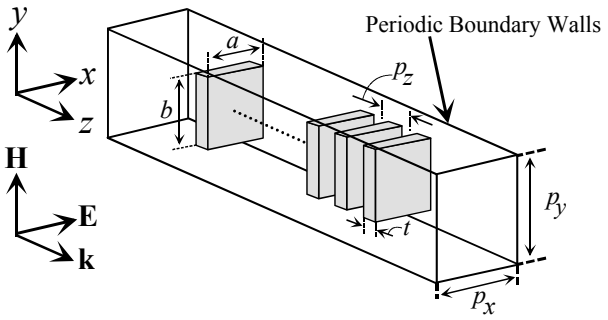

Figure 3: Analysis model with periodic boundary walls for estimation of phase delay.

Table 1: Lens parameters for reference model.

a	120 μm(0.20λ)
b	120 μm(0.20λ)
t	20 μm(0.033λ)
p_x	160 μm(0.27λ)
p_y	160 μm(0.27λ)
p_z	70 μm(0.12λ)

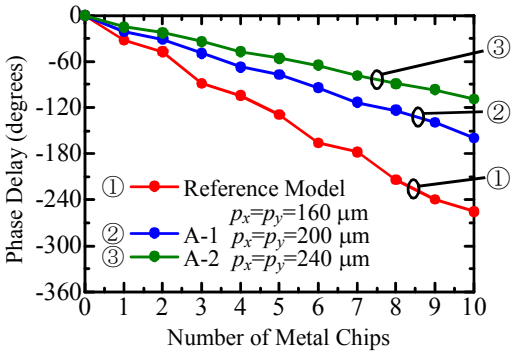

(a) Pattern A

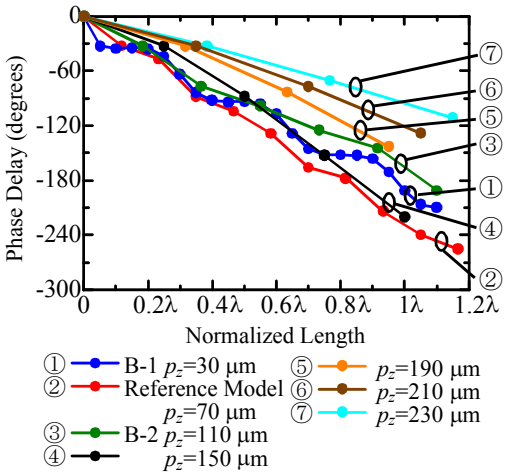

(b) Pattern B

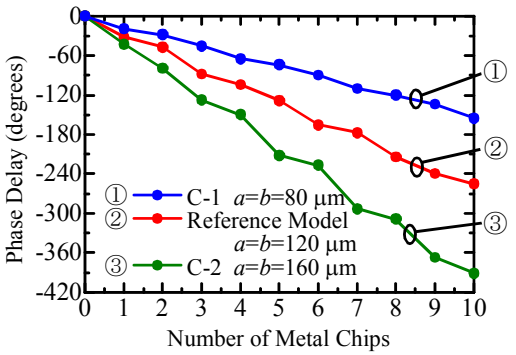

(c) Pattern C

Figure 4: Phase delay for analysis model with periodic boundary walls.

4.1. Pattern A

Figure 6 (a) shows the full model analysis result for Pattern A-1, p_x=p_y=200 μm (0.33λ). For Pattern A-1, the local maximum value of the electric field magnitude is 3.0 times that of the incident wave at 1.89 mm (3.15λ) from the top of the lens sphere, as shown in Figure 9 (b). Fig. 6 (b) shows the full model analysis result for Pattern A-2, p_x=p_y=240 μm (0.40λ). For Pattern A-2, the local maximum value of the electric field magnitude is 2.4 times that of the incident wave at 2.25 mm (3.75λ) from the top of the lens sphere, as shown in Fig. 9 (b). The periodic model results in

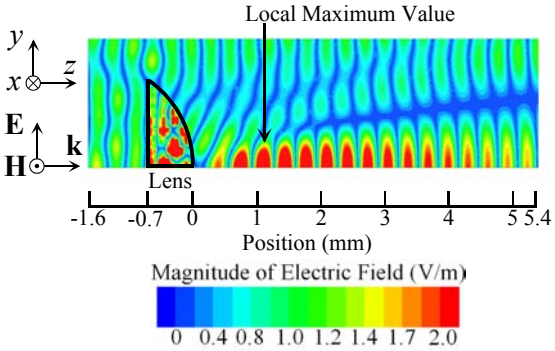

Fig. 5 Full wave analysis results for reference model.

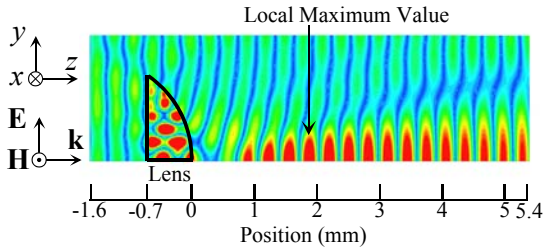

(a) A-1 p_x= p_y=200 μm (0.33λ)

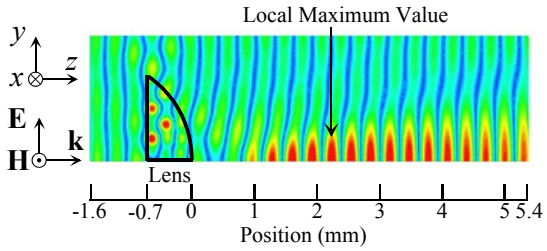

(b) A-2 p_x= p_y=240 μm (0.40λ)

Figure 6: Full wave analysis results for pattern A.

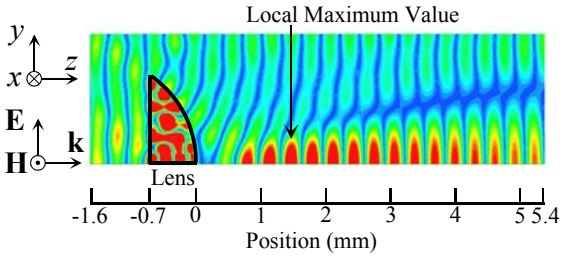

(a) B-1 p_z=30 μm (0.050λ)

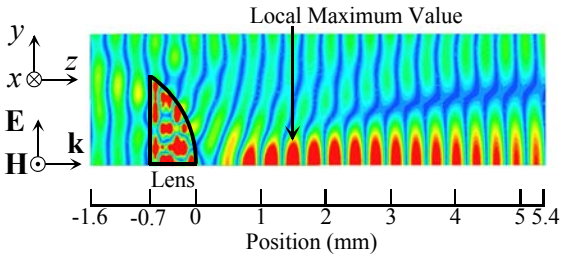

(b) B-2 p_z=110 μm (0.18λ)

Figure 7: Full wave analysis results for pattern B.

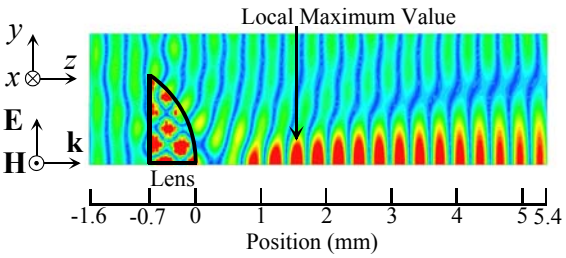

(a) C-1 a=b=80 μm (0.13λ)

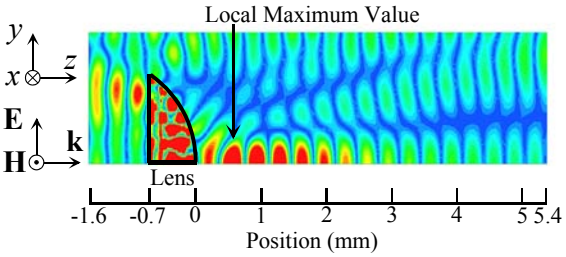

(b) C-2 a=b=160 μm (0.27λ)

Figure 8: Full wave analysis results for pattern C.

Fig. 4 (a) are qualitatively consistent with those of full model because the focusing length increases as the periodicity p_x and p_y increases. The equivalent refractive index decreases as the periodicity p_x and p_y increases.

4.2. Pattern B

Figure 7 (a) shows the full model analysis result for Pattern B-1, p_z=30 μm (0.050λ). For Pattern B-1, the local maximum value of the electric field magnitude is 3.0 times that of the incident wave at 1.49 mm (2.48λ) from the top of the lens sphere, as shown in Fig. 9 (b). Fig. 7 (b) shows the full model analysis result for Pattern B-2, p_z=110 μm (0.18λ). For Pattern B-2, the local maximum value of the electric field magnitude is 3.4 times that of the incident wave at 1.50 mm (2.50λ) from the top of the lens sphere, as shown in Fig. 9 (b). The phase delay for p_z=30 μm exists between that for p_z=70 μm and p_z=110 μm, as shown in Fig. 4 (b). Fig. 4 shows a nonuniform change for the periodicity along the propagation direction and a longer focusing length with narrower rectangular chips. The periodic model results shown in Fig. 4 (b) are qualitatively consistent with those of full model because the focusing length for p_z=30 μm exists between that for p_z=70 μm and p_z=110 μm, as shown in Fig. 9 (b). This suggests we can simplify the design of unit cell array with exact size to an iterative one by using a periodic model, even under nonuniform changes with parameters.

4.3. Pattern C

Figure 8 (a) shows the full model analysis result for Pattern C-1, a=b=80 μm (0.13λ). For Pattern C-1, the local maximum value of the electric field magnitude is 3.0 times that of the incident wave at 1.57 mm (2.62λ) from the top of the lens sphere, as shown in Fig. 9 (c). Fig. 6 (b) shows the full model analysis result for Pattern C-2, a=b=160 μm (0.27λ). For Pattern C-2, the local maximum value of the

electric field magnitude is 4.0 times that of the incident wave at 0.59 mm (0.98λ) from the top of the lens sphere, as shown in Fig. 9 (c). The results of periodic model in Fig. 4 (c) are qualitatively consistent with those of full model because the focusing length decreases as the periodicity *a* and *b* increases. The equivalent refractive index increases as the periodicity *a* and *b* increases.

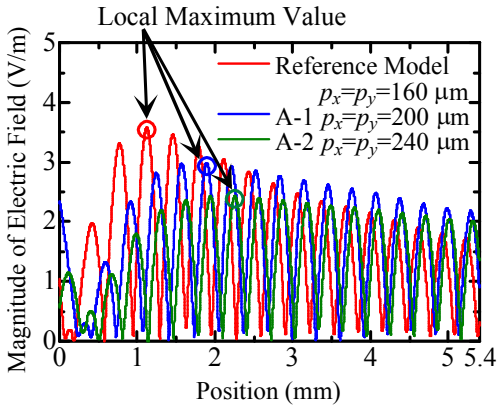

(a) Pattern A

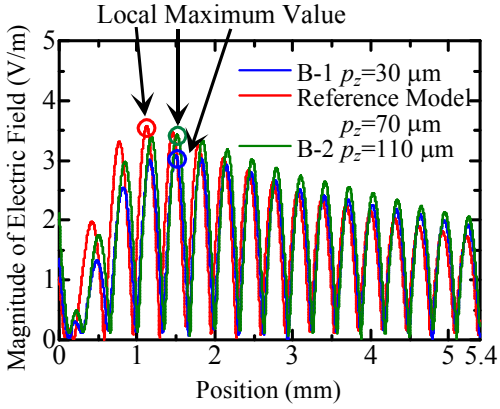

(b) Pattern B

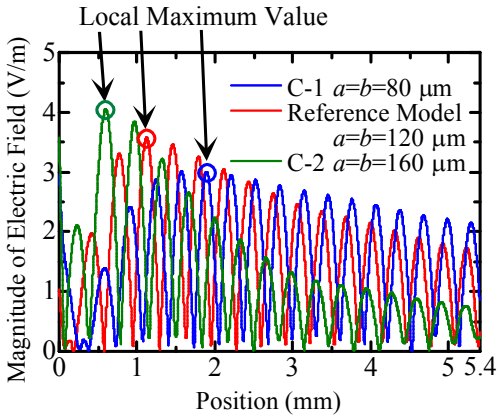

(c) Pattern C

Figure 9: Electric field.

5. Conclusions

This paper presents the focusing effect of an artificial dielectric lens that consist of metallic rectangular chips in the terahertz wave band and an explanation of the focusing length using a periodic analysis model. The periodic model analyses confirm the phase delay, and the full model analyses confirm the focus effect. The full model analysis confirms that the focusing length is longer with the larger periodicity of rectangular metal chips along the direction transverse to the propagation direction. It also confirms a nonuniform change for the periodicity along the propagation direction and a longer focusing length with narrower rectangular chips. The periodic model analysis can be used for iterative design of the refractive index for artificial dielectric lens with metallic rectangular chips, even under nonuniform changes with parameters. We are planning to fabricate the lenses and measure the focusing effect and the equivalent refractive index.

Acknowledgements

This research was supported by the Ministry of Education, Science, Sports and Culture, Grant-in-Aid for Scientific Research on Innovative Areas under Grant No. 23109505, Adaptable and Seamless Technology Transfer Program through Target-driven R&D, Japan Science and Technology Agency No. AS231Z04696B, and aid for scientific research from Takayanagi Memorial Foundation.

References

[1] W. E. Kock, "Metallic delay lenses," Bell Syst. Tech. J., vol. 27, no. 1, pp. 58-82, Jan. 1948.

[2] S. S. D. Jones, and J. Brown, "Metallic delay lenses," Nature, vol. 163, pp. 324-325, Feb. 1949.

[3] J. Brown, "The design of metallic delay dielectrics," Proceedings of the IEE - Part III: Radio and Communication Engineering, vol. 97, no. 45, pp. 45-48, Jan. 1950.

[4] S. B. Cohn, "Microwave measurements on metallic delay media," Proceedings of the IRE, vol. 41, no. 9, pp. 1177-1183, Sep. 1953.

[5] J. Brown, W. Jackson, "The relative permittivity of tetragonal arrays of perfectly conducting thin discs," vol. 102, no. 1, pp. 37-42, Jan. 1955.

[6] W. E. Kock, "Metal-lens Antennas," Proceedings of the I. R. E. and Waves and Electrons, vol. 34, no. 11, pp. 828-836, Nov. 1946.

[7] N. I. Landy, S. Sajuyigbe, J. J. Mock, D. R. Smith, and W. J. Padilla, "Perfect metamaterial absorber," Phys. Rev. Lett., vol. 100, pp. 207402-1-207402-4, May 2008.

[8] H. Tao, N. I. Landy, C. M. Bingham, X. Zhang, R. D. Averitt, W. J. Padilla, "A metamaterial absorber for the terahertz regime: design, fabrication and characterization," Opt. Express, vol. 16, no. 10, pp. 7181-7188, May 2008.

[9] H. Tao, C. M. Bingham, A. C. Strikwerda, D. Pilon, D. Shrekenhamer, N. I. Landy, K. Fan, X. Zhang, W. J. Padilla, and R. D. Averitt, "Highly flexible wide angle of incidence terahertz metamaterial absorber: Design, fabrication, and characterization," Phys. Rev. B, vol. 78, pp. 241103-1-241103-4, Dec. 2008.

[10] N. I. Landy, C. M. Bingham, T. Tyler, N. Jokerst, D. R. Smith, and W. J. Padilla, "Design, theory, and measurement of a polarization-insensitive absorber for terahertz imaging," Phys. Rev. B, vol. 79, pp. 125104-1-125104-6, Mar. 2009.

[11] H.-T. Chen, J. Zhou, J. F. O'Hara, F. Chen, A. K. Azad, and A. J. Taylor, "Antireflection coating using metamaterials and identification of its mechanism," Phys. Rev. Lett., vol. 105, pp. 073901-1-073901-4, Aug. 2010.

[12] M. Choi, S. H. Lee, Y. Kim, S. B. Kang, J. Shin, M. H. Kwak, K.-Y. Kang, Y.-H. Lee, N. Park and B. Min, "A terahertz metamaterial with unnaturally high refractive index," Nature, vol. 470, pp. 369-374, Feb. 2011.

[13] F. Miyamaru, M. W. Takeda, and K. Taima, "Characterization of terahertz metamaterials fabricated on flexible plastic films: toward fabrication of bulk metamaterials in terahertz region," Appl. Phys. Express, vol. 2, pp. 042001-1-042001-3, Mar. 2009.

[14] F. Miyamaru, S. Kubota, K. Taima, K. Takano, M. Hangyo, and M. W. Takeda, "Three-dimensional bulk metamaterials operating in the terahertz range", Appl. Phys. Lett., vol. 96, pp. 081105-1-081105-3, Feb. 2010.

[15] K. Sakakibara, J. Hirokawa, M. Ando, and N. Goto, "Periodic Boundary Condition for Evaluation of External Mutual Couplings in a Slotted Waveguide Array," IEICE Trans. Commun., vol.E79-B, no.8, pp.1156-1164, Aug. 1996..

[16] C. A. Balanis, *Antenna Theory*: *Analysis and Design* (3rd edition), John Wiley & Sons, 2005, sec. 4. 7. 1.

Arrays of doped and un-doped semiconductors for sensor applications

Thierry Taliercio*, Vilianne Ntsame Guilengui, and Eric Tournié

Institut d'Electronique du Sud, CNRS-INSIS-UMR 5214, Université Montpellier 2,
34095 MONTPELLIER cedex 05 (France)
*corresponding author, E-mail: thierry.taliercio@univ-montp2.fr

Abstract

This numerical investigation proposes to use a lamellar grating of doped semiconductors as the active region of a nanoplasmonic biosensing device. Working with highly doped semiconductors instead of a metal allows controlling the value of the plasma frequency. It is possible to reach the plasma frequency close to the range of detection of the sensor to improve its sensitivity. A red-shift of the plasmonic resonance of 10.2 nm for a 10^{-2} refractive index unit (RIU) increase can be achieved.

1. Introduction

Surface Plasmon Resonance (SPR) [1] sensing is a leading technology for biosensing [2]. The principle is to detect small changes in the optical refractive index using the high sensitivity of the frequency of SPR. Until now SPR biosensors are mainly based on glass technology which is not well adapted for integration and limited to the visible or near infrared ranges. Midinfrared (MIR) surface plasmon resonance has been recently investigated and showed a real potential [3] although based only on surface electromagnetic waves propagating at the metal-dielectric interface. To work at MIR wavelengths ZnS prisms replace glass prisms.

Nanoplasmonic offers the possibility of high integration without degrading the sensitivity of the device. Several works exploit the unique optical properties of nanoplasmonic structures on Si substrates, allowing proposing new architectures for biosensing [4, 5]. These new designs are based on gold or silver for the sensitive layer. Unfortunately both metals have drawbacks: Au is forbidden in microelectronic environment, and Ag is highly reactive in aqueous media. It is thus interesting to investigate new materials to bypass these limitations while maintaining high sensitivity. In the present work we propose to use a lamellar grating of doped semiconductors as active region for biosensing applications. The period of the grating is chosen to be largely sub-wavelength compared to the plasma wavelength of the doped semiconductor and of the wavelength of detection. This allows exciting mainly localized surface plasmon (LSP) modes propagating vertically into the slits [6].

2. The metamaterial as sensing media

We used two approaches to model the optical properties of the lamellar structure: i) an analytical model recently developed [7] which allows to save considerable time to roughly depict the adapted structure, ii) a finite difference time domain (FDTD) software [8] to valid the selected structure. Indeed, the analytic model does not take into account the surface plasmon polaritons (SPP) propagating at the surface of the lamellar structure while in some cases it is necessary to consider them. Figure 1 represents a scheme of the structure. It consists of a highly anisotropic plasmonic media (yellow).

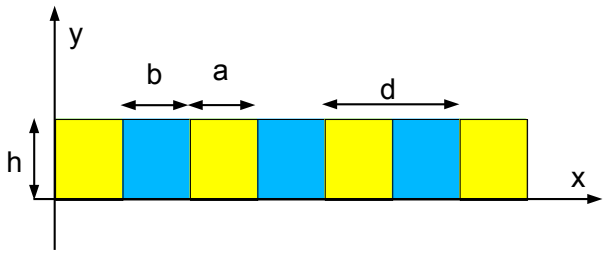

Figure 1: Schema of the lamellar grating of the doped semiconductors (yellow) and the dielectric or liquid (blue). The thickness of the lamellar grating is h, the period is d. a and b are respectively the width of the doped semiconductor and of the studied liquid.

The structure consists in a grating with a 520 nm period and a thickness of 1 µm. The widths of the slit and of the doped semiconductor are equal to 260 nm. The dielectric or liquid to analysis will be sitting into the slit. The wavelength corresponding to the plasma frequency of the semiconductor is chosen close to 6 µm which is a reasonable value to reach [12]. In these conditions, we have recently demonstrated that the lamellar grating can be viewed as an ionic crystal characterized by an oscillator wavelength λ_r under a transvers magnetic (TM) field and as a metal characterized by a pseudo-volume plasmon wavelength λ_t under a transverse electric (TE) field [7]. We look at the transmission of this metamaterial and try to evaluate its sensitivity to index variation of the dielectric material. It is

also possible to investigate the metamaterial in reflectance which gives us equivalent sensitivity to the index variation. We focus ourselves on the experimental configuration proposed in ref. 5. They proposed a setup based on orthogonal linearly light polarization of a laser beam. This particular optical configuration leads to a sensitivity improvement and noise reduction.

3. Results and discussion

Before investigating a particular structure we compare both models used in this study. Figure 2 shows calculated transmittance of the previously-defined lamellar grating using the analytic model or the FDTD method. We can see a good agreement between both methods. The differences are due to the approximation of the analytic model that supposes that we are in the long wavelength limit. However, the essential results are similar: resonances, amplitudes… The real advantage of the analytic model is saving much time (several orders of magnitude) that allows to quickly identify the best structure. In the following of the article we just present FDTD results except when it will be specified.

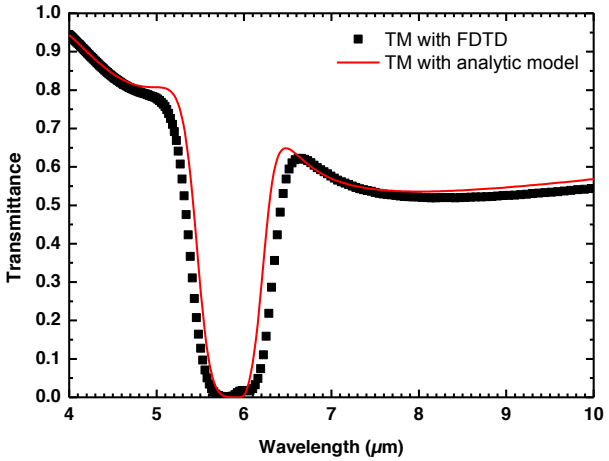

Figure 2: Calculated transmittance in normal incidence of the lamellar grating with a = b = 260 nm, d = 520 nm, h = 1 µm, using the FDTD method (dark symbols) or analytic model (red curve). The index of the dielectric part is taken equal to 1.5. The polarization is TM.

We now study the lamellar structure to identify the more sensitive wavelength range. Figure 3 shows the calculated transmittance in normal incidence of the lamellar grating with a = b = 260 nm, d = 520 nm, h = 1 µm, in TM polarization (black squares and red curve) or in TE polarization (green squares and blue curve). The vertical black arrows show respectively the wavelength associated to the plasma wavelength of the doped semiconductor λ_p, of λ_t and of λ_r. The index of the liquid is taken equal to 1.5 (solid symbols) or 1.51 (solid lines). We can see that λ_t is associated to the small shoulder at 5.95 µm TM polarization (dark symbols). In the same time, λ_r corresponds exactly to the pseudo volume plasma wavelength in TE polarization (green symbol). Both wavelengths are degenerate due to identical b (see ref. 7 for more details).

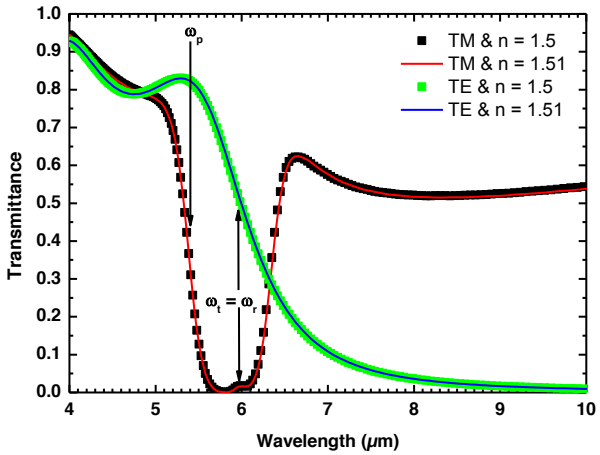

Figure 3: Calculated transmittance in normal incidence of the lamellar grating with a = b = 260 nm, d = 520 nm, h = 1 µm, in TM polarization (black symbols and red curve) or in TE polarization (green symbols and blue curve). The index of the liquid is taken equal to 1.5 (symbols) or 1.51 (lines). Vertical arrows show the frequency associated to λ_p, to λ_t and λ_r.

The modulation of the transmitted signal at wavelengths larger than λ_p is due to interference effects in the metamaterial layer which selects some LSP modes. To identify the best working area it is interesting to draw the transmittance modification, ΔT, for an index variation of the dielectric media from 1.50 to 1.51, that is $\Delta n = 0.01$. Results are represented in figure 4. ΔT are drawn for TM (dark) and TE polarization (red). The blue curve corresponds to the summation of the absolute value of ΔT of both polarizations.

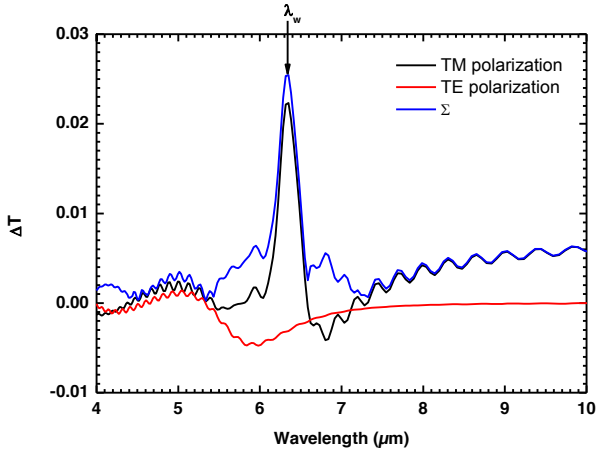

Figure 4: Transmission variation ΔT for an index modification of $\Delta n = 0.01$, under TM polarization (dark curve) or TE polarization (red curve). The summation of the absolute value of ΔT for both polarizations is the curve Σ (blue).

The small amplitude interferences observed for each spectrum are due to numerical artifacts arising from the step size in time and in space of FDTD techniques. They have no physical meaning. The zone of interest is obtained for the

maximum amplitude of Σ. Indeed, this corresponds to the maximum sensitivity of the metamaterial. We obtain an amplitude modulation of 2.5 % for a wavelength of 6.32 µm corresponding to λ_W. This is exactly the spectral range where spectra in both polarizations cross (see Fig. 4).

Figure 5 demonstrates the impact of the index variation on the calculated transmittance spectra in TE and TM polarization. Figure 5 corresponds to a zoom of the Figure 3 for a wavelength around λ_W. The red arrow shows the red-shit of the LSP resonance, 10.2 nm, due to a 10^{-2} refractive index unit (RIU) modification. This corresponds to a sensitivity of 1.02 10^3 nm/RIU.

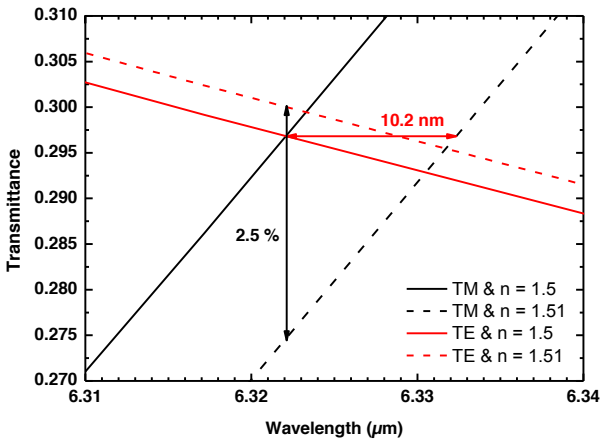

Figure 5: Zoom of the intersection between both spectra in TM and TE polarization of the Fig.2. The dark and red arrows are respectively the amplitude modification between both polarization and the red-shift of the spectra in TM polarization due to index variation.

The nanoplasmonic sensors are generally based on the measurement of the wavelength of the localized plasmons. It is also possible to propose intensity plasmonic sensing. In this configuration the wavelength is fixed (for example at λ_W) and the amplitude variation is measured for both polarizations by a detector behind the metamaterial [5]. In our case, an index variation of $\Delta n = 0.01$ at a wavelength of λ_W provokes an amplitude modification of 2.5 %. This is in the same order of magnitude than in ref. 5.

It is necessary to integrate this metamaterial into a complete device and evaluate its sensitivity in the MIR range.

4. Device proposition

We propose to study a device equivalent to that adopted in ref. 5. Figure 6 represents a scheme of the structure. It consists on a highly anisotropic plasmonic media (yellow) deposited onto a MIR detector (grey). A linearly polarized light is injected backward the y direction. The light to be detected should be a laser polarized along x (TM polarized), or z axes (TE polarized). The MIR detector should be a quantum well infrared photodetector (QWIP) [9], a quantum dot infrared photodetector (QDIP) [10] or a superlattice infrared photodetector (SLIP) [11].

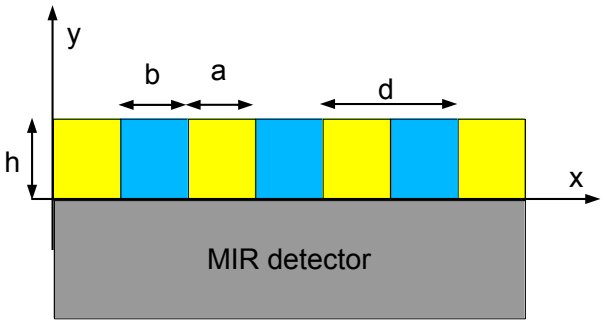

Figure 6: Schema of nanoplasmonic sensing. The lamellar grating of doped semiconductors (yellow) deposited onto a MIR detector (grey). The blue parts correspond to the liquid that will be analyzed.

Simulations of the complete structure are shown in Figure 8. Spectra are somewhat modified by the presence of the detector layer behind the metamaterial. This is mainly due to the refractive index difference between both faces of the metamaterial (n_{det} = 3.6). The resonance associated to LSP is not deeply modified. As we can see we conserve a good agreement between the FDTD simulation and the analytic model (red dash line) around 6 µm. On the other hand, at longer wavelengths we can see two resonances at 8 µm and 9.3 µm associated to SPP propagating at both interfaces of the metamaterial. We do not detail much more this point and focus ourselves on the LSP resonance.

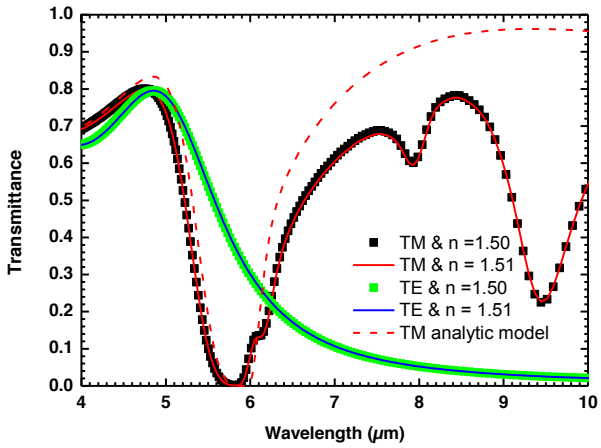

Figure 7: Calculated transmittance in normal incidence of the lamellar grating deposited on a detector modeled by a dielectric with an index of refraction n_{det} = 3.6, in TE polarization (dark curves) or in TM polarization (red curves). The index of the liquid is taken equal to 1.5 (solid lines) or 1.51 (dashed lines).

The LSP resonance modifies a little bit their shape and wavelength as compared to the lamellar grating alone. This provokes a small blue-shift until 6.24 µm. This demonstrates that the LSP is essentially sensitive to what is happening into the metamaterial.

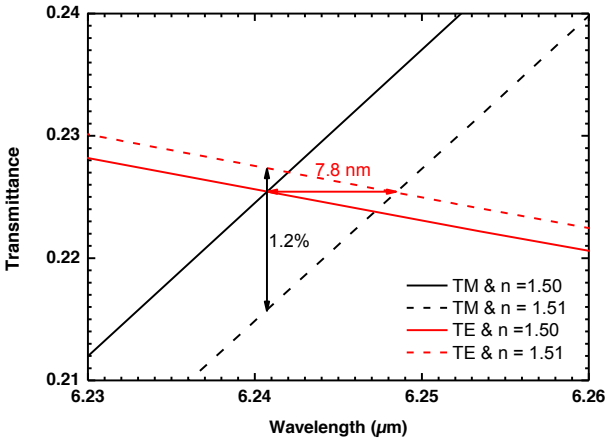

Figure 8: Zoom of the intersection between both spectra in TM and TE polarization of the Fig.6. The dark and red arrows are respectively the amplitude modification between both polarizations and the red-shift of the spectra in TM polarization due to index variation.

Figure 8 shows a zoom of the transmittance spectra in TM (dark) and TE (red) polarizations for different indexes of liquid (n = 1.50 for solid line curves and n = 1.51 for dashed line curves). The sensitivity of the device is slightly degraded. We obtain a sensitivity of 7.8 10^{-2} nm/RIU.

The sensitivity of our devices should be comparable to this recently proposed [5]. To increase the sensitivity of the metamaterial we can adjust the size of the slit. Decrease the slit increases the sensitivity. It is also quite easy to extend the validity of our metamaterial to longer wavelength by modifying the doping level [12] of the semiconductor or the geometry of the system [7].

5. Conclusions

Lamellar gratings of doped semiconductors are very interesting for the fabrication of integrated biosensors operating in the IR wavelength range. We have demonstrated that a sensitivity of 10^{-3} nm/RIU can be reached. Experimental validation of this concept in the IR range is now needed. The use of doped semiconductors allows easy integration into silicon technology while maintaining high sensitivity. By simply adjusting the geometry or the doping level it is possible to control efficiently the resonance position of the LSP. This allows finely defining the kind of biological material to be detected to be much more selective. It is also possible to extend the use of doped semiconductors to experimental techniques such as surface enhanced infrared absorption spectroscopy (SIERA) by adapting the geometry of the metamaterial.

References

[1] H. Reather, "Surface plasmons on smooth and Rough surfaces and on gratings," Springer-Verlag Tracts Mod. Phys. **111** (Spring-Verlag, 1988).

[2] [B. Liedberg, C. Nylander, and I. Lundström, "Biosensing with surface plasmon resonance-how it all started," Biosens. Bioelectron. **10**(8), i-ix (1995).

[3] M. Golosovsky, V. Lirtsman, V. Yashunsky, D. Davidov, and B. Aroeti, "Midinfrared surface-plasmon resonance: A novel biophysical tool for studying living cells," Journal Appl. Phys. **105**, 102036, 2009.

[4] Y. Wang, X. Su, Y. Zhu, Q. Wang, D. Zhu, J. Zhao, S. Chen, W. Huang, and S. Wu, "Photocurrent in Ag-Si photodiodes modulated by plasmonic nanopatterns," Appl. Phys. Lett. **95**, 241106, 2009.

[5] L. Guyot, A-P Blanchard-Dionne, S. Patskovsky, and M. Meunier, "Integrated silicon-based nanoplasmonic sensor," Optics Exp. **19**, 9962, 2011.

[6] J. A. Porto, F. J. Garcia-Vidal, and J. B. Pendry, "Transmission Resonances on metallic gratings with very narrow slits," Phys. Rev. Lett. **83**, 2845, 1999.

[7] J. Léon and T. Taliercio, "Large tunable photonic band gaps in nanostructured doped semiconductors," Phys. Rev B **84**, 195301, 2010.

[8] FDTD SOLUTIONS 7.5, Lumercial Solution Inc., Canada.

[9] J. Y. Andersson and L. Lundqvist, "Near-unity quantum efficiency of AlGaAs/GaAs quantum well infrared detectors using a waveguide with a doubly periodic grating coupler", Appl. Phys. Lett **59**, 857, 1991.

[10] K. W. Berryman, S. A. Lyon, and M. Segev, "Mid-infrared photoconductivity in self-organized InAs quantum dots," Appl. Phys. Lett. **70**, 1861, 1997.

[11] J. B. Rodriguez, C. Cervera, and P. Christol, "A type-II superlattice period with a modified InAs to GaSb thickness ratio for midwavelength infrared photodiode performance improvement," Appl. Phys. Lett. **97**, 251113, 2010.

[12] Y.B. Li, R. A. Stradling, T. Knight, J. R. Birch, R. H. Thomas, C. C. Philips and I. T. Ferguson, "Infrared reflection and transmission of undoped and Si-doped InAs grown on GaAs by molecular beam epitaxy," Semicond. Sci. Technol. **8**, 101, 1993.

A smart plasmonic transparent conductor with a gas sensing ability

M. K. Hedayati[1], Javaherirahim[1], M. Elbahri[*1, 2]

[1]Nanochemistry and Nanoengineering, Institute for Materials Science, Faculty of Engineering, University at Kiel, Kaiserstrasse 2, 24143 Kiel, Germany

[2] Helmholtz-Zentrum Geesthacht, Institute of Polymer Research, Nanochemistry and Nanoengineering, Max-Planck-Str.1, 21502, Geesthacht, Germany

[*]corresponding author: me@tf.uni-kiel.de

Abstract

Smart materials drawn the attention of the scientists due to their promising potential application in modern society. Among the demanded materials for opto-electronics, transparent conductors are highly requested and possibility to control their optical transparency opens up a new door in optical industry. Here we experimentally demonstrate a smart transparent conductive metal based on plasmonics. We show that by coating a thin gold film with polymeric/Spiro-molecules composite the transparency of the film not only be enhanced rather than the resonance transmission peak can be tuned by adjusting the coating thickness and the wt% of Spiro-molecules content. Using photoswitchable molecules as plasmonic coupler give us the opportunity to demonstrate the first photoswitchable transparent conductor. In other words, the transmission of our device can be enhanced/reduced upon VIS or UV illumination, respectively which demonstrates its potential application for smart optical devices such as smart windows. Although the recovery time takes almost one day, we tremendously reduced it to a short time by exposing the device to certain organic vapors, demonstrating a photobleaching gas sensor.

1. Introduction

Transparent conductors (TCs) are in high demand because of ever increasing growth of solar power industry and optical displays. There have been tremendous efforts to finding a replacing materials with comparable or even superior properties to that of conventional TCs (e.g. ITO) [1-5]. (For review refer to [6]). Thin metallic films due to their high electrical conductivity could be one of the best replacing materials for ITO, however their poor transparency makes their application as TCs limited. Recently a new plasmonic coating method is developed in our group to improve the optical transparency of the thin metallic film with the aid of dipole-dipole interaction [7]. Since the fabrication method of the mentioned system is PVD (Physical vapor deposition), applying chemical techniques could make the final device even more cost effective and simple. We have found out that deposition of Spiro molecules embedded in a polymeric matrix fabricated with spin coating on a thin metallic film give a high transparency to the metal substrate while having a high electrical conductivity [8].

In this work we show that the similar optical response can be extracted from the system out of Gold. In other word, here we show that the Spiro molecule embedded in polymeric matrix can enhance significantly the transparency of thin gold film. In addition, we show that the transmission intensity and peak position of our device can be tuned by adjusting the coating thickness or filling factor of Spiro-molecules in composite. Furthermore the developed plasmonic transparent device shows gas detection potential which makes it as a new smart optical sensor.

2. Experimental procedure

Spirophenanthrooxazine (SPO) was provided by Sigma Aldrich. For making solution out of SPO, general laboratory grade acetone was used. Polystyrene (PS) grain was dissolved in toluene and stirred before further usage. All the metallic film were deposited by sputtering. For that, a home made vacuum chamber is used. The 0.026 M solution of SPO was prepared by dissolving SPO powder in acetone. The 1 wt% PS solution was diluted with toluene to different concentration in order to have different thicknesses after spin coating. The spin coating was done on the gold coated glass plate by means of Spincoater® (P6700 Series). The rate of spinning was changed and optimized to achieve the desire thickness. Optimization showed that 1000 rpm rotation speed for 60 seconds gives the best uniform film. The samples thickness were measured by a profilometer (Dectak 8000 surface profile measuring system).

To analyze the switchability of the coatings, a 35W UV spot light lamp (LABINO-AB) was utilized and irradiation time kept constant for all experiments (20 seconds). Optical measurements were carried out by UV-Vis/IR spectrometer (Lambda 900). In all cases, the transmission value was normalized to the transmission of bare glass substrate to exclude the intrinsic reflectivity of glass.

To speed up the switching of the stacks, the samples after UV illumination were exposed to Acetone, Isopropanol, Toluene and Ethanol vapors. For that purpose, the samples placed as a top lid of a beaker containing 5 ml solution and the distance between the lid and the surface of the solvent kept constant for all the samples (8 cm). Right away after the samples were exposed, the optical spectra were measured to observe the role of the solvent vapor on the switching properties. The mentioned process was done for different time periods to calculate the right time of recovery for each sample. All experiments were done in air and room temperature.

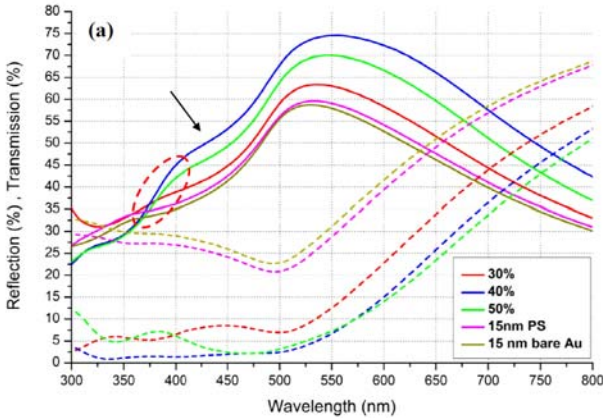

Figure 1: (left)Transmittance (solid lines) and refection (dashed lines) spectra of 15nm gold film coated with 15nm of spiro/polymer composite with different filling factor of SPO.

3. Results and Discussion

It is well known that the excitation of the surface plasmon associated with the trapping of the light, leading to a significant reflection drop while the induced charges on the metal mirror by dipole/image reduce the absorption/scattering of the structure. Both of the two mentioned phenomena enhance the transparency of metal films [7-8]. In the present work, we implemented the mentioned concept to make thin gold film highly transparent by using photoswitchable molecules (acting as dipoles) incorporated in Polystyrene. Our structure shows gas detection potential which makes it as a new smart optical sensor.

Although Spiro molecules are known as light absorbers, by proper design of the SPO doped coating one can enhance the transmission of metal film as well [8]. In Figure 1, the transmission spectra of 15nm gold film coated with 15nm of spiro/polymer composite with different filling factor of SPO is shown. It is clear that depending on the filling factor of SPO, the transparency of gold film is changed however the best efficiency of the film achieved when the concentration of molecules was set to 40%. Interestingly the change in transmission intensity for the pure PS film deposited on gold is negligible which shows that molecules (dipoles) plays a significant role in the observed phenomena. Reflection spectra is influenced the same by composite film and the 40% concentrated coating reduces the reflectivity more efficiently (Figure 1).

Spiro molecules (SPO) are chemical species in which the dipole moments amend their conformation upon UV illumination from close (off) to open (on) states [9-10]. However, even in the close form the SPO molecules could be polarized because of thermal equilibrium with its open form[11]. Therefore those polarized molecules near the base metallic film (gold) can induce a dipole image on the film and changes the charge distribution on the surface which can be considered as an in-plane wave-vector (k_{Ind}).[12] This distribution will be altered when the concentration of molecules varies (Figure 2) and when the k_{Ind} vector reaches the value that of plasmon of gold, matching condition if fulfilled and consequently the reflection significantly dropped due to the plasmon excitation. In other words, as soon as the dipole/image interaction of the chromophores strongly interact with the free electrons of the metal, a plasmon resonance activates and the broad drop in the reflectivity as well as high transmission happens. other interesting observation is the reflectivity dips occur in the range of 300-450 nm (Figure 1 dashed area) where the screening plasma frequencies of the metal film are expected. However further investigation is still needed to explore this phenomenon. On the other hand, exceeding the critical concentration of molecules results in a larger wave-vector which is comparable or even larger than the wavevector of internal reflection of the sample and the reflectivity start to increases. Additionally, since the interaction between molecules related to the space between them, it seems that enhanced reflection by concentration is also related to the inter-molecular interaction[12].

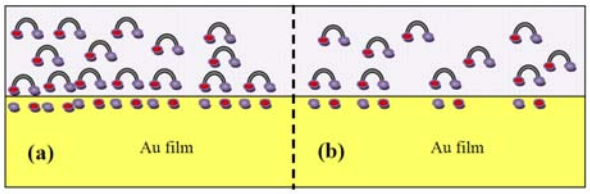

Figure 2: Schematic dipole-film interaction of a (a) high concentration (Closely separated dipole images) and (b) low concentrated (Highly separated dipole images) PS-SPO solution on the Au film surface. The induced dipole images are shown immediately under the interface.

Calculation showed that the transmission enhancement up to 65% in red part of spectrum can be achieved which is less than the silver system where the enhancement was greater in the UV to green part of frequencies [8] . We attribute the difference to the intrinsic optical properties of the metal layers. In fact we believe that using alloys instead of single metal would give rise into a broader transparency peak.

SPO under UV illumination switches to photomerocyanine (PMC) form which absorbs light at visible frequencies due to its HOMO/LUMO transition[13]. Illumination of composite coating showed that a drastic drop in transmission. The relative changes in intensity is also around 65% which means, by switching one can tune the optical transparency of gold.

One problem regarding application of SPO is that the recovery time of the system after illumination with UV-light is pretty long (almost one day). We demonstrated a method to accelerate recovery time of this molecules to very short time by exposing the molecules in on state to some gas vapor [3]. The method worked by considering the fact that the conformation changes of the molecules in soft matrix is easier than hard one. Therefore, when the SPO embedded in polymeric matrix come to contact with some solvent gas vapor, the polymer matrix expand due to the swelling and it turns softer. Consequently, the movement of molecules in the matrix is fastened and correspondingly the switchability process accelerated. In other words, exposing the sample to organic vapor of a good solvent which acts as plasticizer for PS, the polymer film should expand and facilitate reverse-switching of SPO i.e. bleaching process.

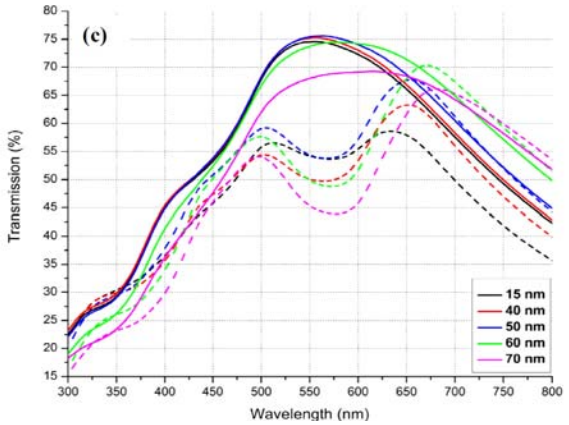

Figure 3: The comparison between before (solid) and after (dashed line) UV light illumination the thin film Spiro molecule composites of 40% SPO with different thickness on 15nm gold film.

Based on kinetically study of the recovery percentage of the device upon exposure to different solvent is illustrated in Figure 4. The response for Toluene and Acetone are very fast, however response for Ethanol was slower and takes more than 20 minutes. In the case of Isopropanol, the optical recovery was the slowest and in the measured period of experiments, full recovery was not achieved. It seems that photoresponse of the developed stacks highly depends on the gas type (solvent) and therefore can be used as a selective gas sensor.

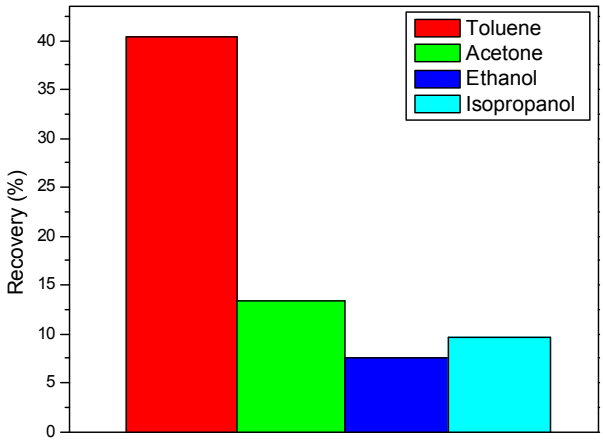

Figure 4: Recovery percentage of the device exposed to different gas vapours.

To implement our device as transparent conductor, in addition to a high transparency, high conductivity is also required. Indeed, the conductivity measurements showed that the electrical resistively of the coated gold film is comparable to that of the bare gold. It is worth mentioning that a photovoltaic device based on our plasmonic transparent conductor is under investigation.

4. Conclusions

As summary, here in this work, we study a new kind of smart transparent conductive metal based on a thin gold film coated with Spirophenanthrooxazine (SPO)/polymer composite. Our results showed that transparency enhancement up to 65% (relative to the intrinsic value of thin metal film) can be achieved in a system composed on 15nm PS/SPO (40%) composite deposited on 15nm gold film. We attributed the observed phenomena to the induced charge from the molecular dipole onto the base film which can excite plasmon at certain concentration of molecules and diminish the reflectivity of the film. Moreover fast recovery of the molecules from on to off state by exposing the UV-illuminated samples (low transparent ones) to organic vapor gases is realized. The recovery time of the SPO was extremely reduced to few seconds and hence established a new optical gas sensor.

Acknowledgements

The funds by DFG through the projects EL 554/1-1 and SFB 677 (C1,C9) are acknowledged. M.E. would like to thank the Initiative and Networking Fund of the Helmholtz Association's (grant No. VH-NG-523) for providing the financial base for the start-up of his research group.

References

1. A. Kumar, C. Zhou, ACS Nano 2010, 4, 11.
2. H. Wu, L. Hu, M. W. Rowell, D. Kong, J. J. Cha, J.

R. McDonough, J. Zhu, Y. Yang, M. D. McGehee, Y. Cui, Nano Lett. 2010, 10, 4242.
3. X.-Y. Zeng, Q.-K. Zhang, R.-M. Yu, C.-Z. Lu, Adv. Mater. 2010, 22, 4484.
4. K. Fehse, K. Walzer, K. Leo, W. Lövenich, A. Elschner, Adv. Mater. 2007, 19, 441.
5. E. M. Doherty, S. De, P. E. Lyons, A. Shmeliov, P. N. Nirmalraj, V. Scardaci, J. Joimel, W. J. Blau, J. J. Boland, J. N. Coleman, Carbon 2009, 47, 2466
6. Hecht, D. S., Hu, L., Irvin, G., "Emerging Transparent Electrodes Based on Thin Films of Carbon Nanotubes, Graphene, and Metallic Nanostructures, " Adv. Mater., Vol. 23, 1482–1513, 2011.
7. Elbahri, M, Hedayati, M.K., Chakravanadhanula, V.S.K., Jamali, M., Strunkus, T., Zaporojtchenko, V., Faupel, F., "An Omnidirectional Transparent Conducting-Metal-Based Plasmonic Nanocomposite, " Adv. Mater., Vol. 23, 1993-1997, 2011.
8. Jamali, M., Hedayati, M.K., Mozooni, B., Javaherirahim, M., Abdelaziz, R., Zillohu, A.U., Elbahri, M., "Photoresponsive Transparent Conductive Metal with a Photobleaching Nose," Adv. Mater., Vol. 23, 4243-4247, 2011.
9. V. Malatesta, G. Ranghino, U. Romano, P. Allegrini, Int. J. Quantum Chem. 1992, 42, 879.
10. Y.-R. Yi, I.-J. Lee, J. Photochem. Photobiol. A 2002, 151, 89.
11. Chibisov, K., Gorner, H., "Photoprocesses in Spirooxazines and Their Merocyanines," J. Phys. Chem. A 1999, 103, 5211.
12. A. Grigorenko, A. Geim, H. Gleeson, Y. Zhang, A. Firsov, I. Khrushchev, J. Petrovic, Nature 2005, 438, 335
13. A. l. Perrier, F. o. Maurel, E. A. Perpéte, V. r. Wathelet, D. Jacquemin, J. Phys. Chem. A 2009, 113, 13004.

Effects of Disorder in Metamaterial Structures

Agnès Maurel [1], Abdelwaheb Ourir [1] Jean-François Mercier [2] and Vincent Pagneux [3]

[1] LOA/Institut Langevin, ESPCI, UMR CNRS 7587, 10 rue Vauquelin, 75005 Paris, France,
[2] Laboratoire Poems, ENSTA, UMR CNRS 7231, 32 bd Victor, 75015 Paris, France,
[3] LAUM, Université du Maine, UMR CNRS 6613, Av. Olivier Messiaen, 72085 Le Mans, France.
*corresponding author, E-mail: a.ourir@espci.fr,

Abstract

We present a study of the attenuation length in a one-dimensional array of alternating left- and right- handed materials in which both the permittivities and the permeabilities are disordered. This type of structure has been shown to present an anomaly in the attenuation length when only permeabilities are disordered. We derive a simple analytical expression of the attenuation length, when the disorder in the refraction index is due to perturbations in both the permeability and the permittivity. Our expression is able to explain the transition to the anomalous behavior when perturbation only in the permeability or only in the permittivity is considered. Besides, we show that the anomaly is dramatically affected when considering perturbations in permeability and permittivity. The coupling effects are able to restore the ordinary localization length.

1. Introduction

In electromagnetism, the design of materials with negative index has offered new perspectives in nano science [1, 2]. In light of the properties of these new materials, the propagation and localization in periodic one-dimensional system has been revisited (*e.g.* [3], see also [4, 5] for a review on 1D propagation in disordered media). Recently, periodic bilayered structures formed by alternating left-handed and right-handed materials have been investigated and they revealed the surprising behavior of the so-called mixed-stack [6, 7]. A mixed-stack is a particular periodic structure with a unit cell formed of two layers of same length $d = d_1 = d_2$ and opposite refractive indices $n_1 = -n_2$. Such unit cell does not accumulate phase and leads to a transparent structure with perfect transmission. When perturbation in the permittivity is introduced, leading to perturbed refractive index and perturbed impedance, an anomaly in the attenuation length has been exhibited, resulting in a significant suppression of Anderson localization [6, 7]. Very recently, the localization length L_{loc} has been derived for this case [8], leading to the prediction $L_{loc} \propto Q^{-4}(kd)^{-8}$ (Q being the perturbation strength and $k = 2\pi/\lambda$ the wavenumber) which is valid in the low frequency regime.

In this Letter, we revisit this anomaly. By deriving a simple analytical expression for the attenuation length in mixed-stacks, we can analyze the conditions leading to the transition to the anomalous behavior. We show that the transition begins for $NQ^2(kd)^2 = 1$ and that increasing the length N of the structure produces an increase in the attenuation length until it reaches the localization length as $N \to \infty$. For $\lambda/d \lesssim 10$, the localization length is reached after $NQ^2(kd)^2 > 100$ and our analytical expression is accurate to characterize the transition. For $\lambda/d \gtrsim 10$, at lower frequency, we may notice in the numerical results of [7, 8] that the localization length is reached after $NQ^4(kd)^8 > 100$, that is for much larger structure sizes (and this is the regime predicted in [8]). Of course, this raises the question of whether or not such regimes can take place in the experiments involving actual designed structures. Currently, designed metamaterial layers work at typically $\lambda \sim d$ [9, 10]. This is the case because such layers are realized by stacking two dimensional arrays of resonators of thickness $\sim \lambda/10$ (for instance, split ring resonators combined with continuous wires [9], or fishnets [10]) and, to limit the losses, a small number (about 10) of stacks is used. In optics, the problem of losses in metal is crucial and the most recent metamaterial layers have micrometer lengths in the infrared frequency regime [10]. For the application to bilayered structures using left-handed materials, the problem of losses remains, in addition to compactness constraints, which limits also the value of N. Under these conditions, it is of importance to carefully describe the transmission properties of structures with moderate size and working in the frequency regime $\lambda \sim d$.

Another important practical aspect is the fact that a perturbation in the refractive index results in general from simultaneous perturbations in permittivity ϵ and in permeability μ. These perturbations can be evaluated but they cannot be controlled, in particular at micro and nano-scales because of manufacturing inaccuracies. In this Letter, we show that the behaviors of the attenuation and localization lengths are dramatically different when including a perturbation in the permeability $\delta\mu$ in addition to the previously considered perturbation in permittivity $\delta\epsilon$. Although the resulting perturbation in the refractive index simply follows from superposition, $\delta n = \delta\mu + \delta\epsilon$ at dominant order, the obtained attenuation length does not follow from superposition. Indeed, coupling effects in ϵ and μ are able to make the anomaly to disappear, or in other words, coupling effects restore the ordinary localization.

2. Perturbative expansion

We propose a derivation of the attenuation length l_N (with $1/l_N \equiv -\langle \log |T_N| \rangle / N$ and T_N is the transmission coefficient) based on the analysis of the electric and magnetic fields E, H in a structure of length $N(d_1+d_2)/2$, with $N/2$ unit cells (N is an even number). In the unperturbed structure, the unit cell is formed of two layers 1-2, of lengths d_a ($a = 1, 2$), with refractive indices $n_a = \pm\sqrt{\epsilon_a \mu_a}$ (the upper and lower signs, respectively, refer to right-handed and left-handed materials). The unperturbed structure is transparent when $Z_1 = Z_2$, with $Z_a = Z_0 \sqrt{\mu_a/\epsilon_a}$ (perfect impedance matching without reflection). In each layer j, perturbations in both ϵ and μ are considered, $\mu_j = \mu_a(1+\delta\mu_j)^2$ and $\epsilon_j = \epsilon_a(1+\delta\epsilon_j)^2$ with uncorrelated $\delta\mu_j$ and $\delta\epsilon_j$, distributed uniformly on $[-Q_\mu, Q_\mu]$ and $[-Q_\epsilon, Q_\epsilon]$ respectively. The resulting perturbation in the refractive index δn_j is distributed on $[-Q, Q]$ with $Q = \sqrt{Q_\epsilon^2 + Q_\mu^2}$.

We define the electric and magnetic fields E_j and H_j at the boundary between the layers j and $(j+1)$, satisfying

$$\begin{pmatrix} E_{j-1} \\ H_{j-1} \end{pmatrix} = \begin{pmatrix} \cos\varphi_j & iZ_j \sin\varphi_j \\ i\sin\varphi_j/Z_j & \cos\varphi_j \end{pmatrix} \begin{pmatrix} E_j \\ H_j \end{pmatrix} \tag{1}$$

with $\varphi_j \equiv k_j d_j$ and where the time dependence $e^{i\omega t}$ has been considered. For small disorder, the impedances remain close to each other and we introduce a small parameter $\delta_j \equiv (Z_j/Z_{j-1} - 1)/2$. Decomposing E_j into right-going E_j^+ and left-going E_j^- waves, we get

$$\begin{aligned} e^{ik_j d} E_j^+ &= E_{j-1}^+ + \delta_j (E_{j-1}^+ - E_{j-1}^-), \\ e^{-ik_j d} E_j^- &= E_{j-1}^- - \delta_j (E_{j-1}^+ - E_{j-1}^-), \end{aligned} \tag{2}$$

with the boundary conditions $E_1^+ = 1$, $E_{N+2}^+ = T$, $E_1^- = R$, $E_{N+2}^- = 0$. Defining a term of phase accumulation $\phi_j \equiv \sum_{l=2}^{j} \varphi_l$, and the quantities $P_j \equiv e^{i\phi_j} E_j^+$ and $D_j \equiv e^{-i\phi_j} E_j^-$, we obtain

$$\begin{aligned} P_j &= 1 + \sum_{l=2}^{j} \delta_l \left[P_{l-1} - e^{2iK_{l-1}d} D_{l-1} \right], \\ D_j &= \sum_{l=j+1}^{N+2} \delta_l \left[e^{-2iK_{l-1}d} P_{l-1} - D_{l-1} \right], \end{aligned} \tag{3}$$

where we used $P_1 = 1$ and $D_{N+2} = 0$. The transmission coefficient is $T_N = e^{-i\phi_{N+1}} P_{N+2}$ and the aim is to derive the attenuation length l_N. This is achieved by solving (3) iteratively owing to the small parameter δ_j. Analytical expressions presented in this Letter are obtained at the second iteration, leading to a prediction accurate up to $O(Q^3)$. Note that this second order in Q is also the approximation used in the semi analytical WSA used in [6, 7] [see Eq. (12) in [7] where the term $R_{n-1}^2 t_n^2 r_n$ is omitted, and this term is $O(Q^3)$ at best]. In the following, for clarity, we first inspect the case where only a perturbation in ϵ is considered, and then, we inspect the case with perturbations both in ϵ and μ for a unit cell with no phase accumulation.

3. Layers with perturbations only in ϵ

– We first consider the case where $Q_\mu = 0$ and $Q = Q_\epsilon$, corresponding to the situation considered in [6, 7, 8]. We can notice that the result is the same if $Q = Q_\mu$, $Q_\epsilon = 0$. The attenuation length for a structure of size $N(d_1+d_2)/2$ is

$$\frac{1}{l_N} = \frac{1}{l_1} - \frac{Q^2}{12}\, \mathcal{A}(k_1 d_1, k_2 d_2, Q, N), \tag{4}$$

$$\frac{1}{l_1} = \frac{Q^2}{12} \left\{ 1 - \frac{1}{2} \left[f(x_1)\cos 2k_1 d_1 + f(x_2)\cos 2k_2 d_2 \right] \right\}, \tag{5}$$

with $x_a \equiv 2Qk_a d_a$ ($a = 1, 2$) and $f(x) \equiv 3\mathrm{sinc}x - 6(\mathrm{sinc}x - \cos x)/x^2$, where $\mathrm{sinc}x \equiv \sin x/x$. The general form of $\mathcal{A}$ has no particular interest and we refer to the appendix for its expression (simplified expressions are given in the following).

The key point is the following: $\mathcal{A}$ depends on N, and it is responsible for the anomaly that occurs **only** for $k_2 d_2 = -k_1 d_1$ (this agrees with the observation of [11] that a structure, with $d_1 \neq d_2$ and $k_2 = -k_1$, does not present the anomaly). This is illustrated in Fig. 1: it can be seen that $\mathcal{A}$ has amplitude unity only in the vicinity of $k_2 d_2 = -k_1 d_1$; otherwise it is at least one order of magnitude smaller. In this latter case, it is negligible and the attenuation length takes a simple form, independent of N, $l_N = l_1$ that characterizes the transmission properties of the structure for any size N. Moreover, we recover the expected behavior of the localization length in the high frequency regime, $l_1 \to 12/Q^2$ since $f \to 0$, and in the low frequency regime, $1/l_1 = Q^2/12\ (\sin^2 k_1 d_1 + \sin^2 k_2 d_2)$ since $f \to 1$, as obtained in [11]. Of course, taking into account the exact form of the function f allows to better describe the attenuation length for intermediate values of the wavelength λ.

If the unit cell does not accumulate phase, for alternating right-handed and left-handed materials with $kd = k_1 d_1 = -k_2 d_2$, Eq. (4) simplifies to

$$\frac{1}{l_N} = \frac{Q^2}{12} \left[1 - f(x)\cos 2kd - h^2(x)\mathcal{B}(\mathrm{sinc}x, kd, N) \right], \tag{6}$$

with $x \equiv 2Qkd$, $h(x) \equiv \sqrt{3}[\mathrm{sinc}x - \cos x]/x$ (such that $\mathcal{A} = h^2(x)\mathcal{B}$) and

$$\mathcal{B}(r, kd, N) \equiv \frac{1 - r^N}{N(1-r^2)^2} \left[1 + r^2 - 2r\cos 2kd \right] - \frac{1 - r\cos 2kd}{1 - r^2}. \tag{7}$$

The main characteristics of $\mathcal{A}$ are illustrated in the inset of Fig. 1. A transition can be observed for $NQ^2(kd)^2 \sim 1$. For $\lambda/d \lesssim 10$, $\mathcal{A}$ reaches asymptotically a value that does not compensate the $1/l_1$ term in Eq. (4). Consequently, $1/l_N$ is of the same order as $1/l_1$ and there is no anomaly. For $\lambda/d \gtrsim 10$, $\mathcal{A}$ reaches asymptotically a value that compensates the $1/l_1$ term in Eq. (4), leading to an increase in l_N and thus to the aforementioned anomaly; this is consistent with the results of [8]. This means also that in this low

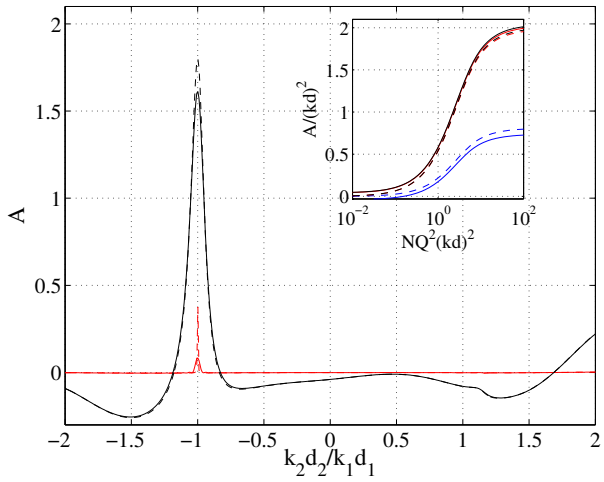

Figure 1: $\mathcal{A}$ as a function of k_2d_2/k_1d_1, curves given for $k_1d_1 = 2\pi/4.3$: lower red curve $Q = .025$ and upper black curve $Q = 0.25$ (plain line $N = 100$ and dotted line $N = 1000$). The inset shows $\mathcal{A}$ as a function of N, for $kd = k_1d_1 = -k_2d_2$. N is normalized to $NQ^2(kd)^2$ and $\mathcal{A}$ normalized to $\mathcal{A}/(kd)^2$. $\lambda/d = 4$ (blue lower curve), and $\lambda/d = 40$, 400 (upper red and black curves, almost undistinguishable) for $Q = 0.025$ (plain line) and $Q = 0.25$ (dotted line).

frequency regime, our perturbation expansion is no more valid and, as suggested by [8], would necessitate to go to order 4 in Q. Finally, note that the wavelengths smaller than the unit cell length ($\lambda/d < 1$) are not concerned by the anomaly because the term $(1 - f(2Qkd)\cos 2kd) \to 1$ while $\mathcal{A}$ remains smaller than 0.1 (the behavior of $\mathcal{A}$ for small wavelengths is not reported here).

4. M-stack with disorder in ϵ and μ

– To assess the robustness of the anomaly, we consider now perturbations both in ϵ and μ but still under the condition of no phase accumulation in the unit cell, $kd = k_1d_1 = -k_2d_2$. Using the same perturbation technique, we find a generalized expression of Eq. (6):

$$\begin{aligned}\frac{1}{l_N} &= \frac{Q_\epsilon^2}{12}\left[1 - f(x^\epsilon)\ \mathrm{sinc}x^\mu \cos 2kd\right] \\ &+ \frac{Q_\mu^2}{12}\left[1 - f(x^\mu)\ \mathrm{sinc}x^\epsilon \cos 2kd\right] \\ &+ \frac{Q_\epsilon Q_\mu}{6}\cos 2kd\ h(x^\epsilon)h(x^\mu) \\ &- \left[Q_\epsilon h(x^\epsilon)\mathrm{sinc}x^\mu - Q_\mu h(x^\mu)\mathrm{sinc}x^\epsilon\right]^2 \frac{\mathcal{B}(R, kd, N)}{12},\end{aligned} \tag{8}$$

with $R \equiv \mathrm{sinc}x^\epsilon\ \mathrm{sinc}x^\mu$. Here, the first three terms are independent of N and they essentially follow from the superposition of l_1 values ($Q = Q_\epsilon$ and Q_μ in Eq. (5)) . The fourth term is dependent on N. This term, responsible for the anomaly when $Q_\mu = 0$, has here a much more complex structure that is not in general able to compensate the first three terms. For instance, in the case $Q_\epsilon = Q_\mu$, this term vanishes, which restores the ordinary Anderson localization.

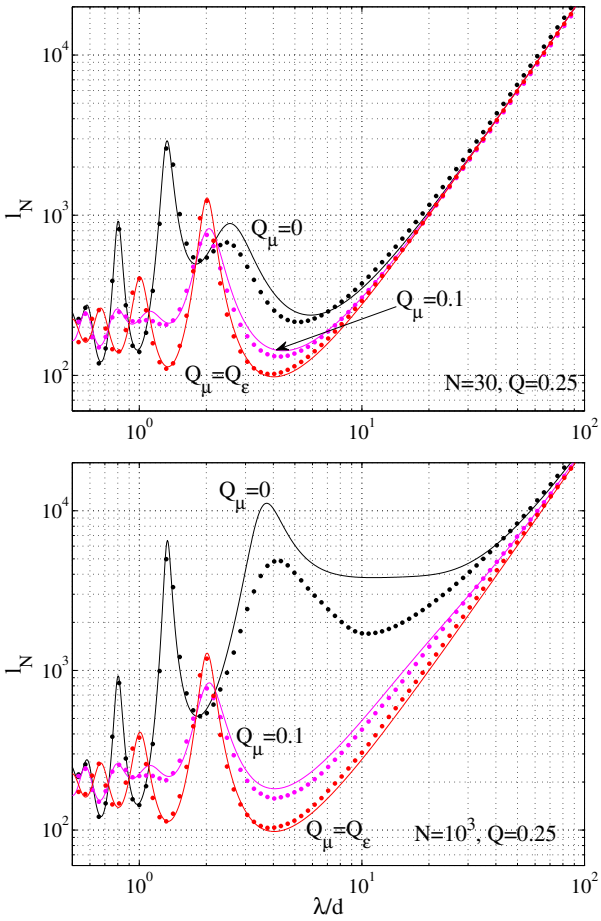

Figure 2: Attenuation length l_N of a mixed-stack for lengths $N = 30$ and $N = 10^3$ as a function of λ/d. Dots show the numerical results and plain lines correspond to our prediction in Eq. (8). Different curves correspond to $Q_\mu = 0$ (black dots), $Q_\mu = 0.1$ (magenta dots) and $Q_\mu = Q_\epsilon = Q/\sqrt{2}$ (red dots) for constant $Q = \sqrt{Q_\mu^2 + Q_\epsilon^2} = 0.25$ (constant perturbation strength in the refractive index). Result for the homogeneous stack (usual Anderson localization) are not represented and would be superposed on the $Q_\epsilon = Q_\mu$ case (red dots).

Our results are exemplified in Figs. 2 and 3 and compared with direct numerical calculations (numerics have been done with $10^3 - 10^4$ averages). We considered two different sizes of mixed-stacks $N = 30$ and $N = 10^3$ for a constant refractive index perturbation $Q = 0.25$, resulting from $Q_\mu = 0$, 0.1 and $Q/\sqrt{2}$ (and $Q_\epsilon = \sqrt{Q^2 - Q_\mu^2}$). Our conclusions are twofold:

1) When the perturbation in the refractive indices result from perturbations both in ϵ and μ, a significant decrease in the attenuation length is visible at low frequency (Fig. 2). For $Q_\mu \sim Q_\epsilon$, the usual localization is restored, similar to the localization observed in the so-called homogeneous-

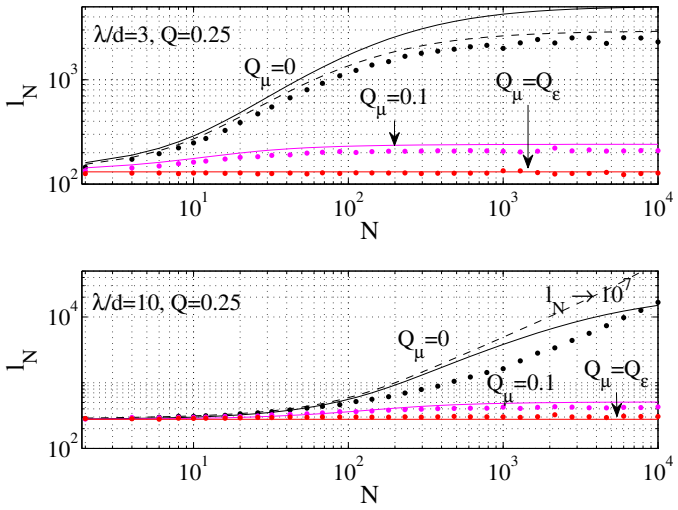

Figure 3: Attenuation length l_N of a mixed-stack as a function of N for $\lambda/d = 3$ and $\lambda/d = 10$. Same convention as on Fig. 2 is used. The transition starts for $N = 1/Q^2(kd)^2$ ($N \sim 4$ for $\lambda/d = 3$ and $N \sim 40$ for $\lambda/d = 10$). For $\lambda/d = 10$, $Q_\mu = 0$, the asymptotic $l_N = L_{loc} \sim 10^7$ is found from [6, 7] for $N > 10^7$.

stack (corresponding to a unit cell with $kd = k_1 d_1 = k_2 d_2$ [6, 7]). In this case, the validity of our expression in Eq. (8) is satisfactory in the whole range of frequencies.

2) It is confirmed that, when perturbation only in ϵ is considered, the anomaly starts for $NQ^2(kd)^2 = 1$ (Fig. 3). For $\lambda/d \lesssim 10$, the saturation at the localization length occurs for $NQ^2(kd)^2 > 100$ and our calculation at second order, Eq. (6), is accurate to describe the whole transition (in this regime, the prediction of [8] does not apply). We derived the attenuation length at third order and it appears to be more accurate although still unsatisfactory for low frequencies (Fig. 3). Indeed, for $\lambda/d \gtrsim 10$, in light of the calculations in [8], the next order in Q^4 is necessary to entirely capture the transition in the low frequency regime and, by analyzing the numerical results in [7, 8], it appears that the attenuation length reaches the localization length for typically $NQ^4(kd)^8 > 100$. This corresponds to the anomaly with a huge localization length.

5. Conclusions

Our results concern the attenuation length l_N in bilayered structures with a unit cell composed of left-handed and right-handed materials. When perturbation only in the permittivity or in the permeability is considered, our analytical expression is accurate for structure of moderate size and for high frequencies (wavelengths of order or smaller than the unit cell size). It must be stressed that real left-handed layer as can be designed nowadays precisely works in this range of wavelengths and structure sizes. More importantly, our result applies for perturbation in the refractive indices resulting from perturbations in the permeability and in the permittivity, which is the case when designing left-handed material. This is of particular practical interest since we have shown that the combined effects of perturbations in permeability and permittivity strongly affect the behavior of the attenuation length and they are able to restore the ordinary Anderson localization.

6. Appendix– Technical calculations

The term $\mathcal{A}$ is given by

$$\mathcal{A}(\varphi_1, \varphi_2, Q, N) = \left[e^{-2i\varphi_1} X_2 h^2(x_1) + e^{-2i\varphi_2} X_1 h^2(x_2)\right] \sigma + h(x_1)h(x_2)\left[2\sigma + \sigma_0\right] \tag{9}$$

with $X_a \equiv \mathrm{sinc} x_a$, $\varphi_a \equiv k_a d_a$ $(a = 1, 2)$, $X^2 \equiv X_1 X_2$, $\varphi \equiv \varphi_1 + \varphi_2$, and $\sigma_0 \equiv [1 - (Xe^{-i\varphi})^N]/[1 - (Xe^{-i\varphi})^2]$ $e^{-2i\varphi}/N$, $\sigma \equiv \left[e^{-2i\varphi}/2 - \sigma_0\right] / \left[1 - (Xe^{-i\varphi})^2\right]$.

The third iteration has been done for mixed-stack, with $kd = k_1 d_1 = -k_2 d_2$ and $Q = Q_\epsilon$. The extra term in Q^3 is $1/l_N^{(3)}$:

$$\frac{1}{l_N^{(3)}} = \frac{Q^3}{4} \sin 2kd \quad \left[F(X, kd, Q) \frac{1 - X^N}{N(1 - X^2)^2} + \frac{G(X, kd, Q)}{(1 - X^2)}\right], \tag{10}$$

with $F \equiv m_1 \left[(1 + X^2)/3 - m_1^2(1 - X^2) - 2X m_2\right]$, $G \equiv X m_1 m_2 - m_1/3 + m_3(1 - X^2)$. m_1, m_2, m_3 are explicit functions defined by $m_1(aQ) \equiv i\langle x e^{iax}\rangle/Q$, $m_2(aQ) \equiv \langle x^2 e^{iax}\rangle/Q^2$ and $m_3(aQ) \equiv i\langle x^3 e^{iax}\rangle/Q^3$ for x distributed uniformly on $[-Q, Q]$.

Acknowledgement

We acknowledge the support from the Agence Nationale de la Recherche, ANR-10-INTB-0914 ProComedia .

References

[1] D. R. Smith, J. B. Pendry and M. C. K. Wiltshire, Metamaterials and Negative Refractive Index, Science Vol. 305 no. 5685 pp. 788-792 (2004).

[2] N. Engheta, R. W. Ziolkowski, Metamaterials: Physics and Engineering Explorations. Wiley & Sons. pp. 3-30 (2006).

[3] Y. Dong, X. Zhang, Phys. Lett. A **359** 542-546 (2006).

[4] I.M. Lifshits, S.A. Gredeskul, L.A. Pastur, 1988, Introduction to the Theory of Disordered Systems (New York: John Wiley).

[5] P. Markos, C.M. Soukoulis, Wave Propagation: From Electrons to Photonic Crystals and Left-Handed Materials, Princeton University Press (2008).

[6] A.A. Asatryan, L.C. Botten, M.A. Byrne, V.D. Freilikher, S.A. Gredeskul, I.V. Shadrivov, R.C. McPhedran, Y.S. Kivchar, Phys. Rev. Lett. **99** 193902 (2007).

[7] A.A. Asatryan, S. A. Gredeskul, L. C. Botten, M.A. Byrne, V.D. Freilikher, I. V. Shadrivov, R. C. McPhedran, and Y. S. Kivshar, Phys. Rev. B **81**, 075124 (2010).

[8] E.J. Torres-Herrera, F.M. Izrailev, N.M. Makarov, Non conventional Localization in Bilayered Structures with Metamaterials, arXiv:1111.3397v1 (2011).

[9] D. R. Smith, Willie J. Padilla, D. C. Vier, S. C. Nemat-Nasser and S. Schultz, Phys. Rev. Lett., 84, 4184 (2000)

[10] J. Valentine, S. Zhang, T. Zentgraf, E. Ulin-Avila, D.A. Genov, G. Bartal and X. Zhang, Nature **455**, 376-379 (2008).

[11] F.M. Izrailev, N.M. Makarov, E.J. Torres-Herrera, Physica B **405** 3022-3025 (2010).

A Fourier-Bessel Expansion Method Applied to Photonic Crystals: Theory and Accuracy

Scott R. Newman*, and Robert C. Gauthier

Department of Electronics, Carleton University, Ottawa, Canada
*corresponding author, E-mail: snewman@doe.carleton.ca

Abstract

Fourier-Bessel functions are used to expand the field and dielectric in the 2D cylindrical Maxwell's equations recasting their solutions into eigenvalue problems. The eigenvalues obtained are the localized states of the given structure with their density indicating optical band gaps. The technique is shown for both TE and TM polarizations within a triangular lattice photonic crystal. The accuracy and efficiency of the results are compared relative to finite difference techniques.

1. Introduction

Photonic crystals (PCs) are typically characterized based on the translational periodicity that is present within the dielectric layout. Accordingly methods for analyzing these structures are often set in Cartesian coordinates. Two common techniques are finite-difference time-domain (FDTD)[1] or the plane-wave expansion method (PWEM)[2]. The FDTD method is robust through its discretization of Maxwell's equations and the dielectric. However, there are significant computational requirements. The more efficient PWEM expands the dielectric and field terms within Maxwell's equations in order to recast the equations as eigenvalue expressions. This technique operates in Fourier space and requires the presence of the unit cell that is a feature within translational structures.

The configuration of translational structures requires the introduction of rotational symmetry such as the 6-fold symmetry within the triangular lattice. There are also other structures such as photonic quasi-crystals that only have rotational symmetry about a central point. Analyzing structures with only rotational symmetry and their optical characteristics is normally done using FDTD or a supercell variation to the PWEM [3-4].

This work proposes a biorthonormal basis method for the analysis of 2D structures containing rotational symmetry. The analysis will be completed in cylindrical coordinates using Fourier-Bessel (FB) functions[5]. The structures are defined in r and θ while they are taken to be infinite in z. Biorthonormal basis solutions have been used in optical fibers [6-7] and outside of the field of optics FB functions have been used in the study of circular patterns [5]. Section 2 will examine the use of FB functions in the recasting of Maxwell's equations into eigenvalue expressions. It will show how the eigenvalue solutions provide the frequencies (eigenvalues) and mode profiles (eigenvectors) for supported localized modes. Section 3 will make use of the technique on the triangular lattice PC, presenting the resulting data and discussing convergence criteria. Section 4 will provide a brief summary and conclusions.

2. Theory

Maxwell's equations can be combined to give what are known as the master equations for both TE and TM polarizations respectively [8].

$$\nabla\times\left(\frac{1}{\varepsilon_r(\mathbf{r})}\nabla\times\mathbf{H}(\mathbf{r})\right)=\left(\frac{\omega}{c}\right)^2\mathbf{H}(\mathbf{r}) \tag{1}$$

$$\nabla\times\left(\nabla\times\frac{1}{\varepsilon_r(\mathbf{r})}\mathbf{D}(\mathbf{r})\right)=\left(\frac{\omega}{c}\right)^2\mathbf{D}(\mathbf{r}) \tag{2}$$

where $\mathbf{D}(\mathbf{r})=\varepsilon_o\varepsilon_r(\mathbf{r})\mathbf{E}(\mathbf{r})$. In the case of (2) the relative dielectric constant, $\varepsilon_r(\mathbf{r})$, is treated as a single value and the equation to be rewritten as

$$\frac{1}{\varepsilon_r(\mathbf{r})}\nabla\times(\nabla\times\mathbf{E}(\mathbf{r}))=\left(\frac{\omega}{c}\right)^2\mathbf{E}(\mathbf{r}) \tag{3}$$

The goal of using these equations is to express them as eigenvalue expressions such that the eigenvalues and eigenvectors can be determined. In PWEM analysis the dielectric and fields are expanded using Fourier functions as the basis. The eigenvalues thus obtained are the frequencies for the propagating Bloch modes through the structure. In our analysis, Fourier-Bessel functions, (4) and (5), are used to expand the inverse dielectric and the desired field component, H_z or E_z for TE and TM polarizations respectively.

$$\frac{1}{\varepsilon_r(r)}=\sum_{q,m_\varepsilon}\kappa^{\varepsilon}_{q,m_\varepsilon}J_0(\rho_q r)e^{-jm_\varepsilon\theta} \tag{4}$$

$$Field=\sum_{n,\Gamma}\kappa^{Field}_{n,\Gamma}J_0(\rho_n r)e^{-j\Gamma\theta} \tag{5}$$

where *Field* is the respective H_z or E_z field component for the given polarization, ρ_n is the nth zero of the Bessel

function scaled by the radius, b, of the dielectric extent. m_ε and Γ are integers related to the rotational symmetries in the inverse dielectric and field respectively. In previous work it was shown that the field profile within the structure would only have significant expansion coefficients when the rotational symmetries, Γ , followed the relationship $\Gamma = m_\varepsilon \pm k_\theta$; k_θ is defined as an integer related to the base rotational order of the mode being sought, i.e. 1 for a dipole-like mode [9].

The advantage to using FB functions is that they are the sum of the products of two distinct profiles, Fig. 1. The incorporation of the two profiles allows the FB functions to efficiently model the general radial shape of the centrally localized modes while also modeling the rotational symmetry present in both the modes and dielectric structure.

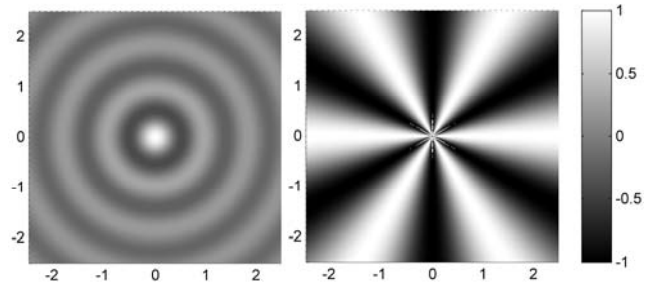

Fig. 1: Two example profiles used in a Fourier-Bessel product. The profile on the left is the Bessel function, $J_0(\rho_6 r)$, while the profile on the right is the exponential term, $e^{j6\theta}$.

In order to recast equations (1) and (3) the curls must be expanded into cylindrical coordinates. The FB expansions, (4) and (5), can then be inserted and using the orthogonality conditions [5] of the Bessel and exponential functions the master equations can be rewritten into the following expressions.

$$\sum_{\Gamma,n,q} \kappa^{\varepsilon}_{(\Gamma'-\Gamma),q}\left(\rho_n^2 S + \Gamma'\Gamma T - \rho_n \rho_q U\right)\kappa^{H_z}_{\Gamma,n} = \frac{\omega^2}{c^2}\kappa^{H_z}_{\Gamma',n'} \tag{6}$$

$$\sum_{\Gamma,n,q} \kappa^{\varepsilon}_{(\Gamma'-\Gamma),q}\left(\rho_n^2 S + \Gamma^2 T\right)\kappa^{H_z}_{\Gamma,n} = \frac{\omega^2}{c^2}\kappa^{H_z}_{\Gamma',n'} \tag{7}$$

Where S, T, and U are given below and used to simplify the expressions.

$$S = \frac{2\int_0^b rJ_0(\rho_{n'}r)J_0(\rho_n r)J_0(\rho_q r)dr}{b^2 J_1^2(\rho_{n'}b)} \tag{8}$$

$$T = \frac{2\int_0^b \frac{1}{r}J_0(\rho_{n'}r)J_0(\rho_n r)J_0(\rho_q r)dr}{b^2 J_1^2(\rho_{n'}b)} \tag{9}$$

$$U = \frac{2\int_0^b rJ_0(\rho_{n'}r)J_1(\rho_n r)J_1(\rho_q r)dr}{b^2 J_1^2(\rho_{n'}b)} \tag{10}$$

Equations (7)-(10) can be rewritten to be independent of the radial extend, b, by performing a change of variable r_{new} = r/b and letting r_{new} be over the interval [0,1]. These are calculated for all required ranges of n', n, and q and stored as look-up tables. It should also be noted that the integrand within (10) included a 1/r term. If the origin is included in the interval of integration the resulting values of the integral would be infinity. Fortunately (10) results from both first and second order derivatives of the field with respect to θ. The first and second order derivatives of the field around the origin are zero allowing us to leave the origin out of the integration. In the calculations this is achieved by integrating from δr to b. Convergence testing with a radial extent, b, of 2.5 μm showed that the results from both (6) and (7) converged to eigenvalue wavelength variations of less than 5 nm as δr decreases from 24.30 nm to 5.20 nm. Values of δr below 5.20 nm caused the results to diverge rapidly resulting in solutions to the expressions that were either undefined or infinite in value.

3. Results

Practical testing of the FB expansion method was conducted using a triangular array of circular air holes (ε_r = 1.00) in a silicon background (ε_r = 12.1104), Fig. 2. The PC was designed with a lattice constant, a, of 0.630 μm and a hole radius to lattice constant, r/a, ratio of 0.48. The parameters were chosen to ensure a complete TE/TM band gap.

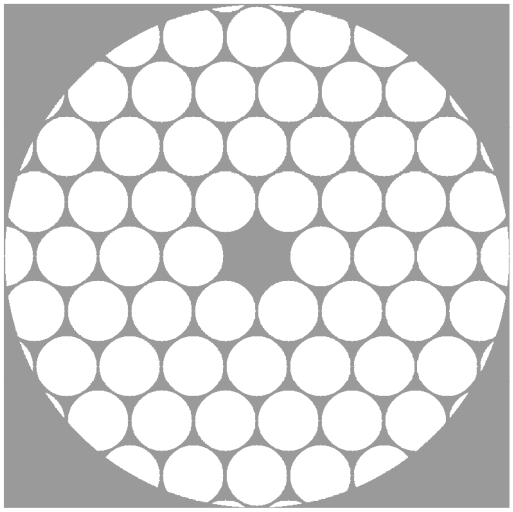

Fig. 2: Triangular lattice of air holes (ε_r = 1.00, white) in a silicon background (ε_r = 12.1104, gray) with a lattice constant, a, of 0.630 μm and r/a = 0.48.

In order to evaluate the accuracy of the FB expansion method a baseline is established using FDTD. The structure was discretized on a 160 point/μm Cartesian grid and excited with a noise source, with the desired polarization, located at the origin. The noise source contains sufficient spectral randomness to partially excite any modes supported by the structure. The temporal progression of the desired field component is monitored at points about the center and along the edge of the structure for defining localized state and band gap wavelengths respectively. Fourier transforms

are performed using the time information to obtain the frequency spectrums. The TE FDTD simulations show that the band gap is located from 1.176 μm to 1.810 μm. The nature of the band edges allows a +- 20 nm range from the higher to lowest amplitude over which the band edge is identified. The stated values are located in the middle of this range. The TM simulations give a band gap location from 1.221 μm to 1.461 μm.

To perform the FB expansion the Cartesian grid from the FDTD calculations is converted to a grid in cylindrical coordinates with 576 points/μm in r and 1440 points/2π in θ using Taylor expansions. The FB expansion coefficients, 200 Bessel terms and 100 exponential terms, for ε_r^{-1} are calculated over a 5 μm diameter circle about the center of the rotational symmetry. In order to focus on the angular symmetry, the magnitude of the expansion coefficients are plotted, Fig. 3, such that the radial components are overlapped at their rotational order. Each order m_ε has 100 points for the 200 radial components, q, used in the expansion. For clarity only the first 48 rotational orders are shown. Convergence tests addressing the density of the cylindrical grid showed that increasing the resolution would reduce the minor contributions at m_ε = 2, 4, etc. but would only result in the final results for mode wavelengths, varying by less than 1%. Additionally this would only affect terms that included these rotational orders i.e. k_θ = 2 or 4 for the triangular lattice.

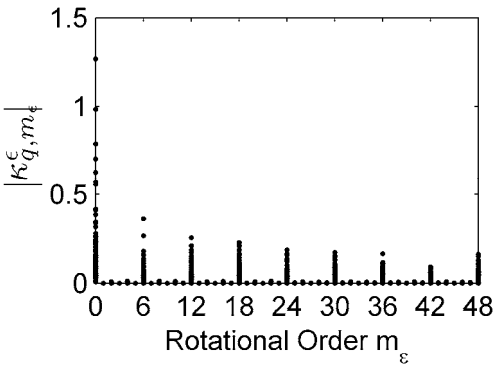

Fig. 3: Magnitude of the Fourier-Bessel expansion coefficients for the triangular lattice, 6-fold rotational. The expansion was done for a 5 μm diameter circle about the center of the PC with 200 Bessel and 100 exponential terms.

The results in Fig. 3 show that the expansion coefficients can be used to determine rotational symmetry of the structure as only expansion coefficients with significant values correspond to the multiples of the rotational order of the dielectric, in this case the 6-fold of the triangular lattice.

The expansion coefficients are then used in (6) and (7) along with the k_θ of the mode being sought. The expressions are then recast into an eigenvalue solution and solved to obtain the eigenvalues, ω^2/c^2. The sorted absolute values of the eigenvalues are converted to wavelength and shown in Fig. 4. Each eigenvalue corresponds to a state supported by the structure under examination. The regions where the states are sparse indicate band gaps. Fig. 4 shows the strong agreement between the Bessel expansion TE band gap regions and those determined by FDTD simulations shown in gray. The gaps within the clustered eigenvalues indicate the band gap to be from approximately 1.131 μm to 1.861 μm. The determination of the upper edge of the band gap is based on the combined information from the monopole (k_θ = 0) and dipole (k_θ = 1) results around this region. Further reconstruction of the modes is necessary for a more accurate estimate. The estimated values correspond to the FDTD band gap edges to within less than 4% error. The major difference between the two techniques is that the FDTD method shows the wavelengths that propagate versus those that are forbidden. The FB method is showing stationary states whose density allows approximate gaps to be determined.

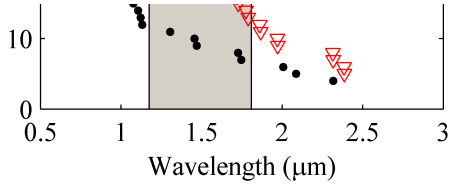

Fig. 4: The TE monopole and dipole FB expansion results for the triangular lattice with shaded area indicating the band gap obtained from FDTD simulations.

The accuracy of the technique is dependent upon the number of Bessel terms, n and q, and exponential terms, m_ε and Γ, used in the calculations. These values were verified in convergence tests showing that an increase from 100 Bessel terms to 200 terms causes wavelength shifts of less than 1% for both polarizations. An increase of 100 exponential terms to 150 terms resulted in wavelength changes of less than 7%.

The nature and location of the band gap determined through the Bessel expansion method can be further explored by examining the eigenvectors as they provide the $\kappa^{Field}_{n,\Gamma}$ terms that are then used in (4) to reconstruct the field profile of a given state. The modes within the band gap are either centrally localized modes or interfaces states. The interface states are the result of the boundary conditions at r = b imposed by the use of Bessel functions in the radial direction. These functions force the field and inverse dielectric to be zero at this boundary. As these states result from the boundary conditions they are ignored in the comparison with FDTD. Fig. 5 shows the centrally localized TE monopole state present within the indicated band gap. The wavelength for the monopole was calculated

to be 1.469 μm using the FB expansion method. This value gives has a 0.41% error when compared to the 1.475 μm value determine through FDTD simulations. Neither the FDTD simulations nor the FB expansion method found dipole states within the given band gap.

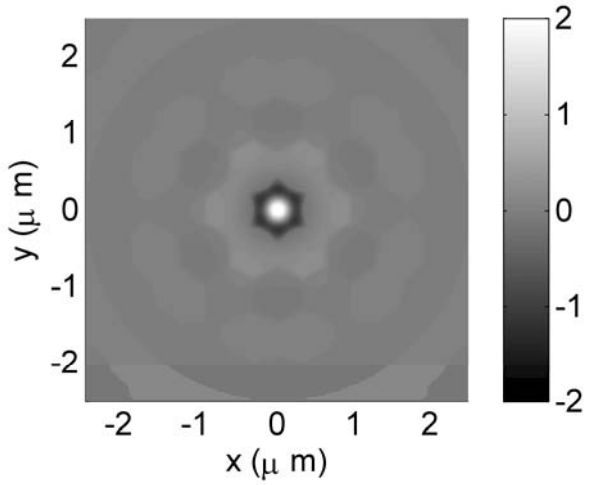

Fig. 5: TE Monopole field profile obtained using eigenvectors in a Fourier-Bessel reconstruction.

Using (7) the TM analysis of the structure was also completed with the sorted eigenvalues are shown in Fig. 6. The FB expansion method indicates an approximate band gap with lower and upper edges at 1.114 μm and 1.476 μm respectively. These are within 110 nm, less than 9% error, of the FDTD results, shown in gray.

Fig. 6: The TM monopole and dipole FB expansion results for the triangular lattice with shaded area indicating the band gap obtained from FDTD simulations.

The TM centrally localized modes can also be reconstructed and verified with the FDTD findings. Both the FDTD and Fourier-Bessel calculations determined that there was a monopole within the TM band gap. The Fourier-Bessel expansion solution gave a wavelength of 1.293 μm and a mode profile shown in Fig. 7. This value gives a 0.84% error from the 1.304 μm value determined with FDTD. As with the TE polarization neither technique located a dipole within the given band gap.

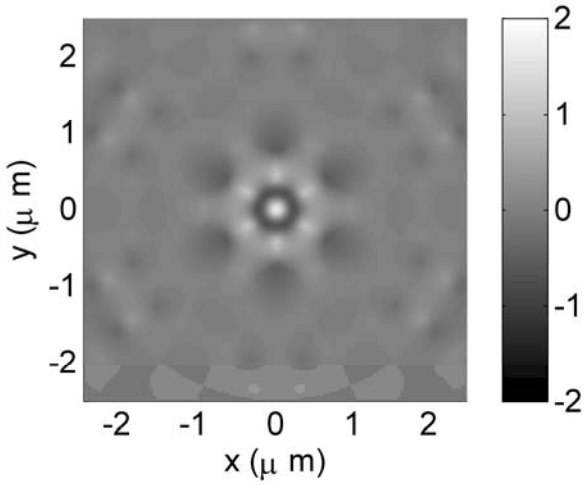

Fig. 7: TM Monopole field profile obtained using eigenvectors in a Fourier-Bessel reconstruction.

4. Conclusions

This work has proposed a new method for the study of dielectric structures that contain rotational symmetry using Fourier-Bessel functions as the basis. The technique has been shown to be effective in studying both TE and TM polarizations giving band gaps that are in good agreement with FDTD simulations. The Fourier-Bessel expansions method was also able to find modes and calculate their wavelength values to within 1% error of the FDTD results.

The use of the Fourier-Bessel expansion method does introduce interface states due to the boundary conditions imposed by the Bessel functions at the radial extent of the photonic crystal being studied. Removal of these states will be one aspect that will be addressed moving forward with this research. Future work will also focus on the use of the technique to generate full band structures akin to those obtained using the more traditional plane-wave expansion-method.

Acknowledgements

The authors would like to thank the funding support of Natural Sciences and Engineering Research Council of Canada (NSERC) and the Canadian Institute for Photonics Innovations (CIPI).

References

[1] Taflove, A., and S.C. Hagness, *Computational electrodynamics : the finite-difference time-domain method*, Artech, 2000.

[2] K. Ho, C. Chan, and C. Soukoulis, Existence of a photonic gap in periodic dielectric structures, *Phys. Rev. Lett.* 65: 3152 – 3155 (1990).

[3] S. Johnson and J. Joannopoulos, Block-iterative frequency-domain methods for Maxwell's equations in a planewave basis, *Opt. Exp.* 8: 173 (2001).
[4] D.M. Beggs, M.A. Kaliteevski, and R.A. Abram, Properties of microcavities in two-dimensional photonic quasicrystals with octagonal rotational symmetry, *J. Mod. Opt.* 54: 881 – 893 (2007).
[5] Guan, S., Fourier–Bessel analysis of patterns in a circular domain, *Physica D: Nonlinear Phenomena*, 151: 83 - 98, (2001).
[6] Silvestre, E., M.V. Andres, and P. Andres, "Biorthonormal-basis method for the vector description of optical-fiber modes," *Journal of Lightwave Technology*, Vol. 16, No. 5, 923-928, 1998.
[7] A. Ortega-Monux, J.G. Wanguemert-Perez, and I. Molina-Fernandez, Accurate Analysis of Photonic Crystal Fibers by Means of the Fast-Fourier-Based Mode Solver, *IEEE Photon. Technol. Lett.* 19: 414 – 416, (2007).
[8] Johnson, S.G., A. Mekis, S. Fan, and J.D. Joannopoulos, *Molding the flow of light*, IEEE, 2001.
[9] S.R. Newman, R.C. Gauthier, Representation of photonic crystals and their localized modes through the use of Fourier-Bessel Expansions, *IEEE Photon. J.* 3: 1133 – 1141, (2011).

Circular-Lattice Photonic Crystal Taper for Optical Waveguides

Gilliard N. Malheiros-Silveira[1], and Hugo E. Hernández-Figueroa[1]

[1]School of Electrical and Computer Engineering (FEEC), State University of Campinas (Unicamp), Department of Microwaves and Optics (DMO), 13083-970 – Campinas/SP, Brazil.
*corresponding author, E-mail: gilliard@dmo.fee.unicamp.br

Abstract

A new taper based on curvilinear-lattice photonic crystal used for coupling two ridge waveguides with different widths has been theoretically investigated. The studies were carried out by using the finite-difference time-domain (FDTD) method. Coupling efficiency around 75 % was obtained for waveguides whose widths were related by a factor of eleven.

1. Introduction

Photonic Crystals (PCs) are structures with a periodic modulation of dielectric materials which can occur in one, two or three dimensions. This kind of material can possibly inhibit the propagation of the light in one or more bands of frequencies [1]. The bandwidth of light that can not go through the material is known as Photonic Band Gap (PBG). Furthermore, parameters like materials, lattice type, geometrical distribution of materials in an unitary cell, among others, have a huge influence on the PBG behavior.

There are practically infinite combinatorial possibilities of geometry and material for structuring a PC. The first PCs proposed and studied were composed of simple geometric forms. However, in the last few years many researchers have used several methods of search and optimization to explore new configurations of PCs with optimized properties [2,3,4,5].

By using PCs it is possible to obtain more compact devices in integrated optics [6]. An interesting class of integrated devices based on PCs emerge as an alternative to the coupling light between different waveguides (optical fibers, ridge waveguide, PBG waveguide, among others) [7,8,9]. Generally, these devices (based on PCs) are a kind of tapers or lenses [1], [10,11].

This work presents a new optical taper based on curvilinear-lattice PC using silicon rods and air as a background material. The simulations were carried out by means of a FDTD code in a 2-D approach. In the device analysis, the transverse magnetic (TM) polarization, was considered. The remainder sections describe the design approach, the numerical results, the discussions, and the conclusions.

2. Design Approach

In general, the sub-class of PBG materials with curvilinear lattice has scatters positioned in curvilinear arrangement. J. Zarbakhsh et al. [12] have stated that square and triangular lattices presented a large complete PBG for the TM light polarization for 2-D PCs made up silicon cylinders with the same radii in an air background. Besides that, they presented a small difference in the spectral position of the PBG, while the cylinder systems assumed different types of lattices. In their investigation, they proposed a PC based on curvilinear lattice, with short-range periodicity. They also investigated a waveguide bend (Figure 1) where they observed very small local density of states (LDOS) in the outer region of waveguide and a high transmission in the inner region.

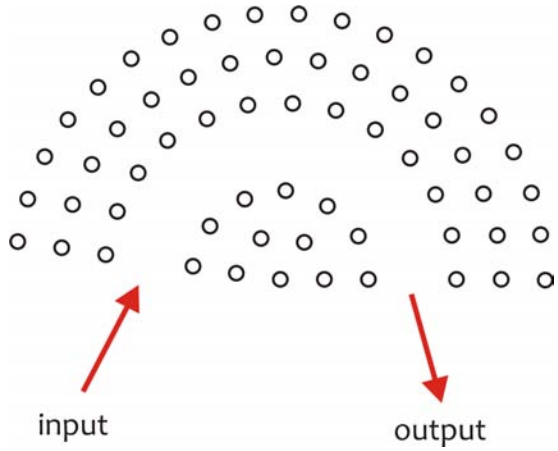

Figure 1: Waveguide bend based in curvilinear-lattice PC [12]. The cylinders consist of silicon and are immersed in air background.

Considering this material arrangement we have proposed a taper for coupling waveguides whose widths were related by a factor of eleven.

Figure 2(a)-(b) shows the two PBG waveguides without and with the new taper, respectively. Waveguides W11 and W1 are formed by removing eleven and one silicon rod layers in the square-lattice PC. The distance between them corresponds to 8 times the lattice constant (a).

The new taper is shown in Figure 2 (b), where the PC structure is formed by curvilinear lattice with silicon rods and with air in the background. The lattice constant is the same as that of the PC which composes the waveguides, but using curvilinear instead of square lattice.

(a)

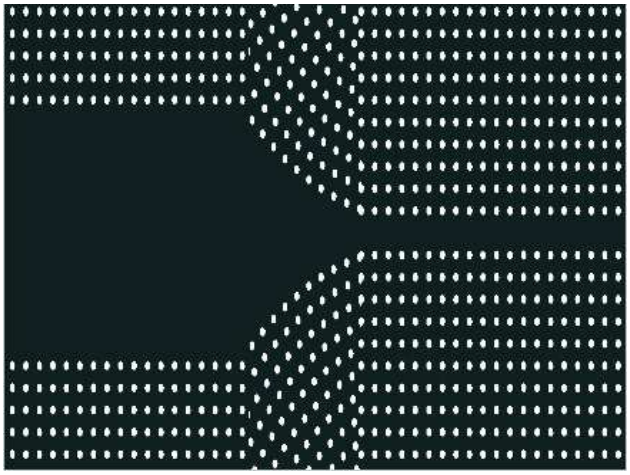

(b)

Figure 2: The PBG waveguides (W11 and W1) to be coupled. (a) it shows the waveguides without taper. (b) it shows the waveguides with taper.

In Figure 2 the silicon region is in white and the air region is in black. The input and output waveguides are in left and right regions, respectively. Figure 2(b) shows, intuitively, that the PC itself (with curvilinear-lattice) is used to strangle the incident light (from W11) towards the output waveguide (W1).

3. Numerical Results and Discussions

In the numerical analyses, we consider the coupling between two waveguides with distinct widths: one with 11a and the other with 1a, were "a" is the lattice constant of the square and curvilinear lattices of the PCs. The considered taper for this setup has length of 8a and it was designed with silicon rods, with radii of 0.2a and n=3.4 [13], in the air background, as shown in Figure 2(b).

The simulations were carried out in time-domain using an implementation of FDTD [14]. The input was excited with a gaussian pulse with a central frequency at 0.37a/λ and w=0.007. The material dispersion was not considered. Each simulation took around 1:10 hours. First, we simulated the coupling between the waveguides without the taper. Figure 3 shows the normalized transmission of the setup; depicted in Figure 2(a).

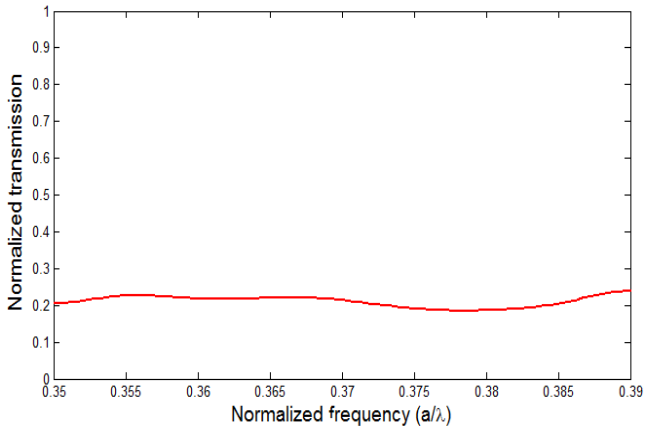

Figure 3: Normalized transmission of coupling between the waveguides without curvilinear taper.

In Figure 3 one can observe that the coupling works badly. The transmission of around 20% between the waveguides was observed.

After that, we investigated the coupling achieved when the taper is part of the setup (Figure 2(b)). Figure 4 shows its normalized transmission.

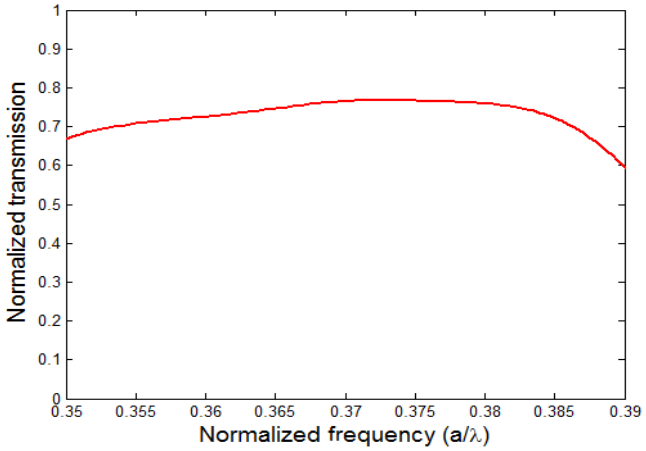

Figure 4: Normalized transmission curve of the setup in Figure 2(b).

In Figure 4, the normalized transmission between the optical waveguides can be seen; one can observe that the device works as predicted. The transmissions around 75 % at normalized frequency (a/λ) within the range of bandwidth 0.35 to 0.39 (a/λ). Although a normalized transmission around 75 % may seem reasonably good for this taper, it is important to highlight that the width factor of the waveguides is 11:1, and this coupling occurs in a short distance (8a).

Figure 5 shows pulse snapshots in the above mentioned setup for distinct time steps; one can see the pulse shape being accommodated by the taper and by the output waveguide.

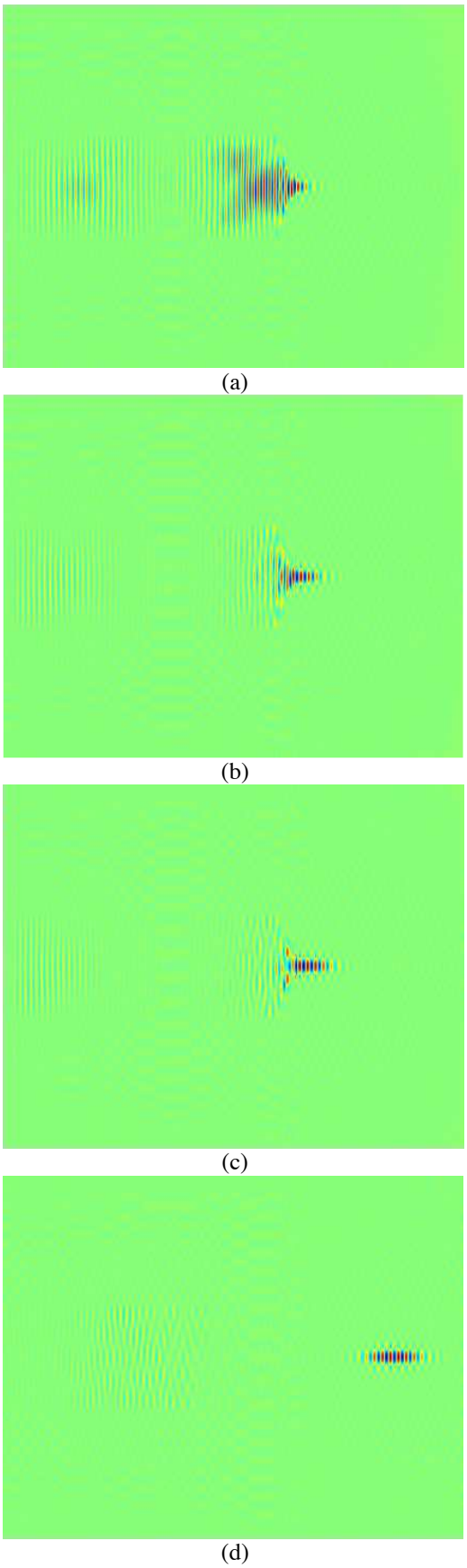

(a) (b) (c) (d)

Figure 5: Pulse snapshots at curvilinear-lattice PC based taper for distinct time steps.

Figure 5 shows that the mode is being strangled by the taper in order to adjust it to the output waveguide, as predicted.

Moreover, the new configuration of taper for optical waveguides presents an easy geometry allowing its fabrication using traditional techniques [15].

4. Conclusions

In conclusion, we have proposed and theoretically designed a taper based on a curvilinear-lattice PC for coupling ridge waveguides with distinct widths. Coupling efficiency around 75 % has been achieved for a wideband and for a relatively short distance between the waveguides. In future works, optimized versions of this taper considering a wideband, a higher transmission and a shorter length will be addressed.

Acknowledgements

The authors acknowledge the financial support from FAPESP (State of Sao Paulo Research Foundation) under contract 2010/18857-7, Capes, CePOF, and CNPq-FAPESP INCT FOTONICOM.

References

[1] J.D. Joannopoulos, R.D. Meade, and J.N. Winn, *Photonic Crystals: Molding the Flow of Light*, Princeton University Press, Princeton, New Jersey, 1995.

[2] G.N. Malheiros-Silveira, V.F. Rodríguez-Esquerre, and H.E. Hernández-Figueroa, Strategy of Search and Refinement by GA in 2-D Photonic Crystals With Absolute PBG, *IEEE Journal of Quantum Electronics* 47, 431-438, 2011.

[3] D. Wang, Z. Yu, Y. Liu, P. Lu, L. Han, H. Feng, X. Guo, and H. Ye, The optimal structure of two dimensional photonic crystals with the large absolute band gap, *Opt. Express* 19, 19346-19353, 2011.

[4] H. Men, N.C. Nguyen, R.M. Freund, P.A. Parrilo, and J. Peraire, Bandgap optimization of two-dimensional photonic crystals using semidefinite programming and subspace methods, *Journal of Computational Physics* 229, 3706-3725, 2010.

[5] C.Y. Kao, S. Osher, and E. Yablonovitch, Maximizing band gaps in two-dimensional photonic crystals by using level set methods, *Appl. Phys. B* 81, 235-244, 2005.

[6] T.D. Happ, M. Kamp, and A. Forchel, Photonic crystal tapers for ultracompact mode conversion, *Opt. Lett.* 26, 1102-1104, 2001.

[7] A. Mekis and J.D. Joannopoulos, Tapered Couplers for Efficient Interfacing Between Dielectric and Photonic Crystal Waveguides, *J. Lightwave Technol.* 19, 861-865, 2001.

[8] M.I. Kotlyar, Y. R. Triandaphilov, A.A. Kovalev, V.A. Soifer, M.V. Kotlyar, and L. O'Faolain, Photonic crystal

lens for coupling two waveguides, *Appl. Opt.* 48, 3722-3730, 2009.

[9] P. Shi, K. Huang, and Y.-P. Li, Subwavelength imaging by a graded-index photonic-crystal flat lens in a honeycomb lattice, *J. Opt. Soc. Am. A* 28, 2171-2175, 2011.

[10] M. Notomi, Manipulating light with strongly modulated photonic crystals. *Rep. Prog. Phys.* 73, 096501, 2010.

[11] M.G. Scullion, T.F. Krauss, and A. Di Falco, High Efficiency Interface for Coupling Into Slotted Photonic Crystal Waveguides, *IEEE Photon. J.* 3, 203-208, 2011.

[12] J. Zarbakhsh, F. Hagmann, S.F. Mingaleev, K. Busch, and K. Hingerl, Arbitrary angle waveguiding applications of two-dimensional curvilinear-lattice photonic crystals, *Appl. Phys. Lett.* 84, 4687-4689, 2004.

[13] J. Zhou, Q. Chang, D. Mu, J. Yang, W. Han, and L. Wang, Theoretical investigation of waveguide power splitters with parallel output ports in two-dimensional square-lattice photonic crystals, *J. Opt. Soc. Am. B* 26, 2469-2472, 2009.

[14] A. Taflove and S.C. Hagness, *Computational Electrodynamics: The Finite-Difference Time-Domain Method*, Boston, Artech House, 2000.

[15] W. Bogaerts, D. Taillaert, B. Luyssaert, P. Dumon, J. Van Campenhout, P. Bienstman, D. Van Thourhout, R. Baets, V. Wiaux, and S. Beckx, Basic structures for photonic integrated circuits in Silicon-on-insulator, *Opt. Express* 12, 1583-1591, 2004.

New Application to Microstrip Antennas with Metamaterial Substrates

Marinaldo Neto • Humberto Fernandes • Valentin Roda

Abstract The propagation characteristics of the rectangular microstrip patch antenna on metamaterial substrate are determined via full wave method, Transverse Transmission Line – TTL. Compared to other full wave methods, the TTL is an efficient tool to determine the resonant frequency, making possible a significant algebraic simplification of the equations involved in the process. Numerical results of resonant frequencies and return loss are found as functions of the metamaterial properties.

1 Introduction

Recently, a great deal of attention has been given to the properties of the artificial materials, named metamaterials, due to their interesting anomalous electromagnetic features and wide variety of applications. The metamaterial consist of periodic metallic arrangements, embedded in a low dielectric host medium, providing an effective medium with effective permittivity and permeability at any frequency of interest [1-7].

This work presents a rigorous full-wave analysis of rectangular microstrip patch antenna printed on a metamaterial substrate. Microstrip antennas consist of a patch conductor on a dielectric substrate and a ground plane at the bottom [8], as shown in Fig. 1. The analysis uses TTL method in the Fourier transform domain, and combines dyadic Green's functions with Galerkin's method to determine the radiation properties of rectangular microstrip patch antenna [9].

M.P.S. Neto • H.C.C. Ferandes • V.O. Roda
H.C.C. Ferandes (✉)

Department of Electrical Engineering, University of Rio Grande do Norte, 1583, Natal, Brazil
e-mail: humbeccf@ct.ufrn.br
Fax: +55-84-3215-3767

M.P.S. Neto
e-mail: sousaneto1@gmail.com

V.O. Roda
e-mail: Valentin@ct.ufrn.br

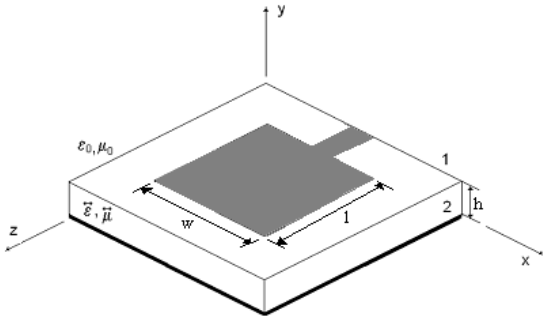

Fig. 1 Rectangular microstrip patch antenna on metamaterial substrate

2 Theory of metamaterials

Artificial materials have been developed with certain desirable dielectric and magnetic characteristics. New techniques and means of production have enabled the development of new materials with characteristics that cannot be found in nature [4]. Such artificial materials with properties that are not found in ubiquitous materials are called metamaterials. These can also be defined as artificial effectively homogeneous electromagnetic structures with unusual properties not readily available in nature [5].

An effectively homogeneous structure is a structure whose structural average cell size p is much smaller than the guided wavelength λ_g, as shown in Fig. 2. Therefore, this average cell size should be at least smaller than a quarter of wavelength $p < \lambda_g/4$. The condition $p = \lambda_g/4$ will refer to the effective – homogeneity limit, to ensure that refractive phenomena will dominate over scattering/diffraction phenomena when a wave propagates inside the MTM medium. The constitutive parameters are the permittivity ε and the permeability μ, which are related to the refractive index n in [5]:

$$n = \pm\sqrt{\mu_r \varepsilon_r} \tag{1}$$

The Fig. 2 shows the first metamaterial proposed by Pendry, consisting of metals and dielectrics and following the actual condition of homogeneity [5].

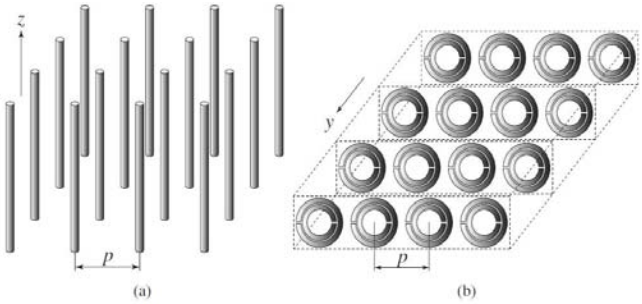

Fig. 2 (a) Structure consisting Thin-wire (TW). (b) Structure consisting Split-ring resonator (SRR)

For TW structure the negative permittivity is theoretically obtained from [10].

$$\varepsilon_{eff}(\omega) = 1 - \frac{\omega_{pe}^2}{\left(\omega^2 + j\omega\xi_e\right)} \tag{2}$$

where is the plasma frequency, which is given by:

$$\omega_{pe}^2 = \frac{2\pi c_0^2}{p^2 \ln\left(\frac{p}{r}\right)} \tag{3}$$

c_0 is the velocity of light in free space, p is the period of the arrangement and r is the radius of the wires. Therefore, it is possible to manipulate the plasma frequency only through the dimensions of the wires, ***p*** and ***r***.

The metal loss factor ζ_e is given by

$$\zeta_e = \frac{\varepsilon_0 \left(\frac{p\omega_{ep}}{r}\right)^2}{\pi\sigma} \tag{4}$$

where σ is the conductivity of metal.

For Re(ε_r) < 0 we have $\omega^2 < \left(\omega_{ep}^2 - \zeta_e^2\right)$. Reducing $\zeta_e = 0$ we have $\varepsilon_r < 0$ when $\omega < \omega_{ep}$, Fig. 3.

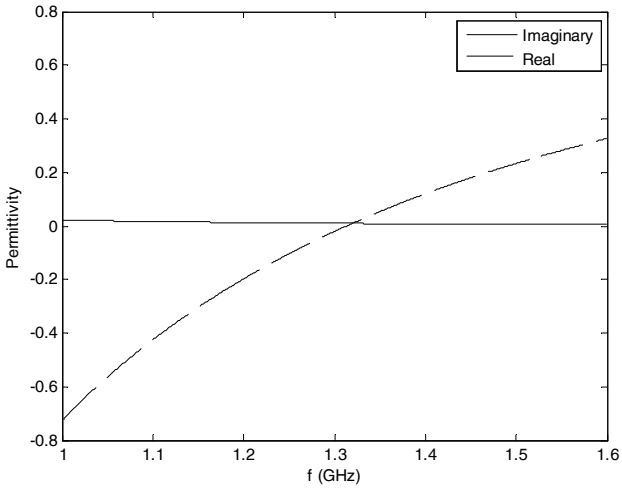

Fig. 3 Resonance frequency as a function of effective relative permittivity

A periodic arrangement of SRRs has an effective magnetic permeability given by [10]:

$$\mu_{eff}(\omega) = 1 - \frac{F\omega^2}{\omega^2 - \omega_{0m}^2 + j\omega\zeta_m} \tag{5}$$

Where **ω** is the magnetic resonant frequency resonance, ***F*** is the factor of the cell and ***r*** is the inner radius of the smaller ring.

$$F = \frac{\pi r^2}{p^2} \tag{6}$$

$$\omega_{0m}^2 = \frac{3pc_0^2}{\pi \ln\left(\frac{2w}{d}\right) r^3} \tag{7}$$

Where ***d*** is the distance between the rings and ***w*** is the width of the rings. is the loss factor of the metal, given by:

$$\zeta_e = \frac{2pR'}{r\mu_0} \tag{8}$$

Where R' is the metal resistance.

Of considerations we can say that to $\mu_r < 0$ we have $\omega_{0m} < \omega < \omega_{0m} \Big/ \sqrt{(1-F)} = \omega_{mp}$, Fig. 4 .

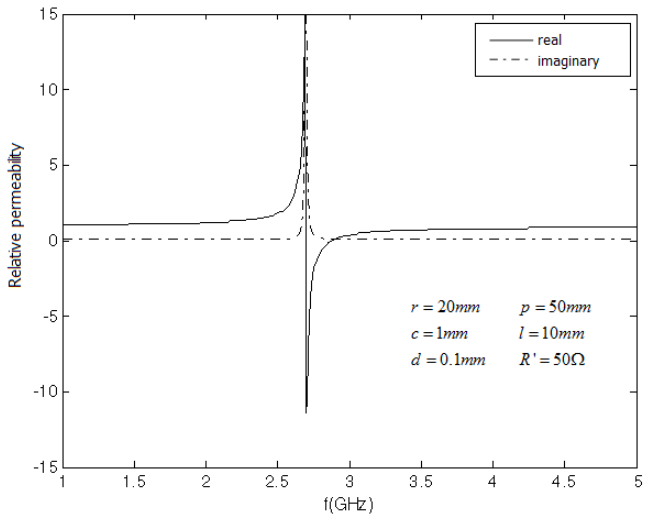

Fig. 4 Resonance frequency as a function of effective relative permeability

Therefore, values of a material with negative ε and μ can be made to certain frequency bands.

3 Theory

The MTM used in the structure described in Fig. 1 can be characterized by the tensor matrix below [4]:

$$\vec{\vec{\mu}} = \mu_0 \begin{bmatrix} \mu_{xx} & 0 & 0 \\ 0 & \mu_{yy} & 0 \\ 0 & 0 & \mu_{zz} \end{bmatrix} \quad (9)$$

$$\vec{\vec{\varepsilon}} = \varepsilon_0 \begin{bmatrix} \varepsilon_{xx} & 0 & 0 \\ 0 & \varepsilon_{yy} & 0 \\ 0 & 0 & \varepsilon_{zz} \end{bmatrix} \quad (10)$$

3.1. Field Structure

Starting from the general field equations of the LTT method and applying the tensors in (1) and (2), the field equations in the Fourier transform domain for the microstrip antenna with metamaterial substrate shown in Fig. 1 are given by:

$$\tilde{E}_{xi} = \frac{1}{k_0^2 \varepsilon_{xx} \mu_{zz} + \gamma_1^2} \left[-j\alpha_n \frac{\partial}{\partial_y} \tilde{E}_y + \beta_k \varpi \mu_0 \mu_{zz} \tilde{H}_y \right] \quad (11)$$

$$\tilde{E}_{zi} = \frac{1}{k_0^2 \varepsilon_{zz} \mu_{xx} + \gamma_i^2} \left[-j\beta_k \frac{\partial}{\partial_y} \tilde{E}_y + \alpha_n \varpi \mu_0 \mu_{xx} \tilde{H}_y \right] \quad (12)$$

$$\tilde{H}_{xi} = \frac{1}{k_0^2 \varepsilon_{zz} \mu_{xx} + \gamma_i^2} \left[-j\alpha_n \frac{\partial}{\partial_y} \tilde{H}_y + \beta_k \varpi \varepsilon_0 \varepsilon_{zz} \tilde{E}_y \right] \quad (13)$$

$$\tilde{H}_{zi} = \frac{1}{k_0^2 \varepsilon_{xx} \mu_{zz} + \gamma_i^2} \left[-j\beta_k \frac{\partial}{\partial_y} \tilde{H}_y + \alpha_n \varpi \varepsilon_0 \varepsilon_{xx} \tilde{E}_y \right] \quad (14)$$

The fields and of equations (11)-(14) are determined from wave equations in the spectral domain (15) and (16):

$$\frac{\partial^2 \tilde{E}y}{\partial y^2} - \gamma^2 \tilde{E}y = 0 \quad (15)$$

$$\frac{\partial^2 \tilde{H}y}{\partial y^2} - \gamma^2 \tilde{H}y = 0 \quad (16)$$

3.2. Admittance Matrix

Applying equations (11) - (14) the boundary conditions appropriate to the structure a system of equations is obtained in matrix form. This matrix is called the admittance or impedance matrix, depending on how the matrix equation is represented:

$$\begin{bmatrix} \mathrm{Y}_{xx} & Y_{xz} \\ Y_{zx} & Y_{zz} \end{bmatrix} \begin{bmatrix} \tilde{\mathrm{E}}_{\mathrm{xh}} \\ \tilde{\mathrm{E}}_{\mathrm{zh}} \end{bmatrix} = \begin{bmatrix} \tilde{\mathrm{J}}_{\mathrm{x}} \\ \tilde{\mathrm{J}}_{\mathrm{z}} \end{bmatrix} \quad (17)$$

Where for example:

$$Y_{xx} = \frac{j}{\gamma_1 \gamma_2 \varpi \mu_0} \left[\frac{\gamma_2 \cot gh(\gamma_1 h)(k_0^2 \varepsilon_{xx} \mu_{xx} \alpha_n^2 - \beta_k^2 \gamma_1^2)}{(\beta_k^2 \mu_{zz} + \alpha_n^2 \mu_{xx})} + \gamma_1 (k_2^2 - \beta_k^2) \right] \quad (18)$$

The matrix inversion is used and the current densities in the interface are expanded using basis functions:

$$\begin{bmatrix} Z_{xx} & Z_{xz} \\ Z_{zx} & Z_{zz} \end{bmatrix} \begin{bmatrix} \tilde{J}_{zh} \\ \tilde{J}_{xh} \end{bmatrix} = \begin{bmatrix} \tilde{E}_{xh} \\ \tilde{E}_{zh} \end{bmatrix} \quad (19)$$

$$\tilde{J}_{xh} = \sum_{i=1}^{n} a_{xi} \cdot \tilde{f}_{xi}(\alpha_n, \beta_k) \quad (20)$$

$$\tilde{J}_{zh} = \sum_{j=1}^{m} a_{zj} \cdot \tilde{f}_{zj}(\alpha_n, \beta_k) \quad (21)$$

The Fourier transform of the basis function used in the study is given by:

$$\tilde{f}_x(\alpha_n, \beta_k) = \frac{2\pi^2 l \cdot \cos\left(\frac{\beta_k l}{2}\right)}{\pi^2 - (\beta_k l)^2} \cdot Jo\left(\alpha_n \frac{w}{2}\right) \quad (22)$$

Equation (19) is transformed into a homogeneous matrix equation - provided that the determinant of the matrix is zero. The non-trivial solution corresponding to the characteristic equation of the structure and its roots provide a complex resonant frequency.

$$\begin{bmatrix} K_{xx} & K_{xz} \\ K_{zx} & K_{zz} \end{bmatrix} \cdot \begin{bmatrix} a_x \\ a_z \end{bmatrix} = \begin{bmatrix} 0 \\ 0 \end{bmatrix} \quad (23)$$

For Example:

$$K_{xx} = \sum_{-\infty}^{\infty} \tilde{f}_x \cdot Z_{xx} \cdot \tilde{f}_x^{\,*} \; ; \; K_{xz} = \sum_{-\infty}^{\infty} \tilde{f}_z \cdot Z_{xz} \cdot \tilde{f}_x^{\,*} \quad (24)$$

4 Results

The developed formulation has been used for the calculation of the resonance frequency of the proposed antenna supported by metamaterial substrate. This artificial medium exhibits anisotropic properties with effective permittivity ε_{eff} and permeability μ_{eff} [4-6]. Results are obtained taking into account two possible configuration of the metamaterial tensors by considering the variations of the effective permittivity and permeability [1].

In the first configuration (CASE 1), we consider that the components of the permittivity assume values $\varepsilon_{zz} = \varepsilon_{eff}$ and $\varepsilon_{xx} = \varepsilon_{yy} = 1$. On the other hand, the permeability elements are $\mu zz = 1$ and $\mu_{xx} = \mu_{yy} = \mu_{eff}$, so for these2-D structures, we have

$$\vec{\vec{\varepsilon}} = \varepsilon_0 \begin{bmatrix} 1 & 0 & 0 \\ 0 & 1 & 0 \\ 0 & 0 & \varepsilon_{eff} \end{bmatrix} \quad \vec{\vec{\mu}} = \mu_0 \begin{bmatrix} \mu_{eff} & 0 & 0 \\ 0 & \mu_{eff} & 0 \\ 0 & 0 & 1 \end{bmatrix} \quad (17)$$

In the second case (CASE 2), the analysis considers that the periodic arrangement of metallic elements is embedded in a dielectric with permittivity ε_r and permeability μ_r, therefore $\varepsilon_{zz} = \varepsilon_{eff}$, $\varepsilon_{xx} = \varepsilon_{yy} = \varepsilon_r$, $\mu_{zz} = \mu_{eff}$, and $\mu_{xx} = \mu_{yy} = 1$,as follows:

$$\vec{\vec{\varepsilon}} = \varepsilon_0 \begin{bmatrix} \varepsilon_r & 0 & 0 \\ 0 & \varepsilon_r & 0 \\ 0 & 0 & \varepsilon_{eff} \end{bmatrix} \quad \vec{\vec{\mu}} = \mu_0 \begin{bmatrix} 1 & 0 & 0 \\ 0 & 1 & 0 \\ 0 & 0 & \mu_{eff} \end{bmatrix} \quad (18)$$

Numerical computations are performed considering that the metamaterial has $\varepsilon_{eff} = 9.8$ and $\mu_{eff} = 3.1$.The resonant size of the patch is calculated at 250 MHz, as presented in [5]. We consider enhanced positive electric permittivity and magnetic permeability for microwave applications [5].

Fig. 3 shows the behavior of the resonant frequency as a function of the length l, (w = 93.0 mm and h = 0.127 cm). The metamaterial substrate is defined as given by (17). It is observed that as the dimension of the length increases, the resonant frequency decreases, as expected. Also, the use of magneto-dielectric materials, as antenna substrate, yields to the miniaturization of the antenna.

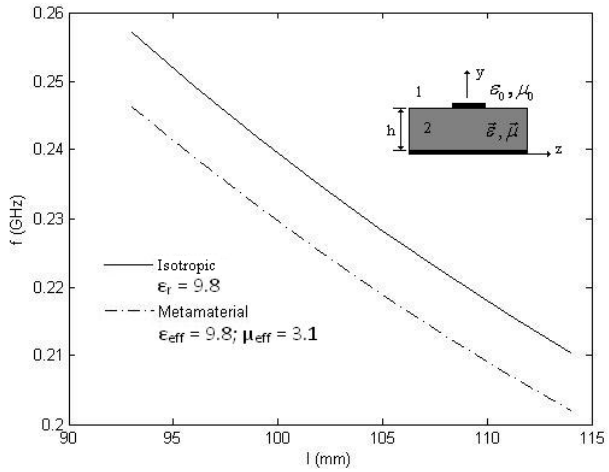

Fig. 3 Resonance frequency as function of the patch length

In Figure 3 numerical results are presented for the resonant frequency versus patch length with different values of effective permittivities along the same optical axis (z - axis), CASE 1. It appears that the antenna printed on a substrate with high dielectric constant has a low resonance frequency, which contributes to miniaturization of the device. The behavior of resonance frequency when the change occurs over μ_{eff} is similar to that observed in ε_{eff} as shown in Fig. 5.

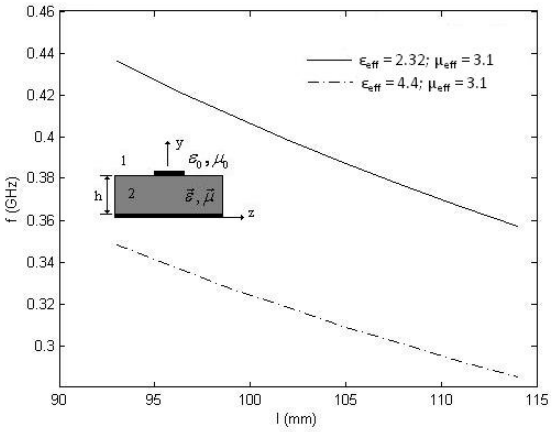

Fig. 4 Resonance frequency as function of the patch length

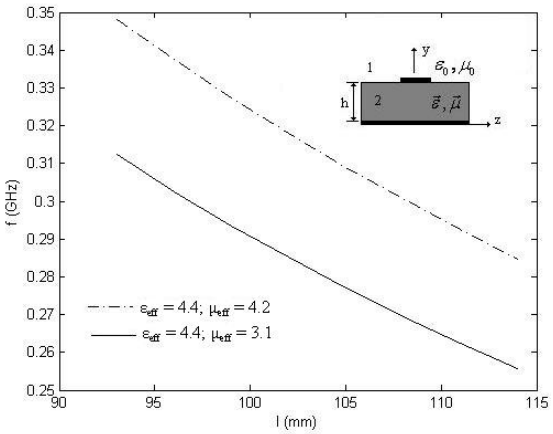

Fig. 5 Resonance frequency as function of the patch length

Using the Ansoft HFSS®, the return loss of the structure with bianisotrópico substrate (h = 0,127 cm) is obtained, as shown in Fig. 6. It appears that for the square patch, with $w = l = 9{,}3$ cm, the return loss is -22 dB.

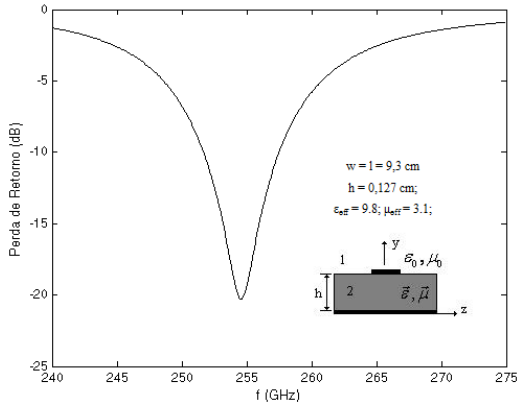

Fig. 6 Return loss as function of the resonance frequency

Fig. 7 shows curves of the resonant frequency as a function of the length l for an rectangular patch with w = 93.0 mm and h = 0.127 cm. The metamaterial is characterized by ε_{eff}, = 9.8, ε_r = 3.38, μ_{eff} = 3.1 and μr = 3.1 (CASE 2). We can see that the antenna with an isotropic substrate has a higher resonance frequency compared to the antenna with uniaxial material bianisotropic. The same behavior can be observed in Fig. 8, for w = 46.5 mm.

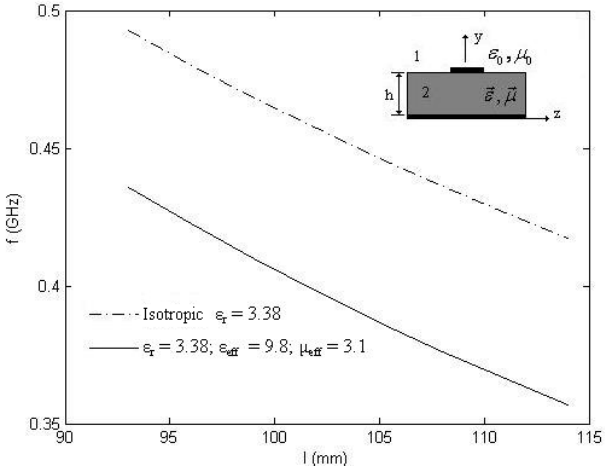

Fig.7 Resonance frequency as function of the patch length

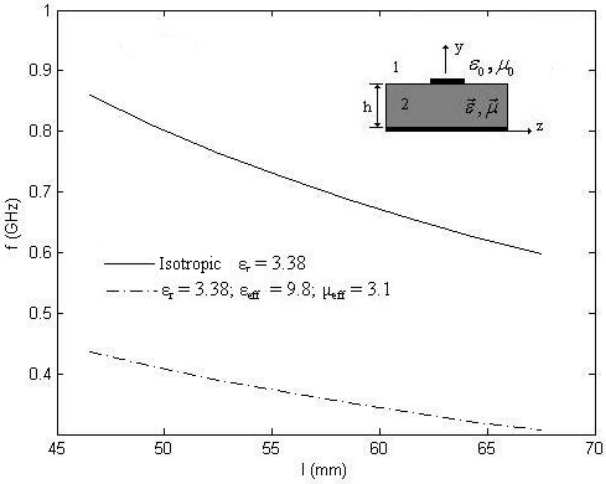

Fig. 8 Resonance frequency as function of the length

5 Conclusions

Theoretical and numerical results have been presented for the rectangular microstrip patch antenna on metamaterial substrate. The TTL method, in the Fourier transform domain

was used in the determination of the electrical and magnetic fields, in all regions.

The results were obtained for the complex resonance frequency. It can be seen that the use of magneto-dielectric materials, as substrate's antenna, yields to the miniaturization of these structures.

Acknowledgements The authors wish to acknowledge the assistance and support of CNPQ and CAPES, Brazilian Agencies and INCT-CSF.

References

1. C. F. L. Vasconcelos, M. R. M. L. Albuquerque, A. G. D'assunção, J. R. S. Oliveira and S. G. Silva , "Full Wave Analysis of Annular Ring Microstrip Antenna on Metamaterial" IEEE Transactions on Magnetics, v. 47, p. 1110-1113, 2011.
2. V. G. Veselago," The electrodynamics of substances with simultaneously negative values of ε and μ," Sov. Phys. Uspekhi, vol. 10, pp. 509–514, Jan.–Feb. 1968.
3. D. R. Smith, W. J. Padilla, D. C. Vier, S. C. Nemat-Nasser, and S. Schultz, " Composite medium with simultaneously negative permeability and permittivity," Phys. Rev. Lett., vol. 84, pp. 4184–4187, May2000.
4. C. Caloz and T Itoh, "Electromagnetic Metamaterials: Transmission line Theory and Microwave Applications: The Engineering Approach" John Wiley & Sons, Inc, Hoboken, New Jersey USA, 2006.
5. K. Buell, H. Mosallaei, and K. Sarabandi, "A substrate for small patch antennas providing tunable miniaturization factors," IEEE Trans. Micr. Theory Tech., vol.54, no.1, pp. 135–146, Jan. 2006..
6. Z. Li, K. Aydin, and E. Ozbay, "Determination of the effective constitutive parameters of bianisotropic metamaterials from the reflection and transmission coefficients," Phys. Rev. E, vol. 79, pp. 026610-1–026610-7, Feb.2009.
7. H. Mosallaei and K. Sarabandi, "Design and modeling of patch antenna printed on magneto-dielectric embedded-circuits metasubstrate," IEEE Trans. Antennas Propag., vol.55, no.1, pp.45–52, Jan.2007.
8. I..J. Bahl e P. Barthia, "Microstrip Antennas", Artech House, 1982.
9. H.C.C. Fernandes and M.P. Sousa Neto. "Metamaterials applied to microstrip antennas" MOMAG2010, Vila Velha-ES., V. 1. PP 1050 – 1052, Nov. 2010.
10. J. B., PENDRY Negative refraction makes a perfect lens, Physical Review Letters, Vol. 85, pp. 3966-3969, 2000.

METALLIC GRADED PHOTONIC CRYSTALS FOR GRADED INDEX LENS

Fabian Gaufillet, Éric Akmansoy

Institut d'Électronique Fondamentale,UMR8622,
Université Paris-Sud,
Orsay, F-91405 ; CNRS, Orsay, F 91405.
E-mail: eric.akmansoy@u-psud.fr

Abstract

We have designed a flat graded index lens made from a metallic graded 2D photonic crystal. The gradient of index has been obtained by varying the filling factor of a flat slab of photonic crystal in the direction perpendicular to that of the propagation of the electromagnetic field. This gradient has been designed in such a way that the flat slab focuses a plane wave. With applications in the microwave range in view, we considered a photonic crystal which consists of copper strips.

1. Introduction

The relation of dispersion of photonic cristals $\omega = \omega(\mathbf{k})$ is as a band structure, so that there are bandgaps in which the electromagnetic field cannot propagate. Apart from the bandgaps of photonic crystals, that is, in the photonic bands, the propagation of the electromagnetic field is governed by the shape of these bands [1]. Besides, graded photonic crystals (GPC) have been demonstrated to enhance the ability of photonic crystals to control the light propagation [2]. GPC are obtained by gradual modications of photonic crystal parameters, such as the lattice period, the filling factor or the dielectric constant. Several phenomena involving GPC have already been demonstrated such as light bending, quasi-transparency or focusing [3, 4, 5, 6]. In this communication, we report on the design of a GPC slab whose filling factor was varied. The gradient of the filling factor results in a gradient of the index of refraction, which allows the slab to focus a plane wave. The GPC was designed so as to it behaves as an homogeneous isotropic material. We consider a metallic photonic crystal for applications in microwave domain, such as antenna applications [7, 8, 9, 10], because in this domain of frequency, losses are very low [11].

2. Design

On one hand, gradient-index optics finds many applications in imagery and in telecommunications and has been quite studied for a long time (see reference [12] for a review). On the other hand, photonic crystals permit to control the flow of the electromagnetic field *via* the shape of their photonic bands which rely the group velocity $\mathbf{v_g}$ to the wave vector $\mathbf{k}$, according to the relation [1]

$$\mathbf{v_g} = \nabla_{\mathbf{k}}\, \omega(\mathbf{k})\,.$$

Thereby, the wave vector $\mathbf{k}$ is perpendicular to the iso-frequency curves (IFC). These represent the relation of dispersion at a given frequency.

On their part, GPC rely on a small variation of one of the parameters over one period of the lattice of the photonic crystal. This small variation gradually modifies the dispersion properties. Consequently, engineering the IFC allows the control of the direction of the wave vector $\mathbf{k}$. IFC may have a great variety of shapes. If these are circular shapes, the photonic crystal can be assumed as a homogeneous isotropic medium. Moreover, at the interface of the photonic crystal with vacuum, the tangential component of the wave vector $\mathbf{k}$ is continuous. These are the key points to

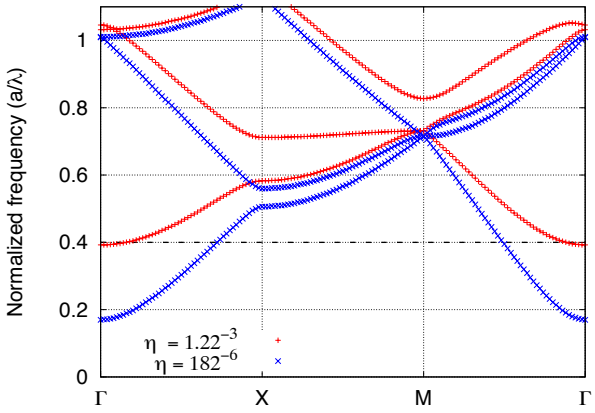

Figure 1: Band structures of two 2D metallic photonic crystals made of copper strips arranged in a square lattice with lattice constant $a = 12\,\text{mm}$. The incident electric field is parallel to the axis of the strips (TM mode). In the first photonic band, at the frequency $\lambda/a = 0.4$, the IFC are circular. The width of the strips of each photonic crystal is constant. The blue and the red curves correspond to the smallest width and to the greatest width of the strips, respectively.

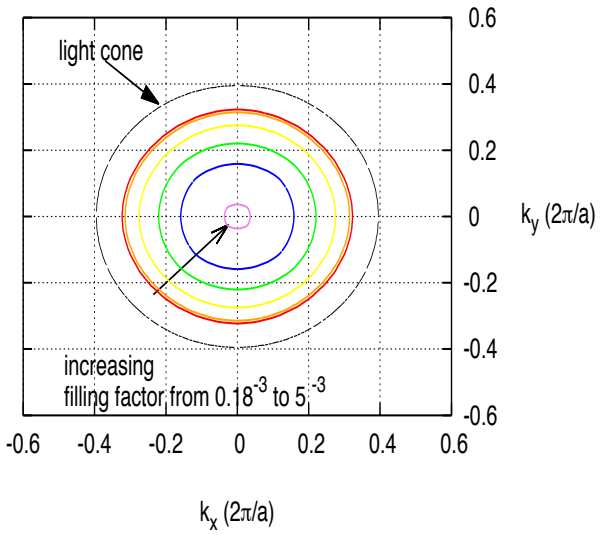

Figure 2: Six iso-frequency curves and that of the vacuum at $\lambda/a = 0.4$, the latter being referred to as the light cone. Each of these curves is circular and corresponds to width of the constitutive of the GPC. The filling factor varies from $0.18\,10^{-3}$ (red curve) to $5\,10^{-3}$ (purple curve).

design a graded index lens from a graded photonic crystal.

For applications in the X band frequency range, we considered a 2D photonic crystal made of metallic strips periodically arranged in a square lattice whose side is a. The strips are onto a dielectric substrate. Indeed, in the microwave range, metals can be considered as ideal metals, because ohmic losses are very low [11]. Thus, the elementary cell of the considered photonic crystal consists of a 12 mm wide square within which a 35 μm thick strip is centered. The filling factor η is given by

$$\eta = \frac{t\,w}{a^2}$$

So as to design the GPC, the filling factor η has been varied by varying the width w of the strips. We calculated band structures and IFC for several values of the filling factor η *via* a "home made" Finite Difference Time Domain (FDTD) code source which describes the unit cell with Periodic Boundaries Conditions [13]. The polarization of the incident wave was transverse magnetic (TM), the electric field being parallel to the axis. The conductivity of the copper strips is taken into account ($\sigma = 5.9\,10^7 S/m$) in the simulations. As the thickness of the strips is very small against their width, this would have necessitated a very fine mesh size and consequently very long numerical calculations. Consequently, we carried out the FDTD simulations using a subgridding scheme based on mesh nesting [14]. Thereby, the dielectric substrate is not simulated.

In the first photonic band of square metallic lattices, the IFC may be circular. Two band structures, which give rise to circular IFC, are reported in Fig. 1, that of the smallest width of the strips and that of the greatest width of the strips. The working frequency is $\lambda/a = 0.4$. The corresponding IFC for six values of the filling factor η and that of the vacuum are shown on Fig. 2. When the IFC are circular, the effective index n_{eff} can be calculated from the ratio of the radius of the IFC to that of the relation of dispersion of the vacuum. This latter is generally called the "light cone". Thus, we deduced a "calibration curve", that is, the variation of the effective index n_{eff} with the filling factor η, $n_{eff} = n_{eff}(\eta)$. The former decreases as the latter increases.

Then, we considered the graded index lens, that is, a slab of homogeneous medium, whose index of refraction is modified from center towards the edges. Graded index lens acts as a phase compensator (see Fig. 3), that is, all optical paths across the slab are equal [15]. The shape of the positive index of refraction is given by [15]

$$n(r) = n(0) - \frac{\sqrt{r^2 + f^2} - f}{d}\,,$$

where f is the focal length of the lens, d is its thickness, r is the radial distance from the optical axis and $n(0) = 1$ is the index of refraction along the optical axis of the lens. The focal length and the thickness were chosen $f = 15\,\text{cm}$ and $d = 6\,\text{cm}$, respectively. Thanks to the previously deduced relation between the effective index n_{eff} and the filling factor η ($n_{eff} = n_{eff}(\eta)$), we extrapolated the different widths of the constitutive strips in order to design the required gradient index $n(r)$. The width of the strips increases from the optical axis towards the edges. As the width w of the strips increases, the effective index n_{eff} decreases. A sketch of the whole device, made of printed circuit board (PCB), is reported in Fig. 4.

3. Simulations

Then, we simulated the whole device *via* a "home made" FDTD code source which involves Perfectly Matched Layer boundaries conditions and the Total Field/Scattered Field method [13]. It consisted of five layers of copper strips. Simulations were carried out at 10 GHz (normalized frequency $a/\lambda = 0.4$), firstly with a plane wave incident on the lens. The results of the simulations are reported in Fig. 5 and the map of the mean value of the square of the electric field ($\overline{E_z^2}$) highlights that the simulated focal length is around $f = 15\,\text{cm}$. Actually, the thickness d of the slab is not negligible compared to the focal length f, so that the slab cannot be assumed as a thin lens. The corresponding shape of the electric field in the focal plane is reported in Fig. 6. Full width at half maximum (FWHM) is 2.35 cm, so that FWHM $= 0.78\lambda$. It can be seen that the outer secondary maximum are high. Edge effects have been attributed to this. Indeed, it can be noticed in Fig. 5 that the electric field is not null on the edges of the domain of simulation. The discretization of the constitutive strips

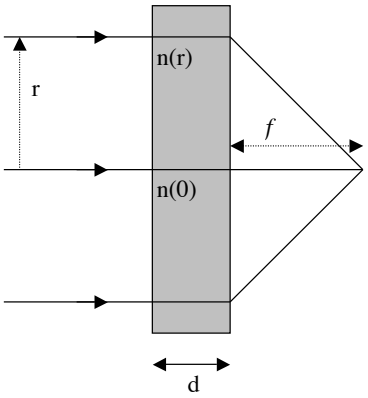

Figure 3: Gradient index lens which behaves as a phase compensator, that is, all the incident parallel rays converge towards the focal point with the same optical path. The index of refraction $n(r)$ is varied symmetrically and perpendicularly to the axis of the lens, from $r = 0$ (optical axis of the lens) towards the edges. f is the focal length of the lens and d is its thickness.

by a square mesh also brings about discrepancy in the simulations.

Secondly, so as to confirm our device really works as a graded index lens, we carried out further simulations with a punctual source located at the focal point. The results of the simulations are reported in Fig. 7 and it can be noticed that the designed GPC actually transforms a cylindrical incident wave into a plane wave. Both cases of simulations showed that the slab acts as a convex lens which focuses an incident plane wave and which transforms a cylindrical wave into a plane wave. Besides, this devices comprised only a few layers, so that it proves that GPC have the ability to efficiently control the propagation of light.

4. Conclusions

We designed a metallic graded photonic crystal slab so that its gradient of filling factor reproduces a gradient of index resulting in a given focal length. Then, we demonstrated firstly, that this device focuses a plane wave at the requisite focal length and secondly, that it transforms a cylindrical wave issued from a punctual source located at the focal point into a plane wave. Therefore, the graded photonic crystal slab behaves like a convex lens. Although this device applies to the microwave frequency range, GPC have the potential to optical components and would efficiently apply to integrated optics devices. Moreover, the engineering of the IFC should permit to design of gradient of negative index and that way, the design gradient index lens with sub-wavelength resolution. Therefore, GPC can find a great variety of applications from the microwave range to the optical domain and may be easily used in various integrated photonic devices.

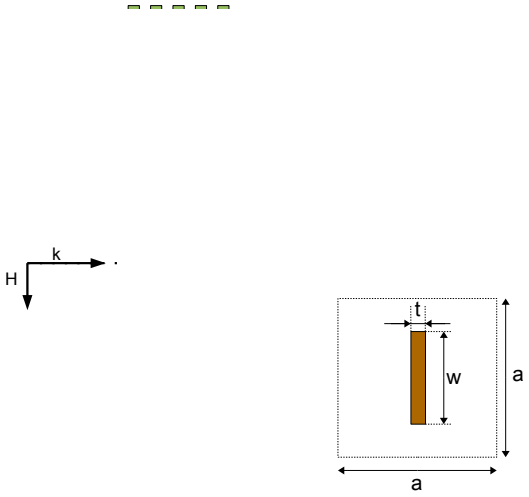

Figure 4: Sketch of the graded 2D photonic crystal slab made of metallic strips onto a dielectric substrate. The width w of the strips increases from the axis of the slab towards the edges, whereas their thickness t is constant to 35 μm. a is the period lattice which is constant. The direction of the wave vector $\mathbf{k}$ is shown and is perpendicular to the gradient. There is no strip along the axis of the lens since $n(0) = 1$. Inset : The elementary cell is a square of side a within which a 35 μm thick strip is centered.

References

[1] M. Notomi, "Theory of light propagation in strongly modulated photonic crystals: Refractionlike behavior in the vicinity of the photonic band gap," *Phys. Rev. B*, vol. 62, no. 16, pp. 10 696–10 705, Oct 2000.

[2] E. Centeno and D. Cassagne, "Graded photonic crystals," *Optics Letters*, vol. 30, no. 17, pp. 2278–2280, SEP 1 2005.

[3] E. Akmansoy, E. Centeno, K. Vynck, D. Cassagne, and J.-M. Lourtioz, "Graded photonic crystals curve the flow of light: An experimental demonstration by the mirage effect," *Applied Physics Letters*, vol. 92, no. 13, MAR 31 2008.

[4] E. Centeno, E. Akmansoy, K. Vynck, D. Cassagne, and J.-M. Lourtioz, "Light bending and quasi-transparency in metallic graded photonic crystals," *Photonics And Nanostructures-Fundamentals And Applications*, vol. 8, no. 2, pp. 120–124, MAY 2010.

[5] H. Kurt, E. Colak, O. Cakmak, H. Caglayan, and E. Ozbay, "The focusing effect of graded index photonic crystals," *Applied Physics Letters*, vol. 93, no. 17, p. 171108, 2008.

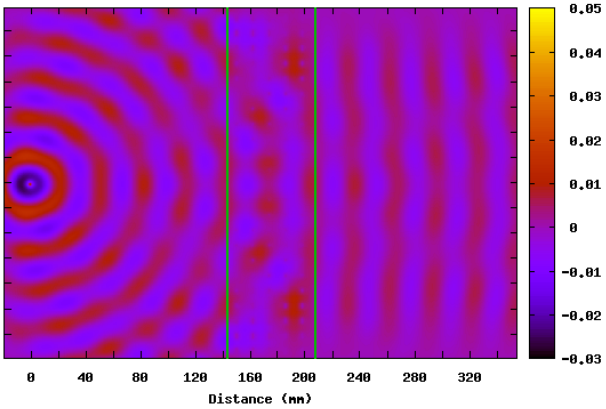

Figure 5: Map of the mean value of the square of the electric field ($\overline{E_z^2}$) of an incident TM plane wave on a graded index lens of focal length $f = 15\,cm$. The lens consists of a graded photonic crystal made of five layers of copper strips whose width is varying perpendicularly to the direction of propagation. The two vertical green lines delimit the lens.

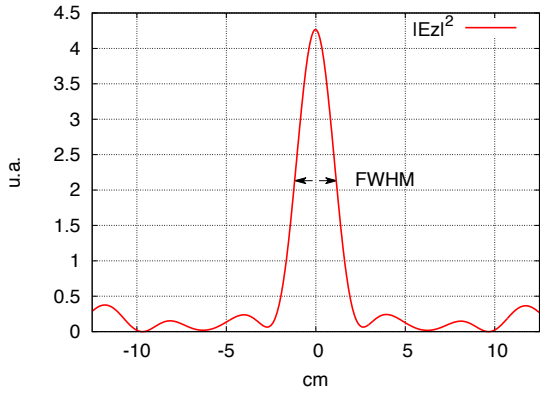

Figure 6: Shape of the mean value of the square of the electric field ($\overline{E_z^2}$) in the focal plane extracted from Fig. 5. FWHM $= 0.78\lambda$.

Figure 7: Map of the instantaneous electric field E_z of a punctual TM source located at the focal point and illuminating the graded index lens. The two vertical black lines delimit the lens.

[6] H. Kurt and D. S. Citrin, "Graded index photonic crystals," *Opt. Express*, vol. 15, no. 3, pp. 1240–1253, 2007.

[7] N. Guerin, S. Enoch, G. Tayeb, P. Sabouroux, P. Vincent, and H. Legay, "A metallic fabry-perot directive antenna," *Antennas and Propagation, IEEE Transactions on*, vol. 54, no. 1, pp. 220 – 224, jan. 2006.

[8] H. Boutayeb, T. Denidni, K. Mahdjoubi, A. Tarot, A. Sebak, and L. Talbi, "Analysis and design of a cylindrical EBG-based directive antenna," *IEEE Transactions On Antennas And Propagation*, vol. 54, no. 1, pp. 211–219, 2006.

[9] P. Ikonen, C. Simovski, and S. Tretyakov, "Compact directive antennas with a wire-medium artificial lens," *Microwave and Optical Technology Letters*, vol. 43, no. 6, pp. 467–469, 2004.

[10] A. de Lustrac, F. Gadot, E. Akmansoy, and T. Brillat, "High-directivity planar antenna using controllable photonic bandgap material at microwave frequencies," *Applied Physics Letters*, vol. 78, no. 26, pp. 4196–4198, 2001.

[11] J. Lourtioz, *Photonic crystals: towards nanoscale photonic devices*. Springer, 2005.

[12] D. T. Moore, "Gradient-index optics: a review," *Appl. Opt.*, vol. 19, no. 7, pp. 1035–1038, 1980.

[13] A. Taflove and S. C. Hagness, *Computational Electrodynamics: The Finite-Difference Time-Domain Method, 2nd ed.* Artech House Publishers, 2005.

[14] S. Chaillou, J. Wiart, and W. Tabbara, "A subgridding scheme based on mesh nesting for the fdtd method," *Microwave and Optical Technology Letters*, vol. 22, no. 3, pp. 211–214, 1999.

[15] A. O. Pinchuk and G. C. Schatz, "Metamaterials with gradient negative index of refraction," *J. Opt. Soc. Am. A*, vol. 24, no. 10, pp. A39–A44, 2007.

Synthesis of RF Circuits with Negative Time Delay by Using LNA

Blaise Ravelo

IRSEEM (Institut de Recherche en Systèmes Electroniques Embarqués), EA 4353, ESIGELEC,
Avenue Galilée, 76801 Saint Etienne du Rouvray, France.
Tel.: +33 (0)2 32 91 59 71 / +33 (0)6 45 33 47 22
Fax: +33 (0)2 32 91 58 59
*corresponding author, E-mail: blaise.ravelo@yahoo.fr

Abstract

A demonstration of the negative time-delay by using active circuit topologies with negative group delay (NGD) is described in this paper. This negative time delay is realized with two different topologies operating in base band and modulated frequencies. The first NGD topology is composed of an RL-network in feedback with an RF/microwave amplifier. Knowing the characteristics of the amplifier, a synthesis method of this circuit in function of the desired NGD values and the expected time advance is established. The feasibility of this extraordinary physical effect is illustrated with frequency- and time-domain analyses. It is shown in this paper that by considering an arbitrary waveform signal, output in advance of about 7 ns is observed compared to the corresponding input. It is stated that such an effect is not in contradiction with the causality. The other NGD topology is comprised of a microwave amplifier associated with an RLC-series resonant. The theoretical approach illustrating the functioning of this NGD circuit is established by considering the amplifier S-parameters. Then, synthesis relations enabling to choose the NGD device parameters according to the desired NGD and gain values are also established. To demonstrate the relevance of the theoretic concept, a microwave device exhibiting NGD function of about -1.5 ns at around 1.19 GHz was designed and analyzed. The NGD device investigated in this paper presents advantages on its faculty to exhibit positive transmission gain, the implementation of the bias network and matching in the considered NGD frequency band.

Keywords*: Negative group delay (NGD), active topology, time-advance*.

1. Introduction

Recent studies revealed that certain passive [1-8] and active [9-18] circuits are susceptible to exhibit the negative group delay (NGD) function at low- and RF-/microwave-frequencies. Theoretical and experimental analyses confirm that this innovative physical function allows to generate an output signal with wave fronts propagating in advance of its input under certain conditions [7-14]. Inversely to the ordinary medium, in this case, the time delay can be assumed as negative [4-5, 9-16]. It was pointed out [19-20] that this NGD effect does not forbid the causality principle. The limits and physical meaning of the negative time delay in function of the NGD transfer function parameters are stated in [21-22].

At the beginning, the occurrence of the NGD was initially explained with the anomalous dispersion [23-27]. The original theoretical study on the abnormal media with negative group velocity is introduced in [24]. In fact, it was shown that at certain wavelengths, these media is capable to present refractive group index n_g can be negative. The theoretical demonstration of the NGD can be illustrated with the following simple mathematical analysis. First of all, it is well-known that the group velocity is linked to the speed of light in the vacuum c by the expression:

$$v_g = c/n_g. \tag{1}$$

Clearly, if n_g is negative, the group velocity v_g is also negative. It means that when using a physical medium with geometrical length d, the group delay, by definition given by:

$$\tau_g = d/v_g, \tag{2}$$

can also be negative. Because of the inherent fact of the wave reshaping or the combination of the constructive and destructive interferences at the edge of the abnormal dispersive passive medium, the NGD phenomenon is systematically accompanied with significant losses, in particular, at microwave wavelengths [1-8]. So, the applications of NGD passive circuits are still limited before the middle 2000s.

To overcome this limitation, active microwave topologies based on the RF/microwave transistors have been developed [14-18, 21-22]. Then, different applications of the NGD function were proposed in the literature. One of the most published applications are the design of independent frequency NGD phase shifter [28-31] and broadband active balun [32], feed forward amplifier [33-34], microwave circuit with pulse compression [35] and also the reduction

of the propagation delay in the microelectronic interconnect with the NGD equalization technique [36-40].
However, because of the transistor access-matching difficulties, the complexity of the biasing networks and the output voltage sign inversion compared to the input is found with certain NGD topologies as proposed in [14-18]. It means that somehow the use of the transistors is more and more sophisticated. To avoid the complexity of bias network and the issues related to the matching level, the replacement of the transistor by an integrated low noise amplifier (LNA) was introduced in [41] for the base band applications.
The present paper is focused on the study of NGD topologies using microwave LNA. For the better understanding, this paper is organized in three main sections. Section 2 presents the analysis of the base band NGD topology proposed briefly in [41]. This first NGD circuit is aimed to the base band applications. Section 3 is focused on the investigation of the NGD LNA topology dedicated to the modulated microwave signals application. Section 4 is the general conclusion of the paper.

2. Investigation on an NGD circuit with LNA operating in baseband frequencies

Figure 1 presents the topology of the NGD circuit understudy for the base band frequencies. It is comprised of an RL-network in feedback with an LNA ***A***.

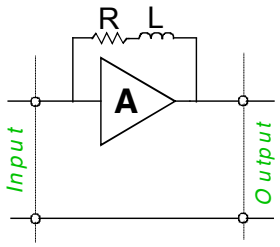

Figure 1: Amplifier in feedback with an RL-series network.

In order to achieve a global perspective on the frequency analysis including the stability, transfer function and matching access, the present analytical approach is based on the S-parameters analysis. To do this, an ideal microwave LNA operating in base band frequencies is considered. For the sake of the analytical expression simplification, in the remainder of this section, the considered amplifier is substituted by the ideal S-parameters expressed as:

$$S_A = \begin{bmatrix} \rho & 0 \\ T & \rho \end{bmatrix}, \tag{3}$$

where ρ and T represent respectively the return loss and transmission parameter. Moreover, this amplifier is supposed perfectly unilateral, S_{A12} = 0. The theoretical analysis of this topology by using the S-parameters is introduced in the next subsection. Then, numerical demonstrations of the negative time delay will be explored based on the analyses in frequency- and time-domains.

2.1. Theory on the baseband topology proposed

After the calculation of the S-parameters of the cell shown in Figure 1, we will establish the synthesis relations enabling to determine the elements R and L in function of the desired gain and NGD values knowing the characteristics of the amplifier.

2.1.1. S-parameter analysis of the NGD cell for base band frequencies

As the circuit proposed is comprised of an RL-network in feedback with an amplifier, it is easier to calculate the S-parameters from the admittance matrix. According to the circuit and system theory, the admittance matrix of the whole circuit which is also the sum of the passive part admittance matrix and that of the amplifier is expressed as:

$$[\underline{Y}] = \begin{bmatrix} \underline{Y}_{11}(j\omega) & \underline{Y}_{12}(j\omega) \\ \underline{Y}_{21}(j\omega) & \underline{Y}_{22}(j\omega) \end{bmatrix}, \tag{4}$$

with

$$\underline{Y}_{11}(j\omega) = \underline{Y}_{22}(j\omega) = \frac{1}{R + jL\omega} - \frac{\rho - 1}{R_0(\rho + 1)}, \tag{5}$$

$$\underline{Y}_{12}(j\omega) = \frac{-1}{R + jL\omega}, \tag{6}$$

$$\underline{Y}_{21}(j\omega) = \frac{-1}{R + jL\omega} - \frac{2T}{R_0(\rho + 1)^2}, \tag{7}$$

where ω is the angular frequency, $j = \sqrt{-1}$ and R_0 = 50 Ω is the reference impedance of the source and the load. Through the admittance to S-matrix transform, one establishes that the following S-parameters of the NGD cell understudy are:

$$\underline{S}_{11}(j\omega) = \underline{S}_{22}(j\omega) = \frac{R_0(T-1) + \rho(2\underline{Z} + \rho \cdot R_0)}{2\underline{Z} + R_0(2\rho - T + 2)}, \tag{8}$$

$$\underline{S}_{12}(j\omega) = \frac{R_0(\rho + 1)^2}{2\underline{Z} + R_0(2\rho - T + 2)}, \tag{9}$$

$$\underline{S}_{21}(j\omega) = \frac{2T\underline{Z} + R_0(\rho + 1)^2}{2\underline{Z} + R_0(2\rho - T + 2)}, \tag{10}$$

where

$$\underline{Z} = R + jL\omega. \tag{11}$$

Therefore, the transmission phase $\varphi(\omega) = \angle \underline{S}_{12}(j\omega)$ is expressed as:

$$\varphi(\omega) = \arctan\left[\frac{2T \cdot L\omega}{2T \cdot R + R_0(\rho+1)^2}\right] - \arctan\left[\frac{2L\omega}{2R + R_0(2\rho - T + 2)}\right], \quad (12)$$

We find that at very low frequencies ($\omega \approx 0$), these S-parameters become:

$$S_{11}(0) = S_{22}(0) = \frac{R_0(T-1) + \rho(2R + \rho \cdot R_0)}{2R + R_0(2\rho - T + 2)}, \quad (13)$$

$$S_{12}(0) = \frac{R_0(\rho+1)^2}{2R + R_0(2\rho - T + 2)}, \quad (14)$$

$$S_{21}(0) = \frac{2T \cdot R + R_0(\rho+1)^2}{2R + R_0(2\rho - T + 2)}. \quad (15)$$

According to relation (13), the NGD cell requires the following stability condition:

$$|S_{11}(0)| < 1 \quad \Leftrightarrow \quad R > R_{\min} = R_0 \frac{\rho^2 - 2\rho + 2T - 3}{2(1-\rho)}. \quad (16)$$

Moreover, it can be demonstrated from equation (10) that at very low frequencies ($\omega \approx 0$), the group delay of the circuit which is analytically defined as:

$$\tau(\omega) = -\frac{\partial \angle \underline{S}_{21}(j\omega)}{\partial \omega}, \quad (17)$$

is expressed as:

$$\tau(0) = \frac{2L \cdot R_0(\rho - T + 1)^2}{[2R + R_0(2\rho - T + 2)][R_0(\rho+1)^2 + 2T \cdot R]}. \quad (18)$$

It means that to generate NGD with the circuit introduced in Figure 1 at very low frequencies ($\tau(0) < 0$), the following condition must be satisfied:

$$2R + R_0(2\rho - T + 2) < 0 \Leftrightarrow R < (T/2 - \rho - 1)R_0. \quad (19)$$

2.1.2. Synthesis relations

At the beginning of the synthesis process, the used amplifier is supposed characterized by its S-parameter elements T and ρ. Thus, from the desired values of gain $|S_{21}(0)|$ and NGD $\tau(0)$, the synthesis relations enabling to determine the NGD circuit parameters R and L are extracted by inverting relations (15) and (18) respectively. From where are established the following formulations [16]:

$$R = R_0 \frac{S_{21}(0)(T - 2\rho - 2) + (\rho+1)^2}{2[S_{21}(0) - T]}, \quad (20)$$

$$L = \tau(0) \frac{\left\{[2R + R_0(2\rho - T + 2)]\right\}}{2R_0(\rho - T + 1)^2}. \quad (21)$$

This expression is dedicated to the synthesis with $\tau(0)$ assigned as a real negative. Under the following condition:

$$T > \rho + 2, \quad (22)$$

the result of expression (20) is physically meaningful only under the following condition:

$$S_{21}(0) > S_{21\min}(0) = \frac{(\rho+1)^2}{\rho - T + 2}. \quad (23)$$

2.1.3. Fundamental characteristics of the baseband NGD cell understudy

One of the main properties which characterizes the NGD cell understudy is based on the relation between its transmission parameter $S_{21}(0)$ and its reflection parameters $S_{11}(0) = S_{22}(0)$. In fact, giving the transmission parameter T and the return loss ρ of the amplifier A, one demonstrates that the return losses $S_{11}(0) = S_{22}(0)$ are mathematically linked to the insertion gain $S_{21}(0)$ by the relation:

$$S_{11}(0) = S_{22}(0) = \frac{(\rho+1)[\rho + 1 - S_{21}(0)] + T}{\rho - T + 1}. \quad (24)$$

To achieve the basic stability condition:

$$|S_{11}| = |S_{22}| < 1, \quad (25)$$

once again, the transmission parameter $S_{21}(0)$ must verify inequality (23). Furthermore, under condition (19), the group delay $\tau(\omega)$ of the NGD cell can be negative from $\omega \approx 0$ to the cut-off frequency ω_c. Via the derivation of the transmission phase with respect to ω, it is established that this cut-off frequency is expressed as:

$$\omega_c = \frac{\sqrt{[(\rho+1)^2 R_0 + 2T \cdot R] \cdot [R_0(2\rho + 2 - T) + 2R]}}{2L\sqrt{T}}. \quad (27)$$

In order to verify the relevance of the above theoretic concept, in the next section, we will examine the S-parameters and the group delay of a proof of concept device designed with the NGD topology proposed.

2.2. Numerical demonstration of the negative time effects

The simulation results presented in this section were generated from the well-known the commercial software Advanced Design system (ADS) from Agilent™.

2.2.1. Design of the prototype of base band NGD device tested

As illustrated in Figure 2, a circuit composed of two-stage NGD cells was designed and simulated. After the application of the previous synthesis relations accompanied with a slight optimization of the RF-components, the choice of the relevant nominal values of passive elements were carried out.

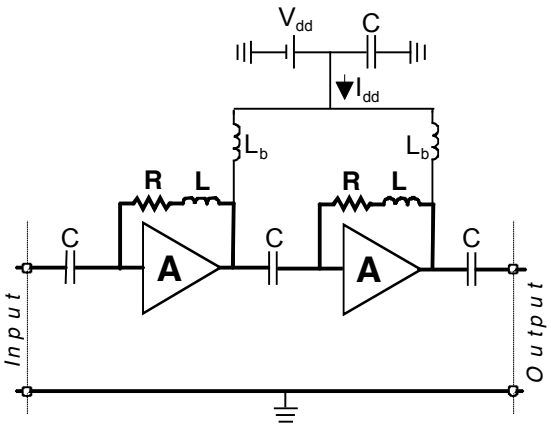

Figure 2: Prototype of two-stage NGD circuit for testing the time advance.

Then, comparative simulations were performed between the circuit comprised of ideal RF-part and the complete circuit shown in Figure 2. This latter was simulated with the S-parameter realistic models of passive components R, L and C available in ADS library. Table 1 indicates the references of the components employed. The employed amplifiers are MMIC LNAs HMC 395 provided by HITTITE™. In this study, the amplifiers were biased with the DC voltage V_{dd} = 5 V and I_{dd} = 20 mA.

The considered MMIC LNAs were replaced by the measured S-parameters including the bias networks provided by the manufacturer.

Table 1: References of the passive components constituting the circuit shown in Figure 2.

	Nominal value	Reference	Manufacturer
Resistance	R = 27 Ω	AVX CR 10-270J	AVX
Inductance	L = 100 nH	LQG15HSR 10J02	MURATA
	L_b = 100 µH	AIC1210-101J	COILCRAFT
Capacitor	C = *1 nF*	-	MURATA

2.2.2. Frequency domain investigations

One points out that the simulation results presented in this paragraph were realized by considering first the ideal RF circuit and then, the realistic circuit shown in Figure 2 by considering the touchstone or S_2P (or two-ports S-parameter) models of the passive components provided by the manufacturer. According to the frequency bands of the components utilized, S-parameter simulations were performed. As displayed in Figure 3, a good agreement between the frequency simulations with the ideal and realistic circuits is found in the NGD frequency band.

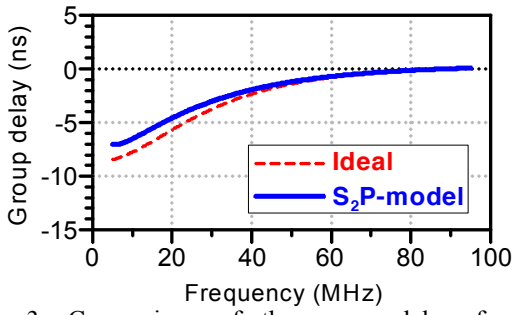

Figure 3: Comparison of the group delay frequency responses from ideal RF circuit and realistic circuit with S2P models including the bias networks.

As forecasted in theory, group delay presenting negative values were realized up to about 90 MHz. This NGD value goes down to about -7 ns at very low frequencies ($\omega \approx 0$). As shown in Figure 4, the circuit simulated guarantees an average gain more than 0 dB from very low frequencies up to hundreds MHz.

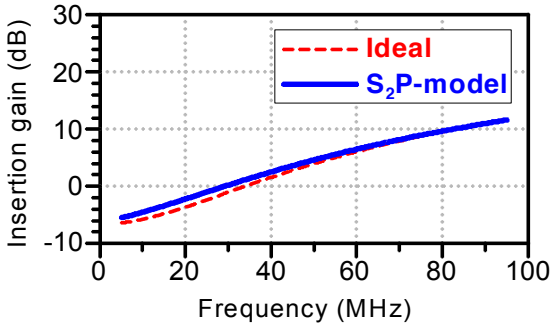

Figure 4: Comparison of the group delay frequency responses from the ideal RF circuit and realistic circuit with S2P models including the bias networks.

2.2.3. Stability analysis

The access parameters S_{11} and S_{22} of the circuit tested are plotted in Figure 5. We remark that these parameters confirm the stability of the circuit from DC to 5 GHz. Moreover, in this ultra wide frequency band, the isolation parameter S_{12} is better than -20 dB. To strengthen the stability of the tested device, the stability factor was also examined. One recalls that this factor is defined by:

$$\mu(\omega)=\frac{1-\left|S_{11}(j\omega)\right|^2}{\left|S_{22}(j\omega)-S_{11}^{*}(j\omega)\Delta(j\omega)\right|+\left|S_{12}(j\omega)S_{21}(j\omega)\right|}, \quad (28)$$

with

$$\Delta(j\omega)=S_{11}(j\omega)S_{22}(j\omega)-S_{12}(j\omega)S_{21}(j\omega), \quad (29)$$

and $S_{11}^{*}(j\omega)$ is the conjugate of $S_{11}(j\omega)$.

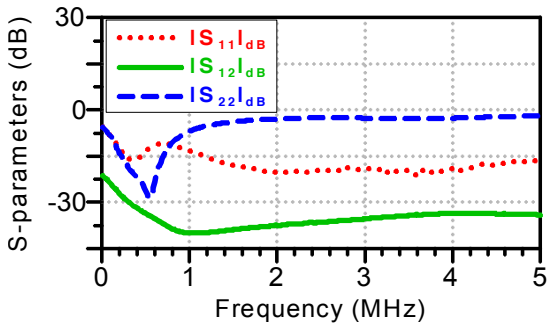

Figure 5: Isolation and return losses of the NGD device shown in Figure 2.

As reported in [17], this behaviour of the transmission parameter magnitude can be exploited to generate the pulse compression effect. The Rollet factor of the circuit is also plotted in Figure 6.

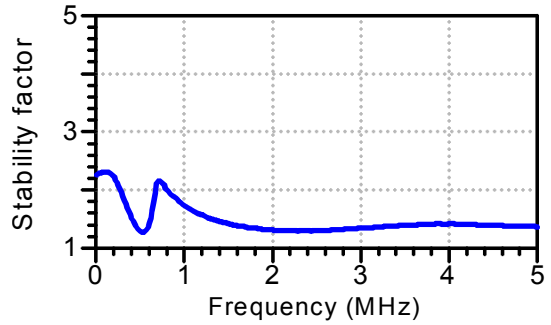

Figure 6: Rollet's factor of the NGD device shown in Figure 2.

As conclusion, the NGD topology proposed in this section respects all the constraints of classical RF active devices as the stability condition in UWB frequency band.

2.2.4. Time-domain investigations

For the better understanding about the meaning of the NGD effect generated by the circuit understudy, time-domain simulations were also performed in the transient option of SPICE-ADS environment. Figure 7 displays the configuration of the simulated circuit which is loaded by R_0 = 50 Ω. After ADS time-domain simulations, the results plotted in Figure 8 and Figure 9 were obtained.

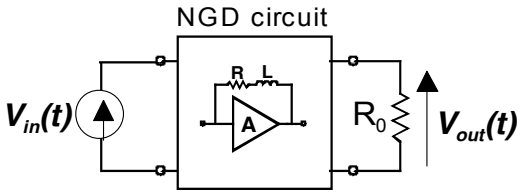

Figure 7: NGD circuit shown in Figure 2 loaded by R_0 = 50 Ω.

We can see that as explained by Figure 8, the output V_{out} of the NGD circuit is practically conform to the Gaussian input V_{in} which presents here a half height half width of about 18 ns. Moreover, contrarily to the ordinary circuit transient response, thanks to the NGD phenomenon, the wave fronts of the output V_{out} is slightly in advance of about 7 ns compared to the input V_{in}.

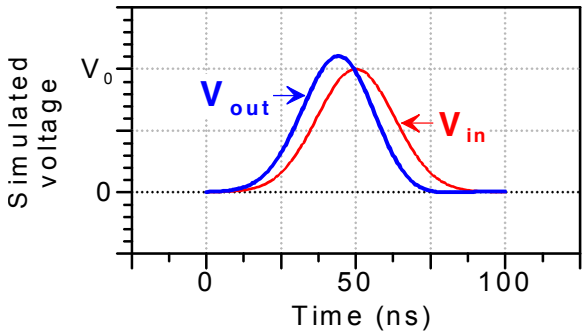

Figure 8: NGD circuit transient analysis results.

In other hand, by injecting an arbitrary waveform input signal presented by V_{in} of Figure 9, once again, an effect of the negative time-delay with time-shift of about 7 ns is found.

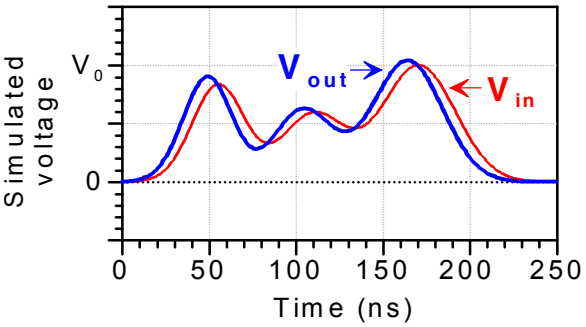

Figure 9: NGD circuit transient analysis results.

Despite this outstanding effect, it is interesting to note that the output signal appears after the input at the starting point t = 0 s. So, the causality principle is still respected. As reported in [18], this advance phenomenon occurs only when the input spectrum belongs in the NGD frequency band.

2.3. Comments and discussions

An innovative NGD active circuit topology susceptible to operate at baseband frequencies is developed by using a microwave amplifier. Compared to the NGD topologies

introduced in [14], the proposed one presents a facility to achieve a good access matching and enables to avoid the opposite sign between the output and input voltages for the single or odd number of stage circuit. Theoretical approaches based on the S-parameter analysis were proposed. Then, the synthesis relations enabling to design the electronic device with the NGD topology understudy were analytically demonstrated according to the desired values of the gain and NGD. Then, the theoretic characteristic specific to the circuit analyzed vis-à-vis the NGD effects were also established. To illustrate the relevance of the theoretic principle proposed, design and simulations of two-stage circuit based on the use MMIC LNA device were carried out. So, it demonstrates the possibility to generate NGD simultaneously with gain in baseband up to microwave frequencies. Moreover, it was stated with SPICE simulation that the presented NGD topology respects all the criteria of classical active RF circuits.

Furthermore, it was shown also that the NGD circuit investigated can be employed to reduce the pure delay induced by telecommunication devices as the microwave TLs. As application, this NGD circuit is potentially useful for the delay reduction as proposed in [37-40] notably for the correction of interconnections degradation on the PCB and for the high-speed microelectronic systems as illustrated in [41-43].

3. Examination of the NGD circuit formed by an LNA for RF/microwave applications

Figure 10 presents the microwave NGD circuit using LNA understudy in the present section. This unit cell of the understudy NGD circuit topology is composed of an amplifier in cascade with an RLC-series resonant network.

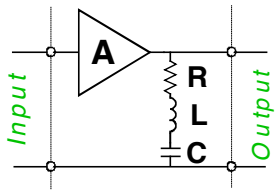

Figure 10: Microwave amplifier cascaded with a shunt series RLC resonant network.

3.1. Theory on the NGD circuit operating in RF/microwave frequencies

Similar to the previous section, to examine the functioning of the circuit described in Figure 10, we analyse its S-parameters and establish the synthesis relations enabling to determine the elements of the NGD topology in function of the desired NGD and gain values. Then, properties of the topology will be established.

3.1.1. S-parameters analysis

Through the S-parameter theory, by considering the reference impedance R_0, one demonstrates that the S-parameters of the NGD topology presented in Figure 10 are expressed as:

$$S_{11} = \rho\,, \tag{27}$$

$$S_{12} = 0\,, \tag{28}$$

$$\underline{S}_{21} = \frac{2T \cdot \underline{Z}}{R_0(\rho+1) + 2\underline{Z}}\,, \tag{29}$$

$$\underline{S}_{22} = \frac{2\rho \cdot \underline{Z} - R_0(\rho+1)}{R_0(\rho+1) + 2\underline{Z}}\,. \tag{30}$$

where

$$\underline{Z} = R + jL\omega + \frac{1}{jC\omega}\,, \tag{31}$$

is the impedance of the series RLC resonant network. The transmission phase of this microwave NGD topology is expressed as:

$$\varphi(\omega) = \arctan\left(L\omega - \frac{1}{C\omega}\right) - \arctan\left[\frac{2\left(L\omega - \frac{1}{C\omega}\right)}{2R + R_0(\rho+1)}\right], \tag{32}$$

One demonstrates that at the resonance frequency:

$$\omega_0 = \frac{1}{\sqrt{L \cdot C}}\,, \tag{33}$$

the transmission parameter S_{21} and the output return loss S_{22} become respectively:

$$S_{21}(\omega_0) = \frac{2T \cdot R}{R_0(\rho+1) + 2R}\,, \tag{34}$$

$$S_{22}(\omega_0) = \frac{2\rho \cdot R - R_0(\rho+1)}{R_0(\rho+1) + 2R}\,. \tag{35}$$

Similarly to the NGD cell introduced in [14-16], the group delay will be also always negative at this resonance frequency:

$$\tau(\omega_0) = \frac{-2L \cdot R_0(\rho+1)}{R\left[R_0(\rho+1) + 2R\right]}\,. \tag{36}$$

3.1.2. Properties of the NGD circuit understudy

One can establish also that this microwave NGD value belongs in the frequency band corresponding to

$[\omega_1, \omega_2]$ which is delimited by the following cut off frequencies:

$$\omega_1 = \sqrt{\frac{4L + L_0 - \sqrt{L_0(8L + L_0)}}{4L^2 C}}, \quad (37)$$

$$\omega_2 = \sqrt{\frac{4L + L_0 + \sqrt{L_0(8L + L_0)}}{4L^2 C}}. \quad (38)$$

where

$$L_0 = R \cdot C[R_0(\rho + 1) + 2R]. \quad (39)$$

It is interesting to note that the product of these NGD cut-off frequencies verify the following relation:

$$\omega_1 \cdot \omega_2 = \omega_0^2, \quad (40)$$

But one points out that at very low frequencies $\omega \approx 0$, the group delay is always positive.

$$\tau(0) = \frac{C \cdot R_0(\rho + 1)}{2}. \quad (41)$$

This last expression leads us to the synthesis method of the NGD passive elements in the next paragraph.

3.1.3. Synthesis method

By inverting formulae (34) and (36) and the resonance frequency expression ω_0, it yields the following synthesis relations:

$$R = \frac{S_{21} R_0(\rho + 1)}{2(T - S_{21})}, \quad (42)$$

$$L = -\frac{\tau |S_{21}| R_0(\rho + 1 - T)^2}{2(T + |S_{21}|)^2}, \quad (43)$$

$$C = \frac{1}{L \cdot \omega_0^2}. \quad (44)$$

In this case, the output return loss S_{22} will be systematically fixed to:

$$S_{22}(\omega_0) = \frac{\rho + 1}{T} |S_{21}(\omega_0)| - 1. \quad (45)$$

Of course, for one cell, the gain S_{21} can not be greater than T. Moreover, to provide a significant NGD with amplification in the wide bandwidth, the investigation of the cascaded structure is provided in the next subsection.

In order to verify the efficiency of the proposed theory, analysis of validation results will be proposed in the next section.

3.2. Numerical validation of the proposed NGD circuit for the modulated signals

The present design and simulation results were performed by using the microwave and electronic circuit simulator Advanced Design System (ADS) from Agilent™.

3.2.1. Design of the microwave NGD device tested

The poof of concept to validate the former theoretic approach is comprised of the one-stage NGD active circuit shown in Figure 11. This later is designed with the LNA implemented in non-linear model using the package transistor AT-41411 provided by Agilent™. Moreover, the considered passive components are from passive SMT models available in ADS library.

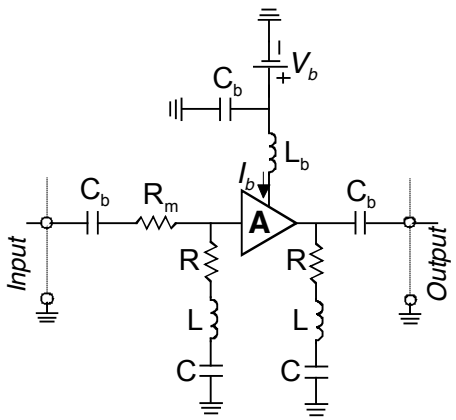

Figure 11: Simulated one stage NGD circuit. (R = 36 Ω, R_m = 22 Ω, L = 33 nH, C = 0.5 pF, L_b = 220 nH, C_b = 10 nF).

The tested NGD device is biased at the DC voltage V_b = 9 V and I_b = 3.9 mA.

3.2.2. Frequency-domain analysis

Through the electromagnetic (EM) and circuit co-simulations in SPICE-Momentum ADS environment, the results obtained are sketched in Figure 12 and Figure 13. As illustrated in Figure 12, the tested circuit introduced in Figure 11 enables to generate a narrow-band NGD from 1.09 GHz to 1.26 GHz which can go down below -1.5 ns.

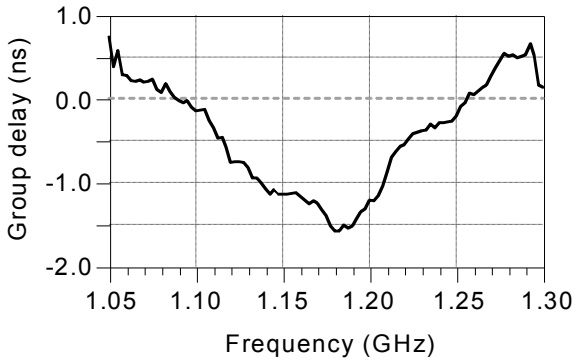

Figure 12: Group delay $\tau(f)$ of the designed NGD circuit tested.

Thus, one evaluates over the bandwidth of about 170 MHz. As displayed in Figure 13, in the considered frequency band, the insertion gain is above 0.5 dB and a good matching at the two accesses is achieved.

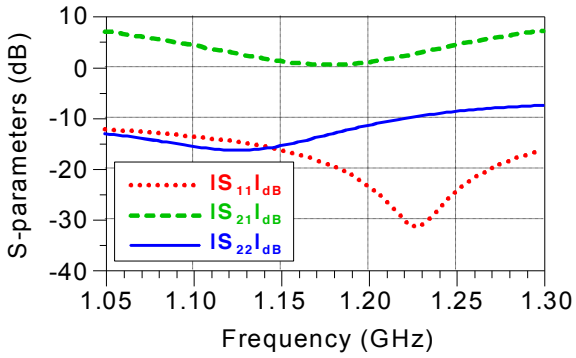

Figure 13: S-parameters ($|S_{11}(f)|_{dB}$, $|S_{21}(f)|_{dB}$ and $|S_{22}(f)|_{dB}$) of the designed NGD circuit shown in Figure 11.

3.2.3. Analysis of the proposed NGD device non-linearity

To carry out a non-linear analysis of the circuit shown in Figure 11, harmonic balance simulations with the considerations of harmonics up to 11th order were realized in the SPICE schematic environment of ADS. For that, a single tone harmonic signal with power P_{in_dBm} at the single frequency f_0 = 1.18 GHz and varied from -15 dBm to 10 dBm was injected in the circuit tested. As consequence, the plot of the output power P_{out_dBm} are obtained in function of the input level P_{i_ndBm} depicted in Figure 14.

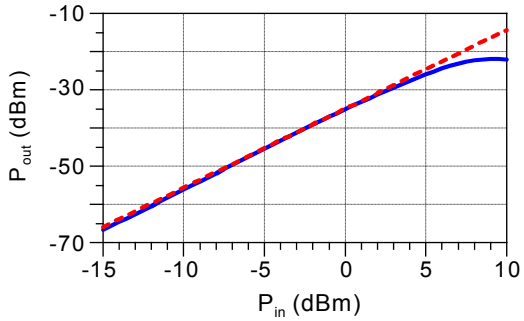

Figure 14: Harmonic balance simulation results: P_{out_dBm} vs P_{indBm}.

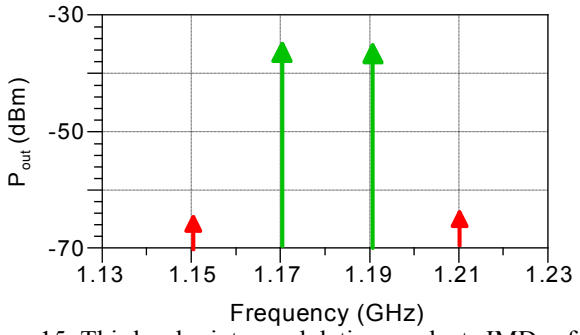

Figure 15: Third order intermodulation products IMD_3 of the device shown in Figure 11.

So, one can see that the device understudy presents P_{in1dBC} of about 5 dBm. Furthermore, by injecting two tones signal centred at the NGD centre frequency f_0 = 1.19 GHz with frequency shift of about 20 MHz. The input powers P_{in_dBm} of these signals are set at around 5 dBm. After simulations, the result obtained is displayed in Figure 15.

Due to the non-linearity of the considered NGD circuit, for the first order harmonic with frequencies f_1 = 1.17 GHz and f_2 = 1.19 GHz, it appears P_{out}(1st order) ≈ -31 dBm and P_{out}(3rd order) ≈ -65 dBm in the operating frequency band.

3.3. Discussions

A microwave topology of active circuit susceptible to exhibit the NGD function with modulated signals is proposed in this section. The NGD topology investigated is comprised of an LNA in cascade with a shunt RLC-series network. The analysis of the proposed NGD topology S-parameters was conducted. The theoretic concept is then, completed by the establishment of synthesis methods of the NGD circuit parameters. This synthesis must be realized knowing the characteristics of the used amplifier and also the desired values of gain and NGD at the given specific frequency. The relevance of the theory was confirmed by the simulation results of one-stage NGD device designed with a hybrid LNA based on the package transistor AT-41411 from Agilent^{TM}. Against the NGD active topology proposed in [15-18], through the present study, it is proved that a better access matching easily is achieved with a simpler biasing network.

4. General conclusions

A theory on the active topologies of electronic circuit susceptible to generate the NGD function is successfully investigated in this paper. Two different types of active topology were analyzed and synthesized.

The first topology, mainly dedicated to the base band frequencies, is comprised of an RL-passive network in

feedback with an RF/microwave amplifier. The other one, mainly operating with the modulated RF/microwave signals, is formed by an RLC-passive network associated in cascade with the amplifier. Theoretical analyses based on the S-parameters are presented by considering the gain and the matching access of the amplified used. Then, synthesis formulae for determining the elements R, L and C of the NGD circuits in function of the desired values of the gain and NGD are established. In addition, the basic properties of the NGD topologies investigated were also proposed. For checking the validity of the theoretical approaches, simulations both in frequency- and time-domains were performed.

With the base band NGD topology, NGD from DC up to tens MHz were realized accompanied with loss compensation. It was shown that the matching access levels of the proof of concept were widely lower than 0 dB up to 5 GHz. It was stated that the tested NFD circuit is unconditionally stable. Then, time-domain simulations confirm the functioning of the NGD circuit. It was observed that by injecting arbitrary wave form signals to the NGD circuit, it was demonstrated that the output signal wave fronts exit the circuit before those of the input penetrating in the circuit. As argued in [10-14, 19-20], this effect is not in contradiction with the causality because the input bandwidth is sufficiently limited. Whereas with the second NGD topology investigated, NGD around 1.19 GHz with minimal value of about -1.5 ns was generated. It is shown that the proof of concept circuit presents good level of matching and excellent isolation loss. Finally, non-linear analyses were proposed to show the reaction of the NGD circuit with the power of the operating signals.

In the continuation of this work, the NGD topologies investigated will be integrated in the telecommunication systems for the enhancement of architectures notably for the delay cancellation.

As ongoing research, design of circuit using MMIC LNA operating with base band signals up to RF/microwave frequencies is planned. The design of the NGD device capable to work up to several tens GHz based on distributed elements is also in progress. Lastly, the NGD concept is envisaged to be used for reducing the delays and also for enhancing the radio communication systems as reported in [45-48].

Acknowledgements

Acknowledgement is made to European Union (EU) and Upper Normandy region (FRANCE) for the support of this research through the European Interreg IVA project No 4081 entitled "Time-Domain Electromagnetic Characterization and Simulation (TECS)".

References

[1] S. Lucyszyn, I. D. Robertson and A. H. Aghvami, "Negative group delay synthesiser", *Electronic Letters*, Vol. 29, pp. 798-800, 1993.

[2] S. Lucyszyn, "Lies, damn lies and measurements," *in Proc. of 16th APMC E4*, New Delhi, India, Dec. 2004.

[3] C. D. Broomfield and J. K. A. Everard, "Broadband negative group delay networks for compensation of oscillators using feedforward amplifiers", *Electronics Letters*, Vol. 20, 1710-1711, Sep. 2000.

[4] G. V. Eleftheriades, O. Siddiqui and A. K. Iyer, "Transmission line for negative index media and associated implementations without excess resonators," *IEEE MWC Lett.*, Vol. 13, No. 2, pp. 51-53, Feb. 2003.

[5] O. F. Siddiqui, M. Mojahedi, and G. V. Eleftheriades, "Periodically loaded transmission line with effective negative refractive index and negative group velocity," *IEEE Trans. Ant. Prop.*, Vol. 51, No. 10, pp. 2619-2625, Oct. 2003.

[6] N. S. Bukhman and S. V. Bukhman, "On the negative delay time of a narrow-band signal as it passes through the resonant filter of absorption," *Radiophysics and Quantum Electronics*, Vol. 47, No. 1, pp. 66-76, 2004.

[7] O. F. Siddiqui, M. Mojahedi and G. V. Eleftheriades, "Periodically Loaded Transmission Line With Effective Negative Refractive Index and Negative Group Velocity", *IEEE Transactions on Antennas and Propagation*, Vol. 51, No. 10, pp. 2619-2625, Oct. 2003.

[8] J. F. Woodley and M. Mojahedi, "Negative Group Velocity and Group Delay in Left-Handed Media", *Phys. Rev. E*, Vol. 70, pp. 046603.1-046603.6, 2004.

[9] R. Y. Chiao, E. L. Bolda, J. Bowie, J. Boyce and M. W. Mitchell, "Superluminality and Amplifiers," *Prog. Crystal Growth Charact. Mat.* 33, pp. 319-325, 1996.

[10] D. Solli, and R. Y. Chiao, "Superluminal effects and negative delays in electronics, and their applications," Phys. Rev. E, No. 5, Nov. 2002.

[11] M. Kitano, T. Nakanishi and K. Sugiyama, "Negative group delay and superluminal propagation: An electronic circuit approach," *IEEE J. Selected Topics in Quantum Electronics*, Vol. 9, No. 1, pp. 43-51, 2003.

[12] J. N. Munday and R. H. Henderson, "Superluminal time advance of a complex audio signal", *Appl. Phys. Lett.*, Vol. 85, pp. 503-504, Jul. 2004.

[13] S. J. Erickson, M. Khaja and M. Mojahedi, "Time- and frequency-domain measurements for an active negative group delay circuit", *in Proc of IEEE Ant. Prop. Soc. Int. Symp.*, Vol. 3A, pp. 790-793, 2005.

[14] B. Ravelo, "Demonstration of negative signal delay with short-duration transient pulse", *Eur. Phys. J. Appl. Phys.* (*EPJAP*), Vol. 55, 10103-pp. 1-8, 2011.

[15] B. Ravelo and S. De Blasi, "An FET-based microwave active circuit with dual-band negative group delay", *Journal of Microwaves, Optoelectronics and Electromagnetic Applications* (*JMOe*), Vol. 10, No. 2, pp. 355-366, Dec.2011.

[16] B. Ravelo, "Investigation on microwave negative group delay circuit", *Electromagnetics*, Vol. 31, No. 8, pp. 537-549, Nov. 2011.

[17] B. Ravelo, A. Perennec, M. Le Roy and Y. Boucher, "Active microwave circuit with negative group delay," *IEEE MWC Lett.*, Vol. 17, No. 12, pp. 861-863, Dec. 2007.

[18] B. Ravelo, A. Perennec and M. Le Roy, "Synthesis of broadband negative group delay active circuits," *IEEE MTT-Symposium IMS 2007*, Honolulu, Hawaii, pp. 2177-2180, 3-8 June 2007.

[19] M.W. Mitchell and R.Y. Chiao, "Causality and negative group delays in a simple bandpass amplifier", *Am. J. Phys.* 66, 14-19, 1998.

[20] M.W. Mitchell and R.Y. Chiao, "Negative group delay and 'Fronts' in a causal systems: An experiment with very low frequency bandpass amplifiers", *Phys. Lett.*, Vol. A230, 133-138, June 1997.

[21] M. Kandic and G. E. Bridges, "Asymptotic Limits of Negative Group Delay in Active Resonator-Based Distributed Circuits", *IEEE Transactions on Circuits and Systems I: Regular Papers*, Vol. 58, No. 8, pp. 1727 – 1735, Aug. 2011.

[22] M. Kandic and G. E. Bridges, "Transient-Imposed Limitations of Negative Group Delay Circuits", *in Proc. of 14th International Symposium on Antenna Technology and Applied Electromagnetics & the American Electromagnetics Conference (ANTEM-AMEREM), 2010,* Ottawa, ON, Canada, pp. 1-4, 5-8 July 2010.

[23] A. Dogariu, A. Kuzmich and L. J. Wang, "Transparent anomalous dispersion and superluminal light-pulse propagation at a negative group velocity", *Phys. Rev. A*, Vol. 63, pp. 053806.1-053806.12, 2001.

[24] L. Brillouin and A. Sommerfeld, *Wave propagation and group velocity*, Academic Press, New York, 113-137, 1960.

[25] G. B. Garrett and D. E. McGumber, "Propagation of a Gaussian light pulse through an anomalous dispersion medium", *Phys. Rev. A*, Vol. 1, pp. 305-313, 1970.

[26] S. Chu. and S. Wong, "Linear pulse propagation in an absorbing medium", *Phys. Rev. Lett.*, Vol. 48, pp. 738-741, 1982.

[27] Ségard and B. Macke, "Observation of negative velocity pulse propagation", *Phys. Lett.* 109, pp. 213-216, 1985.

[28] B. Ravelo, M. Le Roy and A. Perennec, "Application of negative group delay active circuits to the design of broadband and constant phase shifters", *Microwave and Optical Technology Letters*, Vol. 50, No. 12, pp. 3077-3080, Dec. 2008.

[29] S. Keser and M. Mojahedi, "Broadband negative group delay microstrip phase shifter design", *in Proc. of IEEE Ant. Prop. Soc. Int. Symp. 2009* (*APSURSI'09*), Charleston, SC, pp. 1-4, 1-5 June 2009.

[30] B. Ravelo, A. Perennec and M. Le Roy, "Synthesis of frequency independent phase shifter using negative group delay active circuit," *Int. J. RF and Microwave Computer-Aided Engineering (RFMiCAE)*, Vol. 21, No. 1, pp. 17-24, Jan. 2011.

[31] B. Ravelo, M. Le Roy and A. Pérennec, "Frequency-independent active phase shifters for UWB applications", *Proc. of the 40th European Microwave Conference*, Paris, France, pp. 1774-1777, 28-30 Sep. 2010.

[32] B. Ravelo, A. Perennec and M. Le Roy, "Broadband balun using active negative group delay circuit", *in Proc. of 37th European Microwave Conference*, Munich, Germany, pp. 466-469, Oct. 2007.

[33] H. Noto, K. Yamauchi, M. Nakayama, and Y. Isota, "Negative group delay circuit for feed-forward amplifier", *IEEE Int. Microw. Symp. Dig.*, Honolulu, Hawaii, pp. 1103-1106, Jun. 2007.

[34] H. Choi, Y. Jeong, C. D. Kim, and J. S. Kenney, "Bandwidth enhancement of an analog feedback amplifier by employing a negative group delay circuit", *Progress In Electromagnetics Research*, Vol. 105, 253-272, 2010.

[35] B. Ravelo, "Investigation on the microwave pulse signal compression with NGD active circuit", *PIER C Journal*, Vol. 20, pp. 155-171, 2011.

[36] B. Ravelo, *Étude des circuits analogiques-numériques NGD et leurs applications: Théorie fondamentale et expérimentations des circuits analogiques et numériques à temps négatif et leurs applications*, (in French) Chapters 8, Éditions Universitaires Européennes (EUE), Ed. by M. Fabre, 432 Pages, 13 Jan. 2012.

[37] B. Ravelo and J. Ben Hadj Slama, "Equalization of digital/mixed-signal disturbances with an negative group delay circuit", (*Accepted for communication*) *Proceedings of the 16th IEEE Mediterranean Electrotechnical Conference* (*MELECON 2012*), 25-28 March 2012, Medine Yasmine Hammamet, Tunisia.

[38] T. Eudes and B. Ravelo, "Cancellation of delays in the high-rate interconnects with UWB NGD active cells", *Applied Physics Research*, Vol. 3, No. 2, Nov. 2011, pp. 81-88.

[39] B. Ravelo, A. Perennec and M. Le Roy, "Experimental validation of the RC-interconnect effect equalization with negative group delay active circuit in planar hybrid technology", *in Proc. of 13th IEEE Workshop on Signal Propagation Interconnects (SPI)*, Strasbourg, France, May 2009.

[40] B. Ravelo, A. Perennec and M. Le Roy, "New technique of inter-chip interconnect effects equalization with negative group delay active circuits", *VLSI*, Chap. 20, Ed. by Z. Wang, INTECH book, 409-434, Feb. 2010.

[41] B. Ravelo, "Baseband NGD circuit with RF amplifier", *Electronic Letters*, Vol. 47, No. 13, June 2011.

[42] B. Ravelo, "Delay modelling of high-speed distributed interconnect for the signal integrity prediction", *To be published in Eur. Phys. J. Appl. Phys.* (*EPJAP*), 2012, DOI: 10.1051/epjap/20121103742012.

[43] B. Ravelo, "Lumped RC-tree network propagation-delay modeling", *To be published in Int. J. Communication Engineering Applications* (*IJCEA*), 2012.

[44] R. Mumford, “European carriers face capacity crunch challenges”, *Int. Report, Microwave J.*, 169-170, Apr. 2010.

[45] A. Lazaro, D. Girbau and R. Villarino, “Effects of interferences in UHF RFID systems”, *Progress In Electromagnetics Research*, Vol. 98, 425-443, 2009.

[46] P. White, “Group delay explanations and applications”, *Applied Radio Labs,* pp. 1-6, 1999.

[47] Z. Abate, *WiMAX RF systems engineering*, Mobile communication series, Artech House 2009, Norwood, MA, USA.

[48] S.-S. Myoung, B.-S. Kwon, Y.-H. Kim and J.-G. Yook, “Effect of group delay in RF BPF on impulse radio systems”, *IEICE Tran. Communications*, Vol. 90, No. 12, pp. 3514-3522, 2007.

Neutralization of LC- and RC-Disturbances with Left-Handed and NGD Effects

Blaise Ravelo

IRSEEM (Institut de Recherche en Systèmes Electroniques Embarqués), EA 4353, ESIGELEC,
Avenue Galilée, 76801 Saint Etienne du Rouvray, France.
Tel.: +33 (0)2 32 91 59 71 / +33 (0)6 45 33 47 22
Fax: +33 (0)2 32 91 58 59
*corresponding author, E-mail: blaise.ravelo@yahoo.fr

Abstract

This paper focus is on the neutralization technique of the unwanted physical disturbances in the radio frequencies (RF) and digital electronic structures. Most of parasitic effects induced in these systems can be modeled by RC- and LC- passive networks. For canceling these disturbing effects, we can proceed with the transfer function neutralization in the considered operating frequency bands. This neutralization concept is developed by using first, a left-handed (LH) and negative group delay (NGD) circuits inspired from metamaterials. The fundamental theoretical approach illustrating the RC- and LC-effects transfer function neutralization is described. Synthesis relations enabling to determine the elements of the LH and NGD circuit correctors in function of the perturbation parameters are established. Numerical and experimental demonstrators are presented to validate the technique proposed. This later is particularly useful for the improvement of the analogue and digital signal integrity degraded by electromagnetic interferences.

Keywords: *Negative group delay (NGD), RC-/LC-disturbances, neutralization technique, left-handed circuit, signal integrity*.

1. Introduction

Long ago, Sommerfeld and Brioullin [1-6] investigated the problem of the light propagation in the region of the dispersive media having dispersive refractive index $n(\omega)$ at the angular frequency ω. They pointed out by theory that in this region which appeared generally within an absorption line, the group velocity $v_g(\omega)$ can be superluminal, i.e., greater than the vacuum speed of light c and can even become negative:

$$v_g(\omega) = c/\{\Re e[n(\omega)] + \omega \cdot \Re e[\partial n(\omega)/\partial \omega]\}. \quad (1)$$

In this case, we realize negative group velocity (NGV) phenomena. These later were confirmed by Garrett and McCumber by calculating in details, the possibility to propagate superluminally a Gaussian pulse [7]. They underlined that the Gaussian output pulse still suffer little distortion from its initial one. The first experimental verification of this NGV phenomenon was performed in 1982, by Chu and Wong by using laser pulses propagating a GaP:N sample as shown in Figs. 1 [8].

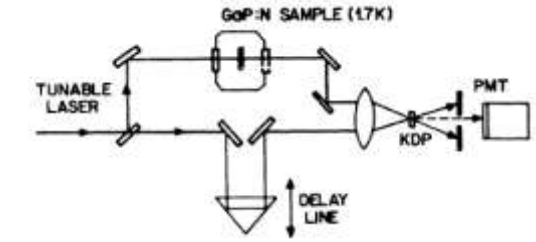

(a)

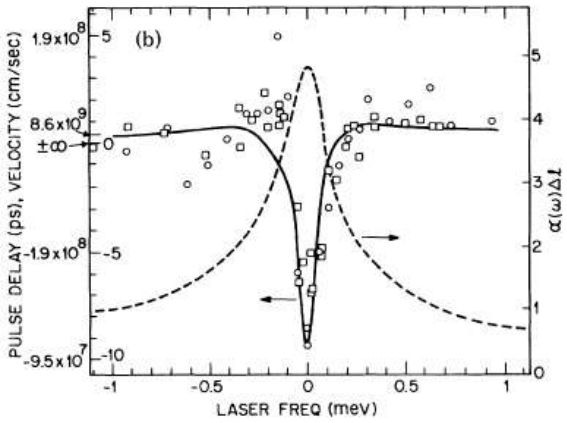

(b)

Figure 1: (a) Chu and Wong experimental setup and (b) frequency response of pulse delay and group velocity [8].

To verify the existence and illustrate the significance of this extraordinary phenomenon, many theoretical and experimental demonstrations, was performed in several physical domains [8-16]. This counterintuitive phenomenon was explained from the pulse reshaping because of constructive and destructive interferences in the frequency band of anomalous dispersion. In this region, it was shown several times, that the group refractive index $n_g(\omega)$ can

become negative [12-18]. In this case, the group velocity, which is defined as:

$$v_g(\omega) = c / n_g(\omega), \quad (2)$$

and the group delay $\tau(\omega)$ whose both are related by:

$$\tau(\omega) = L / v_g(\omega), \quad (3)$$

By considering a medium with length L can be also negative. To study this counterintuitive phenomenon in electronic domain, it is more general to start with the group delay parameter $\tau(\omega)$ instead of the group velocity $v_g(\omega)$. Moreover, for all devices modelled by a transfer function $T(j\omega)$, the group delay can be determined directly via the analytical definition:

$$\tau(\omega) = -\partial \angle T(j\omega) / \partial\omega. \quad (4)$$

Since the early 1990s, the possibility to generate negative group delay (NGD) phenomenon was confirmed in electronic domain thanks to the topology of circuit proposed by Chiao and his co-workers [19-22]. The first NGD circuit composed of an operational amplifier in feedback with passive networks mainly composed of resistor(s), inductance(s) and capacitance(s) as depicted in Fig. 2.

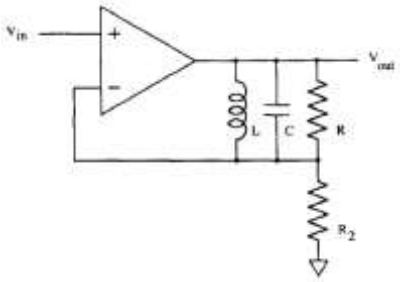

Figure 2: Topology of NGD electronic circuit for low frequencies.

With this topology, Kitano and his collaborators highlights the meaning of the NGD phenomenon by using a circuit showing the occurrence of output voltage pulse wave front before the input one penetrating in the circuit [23-24]. In this case, they demonstrated visually that a LED at the output can be turned on before that one connected at the input of the NGD circuit. However, such NGD circuit works only up to some hundreds kHz [23-25]. It was stated that the NGD effect does not contradict the causality principle [19-26]. In addition, the left-handed (LH) lumped passive circuit shown in Fig. 3 capable to generate NGD effect for microwave signals up to GHz has been introduced by the group of Mojahedi [15-16].

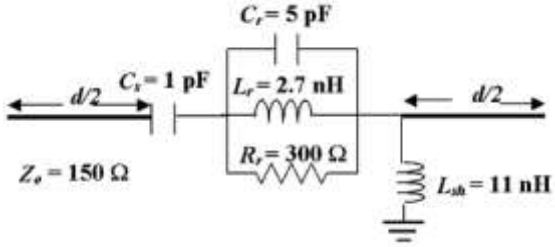

Figure 3: Microwave LH NGD passive cell [15-16].

The topology of this circuit was established from the 1D metamaterials modelling of the array split ring resonators having simultaneously negative permittivity and negative permeability. This unnatural physical concept was, first, proposed by Veselago in 1968 [27] and then, experimented in the early 2000s by Pendry and Smith [28-31]. Several experiments confirmed the physical existence of the superluminal and NGD phenomena with negative refractive index media [32-37]. In the presence of losses, the NGD generated by NGD passive media is accompanied by excessive losses [15-16, 38-40]. So, the applications are still limited in low frequencies. To overcome this physical roadblock, more recently, NGD active topologies for microwave signals were proposed [41-44]. These active topologies are constituted by RF transistor or amplifier associated with passive lumped networks. Lastly, it was demonstrated theoretically and experimentally that this circuit is capable to generate simultaneously significant NGD and amplification, and respecting all criteria of microwave active devices as the access matching and stability. The time delay limitation of NGD circuits is investigated in [45-46].

Based on the NGD function, different applications for the design of innovative oscillator [47], balun [48], phase shifters [49-52], pulse compression generator [53] and feed forward amplifier [54-55] were developed in electronic areas. In addition, further applications for the reduction of signal delays were also proposed based on the neutralization of the disturbing effects in the electronic systems [51][56-59]. The neutralization technique proposed in [58-59] is interesting for reducing the degradation caused the electrical interconnections in the printed circuit board (PCB) and microelectronic systems.

With the increase of the operating data speed, the microelectronic signals propagating through the PCB interconnections and wireless propagation channels suffer of undesired degradations, for example, caused by the electromagnetic interference (EMI) [60-64]. This later can be usually modeled by RC-, LC- and RLC-networks. To reduce these effects, efficient technique enabling to annihilate the RC-delay was also introduced by using base band NGD circuits [58-59]. It was shown that the RC-effect for high-speed applications can be cancelled [51]. Till now few methods are available to neutralize the typically resonating disturbance effects modeled by LC-networks. For this reason, LC-effect neutralization techniques are developed in this paper by using LH- and NGD-circuits operating with modulated signals.

To highlight the feasibility of this concept, theoretic, simulation and experimental analyses are performed. Section 2 introduces the fundamental principle of the neutralization technique proposed. The next three sections are the applications of this technique for canceling the undesired electrical effects modeled by base band and resonating networks. The final section is the general conclusion.

2. Fundamental principle of the neutralization technique proposed

The unintentional disturbances as the EMI in the most of physical systems can be modeled by black box of the transfer function denoted T_d. Ideally, the neutralization technique can be traduced by the implementation of a system with outputs equal to its inputs ($v_{in} = v_{out}$). In this case, by denoting s the Laplace variable, the transfer function should be equal to unity as introduced in chapter 11 of [51]:

$$T(s) = V_{out}(s)/V_{in}(s) = 1. \quad (5)$$

To achieve this operation, the disturbance function can be multiplied with the corrector transfer function mathematically defined as [51]:

$$T(s) = T_d(s) \cdot T_{corrector}(s) \approx 1 \Rightarrow T_{corrector}(s) = 1/T_d(s). \quad (6)$$

This analytical solution can be implemented by cascading the system T_d with $T_{corrector}$. So, one proposes to exploit the configuration presented by the block diagram depicted in Fig. 4.

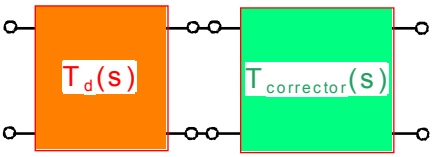

Figure 4: Disturbing system in cascade with the correction system [50].

In the ideal case, the frequency responses as the magnitude, phase and group delay of the correction system must be respectively expressed as:

$$T_{corrector}(\omega) = 1/T_d(\omega), \quad (7)$$

$$\varphi_{corrector}(\omega) = \angle T_{corrector}(j\omega) = -\angle T_d(j\omega), \quad (8)$$

$$\tau_{corrector}(\omega) = -\partial\varphi_{correction}(\omega)/\partial\omega = \partial\angle T_d(j\omega)/\partial\omega. \quad (9)$$

In the remainder of this paper, these expressions will be used for synthesizing neutralization circuits in function of the disturbances.

3. LC-effect cancellation with LH active circuits

Since the early 2000s, various microwave engineering applications of the LH concept have been proposed in the literature [65-68]. So, innovative microwave devices (filter, antenna, power divider, coupler…) were designed [65-68]. At the beginning, the LH-circuits were inspired thanks to the analogy with the metamaterials susceptible to operate with negative phase- and/or group-velocities [69-71]. Contrarily to the classical transmission lines which are categorized as right-handed (RH) structures, these LH circuits are susceptible to generate positive phase values in certain frequency bands. One of the most expanded applications of these circuits is based on the use of composite right- and left- handed (CRLH) cells which are composed of the combination of LC- and CL-circuits shown in Fig. 5 [70-71].

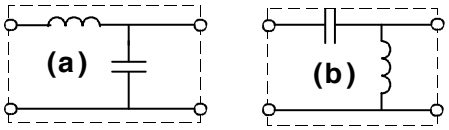

Figure 5: Purely (a) RH- and (b) LH- elementary cells.

However, the application of LH circuits is somehow restricted due to its inherent undesired losses. Therefore, different numerical approaches dedicated to the analysis of LH structures were proposed [72-75]. In this section, a synthesis method of LH active cell for the neutralization of the LC-effect is introduced. To get more insight about the functioning of this LH active concept, a theoretical analysis on the cancellation technique of the LC-effect is presented based on the examination of the S-parameters. Then, validation results are presented and discussed.

3.1. Theoretical approach on the LC-effect neutralization technique

For compensating the LC-effect, we use the LH active circuit with the configuration explained in Fig. 6. It consists of cascading the disturbing LC-network with an active circuit formed by a transistor ended by an LH cell.

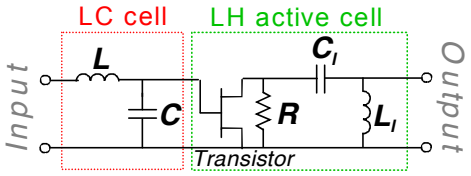

Figure 6: LC-circuit compensated with LH active circuit.

Along this study, for the analytical demonstration, the transistor is supposed comprised of a transconductance g_m and a drain-source resistance R_{ds}, here, included in the matching resistance R. Therefore, the scattering parameters of the circuit shown in Fig. 6 are expressed as:

$$S_{11}(j\omega) = (LC\omega^2 - 1 + j\omega Z_0 C)/(LC\omega^2 - 1 - j\omega Z_0 C), \quad (10)$$

$$S_{12}(j\omega) = 0, \quad (11)$$

$$S_{21}(j\omega)=\frac{-2g_m R_{ds} Z_0 L_l C_l \omega^2}{(LC\omega^2-1+j\omega Z_0 C)\left[Z_0(L_l C_l\omega^2-1)-j\omega(L_l-R_{ds}Z_0C_l)\right]\; Z_0(1-L_l C_l\omega^2)+R_{ds}L_l C_l\omega^2}, \quad (12)$$

$$S_{22}(j\omega)=\frac{-j\omega(L_l-R_{ds}Z_0C_l)}{Z_0(L_l C_l\omega^2-1)+R_{ds}L_l C_l\omega^2-j\omega(L_l+R_{ds}Z_0C_l)}. \quad (13)$$

For the reference impedance denoted Z_0 = 50Ω, by supposing:

$$C=1/(L\cdot\omega_0^2), \quad (14)$$

with ω_0 is an angular frequency, the magnitude and phase of the transmission parameter S_{21} of the LC-circuit alone are respectively given by:

$$A_{LC}(\omega)=\frac{2Z_0L\omega_0^2}{\sqrt{Z_0^2L^2(\omega^2-2\omega_0^2)^2+\omega^2(L^4\omega_0^4+Z_0^4)}}, \quad (15)$$

$$\varphi_{LC}(\omega)=\arctan\left\{\omega(Z_0^2+L^2\omega_0^2)/\left[Z_0L(\omega^2-2\omega_0^2)\right]\right\}. \quad (16)$$

To neutralize this attenuation and this phase shift at the given frequency ω_1, we must verify:

$$S_{21}(j\omega_1)=1\Leftrightarrow\begin{cases}|S_{21}(j\omega_1)|=1\\ \varphi_{S_{21}}(\omega_1)=0\end{cases}. \quad (17)$$

By solving this equation system, the following synthesis relations are established:

$$L_l=Z_0\sqrt{R}/\left[\omega_0\sqrt{R+Z_0}\right], \quad (18)$$

and

$$C_l=1/\left[\omega_0\sqrt{R(R+Z_0)}\right]. \quad (19)$$

According to the desired value of the total transmission gain $|S_{21}|$, the transistor characteristic g_m must be equal to:

$$g_m=\frac{S_{21}\sqrt{\left|Z_0^4-Z_0^2\cdot R^2+4\omega_0^2\cdot L^2\cdot R^2\right|}}{\omega_0\cdot L|Z_0-R|\sqrt{Z_0\cdot R}}. \quad (20)$$

In this case, the minimal value of the output parameter $S_{22}(\omega_1)=0$ is achieved if:

$$R=Z_0(\omega_1^2-\omega_0^2)/(\omega_1^2+\omega_0^2), \quad (21)$$

It is noteworthy that when $\omega_1=\omega_0$, the expressions of the compensating LH-cell elements introduced in (18) and (19) are transformed as:

$$L_l=\sqrt{Z_0\cdot R}/(2\omega_0) \quad (22)$$

and

$$C_l=1/(L_l\cdot\omega_0^2) \quad (23)$$

In this case, the transistor parameters can be extracted from the desired value of the output parameter S_{22} with formulae:

$$g_m=S_{21}\sqrt{Z_0+R}/(\omega_0\cdot L\sqrt{R}), \quad (24)$$

$$R=4Z_0\cdot S_{22}^2/(1-S_{22}^2). \quad (25)$$

One recalls that the matching resistance R_m can be determined from the equivalent resistance relation $1/R=1/R_{ds}+1/R_m$. Meanwhile, the matching resistance can be defined with the equation $R_m=R_{ds}\cdot R/(R_{ds}-R)$.

To verify the relevance of this LC-effect cancellation technique, an application is presented in the next subsection.

3.2. Validation with SPICE simulations

The simulation results presented in this paper were run with the electronic and microwave circuit simulator Advanced Design System (ADS) from Agilent™.

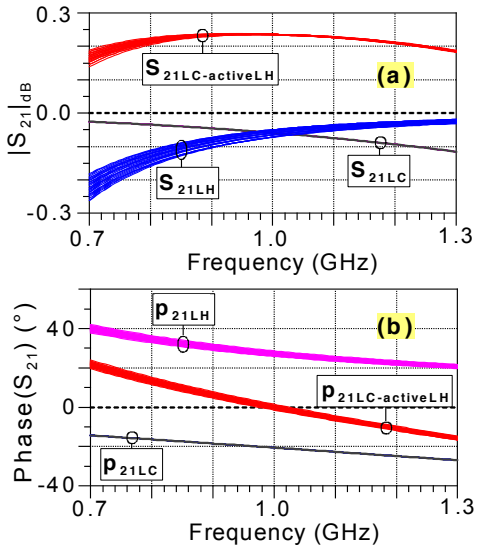

Figure 7: Magnitudes (a) and phases (b) of the LC, LH-cell and compensated circuit transmission parameters.

During the simulations, an arbitrary LC-network with parameters L = 2 nH and C = 2.2 pF was considered. At the given frequency f_1 = 1 GHz, the LH active circuit elements L_l = 15 nH, C_l = 7.8 pF and R = 62 Ω are synthesized. Then, after sensitivity studies with tolerances fixed to ±10%, one gets the simulation results displayed in Figs. 7. These graphs illustrate the feasibility of the transmission gain S_{21} and phase p_{21} neutralizations. One can see that with LH active circuit parameter variations of 10%, S_{21} and p_{21} relative variations only of about 1.5% are found. In addition, analysis of the transistor parameter influences was also performed by varying first, g_m and fixing the drain-source resistance R_{ds} = 100 Ω, and then, varying R_{ds} and fixing g_m = 20 mS. Therefore, the results shown in Figs. 8 were realized. These later explain that the gain compensations can be carried out from certain values of the used transistor parameters.

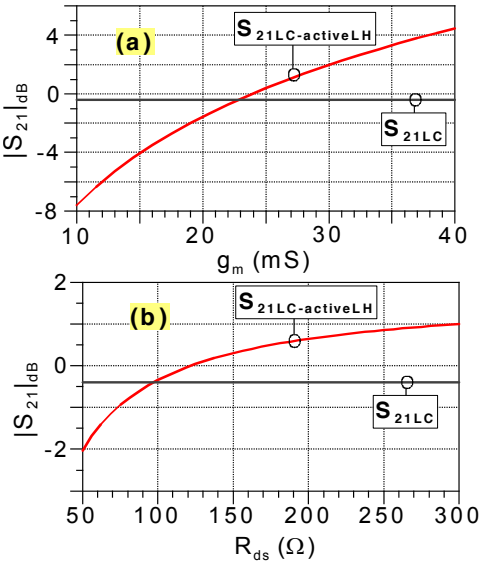

Figure 8: (a) $S_{21}(f_1)$ vs g_m and (b) $S_{21}(f_1)$ vs R_{ds}.

3.3. Remarks and discussions

A neutralization technique enabling to cancel out the LC-effect degradation is presented by using an LH active circuit comprised of a transistor cascaded with a series capacitor ended by a parallel inductance. Synthesis expressions enabling to determine the compensator are established according to the operating frequency and the LC-parameters. To validate the synthesis method, results in very good agreement with the theory were realized. In the continuation of this work, this technique will be used for improving the microwave device performances and the signal integrity.

4. Disturbing resonating effects cancellation with NGD circuit for modulated microwave signals

The resonance phenomenon is one of the effects susceptible to disturb most of physical systems. In this section, we propose a cancellation technique of the resonance effect essentially modeled by parallel LC-network. To do this, the microwave NGD circuit formed by a transistor associated with RLC series network developed in [41-42] is used. Fig. 9 represents the configuration considered to perform this neutralization technique.

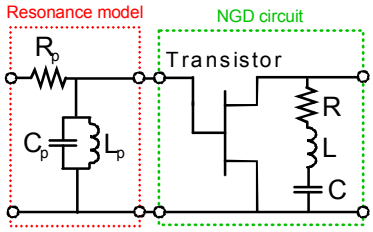

Figure 9: Resonating cell model in cascade with an NGD circuit.

Similar to the previous study established in section 3, the resonating circuit generating the perturbation is cascaded with the NGD circuit corrector.

4.1. Synthesis of the NGD circuits in function of the considered resonance parameters

The synthesis process introduced in this subsection is aimed to the determination of neutralizer elements in function of the perturbation $R_pL_pC_p$ around the resonance:

$$\omega_0 = 1/\sqrt{L_pC_p} = 1/\sqrt{L\cdot C}\,. \tag{26}$$

Around this frequency, one establishes that knowing the transistor characteristics, the S-parameters of the whole circuit shown in Fig. 9 are expressed as:

$$S_{21RLC-NGD}(\omega_0) = 2g_mZ_0R/(R+Z_0)\,, \tag{27}$$

$$S_{22RLC-NGD}(\omega_0) = |R-Z_0|/(R+Z_0)\,, \tag{28}$$

The corresponding group delay is equal to:

$$\tau_{RLC-NGD}(\omega_0) = \frac{2\left[\begin{array}{l}(R^2+Z_0R)(R_p+Z_0)\\ -Z_0L_pL\omega_0^2\end{array}\right]}{L_pR\omega_0^2(R+Z_0)}\,. \tag{29}$$

As aforementioned, the neutralization is realized when:

$$\begin{cases} S_{21RLC-NGD}(\omega_0) = 1 \\ \tau_{RLC-NGD}(\omega_0) = 0 \end{cases}. \tag{30}$$

By solving this last equation, we obtain the following synthesis formulae in function of the parameters R_p, L_p and C_p:

$$R = Z_0/(2Z_0\cdot g_m - 1)\,, \tag{31}$$

$$L = R(R+Z_0)(R_p+Z_0)/(L_p\omega_0^2Z_0)\,. \tag{32}$$

In this case, the capacitance value can be deduced by inverting equation (26).

4.2. Application results

To validate the concept, neutralization of resonating network with arbitrary parameters R_p = 43 Ω, L_p = 5 nH, C_p = 5 pF was performed. In this case, the resonance frequency is f_0 = 1 GHz. The employed transistor is characterized by the transcoductance g_m = 100 mS and the drain-source resistance R_{ds} = 200 Ω. By using relations (31) and (32), the following NGD circuit parameters R = 5.5 Ω, L = 2.9 nH and C = 8.7 pF are synthesized for the correction. The frequency responses of the whole circuit RLC-NGD understudy are displayed in Fig. 10. As we can see that $R_pL_pC_p$ circuit generates a significant attenuation more than -3 dB and positive group delay close to 400 ps around f_1.

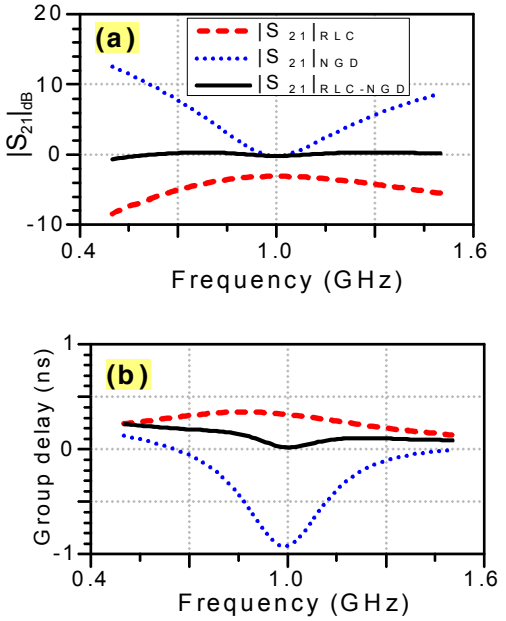

Figure 10: Transmission parameters of the circuit presented in Fig. 9. (a) Magnitude and (b) group delay.

Thus, thanks to the gain and group delay behaviors of the NGD circuit, a total gain around 0 dB with very good flatness and a group delay near zero thanks to the NGD going down up to about -1 ns are realized. As expected, we find that the total transmission parameter responses (plotted in black full lines) are close to unity.

5. RC-effect cancellation with base band NGD circuits for the analogue-numerical signal

In this section, the neutralization technique understudy is applied for enhancing the high-speed analogue-digital or mixed signal integrity. To do this, after illustration on the used NGD circuit functioning developed in [51, 58-59], the analytical approach based on the transfer function of the RC-model and the RCNGD-circuit including the corrector NGD circuit will be explored. Then, validation experimental results will be laid out.

5.1. Experimentation of the proposed base band NGD circuit

Fig. 11 depicts the base band NGD cell under study. The fabricated proof of concept under test is comprised of the PHEMT ATF-34143 transistor manufactured by Avago Technology™ supplied with $V_{gs} = 0$, $V_{ds} = 3$ V and $I_{dss} = 110$ mA. By using the ADS Momentum environment, the layout of the hybrid planar circuit was designed and implemented. It is noteworthy that this circuit is printed on the epoxy substrate FR4 with permittivity $\varepsilon_r = 4.3$ and thickness $h = 800$ µm [41].

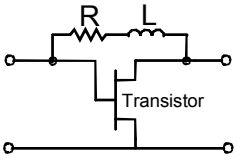

Figure 11: NGD circuit used ($R = 56\ \Omega$ and $L = 220$ nH).

3.1.1. Frequency-domain results

To generate the magnitude and the group delay responses of the fabricated circuit, one proceeds with the traditional RF-circuit frequency measurement with the vector network analyzer (VNA) *R&S* (*ZVRE 9 kHz - 4 GHz*).. Then, the transfer function was determined with the following relationship:

$$T(j\omega) = \frac{2S_{21}(j\omega)}{1 + S_{11}(j\omega) - S_{22}(j\omega) - S_{11}(j\omega)S_{22}(j\omega) + S_{12}(j\omega)S_{21}(j\omega)}. \quad (33)$$

As illustrated in Fig. 12(a), a positive gain is realized. The measured gain slightly above the simulation mainly is due to the imperfection of the non linear model of the transistor used during the simulation. As revealed in Fig. 12(b), the measured group delay is well-correlated with the simulation. As expected, one observes that the prototype of the circuit tested provides a base band NGD up to 63 MHz which can go down below –2.5 ns.

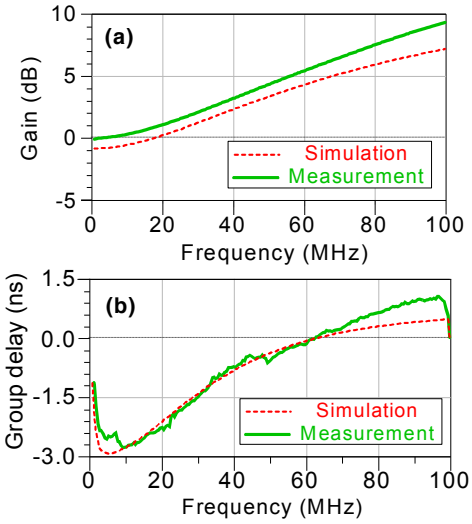

Figure 12: Comparisons of the simulated and measured frequency responses: (a) gain and (b) group delay [41].

3.1.2. Time-domain measurements:

The diagram presented in Fig. 13 illustrates the considered experimental setup. It consists to retrieve the input (CH1) and output (CH2) signals successively with the same reference of synchronization. The time domain measured result is displayed in Fig. 14. Thanks to the NGD effect illustrated in Fig. 12(b), an output signal in time-advance of about 1.5 ns compared to the input one was observed. As sketched by the zoom in graph in the bottom of Fig. 14, the leading and trailing edges of the output are equally in time-advance of 1.5 ns. This result reveals the apparition of negative frontal velocity corresponding to the signal levels

included in 10 % and 90 % of its maximal value. In fact, this extraordinary physical phenomenon can occur only when more than 95 % of the input power spectrum density belongs in the NGD frequency band. So that, a smoothed input signal is necessary in order to realize this time-advance effect. However, the signals presenting discontinuity as unit step Heaviside cannot propagate in negative delay because its frequency spectrum is ideally infinite.

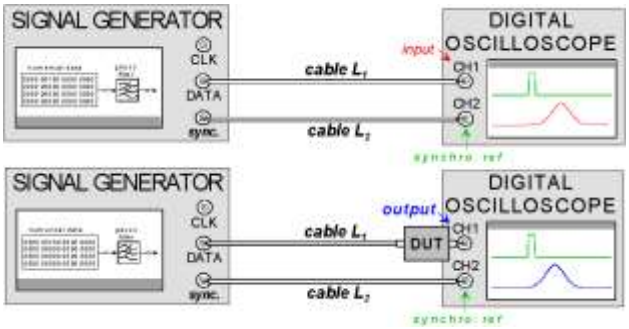

Figure 13: Diagram of the experimental setup [41].

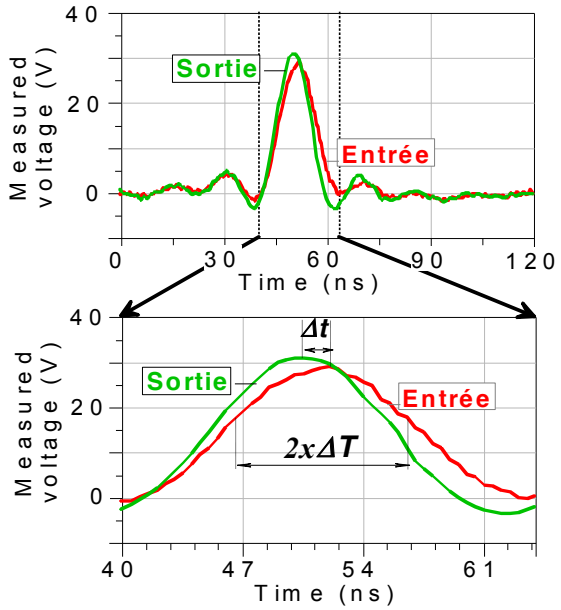

Figure 14: Time-domain measured input and output (opposite sign) pulses.

One points out that the group velocity of the structure tested is v_g = -0.13c (c is the vacuum light speed).
In the next subsection, this NGD topology will be employed for neutralizing RC-perturbations.

5.2. Illustration of the neutralization effect in base band frequencies

As argued in section 2, to realize the neutralization effect, we use the NGD circuit in cascade with the disturbance model. According to relation (7), the corrector magnitude response T_{NGD} must behave as plotted in full line of Fig. 15(a) to cancel the attenuation induced by T_p [58]. Similarly for the group delay according to relation (9), we must generate the NGD τ_{NGD} as illustrated in Fig. 15(b) in base band frequencies to annihilate the delay τ_p.

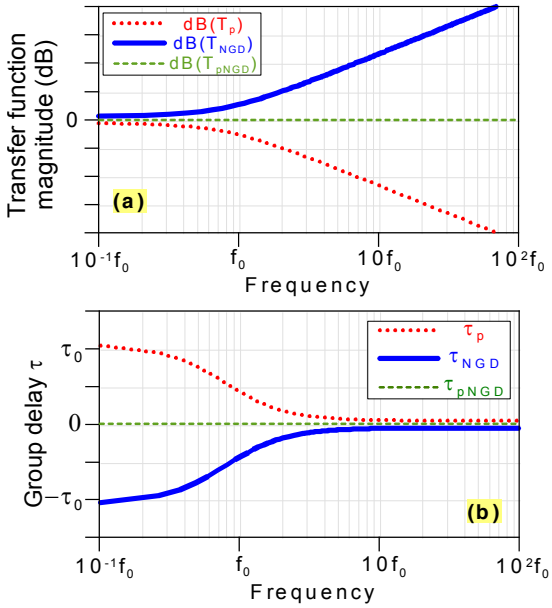

Figure 15: Illustration of the neutralization principle with frequency responses. (a) Magnitude and (b) group delay of the transfer functions $T_d(s)$ for the passive circuit, $T_{NGD}(s)$ for the NGD circuit and $T_{NGD}(s)$ for the cascaded system.

In the next subsection, these frequency responses will be experimented with the neutralization of the RC-effect with the NGD circuit presented in Fig. 9.

5.3. Analytical investigation of the RC-effect neutralization

Fig. 16 represents the diagram of the RC-circuit neutralized by the base band NGD circuit. One can establish that this circuit presents the transfer function and DC gain, respectively expressed as:

$$T(s) = \frac{R_{ds}(1-g_mR)-g_mR_{ds}Ls}{R+R_{ds}+R_c(1+g_mR_{ds})} + \left[R_cC(R+R_{ds})+L\right]s+R_cCLs^2, \quad (34)$$

$$T(0) = \frac{R_{ds}(1-g_mR)}{R+R_{ds}+R_c(1+g_mR_{ds})}. \quad (35)$$

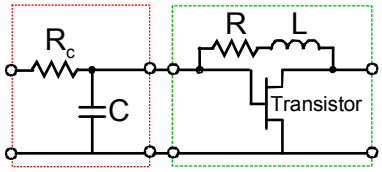

Figure 16: RC- and NGD active-circuit cascaded [51, 58].

With the neutralization technique, we are aimed also to reduce the 50% propagation delay induced by the RC-circuit alone which is analytically expressed as:

$$T_{rc} = R_cC\,ln(2). \quad (36)$$

To do this, in the next paragraphs, we will examine the frequency- and unit-step responses of the system defined by

expression (34).

5.3.1. Frequency responses of the RCNGD-system understudy

The transfer function expressed in (34) can be presented with the canonical form [58]:

$$T(j\omega)=\frac{\alpha_0+j\omega\alpha_1}{\omega_n^2-\omega^2+2j\zeta\omega_n\omega}. \quad (37)$$

where α_0 and α_1 are the real constants, and ω_n and ζ are respectively the undamped natural frequency and the damping ratio. Then, it yields the following magnitude and phase responses, respectively written as:

$$|T(j\omega)|=\frac{\sqrt{\alpha_0^2+\alpha_1^2\omega^2}}{\sqrt{(\omega_n^2-\omega^2)^2+4(\zeta\omega_n\omega)^2}}, \quad (38)$$

$$\varphi(\omega)=\arctan(\frac{\alpha_1}{\alpha_0}\omega)-\arctan(\frac{2\zeta\omega_n\omega}{\omega_n^2-\omega^2}). \quad (39)$$

The corresponding group delay is given by:

$$\tau(\omega)=\frac{2\zeta\omega_n(\omega^2+\omega_n^2)}{\omega^4+2(2\zeta^2-1)\omega_n^2\omega^2+\omega_n^4}-\frac{\alpha_0\alpha_1}{\alpha_0^2+\alpha_1^2\omega^2}. \quad (40)$$

As reported in [75], with $y(t)$ the unit step response of $T(s)$, the 50% Elmore propagation delay $T_{pd50\%}$ which is defined as:

$$y(T_{pd50\%})=y(\infty)/2, \quad (41)$$

will be [64]:

$$\tau(0)=2\zeta/\omega_n-\alpha_1/\alpha_0. \quad (42)$$

Knowing that compared to the exact value of the 50% propagation delay, (42) presents a relative error more than 30% due to the simplification of the exact model. For this reason, the study of the unit step response of $T(s)$ in the next paragraph.

5.3.2. RCNGD-circuit unit step responses

This response is obtained when the unit step signal presenting Laplace transform:

$$X(s)=1/s. \quad (43)$$

is applied at the input of the circuit shown in Fig. 16. The Laplace transform of the unit step response is given by:

$$Y(s)=T(s)X(s)=(\alpha_0+\alpha_1 s)/(s^2+2\zeta\omega_n s+\omega_n^2)/s. \quad (44)$$

Similar to the classical second order passive system with constant numerator, according to the $T(s)$ pole nature of or the damping ratio ζ compared to 1, we classify three categories of the unit step response $y(t)$ as shown by Fig. 17. We recall that according to the final value theorem:

$$y(\infty)=T(0)=\alpha_0/\omega_n^2. \quad (45)$$

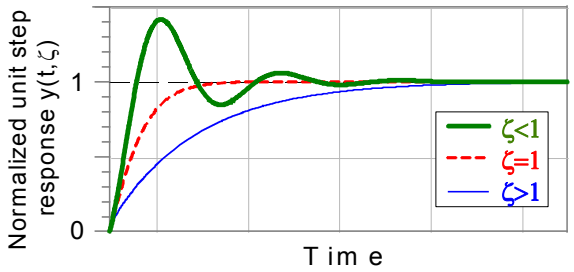

Figure 17: Three types of the unit step response of system (36) according to the damping factor ζ.

In the remainder of the paper, we denote y_{max} the maximum value of $y(t)$ at instant time t_{max}. So that, the overshoot is expressed as:

$$\xi=[1-y(\infty)/y_{\max}]=[1-T(0)/y_{\max}], \quad (46)$$

and the 50% propagation delay is the root of the equation:

$$y(T_{pd})=\alpha_0/(2\omega_n^2). \quad (47)$$

5.3.3. Case 1: $\zeta=1$ Critically damping system analysis

In this case, we have the unit step response:

$$y_1(t)=\{\alpha_0-[\alpha_0+(\alpha_0-\alpha_1\omega_n)\omega_n t]e^{-\omega_n t}\}/\omega, \quad (48)$$

with maximal value y_{1max} and overshoot ξ_1 at the instant time t_{1max} respectively given by:

$$y_{1\max}=\{\alpha_0-(\alpha_0-\alpha_1\omega_n)e^{-\alpha_1\omega_n/(\alpha_0-\alpha_1\omega_n)}\}/\omega_n^2, \quad (49)$$

$$\xi_1=(\alpha_1\omega_n/\alpha_0-1)e^{-\alpha_1\omega_n/(\alpha_0-\alpha_1\omega_n)}, \quad (50)$$

$$t_{1\max}=\alpha_1/(\alpha_1\omega_n-\alpha_0). \quad (51)$$

It means that, the last one exists ($t_{1max}>0$) when:

$$\alpha_1\omega_n-\alpha_0\geq 0 \quad \Leftrightarrow \quad \alpha_1>\alpha_0/\omega_n. \quad (52)$$

To keep the condition:

$$y_{1\max}\leq y_1(\infty)=\alpha_0/\omega_n^2, \quad (53)$$

we should expect the condition below:

$$\alpha_0-\alpha_1\omega_n\geq 0. \quad (54)$$

Clearly, we see that this last condition is absolutely contrary to condition (52). According to expression (47), we propose another high accurate even exact solution below using the Lambert function W(x) [77-78] defined as:

$$W(x)\exp[W(x)]=x. \quad (55)$$

Consequently, the 50% propagation delay will be:

$$T_{pd1}=[\alpha_0+(\alpha_0-\alpha_1\omega_n)W(x)]/[\omega_n(\alpha_1\omega_n-\alpha_0)]. \quad (56)$$

where:

$$x=(2\alpha_0-\omega_n^2)e^{\alpha_0/(\alpha_1\omega_n-\alpha_0)}/[2(\alpha_1\omega_n-\alpha_0)]. \quad (57)$$

5.3.4. Case 2: $\zeta>1$ Over-damping system analysis

In this case, the unit step response can be expressed as:

$$y_2(t)=y_{21}(t)+y_{22}(t), \quad (58)$$

where:

$$y_{21}(t)=\frac{\alpha_0}{\omega_n^2}+\frac{1}{2\omega_n^2}(\frac{\alpha_1\omega_n-\zeta\alpha_0}{\sqrt{\zeta^2-1}}-\alpha_0)e^{(\sqrt{\zeta^2-1}-\zeta)\omega_n t}, \quad (59)$$

$$y_{22}(t)=\frac{1}{2\omega_n^2}\left(\frac{\zeta\alpha_0-\alpha_1\omega_n}{\sqrt{\zeta^2-1}}-\alpha_0\right)e^{-(\sqrt{\zeta^2-1}+\zeta)\omega_n t}, \quad (60)$$

The optimal instant time is expressed as:

$$t_{2\max}=\frac{\ln\left(\frac{\zeta\alpha_1\omega_n-\alpha_0+\alpha_1\omega_n\sqrt{\zeta^2-1}}{\zeta\alpha_1\omega_n-\alpha_0-\alpha_1\omega_n\sqrt{\zeta^2-1}}\right)}{2\omega_n\sqrt{\zeta^2-1}}. \quad (61)$$

This optimum exists when we have the condition:

$$\frac{\zeta\alpha_1\omega_n-\alpha_0+\alpha_1\omega_n\sqrt{\zeta^2-1}}{\zeta\alpha_1\omega_n-\alpha_0-\alpha_1\omega_n\sqrt{\zeta^2-1}}>0. \quad (62)$$

However, like the previous case, to avoid the overshoot or to keep:

$$y_{2\max}<y_2(\infty)=\alpha_0/\omega_n^2, \quad (63)$$

we must verify the opposite condition that is reduced to:

$$\alpha_1\omega_n(\zeta-\sqrt{\zeta^2-1})<\alpha_0<\alpha_1\omega_n(\zeta+\sqrt{\zeta^2-1}). \quad (64)$$

We can find that, $y_2(t)$ is dominated by $y_{21}(t)$ because $y_{22}(t)$ decreases rapidly when t increases. Since, the expanding second order Maclaurin series $y_{2a}(t)$ defined in (65) presents T_{pd} inaccurate than that involving from $y_{21}(t)$. So, we have the T_{pd2} in (66) yielded from the equation $y_{21}(T_{pd2})=\alpha_0/(2\omega_n^2)$.

$$y_{2a}(t)=\alpha_1 t+\left(\frac{\alpha_0}{2}-\zeta\alpha_1\omega_n\right)t^2+O(t^3). \quad (65)$$

$$T_{pd2}\approx\frac{\ln\left[\frac{\alpha_0^2(\zeta^2-1)}{(\alpha_0(\zeta+\sqrt{\zeta^2-1})-\alpha_1\omega_n)^2}\right]}{2\omega_n(\sqrt{\zeta^2-1}-\zeta)}. \quad (66)$$

5.3.5. *Case 3: $\zeta<1$ Under damping system analysis*

In this last case, we have the unit step response $y_3(t)$ and the overshoot ξ_3 at t_{3max} respectively expressed as:

$$y_3(t)=\frac{\alpha_1\omega_n-\alpha_0\zeta}{\omega_n^2\sqrt{1-\zeta^2}}\sin(\omega_n t\sqrt{1-\zeta^2})e^{-\zeta\omega_n t}+\alpha_0/\omega_n^2\left[1-e^{-\zeta\omega_n t}\cos(\omega_n t\sqrt{1-\zeta^2})\right], \quad (67)$$

$$\xi_3=e^{-\zeta\omega_n t_{3\max}}/\omega_n^2\sqrt{\alpha_0^2-2\zeta\alpha_0\alpha_1\omega_n+\alpha_1^2\omega_n^2}, \quad (68)$$

$$t_{3\max}=\pi-\frac{\arctan\left[(\alpha_1\omega_n\sqrt{1-\zeta^2})/(\alpha_0-\zeta\alpha_1\omega_n)\right]}{\omega_n\sqrt{1-\zeta^2}}, \quad (69)$$

Based on the time-domain behaviour of $y_3(t)$, we can assume that it presents an inflection point T_i ($y_3''(T_i)=0$) which can be considered as its propagation delay and given by :

$$T_i=\frac{\arctan\left[\frac{(2\zeta\alpha_1\omega_n-\alpha_0)\sqrt{1-\zeta^2}}{\alpha_1\omega_n(2\zeta^2-1)-\zeta\alpha_0}\right]}{\omega_n\sqrt{1-\zeta^2}}. \quad (70)$$

More accurate value of T_{pd} can be obtained by assuming $y_3(t)$ as its steepest slope of the thin black line displayed in Fig. 18. This line is defined from the tangent at the inflection point. Thereby, T_{pd3} will be the root of equation:

$$y_3'(t_i)(T_{pd3}-t_i)+y_3(t_i)=y_3(\infty)/2. \quad (71)$$

As result, the propagation delay can be written as:

$$T_{pd3}=t_i+\left[\alpha_0/(2\omega_n^2)-y_3(t_i)\right]/y_3'(t_i). \quad (72)$$

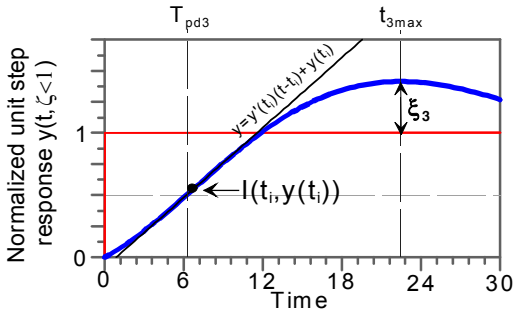

Figure 18: Unit step response of the second order active system for $\zeta=0.3, \omega_n=4\pi 10^7, \alpha_0=2.25\omega_n^2$ and $\alpha_1=\omega_n$ illustrating the T_{pd3} approximation associated to the response to $\zeta<1$.

5.4. Validation results

Fig. 19 displays the detailed circuit diagram of the proof of concept under test. The PHEMT/ATF-34143 from Avago Technology™ was employed to implement the NGD circuit values compensating the RC-effect. After application of the synthesis relations proposed in [51], the hybrid planar circuit comprised of surface-mount chip passive components R, L, and C displayed in Fig. 20 was manufactured.

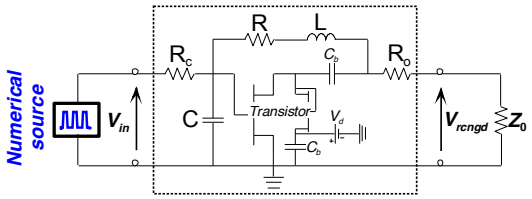

Figure 19: Schematics of the RCNGD-circuit including biasing network using an FET = PHEMT ATF-34143 (V_{gs} = 0V, V_d = 3V, I_d = 110 mA), for R_c = 33 Ω, C = 680 pF, and R = 56 Ω, R_o = 10 Ω, L=220 nH, C_b=100 nF, Z_0 =50 Ω.

This prototype was printed on the FR4 substrate with permittivity ε_r = 4.4 and thickness h = 800 µm.

Figure 20: Photograph of the RCNGD-circuit implemented.

5.4.1. Measured frequency results of the neutralized circuit

The measured frequency results analysed in this paragraph were extracted from the S-parameters as in 3.1.1. Figs. 21 display the frequency responses of the RC-, NGD- and RCNGD-circuits from the experimentations from DC to 100 MHz. We can see that a very good correlation between the expected theoretic concept illustrated in Figs. 15 and the measurements is observed.

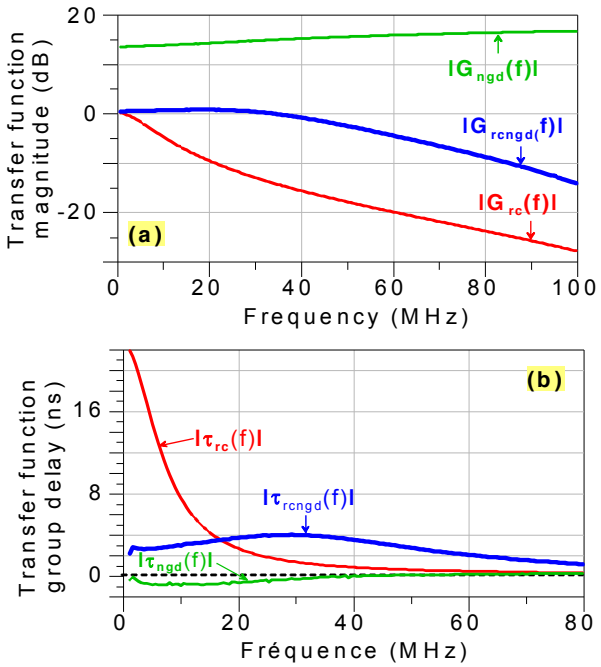

Figure 21: Measurement results of the transfer functions from the RC-, NGD- and RCNGD-circuits tested. (a) Magnitude and (b) group delay.

Once again, thanks to the gain more than 10 dB up to 80 MHz and NGD of about -2 ns up to 55 MHz, a significant reduction of the RC-effects is observed. As consequence, the gain of the RCNGD-circuit is close to 0 dB up to 40 MHz whereas as shown in Fig. 21(b) the group delay is reduced strongly up to 20 MHz. These frequency responses illustrate the mechanism of the neutralization method proposed. To highlight more concretely the interpretation of this method, time-domain measurements were also performed. The next paragraph presents results obtained by considering analogue-numerical input signals.

5.4.2. Time-domain experimental results

To confirm the proposed neutralization technique effectiveness for the signal integrity improvement, we compare the square wave pulse v_{in}, and the RC- and RCNGD-circuit outputs, respectively denoted v_{rc} and $-v_{rcngd}$ as plotted in Fig. 22. So, we observe that compared to v_{rc}, the output $-v_{rcngd}$ is well-reconstructed and less distorted according to the input, v_{in}. As we can see in Fig. 22, the RC-circuit degrades the output leading edge with a rise time and a 50 % propagation delay respectively of $t_r \approx 35\,ns$ and $T_{rc} \approx 18.50\,ns$.

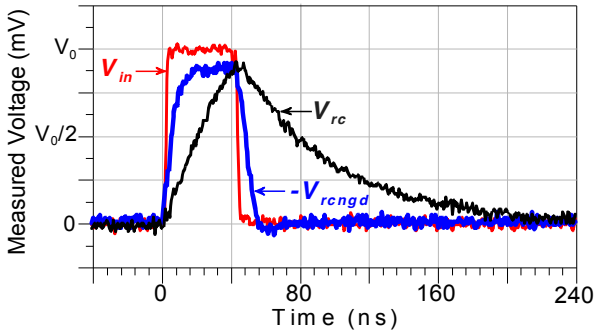

Figure 22: Measured time domain results for an input square wave pulse with V_0 = 1 V with a 40 ns duration or 25-Msym/s rate, 2 ns rise- and fall-times.

Hence, due to the NGD circuit compensation, these parameters were respectively reduced to $t_{rngd} \approx 10\,ns$ and $T_{rcngd} \approx 2.50\,ns$. It corresponds to a relative reduction: $(1-T_{rcngd}/T_{rc})$ =71.4 %, and $(1-t_{rngd}/t_r)$ =86.4 %. In addition, an excellent improvement of the signal rising trailing edges is also achieved.

6. Conclusions

A neutralization technique enabling to suppress the electromagnetic and parasitic disturbances modeled by LC- and RC-networks is developed in this paper. The basic principle of the neutralization concept is explained. The technique is based on the use of LH [71-72] and NGD active circuits presenting transfer function inverse of the disturbing networks.

Applications with various application examples of unwanted disturbances cancellation are developed theoretically, numerically and experimentally. First, a possibility of the LC-effect neutralization is performed by using an LH active circuit. The synthesis relations in function of the LC-parameters are established. Then, simulations confirm the feasibility of the technique proposed around 1 GHz. Then, a compensation of the resonance effect modeled by LC-parallel network by using an NGD circuit comprised of a transistor associated with an RLC-series network was also investigated. Numerical verifications confirm once again, the utility of the technique. The last case concerns the neutralization of the RC-effect with the base band NGD circuit proposed in [41]. The functioning of the NGD effect in base band frequencies was illustrated with experimentation of a circuit in hybrid planer technology. Output signal with front waves in time-advance of about 1.5 ns compared to the input ones is observed. Then, analytical investigation on the frequency-response and unit step responses of the compensated RCNGD-circuit is presented. The relevance of the technique is confirmed with measured results both in frequency- and in time-domains. By considering analogue-digital signal with 25

Msym/s rate, a mixed signal integrity improvement is demonstrated experimentally.

In the continuation of this work, the application of the present neutralization technique for cancelling the degradation of electro-optic perturbations is in progress.

References

[1] Sommerfeld, "Ein Einwand gegen die Relativtheorie der Elektrodynamik und seine Beseitigung", *Physik. Z.* 8, pp. 841-842, 1907.

[2] Sommerfeld, "Uber die Fortpflanzung des Lichtes in Dispergierenden Medien", *Ann. Physik.* 44, pp. 177-201, 1914.

[3] L. Brillouin, *Wave Propagation in Periodic Structures*, McGraw-Hill, New York, 1946.

[4] Sommerfeld, *Vorlesungen über Theoretische Physik*, Band IV, Optik, Dieterich'sche Verlagsbuchhandlung, 1950.

[5] Sommerfeld, *Lectures on Theoretical Physics*, Optics. Academic Press Inc. US, 1954.

[6] L. Brillouin, *Wave propagation and group velocity*, Academic Press, New York, pp. 1-83 & 113-137, 1960.

[7] G. B. Garrett and D. E. McGumber, "Propagation of a Gaussian light pulse through an anomalous dispersion medium", *Phys. Rev. A*, Vol. 1, pp. 305-313, 1970.

[8] S. Chu. and S. Wong, "Linear Pulse Propagation in an Absorbing Medium", *Phys. Rev. Lett.*, Vol. 48, pp. 738-741, 1982.

[9] Ségard and B. Macke, "Observation of negative velocity pulse propagation", Phys. Lett. 109, pp. 213-216, 1985.

[10] Macke and B. Segard, "Propagation of light-pulses at a negative group-velocity", *Eur. Phys. J. D* 23, pp. 125-141, 2003.

[11] A. M. Steinberg and R. Y. Chiao, "Dispersionless, highly superluminal propagation in a medium with a gain doublet", *Phys. Rev. A*, Vol. 49, pp. 2071–2075, 1994.

[12] A. Dogariu, A. Kuzmich and L. J. Wang, "Transparent anomalous dispersion and superluminal light-pulse propagation at a negative group velocity", *Phys. Rev. A*, Vol. 63, pp. 053806.1-053806.12, 2001.

[13] L. J. Wang, A. Kuzmich and A. Dogariu, "Gain-assisted superluminal light propagation", *Nature 406*, pp. 277 – 279, 2000.

[14] K. T. McDonald, "Negative group velocity", *Amer. J. Phys.*, Vol. 69, No. 5, pp. 607–614, May 2001.

[15] O. F. Siddiqui, M. Mojahedi and G. V. Eleftheriades, "Periodically loaded transmission line with effective negative refractive index and negative Group velocity", *IEEE Transactions on Antennas and Propagation*, Vol. 51, No. 10, pp. 2619-2625, Oct. 2003.

[16] J. F. Woodley and M. Mojahedi, "Negative group velocity and group delay in left-handed media", *Phys. Rev. E*, Vol. 70, pp. 046603.1-046603.6, 2004.

[17] R. Y. Chiao, "Superluminal (but causal) propagation of wave packets in transparent media with inverted atomic populations", *Phys. Rev. A*, Vol. 48, pp. R34-R37, 1993.

[18] R. Y. Chiao, *Population inversion and superluminality, in amazing light*, Springer-Verlag, New York, pp. 91-108, 1996.

[19] R. Y. Chiao, E. L. Bolda, J. Bowie, J. Boyce and M. W. Mitchell, "Superluminality and amplifiers", *Prog. Crystal Growth Charact. Mat.* 33, pp. 319-325, 1996.

[20] M. W. Mitchell and R.Y. Chiao, "Causality and negative group delays in a simple bandpass amplifier", *Am. J. Phys.*, Vol. 66, pp. 14–19, 1998.

[21] M. W. Mitchell and R.Y. Chiao, "Negative group delay and 'Fronts' in a causal systems: An experiment with very low frequency bandpass amplifiers", *Phys. Lett. A*, Vol. 230, pp. 133–138, Jun. 1997.

[22] D. Solli, R. Y. Chiao and J. M. Hickmannn, "Superluminal effects and negative group delays in electronics, and their applications", *Phys. Rev. E*, Vol. 66, pp. 056601.1-056601.4, 2002.

[23] M. Kitano, T. Nakanishi and K. Sugiyama, "Negative group delay and superluminal propagation: An electronic circuit approach", *IEEE Journal of Selected Topics in Quantum Electronics*, Vol. 9, No. 1, pp. 43-51, Feb. 2003.

[24] T. Nakanishi, K. Sugiyama and M. Kitano, "Demonstration of negative group delays in a simple electronic circuit", *Am. J. Phys.*, Vol. 70, No. 11, pp. 1117-1121, 2002.

[25] J. N. Munday and R. H. Henderson, "Superluminal time advance of a complex audio signal", *Appl. Phys. Lett.*, Vol. 85, pp. 503-504, Jul. 2004.

[26] S. J. Erickson, M. Khaja and M. Mojahedi, "Time- and frequency-domain measurements for an active negative group delay circuit", *in Proc of IEEE Ant. Prop. Soc. Int. Symp.*, Vol. 3A, pp. 790-793, 2005.

[27] V. Veselago, "The electrodynamics of substances with simultaneously negative values of ε and μ", *Soviet Physics Uspekhi*, Vol. 10, No. 4, pp. 509-514, 1968.

[28] J. B. Pendry, "Negative refraction make a perfect lens", *Phys. Rev. Lett.*, Vol. 85, pp. 3966-3969, Oct. 2000.

[29] R. A. Shelby, D. R. Smith and S. Schultz, "Experimental verification of a negative index of refraction", *Science*, Vol. 292, No. 5514, pp. 77 - 79, Apr. 2001.

[30] J. B. Pendry, "Negative refraction", *Contemporary Physics*, Vol. 45, pp. 191-202, 3 May-June 2004.

[31] R. Smith, J. B. Pendry and M. C. K. Wiltshire, "Metamaterials and negative refractive index", *Science*, Vol. 305, pp. 788-792, 6 Aug. 2004.

[32] R. W. Ziolkowski and E. Hayman, "Wave propagation in media having negative permittivity and permeability", *Phys. Rev. E*, Vol. 64, pp. 056625.1-056625.15, 2001.

[33] R. W. Ziolkowski and A. D. Kipple, "Causality and double-negative metamaterials", *Phys. Rev. E*, Vol. 68, Part 2, pp. 026615, Aug. 2003.

[34] A. Dogariu, A. Kuzmich and L. J. Wang, "Transparent anomalous dispersion and superluminal light-pulse propagation at a negative group velocity," *Phys. Rev. A*, Vol. 63, pp. 053806.1-053806.12, 2001.

[35] R. W. Boyd and D. J. Gauthier, *'Slow' and 'Fast' light*, Ch. 6 in Progress in Optics 43, E. Wolf, Ed. Elsevier, Amsterdam, pp. 497-530, 2002.

[36] J. Gauthier and R. W. Boyd, "Fast light, slow light and optical precursors: What does it all mean", *Photonics Spectra*, pp. 82-90, Jan. 2007.

[37] A. Kuzmich, A. Dogariu, L. J. Wang, P. W. Milonni and R. Y. Chiao, "Signal velocity, causality and quantum noise in superluminal light pulse propagation", *Phys. Rev. Lett.* 86, pp. 3925–3929, 2001.

[38] S. Lucyszyn, I. D. Robertson and A. H. Aghvami, "Negative group delay synthesiser", *Electronic Letters*, Vol. 29, pp. 798-800, 1993.

[39] C. D. Broomfield and J. K. A. Everard, "Broadband negative group delay networks for compensation of oscillators using feedforward amplifiers", *Electronic Letters*, Vol. 20, pp. 1710-1711, Sep. 2000.

[40] N. S. Bukhman, and S. V. Bukhman, "On the negative delay time of a narrow-band signal as it passes through the resonant filter of absorption", *Radiophysics and Quantum Electronics*, Vol. 47, No. 1, pp. 66-76, 2004.

[41] B. Ravelo, "Demonstration of negative signal delay with short-duration transient pulse", *Eur. Phys. J. Appl. Phys.* (*EPJAP*), Vol. 55, 10103-pp. 1-8, 2011.

[42] B. Ravelo and S. De Blasi, "An FET-based microwave active circuit with dual-band negative group delay", *Journal of Microwaves*, *Optoelectronics and Electromagnetic Applications* (*JMOe*), Vol. 10, No. 2, pp. 355-366, Dec. 2011.

[43] B. Ravelo, "Investigation on microwave negative group delay circuit", *Electromagnetics*, Vol. 31, No. 8, pp. 537-549, Nov. 2011.

[44] B. Ravelo, "Baseband NGD circuit with RF amplifier", *Electronic Letters*, Vol. 47, No. 13, pp. 752-754, June 2011.

[45] M. Kandic, and G. E. Bridges, "Asymptotic limits of negative group delay in active resonator-based distributed circuits", *IEEE Transactions on Circuits and Systems I: Regular Papers*, Vol. 58, No. 8, pp. 1727 – 1735, Aug. 2011.

[46] M. Kandic and G. E. Bridges, "Transient-imposed limitations of negative group delay circuits", *14th International Symposium on Antenna Technology and Applied Electromagnetics & the American Electromagnetics Conference (ANTEM-AMEREM), 2010,* Ottawa, ON, Canada, pp. 1-4, 5-8 July 2010.

[47] C. D. Broomfield and J. K. A. Everard, "Broadband negative group delay networks for compensation of oscillators using feedforward amplifiers", *Electronic Letters*, Vol. 20, pp. 1710-1711, Sep. 2000.

[48] B. Ravelo, A. Perennec and M. Le Roy, "Broadband balun using active negative group delay circuit", in *Proc. of the 37th European Microwave Conference*, Munich, Germany, pp. 466-469, Oct. 2007.

[49] S. Keser and M. Mojahedi, "Broadband negative group delay microstrip phase shifter design", *in Proc. of IEEE Ant. Prop. Soc. Int. Symp. 2009* (*APSURSI'09*), Charleston, SC, pp. 1-4, 1-5 June 2009.

[50] B. Ravelo, A. Perennec and M. Le Roy, "Synthesis of frequency-independent phase shifters using negative group delay active circuit", *Int. J. RF and Microwave Computer-Aided Engineering* (*RFMiCAE*), Vol. 21, No. 1, pp. 17-24, Jan. 2011.

[51] B. Ravelo, *Étude des circuits analogiques-numériques NGD et leurs applications: Théorie fondamentale et expérimentations des circuits analogiques et numériques à temps négatif et leurs applications*, (in French) Chapters 10 and 11, Éditions Universitaires Européennes (EUE), Ed. by M. Fabre, 432 Pages, 13 Jan. 2012.

[52] B. Ravelo, M. Le Roy and A. Pérennec, "Frequency-independent active phase shifters for UWB applications", *Proc. of the 40th European Microwave Conference*, Paris, France, pp. 1774-1777, 28-30 Sep. 2010.

[53] B. Ravelo, "Investigation on the microwave pulse signal compression with NGD active circuit", *PIER C Journal*, Vol. 20, pp. 155-171, 2011.

[54] H. Noto, K. Yamauchi, M. Nakayama, and Y. Isota, "Negative group delay circuit for feed-forward amplifier", *IEEE Int. Microw. Symp. Dig*., Honolulu, Hawaii, pp. 1103-1106, June 2007.

[55] H. Choi, Y. Jeong, C. D. Kim, and J. S. Kenney, "Bandwidth enhancement of an analog feedback amplifier by employing a negative group delay circuit", *PIER*, Vol. 105, pp. 253-272, 2010.

[56] K.-P. Ahn, R. Ishikawa, and K. Honjo, "Group delay equalized UWB InGaP/GaAs HBT MMIC amplifier using negative group delay circuits", *IEEE Tran. MTT*, Vol. 57, No. 9, pp. 2139- 2147, Sep. 2009.

[57] S. K. Podilchak, B. M. Frank, A. P. Freundorfer, and Y. M. M. Antar, "High speed metamaterial-inspired negative group delay circuits in CMOS for delay equalization", *in Proc. of 2nd Microsystems and Nanoelectronics Research Conference 2009 (MNRC 2009*), Ottawa, ON, Canada, pp. 9-12, 13-14 Oct. 2009.

[58] B. Ravelo and J. Ben Hadj Slama, "Equalization of digital/mixed-signal disturbances with an negative group delay circuit", (Accepted for communication) *Proceedings of the 16th IEEE Mediterranean Electrotechnical Conference* (*MELECON 2012*), Medine Yasmine Hammamet, Tunisia, 25-28 March 2012.

[59] T. Eudes, and B. Ravelo, "Cancellation of delays in the high-rate interconnects with UWB NGD active cells", *Applied Physics Research*, Vol. 3, No. 2, pp. 81-88, Nov. 2011.

[60] B. Ravelo, "Delay modelling of high-speed distributed interconnect for the signal integrity prediction", *To be published in Eur. Phys. J. Appl. Phys.* (*EPJAP*), 2012, DOI: 10.1051/epjap/20121103742012.

[61] B. Ravelo, "Microelectronic interconnect modeling with periodical lumped RLC-network", *To be published in Turkish Journal of Electrical Engineering & Computer Sciences* (*TJCEES*), 2012.

[62] B. Ravelo, "Lumped RC-tree network propagation-delay modeling", *To be published in Int. J.*

Communication Engineering Applications (*IJCEA*), 2012.

[63] S.-S. Myoung, B.-S. Kwon, Y.-H. Kim and J.-G. Yook, "Effect of group delay in RF BPF on impulse radio systems", *IEICE Trans. Communications*, Vol. 90, No. 12, pp. 3514-3522, 2007.

[64] W. C. Elmore, "The transient response of damped linear networks", *J. Appl. Phys.*, Vol. 19, pp. 55-63, Jan. 1948.

[65] C.-Y. Liu, Q.-X. Chu and J.-Q. Huang, "A planar D-CRLH and its application to bandstop filter and leaky-wave antenna", *PIER Letters*, Vol. 19, pp. 93-102, 2010.

[66] O. Siddiqui, A. S. Mohra, and G. V. Eleftheriades, "Quad-band power divider based on left-handed transmission lines", *Electronic Letters*, Vol. 46, No. 21, pp. 1441-1442, Oct. 2010.

[67] C. Caloz, A. Sanada, and T. Itoh, "A novel composite right/left-handed coupled-line directional coupler with arbitrary coupling level and broad bandwidth", *IEEE Tran. MTT*, Vol. 52, pp. 980-992, Mar. 2004.

[68] R. Islam and G. V. Eleftheriades, "Phase-agile branch-line couplers using metamaterial lines", *IEEE MWC Lett*., Jul. 2004, 14, Vol. 7, pp. 340-342.

[69] G. V. Eleftheriades, O. Siddiqui and A. K. Iyer, "Transmission line for negative refractive index media and associated implementations without excess resonators", *IEEE MWC Lett.*, Vol. 13, No. 2, pp. 51-53, Feb. 2003.

[70] A. Lai, C. Caloz and T. Itoh, "Composite right/left-handed transmission line metamaterials", *IEEE Microwave Magazine*, Vol. 5, pp. 34-50, Sep. 2004.

[71] T. Itoh, "Invited paper: Prospects for metamaterials", *Electronic Letters*, Vol. 40, No. 16, pp. 972-973, Aug. 2004.

[72] A. Levy, R. Shavit and L. Habib, "Optimisation of a microstrip left-handed transmission line using circuit modelling", *IET Microwaves, Antennas & Propagation*, Vol. 4, No. 12, pp. 2133-2143, 2010.

[73] S.-G. Mao, M.-S. Wu, Y.-Z. Chueh and Chen Chun Hsiung, "Modeling of symmetric composite right/left-handed coplanar waveguides with applications to compact bandpass filters", *IEEE Trans. MTT*, Vol. 53, No. 11, pp. 3460-3466, Nov. 2005.

[74] W.-R. Zhu, and X.-P. Zhao, "Numerical study of low-loss cross left-handed metamaterials at visible frequency", *Chinese Phys. Lett.*, 2009, 26 074212.

[75] Fu Jia-Hui, Wu Qun, Yang Guo-Hui, Meng Fan-Yi and Lee Jong-Chul, "Effective electromagnetic parameters of left-handed coplanar waveguide transmission lines", J. Appl. Phys., Vol. 109, 07A333, 2011.

[76] J. Vlach, J. A. Barby, A. Vannelli, T. Talkhan, and C. J. Shi. Neves, "Group delay as an estimate of delay in logic", *IEEE Trans. Computed-Aided Design*, Vol. 10, No. 7, pp. 949-953, Jul. 1991.

[77] R. M. Corless, G. H. Gonnet, D. E. G. Hare, D. J. Jeffrey and D. E. Knuth, "On the Lambert W Function", *Advances in Computational Mathematics*, Vol. 5, pp. 329-359, 1996.

[78] D. J. Jeffrey, D. E. G. Hare and R. M. Corless, "Unwinding the branches of the Lambert W function", *Math. Scientist*, Vol. 21, pp. 1-7, 1996.

Experimental Measurement of Reverse Doppler Effect with Tunable Composite Right/Left Handed Transmission Line

Z. Li[1], Y. W. Zhang[1*], J. F. Zhao[1],L. W. Zhang[1,2]

[1] MOE Key Laboratory of Advanced Micro-structure Materials,Department of Physics, Tongji University, Shanghai 200092, PR China
[2] School of Physics and Chemistry, Henan Polytechnic University, Jiaozuo 454000
*corresponding author: yewen.zhang@tongji.edu.cn

Abstract

The reverse Doppler Effect only is observed in metamaterial with both negative permittivity and negative permeability. A new way to observe reverse Doppler Effect using a simple circuit configuration is presented. The experimental results show good agreement with the theoretical prediction.

1. Introduction

The Doppler Effect is a well-known phenomenon by which the frequency of a wave is shifted according to the relative velocity of the source and the observer [1]. The application of this phenomenon have been widely used and include weather and aircraft radar, blood flow measurement and the detection of extra solar planets. However, the reverse Doppler Effect refers to frequency shifts are in the opposite way to those phenomenons mentioned above. For example, the frequency increasing of a wave would be measured on reflection from a receding boundary [2-7]. The expiation is that in left-handed media the group and phase velocities of the waves are in opposite directions. If we can construct such a moving reflecting boundary and find a method of measuring the frequency shifts of reflected wave from the boundary, the reversed Doppler Effect can be verified easily.

The basis of the Doppler effect is determined by the affect that reflecting boundary motion has on observed frequency. A composite wavefront is created because the reflecting boundry is in motion and the emitted wavefronts experience different propagation distances to the observer. The phase of the wavefront can be expressed as

$$\varphi=2\pi f_s - \beta v_b t \qquad (1)$$

where f_s is the source frequency, v_b is the velocity of the reflecting boundary, and β is the propagation phase constant. The frequency of the wave is determined by the time derivative of the phase, given by

$$2\pi f_r = 2\pi f_s - \beta v_b \qquad (2)$$

It is noticed that whether received frequency f_r higher or lower than the original frequency f_s is determined by the sign of the propagation phase constant β. Thus, if the reflecting boundary is moving through an LH medium where β is a negative value rather than a positive value, a reverse Doppler effect will be induced.

In this paper, the experiment was performed using the tunable Composite Right/Left Handed Transmission Line (CRLH-TL) as its experimental platform. Composite Right/Left Handed Transmission Line (CRLH-TL) is an important artificial electromagnetic structure to implement microwave metamaterial. CRLH-TL is analyzed based on transmission line approach, and fabricated by surface micro-machining and surface-mount technology. In recent years, there has been an intensive interest in CRLH-TL because of its obvious advantages, such as simple structure, compact size, easy to fabricate, low loss and broadband. CRLH-TL provides an efficient design tool for left-handed applications and provides insight into the physical phenomena of metamaterial.

2. Experimental Design

2.1 The structure of tunable CRLH_TL

The structure of the tunable CRLH-TL is shown in Fig. 1. In the structure of CRLH-TL, the inductance and

capacitance both have decisive impact to the left-handed passband characteristics in bandgap materials composed by lumped elements when unit length of periodic structure is very short compared with the wavelength. When the inductance or capacitance is varied, the frequency range of the left-handed passband changed accordingly. In the microwave band, it is very difficult to

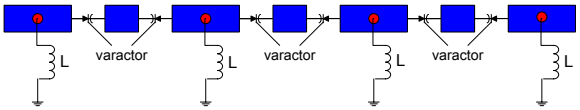

Figure 1: The structure of the CRLH-TL. The blue square is microstripline. There are three cells of the CRLH-TL shown in the figure.

change the inductance of surface-mount components continuously. But the left-handed passband can be easily adjusted if we use varactor diodes instead of the lumped capacitance. Varactor diode is a kind of device that its capacitance will change with the bias voltage. The capacitance of varactor diode will decrease when its bias voltage increase and vice verse. On this basis, a special CRLH-TL that its transmission characteristics can be tuned is designed. The structure using double-sided printed circuit board, the varactor connected by microstripline and the SMD inductor L connecting the upper and lower surfaces of the printed circuit board through the hole which mentioned by the red circle. V_b is a external voltage using to adjust the bias voltage of the varactor. The inductance of the SMD inductor is 4.7nH. The model of the varactor is BB135 which manufactured by Philips. The length of a cell is 10.5mm. The relationship between the changes of the varactor's capacitance and the dispersion relationship of the CRLH-TL is shown in Fig.2.

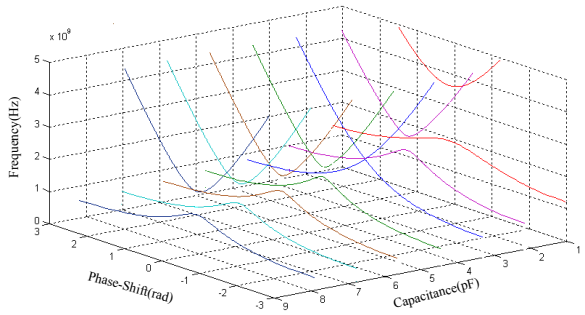

Figure 2: The dispersion relation map

2.2 The establishment of the moving reflecting boundary

How to build a moving reflecting boundary in this kind of transmission line is the key point of this experiment. The schematic diagram of experimental platform is shown in Fig. 3.

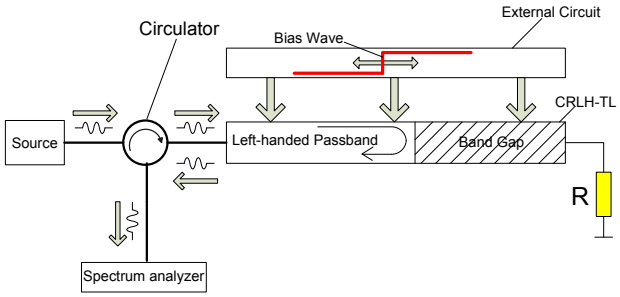

Figure 3: Schematic diagram of experimental platform.

The frequency of the original electromagnetic wave using in this experiment is 1GHz. The number of CRLH-TL cells of the transmission line is fourteen. The external circuit is used to generate a "bias wave" to vary the bias voltage of each unit varactor diode successively. When the bias voltage of the varactor is 0V, the state of the transmission line is in the band gap, electromagnetic wave can not propagate and all reflected back. When the bias voltage is increased, the capacitance of the varactor is decreased, the state of the transmission line is changed, turned into the passband. The relationship between the state of the transmission line and the changes of the bias voltage is shown in Fig 4.

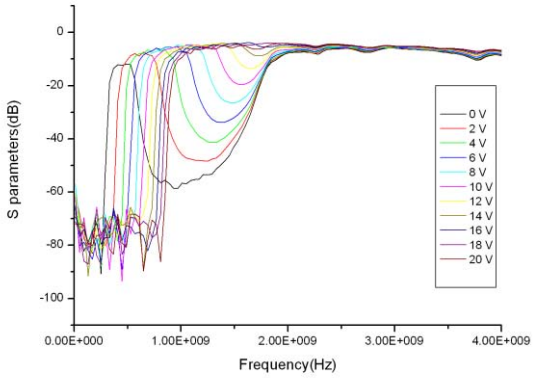

Figure 4: The relationship between the state of the transmission line and the changes of the bias voltage.

Since the bias voltage of each unit varactor diode is changing successively, the entire transmission line is also

getting into the passband gradually. For the electromagnetic wave, it is like there is a reflecting boundary moves in the transmission line. The bias voltage of varactors is varied from left to right successively by using the "bias wave". It constructs a reflecting boundary moving from left to right which is away from the source. Using a similar way, a reflecting boundary moving toward the source can also be generated. The circulator in this construct is using to separate the reflected wave and incident wave, so the spectrum analyzer can get the frequency shift of the reflected wave.

The velocity of the reflecting boundary v_r is defined by the time interval Δt and the length of the CRLH-TL cell d_0, given by

$$v_r = d_0 / \Delta t \qquad (3)$$

The phase velocity of the source wave which propagating in the CRLH-TL. v_s is derived from the dispersion relation of the CRLH-TL.

$$f_r = f_s \times \left(\frac{v_s \pm s \times v_r}{v_s \mp s \times v_r} \right) \qquad (4)$$

$$\Delta f = f_r - f_s \qquad (5)$$

s is the sign of the propagation phase constant β, since s is equal to -1 in that case, the received frequency f_r is higher than the original frequency f_s when the reflecting boundary is moving away from the source and the frequency shift Δf is positive. The received frequency f_r is lower than the original frequency f_s when the reflecting boundary is moving toward the source and the frequency shift Δf is negative. The reverse Doppler effect is induced.

3. Experimental Results

The source signal in this experiment is generated by the Agilent PSG Vector Signal Generator E8267D, the frequency is 1GHz. The spectrum analyzer using the Agilent MXA Signal Analyzer N9020A, the frequency shift of the reflected wave is measured by the spectrum analyzer. The result of the spectrum analyzer is shown in Fig. 5. The results show the frequency shift is positive when the reflecting boundary is moving away from the source in Fig. 5(a) and the frequency shift is negative when the reflecting boundary is moving toward the source in Fig. 5(b).

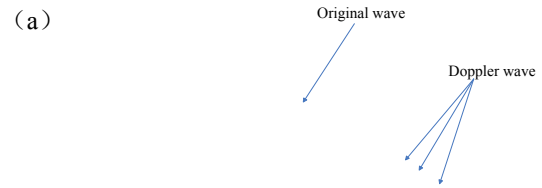

(a) The reflecting boundary is moving away from the source.

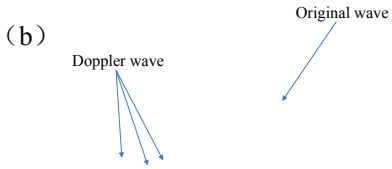

(b) The reflecting boundary is moving toward the source

Figure5: The result of Frequency shift.

The three different lines in each figure represent the result obtained by different speed of the moving reflecting boundary. The relationship between the speed of the moving reflecting boundary and the frequency shift is shown in Fig. 6.

4. Conclusion

To summarize, the experiments verified the reversed Doppler Effect by construct a moving reflecting boundary using the tunable CRLH transmission line. Implementation method is relative simple, and the results consistent with theory.

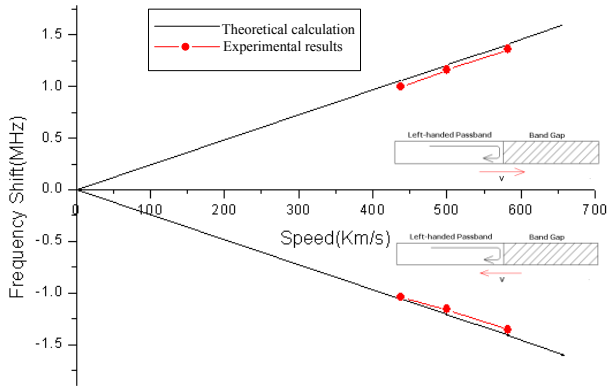

Figure 6: The relationship between the speed of the moving reflecting boundary and the frequency shift. The horizontal axis is the frequency shift of the reflected wave; the vertical axis is the speed of the moving reflecting boundary. The black line is theoretical calculation; the red dash-dot is experimental result.

Acknowledgements

This research is supported by National Basic Program (973) of China (No.2011CB922001), and by the National Natural Science Foundation of China (No.10904032).

References

1. C.H. Papas, *Theory of Electromagnetic Wave Propagation*, McGraw-Hill, New York, 1965.
2. V.G. Veselago, The electrodynamics of substances with simultaneously negative values of ε and μ, *Sov. Phys. Usp.*, Vol.10, 509-514, 1968.
3. N.Seddon, T.Bearpark, Observation of the inverse Doppler Effect, *Science*, Vol. 302, 1537, 2003.
4. M. Kevin, K.H. Leong, A. Lai, T. Itoh, Demonstration of reverse Doppler effect using a left-handed transmission line, *Microwave and Optical technology letters*, Vol. 48, No. 3, 545-547, 2006.
5. E.J. Reed, J.D. Joannopoulos, Reversed Doppler Effect in Photonic Crystals, *Phys. Rev. Lett.*, Vol. 91, No. 13, 133901, 2003.
6. A.V. Chumak, P.Dhagat, A. Jander, A.A. Serga, B. Hillebrands, Reverse Doppler effect of magnons with negative group velocity scattered from a moving Bragg grating, *Phys. Rev. B*, Vol. 81, 140404, 2010.
7. D.D. Stancil, B.E. Henty, A.G. Cepni, J.P. Van't Hof, Observation of an inverse Doppler shift from left-handed dipolar spin waves, *Phys. Rev. B*, Vol. 74, 060404, 2006.

Gain Compensated Symmetric Loaded Transmission Line Exhibiting Bidirectional Negative Group Delay

Greg E Bridges[1*], Miodrag Kandic[1]

[1]Electrical and Computer Engineering, University of Manitoba, Winnipeg, Canada
*corresponding author, E-mail: bridges@ee.umanitoba.ca

Abstract

A one-dimensional transmission line-based medium capable of bidirectional lossless negative group delay signal propagation is described. The microwave circuit comprises two symmetric resonator loaded transmission lines with active gain compensation and coupled through power combiners. We demonstrate the circuit is conditionally stable and capable of transmitting a finite bandwidth pulse in both directions. A group delay of -600 ps in either direction is achieved for a Gaussian pulse with a bandwidth of 14 MHz modulated at a frequency of 280 MHz.

1. Introduction

Media exhibiting superluminal or negative group delay (NGD) have been explored in the optical regime [1] as well as the microwave regime where they are commonly implemented using loaded transmission lines [2]. Passive devices based on resonator loaded transmission lines can provide NGD in regions of anomalous dispersion but are accompanied by loss. Several active circuit designs, which incorporate gain elements, have been proposed to compensate for this loss [3-9]. These circuit topologies are, however, inherently unidirectional. Bidirectional transmission line media have recently been demonstrated that are capable of superluminal group velocity using shunt negative capacitance devices [10], and negative group velocity using symmetric coupled active transmission lines [11]. In this paper we present a bidirectional lossless NGD transmission line and demonstrate measurements of stable time-domain pulse propagation with NGD in both directions through this media.

Circuits exhibiting superluminal or negative group delay have enabled many novel microwave devices through their ability to provide phase equalization or delay compensation. Several passive NGD circuits, mostly based on series or parallel RLC resonators have been reported [2,12,13]. These devices exhibit large attenuation for any reasonable NGD, and there is a trade-off between the achieved NGD and attenuation at the resonance frequency [7]. The attenuation can be compensated by cascading active elements with resonators or by integrating the resonator within the amplifier feedback circuitry. The use of active elements limits the signal transmission in gain-compensated NGD media to be unidirectional and places restrictions on their application. For example, the gain-compensated NGD application in series-fed phased arrays [14,15] can be used for either transmit or receive modes, but not simultaneously. In [11] a symmetric bilateral gain-compensated NGD circuit was presented which enabled a bilateral lossless constant phase shifter. Most studies of NGD microwave devices present the frequency behavior, with few examining the time-domain response to finite bandwidth waveforms and their associated distortion [16].

2. Bidirectional NGD Media

In this paper we present a one-dimensional medium that exhibits NGD without absorption in both directions. The medium enables finite bandwidth pulses to propagate in both directions without loss as shown in Fig. 1a. This would also enable construction of a finite sized (delay) medium exhibiting lossless zero delay.

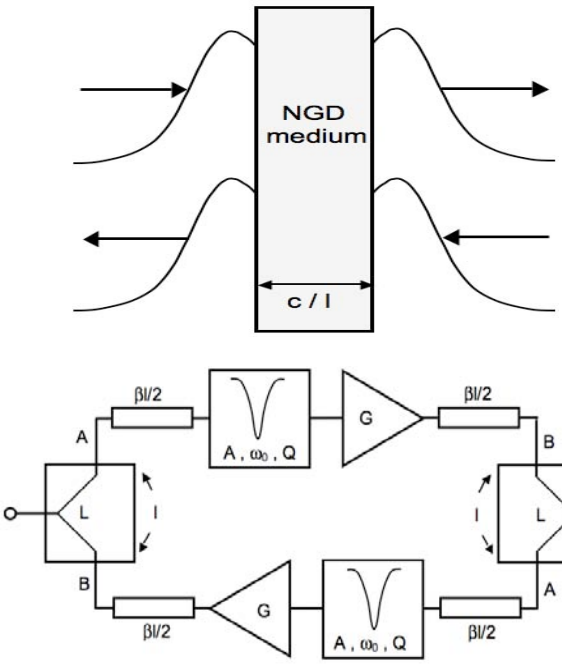

Figure 1a) Bidirectional medium with length τ_0=c/l exhibiting negative group delay and b) its implementation using a symmetric coupled resonator-loaded transmission line circuit with active gain compensation.

The bidirectional NGD device comprises two symmetric resonator loaded transmission lines with active gain compensation, which are coupled through power combiners as shown in Fig. 1b. The resonator-loaded transmission lines in each of the branches (A-B) are used to produce the NGD and can be constructed using several different topologies as previously described in [6]. A passive resonator based circuit exhibiting negative group delay will inherently have attenuation associated with it. The attenuation is compensated by cascading an active gain stage with the NGD circuit. Various approaches, involving cascaded NGD circuit-amplifiers [3], integration of the NGD resonator in the feedback path of an op-amp [7] or use of the out-of-band negative phase characteristic in the roll-off of an amplifier has been used to achieve lossless NGD [17] in transmission line based media. However, all these previous approaches are unidirectional due to the active gain stages in these circuits.

The 2-port description of the circuit in Fig. 1b will be derived by considering the transmission and reflection coefficients of the branches (A-B). A passive resonator-based NGD circuit comprised of simple resonators can be modeled using a cascaded second-order transfer function [7]. For the generic gain-compensated case of Fig. 1, the transmission coefficient of a matched cascaded *N*-stage design is

$$S_{21}^{AB}(\omega) = -G\left[\frac{1+jQ(\omega/\omega_0-\omega_0/\omega)}{A_{tot}^{1/N}+jQ(\omega/\omega_0-\omega_0/\omega)}\right]^N e^{-j\beta l}, \quad (1)$$

where Q is the chosen quality factor of individual resonators, ω_0 is the resonance frequency, and A_{tot} is the maximum out-of-band magnitude swing of the overall *N*-stage design ($A_{tot}=A^N$). Here, G is the compensating amplifier gain and compensates for the NGD resonator loss as well as losses in the splitters and $|G/A_{tot}|>1$ or $|S_{21}{}^{AB}(\omega)|>1$. The $exp(-j\beta l)$ term accounts for the phase shift due to finite physical dimensions. Expression (1) assumes ideal wideband input and/or output matching of the cascaded stages. The overall *N*-stage bandwidth is determined by the overall quality factor $Q_{tot}=\omega_0/\Delta\omega$. Assuming $1/(2Q_{tot})<<1$, and with $A_{tot} > 2^{1/2}$ yields

$$Q_{tot} = Q\frac{\sqrt{1-(2/A_{tot}^2)^{1/N}}}{\sqrt{2^{1/N}-1}}. \quad (2)$$

The bidirectional gain-compensated NGD circuit is shown in Fig. 2. It consists of two 3-dB power splitters/combiners with high isolation, and two amplifiers, one for each propagation direction, as shown in Fig. 1b. Assuming the power divider-couplers have an insertion loss, L, and isolation, I, and with $|S_{22}{}^{AB}(\omega)|=0$ the overall transfer and reflection coefficients for the bidirectional circuit is

$$S_{11} = S_{22} = L^2\frac{(S_{21}^{AB})^2 I + S_{11}^{AB}}{1-(S_{21}^{AB})^2 I^2}, \quad (3)$$

$$S_{21} = S_{12} = L^2 S_{21}^{AB}\frac{1+S_{11}^{AB} I}{1-(S_{21}^{AB})^2 I^2}. \quad (4)$$

At the resonance frequency we note that for splitters with good isolation, such that $|S_{21}{}^{AB}I|<<1$ and $|S_{11}{}^{AB}I|<<1$, the transmission coefficient is $S_{21} = L^2 S_{21}{}^{AB}$.

The transmission coefficient phase and the differential-phase group delay can be expressed, respectively, as

$$\phi(\omega) = \tan^{-1}\left(\frac{\mathrm{Im}(S_{21})}{\mathrm{Re}(S_{21})}\right) \text{ and } \tau_g = -\frac{d\phi(\omega)}{d\omega}. \quad (5)$$

The minimum group delay (largest NGD, if it becomes negative) occurs approximately at the resonance frequency, and can be evaluated from (2) as

$$GD_{21} = \tau_g\Big|_{\omega=\omega_0} = -\frac{2Q_{tot}}{\omega_0}N\sqrt{2^{1/N}-1}\frac{1-1/A_{tot}^{1/N}}{\sqrt{1-(2/A_{tot}^2)^{1/N}}} + \tau_{AB} + 2\tau_L, \quad (6)$$

where τ_{AB} is the positive group delay associated with the physical delay of the NGD circuit (A-B) and τ_L is the delay due to the coupler.

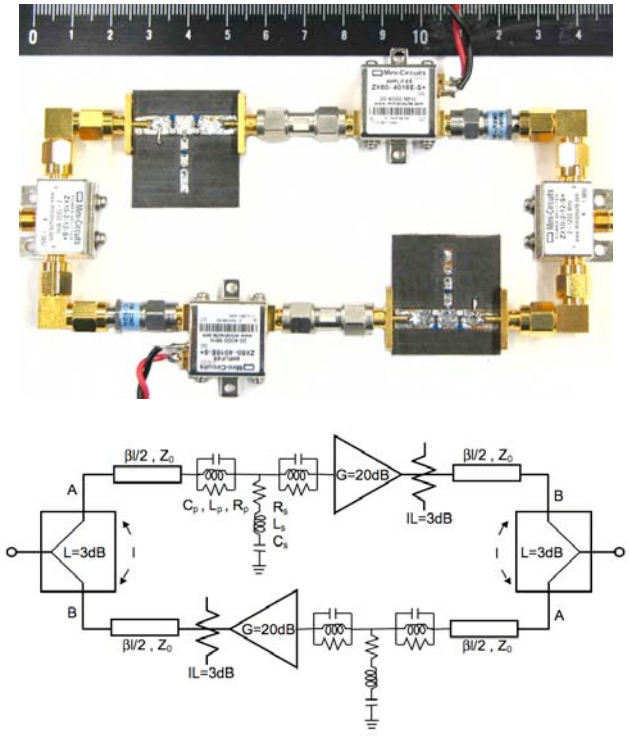

Figure 2a) Bidirectional resonator-loaded transmission line circuit exhibiting NGD and b) its equivalent circuit block diagram.

2.1. Bidirectional gain-compensated NGD circuit

The constructed bidirectional NGD circuit is shown in Fig. 2a, with its equivalent circuit shown in Fig. 2b. In this work we employ a T-network of series / parallel resonators for

the NGD passive circuit [13], equivalent to the N=3 stage cascaded second order filter (1). The resonator is cascaded with a wideband, low group delay, amplifier with a gain, G, and an attenuator with insertion loss L_{ATTN}. The attenuator after the amplifier is used to adjust the total insertion loss of the circuit so that a net gain of the bidirectional circuit is zero. When the resonance frequency and quality factor of the stages are equal, the transmission and reflection coefficients of the individual NGD–gain compensated branches (A-B) is

$$S_{21}^{AB} = G_{tot}\frac{1}{1+z_p}\frac{2}{2+y_s(1+z_p)}e^{-j\omega\tau_{AB}}, \tag{7}$$

$$S_{11}^{AB} = \frac{1}{1+z_p}\frac{2z_p - y_s(1-z_p^2)}{2+y_s(1+z_p)}e^{-j\omega\tau_{AB}}, \tag{8}$$

where

$$z_p = \frac{R_p/Z_0}{1+jQ\left(\frac{\omega}{\omega_0}-\frac{\omega_0}{\omega}\right)} \quad , \quad y_s = \frac{Z_0/R_s}{1+jQ\left(\frac{\omega}{\omega_0}-\frac{\omega_0}{\omega}\right)}, \tag{9}$$

$$Q = Q_p = \frac{R_p}{\sqrt{L_p/C_p}} = Q_s = \frac{\sqrt{L_s/C_s}}{R_s}, \tag{10}$$

$$\omega_0 = \omega_p = \frac{1}{\sqrt{L_pC_p}} = \omega_s = \frac{1}{\sqrt{L_sC_s}}, \tag{11}$$

$$R_s = \frac{Z_0^2 - R_p^2}{2R_p} \quad , \quad A_{tot} = \frac{Z_0 + R_p}{Z_0 - R_p}. \tag{12}$$

Equation (12) puts limits on the possible values of R_p. Here $G_{tot} = GL_{ATTN}$ with L_{ATTN} = -3 dB in the constructed circuit. A resonant frequency of f_0 = 310 MHz, a Q = 2.62 and an out-of-band gain A_{tot} = 2.84 (9.1 dB) were chosen as design parameters along with a reference impedance $Z_0 = 50\Omega$. The gain is chosen so that $G = A_{tot}/(LL_{ATTN})$ where L is the coupler insertion loss.

2.2. Measured frequency response and group delay

The measured S-parameters of the single-branch (A-B) gain compensated circuit are shown in Fig. 3a. The measured resonance frequency was 280 MHz, while the gain at the resonance was 7.2 dB. The amplifiers are designed for a gain of slightly over 6 dB at the resonant frequency, in order to compensate for loss at the two splitters. The resonance frequency and matching of the circuit deviate slightly from the theoretically designed values due to the actual chosen values of the R,L,C components and parasitic effects. The values used in the fabricated resonator design were R_p=24Ω, L_p=4.7nH, C_p=56pF and R_s=43Ω, L_s=39nH, C_s=6.8pF. Fig. 3b shows the measured group delay of the single-branch (A-B) circuit. Ignoring the positive delays, τ_{AB} and τ_L, Equation (3) predicts a group delay of GD_{21} = -2.3 ns at the resonance frequency, while the measured value is -1.8 ns.

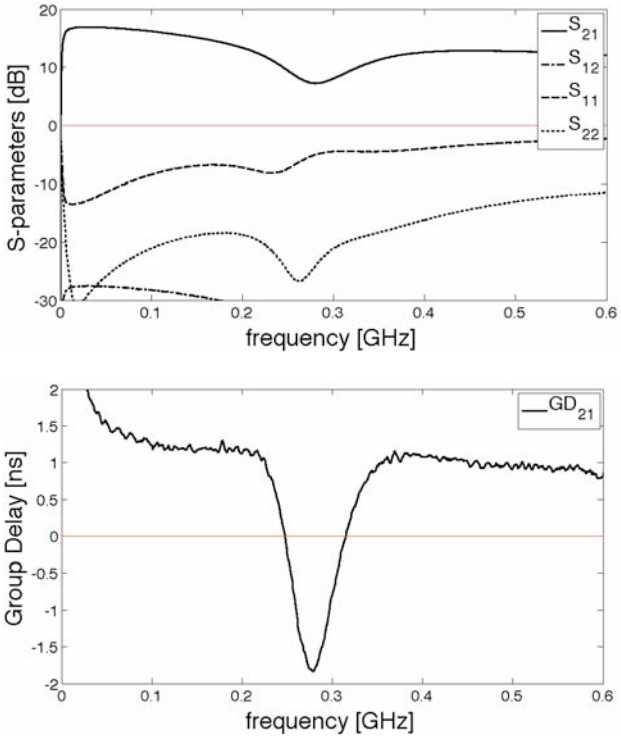

Figure 3a) Measured S-parameters of the gain-compensated resonator-loaded transmission line single branch (A-B) in Fig. 2b and b) its measured group delay.

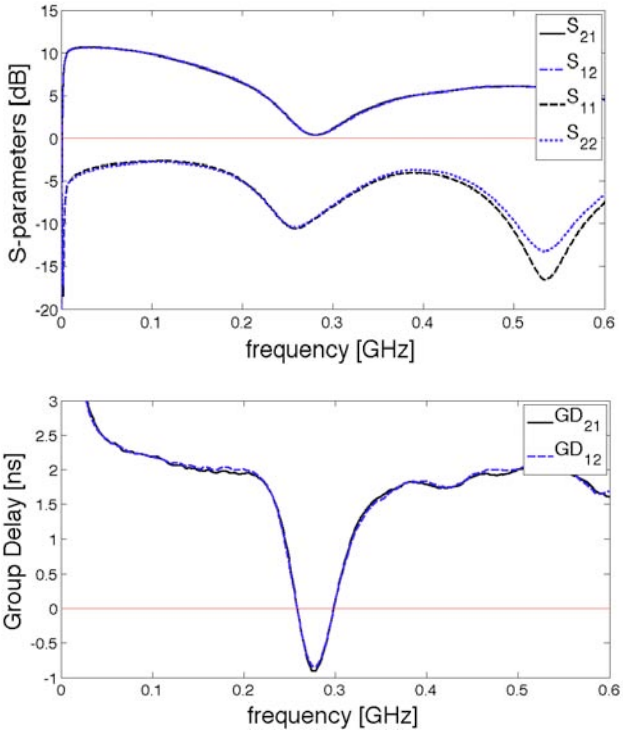

Figure 4a) Measured S-parameters of the entire bidirectional NGD circuit and b) the measured group delay in both directions.

The measured *S*-parameters and group delay of the overall bilateral circuit from Fig. 2 are shown in Fig. 4a and Fig. 4b, respectively. For matched terminations at both ports, the circuit is stable at all frequencies (both $|S_{11}|$ and $|S_{22}|$ are below 0 dB). The transmission coefficients in both directions at the resonance frequency are fully compensated ($|S_{21}|$ and $|S_{12}|$ are both 0.38 dB). The circuit exhibits a maximum negative group delay of 0.85 ns at the resonance frequency, in both directions. This includes the delay of the amplifier, the splitter/combiners and the interconnecting transmission lines. The speed-of-light delay across the physical length of the circuit (14.5 cm) in air would be 483ps. The negative group delay produced by this circuit would enable compensating for a physical length of 0.4 m.

3. Bidirectional Pulse Propagation

The bidirectional and stable NGD operation of the circuit is demonstrated in the time-domain by propagation of the same Gaussian modulated pulse through the circuit in both directions. The time-domain reflectometry experiment shown in Fig. 5a is employed. The setup uses 50Ω delay lines, with delays TD_1 and TD_2, to separate the incident, reflected and two-way transmitted pulses for a device under test (DUT) inserted in the propagation path. A short-circuit load is placed at the end of the second delay line so that the same pulse transmitted in the forward direction through the DUT is reflected back and is transmitted through it in the reverse direction. Fig. 5b shows an example of the measured waveform when the bidirectional NGD circuit is the DUT. It clearly indicates the incident pulse, the reflected pulse from the DUT (due to non-zero S_{11}) and the two-way transmitted pulse. Three different devices were used for the DUT; a very short 15 ps delay line, a 443 ps delay line (approximately equal to the speed-of-light delay across the 14.5 cm physical length of the NGD circuit), and the bidirectional NGD circuit.

The measured two-way transmitted pulses for the three devices are shown in Fig. 6a. Fig. 6b shows the normalized envelopes of the three two-way transmitted pulses. Using a three parameter fit of the Gaussian envelopes, the measured two-way delay of the pulse peak (relative to the 15 ps delay line peak) was 965 ps for the 443 ps delay line. The measured delay was -1.200 ns and for the NGD circuit (one-way group delay of -600 ps). The amplitude of the NGD device waveform is slightly amplified, by a factor of 1.25 (1.12 for one-way transmission), with respect to the other two devices due to the slightly larger overall gain for a finite bandwidth signal ($|S_{21}(\omega)|$ is slightly larger than unity at frequencies other than the resonant frequency). The pulse shape for the NGD device is also slightly distorted, as expected, due to the non-linear frequency response near the resonant frequency. This demonstrates the ability to advance a finite bandwidth pulse in both directions.

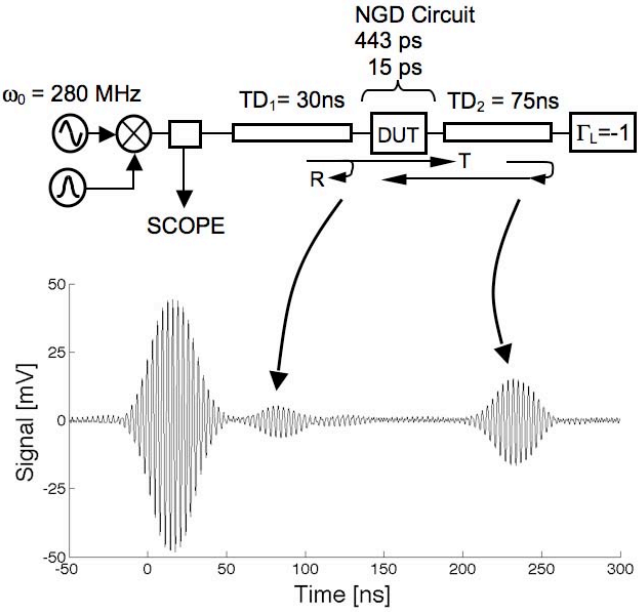

Figure 5a) Time-domain reflectometry measurement of a 14MHz bandwidth Gaussian pulse modulated at 280MHz as it propagates in both directions through the DUT and b) example waveform indicating incident, reflected and two-way transmitted pulses.

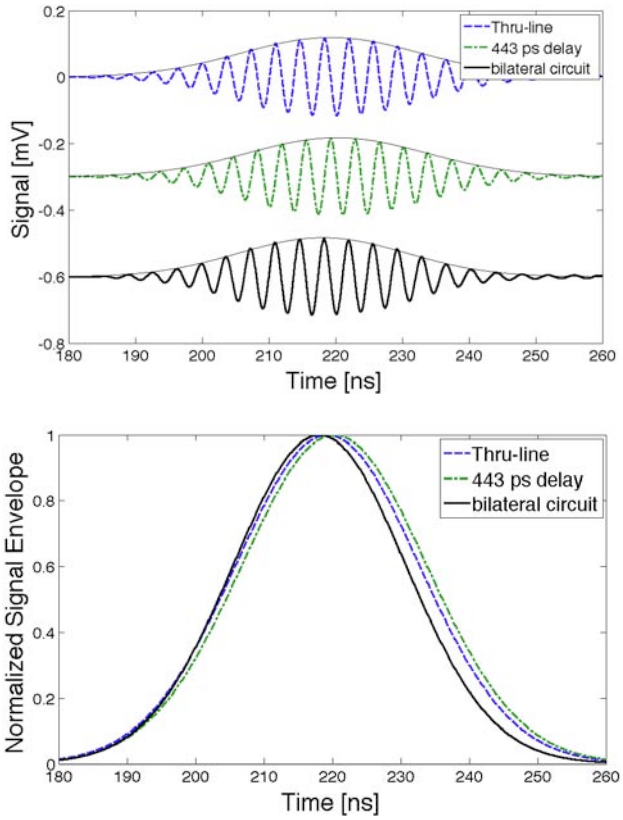

Figure 6a) Measured two-way transmitted modulated pulses through the 15 ps and 443 ps delay line devices and the bidirectional NGD device and b) the envelopes of the pulses, indicating peak delays of 965 ps and -1.201 ns relative to the 15 ps delay line.

4. Bidirectional Circuit Stability

Due to the large out-of-band gain, $|S_{21}(\omega \to 0)| \sim A_{tot} > 1$, and the greater-than-unity reverse transmission coefficient, $|S_{12}(\omega)| = |S_{21}(\omega)| > 1$, the bidirectional circuit is potentially unstable. For the demonstrated NDG circuit, the measured input and output reflection coefficients are less than 0 dB for all frequencies as shown in Fig. 4a, making the bilateral circuit stable for the case of matched terminations ($|\Gamma_{IN}| = |S_{11}(\omega)| = |\Gamma_{OUT}| = |S_{22}(\omega)| < 1$ for $|\Gamma_L|, |\Gamma_S| = 0$, where Γ_L is the load termination reflection coefficient and Γ_S is the source termination reflection coefficient). To analyze the stability of the bidirectional circuit, the input and output reflection coefficients for the general termination case are considered. For stable operation [18],

$$|\Gamma_{IN}| = \left| S_{11} + \frac{S_{21}^2 \Gamma_L}{1 - \Gamma_L S_{22}} \right| < 1, |\Gamma_{OUT}| = \left| S_{22} + \frac{S_{12}^2 \Gamma_S}{1 - \Gamma_S S_{11}} \right| < 1. \quad (13)$$

Using (13), and the S-parameters of the bidirectional circuit, the range of impedances for which the circuit will be stable can be identified. Using expressions for identifying the regions of instability [18] a conditional stability analysis was performed to identify the range of impedances for which the circuit remains stable. The analysis was performed using the NGD design equations (3-4),(7-12), with a resonant frequency of f_0=310 MHz, a Q = 2.62 and an out-of-band gain A_{tot} = 2.84 (9.1 dB). Since the power splitter/combiners have a finite isolation and an insertion loss, these will affect the result. Fig. 7a shows the simulated S-parameters of the NGD circuit for I=-34 dB and L=-3 dB. Fig. 7b indicates the maximum magnitude of the complex termination reflection coefficient, $|\Gamma|_{max}$, for which the circuit is stable ($|\Gamma_L|_{max} = |\Gamma_S|_{max}$ due to the symmetry of S). This is a lower limit since the circuit could be stable for larger magnitudes but only for certain angles. The circuit is conditionally stable for all frequencies. At frequencies near f_0, the circuit is stable for almost all values of $|\Gamma|$. For all possible L, I values, the bidirectional circuit will be conditionally stable since $|S_{12}(\omega)| = |S_{21}(\omega)| > 1$.

5. Conclusions

A bidirectional, conditionally stable gain-compensated circuit exhibiting NGD was presented. The design operates at 280 MHz, but it can be extended to higher frequency through proper choice of amplifiers and power splitters. The bidirectional NGD device has application in minimization of transmitting/receiving beam-squint in linear phased arrays, bidirectional baluns, or bidirectional 90° feed for circular polarization of antennas. By matching the NGD with the medium delay, the bidirectional lossless behavior would enable construction of a finite size medium exhibiting the properties of a spatial void for finite bandwidth signals.

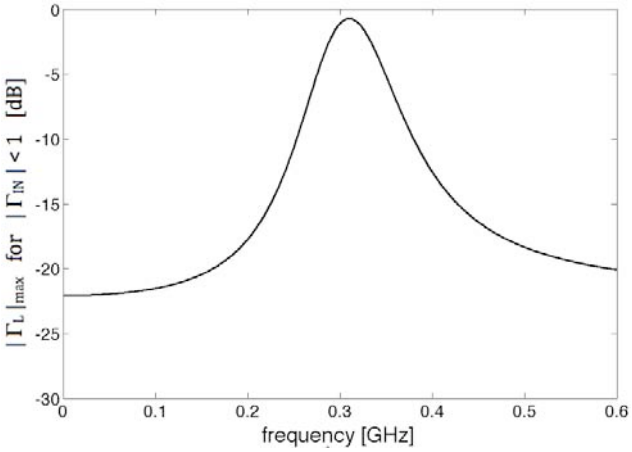

Figure 7a) Simulated S-parameters for a bidirectional NGD circuit and the resonator within branch (A-B) with f_0=310 MHz, Q = 2.62, A_{tot} = 2.84 and I=-34 dB, C=-34 dB and b) maximum allowed termination reflection coefficient magnitude, $|\Gamma_L|_{max}$, for stability.

Acknowledgements

This work was supported by the Natural Sciences and Engineering Research Council of Canada. Use of the facilities of the Advanced RF Systems Lab of the National Microelectronics and Photonics Testing Collaboratory are appreciated.

References

[1] A. Dogariu, A. Kuzmich and L.J. Wang, Transparent anomalous dispersion and superluminal light-pulse propagation at negative group velocity, *Physical Rev. A*, 63-053806, 2001.

[2] O.F. Siddiqui, M. Mojahedi and G.V. Eleftheriades, Periodically loaded transmission line with effective negative refractive index and negative group velocity, *IEEE Trans. Antennas Propag.* 51: 2619–2625, 2003.

[3] B. Ravelo, A. Perannec, M. LeRoy and Y.G. Boucher, Active microwave circuit with negative group delay,

IEEE Microwave Wireless Comp. Lett. 17: 861-863, 2007.

[4] S. Gharavi and M. Mojahedi, Theory and application of gain-assisted periodically loaded transmission lines with negative or superluminal group delays, *Proc. IEEE Intl. Conf. Antennas Propag.*, Aloha, Hawaii, pp. 2373-2376, June 2007.

[5] T. Nakanishi, K. Sugiyama and M. Kitano, Demonstration of negative group delays in a simple electronic circuit, American J. Physics, 70: pp. 1117-1121, Nov. 2002.

[6] B. Ravelo, A. Perennec and M. Le Roy, Negative group delay active topologies respectively dedicated to microwave frequencies and baseband signals, *J. EuMA*, 4: pp. 124-130, Jun. 2008.

[7] M. Kandic and G.E. Bridges, Asymptotic limits of negative group delay in active resonator-based distributed devices, *IEEE Trans. Circuits and Systems-I*, 58: 1727-1735, 2011.

[8] B. Ravelo, A. Perennec, M. Le Roy and Y. Boucher, Synthesis of broadband balun negative group delay active circuits, *Proc. IEEE Intl. Conf. Antennas Propag.*, Aloha, Hawaii, June 2007.

[9] B. Ravelo, A. Perennec and M. Le Roy, Broadband balun using active negative group delay circuit, *Proc.* 2007 *European Microwave Conference*, pp. 466–469, Oct. 2007.

[10] S. Hrabar, I. Krois and A. Kiricenko, Towards active dispersionless ENZ metamaterial for cloaking applications, *Metamaterials* 4: 89-97, 2010.

[11] M. Kandic and G.E. Bridges, Bilateral gain-compensated negative group delay circuit, *IEEE Microwave Wireless Comp. Lett.* 21: 308-310, 2011.

[12] H. Noto, K. Yamauchi, M. Nakayama and Y. Isota, Negative group delay circuit for feed-forward amplifier, *Proc., 2007. IEEE/MTT-S Intl. Microwave Symp.*, pp. 1103–1106, June 2007.

[13] S. Keser and M. Mojahedi, Broadband negative group delay microstrip phase shifter design, *Proc. IEEE Intl. Conf. Antennas Propag.*, Charleston, South Carolina, June 2009.

[14] B. Ravelo, M. Le Roy and A. Perennec, Application of negative group delay active circuits to the design of broadband and constant phase shifters, *Microwave And Optical Technology Letters*: 50: pp. 3078-3080, Dec. 2008.

[15] S.S. Oh and L. Shafai, Compensated circuit with characteristics of lossless double negative materials and its application to array antennas," *IET Microwaves, Antennas Propag.*, 1: pp. 29-38, Jan. 2007.

[16] O.F. Siddiqui, S.J. Erickson, G.V. Eleftheriades and M. Mojahedi, Time-domain measurement of negative group delay in negative-refractive-index transmission-line metamaterials, *IEEE Trans. Microwave Theory Tech.* 52: 1449-1454, 2004.

[17] S.J. Erickson, M. Khaja and M. Mojahedi, Time-and frequency-domain measurements for an active negative group delay circuit, *Proc. IEEE Intl. Conf. Antennas Propag.*, pp. 790-793, July 2005.

[18] D.M. Pozar, *Microwave Engineering*. John Wiley & Sons, New York, 2nd edition, chapter 11, pp. 612-618, 1998.

Pseudo volume-plasmon into arrays of doped and un-doped semiconductors

Thierry Taliercio*, Vilianne N'Tsame Guilengui, and Eric Tournié

Institut d'Electronique du Sud, CNRS-INSIS-UMR 5214, Université Montpellier 2,
34095 MONTPELLIER cedex 05 (France)
*corresponding author, E-mail: thierry.taliercio@univ-montp2.fr

Abstract

We present a theoretical work which shows that for a metamaterial consisting of a periodic array of doped and undoped semiconductors it is possible to define a frequency ω_t corresponding to a pseudo volume-plasmon. ω_t depends on the thicknesses and on the dielectric constants of the components of the metamaterial and on the plasma frequency of the doped semiconductor. As its homologue in noble metal, the pseudo volume-plasmon is the collective oscillation of charges present in the metallic part of the metamaterial leading to a pure longitudinal electric wave. We show that ω_t is the degeneracy frequency between the anti-symmetric mode in transverse magnetic field (TM) and the mode in transverse electric field (TE). We demonstrate that this degeneracy is due to the periodicity of the structure which transforms the imaginary solution of a metal-dieletric interface into a real solution in the case of the periodic metamaterial.

1. Introduction

Recent developments of plasmonics have opened new prospects to control light-matter interactions [1,2]. Surface plasmon polaritons (SPP) result from the coupling between an electromagnetic wave and the collective oscillation of the electrons supported by the metal/dielectric interface. They exhibit unique physical properties due to enhanced nanolocalized optical fields. In the past decade, several breakthroughs have been made to improve the control of the wave propagation via wave-guides [3], plasmonic crystals [4,5] or the so-called extraordinary optical transmission (EOT) [6]. More recently, new applications have been proposed which are based on the exaltation of the electromagnetic field near metallic surfaces. They allow to enhance natural optical properties of materials [7] or to generate nonlinear effects by breaking symmetries [8,9] and induce a control of the optical processes at the femto-second scale [10,11].

The existence of the SPP, and their unique optical properties, is possible because of the presence of the volume plasmon with its characteristic frequency, ω_p. Volume plasmon is a quantum of the oscillating plasma and a pure longitudinal electric wave propagating into the metal. This particular wave can be excited uniquely by electrons, because of its longitudinal nature, by coupling between the electric charge of the electron and the fluctuations of the electrostatic field of the plasma wave. It is necessary to use energy electron loss spectroscopy (EELS) to characterise volume plasmon. An indirect signature can be obtained in optical reflectance spectra because the dielectric function equals 0 for $\omega = \omega_p$. But generally this method is limited to doped semiconductors [12] because ω_p is in the deep UV range and is masked by the interband absorption for noble metal. Controlling the plasma frequency is fundamental for engineering the optical properties of new photonic devices. It is possible to adjust the volume plasmon frequency in the microwave range notably by using thin-wire structures [13-15]. However, realising three-dimensional (3D) structure for IR applications is difficult because of technological limitations. It is however possible to investigate simpler one or two dimensional structures to control the plasma frequency ω_p.

In the case of one dimensional structures such as grids of parallel metallic wires, theoretical works have been done to explain in detail their optical properties [16,17]. They consider structures with a period d larger than l, the aperture of the grating, and much larger than the plasma wavelength λ_p. In other words, $\lambda_p << l < d$. They have shown that their main optical property, the EOT, is due to the coupling of the incident plane wave with cavity resonances located inside the slits, leading to localized SPP, or to the excitation of coupled surface electromagnetic modes on both surfaces of the grid, resulting in coupled SPP (see ref. 18 for more detail).

Theoretical studies dealing with comparable λ_p, l, and d, have been performed on infinite or truncated super-lattices of metal/dielectric or semiconductor/semiconductor [19-22]. They showed in the case of truncated super-lattices that bulk and surface plasmon should exist because of periodicity. The term bulk and surface plasmon are used to describe the coupling through the structure of surface plasmon pinned at each interface and surface plasmon pinned at the truncated surface, respectively. These works however did not investigate the impact of the carrier density

modification given by the fraction of space occupied by the metal.

Recently, this theoretical approach has been simplified and an analytic model has been proposed to treat periodic arrays of doped and un-doped semiconductors in the long wavelength limit to exploit the polaritonic behaviour of the SPP [23]. The main difference between Ref. 23 and previous works on periodic slit arrays is that Ref. 23 considers the case where d << λ_p. This implies fundamental differences: it is no more possible to consider the metal as a perfect conductor and the zero order transmission or reflection is at higher frequency than the plasma frequency. So the optical properties of doped and un-doped semiconductor arrays are essentially governed by SPP located inside the un-doped semiconductor part. One of the main results of this analytic model was to demonstrate the existence of a huge photonic band gap which opens the possibility to realise optical filtering in the IR and THz ranges. Similar structures based on metal and dielectric waveguides have been first studied in 1969 [24]. Three branches appeared in the dispersion relation, two of them corresponding to the symmetric modes and one to the anti-symmetric mode. Several other works have completed the theoretical study of SPP wave-guides [25-26]. However the quasi-bi-dimensional shape of wave-guides makes them difficult to manipulate in free space optic. Periodic arrays in contrast allow avoiding this problem and give access to new optical properties like negative refractive index [27-31] or high index of refraction [32].

In this work, we propose a theoretical work on pseudo volume-plasmons which can be observed in periodic arrays of doped and un-doped semiconductor. We first describe the theoretical framework and highlight the analogy between a SPP and an ionic crystal (Sec. II). We then generalise this approach to periodic structures before defining the concept of pseudo volume-plasmon and studying its properties (Sec. III). Finally, we propose a scheme of the pseudo volume-plasmon (Sec. IV) and discuss the physical meaning of the pseudo volume-plasmon frequency in light of the ionic-crystal analogy (Sec. V).

2. Surface Plasmon Polaritons modelled as an ionic-crystal

2.1. SPP at the metal/dielectric interface

We consider the interface between two semi-infinite materials as depicted in Fig. 1. For simplicity, we normalize all frequencies to the plasma frequency ω_p, the wave numbers to $k_p = \omega_p / c$, the lengths (including spatial variables) to k_p^{-1}, and time to ω_p^{-1}.

The index of the structure is defined as:

$$n^2(z,\omega) = \begin{cases} \varepsilon_b \ for \ z > 0 \\ \varepsilon' = \varepsilon_a \left[1 - \frac{1}{\omega(\omega + i\gamma)}\right] for \ z < 0 \end{cases} \quad (1)$$

where a Drude dielectric function is used to model the behaviour of the doped semiconductor.

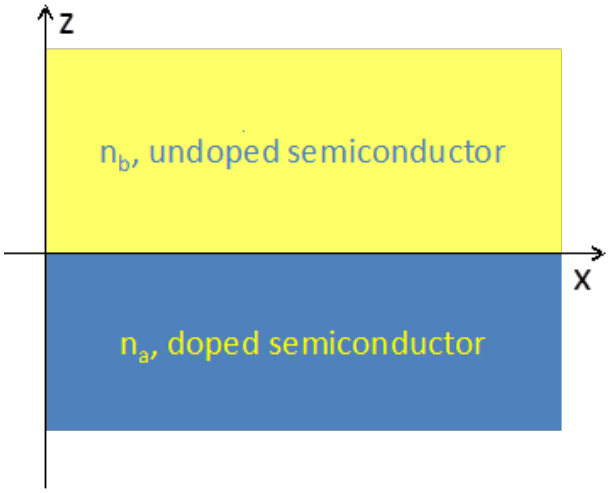

Figure 1: Scheme of the structure corresponding to an interface (x axis) between two materials which are assumed to be semi-infinite in the z direction and infinite in the y direction. The indexes of the doped and un-doped semiconductors are respectively $n_a = \sqrt{\varepsilon'}$ and $n_b = \sqrt{\varepsilon_b}$. The SPP propagates along the x direction.

We consider that the TM field exciting the surface wave that propagates along the interface takes the form:

$$\vec{E}(x,z,t) = \begin{pmatrix} E(z) \\ 0 \\ F(z) \end{pmatrix} e^{i(\omega t - qx)} \quad (2)$$

We study the dependence with the z variable. Computing $\nabla \times \nabla \times \vec{E}(x,z,t)$ in the Maxwell equation $\nabla \times \nabla \times \vec{E} + (n^2/c^2)\partial_t^2 E = 0$, and eliminating $\partial_z F(z)$, we obtain the usual Helmotz equation for E(z), and an explicit expression for F(z):

$$\frac{\partial^2 E}{\partial z^2} + [n^2(z,\omega)\omega^2 - q^2]E = 0 \quad (3)$$

$$[n^2(z,\omega)\omega^2 - q^2]F = -iq\frac{\partial E}{\partial z} \quad (4)$$

Considering the boundary conditions at the interface, that is the continuities of the field components $E_{//}$, $B_\perp$, the discontinuities of the field components $E_\perp$, $B_{//}$ and the Gauss theorem for z < 0, $(\nabla\left(\varepsilon'\overrightarrow{E_a}(x,z,t)\right) = 0)$ and for z > 0, $(\nabla(\varepsilon_b\overrightarrow{E_b}(x,z,t)) = 0)$ allow collecting 6 equations. Manipulating these equations allows obtaining the well-known equation:

$$\frac{\varepsilon_b}{k_b} - \frac{\varepsilon'}{k_a} = 0 \quad (5)$$

where k_a and k_b are respectively the wavenumbers for z < 0 and z > 0 and are given by:

$$k_a^2 = \varepsilon_a(\omega^2 - 1) - q^2 \quad (6)$$

$$k_b^2 = \varepsilon_b\omega^2 - q^2 \quad (7)$$

For more detail the reader should refer to [1]. Injecting Eq. (6) and (7) in (5) gives:

$$q^2 = \frac{\varepsilon_a \varepsilon_b}{\varepsilon_a + \varepsilon_b} \frac{\omega^2 - 1}{\omega^2 - \omega_s^2} \omega^2 \quad (8)$$

where $\omega_s^2 = \frac{\varepsilon_a}{\varepsilon_b + \varepsilon_a}$ (9)

Eq. (8) and (9) are respectively the dispersion relation ω(q) and the expression of the SPP frequency at the metal/dielectric interface.

2.2. Analogy between SPP and ionic crystal

Let us compare the dispersion relation ω(q) in Eq. (8) to the one found in ionic crystals. Ashcroft & Mermin [33] define it in chapter 27 formulae (27.57) and (27.67):

$$\varepsilon(\omega) = \varepsilon_\infty + \frac{\varepsilon_\infty - \varepsilon_0}{(\omega^2/\omega_T^2) - 1} \quad (10)$$

$$\omega_L^2 = \frac{\varepsilon_0}{\varepsilon_\infty} \omega_T^2 \quad (11)$$

where ε_0 and ε_∞ are the dielectric constants at low and high frequencies and the subscripts L and T are meant for *Longitudinal* and *Transverse*. Eq. (11) is the so-called *Lyddane-Sachs-Teller relation*. Combining these two relations gives

$$\varepsilon(\omega) = \varepsilon_\infty \frac{\omega^2 - \omega_L^2}{\omega^2 - \omega_T^2} \quad (12)$$

Taking into account $\omega^2 = c^2 q^2 / \varepsilon(\omega)$, we obtain:

$$q^2 = \epsilon_0 \mu_0 \omega^2 \varepsilon_\infty \frac{\omega^2 - \omega_L^2}{\omega^2 - \omega_T^2} \quad (13)$$

where ϵ_0 and μ_0 are the permittivity and permeability of the vacuum.

Now Eq. (13) is exactly the expression of the dispersion relation given above in Eq. (8) provided that:

$$\varepsilon_\infty = \frac{\varepsilon_a \varepsilon_b}{\varepsilon_a + \varepsilon_b} \quad (14)$$

$$\omega_L = \omega_p \quad (15)$$

$$\omega_T = \omega_s \quad (16)$$

The dielectric constant at high frequencies of the composite material considered in the ionic-crystal model is an average between these of the metal and of the dielectric. If both dielectric constants are equal we obtain the well-known value of the SPP frequency in the case of an interface between a noble metal and the air, $\omega_p/\sqrt{2}$. The longitudinal frequency, associated to the zero of the dielectric function (Eq. (13)), corresponds to the plasma frequency which is of course a pure longitudinal electric wave. The transverse frequency, associated to a pole of the dielectric function (Eq. (13)), corresponds to the SPP frequency. In fact, this is the frequency of the oscillator (or the two level system) necessary to develop the crystal-ionic model. Thus, we can view the SPP as an oscillator pined at the interface between the metal and the dielectric. Finally, considering the *Layddane-Sachs-Teller* relation, we can define the dielectric constant at low frequencies

$$\varepsilon_0 = \varepsilon_b \quad (17)$$

As expected for an ionic crystal, ε_∞ is smaller than ε_0. In addition, ε_0 is simply due to the contribution of the dielectric material. This stems from the fact that the electromagnetic wave does not penetrate the metallic part which can be considered as a perfect conductor at low frequency.

2.3. The SPP dispersion relation ω(q)

Let us consider the dispersion relation eq. (8) which is valid for both real and imaginary solutions of the wave-vector **q**. As an example we show in Figure 2 the solutions obtained when both ε_a and ε_b dielectric constants are taken equal to 11.7 (which is the value of InAs). The real and imaginary solutions are the black and the red-dashed lines, respectively. The SPP frequency is noted ω_s. In the low frequency range (lower than ω_s) one can recognize the dispersion relation law of the SPP which corresponds to the bound mode at the interface. High frequencies (higher than 1) correspond to the radiative regime into the metal. At these frequencies, the metal is transparent. When the normalized frequency lies between ω_s and 1, we obtain a photonic band gap, a range of frequencies where the wavenumber is purely imaginary. No mode is sustained at the interface. The inset in figure 2 shows the x and z components of the electric field through the interface. Note that the electric field of the unique SPP mode is pined at the interface (E_x component). This is the only possible mode at the interface. We will see in the following that this mode can be compared to the symmetric mode of wave-guide [24] or of periodic structures [23,29] whereas the imaginary solution should be compare to the anti-symmetric one. Indeed, for these cases several modes can be sustained. We develop this point in the next section..

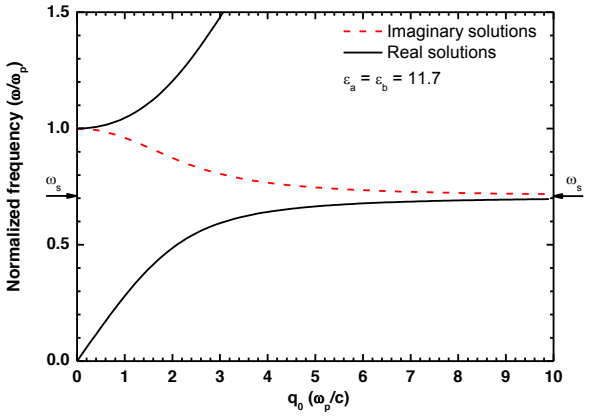

Figure 2: Dispersion relation of SPP at the interface between a doped semiconductor and an un-doped semiconductor. The dielectric constants are equal to 11.7. The dark lines and the red dashed line correspond respectively to the real and the imaginary solutions of eq. (8). The SPP frequency is noted ω_s. Inset shows the z and x components of the electric field along the z axe of the SPP.

3. The periodic array of doped and un-doped semiconductors

We now extend the point of view of the ionic-crystal model to periodic arrays. Let us recall the main results of ref. 23 obtained in the long wavelength limit approximation. Indeed, the main difference between this approach and previous ones [16-18] is the fact that λ_p is larger than the grating period (a + b). This implies, first, the selection of vertical SPP into the un-doped semiconductor and, second, the possibility to obtain SPP modes near the plasma frequency.

Consider the metamaterial composed of a periodic array of doped and un-doped semiconductors (Fig. 3-a and c). When light is under normal incidence, this metamaterial may be considered as ionic-crystal in TM field and as a metal in TE field (Fig. 3-b and d). To reach these results it is necessary to consider the dielectric function and the thickness of the doped (ε' and a) and un-doped (ε_b and b) semiconductors as follows:

$$n^2(z,\omega) = \begin{cases} \varepsilon_b \ \ for\ z \in [-b, 0] \\ \varepsilon' = \varepsilon_a \left[1 - \frac{1}{\omega(\omega+i\gamma)}\right] \ \ for\ z \in [0, a] \end{cases} \quad (18)$$

The doped semiconductor follows a Drude model whereas in the case of the un-doped one we consider its dielectric constant. Afterwards, it is necessary to solve the Maxwell equations in each region and consider the boundary conditions in both interfaces. Several mathematical manipulations are necessary to obtain the dispersion relation in both cases

$$q^2 = \varepsilon_{eff}\omega^2 \quad (19)$$

where q is the wavenumber and ε_{eff} the effective dielectric function. Note that the term effective dielectric function, ε_{eff}, is very restrictive because it is valid for normal incidence or close to the normal incidence. ε_{eff} is well defined essentially along the x direction and is strongly polarisation depend.

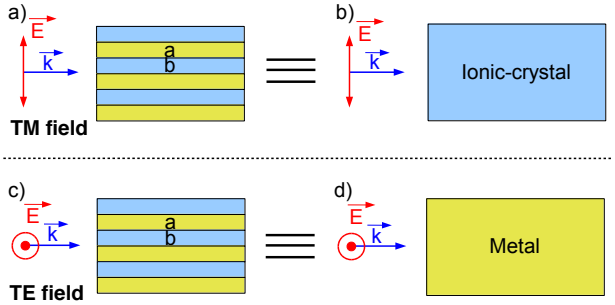

Figure 3: Scheme of the simplification obtained by the model of ref. 23. The periodic arrays of doped and un-doped semiconductors can be view as ionic-crystal under TM filed radiation, a) and b), or as a metal under TE field radiation, c) and d). Materials a and b stand for metal and dielectric, respectively.

Indeed in TM field, ε_{eff} follows the ionic-crystal model with characteristic dielectric constant ε_{TM} and frequency ω_r. ε_{TM} and ω_r correspond respectively to the average dielectric constant and to the frequency associated to the oscillators pined at the interface:

$$\varepsilon_{eff} = \varepsilon_{TM}\frac{\omega(\omega+i\gamma)-1}{\omega(\omega+i\gamma)-\omega_r^2} \quad (20)$$

$$\text{where } \varepsilon_{TM} = \frac{(a+b)\varepsilon_a\varepsilon_b}{a\varepsilon_b+b\varepsilon_a} \quad (21)$$

$$\text{and } \omega_r^2 = \frac{b\varepsilon_a}{a\varepsilon_b+b\varepsilon_a} \quad (22)$$

The associated modes are symmetric. It is important to note that an anti-symmetric mode exists with the following dispersion relation law:

$$\omega(q) = \omega_t \quad (23)$$

with

$$\omega_t^2 = \frac{a\varepsilon_a}{a\varepsilon_a+b\varepsilon_b} \quad (24)$$

The frequency of this anti-symmetric mode is thus independent on q and this mode is not coupled to normal incident light.

At this stage, it is possible to compare the previous expressions with those obtained for the ionic crystal model. As in the case of the SPP at one interface ε_{TM}, ω_p, ω_r are respectively the high frequency dielectric constant, the plasma and oscillator frequencies. It is also possible to define by the way of eq. (11) the static dielectric constant

$$\varepsilon_0 = \frac{a+b}{b}\varepsilon_b \quad (25)$$

As expected, ε_∞ is smaller than ε_0 but contrarily to the SPP at an interface ε_0 depends on the proportion of the dielectric material in the metamaterial. This is coherent with the fact that ε_0 is due to the contribution of the dielectric material.

In TE field, ε_{eff} follows a Drude model with characteristic dielectric constant ε_{TE} and frequency ω_t. ε_{TE} and ω_t correspond respectively to the average dielectric constant and to the frequency associated to the collective oscillation of the free carrier, that is the plasma frequency or the pseudo volume-plasmon for this metamaterial. Note that ω_t naturally appears in the analytic model.

$$\varepsilon_{eff} = \varepsilon_{TE}\left(1 - \frac{\omega_t^2}{\omega(\omega+i\gamma)}\right) \quad (26)$$

$$\text{with} \quad \varepsilon_{TE} = \frac{(a\varepsilon_a+b\varepsilon_b)}{a+b} \quad (27)$$

Of course, these results are valid when a and b are smaller than $k_p^{-1}/2$ (see ref. 34 for more details). Indeed for larger thickness, guided modes appear invalidating our main approximation: the long wavelength limit. ω_t can be also view as the cut off frequency of the waveguide.

4. The pseudo volume-plasmon

The main approximation of the analytic model is to consider that we can linearize the tangent function present in the solutions obtained by resolving the Maxwell equations in

TM field, respectively for the symmetric (28) and anti-symmetric (29) modes:

$$\varepsilon_b k_a \tan(a\,k_a/2) + \varepsilon_a k_b \left(1 - \frac{1}{\omega(\omega+i\gamma)}\right)\tan(b\,k_b/2) = 0 \quad (28)$$

$$\varepsilon_a k_b \left(1 - \frac{1}{\omega(\omega+i\gamma)}\right)\tan(a\,k_a/2) + \varepsilon_b k_a \tan(b\,k_b/2) = 0 \quad (29)$$

Figure 4 shows the dispersion relation of the optical modes propagating into the metamaterial using the analytic model (open circles) or numerical model (lines or dashed-line eq. 28 and 29). The black and red lines or symbols correspond respectively to the symmetric and the anti-symmetric modes in TM field. The dashed blue line corresponds to the fundamental mode in TE field. As we can see, the analytic model and the numerical one are in very good agreement for $\mathbf{q} < 3.5\ k_p^{-1}$. This upper limit of **q** depends directly on the dielectric constant of the constitutive materials of the metamaterial.

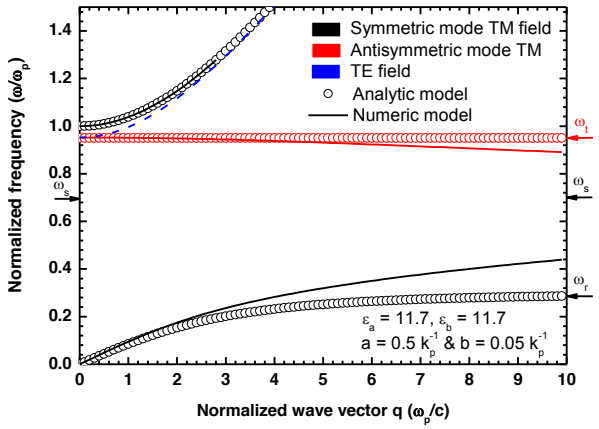

Figure 4: Dispersion relation of SPP into an array of doped and un-doped semiconductors. The dielectric constants are equal to 11.7 and the ratio a/b = 10. The open circle curves correspond to the analytic model. Lines and dashed lines correspond to the numeric model. The dark, red and blue colours correspond respectively to symmetric, anti-symmetric modes in TM filed and the fundamental mode in TE field. The SPP frequency for a single interface is noted ω_s, and ω_t and ω_r are respectively frequencies of the pseudo volume-plasmon and SPP of the analytic model.

We can see that ω_t corresponds exactly to the cut-off frequency for an incident electromagnetic wave in TE field polarisation. But in contrast to a waveguide with perfect electric conductor the cut-off frequency does not depend only on the dielectric constant and on the size of the waveguide but also on the dielectric constant and on the size of the doped semiconductor (the metal here). This new dependence is mainly due to the fact that the electromagnetic wave penetrates in the metallic part. Indeed the proximity of the plasma frequency implies a weak permittivity.

By analogy with the case of a metal, ω_t can be interpreted as the plasma or volume plasmon frequency for the metamaterial under investigation. Thus we define this frequency as the pseudo volume-plasmon frequency where we use pseudo to differentiate from the rigorous definition of the volume plasmon. This approach allows understanding how modifying the size of both materials modifies ω_t. Decreasing the metal thickness decreases the number of charges and thus ω_t, and vice-versa. At a frequency lower than ω_t, the electromagnetic waves in TE field cannot propagate because the dielectric function is negative. The metal is a perfect mirror. At higher frequency than ω_t, the metal becomes transparent. The electromagnetic waves propagate.

Figure 5 shows a scheme of the pseudo volume-plasmon into the metamaterial. The electric field lines are represented by the black arrows and the charge density is represented by the plus or minus charges for ions and electrons, respectively. This is a longitudinal electric wave with a wavelength λ_t.

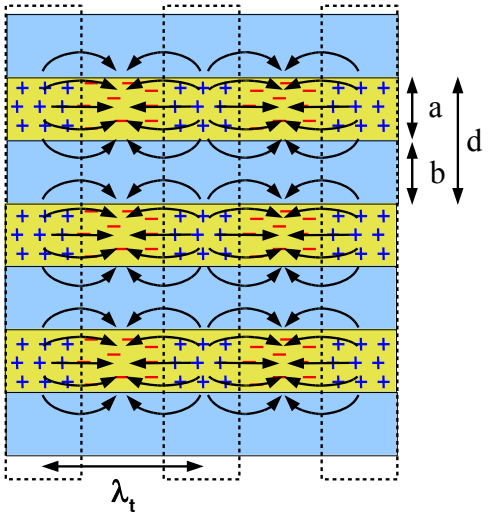

Figure 5: Scheme of the collective oscillation of charges (positive in blue, negative in red) into the metamaterial associated to the pseudo volume-plasmon frequency ω_t and wavelength λ_t. This is a longitudinal wave which is purely electric. The electric field is represented by the black arrows. a, b and d are respectively the thickness of the doped, un-doped semiconductor and the period.

5. Properties of the pseudo volume-plasmon

We will analyse here the behaviour of the pseudo volume-plasmon, particularly near ω_t for **q** =0.

Figure 4 shows that at **q** = 0 there is no degeneracy of the high frequency branches in TE and TM fields ($\omega > \omega_t$). This is not the expected behaviour of a metal. Indeed, if the metamaterial were equivalent to a metal for both polarisations then the lowest frequency of the high frequency mode of the TM field should be resonant with ω_t, the pseudo volume-plasmon frequency.

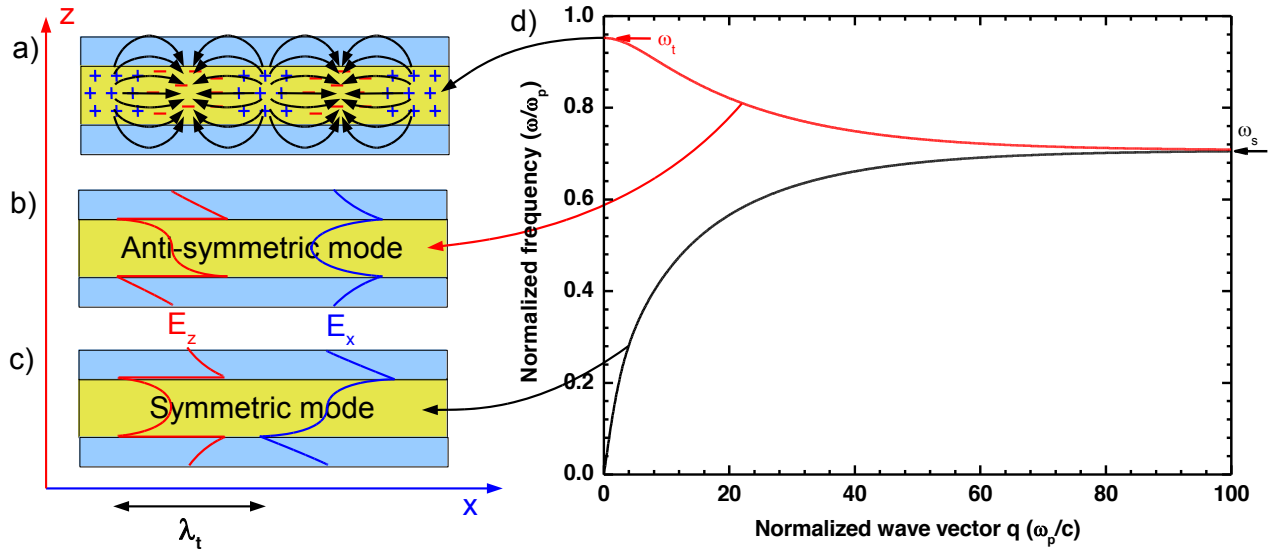

Figure 6: a), b) and c) are respectively schemes of the pseudo volume-plasmon, the anti-symmetric and symmetric modes. The z (red) and x (blue) components of the electric field are depicted. d) Dispersion relations of SPP for the structure shown in fig. 4 obtained with eq. (28)-(29). The dark and red curves correspond respectively to symmetric and anti-symmetric modes in TM filed. The SPP frequency is noted ω_s, and ω_t is the frequency of the pseudo volume-plasmon.

In contrast to this intuition, the lower frequency of the TM branch is ω_p whereas the cut off frequency of the TE branch is ω_t. In fact, in TE polarisation the electromagnetic wave is sensitive to the total carrier concentration into the metamaterial. Thus the cut-off frequency follows the behaviour of ω_t which depends mainly of the geometry of the metamaterial. In revenge, in TM polarisation the low frequency limit of the second symmetric mode depends exclusively on what happens at the metal/dielectric interface. The associated frequency thus depends exclusively on the plasma frequency ω_p of the metallic part of the metamaterial.

In contrast, fig. 4 reveals unambiguously that the anti-symmetric mode in TM field and the TE mode are degenerated at $\mathbf{q} = 0$. This degeneracy does not depend on the structure except when a and b > 0.5 k_p^{-1} which correspond to the limit of validity of the analytic model [34]. This puzzling behaviour can be explained as follows. Let us first remind the results of the Fig. 2 where we modelled the SPP by an ionic crystal approach. We obtained two solutions for the TM polarisation, one corresponding to the propagative wave with a real wave-vector **q** and the second corresponding to the non-propagative wave with a purely imaginary wave-vector **q**. This second solution mode frequency decreases continuously with **q** from the plasma frequency ω_p to the surface plasmon frequency ω_s. There is a photonic band gap in this frequencies range. In TE polarisation, there is no propagation for $\omega < \omega_p$ whereas propagative waves following the dispersion relation law is possible for $\omega_p < \omega$. It is important to notice that the upper value of the imaginary branch in TM field is equal to the lower value of the real branch in TE field, that is ω_p, for $\mathbf{q} = \mathbf{0}$. Now, there exists an analogy between the ionic crystal and the doped/undoped semiconductor periodic array. In the case of the periodic structures (Fig. 6-d), the plasma frequency ω_p is replaced by the pseudo volume-plasmon, ω_t, depicted in the Fig. 6-a. In TE field the propagative waves are allowed for $\omega < \omega_t$. In TM field we obtain two propagative modes for $\omega < \omega_t$, one symmetric and the other one anti-symmetric. But in contrast to the two dimensional case with SPP, the imaginary branch is real which means that both modes propagate. If we compare the dispersion relations of the metal/dielectric interface (Fig. 2) and of the metamaterial at high **q** (Fig. 6-b) we obtain the same behaviour. The upper and lower limit frequencies for the imaginary mode in TM field and the anti-symmetric mode in TM field are identical, ω_p or ω_t and ω_s, respectively. So the anti-symmetric mode of the metamaterial corresponds to the imaginary mode in TM field.

The question is whether this situation is physically sound. In fact, it is the periodicity of the structure that transforms the imaginary solution into a real one. Indeed, an anti-symmetric mode has no meaning at a metal/dielectric interface. Only a symmetric mode can exist (Fig. 6-c). In revenge, anti-symmetric mode is possible in periodic structures because of the possibility to pin the electric field at the interfaces and to extinguish the electric field into the dielectric or metallic part of the metamaterial (Fig. 6-b). When the frequency of this anti-symmetric mode reaches ω_t its longitudinal component become dominant leading to a mode which is not coupled to incident light. This is the definition of the pseudo volume-plasmon.

At this stage, it is interesting to evaluate how modifying the properties of the metamaterial (a, b, n_a and n_b) impacts ω_t the pseudo volume-plasmon. The general expression of the volume plasmon when positive charges are immersed in a material with a dielectric constant ε is:

$$\omega_p = \sqrt{\frac{ne^2}{m\varepsilon\varepsilon_0}} \qquad (30)$$

where n and m are respectively the charge density and the electron effective mass. To modify ω_p, one can play with n, m or ε. As an example, consider dividing the charge density by a factor 2. Eq. (30) shows that ω_p will be divided by $\sqrt{2}$. Now, consider a periodic structure with $\varepsilon_a = \varepsilon_b$, and a = b. Eq. (24) leads to $\omega_t = \frac{1}{\sqrt{2}}$ which means that ω_t is also divided by $\sqrt{2}$. This is a confirmation of the same behaviour for both equations.

These results show that one can easily control ω_t just by modifying the geometrical properties of the metamaterial or by changing the individual materials constituting the periodic array, *i.e.* changing the dielectric constants. This is a very important asset of our system. In the case of metals, it is very difficult to play directly with these parameters to reach wavelength in the IR range. One of the main solution is to consider a metamaterial composed of metallic nano-particles (NP) embedded in host material [35]. Indeed, if the electromagnetic wave averages the metamaterial, changing the size and the density of NP allows playing with the electron density. But it is very difficult to control exactly what occurs in terms of charge density, dielectric constant and homogeneity of the material. In the case of doped semiconductors in contrast, one can select the right semiconductors and adjust at will their doping level to obtain the target m and ε. Eq. (24) shows that in the general case when a, b, ε_a and ε_b can be adjusted, achieving a target volume plasmon frequency is trivial whereas it is not so simple with metals (Eq. (30)). Our simplified model can be used to easily design and fabricate a metamaterial with the expected optical properties. Of course, doped semiconductors cannot be used in the visible range. However, they can be the best choice for IR applications.

6. Summary and conclusion

After having presented the analogy between surface plasmon polaritons and the ionic-cristal model in the case of a single interface and a periodic array of metal/dielectric system, we have shown that an analytic model allows defining a pseudo volume-plasmon frequency, ω_t, associated to the periodic array. By adjusting the physical properties of the structure (a, b, n_a, n_b) it is thus possible to define the characteristic frequencies ω_r, ω_t and ω_s, and to control their optical properties. We have also explained the behaviour of ω_t as a function of the physical parameters. We have also explained why ω_t corresponds to the cut off frequency in TE Field and to the high frequency limit of the anti-symmetric mode in TM field.

References

[1] S. A. Maier, "Plasmonics: Fundamentals and Applications", Springer Science+Buisness Media LLC (2007).

[2] A. V. Zayats, I. I. Smolyaninov, A. A. Maradudin, "Nano-optics of surface plasmon polaritons" Physics Reports **408**, 131–314 (2005)

[3] Dmitri K. Gramotnev and Sergey I. Bozhevolnyi, "Plasmonics beyond the diffraction limit" Nature Photonics **4**, 83 - 91 (2010).

[4] S. C. Kitson, W. L. Barnes, and J. R. Sambles, "Full Photonic Band Gap for Surface Modes in the Visible" Phys. Rev. Lett. **77**, 2670–2673 (1996).

[5] Sergey I. Bozhevolnyi, John Erland, Kristjan Leosson, Peter M. W. Skovgaard, and Jørn M. Hvam, "Waveguiding in Surface Plasmon Polariton Band Gap Structures" Phys. Rev. Lett. **86**, 3008–3011 (2001).

[6] T. W. Ebbesen, H. J. Lezec, H. F. Ghaemi, T. Thio, and P.A. Wolff, "Extraordinary optical transmission through sub-wavelength hole arrays" Nature **391**, 667, (1998).

[7] Vasily V. Temnov, Gaspar Armelles, Ulrike Woggon, Dmitry Guzatov, Alfonso Cebollada, Antonio Garcia-Martin, Jose-Miguel Garcia-Martin, Tim Thomay, Alfred Leitenstorfer & Rudolf Bratschitsch, "Active magneto-plasmonics in hybrid metal–ferromagnet structures" Nature Photonics **4**, 107 - 111 (2010).

[8] Ye Pu, Rachel Grange, Chia-Lung Hsieh, and Demetri Psaltis, "Nonlinear Optical Properties of Core-Shell Nanocavities for Enhanced Second-Harmonic Generation" Phys. Rev. Lett. **104**, 207402 (2010).

[9] Seungchul Kim, Jonghan Jin, Young-Jin Kim, In-Yong Park, Yunseok Kim and Seung-Woo Kim "High-harmonic generation by resonant plasmon field enhancement" Nature 453, 757-760 (2008).

[10] Rohan D. Kekatpure, Edward S. Barnard, Wenshan Cai, and Mark L. Brongersma, "Phase-Coupled Plasmon-Induced Transparency" Phys. Rev. Lett. **104**, 243902 (2010)

[11] Tobias Utikal, Mark I. Stockman, Albert P. Heberle, Markus Lippitz, and Harald Giessen, "All-Optical Control of the Ultrafast Dynamics of a Hybrid Plasmonic System" Phys. Rev. Lett. **104**, 113903 (2010).

[12] Y.B. Li, R. A. Stradling, T. Knight, J. R. Birch, R. H. Thomas, C. C. Philips and I. T. Ferguson, "Infrared reflection and transmission of undoped and Si-doped InAs grown on GaAs by molecular beam epitaxy" Semicond. Sci. Technol. **8**, 101-111 (1993).

[13] J. B. Pendry, A. J. Holden and W. J. Stewart and I. Youngs, "Extremely Low Frequency Plasmons in Metallic Mesostructures" Physical Review Letters 76, 4773 (1996).

[14] P. A. Belov, C. R. Simovski, and S. A. Tretyakov, "Two-dimensional electromagnetic crystals formed by reactively loaded wires", Physcial Review E **66**, 036610 (2002).

[15] Left-Handed-Media Simulation and Transmission of EM Waves in Subwavelength
Split-Ring-Resonator-Loaded MetallicWaveguides
Physical Review Letters 89, 183901 (2002)
R. Marques, J. Martel, F. Mesa, and F. Medina

[16] U. Shröter and D. Heitmann, "Surface-plasmon-enhanced transmission through metallic gratings" Phys. Rev.

B **58**, 15419 (1998)
[17] J.A. Porto, F. J. Garcia-Vidal, and J. B. Pendry, "transmission Resonnances on Metallic Gratings with Very Narrow Slits" Phys Rev. Lett. **83**, 2845 (1999).
[18] F. J. Garcia-Vidal, L. Martin-Moreno, T. W. Ebbesen, and L. Kuipers, "Light passing through subwavelength apertures" Rev. Mod. Phys. **82**, 729 (2010).
[19] R. E. Camley and D. L. Mills, "Collective excitations of semi-infinite superlattice structures : Surface plasmons, bulk plasmons, and the electron-energy-loss spectrum" Physical Review B **29**, 1695 (1984).
[20] R. Szenics, R.F. Wallis, G.F. Giuliani, and J.J. Quinn, "Theory of surface plasmon polaritons in truncated superlattices" Surface Sciences **166**, 45 (1986).
[21] R.F. Wallis, R. Szenics, J.J. Quinn, and G.F. Giuliani, "Theory of surface magnetoplasmon polaritons in truncated superlattices" Physical Review B **36**, 1218 (1987).
[22] R.F. Wallis and J.J. Quinn, "Surface magnetoplsamon polaritons in truncated semiconductor superlattices" Physical Review B **38**, (1988).
[23] J. Léon and T. Taliercio, "Large tunable photonic band gaps in nanostructured doped semiconductors" Phys. Rev. B **83**, 195301 (2010).
[24] E. N. Economou, "Surface Plasmons in Thin Films" Phys. Rev. **182**, 539–554 (1969).
[25] J. J. Burke, G. I. Stegeman, and T. Tamir, "Surface-polariton-like waves guided by thin, lossy metal films" Phys. Rev. B **33**, 5186 (1986).
[26] B. Prade, J. Y. Vinet, and A. Mysyowicz, "Guided optical waves in planar heterostructures with negative dielectric constant" Phys. Rev. B **44**, 13556 (1991).
[27] A. J. Hoffman, L. Alekseyev, S. S. Howard, K. J. Franz, D. Wasserman, V. A. Podolskiy, E. E. Narimanov, D. L. Sivco, and C. Gmachl, "Negative refraction in semiconductor metamaterials" Nature Materials **6**, 946 (2007).
[28] A. J. Hoffman, A. Sridhar, P. X. Braun, L. Alekseyev, S. S. Howard, K. J. Franz, L. cheng, F. S. Choa, D. L. Sivco, V. A. Podolskiy, E. E. Narimanov, and C. Gmachl, "Midinfrared semiconductor optical matamaterials" J. Appl. Phys. **105**, 122411 (2009).
[29] E. Verhagen, R. de Waele, L. Kuipers, and A. Polman, "Three-dimensional negative index of refraction at optical frequencies by coupling plasmonic waveguides" Phys. Rev. Lett. **105**, 223901 (2010).
[30] H. J. Lezec, J. A. Dionne, and H. A. Atwater, "Negative refractive at visible frequencies" Science **316**, 430 (2007).
[31] J. A. Dionne, E. Verhagen, A. Polman, and H. A. Atwater, "Are negative index materials achievable with surface plasmon waveguides? A case study of three plasmonic geometries" Optics express **16**, 19001 (2008).
[32] J. T. Shen, Peter B. Catrysse, and Shanhui Fan "Mechanism for Designing Metallic Metamaterials with a High Index of Refraction" Physical Review Letters **94**, 197401 (2005).
[33] N. W. Ashcroft and N. D. Mermin, "Solid state physics", Saunders College Publishing, Orlando, FL, first edition (1976).
[34] T. Taliercio, V. N'Tsame Guilengui, J. Léon and E. Tournié "Analytical model to describe the optical properties of arrays of doped and un-doped semiconductors" in preparation.
[35] Cheng-ping Huang, Xiao-gang Yin, Qian-jin Wang, Huang Huang, and Yong-yuan Zhu, "Long-Wavelength Optical Properties of a Plasmonic Crystal" Phys. Rev. Lett. **104**, 016402 (2010).

Coupled resonant modes in twisted acoustic metamaterials

Ying Cheng, Xiaojun Liu*

Key Laboratory of Modern Acoustics, Nanjing University, Nanjing 210093, China
*corresponding author, E-mail: liuxiaojun@nju.edu.cn

Abstract

Acoustic metamaterials constructed by resonant microelements in subwavelength scale were generally characterized by the effective medium approximation theory, which neglects the interaction between adjacent elements. In this paper, we show that twisting the orientation of resonators in acoustic metamaterials produces secondary coupled resonant modes by introducing internal vibration interaction. Metamaterials composed of single-slit Helmholtz resonator arranged in two-dimensional square lattice are investigated. We rotate a portion of the resonator so that the adjacent resonators in ΓX direction have a twist angle of φ. For the system with φ = 180°, the coupling interaction produces the symmetric coupled mode in in-phase oscillation and the anti-symmetric coupled mode in out-of-phase oscillation. This acoustic analog of "hybridization effect" leads to a sharp transparency window in the extended locally-resonant forbidden gap, which is analogous to the phenomenon of electromagnetically induced transparency. Such coupled resonant modes may have potential applications in sound wave manipulations such as acoustic filtering and imaging.

1. Introduction

Recently, acoustic metamaterials have received high interest due to their unprecedented physical behavior beyond those found in nature [1, 2]. In particular, the effective bulk modulus and mass density can be simultaneously or independently negative within a certain frequency region, which is unattainable using traditional composites. These intriguing properties allows ability to control sound in novel ways, ranging from acoustic cloaking [3-5] and subwavelength imaging [6-10] to sound energy superabsorption [11]. Most of the acoustic metamaterials reported to date are based on localized resonance induced by the subwavelength microelements. Negative effective bulk modulus and mass density can derive from appropriate monopolar and dipolar resonance, respectively [12]. One famous example is the engineered acoustic metamaterial consisting of Helmholtz resonator (HR), which is a tiny structure featuring a miniature gap analogous to the metal split-ring resonator in electromagnetic metamaterials [13]. Unique properties such as low-frequency locally-resonant band gap and anomalous transmission behavior have been demonstrated theoretically and experimentally [10, 14-17], and further numerical retrieval analysis of transmission-reflection coefficients also confirms the negative bulk modulus in one-dimensional HR chain and two-dimensional HR array [18-20]. Subsequent researches observe negative refraction, surface modes and superlensing effect via homogenization near resonance in a finite array of HRs [9, 10, 15].

The acoustic metamaterials derive their overall properties from individual sub-wavelength resonators. Changing the size and geometry of the HR determines the acoustic properties of the metamaterial and its operation frequency. The general case of describing an acoustic metamaterial uses the effective media approximation (EMA) theory [1, 14]. In EMA model, since the resonator element is much smaller in size than the working wavelength, the response of the acoustic metamaterial is treated as the averaged effects of the individual element's resonance response. Thus the metamaterial can be characterized by the effective parameters of mass density and bulk modulus.

However, the EMA theory ignores the coupling interactions between the resonator elements, which always exist when the elements are structured into metamaterials. Previous studies demonstrate that parallel HRs with identical resonant frequency could couple with each other, and the intensive interaction between adjacent HRs significantly extends the width of the locally-resonant forbidden gap, which is different from the case in solid elastic metamaterials [21]. The aim of our work is to demonstrate the coupled resonant modes in twisted acoustic metamaterials. In this paper, significant modulation to the band structure is investigated using the analyses of the dispersion curves and the transmission spectra. We identify these coupled resonances through the pressure fields of the supercell's eigenmodes. The adjunct resonator elements oscillate in-phase for the symmetric coupled mode and out-of-phase for the anti-symmetric coupled mode. These coupled resonant modes further lead to some "hybridization effect", which split the dispersion curves and causes the occurrence of sharp transparency window in the extended forbidden gap. This kind of coupled resonant mode may be used to develop novel functional acoustic devices in the future, including acoustic imaging with deep subwavelength resolution and acoustic transparency.

2. Description of the model

Figures 1(a) and 1(b) illustrates the schematic configuration of the regular acoustic metamaterial and the proposed twisted metamaterial. The cut-off view of the samples in *x*-*y* plane and the schematics of the corresponding supercells are plotted in the upper and lower panels, respectively. The structure we investigated is comprised of identical HRs periodically arranged in square lattice. The HRs are cylindrical metal shells with single slit. The outer and inner radii of the shells are a and b, respectively. The lattice constant is d and the height of the slit is h. The system is translationally invariant in the z-direction. The host medium is fluid such as water with bulk modulus κ_0 and mass density ρ_0, and the HRs are assumed as rigid-walled due to the mismatched acoustic impedance between metal and fluid. A supercell contains two HRs aligned along the x axis and the right HR is rotated with twist angle of φ [φ = 0° for regular metamaterial in Fig. 1(a) and φ = 180° for twisted metamaterial in Fig.1 (b)].

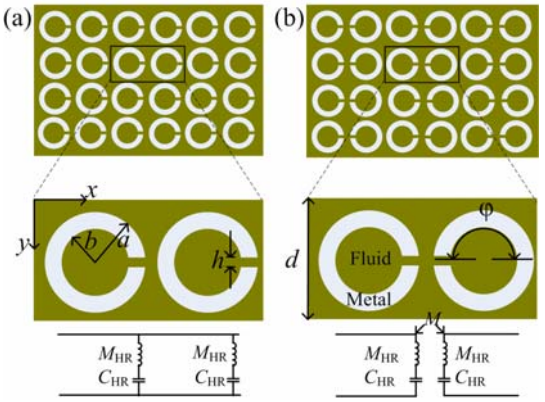

Figure 1: Scheme diagram and the corresponding equivalent acoustic circuit of (a) the regular acoustic metamaterials with φ = 0° and (b) the twisted acoustic metamaterials with φ = 180°.

Let us now consider the behavior of the individual HR. Since the incident wavelength is considerably long compared with the HR's transverse dimensions in *x*-*y* plane, we can employ the well-known theory of equivalent acoustic circuits to model the acoustic metamaterials. For simplicity, we use the 2D model. Figure 1(a) shows a circuit section composed of standard *L*-*C* oscillating circles, and the repeated circuit sections will further construct an acoustic transmission line in *x*-direction. The short slit of the split ring acts as an inductor with acoustic mass $M_{HR}=\rho_0*(a-b)/h$, and the inner cavity acts as a capacity with acoustic capacitance $C_{HR}=\pi b^2/\rho_0 c_0^2$. In all our studies, the host medium is chosen as water with κ_0 = 2.19 GPa and ρ_0 = 998 kg/m^3, and the geometry size of the resonator is set as a=0.48 m, b=0.34 m, h=0.05 m and d=1 m unless otherwise specified. To include the influence of periodicity on the acoustic radiation of the slit, we employ an equivalent extra mass radiation mass and revise the effective acoustic mass as $M_{eff}=\rho_0(a-b+2.85h)/h$. Hence the resonant frequency f_R $[=(1/M_{eff}C_{HR})^{0.5}/(2\pi)]$ of the HR is obtained to be 164 Hz, and the corresponding normalized frequency $f_R d/c_0$ is 0.11. The HR chain in *x*-direction could be modeled as a 1D transmission line with periodic loaded *L*-*C* shunt branches. We further give a qualitative description on the coupling effect from the view point of acoustic circuit. Due to the twisted configuration, the near-field coupling interaction between close-spaced slits is significant enhanced and its influence could be characterized as an mutual acoustic mass M. M takes negative value when the two HRs oscillate in-phase since the mass loading at the outlet of the slit is decreased, and vice versa. Thus a coupled acoustic propagation mode may be established in this case and could be used to open a transparency window in forbidden gap, as illustrated below.

3. Results and discussion

3.1. Band structures

To describe the coupling properties for acoustic wave propagating within the twisted structure, we first calculate the band structure of the metamaterials. The band structure of the composite metamaterial can be calculated by solving the acoustic eigenvalue problem of the supercell. The periodic boundary conditions are applied to the supercell along the *x*-direction and *y*-direction based on Bloch's theorem. The finite element technique transforms the wave equation into a generalized acoustic eigenvalue problem expressed by $[K(k_x)-\omega^2 M]P=0$, where $K(k_x)$ and M are the stiffness and mass matrices. An alternative searching arithmetic is employed to determine the eigenfrequency ω. The spatial discretization is fine enough for the convergence in our numerical experiments.

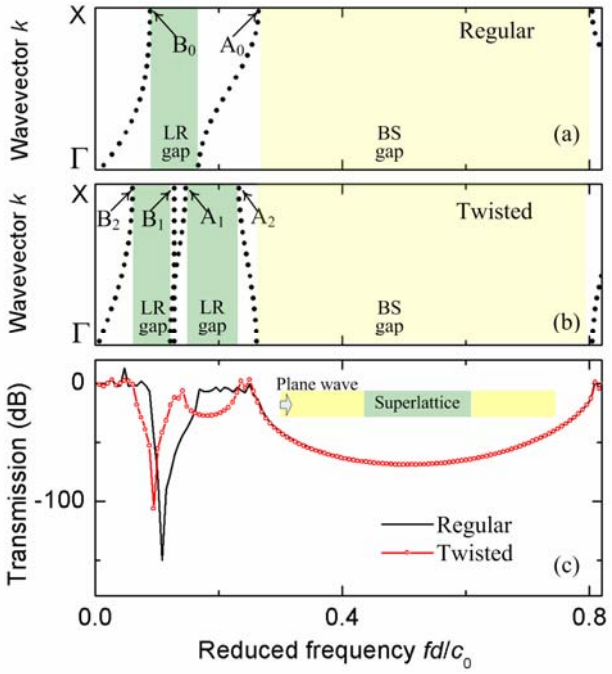

Figure 2: Band structures for (a) regular and (b) twisted acoustic metamaterials. The corresponding normalized transmission spectra are shown in panel (c).

The band structures for regular and twisted metamaterials are shown in Figs. 2(a) and 2(b), respectively. As a first observation, we can see one Bragg-scattering (BR) gap from 0.256 to 0.808 and one locally-resonant (LR) gap from 0.089 ~ 0.167 for regular acoustic metamaterials with $\varphi = 0°$. The phenomenon is consistent with previous studies for regular HR chain and array [14, 15, 21]. In contrast, although the position and width of the BR gap for twisted metamaterial are exactly the same as that for regular metamaterial, the number of transmission bands below BR gap is doubled. Generally, two native bands separated by the only LR gap exist in the frequency range below the BR gap for regular metamaterial [Fig. 2(a)], which originate from the eigen-vibration of the individual HRs. However, four transmission bands intersected by two LR gaps exist in the frequency region below the BR gap for the twisted case [Fig. 2(b)]. The origin of the four transmission bands could be ascribed to the symmetric and asymmetric combination of original eigen-vibration modes by the intensive coupling interaction, which will be discussed in the following section. The calculations assume that the dissipation is weak and the vibration amplitude is limited, hence the viscosity loss is not included in this case. We also take the large loss factor into consideration and find that the band structures change a little.

In order to confirm the analysis of band structures, the transmission spectra through finite supercells are calculated using the full-wave finite element simulations. The computational domain is shown in the inset of Fig. 2(c). Bloch conditions are applied in the y-direction since the structure is supposed to be infinite in this direction. A plane wave source with the amplitude of 1 Pa is added on the left surface of the domain. In order to improve the accuracy of the numerical model, the perfect match layers are added at the external boundaries to simulate the infinite region. Sound wave transmissions through the periodic superlattice are calculated, as shown in Fig. 2(c). We note that the LR transmission gap appears at 0.089 ~ 0.167 for the case of regular acoustic metamaterials, which is in agreement with the dispersion curves [as shown in Fig. 2(a)]. On the other hand, the LR gaps appear at 0.060 ~ 0.121 and 0.146 ~ 0.233 for the case of twisted acoustic metamaterials. Note that a narrow transparency window extends from 0.121 to 0.146 which located between the two LR gaps [see Fig. 2(b)]. This secondary transparency window should be attributed to the splitting of the dispersion curves. We also note that both BR gaps appear at 0.256 ~ 0.808 for the two cases. In general, the transmission spectra are in agreement with the dispersion curves. The consistency demonstrates the drastic effect of subwavelength coupling interaction on the propagation of acoustic waves.

We continue to study the transparency window inside the extended LR gap through the pressure field of wave propagation. The edge of third dispersion curve is utilized as load frequency since only one eigenmode is supported in this case. The pressure fields at the load frequencies of 200 Hz for the two cases are shown in Figs. 3(a) and 3(b), respectively. For comparison, the corresponding profile along the cross-section line of $y=d/2$ are plotted in each panel. Since the frequency of incident wave is inside the LR gap for the case of regular metamaterials, the incident wave could only penetrate the first few HRs and the interior field is nearly zero. In this case, the propagation of the wave is forbidden, and most of the incident energy is reflected backward. These results are consistent with the dispersion curves and transmission spectra. On contrary, the incident wave could effectively propagate through the superlattice for the case of twisted metamaterials. The variation trend of the absolute value of the pressure field is periodic, which can be determined by the periodicity of the supercell. In this case, the supercells exhibit unique oscillation modes in which the two HRs in each supercell vibrate in-phase with each other. Note that the pressure amplitude in the supercell region is significantly higher than that of the incident and transmitted wave. This phenomenon should be attributed to the intensive resonance in the HRs through coupling interaction. This finding should have substantial practical applications, for example in controlling and filtering the propagation wave via tuning the twisted structure.

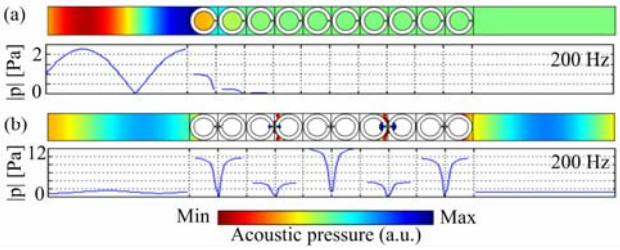

Figure 3: Pressure fields and the corresponding profile along the cross-section line of $y=d/2$ at the load frequency of 200 Hz for (a) regular and (b) twisted acoustic metamaterials. The red (blue) corresponds to the maximum (minimum) pressure. The plane wave with the amplitude of 1 Pa travels along the x-direction.

It is interesting to note that the acoustic transparency window induced by coupled resonance is different from that induced by coupling between the rod-resonator modes [22], although both structures employ twisted configuration. In the rod-resonators with a twist angle of 45° relative to each other, the surface resonant modes with identical resonant frequencies but different quality factors respectively act as radiative mode and dark mode, and the destructive interference of them results in electromagnetically-induced-transparency like effect. Importantly, the distance of the rod-resonators is much longer than the wavelength. In contrast, the HRs in our proposal can be deep subwavelength spaced, which is very compact for construction. The transparency is achieved through the cancellation of opposite contributions from the two HRs.

3.2. Eigenmodes distributions

In order to explore the physical mechanism causing such splitting of the dispersion curves illustrated in Fig. 2, we further investigate the recombination of acoustic vibration modes induced by the twisted structure. Sound waves in the metamaterials propagate through the particle vibrations in the constructive resonant microelements in subwavelength

scale, which can be decomposed into eigenmodes with the characteristic oscillation pattern. In this section, we characterize the eigenmodes through the pressure field distribution of the supercell. By assigning both the wave-vector k_x and frequency ω, the specific eigenmodes are excited and the pressure data at each node are recorded to reconstruct the eigenmodes. The eigenmodes defined at the zone edge below the BS gap are discussed. We have also investigated the other modes with k values located at general positions of the dispersion curves, e.g. at zone center. The results show that the coupling interaction maintains the effect of mode recombination, which are not listed in the paper.

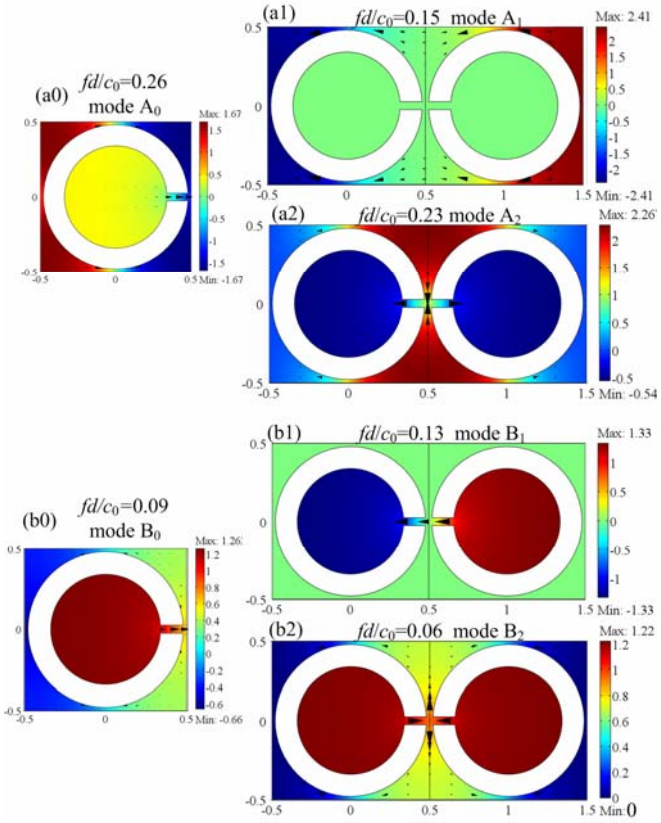

Figure 4: Pressure field distributions of the eigenmodes. Panels (a0) and (b0) correspond to modes A_0 and B_0 for the regular acoustic metamaterials, and panels (a1), (a2), (b1) and (b2) correspond to modes A_1, A_2, B_1 and B_2 for the twisted acoustic metamaterials. The direction (size) of the cones indicates the direction (magnitude) of velocity vector, and the red (blue) correspond to the maximum (minimum) pressure.

Based on the mode characterization method, we first depict the pressure fields of the eigenmodes A_0 [marked in Fig. 2(a)] for regular acoustic metamaterials with the twist angle of $\varphi = 0°$ in Fig. 4(a0). In this case, the dominant particle motion occurs in the short neck, and the upper/lower region outside the resonator. The pressure distribution exhibits symmetric variation with respect to the mid-plane of the short-neck (the plane of $y = d/2$). Note that the eigenmodes are defined at the zone edge with $k_x d/\pi = 1$ and $\lambda = 2d$, for which the adjacent unit cells move in antiphase.

Comparing mode A_0 with mode A_1 and A_2 for the twisted acoustic metamaterials with $\varphi = 180°$ [see Figs. 4(a1) and 4(a2)], an interesting observation is that the oscillation of the adjacent cells exhibit in both in-phase and out-of-phase patterns. For the case of mode A_1, the left and right HRs exhibit in-phase vibration along the x-direction [Fig. 4(a1)]. As a result, the entire supercell also shows antisymmetric pressure field distribution with respect to the mid-plane along x-direction (the plane of $x = d$). In contrary, the left and right HRs vibrate out of phase for the case of mode A_2, leading to the symmetric variation of the pressure field [Fig. 4(a2)]. Therefore, the twisted structure combines the vibration mode of standalone HR into a pair of asymmetric and symmetric modes, which is analogous to the bonding and anti-bonding magnetic plasmon modes in magnetic dimer [23]. Similar effect of eigenmode recombination is also found in other transmission band. For example, the mode B_0 [Fig. 3(b0)] constructs the symmetric mode B_1 [Fig. 4(b1)] and antisymmetric mode B_2 [Fig. 5(b2)]. We outline the physical mechanism which leads to the combination effect as follows. The hybridization of the acoustic response in the case of $\varphi = 180°$ is mainly due to vibration coupling between the HRs. Each HR in deep subwavelength scale can be viewed as a quasi-atom, and the supercell of the coupled metamaterial with $\varphi = 180°$ can be regarded as a quasi-molecule. The quasi-atom possesses strong polarity caused by its nonaxisymmetrical structure, and the local amplitude at the short neck may be extremely high. For regular metamaterial with $\varphi = 0°$, the polar axes of all of the HRs lie in the same direction, and the interactions between adjacent cells are so weak that the periodic cells vibrate in-phase independently [as shown in Fig. 3(a)]. On contrary, for twisted metamaterial with $\varphi = 180°$, the polar axes of the two HRs in the quasi-molecule lie in opposite direction, and the significantly enhanced interaction couples the left and right HRs without obvious modification to their standalone eigenmodes. The decoupled eigenmode A_0 can combine in symmetric and asymmetric manners, leading to the splitting of the dispersion relations (e.g. the two transmission bands for regular acoustic metamaterials with $\varphi = 0°$ below the BR gap split into four transmission bands for twisted metamaterials with $\varphi = 180°$ as illustrated in Fig. 2). In general, the splitting of the dispersion curves originates from the hybridization of the original decoupled modes with small frequency offset.

3.3. Evolution of coupling effect with the lattice constant

As illustrated above, the coupling interaction is crucial in the hybridization effect of the transmission bands. The strength of the coupling interaction depends strongly on the distance between the quasi-atoms and for the considered geometry can be tuned by changing the lattice constant d. Therefore, we investigate the band structure with the lattice constant ranging from $d = 0$ to 1.6 m. The evolution of bandgap extent is extracted from the band structures and illustrated as a function of the lattice constant d in Fig. 5, where panels (a) and (b) correspond to the regular acoustic metamaterials with $\varphi = 0°$ and twisted acoustic metamaterials with $\varphi = 180°$, respectively. It is found that the sensitivity of the

bandgaps to the lattice constant is different. Three remarks should be noted. (1) Both BS gaps for the two cases (bounded by curves with blue open squares and blue open circles) gradually shrink in the same trend and the midgap frequencies move downward. Its upper (lower) band-edge frequency decreases from 0.80 (0.26) to 0.37 (0.23) when the lattice constant d is increased from 1 m to 1.6 m. This phenomenon, which is analogous to the BS gap in phononic-crystals composed of solid cylinders periodically arranged in the background of fluid, should be attributed to the fact that the periodicity of the scatterer has to be of the same length-scale as half the wavelength of the sound waves. (2) The width of the LR gap for the case of regular metamaterial also gradually shrinks. However, its midgap frequency eventually approaches 0.12, which is almost unchanged and equals the resonant frequency of the individual HR. (3) For the case of twisted metamaterial, similar dependence on the lattice constant is also observed in both the first and the second LR gap. In addition, the transparency window between the two LR gaps also depends on the lattice constant. Its upper edge frequency (indicated by curve with red solid up-triangles and) first slightly increases from 0.15 at d = 1 m to 0.16 at d = 1.1 m and then decreases to 0.13 at d = 1.6 m. Meanwhile, its lower edge frequency (indicated by curve with black solid circles) maintains the value of 0.12 which is almost unchanged.

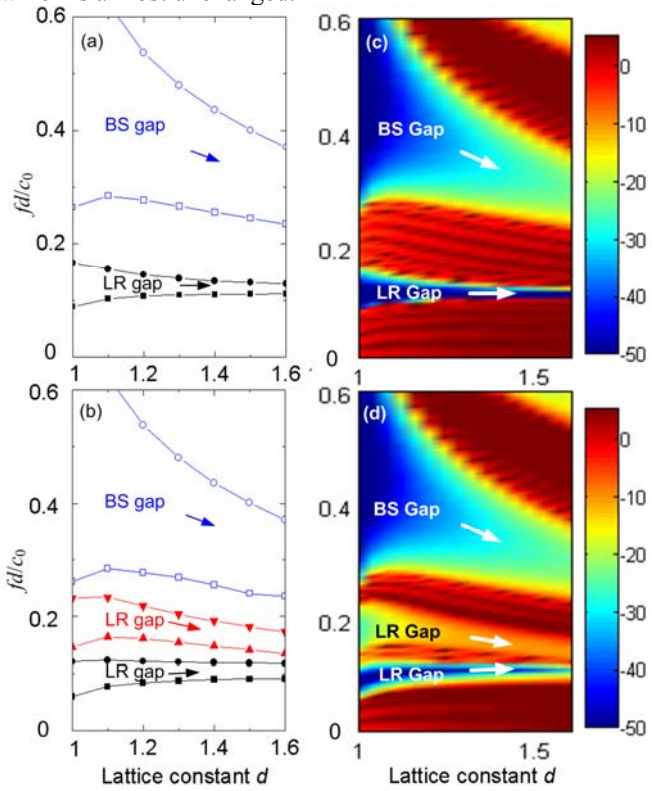

Figure 5: Complete phononic band gap extent as a function of the lattice constant for (a) regular and (b) the twisted acoustic metamaterials. The corresponding normalized transmission spectra are plotted in panels (c) and (d), respectively.

To confirm the bandgap extent in Figs. 5(a) and 5(b), the transmission spectra maps with the variation of the lattice constant are shown in Figs. 5(c) and (d). It is found that the location and width of transmission gaps agree with the band structures. In addition, the transparency window lies within the frequency region defined by the transmission bands of the infinite system. From above observations, we can conclude that the strength of the coupling interaction depends strongly on the lattice constant, which performs as a key factor in engineering the band gap and acoustic transparency window.

4. Conclusions

In conclusion, we have studied the coupled resonant modes in acoustic metamaterials composed of single-slit Helmholtz resonators with twist angle between adjacent cells. The coupling effects are demonstrated by the consistent band structures and transmission spectra, in which doubled dispersion curves and a sharp transparency window in the extended LR gap are observed. Due to the resonance interaction, eigen-vibration mode of individual HR recombined into a pair of symmetric coupled mode in in-phase oscillation and anti-symmetric coupled mode in out-of-phase oscillation. By adjusting the coupling strength which strongly depends on the separation distance determined by the lattice constant, transmission and modes of an acoustic metamaterial are highly tunable. Thus, the coupled resonant modes, introduced by twisting the orientation of resonators in acoustic metamaterial, may provide a new way of tailoring their acoustic properties.

Acknowledgements

This work was supported by the National Basic Research Program of China under Grant No. 2012CB921504, NSFC (11074124, 11104139 and 10904052), SRFDP 20110091120040, and Jiangsu Provincial Natural Science Foundation (BK2011542) and PAPD of Jiangsu higher education institutions.

References

[1] L. Fok, M. Ambati, X. Zhang, Acoustic metamaterials. *MRS Bull*. 33: 931-934, 2008.

[2] B. I. Popa, S. A. Cummer, Design and characterization of broadband acoustic composite metamaterials. *Phys. Rev. B* 80: 174303, 2009.

[3] S. Zhang, C. Xia, N. Fang, Broadband acoustic cloak for ultrasound waves. *Phys. Rev. Lett.* 106: 024301, 2011.

[4] N. Stenger, M. Wilhelm, M. Wegener, Experiments on Elastic Cloaking in Thin Plates. *Phys. Rev. Lett.* 108: 014301, 2012.

[5] Y. Cheng, F. Yang, J. Y. Xu, X. J. Liu, A multilayer structured acoustic cloak with homogeneous isotropic materials. *Appl. Phys. Lett.* 92: 151913, 2008.

[6] J. S. Li, L. Fok, X. B. Yin, G. Bartal, X. Zhang, Experimental demonstration of an acoustic magnifying hyperlens. *Nat. Mater.* 8: 931-934, 2009.

[7] C. M. Park, J. J. Park, S. H. Lee, Y. M. Seo, C. K. Kim, S. H. Lee, Amplification of Acoustic Evanescent Waves Using Metamaterial Slabs. *Phys. Rev. Lett.* 107: 194301, 2011.

[8] X. Y. Ao, C. T. Chan, Far-field image magnification for acoustic waves using anisotropic acoustic metamaterials. *Phys. Rev. E* 77: 025601, 2008.

[9] M. Farhat, S. Guenneau, S. Enoch, A. B. Movchan, Negative refraction, surface modes, and superlensing effect via homogenization near resonances for a finite array of split-ring resonators. *Phys. Rev. E* 80: 046309, 2009.

[10] S. Zhang, L. L. Yin, N. Fang, Focusing ultrasound with an acoustic metamaterial network. *Phys. Rev. Lett.* 102: 194301, 2009.

[11] R. Q. Li, X. F. Zhu, B. Liang, Y. Li, X. Y. Zou, J. C. Cheng, A broadband acoustic omnidirectional absorber comprising positive-index materials. *Appl. Phys. Lett.* 99: 193507, 2011.

[12] J. Li, C. T. Chan, Double-negative acoustic metamaterial. *Phys. Rev. E* 70: 055602, 2004.

[13] D. R. Smith, Willie J. Padilla, D. C. Vier, S. C. Nemat-Nasser, S. Schultz, Composite medium with simultaneously negative permeability and permittivity. *Phys. Rev. Lett.* 84: 4184-4187, 2000.

[14] N. Fang, D. J. Xi, J. Y. Xu, M. Ambati, W. Srituravanich, C. Sun, X. Zhang, Ultrasonic metamaterials with negative modulus. *Nat. Mater.* 5: 452-456, 2006.

[15] S. Guenneau, A. Movchan, G. Petursson, S. A. Ramakrishna, Acoustic metamaterials for sound focusing and confinement. *New J. Phys.* 9: 399, 2007.

[16] A. B. Movchan, S. Guenneau, Split-ring resonators and localized modes. *Phys. Rev. B* 70: 125116, 2004.

[17] Z. G. Wang, S. H. Lee, C. K. Kim, C. M. Park, K. Nahm, S. A. Nikitov, Effective medium theory of the one-dimensional resonance phononic crystal. *J. Phys.-Condens. Mat.* 20: 055209, 2008.

[18] V. Fokin, M. Ambati, C. Sun, X. Zhang, Method for retrieving effective properties of locally resonant acoustic metamaterials. Phys. Rev. B 76: 144302, 2007.

[19] S. H. Lee, C. M. Park, Y. M. Seo, Z. G. Wang, C. K. Kim, Composite acoustic medium with simultaneously negative density and modulus. *Phys. Rev. Lett.* 104: 054301, 2010.

[20] Y. Cheng, J. Y. Xu, X. J. Liu, One-dimensional structured ultrasonic metamaterials with simultaneously negative dynamic density and modulus. *Phys. Rev. B* 77: 045134, 2008.

[21] Y. Cheng, J. Y. Xu, X. J. Liu, Broad forbidden bands in parallel-coupled locally resonant ultrasonic metamaterials. *Appl. Phys. Lett.* 92: 051913, 2008.

[22] F. Liu, M. Ke, A. Zhang, W. Wen, J. Shi, Z. Liu, P. Sheng, Acoustic analog of electromagnetically induced transparency in periodic arrays of square rods. *Phys. Rev. E* 82: 026601, 2010.

[23] H. Liu, D. A. Genov, D. M. Wu, Y. M. Liu, Z. W. Liu, C. Sun, S. N. Zhu, X. Zhang, Magnetic plasmon hybridization and optical activity at optical frequencies in metallic nanostructures. *Phys. Rev. B* 76: 064304, 2007.

Laser-ultrasonic investigation on Lamb wave band gaps in two-dimensional phononic crystal plates

Jingshi Wang[1, 2], Ying Cheng[1*], Xiaodong Xu[1], Xiaojun Liu[1]

[1]Laboratory of Modern Acoustics, Nanjing University, Nanjing 210093, China
[2] School of Electronics and Information, Nantong University, Nantong 226019, China
*corresponding author, E-mail: chengying@nju.edu.cn

Abstract

Phononic crystals (PCs) commonly consisted of two materials with huge contrasted elastic properties and mass densities are generally studied in theory such as the finite element method for many difficulties in the experiments. In this paper, the laser-ultrasonic non-destructive testing is introduced to investigate the propagation of Lamb waves in two-dimensional PC plates. The existence of band gaps for low order Lamb wave modes is demonstrated experimentally. Crucial parameters such as the thickness of PC plate and the periodical arrangement of scatterers are discussed in detail for the influence of location of band gaps. The finite element analysis agrees well with the result of the laser-ultrasonic measurement.

1. Introduction

Phononic crystals (PCs) are periodic elastic structures which consist of two or more materials with much different elastic properties such as mass density and elastic constants. For frequencies within a complete band gap, the vibration and propagation of acoustic waves are forbidden, whatever the polarization and the wave vector. Absolute forbidden band gaps donate many potential applications, such as acoustic filters, elastic wave guides, vibration isolators, and chemical and biological sensors [1-7]. Sigalas *et al.* [8] theoretically proved the existence of frequency gaps in the periodic elastic solid materials by imbedding golden/lead spheres in the host medium of aluminum/silicon. From then on, many efforts have been devoted to studies of forbidden band gaps of bulk and surface acoustic waves propagating in phononic crystals with one-, two- and three-dimensional periodic arrays theoretically and experimentally [9-15].

Due to the coupling of longitudinal and transversal strain components at the plate boundaries with complex wave vectors, Lamb waves in PC plate are more interesting and complicated. Earlier studies mainly focus on the calculation of Lamb waves propagating in the one-dimension (1D) PC plate in theory. Chen *et al.* [15] has studied the propagation of the lower-order Lamb waves in 1D composite thin plates. Gao *et al.* [16] have studied the band gap structures of Lamb waves in 1D quasiperiodic composite thin plates and the thin PC plate with 1D PC layer coated on a substrate by using the finite element method. Hsu *et al.* [17] has investigated the band gap structures of Lamb waves in two-dimension composite thin plates according to the plane wave expansion method. However, little experimental observation and the research in a higher dimension are known.

2. Laser-ultrasonic detection of Lamb waves

2.1. Experiment system

The Laser-ultrasonic measurement is an effective means to determine the vibrations in solid materials due to its advantages of non-contact and non-destruction. For the Lamb wave measurements, a modified optical detection system with the laser-induced vibrations based on the study of Kavalerov *et al.* [18] is employed, as schematically shown in Fig. 1. The detection is performed with a 632.8 nm reflected probe beam by means of a balanced photo receiver (BPR) that measures the optical intensity difference between the two parts of the probe beam detached by the mirror set M3, which implies information of the propagation of acoustic waves in the sample plate.

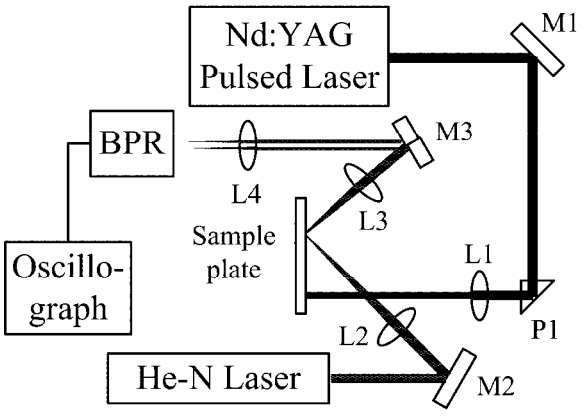

Figure 1: Schematic diagram of the Laser-ultrasonic detection system.

2.2. Principal of the detection

When the system is in the static balance with no vibration in the sample plate, the optical spot is divided by two mirrors of M3, seeing the solid line in Fig. 2. The amplitude distribution of the Gaussian probe beam can be written as

$$E(x,y)=\frac{E_0}{2\pi R^2}\exp(-\frac{x^2+y^2}{R^2}), \tag{1}$$

where E_0 is the amplitude of the probe beam at the central of the beam, R is radius of the optical spot on M3. Then the intensity of the divided two parts is

$$\begin{aligned} P_1&=\int_s^R\int_{-\sqrt{R^2-x^2}}^{\sqrt{R^2-x^2}}E^2(x,y)dxdy \\ P_2&=\int_{-s}^R\int_{-\sqrt{R^2-x^2}}^{\sqrt{R^2-x^2}}E^2(x,y)dxdy \end{aligned}, \tag{2}$$

where S is the deflection of the probe beam which is practically negligible in the static balance condition.

While Lamb waves pass the detection point, the reflected probe beam is disturbed and the deflection of the spot on M3 δs is shown in Fig. 2. Then the intensity variation of the two parts of the probe beam is obtained

$$\begin{aligned} \Delta P_1&=\frac{2E_0^2(1-\exp(-1/2))\delta s}{R} \\ \Delta P_2&=-\frac{2E_0^2(1-\exp(-1/2))\delta s}{R} \end{aligned}. \tag{3}$$

The two parts of the detection beam are absorbed at two photodiodes of BPR, and the output i which is the difference of the two can be described as

$$i=\Delta P_1-\Delta P_2=\eta_t\frac{4E_0^2(1-\exp(-1/2))\delta s}{R}, \tag{4}$$

where η_t is the transformation efficiency of two photodiodes.

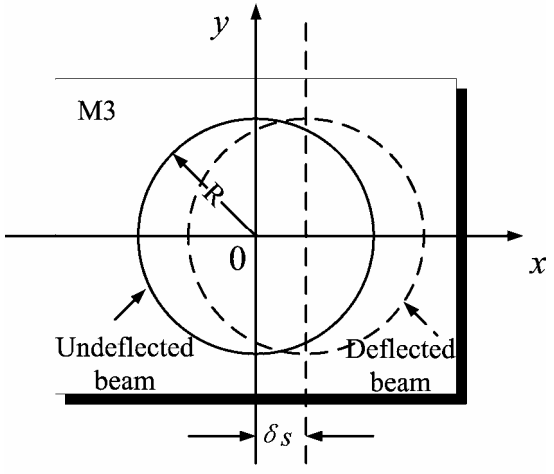

Figure 2: The deflection of the reflected probe beam in the cross section.

The displacement of Lamb waves induced by the pulse laser propagated in the sample plate is

$$u(x,t)=u_0\cos(\omega t-kx), \tag{5}$$

where u_0 is the amplitude of Lamb waves, ω is the angular frequency and k is the wave number. The deflection angle of the reflected probe beam caused by the propagation of acoustic waves in the sample plate at the detection point can be approximated as

$$\theta=\frac{\partial u}{\partial x}=ku_0\sin(\omega t-kx)\cdot \tag{6}$$

And the deflection shift of the optical spot on M3 is

$$\delta s=F_3\cdot\theta, \tag{7}$$

where F_3 is the focal length of the collimating lens L3.

Then combining Equation (4) and (7), the output signal of BPR can be express as

$$i=\frac{4\eta_t E_0^2F_3\theta}{R}(1-\exp(-1/2))\cdot \tag{8}$$

For wideband Lamb waves, Equation (8) can be written as

$$\begin{aligned} i&=\frac{4\eta_t E_0^2F_2}{R}(1-\exp(-1/2))\sum_{i=1}^{n}\theta_i \\ \theta&=k_iu_{0i}\sin(\omega_i t-k_ix) \end{aligned}. \tag{9}$$

3. Experimental results and numerical simulations

We investigate theoretically and experimentally the propagation of Lamb waves in two-dimension (2D) PC plates. The laser-ultrasonic measurement is introduced to detect surface particle displacements of composite thin plates caused by the propagation of Lamb waves. The transmission properties of Lamb waves in PC plate are calculated employing the finite element method.

Table 1: Thermal conductivity k_{xx}, thermal expansion coefficient α, heat capacity c, density ρ, bulk modulus K and Poisson's ratio σ of aluminum (A) and air (B).

Material	Aluminum (A)	Air (B)
k_{xx} [W/m×K]	240	0.026
α [10^{-6}/K]	23.2	3700
c [J/kg×K]	880	1005
ρ [kg/m^3]	2.7	1.29
K [10^5N/m^2]	6.8*10^5	1.01
σ	0.34	-

Two patterns of composite thin plates (foursquare and triangular distribution) are schematically shown in Fig. 3(a) and (b), respectively. The PCs are created by patterning air (B) filled holes in the aluminum (A) thin plates with the thickness of 0.3 mm. The radius of air holes is r= 1.5 mm, the lattice constant is a= 4 mm, and the filling rate of 2D

PCs systems is $\tau = \pi r^2 / a^2 = 0.442$. Table 1 shows the parameters of the samples used in the experiments and numerical simulations.

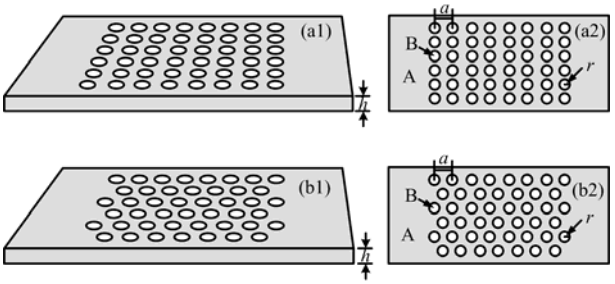

Figure 3: Schematic configuration of the 2D phononic-crystal plate: (a) foursquare distribution; (b) triangular distribution.

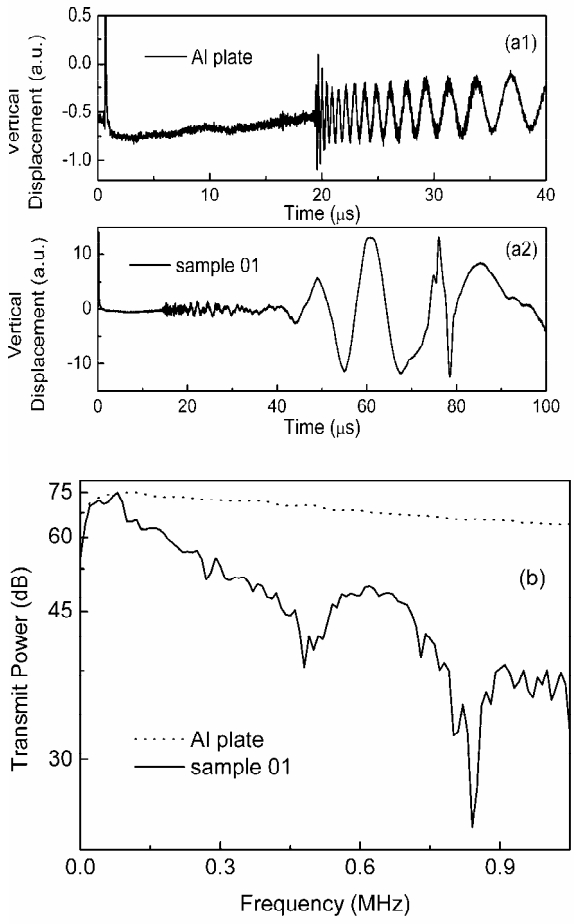

Figure 4: Transmitted waveforms of Lamb waves propagated in (a1) aluminum plate; (a2) sample 01 (foursquare distribution); (b) transmission spectra in aluminum plate (dot curve) and sample 01 (solid curve).

Figure 4 (a2) shows that the transmitted waveform for the 2D composite plate with foursquare distribution PCs (sample 01) is distorted visibly, compared to the aluminum thin plate presented in Fig. 4 (a1). Three acoustic band gaps are noted in the transmission spectra of Lamb waves propagated in sample 01 [see the solid curve in Fig. 4 (b)], which are obtained from 0.24 MHz to 0.3 MHz (the bandwidth δf= 0.06 MHz, corresponding bandwidth/center frequency ratio $\delta f / f_m$= 0.222), 0.45 MHz to 0.54 MHz (δf= 0.09 MHz, $\delta f / f_m$= 0.182) and 0.77 MHz to 0.91 MHz (δf= 0.14 MHz, $\delta f / f_m$= 0.167), respectively.

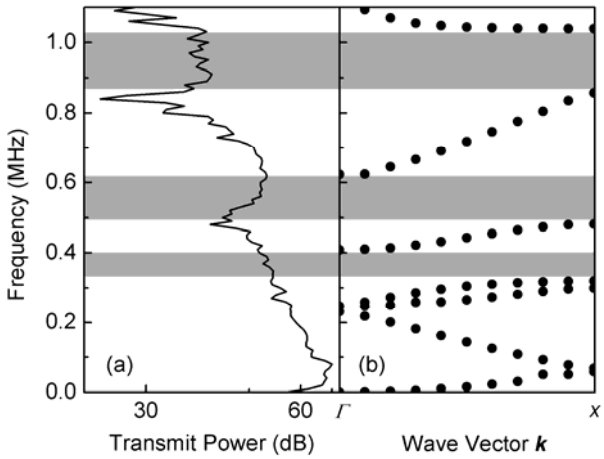

Figure 5: (a) The detected transmission spectrum of Lamb waves in sample 01; (b) Dispersion curves of Lamb waves.

The calculated results of sample 01 are shown in Fig. 5 (b). As shown by the hatched region in Fig. 5, the first absolute forbidden band gap of calculated results is obtained from 0.32 MHz to 0.41 MHz with the bandwidth of 0.09 MHz ($\delta f / f_m$= 0.246), which is wider slightly than the experimental result with a little blue shift of center frequency f_m. The dispersion curves reveal three absolute forbidden band gaps in low frequency, which bring out the location characters of Lamb wave band gaps in the 2D PC thin plate and basically agreed with the experimental results. There are two mainly possible causes of variances. On the one hand restricted by the mechanical process, the structural parameters and material parameters of the sample composite thin plate do not strictly equal to that of the calculated model, which affect much on the band structure of Lamb waves[19]. And there are some unavoidable systematic and measurement errors. On the other hand the infinite PC model is employed neglected boundary problems such as reflection and dispersion which exist in experiment detection. The locations of the other two absolute forbidden band gaps are also plotted in Fig. 5 (b). Based on the calculation, the second band gap is found from 0.48 MHz to 0.62 MHz with the bandwidth of 0.14 MHz ($\delta f / f_m$= 0.254), which is comparable to the case of the first one. The third one is localized from 0.86 MHz to 1.04 MHz (compared with the detected result 0.77 MHz to 0.91 MHz in Fig. 5 (a)) with the bandwidth of 0.18 MHz (0.14 MHz) and the ratio $\delta f / fm$ of 0.189 (0.167). Thus, the bandwidths of three calculated absolute forbidden band gaps are broad slightly with a little shift of center frequency.

We patterned the scatterers in the triangular arrangement in a thin aluminum plate, while other parameters of the

composite plate remain constant as shown in Fig. 3 (b). Figure 6 (a) indicates that periodic structures have a strong impact on the propagation of Lamb waves. On the basis of experiment results, the spectrum of transmission for Lamb waves in composite sample plate 02 is plotted (the solid curve in Fig. 6 (b)) and presents three acoustic band gaps compared with the one of aluminum plate (dot curve).

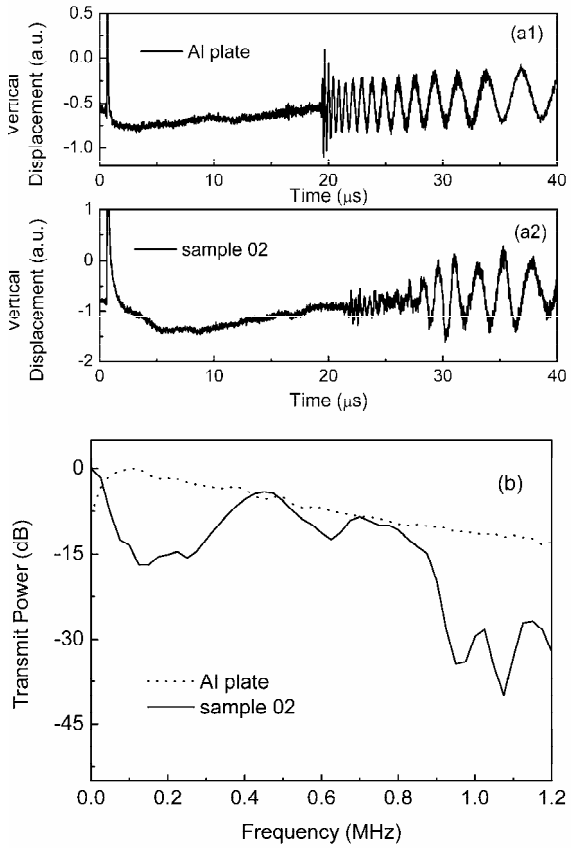

Figure 6: Transmitted waveforms of Lamb waves propagated in (a1) aluminum plate; (a2) sample 02 (triangular distribution); (b) transmission spectra: aluminum plate (dot curve) and sample 02 (solid curve).

Figure 7 shows the band structure of Lamb waves propagated in the composite plate with triangular distribution PCs (sample 02). Compared with the dispersion curves (Fig. 7 (b)), it is found that the first slit on transmission spectrum indicated by the arrows is not absolute forbidden band. The second absolute forbidden band obtained by experimental detection (numerical calculation) is localized from 0.6 MHz to 0.72 MHz (0.71 MHz to 0.82 MHz) with the bandwidth of 0.12 MHz (0.11 MHz) and the ratio $\delta f / f_m$ of 0.182 (0.144). And the third absolute forbidden band obtained by detection is extends from the frequency of 0.9 MHz to 1.03 MHz with δf = 0.13 MHz and f_m= 0.965 MHz, while the calculated one is localized from 1.04 MHz to 1.15 MHz with δf = 0.11 MHz and f_m= 1.095 MHz. The bandwidths of two results are mainly closely while the center frequencies have little shift, and the characters of the variances between two results are much similar to the case of sample 01. Figure 7 (a) and (b) exposit that there are one partial forbidden band and two absolute forbidden bands of Lamb waves in low frequency range for sample 02, which is great different with .the case for sample 01. Comparing Fig. 5 with Fig. 7, the huge influence of the arrangement of scatterers on the band structure of Lamb waves in a 2D PC plate is confirmed not only in theory but also in experiment.

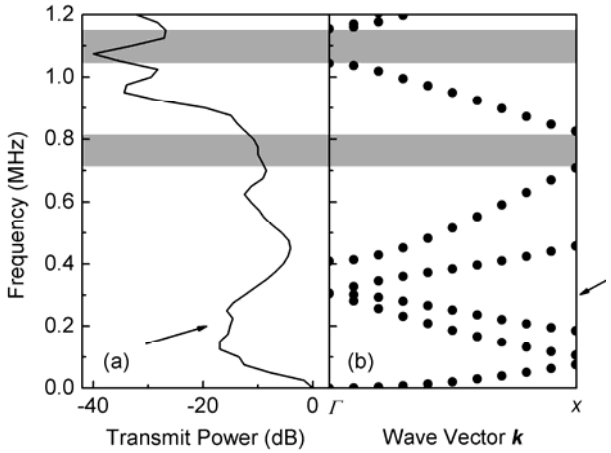

Figure 7: (a) The detected transmission spectrum of Lamb waves in sample 02; (b) Dispersion curves of Lamb waves.

4. Conclusions

The propagation of Lamb wave in 2D PC thin plate is studied. The calculated results show the periodical arrangement of scatterers strongly modifies the location of Lamb wave band gaps. The PC with scatterers patterned squarely shows three absolute forbidden bands, while the PC with scatterers patterned triangularly presents one partial forbidden band and two absolute forbidden bands in low frequency domain. On the basis of calculations, 2D PC plates are manufactured. Through laser-ultrasonic measurements, acoustic band gaps in the PC plates are observed experimentally, which confirms the existence of Lamb wave band gaps in 2D PC plates. The transmit power spectra detected in the experiments mainly agree with the calculated results.

Acknowledgements

This work was supported by the National Basic Research Program of China (2012CB921504), the National Natural Science Foundation of China (11074124, 11104139, and 10904052), and Jiangsu Provincial Natural Science Foundation (BK2011542).

References

[1] M. M. Sigalas, E. N. Economou, Band structure of elastic waves in two dimensional systems, *Solid State Commun.* 86: 141-143, 1993.

[2] M. S. Kushwaha, P. Halevi, L. Dobrzynski, B. Djafari-Rouhani, Acoustic Band-Structure of Periodic Elastic Composites, *Phys. Rev. Lett.* 71: 2022-2025, 1993.

[3] L. S. Cao, R. W. Peng, R. L. Zhang, X. F. Zhang, M. Wang, X. Q. Huang, A. Hu, S. S. Jiang, Delocalization of phonons and quantized thermal conductance in a random n-mer system, *Phys. Rev. B* 72: 214301, 2005.

[4] D. Sutter-Widmer, P. Neves, P. Itten, R. Sainidous, W. Steurer, Distinct band gaps and isotropy combined in icosahedral band gap materials, *Appl. Phys. Lett.* 92: 073308, 2008.

[5] Y. Lai and Z. Q. Zhang, Large band gaps in elastic phononic crystals with air inclusions, *Appl. Phys. Lett.* 83: 3900-3902, 2003.

[6] S. X. Yang, J. H. Page, Z. Liu, M. L. Cowan, C. T. Chan, P. Sheng, Focusing of sound in a 3D phononic crystal, *Phys. Rev. Lett.* 93: 024301, 2004.

[7] J. S. Wang, X. D. Xu, X. J. Liu, G. C. Xu, A tunable acoustic filter made by periodical structured materials, *Appl. Phys. Lett.* 94: 181908, 2009.

[8] M. M. Sigalas, E. N. Economou, Elastic and Acoustic-Wave Band-Structure, *J. Sound Vib.* 158: 337-382, 1992.

[9] Y. Tanaka, S. I. Tamura, Surface acoustic waves in two-dimensional periodic elastic structures, *Phys. Rev. B* 58: 7958-7965, 1998.

[10] Y. Tanaka, S. I. Tamura, Acoustic stop bands of surface and bulk modes in two-dimensional phononic lattices consisting of aluminum and a polymer, *Phys. Rev. B* 60: 13294-13297, 1999.

[11] Y. Tanaka, Y. Tomoyasu, S. I. Tamura, Band structure of acoustic waves in phononic lattices: Two-dimensional composites with large acoustic mismatch, *Phys. Rev. B* 62: 7387-7392, 2000.

[12] Q. Ni, J. C. Cheng, Anisotropy of effective velocity for elastic wave propagation in two-dimensional phononic crystals at low frequencies, *Phys. Rev. B* 72: 014305, 2005.

[13] J. O. Vasseur, P. A. Deymier, B. Chenni, B. Djafari-Rouhani, L. Dobrzynski, D. Prevost, Experimental and theoretical evidence for the existence of absolute acoustic band gaps in two-dimensional solid phononic crystals, *Phys. Rev. Lett.* 86: 3012-3015, 2001.

[14] T. T. Wu, Z. C. Hsu, Z. G. Huang, Band gaps and the electromechanical coupling coefficient of a surface acoustic wave in a two-dimensional piezoelectric phononic crystal, *Phys. Rev. B* 71: 064303, 2005.

[15] J. J. Chen, K. W. Zhang, J. Gao, J. C. Cheng, Stopbands for lower-order Lamb waves in one-dimensional composite thin plates, *Phys. Rev. B* 73: 094307, 2006.

[16] J. Gao, J. C. Cheng, B. W. Li, Propagation of Lamb waves in one-dimensional quasiperiodic composite thin plates: A split of phonon band gap, *Appl. Phys. Lett.* 90: 111908, 2007.

[17] J. C. Hsu, T. T. Wu, Efficient formulation for band-structure calculations of two-dimensional phononic-crystal plates, *Phys. Rev. B* 74: 144303, 2006.

[18] V. Kavalerov, T. Fujii, M. Inoue, Observation of highly nonlinear surface-acoustic waves on single crystal lithium-niobate plates by means of an optical sampling probe, *J. Appl. Phys.* 87: 907-913,2000.

[19] T. Brunet, J. Vasseur, B. Bonello, B. Djafari-Rouhani, A. C. Hladky-Hennion, Lamb waves in phononic crystal slabs with square or rectangular symmetries, *J. Appl. Phys.* 104: 043506, 2008.

Acoustic cloak with duplex communication ability constructed by multilayered homogeneous isotropic materials

Q. Wei, Y. Cheng, and X. J. Liu*

Institute of Acoustics, Nanjing University, Nanjing 210093, China
*corresponding author, E-mail: liuxiaojun@nju.edu.cn

Abstract

Based on the effective medium approximation, we propose a practical implementation of cylindrical acoustic cloak with concentric alternating multilayered structure of homogeneous isotropic materials, which can perfectly mimic the ideal radius-dependent and anisotropic ordinary lens cloak. The proposal exhibits near-ideal cloaking performance such as low-scattering and shadow-reducing at a wide range frequency, thus can hide an object from the detection of acoustic wave. The acoustic waves can pass through the cloaking shell with unchanged wavefront shape, which endues the cloaked object with duplex communication ability. More simulations on the acoustic far-field scattering patterns and total scattering cross-section (TSCS) are performed to investigate the layer number and frequency dependence of cloaking effect, and the results show that the thinner layers exhibit better cloaking effect. The proposal may significantly facilitate the experimental demonstration of acoustic cloak.

1. Introduction

Recently, transformation optics has attracted increasing interest, since it offers a conceptual design technique to create a wide variety of unprecedented optical effects and functional devices by controlling the paths of electromagnetic (EM) wave propagation at will [1-8]. One of the most remarkable applications enabled by this technique is the so-called invisibility cloak, which can bend light around a region of space and make any object in the region seem invisible. The invisibility cloak has been experimentally realized at microwave [4] and optical [8] frequencies with the aid of artificial EM metamaterials. Since the acoustic wave equation is also transformation invariant, the transformation-based method was then further extended to manipulate acoustic wave in similar manner and design the inaudibility cloak, which may significantly reduce the acoustic signature of the cloaked object and make it acoustically undetectable [9-26].

There are two schemes been developed to achieve the cloaking effect of scattering cancellation and acoustic transparency, according to whether the cloaked object has capability of sending and receiving information. The first scheme is to expand a point or a line in one coordinate system into a hole (cloaked region with spherical, cylindrical, wedged or other shapes) in another [9-21]. Since a point/line is defined as the smallest/thinnest mathematical entity, nothing can penetrate them, i.e. in the transformed coordinate system the wave can not get into the hole because it must locally follow the coordinate system. The object inside the hole thus becomes invisible, but meanwhile it loses communication with the surroundings because no wave can penetrate the cloak. In order to get around such an inherent limitation, the second scheme was then proposed in which the object lies outside the cloak or encircled by lens [7, 22-26]. In the external cloak scheme the object is canceled out by its anti-object made of negative materials for the propagating waves [7, 22-24], while the lens can be regarded as perfectly-matched layer which can mach two mismatched domains, so it can cloak object from external illumination too [25-26]. Both in anti-object and hyperlens proposal, single-negative even left-hand materials were needed until it was subsequently found that ordinary lens made of positive materials can also hide an object from detection of acoustic wave [26]. However, the implement of ordinary lens cloak depends on the medium with radius-dependent and anisotropic density and bulk modulus, which is still difficult to realize because of the limited resource of natural materials with radial anisotropy. One possible solution is to use acoustic artificial metamaterial composed of subwavelength resonant inclusions, but the metamaterial works in a limited frequency range and its local resonance may result in considerable absorption of wave [15, 27-29].

In this paper, we employ the principle of layered system used in invisibility cloak [5-6] and the first scheme inaudibility cloak [16-20] to design two-dimensional (2D) ordinary lens acoustic cloak. The proposed cloak is implemented with concentric alternating multilayered structure of homogeneous isotropic materials. Based on the effective medium approximation [30], when each layer has proper parameters and enough thin thickness, the multilayered structure can behave as a single effective medium with radius-dependent and anisotropic density and bulk modulus. Full-wave simulations by finite element method (FEM) are performed to demonstrate the properties of the proposed structure. The simulation results clearly show near-ideal cloaking performance such as low-scattering and shadow-reducing. Meanwhile, the acoustic wave can pass through the cloaking shell changelessly

which makes the cloaked object capable of exchanging information with the surroundings by acoustic wave for any purpose. It is noteworthy that the proposed cloak has a wide operating frequency region in which the upper limit is only determined by layer thickness. With the feasibility of designing an acoustic cloak by ordinary isotropic materials instead of acoustic metamaterial with complex structured inclusions, this proposal may significantly facilitate the experimental demonstration of acoustic cloak.

2. Ideal cloak

According to the acoustic transformation theory, when original space $x'(r', \theta', z')$ is transformed into physical space $x(r, \theta, z)$ by a radial mapping in cylindrical geometry ($r'=f(r)$, $\theta'=\theta$, $z'=z$), the density and bulk modulus in the physical space can be expressed as

$$\rho_r = \rho' f'(r) r / f(r),\ \rho_\theta = \rho' f(r) / (r f(r)),$$
$$\kappa = \kappa' r / (f'(r) f(r)), \qquad (1)$$

where ρ' and κ' are the density and bulk modulus in the original space. It can be noticed in Eq. (1) that ρ_r/ρ' and ρ_θ/ρ' are reciprocal. In order to simplify the parameters, we set ρ_r as a constant, then ρ_θ becomes constant too. Suppose $f'(r)r/f(r)=n$, then the general form of transformation function $f(r)$ which yields constant ρ_r and ρ_θ can be obtained as

$$f(r) = mr^n. \qquad (2)$$

Here, m and n are two unknown coefficients which can be obtained by the requirement of continuous condition of $f(r)$ at boundary.

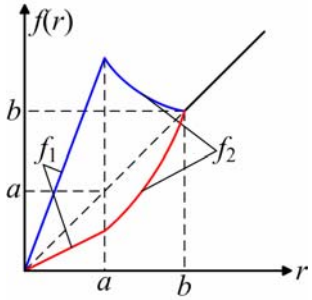

Figure 1: The transformation function $f(r)$ of the cloak.

For a central cylindrical object with density ρ_0, bulk modulus κ'' and radius a, its corresponding transformation function is

$$f_1(r) = r\sqrt{\kappa_0 / \kappa''}, \qquad (3)$$

as shown in Fig. 1. Here ρ_0 and κ_0 are the density and bulk modulus of the host medium. In order to cancel the scattering of the object, we shield it by an acoustic cloaking shell with inner (outer) radius a (b). As is shown in Fig. 1, the transformation function $f_2(r)$ to produce acoustic cloaking must fulfill the continuous conditions that

$$f_2(a) = f_1(a),\ f_2(b) = b. \qquad (4)$$

By solving Eq. (4), we eventually obtain the parameters of the 2D ideal acoustic cloak [26]

$$\rho_r = n\rho_0,\ \rho_\theta = \rho_0 / n,\ \kappa = (r/b)^{2-2n}\kappa_0 / n, \qquad (5)$$

with coefficient $n=1+0.5\lg(\kappa''/\kappa_0)/\lg(b/a)$. It can be noticed in Eq. (5) that, the density of the cloak is anisotropic but homogeneous, and only the bulk modulus is spatially variant.

As is shown in Fig. 1, there are two cases. (1) $\kappa'' > \kappa_0 a^2/b^2$, then the coefficient n should locate at the range $(0, +\infty)$ and the parameters of the cloak are all positive. (2) $\kappa'' < a^2\kappa_0/b^2$, then the coefficient n locates at the range $(-\infty, 0)$ and the parameters of the cloak are all negative. The cloak with negative parameters has been discussed, so we only consider the first case in this paper.

Full-wave simulations are performed by FEM to demonstrate the cloaking effect. In all simulations in this paper, the host medium is set as water with the density ρ_0=998 kg/m^3 and the bulk modulus κ_0=2.19 GPa, the cloaked object has density ρ_0, bulk modulus $\kappa''=2.25\kappa_0$ and radius a=1.0 m, the outer and inner radius of the cloaking shell are chosen as b=1.5 m and a=1.0 m, and the acoustic plane wave travels from left to right with spatial frequency in host medium $k_0=4\pi$, unless otherwise specified. The acoustic parameters of the cloaking shell can be readily obtained by inserting the corresponding coefficients into Eq. (5).

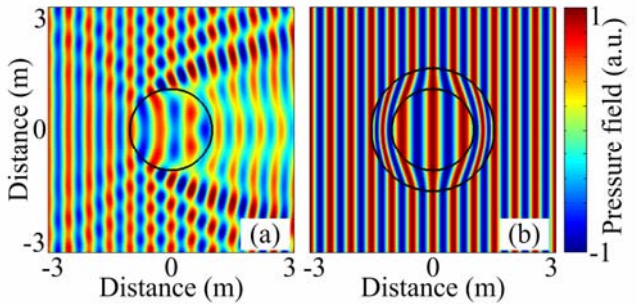

Figure 2: Acoustic pressure field distributions for (a) uncloaked scatterer and (b) cloaked scatterer.

The acoustic pressure field distributions for uncloaked and cloaked scatterer are shown in Figs. 2(a) and 2(b), respectively. As observed, without the cloak the plane wave is strongly disturbed by the scatterer, which results in the remarkable backward reflection and the sharp-edged acoustic shadow. With the cloak, both the backward reflection and shadow are significantly suppressed, which results in the undisturbed pressure field outside the shell. Moreover, the incident plane wave can pass through the cloaking shell with unchanged wavefront shape, which makes the cloaked object capable of receiving information from the surroundings without distortion.

It should be noted that, the density ρ_0 and bulk modulus κ'' of the cloaked object is in fact the effective parameters. Because the object in water generally has a composite structure, we treat the object as a homogeneous effective medium. In Figs. 3 a square region (-0.25 m$<x<$0.25m, -0.25 m$<y<$0.25 m) within the object is constructed by two kinds of alternately stacking layers with same geometry size. The width and length of each layer are 0.05 m and 0.5 m. The

mass density and bulk modulus of the two kind layers are $\rho_1=1.5\rho_0$, $\kappa_1=2\kappa''$ and $\rho_2=0.5\rho_0$, $\kappa_2=2\kappa''/3$, respectively. The other region of the cloaked object has density ρ_0 and bulk modulus $\kappa''=2.25\kappa_0$. The total effective parameters of the cloaked object are ρ_0 and κ'', so the parameters of the cloaking shell are same with that in Fig. 2(b). Comparing Fig. 3(b) with Fig. 3(a), the cloaking shell can significantly reduce the scattering and the cloaking effect is valid for the composite object.

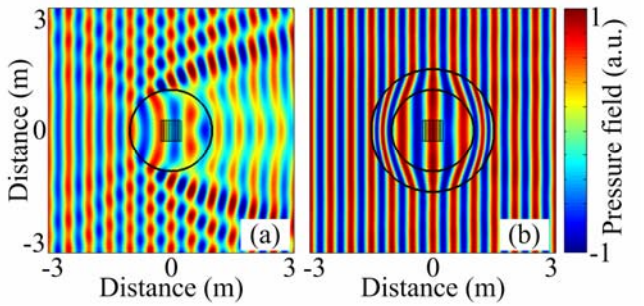

Figure 3: Acoustic pressure field distributions for (a) uncloaked composite scatterer and (b) cloaked composite scatterer.

In order to yield perfect cloaking effect, the effective mass density of the object must equal ρ_0 exactly. However, the density of the object suspending underwater is just approximately same with ρ_0, and it may be variation with the work condition (e.g., submarine). Now we maintain the parameters of the cloaking shell in Fig. 2(b) and multiply the mass density and bulk modulus of the cloaked object by a factor η. In Figs. 4(a) and 4(b) the factor are chosen as $\eta=0.7$ and $\eta=1.5$, respectively. It is apparent that at a relatively wide range ($0.7<\eta<1.5$) of objects, the cloaking effect is robust because the change of the parameters of the cloaked object only induces slight turbulences.

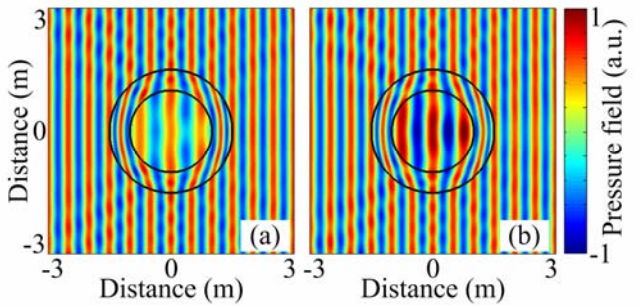

Figure 4: Acoustic pressure field distributions for cloaked object with (a) $\eta=0.7$ and (b) $\eta=1.5$.

3. Layered cloak

The parameters of the cloaking shell are anisotropic and inhomogeneous, which makes it difficult to experimentally realize. So we further construct the cloak by alternating homogeneous isotropic materials. As verified in Ref. [16, 30], the transverse isotropic density can be mimicked by an alternating layered system. Figure 5(a) shows the structure of acoustic layered system in cylindrical coordinates. For a concentric layered structure consisting of two kinds of alternating layers A (B) whose parameters are homogeneous and isotropic density ρ_A (ρ_B) and bulk modulus κ_A (κ_B), it can be properly treated as a single anisotropic medium which has the transverse isotropic density along the r-direction and θ-direction based on the effective medium approximation, if only the thickness of each layer is much smaller compared with the incident wavelength. The effective density tensor and bulk modulus of the layered structure take the following form

$$\rho_r=\frac{\rho_A+\eta\rho_B}{1+\eta},\ \frac{1}{\rho_\theta}=\frac{1}{1+\eta}\left(\frac{1}{\rho_A}+\frac{\eta}{\rho_B}\right),$$
$$\frac{1}{\kappa}=\frac{1}{1+\eta}\left(\frac{1}{\kappa_A}+\frac{\eta}{\kappa_B}\right), \qquad (6)$$

where, ρ_r and ρ_θ are the radial and angular components of the effective anisotropic density tensor, respectively, κ is the effective bulk modulus, and η is the ratio for the thicknesses of B layers (d_B) and A layers (d_A).

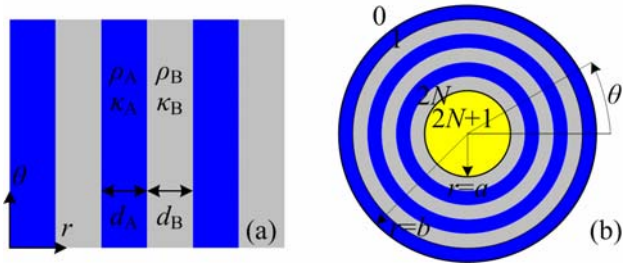

Figure 5: (a) The structure of acoustic layered system. (b) The schematic of 2N-layered acoustic cloak.

Now we come to realize the radius-dependent, anisotropic acoustic cloaking shell described by Eq. (5) using layered structures of homogeneous isotropic materials described by Eq. (6). First, break the ideal continuous shell into N layers which have stepwise discrete parameters distribution. The material in each layer is thus anisotropic and homogenous. Then, mimic each anisotropic layer by alternating layers of isotropic materials A and B whose parameters are precisely designed by Eq. (6) from the corresponding anisotropic layer. If N is large enough, each anisotropic but homogeneous layer can be mimicked by only two isotropic and homogeneous layers A and B. Finally, the inhomogeneous anisotropic cloaking shell is approximately implemented by 2N discrete layers of homogeneous isotropic materials, as shown in Fig. 5(b). Suppose the layers have equal thickness ($\eta=1$) and substitute Eq. (5) into Eq. (6), then the density and bulk modulus of each layer can be obtained as follows

$$\rho_{2i-1}=(n+\sqrt{n^2-1})\rho_0,$$
$$\rho_{2i}=(n-\sqrt{n^2-1})\rho_0,\ i=1, 2, 3, \ldots, N,$$
$$\kappa_i=\frac{\kappa_0}{n(r_i/b)^{2n-2}},\ i=1, 2, 3, \ldots, 2N, \qquad (7)$$

with $r_i=a+(2i-1)(b-a)/4N$, $i=1, 2, 3, \ldots, 2N$.

The acoustic pressure field distributions for cylindrical scatterer shielded by the 10-layered cloak and 40-layered cloak are shown in Figs. 6(a) and 6(b), respectively. Comparing Fig. 6(a) with Fig. 6(a), when the scatterer is

shielded by the 10-layered cloak ($2N$ = 10, $d_A = \lambda/10$), the deformation of pressure field decreases but the scattering is still very large. Figure 6(b) shows the efficient cloaking effect by the 40-layered cloak ($2N$ = 40, $d_A = \lambda/40$). Outside the cloaking shell, the scattering is greatly reduced and the plane wave field is almost undisturbed. For an exterior observer, the acoustic field seems to be emitted from the source directly as if there is no scatterer in the host medium. The absence of scattered waves clearly verifies the efficient cloaking effect of the proposed layered cloak. And it is worth pointing out that the incident plane wave can pass through the cloaking shell with the shape of the wavefront unchanged, which makes it capable of receiving information from the surroundings. Figures 6(a) and 6(b) imply that the proposed cloak with larger layer number $2N$ produces smaller scattering for external illumination, and the cloaking performance is quite excellent when $2N$ becomes large enough (e.g., $2N$ = 40).

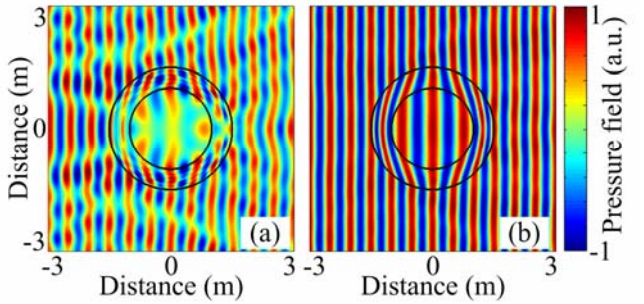

Figure 6: Acoustic pressure field distributions for (a) 10-layered cloak and (b) 40-layered cloak.

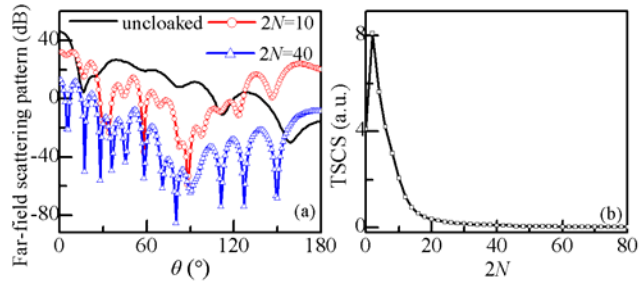

Figure 7: (a) The acoustic far-field scattering patterns and (b) TSCS for different $2N$-layered cloak.

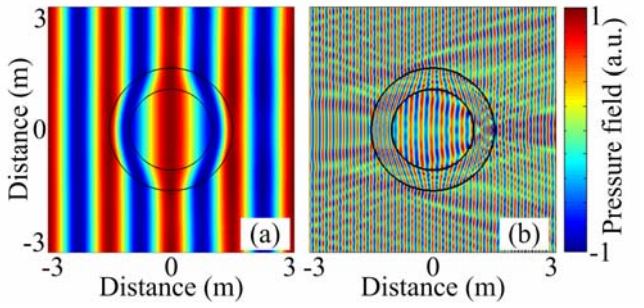

Figure 8: Acoustic pressure field distributions of 40-layered cloak with (a) $\lambda = 1.5a$ and (b) $\lambda = a/6$.

We further investigate the acoustic total scattering cross-section (TSCS) [11] which is defined as the ratio of the total scattered power to the incident power and can be calculated by integrating the far-field scattering pattern over θ. Figure 7(b) depicts the TSCS as a function of layer number $2N$ at $\lambda = 0.5a$. For the bare scatterer ($2N$ = 0), the TSCS is about 4.1. When the scatterer is shielded by a 2-layered cloak, the TSCS is 8.1 and it may significantly drop as the layer number $2N$ increases. Finally, the TSCS will decrease to zero when $2N$ is large enough. It is clearly shown in Fig. 7(b) that the larger layer number, the smaller this $2N$-layered cloak produces scattering for fixed external illumination.

For the purpose of quantitatively analyzing the cloaking effect, the acoustic far-field scattering pattern [5, 11] is calculated by using the acoustic scattering theory under plane wave incidence. Figure 7(a) plots the acoustic far-field scattering patterns for different $2N$-layered cloak at $\lambda = 0.5a$. For the bare scatterer, the maximum scattering is 46.12 dB at $\theta = 0°$ which corresponds to the sharp forward shadow behind the scatterer. When it is shielded by the 40-layered (10-layered) cloak, the forward ($\theta = 0°$) scattering dramatically decreases to 12.98 dB (32.21 dB). The maximum reduction (94.17 dB) of scattering due to the presence of 40-layered cloak occurs in $\theta = 80°$, and at most angles (≥71.11%) the reduction is more than 25 dB. It can be found in Fig. 7(a) that, when the layer number $2N$ is increasing the scattering of such $2N$-layered cloak significantly drops compared with that of a bare cylindrical scatterer, which clearly demonstrates the efficiency of the layered cloaking system.

We also investigate the performance of the multilayered cloak with different wavelengths. The acoustic pressure field distributions of 40-layered cloak for plane wave incidence with wavelength $\lambda = 1.5a$ ($d_A = \lambda/120$) and $\lambda = a/6$ ($d_A = 3\lambda/40$) are shown in Figs. 8(a) and 8(b), respectively. Compared to Fig. 6(b), the pressure field in Fig. 8(a) suffers so smaller disturbance from the scatterer that the deformation of exterior plane wave can not been caught by the naked eye. Namely, the cloaking effect improves as the wavelength increases from $\lambda = 0.5a$ to $\lambda = 1.5a$, but in contrast the cloaking effect markedly degrades when the wavelength is decreased to $a/6$, as shown in Fig. 8(b). It is clearly seen that the plane wave field is strongly disturbed and the wavefront becomes discontinuous, indicating non-negligible scattering appears.

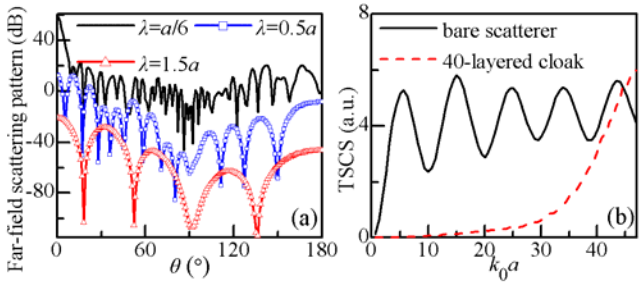

Figure 9: (a) The far-field scattering patterns of 40-layered cloak under plane wave incidence with different wavelength λ. (b) The frequency dependence of TSCSs for bare scatterer and 40-layered cloak.

We further quantify the directional performance of the cloak with different wavelengths. Figure 9(a) plots the

scattering patterns of 40-layered cloak for wavelength $\lambda = a/6$, $\lambda = 0.5a$ and $\lambda = 1.5a$. As observed, when the wavelength decreases from $1.5a$ to $0.5a$ and further to $a/6$, the scattering increases dramatically in all directions. For $\lambda = 1.5a$ and $\lambda = a/6$, the scatterings in the direction $\theta = 0°$ ($\theta = 180°$) are -20.79 dB and -46.42 dB (59.17 dB and 0.59 dB), respectively. Namely, the forward shadow (backward reflection) increases 79.96 dB (47.01 dB) as λ only decreases from $1.5a$ to $a/6$. The scattering patterns accurately match the pressure field distributions in Fig. 8.

In order to present an overall performance on the cloak's operating frequency, we further calculate the acoustic TSCS spectra under different frequency, and depict it as a function of the normalized frequency k_0a ($2\pi/\lambda$) in Fig. 9(b). At extremely low frequency ($k_0a \to 0$), the size of the scatterer and 40-layered cloak are much smaller than the wavelength, the TSCSs for three cases thus approach zero. As k_0a increases from 0 to 5.66 and further to 45, the TSCS of the bare scatterer first rapidly increases to 5.3 and then oscillates around average value 4, while the TSCSs for two types of 40-layered cloak increase monotonously with k_0a. However, the TSCS of the 40-layered cloak is always smaller than that for bare scatterer in the range of k_0a = 0 - 44.55, which distinctly confirms the efficient cloaking effect of the proposed layered structure, and the cloaking effect is gradually degraded as the frequency increases (or wavelength decreases). In the range of k_0a = 0 – 27.02, the TSCS of the cloak maintains below 0.44 and the cloaking efficiency keeps above 90%. As k_0a is further increased to 44.55, the TSCS of the cloak increases dramatically and equals to that for bare scatterer at last, the cloaking efficiency thus vanishes. If the cutoff frequency is defined as a benchmark distinguishing whether the cloaking effect exists, then the operating frequency of the 40-layered cloak is 0 - 44.55. The frequency dependence of the cloaking effect agrees well with Figs. 8 and 9(a).

The investigation about the layer number and frequency dependence of the cloaking effect clearly show that the thinner the layers compared with incident wavelength, the better this 2N-layered structure cloaks the scatterer. This character can be easily explained by effective medium approximation. The layered cloak is characterized as an effective anisotropic material, and the mimic works if only d_A (d_B) << λ. When the wavelength decreases or the layers become thick the long-wavelength limit will be destroyed, which directly degrades the working condition of the approximation, and hence, attenuates the cloaking effect. As a result, the better cloaking effects and wider operating frequency could be obtained by thinner alternating layers. However, in practical realization it is difficulty to coat too many thin layers which follow the parameter described by Eq. (3), we thus have to terminate the coating process at a proper medium value of layer number 2N considering the fabrication cost and implementation difficulty.

Since the wave from external sources can pass through the cloaking shell, we have also considered the case where a source is put inside the cloaked region to decide whether the wave can travel from inside to external region. The simulation results are given in Fig. 10 in which the point source is located at (1.0 m, 180°). Without cloak, the wave directly travels into the distance, but the wavefront shape no longer keeps cylindrical because of the scattering by the cylinder, as shown in Fig. 10(a). In Fig. 10(b) the cylindrical wave can pass through the cloaking shell and reach the outside with changeless wavefront shape, which makes it capable to send information to outside. In addition, the cloaking shell produces an imaginary image P' at (0.67 m, 180°), which results in an intriguing effect that for an exterior observer the acoustic wave appears to be radiated from the point P'.

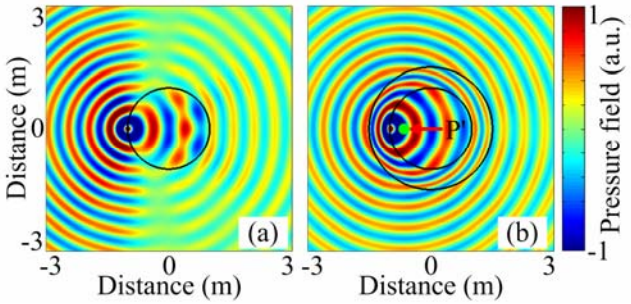

Figure 10: Acoustic pressure field distributions for (a) bare scatterer and (b) 40-layered cloak. The acoustic wave is incident from a point source located at (1.0 m, 180°) with wavelength in host medium $\lambda = 0.5a$.

4. Conclusions

In conclusion, we have presented an inaudibility cloaking scheme by mimicking the radius-dependent and anisotropic ordinary lens through alternating layered structures of homogeneous isotropic materials based on the effective medium approximation. The low-scattering and shadow-reducing properties have been demonstrated, which make an acoustic sensor undetectable. Since the wave can pass through the cloaking shell with changeless wavefront shape, the cloaked object is able to exchange information with the outside environment by acoustic wave for the purpose of communication or detection. The investigation about layer number and operating frequency show that the thinner layers produce better cloaking effect. Moreover, the proposed scheme has no requirement of any anisotropic or inhomogeneous materials which are usually constructed by resonant metamaterial, thus the layered cloak may have a wide operating frequency range in which the upper limit is only decided by layer thickness. The proposal may significantly facilitate the experimental demonstration of acoustic cloaking.

Acknowledgements

This work was supported by the National Basic Research Program of China under Grant No. 2012CB921504, NSFC (11074124, 11104139 and 10904052), SRFDP 20110091120040, and Jiangsu Provincial Natural Science Foundation (BK2011542) and PAPD of Jiangsu higher education institutions.

References

[1] U. Leonhardt, Optical conformal mapping, *Science* 312: 1777−1779, 2006.

[2] J. B. Pendry, D. Schurig, D. R. Smith, Controlling electromagnetic fields, *Science* 312: 1780−1782, 2006.

[3] S. A. Cummer, B. I. Popa, D. Schurig, D. R. Smith, J. B. Pendry, Full-wave simulations of electromagnetic cloaking structures, *Phys. Rev. E* 74: 036621, 2006.

[4] D. Schurig, J. J. Mock, B. J. Justice, S. A. Cummer, J. B. Pendry, A. F. Starr, D. R. Smith, Metamaterial electromagnetic cloak at microwave frequencies, *Science* 314: 977−980, 2006.

[5] Y. Huang, Y. Feng, T. Jiang, Electromagnetic cloaking by layered structure of homogeneous isotropic materials, *Opt. Express* 15: 11133−11141, 2007.

[6] C. W. Qiu, L. Hu, X. Xu, Y. Feng, Spherical cloaking with homogeneous isotropic multilayered structures, *Phys. Rev. E* 79: 047602, 2009.

[7] Y. Lai, H. Y. Chen, Z. Q. Zhang, C. T. Chan, Complementary media invisibility cloak that cloaks objects at a distance outside the cloaking shell, *Phys. Rev. Lett.* 102: 093901, 2009.

[8] J. Valentine, J. Li, T. Zentgraf, G. Bartal, X. Zhang, An optical cloak made of dielectrics, *Nature Mater.* 8: 568−571, 2009.

[9] G. W. Milton, M. Briane, J. R. Willis, On cloaking for elasticity and physical equations with a transformation invariant form, *New J. Phys.* 8: 248, 2006.

[10] S. A. Cummer, D. Schurig, One path to acoustic cloaking, *New J. Phys.* 9: 45, 2007.

[11] L. W. Cai, J. Sánchez-Dehesa, Analysis of Cummer-Schurig acoustic cloaking, *New J. Phys.* 9: 450, 2007.

[12] H. Chen, C. T. Chan, Acoustic cloaking in three dimensions using acoustic metamaterials, *Appl. Phys. Lett.* 91: 183518, 2007.

[13] S. A. Cummer, B. I. Popa, D. Schurig, D. R. Smith, J. Pendry, M. Rahm, A. Starr, Scattering theory derivation of a 3D acoustic cloaking shell, *Phys. Rev. Lett.* 100: 024301, 2008.

[14] A. N. Norris, Acoustic cloaking theory, *Proc. R. Soc. A* 464: 2411−2434, 2008.

[15] S. Zhang, C. G. Xia, N. Fang, Broadband acoustic cloak for ultrasound waves, *Phys. Rev. Lett.* 106: 024301, 2011.

[16] Y. Cheng, F. Yang, J. Y. Xu, X. J. Liu, A multilayer structured acoustic cloak with homogeneous isotropic materials, *Appl. Phys. Lett.* 92: 151913, 2008.

[17] D. Torrent, J. Sánchez-Dehesa, Acoustic cloaking in two dimensions: a feasible approach, *New J. Phys.* 10: 063015, 2008.

[18] H. Y. Chen, T. Yang, X. D. Luo, H. R. Ma, Impedance-matched reduced acoustic cloaking with realizable mass and its layered design, *Chin. Phys. Lett.* 25: 3696−3699, 2008.

[19] Y. Cheng, X. J. Liu, Three dimensional multilayered acoustic cloak with homogeneous isotropic materials, *Appl. Phys. A* 94: 25−30, 2009.

[20] H. Y. Chen, C. T. Chan, Acoustic cloaking and transformation acoustics, *J. Phys. D: Appl. Phys.* 43: 113001, 2010.

[21] B. I. Popa, L. Zigoneanu, S. A. Cummer, Experimental acoustic ground cloak in air, *Phys. Rev. Lett.* 106: 253901, 2011.

[22] B. Liu, J. P. Huang, Acoustically conceal an object with hearing, *Eur. Phys. J. Appl. Phys.* 48: 20501, 2009.

[23] J. J. Yang, M. Huang, C. F. Yang, J. H. Peng, J. Chang, An external acoustic cloak with N-sided regular polygonal cross section based on complementary medium, *Comput. Mater. Sci.* 49: 9−14, 2010.

[24] Q. Su, B. Liu, J. P. Huang, Remote acoustic cloaks, *Front. Phys.* 6: 65−69, 2011.

[25] X. F. Zhu, B. Liang, W. W. Kan, X. Y. Zou, J. C. Cheng, Acoustic cloaking by a superlens with single-negative materials, *Phys. Rev. Lett.* 106: 014301, 2011.

[26] X. F. Zhu, *The investigation of phononic crystal and acoustic metamaterials*, PhD thesis, Nanjing University, Nanjing, 2011.

[27] Z. Liu, X. Zhang, Y. Mao, Y. Y. Zhu, Z. Yang, C. T. Chan, P. Sheng, Locally resonant sonic materials, *Science* 289: 1734−1736, 2000.

[28] G. W. Milton, New metamaterials with macroscopic behaviour outside that of continuum elastodynamics, *New J. Phys.* 9: 359, 2007.

[29] J. Li, L. Fox, X. Yin, G. Bartal, X. Zhang, Experimental demonstration of an acoustic magnifying hyperlens, *Nature Mater.* 8: 931−934, 2009.

[30] M. Schoenberg, P. N. Sen, Properties of a periodically stratified acoustic half-space and its relation to a biot fluid, *J. Acoust. Soc. Am.* 73: 61−67, 1983.

Determining the full transformed relations in transformation method

Jin Hu[1 *], and Xiang-Yang Lu [1, 2]

[1] School of Information and electronics, Beijing Institute of Technology, Beijing, China
[2] School of Electronic and Information Engineering, Zhongyuan University of Technology, Zhengzhou, China
*corresponding author, E-mail: bithj@bit.edu.cn

Abstract

Transformation method provides an efficient way to control wave propagation by materials. The transformed relations for field and material during a transformation are essential to fulfill this method. However, there are no general methods to obtain the transformed relations for a general physic process; all the results in literatures are derived case by case. As a result, the degree to which this transformation concept can be applied to other physical phenomena remains an open question. Recently, Hu et al. present a general framework for determining the transformed relations of physical quantities in arbitrary PDE in its application scope according to the idea of transformation method. In this paper, we will review the main concepts of this general theory, particularly the difference between this idea and the usual method. The flexibility of this method is shown by an example.

1. Introduction

The transformation method proposed for electromagnetic (EM) waves [1-3] has been found many applications to control and manipulate electromagnetic fields with help of electromagnetic metamaterials, such as cloaks [2,4]. The method is also extended to acoustic wave for liquid materials [5,6], heat conduction [7] and matter waves [8]. The basic principle of transformation method is based on the form-invariance of the corresponding equations under a general spatial mapping, and then the needed materials to distribute the fields in a prescribed manner can be constructed directly. Consider a physical process described on an initial space Ω, the field $\mathbf{u}$ and material $\mathbf{C}$ are related together at a point $\mathbf{x}$ and time t by a differential equation F as

$$F(\mathbf{x},t,\mathbf{u}(\mathbf{x},t),\mathbf{C}(\mathbf{x}))=0,\ \mathbf{x}\in\Omega. \qquad (1)$$

The operator F announces the certain physical mechanism between $\mathbf{C}$ and $\mathbf{u}$ in every point within Ω. If F is form-invariant under the mapping which transform the space Ω to Ω' by $\mathbf{x}'=\mathbf{x}'(\mathbf{x})$, i.e. there is

$$F(\mathbf{x}',t,\mathbf{u}'(\mathbf{x}',t),\mathbf{C}'(\mathbf{x}'))=0,\ \mathbf{x}'\in\Omega', \qquad (2)$$

then the attached field $\mathbf{u}$ and materials $\mathbf{C}$ in Ω can also be mapped to Ω' as $\mathbf{u}'$ and $\mathbf{C}'$. The idea of transformation method is to carefully perform a specifical mapping so that the transformed field $\mathbf{u}'$ in the transformed space follows a designed way, and $\mathbf{C}'$ then tells how to realize this function by the material distribution. Hence, the transformed relations for field and material during a transformation, i.e.,

$$T_u:\mathbf{u}\mapsto\mathbf{u}',\ T_C:\mathbf{C}\mapsto\mathbf{C}', \qquad (3)$$

are essential to fulfill this method.

To obtain Eq. (3) for different equations, different groups have come up with different methods. Pendry et al. [2] rebuild the Maxwell's equations in a small parallelepiped and find the transformed relations with help of both the contravariant and covariant components of vectors. The similar method is used by Cummer et al. [9] to obtain the velocity transformation for scalar acoustic equations. Greenleaf et al. [10] analyze the Helmholtz equation with respect to Riemannian metrics, and then the transformed relations can be obtained by comparison of the equations in Riemannian space and Euclidian space. Milton et al. [11] give another concise mathematical formulation. They utilize tensor calculation to prove that for a given transformation of field and material in the Maxwell's equations, the equations can retain their form. Norris [12] shows that the material transformations of generalized-acoustic equations are not uniquely defined based on the pentamode elastic material theory [13]. Interestingly, Leonhardt et al. [14] find that general relativity provides the recipes for calculating the required electromagnetic material properties. Recently, the so-called "change of variable" method which was developed by Milton et al. [11] has been extended by Vasquez et al. [15] and Norris et al. [16] to obtain the transformations of the elastodynamics equations. The main idea of the this "change of variable" method is: one should first assume certain transformed relations for some physical quantities between $\mathbf{x}$ and $\mathbf{x}'$, and then reestablish the whole equations and other quantities also respect to $\mathbf{x}'$, according to the calculus rules. If the reestablished equations have the same form as the original one, then the equations are declared to be form-invariant, and the transformed relations Eq. (3) can be easily obtained by comparing the two sets of equations; otherwise, the equations are considered as form-variant and thus the transformation method can not be applied. By this method, the two groups achieve coincident results for transformation elastodynamics: if the transformed elasticity tensor is

assumed to be full symmetric, then the reestablished elastodynamics equations are changed from Navier's equations to Willis' equation; if one want to retain the form of Navier's equations, the transformed elasticity tensor should be asymmetric, which is first shown by Brun et al. [17] for the transformation elastodynamics as a special case.

The abovementioned methods are, generally speaking, based on the mathematical interpretation of the form-invariance. In this interpretation, the "form-invariance" is a pure mathematical property of a given set of equations. One needs first to find the transformed equations to verify whether they have the same forms as the original ones, if that is the case, the transformed relations for fields and materials can be obtained. Recently, Hu et al. and Chang et al. [18-20] have proposed another method to obtain the Eq. (3). In their method, the "form-invariance" is interpreted from the physical point of view, i.e., if the governing equation Eq. (1) is used for both homogeneous (isotropous) and inhomogeneous (anisotropic) materials, it is considered as form-invariant. In this framework, there is no need to find the transformed governing equation, because any reasonable governing equation must have clear answer for their application scope. The physical interpretation of form-invariance bring about conveniences in obtaining the transformed relations for field and material during a transformation, however as it is totally different to the usual methods, the difference and relationship between these two ideas should be give more clarifications. That is the objective of this paper.

The paper is arranged as follows: In Section 2, the "change of variable" method in transformation method is discussed, and the ambiguity implied in this idea is pointed out, then in Section 3 the method based on the physical interpretation of form-invariance is discussed. A sample is given to show the flexibility of this method in Section 4, with a concluding summary of the paper in Section 5.

2. The "change of variable" method in transformation method

The "change of variable" method is a representative method to obtain the Eq. (3) based on the mathematical interpretation of form-invariance. The main idea of this method has been briefly introduced in Section 1. In this section, we will give more detailed introduction to this method in context of elastodynamics according to Ref. [11, 15-16], and the ambiguity of this method will be demonstrate subsequently.

The governing equations of elastodynamics are

$$\nabla \cdot \boldsymbol{\sigma} = -\omega^2 \rho \mathbf{u}\,, \quad \boldsymbol{\sigma} = \mathbf{C} \nabla \mathbf{u}\,, \tag{4}$$

where $\mathbf{u}$ denotes displacement vector, $\boldsymbol{\sigma}$ is 2-order stress tensor, $\mathbf{C}$ is 4-order elasticity tensor, ρ is density and ω is the frequency. If one physical quantity transformation can be given first, then all the others can be obtained. For example, if one assumes the displacement vector has this transformation [11]

$$\mathbf{u}' = (\mathbf{A}^{\mathrm{T}})^{-1} \mathbf{u}\,, \tag{5}$$

where $\mathbf{A}$ is the Jacobian transformation tensor with the components $A_{ij} = \partial x'_i / \partial x_j$, then the transformations of other physical quantities, $\boldsymbol{\sigma}$, $\mathbf{C}$, ρ can be derived by submitting Eq. (5) to (4) and rewriting the equations respect to $\mathbf{x}'$. The "test function" method can be introduced to simplify the derivation [11]. One can find that the chain rule in calculus will lead to the form-variance of Eq. (4) in the new space Ω' [11]

$$\nabla' \cdot \boldsymbol{\sigma}' = \mathbf{D}' \nabla \mathbf{u}' - \omega^2 \boldsymbol{\rho}' \mathbf{u}'\,, \ \boldsymbol{\sigma}' = \mathbf{C}' \nabla' \mathbf{u}' + \mathbf{S}' \mathbf{u}'\,, \tag{6}$$

which are of the form of Willis' equations.

Realizing that the assumption of Eq. (5) is just a special case, Vasquez et al. [15] and Norris et al. [16] then propose a more general transformation of the displacement vector

$$\mathbf{u}' = \mathbf{B}^{-\mathrm{T}} \mathbf{u}\,, \tag{7}$$

where $\mathbf{B}$ is an arbitrary invertible matrix-like transformation operator. As the arbitrary operator $\mathbf{B}$ is introduced, the transformations of quantities in Eq. (6) are nonunique [15,16]

$$\begin{aligned} C'_{ijkl} &= J^{-1} A_{im} B_{jn} A_{kp} B_{lq} C_{mnpq}\,, \\ S'_{ijk} &= J^{-1} A_{im} B_{jn} \frac{\partial B_{kq}}{\partial x'_p} C_{mnpq}\,, \\ D'_{kij} &= B'_{ijk}\,, \\ \rho'_{ij} &= J^{-1} B_{ik} B_{jk} \rho - J^{-1} \omega^{-2} \frac{\partial B_{in}}{\partial x'_m} \frac{\partial B_{jq}}{\partial x'_p} C_{mnpq}\,, \end{aligned} \tag{8}$$

where $J = \det \mathbf{A}$. Hence, it is obvious that

(a) If $\mathbf{C}'$ needs to be full symmetric, i.e., $C'_{ijkl} = C'_{jikl} = C'_{klij}$, then one has to set $\mathbf{B} = \mathbf{A}$, the transformed equations become Eq. (6), and this the case by adopting the assumption of Eq. (5);

(b) If the transformed equations need to be keep their original form as Eq. (4), i.e., $\mathbf{D}' = \mathbf{S}' = 0$ in Eq. (6), then one has to set $\mathbf{B}$ = const, and thus $\mathbf{C}'$ loses it full symmetry because there may has $C'_{ijkl} \neq C'_{jikl}$. If $\mathbf{B} = \mathbf{I}$, the result of Brun et al. [17] can be included as a specifical case.

So far it is seems that the analyses are complete. However, the following question makes the above result becomes debatable: although Eq. (7) is more general than Eq. (5), it is still a special case, so why the special result should be think as the general one, and assert that Eq. (4) can not retain their form if the transformed elasticity tensor $\mathbf{C}'$ needs to be full symmetric? The real general transformation of displacement vector is

$$\mathbf{u}'(\mathbf{x}') = f(\mathbf{x}', \mathbf{x}, \mathbf{u}(\mathbf{x}))\,, \tag{9}$$

where f is an arbitrary continuous function, it can be much more complex than Eq. (7). In fact, as shown by Cevery [21], a time-harmonic solution of the elastodynamic

equation (4) for an inhomogeneous medium can be written in the form of a vectorial ray series

$$\tilde{\mathbf{u}}(\mathbf{x}',t)=\left[\sum_{n=0}^{\infty}\frac{\mathbf{U}_n(\mathbf{x}')}{(-i\omega)^n}\right]\exp[-i\omega(t-T(\mathbf{x}')], \quad (10)$$

and the system can be solved successively according to its recurrent character. Other literatures about the displacement solutions of inhomogeneous elastodynamic can be found in Ref. [22]. This type of displacement vector can not be expressed by the simple transformation Eq. (7). For the isotropous homogeneous medium, we can assume the transformations of the material parameters from space Ω to Ω', which transform the medium to anisotropies inhomogeneous one

$$g(\mathbf{x}',\mathbf{x},\mathbf{C}):\mathbf{C}\mapsto\tilde{\mathbf{C}}(\mathbf{x}'),$$
$$h(\mathbf{x}',\mathbf{x},\rho):\rho\mapsto\tilde{\rho}(\mathbf{x}'), \quad (11)$$

where g and h are given functions, and $\tilde{\mathbf{C}}$ is of full symmetric by this transformation, then the displacement solution $\tilde{\mathbf{u}}$ can be obtained by Eq. (10) in space Ω'. We have

$$\nabla\cdot\boldsymbol{\sigma}=-\omega^2\rho\mathbf{u},\ \ \boldsymbol{\sigma}=\mathbf{C}\nabla\mathbf{u},\ \ \mathbf{x}\in\Omega$$
$$\nabla'\cdot\tilde{\boldsymbol{\sigma}}=-\omega^2\tilde{\rho}\tilde{\mathbf{u}},\ \ \tilde{\boldsymbol{\sigma}}=\tilde{\mathbf{C}}\nabla'\tilde{\mathbf{u}},\ \ \mathbf{x}'\in\Omega' \quad (12)$$

where $\mathbf{u}$ is the solution of the isotropous homogeneous medium in space Ω, which can be of a harmonic plane wave form

$$\mathbf{u}(\mathbf{x})=\mathbf{U}(\mathbf{x})\ \exp\ (-i\omega(t-T(\mathbf{x}))). \quad (13)$$

Thus, according to Eq. (12), there must exist point-to-point mapping between space Ω and Ω'

$$\mathbf{C}\mapsto\tilde{\mathbf{C}}(\mathbf{x}'),$$
$$\rho\mapsto\tilde{\rho}(\mathbf{x}'), \quad (14)$$
$$\mathbf{u}(\mathbf{x},t)\mapsto\tilde{\mathbf{u}}(\mathbf{x}',t).$$

Equations (14) clearly show that even if the elasticity tensor keeps full symmetric, the elastodynamic equation (4) can be form-invariant for a general space mapping, provide the transformation of the displacement vector can be properly assumed. This result disagrees with the assertions (a) and (b) in this section.

However, although the elastodynamic equation can, in principle, be form-invariant from the pure mathematic point of view, it not indicates that Eq. (14) can be used in the framework of transformation method to control the displacement field. This is because the inhomogeneous elastodynamic equations are equivalent to have non-physical sources term, thus the displacement solution Eq. (10) is not a smooth wave field, but a scattered wave field [21], which usually can not satisfy the engineering design requirement.

This fact demystifies the key point in the transformation method: the method does not concern for *whether* the governing equations can be mapped (form-invariance) or not, instead, it concern for *what kind of* mapping (form-invariance) the equations have, or the characters of the transformed relations Eq. (3).

For high frequency elastic waves (ω >>1), one can only use the zeroth-order term in the series of Eq. (10)

$$\tilde{\mathbf{u}}_0(\mathbf{x}',t)=\mathbf{U}_0(\mathbf{x}')\exp[-i\omega(t-T(\mathbf{x}')]. \quad (15)$$

In this approximation, Eq. (10) is reduced to the form of plane wave form Eq. (13), which presents a smooth wave field, and can be used in the frame work of transformation method. The local linear transformation must exist between the displacement vectors $\mathbf{u}$ and $\tilde{\mathbf{u}}_0$ because of their identical forms. This condition is also true for electromagnetic and acoustic waves, if the local linear transformation can be found, then Eq. (3) can be used in transformation method. However, this "local linear" restrict can not be naturally introduced into the "change of variable" method, because this restrict is based on the strong physical and engineering background, while the "change of variable" method is based on the mathematical interpretation of the "form-invariance". Thus, deeper physical insight should be introduced into the transformation method.

3. Physical interpretation of the form-invariance

The objective of the transformation method is to control some physical fields by designed appropriate materials, and the achieved materials are usually inhomogeneous and anisotropic. Thus, if one wants to manipulate the physical fields in such media, he must in advance know the governing equations for these materials. In view of this, Hu et al. [18] give the physical interpretation of the form-invariance: the governing equation (1) is used for isotropic homogeneous materials, if it can also be used for the anisotropic inhomogeneous materials, then it is considered as form-invariant. Namely, in this interpretation, Eq. (1) and Eq. (2) are the governing equations for isotropic homogeneous and anisotropic inhomogeneous materials, respectively. For example, in classical physics, Maxwell's equations

$$\nabla\times\mathbf{E}=-\boldsymbol{\mu}\frac{\partial\mathbf{H}}{\partial t},\quad \nabla\times\mathbf{H}=+\boldsymbol{\varepsilon}\frac{\partial\mathbf{E}}{\partial t}, \quad (16)$$

can be equally used for both isotropic homogeneous materials and anisotropic inhomogeneous materials. Similarly, the classical acoustic wave equation

$$\nabla p=\rho\ddot{\mathbf{u}},\ \ p=\kappa\nabla\cdot\mathbf{u}, \quad (17)$$

can also be equally used for both isotropic homogeneous materials and anisotropic inhomogeneous materials, where the mass density is assumed to have a tensor form in general. For the classical elastodynamics equations (4), although some use it for inhomogeneous materials, but as shown in Ref. [23,24], in such cases elastodynamics should be governed by Willis equations.

The essential difference between acoustics (or optics) and elastodynamics is that the former is established by the

first-order approximation, i.e., the variation of a quantity around a point is expressed by Taylor series expansion with higher-order terms being neglected. Then the physical model of the Eq. (16) or (17) is simply based on a point, which can be used for both homogeneous and inhomogeneous materials. In contrast, elastodynamics must consider the moment effect, thus the physical model is based on a finite area rather than a point that cannot support moment. The balance equation of angular momentum by first-order approximation is written as (without summation)

$$\sigma_{ij} + \frac{1}{2}\frac{\partial \sigma_{ij}}{\partial x_i} dx_i = \sigma_{ji} + \frac{1}{2}\frac{\partial \sigma_{ji}}{\partial x_j} dx_j , \qquad (18)$$

where i,j=1,2,3 $i \neq j$. Equations (18) complete the elastodynamics equations in addition to Eq. (4). However, Eq. (18) are difficult to solve, so one can simplified it to

$$\sigma_{ij} = \sigma_{ji} \qquad (19)$$

by zero-order approximations. Equation (19) is usually omitted in Navier's equation because it is included by the symmetry of classical elasticity tensor. Thus, equations (4) with symmetric elasticity tensor in fact use zero-order approximation and are proper only for slowly varying materials (or high-frequency waves).

The detailed discussions on the precision of the governing equations are beyond the scope of this paper. What we want to emphasize is that in the physical interpretation, the "form-invariance" or "form-variance" of the governing equations is already known before obtaining Eq. (3). The anisotropic inhomogeneous material can be regarded as transformed from the isotropic homogeneous one. However the transformation can be arbitrary, different transformations will lead to different material, then how to find the appropriate transformation that can be used to control the physical fields? The transformation method gives a graceful solution: it connects the material transformation to a point-to-point coordinates mapping between the two materials and the local properties of the transformed material is determined by the local geometrical property of this space mapping. Though this way, the material can be transformed via a certain visualized method point by point, in turn the physical fields related to material.

Hu et al. [25] further recognize that the space mapping is equivalent to space deformation. If Eq. (1) and Eq. (2) are established by first-order approximation, the local linear transformation must exist between them. So the space deformation can also be interpreted by first-order approximation, or the space deformation is regarded as local affine deformation point-by-point, and the physical quantities transformations are equivalent to physical quantities deformations arouse by space deformation. Afterwards, according to continuum mechanics, the deformation gradient tensor $\mathbf{A}$ (equals to the Jacobian transformation tensor) induced by the space mapping can be decomposed by a rotation (orthogonal) tensor $\mathbf{R}$ and a pure stretch tensor $\mathbf{V}$ as $\mathbf{A} = \mathbf{VR}$. Suppose at each point $\mathbf{e}'_i$ and λ_i respectively the eigenvectors and eigenvalues of $\mathbf{V}$, then there are $\mathbf{V} = \lambda_1 \mathbf{e}'_1 \mathbf{e}'_1 + \lambda_2 \mathbf{e}'_2 \mathbf{e}'_2 + \lambda_3 \mathbf{e}'_3 \mathbf{e}'_3$. The physical field $\mathbf{u}$ and material $\mathbf{C}$ in the initial space are rigidly rotated with the element to the local system $\mathbf{e}'$ of the transformed space, in the new local Cartesian system $\mathbf{e}'$ the components of the field $\mathbf{u}$ and material $\mathbf{C}$ will then be rescaled along $\mathbf{e}'_i$. Symbolically the transformations can be written as

$$\mathbf{V_q R}: \mathbf{q} \mapsto \mathbf{q}', \quad \mathbf{q} = \mathbf{u}, \mathbf{C} , \qquad (20)$$

where $\mathbf{V_q}$ is the scaling tensor for the quantity $\mathbf{q}$, and has a diagonal form in the specially established frame $\mathbf{e}'$, i.e., $\mathbf{V_q} = \mathrm{diag}[q_1, q_2, q_3]$, where q_i are scaling factors to be determined. The form-invariance of Eq. (1) and (2) and differential relation between the two spaces $\partial / \partial x'_i = (1/\lambda_i)\partial / \partial x_i$ can lead to the some conditions for determining the scaling factors. In addition, one should assume during the mapping, each type of energy is conserved and there is not energy conversion. If $w(\mathbf{u}, \mathbf{C})$ and $w'(\mathbf{u}', \mathbf{C}')$ denote respectively any type of energy densities in the initial and transformed spaces, the volume of an element dv becomes $\lambda_1 \lambda_2 \lambda_3 dv$ during the mapping, so the energy conservation of each point leads to the following physical constraint condition

$$w(\mathbf{u}, \mathbf{C}) = w'(\mathbf{u}', \mathbf{C}') \lambda_1 \lambda_2 \lambda_3 . \qquad (21)$$

The energy conservation will provide other constraint condition for the scaling factors. The constraint conditions will allow one finally to determine the transformed relations for the field and material.

This theory provides a general method to determine the transformed relations for any physical process governed by a set of PDE, if the PDEs are established by the first-order approximation. Hu et al. [18] show that the constraint conditions are not enough to determine completely the transformed relation for transformation acoustics, leaving a possibility to define them differently as found in the literature. New acoustic transformations with constant density or modulus are also proposed. They also show that the transformed relation is uniquely determined for transformation optics. With help of this theory, we have a convenient method to explore the transformation method in a vast range of potential dynamical systems.

4. Transformation elastodynamics sample

The theory based on the physical interpretation of the form-invariance can work well for those equations established by the first-order approximation, because in these cases the equations can be equally used for both homogeneous and inhomogeneous materials. However, the method is not limited for those equations; the physical view make it has more flexibility in material design compared to the usual method such as change of variable method.

Recall the physical interpretation of the form-invariance, the designer should in advance knows the governing equations for the inhomogeneous and anisotropic material, thus, even if the equations is not a standard first-order

approximation but within some application scope they can be used in the inhomogeneous media, then the form-invariance still exists. Take the elastodynamics as an example. It is known that Eq. (4) with symmetric elasticity tensor can not be used in inhomogeneous materials, however, in the high-frequency waves or slowly varying materials cases, these equations can be used approximatively. Therefore, in this limit, one can still explore the method introduced in the previous section to obtain the transformed relations of Eq. (4).

As shown in Ref. [21,26], the researches on the high frequency (short wavelength) have a long history in acoustic and elastodynamic wave propagation problems for various important applications, such as in seismology, petroleum exploration, nondestructive ultrasound evaluation and other important areas. In addition, as shown in Ref. [21], the condition of high frequency has only a relative meaning. It requires that the appropriate material parameters of the media do not vary greatly over an order of wavelength, for example, in seismology, sometime the wave with frequency ≈ 8 Hz can be considered as high frequency. Thus, the high frequency transformation elastodynamics is useful in practice.

The transformed relations are derived directly from the constraint conditions, none of transformed relation is pre-assumed, and as the constraint equations of elastodynamics have non-unique solution, various transformations can be obtained [19-20]. Interestingly, in the local conformal space mapping, which will lead to both isotropic transformed modulus and density, the impedance-matched condition for both S and P waves in perpendicularly incident cases exists

$$E' = \lambda E, \quad \upsilon' = \upsilon, \quad \rho' = \rho / \lambda , \tag{22}$$

where E and υ denote Young's modulus and Poisson's ratio of the media, respectively, and λ is the local scaling factors of the conformal space mapping. Equations (22) show that for the perpendicularly incident elastic waves, the impedance-matched condition does not require the boundary between the transformed media and the background media to be fixed, in contrast to the electromagnetic waves [27,28]. Thus, we can design an approximative elastic waves cloak with isotropous homogeneous material. Let a region with a hole has a uniform magnifying

$$\mathbf{x}' = \lambda \mathbf{x} ,. \tag{23}$$

where λ >1 is a constant real. Then with help of the designed cloak, the scattering arouse by the obstacle in the hole can be smaller compared to that without the cloak, because the cloak as effective as to "compress" the obstacle size. Equations (22) guarantee there are no scattering in the incident boundary, and the cloak is of isotropous and homogeneous. The space mapping is shown in Fig. 1. The simulation result is shown in Fig. 2, where the constant scaling factor λ =3 and the background media is the structural steel with material parameters $E = 200\text{Gpa}$, $\upsilon = 0.33$ and $\rho = 7850\ \text{kg/m}^3$. The obstacle has material parameter $E_{obs} = 10E$ and other parameters are as same as the background. It is shown that the cloak can obviously reduce the scattering.

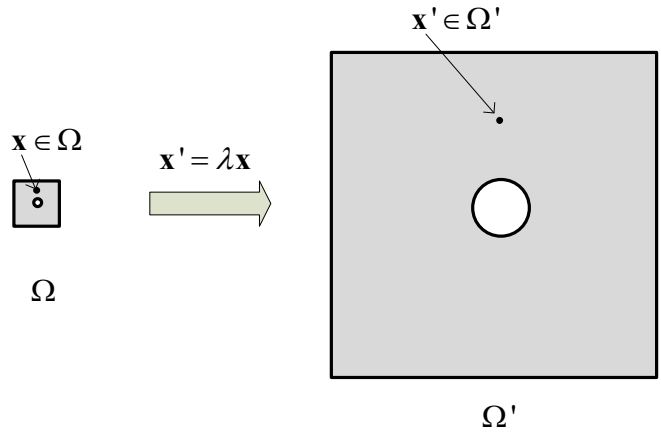

Figure 1: The space mapping of the approximative elastic waves cloak with isotropous homogeneous material.

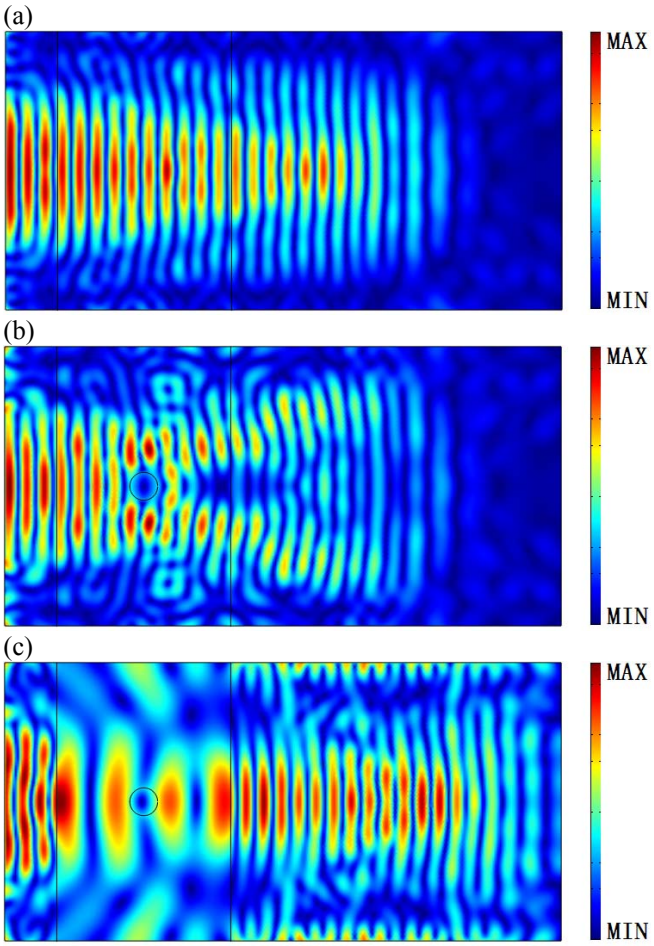

Figure 2: The simulation result (total displacement) of the designed elastic waves cloak. (a) Original waves without obstacle; (b) waves without cloak; (c) waves with the designed cloak.

5. Discussion and conclusions

This paper review some important concepts and methods contained in transformation method. The transformed relations for field and material during a transformation, equations (3), are very important in the framework of transformation method. The usual methods to obtain Eq. (3) are based on the mathematical interpretation of the form-invariance, where the form-invariance is a pure mathematical property of a given set of equations, that one need to verify. The "change of variable" method is a representative method of this idea. It needs to assume certain transformed relations for some physical quantities first, and then express the others in a general arbitrary curvilinear coordinate system according to the coordinate transformation laws. Thus the results depend on the pre-assumed transformed relations and this method can not obtain the full transformed relations. More important, the mathematical interpretation of the form-invariance masks the physical essence implicated in the transformation method, i.e., the most important question need to answer is not whether the governing equations can be mapped or not, but what kind of mapping the equations have.

An alternative interpretation to the form-invariance is explored. The main idea is that if the governing equation is used for both homogeneous and inhomogeneous materials in its known scope, or it is physically form-invariant, then there is no need to find the governing equation for the inhomogeneous materials by "change of variable" method. If the governing equation is established by the first-order approximation, one can also interpret the general mapping by first-order approximation. The transformed material property and physical field are constrained by some constraint conditions. The flexibility of this method is discussed, followed by a demonstration of an isotropous homogeneous approximative elastic cloak.

Acknowledgements

This work was supported by the National Natural Science Foundation of China (11172037).

References

[1] A. Greenleaf, M. Lassas, and G. Uhlmann, Math. Res.Lett. 10, 685-693 (2003).

[2] J. B. Pendry, D. Schurig, and D. R. Smith, Science 312, 1780-1782 (2006).

[3] U. Leonhardt, Science 312, 1777-1780 (2006).

[4] D. Schurig, J. J. Mock, B. J. Justice, S. A. Cummer, J. B. Pendry, A. F. Starr, and D. R. Smith, Science 314, 977-980 (2006).

[5] H. Chen and C. T. Chan, Appl. Phys. Lett. 91, 183518 (2007).

[6] S. A. Cummer, B. Popa, D. Schurig, D. R. Smith, J. Pendry, M. Rahm and A. Starr, Phys. Rev. Lett. 100, 024301 (2008).

[7] T. Chen, C. N Weng and J. S. Chen, Appl. Phys. Lett. 93, 114103 (2008).

[8] S. Zhang, D. A. Genov, C. Sun and X. Zhang, Phys. Rev. Lett. 100, 123002 (2008).

[9] S. A. Cummer, M. Rahm and D. Schurig, New J. Phys. 10, 115025(2008).

[10] A. Greenleaf, Y. Kurylev, M. Lassas and G. Uhlmann,, Comm. Math. Phys. 275, 749 (2007).

[11] G. W. Milton, M. Briane and J. R. Willis, New J. Phys. 8, 248(2006).

[12] A. Norris, Proc. R. Soc. A 464, 2411 (2008).

[13] G. W. Milton and A. V. Cherkaev, J. Eng. Mater. Technol. 117, 483 (1995).

[14] U. Leonhardt and T. G. Philbin, New J. Phys. 8, 247(2006).

[15] F. G. Vasquez, G. W. Milton, D. O. and P. Seppecher, arXiv:1105.1221v1.

[16] N. Norris, A. L. Shuvalov. Wave Motion 48, 525(2011).

[17] M. Brun, S. Guenneau and A. B. Movchan, Appl. Phys. Lett. 94, 061903 (2009).

[18] J. Hu, X. N. Liu and G. K. Hu, arXiv:0912.5462.

[19] J. Hu J, Z. Chang, and G. Hu, Phys. Rev. B 84, 201101(R) (2011).

[20] Z. Chang, J. Hu, G .Hu, R. Tao and Y. Wang, Appl. Phys. Lett. 98, 121904(2011).

[21] V. Cerveny, *Seismic Ray Theory* (Cambridge University Press, Cambridge, 2001).

[22] Y-H. Pao, J. Appl. Mech. 50, 1152 (1983).

[23] G. W. Milton and J. R. Willis, Proc. Roy. Soc. A 463, 855 (2007).

[24] J. R. Willis, *Dynamics of composites In Continuum Micromechanics*, pp 265–90 (CISM Lecture Notes, Springer, New York, 1997).

[25] J. Hu, X. Zhou and G. Hu, Opt. Express 17, 1308 (2009).

[26] V. Pereyra, Inverse Problem. 16, R1–R35 (2000)

[27] J. Hu, X. Zhou, G. Hu, Appl. Phys. Lett., 95, 011107(2009).

[28] W. Yan, M. Yan, Z. Ruan and M. Qiu, New J. Phys. 10, 043040 (2006).

Ultra-thin electromagnetic absorbers for mm- and submm-waves: from fundamentals towards applications in bolometric sensors

Sergey Kuznetsov[1,2], Andrey Arzhannikov[1,2], Manfred Thumm[1,3], Andrey Paulish[1,4], Alexander Gelfand[1,4], Victor Fedorinin[1,4], Miguel Beruete[5], Miguel Navarro-Cía[6], and Mario Sorolla[5]

[1]Analytical and Technological Innovation Center "High Technologies and Novel Materials," Novosibirsk State University, Novosibirsk, Russia
[2]Budker Institute of Nuclear Physics SB RAS, Novosibirsk, Russia
[3]Karlsruhe Institute of Technology, Karlsruhe, Germany
[4]Institute of Semiconductor Physics SB RAS, Novosibirsk Branch "TDIAM", Novosibirsk, Russia
[5]Millimeter and Terahertz Waves Laboratory, Public University of Navarre, Pamplona, Spain
[6]Experimental Solid State Group, Department of Physics, Imperial College London, London, UK
*corresponding author, E-mail: SAKuznetsov@nsm.nsu.ru

Abstract

We overview the results of theoretical and on-going experimental investigations of electrically ultra-thin metamaterial-inspired absorbers operating in the range of millimetre and submillimetre waves and intended for integration with spectrally-selective bolometric devices. The attainability of values up to 180 for the ratio of the free-space wavelength to the absorber's thickness is experimentally demonstrated. The first prototypes of spectrophotometric and imaging detectors utilizing metamaterial-based radiation-sensitive pixels are presented.

1. Introduction

The range of short millimeter and submillimeter waves of the terahertz spectrum (0.1-1 THz) remains an attractive area for applied sciences and technologies due to high penetrability of T-rays through various optically opaque materials and media, as well as attainability of a sufficient spatial resolution upon object imaging [1, 2]. When investigating objects, their data information can be noticeably increased if different spectral bands and polarization discrimination are involved in data processing. Such terahertz sensors or cameras, combining the options of high spatial resolution, multispectral capability, polarization sensitivity, low cost and real-time operation are commercially unavailable and remain much demanded.

In this contribution we discuss the concepts of micro-Golay cell arrays and THz-to-IR converters, as the flexible uncooled bolometric detectors with the aforementioned functional capabilities that were recently developed by our group for spectropolarimetric applications and imaging with CW terahertz oscillators [3-5]. Both the micro-Golay cell array detector and the THz-to-IR converter are estimated to be flexible to the choice of the operating wavelength and have no principle constraint on the array's overall dimensions due to an optical readout system, which does not demand development of a specially designed multiplexer system integrated with sensitive elements. It is essential that adaptation of these detectors to the THz band became feasible due to elaboration of the concept of electrically thin electromagnetic absorbers with a close to unity absorptivity within a desired frequency range [6, 7]. Such absorbers are frequently considered as a kind of artificial engineered or metamaterial structures and can be effectively designed by using the concept of high-impedance or artificial impedance surfaces (AISs) [7]. Unlike the classical Salisbury, Jaumann, or Dallenbach electromagnetic absorbers based on unfavorably thick quarter-wave absorbing layers, the AIS absorbers allow one to attain the ratio of the free-space wavelength λ to the absorber's thickness d of at least several tens. The condition $\lambda / d >> 1$ is essential for decreasing the absorber's heat capacity that enables achieving high sensitivity and low response time of the bolometric detector. The investigations also show that the increase of the λ / d ratio inevitably leads to decreasing the absorption bandwidth, making AIS absorbers ideally applicable to bolometric detectors with a high spectral resolution.

In this work we overview the results of theoretical and experimental investigations of ultra-thin AIS absorbers of different configurations, designed for narrow-band operation in the frequency range 0.05-0.5 THz. The prospects for application of such absorbers in uncooled bolometric sensors are experimentally demonstrated.

2. Ideology of ultra-thin absorbers

The ideology of high-performance electromagnetic absorbers, exhibiting a considerable excess of the operating free-space wavelength λ over the absorber thickness d, is built on manipulating a spatial distribution of the electromagnetic field to shift the electric field antinode onto the lossy surface of the absorber. This goal can be effectively achieved by using a high-impedance surface

(HIS) approach [7]. The conventional HIS is represented by a subwavelength single-layer frequency-selective surface (FSS) of a capacitive kind placed over a thin grounded dielectric slab. At the HIS resonance frequency, the surface impedance tends to infinity, yielding a zero reflection phase. In this case, the tangential component of the total magnetic filed formed by the incident and reflected waves vanishes upon the HIS surface (the "magnetic wall" condition), while the electric component is maximized. By properly incorporating dissipative losses into FSS or the dielectric slab, the regime of perfect absorption can be further easily realized. If a dissipative parameter is chosen to be small enough, the absorption resonance Q-factor and the absorber's λ/d ratio can reach the level of several hundreds that is attractive for spectrophotometric applications.

3. Selected results

By appealing to an equivalent circuit model analysis and 3D full-wave electromagnetic simulations, we thoroughly analyze the ultimate performance of ultra-thin absorbers with different FSS geometries and establish fundamental relations between the resonant absorption bandwidth, wavelength-to-thickness ratio, FSS conductivity, dielectric slab loss tangent, and other parameters (see [3] for details). Through the performed analysis we highlight the advantage of the low-loss bulk materials to maximize the absorber's λ/d ratio and spectral selectivity. As a result, when implementing experimentally, polypropylene (PP) material was chosen as the caring dielectric for the absorber's substrates (PP permittivity: $\varepsilon \cong 2.27 - j \cdot 4 \times 10^{-4}$), while highly conductive metallization (with typical conductivity $\sigma \geq 2 \times 10^7$ S/m and thickness 0.4 μm) was utilized in the FSS and "ground" layers. Our analysis shows that for PP-based absorbers the energy dissipation occurs mainly in the metallized FSS layer, unlike the results of other research groups reported on absorption predominance in the dielectric slab [6, 7].

Designed for operation in the frequency range 0.05–0.5 THz and utilizing FSS of different geometries, the experimental prototypes of ultra-thin absorbers were fabricated via a contact photolithography technique. Limited by the fabrication technology, the absorber's λ/d ratios in our case were shown to attain the values ~50 for FSS with split-ring resonator elements, while reaching the record-breaking magnitudes ~180 for FSS comprised by metallic patches. The results of the electromagnetic modeling for such ultra-thin absorbers are in a good agreement with their experimental characterization by using a subTHz BWO-spectrometer and AB mm™ Vector Network Analyzer, which demonstrated 90-99.9% of the resonant absorptivity for the designed wavelengths at bandwidth selectivity of several percent.

The developed absorbers were further effectively used for integration with T-ray sensing devices (single-channel and matrix sensors), and we present the first results on single- and multi-spectral subterahertz imaging and spectropolarimetry using such detectors (Fig. 1).

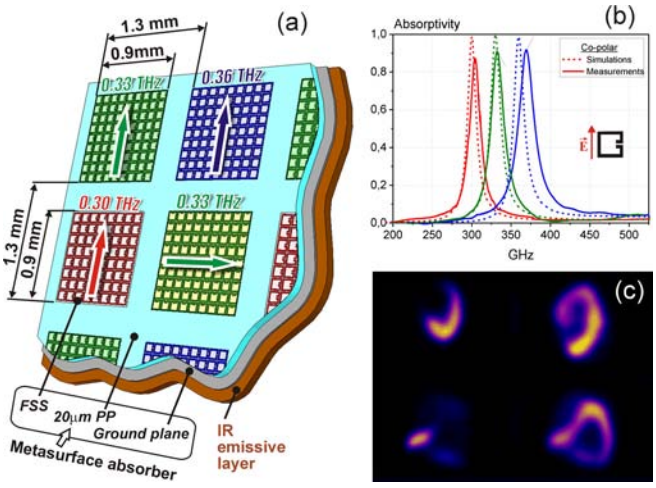

Figure 1: Implementing a 3-spectral polarization-sensitive terahertz imager based on the THz-to-IR converter concept [3]–[5]. (a) Matrix structure of absorbers with split ring resonator elements. (b) Spectral absorptivity of matrix pixels for optimal polarization. (c) Movie's screen-shots at real-time imaging of the radiation beam from a backward-wave oscillator of the milliwatt output radiation power level.

Acknowledgements

This work is supported by the grant 11.G34.31.0033 of the Russian Federation Government, the contract 16.740.11.0377 via the Federal Target Program and by the Spanish Government and E.U. FEDER funds under contracts Consolider "Engineering Metamaterials" CSD2008-00066.

References

[1] L. Yun-Shik, *Principles of THz Science and Technology*, Springer, 2009.

[2] K. Sakai, ed., *Terahertz Optoelectronics*, Springer-Verlag, New York, 2005.

[3] S.A. Kuznetsov et al., Ultrathin electromagnetic absorbers for uncooled subterahertz imagers, to be published in *IEEE Trans. THz Sci. and Tech.*, 2012.

[4] S.A. Kuznetsov et al., Bolometric THz-to-IR converter for terahertz imaging, *APL*, V. 99, Iss. 2, 023501, 2011.

[5] S.A. Kuznetsov et al., Matrix structure of metamaterial absorbers for mutispectral terahertz imaging, *PIER*, Vol. 122, 93–103, 2012.

[6] W. Padilla and X. Liu, Perfect electromagnetic absorbers from microwave to optical, *Optical Design & Engineering,* SPIE Newsroom, 2010, 10.1117/2.1201009.003137, pp 1-3.

[7] N. Engheta, R. W. Ziolkowski, *Electromagnetic Metamaterials: Physics and Engineering Explorations*, Wiley and IEEE Press 2006.

Control the phase by using the mimicking electromagnetically induced transparency in planar metamaterial

J. F. Zhao[1], Y. W. Zhang[1*], L. W. Zhang[1,2]

1 MOE Key Laboratory of Advanced Micro-structure Materials, Department of Physics, Tongji University, Shanghai 200092, PR China
2 School of Physics and Chemistry, Henan Polytechnic University, Jiaozuo 454000
*corresponding author: yewen.zhang@tongji.edu.cn

Abstract

The mimicking electromagnetically induced transparency (EIT) can be achieved by the concentric double rings structure in planar metamaterial. The transmission phases in the transparency window are simulated by Finite Difference Time Domain method. It is shown that the wide nearly linear tuning can be achieved by varying the structure parameters. By using this kind of planar structure, the phase of plane wave can be controlled clearly.

1. Introduction

Planar metamaterial attracts much attention due to their singular properties, such as mimicking electromagnetically induced transparency (EIT), extraordinary transmission [1] and negative refraction [2]. EIT is caused by destructive quantum interference in atomic systems, which lead to the reduced absorption of the incident light or even complete transparency around the resonance frequency [3-4]. This strong dispersion has important consequences in reducing the group velocity and enhancing nonlinear interactions [5-6]. Recently, by the artificial "atoms" in planar metamaterial, the mimicking EIT spectrum were achieved in classic systems [7-9] whose operating frequency can be easily tuned by the geometry of the structures. Among these structures the Double-Ring (DR) structure which consists of pairs of concentric metal rings is insensitive with the polarization and direction of the incident wave in mimicking EIT [10].

In this paper, the transmission phase properties of the DR-structure are studied by simulation, and the linearly variation of the transmission phase is achieved by tuning the geometry parameters.

2. Theory model and analysis

This planar metamaterial consists of array of pairs of concentric rings is shown in Figure 1(a). The dimension of the unit cell which contains one pair of concentric copper rings is $10 \times 10\text{mm}^2$ (Figure 1(b)) and the thickness of the copper pattern is 18μm. The host medium is designed with a dielectric substrate ($\varepsilon_r = 2.2$) with the height h=0.787mm. Wi and Wo indicate the line width of the inner ring and outer ring respectively. Ri and Ro represent the radius of the inner ring and outer ring. In simulation Wi= Wo= 0.2mm, Ro= 4.1mm, Ri=3.61mm.

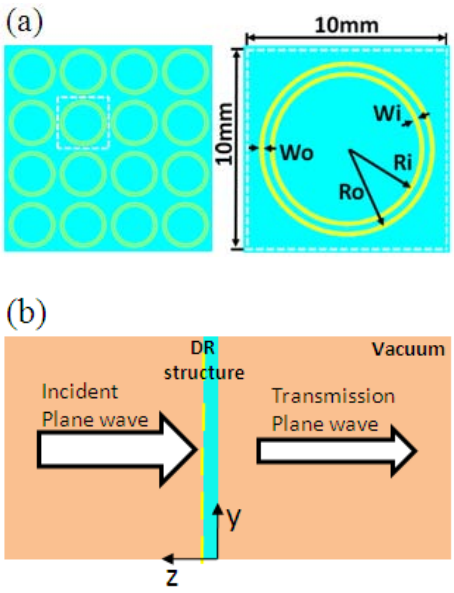

Figure 1: Model of the simulation, (a) Diagram of the DR-structure, dashed box indicates the unit cell. (b) Schematic diagram of the simulation. The yellow dashed lines indicate the DRs and the blue rectangle indicates the substrate of the planar metamaterial.

The plane wave source is put in the left side in vacuum where z>0 is shown in Figure 1(b). The planar metamaterial locates around z=0. For normal incidence, Spectra is simulated by using the time domain simulator of the commercial software CST as show in Figure 2.The red solid line indicates the transmission phase advance and the red dash line indicates the transmission. The transparency window caused by interference of the two resonances is around the frequency of 10 GHz (vertical dot line) with quality (Q) factors (define as the ratio of the resonance frequency to the bandwidth) is about 8.2. We can also find a sharp phase dispersion around 10GHz. This mimicking EIT phenomenon is based on the existence of the trapped mode, which is caused by the inner ring and the outer ring excited equally but in opposite phase [10]. This current distribution make the scattered field is very weak and high Q factor.

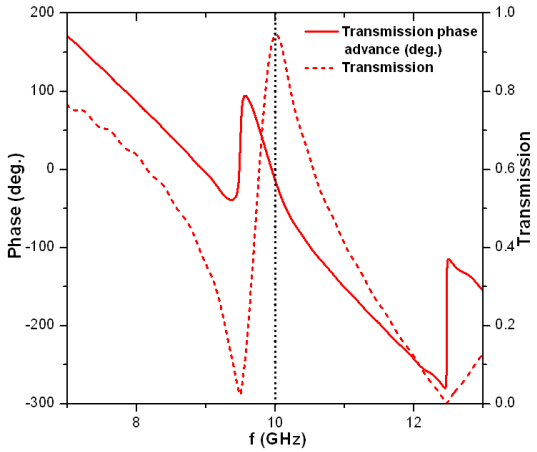

Figure 2: Transmission spectrum of the planar metamaterial with corresponding phase.

3. Results and discussion

Based on the model above, the fact that the transmission phase and transmission varies rapidly with the geometric parameters has been found. Farther research shows that by fine tune the radius of the inner rings (Ri) at 10GHz while fix the other geometric parameters, the most rapidly phase changes can be obtained as shown in Figure 3. The transmission phase advance and transmission are indicated by blue empty triangle and blue empty circle. The blue solid line is the linear fit of the transmission phase advance, from where we can find the linear relation between the radius of the inner ring and the transmission phase clearly. 104 degree' changes can be got with the minute variation of Ri ranging from 3.45mm to 3.8mm.At the same time, the transmission can be ensured greater than 50% by eliminating marginal points.

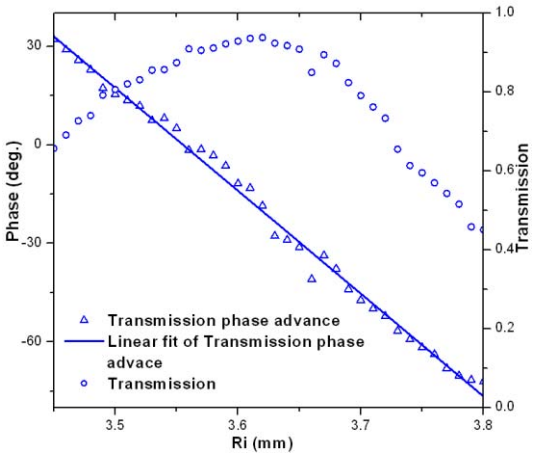

Figure 3: Transmission phase advance vary along with radius of the inner ring at 10GHz.

The phase control by tuning the geometry parameters has important consequence in antenna design. Transplant concept from the optics [9], a new way to control the wavefront can be attained by introducing this kind of phase shift to the path. For example, the angle of the refraction of normal incidence plane wave can be controlled.

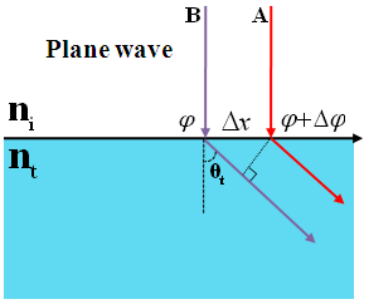

Figure 4: Schematics of the deformation of the Fermat's principle. Red solid line indicate the Way1, Purple solid line indicate the Way2. Φ and $\varphi + \Delta\varphi$ (Radian) are the phase shifts between two path way cross the interface

Based on Fermat's principle, the phase shift between two paths should be zero

$$[k_0 n_t \sin(\theta_t)\,\Delta x + \varphi] - [\varphi + \Delta\varphi] = 0 \qquad (1)$$

Where θ_t is the angle of the refraction; Δx is the distance between the crossing points; Φ and $\varphi + \Delta\varphi$ (Radian) are the phase shifts between two paths cross the interface; n_t is the index of the refraction of the transmission medium; $k_0 = 2\pi/\lambda_0$ and λ_0 the vacuum wavelength.

$$\sin(\theta_t) = \frac{\lambda_0}{2\pi n_t}\frac{\Delta\varphi}{\Delta x} \quad (2)$$

and

$$\theta_t = \arcsin\left(\frac{\lambda_0}{2\pi n_t}\frac{\Delta\varphi}{\Delta x}\right) \quad (3)$$

From what we study above, $\frac{\Delta\varphi}{\Delta x}$ along the interface can be achieved by configuring the proper geometry of this kind of planar metamatrials. And since $\frac{\Delta\varphi}{\Delta x}$ can be negative, the negative refraction can be attained.

To demonstrate the angle of the refraction that can be adjusted, a simple simulation has been carried out. The group a b c and d indicate different configurations of Ri which listed in the Table 1. The difference of the phase shift crossing the interface between two adjacent configurations is 25 degree ($\Delta\varphi$). Δx is the side length of the unit cell. λ_0 is the vacuum wavelength at 10GHz.For the simulation as shown in Figure 1(b), $n_t = n_0 = 1$.

$$\theta_t = \arcsin\left(\frac{30\text{mm}}{2\pi}\frac{25}{10\text{mm}}\frac{2\pi}{360}\right) = 12^o \quad (4)$$

From the simulation of the scattered electric field for the individual configuration as showed in Figure 5(the difference of the scattered electric field strength is caused by the different transmission), an angle about 12 degree of inclination (θ_i) was obtained, which is in good agreement with the calculation (θ_t).

Table 1: the configuration of the Ri

Group	Ri [mm]
a	3.49
b	3.59
c	3.65
d	3.73

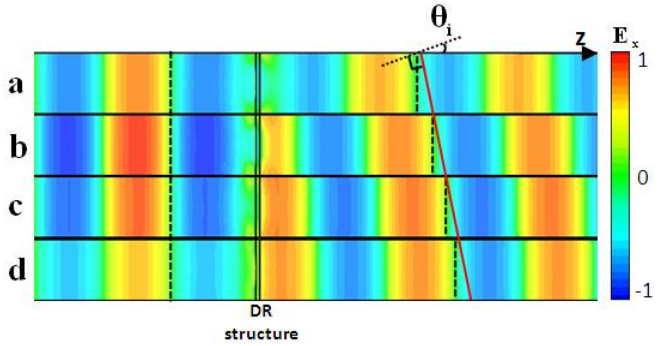

Figure 5: Simulation of the scattered electric field for the individual configuration of the DR structure. Black dash lines indicate the wave front of the individual electric field. Red solid line indicates the co-wavefront, and θ_i is the angle of the inclination.

4. Conclusions

To summarize, the DR structure has been studied in theory. And the linearly variation of the transmission phase was achieved. That is to say that by using planar structure we can control the phase of plane wave. Combining this property and Fermat's principle we can develop a novel lens antenna, which may lead to a significant decrease in volume compare to the traditional ones.

Acknowledgements

Supported by National Basic Program (973) of China (No.2011CB922001), and by the National Natural Science Foundation of China (Nos. 10904032).

References

[1] W.L. Barnes, W.A. Murray, J. Dintinger, E. Devaux, T.W. Ebbesen, Surface plasmon polaritons and their role in the enhanced transmission of light through periodic arrays of subwavelength holes in a metal film, *Phys. Rev. Let*, Vol. 92, 107401, 2004.

[2] Y.Z. Cheng, H.L. Yang, Y. Nie, R.Z. Gong, Z.Z. Cheng, Investigation of negative index properties of planar metamaterials based on split-ring pairs, Appl Phys A 103: 989-994, 2011.

[3] S.E. Harris, J.E. Field and A. Imamoglu, Nonlinear optical processes using electromagnetically induced transparency, *Phys. Rev. Let*, Vol. 64, 1107, 1990.

[4] M. Fleischhauer, A. Imamoglu, J.P. Marangos, Electromagnetically induced transparency: Optics in coherent media, *Rev. Mod. Phys*, Vol. 77, 633, 2005.

[5] L.V. Hau, S.E. Harris, Z.Dutton, C.H.Behroozi, Light speed reduction to 17 metres per second in an ultracold atomic gas, *Nature* 397, 594 , 1999.

[6] S.E. Harris, L.V. Hau, *Phys. Rev. Lett.* 64, 1107, 1999.

[7] V.A. Fedotov, M. Rose, S.L. Prosvirnin, N. Papasimakis, N.I. Zheludev, Sharp trapped-mode resonances in planar metamaterials with a broken structural symmetry, *Phys. Rev. Lett*, Vol. 99, 147401, 2007

[8] S. Zhang, D.A. Genov, Y. Wang, M. Liu and X. Zhang, Plasmon-indced transparency in metamaterial, *Phys. Rev. Lett*, Vol. 101, 047401, 2008

[9] S.Y. Chiam, R.J. Singh, C. Rochstuhl, F. Lederer, W.L. Zhang, A.A. Bettiol, Analogue of electromagnetically induced transparency in a terahertz metamaterial, *Phys. Rev. B*, Vol. 80, 153103, 2009

[10] N. Papasimakis, Y.H. Fu, V.A. Fedotov, S.L. Prosvirnin, D.P. Tsai, N.I. Zheludev, Metamaterial with polarization and direction insensitive resonant transmission response mimicking electromagnerically induced transparency, *Appl. Phys. Lett*, Vol.94, 211902, 2009.

[11] N.F. Yu, P. Genevet, M.A. Kats, F. Aieta, J.-P. Tetienne, F. Capasso, Z. Gaburro, Light propagation with phase discontinuities: generalized laws of reflection and refraction, *Science,* Vol.334, 6054, 2011.

Temperature-agile and Structure-tunable Optical Properties of VO_2/Ag Thin Films

X. R. Zhang[1], W. Wang[2,3], Y. Zhao[2], X. Hu[1], K. Reinhardt[4], R. J. Knize[5] and Yalin Lu[1,2,5 *]

[1]Advanced Applied Research Center, HeFei National Laboratory for Physical Sciences at the Microscale, University of Science and Technology of China, Anhui 230026, P. R. China
[2] CAS Key Laboratory of Materials for Energy Conversion, Department of Materials Science and Engineering, University of Science and Technology of China, Hefei 230026, P. R. China
[3] Materials Science and Engineering, the University of Texas at Austin, Austin, TX 78712, USA
[4]United States Air Force Office of Scientific Research, 875 North Randolph Street, Arlington, VA 22203, USA
[5]Laser Optics Research Center, Physics Department, United States Air Force Academy, CO 80840, USA
[*]Corresponding author, E-Mail: yllu@ustc.edu.cn or yalin.lu@usafa.edu

Abstract

By integrating together the VO_2's unique near room-temperature (RT) semiconductor-metal (S-M) phase transition with a thin layer silver's (Ag) plasmonic properties, VO_2/Ag multilayers could present a much enhanced optical transmission change when increasing the temperature from RT to over VO_2's S-M phase transition temperature. Changing VO_2 and Ag layer thicknesses can also significantly tune their transmission and absorption properties, which could lead to a few useful designs in optoelectronic and energy-saving industries.

1. Introduction

A multilayer with its optical properties to be actively modulated via external physical parameters can find many potential applications in a few emerging technology areas including optoelectronics as either components or sub-systems. In certain security-related cases a smart window for those sensors monitoring various external physical parameters requires an instant response to an unexpected incident radiation. For example when incident with a thermal radiation in a harsh environment, the window should instantly become highly reflective, realizing a unique sensor protection function. Similarly, this function can also be applied to building windows for energy-saving. A thermochromic window highly reflective to thermal radiation and automatically switchable by the temperature can effectively prevent a building from overheating by solar irradiation in summer time. In these regards, a temperature-agile and structurally tunable multilayer coating combining the use of temperature-active materials is highly desirable, and the coating should be simple in structure, cost effective in material usage, easy in film fabrication, and flexibility to be coated on substrate materials such as regular glasses.

Vanadium dioxide (VO_2) thin films have been the subject of intensive research in recent years. It has a reversible first-order semiconductor-metal (S-M) phase transition under a few different external excitations. When changing the temperature, for example, it has a phase transition at around 68℃. During the S-M phase transition, VO_2 experiences dramatic changes in many properties incldluing dielectric constant and electrical conductivity [1, 2]. Very encouragingly, via doping this phase transition temperature can be almost linearly lowered to ~40 ℃[3], and its closeness to RT makes the material more attractive to the above-discussed security photonics and energy-saving windows applications. In the past, there are a few researches reported the use of VO_2-embedded noble metal/VO_2 films to improve their optical performance [4-6]. In those designs, thin layer noble metal such as platinum was usually used as the surface layer with a goal to modify the refection to the infrared. This layer of noble metal has to be very thin in order not to sacrifice the optical transmission to the visible light, and this causes technical problems related to the film growth and then adds limitation to material selection on the noble metal only. In this research via simulations we have used a simple structure of VO_2 and plasmonic metallic silver (embedded beneath the VO_2 layer) to be potentially made on glass substrates, and investigated their optical transmission and absorption over a wide temperature range crossing through the VO_2 phase transition temperature and over a range of structural changes. It was experimentally demonstrated before that by adding a thin layer of Ag beneath to a semiconductor layer the optical transmission can be significantly modified [7], due to the plasmonic behavior and the thickness change of the Ag layer. Here embedding a thin Ag layer could therefore utilize both benefits from the temperature agility of VO_2 and from the plasmonic enhancement of the embedded Ag thin layer. An additional benefit is that the structure could tolerate relatively thicker metallic layer which may ease the thin film deposition.

2. Computational method

The schematic structure includes a thin Ag layer sandwiched between a VO_2 layer and a K9 glass substrate. In our simulations, we mapped the VO_2 thickness from very thin to about 200 nm, and changed the Ag thickness from 0 (no Ag layer) to 15 nm at an interval of 5 nm. A wavelength range from 0.35 to 2 μm, from ultraviolet (UV) to the mid-infrared (IR) covering the major solar spectrum, was also swept through in the investigation. Dielectric constants (*n* and *k*) of VO_2 used in our simulations was taken from interpolating of the reported experimental spectroscopic data [8-9], and were shown in Fig.1a and Fig.1b, respectively. To be brief and simple, only a few lines corresponding to a few temperatures aside the phase transition temperature were shown. Normally the material is relatively transparent in its semiconductor state, and reflective and absorptive in the metal state, in the near-infrared spectrum. Dielectric constant of silver is taken from the tabulated data in [10]. In the interested wavelength range, the K9 glass's dispersion is small comparing to those of silver and VO_2, and was then neglected. We used a constant K9's refractive index of 1.51. The simulations were executed following the transfer matrix method [11].The method generates analytic results from the Maxwell's equations in horizontally infinite multilayer structures in our cases here, which are equivalent to the Fresnel's formulation but much more convenient [12].

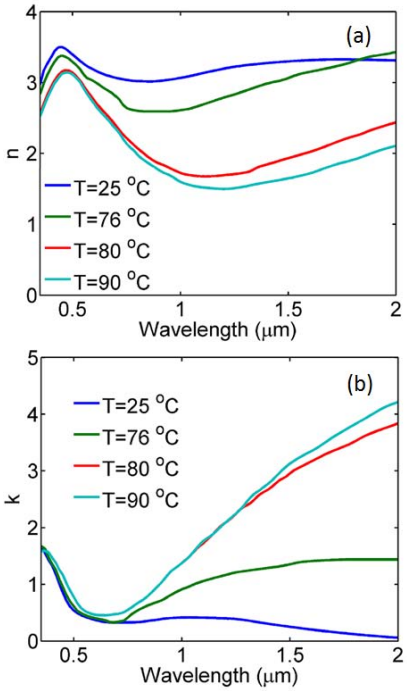

Fig.1 (a) and (b) are real and imaginary refractive indices of VO_2 in the visible to near-IR spectrum range at a few different temperatures.

3. Results and discussion

3.1. Adding a ultra-thin silver layer

We first investigated the case of embedding a thin Ag layer to the structure with a fixed VO_2 thickness of 50 nm, comparing to the case of no Ag layer. Fig. 2a and 2b show both transmission and absorption spectra for the structure with different Ag thicknesses of 0, 5, 10 to 15 nm, respectively, with the VO_2 in its semiconductor (solid lines marked with 's', selected at 25 °C) and metallic phases (dotted lines as 'm', selected at 80 °C). In Fig. 2a, optical transmission for the metallic VO_2 state always reduces as the Ag thickness increases. Whereas in the dielectric state, change of the optical transmission can be roughly divided into three wavelength sections: < 0.6, 0.6-1.2, and > 1.2 μm. When below 0.6 μm, the transmission presents a monotonous reduction as the Ag thickness increasing. When above 0.6 μm, adding a thin Ag layer first enhances the transmission, and then reduces it. In the range of 0.6-1.2 μm, however, this enhancement extends to the case with an Ag thickness of 10 nm, from that of 5nm when the wavelength is > 1.2 μm.

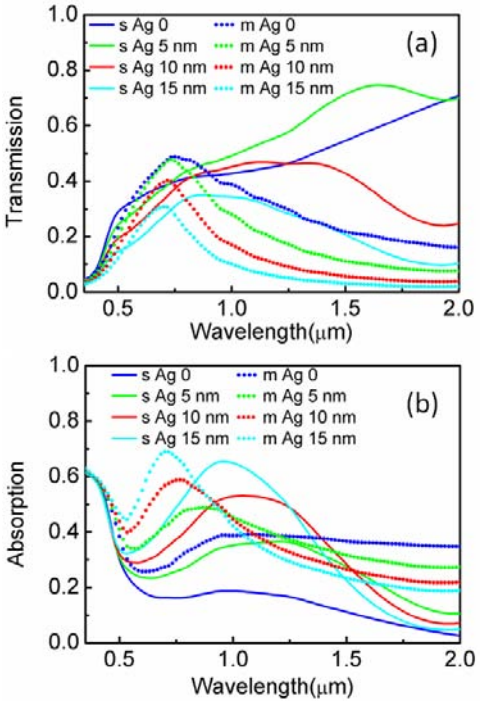

Fig. 2 Transmission and absorption in cases with and without the thin Ag layer, with 's' stands for the semiconductor VO_2, and 'm' for metallic. The VO_2 layer thickness is fixed at 50nm.

In general, optical transmission of a multilayer may reflect the variations in absorption of the materials and the reflection by multiple interfaces. Fig. 2b shows the optical absorption in dielectric (semiconductor) and metallic VO_2 states when increasing the Ag thickness, monitored by simulating the exact electrical field inside the multilayer. In the metallic state, the multilayer is all metallic and it shows three distinct absorptions: sharp increasing in absorption from photoionization inside the skin layer under high energy UV photon irradiations, plasmon absorption as the peak at ~0.6 μm, and absorption from free carriers excited by the near IR photons (> 1 μm). The monotonous reduction in transmission as the Ag thickness increasing in the metallic VO_2 shown in Fig 2a can be explained by the superposition of all three absorption mechanisms discussed above.

When VO_2 is in the dielectric state, however, as usual it presents photoionization absorption for high energy UV photons and then multiple interface reflections for visible and IR photons at the case of no Ag layer. Adding a thin layer of Ag to the structure excites the plasmon absorption in the wavelength range around 1 μm. This plasmon absorption is enhancing and then blue-shifts as the Ag thickness increases. This corresponds well to the observation in Ag nanoparticles [13]. In the long wavelength range, adding the Ag layer raises the free carrier absorption from the near IR photon excitation. Additionally, a planar cavity resonance inside the dielectric VO_2 layer has to be considered here for those photons having wavelengths shorter than an effective quarter wavelength of the cavity ($\lambda/4n$, for a 50 nm thick VO_2 this is around 0.6 μm). This resonance will overlap and modulate the reflection when the spectrum having wavelengths smaller than $\lambda/4n \sim 0.6$ μm, and when the Ag thickness changes.

3.2. Structure-tunable optical transmission and absorption

For a particular application, a useful parameter to be derived from Fig. 2a is the optical transmission difference between the VO_2's dielectric and metallic states. For potential photonic applications involving lasers, for example, wavelengths of 1.064 μm (Nd^{3+}:YAG) and 1.55 μm (Er^{3+}:Fiber) would be of the major interests. For solar energy applications, for another example, we may be interested in the 'hot' IR wavelength range. According to above Fig. 2a results and considering the Ag thin film's fabrication/quality issue, in our subsequent simulations we will choose the Ag's thickness of 10 nm, which is not too thin but still maintains acceptable bi-status transmission contrasts over a fairly large IR wavelength range. We were then mapping both transmission and absorption over a wavelength range from 0.35 to 2 μm and over a VO_2 thickness from very thin to 0.2 μm (in the semiconductor state), at both cases of without and with Ag (10 nm thick). Fig.3 (a-d) shows the optical transmission (a and c) and absorption (b and d) mapping spectra for the bare VO_2 film (a and b) and the structure with Ag layer (c and d), with the varying VO_2 thickness and the wavelength.

Apparently, an enhanced optical transmission occurs as a dark strip in Fig. 3c in the case of adding the Ag layer, and the enhancement shifts to longer wavelength as the VO_2 thickness increases. This is a mainly from the cavity resonance response inside the VO_2 layer that is affected by plasmon and free carrier absorptions inside the metallic layer and also possibly inside the semiconductor layers (the changing amplitude along the dark strip). Possible plasmon and free carrier contribution to the absorption inside the semiconductor layer can be clearly seen in Fig. 3d. They are very weak in the case of the bare VO_2 structure, as only a few light color contours can be seen in the similar area in a Fig. 3b to that in Fig. 3d. Fig. 3 gives the necessary instruction to further device designing, and indicates the structure's better performance for long wavelengths where the plasmon-related absorption is reducing (beyond the 2 μm wavelength range).

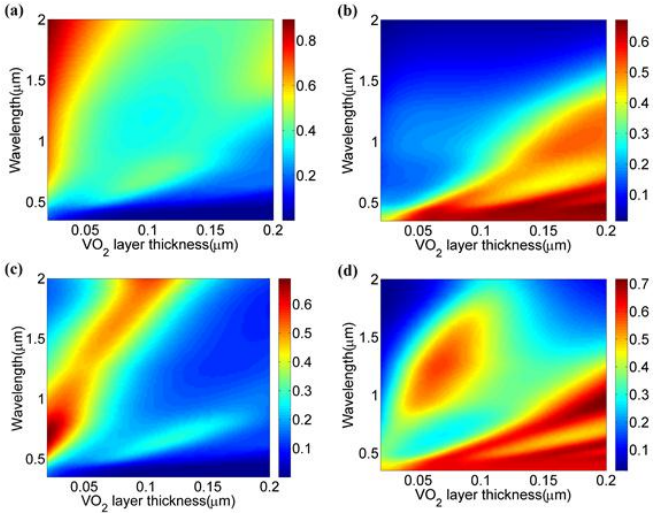

Fig. 3 Mapping transmission and absorption with varying VO_2 thickness and incident wavelength. (a) and (b) are for bare VO_2, respectively. (c) and (d) are for the case with a 10 nm Ag layer.

3.3. Temperature-agile transmission and absorption

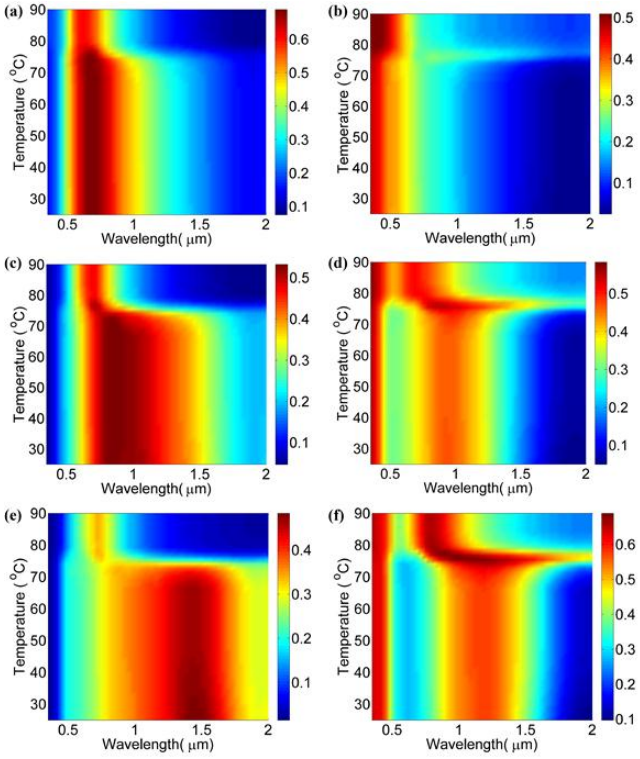

Fig. 4 Mappings transmission (a, c, e) and absorption (b, d, f) spectra with varying temperature and VO_2 layer thicknesses ((a, b) for 20 nm, (c, d) for 40 nm, (e, f) for 60 nm). The Ag layer was fixed at 10 nm.

Figure 4 shows the optical transmission and absorption spectra with varying temperature and VO_2 layer thickness, when the silver layer was fixed at 10 nm. We neglected a possible reduction of the VO_2's S-M phase transition temperature caused by overlapping the VO_2 with Ag, and

fixed the phase transition temperature at ~70 ^{o}C in all the following simulations. A noticeable phenomenon is the abrupt change (from high to low) in optical transmission when the VO_2 layer changes its state from semiconductor to metallic. This change occurs mainly in the visible to near infrared wavelength range, which shifts and expands in range when increasing the VO_2 thickness from 20 to 60 nm. This range is roughly in 0.5-1.0 μm at the VO_2 thickness of 20 nm, shifts and expands to 0.6 to 1.5 μm at 40 nm, and further to 0.75 to 1.75 μm at 60 nm. This change can be explained by overlapping the plasmon absorption, free carrier absorption, and resonance cavity effect discussed above, and can be also clearly seen in Fig. 4b, 4d, and 4f. When below 0.4 μm, that little optical transmission change when crossing the phase transition temperature is because of the high absorption of both VO_2 states over those short UV photons. Such results in Fig. 4 are attractive to future energy-saving and specific photonic applications.

4. Conclusions

An integration of near RT phase-transition material VO_2 with plasmonic metallic silver as temperature-agile and structure-tunable coatings on glasses was proposed and fully investigated by simulations. Adding a thin Ag layer enhances the optical transmission when VO_2 is in its dielectric state. The optical performance can be further tuned by changing the layer thicknesses. Such properties can be explained by photoionization by UV, plasmon absorption, free-carrier absorption, and resonant cavity effect.

Acknowledgements

Financial support from the National Basic Research Program of China (2012CB922001) and the Air Force Office of Scientific Research (AFOSR) is greatly appreciated.

References

[1] F. J. Morin: Phys. Rev. Lett. 3: 34, 1959.

[2] L. Kang, Y. Gao, H. Luo: ACS Appl. Mater. Interfaces, 1 : 2211, 2009.

[3] J. M. Wu, L. B. Liou: J. Mater. Chem., 21: 5499, 2011.

[4] L. Kang, Y, Gao, Z, Chen, J. Du, Z. Zhang, H. Luo: Sol. Energy Mater. Sol. Cells, 94 : 2078, 2010.

[5] L. Kang, Y. Gao, H. Luo, J. Wang, B. Zhu, Z. Zhang, J. Du, M. Kanehira, Y. Zhang: Sol. Energy Mater. Sol. Cells, 95: 3189, 2011.

[6] Z. Zhang, Y. Gao, H. Luo, L. Kang, Z. Chen, J. Du, M. Kanehira, Y. Zhang, Z. L. Wang: Energy Environ. Sci., 4: 4290, 2011.

[7] Yalin Lu, J. F. Sell, M. D. Johnson, K. Reinhardt, R. J. Knize: Phys. Status Solidi C, 8: 843, 2011

[8] A. Gavini, C. Kwan: Phys. Lett. B, 5: 3138, 1972.

[9] J. B. Kana, J. M. Ndjaka, G. Vignaud, A. Gibaud, M. Maaza: Opt. Commun., 284: 807, 2011.

[10] E. D. Palik: Handbook of Optical Constants of Solid (Academic 1985).

[11] E. Anemogiannis, T. K. Gaylord: J. Lightwave Technol., 17: 929, 1999.

[12] M. Born, E. Wolf: Principles of Optics (Cambridge University Press 1980).

[13] Yalin Lu and X. B. Chen, Appl. Phys. Lett. 94: 193110 2009.

Experimental study on the transient establishment of the tunneling mode in ENG/MNG structure

Liwei Zhang[1, 2], Yewen Zhang[2*], Xiaodong Chen[3], Xiaoming Liu[3], Li Zhang[2], Hong Chen[2]

[1] School of Physics and Chemistry, Henan Polytechnic University, Jiaozuo 454000, PR China
[2] MOE Key Laboratory of Advanced Micro-structure Materials, Department of Physics, Tongji University, Shanghai 200092, PR China
[3] School of Electronic Engineering and Computer Science, Queen Mary, University of London, London E1 4NS, UK
*corresponding author, E-mail: yewen.zhang@tongji.edu.cn

Abstract

We theoretically and experimentally investigate the establishment process of the tunneling mode in the conjugate matched pair consisting of ε-negative (ENG) and μ-negative (MNG) materials based on time-domain method. The one-dimensional conjugate matched pair is realized by using transmission line approach and the position and time behavior of the transmitted signal along the pair is measured and recorded by oscilloscope. It is found that the field does not decay to zero in a finite length single negative material and the average power flow is a constant. While for a conjugate matched ENG/MNG pair, the incident field attenuates in ENG material in the first instance and then the fields are rapidly enhanced at ENG-MNG interface due to the strong interaction between the evanescent wave and MNG material. After a certain time, the steady state resonance is eventually achieved. It is revealed that there is a combination of travelling wave and reactive standing wave inside the bilayer with the ratio between them varying with the position and time. It is also proved that the bilayer can be treated as an open resonator, in which the charging up characteristic time is in proportion to the Q factor of the structure.

1. Introduction

Metamaterials, including negative-index materials [1,2] and single negative materials [3-6] have attracted intensive studies in the past few years, due to their unique electromagnetic properties and potential applications [7-13]. One of the most important applications of negative-index material is super-resolution imaging which come from the amplification of evanescent waves[6,7]. The studies of the evanescent wave amplification becomes very important and desirable. There are two kinds of single negative metamaterials: one is the ε-negative (ENG) medium and the other is the μ-negative (MNG) medium. For the single negative materials, the electromagnetic(EM) wave is evanescent, but it is surprising that the complete tunneling mode was found in a conjugate matched pairing structure made of ENG and MNG metamaterials, where the evanescent field is amplified [5]. For the steady state case, the EM field of the tunneling mode is exponentially increase from the boundary to the center of the pair and strongly localized on the interface. Many applications based on the tunneling mode such as transparency, subwavelength imaging and self-collimation properties have been studied [5,8,14]. A single-mode cavity with sub-wavelength size has also been proposed based on the ENG-MNG pair and lead to unusual Rabi splitting when an artificial "atom" was put into the interface[13]. The conjugate matched ENG-MNG pair can be reduced to nihility without any reflection and phase shift when steady state response is built, whereas the foundation of the steady state resonance is not instantaneous, it requires a certain time. In Ref.14, Andrea et al studied the tunneling mechanics theoretically by using finite-difference time-domain (FDTD) method. The studies about instantaneous process of the interaction between wave and metamaterials will help us to understand some interesting physical phenomenon [15]. In this paper, the (near) conjugate matched pair containing ENG and MNG materials are made of L-C loaded transmission lines, the establishment process of the tunneling mode is investigated by time domain analysis, simulation and measurement.

2. Model and theory

We consider a single ENG slab with the thickness of d_{ENG} in free space using the coordinates shown in Fig.1 firstly. For the sake of simplicity, we only consider a TM plane wave (E_x, H_y) incident normally on the slab. The general solution of electric field in phasor form can be written as: $E_x = E^+ e^{-jk_i z} + E^- e^{+jk_i z}$, where wave number $\mathrm{k}_i = \omega\sqrt{\mu_i \varepsilon_i}$, and E^+ and E^- are the electric field coefficients of forward wave and backward wave, ε_i and μ_i are the permittivity and permeability respectively. In free space, the wave number $\mathrm{k}_i = \omega\sqrt{\mu_0 \varepsilon_0}$ is real, so the solution represents the traveling wave. However, inside the ENG slab, the wave number $\mathrm{k}_i = j\omega\sqrt{|\mu_i \varepsilon_i|}$ becomes imaginary. People tend to simply regard the solution here as the evanescent wave, and the single negative material can not support power flow. In fact the situation is not rigorous exponentially decay in a finite ENG slab. After applying the boundary conditions on the two interfaces of the ENG slab and some mathematical manipulation, the EM field can be expressed as:

$$E_x = |E_x| e^{j\theta_E} \quad \text{and} \quad H_y = |H_y| e^{j\theta_H} \qquad (1)$$

the phase difference θ_1 between the electric field and magnetic field in Regions 1 is $\theta = \theta_E - \theta_H$. It is easy to obtain that the average power flow p_{ENG} in the finite ENG material is constant,

$$p_{ENG} = \frac{1}{2}\mathrm{Re}\left(E_x H_y^*\right) = \frac{1}{2}\left|E_x\right|\left|H_y\right|\cos(\theta) = \frac{E_0^2}{2\eta_0}\left[1-\tanh^2(kd)\right] \quad (2)$$

where $k = \omega\sqrt{|\mu\varepsilon|}$. The propagation property is similar in a finite MNG slab. So in a finite single negative metamaterial, the power flow decrease with the thickness but not zero, the average power flow is constant along the slab since the phase difference between electric field and magnetic field varies with the position. For the ENG/MNG bilayer shown in the inset of Fig. 1, People also tend to simply regard the solution here as the evanescent wave, and the structure can not support power flow. In fact the situation is more complicated and needs a rigorous analysis. After applying the boundary conditions on the three interfaces of the ENG/MNG slabs and some mathematical manipulation, the EM field can be obtained. Interesting, the complete tunneling can happen in the ENG/MNG bilayer when the condition is satisfied [4,14]:

$$\sqrt{|\mu_1||\varepsilon_1|}d_1 = \sqrt{|\mu_2||\varepsilon_2|}d_2 \quad \text{and} \quad \sqrt{|\mu_1|/|\varepsilon_1|} = \sqrt{|\mu_2|/|\varepsilon_2|} \quad (3)$$

where d_1 and d_2 are the thickness of ENG and MNG slabs, respectively.

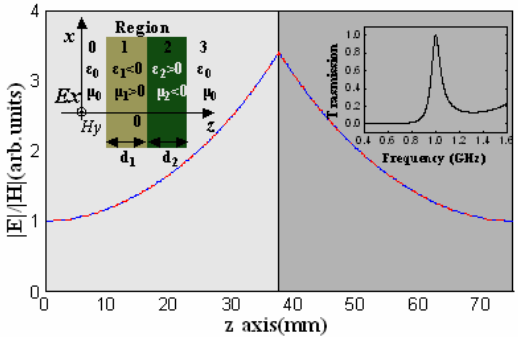

Figure 1 The EM field distribution of the conjugate matched bilayer of ENG/MNG at the resonance frequency, the insets are the schematics and the transmission spectrum of the bilayer of ENG and MNG slabs.

As a special case, a conjugate matched blayer is denoted by: $\varepsilon_1 = -\varepsilon_2 = -\varepsilon$, $\mu_1 = -\mu_2 = \mu$ and d_1=d_2=d, we have: $k = \omega\sqrt{\mu\varepsilon}$, ($i$=1, 2). The steady state EM fields in the bilayer can be expressed as follows.

Region 1 (0< z <d):

$$E_{x1} = E_0\cosh(kz) - j\frac{\eta}{\eta_0}E_0\sinh(kz) = \left|E_{x1}\right|e^{j\theta_{E1}} \quad (4)$$

$$H_{y1} = \frac{E_0}{\eta_0}\cosh(kz) + j\frac{E_0}{\eta}\sinh(kz) = \left|H_{y1}\right|e^{j\theta_{H1}} \quad (5)$$

Region 2 (d< z <2d):

$$E_{x2} = E_0\cosh[k(z-2d)] + j\frac{\eta}{\eta_0}E_0\sinh[k(z-2d)] = \left|E_{x2}\right|e^{j\theta_{E2}} \quad (6)$$

$$H_{y2} = \frac{E_0}{\eta_0}\cosh[k(z-2d)] - j\frac{E_0}{\eta}\sinh[k(z-2d)] = \left|H_{y2}\right|e^{j\theta_{H2}} \quad (7)$$

where the wave impedance $\eta = \sqrt{\mu/\varepsilon}$ and $\eta_0 = \sqrt{\mu_0/\varepsilon_0}$. It is quite easy to prove that the average power flow p_{avi} in Regions 1 and 2 is constant (i = 1, 2),

$$p_{avi} = \frac{1}{2}\mathrm{Re}\left(E_{xi}H_{yi}^*\right) = \frac{1}{2}\left|E_{xi}\right|\left|H_{yi}\right|\cos(\theta_i) = \frac{E_0^2}{2\eta_0} \quad (8)$$

being equal to the average power flow in Regions 0 and 3. where $\theta_1 = \theta_{E1} - \theta_{H1}$ and $\theta_2 = \theta_{E2} - \theta_{H2}$, which change with the position. The constant power flow has confirmed the complete tunneling inside this conjugate matched ENG/MNG bilayer, and the EM fields inside the conjugate matched ENG/MNG bilayer is a hybrid of the traveling wave and the reactive standing wave[16].

Consider an example where the Drude models for the permittivity and permeability in the lossless ENG and MNG slabs are: $\varepsilon_1/\varepsilon_0 = 2 - 4/f^2$, $\mu_1/\mu_0 = 2$, $\mu_2/\mu_0 = 2 - 4/f^2$, $\varepsilon_2/\varepsilon_0 = 2$, where f is frequency measured in GHz and $d_1 = d_2 = 37.5mm$. According to the conjugate matched condition Eq.(3), the bilayer exhibits a complete tunneling mode at f_0=1GHz shown in the inset of Fig.1. The analytical amplitude of the steady electric and magnetic fields are plotted in Fig. 1. It is clear that the amplitudes of *Ex* and *Hy* reach to their peaks at the interface of the bilayer and decay 'exponentially' towards either edge of ENG/MNG slab.

At the tunneling frequency, there is a substantial amount of EM energy ($W_{EM} = W_{ENG} + W_{MNG}$) stored in the tunneling structure which work as a resonator and the total instantaneous EM energy can be calculated. Under the lossless condition, the output quality (Q) factor of the tunneling mode can be define as $Q = \omega W_{EM} / p_{avi}$.

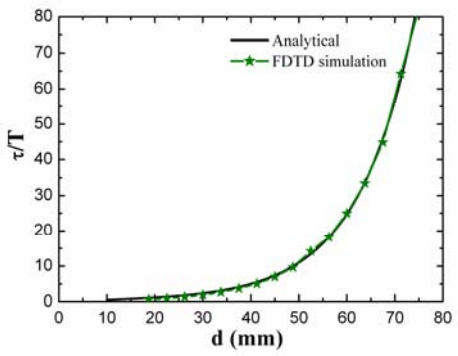

Figure 2. The analytical and FDTD simulated charging-up characteristic times τ/T vs thickness d of the conjugated matched ENG/MNG slabs, the parameters are the same as those in Fig.1.

It will takes a certain amount of time to tunnel thought the ENG/MNG and reach to its steady state [14]. The transient process of the complete tunneling can be quantitatively described by the charging up characteristic time τ. The charging up process of the resonator with a rectangular waveform signal follows 1-exp(-αt)[17], where the charging up coefficient α=ω/2Q. So the charging up characteristic time $\tau/T = (2/\pi)[(\sinh(2kd))/2 + \tan^{-1}(e^{2kd}) - \pi/4]$ [16] under the conditions in Fig. 1, where T is the cycle of the wave and d is the thickness of the slab. It increases exponentially with the thickness of the slabs, corresponding to the increase

of Q factor of the tunneling mode as shown in Fig.2 (the solid line).

In order to study the transient process, we have simulated the building up of the complete tunneling mode in this conjugate matched pair of ENG/MNG slabs by using FDTD method [18]. The problem space is 1500 cells long, where $\Delta z = \lambda_0 / 1120$ with $\lambda_0 = 300mm$, the thicknesses of the ENG and MNG layers are $d_{ENG} = d_{MNG} = 140\Delta z$, the time step is set to be $\Delta t = 0.5\Delta z / c = 0.4464 ps$. A plane sinusoidal wave is launched at about a half wavelength away from the surface of ENG with a rectangular waveform.

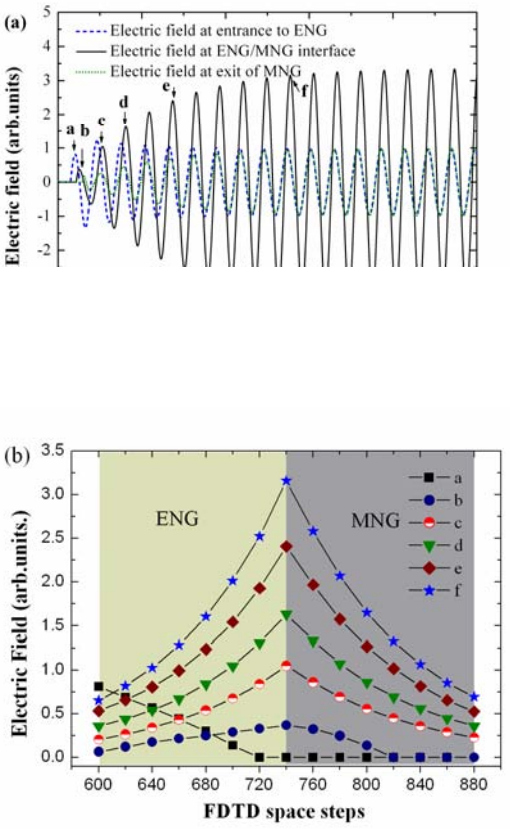

Figure 3. (a) FDTD simulated time histories of the electric field at the entrance to ENG, at the ENG/MNG interface and at the exit of MNG slab, respectively. (b) The electric field distribution along ENG/MNG pair at different time points marked by *a, b, c, d, e* and *f* in Fig.3 (a), respectively.

The amplitude and the phase information of the electric and magnetic fields at any position can be obtained from the temporal evolution. In Fig. 3(a), the time histories of the electric field (magnetic fields are not shown here) at the entrance of ENG, at the ENG/MNG interface and at the exit of MNG slab are plotted respectively. In Fig. 3(b), the transient field distributions built inside the pair are plotted at different time points which are marked by *a, b, c, d, e* and *f* as shown in Fig. 3(a). It is evident that the electric field amplitude begins to attenuate in ENG material when the wave incidents on the first interface between air and ENG material until arrive at the ENG/MNG interface, then the field amplitude begins to increase because of the multiple reflections within the bilayer. Especially, the field amplitude at the ENG-MNG interface is rapidly improved due to a strongest reactive field. When the EM field reaches to the steady state, the field amplitude is equal at the entrance and the exit faces of the bilayer without any phase shift.

3. Experiment and simulation

Single negative metamaterials can be realized by periodically arranged metallic structures and dielectric composite [3,4]. In addition, in a transmission line (TL) loaded with lumped elements characterized by nonresonance, MNG and ENG metamaterials can also be realized with low loss[19]. For the sake of simplicity, the transmission lines loading shunt inductor L (series capacitor C) possessing ENG (MNG) properties in a certain range of frequencies are termed as ENG (MNG) TLs, the circuit models of ENG TL and an MNG TL are shown in Fig. 4(a). In experiment, ENG and MNG TL units have been fabricated on a FR-4 substrate (with relative permittivity of 4.75, thickness of 1.6mm). Fig 4(b) shows the photograph of the fabricated pair structure ENG_6MNG_6 by cascading six ENG TL units with six MNG TL units. The S-parameters of the units are simulated by Agilent Advanced Design system (ADS) and measured by means of an Agilent 8722ES vector network analyzer. The ENG TL unit with the characteristic impedance of 50Ω is designed to have the unit length of d_{ENG}=7mm, the loaded shunt inductor L_{ENG}=15nH, and the MNG TL unit to have d_{MNG}=7mm, series capacitor C_{MNG}=6pF, respectively. They can be regarded as single negative materials below 1.3GHz, and the ENG/MNG pairs possess tunneling mode at the resonance frequency [16]. The simulated and measured S-parameters of the MNG TL, ENG TL containg ten TL units and the paired structure MNG_nENG_n (n=4,6,8) are shown in Fig.5. The simulated tunneling frequency f_0=1.04GHz accords well with the experimental data f_0=1.01GHz. It is evident that the tunneling mode is robust against the scaling change of the pair structure and the pair can work as a sub-wavelength open-cavity resonator [13].

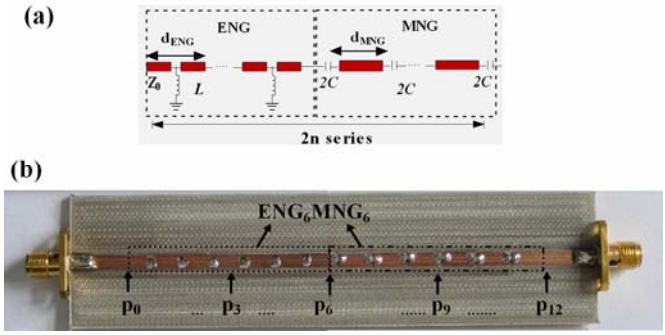

Figure 4 (a) The circuit model of ENG and MNG TLs with the loading shunt inductor (L) and series capacitors (C); (b) The photograph of the fabricated pair structure ENG_6MNG_6 by cascading six ENG TL units with six MNG TL units.

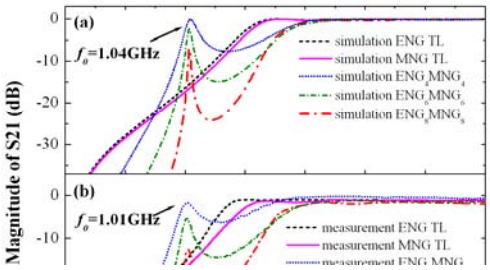

Figure 5 The simulated (a) and measured (b) S-parameters of the MNG TL, ENG TL and the paired structure MNG_nENG_n with n=4, 6 and 8.

In order to investigate the field establishment process of the tunneling mode in experiments, a time-domain measurement system is setup. The Tektronix arbitrary waveform generator (AWG710) is used to generate the rectangle envelope of signal, while the Agilent vector signal generator (E8267D) is used to generate the carrier wave with the tunneling frequency(1.01GHz in measurement). The rectangle modulated signal is then injected into the *ENG*/*MNG* pair. A Tektronix P7350 differential probe with the input impendence 100 kΩ is used to measure the waveform at P_0, P_1, P_2.....P_{12}, along the pair. The position and time behavior of the transmitted signal along the pair are measured and recorded by oscilloscope. The detailed time-domain measurement information could be found in Ref. 20. Fig. 6(a) shows the measured time histories of the voltage distribution at the 3rd, 6th and 9th unit of the fabricated sample, respectively, that is p_3, p_6 and p_9. There are some small fluctuations in the first instance because of reflection. Fig. 6(b) shows the measured voltage distribution along ENG_6MNG_6 at different time points which marked by *a, b, c* and *d* shown in Fig. 6(a). The voltage distribution along the ENG_6MNG_6 transmission line changes with time and position and the tendency agrees well with that obtained in FDTD simulation. This clearly illustrates the instantaneous response of the tunneling mode in the conjugate matched ENG/MNG pair.

Furthermore, the charging up characteristic time τ can also be obtained by fitting the signal magnitude probed at P_{12} as shown in Fig.4(b) with decay-exponential function. In measurement, a rectangle modulated sinusoidal signal with $f = 1.01GHz$ is used. The charging up characteristic time of ENGn/MNGn vs the unit number n is plotted in Fig.7. It is shown that τ increases exponentially with the pair length under the lossless condition. The building up process of the tunneling mode in the lossy ENG/MNG TL pair is also modeled in ADS. While with the increase of the dielectric loss $\tan\delta$, the tunneling mode needs less time to reach to the steady state since the total Q factor of the resonator decreases. It can be seen that the measured charging up characteristic times fit well in the range of simulated ones with losses.

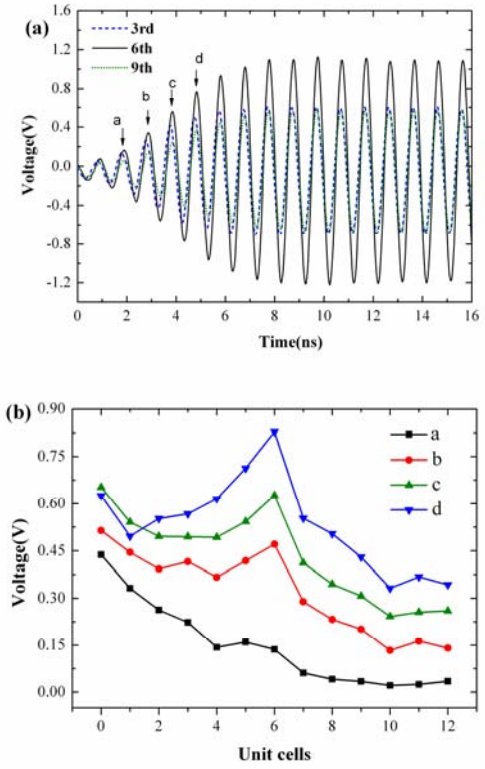

Figure 6. (a) The measured time histories of the incident rectangle modulated sinusoidal signal with carrier frequency of 1.01GHz at 3rd, 6th and 9th unit respectively, the marker points *a, b, c, d* denote different time points. (b) The measured voltage distribution along the ENG_6MNG_6 at different time points.

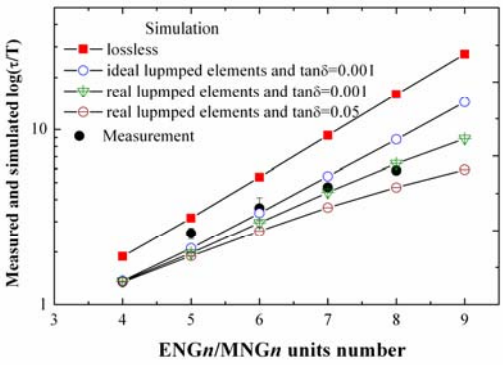

Figure 7 The ADS simulated and measured charging up characteristic time (τ/T) (logarithmic scale) of ENG*n*/MNG*n* vs the unit number *n* with different dielectric loss.

4. Conclusions

In conclusion, the instantaneous establishment process of the tunneling mode in a conjugate matched ENG-MNG pair is theoretically and experimentally studied based on transmission line approach. It is found that the field does not decay to zero in a finite length single negative material and the average power flow is a constant. For a conjugate matched ENG/MNG bilayer, it can be work as a

sub-wavelength open-cavity resonator. The transient process of the complete tunneling can be quantitatively described by the charging up characteristic time, which increases exponentially with the thickness of the slabs.

Acknowledgements

This research was supported by National Basic Research program (973) of China (No. 2011CB922001) and by NFSC (No.10904032).

References

[1] C. Garcı´a-Meca, J. Hurtado, J. Martı´, and A. Martı´nez, "Low-Loss Multilayered Metamaterial Exhibiting a Negative Index of Refraction at VisibleWavelengths," *Phys. Rev. Lett.* vol. 106, no. 6, p. 067402, Feb. 2011

[2] J. Yang, C. Sauvan, H. T. Liu, P. Lalanne, "Theory of Fishnet Negative-Index Optical Metamaterials," *Phys. Rev. Lett.* vol. 107, no. 4, p. 043903, Jul. 2011

[3] Q. Zhao, L. Kang, B. Du, H. Zhao, E. Ulin-Avila, D. A. Genov, G. Bartal, X. Zhang, "Experimental Demonstration of Isotropic Negative Permeability in a Three-Dimensional Dielectric Composite," *Phys. Rev. Lett.* vol. 101, no. 2, p.027402, Jul.2008

[4] A. Dhouibi · S. N. Burokur · A.Lustrac · A. Priou, "Z-shaped meta-atom for negative permittivity metamaterials ," *Appl Phys A*, vol. 106, no. 1, pp. 47–51, Jan. 2012

[5] A. Alù and N. Engheta, "Pairing an epsilon-negative slab with a mu-negative slab: resonance, tunneling and transparency," *IEEE Trans. Antennas Propagat.* vol. 51, no. 10, pp.2558-2571, Oct.2003

[6] X. Zhang and Z.W. Liu, "Superlenses to overcome the diffraction limit," *Nature Mater*. vol. 7, pp.435-441, Jun.2008

[7] A. Grbic, G. Eleftheriades, "Overcoming the Diffraction Limit with a Planar Left-Handed Transmission-Line Lens," *Phys. Rev. Lett.* vol. 92, no. 11, p.117403, Mar.2004

[8] Z. L. Wang, H.t. Jiang, Y.h. Li, and H. Chen, "Enhancement of self-collimated fields in photonic crystals consisting of two kinds of single-negative materials," *Opt. Express.* vol. 18, no. 14, pp. 14311-14318, Jun. 2010

[9] K. L. Tsakmakidis, A. D. Boardman and O. Hess, "Trapped rainbow' storage of light in metamaterials," *Nature,* vol. 450, pp.397-401, Nov.2007

[10] T. Ergin, N. Stenger, P. Brenner, J. B. Pendry, M. Wegener, "Three-Dimensional Invisibility Cloak at Optical Wavelengths," *Science*, vol. 328, no. 5976, pp.337-339, Apr.2010

[11] M. Choi, S. H. Lee,Y. Kim,S. B. Kang, J. Shin, M. H. Kwak, K. Y. Kang, Y. H. Lee, N. Park, B. M, "A terahertz metamaterial with unnaturally high refractive index," *Nature,* vol. 470, no. 7334, pp.369-373, Feb.2011

[12] C. Wu, A. B. Khanikaev, and G. Shvets, "Broadband Slow Light Metamaterial Based on a Double-Continuum Fano Resonance," *Phys. Rev. Lett.* vol. 106, no. 11, p.107403, Mar.2011

[13] L. W. Zhang, Y. W. Zhang, Y. P. Yang, H. Chen, "Experimental study of Rabi-type oscillation induced by tunneling modes in effective near-zero-index metamaterials," *Phys .Rev. E*, vol. 83, no. 4, p.046604, Apr. 2011

[14] A. Alù, N. Engheta and R. W. Ziolkowski, "Finite-difference time-domain analysis of the tunneling and growing exponential in a pair of ε-negative and μ-negative slabs," *Phys. Rev. E* vol. 74, no. 4, p.016604, Jul. 2006

[15] S. Foteinopoulou, E. N. Economou, C. M. Soukoulis, "Refraction in Media with a Negative Refractive Index," *Phys. Rev. Lett.* vol. 90, no. 10, p.107402, Mar. 2003

[16] L. W. Zhang, Y. W. Zhang, X. D. Chen, X .M. Liu, L. Zhang, H. Chen, "Energy transport in a metamaterial subwavelength open-cavity resonator," *Opt. Lett.* vol. 36, no. 12, pp. 2224-2226, Jun. 2011

[17] T. L. Floyd, Electric Circuit Fundamentals, 2nd ed. (Prentice Hall, 2006).

[18] D. M. Sullivan, Electromagnetic Simulation Using the FDTD Method, (IEEE Press: New York, 2000).

[19] C. Caloz, T. Itoh, Electromagnetic Metamaterials: Transmission Line Theory and Microwave Applications (Wiley & Sons, New York, 2006)

[20] Y. Z. Wang, Y. W. Zhang, L. He, H. Q. Li, H. Chen, F. Q. Liu, C. Caloz, "Direct observation of negative phase velocity and positive group velocity in time domain for composite right/left-handed transmission lines, " *J. Appl. Phys,* vol. 100, no. 11, p. 113503, Apr. 2006

Tamm plasmon polaritons in composite structures composed of the metal film and truncated photonic crystals

Guiqiang Du[1, 3, *], Liyong Cui[1], Liwei Zhang [2, 3], Haitao Jiang[3, 4]

[1] School of Space Science and Physics, Shandong University at Weihai, Weihai 264209, China

[2] School of Physics and Chemistry, Henan Polytechnic University, Jiaozuo 454000, China

[3] Laboratory of Special Artificial Microstructure Materials and Technology, Shanghai 200092, China

[4] Pohl Institute of Solid State Physics, Tongji University, Shanghai 200092, China

[*]corresponding author: *dgqql*@sdu.edu.cn

Abstract

Tamm plasmon polaritons (TPPs) are studied theoretically and experimentally in heterostructures and sandwiched structures with the metallic film and truncated photonic crystals. Different from conventional surface plasmon polaritons, TPPs can be realized in both the transverse electric (TE) and transverse magnetic (TM) polarizations, and they can be excited from a free space. Because of nonreciprocal electromagnetic field distributions of TPPs, the structures possess strongly nonreciprocal absorption and reflection. Moreover, two tunneling peaks or a narrow transmission band can be realized in sandwiched structures for both polarizations due to the coupling effect between two TPPs.

1. Introduction

The metals have larger optical nonlinearity and absorption coefficient than those of many dielectrics. For example, third-order nonlinear susceptibility of noble metals is nearly 10^6 times larger than those of typical dielectrics [1-3]. However, such properties are difficult to realize high-quality nonlinear devices or optical absorbers for bulk metals since they are opaque epsilon-negative (ENG) materials below their plasma frequencies. Transparent metals [4-6], which are composed of an alternating thin metal film and a thick dielectric material, can enhance transmission, absorption and nonlinearity through Bragg resonance [2-7], but the nodes of the electric field usually locate within thin metal layers which limits the absorption and nonlinearity enhancement. One the other hand, nanostructured metals can enhance transmission and absorption [8-11], while it is difficult to fabricate such metallic structures in visible and near infrared regions. Therefore, it is desirable to realize transmission, absorption and nonlinearity enhancement by inducing strong localized intensity of electromagnetic (TM) fields in thick unstructured metals.

Recently, Tamm plamon polaritions (TPPs) [12, 13] are proposed in heterostructures constituted by the thick unstructured metal and truncated dielectric photonic crystals (PCs), where the frequencies of TPPs locate in the forbidden gap of the PCs which have the effect of mu-negative (MNG) materials [14-17]. The tunneling mechanism is similar to that in the heterostructure composed of ENG and MNG media [18]. TPPs can enhance field intensities considerably within thick metals so that the composite structures containing thick metals have much larger nonlinearity enhancement [16, 19] and can realize near total absorption [17, 20]. TPPs provide a new method to induce EM waves entering the metals. Due to the large absorption coefficient of metals and the asymmetry of heterostructures, the reflection and absorption are found to be nonreciprocal noticeably when EM waves propagate from two opposite directions. Such properties are important to design optical nonlinear devices. Different from conventional surface plasmon polaritions (SPPs), TPPs depend on the forbidden gap of PCs and can be excited for two polarizations. Especially, two TPPs are found theoretically and experimentally to have strong coupling effect in sandwiched structures centered with the thick metallic film. It is significant to bring potential important applications.

The paper is organized as follows. In section 2, we report the theoretical and experimental results on nonreciprocal reflection and absorption of heterostructures. The transmission, reflection and absorption spectra are shown and EM field intensity distributions are given both in two opposite incident directions. In section 3, we study the optical properties of the sandwiched structures. It is demonstrated

experimentally that the degenerated TPPs in TE polarization may split into two discrete modes at large oblique angles due to the strong coupling of two TPPs in front of and behind the metallic film. Finally, we sum up in section 4.

2. Nonreciprocal reflection and absorption in heterostructures

Considering the effect of the substrate and the metallic loss, the heterostructure is designed with BA(DC)^{18}S which is fabricated by the electronic beam evaporation. Where, the substrate S is K9 with n_S =1.52, the protection film B is SiO_2 with d_B =50 nm, and the dielectric C (D) is selected to be SiO_2 (TiO_2) with refractive index $n_C = 1.46$ ($n_D = 2.13$) [21] and the thickness d_C =91.44 nm (d_D =62.68 nm). The metal A is chosen to be silver whose refractive indices are referred from [22]. The thickness of the silver film is selected with 57.57nm to satisfy the near-zero reflection at the tunneling wavelength when normal incident EM waves propagate from left to right. The transmission (*T*) and reflection (*R*) of the samples are measured by a UV-Vis-Near IR Spectrophotometer. The absorbance (*A*) is calculated from *A*=1-*T*-*R*. Firstly, the normal incidence is considered at two opposite directions. Figures 1 (a) (b) and (c) give the transmittance *T*, the reflectance *R* (the light through from left to right) and *R* (the light through from right to left) of the heterstructure BA(DC)^{18}S, respectively. The solid blue lines show the numerical results using the transfer-matrix method [23], and the wavelength of the numerical tunneling mode (TPP) λ_0 is 590.09 nm. The red circles represent measured values and the measured wavelength λ_0 is 597.60 nm. Considering the light propagating from left to right for BA(DC)^{18}S, as shown in Fig. 1 (b), numerical *T*, *R* and *A* at 590.09 nm are 0.0141, 2×10^{-6} and 0.9859 respectively, and measured *T*, *R* and *A* at 597.60 nm are 0.0010, 0.0251 and 0.9739 respectively. When the EM

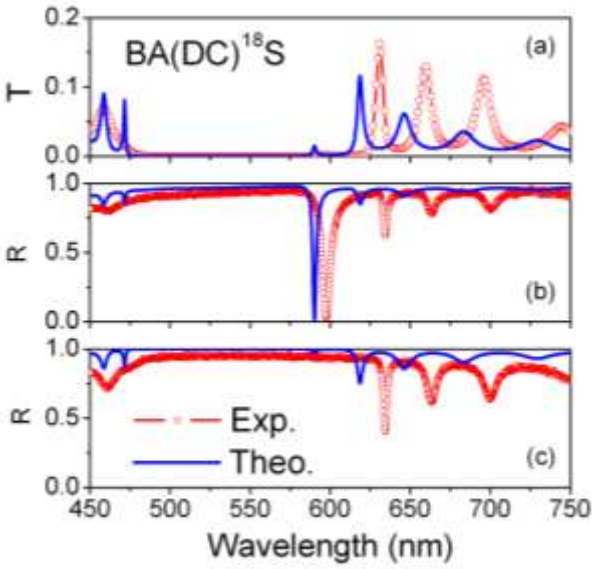

Fig. 1 (a), (b) and (c) show *T*, *R* (the light through from left to right) and *R* (the light through from right to left) for BA(DC)^{18}S. The solid blue (dotted red) lines show the numerical (measured) results.

wave transmits through BA(DC)^{18}S from right to left, as shown in figure 1 (c), numerical *R* and *A* at 590.09 nm are 0.9707 and 0.0152 respectively, and measured *R* and *A* at 597.60 nm are 0.9388 and 0.0602 respectively. The measured values are in good agreement with the theoretical one although there is minor difference on account of monitoring errors of layer thickness and the discrepancy of refractive indices between numerical and real deposited materials. Considering the EM wave propagating from left to right**,** figure 2 (a) and (b) give simulated distributions of intensities of electric field $|E|^2$ (solid lines) and magnetic field $|H|^2$ (dashed lines) for BA(DC)^{18}S and S(CD)^{18}AB at the tunneling wavelength (λ_0 =589.14nm), respectively. The thickness of the silver is 5 times of its real thickness. The field intensity of the incident wave is supposed to be 1. One can see that EM fields are localized highly near the interface between the metal and the truncated PC in figure 2 (a), but those are weak in the latter structure as shown in figure 2 (b). The reason is that the metal loss results in that the impedance conditions [17, 20] are satisfied only for BA(DC)^{18}S at the incident direction from left to right. Because the intensity of the electric field in the silver of figure 2 (a) is much larger than that

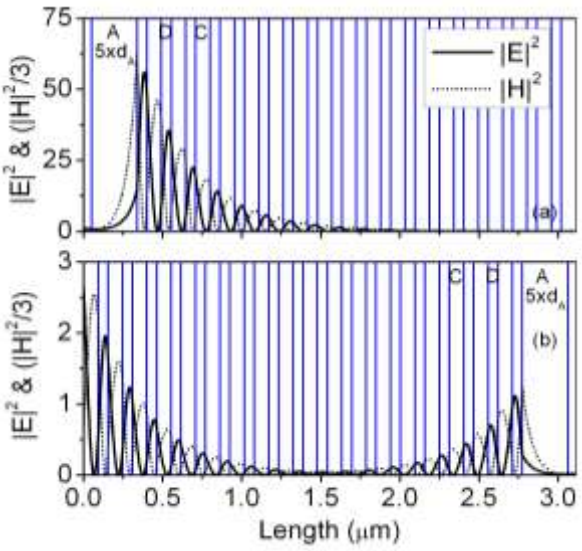

Fig. 2 (a) and (b) give simulated intensities of the electric fields (solid lines) and magnetic fields (dotted lines) in samples $BA(DC)^{15}S$ and $BA(DC)^{18}S$, respectively. Where, the light propagates from left to right at the normal incidence. The thickness of Ag in the schematic is 5 times of its real thickness.

in the latter of figure 2 (b), the absorbance of the former heterostructure is near unit at the wavelength of TPP. The nonreciprocal EM field distributions of TPP induce strongly nonreciprocal absorption and reflection of the heterostructure. Such properties can be used to design the reflection-typed and absorption-typed light-emitting diode etc..

3. The coupling effect of TPPs in sandwiched structures

In a sandwiched structure composed of a thick metal film and two symmetrical truncated PCs, two TPPs can be realized in front of and behind the metal film [24]. Compared to that of the heterostructure, the transmission of the sandwiched structure can be enhanced through a thicker metal film due to the coupling effect of the two interface modes [24]. However, the dispersion relations of TPPs at the PC/Ag/PC interfaces for TE and TM waves were only studied theoretically, and the transmission and reflection properties were investigated at the normal incidence [24]. In this section, these properties are demonstrated experimentally for both two polarizations. The sandwiched structure PC/Ag/PC $[(CD)^6A(DC)^6S]$ are fabricated by the electronic beam evaporation. Where, the thickness of the silver film (A) is 80.2 nm and the other material parameters are the same to those in section 2. The coupling effect between two TPPs is related with the thickness of the metallic film and the periodic number of the PC. The sandwiched structure is selected to satisfy the degeneracy of two TPPs when the light propagates at the normal incidence. Different from conventional SPPs, TPPs can be realized for both TE and TM polarizations. For $(CD)^6A(DC)^6S$, figure 3 (a) and (b) show the T and R at the normal incidence, and (c) and (d) show the R under 45° of TE and TM polarizations, respectively. Where, the EM wave propagates from left to right. The black (blue) lines show the numerical (measured) results. Due to the limitation of the spectrophotometer, reflection spectra are only scanned at oblique angles for two polarizations. The reason to induce the discrepancy between theoretical and

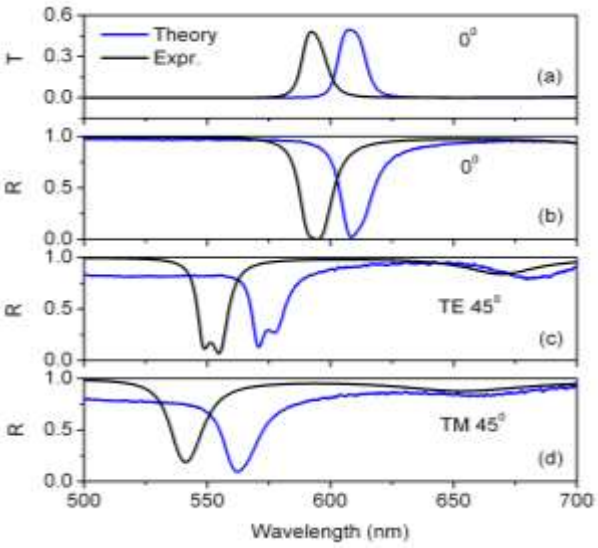

Fig. 3 (a) and (b) show the T and R at the normal incidence, and (c) and (d) show the R under 45° of TE and TM polarizations for $(CD)^6A(DC)^6S$, respectively. Where, the light propagates from left to right. The black (blue) lines show the numerical (measured) results

measured results is the same as that of the heterostructure. Especially, two minimal peaks in figure 3 (c) demonstrate the nondegeneracy of two TPPs. In order to illustrate the coupling effect of two TPPs more clearly at the PC/Ag/PC interfaces for TE and TM waves, figure 4 (a) and (b) give the dispersion relations of TPPs for two polarizations, respectively. The solid (circled or squared)

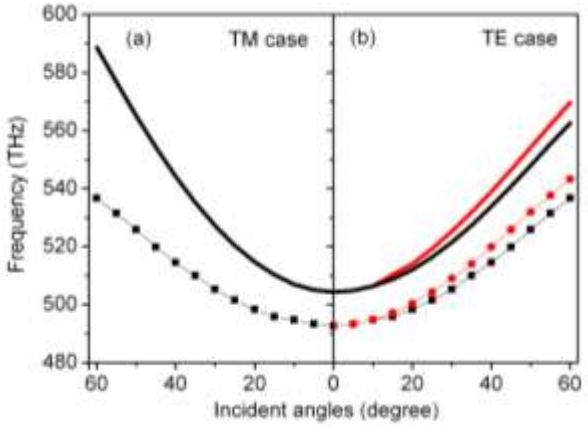

Fig. 4 (a) and (b) show the numerical (solid lines) and measured (circled or squared lines) dispersion relations of TPPs at the PC/Ag/PC interfaces for TE and TM waves, respectively.

lines show the numerical (measured) results. The theoretical results have been demonstrated in Ref. [24]. The dispersion relations show that the degenerated TPPs in TE case can split into two discrete modes at large oblique angles. The forbidden gap becomes broader with the increase of the incident angles for the TE waves but it becomes narrower with that for the TM waves [24], which induces that the EM waves are evanescent more sharply in the PC at larger incident angles of TE polarization. Therefore, stronger localized TPPs are realized between the metallic film and the truncated PC. The stronger coupling effect between two TPPs in front of and behind the silver film leads to the degenerated tunneling mode splitting into two discrete modes at oblique angles of TE waves. Moreover, such properties prove that larger localized intensity of electromagnetic fields for TPPs can be realized for TE waves.

4. Conclusion

In conclusion, we have demonstrated theoretically and experimentally that the TPP can be totally absorbed or reflected in one propagation direction for heterostructures composed of the thick metallic film and the truncated photonic crystal. Moreover, two nondegenerate tunneling modes are illustrated experimentally in the sandwiched structures due to the strong coupling effect between two TPPs in front of and behind the thick metallic film. These structures will play important roles in new types of optical and photonic devices.

Acknowledgements

This research was supported by the National Natural Science Foundation of China (Nos. 11004121, and 10904032), by the Program for Young Excellent Teacher in Shandong University (No. 2010ZRJQ004), by the Opening Project of Shanghai Key Laboratory of Special Artificial Microstructure Materials and Technology (ammt2011A-1), and by China Postdoctoral Science Foundation Funded Project (No. 20100480629).

References

[1] T. Tokizaki, A. Nakamura, S. Kaneko, K. Uchida, S. Omi, H. Tanji, Y. Asahara, Subpicosecond time response of third‐order optical nonlinearity of small copper particles in glass, Appl. Phys. Lett. 65: 941-943, 1994.

[2] R. S. Bennink, Y. Yoon, R. W. Boyd, J. E. Sipe, Accessing the optical nonlinearity of metals with metal-dielectric photonic bandgap structures, Opt. Lett. 24: 1416-1418, 1999.

[3] N. N. Lepeshkin, A. Schweinsberg, G. Piredda, R. S. Bennink, R. W. Boyd, Enhanced nonlinear optical response of one-dimensional metal-dielectric photonic crystals, Phys. Rev. Lett. 93: 123902, 2004.

[4] M. Scalora, M. J. Bloemer, A. S. Manka, S. D. Pethel, J. P. Dowling, C. M. Bowden, Transparent, metallo-dielectric, one-dimensional, photonic band-gap structures, J. Appl. Phys. 83: 2377-2383, 1998.

[5] M. J. Bloemer, M. Scalora, Transmissive properties of Ag/MgF_2 photonic band gaps, Appl. Phys. Lett. 72: 1676-1678, 1998.

[6] M. J. Keskinen, P. Loschialpo, D. Forester, J. Schelleng, Photonic band gap structure and transmissivity of frequency-dependent metallic-dielectric systems, J. Appl. Phys. 88: 5785-5790, 2000.

[7] J. F. Yu, Y. F. Shen, X. H. Liu, R. T. Fu, J. Zi, Z. Q. Zhu, Absorption in one-dimensional metallic-dielectric photonic crystals, J. Phys.: Condens. Matter 16: L51-L56, 2004.

[8] T. W. Ebbesen, H. J. Lezec, H. F. Ghaemi, T. Thio, P. A. Wolff, Extraordinary optical transmission through sub-wavelength hole arrays, Nature, 391: 667-669, 1998.

[9] J. A. Porto, F. J. García-Vidal, J. B. Pendry, Transmission Resonances on Metallic Gratings with Very Narrow Slits, Phys. Rev. Lett. 83: 2845-2848, 1999.

[10] G. Sun, C. T. Chan, Frequency-selective absorption characteristics of a metal surface with embedded dielectric microspheres, Phys. Rev. E 73: 036613, 2006.

[11] T. V. Teperik, F. J. García De Abajo, A. G. Borisov, M. Abdelsalam, P. N. Bartlett, Y. Sugawara, J. J. Baumberg, Omnidirectional absorption in nanostructured metal surfaces, Nature Photonics 2: 299-301, 2008.

[12] M. Kaliteevski, I. Iorsh, S. Brand, R. A. Abram, J. M. Chamberlain, A. V. Kavokin, and I. A. Shelykh, Tamm plasmon-polaritons: Possible electromagnetic states at the interface of a metal and a dielectric Bragg mirror, Phys. Rev. B 76: 165415, 2007.

[13] M. E. Sasin, R. P. Seisyan, M. A. Kalitteevski, S. Brand, R. A. Abram, J. M. Chamberlain, A. Yu. Egorov, A. P. Vasil'ev, V. S. Mikhrin, and A. V. Kavokin, Tamm plasmon polaritons: Slow and spatially compact light, Appl. Phys. Lett. 92: 251112, 2008.

[14] J. Y. Guo, Y. Sun, Y. W. Zhang, H. Q. Li, H. T. Jiang, and H. Chen, Experimental investigation of interface states in photonic crystal heterostructures, Phys. Rev. E 78: 026607, 2008.

[15] T. Goto, A.V. Dorofeenko, A. M. Merzlikin, A.V. Baryshev, A. P. Vinogradov, M. Inoue, A. A. Lisyansky, and A. B. Granovsky, Optical Tamm States in One-Dimensional Magnetophotonic Structures, Phys. Rev. Lett. 101: 113902, 2008.

[16] G. Q. Du, H. T. Jiang, Z. S. Wang, and H. Chen, Optical nonlinearity enhancement in heterostructures with thick metallic film and truncated photonic crystals, Opt. Lett. 34: 578-580, 2009.

[17] G. Q. Du, H. T. Jiang, Z. S. Wang, and H. Chen, Zero-reflection metal slabs: A mechanism of light tunneling in metamaterials, Applied Physics A, 103: 567-570, 2011.

[18] A. Alù, and N. Engheta, Pairing an epsilon-negative slab with a mu-negative slab: resonance, tunneling and transparency, IEEE Trans. Antennas Propagat. 51: 2558-2571, 2003.

[19] C. H. Xue, H. T. Jiang and H. Chen, Highly efficient all-optical diode action based on light-tunneling heterostructures, Opt. Express 18: 7479-7487, 2010.

[20] G. Q. Du, H. T. Jiang, Z. S. Wang, Y. P. Yang, Z. L. Wang, H. Q. Lin, and H. Chen, Heterostructure-based optical absorbers, J. Opt. Soc. Am. B **27**: 1757-1762, 2010.

[21] J. C. Manifacier, J. Gasiot and J. P. Fillard, A simple method for the determination of the optical constants n, k and the thickness of a weakly absorbing thin film, J. Phys. E: Scientific instruments, 45: 1002-1004, 1976.

[22] E. D. Palik, ed., *Handbook of Optical Constants of Solids*, Academic, Orlando, 1985.

[23] A. Yariv and P. Yeh, ed., *Optical waves in Crystals*, Wiley, New York, 1984.

[24] G. Q. Du, H. T. Jiang, L. Wang, Z. S. Wang, and H. Chen, Enhanced transmittance and fields of a thick metal sandwiched between two dielectric photonic crystals, J. Appl. Phys. 108: 103111, 2010.

Vortexlike Power Flow at the Interfaces of Metamaterial Lens

K. Fang[1], Y. W. Zhang[1*], L. W. Zhang[1,2]

[1] MOE Key Laboratory of Advanced Micro-structure Materials, Department of Physics, Tongji University, Shanghai 200092, PR China
[2] School of Physics and Chemistry, Henan Polytechnic University, Jiaozuo, 454003, China
*corresponding author, E-mail: yewen.zhang@tongji.edu.cn

Abstract

The metamaterial lens with DPS/DNS/DPS structure has been realized by using the two-dimensional (2D) isotropic transmission line approach. We studied the vortexlike power flow at the interfaces of metamaterial lens and validated by the finite-difference time-domain (FDTD) simulator. The computational results showing its different conditions near DPS/DNS and other kinds of interfaces are obtained by CST STUDIO SUITE at different frequencies, and demonstrate the intuitionistic power location at the metamaterial lens interfaces.

1. Introduction

Since the pioneer work of Veselago's paper about left-handed media in 1968, the studies of metamaterials have intrigued researchers in the last decade mainly due to the remarkable properties, such as imaging in negative refraction, perfect lens with imaging resolution beyond the usual diffraction limit [1-3]. Researches confirmed the existences of the perfect imaging with metamaterial lens based on the transmission line and other structures [4-7]. The dispersion relations of the wavevector components in the negative index medium over a frequency range are different from that in a conventional medium [8]. With the changing of frequency, the permittivity, permeability and refractive index of metamaterials can be positive, negative and zero, as the phenomena in the phononic crystal depending on the angle of incidence [9]. Metamaterials essentially characterized by negative value of the permittivity, permeability and refractive index result in opposite directions of the wave vector and the Poynting vector. Near the interface between left-handed media and convectional media, the power flow is inevitably vortexlike because of negative refraction. The properties of vortexlike interface mode in one-dimensional metamaterials were studied, and the group delay from the composite right-left-handed transmission line to the right-handed transmission line was shown much longer because the vortex mode leads to slow propagation [10]. The vortex-like surface modes inducing image oscillation and the linear guided waves with a dipole-vortex internal structure of the Poynting vector in left-handed slab waveguides have been demonstrated [11,12].

2. Theory

In this paper, we studied the vortexlike power flow at the different interfaces of two-dimensional metamaterial perfect lens with sandwich structure shown in Figure1 (i.e. DPS/DNG/DPS). In some frequency bands, the two-dimensional microwave metamaterial lens consists of the negative refractive index (NRI) region with negative permittivity and permeability (DNG), and positive refractive index (PRI) region with positive permittivity and permeability (DPS) which can be realized by using transmission lines [13,14]. From Maxwell's source free equations, we can get the electric field E and the magnetic field H, the plane electromagnetic TEM wave in the homogenous media can be written as

$$E_z = E_0 e^{i(k_x x + k_y y - \omega t)} \tag{1}$$

$$H_x = H_0 e^{i(k_y y + k_z z - \omega t)} = \frac{k_y}{\omega\mu} E_0 e^{i(k_y y + k_z z - \omega t)} \tag{2}$$

$$H_y = H_0 e^{i(k_x x + k_z z - \omega t)} = -\frac{k_x}{\omega\mu} E_0 e^{i(k_x x + k_z z - \omega t)} \tag{3}$$

where the wavevector obeys $k^2 = k_x^2 + k_y^2 = \omega^2\mu\varepsilon$. ε and μ refer to the permittivity and permeability in the isotropic media, while $\vec{E}$ and $\vec{H}$ are functions of position. In the isotropic media, the time average of the Poynting vector is

$$\langle S \rangle = \frac{1}{2}\mathrm{Re}\left(\vec{E} \times \vec{H}^*\right) = \frac{\vec{k}}{2\omega\mu}\left|\vec{E}\right|^2 = \frac{\vec{k}}{2\omega\varepsilon}\left|\vec{H}\right|^2 \tag{4}$$

We conceptually assume the media to be lossless for simplicity and, therefore, the material parameters are taken to be real-valued quantities. In the DPS region, Poynting vector possesses the same direction with the wave vector because ε and μ are positive simultaneously. On the contrary, the Poynting vector changes to the opposite direction of the wave vector in DNG region. Therefore, the plane wave is the backward wave in the DNG material. Near the interface between the positive material and the negative material, the Poynting vector changes its direction and result in the vortexlike power flow.

3. Discussion

In our metamaterial lens model, the NRI metamaterial region is constructed by periodically isotropic transmission line medium loaded inductors and capacitors, while the PRI one is constructed of the isotropic microstrip grids. And the sample of the metamaterial lens consists of the first DPS region with 5×11 cells, an adjacent DNG region with 10×11 cells, and the second DPS region with 11×11 cells in (x, y) plane. The DPS medium and the DNG host medium are designed on a dielectric substrate (ε_r=4.75) which height h is 1.6mm with a square grid of w=2.8mm wide microstrip lines. The unit period d is 1 cm in x and y directions. Inductances and shunt capacitances are 3.3nH and 2.5 pF in the DNG region. The schemes are shown in the inset of Figure1. In the long-wavelength regime, the permittivity and permeability of metamaterials can be artificially synthesized with periodic L-C networks and double negative values with a negative refractive index in the high-pass configuration [13, 14]. Here the unit cell dimensions along both of the x-axis and the y-axis are same and much smaller than a wavelength and these arrays of these unit cells can be viewed as isotropic and effective media.

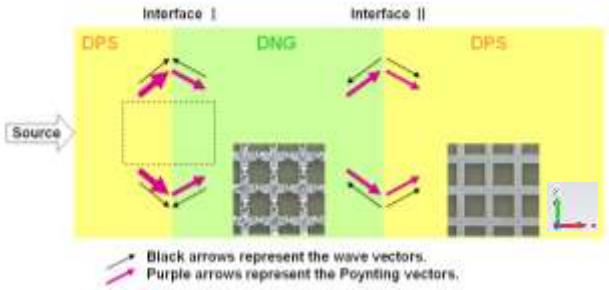

Figure 1: Structure of the metamaterial lens.

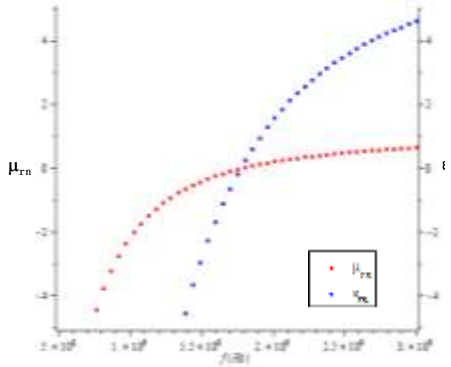

(a) The permittivity and permeability of metamaterial region.

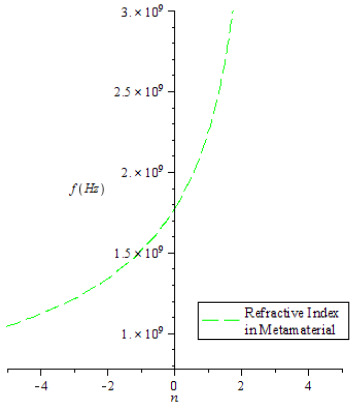

(b) The refractive index of metamaterial region.

Figure 2: The permittivity, permeability and refractive index of metamaterial region.

In the loaded transmission line regions, with the intrinsic dispersions and the parameters as mentioned above, we find three different behaviors according to the signs of permittivity, permeability and refractive index as follows: (i) The double negative (DNG) with permittivity, permeability and refractive index < 0, within the frequency regime of 0.876GHz < f < 1.77GHz. Bragg frequency in this structure is 0.876GHz. The focus frequency is 1.25GHz in the lens which predicts a relative refractive index of n= –1. Within this band, the Poynting vector has opposite direction of wavevector, because the relative permeability and permittivity are negative. (ii) Zero refraction, with the permittivity, permeability and refractive index in metamaterial are nearly zero while the frequency is about 1.77GHz. Most power flow is reflected at the interface between the DPS region and the zero refraction one. (iii) The double positive (DPS) with the permittivity, permeability and refractive index > 0, when f >1.77GHz, and the Poynting vector has same direction with wavevector. The permittivity, permeability and refractive index of metamaterial region are shown in Figure 2 produce positive, negative or zero value at different frequencies.

4. Simulation

A time domain simulation was carried out by CST simulator. The Gauss source signal inputs from the middle point in the left side of the first DPS region to the x-y plane of the lens. In the DPS region, the fields decay away from the source, as expected. On the contrary, in the DNG region, Poynting vector should be pointed away from the point source, the phase velocity vector should be pointed toward the source, as depicted in Figure 1. Figure 3 shows the Poynting vector distribution near the interfaces at different frequencies. The blue dashed lines show the interface between the different regions, and the yellow arrows show the direction of the vortexlike power flow. In Figure 3(a) and (b), the computational results showing the vortexlike power flow near the DPS/DNG and DNG/DPS interfaces are obtained at the focus frequency of 1.25 GHz via metamaterials lens, while the relative refractive index of

DPS and DNG is -1. At the focus frequency, the wave impedance in DNG region is about 141 Ohm, similar to the wave impedance in DPS, while relative permeability and permittivity are about negative one. Therefore, the impedance is matched in different regions of the medium. At the interfaces between DPS and DNG media, the direction of the Poynting vector will differ considerably from those existing at interfaces between two DPS materials. The direction of Poynting vector in one grating unit is clockwise in the upper part of the region, while the one is anticlockwise in the underside. Similar behaviors show in the other regions near the interface. Contrastively, when the simulation signal frequency is 2GHz, the value of refraction index in the two dimensional loaded transmission lines becomes positive, and the interfaces changes to DPS/DPS. Therefore, the interface between the DPS and the zero refraction regions becomes a reflecting interface, shown in Figure 3 (c).

There is a special frequency region, around 1.77GHz, while the permeability, the permittivity and group velocity in the DNG region approach zero. The amplitude of the wavevector in the two dimensional loaded transmission lines is nearly zero. Therefore, the transmission through the interface between the DPS and the zero refraction regions is almost forbidden, and the interface becomes a reflecting interface, shown in Figure 3 (d).

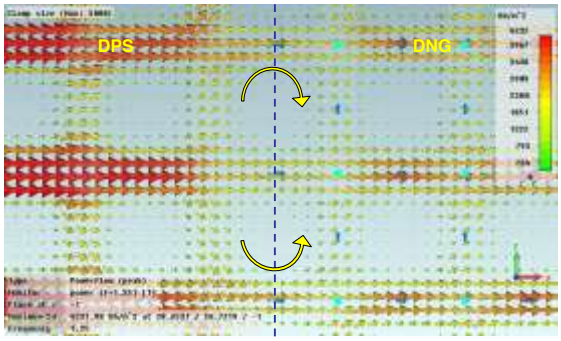

(a) Vortexlike power flow at the DPS/DNG interface in 1.25GHz near the interface Ⅰ in the black dashed rectangle region in Figure1.

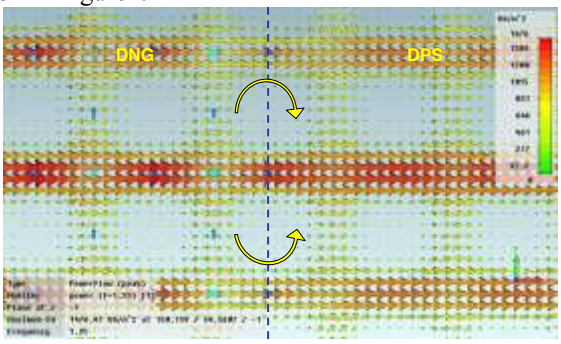

(b) Vortexlike power flow at the DNG/DPS interfaces in 1.25GHz near the interface Ⅱin Figure1.

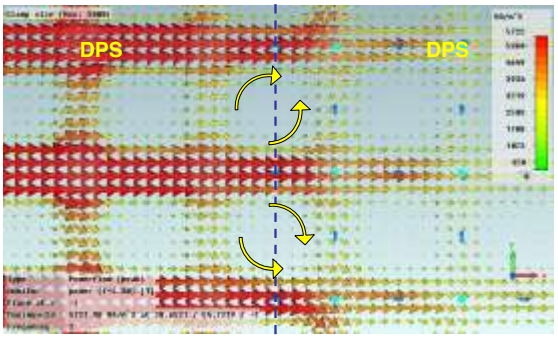

(c) Power flow in 2.00GHz near the interface Ⅰin the black dashed rectangle region in Figure1.

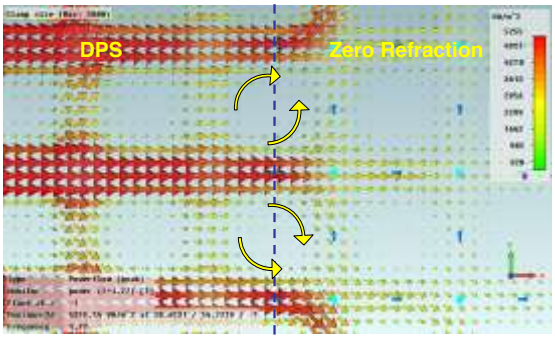

(d) Power flow at the DPS/Zero Refraction interface in 1.77GHz near the interface Ⅰ in the black dashed rectangle region in Figure1, resulting in little transmission.

Figure 3: The power flow at the interfaces of metamaterial lens.

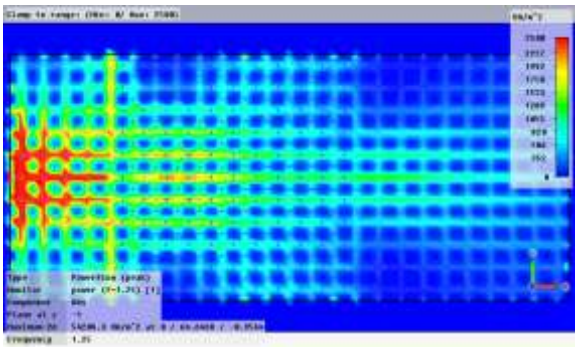

(a) 1.25GHz

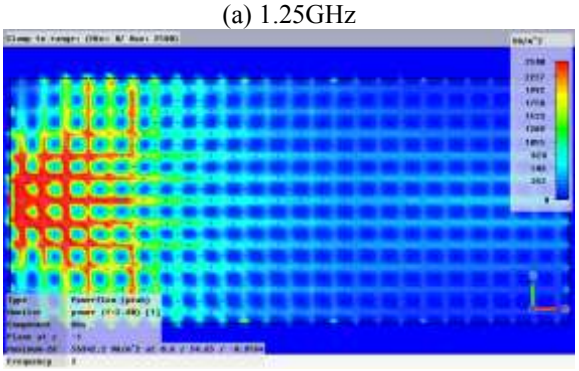

(b) 2.00GHz

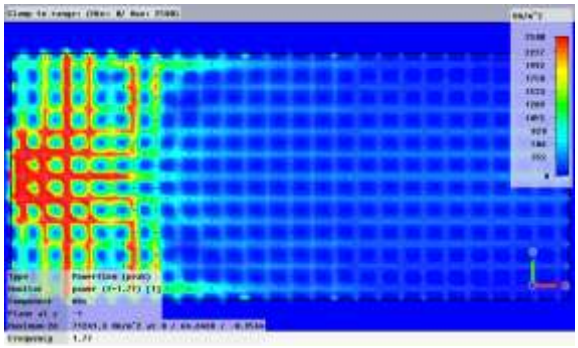

(c) 1.77GHz

Figure 4: Amplitudes of power flow of the sample at different frequencies. (a) Amplitudes of power flow focused in the DNG region and the second DPS region in 1.25GHz. (b) Amplitudes of power flow are decaying away from the interface in 2.00GHz. (c) Amplitudes of power flow in the DPS/Zero Refraction/DPS regions in 1.77GHz.

The vortexlike power flow on the interfaces changes the directions of power flow in the metamaterial lens, and produces the first focus phenomenon in the DNG region and the second focus in the second DPS region mentioned, shown in Figure 4 (a). The change of the vortexlike Poynting vector direction at the DPS/DNG interface is also an important feature that makes the localization for focus in the metamaterial lens. On the contrary, at the DPS/DPS interface, the power flow of electromagnetic wave scatters through the interface and its amplitude decay, shown in Figure 4 (b). Near the interface between the DPS/Zero refraction regions, most of the wave and the power flow can not pass the interface and be dispersed along the DPS side of the interface, shown in Figure 4 (c).

5. Conclusion

To summarize, we have studied the characters of power flow at the interface in the metamaterial lens. The energy flow forms vortices at the interfaces between the DPS and DNG regions and the energy was partly trapped. Therefore, the location at the metamaterial lens interfaces can be explained. The new message in this paper is analysis of the vortexlike power flow and the explanation of the location at the metamaterial lens interfaces which may have potential applications in metamaterials-based imaging system.

Acknowledgements

The present research was supported by National Basic Program (973) of China (No.2011CB922001), and by the National Natural Science Foundation of China (Nos. 10634050, 10904032).

References

[1] V. G. Veselago, The electrodynamics of substances with simultaneously negative values of ε and μ, *Sov. Phys. Usp*., 10: 509-514, 1968.

[2] J. B. Pendry, Negative Refraction Makes a Perfect Lens, *Phys. Rev. Lett*., 85: 3966-3969, 2000.

[3] D. R. Smith, J. B. Pendry, M. C. K. Wiltshire, Metamaterials and negative refractive index, *Science,* 305: 788-792, 2004.

[4] A. K. Iyer, P. C. Kremer, and G. V. Eleftheriades, Experimental and theoretical verification of focusing in a large, periodically loaded transmission line negative refractive index metamaterial, *Opt. Express*. 11(3): 696-708, 2003.

[5] G. V. Eleftheriades, Negative Refraction and Focusing in Hyperbolic Transmission-line Periodic Grids, *IEEE Trans. Microw. Theory Tech*., 53(1): 396-403, 2005.

[6] P. Alitalo, S. Maslovski, and S. Tretyakov, Three-dimensional isotropic perfect lens based on LC-loaded transmission lines, *J. Appl. Phys*., 99, 064912, 2006.

[7] T. J. Cui, Q. Cheng, W. B. Lu, Q. Jiang, and J. A. Kong, Localization of electromagnetic energy using a left-handed-medium slab, *Phys. Rev. B*, 71, 045114, 2005.

[8] G. V. Eleftheriades, K. G. Balmain, *Negative-Refraction Metamaterials: Fundamental Principles and Applications*, Wiley, New York, pp.214-219, 2005.

[9] J. Bucay, E. Roussel, J. O. Vasseur, P. A. Deymier, A-C. Hladky-Hennion, Y. Pennec, K. Muralidharan, B. Djafari-Rouhani, and B. Dubus, Positive, negative, zero refraction, and beam splitting in a solid/air phononic crystal: Theoretical and experimental study, *Phys. Rev. B*, 79, 214305, 2009.

[10] Y. Wang, Y. Zhang, L. He, H. Li, H. Chen, F. Liu, C. Caloz, Time-domain study of vortexlike interface mode in metamaterials, *Appl. Phys. Lett*. 91, 221907, 2007.

[11] L. Zhou, and C. T. Chan, Vortex-like surface wave and its role in the transient phenomena of meta-material focusing, *Appl. Phys. Lett.,* 86, 101104, 2005.

[12] I. V. Shadrivov, A. A. Sukhorukov, and Y. S. Kivshar, Guided modes in negative-refractive-index waveguides, *Phys. Rev. E*, 67, 057602, 2003.

[13] A. K. Iyer, P. C. Kremer, and G. V. Eleftheriades, Experimental and theoretical verification of focusing in a large, periodically loaded transmission line negative refractive index metamaterial, *Opt. Express*, 11(7): 696-708, 2003.

[14] A. Grbic, and G. V. Eleftheriades, Periodic analysis of a 2-D negative refractive index transmission line structure, *IEEE Trans. Antennas Propag.*, 51(10): 2604-2611, 2003.

Lower RCS Directional Antenna by Left-Handed Material

Rui-xin Wu*, Jiang Zhu and Li-rong Tan,

School of Electronic Science and Engineering, Nanjing University, Nanjing 210093, China
* E-mail: rxwu@nju.edu.cn

Abstract

The emission of a current line source surrounded by a cylindrical shell of left-handed material (LHM) is studied theoretically. The use of LHM shell greatly improves the directional emission of the line source, while in a broadband frequency range its radar cross-section is lower than that of a parabolic reflector antenna with the same aperture size. This may be useful in stealth antenna design. We prove the directive emission is due to the negative refraction and the focus effect occurring at the interface of the LHM shell.

1. Introduction

Metamaterials are engineered composites that exhibit superior properties that do not find in nature and not observed in the constituent materials. Owing to their abnormal electromagnetic characteristics, metamaterials have drawn significant scientific and engineering interest. Many works have devoted to the physics and possible applications of the metamaterials. The most well-known applications are superlens [1] and cloaking [2]. Besides, theoretical studies predict the great advantages from metamaterials in antenna design. For example, resonant conditions for strongly subwavelength patch antennas and using metamaterials to improve the source radiation have been discussed. Ziolkowski [3] proved that double negative metamaterials could increase the power radiation of electrically small antenna. Ghoshm [4] studied gain enhancement of antennas using metamaterials, which including left-handed materials (LHM) and single-negative materials. Enhancing the directional emission is another important application of metamaterials. Enoch [5] first showed that energy radiated by a source embedded in an isotropic metamaterial was concentrated in the narrow cone in the surrounding media. After that, directive emission enhancement was studied for the radiators with anisotropic metamaterials [6] and cylindrical metamaterials [7-8]. Many theoretical works have been backed up with prototypes experimentally verifying the proposed ideas, which stimulate many interests in antenna design [9-14]. People are trying to design new antennas with metamaterials to improve the antenna performances.

In this work, we will show that the line source surrounded by a cylindrical shell of left-handed metamaterial has a very good directional emission; while it has a lower radar cross section in a broadband frequency range. This feature provides a new way for designing stealth antennas. We prove that the directive emission is caused by the negative refraction and focus effects at the interface of the LHM shell.

2. Theoretical model

Consider that a radiator consists of a line source and a surrounding cylindrical shell as shown in Fig.1. The line source and the shell are infinite long along z-axis, so the source emission reduces into a two-dimensional problem. The shell is with the inner radius a and outer radius b, respectively, which separating the calculation area into the regions I, II and III. Without loss of the generality, we assume the current line source is on x-axis in the region I. It produces a TMz mode electromagnetic (EM) wave, which can be expressed, in cylindrical coordinate, as [15]

$$E_z^i(\bar{\rho}) = -\frac{k_0^2 i_0}{4\omega\varepsilon_0} H_0^{(2)}\left(k_0|\bar{\rho}-\bar{\rho}_0|\right) = \begin{cases} -\frac{k_0^2 i_0}{4\omega\varepsilon_0}\sum_n H_n^{(2)}(k_0\rho_0)J_n(k_0\rho)e^{in(\phi-\phi_0)} & (\rho<\rho_0) \\ -\frac{k_0^2 i_0}{4\omega\varepsilon_0}\sum_n J_n(k_0\rho_0)H_n^{(2)}(k_0\rho)e^{in(\phi-\phi_0)} & (\rho>\rho_0) \end{cases} \quad (1)$$

where $k_0 = \omega\sqrt{\varepsilon_0\mu_0}$ is the wave number in free space. The excited EM wave spreads outward and at steady state, the total field in each region is:

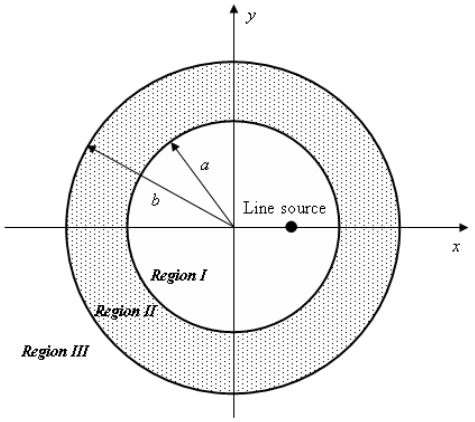

Figure 1. Schematic diagram of LHM directional antenna, which includes a line source and an LHM shell

$\rho \le a$:

$$E_z^t = E_z^i(\bar{\rho}) - \frac{k_0^2 I_0}{4\omega\varepsilon_0} \sum_{n=-\infty}^{\infty} J_n(k_0\rho_0)\left[A_n J_n(k_0\rho)\right] e^{in(\varphi-\varphi_0)} \quad (2)$$

$a < \rho \le b$:

$$E_z^t = -\frac{k_0^2 I_0}{4\omega\varepsilon_0} \sum_{n=-\infty}^{\infty} \left[B_n H_n^{(2)}(k\rho) + C_n J_n(k\rho)\right] e^{in(\varphi-\varphi_0)} \quad (3)$$

$\rho > b$:

$$E_z^t = -\frac{k_0^2 I_0}{4\omega\varepsilon_0} \sum_{n=-\infty}^{\infty} D_n H_n^{(2)}(k_0\rho) e^{in(\varphi-\varphi_0)} \quad (4)$$

In the above J_n is the Bessel function of first kind and H_n is the Hankel function of second kind. The coefficients A_n, B_n, C_n and D_n are unknowns. Using the continuous conditions of the electric and magnetic fields at boundaries $r = a$ and b, we have a system of linear equations with four unknowns. Solving the equations, the field distribution in each region is obtained, and then the far-field radiation pattern can be derived. Corresponding magnetic fields can be derived by Maxwell equation, which are:

$$H_\rho = -\frac{i}{\omega\mu\rho}\frac{\partial E_z}{\partial\varphi}, \quad H_\varphi = -\frac{i}{\omega\mu}\frac{\partial E_z}{\partial\rho} \quad (5)$$

3. Radiation of a line source with LHM shell

We suppose the shell in Fig.1 is made of a uniform dispersive material. Its permittivity ε_r and permeability μ_r follows Drude model and Lorentz model [17], respectively, i.e.

$$\varepsilon_r = 1 - \frac{\omega_{ep}^2}{\omega(\omega - i\gamma_e)} \quad (6)$$

$$\mu_r = 1 + \frac{F\omega_{mp}^2}{\omega_{m0}^2 - \omega(\omega - j\gamma_m)} \quad (7)$$

where ω_{ep} and γ_e are electric plasma frequency and damping coefficient; ω_{mp}, ω_{mo} and γ_m are magnetic plasma frequency, magnetic resonance frequency and magnetic damping coefficient, respectively. We assume $f_p=\omega_p/2\pi$=4.24GHz, $f_{mp}=\omega_{mp}/2\pi$=6.5GHz, $f_{m0}=\omega_{m0}/2\pi$=2.1GHz and F=0.22. For simplicity, the damping coefficient γ_e and γ_m are supposed zero in this work. It is easy to verify ε_r and μ_r are both negative in the frequency range 2.1 to 3.7GHz. Specifically, at 3GHz both ε_r and μ_r are negative one; the impedance of shell matches that of free space.

The normalized electric far-field radiation pattern at 3GHz is shown in Fig. 3(a) in solid line. The shell is assumed, respectively, with inner radius a=1.5λ_0 and outer radius b=3.5λ_0 where λ_0 is the wavelength in free space at the working frequency. The line source is near the inner wall at ρ_0=1.35λ_0. We see the radiation has a sharp main beam along x-axis. The sharp beam marks the EM energy mostly focusing on that direction. To display this feature intuitively, we did simulation of the time averaged power flow by the finite element solver COMSOL. The result, shown in Fig. 3(b), illustrates the most of the outgoing EM energy concentrates in a small angle along x-axis forming a narrow beam. The power flow distribution is the same as that of the far-field radiation pattern though they are obtained by the different methods. This confirms the computing results of the field distribution. The directivity derived from radiation pattern is about 20, much greater than that of the line source without LHM shell. As a compare, we replace the LHM by a normal material with $\varepsilon_r=\mu_r$=+1.2, and recalculated the radiation pattern. The result is shown in Fig. 3(a) in dash line. Quit different from the radiation pattern of the LHM shell, the radiation does not focus on any direction but almost radiates uniformly.

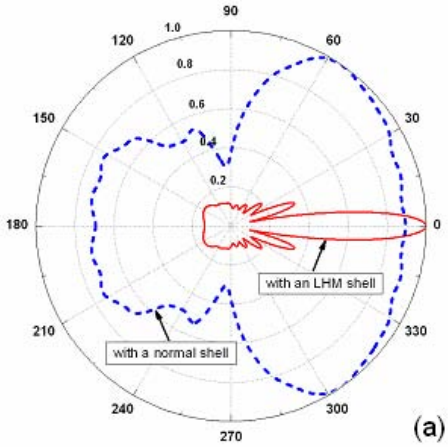

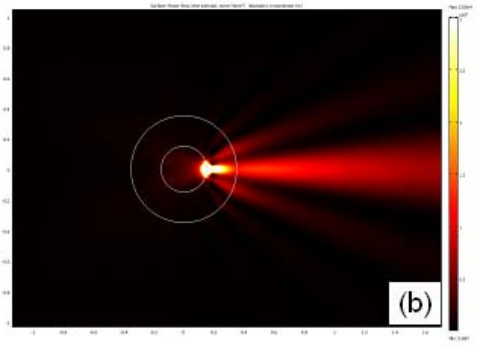

Figure 3. (a) Far-field radiation pattern of the line source at 3GHz at which the shell has $\varepsilon_r=\mu_r$=-1 (solid line). The dash line is for the shell with $\varepsilon_r=\mu_r$ =1.2. (b) Power flow distribution of the line source radiation for LHM shell.

The difference between the two radiation patterns demonstrates the LHM shell greatly improves the directive emission of the line source when it locates at a proper position; this system can be considered as a directional antenna (LHM antenna). With the far-field distribution, we have the total radiation power of the line source. It is about 1.15P_0, where P_0 is total radiation power of the line source in free space. The LHM shell does not reduce total power delivered by the line source because of the impedance match at working frequency. The slight increase of the total power is related to the high mode excitation [3].

It may be helpful to compare the directive emission of the LHM antenna with a known directional antenna having the same aperture size. Here, a parabolic reflector antenna is used for a comparison. The aperture size of the parabolic antenna is $2a$, same as the diameter of the LHM shell. Figure 4 is the far-field radiation pattern of two antennas, and the inset shows a comparison of their feature size. We see two antennas all have a sharp main beam. The half-power bandwidth HPBW, which measures the main beam width, is about 11° for the LHM antenna, slightly larger than that of the parabolic antenna 9°. The two main beams are almost the same, indicating their similar directional emission characteristics. Though the larger sidelobe and backlobes cause the directivity of the LHM antenna is lower than that of parabolic antenna, the use of LHM shell increases the focusing ability of the line source obviously.

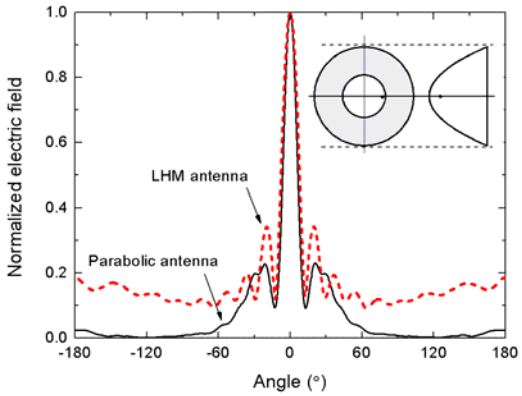

Figure 4. Far-field radiation patterns for LHM antenna and a parabolic antenna with same feature aperture size of LHM antenna. The inset shows the compare of the feature size of two antennas.

Another advantage using LHM shell is its lower radar cross section. In 2D, the radar cross-section is defined as,

$$\sigma = 2\pi\rho \lim_{\rho\to\infty} \frac{E_s^2}{E_i^2} \qquad (8)$$

where E_s is the scattering field and E_i is the incident field. We compare the radar cross-section of our antennas with a parabolic reflector antenna having the same feature size. Figure 5 shows the ratio $\sigma = \sigma_{LHM}/\sigma_P$, where σ_{LHM} and σ_P are the radar cross-section of LHM shell and parabolic reflector, respectively. The dispersive ε and μ of LHM is considered in calculations. We see in broadband frequencies the σ for LHM antenna is never greater, but mostly much smaller than that of parabolic antenna. This is due to the impedance mismatch at the interface of the LHM shell and free space is much smaller than that of for metallic reflector. The relative larger σ of the LHM shell at 3 GHz is due to the focus effects, which will be explained below. The high directivity with lower radar cross-section in broadband frequency makes the LHM antenna useful in design of stealth antennas, which has been becoming more and more important in stealth technology today.

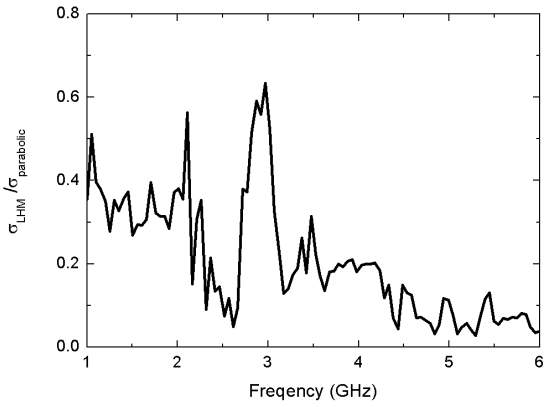

Figure 5. RCS ratio of LHM antenna to parabolic antenna shown in the inset of Fig. 4.

The directive emission shown above can be explained by the negative refraction at outer interface and the focus effect at inner interface of the LHM shell. The process can be proved by the LHM shell illuminated by a plane wave. According to the reciprocal principle of the antenna, if the incident plane wave can create a focus point within the region I, a real source at this point will produce a plane wave out of the LHM shell. We did simulations with shell parameters a=1.5λ_0, and b=3.5λ_0 at 3GHz at which ε and μ are both negative one. Figure 6 gives time averaged power flow density distribution when the plane wave incident from the right-hand side. In the figure, we see a sharp light spot S_1, representing the high power flow density, is on x-axis in the region I near the inner wall of the shell. The spot position is about 1.35λ_0, same as the source position in radiation pattern calculation in Fig. 3. The ray tracing can explain the presence of the light spot. As the incident ray meets the outer interface, negative refraction occurs. The refracted rays will form a focus. Its position is $b/2$ according to the Gauss' formula since the shell's index n is -1 at 3GHz. Thus, we need the inner radius a be smaller than $b/2$. Otherwise, the refracted rays will meet the inner interface of the LHM shell, and then second refraction at the interface causes the rays diversity in region I. If the condition $a<b/2$ is satisfied, a focus will appear within the LHM shell due to the refraction at the inner interface. This focus as a second source generates a high quality image source, the light spot S_1, in the region I according to the near field imaging principle of LHM. Indeed, in Fig. 6 we can find the light spot S_2 within the LHM shell; the position is about 1.6λ_0 slightly smaller than $b/2$. This is because the shell size is not much larger than the operating wavelength as required by geometric optics. Therefore, it can be expected that a good directional radiation is formed as the line source sets at the position light spot S_1.

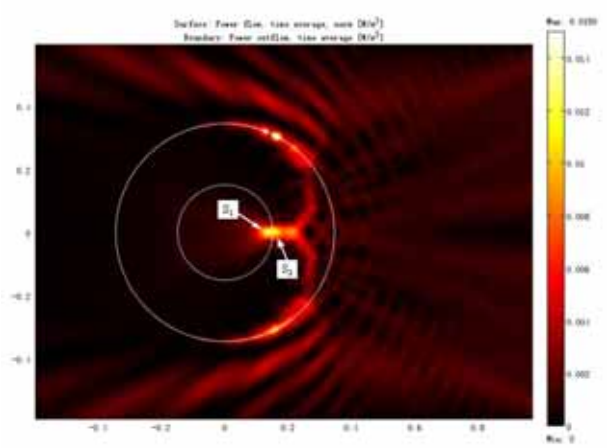

Figure 6. Power flow distribution for the LHM shell illuminated by the plane wave incident from right-hand side. The negative refraction at the outer interface of LHM forms the light spots S_2, which in turn as a second source creates the spot S_1 by the image process of LHM at inner interface.

4. Conclusions

We have explored the radiation property of the LHM antenna made of the current line source and the surrounding LHM shell. The study shows this antenna has a good directional emission when the line source locates near the inner wall of the LHM shell. The directive emission is attributed to the negative refraction and the focus effect happening at the interface of the LHM shell, and can be well explained by ray tracing. The lower radar cross-section in broadband frequencies makes the LHM antenna useful in designing stealth antennas.

Acknowledgements

This work is supported by National Natural Science Foundation of China (60771013, 61071007, 61001017) and Specialized Research Fund for the Doctoral Program of Higher Education (20110091110030, 20100091120045).

References

[1] N. Fang, H. Lee, C. Sun and X. Zhang, Sub-diffraction-limited optical imaging with a silver superlens, *Science* 308: 534-537, 2005

[2] D. Schurig, J. J. Mock, B.J Justice, S. A. Cummer, J. B. Pendry, A. F, Starr and D. R. Smith, Metamaterial electromagnetic cloak at microwave frequencies, *Science* 314: 977-980, 2006

[3] R. W. Ziolkowski and A. D. Kipple, Application of double negative materials to increase the power radiated by electrically small antennas, *IEEE Trans. Antennas Propag.* 51:2626-2640, 2003

[4] B. Ghoshm, S. Ghosh, and A. B. Kakade, Investigation of gain enhancement of electrically small antennas using double-negative, single-negative, and double-positive materials, *Phy. Rev. E* 78: 026611, 2008

[5] S. Enoch, G. Tayeb, P. Sabouroux, N. Guerin and P. Vinvent, A metamaterial for directive emission, *Phys. Rev. Lett.* 89: 213902, 2002

[6] I. Bulu, H. Caglayan, K. Aydin and E. Ozbay, Compact size highly directive antennas based on the SRR metamaterial medium, *New J. Phys.* 7: 223, 2005

[7] S. Arslanagic and O. Breinbjerg, Electric-line-source illumination of a circular cylinder of lossless double-negative material: An investigation of near field, directivity, and radiation resistance, *IEEE Antennas Propag. Magazine* 48: 38-54, 2006

[8] S. Arslanagic, R. W. Ziolkowski, and O. Breinbjerg, Excitation of an electrically small metamaterial-coated cylinder by an arbitrarily located line source, *Microwave Opt. Technol. Lett.* 48: 2598-2606, 2006

[9] L. W. Li, Y. N. Li, T. S. Yeo, J. R. Mosig and O. J. F. Martin, A broadband and high-gain metamaterial microstrip antenna, *Appl. Phys. Lett.* 96: 164101, 2010

[10] H. K. Liu and K. J. Webb, Leaky wave radiation from planar anisotropic metamaterial slabs, *Phys. Rev. B* 81: 201404, 2010

[11] Y. Luo, J. J. Zhang, H. S. Chen, J. T. Huangfu and L. X. Ran, High-directivity antenna with small antenna aperture, *Appl. Phys. Lett.* 95: 193506, 2009

[12] H. F. Ma, X. Chen, H. S. Xu, X. M. Yang, W. X. Jiang and T. J. Cui, Experiments on high-performance beam-scanning antennas made of gradient-index metamaterials, *Appl. Phys. Lett.* 95: 094107, 2009

[13] A. Alu and N. Engheta, Enhanced directivity from subwavelength infrared/optical nano-antennas loaded with plasmonic materials or metamaterials, *IEEE Trans. Antennas Propag.* 55: 3027-3039, 2007

[14] F. P. Casares-Miranda, C. Camacho-Penalosa and C. Caloz, High-gain active composite right/left-handed leaky-wave antenna, *IEEE Trans. Antennas Propag.* 54: 2292-2300, 2006

[15] R. F. Harrington, *Time-Harmonic Electromagnetic Fields*, Wiley-IEEE Press, New York, 2001

[16] D.M. Pozar, *Microwave Engineering*, John Wiley & Sons, New York, 2005

[17] S. A. Ramakrishna, Physics of negative refractive index materials, *Rep. Prog. Phys.* 68: 449–521, 2005

Experimental Observation on Building-up of Negative Refraction

F. F. Li, K. Fang ,Y. W. Zhang*

MOE Key Laboratory of Advanced Micro-structure Materials, Department of Physics,
Tongji University, Shanghai 200092, PR China
*corresponding author: yewen.zhang@tongji.edu.cn

Abstract

The two-dimensional (2D) metamaterial is realized by using the isotropic transmission line approach. When an electromagnetic (EM) wave hits the interface between the positive and negative refractive index materials, the reflected wave will build up firstly, and after a while, the wave front moves eventually in the negative refracted direction. Finite-difference time-domain (FDTD) simulations and experiment are used to study the time evolution of an EM wave as it hits the interface.

1. Introduction

In 1904, Schuster firstly came up with the concept of negative refraction in his book [1]. At the end of 1960s, Veselago [2] discussed the material which possessed simultaneously negative permittivity, and negative permeability, would exhibit unusual properties such as negative index of refraction. In 1998, Pendry suggested that some specific structures would have both ε_{eff} and μ_{eff} negative (over a range of frequencies). After that, there have been numerous theoretical and experimental studies. In particular, Markos˘ and Soukoulis [3] have employed the transfer matrix technique to calculate the transmission and reflection properties of the structure suggested by Pendry [4] and realized experimentally by Smith et al.. Later, Smith et al. proved that the data of Ref. [3] can be fitted by length independent and frequency dependent ε_{eff} and μ_{eff}. They found that in a frequency region both ε_{eff} and μ_{eff} were negative with negligible imaginary parts. In this negative region, n was found to be unambiguously negative. These unusual results have raised objections both to the interpretation of the experimental data and to the realizability of negative refraction. Since then, metamaterial became an exciting researching field with much different future advancements in physics, material sciences and telecommunications. [6-9]

In this paper, we report a two-dimensional microwave metamaterial composed of the isotropic periodically loaded transmission line structure which can exhibit the negative refraction phenomenon. With the time-domain experiment, we find that when the electromagnetic wave hits the interface between PRI region and NRI region, the reflective wave will build up firstly then the refractive wave will turn up. In the time domain experiment we use the Gaussian modulated pluses as the input signal.

2. Negative refraction in metamaterial

2.1 Parameters calculation

In particular frequency band, the two-dimensional microwave metamaterial consists of negative refractive index (NRI) metamaterial region with simultaneously negative permittivity and permeability, and positive refractive index (PRI) region with simultaneously positive permittivity and permeability [10-13]. The NRI metamaterial region is constructed by periodically transmission line medium with inductors and capacitors. And the PRI one is consisted of the microstrip grids.

We structured a negative refraction sample with isotropic periodically loaded transmission line. The height of bottom metal layer is 0.018mm. The sample is fabricated on a ceramic ($\varepsilon_r = 4.75\ \mu_r = 1$) substrate of height h=1.6mm and form the PRI region measuring 3×4 cells. The adjacent NRI region shaped isosceles triangle is measured 11×11 cells. Both the PRI medium and the NRI medium are consisted of a square grid of w=2.8mm wide microstrip lines with d=10mm period. The shunt inductance is L = 15nH and the series capacitance is C= 3.3 pF.

In the PRI region,

$$\varepsilon_{re} = \frac{\varepsilon_r + 1}{2} + \frac{\varepsilon_r - 1}{2} \cdot \frac{1}{\sqrt{1 + \frac{12 \cdot h}{w}}} \quad (1)$$

$$\varepsilon_p = 2 \cdot \varepsilon_{re} \cdot \varepsilon_0 \quad (2)$$

$$\mu_p = \mu_0 \quad (3)$$

$$g = \frac{1}{2\pi} \cdot \ln\left(\frac{8 \cdot h}{w} + \frac{w}{4 \cdot h}\right) \quad (4)$$

where ε_p is effective permittivity of PRI region, μ_p is effective permeability and g is conduct factor which is decided by the structure.

In the NRI region,

$$\mu_n = \mu_p - \frac{1}{g \cdot C \cdot d \cdot \omega^2} \quad (5)$$

$$\varepsilon_n = \varepsilon_p - \frac{g}{L \cdot d \cdot \omega^2} \quad (6)$$

where ε_n and μ_n are effective permittivity and permeability of NRI region. The relative index of refraction in PRI and NRI region is

$$n_{rP} = \sqrt{2 \cdot \varepsilon_{re} \cdot \mu_r} \quad (7)$$

$$n_{rN} = \sqrt{\varepsilon_{rn} \cdot \mu_{rn}} \quad (8)$$

2.2 Negative refractive index

So, we have the dispersion figure of refractive index in PRI and NRI region shown in Fig. 1. The x axis is frequency and the y axis is square power of refractive index n. We want to have the -1 relative refractive index, so we have the next equation. According to the transfer matrix, we can calculate the wave vector, phase velocity and group velocity.

$$n_{rP} = -n_{rN} \quad (9)$$

$$\beta d = \pm \omega d \sqrt{\left(L_0 - \frac{1}{\omega^2 C d}\right)\left(2C_0 - \frac{1}{\omega^2 L d}\right)} \quad (10)$$

$$v_p = \omega / \beta \quad (11)$$

$$v_g = \partial\omega / \partial\beta \quad (12)$$

L_0 and C_0 are distributed parameter of PRI transmission line. C and L are loaded capacitance and inductance. v_p is phase velocity and v_g is group velocity.

.

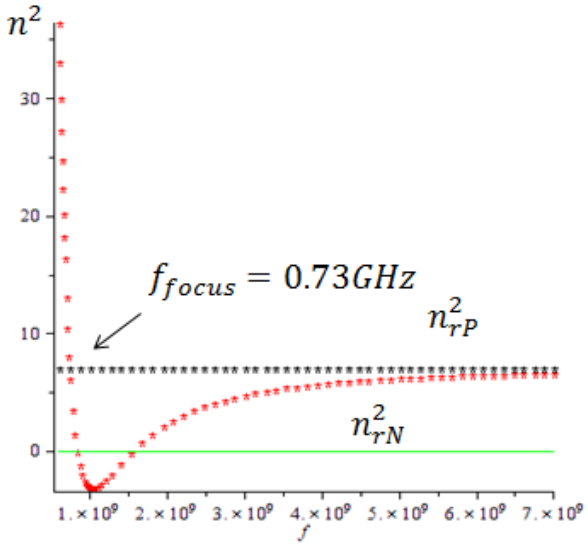

Figure 1: Dispersion figure of refractive index

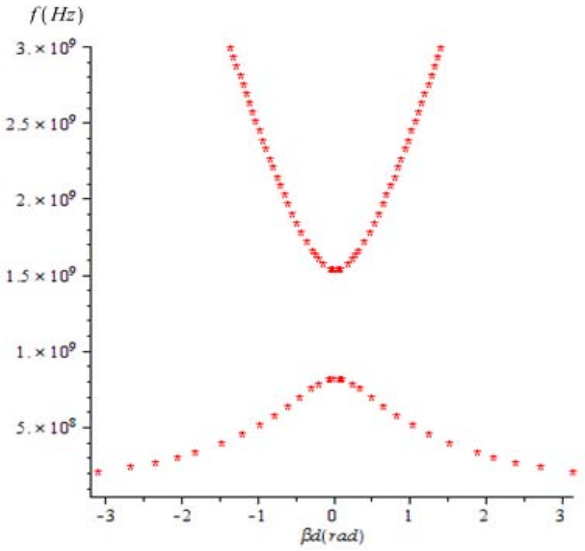

Figure 2: Dispersion figure of wave vector.

The frequency band with the negative permittivity and permeability in first passband is from Bragg frequency to the cutoff frequency. The focus frequency in this band is in the condition that the relative refractive index is –1. The second passband over 1.54GHz has the simultaneously positive permittivity and permeability.

So we have the results that the broadband region from 0.36GHz to 1.54GHz has the negative refractive index.

When the frequency equals 0.73GHz, the sample presents a relative refractive index of –1 and the best impedance match. We put 0.73GHz to the equation (11) and (12), so in the NRI region, v_p=-1.1*10^8 m/s, v_g=2.4*10^7 m/s.

3. Experimental observation on building on negative refraction

3.1 Negative refraction sample

Fig.3 is the experimental negative refraction sample. Port 1 is input terminal, while Port 2 and Port 3 are the reflection and refraction ones. Horizontal side is signed with numbers and vertical side is expressed with letters. We put 50Ω resistance on the sample boundry to match the impedance.

3.2 Time domain measurement

In CST simulation and experiment, we use the time-domain method to measure all the data and compare with the theoretical results. The experimental instruments of time-domain measurement are shown schematically in Fig.4. The Tektronix arbitrary waveform generator (AWG710) is used to generate the Gaussian envelope of signal while the Agilent vector signal generator (E8267D) is used to generate the carrier wave with the same frequency of focus, 0.73GHz. Because the AWG710 gives a 10MHz reference clock signal to the E8267D and a trigger signal to the oscilloscope, these three instruments are synchronized. So the waveforms tested from different positions could be compared. The Tektronix P7260 probe with an input impendence of 20kΩ and bandwidth of 6GHz detects the waveforms at different positions. Finally, the oscilloscope shows the waveforms and outputs the data.

We measure the sample in three routes point by point. Then pick up 4F, 6D and 6H three dots. These three points have the same distance from the interface. The waveform of these three points is shown in Fig. 5. Point 4F is in the input region, point 6H is in the reflection region and point 6D is in the refraction region. From the figure we can see the reflected wave build up firstly then the refracted wave turned up. Table 1 is the time difference between these points.Six points are picked up to be the example. Three of them are in the reflection region, another three are in the refraction refion. At the same time, they are all symmetrical around the interface. From Table we can see the time that wave reach to the reflection refion is shorter than the refrction region, and the time difference between symmetrical points are all about 0.94ns. v_p=-1.0*10^8 m/s, v_g=2.7*10^7 m/s the data of experiment are much closed to the theory. According that we observe that when electromagnetic (EM) wave hits the interface between a positive and negative refractive index material, the reflected wave will build up firstly, and after a while, the wave moves in the negative refracted direction.

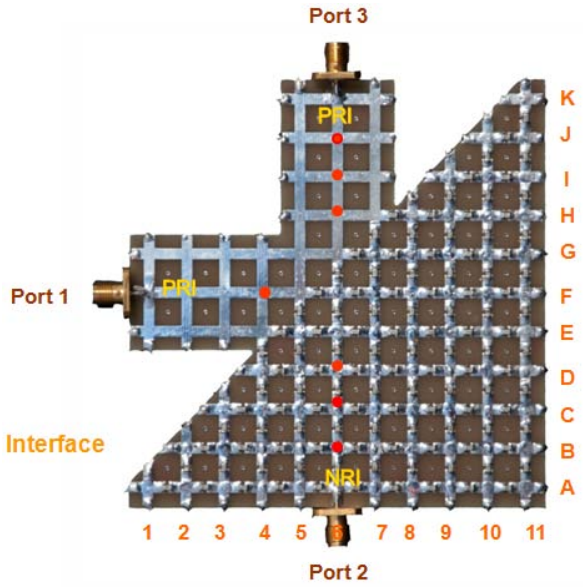

Figure 3 Negative refraction sample

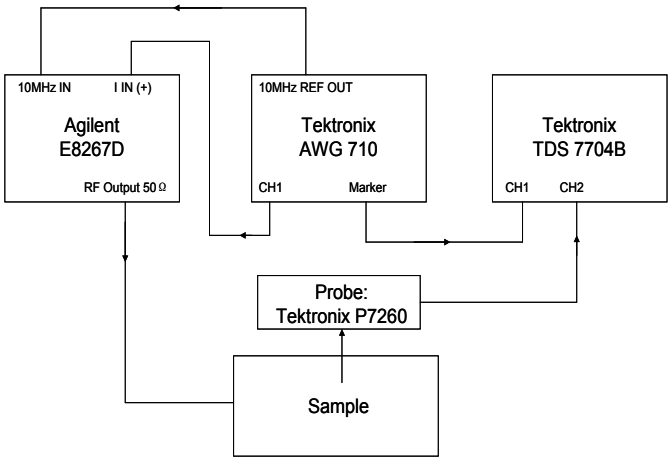

Figure 4 Time domain measurement.

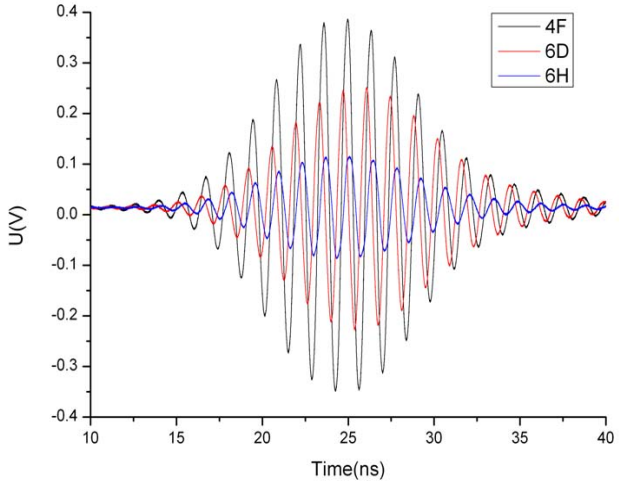

Figure 5 Waveforms in 3 points

Table 1: Time difference

Point	Time difference with 4F Δt_1(ns)	Time difference Δt_2 (ns)
6B	1.51	Between 6B and 6J
6J	0.57	0.94
6C	1.21	Between 6C and 6I
6I	0.27	0.94
6D	0.95	Between 6D and 6H
6H	< 0.01	0.95

4. Conclusion

To summarize, negative refraction creation process on the two-dimensional metamaterial is studied in time-domain methods. The simulation and experimental results show that when the electromagnetic (EM) wave hits the interface between a positive and negative refractive index material, the reflected wave will build up firstly, and after a while, the wave front moves eventually in the negative refracted direction. By means of that, we can understand the characters and the processes of negative refraction in detail.

Acknowledgements

This research is supported by National Basic Program (973) of China (No.2011CB922001), and by the National Natural Science Foundation of China (No. 10904032).

References

[1]. A. Schuster, *An Introduction to the Theory of Optics*, Edward Arnold, London, 1904.

[2]. V. G. Veselago, The electrodynamics of substances with simultaneously negative values of ε and μ, *Sov. Phys. Usp.* 10, 509-514, 1968.

[3]. P. Markoš , C.M. Soukoulis, Transmission studies of left-handed materials, *Phys. Rev. B* **65**, 033401, 2001; Numerical studies of left-handed materials and arrays of split ring resonators, *Phys. Rev. E* **65**, 036622 , 2002.

[4]. J. B. Pendry et al., Extremely Low Frequency Plasmons in Metallic Mesostructures, *Phys. Rev. Lett.* 76, 4773-4776, 1996; J. B. Pendry *et al.*, Low frequency plasmons in thin-wire structures, *J. Phys. Condens. Matter* 10, 4785-4809, 1998

[5]. D. R. Smith, W. J. Padilla, D. C. Vier, S. C. Nemat-Nasser, S. Schultz, A composite medium with simultaneously negative permeability and permittivity, *Phys. Rev. Lett.* 18, 4184-4187, 2000.

[6]. J. B. Pendry, Negative refraction makes a perfect lens, *Phys. Rev. Let*t. 18, 3966-3969, 2000.

[7]. C. Luo, S. G. Johnson, J. D. Joannopoulos, J. B. Pendry, All-angle negative refraction without negative effective index, *Phys. Rev. B*, 201104, 2002.

[8]. G.V.Eleftheriades, K.G. Balmain, *Negative-refraction Mearmaterials: Fundamental Principles and Applications*, Wiley, New York, pp. 214-219, 2005.

[9]. S. Foteinopoulou, E. N. Economou, C. M. Soukoulis, Refraction in media with a negative refractive index, *Phys. Rev. Lett.* 10, 107402, 2003.

[10]. D. R. Smith, J. B. Pendry, M. C. K. Wiltshire, Metamaterials and negative refractive index, *Science* 5685, 788-792, 2004.

[11]. A. Grbic, G. V. Eleftheriades, Periodic analysis of a 2-D negative refractive index transmission line structure, *IEEE Trans. Antennas Propag*.10, 2604-26 11, 2003.

[12]. W. T. Lu, J. B. Sokoloff, S. Sridhar, Refraction of electromagnetic energy for wave packets incident on a negative-index medium is always negative, *Phys. Rev. E*. 2, 026604 , 2004.

[13]. K. Fang, L. W. Zhang, F. F. Li, W. S. Wang, Y. W. Zhang, Time-domain Measurement of Group locity in the Metamaterial Perfect Lens, *iWAT* , Hongkong, China, pp. 428-431, 2011.

Negative refraction in semiconductor metamaterials based on quantum cascade laser design for the mid-IR and THz spectral range

J. Radovanović[1*], S. Ramović[1], A. Daničić[2] and V. Milanović[1]

[1]School of Electrical Engineering, University of Belgrade, Serbia
[2]Vinča Institute of Nuclear Sciences, University of Belgrade, Serbia
[*]corresponding author: radovanovic@etf.bg.ac.rs

Abstract

We have considered the realization of metamaterials based on semiconductor quantum nanostructures, in particular, with the structural arrangement as in quantum cascade laser (QCL) designed to achieve optical gain in the mid-infrared and terahertz part of the spectrum. The entire structure is placed in a strong external magnetic field which facilitates the attainment of sufficient population inversion, necessary to manipulate the permittivity and enable left-handed regime.

1. Introduction

In recent years a new type of artificial electromagnetic composites termed metamaterials (MTMs) has been extensively studied and developed. The broad range of configurations of these materials has introduced a variety of otherwise unexpected physical phenomena, among which the realization of negative refractive index and cloaking effect have been among the most interesting ones [1]. Composite metamaterial elements are patterned in a periodic array to form metamaterials, and the dimensions of unit cells, which metamaterials are composed of, are significantly less than the wavelength, on the order of tenths of wavelengths. Thus metamaterials can be considered as an effective medium and are well described by magnetic permeability and electric permittivity, in accordance with the macroscopic form of Maxwell's equations.

The advent of MTMs enabled control of electromagnetic properties of materials, going beyond the limit that is attainable with naturally existing structures. This is especially important for the technologically relevant terahertz frequency regime, because the tools that are necessary to construct devices operating within this spectral range are mainly lacking. Considerable efforts are underway to fill this 'THz gap' in view of the useful potential applications of the THz radiation. Techniques to control and manipulate THz waves are lagging behind, but moderate progress has been made in THz generation and detection and one of the recent examples is the THz quantum cascade laser.

In this paper we have considered the realization of metamaterials with the structural composition as in quantum cascade lasers which are intended to exhibit negative refraction in the mid-infrared and terahertz part of the spectrum. Our metamaterials belong to low-loss and active optical materials, and are made of very thin GaAs/AlGaAs layers, whose configuration corresponds to quantum cascade laser. They are subjected to very strong magnetic fields which enable modulation of the optical gain by discretizing the in-plane electron motion and thus make it possible to obtain negative index of refraction.

2. Theoretical consideration

Quantum cascade laser is a low-dimensional semiconductor quantum structure that consists of series of identical stages, allowing each electron to emit many photons during its transit through the structure. This scheme provides excellent laser performance in terms of optical gain and output power, thus it has been successfully utilized in many different applications (high-sensitivity gas sensing, infrared imaging, security monitoring and non-invasive medical diagnostics) in the mid-infrared and far-infrared part of the electromagnetic spectrum [2-7]. However, in spite of impressive properties demonstrated in the mid infrared, the operation in the THz part of the spectrum is subject to inherent limitations. Therefore, a lot of research effort has been invested recently into developing different approaches to overcome these limitations.

Many of the proposed and experimentally demonstrated metamaterials are based on inclusions of smart metallic films, wires, or spheres and therefore exhibit high optical losses which are detrimental to their performance and considerably limit their usefulness [8-10]. One of the major challenges in new metamaterial development is to design active metamaterials, i.e. to compensate the losses by adding gain. Active metamaterials, which comprise thin layers of semiconductors materials with particular layout,

may be used to realize substantial optical gain via carrier injection at frequencies of interest [8,9,11,12]. Specifically, the QCL-like structural profile allows for significant tunability of output properties and offers prospects for efficient engineering of effective permittivity [2,4,13,14]. The relative magnetic permeability of a semiconductor-based non-magnetic material is $\mu = 1$, while the dielectric permittivity tensor may be written as [9]:

$$\left\|\varepsilon\right\| = \begin{Vmatrix} \varepsilon_{\|} & 0 & 0 \\ 0 & \varepsilon_{\|} & 0 \\ 0 & 0 & \varepsilon_{\perp} \end{Vmatrix} \tag{1}$$

This form is valid for quantum well based semiconductor nanostructures which exhibit strong anisotropy of optical properties. Here, $\varepsilon_{\|}$ is the permittivity component along the quantum well planes, and is equal to the average permittivity of the background materials (ε_b), while $\varepsilon_{\perp}$ describes the interaction along the growth (z) axis and may be represented by the Lorentz model [15]:

$$\varepsilon_{\perp} = \varepsilon_b + \frac{e^2}{\varepsilon_0 \hbar L} \sum_{m<n} \left(N_{s,m} - N_{s,n}\right) \cdot \frac{\left|z_{m,n}\right|^2}{\left(\omega_{nm} - \omega\right) - i\gamma_{nm}} \tag{2}$$

Here, L is the length of the unit cell in z direction, $N_{s,i}$ represents the electron sheet density in i-th state, ω_{nm} is the resonant transition frequency between states n and m, ω is the frequency of the input light, γ_{nm} denotes the transition linewidth, while z_{mn} is the transition matrix element between states n and m. According to Eq. (2), the normal component of dielectric permittivity strongly depends on the populations of electron energy levels. Our goal was to meet the criteria for negative refraction, which in case of anisotropic, single-negative, metamaterial read [16]:

$$\varepsilon_{\|} > 0, \quad \mathrm{Re}\left(\varepsilon_{\perp}\right) < 0 \tag{3}$$

In the case of a passive configuration, when the upper levels are less occupied than the lower ones, both parts, the imaginary and the real one, of $\varepsilon_{\perp}$ are always positive. But in the active configuration, the total dielectric permittivity could be made negative by controlling the carrier distribution (Eq. (2)). Hence, in order to obtain negative values of the real part of $\varepsilon_{\perp}$, one clearly has to achieve high enough population inversion $N_{s,n} > N_{s,m}$ to cancel out the background term and reverse the sign of the real part of Eq. (2).

The active region of the QCL structures under consideration consists of two and three coupled quantum wells, for the terahertz and mid-infrared part of the electromagnetic spectrum, respectively, biased by an external electric field. Each period of the structure has three crucial energy states, and the laser transitions occur between the upper (n=3) and the lower (n=2) energy state. The main scattering mechanism is the electron-LO-phonon scattering, which is responsible for depopulation of the lower laser state. The active region is surrounded by the emitter/collector barriers, which enable injection of carriers from the preceding active region/extraction from the lower subband.

The direct use of LO-phonon scattering for lower state depopulation offers two advantages. First, when the ground energy state (n=1) is separated from the lower laser state (n=2) by the resonant LO-phonon energy, depopulation can is extremely fast. Second, the large energy separation between these two states provides intrinsic protection against thermal backfilling of the lower radiative state. Both properties are very important for lasers at longer wavelengths (which are within our subject of interest), because they allow for higher temperature operation. Therefore, our semiconductor QCL structures are designed so that the energy difference between the states E_2 and E_1 is approximately equal to LO-phonon energy in order to maintaining high population inversion.

In normal operating conditions, the electron motion in QCL structure is quantized along the growth direction only and free in the direction parallel to QW planes (x-y). When a strong perpendicular magnetic field is introduced, the in-plane electron motion becomes discretized as well, and continuous two-dimensional energy subbands are split into series of discrete Landau levels (LLs) whose energies, with band nonparabolicity included, are given by [17-21]:

$$E_{n,l}(B) = E_{n0} + \left(l + \frac{1}{2}\right) \frac{\hbar e B}{m_{\|,n}(E_{n0})} - \frac{1}{8}\left[\left(8l^2 + 8l + 5\right)\left\langle \alpha_0 \right\rangle + \left(l^2 + l + 1\right)\left\langle \beta_0 \right\rangle\right]\left(\hbar \omega_c\right)^2 \tag{4}$$

where $\omega_c = eB / m_{\|,n}(E_{n0})$ is the cyclotron frequency, E_{n0} the in-plane energy of the state n for zero in-plane wave vector ($k_{\|} = 0$), l=0,1,2,... is the Landau index, $m_{\|n}(E_{n0})$ represents the energy-dependent in-plane electron effective mass and B is the external magnetic field. The mean values of non-parabolicity parameters $\left\langle \alpha_0 \right\rangle$, $\left\langle \beta_0 \right\rangle$, averaged over the z-coordinate, are given according to [20]. It is obvious from Eq. (4) that the energy separations between Landau levels depends on the strength of the applied magnetic field which influences all the relevant relaxation processes in the structure and consequently the lifetime of carriers in the upper laser level. This enables one to control the population inversion in the active region and to influence the overall operation of the QCL structure, as described in detail in Ref.[18]. Here, such effect may be used to tune the carrier relaxation rates and their distributions over LLs which is important because it strongly affects the permittivity.

To calculate the normal component of the permittivity, one must first find the electron distribution over all Landau levels, by solving the nonlinear system of rate equations [11]:

$$\frac{\partial N_f}{\partial t} = \overline{f}_f \sum_{i \neq f} N_i W_{E_i \to E_f} - N_f \sum_{i \neq f} \overline{f}_i W_{E_f \to E_i} \qquad (5)$$

where indices i,f run over all Landau levels in all of the periods of the QCL and the probability that the state i is unoccupied is given by $\overline{f}_i = 1 - \pi\hbar/(eB) N_i$ according to the Fermi-Dirac distribution. The periodic QCL design enables solving the system of rate equations in a simplified form as described in [18]. Each state and its LLs can be associated with one of the periods of the QCL due to the wave-function localization properties. We assume that inside the cascade there is a globally linear potential variation, which enables the use of periodic boundary conditions for the particle surface densities. Each period is assumed to have an identical set of N Landau levels, with identical electron distributions. Out of the total of N, there are N−1 linearly independent equations, so one of them is replaced by the particle conservation law: $\sum_i N_i = N_S$, where N_S is the total electron sheet density

3. Results and Discussion

The calculations are performed for GaAs/AlGaAs quantum cascade laser structures, designed to emit radiation at mid-infrared and THz frequencies, under the influence of an intense external magnetic field.

The first structure under consideration is a GaAs/$Al_{0.38}Ga_{0.62}$As QCL, comprising three quantum wells per period, gain-optimized by the genetic algorithm for emission at $\lambda = 7.3\mu$m [12]. Starting from the left well the layer widths are: 11Å, 32Å, 39Å, 23Å, 38Å and the barrier height is U_B=0.317eV. The applied electric field in the z-direction is K=48kV/cm, and the minima of energy subbands (prior to the application of external magnetic field) are at $E_1(k_{\|}=0) = 0.083$eV, $E_2(k_{\|}=0) = 0.119$eV and $E_3(k_{\|}=0) = 0.290$eV. The material parameters used in calculations are: $m^* = 0.0665\, m_0$ (m_0 is the free electron mass), $\gamma_{nm} = 5$ meV, $\varepsilon_b \approx 13$ and the one period length (the active region plus the corresponding injector/collector) L=500Å.

Oscillations of the relaxation rate with magnetic field for transitions from the ground LL of the third subband, into which the majority of carriers are injected, into the two sets of LLs of the two lower subbands are very pronounced. The prominent peaks are found at values of the magnetic field which satisfy the resonance conditions for LO phonon emission. On the contrary, when the arrangement of Landau levels is such that there is no level situated at $\approx \hbar\omega_{LO}$ below the state (3,0), this type of scattering is inhibited, and the lifetime of the upper laser state is increased. When the current injection is constant, the modulation of lifetimes of all the states in the system results in either a suppression or an enhancement of population inversion between states (3,0) and (2,0). Thus, for magnetic field values at which the configuration of relevant electronic states leads to maximally enhanced relaxation rate from the (3,0) state, there is a huge drop in the optical gain, and conversely, for certain values of B there appears a peak of the gain. The total permittivity is calculated according to Eq. (2), and two particular cases, one for magnetic fields which enhances the population inversion and one where a minima of population inversion is found, are presented in Fig. 1. The injection current is kept constant for all displayed magnetic field strengths. It is not necessary to reach extremely high values of the optical gain in order to obtain negative real part of the permittivity. As shown, this can be accomplished for regular carrier sheet densities, but at specific values of magnetic at which the population inversion is enhanced.

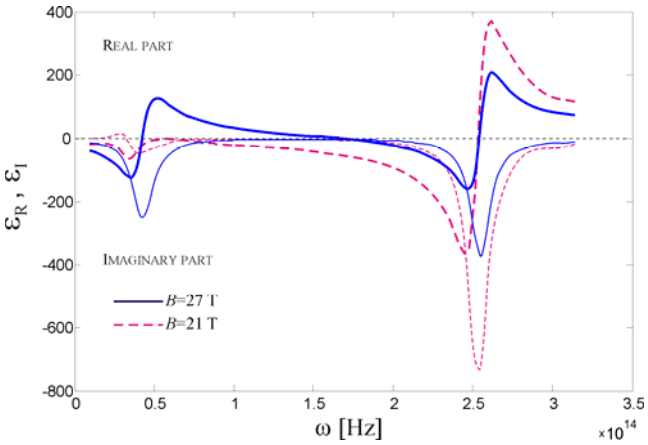

Figure 1: The dependence of $\varepsilon_\perp$ on frequency in a mid-IR QCL for various magnetic field values, at N_S=1·10^{11}cm^{-2} and T=300K

The realistic effects of band non-parabolicity influence the energy separation between the levels relevant for the radiative transition, thus the resonant wavelength becomes dependent on the magnetic field. This allows for the small shift of wavelength at which the minima of ε_R and ε_I are achieved and it may be used for fine-tuning of the permittivity.

Figure 2 illustrates how the frequency range $\Delta\omega$, at which metamaterial behaves as left-handed, depends on the electron sheet densities and on magnetic field values. Dark blue regions correspond to situations at which negative-refraction cannot be obtained. Even if the structure is exposed to very high values of B, in these cases it is impossible to reach high enough population inversion in QCL to obtain a left-handed regime. We observe that it is necessary to set (by doping) the total electron sheet density to at least $N_s \approx 1\cdot10^{10}$ cm^{-2}, so that the metamaterial could enter the desired working regime for some magnetic fields. The increase in the doping level leads to spreading of the magnetic field range at which negative-refraction may be reached, and the frequency range at which material behaves as left-handed. The widest range $\Delta\omega$ occurs at magnetic field which enhances the population inversion (B=27T) and

it is quite large for all electron sheet densities above $N_{s(\min)}$. On the other hand, the narrowest bandwidth corresponds to B at which the configuration of relevant electronic states leads to a maximally enhanced relaxation rate from the (3,0) state and that is for B=30T

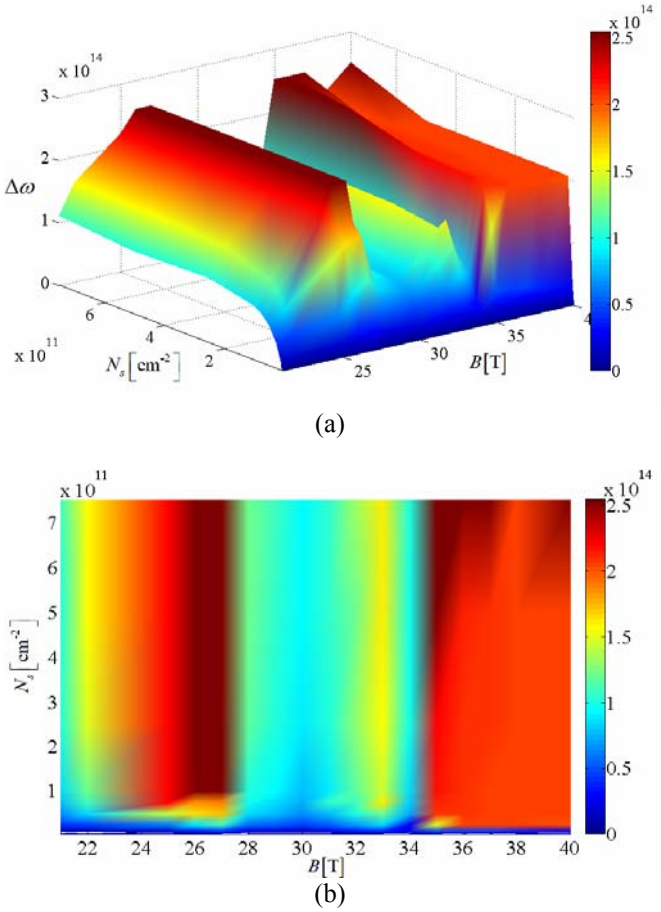

Figure 2: (a) The dependence of $\Delta\omega$ on electron sheet densities for various magnetic field values presented as a 3D plot, at T=300K. (b) Orthographic projection of the dependence of $\Delta\omega$ on electron sheet densities N_S and magnetic field B.

In order to present some results of our ongoing work, which is focused on designing negative-index metamaterials based on terahertz QCLs, we describe the second analyzed structure. It is a GaAs/$Al_{0.15}Ga_{0.85}As$ QCL, comprising two quantum wells per period, designed to emit radiation at 4.6 THz [13]. The layer widths are 56, 71, 31, 167 Å, starting from the emitter towards the collector barrier, and the electric field is 17 kVcm^{-1}. The calculated energy difference between subbands 3 and 2 is 20.9 meV, while the difference between the lower laser state and the ground state is $E_2 - E_1 = 36\text{meV} \approx \hbar\omega_{LO}$. The conduction band diagram of one period of the structure is illustrated in Figure 3.

In modeling this THz QCL an additional nonradiative relaxation mechanism that affects the operation of the structure must be included: the interface roughness scattering [22,23]. This type of scattering must be accounted for in calculations because of the small difference between adjacent levels. The numerical parameters used in calculations (in addition to the above parameters for MIR QCL) are: U_B=0.125eV, relevant parameters for interface roughness scattering Δ=1.5Å (height of roughness) and Λ=60Å (correlation length).

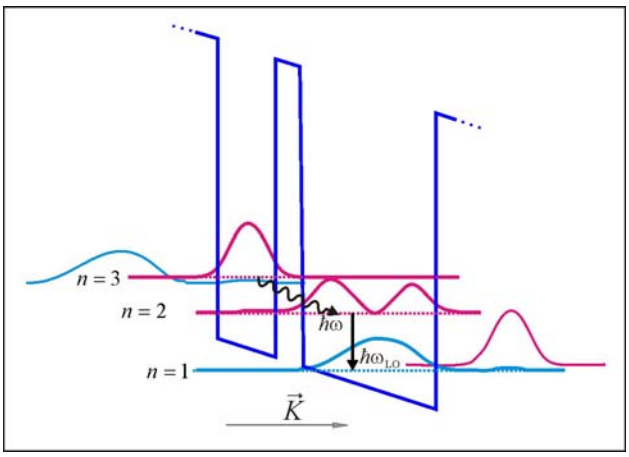

Figure 3: Conduction band profile of a single period of two-well THz quantum cascade laser.

The dependence of the modal gain on the applied magnetic field for this structure is illustrated in Figure 4. The oscillations of the relaxation rate with B are again very pronounced, with two distinct peaks around B=9 T and B=17.5 T. When the arrangement of LLs is such that there is no level situated near the state (3,0), or at $\approx \hbar\omega_{LO}$ below it, the relevant scattering rates are minimal and the modal gain is significantly increased.

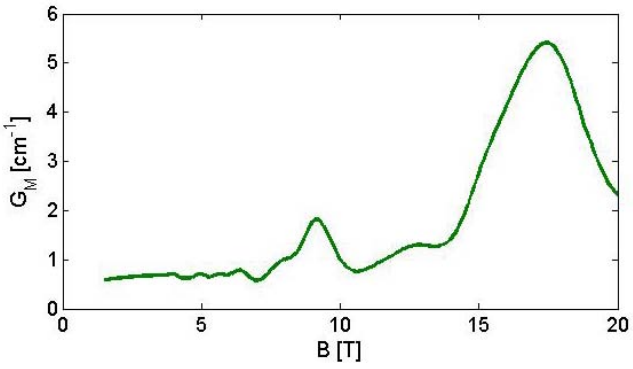

Figure 4: The modal gain in a THz QCL as a function of the applied magnetic field at N_S=2.2·10^{12}cm^{-2} and T=77K

For magnetic field which maximizes the optical gain in this structure (B=17.4T), with high enough doping level (N_S=5·10^{11}cm^{-2}) it is possible to achieve negative values of the real part of $\varepsilon_\perp$ (Fig. 5).

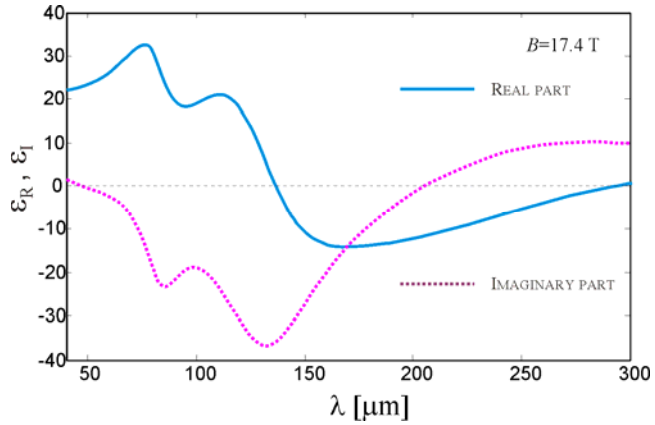

Figure 5: The dependence of $\varepsilon_{\perp}$ on the radiation wavelength in a THz QCL, for B=17.4 T at N_S=5·10^{11}cm^{-2} and T=77K.

4. Conclusions

The calculations are performed for GaAs/AlGaAs quantum cascade laser structures, design to emit radiation at mid-infrared and THz frequencies, under the influence of an intense external magnetic field. Their energies depend on the field, which, together with the fact that scattering rates between states are sensitive to their energy spacing, enables one to selectively enhance or inhibit different relaxation channels by varying the magnetic-field strength, which translates into a field-induced modulation of the population inversion.

The results presented in this paper show that it is possible to obtain a sufficiently high degree of population inversion to invert the sign of $\mathrm{Re}(\varepsilon_{\perp})$ i.e. to obtain its negative values. In fact, for mid-infrared structure we can even distinguish two frequency ranges where the structure behaves as left-handed. For certain magnetic fields that enhance the optical gain, those two regions may even merge into a very wide one. However, the fact that the structure is exposed to a very strong magnetic field, may not be sufficient condition to obtain high enough population inversion in the QCL active region to enable the left-handed regime. The other condition that must be fulfilled is the total electron sheet density, which in our case needs to be at least $N_s \approx 1 \cdot 10^{10}$ cm^{-2}. An increase in the doping level leads to extension of magnetic field range at which negative-refraction is achieved and the corresponding frequency span.

For the THz metamaterial structure we have also achieved the desired operating regime, but only for higher doping levels and applied magnetic fields which maximize the optical gain. This is due to a large background permittivity of GaAs, so our future work will focus on exploring other semiconductor materials, with lower background permittivity, in order to design left-handed metamaterials which require much lower magnetic field strengths.

Acknowledgements

This work was supported by the Ministry of Science (Republic of Serbia), ev. no. III 45010 and NATO SfP Grant, ref. no. ISEG.EAP.SFPP 984068.

References

[1] D. Schurig, J. J. Mock, B. J. Justice, S. A. Cummer, J. B. Pendry, A. F. Starr, D. R. Smith, Metamaterial electromagnetic cloak at microwave frequencies, *Science* 314: 977-980, 2006.

[2] J. Faist, F. Capasso, D. L. Sivco, C. Sirtori, A. L. Hutchinson , A. Y. Cho, Quantum Cascade Laser, *Science* 264: 553-556, 1994.

[3] C. Gmachl, F. Capasso, D. L. Sivco, A. Y. Cho, Recent progress in quantum cascade lasers and applications, *Rep. Prog. Phys.* 64, 1533-1601, 2001.

[4] B. S. Williams, Terahertz quantum-cascade lasers, *Nat. Photonics* 1: 517-525, 2007.

[5] O. Drachenko, S. Winnerl, H. Schneider, M. Helm, J. Wosnitza, J. Leotin, Compact magnetospectrometer for pulsed magnets based on infrared quantum cascade lasers, *Rev. Sci. Intrum.* 82**:** 033108 , 2011.

[6] A. Hugi, R. Maulini, J. Faist, Topical review—external cavity quantum cascade laser, *Semicond. Sci. Technol.* 25: 083001 , 2010.

[7] R.F. Curl, F. Capasso, C. Gmachl, A. A. Kosterev, B. McManus, R. Lewicki, M. Pusharsky, G. Wysocki, F. K. Tittel, Quantum cascade lasers in chemical physics, *Chem. Phys. Lett.* 487: 1-18, 2010.

[8] P. Ginzburg, M. Orenstein, Metal-free quantum-based metamaterial for surface plasmon polariton guiding with amplification, *J. Appl. Phys*. 104: 063513 (1-5), 2008.

[9] P. Ginzburg, M. Orenstein, Nonmetallic left-handed material based on negative-positive anisotropy in low-dimensional quantum structures, *J. Appl. Phys*. 103: 083105 (1-5), 2008.

[10] V. M. Shalaev , Optical negative-index metamaterials, *Nat. Photonics* 1: 41-48, 2007.

[11] I. Savić, N. Vukmirović, Z. Ikonić, D. Indjin, R. W. Kelsall, P. Harrison, V. Milanović, Density matrix theory of transport and gain in quantum cascade lasers in a magnetic field , *Phys. Rev. B* 76: 165310 , 2007.

[12] S. Ramović, J. Radovanović, V. Milanović, Tunable Semiconductor Metamaterials Based On Quantum Cascade Laser Layout Assisted By Strong Magnetic Field, *J. Appl. Phys*. 110: 123704 (1-5), 2011.

[13] S. Kumar, C. W. I. Chan, Q. Hu, J. Reno, Two-well terahertz quantum-cascade laser with direct intrawell-phonon depopulation, *Appl. Phys. Lett*. 95: 14110 (1-3), 2009.

[14] A. Wade, G. Fedorov, D. Smirnov, S. Kumar, B. S. Williams, Q. Hu, J. L. Reno, Magnetic-field-assisted terahertz quantum cascade laser operating up to 225 K, *Nature Photon*. 3: 41-45, 2007.

[15] P. Basu, *Theory of Optical Processes in Semiconductors: Bulk and Microstructures*, Clarendon Press, Oxford, 1997.

[16] V. A. Podolskiy, E. E. Narimanov, Strongly anisotropic waveguide as a nonmagnetic left-handed system, *Phys. Rev B* 71: 201101R (1-4), 2005.

[17] J. Radovanović, V. Milanović, Z. Ikonić, D. Indjin, P. Harrison, Electron-phonon relaxation rates and optical gain in a quantum cascade laser in a magnetic field, *J. Appl. Phys.* 97: 103109 (1-5), 2005.

[18] A. Daničić, J. Radovanović, V. Milanović, D. Indjin, Z. Ikonić, Optimization and magnetic-field tunability of quantum cascade laser for applications in trace gas detection and monitoring, *J. Phys. D: Appl. Phys*. 43: 045101 (1-8), 2010.

[19] J. Radovanović, A.Mirčetić, V. Milanović, Z. Ikonić, D. Indjin, P. Harrison, R.W. Kelsall, Influence of the active region design on output characteristics of GaAs/AlGaAs quantum cascade lasers in a strong magnetic field, *Semicon. Sci. Technol.* 21: 215-220, 2006.

[20] U. Ekenberg, Nonparabolicity effects in a quantum well: Sublevel shift, parallel mass, and Landau levels, *Phys. Rev. B* 40: 7714-7726, 1989

[21] J.Radovanović and Milanović, Quantum Cascade Laser: Applications In Chemical Detection And Environmental Monitoring, *Nucl. Technol. Radiat*. 24: 75-81, 2009.

[22] A. Leuliet, A. Vasanelli, A. Wade, G. Fedorov, D. Smirnov, G. Bastard and C. Sirtori, Electron scattering spectroscopy by a high magnetic field in quantum cascade lasers, *Phys. Rev. B* 73: 085311 (1-9), 2006.

[23] T. Unuma, M. Yoshita, T. Noda, H. Sakaki and H. Akiyama, Intersubband absorption linewidth in GaAs quantum wells due to scattering by interface roughness, phonons, alloy disorder, and impurities, *J. Appl. Phys* 93: 1586 (1-12), 2003.

Comparison of tunneling times in isotropic and anisotropic media

Jelena Radovanović[1,*], Igor Ilić[2], Petra Beličev[2], Vitomir Milanović[1] and Ljupčo Hadžievski[2]

[1]Faculty of Electrical Engineering, University of Belgrade, Belgrade, Serbia
[2]Vinča Institute of Nuclear Sciences, Department of Atomic Physics, Belgrade, Serbia
*corresponding author, E-mail: radovanovic@etf.rs

Abstract

In this paper, a comparative analysis of the tunneling times of electromagnetic waves (EM) propagating in isotropic and anisotropic media is presented. The expressions for calculating the tunneling times in layered periodic material, which possesses anisotropic properties due to its structure, are derived. Corresponding numerical calculations are performed for a new types of anisotropic semiconductor metamaterial. In the first case the analyzed layered structure consists of two differently doped $In_{0.53}Ga_{0.47}As$ semiconductor. In the second observation, the layered structure is made of alternately placed layers of doped $In_{0.53}Ga_{0.47}As$ and undoped $Al_{0.48}Ga_{0.52}As$. It is shown that two peaks emerge in the dependence of the dwell time on the incident wave frequency, one of which corresponds to the peaks of absorption and the group delay, while the other one is a consequence of anisotropy. These two peaks are affected by variations of layers' doping densities Furthermore, with the increase of the incident angle of incoming EM wave, the dwell time peak occurs at the upper boundary frequency of the frequency interval for which the structure exhibits negative refractive index.

1. Introduction

Recently, a lot of attention has been paid to a specific class of artificial materials, called negative-refractive-index metamaterials (NIMs). The theoretical concept of interesting feature of negative index of refraction dates back to the beginning of the 20th century as reported in [1], although most of the references point to the work of Veselago [2]. Depending on the sign of the constitutive parameters of a certain material (permittivity 1 and permeability μ), two types of NIMs can be distinguished: single-negative NIMs (SN NIMs) [3] and double-negative NIMs (DN NIMs) [4]. The latter ones are also known as left-handed metamaterials (LHMs), since the electric field, magnetic field and wave vector of propagating EM wave follow a left-hand rule. With ongoing progress in technology, the gap between theoretical predictions of negative refraction and realization of materials that exhibit such behavior has been overcome. A number of pioneering theoretical studies [5-7] suggested how these peculiar properties could be realized in funcionally-designed and built materials, and experiments subsequently confirmed those predictions [8-10]. Design and production of NIMs have experienced rapid progress in the past decade, especially in the field of optics where they found a lot of applications using unusual properties such as inverse Snell's law, inverse Doppler shift, backward Cerenkov radiation, etc [11-13]. Furthermore, novel designs also provide NIMs that exhibit negative refractive index at near-infrared and optical frequencies [4,14-16].

Another way to obtain negative refractive index in a material is to introduce anisotropy in the system, keeping the resonance only in one of the constitutive parameters, e.g. ε [17]. Based on this concept, one class of SN NIMs named semiconductor metamaterials, experienced a rapid progress in past few years [18,19]. These artificial materials represent anisotropic layered semiconductor structures which exhibit negative refractive index properties in a certain range of frequencies. Such design facilitates the fabrication of metamaterials with reduced losses.

From a point of a quantum description, photons and electrons can be treated analogously and exhibit many similar characteristics. Similarities in their behavior provide numerous opportunities for studying interesting electromagnetic effects that also occur in quantum mechanics [20]. As a consequence of this correspondence, the concept of quantum tunneling can be used for description of an EM wave encountering the obstacle with lower refractive index than the surrounding medium. One of the quantities that describes tunneling phenomenon is the tunneling time. The debate about the most appropriate definitions for tunneling times has been on for many years. Two of them, the dwell time and the group delay, are accepted as the most apt [21]. The first one is related to propagation of electromagnetic energy through the barrier, while the second one refers to the wave phase propagation. The relation between these times was first derived by Winful. Presuming an obstacle made of a nonmagnetic material ($\mu = 1$) with a positive index of refraction, he expressed the group delay as the sum of the dwell time and a term called the self-interference time [22,23], which represents the time that a wave packet spends in front of the obstacle interfering with its reflected part. Only when the

background medium is dispersive this time is nonzero. Furthermore, the more general relations between tunneling times have been calculated for different types of isotropic NIMs, such as: linear absorptive dispersive [24,25], nonlinear non-absorptive non-dispersive [26] and nonlinear absorptive dispersive NIMs [27]. The impact of the Goos-Hänchen shift on these times has been calculated, as well [28,29].

Relying on the design of the above mentioned anisotropic layered structure, we derive appropriate expressions for determination of tunneling times in such type of media. Corresponding numerical results, performed by using the parameters of semiconductor NIMs provided in [19], indicate strong impact of anisotropy on tunneling of EM wave through such a structure.

2. Theoretical consideration

The observed model considers a non-magnetic obstacle ($\mu = 1$) made of a large number of alternately placed layers of two different semiconductors (both linear, absorptive and dispersive), so that the whole structure exhibits anisotropy via the effective permittivity ε . The obstacle is placed inside the waveguide with given constitutive parameters: permittivity ε_b and permeability μ_b ($\varepsilon_b, \mu_b > 0$), as depicted in Fig. 1. Incident planar wave is TM polarized.

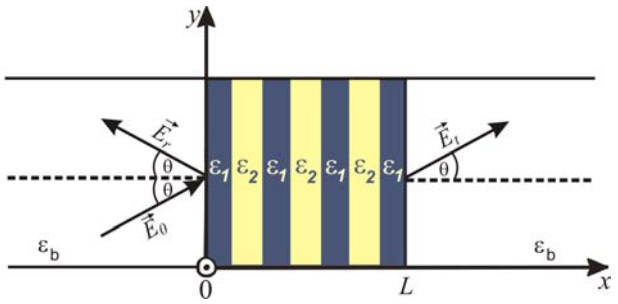

Figure 1. The model of anisotropic obstacle with thickness *L*, placed inside a planar waveguide. *x* is the propagation axis, while θ stands for the incident angle.

The permittivity tensor for this structure is given by the following expression:

$$\varepsilon = \begin{vmatrix} \varepsilon_\perp & 0 & 0 \\ 0 & \varepsilon_\parallel & 0 \\ 0 & 0 & \varepsilon_\parallel \end{vmatrix}, \tag{1}$$

$$\varepsilon_\perp = \frac{2\varepsilon_1\varepsilon_2}{\varepsilon_1 + \varepsilon_2}, \ \varepsilon_\parallel = \frac{\varepsilon_1 + \varepsilon_2}{2}, \tag{2}$$

where $\varepsilon_\perp$ and $\varepsilon_\parallel$ represent the permittivity for orthogonal and parallel polarization, respectively, and ε_1 and ε_2 stand for the permittivities of the two types of semiconductors which constitute the structure. Relations for permittivity of each layer can be expressed by the Drude model:

$$\varepsilon_{1(2)} = \varepsilon_{\infty 1(2)}\left(1 - \frac{\omega_{p1(2)}^2}{\omega^2 + i\Gamma_{e1(2)}\omega}\right). \tag{3}$$

Here, $\varepsilon_{\infty 1}$ and $\varepsilon_{\infty 2}$ are the semiconductors' background permittivities, $\omega_{p1(2)}$ are the plasma frequencies, while $\Gamma_{1(2)}$ stand for the damping frequencies of these layers. For simplicity, here we assume $\Gamma_{e1} \approx \Gamma_{e2} = \Gamma_e$. Furthermore, ω is the incident EM wave frequency. The analysis takes into consideration only non-magnetic materials, i.e. permeabilities of the obstacle and the surrounding waveguide are equal to 1 (μ =1 and μ_b =1). As shown in [18], the presented system possesses negative index of refraction when $\mathrm{Re}(\varepsilon_\perp) < 0$ and $\mathrm{Re}(\varepsilon_\parallel) > 0$ in a certain range of frequencies. Additionally, such anisotropy of the system affects only the propagation of TM modes, since boundary conditions imply negative refraction only in this case.

In isotropic media, the negative refractive index of the obstacle causes the directions of energy flow and the phase velocity, i.e. the Poynting and the wave vector, to be opposite therein [16]. However both vectors refract negatively. In an anisotropic medium the situation is different. Due to the anisotropy of the material the Poynting vector, which points in the direction of energy flow, and the wave vector, directed along the wave front normal, are usually non-parallel. As the geometry of the system implies solely the conservation of tangential components of the wave vector at an interface of two layers, the travelling wave can experience positive refraction with respect to the wave vector and negative refraction with respect to the Poynting vector [30].

Therefore, the expression for the effective refractive index of Poynting vector in anisotropic structure presented in [19] is given by:

$$n_{eff} = \frac{\varepsilon_\perp}{\varepsilon_\parallel}\sqrt{\varepsilon_\parallel + \varepsilon_b \sin^2\theta\left(\frac{\varepsilon_\parallel^2}{\varepsilon_\perp^2} - \frac{\varepsilon_\parallel}{\varepsilon_\perp}\right)}. \tag{4}$$

This expression describes the refraction of the Poynting vector at the boundary between isotropic and anisotropic medium and is valid in case of a structures with small losses, as indicated in [19]. If we observe an anisotropic structure whose absorption cannot be neglected, the following expression for the effective refractive index can be obtained (the derivation is given in the Appendix):

$$n_{eff} = \mathrm{sgn}(\varepsilon_\perp')\cdot\left|\frac{\varepsilon_\parallel'}{\varepsilon_\perp'}\right|\frac{|\varepsilon_\perp|^2}{|\varepsilon_\parallel|^2}\cdot \mathrm{M}, \tag{5}$$

where:

$$\mathrm{M}=\sqrt{\frac{\left|\varepsilon_{\|}\right|^{2}\Theta}{\varepsilon_{\|}^{'}}-\varepsilon_{b}\sin^{2}\theta\left[\frac{\varepsilon_{\perp}^{'}\left|\varepsilon_{\|}\right|^{2}\Theta}{\varepsilon_{\|}^{'}\left|\varepsilon_{\perp}\right|^{2}}\left(1-\frac{\varepsilon_{\perp}^{''}}{\varepsilon_{\|}^{'}}\right)-\left(\frac{\varepsilon_{\perp}^{'}\left|\varepsilon_{\|}\right|^{2}}{\varepsilon_{\|}^{'}\left|\varepsilon_{\perp}\right|^{2}}\right)^{2}\right]} \quad (6)$$

Here, $\varepsilon_{\perp,\|}^{'}=\mathrm{Re}(\varepsilon_{\perp,\|})$, $\varepsilon_{\perp,\|}^{''}=\mathrm{Im}(\varepsilon_{\perp,\|})$, while the parameter Θ is derived according to the Snell's law for anisotropic medium:

$$\Theta=\frac{1}{2}\left(1+\sqrt{1+\frac{\left\{\mathrm{Im}\left[\left(\frac{k_{xt}}{\varepsilon_{\|}}\right)^{2}\right]\right\}^{2}}{\left\{\mathrm{Re}\left[\left(\frac{k_{xt}}{\varepsilon_{\|}}\right)^{2}\right]\right\}^{2}}}\right). \quad (7)$$

The parameter $k_{xt}^{2}=\varepsilon_{\|}\left(1-\varepsilon_{b}\sin^{2}\theta/\varepsilon_{\perp}\right)k_{0}^{2}$ represents the x-component of the transmitted wave vector, while k_0 and θ stand for the wave vector in vacuum and the incident angle, respectively. Note that the negative refraction of the Poynting vector occurs only in case when the expression in Equation (5) has negative value, i.e. when $\varepsilon_{\perp}^{'}<0$. In the limit case of low material absorption, $\Omega=1$, $\varepsilon_{\perp}=\varepsilon_{\perp}^{'}$, $\varepsilon_{\|}=\varepsilon_{\|}^{'}$ and Equation (5) reduces to the Equation (4).

2.1.1. Tunneling times definitions

The dwell time is defined as the time spent by a wave packet in a given region of space [22,31,32]:

$$\tau_{d}=\frac{\langle W\rangle}{\langle P_{in}\rangle}, \quad (8)$$

where W stands for the stored EM energy inside the obstacle and $P_{in}=\gamma_{0}\left|H_{0}\right|^{2}S_{CS}/(4\varepsilon_{0}\varepsilon_{b}\omega)$ represents the time averaged incident power. Here, $\gamma_{0}=\sqrt{\varepsilon_{b}}k_{0}\cos\theta$, S_{CS} stands for the cross-section and $\left|H_{0}\right|$ is the incident magnetic field amplitude.

In order to calculate the stored EM energy, we start from the Helmholtz equation for anisotropic media:

$$\frac{\varepsilon_{\perp}}{\varepsilon_{\|}}\frac{d^{2}H_{y}(x)}{dx^{2}}+(\varepsilon_{\perp}k_{0}^{2}-\beta^{2})H_{y}(x)=0. \quad (9)$$

and apply the Equivalent Circuit (EC) method [33], which is based on analogy between electric energy density in the material and the work done by the corresponding (analogous) electrical circuit. Here, H_y is the y component of the magnetic field inside the obstacle. In addition, $\beta=\sqrt{\varepsilon_{b}}k_{0}\sin(\theta)$ is the propagation constant and L is the obstacle length. The other way for calculating the stored EM energy is based on determining the EM energy density inside the obstacle as described in [34]. However the energy density (ED) method offers exact solutions only in cases when it is possible to determine all losses in the material, as for instance in structures whose permittivity and permeability are described by the Drude and the Lorentz model, respectively [35,36]. If these parameters are arbitrarily complex functions, it is usually not possible to derive the exact expression for EM energy density, primarily due to impossibility of separating the contributions which are related to losses in the medium, from those that are related to the time derivative of EM density. Therefore, to avoid these problems and in order to obtain accurate results, we opted for the EC method.

The EM energy density can be represented as a sum of two contributions, one originating from the electric field and the second one originating from the magnetic field. Since our model describes a nonmagnetic obstacle, the magnetic part of the EM magnetic energy density equals [34]:

$$\langle w_{m}\rangle=(\mu_{0}\left|H\right|^{2})/4. \quad (10)$$

Starting from the expression for the work per unit volume (i.e., energy density), necessary for establishing the electric field E in an isotropic media with permittivity $\varepsilon(\omega)$, we have [33]:

$$w_{e}=\int_{t}E\frac{\partial D}{\partial t}dt, \quad (11)$$

where D represents the corresponding electric displacement field. Similarly, the work done by electrical circuit equals:

$$W_{ec}=\int_{t}VIdt=\int_{t}V\frac{\partial q}{\partial t}dt, \quad (12)$$

where V is the electrical potential difference between two ends of a circuit, while $I=\partial q/\partial t$ represents the current of a branch of the circuit. In case of a circuit with linear electric response, expression for the electric charge reads:

$$\hat{q}(\omega)=\frac{1}{j\omega}\hat{I}(\omega)=\frac{1}{j\omega Z(\omega)}\hat{V}(\omega). \quad (13)$$

Here, $\hat{I}(\omega)$, $\hat{V}(\omega)$ and $Z(\omega)$ represent the current, the voltage and the circuit impedance in the frequency domain, respectively, while $q(t)=\mathrm{Re}\left[\hat{q}(\omega)\exp(j\omega t)\right]$. Adopting the following analogies: $V\leftrightarrow E$ and $q\leftrightarrow D$ and comparing the Equation (13) with expression $\hat{D}(\omega)=\varepsilon(\omega)\hat{E}(\omega)$, we find:

$$\frac{1}{j\omega Z(\omega)} \leftrightarrow \varepsilon(\omega)\,. \tag{14}$$

Schematic of the equivalent circuit of the permittivity of parallel polarization $\varepsilon_{\parallel}$ in a semiconductor metamaterial is depicted in Fig. 2.

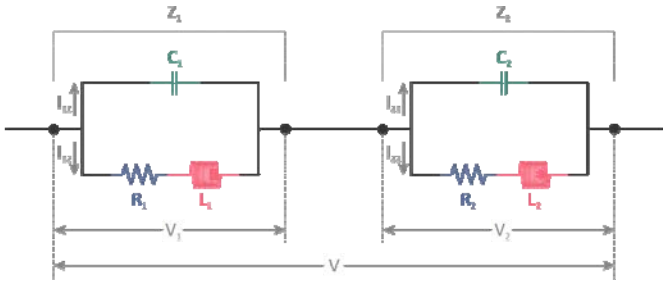

Figure 2. Schematic of the equivalent circuit of $\varepsilon_{\perp}$ in a semiconductor metamaterial.

In the direction of the EM field flow, the permittivity of the structure reads:

$$\frac{1}{2\varepsilon_{\perp}} = \frac{1}{\varepsilon_1} + \frac{1}{\varepsilon_2} \Rightarrow, \tag{15}$$

$$Z(\omega) = \frac{1}{j\omega\varepsilon_1} + \frac{1}{j\omega\varepsilon_2} = Z_1(\omega) + Z_2(\omega)\,. \tag{16}$$

Based on the above analysis, it is easy to conclude that the equivalent circuit of this material can be represented by the serial connection of two RLC circuits shown in Fig. 2. By calculating the work done by electric circuit depicted in Fig. 2, the expression for the electric energy density for normal polarization is derived to be:

$$\left\langle w_{e\perp} \right\rangle = \frac{2\varepsilon_0\varepsilon_{\infty 1}\varepsilon_{\infty 2}}{\varepsilon_{\infty 1}+\varepsilon_{\infty 2}} \frac{\left|\vec{E}_x\right|^2}{4} \left\{ 1 + \frac{\omega_s^2\left(\omega_s^2+\omega^2\right)\left(\omega^2+{\Gamma_e}^2\right)}{\left[\left(\omega^2-\omega_s^2\right)^2+\omega^2{\Gamma_e}^2\right]\left(\omega^2+\mathrm{I}\right.} \right.$$
$$\left. + \frac{\omega_p^4\left(\omega_s^2-{\Gamma_e}^2-3\omega^2\right)}{\left[\left(\omega^2-\omega_s^2\right)^2+\omega^2{\Gamma_e}^2\right]\left(\omega^2+{\Gamma_e}^2\right)} \right\}. \tag{17}$$

Using the similar procedure, the expression for the electric energy density for parallel polarization reads:

$$\left\langle w_{e\parallel} \right\rangle = \frac{\varepsilon_0(\varepsilon_{\infty 1}+\varepsilon_{\infty 2})\left|\vec{E}_z\right|^2}{4} \left[1 + \frac{\dfrac{\varepsilon_{\infty 1}\omega_{p1}^2+\varepsilon_{\infty 2}\omega_{p2}^2}{\varepsilon_{\infty 1}+\varepsilon_{\infty 2}}\omega^2}{\omega^2\left(\omega^2+{\Gamma_e}^2\right)} \right], \tag{18}$$

where

$$E_x = \frac{\beta}{\varepsilon_{\perp}\varepsilon_0\omega} H_y\,,\; E_z = \frac{i}{\varepsilon_{\parallel}\varepsilon_0\omega}\frac{dH_y}{dx}\,.$$

By adding Equations (10), (17) and (18), and integrating spatially, we arrive to a relation for the stored electromagnetic energy density in the obstacle

$$\left\langle W \right\rangle = \frac{\varepsilon_0 S}{4}\frac{\left(\varepsilon_{\parallel}\right)_{eff}}{\left(\varepsilon_{\parallel}\varepsilon_0\omega\right)^2}\left(-2\gamma_0\,\mathrm{Im}(R)\left|H_0\right|^2 - S_1\right) +$$
$$+\frac{\varepsilon_0 S}{4}\left[\left(\varepsilon_{\perp}\right)_{eff}\frac{\beta^2}{\left(\varepsilon_{\perp}\varepsilon_0\omega\right)^2} + \left(\varepsilon_{\parallel}\right)_{eff}\frac{\mathrm{Re}(\gamma^2)}{\left(\varepsilon_{\parallel}\varepsilon_0\omega\right)^2}\right]\int_0^L \left|H_y\right|^2 dx, \tag{19}$$

where:

$$S_1 = \mathrm{Re}\left\{\left(\varepsilon_{\parallel}^* - \varepsilon_b\right)\left[H_y\left(\frac{dH_y/dx}{\varepsilon_{\parallel}}\right)^*\right]\right\}_{x=0}^{L}, \tag{20}$$

$$\left(\varepsilon_{\perp}\right)_{eff} = \frac{2\varepsilon_{\infty 1}\varepsilon_{\infty 2}}{\varepsilon_{\infty 1}+\varepsilon_{\infty 2}}\left[1 + \frac{\left(\omega_s^2+\omega^2\right)\omega_s^2}{\left|\Omega^2-\omega_s^2\right|^2} + \right.$$
$$\left. + \frac{\omega_p^2\left(\omega_s^2-{\Gamma_e}^2-3\omega^2\right)\omega^2}{\left|\Omega^2-\omega_s^2\right|^2\cdot\left(\omega^4+\omega^2{\Gamma_e}^2\right)}\right], \tag{21}$$

$$\left(\varepsilon_{\parallel}\right)_{eff} = \frac{1}{2}\left[\mathrm{Re}(\varepsilon_1) + \frac{2\omega\,\mathrm{Im}(\varepsilon_1)}{\Gamma_e}\right] + \frac{1}{2}\left[\mathrm{Re}(\varepsilon_2) + \frac{2\omega\,\mathrm{Im}(\varepsilon_2)}{\Gamma_e}\right], \tag{22}$$

Here, the following substitutions have been introduced: $\Omega = \sqrt{\omega^2 + i\Gamma_e\omega}$, $\omega_s^2 = \left(\omega_{p1}^2+\omega_{p2}^2\right)/2$ and $\omega_p^2 = \omega_{p1}\omega_{p2}$. Finally, the expression for the dwell time in a semiconductor metamaterial reads:

$$\tau_d = \frac{\varepsilon_b}{2\gamma_0\omega\left|H_0\right|^2}\left[\frac{\beta^2\left(\varepsilon_{\perp}\right)_{eff}}{\varepsilon_{\perp}^2} + \frac{\mathrm{Re}\left(\gamma_s^2\right)\cdot\left(\varepsilon_{\parallel}\right)_{eff}}{\varepsilon_{\parallel}^2} + k_0^2\right]\int_0^L \left|H_y\right|^2 dx -$$
$$-\frac{\varepsilon_b\left(\varepsilon_{\parallel}\right)_{eff}}{\varepsilon_{\parallel}^2}\frac{\mathrm{Im}(R)}{\omega} - \frac{1}{2}\frac{\varepsilon_b}{\gamma_0\left|H_0\right|^2}\frac{\left(\varepsilon_{\parallel}\right)_{eff}}{\varepsilon_{\parallel}^2\omega}S_1, \tag{23}$$

where H_0 stands for the incident magnetic field strength and $\gamma_s^2 = k_0^2\varepsilon_{\parallel} - \left(\varepsilon_{\parallel}/\varepsilon_{\perp}\right)\beta^2$.

On the other hand, the group delay can be determined from the frequency derivative of the transmission phase shift, i.e.:

$$\tau_g = \left|T\right|^2\frac{d\phi_0}{d\omega} + \left|R\right|^2\frac{d\phi_r}{d\omega}\,, \tag{24}$$

where $T = \left|T\right|\exp\left(i\phi_t\right)$ and $R = \left|R\right|\exp\left(i\phi_r\right)$ are the transmittance and the reflectance, respectively, while $\phi_0 = \phi_t + \gamma_0 L$ stands for the phase of the transmitted wave.

With the standard procedure of subtracting the conjugate of the Helmholtz equation multiplied by dH_y/dx from the derivative of the Helmholtz equation, with respect to ω multiplied by H_y^*, and integrating this expression along the obstacle, the integral in Equation (23) can be derived as a function of the group delay. Now, the relationship between the tunneling times, the group delay and the dwell time, reads:

$$\tau_g = \frac{1}{f}\cdot\tau_d + \tau_i + \tau_{loss} + \tau_{interface}\,, \tag{25}$$

where:

$$f = \frac{\tilde{\varepsilon}_\perp\beta^2 + \tilde{\varepsilon}_\parallel\gamma_0^2 + \varepsilon_b k_0^2}{\omega\,\mathrm{Re}\left(d\gamma_s^2/d\omega\right)}\,, \tag{26}$$

$$\tilde{\varepsilon}_\perp = \frac{\varepsilon_b\left(\varepsilon_\perp\right)_{eff}}{\left|\varepsilon_\perp\right|^2}\,,\ \tilde{\varepsilon}_\parallel = \frac{\varepsilon_b\left(\varepsilon_\parallel\right)_{eff}}{\left|\varepsilon_\parallel\right|^2}\,. \tag{27}$$

As shown in Equation (25), the group delay can be represented as a sum of several contributions, one of which is the dwell time. These contributions are consequences of:

1) interference of the incident wave with its reflected part in front of the obstacle, named the self-interference time:

$$\tau_i = \tilde{\varepsilon}_\parallel\frac{\mathrm{Im}(R)}{\omega}\frac{1}{f} - \frac{1}{\gamma_0}\frac{d\gamma_0}{d\omega}\mathrm{Im}(R)\,, \tag{28}$$

2) the absorptive nature of the obstacle:

$$\tau_{loss} = \frac{\mathrm{Im}(\gamma_s)\int_0^L \mathrm{Im}\left(H_y^*\frac{dH_y}{d\omega}\right)dx}{\gamma_0\left|H_0\right|^2}\,, \tag{29}$$

and

3) the difference in permittivities between the obstacle and the surrounding waveguide:

$$\tau_{interface} = \frac{1}{2\gamma_0\left|H_0\right|^2}\left\{-\mathrm{Re}\left\{\left(\frac{d\varepsilon_\parallel}{d\omega}-\frac{d\varepsilon_b}{d\omega}\right)\frac{H_y^*H_y}{\varepsilon_\parallel}\right\}\right|_L^0 + \\ +\mathrm{Re}\left\{\left(\varepsilon_\parallel-\varepsilon_b\right)\left[\frac{H_y}{\varepsilon_\parallel}\frac{dH_y^*}{d\omega} - H_y^*\frac{d}{d\omega}\left(\frac{H_y}{\varepsilon_\parallel}\right)\right]\right\}\Bigg|_L^0 + \frac{\tilde{\varepsilon}_\parallel f S_1}{\omega}\Bigg\} \tag{30}$$

The latter has non-zero value only if the condition $\varepsilon_\parallel \neq \varepsilon_b$ is satisfied, which is always fulfilled since $\varepsilon_\parallel$ has a complex value.

3. Numerical results

Numerical calculations were carried out for three different structures, two of which are anisotropic semiconductor metamaterials, while the last one represents the isotropic NIMs.

In the first setting, the structure from Fig. 1 is composed of a large number of alternately placed absorptive layers of two differently doped $In_{0.53}Ga_{0.47}As$ samples. The doping density of even layers is fixed and equals $n_d = 7.5\cdot10^{24}$ cm^{-3} ($\omega_p \sim n_d$), while the odd layers' doping density is varied in the range of $0 < n_d < 12\cdot10^{24}$ cm^{-3}. The parameters of these materials used in our calculations were: $\varepsilon_{\infty 1} = \varepsilon_{\infty 2} = 12.15$, $\omega_{p1} = 214.75$ THz, $\Gamma_e = 10$ THz, $\omega_{p2} \in (\omega_{p1}/1.6,\ \omega_{p1}\cdot1.6)$ and the incident angle θ is equal to $\pi/3.2$. The length of the barrier is set to $L = 3.6$ μm, and the surrounding medium is air ($\varepsilon_b = 1$, $\mu_b = 1$).

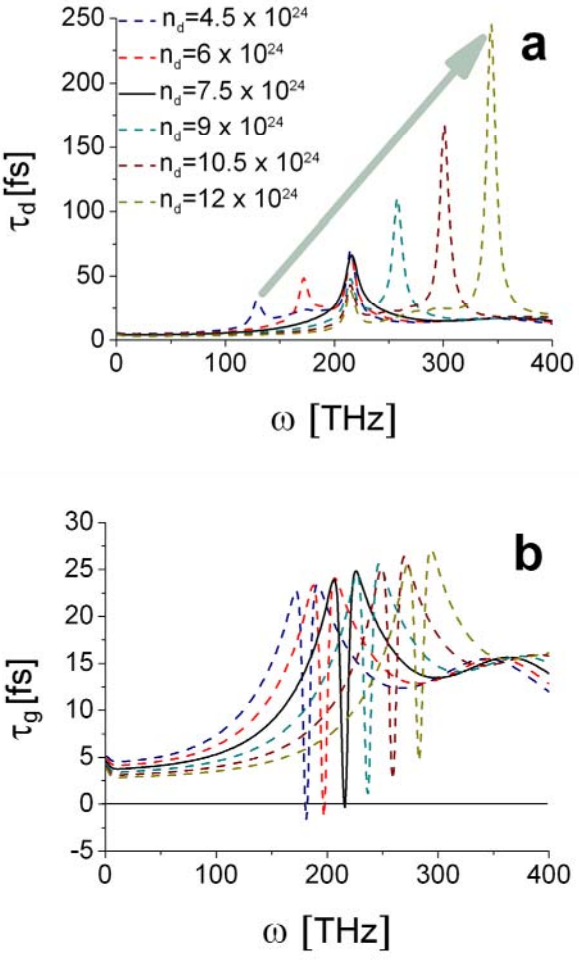

Figure 3. (a) The dwell time and (b) the group delay vs. incident field frequency in anisotropic media for different doping densities of odd layers (the arrow depicts increasing doping density).

Fig. 3 depicts dependence of tunneling times on incident field frequency for different doping densities. It can be seen that the anisotropy of the obstacle causes the emergence of two peaks in dwell time, i.e. the peaks are a consequence of two plasma resonance frequencies of layers. The increase of odd layers' doping density shifts and enhances the regular dwell time's peak which is the consequence of the absorption of the obstacle toward higher frequencies. The second peak of dwell time dependence on ω corresponds to the peaks of absorption and group delay in the structure. In the case of isotropic medium only one peak exists, which is depicted by solid black line.While the dwell time has local maxima for the boundary frequencies of the frequency ranges when effective refractive index is negative, group delay reaches minima. With the decrease of doping density, the group delay becomes smaller and even negative at its first local minimum meaning that in narrow frequency region, both the group velocity and phase velocity are negative. This phenomenon indicates that the output wave leaves the obstacle prior than the input wave enters [37]. On the other hand, for doping densities $n_d > 7.5 \cdot 10^{24}$ cm^{-3} group delay remains positive.

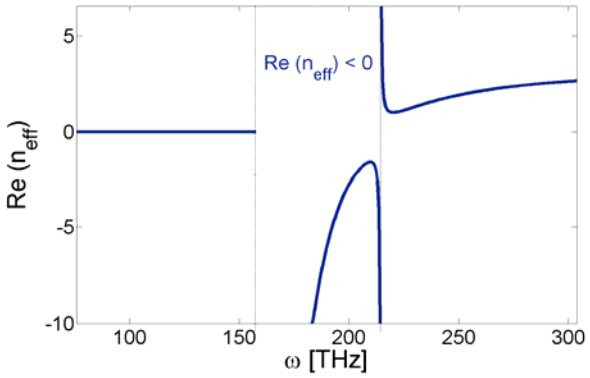

Figure 4. The real part of effective index of refraction vs. incident field frequency. For low frequencies, effective refractive index is pure imaginary quantity.

The second investigated structure is made of alternately placed layers of $In_{0.53}Ga_{0.47}As$ (in Fig. 1 material with permittivity ε_1) and $Al_{0.48}Ga_{0.52}As$ (in Fig. 1 material with permittivity ε_2). This semiconductor metamaterial is developed by Hoffman [19] and exhibits negative index of refraction in infrared frequency domain. In order to ensure plasma resonance for free carriers the layers of InGaAs are uniformly doped ($\omega_{pInGaAs} \neq 0$), while the layers of AlGaAs remain undoped, which leaves them non-dispersive and non-absorptive. The parameters of these materials are: $\varepsilon_{\infty 1} = 12.15$, $\omega_{p1} = 214.75$ THz, $\Gamma_e = 10$ THz, $\varepsilon_{\infty 2} = 10.23$, $\omega_{p2} = 0$. The length of the obstacle is set to $L = 1$ μm, and the surrounding medium is air ($\varepsilon_b = 1$, $\mu_b = 1$). The real part of effective index of refraction of this particular structure is negative for frequencies 158.7 THz $< \omega < \omega_{p1}$. Its dependence on incident field frequency is depicted in Fig. 4.

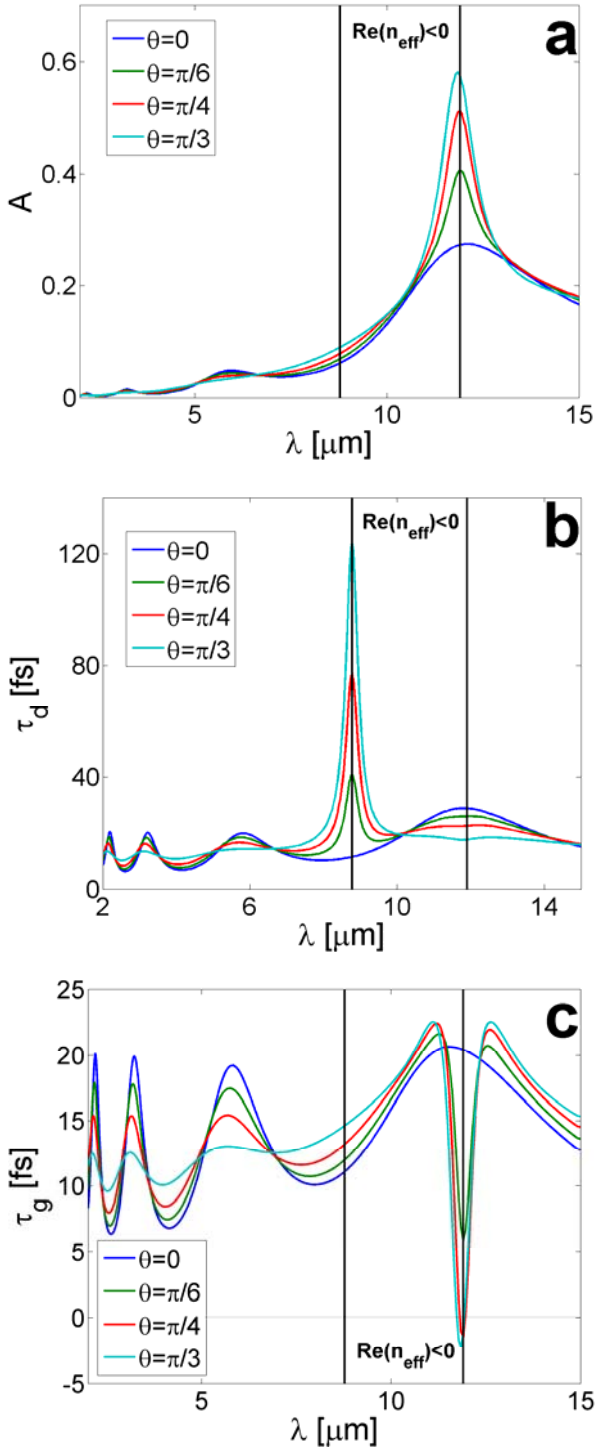

Figure 5. Dependence of (a) absorption (b) dwell time and (c) group delay on the wavelength of incident EM wave for different angles of incidence. Vertical black lines indicate the boundaries of the area of negative refractive index of anisotropic obstacle for TM polarized EM waves.

Numerical results obtained for quantities of interest are depicted in Fig. 5. As shown in Fig. 5b which describes the dependence of the dwell time on the wavelength of incident wave λ, the dwell time exhibits small oscillations for incident wavelengths lower than 8 μm. This dwell time's oscillating nature arises from the structure of the system, since in this interval of incident wavelengths the obstacle behaves like a Bragg grating, because the period of the observed structure is comparable with λ. For higher incident wavelengths ($\lambda > 8$ μm) the oscillations vanish. The angle of incident wave also affects the behavior of the dwell time. The increase of incident angle causes the decrease in oscillations. The interesting feature of the dwell time is that, for non-zero incident angles, it reaches a maximum at frequency ω_{p1} for which the index of refraction becomes negative.

On the other hand, the absorption (Fig. 5a) peaks at the second boundary of the interval of negative index of refraction (158.7 THz) for all incident angles. Similar situation can be noticed in the behavior of the group delay, which can reach even negative values at this frequency for some incident angles (Fig. 5c).

The peak position frequency mismatch between the group delay and the dwell time has not been evidenced so far in the linear media, and is a direct consequence of anisotropy. This difference in peak position frequency can be observed between the absorption and the dwell time, as well. Only in the case of zero angle of incidence (blue solid line) both tunneling times, the dwell time and the group delay, and the absorption have maximum values at the second boundary of the frequency interval for which the structure exhibits negative refractive index.

As already mentioned, in case of isotropic media, negative refractive index can be achieved only if the obstacle has resonances in both of constitutive parameters, i.e. in ε and μ. Therefore, the permeability of such an obstacle can be described as [24]:

$$\mu = 1 - \frac{F\omega_0^2}{\omega^2 - \omega_0^2 + i\Gamma_m\omega}, \qquad (31)$$

where ω_0 is the resonance frequency of the magnetic dipole oscillators, F is a measure of the strength of interaction between the oscillators and the magnetic field and Γ_m stands for the damping frequency for the magnetic field. The permittivity of the obstacle is expressed by the Drude model.

The third analyzed structure is a magnetic obstacle, whose parameters are [32]: ω_p =10 GHz, ω_0 =4 GHz, F=1.25, ε_∞ =1, Γ_e =0.05 ω_p, and Γ_m =0.05 ω_0. The obstacle is placed in air and it possesses negative refractive index for 3.52 GHz$\le \omega \le$6.57 GHz, as depicted in Fig. 6. The length of the obstacle is $L = 1$ cm.

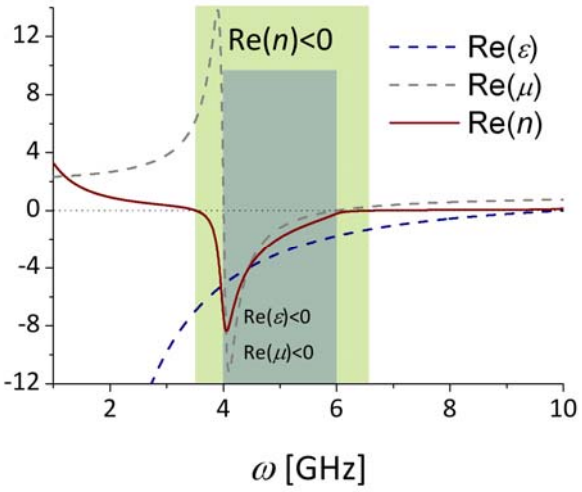

Figure 6. Dependence of the real part of refractive index (red solid line), the real part of permittivity (blue dashed line) and the real part of permeability (grey dashed line) of isotropic metamaterial on incident wave frequency.

In this case, the refractive index of the obstacle is calculated from an expression $n = \sqrt{\varepsilon\mu}$ if $\varepsilon(\omega \to \infty) > 0$ and $\mu(\omega \to \infty) > 0$, as derived in [38]. Assuming the following dependences: $\varepsilon = |\varepsilon|\exp(i\Phi_\varepsilon)$, $\mu = |\mu|\exp(i\Phi_\mu)$, where $(\Phi_\varepsilon, \Phi_\mu \in [0, \pi])$, since $\Gamma_e, \Gamma_m > 0$, index of refraction can be derived as $n = \pm\sqrt{|\varepsilon||\mu|}\exp[i(\Phi_\varepsilon + \Phi_\mu)/2]$. For the observed obstacle, it is evident that $\varepsilon(\omega \to \infty) \to \varepsilon_\infty > 0$ and $\mu(\omega \to \infty) \to 1 > 0$, which implies that for all frequencies the refractive index of isotropic obstacle can be represented by $n = \sqrt{\varepsilon\mu}$. Consequently, it can be shown that the sign of the real part of the refractive index is directly proportional to the sign of the expression $\mathrm{Re}(\varepsilon)\,\mathrm{Im}(\mu) + \mathrm{Im}(\varepsilon)\,\mathrm{Re}(\mu)$ [38].

Here, two frequency regions in which the material has negative index of refraction can be distinguished. The green one corresponds to the frequency region in which only the real part of permittivity is negative, while the permeability remains positive. On the other hand, for frequencies in the grey region (4 GHz $\le \omega \le$ 6 GHz), both ε and μ have negative values, and in this frequency interval the obstacle behaves as a DN NIM.

Fig. 7 depicts the dependences of the absorption, the dwell time and the group delay on incident field frequency for three different incident angles. For θ greater than $\pi/6$, the negative Goos-Hänchen shift occurs [39], hence they are not considered. From Fig. 7a and Fig. 7b, it is evident that the absorption and the dwell time have a similar profile, in contrast to group delay. Both the absorption and the dwell time reach local maxima at the boundary frequencies of the interval for which the obstacle behaves as DN NIM (grey area in Fig. 6). Unlike the situation in an anisotropic

obstacle, the peak position frequencies of absorption and the dwell time match. On the other hand, the group delay has local minima at these frequencies, and, the same as in case of anisotropic medium, it can reach negative value in a narrow frequency range for nonzero incident angles. For zero incident angle, the peaks positioned at the frequency $\omega = 6$ GHz vanish for all three quantities, leaving only those centered at resonant frequency $\omega_0 = 4$ GHz.

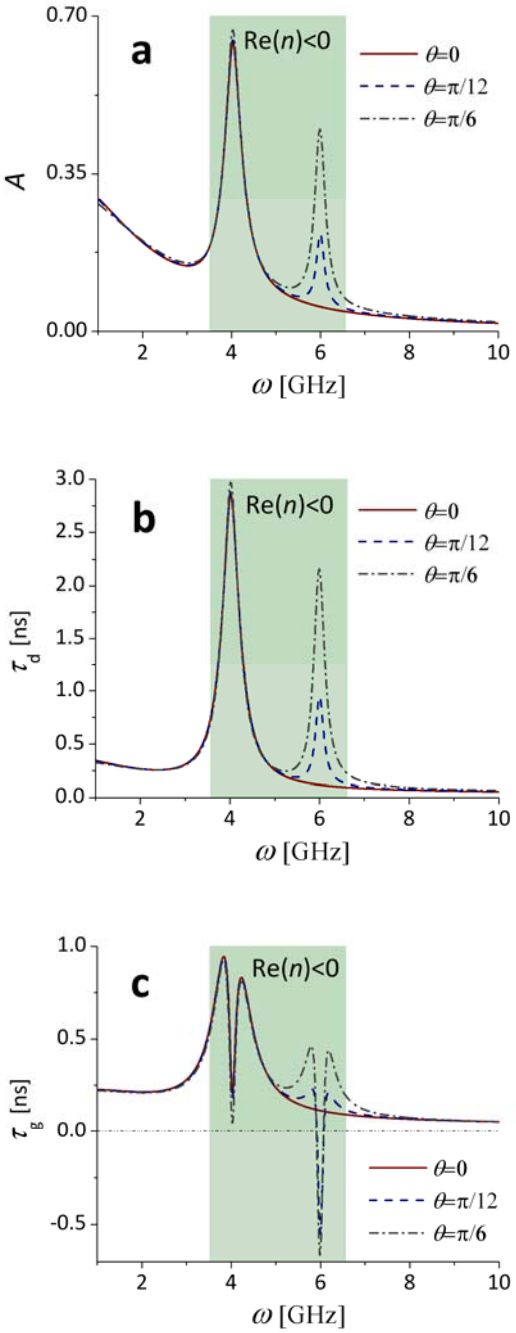

Figure 7. Dependence of (a) the absorption (b) the dwell time and (c) the group delay on the incident field frequency for different angles of incidence. Green area indicates the frequency region for which the isotropic obstacle possesses negative refractive index.

4. Conclusions

In this paper, the influence of properties of two types of anisotropic media on tunneling times has been investigated and compared to the case of isotropic materials. For the model that considers an obstacle made of alternately placed layers of two linear, absorptive and dispersive materials with anisotropic properties placed inside air, we obtained the expressions for calculating the tunneling times. The derivation shows that the group delay may be expressed as a sum of different times related to the tunneling effect: the dwell time, the self-interference time, the time related to the absorptive nature of the obstacle and the time which is a consequence of the permittivity difference between the obstacle and the surrounding waveguide. In case of a structure which is made of a large number of alternately placed absorptive layers of two differently doped $In_{0.53}Ga_{0.47}As$ samples, numerical calculations showed that the anisotropy of the structure causes the emergence of an additional peak in the dwell time, compared to the situation in isotropic media. With the increase of the odd layers' doping density, the regular dwell time peak which exists due to the absorption of the obstacle shifts and enhances toward higher frequencies. On the other hand, the change in the doping density of the second layer causes the group delay to reach minimal values at the boundary frequencies of the frequency ranges where the effective refractive index is negative. The decrease of the doping density is followed by the decrease of the group delay, too. It may even become negative at its first local minimum in a narrow frequency region. For the second structure, we used a new type of semiconductor metamaterial: layered anisotropic structure made of alternately placed layers of $In_{0.53}Ga_{0.47}As$ and $Al_{0.48}Ga_{0.52}As$. The first material is doped, while the other one remains undoped and therefore non-dispersive. Numerical results showed that this structure possesses negative refractive index for incident frequencies in the range 158.7 THz $\leq \omega \leq$ 214.75 THz. The increase of the angle of incident wave causes the increase of tunneling times and absorption in the frequency range for which the structure has negative refractive index. At higher frequencies, the oscillations caused by Bragg reflections become smaller as the incident angle grows. The results also indicate a peak frequency mismatch between the dwell time and the group delay, on one hand, and the dwell time and the absorption, on the other hand, and this phenomenon is noticed for the first time in linear media. Only in case of the zero angle of incidence all three quantities, i.e. the dwell time, the group delay and the absorption, reach their maximum values at the second boundary of the frequency interval for which the structure exhibits negative refractive index.

In a case of EM wave propagation through an obstacle made of isotropic NIM, we showed that, unlike the situation observed in anisotropic obstacles, the peak position frequencies of absorption and the dwell time match for all incident angles. On the other hand, the group delay exhibits similar behavior as in anisotropic media.

Appendix

The Poynting vector for the observed structure is equal to:

$$\vec{S} = \frac{1}{2}\vec{E}\times\vec{H}^{*} = -\frac{1}{2}\vec{i}_x E_z H_y^{*} + \frac{1}{2}\vec{i}_z E_x H_y^{*}. \tag{A1}$$

From Maxwell's equations it follows:

$$E_x = \frac{k_{zt}}{\varepsilon_0\varepsilon_{\perp}\omega}H_y, \quad E_z = -\frac{k_{xt}}{\varepsilon_0\varepsilon_{\parallel}\omega}H_y, \tag{A2}$$

where k_{zt} represents the z-component of the transmitted wave vector. Inserting Equations (A2) into Equation (A1), and neglecting the imaginary parts, the Poynting vector in anisotropic structure reads (Fig. 8):

$$\vec{S}_t = \left[\vec{i}_x \,\mathrm{Re}\left(\frac{k_{xt}}{\varepsilon_{\parallel}}\right) + \vec{i}_z \frac{k_z}{\tilde{\varepsilon}_{\perp}^{'}}\right]\frac{|H_0|^2\left(1-|R|^2\right)}{2\varepsilon_0\omega}, \qquad \frac{1}{\tilde{\varepsilon}_{\perp/\parallel}^{'}} = \frac{\mathrm{Re}(\varepsilon_{\perp/\parallel})}{\left|\varepsilon_{\perp/\parallel}\right|^2}. \tag{A3}$$

Analogously, the Poynting vector of the incident wave is equal to:

$$\vec{S}_i = \left(\vec{i}_x k_{xi} + \vec{i}_z k_z\right)\frac{|H_0|^2}{2\varepsilon_0\varepsilon_b\omega}. \tag{A4}$$

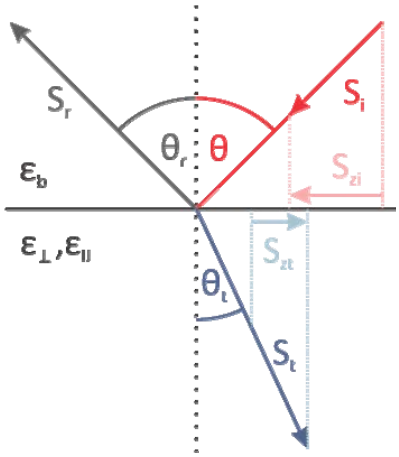

Figure 8. Schematic representation of the Poynting vector refraction. S_r and θ_r are the Poynting vector of reflected wave and reflected angle, respectively.

From the Snell's law, effective index of refraction is:

$$n_s = \sqrt{\varepsilon_b}\frac{\sin\theta}{\sin\theta_t}, \tag{A5}$$

where θ_t represents the refraction angle. From Equations (A3) and (A4) it follows:

$$\frac{S_{zt}}{S_{zi}} = \frac{S_t\sin\theta_t}{S_i\sin\theta} = \frac{\varepsilon_b}{\tilde{\varepsilon}_{\perp}^{'}}\left(1-|R|^2\right) \Rightarrow \tag{A6}$$

$$\left(\frac{\sin\theta}{\sin\theta_t}\right)^2 = \frac{\tilde{\varepsilon}_{\perp}^{'2}\left[\mathrm{Re}\left(\frac{k_{xt}}{\varepsilon_{\parallel}}\right)\right]^2 + k_z^2}{k_{xi}^2 + k_z^2}. \tag{A7}$$

Adopting the identity: $\left[\mathrm{Re}(d)\right]^2 = \left(a+\sqrt{a^2+b^2}\right)/2$, where $d^2 = a + jb$, the previous expression becomes:

$$\left(\frac{\sin\theta}{\sin\theta_t}\right)^2 = \frac{\tilde{\varepsilon}_{\perp}^{'2}}{\varepsilon_b k_0^2}a\frac{1+\sqrt{1+\frac{b^2}{a^2}}}{2} + \frac{k_z^2}{\varepsilon_b k_0^2}, \tag{A7}$$

$$a = \mathrm{Re}\left[\left(\frac{k_{xt}}{\varepsilon_{\parallel}}\right)^2\right], \quad b = \mathrm{Im}\left[\left(\frac{k_{xt}}{\varepsilon_{\parallel}}\right)^2\right].$$

The dispersion relations for the isotropic (surrounding waveguide) and the anisotropic (semiconductor metamaterial) medium are:

$$k_0^2 = \frac{k_{xi}^2 + k_z^2}{\varepsilon_b}, \tag{A8}$$

$$k_0^2 = \frac{k_{xt}^2}{\varepsilon_{\parallel}} + \frac{k_z^2}{\varepsilon_{\perp}}, \tag{A9}$$

respectively. From Equations (A8) and (A9) we obtain:

$$\mathrm{Re}\left[\left(\frac{k_{xt}}{\varepsilon_{\parallel}}\right)^2\right] = \left(\frac{1}{\tilde{\varepsilon}_{\parallel}^{'}} - \frac{\varepsilon_{\perp}^{'}\varepsilon_{\parallel}^{'} - \varepsilon_{\perp}^{''}\varepsilon_{\parallel}^{''}}{\left|\varepsilon_{\perp}\right|^2\left|\varepsilon_{\parallel}\right|^2}\varepsilon_b\sin^2\theta\right)k_0^2, \tag{A10}$$

$$\mathrm{Im}\left[\left(\frac{k_{xt}}{\varepsilon_{\parallel}}\right)^2\right] = \left(-\frac{\varepsilon_{\parallel}^{''}}{\left|\varepsilon_{\parallel}\right|^2} + \frac{\varepsilon_{\perp}^{'}\varepsilon_{\parallel}^{''} - \varepsilon_{\perp}^{''}\varepsilon_{\parallel}^{'}}{\left|\varepsilon_{\perp}\right|^2\left|\varepsilon_{\parallel}\right|^2}\varepsilon_b\sin^2\theta\right)k_0^2. \tag{A11}$$

Finally, by inserting Equations (A7), (A10) and (A11) in Equation (A5), we arrive to the expression for effective refractive index (5).

Acknowledgements

This work has been supported by the Ministry of Education and Science, Republic of Serbia (Project III45010).

References

[1] V. M. Agranovich and Yu. N. Gartstein, Spatial dispersion and negative refraction of light, *Phys. Usp.* 49: 1029-1044, 2006.

[2] V. G. Veselago, "The electrodynamics of substances with simultaneously negative values of ε and μ, *Sov. Phys. Usp.* 10: 509-514, 1968.

[3] R. A. Shelby, D. R. Smith, S. Schultz, Experimental verification of a negative index of refraction, *Science* 292: 77-79, 2001.

[4] U. K. Chettiar, A. V. Kildishev, H.-K. Yuan, W. Cai, S. Xiao, V. P. Drachev, V. M. Shalaev, Dual-band negative index metamaterial: Double negative at 813 nm and single-negative at 772 nm, *Opt. Lett.* 32: 1671-1673, 2007.

[5] J. B. Pendry, A. J. Holden, W. J. Stewart, I. Youngs, Extremely low frequency plasmons in metallic mesostructures, *Phys. Rev. Lett.* 76: 4773-4776, 1996.

[6] J. B. Pendry, A. J. Holden, D. J. Robbins, W. J. Stewart, Magnetism from conductors and enhanced nonlinear phenomena, *IEEE Trans. Microwave Theory Tech.* 47, 2075- 2084, 1999.

[7] D. R. Smith and N. Kroll, Negative refractive index in left-handed materials, *Phys. Rev. Lett.* 85: 2933-2936, 2000.

[8] D. R. Smith, W. J. Padilla, D. C. Vier, S. C. Nemat-Nasser, S. Schultz, Composite medium with simultaneously negative permeability and permittivity, *Phys. Rev. Lett.* 84: 4184-4187, 2000.

[9] A. N. Grigorenko, A. K. Geim, H. F. Gleeson, Y. Zhang, A. A. Firsolv, I. Y. Khrushchev, J. Petrovic, Nanofabricated media with negative permeability at visible frequencies, *Nature* 438: 335-338, 2005.

[10] C. G. Parazzoli, R. B. Greegor, K. Li, B. E. C. Koltenbah, Tanielian, Experimental verification and simulation of negative index of refraction using Snell.s law, *Phys. Rev. Lett.* 90: 107401-1-4, 2003.

[11] J. B. Pendry, Negative refraction makes perfect lens, *Phys. Rev. Lett.* 85: 3966-3969, 2000.

[12] A. Greenleaf, Y. Kurylev, M. Lassas, G. Ulhmann, HYPERLINK "http://www.math.washington.edu/~gunther/publications/Papers/siamreviewfinal.pdf" Cloaking Devices, Electromagnetic Wormholes and Transformation Optics , *SIAM Review* 51: 3-33, 2009.

[13] J. A. Ferrari, E. Frins, Negative refraction and lensing at visible wavelength: experimental results using a waveguide array, *Opt. Express* 19**:** 13358-13364 , 2011.

[14] S. Zhang, W. Fan, N. C. Panoiu, K. J. Malloy, R. M. Osgood, S. R. J. Brueck, Experimental demonstration of near-infared negative-index metamaterials, *Phys. Rev. Lett.* 95: 137404-1-4, 2005.

[15] V. M. Shalaev, W. Cai, U. K. Chettiar, H.-K. Yuan, A. K. Sarychev, V. P. Drachev, A. V. Kildishev, Negative index of refraction in optical metamaterials, *Opt. Lett.* 30: 3356-3358, 2005.

[16] V. M. Shalaev, Optical negative-index metamaterials , *Nat. Photonics* 1: 41-48, 2007.

[17] A. J. Hoffman, A. Sridhar, P. X. Braun, L. Alekseyev, S. S. Howard, K. J. Franz, L. Cheng, F.-S. Choa, D. L. Sivco, V. A. Podolskiy, E. E. Narimanov, C. Gmachl, J., Mid-infrared semiconductor optical metamaterials, *Appl. Phys.* 105: 122411-1-7, 2009.

[18] V. A. Podolskiy, E. E. Narimanov, Strongly anisotropic waveguide as a nonmagnetic left-handed system, *Phys. Rev. B* 71**:** 201101(R)-1-4, 2005.

[19] A. J. Hoffman, L. Alekseyev, S. S. Howard, K. J. Franz, D. Wasserman, V. A. Podolskiy, E. E. Narimanov, D. L. Sivco, C. Gmachl, Negative refraction in semiconductor metamaterials, *Nat. Mater.* 6**:** 946-950, 2007.

[20] P. N. Prasad, *Nanophotonics*, John Wiley & Sons, Inc., New Jersey, 2004.

[21] E. H. Hauge and J. A. Støvneng, Tunneling times: a critical review, *Rev. Mod. Phys* 61: 917-936, 1989.

[22] H. G. Winful, Group delay, stored energy, and the tunneling of evanescent electromagnetic waves, *Phys. Rev. E* 68: 016615-1-9, 2003.

[23] H. G. Winful, Tunneling time, the Hartman effect, and superluminality: A proposed resolution of an old paradox, *Phys. Rep.* 436: 1–69, 2006.

[24] I. Ilić, P. P. Beličev, V. Milanović, J. Radovanović, Analysis of tunneling times in absorptive and dispersive media, *J. Opt. Soc. Am. B* 25: 1800-1804, 2008.

[25] I. Ilić, P. P. Beličev, V. Milanović, J. Radovanović, Modeling of dwell time and group delay in dispersive and absorptive media, *Phys. Scr.* T135: 014040-1-4, 2009.

[26] G. Isić, V. Milanović, J. Radovanović, Z. Ikonić, D. Indjin, P. Harrison, Time delay in thin slabs with self-focusing Kerr-type nonlinearity, *Phys. Rev. A* 77, 033821-1-5, 2008.

[27] P. P. Beličev, I. Ilić, V. Milanović, J. Radovanović, Lj. Hadžievski, Tunneling times in metamaterials with saturable nonlinearity, *Phys. Rev. A* 80: 023821-1-7 , 2009.

[28] I. Ilić, P. P. Beličev, V. Milanović, J. Radovanović, Lj. Hadžievski, Goos–Hänchen shift and time delay in dispersive nonlinear media, *Phys. Lett. A* 375: 1357-1361, 2011.

[29] I. Ilić, P. P. Beličev, V. Milanović, J. Radovanović, Lj. Hadžievski, Influence of the Goos–Hänchen shift on tunneling times in dispersive nonlinear media, *Acta Phys. Pol. A* 116: 638-641, 2009.

[30] V. G. Veselago and E. E. Narimanov, The left hand of brightness: past, present and future of negative index materials, *Nature Mater.*5:759-762, 2006.

[31] F. T. Smith, Lifetime matrix in collision theory, *Phys. Rev.* 118, 349-356, 1960.

[32] M. Büttiker, Larmor precession and the traversal time for tunneling, *Phys. Rev. B* 27: 6178-6188, 1989.

[33] P. C. W. Fung, K. Young, Electric energy density in a dispersive medium by circuit analog, *Am. J. Phys.* 46: 57-59, 1978.

[34] R. Ruppin, Electromagnetic energy density in a dispersive and absorptive material, *Phys. Lett.* 299: 309–312, 2002.

[35] T. J. Cui and J. A. Kong, Time-domain electromagnetic energy in a frequency-dispersive left-handed medium, *Phys. Rev. B* 70: 205106-1-7, 2004.

[36] R. Zioklowski and E. Heyman, Wave propagation in media having negative permittivity and permeability, *Phys. Rev. E*, 64: 056625-1-15, 2001.

[37] J. G. Muga, I. L. Egusquiza, J. A. Damborenea, F. Delgado, Bounds and enhancements for negative scattering time delays, *Phys. Rev. A* 66: 042115-1-8, 2002.

[38] R. W. Ziolkowski and E. Heyman, Wave propagation in media having negative permittivity and permeability, *Phys. Rev. E* 64: 056625-1-15, 2001.

[39] C.-F. Li, Negative lateral shift of a light beam transmitted through a dielectric slab and interaction of boundary effects, *Phys. Rev. Lett.* 91: 133903-1-4, 2003.

A Flat Profile Cooke Triplet Made from Dielectrics

S. J. Wiggin[1], W. Tang[1], Y. Hao*[1], I. Youngs[2]

[1]School of Electronic Engineering and Computer Science,
Queen Mary, University of London, UK
[2]DSTL, Salisbury, SP4 OJQ, UK
E-mail: yang.hao@eecs.qmul.ac.uk

Abstract

Transformation Optics (TO) can be applied as an alternative to conventional optical design. A Cooke triplet based on TO is re-engineered using metamaterials (MTM). The triplet is simulated using the Finite-Difference Time Domain Method (FDTD). The MTM triplet performs, in terms of Siedel aberrations, as well as a conventional triplet design. A TO-designed triplet with dielectrics, materials without a permittivity less than 1, is also simulated. The device is demonstrated to be broadband and can be easily fabricated.

1. Introduction

Metamaterials could be classified as materials possessing negative values of either permittivity or permeability or both [1]. However, recently the concept has been extended to any materials/structures which are artificially made and possess novel properties that cannot be found in nature. Much interest in MTMs has been generated around the holy-grail applications of sub-wavelength imaging [2]. The more lucrative applications of MTMs are in the field of electromagnetic engineering, where metamaterials potentially offer, for example, a novel way of designing optical systems such as compressed lenses [3]. Negative index MTMs allow aberrations to be minimised more successfully in optical systems [4]. More recently, transformation optics (TO) is developed to manipulate electromagnetic waves and has led to the possibility of invisibility cloak [5]. Most of TO based devices rely on the use of MTMs, however, a carpet cloak [6] which cloaks a grounded metallic object has less of a divergence in material parameters in the construction and operated at a wide band width overcoming two key limitations of MTMs: losses and narrowband operation. Moreover, the concept of TO can be used to modify conventional devices such as lenses, which translate and magnify objects with materials of varying refractive index [7].

In this paper, we intend to apply TO to re-engineer one of the classic optical devices, the Cooke Triplet lens. The lens was invented by Dennis Taylor in 1893 and via an elegant design it is able to minimise all five major Seidel aberrations. The triplet consists of three lenses, two made of crown glass either side of one lens made of flint glass. The five major aberrations were described by Siedel and are spherical, coma, astigmatism, distortion and field curvature. A triplet eliminates the aberrations at the edges of the image compared with a single lens minimising the distortion and field curvature. The removal of aberrations from images is one of the key goals for optics designers in camera and film technology. The objective of this study is to derive material properties of a single device designed using TO to control the propagation of light in the same way as the Cooke Triplet lens does in a conventional system. Exotic material properties are generated from a rigorous transformation therefore MTMs are required in the design of the proposed lens. In this paper, we apply the Finite-Difference Time Domain (FDTD) technique to evaluate lens performance. Additionally, we hope to compare the MTM lens with a simplified one, where MTMs are replaced with conventional dielectrics. We expect that the simplified lens will be able to perform better at a broad band of frequencies than the MTM design but with a slightly degraded performance.

2. The method for designing a MTM triplet

Ray tracing is a key concept in lens design based on Snell's law of refraction and that light travels along a straight line in a medium of constant refractive index. The theory of TO says that light perceives a virtual or distorted space when it enters a medium and is distorted in a similar manner to the bending of spacetime due to large masses in the theory of relativity. Ray tracing was carried out on a Cooke Triplet in the lens library in **OSLO**, see Fig.1. The materials properties of the Cooke Triplet were then re-engineered using TO.

A distorted coordinate system is generated from the ray tracing procedure. These rays form the boundary between 8 different grid blocks. A quasi-orthogonal, structured grid was generated by solving for the partial differential equation via an iterative solution with the rays forming the boundary of the blocks. As the triplet is symmetrical about the optical axis only the top half is presented, see Fig.2. The smoothness of the permittivity values and hence the performance of the device were very sensitive to detrimental changes in the smoothness and orthogonality of the grid. The grid was made smoother and more orthogonal by using the Laplace control function. The outermost wings

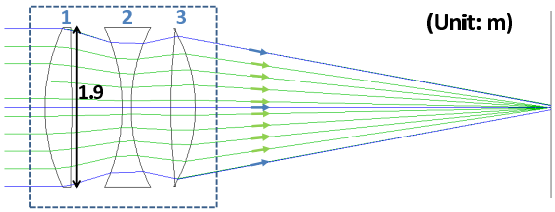

Figure 1: *The rays for the transformation used as the distorted geometry were taken from the dashed box region.*

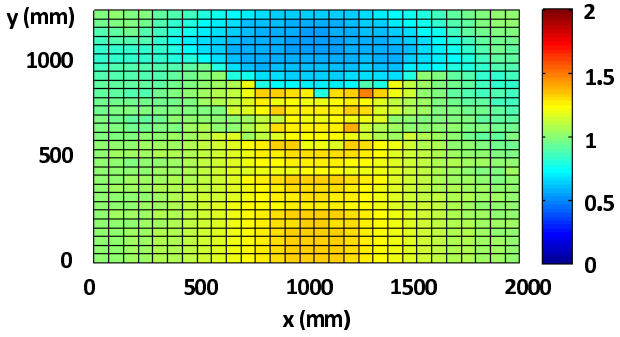

Figure 2: *The plot shows the discrete permittivity map for the top half of the Cooke triplet where the cell size is about $\lambda/10$.*

have ϵ less than that of free space due to the expansion of space in this region.

The metric tensor defines a metric for distance in a coordinate system. A metric tensor was calculated for each grid cell, see Fig. 2 is a discrete calculation. The vector defining the coordinate system in the x direction, **x**, and the vector defining the coordinate system in the y direction, **y** were combined to yield the metric tensor as follows:

$$g = \begin{pmatrix} g_{xx} & g_{xy} \\ g_{xy} & g_{yy} \end{pmatrix} \quad (1)$$

where $g_{xy} = \mathbf{x} \cdot \mathbf{y}$ and **x** and **y** are basis vectors of each unit cell.

Maxwell's equations are invariant under coordinate transformation therefore, if we take the materials interpretation for the transformation where where the permittivity and permeability tensors are expressed in terms of the metric tensor, a material can be designed with the material properties for the propagation characteristics for the distorted geometry.

$$\epsilon^{ij} = \mu^{ij} = +/- \sqrt{g} g^{ij} \quad (2)$$

The device is engineered to be an all-dielectric device where the permeability does not vary in the device and the refractive index only depends on permittivity. Materials with a permeability which is not equal to one are rare in nature. The permeability can be held constant and the permittivity tensor varied during the transformation to allow for the design of a device which only varied in terms of permittivity. This condition is true so long as the grid is quasi-orthogonal [6].

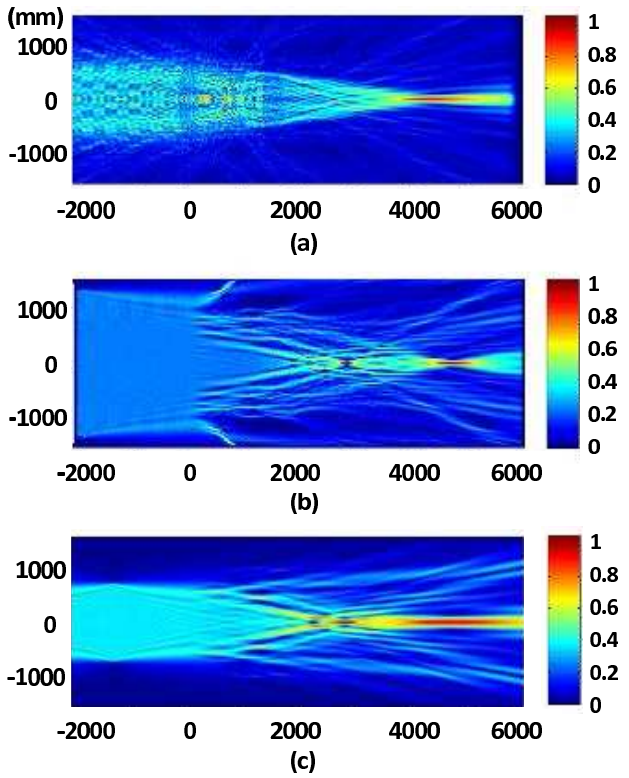

Figure 3: *Electric field distributions when (a) a conventional triplet, (b) a MTM triplet and (c) a reduced non-MTM triplet is applied. The focusing of the lens is evident in this plot of the field distribution following the FDTD simulation. Major losses occur by reflection and by scattering from the lens. The true focus is taken in all results as the extended maximum far from the lens rather than the maximum close to the lens surface.*

3. Results

An FDTD simulation was carried out to simulate the electromagnetic interaction with the lens. The FDTD Method is a common tool for simulating electromagnetic fields and has been used widely in the study of metamaterials [8]. The simulation was made in 2D using the TM mode as 3D can be achieved using rotation or extending the 2D model. A rectangular computational domain is truncated with perfectly matched layers. The simulation was carried out with a Total Field Scattering Field (TFSF) continuous plane wave source at 8 GHz. The simulation uses a cell size of $\lambda/10$. The MTM parts are dispersive and are simulated using the Drude model [9]. The energy map derived from the Ez component of the electromagnetic field for a conventional triplet, a MTM triplet, and a reduced non-MTM triplet is displayed in figure 3. When a plane wave is launched from the left, the focal length, as can be seen from Fig.3, is approximately the same for all three lenses. We also investigate five major abbreviations of the proposed MTM triplet related to conventional optical systems.

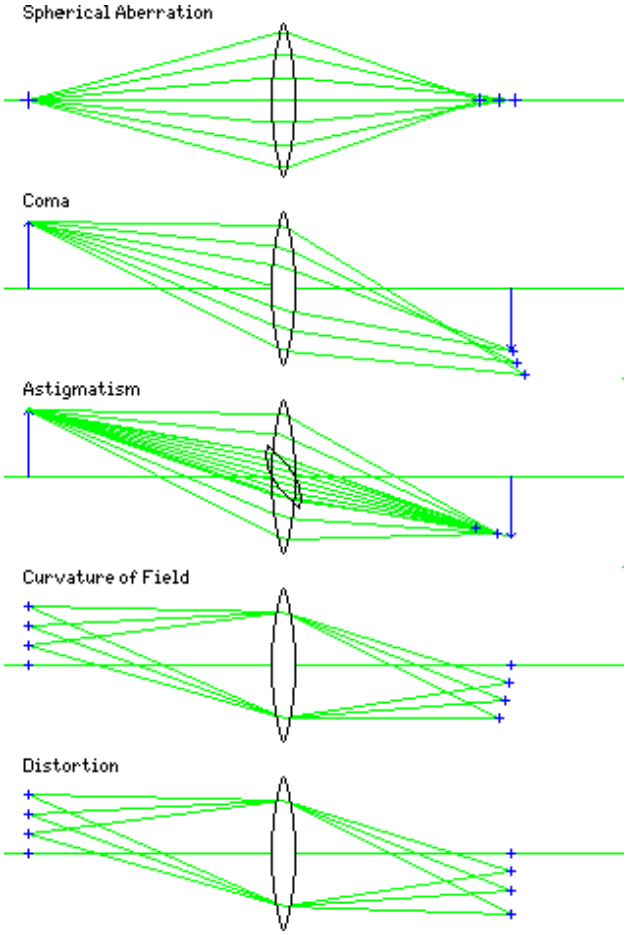

Figure 4: *The five Siedel aberrations results from a deviation from the paraxial approximation resulting in a shift in focal point. This diagram describes each Siedel aberration. It serves as the basis for calculating the aberrations in this paper.*

3.1. Spherical aberration

Spherical aberration occurs due to the focus for the rays at the edge of the lens being a different focal length than for those rays close to the optical axis. This is simulated by using a plane wave incident on the lens and investigating the distribution of irradiance along the optical axis around the true focal length, see Fig. 4. The transverse spherical aberration for the MTM triplet is similar to the conventional triplet but with less energy scattered outside the main beam. The spherical aberration for the reduced lens is poorer in the reduced lens.

3.2. Chromatic aberration

Chromatic aberration is due to the permittivity of a material being dependant on frequency. The chromatic aberration is simulated used a Gaussian pulse as a source in FDTD and sampling the electric field at 5.63 GHz, 6.67 GHz and 8 GHz. The simulation results show that the displacements of the focal point at different frequencies are similar for all three lenses.

3.3. Coma

The coma is due to oblique rays being refracted more at the edge of the lens than at the centre of the lens. This behaviour results in a comet-shaped blur as the image is formed at diminishing focal point perpendicular to optical axis. This aberration is simulated for a lens in FDTD by using a plane wave source angled at 18 degrees to the optical axis and measuring the irradiance distribution at the focus perpendicular to the optical axis. The coma in the MTM triplet is half the spread and with fewer peaks compared to the coma from the non-MTM triplet.

3.4. Distortion

Distortion occurs when a source far away from the optical axis is imaged and sufferers a greater magnification than a source close to the optical axis. The magnification is the ratio of the image height over the object height. The image height is the distance of the focus from the perpendicular optical axis; the object height is the height of the chief ray extended backwards to the start of the simulation. The results of the distortion in a conventional triplet design are given in Fig. 4. Barrel distortion is visible for the conventional lens. The distortion is clearly much greater in the MTM Cooke Triplet and the single lens. The MTM triplet has a similar distortion to the single lens rather than the triplet lens because it behaves as a single concave lens would and does not act as a Cooke Triplet. The off-axis simulations also reveal that the MTM triplet is able to focus at much larger angles than the conventional lens.

4. Discussion

We have presented a method to design a Cooke Triplet that can be generalised to design any optical system containing multiple lenses with transformation optics. The optical system designed with this method will benefit from having a flat profile and be made of only a single dielectric block compared with a conventional optical system made from many lenses with curved surfaces. This design is broadband and can be fabricated with low-cost dielectric materials. To the authors' knowledge this is the first use of ray tracing to define the electromagnetic propagation characteristics of an optical system for spatial transformation and serves as a key step in speeding the design methodology for using transformation media to design optical systems.

The results show that the field distribution outside the MTM device is very much like the field distribution outside the conventional triplet however there are slight differences in the distortion and coma in the two. The reduced, non-MTM triplet suffers from a serious coma and generally suffers from poorer image aberrations. The distortion for the MTM triplet is much larger than the conventional design and is close to that of a single lens. A limitation of the work is the lack of geometrical optics and ray tracing analysis available to the FDTD method which would allow a direct comparison with work on meta material lens aberrations which use analytical formulae for the Siedel aberra-

tions [4] rather than full wave electromagnetic simulations which restricts the results of this paper to that of plots of the EM field rather than numbers and coefficients. Further work would include fabrication of the triplet using dielectric materials and a hole-drilling fabrication technique with experimental verification on a near field scanner.

5. Acknowledgement

SW acknowledges the support of Dstl and EPSRC through an industrial CASE studentship. Crown copyright 2011. This work is part funded by the Ministry of Defence and is published with the permission of the Defence Science and Technology Laboratory on behalf of the Controller of HMSO.

References

[1] V.-G. Veselago, "The Electrodynamics of Substances with Simultaneously Negative Values of Epsilon and Mu," *Soviet Physics Uspekhi* 10: 509–, 1968.

[2] J.B., Pendry, "Negative Refraction Makes a Perfect Lens," *Physical Review Letters* 85: 18: 3966-3969, 2000.

[3] D. -A. Roberts, N. Kundtz and D. -R. Smith, "Optical Lens Compression by Transformation Optics," *Optics Express* 17: 19: 16535-16542, 2009.

[4] D. Schurig and D. -R. Smith, "Negative Index Lens Aberrations," *Physical Review E* 70: 065601, 2004.

[5] J. -B. Pendry, D. -Schurig, D. -R. Smith, "Controlling Electromagnetic Fields," *Science* 321: 1780-1782, 2006.

[6] J. Li and J. B. Pendry, "Hiding under the carpet: a new strategy for cloaking," *Phys. Rev. Lett.* 101: 20:203901, 2008.

[7] D. Schurig, J. -B. Pendry and D. -R. Smith, "Transformation-designed Optical Elements," *Optics Express* 15: 22: 14772-14782, 2007.

[8] Y. Hao, R. Mitra, *FDTD Modelling of Metamaterials: Theory and Applications* Artech House, MA, 2009.

[9] Y. Zhao, C. Argyropoulos and Y. Hao, "Full-wave finite-difference time-domain simulation of electromagnetic cloaking structures," *Optics Express* 16: 9: 6717 – 6730, 2008.

Novel antenna concepts via coordinate transformation

Paul-Henri Tichit, Shah Nawaz Burokur, Xinying Wu, Dylan Germain, André de Lustrac*

IEF, Univ. Paris-Sud, CNRS, UMR 8622, 91405 Orsay cedex, France
*corresponding author, E-mail: andre.de-lustrac@u-psud.fr

Abstract

Coordinate transformation is an emerging field which offers a powerful and unprecedented ability to manipulate and control electromagnetic waves. Using this tool, we demonstrate the design of novel antenna concepts by tailoring their radiation properties. The wave manipulation is enabled through the use of engineered dispersive composite metamaterials that realize the space coordinate transformation. Three types of antennas are considered for design: a directive, a beam steerable and a quasi-isotropic one. Numerical simulations together with experimental measurements are performed in order to validate the coordinate transformation concept. Near-field cartography and far-field pattern measurements performed on a fabricated prototype agree qualitatively with Finite Element Method (FEM) simulations. It is shown that a particular radiation pattern can be tailored at ease into a desired one by modifying the electromagnetic properties of the space around radiator. This idea opens the way to novel antenna design techniques for various application domains such as the aeronautical and transport fields.

1. Introduction

Coordinate transformation (also called transformation optics or transformation electromagnetics) is a powerful mathematical tool that is used to generate a new transformed space from an initial one where solutions of Maxwell's equations are known by manipulating electromagnetic waves. As a first step, it consists in imagining a virtual space with desired topological properties, which will contain the underlying physics. This approach has been revived when J. B. Pendry et al. [1] have proposed an interpretation where permeability and permittivity tensors components can be viewed as a material in the original space. It is as if the new material mimicks the defined topological space. Since this pioneering work of J. B. Pendry and that of U. Leonhardt et al. [2], transformation optics is an emerging field where Maxwell's equations are form invariant under a coordinate transformation. It offers an unconventional strategy to the design of novel class metamaterial devices. The most striking application conceived so far via coordinate transformation concept is the invisibility cloak for which various designs have been presented in microwave [3-5] and optical regimes [6-8]. Other interesting wave manipulation applications such as wave concentrators [9], field rotators [10], electromagnetic wormholes [11], waveguide transitions and bends [12-16] have also been proposed. Concerning antenna applications, focusing lens antennas [17-19] and the engineering of radiation patterns [20] have been proposed. The performances of an omnidirectional retroreflector [21] based on the transmutation of singularities [22] and Luneberg lenses [23] have also been experimentally demonstrated. An octave-bandwidth horn antenna has experimentally validated for satellite communications [24]. Recently, techniques of source transformation [25-27] have offered new opportunities for the design of active devices with source distribution included in the transformed space.

Using this last approach, we review the design of three antenna models where the radiation pattern is tailored specifically in each case. The first one concerns an ultra-directive antenna obtained by stretching a source into an extended coherent radiator [28-30]. The design has been implemented through the use of judiciously engineered metamaterials and the device is shown experimentally to produce an ultra-directive emission. The idea has been extended to a second device, a wave bending one, so as to achieve a steered beam antenna via a rotational coordinate transformation. Experimental measurements have shown a beam steering as much as 66°. Finally, we present the numerical design of a quasi-isotropic antenna achieved by expanding the space around a directive source [31].

2. Ultra-directive antenna

The ultra-directive antenna is based on the transformation of a cylindrical space into a rectangular one. The schematic principle of the transformation is presented in Fig. 1. The theoretical underlying physics of the transformation involved here has been detailed recently in [28]. The concept is as follows: the imagined space of our proposed antenna is obtained by transforming a flat isotropic cylindrical half-space with zero Riemann curvature tensor described in polar coordinates $\{r, \theta\}$ into a flat space in squeezed Cartesian coordinates. x', y' and z' are the coordinates in the virtual transformed rectangular space and x, y, z are those in the initial real cylindrical space. We assume free space in the cylinder, with isotropic permeability and permittivity tensors ε_0 and μ_0. In the theoretical study of [28], we have shown that the coordinate transformation can be implemented by a material obeying the following tensors:

$$\psi^{i'j'} = g^{i'j'}\left|\det\left(g^{i'j'}\right)\right|^{-\frac{1}{2}}\psi\,, \qquad (1)$$

where ψ represents the permittivity or permeability tensor and g, the metric tensor of our designed space. The material must then be able to produce the following dielectric tensors presenting no non-diagonal components (2):

$$\varepsilon^{ij} = \mu^{ij} = diag\left(\varepsilon_{xx}(x'), \frac{1}{\varepsilon_{xx}(x')}, \alpha\varepsilon_{xx}(x')\right), \quad (2)$$

where $\varepsilon_{xx}(x') = \frac{\pi x'}{e}$ and $\alpha = \frac{d^2}{4L^2}$, with d representing the diameter of the initial cylindrical space and e and L, respectively, the width and length of the rectangular target space. For a practical implementation using metamaterials, the dimensions of the semi-cylindrical space is set so that α = 4 in order to obtain achievable values for the electromagnetic parameters. We also consider a polarized electromagnetic wave with an electric field pointing in the z-direction, which allows modifying the dispersion equation in order to simplify the electromagnetic parameters without changing Maxwell's equations and propagation in the structure. This leads to a metamaterial which is described with e = 0.15 m and L = 0.05 m by:

$$\mu_{xx} = 1\ ;\ \mu_{yy} = \frac{1}{(\varepsilon_{xx})^2}\ ;\ \varepsilon_{zz} = 4(\varepsilon_{xx})^2\,, \qquad (3)$$

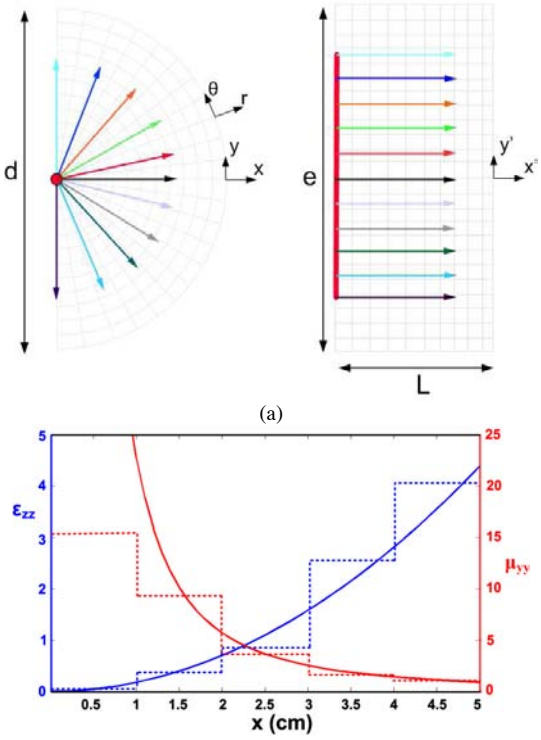

Figure 1: (a) Transformation of a cylindrical space into a rectangular one. (b) Continuous (continuous lines) and discretized (dashed lines) variations of permeability and permittivity of the material.

Discrete values are then created for the desired variation of μ_{yy} and ε_{zz} to secure a practical realization producing experimental performances close to theory. Fig. 2 shows the photography of the fabricated prototype. A microstrip square patch antenna printed on a 0.787 mm thick low-loss dielectric substrate (Rogers RT/Duroid 5870TM with 17.5 μm copper cladding, ε_r = 2.33 and tanδ = 0.0012) is used as radiating source. A surrounding material made of alternating electric metamaterial and magnetic metamaterial layers is used to capture the emanating omnidirectional radiation from the patch source and transform it into a directive one. The metamaterial is a discrete structure composed of five different regions where permittivity and permeability vary according to (3) and to the profile of Fig. 1(b).

The axial permittivity ε_{zz} and permeability μ_{yy} show respectively values ranging from 0.12 to 4.15 and from 1.58 to 15.3. The bulk metamaterial is assembled using 56 layers of dielectric boards on which subwavelength resonant structures are printed. 28 layers contain SRRs [32] and 28 others contain ELCs [33], shown in the insets of Fig. 2 and known to provide respectively a magnetic and an electric response. Each layer is made of 5 regions of metamaterials corresponding to the discretized values of Fig. 1(b). Because of constraints of the layout, we choose a rectangular unit cell with dimensions 3.333 mm for both resonators. The layout consists of 5 regions, each of which is three unit cells long (10 mm). We are able to obtain the desired ε_{zz} and μ_{yy} by tuning the resonators' geometric parameters, as illustrated and detailed in Fig. 3. The SRR and ELC resonators are simulated with finite-element method based Ansys HFSS commercial code for the [8 GHz – 15 GHz] frequency band. The calculated S-parameters are then utilized to extract the effective material parameters μ_{yy} and ε_{zz}, through the use of a retrieval process described in [34]. μ_{yy} and ε_{zz} are respectively shown in Fig. 4(a) and 4(b). The insets of Fig. 4 show the variation of the two material parameters in the vicinity of 10 GHz.

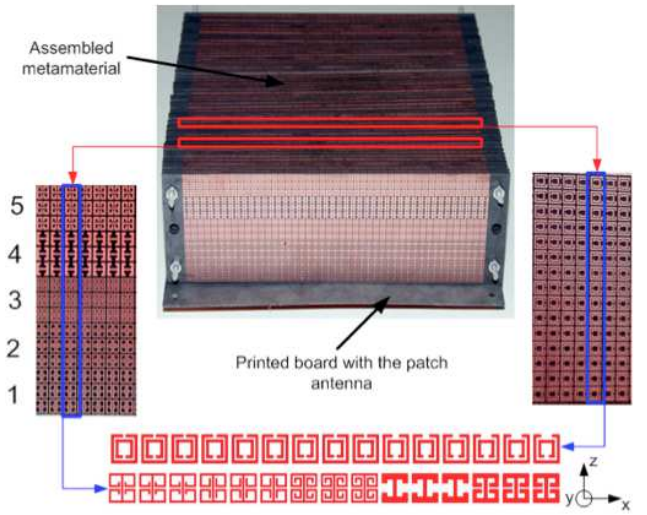

Figure 2: Photography of the structure of the antenna. The inserts show the permittivity (left) and the permeability (right) layers of the material.

SRR

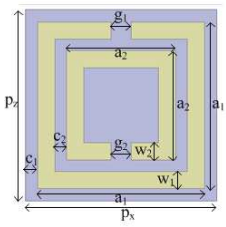

region	a_2	c_2	g_1	g_2	μ_{yy}
1	1.9	0.2	0.35	0.35	15.3
2	1.9	0.2	0.38	0.38	10
3	1.8	0.25	0.36	0.3	3.66
4	1.8	0.25	0.8	0.6	1.89
5	1.8	0.25	1.2	0.6	1.58

$p_x = p_z = 10/3$, $a_1 = 2.9$, $w_1 = w_2 = 0.3$, $c_1 = 0.2165$

ELC

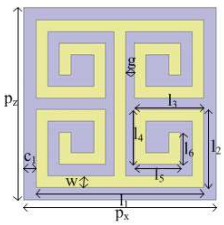

region	l_4	l_5	l_6	ε_{zz}
1	0.5	0	0	0.15
2	0.9	0	0	0.4
3	0.95	0.8	0.55	0.65

$p_x = p_z = 10/3$, $l_1 = 2.9$, $l_2 = 1.35$, $l_3 = 1.2$, $w = 0.2$, $g = 0.15$, $c_1 = 0.2165$

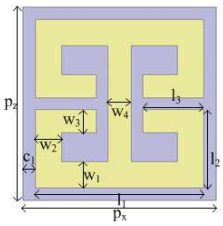

region	l_2	l_3	w_3	ε_{zz}
4	1	0	0	2.74
5	1.35	1.05	0.4	4.15

$p_x = p_z = 10/3$, $l_1 = 2.9$, $w_1 = w_2 = 0.6$, $w_4 = 0.4$, $c_1 = 0.2165$

All dimensions are in mm.

Figure 3: Unit cell of the SRR used as magnetic material and of the ELC used as electric material. The tables summarize the dimensions of these two metamaterial cells to achieve the different values of the electromagnetic parameters needed for the transformation.

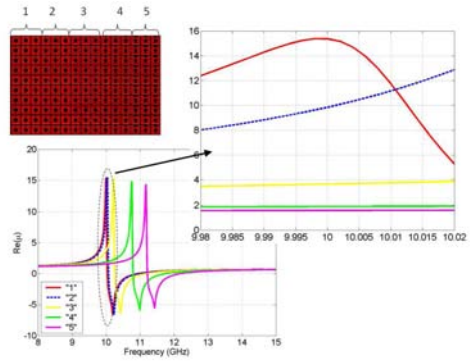

(a)

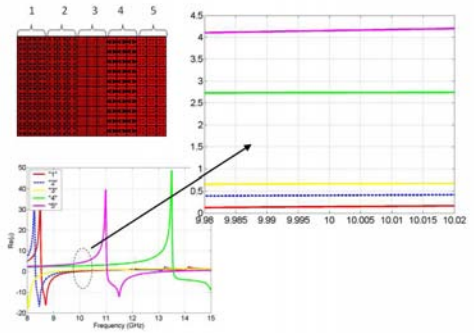

(b)

Figure 4: (a) Magnetic response of the SRR for the 5 regions. (b) Electric response of the ELC for the 5 regions.

The metamaterial layers are mounted 2 by 2 with a constant air spacing of 2.2 mm between each. Overall dimensions of the antenna are 15 cm x 15 cm x 5 cm. Far-field patterns measurements are performed in an anechoic chamber, where the metamaterial-based antenna is used as emitter and a wideband [2 GHz – 18 GHz] is used as receiver. The E-plane radiation pattern is measured at 10.6 GHz for computer-controlled elevation angle varying from -90° to +90°. Fig. 5 presents the comparison between simulations and experiments for the patch source alone and the metamaterial antenna. The transformation of the patch's omnidirectional radiation into a directive is clearly established. A narrow half-power beamwidth of 13° is observed for the measured antenna. These performances are competitive with classical high directivity antennas such as parabolic reflector antennas.

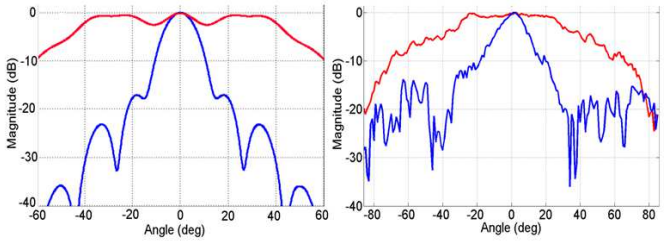

(a) (b)

Figure 5: (a) Calculated and (b) measured radiation pattern at 10.6 GHz of the proposed metamaterial antenna (blue) and the microstrip patch radiator alone (red).

3. Azimuthal antenna

Here, we propose a two-dimensional coordinate transformation, which transforms the vertical radiation of a plane source into a directive azimuthal emission. Let us consider a source radiating in a rectangular space. Theoretically this radiation emitted from the latter source can be transformed into an azimuthal one using transformation optics. The transformation procedure is noted F(x',y') and consists in bending the emission. Fig. 6 shows the operating principle of this rotational coordinate transformation. Mathematically, F(x',y') can be expressed as:

$$\begin{cases} x' = ax\cos(by) \\ y' = ax\sin(by) \\ z' = z \end{cases}, \qquad (4)$$

where x', y', and z' are the coordinates in the bent space, and x, y and z are those in the initial rectangular space. In the initial space, we assume free space. L_2-L_1 and L are respectively the width and the length of the rectangular space. The rotational transformation of Fig. 6 is defined by parameter *a* considered as an "expansion" parameter and parameter *b* which controls the rotation angle of the transformation F(x',y'). By substituting the new coordinate system in the tensor components, and after some simplifications, the material parameters are derived. After

diagonalization, calculations lead to permeability and permittivity tensors given in the diagonal base by:

$$\overline{\overline{\varepsilon}} = \begin{pmatrix} \psi_{rr} & 0 & 0 \\ 0 & \psi_{\theta\theta} & 0 \\ 0 & 0 & \psi_{zz} \end{pmatrix} \varepsilon_0 \qquad \overline{\overline{\mu}} = \begin{pmatrix} \psi_{rr} & 0 & 0 \\ 0 & \psi_{\theta\theta} & 0 \\ 0 & 0 & \psi_{zz} \end{pmatrix} \mu_0$$

with: $$\psi_{rr} = \frac{a}{br}; \psi_{\theta\theta} = \frac{a}{b} r; \psi_{zz} = \frac{1}{abr}, \quad (5)$$

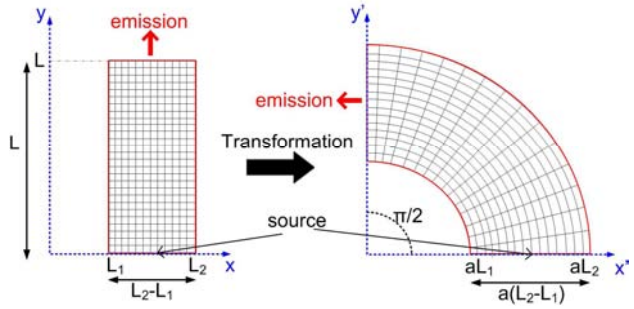

Figure 6: Schematic principle of the 2D rotational coordinate transformation. The emission in a rectangular space is transformed into an azimuthal one.

The transformation formulation is implemented using finite-element method based commercial solver Comsol Multiphysics. Fig. 7 shows the comparison of 2D simulation between a plane source made of current lines in *yz* plane above a limited metallic ground plane (Fig. 7(a)) and the same source surrounded by a metamaterial defined by Eq. (5) [Fig. 7(b)]. Fig. 7(c) and 7(d) show respectively the far-field patterns of the plane source without and with the metamaterial structure. The left shift of the peak corresponds to a rotation of 76° of the emitted radiation.

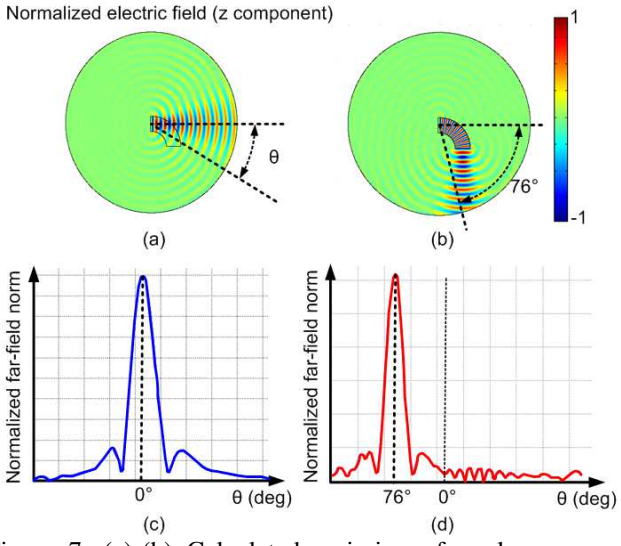

Figure 7: (a)-(b) Calculated emission of a plane current source above a limited metallic ground plane without and with the metamaterial structure. (c)-(d) Calculated normalized far field of the antenna without and with metamaterial. A 76° rotation of the radiation is clearly observed.

For the physical prototype fabrication, we simplify the calculated material parameters through a parameter reduction procedure. We set a polarization of the electromagnetic field such that the magnetic field is along the z-direction. In this case, the relevant electromagnetic parameters are μ_{zz}, $\varepsilon_{\theta\theta}$ and ε_{rr}. We maintain $\varepsilon_{\theta\theta}$ and μ_{zz} constant and the new set of coordinates is given by (6):

$$\varepsilon_{rr} = \left(\frac{1}{br}\right)^2 \div 1.7; \varepsilon_{\theta\theta} = 2.8; \mu_{zz} = 1.7, \quad (6)$$

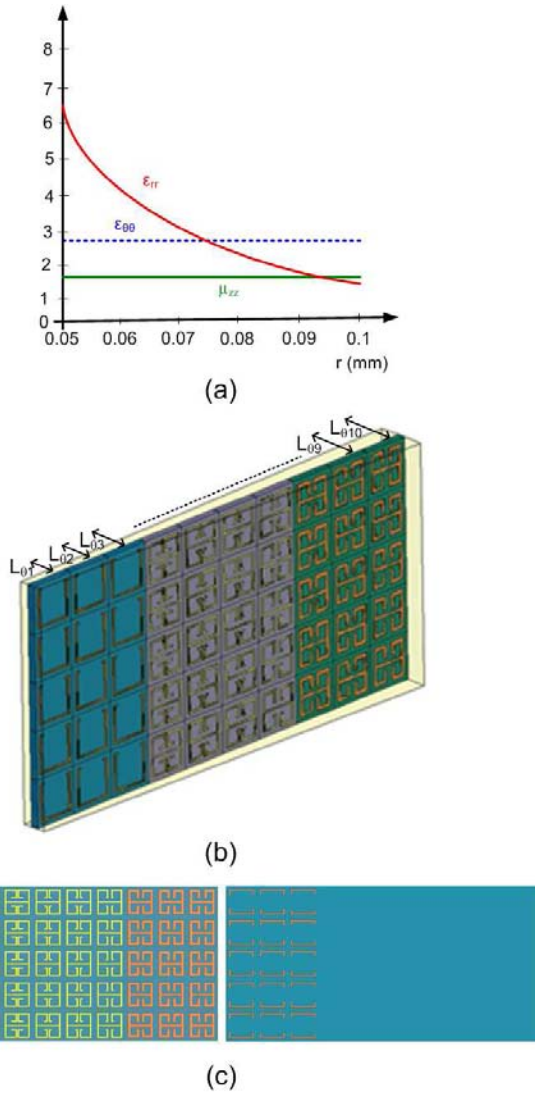

Figure 8: (a) Profile of the material parameters. (b) Single metamaterial layer composed of 10 unit cells providing the material parameters necessary for the coordinate transformation. (c) Front and rear view of the metamaterial cells.

Setting physical parameter $b = 6$ allows an optimization of the material parameter ε_{rr}. The profile of the different parameters is presented in Fig. 8(a). We consider fabricating the prototype composed of 30 identical layers where each layer is divided in 10 unit cells as illustrated by the single layer in Fig. 8(b). For the discretization of the material

parameters, meta-atoms producing electric resonances are designed on the 0.787 mm thick low loss ($\tan\delta$ = 0.0013) RO3003^{TM} dielectric substrate. We choose a rectangular unit cell with dimensions 5 mm for the resonators. We are able to obtain the desired ε_{zz} and μ_{yy} by tuning the resonators' geometric parameters. The 10 cells presented in Fig. 8(c) are designed to constitute the discrete variation of ε_{rr}. Table I summarizes the corresponding electromagnetic parameters of the cells. The cells are composed of respectively SRRs and ELCs to secure μ_{zz} and ε_{rr}. $\varepsilon_{\theta\theta}$ is produced by a host medium, which is a commercially available resin.

Table 1: Electromagnetic parameters μ_{zz}, and ε_{rr} for the 10 cells of the metamaterial layers. The length L_θ of each cell is given as a function of its position along the layer.

Layer	r_i (mm)	$L_{\theta i}$ (mm)	μ_{zz}	ε_{rr}
1	52.5	2.75	1.7	5.8
2	57.5	3.01	1.7	4.842
3	62.5	3.27	1.7	4.096
4	67.5	3.53	1.7	3.504
5	72.5	3.8	1.7	3.04
6	77.5	4.06	1.7	2.664
7	82.5	4.32	1.7	2.35
8	87.5	4.58	1.7	2.09
9	92.5	4.84	1.7	1.87
10	97.5	5.1	1.7	1.68

For numerical verifications of the proposed device performances, a microstrip patch antenna presenting a quasi-omnidirectional radiation is used as the feeding source of the metamaterial antenna. This patch source is optimized for a 10 GHz operation. A 3D simulation of the patch antenna and the layered metamaterial is performed using HFSS as illustrated in Fig. 9(a). Fig. 9(b) shows the calculated energy distribution in the middle plane of the layered metamaterial structure. We shall note that the latter structure firstly transforms the quasi-omnidirectional radiation of the patch source into a directive one and also maintains this highly directive emission after the 76° rotation.

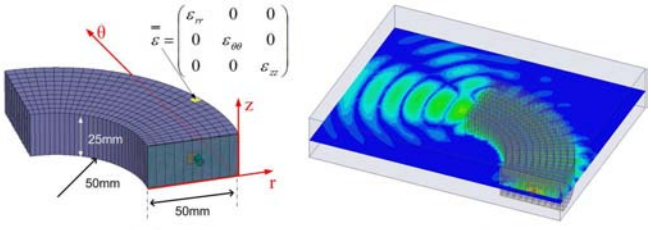

Figure 9: (a) Simulated design consisting of 30 metamaterial layers each composed of 10 cells. (b) Calculated energy distribution at 10 GHz.

To validate experimentally the azimuthal directive emission, the device shown in Fig. 10(a) is fabricated. A microstrip square patch antenna printed on a 1 mm thick epoxy dielectric substrate (ε_r = 3.9 and tanδ = 0.02) is used as radiating source. The metamaterial is a discrete structure composed of 10 different regions where permittivity and permeability vary according to Eq. (6) and to the values of Table 1. The bulk metamaterial is assembled using 30 layers of RO3003^{TM} dielectric boards on which subwavelength resonant structures are printed. The layers are mounted 1 by 1 in a molded matrix with a constant angle of 3° between each. A commercially available liquid resin is then flowed into the mold. This resin constitutes the host medium and is an important design parameter which is closely linked to $\varepsilon_{\theta\theta}$. Its measured permittivity is close to 2.8. The mold is removed after solidification of the resin.

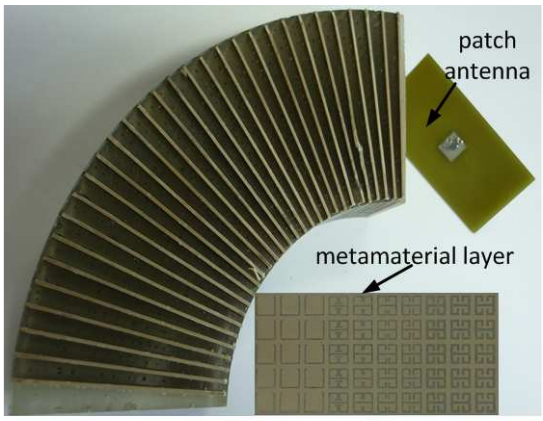

(a)

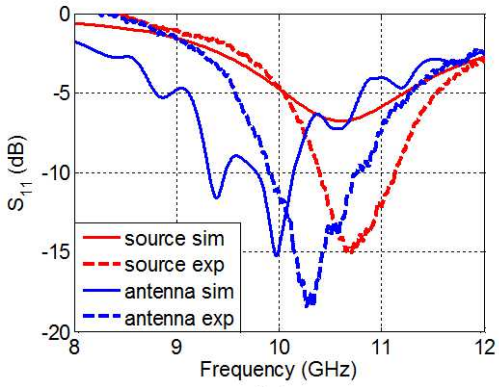

(b)

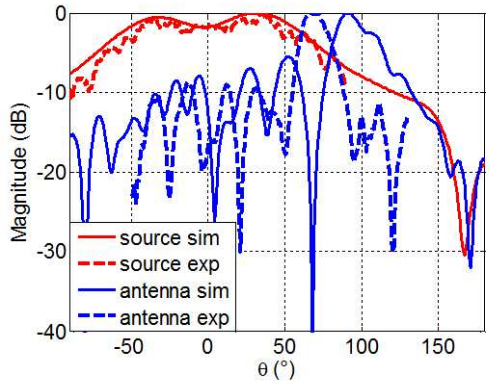

(c)

Figure 10: (a) Photography of the fabricated prototype. (b) Simulated and measured S_{11} parameter of the patch source alone and the metamaterial antenna. (c) Far-field E-plane radiation patterns of the patch source alone and of the metamaterial antenna.

S_{11} parameter measurements are first performed on the fabricated prototype. The measured S_{11} parameter of the metamaterial antenna is compared with the HFSS-simulated one in Fig. 10(b). A good agreement can be observed and return losses reaching 18 dB is observed experimentally at 10.3 GHz compared to 15 dB calculated. This quantity is further compared with that of the feeding patch antenna alone. A better matching can be clearly observed for the metamaterial antenna. The E-plane far-field radiation pattern of the metamaterial antenna is measured in a fully anechoic chamber. Measurements are performed for computer-controlled elevation angle varying from -90° to +90°. The measured far-field radiation pattern is presented for the metamaterial device (Fig. 10(c)). From the experiments, we can clearly observe the transformation of the omni-directional far-field radiation of the patch antenna into a directive one which is further bent at an angle of 66°, which is consistent to the 76° predicted by numerical simulations. The difference in bending angle is due to the fabrication tolerances of the meta-atoms providing the gradient radial permittivity and to the positioning of the patch source.

4. Isotropic antenna

Conversely to the previous sections, here we focus our attention on how coordinate transformation can be applied to transform directive emissions into isotropic ones. An intuitive schematic principle to illustrate the proposed method is presented in Fig. 11. Let us consider a source radiating in a circular space as shown in Fig. 11(a) and a circular region bounded by the blue circle around this source limits the radiation zone. The "space stretching" coordinate transformation consists in stretching exponentially the central zone of this delimited circular region represented by the red circle as illustrated in Fig. 11(b).

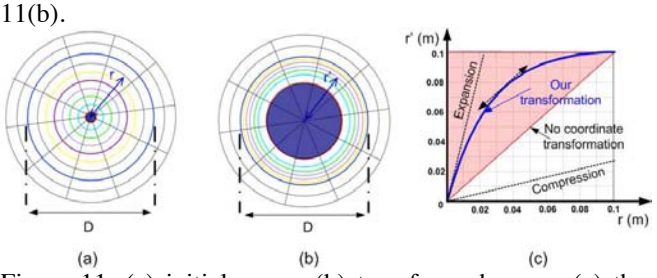

Figure 11: (a) initial space, (b) transformed space, (c) the blue curve shows the transformation rule made of an expansion followed by a compression.

The expansion procedure is further followed by a compression of the annular region formed between the red and blue circles so as to secure a good impedance matching with free space. Fig. 11(c) summarizes the exponential form of our coordinate transformation. The diameter of the transformed (generated metamaterial) circular medium is noted D.

Mathematically this transformation is expressed as [31]:

$$\begin{cases} r' = \alpha(1 - e^{qr}) \\ \theta' = \theta \\ z' = z \end{cases} \quad \text{with} \quad \alpha = \frac{D}{2}\frac{1}{1 - e^{\frac{qD}{2}}} \quad , \quad (7)$$

where r', θ', and z' are the coordinates in the transformed cylindrical space, and r, θ, and z are those in the initial cylindrical space. In the initial space, we assume free space, with isotropic permittivity and permeability tensors ε_0 and μ_0. Parameter q (in m^{-1}) appearing in Eq. (4) must be negative in order to secure the impedance matching condition. This parameter is an expansion factor which can be physically viewed as to what extent space is expanded. A high (negative) value of q means a high expansion whereas a low (negative) value of q means a nearly zero expansion.
Calculations lead to permeability and permittivity tensors given in the diagonal base by:

$$\overline{\overline{\psi}} = \begin{pmatrix} \psi_{rr} & 0 & 0 \\ 0 & \psi_{\theta\theta} & 0 \\ 0 & 0 & \psi_{zz} \end{pmatrix} = \begin{pmatrix} \frac{qr(r'-\alpha)}{r'} & 0 & 0 \\ 0 & \frac{r'}{qr(r'-\alpha)} & 0 \\ 0 & 0 & \frac{r}{r'q(r'-\alpha)} \end{pmatrix}$$

$$\text{with:} \quad r = \frac{\ln\left(1 - \frac{r'}{\alpha}\right)}{q} \quad , \quad (8)$$

The components in the Cartesian coordinate system are calculated and are as follows:

$$\begin{cases} \psi_{xx} = \psi_{rr}\cos^2(\theta) + \psi_{\theta\theta}\sin^2(\theta) \\ \psi_{xy} = \psi_{yx} = (\psi_{rr} - \psi_{\theta\theta})\sin(\theta)\cos(\theta) \\ \psi_{yy} = \psi_{rr}\sin^2(\theta) + \psi_{\theta\theta}\cos^2(\theta) \end{cases} \quad , \quad (9)$$

By fixing the electric field directed along the z-axis and by adjusting the dispersion equation without changing propagation in the structure, the following reduced parameters can be obtained:

$$\begin{cases} \mu_{rr} = 1 \\ \mu_{\theta\theta} = \left(\frac{r'}{qr(r'-\alpha)}\right)^2 \\ \varepsilon_{zz} = \left(\frac{r}{r'}\right)^2 \end{cases} \quad , \quad (10)$$

Fig. 12 presents simulations results of the source radiating in the initial circular space at an operating frequency of 4 GHz for several values of q. The current direction of the source is supposed to be along the z-axis. Simulations are performed in a Transverse Electric (TE) mode with the electric field polarized along z-direction. The surface current source is considered to have a width of 10

cm, which is greater than the 7.5 cm wavelength at 4 GHz. Radiation boundary conditions are placed around the calculation domain in order to plot the radiation properties. Continuity of the field is assured in the interior boundaries. As stated previously and verified from the different electric field distribution patterns, a high negative value of q leads to a quasi-perfect isotropic emission since the space expansion is higher. This phenomenon can be clearly observed in Fig. 12(d) for q = -40 m^{-1}.

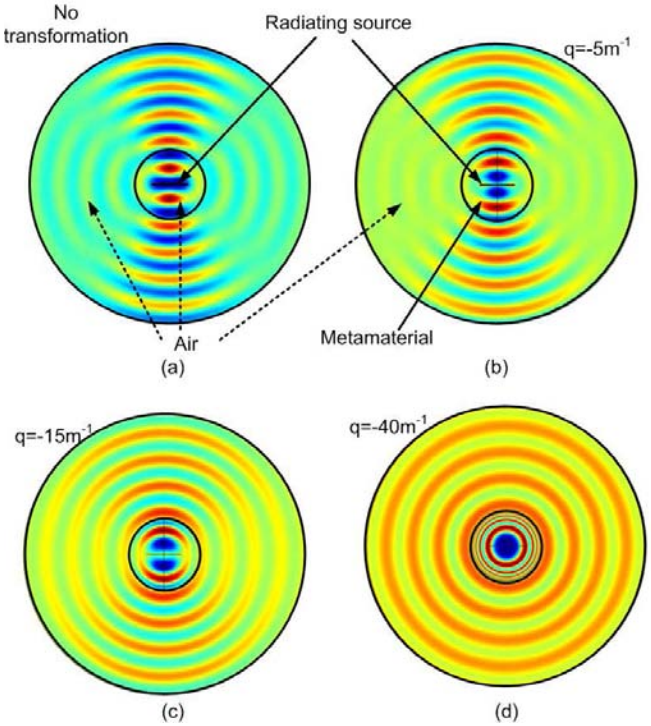

Figure 12: Simulated electric field distribution for a TE wave polarization at 4 GHz. (a) current plane source used as excitation for the transformation. The current direction is perpendicular to the plane of the figure; [(b)-(d)] verification of the transformation for different values of expansion factor q.

The calculated far-field patterns are shown in Fig. 13(a). The source alone produces a directive emission and when it is surrounded by the judiciously engineered coordinate-transformation based metamaterial, an isotropic emission is produced. Fig. 13(b) shows the influence of parameter q on the space expansion in the coordinate transformation. As q becomes highly negative, a greater space expansion is achieved.

5. Conclusions

To summarize, we have presented three types of antennas designed using coordinate transformation concept. The first antenna is a directive one achieved by transforming the omnidirectional radiation of a patch radiator into a directive one. Measurements performed on the fabricated prototype have shown good qualitative agreements with theory and simulations. The second antenna is an extension of the directive one, in the way that it also presents a steered beam. In this case, a rotational coordinate transformation has been elaborated to achieve the azimuthal emission. Measurements have shown as much as 66° beam steering. Finally, a space expansion coordinate transformation has been theoretically presented so as to transform a directive emission into an isotropic one.

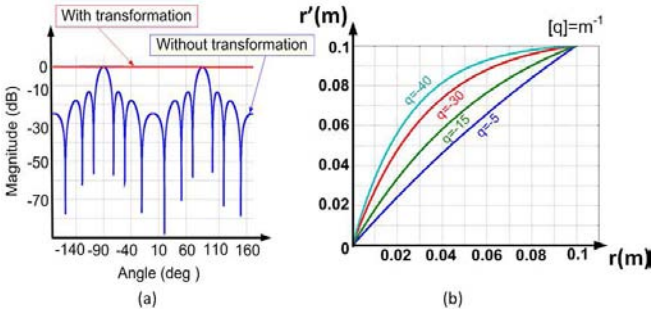

Figure 13: (a) Far field radiation pattern of the emission with (q = -40 m^{-1}) and without transformation. (b) Influence of the expansion parameter q on the proposed coordinate transformation. The emitted radiation is more and more isotropic as q tends to high negative values.

References

[1] J. B. Pendry, D. Schurig, D. R. Smith, Controlling electromagnetic fields, Science 312(5781): 1780-1782, 2006.

[2] U. Leonhardt, Optical conformal mapping, *Science* 312(5781): 1777-1780, 2006.

[3] D. Schurig, J. J. Mock, B. J. Justice, S. A. Cummer, J. B. Pendry, A. F. Starr, D. R. Smith, Metamaterial electromagnetic cloak at microwave frequencies, *Science* 314(5801): 977-980, 2006.

[4] R. Liu, C. Ji, J. J. Mock, J. Y. Chin, T. J. Cui, D. R. Smith, Broadband ground-plane cloak, *Science* 323(5912): 366-369, 2009.

[5] B. Kanté, D. Germain, A. de Lustrac, Experimental demonstration of non-magnetic metamaterial cloak at microwave frequencies, *Phys. Rev. B* 80, 201104(R), 2009.

[6] W. Cai, U. K. Chettiar, A. V. Kildishev, V. M. Shalaev, Optical cloaking with metamaterials, *Nat. Photon.* 1(4): 224-227, 2007.

[7] J. Valentine, J. Li, T. Zentgraf, G. Bartal, X. Zhang, An optical cloak made of dielectrics, *Nat. Mater.* 8: 568-571, 2009.

[8] L. H. Gabrielli, J. Cardenas, C. B. Poitras, M. Lipson, Silicon nanostructure cloak operating at optical frequencies, *Nat. Photon.* 3(8): 461-463, 2009.

[9] M. Rahm, D. Schurig, D. A. Roberts, S. A. Cummer, D. R. Smith, J. B. Pendry, Design of electromagnetic cloaks and concentrators using form-invariant coordinate transformations of Maxwell's equations, *Photon. Nanostruct.: Fundam. Appl.* 6(1): 87-95, 2008.

[10] H. Chen, B. Hou, S. Chen, X. Ao, W. Wen, C. T. Chan, Design and experimental realization of a broadband transformation media field rotator at microwave frequencies, *Phys. Rev. Lett.* 102(18): 183903, 2009.

[11] A. Greenleaf, Y. Kurylev, M. Lassas, G. Uhlmann, Electromagnetic wormholes and virtual magnetic monopoles from metamaterials, *Phys. Rev. Lett.* 99(18): 183901, 2007.

[12] M. Rahm, D. A. Roberts, J. B. Pendry, D. R. Smith, Transformation-optical design of adaptive beam bends and beam expanders, *Opt. Express* 16(15): 11555-11567, 2008.

[13] M. Rahm, S. A. Cummer, D. Schurig, J. B. Pendry, D. R. Smith, Optical design of reflectionless complex media by finite embedded coordinate transformations, *Phys. Rev. Lett.* 100(6): 063903, 2008.

[14] L. Lin, W. Wang, J. Cui, C. Du, X. Luo, Design of electromagnetic refractor and phase transformer using coordinate transformation theory, *Opt. Express* 16(10): 6815-6821, 2008.

[15] J. Huangfu, S. Xi, F. Kong, J. Zhang, H. Chen, D. Wang, B.-I. Wu, L. Ran, J. A. Kong, Application of coordinate transformation in bent waveguide, *J. Appl. Phys.* 104(1): 014502, 2008.

[16] P.-H. Tichit, S. N. Burokur, A. de Lustrac, Waveguide taper engineering using coordinate transformation technology, *Opt. Express* 18(2): 767-772, 2010.

[17] W. X. Jiang, T. J. Cui, H. F. Ma, X. M. Yang, Q. Cheng, Layered high-gain lens antennas via discrete optical transformation, *Appl. Phys. Lett.* 93(22): 221906, 2008.

[18] Z. L. Mei, J. Bai, T. M. Niu, T. J. Cui, A Planar focusing antenna design using quasi-conformal mapping, *PIER M* 13: 261-273, 2010.

[19] Z. H. Jiang, M. D. Gregory, D. H. Werner, Experimental demonstration of a broadband transformation optics lens for highly directive multibeam emission, *Phys. Rev. B* 84(16): 165111, 2011.

[20] C. Garcia-Meca, A. Martinez, U. Leonhardt, Engineering antenna radiation patterns via quasi-conformal mappings, *Opt. Express* 19(24): 23743-23750, 2011.

[21] Y. G. Ma, C. K. Ong, T. Tyc, U. Leonhardt, An omnidirectional retroreflector based on the transmutation of dielectric singularities, *Nat. Mater.* 8: 639-642, 2009.

[22] T. Tyc, U. Leonhardt, "Transmutation of singularities in optical instruments," *New J. Phys.* 10(11): 115038, 2008.

[23] N. Kundtz, D. R. Smith, Extreme-angle broadband metamaterial lens, *Nat. Mater.* 9: 129-132, 2010.

[24] E. Lier, D. H. Werner, C. P. Scarborough, Q. Wu, J. A. Bossard, An octave-bandwidth negligible-loss radiofrequency metamaterial, *Nat. Mater.* 10(3): 216-222, 2011.

[25] Y. Luo, J. Zhang, L. Ran, H. Chen, J. A. Kong, Controlling the Emission of Electromagnetic Source, *PIERS Online* 4(7): 795-800, 2008.

[26] J. Allen, N. Kundtz, D. A. Roberts, S. A. Cummer, D. R. Smith, Electromagnetic source transformations using superellipse equations, *Appl. Phys. Lett.* 94(19): 194101, 2009.

[27] B. I. Popa, J. Allen, S. A. Cummer, Conformal array design with transformation electromagnetics, *Appl. Phys. Lett.* 94(24): 244102, 2009.

[28] P.-H. Tichit, S. N. Burokur, A. de Lustrac, Ultradirective antenna via transformation optics, *J. Appl. Phys.* 105(10): 104912, 2009.

[29] P.-H. Tichit, S. N. Burokur, D. Germain, A. de Lustrac, Design and experimental demonstration of a high-directive emission with transformation optics, *Phys. Rev. B* 83(15): 155108, 2011.

[30] P.-H. Tichit, S. N. Burokur, D. Germain, A. de Lustrac, Coordinate transformation based ultra-directive emission, *Elec. Lett.* 47(10): 580-582, 2011.

[31] P.-H. Tichit, S. N. Burokur, A. de Lustrac, Transformation media producing quasi-perfect isotropic emission, *Opt. Express* 19(21): 20551-20556, 2011.

[32] J. B. Pendry, A. J. Holden, D. J. Robbins, W. J. Stewart, Magnetism from conductors and enhanced non-linear phenomena, *IEEE Trans. Microwave Theory Tech.* 47(11): 2075-2084, 1999.

[33] D. Schurig, J. J. Mock, D. R. Smith, Electric-field-coupled resonators for negative permittivity metamaterials, *Appl. Phys. Lett.* 88(4): 041109, 2006.

[34] A. M. Nicolson, G. F. Ross, Measurement of the intrinsic properties of materials by time-domain techniques, *IEEE Trans. Instrum. Meas.* 19(4): 377-382, 1970.

Multi-hierarchical metamaterials combining conductive inclusions and polymer matrices for Electromagnetic Interference Shielding

Isabelle Huynen[1*], Nicolas Quiévy[2], Pierre Bollen[1,3], Yann Danlée[1,2], Christian Bailly[2], and Thomas Pardoen[3]

[1] Information and Communications Technologies, Electronics and Applied Mathematics (ICTEAM)
[2]Institute Institute of Condensed Matter and Nanosciences (IMCN)
[3]Department Institute of Mechanics, Materials and Civil Engineering (iMMC)
*corresponding author, E-mail: isabelle.huynen@uclouvain.be

Abstract

Multifunctional metamaterials under development in our group are based on a hierarchical combination, from nano to macroscale, of conductive inclusions and polymer matrices. The paper illustrates this hybrid approach for a metallic honeycomb filled with a carbon nanotube-reinforced polymer foam. The waveguide characteristic of the honeycomb combined with the electromagnetic properties of the foam lead to large power absorption above the cut-off frequency of the waveguide, situated in the GHz range. Below cut-off, electromagnetic shielding is also offered by total reflection at input interface of the hybrid, preventing the signal transmission.

1. Introduction

Due to the generalization of electronic devices in most human technologies and the growth of wireless communications and radar detection, electromagnetic interference (EMI) shielding has become essential for keeping the external environment unpolluted from potential radiations as well as for proper operation of the electronic devices. Shielding by EM absorption, which is preferable over reflection in certain instances, requires combining a low dielectric constant with high electrical conductivity, which are antagonist properties in the world of materials. Various topologies based on carbonaceous nanocomposite materials are developed in our group [1-2]. This paper discusses a hierarchical architecture involving a metallic honeycomb filled with a carbon nanotube-reinforced polymer foam (Fig. 1).

2. Multihierarchical topology

Filling insulating polymers with carbon based filler such as carbon nanotubes (CNT) make them conductive. Thanks to the formation of a percolating network, a relatively low amount of CNT is sufficient to raise the electrical conductivity of the insulating polymer [3]. However, this effect goes along with the increase of the relative permittivity of the material promoting EM wave reflections, which is undesirable for radar absorbing materials (RAMs).

Decreasing the permittivity of materials can be achieved by foaming [4]-[5].
The insertion of the nanocomposite foam in the honeycomb lattice contributes to decrease the real part of the relative effective permittivity Re{$\varepsilon_{r,eff}$} of the material, being close to the permittivity of air in a certain frequency range. Below the cut-off frequency of the hexagonal waveguide, shielding by reflection is achieved and above the cut-off frequency, higher EM absorption levels are reached by the hybrid compared to the conductive foam alone. Varying the cell shape of the honeycomb changes the cut-off frequency [1], hence the range for high absorption.

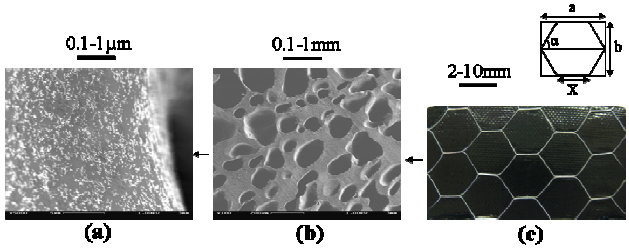

Figure 1: Multimaterial and multiscale strategy developed to reach high EM absorption levels in the GHz range starting from (a) CNT dispersed in a polymer matrix which is (b) foamed and (c) inserted in a metallic honeycomb.

3. Strategy for EMI reduction

Designing materials with high absorption properties is achieved by reducing both reflection and transmission of EM waves. The fraction of EM power absorbed by a slab of material, denoted hereby *absorption index A*, is defined by the ratio between absorbed power P_{abs} and incident power P_{in}, expressed as:

$$A = \frac{P_{abs}}{P_{in}} = 1 - \frac{P_{ref}}{P_{in}} - \frac{P_{out}}{P_{in}} = 1 - \left|S_{11}\right|^2 - \left|S_{21}\right|^2$$

where S_{11}, S_{21} are the S-parameters. This definition of the absorption index, because of its normalization to incoming power, truly characterizes the performances of a microwave absorber, i.e. a material showing simultaneously low reflection at the input interface between air and hybrid and high absorption inside the hybrid: a value of *A* close to 1 (or 100%) implies that both S_{11} associated to input reflection and mismatch, and S_{21} associated to residual power outgoing from the hybrid, are minimized. It is thus an alternate formulation, compared to reflectivity, for characterizing the performances of an absorber. Reversely, the shielding effectiveness of the material results from the sum of the reflected and the absorbed powers by the material

$$SE = \frac{P_{in}}{P_{out}} = \frac{1}{|S_{21}|^2} = 1/(1-|S_{11}|^2 - A)$$

A high SE translates into a low fraction of the power flowing out of the material. EMI shielding can thus be obtained either by maximizing *A* (efficient absorber) or input reflection coefficient S_{11}. Frequency operating range of each mechanism can be tuned by the size of the honeycomb cell.

4. Results

The contribution of the honeycomb waveguide on the real part of the effective permittivity Re{$\varepsilon_{r,eff}$} is highlighted on Fig. 2 for honeycomb filled with polycarbonate (PC) foam containing 1wt.% CNT. Below the cut-off frequency, the effective permittivity is negative for the hybrid while it remains almost constant and positive over the whole frequency range for the nanocomposite foam alone. The conductivity is not significantly modified by the presence of the metallic honeycomb. In this case, the cut-off frequency was measured at 10.4 GHz for the PC based hybrid. In each case, the geometrical parameters were *X*=0 or 4.76mm and α=60° (see Fig.1).

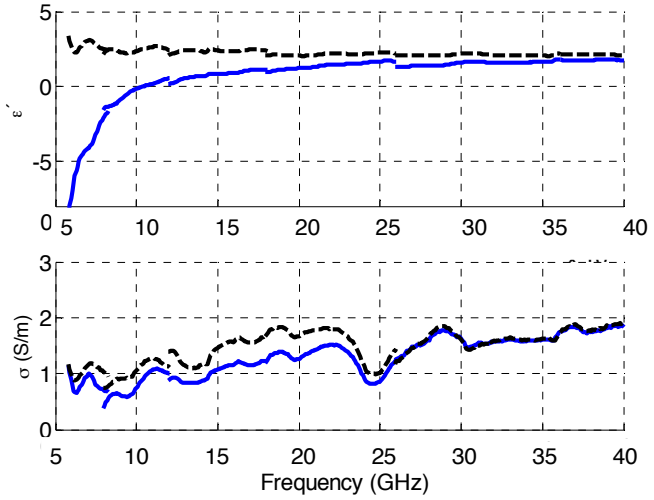

Figure 2: Measured real part ε' of relative effective permittivity (top) and conductivity σ (bottom) for PC-CNT 1wt.% foams with honeycomb (solid blue line, X = 4.76 mm) and without (dashed black line).

A closed form model of the EM reflection and absorption has been developed based on the propagation in the hexagonal waveguide modelled as an equivalent transmission line. It provides a tool for the optimization of the hybrid [6].

The absorption index of the hybrid extracted from the measured S-parameters is shown in Fig. 3 for the PC-CNT 1wt% foam filling a 7mm thick aluminium honeycomb. The cut-off frequency has been measured at 10.5 GHz. The prediction obtained with the analytical model using the electrical properties of the foam, the honeycomb cell size and the material thickness as parameters is in good agreement with the measurement. The inset shows the Shielding Effectiveness (*SE*) of the hybrid. As announced, SE is significantly improved below the cut-off due to the high reflection at the input interface.

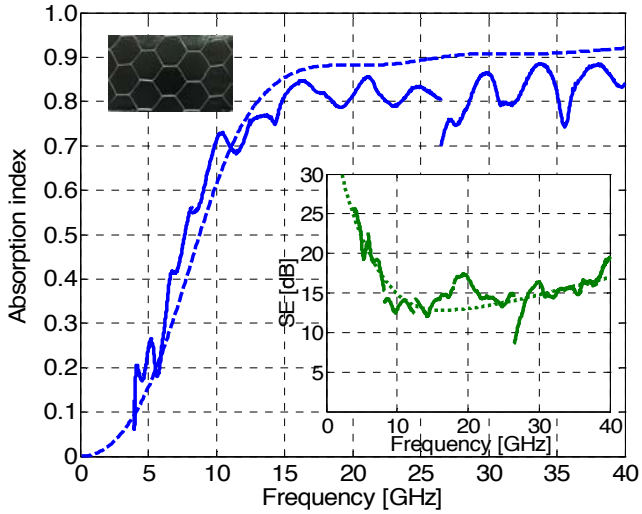

Figure 3: Measured real part ε' of relative effective permittivity (top) and conductivity σ (bottom) for PC-CNT 1wt.% foams with honeycomb (solid blue line, X = 4.76 mm) and without (dashed black line).

5. Conclusions and perspectives

EMI shielding is achieved by combining the waveguide properties of a metallic honeycomb structure filled with a polymer foam reinforced with CNT. Above the cut-off frequency set by the hexagonal waveguide, the nanocomposite filling foam attenuates the propagating EM waves inside the hybrid. The resulting absorption index *A* is higher than for the nanocomposite foam alone. Experimental results validate the developed analytical model. Tuning and optimizing the performance of the hybrid is now possible thanks to the model. While reaching high absorption index below 5 GHz remains difficult with acceptable cell size *X* and material thickness *t*, shielding by total reflection mechanism is acting below the cut-off as in an air vent.

The particular hierarchical organization of the studied hybrid materials offers interesting perspectives for multifunctional structures. In particular, high EM

absorption could be combined with lightness and stiffness if a honeycomb filled with a CNT-polymer foam was sandwiched between rigid dielectric plates. Currently, mechanical test campaigns are being performed to determine the bending and impact resistance of the material and guide the design of sandwich structures with high mechanical performances [7]. Good thermal conductivity across the structure is also achieved owing to the presence of a metallic honeycomb, while foams can help for protection against dust. Finally, synergy with acoustic shielding performances could be considered.

Acknowledgements

The authors are grateful to the Wallonia Region DG06 for supporting this research through a Winnomat II project "Multimasec". The support of D. Spote for the electromagnetic measurements as well as the provision of the Al honeycombs by the company Hexcel are gratefully acknowledged. I.H. is ''Research Director'' by the National Fund for Scientific Research (F.R.S.-FNRS). P.B. and Y.B. are under a FRIA grant from the National Fund for Scientific Research (F.R.S.-FNRS).

References

[1] I. Huynen, N. Quiévy, C. Bailly, P. Bollen, C. Detrembleur, S. Eggermont, I. Molenberg, J.-M. Thomassin, L. Urbanczyk, T. Pardoen, Multifunctional hybrids for electromagnetic absorption, Acta Materialia, 59: 3255–3266, 2011.

[2] Y. Danlée, C. Bailly, I. Huynen, Thin smart multilayer microwave absorber based on hybrid structure of polymer and carbonated nanoparticles, Proc. International Conf. on Electrodynamics of Complex Materials for Advanced Technologies (PLASMETA'11), Samarkand, Uzbekistan, 70, 2011.

[3] A. Saib, L. Bednarz, R. Daussin, C. Bailly, Xudong Lou, J.-M. Thomassin, C. Pagnoulle, C. Detrembleur, R. Jérôme and I. Huynen, Carbon nanotube composites for broadband microwave absorbing materials, IEEE Trans Microw. Theory Tech., 54 : 2745-2754, 2006.

[4] J.-M. Thomassin, Xudong Lou, C. Pagnoulle, A. Saib, L. Bednarz, I. Huynen, R. Jérôme and C. Detrembleur, MWCNT/Poly(ε-caprolactone) nanocomposites with exceptional electromagnetic interference shielding properties, J. Phys. Chem. C, 111: 11186-11192, 2007.

[5] I. Huynen, L. Bednarz, J.-M. Thomassin, C. Pagnoulle, R. Jerome, C. Detrembleur, Proc. 38th European Microw. Conf., October 28–30, Amsterdam; 5–8, 2008.

[6] N. Quiévy, P. Bollen, J.-M. Thomassin, C. Detrembleur, T. Pardoen, C. Bailly and I. Huynen, Electromagnetic absorption properties of carbon nanotube nanocomposite foam filling honeycomb waveguide structures, IEEE Trans. Electromagn. Compat., 54: 43-51, 2012.

[7] P. Bollen, N. Quiévy, I. Huynen, C. Bailly, C. Detrembleur, J.M. Thomassin, T. Pardoen, Multifunctional architectured materials for electromagnetic absorption, submitted for publication in Scripta Materialia.

Axial ratio improvement of an Archimedean spiral antenna over a radial AMC reflector

M. Grelier[1,2*], C. Djoma[1,2], X. Begaud[1], A. C. Lepage[1], M. Jousset[2] and S. Mallégol[2]

[1]Institut Telecom, Telecom ParisTech - LTCI CNRS UMR 5141,
46 rue Barrault 75634 Paris Cedex 13, France
[2]Thales Systèmes Aéroportés, 10 avenue de la 1ère DFL 29238 Brest Cedex 3, France
*Corresponding author: grelier@ieee.org

Abstract

This paper presents a method to improve the circular polarization of an Archimedean spiral antenna placed over a radial Artificial Magnetic Conductor (AMC). Results have been compared with the same radiating element over a more classical AMC reflector. A prototype of an Archimedean two-wire spiral antenna has been built to operate from 0.5GHz to 6GHz. Measurement results with this radial AMC give a relative bandwidth of 79%, in which the broadside RHCP gain is improved. In this bandwidth the axial ratio is less than 2dB whereas it is higher than 3dB with a classical cartesian shape of AMC reflector.

1. Introduction

The needs of the current wireless applications, both civilian and military, require antennas that are at the same time, low cost, low thickness and broadband. Planar spiral antennas are widely used to fulfill the aforementioned specifications. An Archimedean spiral antenna radiates a circularly polarized bi-directional beam. In most applications, this bi-directional beam must be transformed into a unidirectional one. A classical solution consists in backing a cavity filled by an electromagnetic absorber behind the radiating element. However, the antenna is bulky and loses one half of the radiated power.

Another approach consists in taking advantage of the backward radiated electric field by reflecting it in-phase with the forward radiated electric field thanks to an Artificial Magnetic Conductor (AMC) [1]. In [2], a reflector based on AMC called Quasi Artificial Magnetic Conductor (QAMC) has been presented. The term "quasi" has been chosen because the QAMC is composed of a few elementary cells.

In this paper we present the improvement of the cartesian QAMC by a reflector suitable to the geometry and the radiation of the Archimedean spiral antenna. The spiral antenna is presented in section 2. The method to design the QAMC is introduced in section 3. In section 4 the spiral antenna is placed over the two different QAMC and compared in order to validate the new design. Then measurements are presented and discussed.

2. Archimedean spiral antenna

The two-wire Archimedean spiral antenna introduced by Kaiser [3], is widely used in airborne systems due to its wideband intrinsic characteristics. This kind of antenna has active areas which depend of the frequency. Thus, these areas are defined by $D=\lambda/\pi$, where D is the diameter of the area and λ the free space wavelength. The knowledge of these active areas enables to adapt the geometry of the reflector to these areas.

The inner diameter and the outer diameter of the prototype of the Archimedean two-wire spiral antenna are respectively D_{in}=6.3mm and D_{out}=300mm which define, respectively, the highest and the lowest operating frequencies f_{high}=15GHz and f_{low}=0.3GHz. Nevertheless, we are going to present results from 0.5GHz to 6GHz, because it is the required bandwidth for the targeted application. The width of the spiral arms is w_{arm}=1.25mm, the spiral arms are separated with a distance equal to the arm width to produce a self-complementary structure and thus maintain broadband characteristics [4].

The antenna is printed on a dielectric substrate Duroid RT5880, the thickness is h_{sub}=1.575mm, the relative dielectric permittivity is ε_r=2.2 and the dissipation factor is tanδ=0.0009 (@10GHz).

3. AMC Reflector

3.1. Cartesian QAMC reflector

The reflection phase is defined as the phase of the reflected electric field at the reflecting surface.

It is normalized to the phase of the incident electric field at the reflecting surface. The reflection phase method is used to identify the frequency band in which the AMC behavior occurs [5]. In the case which the AMC is an infinite periodic structure, the phase diagram can be obtained by applying periodic conditions of Floquet on an elementary cell in order to simulate an infinite AMC [6].

The AMC bandwidth depends on their dimensions [7] and has been defined for a reflection phase varying between +/-120° [8]. In this bandwidth the spiral antenna placed over an AMC reflector should have a broadside gain higher than the spiral antenna in free space.

The dimensions of the AMC are w=17.35mm and g=2.65mm, where w is the length of a square patch and g the gap between two patches (cf. Fig. 2a).

The AMC substrate is Arlon CuClad 250 with a thickness h_{amc}=4 x 1.565mm, the relative dielectric permittivity is ε_r=2.5 and the dissipation factor is tanδ=0.0018 (@10GHz).

The cartesian QAMC reflector shown in Fig. 2a is composed of a planar array of only 4x4 elementary cells [2]

and it is placed 4mm under the antenna substrate. The diameter of the QAMC reflector is equal to λ_{1GHz}/π (100.8mm).

3.2. Radial QAMC reflector

The radial QAMC reflector resulting from the transformation of the cartesian one is shown in Fig. 2 The method consists in placing the patches under the targeted active area [9]. The active area at a given frequency can be identified by using the electromagnetic energy density (cf. Fig. 1) defines as follows (1).

$$\rho_{EM} = \frac{1}{2}(\varepsilon_0 E^2 + \mu_0 H^2) \quad (1)$$

Where ε_0 and μ_0 are the permittivity and the permeability in free space, E and H are the magnitude of the electric and magnetic fields.

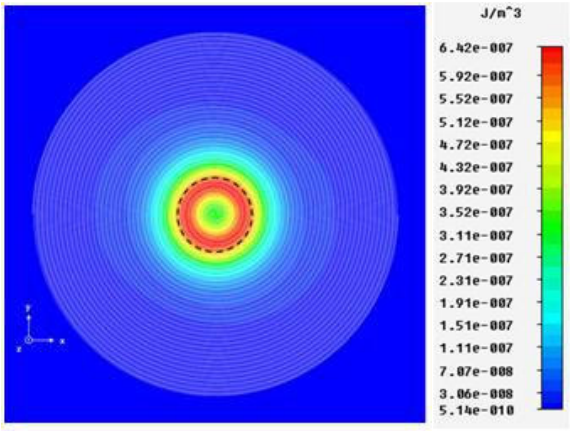

Figure 1: Electromagnetic energy density at 2.5GHz.

The dimensions of the radial patches are the same as for the square patches, i.e. they have a length equal to w and the gap between two patches in the radial or ortho-radial direction is equal to g (cf. Fig. 2b).
The radial QAMC is composed of 2 rows of 12 patches. The distance between the center of the radial QAMC and half the length (w/2) of a patch of the first row (cf. Fig. 2b) is chosen so that the patches operate under this active area at the frequency for which the phase reflection of the AMC is equal to zero. (cf. Fig. 3). This occurs at 2.7GHz and $D_{2.7GHz}$=35.34mm).
The second row is only present to assure the periodicity in the radial direction.

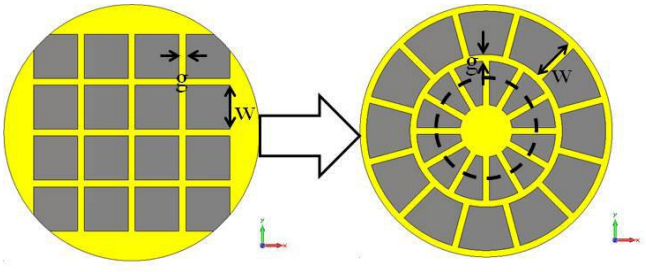

(a) (b)

Figure 2: QAMC top view: (a) Cartesian QAMC, (b) Radial QAMC.

3.3. Results

The Archimedean spiral antenna defined in section 2 has been simulated over the two aforementioned QAMC. Figure 3 presents the broadside realized gain for the co-polarization and the cross-polarization radiated by the antenna and also the phase diagram of the AMC defined in section 3.1. Simulations have been performed with CST Microwave Studio®.

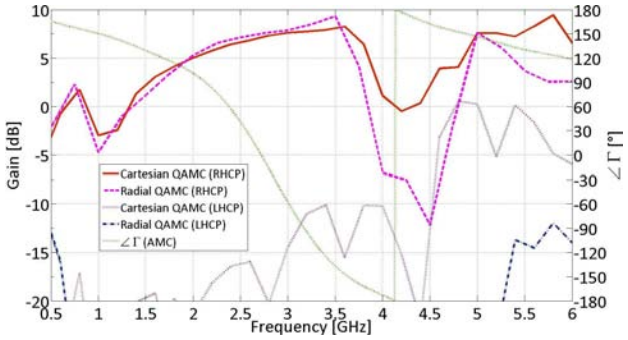

Figure 3: Left scale (simulated gain): Comparison between the two QAMC, Right scale (phase): Reflection phase diagram of the AMC.

According to Fig 3. the reflection phase of the AMC is included between +/-120° from 1.68GHz to 3.36GHz and leads to a relative bandwidth of 66%. Fig. 3 shows that the spiral antenna placed over a cartesian QAMC has a broadside LHCP gain (cross-polarization component) higher than -10dB from 4.5GHz to 6GHz. The spiral antenna placed over a radial QAMC has a broadside LHCP gain less than -10dB from 0.5GHz to 6GHz. The two configurations have a similar broadside RHPC gain (co-polarization component) from 1GHz to 3.5GHz. In order to validate those results, a prototype has been realized.

4. Configurations

We present hereafter the different configurations that have been measured. The configuration named AS_{Ref}, corresponds to the spiral antenna placed above a cavity completely filled with an electromagnetic absorber, with a height h_{abs}=55.26mm (cf. Fig. 4).
This configuration will be used as the reference to evaluate the benefits of the proposed structures.

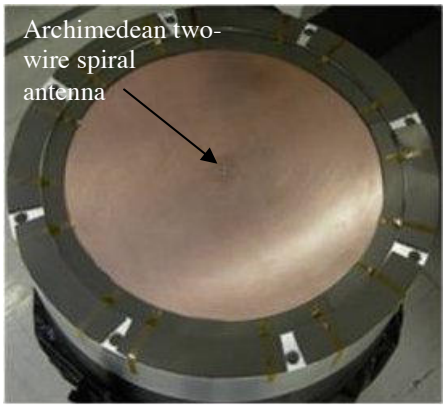

Figure 4: Spiral antenna over the cavity.

The distance between the antenna substrate and the surface of the QAMC reflectors is h_{air}=4mm (cf. Fig. 5).
So the total thickness of the antenna is equal to $h_t=h_{sub}+h_{air}+h_{amc}$=11.835mm i.e. $\lambda_{1.68GHz}/15$. In order to not disturb the behavior of the spiral antenna at low frequency, absorber is put all around the QAMC reflectors (cf. Fig. 5). These two configurations are named $AS_{C\text{-}QAMC}$ and $AS_{R\text{-}QAMC}$ respectively, where $AS_{C\text{-}QAMC}$ refers to the spiral antenna above the cartesian QAMC and $AS_{R\text{-}QAMC}$ to the spiral antenna above the radial QAMC.

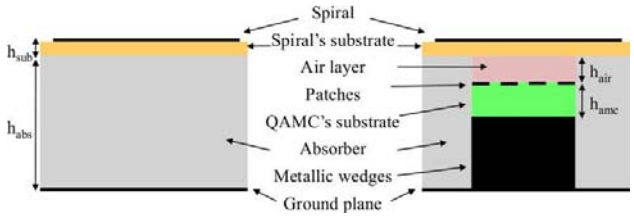

(a) (b)

Figure 5: Configurations: (a) AS_{Ref}, (b) $AS_{C/R\text{-}QAMC}$.

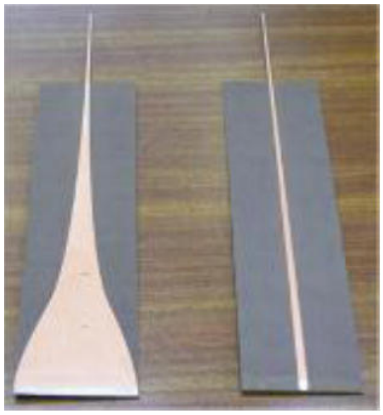

Figure 6: Top and bottom view of the balun.

Figure 7: The whole antenna: Cavity of the antenna assembled with the shielded cavity of the balun.

The antenna is fed at the center of the spiral through a broadband tapered balun (cf. Fig. 6).
It is required to transform the impedance presented by the input balanced line of the spiral equal 160Ω to the unbalanced line of the coaxial connector equal to 50Ω.
The size of the balun is 300mm x 60mm [2], and it is placed in a shielded cavity (cf. Fig. 7).

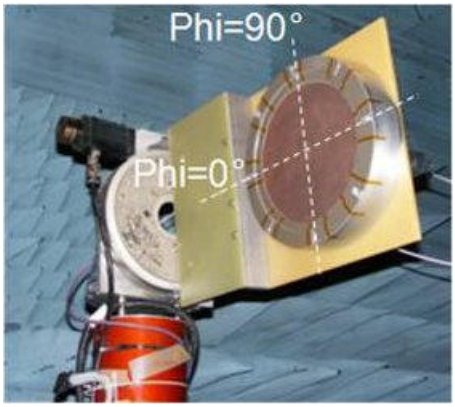

Figure 8: Definition of φ planes.

5. Results and discussion

In this section, measurements of the aforementioned configurations are analyzed.
Fig. 9 shows that the AS_{Ref} has a good impedance matching from 0.5GHz to 6GHz defined for a return loss level less than -10dB.
The $AS_{C\text{-}QAMC}$ has also a good impedance matching from 0.5GHz to 6GHz. The return loss level of the $AS_{Q\text{-}AMC}$ presents a minor increase between 4.7GHz to 4.8GHz.

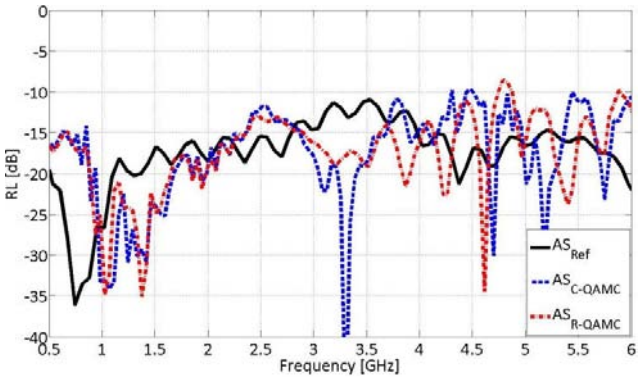

Figure 9: Return loss versus frequency.

Fig. 10 shows the evolution of the broadside RHCP gain (co-polarization component) for the different configurations. We observe the same behavior from 0.5GHz to 3.3GHz for $AS_{C\text{-}QAMC}$ and $AS_{R\text{-}QAMC}$.
For both configurations the broadside RHCP gain is higher than the AS_{Ref} from 1.65GHz to 3.8GHz i.e. a relative bandwidth of 79%. It's interesting to note that this band is greater than the theoretical bandwidth of 66% deduced previously from the phase diagram.

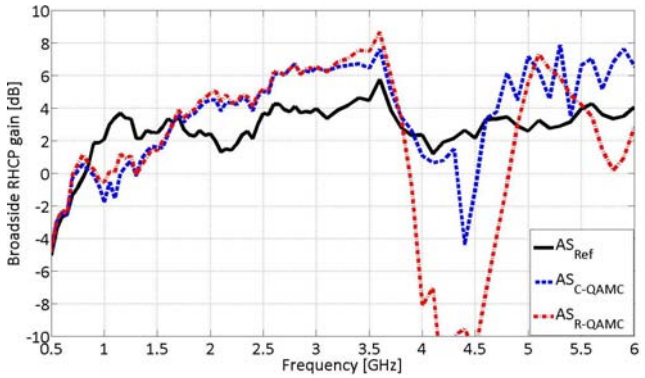

Figure 10: Broadside gain (RHCP) versus frequency.

Fig. 11 presents the broadside LHCP gain (cross-polarization component) for the different configurations. We can see that the broadside LHCP gain of the $AS_{R\text{-}QAMC}$ remains below -10dB from 0.5GHz to 6GHz. Unlike the broadside LHCP gain of the $AS_{C\text{-}QAMC}$ is higher than -10dB for frequencies higher than 3.25GHz.

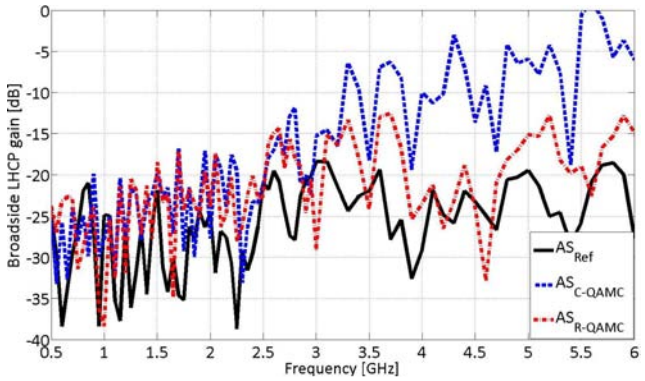

Figure 11: Broadside gain (LHCP) versus frequency.

In order to evaluate the benefits of the radial QAMC the axial ratio (AR), which defines the quality of the circular polarization [10], is presented in figure 12.
The AR level of the AS_{Ref} remains below 3dB from 0.5 GHz to 6GHz i.e. a relative bandwidth of 169%, thanks to the absorber cavity. The AR level of the $AS_{C\text{-}QAMC}$ is less than 3 dB from 0.5GHz to 3.3GHz i.e. a relative bandwidth of 74%. At 4.4GHz broadside RHCP and LCHP gains have the same value and that is why at this frequency the AR level is higher than 10dB. Then the polarization is no more circular but linear.
With the radial QAMC, the AR level of the $AS_{R\text{-}QAMC}$ is less than 3dB from 0.5GHz to 4GHz i.e. a relative bandwidth of 157%. But if we only considered the bandwidth in which the broadside RHCP gain of the $AS_{C\text{-}QAMC}$ and $AS_{R\text{-}QAMC}$ is higher than AS_{Ref}, then the relative bandwidth of the $AS_{C\text{-}QAMC}$ decreases to 67% and the relative bandwidth of the $AS_{R\text{-}QAMC}$ remains to 79% i.e. a difference of 12% between the two configurations.

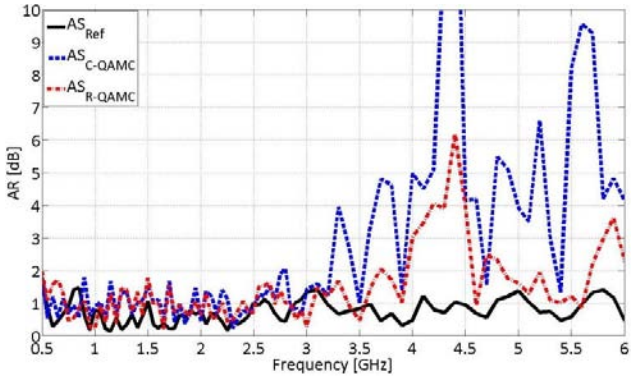

Figure 12: Axial ratio versus frequency.

Table 1 summarizes the measurements results. Those are given from 1.65GHz to 3.8GHz, which corresponds to the operational bandwidth of 79%.

Table 1: Radiation characteristics comparison between the two QAMC.

	$AS_{C\text{-}QAMC}$	$AS_{R\text{-}QAMC}$
Return Loss	< -10dB	< -10dB
Co-polarization Level (RHCP broadside gain)	3dB to 7dB	3dB to 9dB
Cross-polarization Level (LHCP broadside gain)	< -6dB	< -12dB
Axial Ratio	< 5dB	< 2dB

Finally, it is important to check if the radiation pattern is stable on the desired bandwidth. That means that the beam stays directional and the broadside RHCP gain does not present any sharp variations.
The following figures present the radiation patterns (in dB) for all configurations. All results are normalized by the value of the broadside RHCP gain.

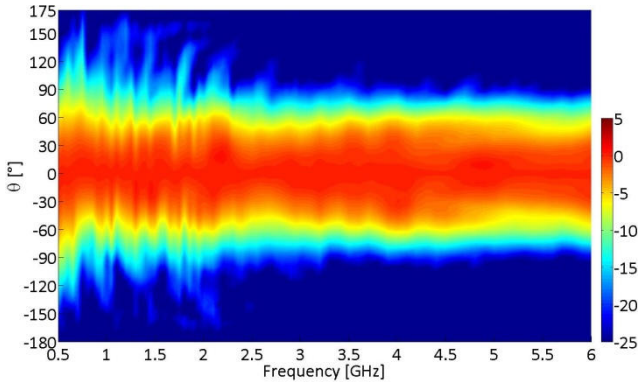

Figure 13: AS_{Ref} radiation pattern versus frequency for φ=0°.

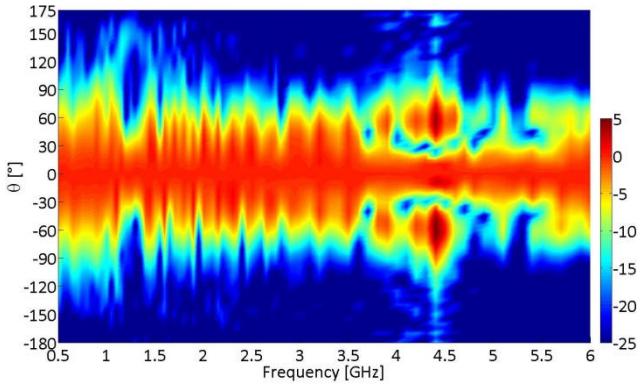

Figure 14: $AS_{C\text{-}QAMC}$ radiation pattern versus frequency for φ=0°.

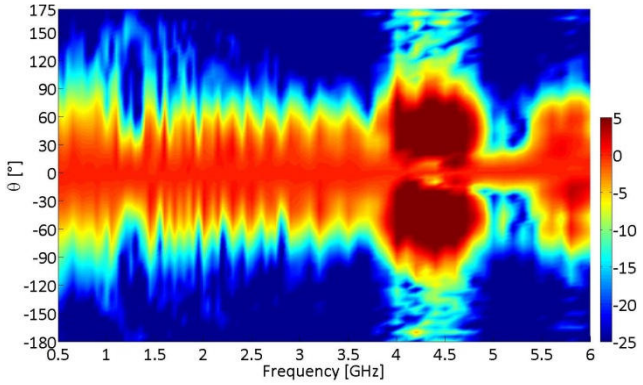

Figure 15: $AS_{R\text{-}QAMC}$ radiation pattern versus frequency for φ=0°.

The radiation pattern of the AS_{Ref} is stable from 0.5GHz to 6GHz, thanks to the absorber cavity (cf. Fig. 13).
Fig. 14 and 15 show that radiation patterns of the $AS_{C\text{-}QAMC}$ and the $AS_{R\text{-}QAMC}$ are almost similar from 0.5GHz to 3.6GHz. For frequencies higher than 3.6GHz the radiation pattern of the $AS_{C\text{-}QAMC}$ begins to be disturbed.
The radiation pattern of the $AS_{R\text{-}QAMC}$ stays stable up to 3.8GHz, and then it also begins to be disturbed, but in the center of the radial QAMC there is enough space to put another reflector in order to reduce this discontinuity.

6. Conclusions

We have shown that it is possible to design a radial QAMC reflector suitable to the geometry and the radiation of the Archimedean spiral antenna. The method consists in determining the active area and in designing circular patches with the dimensions given by the cartesian AMC. The simulation shows that the RHCP broadside gain of the two QAMC is almost similar.
In order to validate these results an Archimedean spiral antenna printed on Duroid RT 5880 substrate has been realized and placed 4mm above the two QAMC. Measurements results show a relative bandwidth of 79%, larger than the theoretical bandwidth of 66%, defined by a reflection phase included between +/-120°. With the radial QAMC the broadside LHCP gain is improved and the axial ratio is below 2dB from 1.65GHz to 3.8GHz.
The paper demonstrates that an Archimedean spiral antenna placed above a radial QAMC can achieve wideband properties with a thickness of only $\lambda_{1.65GHz}/15.3$. This new design can be improved by reducing the dimensions of the patches in order to have different patches for different frequency bands.

References

[1] D. Sievenpiper, L. Zhang, R. F. J. Broas, N. G. Alexopolous and E. Yablonovitch, High impedance electromagnetic surfaces with a forbidden frequency band, *IEEE Trans. on Microwave Theory and Techniques*, Vol. 47, No. 11, 2059–2074, 1999.
[2] M. Grelier, M. Jousset, S. Mallégol, A.C. Lepage, X. Begaud and J.M. Le Mener, Wideband QAMC reflector's antenna for low profile applications, *Applied Physics A: Materials Science & Processing*, Vol. 103, Num. 3, 809-813, 2010.
[3] J.A. Kaiser, The Archimedean two-wire spiral antenna, *IEE Trans. on Antennas and Propagation*, Vol. 8, No. 3, 312-323, 1960.
[4] Y. Mushiake, Self-complementary antennas, *Antennas and Propagation Magazine IEEE*, vol.34, no.6, pp.23-29, Dec 1992.
[5] F. Yang and Y. Rahmat-Samii, Reflection phase characterizations of the EBG ground plane for low profile wire antenna application, *IEEE Trans. on Antennas and Propagation*, Vol. 51, No. 10, 2691-2703, 2003.
[6] F. Linot, R. Cousin, X. Begaud, M. Soiron, Design and measurement of High Impedance Surface, *Antennas and Propagation (EuCAP), Proceedings of the Fourth European Conference on*, pp.1-4, 12-16 April 2010
[7] G. Goussetis, A.P. Feresidis, J.C. Vardaxoglou, Tailoring the AMC and EBG characteristics of periodic metallic arrays printed on grounded dielectric substrate, *Antennas and Propagation, IEEE Transactions on*, vol.54, no.1, pp. 82- 89, Jan. 2006.
[8] C. Djoma, X. Begaud, A.C. Lepage, S Mallégol and M. Jousset, Wideband Reflector for Archimedean Spiral Antenna, *6th European Conference on Antennas and Propagation 2012*.
[9] M. Grelier, M. Jousset, S. Mallégol and X. Begaud, *Antenna device with a planar antenna and a wide band reflector and method of realizing of the reflector*, Patent n° EP 2365584.
[10] M.N. Afsar, W. Yong, D. Hanyi, A new wideband cavity-backed spiral antenna, *Antennas and Propagation Society International Symposium*, vol.4, pp.124-127, 2001.

High performance diffraction gratings made by e-beam lithography

Uwe D. Zeitner[1,2*], Maria Oliva[1], Frank Fuchs[1], Dirk Michaelis[1], Tino Benkenstein[1], Torsten Harzendorf[1], and Ernst-Bernhard Kley[2]

[1]Fraunhofer Institute for Applied Optics & Precision Engineering,
Albert-Einstein-Str.7, 07745 Jena, Germany
[2]Institute for Applied Physics, Friedrich-Schiller-University Jena,
Max Wien Platz 1, 07743 Jena, Germany
*corresponding author, E-mail: uwe.zeitner@iof.fraunhofer.de

Abstract

Gratings are essential components in different high performance optical set-ups such as spectrometers in space missions or ultra-short-pulse laser compression arrangements. Often such kinds of applications require gratings operating close to the technological accessible limits of today's fabrication technology. Typical critical parameters are the diffraction efficiency and its polarization dependency, the wave-front error introduced by the grating, and the stray-light performance. Additionally, space applications have specific environmental requirements and laser application typically demand a high damage threshold. All these properties need to be controlled precisely on sometimes rather large grating areas. Gratings with extensions of up to 200mm or above are not unusual anymore. The paper provides an overview on how such high performance gratings can be realized by electron-beam lithography and accompanying technologies. This approach is demonstrated by different examples. The first example is the design and fabrication of the grating for the Radial-Velocity-Spectrometer of the GAIA-mission of the ESA. The second grating is a reflective pulse compression element with no wavelength resonances due to an optimized design. The last example shows a three level blazed grating in resonance domain with a diffraction efficiency of approximately 86%.

1. Introduction

Even about 200 years after the first grating spectrometer build by Joseph von Fraunhofer exciting grating effects are still discovered and investigated. Diffraction gratings have not lost anything of their attraction; they are key elements for a huge number of applications. The field of grating applications stretches from dispersing elements in spectrometers over beam-splitting elements to pulse-compression gratings for the manipulation of ultra-short laser pulses. The developments in modern lithographic fabrication technologies, especially the advances in resolution and accuracy of e-beam lithography, opened the way for the use of sub-wavelength sized effective media structures and their beneficial use in the realization of high performance diffraction gratings (see Figure 1) in real applications.

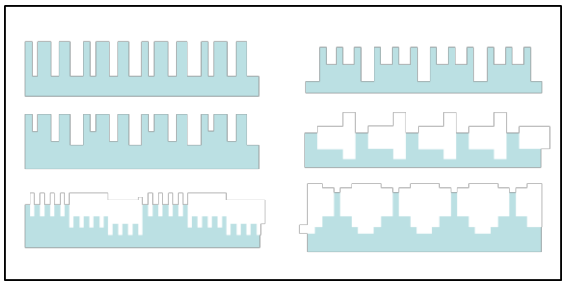

Figure 1: Example profiles for the use of effective media structures in advanced diffraction gratings.

In this paper, we will discuss the developed technology, based on electron beam lithography, used to fabricate such advanced diffraction gratings and show some examples.

2. Electron beam based technology

The core of our fabrication technology is the electron beam lithography process. The system installed at IOF Jena is a Vistec SB350 OS (Vistec Electron beam GmbH, Jena) which has been developed and specially adapted to requirements of optical applications. In fact, the letters OS stand for 'optics special'. The machine can handle substrate sizes up to 310mm extension and 15mm thickness and achieves very high overlay accuracy and writing speed. The minimum feature size achievable is smaller than 50nm, the address grid is 1nm and the overlay accuracy in case of a multi-exposure process is less than 30nm.
The standard process flow for the fabrication of a binary optics structure is sketched in Figure 2. The substrate, usually made of Fused Silica, is covered with 80nm thick Chromium layer, on top of which an e-beam resist layer is coated (see Figure 2(I)). The micro-structure geometry is transferred to the resist by electron beam lithography and successive development of the exposed areas (see Figure 2(II)). Then the structured resist layer is used as mask to transfer the patter into the chromium layer through a RIE process (see Figure 2(III)). After removing the resist, the

patterned chromium layer acts as hard mask for the final deep etching into the substrate (see Figure 2(IV-V)). Finally the chromium layer is removed from the top of the grating.

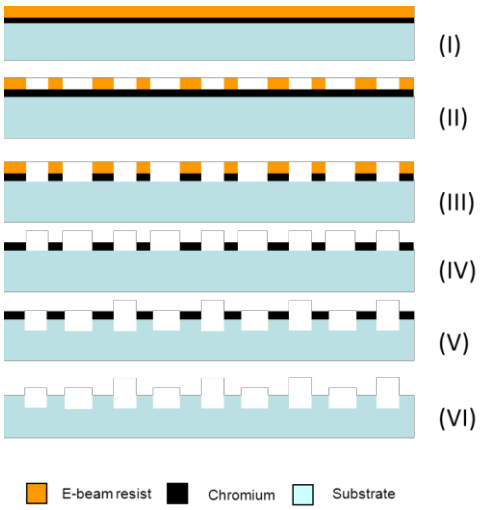

Figure 2: Binary grating fabrication flow.

To reduce the e-beam writing time we use chemically amplified resists (CARs) like FEP171 (Fuji-Film). In the exposure data preparation a structure dependent bias value is considered in order to account for the variation in the final lateral dimensions due to the different process steps.
To fabricate multilevel structures the structure profile is ideally divided in binary substructures and the standard technology consists in a multistep binary optics process [1]. This approach becomes more problematic with the shrinking of the features size and period of the structures: the alignment errors between two exposures become more important. To overcome this problem, two different approaches for the fabrication of multilevel grating have been developed at Fraunhofer IOF. The first, named "three resist layer technology" is only a modification of the standard approach. Here, after the etching of the first binary structure, an additional layer of conventional photoresist is used as a planarization for the chromium- and resist coating of the second binary process step to accurately pattern the second layer [2]. In the second approach, the "Relaxed alignment technology", a unique coded chromium mask (which contains all lateral pattern information) is used for all process steps in order to avoid alignment errors [3].
With the e-beam based technology described here several gratings, binary and multilevel, have been successfully fabricated. In the following three examples will be described in detail.

3. High performance grating examples

The three different examples described in the following are high performance diffraction gratings with special requirements on design and technology. The main focus is on the special design considerations and fabrication of a spectrometer grating for the space mission GAIA [4].

3.1. GAIA spectrometer grating

Special spectrometer gratings are needed for several Earth-observation and scientific space missions. The realization of such kinds of gratings is extremely demanding because several parameters have to be simultaneously satisfied. In particular, critical parameters are the diffraction efficiency and its polarization dependency, the wave-front error introduced by the grating, stray-light performance, and usability in a space environment. To achieve the optimal performance of the grating it is essential to include technological considerations and specifications already into the design. We demonstrate this approach by the design and fabrication of the grating for the Radial-Velocity-Spectrometer (RVS) of the GAIA-mission of the European Space Agency (ESA). The corresponding instrument is dedicated to the measurement of the star distance for objects located in our home galaxy down to a relative brightness of m = 18 light magnitude. The distance measurement is based on a characterization of the red-shift of a Calcium triple spectral line group in the wavelength range λ=847…874nm. In order to achieve the desired sensitivity there is a combination of requirements to be fulfilled by the spectrometer grating which makes it an extremely demanding optical element. An overview of the specification and requirements for the grating is given in the Table 1.

Table 1: Required optical parameters of the spectrometer grating for the GAIA-Satellite of the ESA.

Parameter	**Value**
grating period	3.15µm
wavelength range	847nm … 874nm
diffraction efficiency +1st order	> 70% (>77% goal)
polarization sensitivity $\frac{\lvert\eta_{TE}-\eta_{TM}\rvert}{\eta_{TE}+\eta_{TM}}$	< 7%
angle of incidence	4.5°
wave-front error	< 5nm (rms) on each 50mm x 42mm sub-aperture
grating size	160mm x 208mm

Each single requirement can be satisfied by a grating realized by any standard technology, but their simultaneous implementation makes the fabrication extremely difficult. To achieve the blazing effect for a quasi-normal incidence configuration, a linear phase modulation of the incident wave within one grating period is needed. It is well known that this can be achieved by blazed gratings with a three-dimensional surface profile of the grating, i.e. a saw-tooth like structure or a stepwise approximation of it. However, the smaller the grating period, the more difficult the fabrication of such a 3D-structure becomes. For such small periods typically the blazed profile can be approximated by a multilevel structure which can be fabricated by multiple succeeding binary patterning steps. However, if the alignment of the different lithography steps with respect to each other is not perfect the resulting structure can exhibit a

considerable amount of stray-light, the diffraction efficiency is reduced, and also the quality of the transmitted wave-front is badly affected. As a result the requirements mentioned in the above table will not be achieved with this technology, especially not on the whole grating area.

An alternative approach for the realization of efficient diffraction gratings is based on the modulation of the effective refractive index within the grating period by a binary sub-wavelength structure. This method of realizing high efficient diffraction gratings by an effective index blaze has been experimentally demonstrated for instance by [5, 6]. The sub-wavelength features within the grating period are not resolved by the incident light which instead is experiencing an effective refractive index averaged from the indices n_s and n_e of the substrate material and the environment (typically air), respectively. The particular effective index is a non-trivial function of the local fill-factor and typically also depends on the polarization of the light.

From the technological point of view the important advantage of this approach is the one step lithographic fabrication of the structure. There is no need for multiple succeeding and precisely aligned lithography steps as would be required for the fabrication of multi-level profiles [1].

However, there is also a potential draw back of the effective index approach. The required aspect ratio, i.e. the ratio of structure depth to smallest feature width, is typically very high in such structures, especially if the grating is supposed to operate in the visible or near infrared spectral region. Then the required structures quickly approach the limits of the available fabrication technologies.

For the realization of the GAIA spectrometer grating we thus developed an approach for the relaxation of the fabrication demands based on a combination of 1D and 2D sub-wavelength structures within one grating period. This particular example shall be used for the comparison of the relaxation potential of the transition from a pure 1D binary effective medium structure to a combination of 1D and 2D sub-wavelength features.

In a first grating design we optimized a pure 1D binary blazed structure using a rigorous coupled wave algorithm (RCWA). The resulting structure, made of 5 bars within one grating period, is sketched in Figure 3(a) together with a graph showing the angular dependency of the diffraction efficiency for TE- and TM-polarization at a wavelength of λ=860nm.

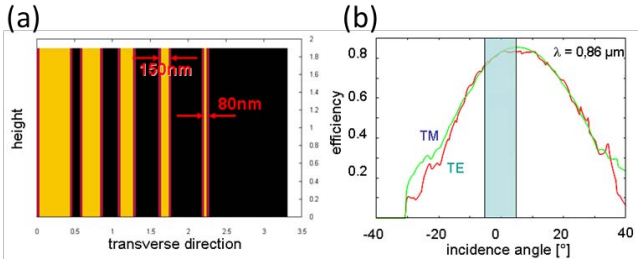

Figure 3: GAIA spectrometer grating. (a) Optimized 1D effective medium structure. (b) Calculated diffraction efficiency as a function of the incidence angle for two orthogonal polarizations.

The required depth of the structure is h=1.83µm. As can be seen from the sketch the smallest lateral bar width is 80nm. Together with the required depth this leads to an aspect ratio (structure height/width) of approximately 23 which is extremely difficult to fabricate.

In order to achieve a good homogeneity in the whole grating area we need to relax the demands on the fabrication process especially by reducing the high aspect ratio of the structures. We consider that for the optical function what is actually important is the local effective refractive index and this depends on the field overlap with the grating bars and grooves. Thus, the relevant parameter is the local filling factor and its variation across the grating period. Based on this idea, we extend the concept of the pure 1D grating structure to a 2D pattern. The smallest 1D bars have been replaced with 2D pillars, generating an additional periodic structure along the y-direction of the grating having a sub-wavelength periodicity of p_y=600nm. Due to the sub-wavelength periodicity of this additional pattern in y-direction it does not lead to additional diffraction orders in this direction. By keeping the local fill-factor almost constant this approach leads to 2D pillars instead of 1D bars with a considerably larger lateral feature size, thus being less demanding from a technological point of view. The resulting grating pattern is a combination of wide 1D bars and 2D pillars.

This combined 1D-2D pattern has been again optimized by a RCWA-algorithm with a constraint about the smallest lateral feature size of 200nm (see Figure 4). The structure depth of the optimized grating remains at about h=1.8µm. Thus, the aspect ratio is reduced from 23 in the pure 1D case to only 9 in the 1D-2D case leading to a much easier fabrication process. The optimized grating structure is shown in Figure 4(a) together with a comparison of the efficiency performance of the two different grating types. It is clearly to be seen that the efficiency performance is similar to the pure 1D-grating but the minimum feature sizes are larger. The maximum theoretical efficiency for the incident angle of 4.5° is approximately 85% for both polarization directions.

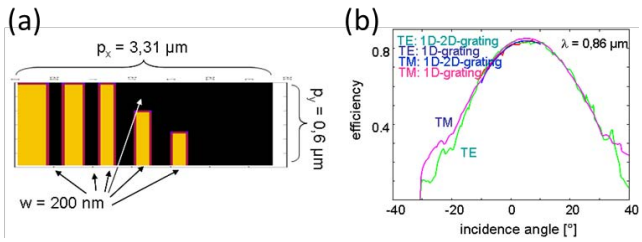

Figure 4: GAIA spectrometer grating (a) Optimized 1D-2D structure for the binary effective medium grating. (b) Comparison of the calculated diffraction efficiency of the two different grating types as a function of the incidence angle for two orthogonal polarizations.

For the fabrication of the spectrometer grating a combination of lithography and reactive ion etching (RIE) processes has been used as described in the section 2 of this paper (see Figure 1).

Achieving a high and polarization independent diffraction efficiency strongly depends on the accurate realization of the lateral features of the sub-wavelength pattern. If the bar width deviates from the design values the efficiency for one of the polarization directions will decrease. Therefore, an extensive optimization of the fabrication technology was necessary. First a number of different grating designs were realized as gratings with a smaller size of only 30mm x 30mm in order to investigate how fabrication tolerances affect the achievable optical performance. From the different sample gratings the most promising pattern geometry has been chosen for the realization of a full-size grating model. By including intermediate results from the technology optimization into a re-design of the grating structure made it possible to further simplify the grating structure without degrading the optical performance. As a result the final grating pattern has a sub-structure within one grating period consisting of three 1D-bars and only one row of pillars, as shown in the SEM picture of Figure 5(a). Their lateral feature sizes have been optimized in a close loop between the achieved experimental results and theoretical calculations which considered also additional fabrication effects like the etch-depth dependence from the local groove width (the so called RIE-lag). One of the full-size "Flight Model" gratings fabricated at IOF is shown in Figure 5(b).

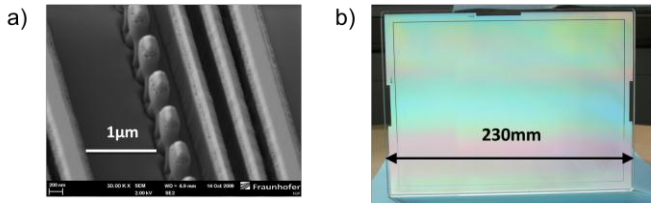

Figure 5: GAIA spectrometer grating (a) SEM-image of the fused silica grating structure fabricated by electron-beam lithography and reactive ion etching. (b) Photograph of the "Flight Model" of the grating.

For these gratings specially shaped 9" sized substrates were used in order to obtain a wave-front error in the sub-apertures below 5nm (rms) and a polarization independent diffraction efficiency above 80%.
The measured efficiency, the polarization sensitivity, and the wave-front accuracy shown in Figure 6 fulfill all the required specifications.

3.2. Resonance-free reflection gratings

The second type of grating that we discuss in this paper is an optimized reflection grating. Reflection gratings are preferable in several applications compared to the transmission ones due to the reduced material interaction and additional freedom for the optical design. Especially, the combination of gratings and dielectric mirrors are promising due to their low losses and consequently high diffraction efficiencies. Using such a setup, almost 100% diffraction efficiency can be achieved with a spectral bandwidth of several 10nm or more and additional polarization-independency, depending on the specific setup. However, such kinds of multilayer dielectric gratings are challenged by the occurrence of guided mode resonances which become noticeable as singular drops in the diffraction efficiency (see red curve in the Figure 7(a)).

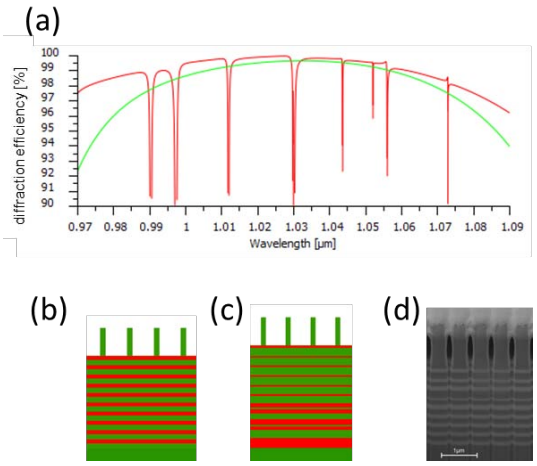

Figure 7: (a) Diffraction efficiency for TE polarized light of a standard grating (red curve & design (b)) and a grating with the resonances removed (green curve & design (c)). Both gratings have a period of 875nm and are illuminated at an incidence angle of 36.05° (Littrow angle for λ=1030nm). (d) FIB Cross-section of a fabricated reflection grating with aperiodic reflector-stack. The platinum layer visible on top of is needed for the focused ion beam cut process.

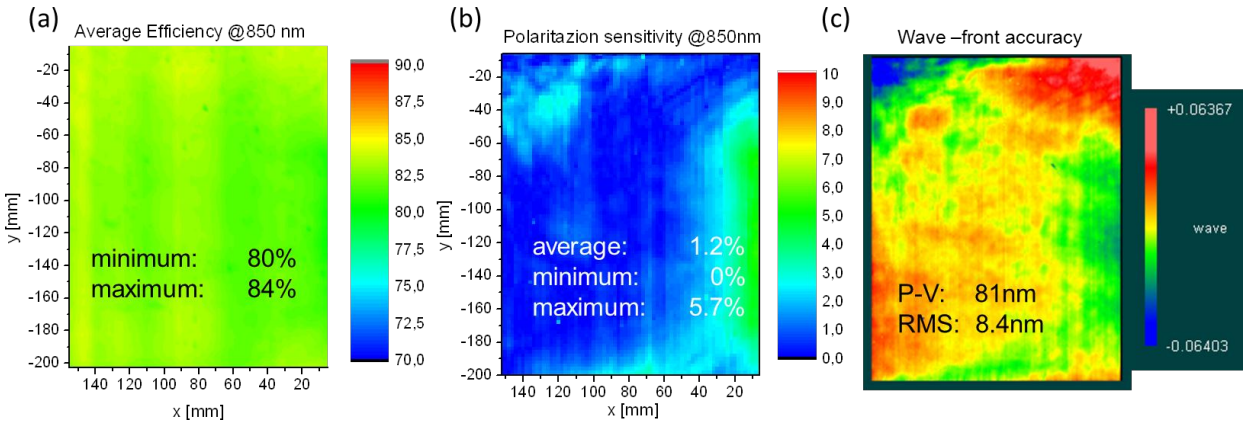

Figure 6: GAIA spectrometer grating (a) Average Efficiency. (b) Polarization sensitivity. (c) Wave-front accuracy.

The problem of undesired resonances can be solved by a significant reduction of the grating period, as suggested in [7]. However, such an approach is often found to be incompatible with the application requirements.
We have investigated and analyzed the physical origin of such guided mode resonances in dielectric reflection gratings. The goal was to find a way to avoid their formation or at least reduce the number of resonances in a given spectral and angular interval for a fixed grating period and incidence conditions. Going beyond the common design of a simple dielectric reflector formed by stacked double layers of λ/4 optical thicknesses we exploit all structural degrees of freedom by a combined optimization of grating and layer stack. Different merit functions were investigated for this optimization and a reliable way of identifying the resonance has been devised by using a merit function based on the analysis of the Poynting-vector inside the grating. The successful removal of resonances is shown in the green curve of Figure 7(a). In the Figure 7(b) and (c), the designs of a standard and resonance-free dielectric reflection grating are shown, respectively. The aperiodicity of the layer stack is fundamental for the resonances elimination. Several resonance-free gratings, with different periods have been successfully fabricated by electron beam lithography and RIE etching into a silicon dioxide layer deposited on the top of the dielectric mirror layers. The FIB (Focused Ion Beam) image of Figure 7(c) shows the profile of one of the fabricated grating profiles.
Such type of gratings having a period of p=667nm was successfully adapted for the NIR-spectrometer grating for the space mission Sentinel IV [8].

3.3. Highly efficient three level grating in resonance domain

The last grating presented here is a multilevel blazed grating working at normal incidence in resonance domain (small period-to-wavelength ratio). In such configurations blazed gratings with a continuous profile as well as traditional multi-level gratings with equidistant phase levels show remarkable efficiency losses due to the shadowing effect [9]. The shadowing can be avoided using simple binary optical elements but their single order efficiency at normal incidence is below 50% due to symmetry reasons. To achieve a high efficiency at normal incidence it is possible to perform a parametric optimization of the width and height of the different phase levels of a multi-level element [9]. We optimized the profile for a three-level grating in fused silica working at λ=633nm at normal incidence operating at the interface from substrate to air. The grating period p=1.266µm is two times the operating wavelength (633 nm). The optimized profile consists of an upper bar with a rather large height (~778nm) and a small width (200nm) and a lower bar with moderate filling factor as well as aspect ratio (height ~ 394nm, width ~ 580nm). The high efficiency can be understood by a three-beam interference mechanism by considering the grating divided in two binary sub-gratings [2] both acting as beam splitting elements.

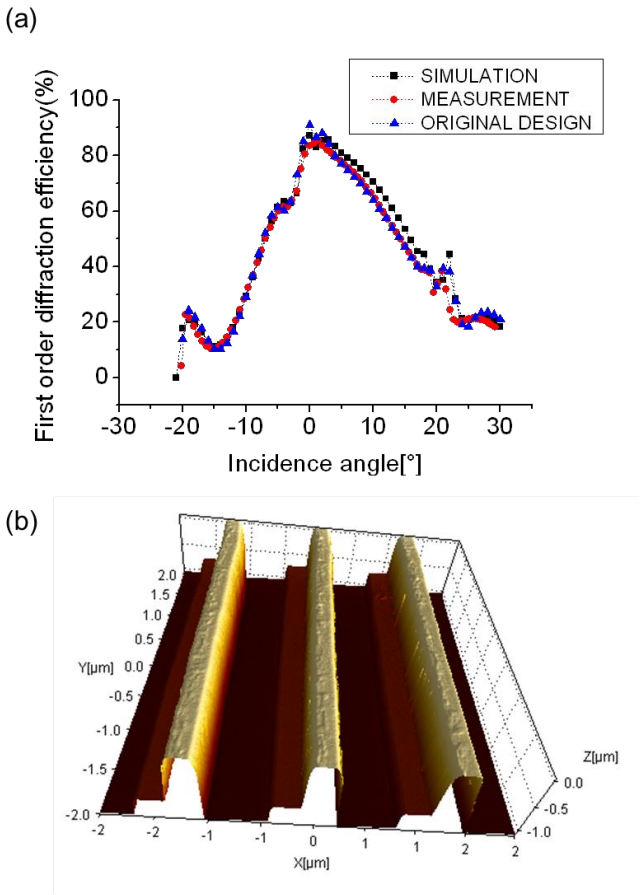

Figure 8: Characterization of the grating, a) Simulation and measurement of the 1st order diffraction efficiency vs. incidence angle b) AFM measurement of the three-level grating.

The three different technological approaches [10] already described for multilevel element fabrication have been tested for the fabrication of the grating in order to overcome inaccuracies and artifacts in the profile. The results of these fabrication tests have shown that all technologies are appropriate but for the profile accuracy the most suitable approach is the “three-resist layer” technology.
In Figure 8 the efficiency measurement and the AFM profile of a grating fabricated with this technological approach is shown. The measured diffraction efficiency of approx. 86% at normal incidence is in very good agreement with the simulation as shown in Figure 8(a). The Atomic Force Microscopy measurement shows an almost perfect grating profile without any artifacts (see Figure 8(b)) revealing that the proposed process is well suited for the fabrication of high quality resonance domain gratings.

4. Conclusions

Modern electron-beam lithography offers the required high accuracy, resolution, and especially a unique flexibility for the realization of high performance micro-structured optical elements such as gratings for spaceborne spectrometers. Such applications often have a collection of extreme demands on the efficiency, polarization dependency, wave-

front quality, stray-light level, and environmental conditions on the gratings. In order to fulfill all requirements at the same time novel grating concepts are necessary which are not accessible by alternative grating fabrication technologies. In the current paper we reported about the realization of three different types of gratings: 1) a binary-blazed transmission grating based on a sub-wavelength effective refractive index pattern for the spectrometer of the GAIA-satellite, 2) a resonance-free dielectric transmission grating for the Earth observation mission Sentinel IV, and 3) a three-level transmission grating in the resonance domain showing a high efficiency at normal incidence.
All examples do exhibit different unconventional grating features which are hard to achieve by gratings realized by ruling or interference lithography due to lag of flexibility in shaping the grating profile with the required accuracy. These examples demonstrate the huge potential of electron beam lithography for the improvement of grating performance in different directions.

Acknowledgements

The authors like to thank their colleagues from the CMN-Optics of the Fraunhofer IOF and the IAP of the FSU-Jena for their contributions to the realization of the gratings. All gratings exposures presented here were done using the e-beam writer SB350 OS at the Fraunhofer IOF whose purchase has been supported by the European Union (FZK: B 408 – 04004). Parts of the technology development presented here where supported by the German Ministry of Science and Education in the frame of the project PhoNa (FZK: 03IS2101D)

References

[1] M. B. Stern, Binary optics fabrication in H. P. Herzig (Ed.): *Microoptics: Elements, Systems, and Applications*. Taylor & Francis, London, 1997.

[2] M. Oliva, D. Michaelis, T. Benkenstein, J. Dunkel, T. Harzendorf, A. Matthes, U. D. Zeitner, Highly efficient three-level blazed grating in the resonance domain, *Opt. Lett.* 35, 2774-2776, 2010.

[3] M. Oliva, T. Harzendorf, D. Michaelis, U. D. Zeitner, A. Tünnermann, Multilevel blazed gratings in resonance domain: an alternative to the classical fabrication approach, *Opt. Express* 19, 14735-14745 2011.

[4] www.gaia.esa.int

[5] W. Stork, N. Streibl, H. Heidner, P. Kipfer, Artifical distributed-index media fabricated by zero-order gratings*, Opt. Lett.* Vol. 16 No. 24, 1921-1923, 1991.

[6] P. Lalanne, S. Astilean, P. Chavel, E. Cambril, H. Launois, Blazed binary subwavelength gratings with efficiencies larger than those of conventional échelette gratings, *Opt. Lett*. Vol. 23 No. 14, 1081-1083, Jul. 1998.

[7] J.-P. Wang, Y.-X. Jin, J.-Y. Ma, J.D Shao, Z.-X. Fan, Analysis of restriction factors of widening diffraction bandwidth of multilayer dielectric grating , *Chinese Phys. B* 19 104201-8, 2010.

[8] U.D. Zeitner, D. Michaelis, E.-B. Kley, M. Erdmann, High performance gratings for space applications, *Proc. SPIE 7716*, 77161K, 2010.

[9] E. Noponen, J. Turunen, A. Vasara, Parametric optimization of multilevel diffractive optical elements by electromagnetic theory, *Appl. Opt*. Vol. 31 No. 28, 5910-5912, 1992.

[10] M. Oliva, T. Benkenstein, J. Dunkel, T. Harzendorf, A. Matthes, D. Michaelis, U. D. Zeitner, Smart technology for blazed multilevel gratings in resonance domain, *Proc. SPIE 7716*, 77161, 2010.

Broadband invisibility cloak with multilayer of normal dielectrics

Yijun Feng, Xiaofei Xu, Junming Zhao, Shuai Xiong, Jinlong Fan, and Tian Jiang

School of Electronic Science and Engineering, Nanjing University, 210093, China
*corresponding author, E-mail: yjfeng@nju.edu.cn

Abstract

Most carpet invisibility cloaks are generated from quasi-conformal transformation, which usually require large number of precisely defined sub-wavelength artificial unit cell structures. We present in this paper the design, fabrication and performance test of a quasi three-dimensional carpet cloak made of normal dielectric in the microwave regime. Taking advantage of a simple linear coordinate transformation we design a carpet cloak with homogeneous anisotropic medium and then practically realize the device with multilayer of alternating normal dielectric slabs based on the effective medium theory. As a proof-of-concept example, we fabricate the carpet cloak with multilayer of FR4 dielectric slabs with air spacing. The performance of the fabricated design is verified through full-wave numerical simulation and measurement of the far-field scattering electromagnetic waves in a microwave anechoic chamber. Experimental results have demonstrated pronounced cloaking effect in a very broad band from 8 GHz to 18 GHz (whole X and Ku band) due to the low loss, non-dispersive feature of the multilayer dielectric structure.

1. Introduction

Recent progress in transformation optics (TO) [1] provides us a precise design tool of engineered metamaterials that could be applied to the manipulation of electromagnetic (EM) waves, such as the invisibility cloaking and other interesting applications [2-4]. However, the perfect invisibility cloak suffers from singular material properties and dispersions, which limits its realization and application. To avoid these limitations, several reduced invisibility cloaks with simplified constitutive parameters have been proposed and realized with the resonant metamaterial structures. Recently, to overcome the narrow-band operation of the resonant metamaterials, a special cloaking scheme, called the 'carpet cloak' which is based on quasi-conformal coordinate transformation, has been proposed and studied [5-12].

Most carpet cloaks are generated from quasi-conformal transformation, which leads to minimal anisotropy and facilitates the fabrications with metamaterials [5]. However, the material properties retrieved from this procedure are highly inhomogeneous, which in the microwave regime usually rely on large number of precisely defined sub-wavelength artificial structures [6], or require accurately defined nano-scale patterns made by sophisticated time-consuming nanofabrication processes in the optical regime [7]. Another drawback, as recently suggested in a theoretical study [8], is that the isotropy cloak structure derived from the quasi-conformal transformation will lead to lateral shift of the scattering fields, making the carpet cloak still visible to near field detection. Another attempt to achieve carpet cloak is to use simple linear coordinate transformation which results in cloak with anisotropic but homogeneous material parameters [9]. This proposal has been applied in the infrared frequency to realize two-dimensional cloak with silicon grating structures [10]. It has also been used recently to achieve macroscopic invisibility cloak based on the natural birefringent crystal calcite and the cloak performance has been experimentally demonstrated for a specific polarization at the visible frequencies [11-12]. However, since the natural transparent birefringent crystals are quite limited and their anisotropy can not be engineered as desired, the design flexibility is restricted for this type of cloak.

In this paper, we will show the design, fabrication and performance test of a quasi three-dimensional (3D) carpet cloak made of normal dielectric in the microwave regime. Taking advantage of a simple linear coordinate transformation [10] we have designed a carpet cloak with homogeneous anisotropic medium and then practically realized the device with multilayer of alternating normal dielectric slabs based on the effective medium theory (EMT). Such design has overcome the problem of lateral shift of the near field scattering. As a proof-of-concept example, we have fabricated the carpet cloak with multilayer of normal dielectric slabs with air spacing. The performance of the carpet cloak through out the whole X, and Ku band (from 8 GHz to 18 GHz) is validated through full wave EM simulation based on finite element method and measurement of the EM scattering fields in a microwave anechoic chamber.

2. Design of the cloak

To avoid the lateral shift of the scattering fields in the carpet cloak designed with the quasi-conformal transformation, we employ a straightforward linear coordinate transformation similar to that discussed in [9-10]. Fig. 1(a) indicates

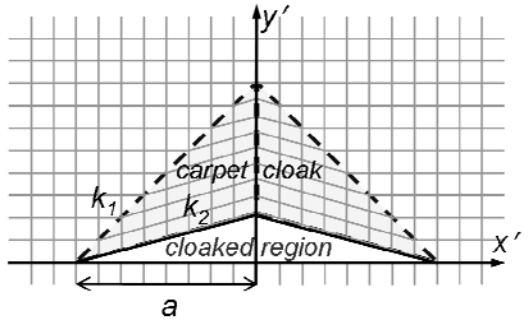

(a)

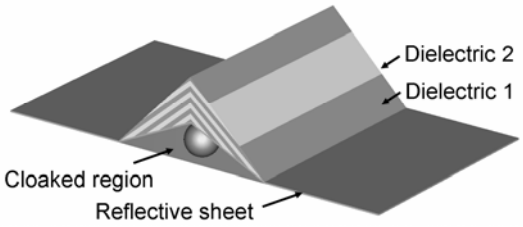

(b)

Figure 1: (a) Scheme of the coordinate transformation and the resulted carpet cloak. (b) Realization of the quasi 3D carpet cloak with multilayer of alternating dielectric 1 and 2. The cloak is covered on a bumped perfect conducting surface enabling a cloaked region underneath.

schematically the coordinate transformation under which a virtual space (x, y, z) with a triangular cross-section in the x-y plane is squeezed into a region with a quadrilateral cross-section (gray region) in the physical space (x', y', z'), leaving the lower triangle part as the cloaked region. The whole carpet cloak is a 3D structure stretched infinitely and uniformly along the z axis. Supposing the outer surface of the carpet cloak or the cloaked region has a the slope of k_1, or k_2, respectively, the transformation can be defined as

$$\begin{aligned} x' &= x \\ y' &= \left(k_1 - k_2\right) y / k_1 + k_2 \left(a + x\right). \\ z' &= z \end{aligned} \tag{1}$$

We could then obtain the material parameters for the left block of the carpet cloak with the standard TO procedures as

$$\overline{\overline{\varepsilon}}' = \varepsilon_r \mathbf{M}, \quad \overline{\overline{\mu}}' = \mu_r \mathbf{M}, \cdot \tag{2}$$

where

$$\mathbf{M} = \begin{pmatrix} k_1/(k_1-k_2) & k_1 k_2/(k_1-k_2) & 0 \\ k_1 k_2/(k_1-k_2) & k_2^2 k_1/(k_1-k_2) + (k_1-k_2)/k_1 & 0 \\ 0 & 0 & k_1/(k_1-k_2) \end{pmatrix}, \tag{3}$$

and $\overline{\overline{\varepsilon}}'$ or $\overline{\overline{\mu}}'$ represents the permittivity or permeability tensor for the cloak in the physical space, while ε_r or μ_r represents the relative permittivity or permeability of the background medium in the virtual space, respectively. We further consider a transverse-magnetic (TM) field polarization for the incident EM wave (the magnetic field along the z axis), and as far as the trajectory of EM wave is concerned, Eq. (3) can be simplified to a nonmagnetic form for the material parameters with $\mu = 1$, and

$$\overline{\overline{\varepsilon}}' = \varepsilon_r \begin{pmatrix} [k_1/(k_1-k_2)]^2 & k_2[k_1/(k_1-k_2)]^2 & 0 \\ k_2[k_1/(k_1-k_2)]^2 & k_2^2[k_1/(k_1-k_2)]^2 + 1 & 0 \\ 0 & 0 & \varepsilon_z \end{pmatrix}. \tag{4}$$

where ε_z can be an arbitrary value for the TM polarization. As a direct consequence of the simple linear coordinate transformation, we find that the material parameters described in Eq. (4) only require a spatially invariant permittivity tensor, and can be easily realized through a certain birefringent dielectric with its optical axis rotated by a certain angle θ with the z-axis. The principal values of the permittivity tensor ε_x^c, ε_y^c and ε_z^c can be determined through diagonalization of the parameters in Eq. (4),

$$\overline{\overline{\varepsilon}}' = \begin{pmatrix} \cos\theta & -\sin\theta & 0 \\ \sin\theta & \cos\theta & 0 \\ 0 & 0 & 1 \end{pmatrix} \begin{pmatrix} \varepsilon_x^c & 0 & 0 \\ 0 & \varepsilon_y^c & 0 \\ 0 & 0 & \varepsilon_z^c \end{pmatrix} \begin{pmatrix} \cos\theta & \sin\theta & 0 \\ -\sin\theta & \cos\theta & 0 \\ 0 & 0 & 1 \end{pmatrix}. \tag{5}$$

For the TM polarization ε_z^c is arbitrary and can be assumed as $\varepsilon_z^c = \varepsilon_x^c$. Therefore the resulted cloak can be realized with a birefringent dielectric crystal described by ε_x^c and ε_y^c. Unlike the previous works that use natural birefringent crystal calcite to design the cloak [11, 12], here we employ a more flexible way to realize the birefringent dielectric through multilayer of alternating dielectric 1 and dielectric 2 (indicated schematically in Fig. 1(b)) based on the EMT [10, 13]. The required dielectric materials in the multilayer are determined through

$$\varepsilon_x^c = \varepsilon_z^c = \frac{\varepsilon_1 + \eta\varepsilon_2}{1+\eta}, \quad \varepsilon_y^c = \frac{(1+\eta)\varepsilon_1\varepsilon_2}{\eta\varepsilon_1 + \varepsilon_2}, \tag{6}$$

where ε_1 and ε_2 are the permittivity and η is the thickness ratio of the two isotropic dielectrics, respectively. We simply let η = 1 for the consideration of achieving maximum anisotropy. This multilayer approach allows us more freedom to design the carpet cloak with desired shape (different slope k_1, or k_2) and material parameters.

3. Implementation and characterization

As a proof-of-concept example of our proposal, we have designed a quasi 3D carpet cloak at microwave regime. Assuming k_1 = 1, k_2 = 0.17, a = 100 mm, and the cloak is immersed in a background medium of ε_r = 1.75. From Eqs. (1) - (6), the relative permittivity of the dielectric 1 and 2 composing the carpet cloak is determined as 4.4 and 1.0, respectively, and the rotation angle θ is about 25.8° with respect to x-axis. Considering the practical realization, we replace the background medium with free space, which in principle will cause slight reflections at the boundary between the cloak and the background medium due to wave

impedance mismatch, but the wave trajectory inside the cloak and thus the cloaking effect will keep unchanged.

To verify the design, we study how the EM waves interact with the carpet cloak with full-wave numerical calculations based on the finite element method (Comsol Multiphysics). Suppose a Gauss beam with TM polarization incidents along an azimuth angle of $\varphi = 135°$ with respect to x-axis. A flat conducting sheet produces a near perfect specular reflection of the incident beam, whereas the presence of a reflective bump structure produces considerable diffuse reflection as shown in Fig. 2 (a) and (b). From the near field distributions of the magnetic field illustrated in Fig. 2 (b), one could easily "detect" the bump structure from the irregular scattering. However, if we consider a background medium with permittivity of 1.75, and cover the bump with an anisotropic carpet cloak determined from Eq. (4), the bump becomes invisible, with a near field distribution of specular reflection (Fig. 2(c)) mimicking that of a flat reflective sheet (Fig. 2(a)). Consider the practical realization, we replace the background medium with free space, and construct the cloak with multilayer of alternating dielectrics as proposed before. FR4 dielectric (usually used in the print circuit board technology) with permittivity of 4.4 and loss tangent of 0.025 has been used for dielectric 1, while air spacing for dielectric 2. Both have a thickness of 1.5 mm. Fig. 2(d) illustrates the near field distributions which represents a specular reflection similar to that of Fig. 2(c) indicating that the reduced multilayer cloak design still has good performance.

We have also calculated the far-field pattern of the scattering field through the near-to-far-field extrapolation algorithm, and compared in Fig. 3. Both the anisotropic and the multilayer cloaks result in confined far-field scattering along the specular direction ($\varphi = 45°$) similar to that from a flat reflective sheet, while the bare bump results in irregular scattering fields with two lobes around $\varphi = 28°$ and $\varphi = 68°$. The slight backward scattering by the anisotropic or the multilayer cloak is due to the nonmagnetic reduction and the removal of the background medium resulting in small impedance mismatching.

To implement the designed cloak, we fabricate a quasi 3D carpet cloak composed of multilayer of FR4 slab and air spacing as depicted in Fig. 4. The cloak is aimed to work in the X and Ku band, covering frequency from 8 GHz to 18 GHz. The center frequency corresponds to a free space wavelength of about 23 mm. The whole structure is about 300 mm long (about 13 times of the wavelength) in the z direction, 200 mm wide in the x direction and 100 mm high, creating a cloak region about 200 mm wide and 17 mm high in the center.

To satisfy the effective medium theory described in Eq. (6), either the FR4 slab or air spacing has a thickness of 1.5mm, about 1/15 of the center free space wavelength. The carpet cloak covers a reflective bump (copper board) on an aluminum perfect conducting board with the size of 300 mm × 300 mm.

The performance of the multilayer cloak is tested in a microwave anechoic chamber. Two standard rectangular horn antennas are used as the transmitter and receiver and

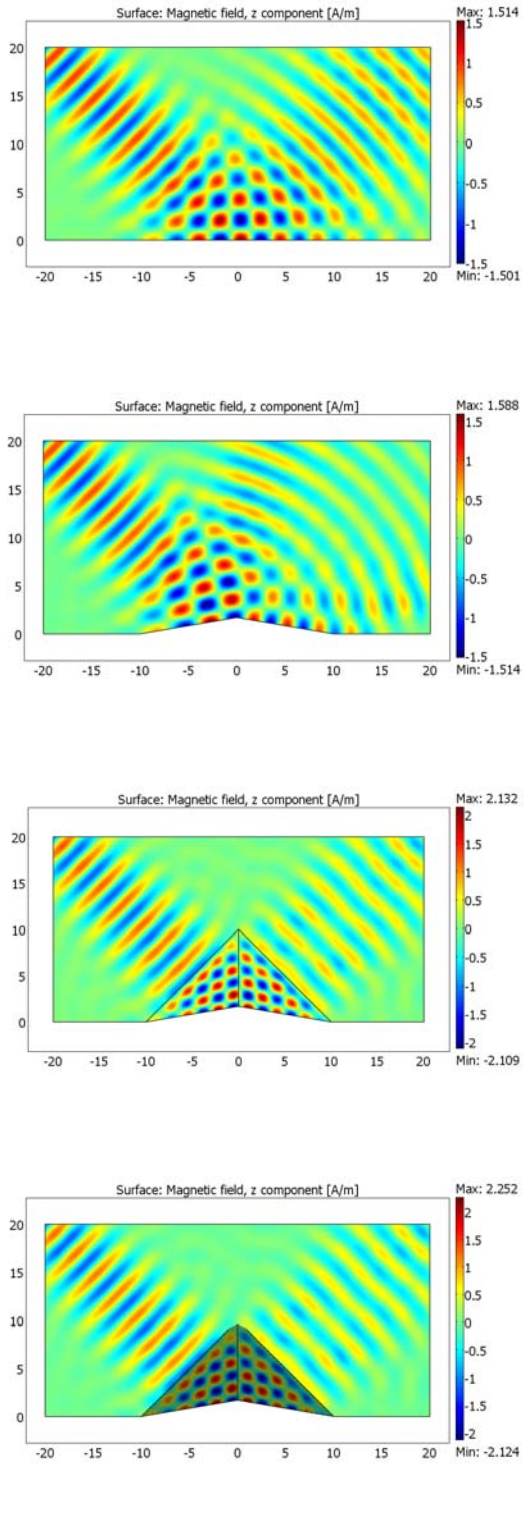

Figure 2: Full-wave simulations of the magnetic field distributions of incident EM beam interacting with (a) flat conducting sheet; (b) bare conducting bump; (c) bump covered by carpet cloak with a background dielectric with permittivity of 1.75; (d) bump covered by carpet cloak composed of multilayer of FR4 slabs with air spacing.

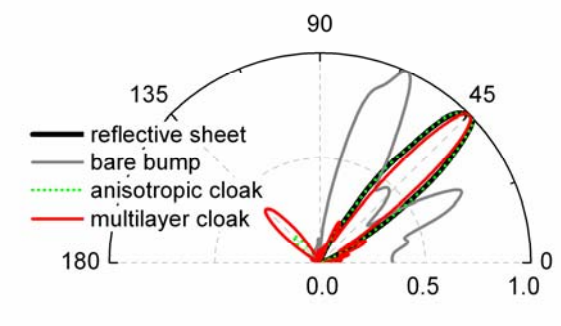

Figure 3: The far field distributions of the scattered EM waves for the different cases indicated by the legends.

linked to a vector network analyzer to measure the scattering field. Both horns can be moved along an arc rail to change their azimuth angles as shown in Fig. 5. To obtain a quasi plane wave of TM polarization, we mainly take advantage of the far field phenomenon of the horns. We fix the incident wave at an azimuth angle of 135°, and record the scattering field as a function of the azimuth angle φ from 10° to 80° through out the whole X and Ku band. The scattering field amplitude has been normalized to that of the specular reflection by a flat conducting plate of 300 mm × 300 mm. We measured the scattering for three different cases: flat conducting plate, conducting bump, and the bump covered by the multilayer cloak as schematically illustrated in Fig. 5(a), (b) and (c), respectively.

The measured results are compared in Fig. 6 for the three different cases. As shown in Fig. 6(a), the flat conducting sheet produce an idea mirror-reflection with single peak scattering at the specular direction ($\varphi = 45°$). However, the bumped conducting sheet generates irregular scattering with two main lobes roughly around $\varphi = 30°$ and $\varphi = 70°$, as shown in Fig. 6(b), which agrees roughly with the simulation in Fig. 3. When the bump is covered with the multilayer cloak, the mirror-reflection is restored with pronounced single peak around $\varphi = 45°$ as shown in Fig. 6(c), imitating that of the flat reflective sheet without any bump. The experiment results have obviously validated the design procedure of realizing the carpet cloak through multilayer of normal dielectrics. The cloak also demonstrates a very broad band performance through out the whole X and Ku band, which is due to the non-dispersive and low loss feature of the multilayer structure.

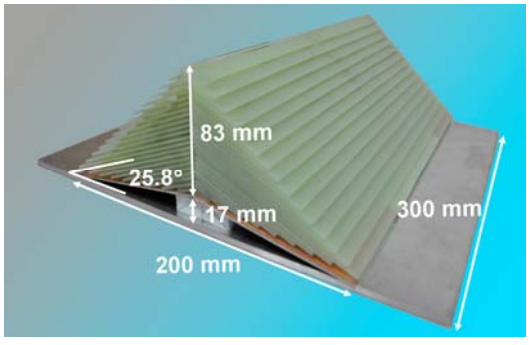

Figure 4: Photograph of the fabricated multilayer cloak.

Since the carpet cloak is designed based on transformation optics; therefore, it should in principle work for all incident angles. We have checked the cases for other incident angles, and pronounced cloaking performance has been verified. In Fig. 7 we show one example for the case of incidence along the azimuth angle of 120°. Both the simulation and the measurement for the far-field scattering indicate that the majority scattering field is along the specular direction at the azimuth angle of 60°, verifying the functionality of the carpet cloak. We notice that a small side lobe appears along the azimuth angle of 150°, which is caused by the reflection at the left surface of the cloak due to wave impedance mismatch.

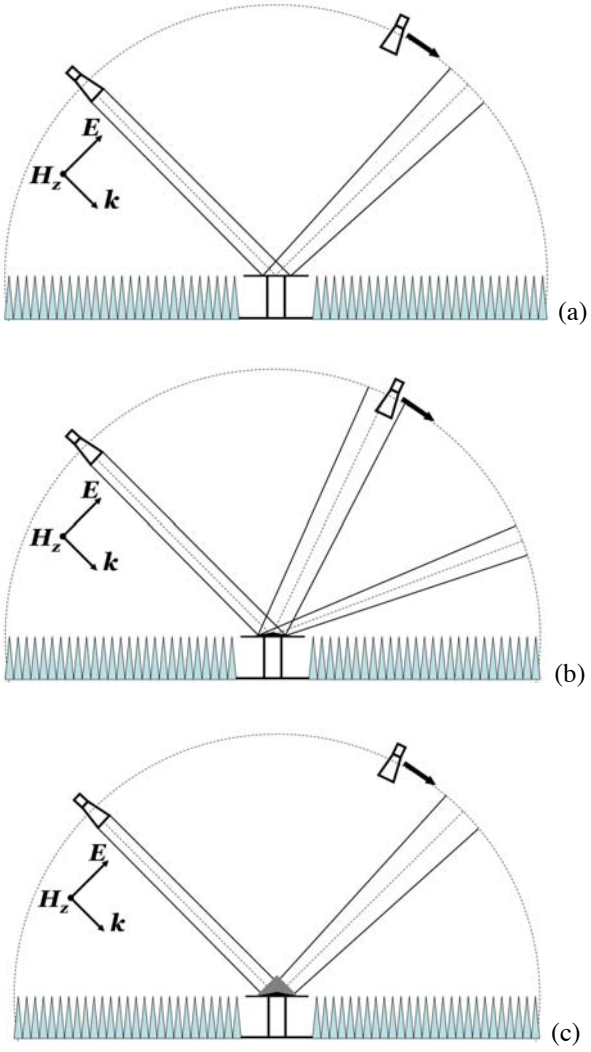

Figure 5: Experimental scheme of measuring the far-field scattering EM field as a function of azimuth angle. (a) the flat conducting sheet; (b) the bare conducing bump; and (c) bump covered by the multilayer carpet cloak.

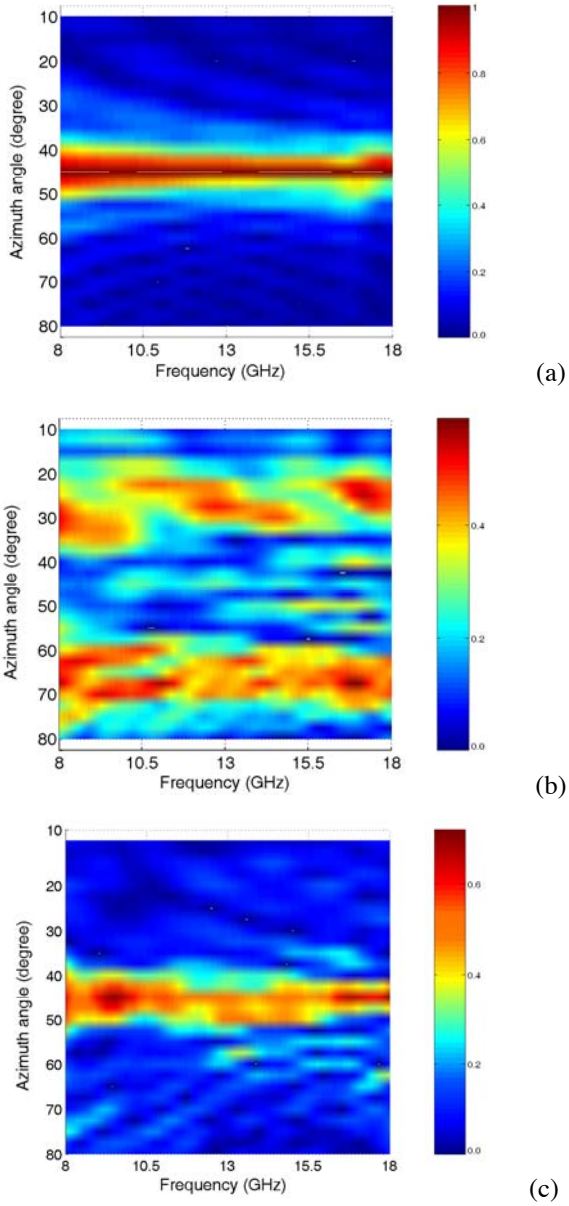

Figure 6: Measured results of the far-field scattering EM field magnitude as a function of azimuth angle and frequency. (a) the flat conducting sheet; (b) the bare conducing bump; and (c) bump covered by the multilayer carpet cloak.

4. Conclusions

In conclusion, we have reported the design, fabrication and performance test of a quasi 3D carpet cloak composed of multilayer of alternating normal dielectric slabs at microwave regime. Through a simple linear coordinate transformation, the carpet cloak can be designed with homogeneous birefringent dielectric medium. Then a practical example of the cloak device has been constructed by realizing the required birefringent dielectric with

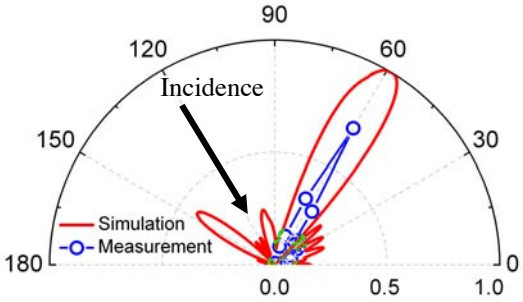

Figure 7: The far field distributions of the scattered EM wave for the incidence along azimuth angle of 120° (at 10 GHz). The measurement is carried out from 10° to 80° with a step of 5°.

multilayer of stacked FR4 dielectric slabs and air spacing based on the EMT. The effectiveness of the device has been verified through full-wave simulation and validated by measurement of the far-field scattering pattern on the fabricated sample, which demonstrated the broad band cloaking effect through out the whole X and Ku band. The proposed design procedure through multilayer of normal dielectrics provides us a cost effective and easy-to-fabricate way to obtain EM cloaking device, and can be further scale to terahertz or optical frequency regime through conventional multilayer thin film technology. We also believe the multilayer approach allows us more freedom in realization of dielectric medium with desired anisotropy of material parameters, and thus can be applied to experimental demonstrations of other transformation optics devices.

Acknowledgements

This work is supported by the National Nature Science Foundation (60990322, 60990320, 60801001 and 61101011), the Fundamental Research Funds for the Central Universities (1111021001, 1104021009, 1085021007), and the Ph.D. Programs Foundation of Ministry of Education of China (20100091110036).

References

[1] J. B. Pendry, D. Schurig, and D. R. Smith, Controlling electromagnetic fields, *Science* 312: 1780, 2006.

[2] H.Y. Chen and C. T. Chan, Transformation media that rotate electromagnetic fields, *Appl. Phys. Lett.* 90: 241105, 2007.

[3] M. Rahm, S. A. Cummer, D. Schurig, J. B. Pendry, and D. R. Smith, Optical design of reflectionless complexmedia by finite embedded coordinate transformations, *Phys. Rev. Lett.* 100: 063903, 2008.

[4] X. Xu, Y. Feng, and T. Jiang, Electromagnetic beam modulation through transformation optical structures, *New J. Phys*. 10: 115027, 2008.

[5] J. Li and J. B. Pendry, Hiding under the carpet: a new strategy for cloaking, *Phys. Rev. Lett*. 101: 203901, 2008.

[6] R. Liu, C. Ji, J. J. Mock, J. Y. Chin, T. J. Cui, and D. R. Smith, Broadband ground-plane cloak, *Science* 323: 366, 2009.

[7] T. Ergin, N. Stenger, P. Brenner, J. B. Pendry, and M. Wegener, Three-Dimensional Invisibility Cloak at Optical Wavelengths, *Science* 328: 337, 2010.

[8] B. Zhang, T. Chan, and B.-I. Wu, Lateral Shift Makes a Ground-Plane Cloak Detectable, *Phys. Rev. Lett*. 104: 233903, 2010.

[9] S. Xi, H. Chen, B. Wu, and J. A. Kong, One-directional perfect cloak created with homogeneous material, *IEEE Microw. Wireless Compon. Lett*. 19: 131, 2009.

[10] X. Xu, Y. Feng, Y. Hao, J. Zhao, and T. Jiang, Infrared carpet cloak designed with uniform silicon grating structure, *Appl. Phys. Lett*. 95: 184102, 2009.

[11] X. Chen, Y. Luo, J. Zhang, K. Jiang, J. B. Pendry, and S. Zhang, Macroscopic invisibility cloaking of visible light, *Nat. Commun*. 2: 176, 2011.

[12] B. Zhang, Y. Luo, X. Liu, and G. Barbastathis, Macroscopic Invisibility Cloak for Visible Light, *Phys. Rev. Lett*. 106: 033901, 2011.

[13] X. Xu, Y. Feng, Z. Yu, T. Jiang, and J. Zhao, Simplified ground plane invisibility cloak by multilayer dielectrics, *Opt. Express*, 18: 24477, 2010.

Experimental study of EIT-Like phenomenon in a metamaterial plasma waveguide

Wusong Wang[1], Liwei Zhang[1,2], Kai Fang[1], Yewen Zhang[1]*

[1] MOE Key Laboratory of Special Artificial Microstructure Materials and Technology
Pohl Institute of Solid State Physics, Tongji University, Shanghai 200092
[2] School of Physics and Chemistry, Henan Polytechnic University, Jiaozuo 454000
*corresponding author: yewen.zhang@tongji.edu.cn

Abstract

This paper demonstrates the realization of the electromagnetically induced transparency (EIT)-like transmission in a metamaterial plasma waveguide with double side defects based on transmission lines. The waveguide with a single side defect works as a plasma resonator and the resonance wavelength is determined by the Fabry-Perot resonance of surface plasma. While in a waveguide with double side defects, a transmission peak appears between the two resonators frequencies because of the destructive interference between the resonance modes of the two resonators, which indicates a pronounced EIT phenomenon. The experiment results agree well with simulations in microwave frequencies.

1. Introduction

The quantum phenomenon of electromagnetically induced transparency (EIT) has become a subject of intensive investigations in recent years [1]. It means regulating and controlling the optical response of the atomic medium by another bunch of laser, which results in the emergence of a narrow transparent window within the original absorption spectrum. At the same time the abnormal dispersion in the transparent window caused by the two energy level resonation changes to the extremely intense normal dispersion [2, 3]. The EIT-related characteristics of strong dispersion and slow propagation within the transmitted frequency domains are showing many potential applications, such as nonlinear mixing and optical storage. But the original EIT was based on the quantum interference of atomic resonances, which makes it difficult to realize in experiments [4]. Recently, the appearance of metamaterials has got the EIT-like transmission to realize under simple experimental conditions [5, 6].

Metamaterials, including double negative materials (DNG, negative ε and μ) and single negative materials (one negative and one positive for ε and μ), have attracted intensive studies in the past few years [7, 8]. A medium with permittivity less than zero and permeability greater than zero is called ε-negative (ENG) material. And a medium with the permittivity greater than zero and permeability less than zero is called μ-negative (MNG) material. Metamaterials can be realized by using transmission lines [7, 8]. One of the most interesting properties is that the metamaterial structures support surface plasma, which is a kind of electromagnetic (EM) waves that propagate along the interface and decay in the transverse direction exponentially into both media. In general SPPs occur in optical frequencies. But they can also occur in microwave frequencies and they are named surface electromagnetic waves at this moment. That is to say surface electromagnetic waves are a mode of SPPs in microwave frequencies. In reference [9] Ruppin pointed out that SPPs appeared when the mathematical signs of permittivity and permeability are different which locate at the two sides of interface.

2. Results of experiment and discussion

In this paper, we demonstrate that EIT-like transmission based on the metamaterial plasma waveguide which is realized by using lumped element loaded transmission lines. As is shown in figure 1(a), a two dimensional metamaterials plasma waveguide with a single side defects with the sandwich structure (MNG-DPS-MNG) is fabricated. The MNG medium and the double positive ones are designed on a dielectric substrate (relative permittivity of 4.75) of height h=1.6mm with a square grid (where the microstrip line width w=1mm) and the period is d=10mm. Unit shunt capacitance of 0.5pF is loaded in the MNG region and the double positive material (DPS) region is consisted of a row of microstrip lines in the middle of the waveguide. In order to prevent the reflection of EM waves by the boundary, the matched resistances of 85ohm are bridged between microstrip lines and ground level. According to the discussion in reference [9] the sandwich structure of MNG-DPS-MNG support the emergence of SPPs. In the left MNG region (figure 1(a)), the region without shunt capacitance is the defect with length L_1=20mm which is calibrated by an elliptically black curve. The input port and output one of electromagnetic (EM) waves are respectively connected through a section of microstrip line with length L=5mm and width w′=2.9mm. The transmission spectrum and electric field distribution of the waveguide with defect are simulated

by Computer Simulation Technology（CST）and measu by means of an Agilent 8722ES vector network analyzer.

When only a single defect exists, our plasma wavegu is not transparent to the EM waves because of the de acting as a resonator. The plasma waveguide which defect exists in the left MNG region is shown in figure 1 Figure 1(b) shows the transmission spectrum and elec field distribution of the defective MNG-DPS-MNG pla waveguide with defect length L_1=20mm at the left side. transparency (dB) of simulation and measurement is general accord and we obtained the transparency of -30 at the frequency of 0.6GHz in measurement. And the inse figure 1(b) reveals that our experimental structure impenetrable to EM waves at the frequency of 0.6C because of the left defect acting as a Fabry-Perot resona of surface plasma. The colors of red (or yellow) and b represent respectively the positive and negative of

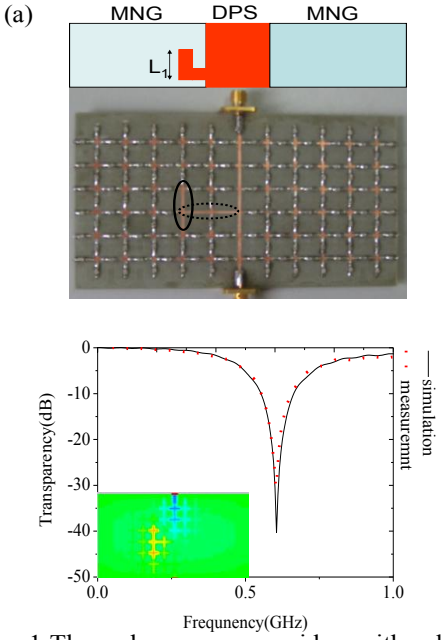

Figure 1:The plasma waveguide with defect len L_1=20mm at the left side (a) and its transmission spectr (b). The inset shows its electric field distribution.

We can also put the defect with length L_2=30mm in right MNG region, which is shown in figure 2(a). T transparency (dB) of simulation and measurement is general accord and we obtained the transparency of abou 30 dB at the frequency of 0.5GHz (figure 2(b)) measurement. And the result of CST simulation in the in states clearly that our plasma waveguide is a impenetrable to EM waves at the frequency of 0.5GHz. H the resonant frequency becomes lower because the def acting as the Fabry-Perot resonator become longer.

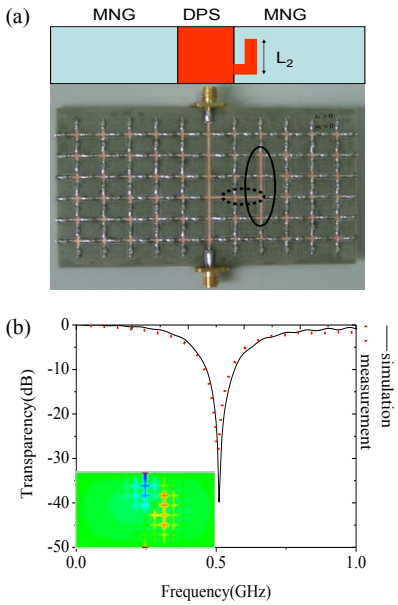

Figure 2: The plasma waveguide with defect length L_2=30mm at the right side (a) and its transmission spectrum (b). The inset shows its electric field distribution.

If the two defects with slightly different resonant frequencies exist simultaneously on the opposite side of the DPS materials (figure 3 (a)), the EIT-like behavior would show up in transmission spectra. As shown in figure 3 (b), the transparency is about equal to -5 dB at 0.55GHz. And the result of CST simulation reveals that EM waves can pass the defective plasma waveguide because the two defects resonate with reversed phase at the frequency 0.55GHz. It is the resonance of reversed phase that caused the reflected EM waves to cancel interference and caused the plasma waveguide to become transparent again

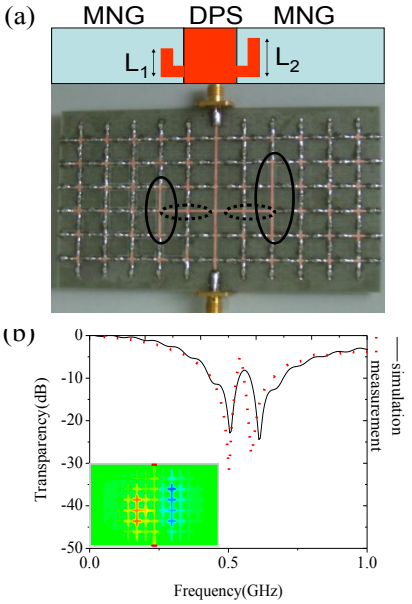

Figure 3: The EIT-like plasma waveguide (a) and its transmission spectrum (b). The inset shows its electric field distribution.

To carry out a thorough study on the physics of the EIT-like transmission in the above paper, the defects lengths were kept to be 20mm and 30mm respectively, but the left defect is moved 10mm upward (figure 4 (a)). The results of simulation and measurement for the shift show that the EIT-like transmission become worse (figure 4 (b)) and EM waves could not penetrate at the frequency of 0.49GHz(between 0.46GHz and 0.52 GHz), because the condition of the cancellation of opposite contributions from the two defects locating at the two sides of DSP is not satisfied well.

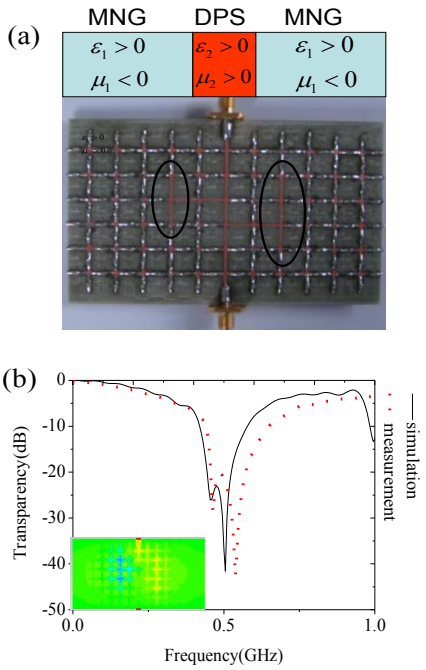

Figure 4: The plasma waveguide with the two defects moving 10mm (a) at the both sides of DPS and its transmission spectrum. (b). The inset shows its electric field distribution.

3. Conclusions

In summary, the EIT-like phenomenon in the sandwich structure composed of defective MNG-DPS-MNG plasma waveguide has been observed in microwave regime. It is shown that the transmission peak can occur between the two resonators frequencies because of the destructive interference effect. And the EIT-like transmission becomes worse while one defect was moved. The measurement and simulation agree well with each other.

Acknowledgements

This research was supported by National Basic Research program (973) of China (No. 2011CB922001) and by the NFSC (No.10904032).

References

[1] F. Michael,Electromagnetically induced transparency: Optics in coherent media, Rev. Mod. Phys., Vol. 77, No.2, pp.633-673, 2005.

[2] S. E. Harris, Electromagnetically Induced Transparency, Phys. Today 50, No. 7, pp.36-42, 1997.

[3] S. E. Harris, J. E. Field, and A. Imamoglu, Nonlinear optical processes using electromagnetically induced transparency, Phys. Rev. Lett. 64, pp.1107-1110, 1990.

[4] F. Phillips, A. Fleischhauer, A. Mair, R. L. Walsworth, M. D. Lukin, Storage of Light in Atomic Vapor, Phys. Rev. Lett. 86, 783, 2001

[5] N Liu, T.Weiss, M. Mesch, L. Langguth,U. Eigenthaler, M. Hirscher, C. Sönnichsen, and H. Giessen, Planar metamaterial analogue of electromagnetically induced transparency for plasmonic sensing, Nano Lett. 10(4), pp.1103-1107, 2010.

[6] S. Zhang, D. A. Genov, Y. Wang, M. Liu, and X. Zhang, Plasmon-induced transparency in metamaterials, Phys. Rev. Lett. 101(4), 047401 , 2008.

[7] C. Caloz, T. Itoh, Electromagnetic Metamaterials: Transmission Line Theory and Microwave Applications (Wiley & Sons, New York, 2006.

[8] A. K. Iyer, P. C. Kremer and G. V. Eleftheriades, Experimental and theoretical verification of focusing in a large, periodically loaded transmission line negative refractive index metamaterial, Opt. Express ,Vol. 11, No.7, pp.696-707, 2003.

[9] R. Ruppin, Surface polaritons of a left-handed material slab, J. Phys.: Condens. Matter 13, pp.1811–1819, 2001.

Surface Plasmon - Guided Mode strong coupling

Aurore Castanié*, Didier Felbacq and Brahim Guizal

University of Montpellier 2
Laboratory Charles Coulomb UMR CNRS-UM2 5221
*E-mail: aurore.castanie@univ-montp2.fr

Abstract

It is shown that it is possible to realize strong coupling between a surface plasmon and a guided mode in a layered structure. The dispersion relation of such a structure is obtained through the S-matrix algorithm combined with the Cauchy integral technique that allows for rigorous computations of complex poles. The strong coupling is demonstrated by the presence of an anticrossing in the dispersion diagram and simultaneously by the presence of a crossing in the loss diagram. The temporal characteristics of the different modes and the decay of the losses in the propagation of the hybridized surface plasmons are studied.

1. Introduction

A surface plasmon (SP) is a transverse magnetic (TM)-polarized electromagnetic wave coupled to the collective longitudinal oscillations of the free electron density existing near the surface of metal [1]. The requirement for the existence of a SP is that the metal in contact with the dielectric must have a relative permittivity whose real part is negative at the frequency of light which will be used to excite the SP.

Besides, emission through SPs is very efficient deexcitation mechanism for emitting materials close to a metallic surface. Indeed, the modification of the spontaneous emission of molecules situated near a metal surface with regard to their emission in the space was experimentally demonstrated by K. H. Drexhage and al. [2]. Furthermore, in 1999, P. T. Worthing and al. [3] etablished that the mode of deexcitation privileged for ions Eu^{3+} close to a metallic surface are the SPs modes. These results were obtained in a weak coupling regime. The dynamics of the excitement is then irreversible and the probability of the presence of the transmitter in the incited state decreases exponentially. SPs were extensively studied in this regime.

When the interaction between an electronic level and an electromagnetic mode increases, it can enter in a regime of strong coupling. This regime was studied in an extensive way in optical microcavities since the works of C. Weisbush and al. [4]. More recently, it was demonstrated between SPs and excitons in organic semiconductors [5, 6, 7]. It is a phenomenon that is interesting both from the point of view of fundamental quantum physics as well as from the point of view of technology.

In the present work, we investigate the strong coupling between a SP and a guided mode in a multilayered planar structure. First of all, the determination of the poles [8] of the S-matrix determinant allows to draw the complex dispersion relation of the structure. Moreover, we used a finite difference time domain (FDTD) algorithm for frequency dependant media which reveals temporal characteristics of the different modes [9].

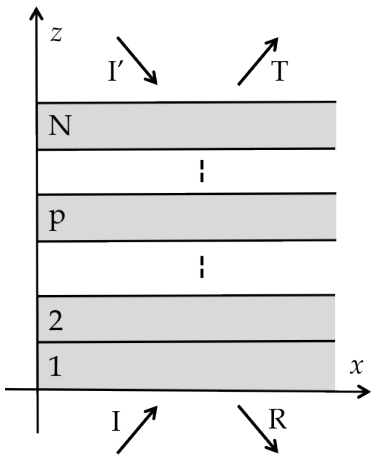

Figure 1: General scheem of a multilayered structure.

2. Theory

It is well known that SPs only exist under TM-polarization. We consider a multilayered structure with N films with dielectric permittivities ε_p. In this case, the transverse magnetic field can be reprensented by :

$$\begin{cases} u_0(x,z) = Ie^{i(\alpha x+\beta_0 y)} + Re^{i(\alpha x-\beta_0 y)} \\ u_p(x,z) = a_p e^{i(\alpha x+\beta_p y)} + b_p e^{i(\alpha x-\beta_p y)} \\ u_N(x,z) = Te^{i(\alpha x+\beta_N y)} + I'e^{i(\alpha x-\beta_N y)} \end{cases} \quad (1)$$

For each medium, $\alpha^2+\beta_p^2 = k_0^2\varepsilon_p\mu_0$. The constants I, I', R, T, a_p and b_p are the amplitudes of the different waves (figure 1). The boundary conditions lead to the system of equations we have to solve with the formalism of the S-matrix.

2.1. The S-matrix formalism

The S-matrix formalism allows to find the coefficients of reflexion and transmission R and T but also all the modes

of the structure. Indeed, it relates the outgoing amplitudes, R and T, to the incoming ones, I and I' :

$$\begin{pmatrix} R \\ T \end{pmatrix} = S(\omega, \alpha) \begin{pmatrix} I \\ I' \end{pmatrix} \quad (2)$$

The modes of the structure are then defined by the existence of outgoing waves in the absence of excitement. With $OUT = (R, T)$, this condition is translated by $S^{-1}OUT = 0$. Thus, to find the modes of the structure, for each frequency ω, we look for the propagation constant α which correspond to the cancellation of the determinant of the matrix S^{-1} or in an equivalent way to the maximization of the determinant of the S-matrix. In other words, we have to find the poles of $detS(\omega, \alpha)$. For each ω, we look for the corresponding poles α_0 in the complex plane by using Cauchy integrals :

$$\alpha_0 = \int_\gamma \alpha S(\omega, \alpha) d\alpha / \int_\gamma S(\omega, \alpha) d\alpha \quad (3)$$

Where γ is a closed loop of the complex plane containing the seeked poles. This method enables to obtain the dispersion and loss diagrams corresponding to the studied structure.

2.2. Finite Difference Time Domain method

A model based on the two-dimensional FDTD method with frequency dependent media is used [10]. We consider an isotropic and non-magnetic multilayered structure (fig. 2) with dielectric functions ε_1, ε_2, ε_g and $\varepsilon_m(\omega) = \varepsilon_\infty - \omega_p/(\omega(\omega + i\gamma))$; where ω_p is the plasma frequency and γ the damping frequency [11]. With ε_0 and μ_0 egal to 1, we have the constitutive relations $\mathbf{B} = \mathbf{H}$ and $\mathbf{D} = \varepsilon_m(\omega)\mathbf{E}$. Therefore, the relationship between $\mathbf{D}$ and $\mathbf{E}$ becomes a convolution in the FDTD algorithm. With the Z transform, it's possible to replace discrete convolution with multiplications [12], so that the constitutive relation for $\mathbf{D}$ and $\mathbf{E}$ becomes :

$$D(z) = \varepsilon_m(z) E(z) \Delta t, \quad (4)$$

where Δt is the time step used in FDTD and $\varepsilon_m(z)$ corresponds to $\varepsilon_m(\omega)$ in z-space :

$$\varepsilon_m(z) = \frac{\varepsilon_\infty}{\Delta t} + \frac{\omega_p^2}{\gamma}\left(\frac{1}{1 - z^{-1}} - \frac{1}{1 - z^{-1}e^{-\gamma \Delta t}}\right). \quad (5)$$

3. Complex dispersion relation

We consider the structure in figure 2 which is a stratified medium containing a dielectric waveguide near a metallic film, the whole being embedded between two dielectric hosts and separated by a dielectric layer of thickness e. This structure supports three different modes : a guided mode (GM) which lives in the medium with ε_g and two SPs over the interfaces of the metal. For this simulations, the permittivity of the metal is taken from the experimental results of E. Palik [13]. All the permittivities values was chosen to allow the manufacturing of this structure to test experimentally our results [14].

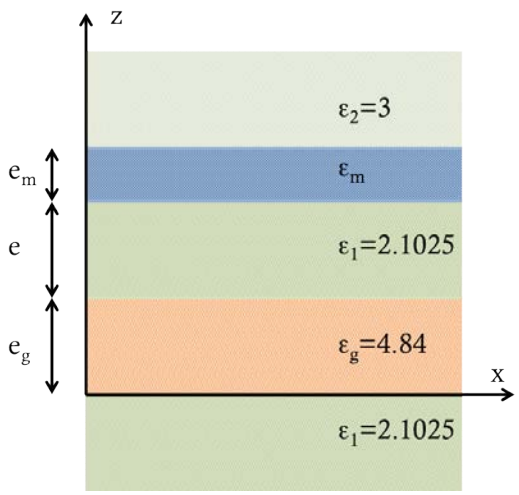

Figure 2: Multilayered structure with a dielectric waveguide (ε_g) with $e_g = 130$ nm and a metallic film (ε_m) with $e_m = 45$ nm inserted between two dielectrics hosts (ε_1 and ε_2) and separated by a dielectric layer. The thickness e is the parameter which is going to change in the simulations.

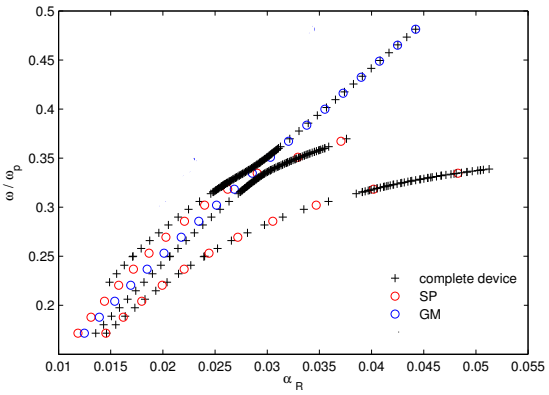

Figure 3: Dispersion relation for a thickness $e = 98$ nm : the normalized frequency (to the plasma frequency ω_p) in function of the real part of the propagation constant α. Taken separately, the modes have the dispersion relations in blue and red.

To reveal the interactions between these modes, we draw the dispersion relations obtained for this structure with the research of the poles of the determinant of the S-matrix. The results are summarized is the figures 3 and 4.

In figure 3, we note the presence of an anticrossing of the dispersion curves (black points) when for the same values of the frequency and the propagation constant, we have a crossing in the uncoupled case (blue and red points). This anticrossing arround $\alpha_R = 0.29$ is the result of hybridization of the guided mode and the SP which lives below the metallic layer, closer to the waveguide. This is the first proof of the strong coupling between these modes.

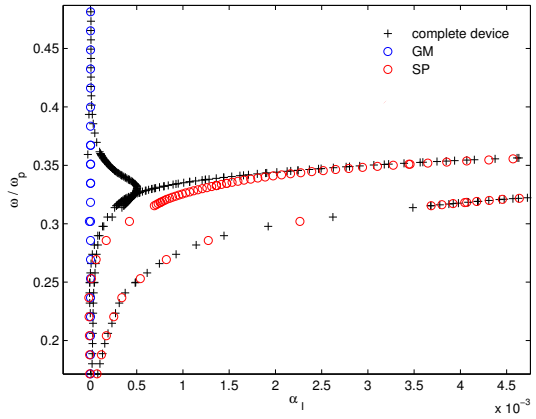

Figure 4: Loss diagram for a thickness $e = 98$ nm : the normalized frequency (to the plasma frequency ω_p) in function of the imaginary part of α. Separately, the absorption of each mode is in blue and red.

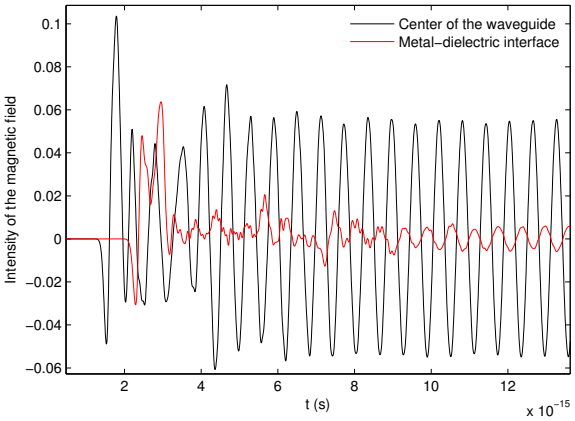

Figure 5: Temporal oscillations between the MG (in black) and the SP under the metal (in red) with a sinusoidal incident beam.

Another way we can illustrate this strong coupling is to consider the curves of the loss diagram in the figure 4. Once again, the blue and ref points are relative to the uncoupled case. The loss diagram reveal the decay of the losses for the SP below the metallic layer. Indeed, whereas the losses for the guided mode increase, those for the SP decrease until obtaining the crossing of the curves : there is an exchange of energy between the guided mode and the plasmon.

Then, it's possible to look at the spatial structure of the hybrid mode. When we excite the structure at the wavelength $\lambda = 409$ nm which corresponds to the anticrossing of the curves, the mode oscillates between the waveguide and the lower interface of the metallic layer. These oscillations are spatial Rabi oscillations with a period bigger than the micrometer.

4. Temporal oscillations

The FDTD allows to study evolution of the structure energy according to time by exciting the structure with a sinusoidal beam. Figure 5 shows oscillations of the field intensity between the center of the waveguide (in black) and the metal-dielectric interface (in red). For this simulations, the permittivity of the metal is taken from equation (5). After the transient regime, the permanent regime takes place at roughly $t = 9$ fs.

In this case, these oscillations can called temporal Rabi oscillations. To obtain a realistic result, we can add a gaussian envelope at the beam. The temporal oscillations decay in time but the life time of the SP is higher than the uncoupled case. The detailed characterization of these oscillations is the next step of our work.

Spatial and temporal oscillations between these modes illustrate the transfert of MG energy towards the SP mode and are associated with the decay of the losses for this last mode.

5. Conclusion

The existence of a strong coupling regime between SP and a guided mode in a multilayered structure was demonstrated. The numerical tools used allow to obtain a rigorous computation of the dispersion relation and loss diagram. The FDTD algorithm reveals temporal oscillations between these modes.

This study is a first step towards the realization of a transfert of energy between these modes like in Spaser [15, 16].

Acknowledgement

The financial support of the Agence Nationale de la Recherche under the project OPTRANS is gratefully acknowledged.

References

[1] H. Raether, Surface plasmons on smooth and rough surfaces and on gratings, *Springer Verlag, Berlin* 1988.

[2] K. H. Drexhage, Interaction of light with monomolecular dye layers, *Progress in Optics*, 12, E. Wolf ed., North-Holland publishing, 1974.

[3] P. T. Worthing, R. M. Amos, W. L. Barnes, Modification of the spontaneous emission rate of Eu^{3+} ions embedded within a dielectric layer above a silver mirror, *Phys. Rev. A*, 59, 865, 1999.

[4] C. Weisbuch, M. Nishioka, A. Ishikawa, Y. Arakawa, Observation of the coupled exciton-photon mode splitting in a semiconductor quantum microcavity, *Phys. Rev. Lett.*, 69 (23), 3314, 1992.

[5] J. Bellessa, C. Symonds, K. Vynck, A. Lemaitre, A. Brioude, L. Beaur, J. C. Plenet, P. Viste, D. Felbacq, E. Cambril, P. Valvin, Giant Rabi splitting between localized mixed plasmon-exciton states in a two-dimensional array of nanosize metallic disks in an organic semiconductor, *Phys. Rev. B.*, 80, 033303, 2009.

[6] J. Bellessa, C. Bonnand, J. C. Plenet, Strong coupling between surface plasmons and excitons in an organic semiconductor, *Phys. Rev. Lett.*, 93, 036404, 2004.

[7] R. L. Chern, D. Felbacq, Artificial magnetism and anticrossing interaction in photonic crystals and split-ring structures, *Phys. Rev. B*, 79, 075118, 2009.

[8] D. Felbacq, Poles and zeros of the scattering matrix associated with defect modes, *J. Phys. A : Math. Gen.*, 33, 7137, 2000.

[9] A. Taflove, S. C. Hagness, Computational electrodynamics : The finite difference time domain method, *Artech House*, 2nd ed., 2000.

[10] A. Mohammadi, M. Agio, Dispersive contour-path finite-difference time-domain algorithm for modelling surface plasmon polaritons at flat interfaces, *Optics Express*, 14 (23), 11330, 2006.

[11] M. Born, E. Worlf, Principles of Optics, *Cambridge U. Press*, 7th ed., 1999.

[12] D. M. Sullivan, Electromagnetic simulation using the FDTD method, *IEEE Press*, 2000.

[13] E. Palik, Handbook of optical constants of solids Academic Press, *Inc., New York*, 1985.

[14] J. Bellessa, S. Rabaste, J. C. Plenet, J. Dumas, J. Mugnier, O. Marty, Eu^{3+}-doped microcavities fabricated by sol-gel process, *Inc., New York*, 1985.

[15] D. J. Bergman, M. I. Stockman, Surface plasmon amplification by stimulated emission of radiation: Quantum generation of coherent surface plasmons in nanosystems, *Phys. Rev. Lett.*, 90, 027402, 2003.

[16] M. A. Noginov, G. Zhu, A. M. Belgrave, R. Bakker, V. M. Shalaev, E. E. Narimanov, S. Stout, E. Herz, T. Suteewong, U. Wiesner, Demonstration of a spaser-based nanolaser, *Nature Letters*, 460, 1110, 2009.

Integrated Localized Surface Plasmon Waveguides

M. Février[1,2], P. Gogol[1,2], A. Aassime[1,2], D. Bouville[1,2], R. Megy[1,2] and B. Dagens[1,2*]
1. Univ Paris-Sud, Laboratoire IEF, UMR 8622, Orsay, F-91405, France
2. CNRS, Orsay, F-91405, France
* corresponding author, E-mail: beatrice.dagens@ief.u-psud.fr

Abstract

Compact plasmonic structures made of gold nanoparticles chains are inserted on silicon optical waveguides. We show that silicon-on-insulator waveguide TE mode energy can be almost totally transferred in a 5 gold nanoparticles plasmonic chain and that this short chain can also behave as a waveguide.

Introduction

The excitation of plasmons in guided configuration remains a crucial step towards a true implementation of plasmonic functions in photonic circuitry. While silicon waveguides allow strong confinement of light and almost transparent propagation, lossy surface plasmon waveguides can exhibit small dimensions at the nanometer scale [1]. Within plasmonics world, localized surface plasmons (LSP) present a decisive advantage for energy concentration in specific spatial region. Electromagnetic wave can indeed be excited and hugely concentrated at the extremities of a non-spherical nanoparticle, or possibly inside a 3D nanogap between two metallic nanoparticle (MNP) [2]. Moreover, localized surface plasmons potentially offer a wide variety of configurations since metallic nanoparticles can be arranged on demand on a waveguide [3, 4].

Several applications could profit from MNP plasmonic waveguides integrated on photonic circuits. The use of long dielectric waveguides would allow positioning optical sources and detectors far from the plasmonic section, thus providing an independent access to this section for optical sensing and biodetection. In addition, the waveguide configuration allows using the entire optical energy available at the waveguide input for launching the plasmon in the coupled MNP chain. In all cases, short MNP chains should be used to avoid excess losses.

Recently we have theoretically and experimentally demonstrated that the transverse plasmonic mode of a 20 gold MNP chain can be efficiently excited by evanescent coupling [5] from a SOI waveguide TE mode, within telecoms wavelength range. Strong coupling between both waveguides occurs as soon as respective propagative mode k-vectors are matched. Coupling strength expresses itself in the very short coupling length, as low as ~560nm on a wide wavelength range. This is attributed both to the high optical confinement in SOI and to the plasmonic resonance.

In this work, we compare the impact of different chain lengths from 5 to 50 MNPs. Especially, we demonstrate that the optical energy carried by the TE silicon-on-insulator (SOI) waveguide mode can be efficiently transferred into the transverse plasmon mode of a coupled metal nanoparticle chain including the case of a very short chain, even if periodic coupling cannot be established.

Sample description and principle

LSP excitation is achieved by interaction between evanescent field of the TE Si waveguide mode and the gold nanoparticles deposited on top (Fig.1). Ellipsoidal shape, size and spacing of MNPs are accurately determined by using finite-difference time-domain (FDTD) simulations so that the transverse plasmonic T1 [6] chain mode can be excited in the transmission range of the SOI waveguide (λ>1.1 µm). Center-to-center distance between particles is equal to 150 nm for optimum dipolar coupling. Silicon ridge waveguides have a 500 × 220 nm^2 cross section. Gold MNP chains were fabricated using electron-beam lithography followed by a lift-off process. They are made of 1 nm thick titanium adhesion layer and 30 nm gold layer deposited by electron-beam evaporation. The as-cleaved Si waveguide supporting MNPs was 4 mm long and was ended by coupling tapers for an easy characterization.

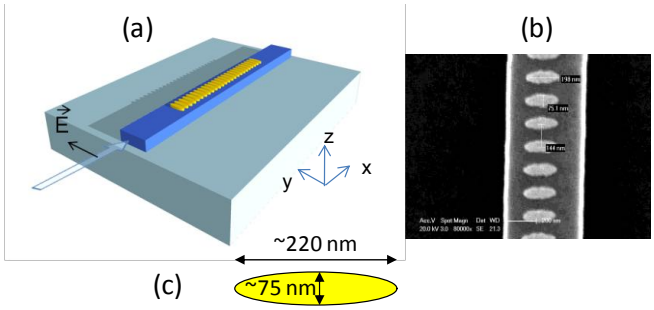

Figure 1: Sample: (a) schematic view of a gold nanoparticle chain on top of a SOI waveguide; (b) scanning electron micrograph of 7 gold nanorods of a 20-nanoparticles chain; (c) typical size of the ellipsoids.

Such structures were fabricated with chains of 5, 20 and 50 MNPs, with ellipsoids typical dimensions of respectively, 200 × 80 × 30 nm^3, 220 × 80 × 30 $nm^3$and 220 × 75 × 30 nm^3.

Experiment

Samples were characterized by optical transmission through the structure. The waveguide transmission spectra were measured with the experimental setup shown in Fig. 2. The output beam of a tunable laser emitting in the wavelength range from 1260 to 1630 nm was injected into the sample using a lensed polarization maintaining fiber (PMF). The PMF was positioned in such a way that the polarization of the light injected into the waveguide was mainly TE. The light at the sample output was collected by an objective with x20 magnification and 0.35 numerical aperture, and was focused onto a power meter**.** A second polarizer was used to eliminate parasitic TM polarized light.
In each case, a reference waveguide without MNP was used on the same chip for transmission normalization.

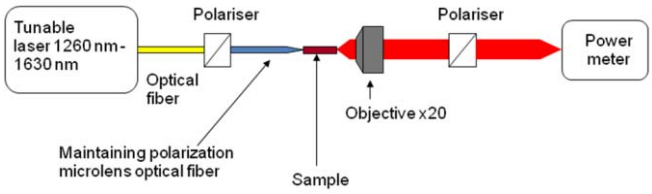

Figure 2: Schematic view of the transmission measurement setup.

Simulation

Numerical simulations were performed using a FDTD model incorporating measured parameters of the fabricated structures. Accurate dispersion data were introduced for home deposited gold after fitting a Drude model to ellipsometric measurements. The presence of a thin layer of native oxide between Si and Ti was also accounted for in FDTD calculations. The layer thickness was measured to be 3nm by scanning electron microscopy for our technological process.

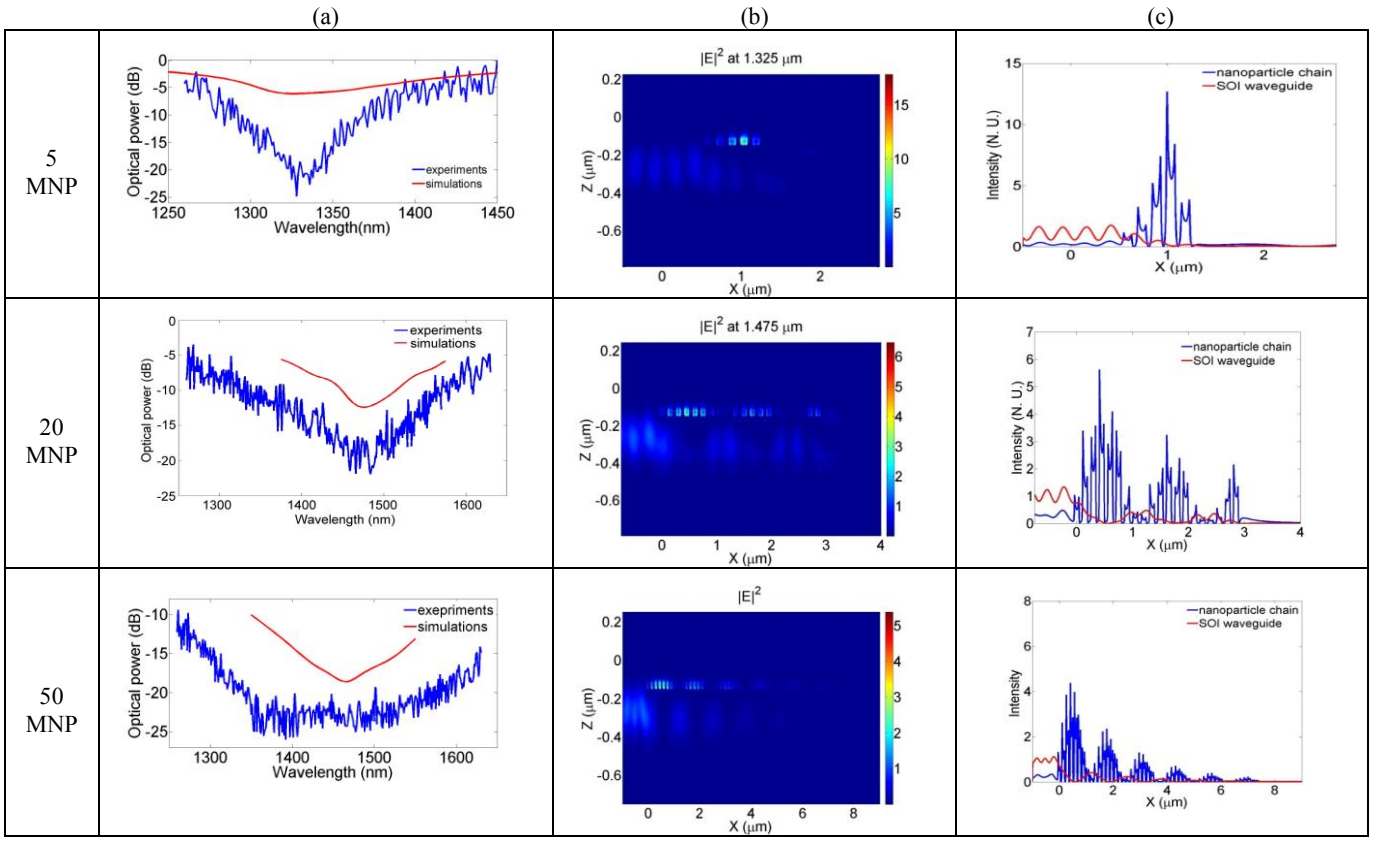

Figure 3: Excitation of LSP for 5 to 50 MNP chains integrated on SOI waveguide: (a) fiber-to-fiber transmission spectra (red: simulation, blue: experiment); electric field intensity evolution along propagation axis x at transmission minimum wavelength: (b) 2D cartographies at the middle of the structure and at minimum transmission wavelength, (c) intensity in the center of SOI waveguide and MNP chain.

The calculated transmission spectrum of Fig. 3(a) was obtained using these input data and 3D mesh with dimensions smaller than 3nm in the MNP region. As seen, there is an excellent agreement between calculations and measurements. The slightly broader resonance found in measurements is readily explained by the size distribution of MNPs.

Results and discussion

The interaction of the SOI and the LSP modes is studied from experimental and theoretical data for three different chain lengths. In Figure 3 are represented, for 5, 20 and 50 MNP chain lengths, respectively (a) the fiber-to-fiber transmission spectrum of the samples, (b) the calculated longitudinal side view of the middle cut structure field intensity cartography at the minimum transmission wavelength, and (c) the corresponding evolution along propagation direction of the intensity in the middle of the MNP chain (blue curves) and of the SOI waveguide (red curves).

LSP waveguide behavior within MNP chain is obtained thanks to energy transfer via dipolar interactions between closely spaced metal nanoparticles [3,6]. However this behavior occurs only if collective (or long distance) oscillation of the dipoles is realized, i.e. if a mode specific to the chain exists. LSP mode excitation is then obtained if the wave vectors of the SOI mode and the LSP mode are similar.

In the longer structures (20 and 50 MNPs), optical intensity oscillates between SOI waveguide and plasmonic chain: the full structures behave like coupled waveguides. We can deduce that MNP chains behave themselves like a waveguide at the considered wavelength.

We have shown previously that this behavior is obtained only in a restricted wavelength range [5]. Indeed, below the light line MNP chain dispersion curve has a maximum (as shown in [7]) near the individual MNP resonance frequency. For this reason, there is no solution for dispersion curve at higher frequency (or shorter wavelength) than this resonant frequency, and then the chain cannot collectively resonate and behave as a waveguide. On the transmission curve, this occurs at ~1440 nm for both 20 and 50 MNPs chains and this coincides with a slope change.

For both chain lengths, when collective excitation occurs, the oscillation period between coupled waveguides is lower than 600nm, which corresponds to a coupling constant as high as 2805 mm^{-1} according to coupled-mode theory [8]. This allows almost totally transferring the incident optical intensity in the fourth or fifth nanoparticle of the chain, during the first oscillation.

Interestingly this property is preserved also in the case of the 5 MNP chain. This very short chain can also behave as a waveguide, and the SOI mode can be then transferred in the fourth MNP as shown in Fig. 3(b) and (c). In that case, waveguide behavior of the 5MNP chain cannot be deduced from periodic oscillation between SOI and plasmonic chain since the latter is too short to allow recoupling in SOI. Let's examine top view of calculated y-component electrical field phase along the chain, at 1325 nm (Fig. 4). Phase is clearly distorted by MNPs. Excitation of collective mode in MNP chain is revealed by this phase distortion which shows independent propagation mode in the chain, similarly to results obtained with 20MNP chain [5]. These assumptions, sustained by dipoles electric field analysis, confirm the excitation of proper LSP modes in 5 MNP chains.

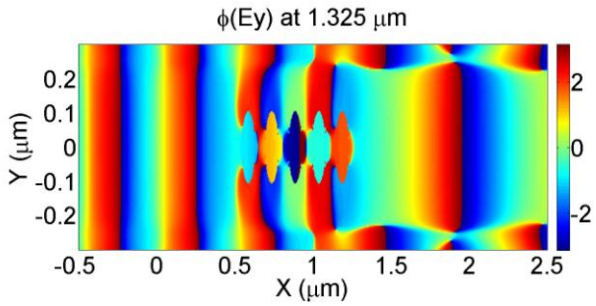

Figure 4: y-component of E-field phase in 5MNP chain at transmission minimum (λ=1325 nm). Cut-view at the middle of MNP chain. SOI waveguide position is at y=+/-0.25μm

Conclusions

As a consequence coupling between a dielectric waveguide and a coupled MNP chain allows not only for a highly efficient excitation of the chain plasmonic collective mode, but also for very short distance (<600 nm) excitation of this mode. We have demonstrated that this behavior can be obtained for long (20 to 50 MNP) or short (5 MNP) chains with similar coupling distance. Since propagation losses decrease with the interaction distance, short MNP chains represent an attractive way to implement LSP based integrated optical devices with nanometer sizes and moderate losses in photonic circuits.

Acknowledgements

This work has been supported by the Agence Nationale de la Recherche under contract PLACIDO N°ANR-08-BLAN-0285-01. The M.F. grant has been funded by Region Ile-de-France.

References

1. Barnes, W. L.; Dereux, A.; Ebbesen, T. W. Surface plasmon subwavelength optics. Nature 2003, 424, 824-511.
2. Juan, M.L.; Righini, M.; Quidant, R. Plasmon nano-optical tweezers, Nature Photon. 2011, 5, 349-356.

3. Brongersma, M.L.; Hartman, J.W.; Atwater, H.A. Electromagnetic energy transfer and switching in nanoparticle chain arrays below the diffraction limit. Phys. Rev. B 2000, 62, R16 356-R16 359.
4. Zou S.; Shatz G.C. Metal nanoparticle array waveguides: proposed structures for subwavelength devices. Phys. Rev. B 2006, 74, 125111.
5. M. Février, P. Gogol, A. Aassime, R. Mégy, C. Delacour, A. Chelnokov, A. Apuzzo, S. Blaize, J;-M. Lourtioz, and B. Dagens, Giant Coupling Effect between Metal Nanoparticle Chain and Optical Waveguide. Nano Letters 2012, 12 (2), pp 1032–1037.
6. Crozier, K. B.; Togan, E.; Simsek, E.; Yang, T. Experimental measurement of the dispersion relations of the surface plasmon modes of metal nanoparticle chains. Optics Express 2007, **15**, 17482-17493.
7. Femius Koenderink, A.; de Waele, R.; Prangsma, J.C.; Polman, A. Experimental evidence for large dynamic effects on the plasmon dispersion of subwavelength metal nanoparticle waveguides. Phys. Rev. B 2007, 76, 201403(R).
8. Chuang, S. L. Physics of optoelectronic devices. Ch 8 (John Wiley & sons, New-York, 1995).

Enhanced Nonlinear Effects in Metamaterials and Plasmonics

Christos Argyropoulos, Pai-Yen Chen, and Andrea Alù

Department of Electrical and Computer Engineering, The University of Texas at Austin
1 University Station C0803, Austin, TX 78712, USA
*corresponding author: alu@mail.utexas.edu

Abstract

In this paper we provide an overview of the anomalous and enhanced nonlinear effects available when optical nonlinear materials are combined inside plasmonic waveguide structures. Broad, bistable and all-optical switching responses are exhibited at the cut-off frequency of these waveguides, characterized by reduced Q-factor resonances. These phenomena are due to the large field enhancement obtained inside specific plasmonic gratings, which ensures a significant boosting of the nonlinear operation. Several exciting applications are proposed, which may potentially lead to new optical components and add to the optical nanocircuit paradigm.

1. Introduction

The research fields of plasmonics and metamaterials have recently led to a series of exciting applications in optics, such as subwavelength imaging [1], the cloak of invisibility [2], [3] and ε-near-zero (ENZ) media [4], [5]. The linear operation of these devices has been widely studied during the last years and successfully implemented experimentally [6]-[11]. However, novel directions to the optical metamaterial research are promised by the inclusion of gain [12] and nonlinear materials [13], [14].

In this work, we mainly focus on an overview of the wave interaction of third-order Kerr nonlinear $\chi^{(3)}$ materials loaded to plasmonic metamaterial waveguides. Kerr optical materials generally exhibit a very weak nonlinearity at optical frequencies, with values in the order of $10^{-20}\, m^2 / V^2$ [15]. In the past, several research studies have focused on enhancing these weak third-order nonlinear effects based on plasmonic structures. For instance, Kerr nonlinear materials may be loaded at the gap of plasmonic nanoantennas to achieve stronger nonlinear effects, such as optical bistability and efficient all-optical switching [16]. The strong resonant fields confined at the nanoantenna's nanogap are the main reason of the boosted nonlinear performance. Nevertheless, these effects are based on narrowband resonant operation characterized by high Q-factors. Even more importantly, the strongly enhanced fields are confined to an extremely small volume at the gap of the nanoantenna, a fact which limits the actual size of the effectively enhanced Kerr material, limiting the overall nonlinear performance.

Alternative approaches to increase third-order nonlinear effects have been based on plasmonic gratings [17], [18] and exotic metamaterial structures [19]. Again, all these works suffer from narrowband operation (high Q-factor resonances). In particular, the authors in [17] proposed to use the extraordinary optical transmission (EOT) concept [20] to achieve broad optical bistability. EOT is based on Fabry-Perot (FP) constructive wave interference, leading to a well-known standing wave distribution in the slits. All these resonant phenomena base the nonlinearity enhancement on field localization and, as in Purcell effect, require high Q-factors and narrow bandwidths to achieve stronger nonlinearity enhancement.

Here, we propose an improved way to achieve strong optical nonlinearities, combining lower Q-factors and a larger available volume over which the nonlinear effect may be increased. An ideal field configuration to efficiently boost optical nonlinear effects would require strong, highly confined, homogeneous electric fields with uniform phase over a large volume. All of these properties surprisingly exist in ENZ metamaterial structures. The quasi-static field distribution inside an ENZ channel can provide highly enhanced homogeneous fields combined with constant phase distribution [4], [5]. Moreover, these effects can be realized for elongated, theoretically infinite, channels, whose shape may be bent in arbitrary ways. Phase matching is also achieved at the ENZ operation, a critical advantage towards boosted nonlinearities, especially when exciting electrically large nonlinear samples.

In this paper, we review and present additional numerical results on the scattering and bistable properties of a three-dimensional (3D) array of plasmonic ENZ channels standing in free-space, a geometry firstly presented in [21]. Inside these plasmonic waveguides, ENZ and FP tunneling can be obtained in distinct frequency regimes, allowing an easy comparison between the two methods to enhance the nonlinear response of Kerr materials. The ENZ resonance is realized at the cut-off frequency of the slits, as it will be discussed in the following, a function of the transverse dimension of the slits, i.e., their width. On the contrary, the FP resonances arise at higher frequencies, when the longitudinal dimension of the slits, i.e., their length, is proportional to half of the guided wavelength in the slit. Note that the proposed structure is different from the one proposed in [17], where only FP resonances are supported, since the slits were 2-D, without cut-off. We will introduce Kerr nonlinear materials inside the plasmonic channels and we will verify that at the ENZ frequency regime stronger bistable effects are dominant compared to FP tunneling

[21]. More importantly, we will explicitly demonstrate that broad bistability and strong all-optical switching can be obtained at the ENZ operation, which is characterized by reduced Q-factor resonances, different to other available techniques for plasmonic enhanced optical nonlinearities [16]-[19]. Finally, the effective permittivity at the cut-off frequency of the array of plasmonic waveguides will be derived applying a homogenization procedure. We will demonstrate that the proposed plasmonic grating in fact constitutes an artificial nonlinear metamaterial with ENZ linear properties and drastically enhanced nonlinear properties. This unconventional response opens the possibility to modulate from low positive to low negative values the effective permittivity, as a function of the applied intensity and of the type of loaded third-order nonlinear material. We envision novel optical nonlinear devices inspired by the proposed structure, such as self-tunable slow-light devices, low-intensity optical memories, switches and tunable sensors.

2. Theoretical analysis of the problem

The geometry of the plasmonic geometry under study is depicted in Fig. 1. Narrow rectangular apertures loaded with third-order $\chi^{(3)}$ Kerr nonlinear optical materials are carved in a thick silver (Ag) screen. The design parameters are chosen to be: height $t = 40nm$, width $w = 200nm$, length $l = 500nm$ and periods $a = b = 400nm$. These dimensions are selected on purpose in order to obtain the ENZ frequency close to first and second FP resonances, in order to be able to clearly compare their performance, as it will be shown later in this paper. Note that the height of the channels is chosen much smaller than their width $t \ll w$ and the periods are selected $a, b \gg t$ with the aim to achieve stronger field confinement at the ENZ operation [5].

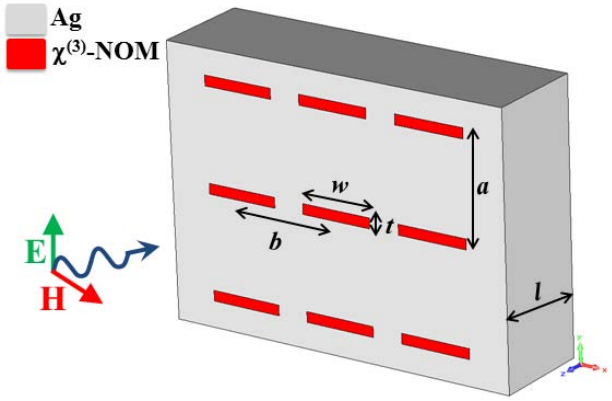

Figure 1: A plane wave impinges at normal incidence on a nonlinear ENZ metamaterial slab. Narrow rectangular apertures loaded with third-order Kerr nonlinear optical materials (red) are carved in an elongated silver screen (light grey).

The slab is composed of Ag and has a relative permittivity which follows the Drude dispersion model at optical frequencies: $\varepsilon_{Ag} = \varepsilon_\infty - f_p^2 / \left[f\left(f + i\gamma\right)\right]$, $f_p = 2175$ THz, $\gamma = 4.35$ THz, $\varepsilon_\infty = 5$ [22]. The apertures are loaded with Kerr nonlinear material with a relative permittivity $\varepsilon_{ch} = \varepsilon_L + \chi^{(3)} \left|E_{ch}\right|^2$. The linear permittivity is chosen $\varepsilon_L = 2.2$ and the nonlinear susceptibility $\chi^{(3)} = 4.4 \times 10^{-20} m^2 / V^2$. These are typical values for nonlinear optical materials [15]. Finally, the magnitude of the localized electric field inside the elongated channels is depicted as $\left|E_{ch}\right|$.

The dominant transmitted mode in this type of rectangular plasmonic waveguides is quasi-TE_{10}. It 'feels' an effective near-zero permittivity, when we operate at the cut-off frequency of the plasmonic channels. In our previous works [5], [21], we derived a simple homogenization approach to describe the effective permittivity of the nonlinear structure shown in Fig. 1. The effective permittivity is given by the formula

$$\varepsilon_{eff} = \frac{\beta_{pp}^2}{k_0^2} - \frac{\pi^2 \varepsilon_{ch}}{\left(\beta_{pp} w + 2\sqrt{\varepsilon_{ch}} / \sqrt{\mathrm{Re}\left[-\varepsilon_{Ag}\right]}\right)^2}, \qquad (1)$$

where β_{pp} is the guided wavenumber in the associated parallel-plate plasmonic waveguide with the same height t as the apertures, but infinite width [23]. Equation (1) is also dependent to the permittivity of the material loaded inside the slits ε_{ch}, the silver's permittivity ε_{Ag} and the width w of the plasmonic waveguides. In the limit $\varepsilon_{Ag} \to -\infty$ (Ag supposed to be perfectly conductor) and $\beta_{pp} = k_0 \sqrt{\varepsilon_{ch}}$, Eq. (1) takes the simple form

$$\varepsilon_{eff} = \varepsilon_{ch} - \left(\frac{\pi}{k_0 w}\right)^2 \qquad (2)$$

and the classic cut-off condition is obtained in order to achieve zero effective permittivity $\varepsilon_{eff} = 0$, which is: $w = \pi / (k_0 \sqrt{\varepsilon_{ch}})$. The nonlinear Kerr permittivity may be substituted into the channel permittivity in Eq. (2) and an elegant and compact formula may be derived for the effective permittivity of the slab:

$$\varepsilon_{eff} = \varepsilon_L - \frac{\pi^2}{k_0^2 w^2} + \chi^{(3)} \left|E_{ch}\right|^2. \qquad (3)$$

At the quasi-static ENZ operation, the enhanced electric field inside the slits can be directly evaluated by power conservation at the discontinuities in the E and H planes of the grating [21]. It varies only with the geometric parameters

of the plasmonic channels and the incident electric field, providing the following result:

$$E_{ch} = \frac{(ba)}{(tw)} E_{in}. \quad (4)$$

Hence, Eq. (4) may be substituted in Eq. (3) to obtain the general formula for the effective permittivity of the nonlinear metamaterial slab shown in Fig. 1 as a function of the structure's geometry, nonlinear material parameters and input intensity:

$$\varepsilon_{eff} = \varepsilon_L - \frac{\pi^2}{k_0^2 w^2} + \frac{b^2 a^2}{w^2 t^2} \chi^{(3)} |E_{in}|^2. \quad (5)$$

Equation (5) explicitly describes the effective permittivity of an artificial nonlinear metamaterial at its ENZ operation. The proposed nonlinear metamaterial has very interesting properties. First, it can realize an enhanced effective nonlinear susceptibility, which varies only with the geometrical parameters of the structure and it is equal to

$$\chi_{eff}^{(3)} = \left(\frac{ba}{wt}\right)^2 \chi^{(3)}. \quad (6)$$

As a result, the effective nonlinearity in the current geometry at the ENZ resonance is strongly enhanced: $\chi_{eff}^{(3)} = 400\chi^{(3)}$. Furthermore, at the cut-off frequency (ENZ operation) $\varepsilon_L = \pi^2/(k_0 w)^2$. The corresponding effective permittivity varies only with its nonlinear part in Eq. (5), and it is given by the simple formula:

$$\varepsilon_{eff} = \frac{b^2 a^2}{w^2 t^2} \chi^{(3)} |E_{in}|^2. \quad (7)$$

Equation (7) clearly shows that the proposed metamaterial design can inherently modulate its effective permittivity only by changing the nonlinear susceptibility of the material or the structure's geometry. It can lead to positive or negative values of effective permittivities, in case focusing nonlinearities $\chi^{(3)} > 0$ or defocusing nonlinearities $\chi^{(3)} < 0$ are employed, respectively.

The aforementioned concept is graphically depicted in Fig. 2(a). It is obvious that the effective permittivity can take positive/negative values with a maximum/minimum value of ±0.4 when focusing/defocusing nonlinearities are loaded inside the slits of the metasurface. In a similar way, the effective permittivity versus the input optical intensity is plotted in Fig. 2(b). Now, a linear curve is obtained due to the relationship: $I_{in} = |E_{in}|^2/2\eta_0$, where $\eta_0 \simeq 377\Omega$ is the free-space impedance. The proposed artificial nonlinear metamaterial can have plenty of interesting potential applications in the research field of metamaterials, such as novel slow-wave devices and nonlinear cloaking coatings.

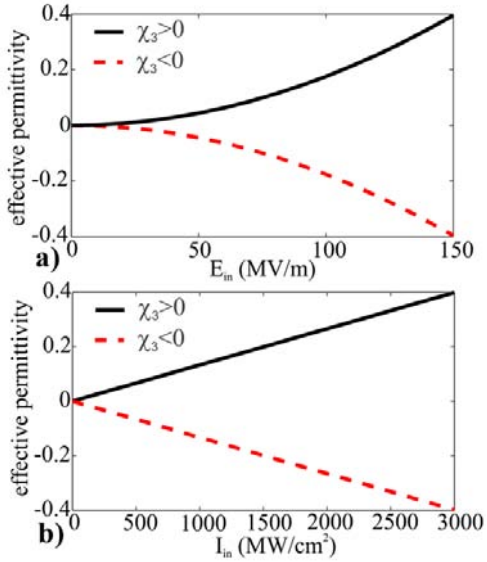

Figure 2: The effective permittivity of an artificial nonlinear ENZ metamaterial as in Fig. 1, as a function of: (a) the input electric field and (b) the input optical intensity. Positive values of effective permittivity are obtained for focusing nonlinearities $\chi^{(3)} > 0$ (black solid lines) and negative values for defocusing nonlinearities $\chi^{(3)} < 0$ (red dashed lines) for both figures.

3. Linear and nonlinear operation

First, we study the linear case, when linear dielectrics are loaded inside the slits of Fig. 1. The material loaded in the channels has similar permittivity as glass, which is given by: $\chi^{(3)} = 0 \rightarrow \varepsilon_{ch} = \varepsilon_L = 2.2$. The transmission coefficient of the proposed structure is computed with rigorous full wave simulations. The numerical simulations are based on finite integration technique and they employ commercially available software [24]. The transmission coefficient of the structure as a function of frequency is plotted in Fig. 3. The first transmission peak is found around $f_{ENZ} = 295THz$ and it corresponds to the cut-off frequency of the plasmonic rectangular waveguide. This peak is independent of the channel's length and it has a moderate Q-factor $Q_{ENZ} \simeq 48$. Two distinct resonances follow the ENZ operation, which correspond to the first and second FP frequency regimes. They are found at approximately $f_{FP1} = 322THz$ and $f_{FP2} = 384THz$ for the current geometry. These resonances depend highly on the channel's length, and they have similar Q-factors as the ENZ operation. Note that with further optimization of the current geometry, these resonances may be easily tuned to optical frequencies rather than infrared. Moreover, the Q-factor of the ENZ resonance can become even lower, if we further decrease the channel's length [5].

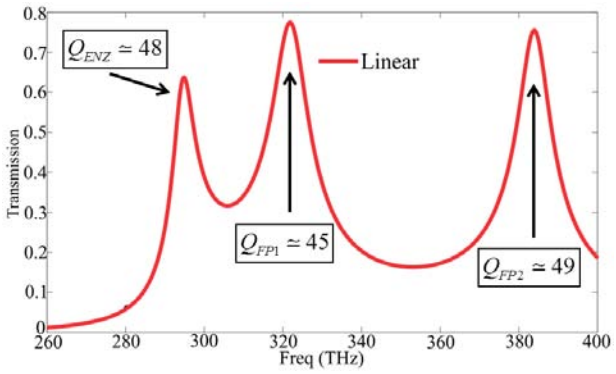

Figure 3: Transmission coefficient versus frequency for linear material loaded in the slits shown in Fig. 1. Three distinct resonances (ENZ, FP 1, FP 2) exist with almost similar, relative low, Q-factors.

Next, the 3D electric field distributions are computed and demonstrated in Fig. 4 inside one plasmonic waveguide slit at the ENZ, first FP and second FP resonances. These distributions further help us to achieve a more in depth physical understanding of each tunneling mechanism. The field distribution in the ENZ case is drastically different compared to the FP resonances. Homogeneous, highly confined and constant phase fields are obtained at the ENZ frequency [Fig. 4(a)], contrary to the standing wave field distributions of the first and second order FP resonances [Figs. 4(b), (c)]. This explains the reason why the transmission at the ENZ is slightly reduced compared to FP resonances (see Fig. 3). The enhanced homogeneous fields will be more dissipated due to the losses in the silver walls of the plasmonic waveguide. In a similar and even stronger way, we expect that the nonlinear effects will be boosted at the ENZ frequency, when the slits will be filled with Kerr nonlinear media, due to the high total field enhancement.

Now, we load Kerr nonlinear materials inside the slits to study the nonlinear response of the geometry of Fig. 1. The nonlinear transmission versus frequency for a moderate input optical intensity of $I_{in} = 3000\,MW/cm^2$ is depicted in Fig. 5. It is obvious that a broader bistable performance is obtained at the ENZ operation compared to weaker bistable curves at both FP resonances. This is a direct consequence of the enhanced homogeneous total field at the ENZ operation (the comparison was shown in Fig. 4). Moreover, it is very important to stress that the current broad bistable effects obtained at the ENZ frequency can be achieved with moderate input intensities and with reduced Q-factor resonances, computed before in Fig. 3. This very interesting enhanced nonlinear optical effect is demonstrated for this specific example, but it may be tuned to different frequencies and geometries, as a function of the desired application. We speculate that this phenomenon can directly lead to more practical and efficient optical memories and switches, due to the larger hysteresis available at the ENZ frequency.

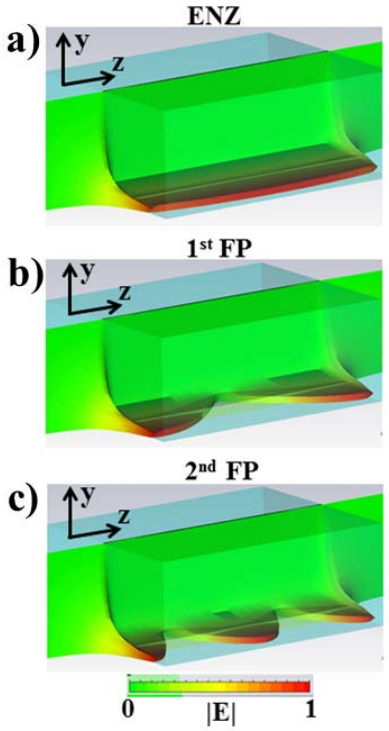

Figure 4: The electric field distributions are computed inside the narrow rectangular apertures at the a) ENZ operation and at the b) 1st FP and c) 2nd FP frequency resonances. Homogeneous and highly confined fields are obtained at the ENZ frequency (a), on the contrary standing wave field patterns are observed at the first (b) and second (c) FP frequencies.

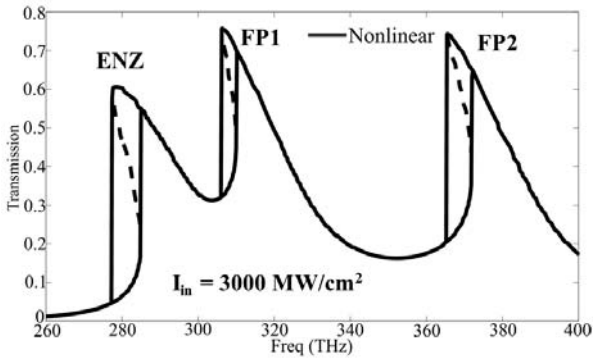

Figure 5: Transmission coefficient versus frequency for the slab nonlinear operation. A strongest hysteresis and bistable response is clearly obtained at the ENZ frequency.

4. Conclusions

In this work, we have demonstrated a robust way to achieve boosted optical nonlinear responses with moderate optical intensities and reduced Q-factor resonances. The design of artificial ENZ metamaterials standing in free-space was proposed and the formula of its effective permittivity was computed. Interestingly, its performance can be purely modulated by the type of nonlinear materials introduced inside its apertures. Positive or negative permittivity values can be obtained with plenty of potential applications in the field of artificially engineered nonlinear metamaterial devices. We believe that the proposed structure can be fabricated within available nanofabrication methods, such as nanoskiving [25]. The peculiar quasi-static properties of effective ENZ media obtained at the channel cut-off were utilized in order to achieve huge bistable response with a low Q-factor resonance confined in a large spatial extent. Finally, in a similar way to nonlinearities, the Purcell factor can be enhanced at the ENZ operation without the usual restrictions of small volumes and high Q-factor resonances [26]. This can have interesting potential applications in future optical nanocircuits and laser designs.

Acknowledgements

This work has been supported by the ONR MURI grant No. N00014-10-1-0942.

References

[1] J. B. Pendry, "Negative refraction makes a perfect lens," *Phys. Rev. Lett.* 85, 3966, 2000.

[2] A. Alù, N. Engheta, "Achieving transparency with plasmonic and metamaterial coatings," *Phys. Rev. E* 72, 016623, 2005.

[3] J. B. Pendry, D. Shurig, D. R. Smith, "Controlling electromagnetic fields," *Science* 312, 1780, 2006.

[4] M. G. Silveirinha, N. Engheta, "Tunneling of Electromagnetic Energy through Subwavelength Channels and Bends using ε-Near-Zero Materials," *Phys. Rev. Lett* 97, 157403, 2006.

[5] A. Alù, N. Engheta, "Light squeezing through arbitrarily shaped plasmonic channels and sharp bends," *Phys. Rev. B* 78, 035440, 2008.

[6] N. Fang, H. Lee, X. Zhang, "Sub–Diffraction-Limited Optical Imaging with a Silver Superlens," *Science* 308, 534, 2005.

[7] D. Schurig, J. J. Mock, B. J. Justice, S. A. Cummer, J. B. Pendry, A. F. Starr, D. R. Smith, "Metamaterial Electromagnetic Cloak at Microwave Frequencies," *Science* 314, 977, 2006.

[8] B. Edwards, A. Alù, M. G. Silveirinha, N. Engheta, "Experimental Verification of Plasmonic Cloaking at Microwave Frequencies with Metamaterials," *Phys. Rev. Lett.* 103, 153901, 2009.

[9] D. Rainwater, A. Kerkhoff, K. Melin, J. C. Soric, G. Moreno, A. Alù, "Experimental Verification of Three-Dimensional Plasmonic Cloaking in Free-Space," *New Journ. of Phys.* 14, 013054, 2012.

[10] B. Edwards, A. Alù, M. E. Young, M. Silveirinha, N. Engheta, "Experimental Verification of Epsilon-Near-Zero Metamaterial Coupling and Energy Squeezing Using a Microwave Waveguide," *Phys. Rev. Lett.* 100, 033903, 2008.

[11] R. Liu, Q. Cheng, T. Hand, J. J. Mock, T. J. Cui, S. A. Cummer, D. R. Smith, "Experimental Demonstration of Electromagnetic Tunneling Through an Epsilon-Near-Zero Metamaterial at Microwave Frequencies," *Phys. Rev. Lett*. 100, 023903, 2008.

[12] S. Xiao, V. P. Drachev, A. V. Kildishev, X. Ni, U. K. Chettiar, H.-K. Yuan, V. M. Shalaev, "Loss-free and active optical negative-index metamaterials," *Nature* 466, 735, 2010.

[13] A. Bouhelier, M. Beversluis, A. Hartschuh, L. Novotny, "Near-Field Second-Harmonic Generation Induced by Local Field Enhancement," *Phys. Rev. Lett.* 90, 013903, 2008.

[14] N. I. Zheludev, "The road ahead for metamaterials," *Science* 328, 582, 2010.

[15] R. W. Boyd, *Nonlinear Optics*, Academic, London, 1992.

[16] P.-Y. Chen, A., Alù, "Optical nanoantenna arrays loaded with nonlinear materials," *Phys. Rev. B* 82, 235405, 2010.

[17] J. A. Porto, L. Martín-Moreno, F. J. García-Vidal, "Optical bistability in subwavelength slit apertures containing nonlinear media," *Phys. Rev. B* 70, 081402(R), 2004.

[18] G. D'Aguanno, D. Ceglia, N. Mattiucci, M. J. Bloemer, "All-optical switching at the Fano resonances in subwavelength gratings with very narrow slits," *Opt. Lett.* 36, 1984, 2011.

[19] M. Ren, B. Jia, J.-Y. Ou, E. Plum, J. Zhang, K. F. MacDonald, A. E. Nikolaenko, J. Xu, M. Gu, N. I. Zheludev, "Nanostructured Plasmonic Medium for Terahertz Bandwidth All-Optical Switching," *Adv. Mater.* 23, 5540, 2011.

[20] F. J. García-Vidal, E. Moreno, J. A. Porto, L. Martín-Moreno, "Transmission of Light through a Single Rectangular Hole," *Phys. Rev. Lett.* 95, 103901, 2005.

[21] C. Argyropoulos, P.-Y. Chen, G. D'Aguanno, N. Engheta, A. Alù, "Boosting Optical Nonlinearities in ε-Near-Zero Plasmonic Channels," *Phys. Rev. B* 85, 045129, 2012.

[22] P. B. Johnson, R. W. Christy, "Optical Constants of the Noble Metals," *Phys. Rev. B* 6, 4370, 1972.

[23] A. Alù, N. Engheta, "Optical nanotransmission lines: synthesis of planar left-handed metamaterials in the infrared and visible regimes," *J. Opt. Soc. Am. B* 23, 571, 2006.

[24] CST Microwave Studio™ 2011, CST of America, Inc.

[25] Q. Xu, R. M. Rioux, M. D. Dickey, G. M. Whitesides, "Nanoskiving: A New Method To Produce Arrays of Nanostructures," *Acc. Chem. Res.* 41, 1566, 2008.

[26] E. M. Purcell, "Spontaneous Emission Probabilities at Radio Frequencies," *Phys. Rev.* 69, 681, 1946.

Multiband Slot-Based Dual Composite Right/Left-Handed Transmission Line

Elena Abdo-Sánchez*, Teresa M. Martín-Guerrero and Carlos Camacho-Peñalosa

Departamento de Ingeniería de Comunicaciones, E. T. S. Ingeniería de Telecomunicación,
Universidad de Málaga, Campus de Teatinos, 29071 Málaga, Spain.
*E-mail: elenaabdo@ic.uma.es

Abstract

A dual Composite Right-/Left-Handed Transmission Line (CRLH TL) implementation that presents multiband behaviour is proposed in this contribution. The artificial TL is realized by loading a host microstrip line with alternate rectangular stubs and slots. The required series and shunt immittances are respectively provided by the slot and the stub. Due to the distributed nature of these immittances, the resultant phase response presents theoretically infinite RH and LH alternate bands, thus being appropriate for multiband applications. The design methodology is described with the help of a proposed TLs-based equivalent circuit and highlights the simplicity for balance condition. Full wave simulated results of the dispersion characteristics and frequency response of a unit-cell and a three-cells structure are presented.

1. Introduction

Although metamaterials have been theoretically studied since the appearance of Veselago's paper [1], this field did not experience much activity until 2002, when three different research groups developed the Transmission Line (TL) approach of metamaterials [2, 3, 4]. This new approach allowed countless applications in microwave engineering to arise. Most of them are based on the so-called Composite Right-/Left-Handed Transmission Line (CRLH), which behaves as a LH medium at low frequencies and as RH at higher frequencies under certain assumptions. After the introduction of the CRLH TL, artificial TLs with different topologies were proposed, like the 'dual' [5] or the 'extended' [6]. Even a derivation of artificial TLs of arbitrary order was presented in [7]. This way, a specific dispersion diagram can be synthesized by simply cascading the necessary unit-cells.

Several realizations of artificial TLs with high order in planar technology can be found in the literature. Recently, a planar dual CRLH TL based on the use of Defected Ground Structure (DGS) with inter-digital gap was demonstrated [8]. An alternative for this structure was presented by the authors in [9], which makes use of alternate dumbbell-shaped DGSs and stubs for building a triband artificial TL and has the advantage of simple design for the balanced case. However, its important stop band and its lack of matching over the rest of the studied bandwidth have limited its possible applications. In this contribution we present a variant of the mentioned structure, which uses alternate rectangular stubs and slots for providing the required shunt and series immittances, respectively. The proposed unit-cell presents improved frequency behaviour, with reduced stop bands. Moreover, the analysis of the structure and design methodology are provided here in terms of the distributed immittances, instead of lumped elements, thus extending its validity and being more accurate.

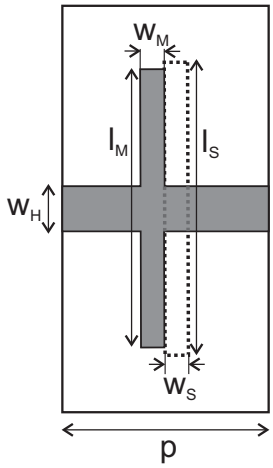

Figure 1: Unit-cell geometry.

This contribution is organized as follows. Section 2 describes the geometry of the proposed unit-cell and its equivalent circuit using TLs. Section 3 deals with the design methodology for achieving a balance CRLH TL. In Section 4, the results for a design example of unit-cell and for the corresponding three-cells CRLH TL are shown. Finally, Section 5 summarizes the main conclusions.

2. Unit-Cell Geometry And Equivalent Circuit

The proposed unit-cell is shown in Fig. 1. It consists of a host microstrip TL loaded by a rectangular stub and a rectangular slot etched on its ground plane. In the figure, w_H stands for the width of the host microstrip line; w_M and l_M, for the stub width and length, respectively, and w_S and l_S represent the slot width and length, respectively. In addition, p stands for the unit-cell length.

A slot etched on the ground plane of a microstrip line behaves as a series impedance. This impedance can be ap-

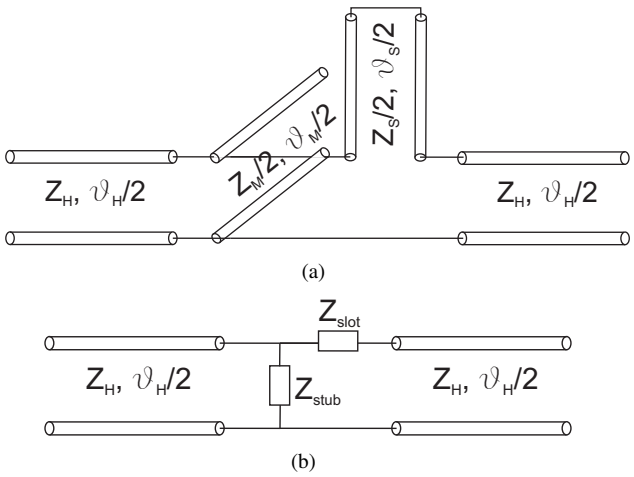

Figure 2: Equivalent circuit of the proposed unit-cell of Fig. 1. (b) is a simplified version of (a).

proximated to the one presented by the corresponding slotline terminated in short circuit. Likewise, a stub behaves as a shunt admittance which is equivalent to the one presented by the corresponding microstrip line terminated by open circuit. Therefore, the slot and stub equivalent impedances can be written as follows:

$$Z_{slot} = -\frac{j}{2} Z_S \cot\frac{\theta_S}{2} \tag{1a}$$

$$Z_{stub} = \frac{j}{2} Z_M \tan\frac{\theta_M}{2} \tag{1b}$$

where Z_S and Z_M are the characteristic impedances and $\theta_S/2$ and $\theta_M/2$, the electrical lengths of the corresponding slotline and microstrip TLs. The resultant impedances in (1a) and in (1b) are the result of the parallel connection of two slotlines terminated in short circuit and two microstrip lines terminated by open circuit. The physical lengths of these transmission lines would be $1/2(l_M - w_H)$ for the stub and $1/2l_S$ for the slot, since the stub is measured from the edge of the host microstrip line and the slot from the middle. However, the short and open circuits effects lengthen the slotline and microstrip line, respectively [10]. Therefore, the equivalent lengths will be slightly greater than the physical ones.

A straightforward equivalent circuit for the proposed unit-cell is shown in Fig. 2, where Z_H and θ_H stand for the characteristic impedance and electrical length of the host microstrip line, respectively.

3. Design

Ignoring the host microstrip sections, the series impedance of the unit-cell corresponds to (1a) and the shunt admittance, to the inverse of (1b). In order to achieve balance condition, they must present exactly the same critical frequencies (poles and zeros). This way, two conditions must be fulfilled for the balanced case:

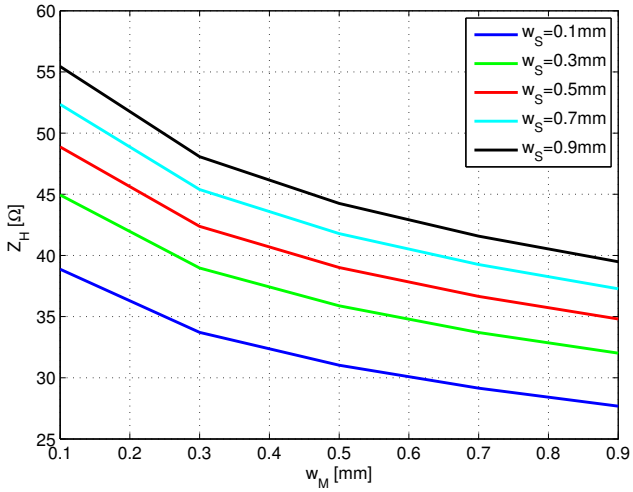

Figure 3: Required characteristic impedance of the host transmission line at 4 GHz as a function of the slot and stub widths, according to (2b).

$$\theta_S = \theta_M \tag{2a}$$

$$Z_H = \frac{1}{2}\sqrt{Z_M Z_S}\,. \tag{2b}$$

It can be assumed that the widths of the stub and slot are the practically only geometric variables that determine the characteristic parameters of the equivalent microstrip and slotline, respectively. This means that, once the widths of the elements are chosen, the parameters Z_M, ε_M, Z_S and ε_S are already determined. Then, the lengths of the elements can be adjusted to make them present the sames poles and zeros. Therefore, the design process can be reduced to a few steps:

- Choose a pair of elements widths w_M and w_S to obtain the desired Z_H according to (2b) or, alternatively, adjust the width of the host transmission line w_H to satisfy (2b).
- Choose the slot length to make it resonate at the desired frequency.
- Adjust the stub length, taking into account the different effective permittivities of the slot and stub, to satisfy (2a).

A unit-cell example on ARLON 1000 substrate with $\varepsilon_r = 10$ and h=50 mil has been designed. We have chosen that substrate in order to reduce as much as possible the radiation losses of the slot, which can be achieved with thick substrates with high permittivity. For this substrate it is possible to obtain the required characteristic impedance of the host TL for the balance condition as a function of the stub and slot widths, according to (2b). This is shown in Fig. 3 for the ARLON 1000 substrate at 4 GHz. Although a 50Ω-characteristic impedance can be achieved using reasonable

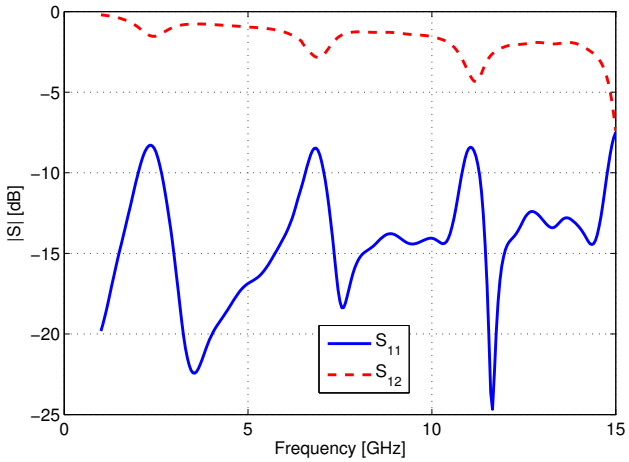

Figure 4: S-Parameters of the unit-cell design example.

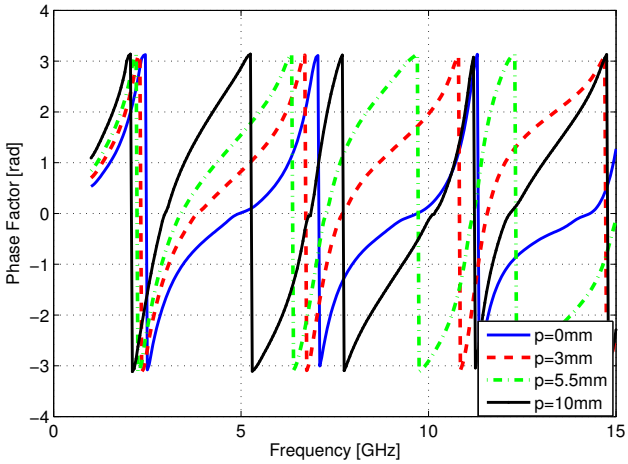

Figure 5: Phase factor for different cell lengths p.

widths on this substrate, we have preferred to choose equal slot and stub widths, since for 50 Ω the slot width has to be higher, thus introducing more radiation losses. Therefore, we have chosen $w_S = w_M = 0.3$ mm, for which the required characteristic impedance of the host TL is 39 Ω, approximately. Therefore, we have adjusted the host TL width to present 39 Ω, that is $w_H = 1.95$ mm. Next, the slot length has been set to 30 mm in order to get the first resonance below 3 GHz (f_{r1}=2.4 GHz) and to obtain several LH-RH transitions in a reasonable bandwidth. Then, the stub length has been adjusted to fulfill (2a). To do that, we use the effective permittivities of the corresponding slotline and microstrip TL to theoretically make an approximation of the required stub physical length. However, an optimization step is needed due to the aforementioned short and end effects, which are not considered in the proposed equivalent circuit of Fig. 2. The resultant stub length is 27.25 mm.

4. Results

The design example, described in Sec. 3 has been analysed by means of full-wave electromagnetic simulation. Fig. 4 shows the S-Parameters of the unit-cell. It can be appreciated that good matching (better than 10 dB) is achieved over the whole band, with the exception of some small stop bands located at the resonance frequencies of the slot/stub. Due to the different frequency dispersion of the equivalent circuit parameters of the slot and stub (characteristic impedance and effective permittivity of the corresponding slotline and microstrip TL), the possibility to achieve good matching in the whole band is limited. This effect is more pronounced at the resonance frequencies, where the equivalent slot and stub impedances in (1a) and (1b) factor of a unit-cell for different present a zero and a pole, respectively.

Fig. 5 shows the phase factor of a unit-cell for different cell lengths p. The curve for $p = 0$ represents the phase factor of the intrinsic unit-cell, that is, the phase that the slot-strip introduces without including the phase that comes from the sections of the microstrip feeding TL that separate adjacent cells. A multiband behaviour can be appreciated, with several RH-LH and LH-RH transitions, with good balance achievement, since practically no stop bands appear when the phase factor takes the null value. Moreover, it can be observed, that as p increases, the phase factor curve is shifted to the left, thus introducing more phase at the same frequency and loosing its non-linearity. This is the effect of the feeding microstrip sections, since for higher lengths the microstrip sections are longer and they contribute to the total phase response to a greater extent. Therefore, the cell length should not be so high that the linear phase response of the host microstrip line disguises the non-linear behaviour of the intrinsic cell.

In order to study the potential of the unit-cell to build a CRLH TL, we have analyzed a three-cells structure. In Fig. 6, the resultant S_{11} for different cell lengths is depicted. It can be observed that the reflection coefficient strongly depends on the cell length (on the distances between adjacent slot/stub elements), experiencing a matching worsening when the cells get closer, which can be attributed to coupling effects.

Keeping a compromise between the linearity effect and the matching worsening, we have selected $p = 5.5$ mm. For this case, Fig. 7 shows the S-Parameters of the resultant three-cells structure. Although, as expected, the behaviour has worsened with respect to that of the unit-cell, three broad pass-bands are obtained, which contain both LH and RH behaviour. For example, good matching has been achieved for $f = 3.4$ GHz, at which a transition from LH to RH occurs, with $|S_{11}|$=-14 dB and $|S_{12}|$=-2.4 dB or for $f = 9.8$ GHz, a transition from RH to LH, with $|S_{11}|$=-10.5 dB and $|S_{12}|$=-1.8 dB.

Finally, in order to check whether the phase factor of a single cell can predict the behaviour of an artificial TL made up of several cells, Fig. 8 shows a comparison between the phase factors of the single cell and the three-cells structure. For the sake of comparison, the phase response of the three-cells structure has been divided by the number of cells. Very good agreement is obtained up to 11 GHz. From

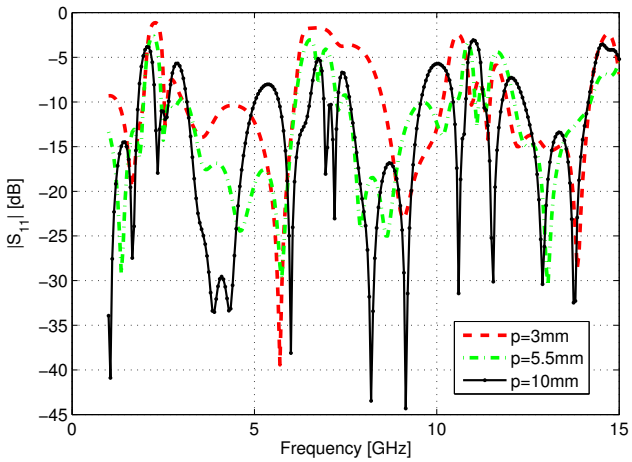

Figure 6: $|S_{11}|$ of the three-cells structure with different cell lengths.

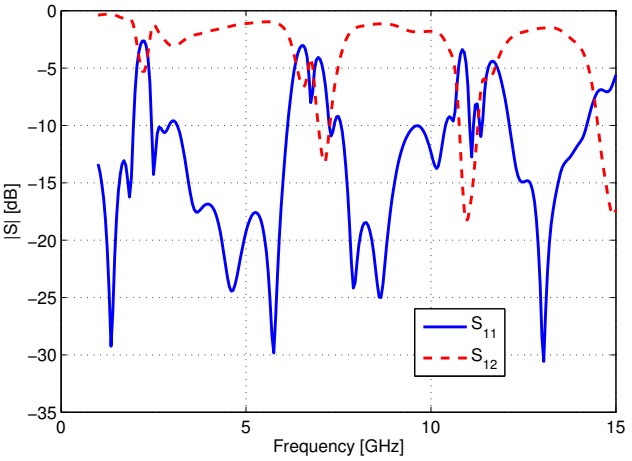

Figure 7: S-Parameters of the three-cells structure with p=5.5mm.

this frequency, the two curves take different behaviours, which indicates that the TL approach is not valid anymore, since the cell length is in the same magnitude order as the wavelength.

5. Conclusions

A CRLH TL implementation has been proposed, which makes use of alternate rectangular stubs and slots to provide the required immittances. Since these immittances are distributed, multiband behaviour has been achieved. An equivalent circuit using TLs has been proposed to model the structure behaviour over a broad bandwidth. With the help of this equivalent circuit, the design methodology has been stated. The design simplicity to fulfill the balance condition has been highlighted.

In order to check the design methodology, simulated results of a unit-cell and a three-cells structure have been analysed. The resultant phase response have confirmed the

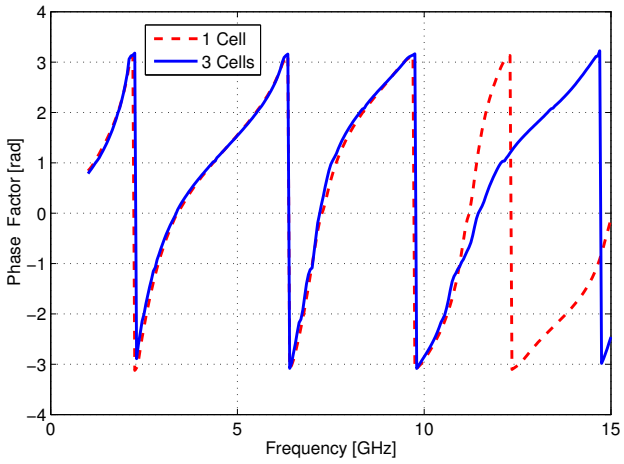

Figure 8: Phase factor of the unit-cell compared to the phase response of the three-cells structure (divided by three), for $p = 5.5$ mm.

design methodology, since balanced multiband behaviour has been achieved. Moreover, the structure presents good matching over some broad frequency bands, which contain LH-RH and RH-LH transitions, making it very appropriate for multiband applications. Since the unit-cell is based on the use of slots, this structure can be a good choice for antenna applications, such as leaky-wave antennas.

Acknowledgement

This work was supported by the Spanish Ministerio de Ciencia e Innovación (Programa Consolider-Ingenio 2010) under Grant CSD2008-00066, EMET, and by the Junta de Andalucía (Spain) under Grant P10-TIC-6883.

References

[1] V. Veselago, "The electrodynamics of substances with simultaneously negative values of ϵ and μ," *Soviet Physics Uspekhi*, vol. 10, no. 4, pp. 509 514, Jan. -Feb. 1968.

[2] C. Caloz, H. Okabe, T. Iwai, and T. Itoh, "Trasmission line approach of lefthanded (LH) materials," in *Proc. USNC/URSI Nat. Radio Science Meeting, San Antonio, TX*, vol. 1, Jun. 2012, p. 39.

[3] A. K. Iyer and G. V. Eleftheriades, "Negative refractive index materials supporting 2-D wave," in *Proc. IEEE-MTTS Int. Microwave Symp., Seattle, WA*, Jun. 2002, pp. 10671070.

[4] A. A. Oliner, "A planar negative refractive index without resonant elements," in *Proc. IEEE-MTTS Int. Microwave Symp., Philadelphia, PA*, Jun. 2003, pp. 191194.

[5] C. Caloz, "Dual Composite Right/Left-Handed (D-CRLH) Transmission Line Metamaterial," *Microwave and Wireless Components Letters, IEEE*, vol. 16, no. 11, pp. 585 587, Nov. 2006.

[6] A. Rennings, S. Otto, J. Mosig, C. Caloz, and I. Wolff, "Extended composite right/left-handed (E-CRLH) metamaterial and its application as quadband quarter-wavelength transmission line," in *Microwave Conference, 2006. APMC 2006. Asia-Pacific*, Dec. 2006, pp. 1405 1408.

[7] C. Camacho-Peñalosa, T. M. Martín-Guerrero, J. E. Page, and J. Esteban,"Derivation and General Properties of Artificial Lossless Balanced Composite Right/Left- Handed Transmission Lines of Arbitrary Order," *Progress In Electromagnetics Research B*, vol. 13, pp. 151 169, 2009.

[8] Y. H. Ryu, J. H. Park, and J. H. Lee, J. Y. Kim, H. S. Tae, "DGS Dual Composite Right/Left Handed Transmission Line," *IEEE Microw. Wireless Compon. Lett.*, vol. 18, no. 7, pp. 434, July 2008.

[9] E. Abdo-Sánchez, J. A. Fernández-Segovia, T. M. Martín-Guerrero and C. Camacho-Peñalosa, "Tri-Band Dual CRLH Transmission Line Using Dumbbell-Shaped DGS and Stub", *4th Young Scientist Meeting on Metamaterials*, Valencia, Feb. 2011.

[10] K. C. Gupta, R. Garg, I. Bahl and P. Bhartia, *Microstrip Lines and Slotlines, 2nd Edition*, Artech House, Norwood, 1996.

Selective Mode Suppression in Coplanar Waveguides Using Metamaterial Resonators

Jordi Naqui, Miguel Durán-Sindreu, and Ferran Martín*

GEMMA/CIMITEC, Departament d'Enginyeria Electrònica, Universitat Autònoma de Barcelona, 08193 Bellaterra (Barcelona), Spain
*corresponding author, E-mail: Ferran.Martin@uab.es

Abstract

In this paper, it is shown that split ring resonators (SRRs) and complementary split ring resonators (CSRRs) can be used to selectively suppress the odd (slot) mode or the even (fundamental) mode, respectively, in coplanar waveguides (CPWs). To this end, it is necessary to symmetrically etch the SRRs and the CSRRs in the line. An interpretation of this behavior is reported. The paper is also supported by experimental results, and some applications are highlighted.

1. Introduction

Coplanar waveguides loaded with pairs of split ring resonators (SRRs) (see Fig. 1a) have been proposed as a mean to achieve one-dimensional planar negative permeability structures [1]. As consequence of the negative effective permeability, these structures inhibit the fundamental (even) mode of the CPW in the vicinity of the resonance frequency of the SRRs. Alternatively, the stop band behavior of these structures can be interpreted as due to the inductive coupling between the CPW and the pairs of SRRs at resonance. The circuit model (unit cell) of CPW transmission lines loaded with pairs of SRRs was first introduced in [1], and later revised in [2]. In [1], the magnetic wall concept was used, taking benefit of the symmetry of the structure and the even nature of the fundamental mode of the CPW. In [2], the unit cell was modeled by considering both SRRs (i.e., the magnetic wall concept was not used). Indeed, the main relevant improvement of the model reported in [2], as compared to the model reported in [1], is the position of the inductance modeling the shunt strips of CPWs loaded with the pairs of SRRs and shunt connected strips (i.e., left handed lines). However, this aspect is not fundamental for this paper since we are not considering left handed lines, that is, the CPW lines are only loaded with SRRs.

The lines considered in this paper are CPWs loaded with single SRRs symmetrically etched in the back substrate side. As will be shown, these lines are transparent to signal propagation for the fundamental (even) CPW mode, whereas they inhibit the odd (slot) mode in the vicinity of SRR resonance. For completeness, we will also analyze CPWs loaded with complementary split ring resonators (CSRRs) [3] symmetrically etched in the central strip. As will be shown, these CSRR-loaded CPW lines are transparent for the slot mode and opaque for the fundamental mode in the vicinity of CSRR resonance. The circuit model of a CPW loaded with symmetrically etched SRRs/CSRRs is provided in this paper, and used to analyze the behavior of the line. The paper is supported by experimental results, and, finally, some potential applications are highlighted.

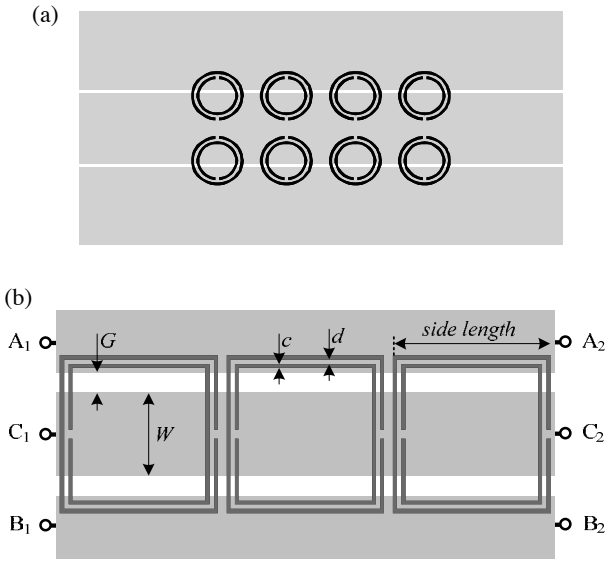

Figure 1: CPW loaded with symmetrically etched SRRs; CPW loaded with pairs of SRRs (a) [1], and CPW loaded with single SRRs (b). The ground plane is depicted in light grey. The SRRs are etched in the back side metallization. The relevant dimensions are indicated.

2. Selective mode suppression in SRR- and CSRR-loaded CPW transmission lines

The first CPW transmission lines under study are loaded with single and symmetrically etched SRRs, as depicted in Fig. 1(b). For the fundamental CPW mode, there is a magnetic wall at the symmetry plane of the structure, and the SRRs cannot be excited at their first resonance since they exhibit an electric wall at their symmetry plane at this

resonance [4]. The magnetic field lines generated by the currents flowing on the CPW structure are contra directional in the slot regions. Since the SRRs are symmetrically etched in the back substrate side, the axial components of the magnetic field lines within the SRR region exactly cancel, there is not a net axial magnetic field in that region, and the SRRs cannot be magnetically driven (the symmetry also precludes that the particles can be excited by means of the electric field present between the central strip and the ground planes). Thus, the structure is transparent for the fundamental CPW mode. However, there is a net axial magnetic field within the SRR region for the slot (odd) mode, the particle is excited at its first resonance and, as a result, the injected power is expected to return back to the source at that frequency.

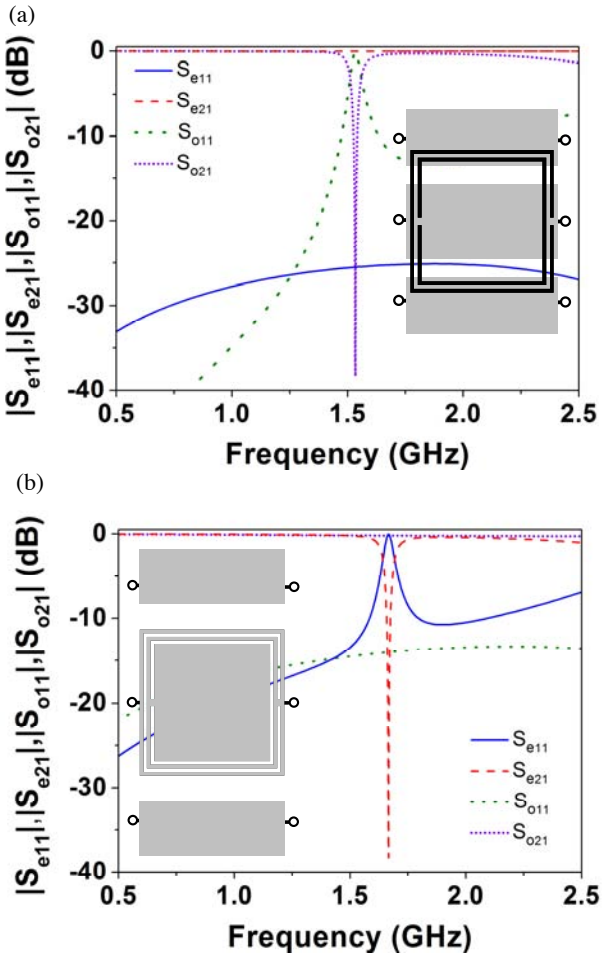

Figure 2: Frequency response for CPW (*e*) and slot (*o*) mode of the indicated CPW loaded with (a) SRR and (b) CSRR. The substrate is the *Rogers RO3010* with thickness h=1.27 mm and dielectric constant ε_r=10.2. The dimensions are: for the SRR and CSRR, c=d=0.2 mm, and *side length*=7.6 mm; for the CPW lines, W=4 mm (a), W=8 mm (b), G=1 mm (a), and G=1.4 mm (b). The characteristic impedance of the CPW mode (even mode) is 50 Ω. The even and odd modes are fed by, respectively, a 50 Ω coplanar port and a 100 Ω differential port.

Let us now consider that the CPW is loaded with a square-shaped CSRR symmetrically etched in the central strip, as the inset of Fig. 2(b) illustrates. In this case, the magnetic wall of the CPW structure (fundamental mode) is perfectly aligned with the magnetic wall of the particle at its resonance frequency [5], and signal is inhibited in the vicinity of CSRR resonance. Conversely, for the slot mode, there is not a net axial electric field in the inner metallic region of the CSRR, the resonator cannot be excited, and the line is transparent for this mode (symmetry also cancels the particle activation through the magnetic field induced in the line).

To demonstrate the previous statements, we have simulated (by means of the commercial software *Agilent Momentum*) the transmission and reflection coefficients of a CPW loaded with a single square-shaped SRR for the even and odd mode (see Fig. 2a). As can be seen, the structure is transparent to the fundamental (even) mode, but a notch is clearly visible at SRR resonance for the slot mode. For the CPW loaded with a CSRR (Fig. 2b), the fundamental mode is inhibited in the vicinity of CSRR resonance, whereas the slot mode is transmitted between the input and output ports.

The main conclusions of this section are: (i) a CPW loaded with a symmetric SRR exhibits for the odd mode an identical behavior to that of a CPW loaded with pairs of SRRs for the fundamental mode, that is, a notch in the transmission coefficient; however, the line is transparent to the fundamental mode; (ii) a CPW loaded with a CSRR in the central strip inhibits the fundamental mode in the vicinity of particle resonance (similar to microstrip lines with CSRRs etched in the ground plane), but it is transparent to the odd mode.

3. Circuit model of a CPW loaded with symmetric SRRs

The lumped element equivalent circuit model of the structure of Fig. 1(b) (unit cell) is depicted in Fig. 3(a). The coupling between adjacent resonators is considered to be negligible. The metallic terminals at ports 1 and 2 (shown in Fig. 1b) are also indicated for a better comprehension. C models the slot capacitance of the CPW line, L_e is the inductance of the line for the fundamental mode, L_o is the inductance of the line for the odd mode, the SRR is modeled as a resonant tank (L_s-C_s), M is the mutual inductance between the SRR and each half of the CPW transmission line, and, finally, C_a accounts for the electric coupling between the line and the SRRs. The electric coupling between the CPW transmission line and the SRR has been neglected so far. However, contrary to previous reported structures (for instance, that shown in Fig. 1a), in the structure of Fig. 1(b), the slits of the SRR are aligned with the line axis. It is well known that SRRs exhibit cross polarization, that is, they can be excited by means of an axial magnetic field, but they can also be driven by means of an electric field with a non negligible component in the plane of the particle and orthogonal to the plane containing the slits. Since for the odd mode of a CPW, there is a net electric field across the slots of the CPW transmission line, the electric coupling cannot be a priori neglected.

For the fundamental (even) mode, the terminals A_1, A_2, B_1 and B_2 are grounded, a magnetic wall arises in the symmetry plane, the SRR is opened, and the equivalent circuit model is simply that of a conventional transmission line (Fig. 3b). For the odd mode, the feeding signal is applied between the terminals A_1 and B_1 (i.e., port 1 and 2 are differential ports). Thus, the symmetry plane exhibits a virtual ground, and the equivalent circuit model that results after applying the electric wall concept is identical to that of a CPW loaded with a pair of SRRs [1], namely a transmission line inductively coupled to a SRR, but including electric coupling as well (Fig. 3c).

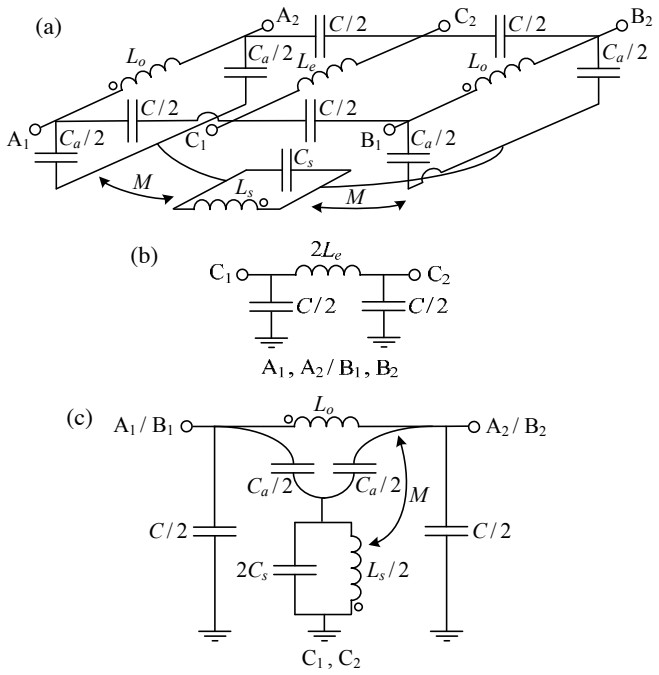

Figure 3: Equivalent circuit model (unit cell) of a CPW loaded with symmetrically etched SRRs (a); equivalent circuit model for the even mode (b); equivalent circuit model for the odd mode (c).

From the electromagnetic simulation of the structure of Fig. 2(a) corresponding to the odd mode, we can extract the parameters of the model of Fig. 3(c), according to the procedure described in [6]. Actually, the procedure described in [6] does not account for electric coupling. The circuit simulation obtained from the extracted parameters does not accurately fit to the full wave simulations of Fig. 2(a) for the odd mode. This means that electric coupling must be considered for an accurate description of the structure. Therefore, we have inferred the new circuit values (including C_a) by curve fitting. The comparison between the circuit and electromagnetic simulations is shown in Fig. 4, where the element values are indicated (see figure caption). As can be appreciated, good agreement is obtained by including electric coupling in the circuit simulation.

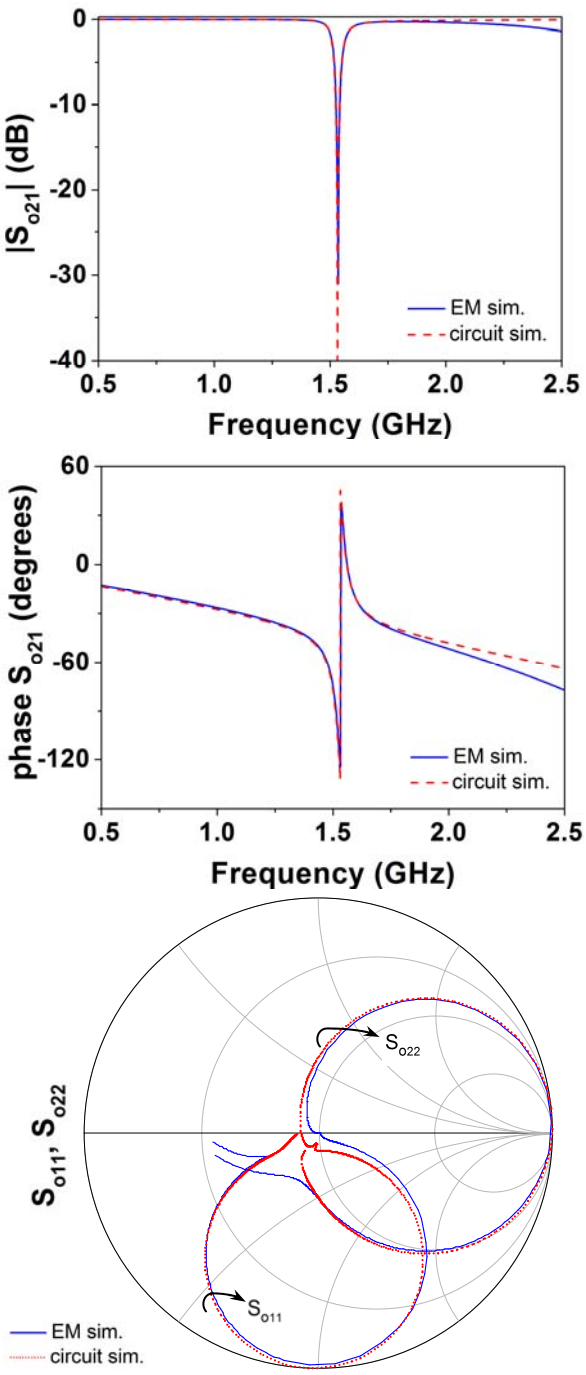

Figure 4: Comparison of the electromagnetic and circuit simulation of the structure of Fig. 2(a) for the odd mode. The element values (referred to the circuit of Fig. 3c) are: C= 1.38 pF, L_o=2.96 nH, L_s=3.66 nH, C_s= 2.73 pF, M=0.66 nH, and C_a= 0.4 pF.

4. Circuit model of a CPW loaded with symmetric CSRRs

The lumped element equivalent circuit model of the CPW loaded with CSRRs in the central strip (Fig. 2b) is shown in Fig. 5 (inter-resonator coupling has not been considered). *C*

models the slot capacitance of the CPW line, L_e is the inductance of the line for the fundamental mode, L_o is the inductance of the line for the odd mode, the CSRR is modeled as a resonant tank (L_c-C_c), and, finally, M accounts for the magnetic coupling between the line and the CSRR. The magnetic coupling between the CPW transmission line and the CSRR has been neglected so far. However, contrary to previous reported structures, in the structure of Fig. 2(b), the slits of the CSRR are aligned with the line axis. Under these conditions, cross polarization effects are present and, hence, inductive coupling must be also included for accurate modeling.

Following a procedure similar to that explained in the previous section, we have extracted the parameters for the even mode corresponding to the electromagnetic simulation of the structure shown in Fig. 2(b) [7]. The comparison between the electromagnetic and circuit simulation is depicted in Fig. 6 (the element values are indicated in the caption), where it can be appreciated that the circuit and electromagnetic simulations are in good accordance.

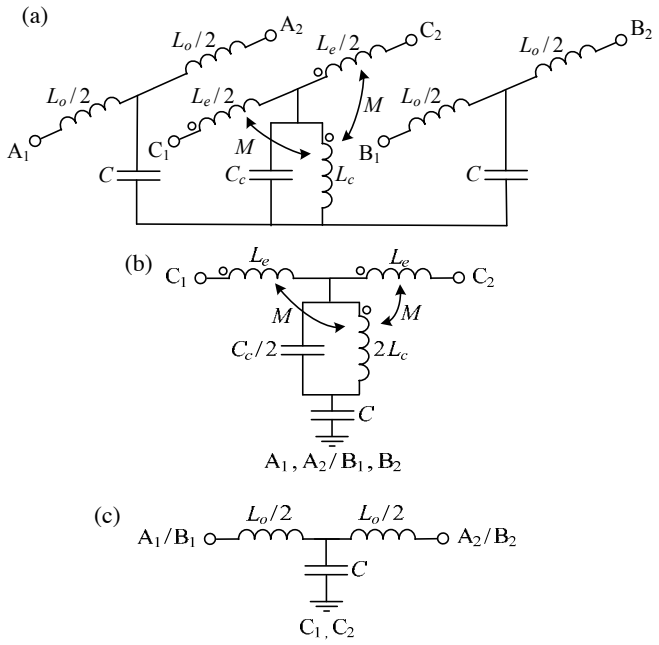

Figure 5: Equivalent circuit model (unit cell) of a CPW loaded with symmetrically etched CSRRs (a); equivalent circuit model for the even mode (b); equivalent circuit model for the odd mode (c).

5. Experimental validation

In order to experimentally validate the selective mode suppression in CPWs, we have designed some structures. One of them consists of a CPW loaded with a SRR in its back substrate side and with a CSRR in the central strip (Fig. 7a), while another structure is the same structure without the SRR. We have fed the CPWs by means of a slot line to generate the odd mode, and it is clear from Fig. 7b that the presence of the SRR inhibits this mode at SRR resonance (while this mode is not affected by the CSRR). On the other hand, we have designed the same structures without the CPW to slot line transition (Fig. 8a), and we have obtained the transmission coefficient (Fig. 8b) which corresponds to the fundamental mode (the structure has not been fabricated; hence it has been obtained through full wave electromagnetic simulation). In this case, the situation is reversed, that is, the notch is caused by the CSRR, and the line is transparent at the resonance frequency of the SRR.

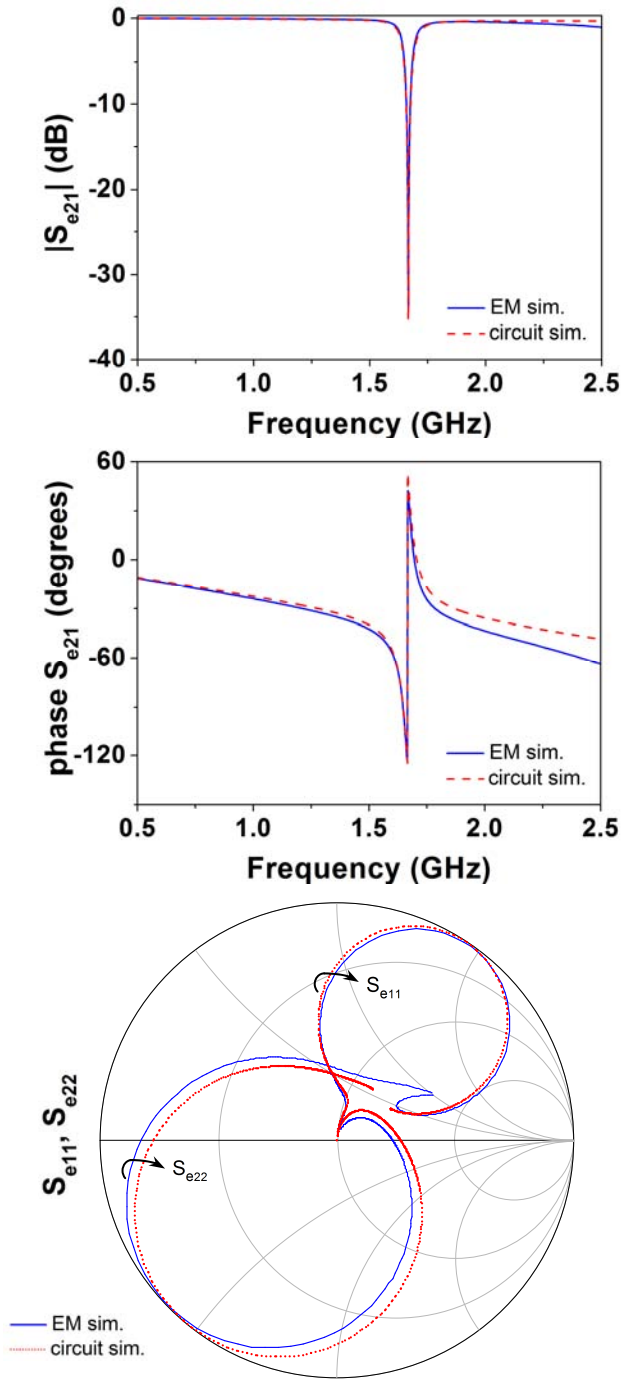

Figure 6: Comparison of the electromagnetic and circuit simulation of the structure of Fig. 2(b) for the even mode. The element values (referred to the circuit of Fig. 5b) are: C= 0.75 pF, L_e=2.13 nH, L_c=0.49 nH, C_c= 17.3 pF, and M=0.2 nH.

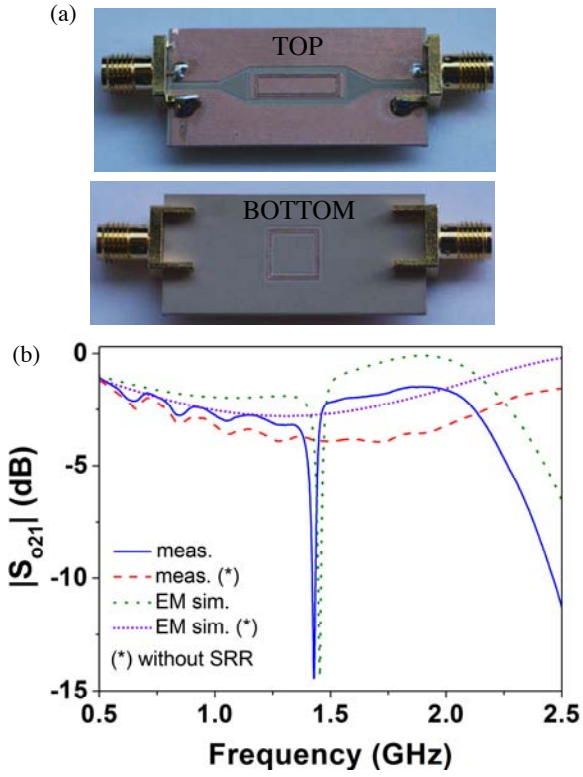

Figure 7: CPW loaded with a SRR and a CSRR and fed through a slot line to generate the slot mode (a) and frequency response (b). The substrate is the *Rogers RO3010* with h=1.27 mm, ε_r=10.2, and loss tangent tanδ=0.0023. The dimensions are: for the SRR, c=d=0.2 mm, and *side length*=7.6 mm; for the CSRR dimensions, c=d=0.2 mm, *longitudinal side length*=12.6 mm, and *transverse side length*=3.6 mm; for the CPW, W=4 mm, and G=1 mm; for the slot line, the slot width is 1.5 mm.

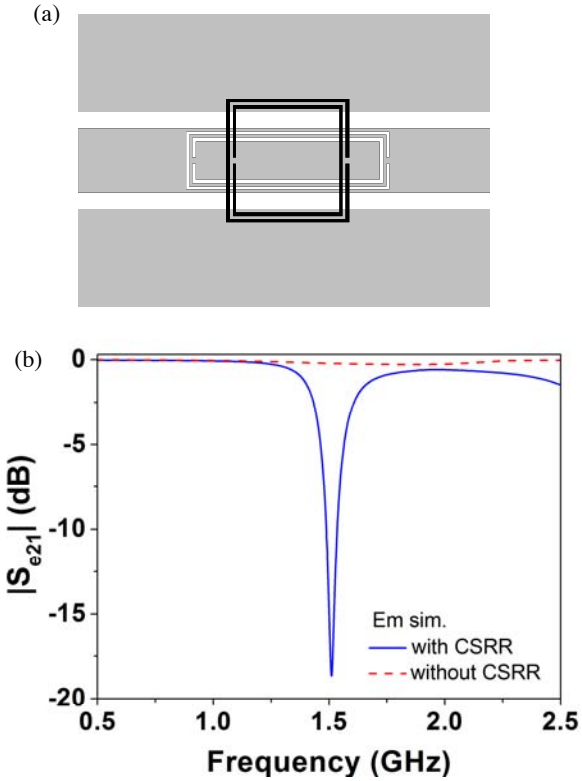

Figure 8: CPW loaded with a SRR and a CSRR and excited through the fundamental (even) mode (a) and frequency response (b). The substrate and dimensions are those indicated in the caption of Fig. 7.

Notice that in Fig. 7(b) the response exhibits certain insertion losses due to the impedance mismatch on the coaxial (50 Ω impedance) to slot line (it has been found that it exhibits about 100 Ω impedance) transition. Nevertheless, this is irrelevant for the purpose of this work, since the main aim is to demonstrate the selective mode suppression of both CPW even and odd modes by using either SRRs or CSRRs.

6. Potential applications

CPW structures loaded with single SRRs or CSRRs may find applications in several fields. For example, CPW transmission lines with symmetrically loaded SRRs inhibit the slot mode, keeping the fundamental mode unaltered. Thus, a set of SRR properly designed can be useful in certain CPW applications where the slot mode typically appears and must be suppressed. Another potential application of SRR-loaded lines concerns the implementation of novel sensors and detectors based on the loss of symmetry of the reported structures [8]. The lack of symmetry can be caused by many different reasons, such as a displacement or rotation, the presence of particles, inhomogeneities in the surrounding medium, etc., and sensing/detection can be simply carried out by measuring the transmission coefficient (many other sensors based on the variation of the resonance frequency of split rings have been reported [9-16]).

For which concern CSRR-loaded CPWs, the presence of these particles causes notches in the transmission coefficient for the fundamental mode, and this can be useful for the rejection of interfering signals in communication systems. As long as the CSRRs are etched in the central strip, this undesired signal suppression can be achieved without the penalty of increasing device area and cost.

In this paper, the potentiality of the reported structures is illustrated by means of a proof-of-concept demonstrator of a radiofrequency bar code [17]. The idea is to each SRRs with different dimensions (i.e., providing different resonance frequencies) in the back substrate side of a CPW transmission line. If the SRRs are aligned with the symmetry plane of the CPW structures, the line is transparent. However, we can codify the line by laterally displacing the SRRs, since this produces a transmission zero in the transmission coefficient at the corresponding frequency, and this can be easily monitored. This frequency domain codification is similar to that reported in [18], but in our case it is not necessary to remove the SRR to set a logic '0'; it suffices by aligning it with the line; hence, our approach opens the possibility to implement reconfigurable radiofrequency bar codes. A 3-bit bar code with the

sequence '101', that is, with two SRRs laterally shifted and with one SRR centered is depicted in Fig. 9(a), whereas Fig. 9(b) shows the simulated frequency response. For comparison, the simulated frequency response corresponding to the code '010', is also depicted. With the purpose to prevent the presence of the odd mode, the ground planes are connected through backside strips and vias. With these results, the radiofrequency bar code proof-of-concept based on CPW structures loaded with SRRs is validated.

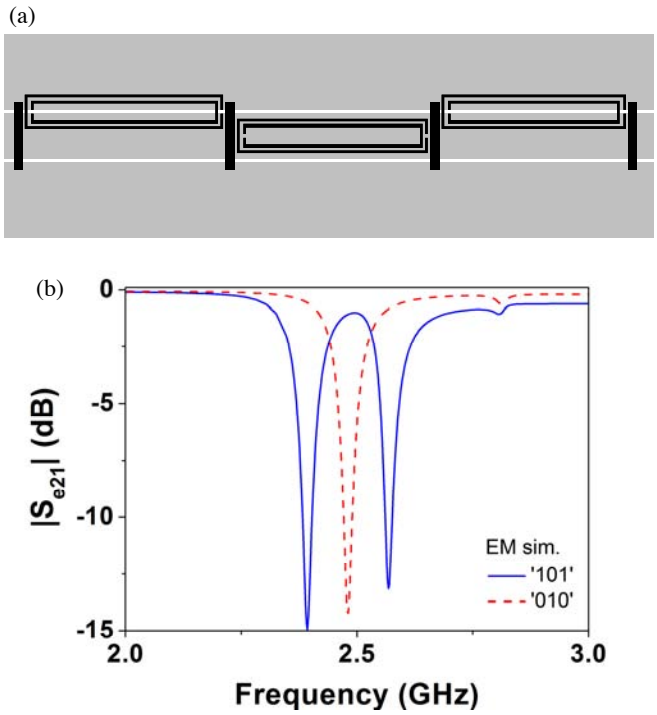

Figure 9: CPW loaded with three SRRs resonating at 2.39 GHz, 2.48 GHz and 2.57 GHz and codified with the code '101' (a), and frequency response (b). The frequency response corresponding to the code '010' is also depicted. The substrate is the *Rogers RO4003C* with h=0.8128 mm, ε_r=3.55, and tanδ=0.0021. The dimensions are: for the SRRs, c=d=0.2 mm, *transverse side length*=2.47 mm, and *longitudinal side length*=14.3 mm, 13.75 mm, and 13.25 mm; for the CPW, W=3.3 mm and G=0.2 mm.

7. Conclusions

In conclusion, the selective suppression of either the fundamental (even) or the slot (odd) mode in CPW structures by using complementary split ring resonators (CSRRs) and split ring resonators (SRRs), respectively, has been demonstrated. In order to preserve the integrity of the mode for which the line is transparent, it is necessary to etch the particles symmetrically in the line. We have provided the circuit models of SRR and CSRR symmetrically loaded CPW transmission lines, including those for even and odd mode excitations, and it has been demonstrated through parameter extraction that these models describe the structures to a good approximation. The selective mode suppression has been experimentally validated and potential applications of these structures have been highlighted, with special emphasis to radiofrequency bar codes. A proof-of-concept demonstrator of a CPW transmission line with a 3-bit spectral signature has been provided. Work is in progress to implement practical bar codes with a higher number of bits, and to the development of new sensors based on the symmetry properties of CPW transmission lines.

Acknowledgements

This work has been supported by MICIIN-Spain (projects TEC2010-17512 and CSD2008-00066) and by AGAUR-*Generalitat de Catalunya*, through project 2009SGR-421.

References

[1] F. Martín, F. Falcone, J. Bonache, R. Marqués and M. Sorolla, "Split ring resonator based left handed coplanar waveguide", *Appl. Phys. Lett.*, vol. 83, pp. 4652-4654, Dec. 2003.

[2] F. Aznar, J. Bonache and F. Martín, "An improved circuit model for left handed lines loaded with split ring resonators", *Appl. Phys. Lett.*, vol. 92, paper 043512, Feb. 2008.

[3] F. Falcone, T. Lopetegi, J.D. Baena, R. Marqués, F. Martín and M. Sorolla, "Effective negative-ε stop-band microstrip lines based on complementary split ring resonators", *IEEE Microwave and Wireless Components Letters*, vol. 14, pp. 280-282, June 2004.

[4] R. Marqués, F. Medina and R. Rafii-El-Idrissi, "Role of bianisotropy in negative permeability and left handed metamaterials", *Phys. Rev. B*, vol. 65, pp. paper 144441(1-6), 2002.

[5] J.D. Baena, J. Bonache, F. Martín, R. Marqués, F. Falcone, T. Lopetegi, M.A.G. Laso, J. García, I Gil, M. Flores-Portillo and M. Sorolla, "Equivalent circuit models for split ring resonators and complementary split rings resonators coupled to planar transmission lines", *IEEE Transactions on Microwave Theory and Techniques*, vol. 53, pp. 1451-1461, April 2005.

[6] F. Aznar, M. Gil, J. Bonache, J.D. Baena, L. Jelinek and R. Marqués and F. Martín, "Characterization of miniaturized metamaterial resonators coupled to planar transmission lines", *J. Appl. Phys.*, vol. 104, paper 114501(1-8), December 2008.

[7] J. Bonache, M. Gil, I. Gil, J. Garcia-García and F. Martín, "On the electrical characteristics of complementary metamaterial resonators", *IEEE Microwave and Wireless Components Letters*, vol. 16, pp. 543.545, October 2006.

[8] J. Naqui, M. Durán-Sindreu and F. Martín, "Novel Sensors Based on the Symmetry Properties of Split Ring Resonators (SRRs)", *Sensors*, vol 11, pp. 7545-7553, 2011.

[9] He, X-J.; Wang, Y.; Wang, J-M.; Gui, T-L. Thin film sensor based tip-shaped splits ring resonator metamaterial for microwave application. *Microsystems Technology*, 2010, 16, 1735-1739.

[10] Cubukcu, E.; Zhang, S.; Park, Y-S.; Bartal, G.; Zhang, X. Split ring resonator sensors for infrared detection of single molecular monolayers. *Appl. Phys. Lett.* 2009, 95, 043113-1-3.

[11] Driscoll, T.; Andreev, G.O.; Basov, D.N.; Palit, S.; Cho, S.Y.; Jokerst, N.M.; Smith, D.R. Tuned permeability in terahertz split ring resonators for devices and sensors. *Appl. Phys. Lett.* 2007, 91, 062511-1-3.

[12] Melik, R.; Unal, E.; Perkgoz, N.K.; Puttlitz, C.; Demir, H.V. Metamaterial-based wireless strain sensors. *Appl. Phys. Lett.* 2009, 95, 011106-1-3.

[13] Yogi, R.A.; Parolia, R.S.; Karekar, R.N.; Aiyer, R.C. Microwave Microstrip ring resonator as a paper moisture sensor: study with different grammage. *Meas. Sci. Technol.* 2002, 13, 1558-1562.

[14] Pattnaik, P.K.; Vijayaaditja, B.; Srinivas, T.; Selvarajan, A. Optical MEMS pressure sensor using ring resonator on a circular diaphragm. *Proc. 2005 Int. Conf. On MEMS, NANO and Smart Systems* (ICMENS'05).

[15] Liu, X.; Xue, C.; Yan, S.; Xiong, J.; Zhang, W. Integrated high sensitivity displacement sensor based on micro ring resonator. *Proc. 2009 4th IEEE Int. Conf. Nano/Micro Engineered and Molecular Systems*, Shenzhen (China), January 5-8, 2009, pp. 1000-1003.

[16] C. Mandel, B. Kubina, M. Schüßler, and R. Jakoby "Passive chipless wireless sensor for two-dimensional displacement measurement", *European Microwave Conf. Dig.* pp. 79-82, October 2011.

[17] S. Preradovic and N.C. Karmakar, "Chipless RFID: the bar code of the future", *IEEE Microwave Magazine*, vol. 11, pp. 87-97, Dec. 2010.

[18] S. Preradovic, I. Balbin, N.C. Karmakar, and G.F. Swiegers, "Multiresonator-based chipless RFID system for low-cost item tracking", *IEEE Transactions on Microwave Theory and Techniques*, vol. 57, pp. 1411-1419, May 2009.

Super-resolution properties of the Spherical Geodesic Waveguides using the perfect drain

Juan Carlos González, Dejan Grabovičkić, Juan Carlos Miñano, Pablo Benítez

Universidad Politécnica de Madrid, Cedint. Campus de Montegancedo 28223 Madrid, Spain
*corresponding author, E-mail: jcgonzalez@cedint.upm.es

Abstract

Perfect drain for the Maxwell Fish Eye (MFE) is a non-magnetic dissipative region placed in the focal point to absorb all the incident radiation without reflection or scattering. The perfect drain was recently designed as a material with complex permittivity ε that depends on frequency. However, this material is only a theoretical material, so it can not be used in practical devices. Recently, the perfect drain has been claimed as necessary to achieve super-resolution [Leonhard 2009, *New J. Phys*. 11 093040], which has increased the interest for practical perfect drains suitable for manufacturing. Here, we analyze the super-resolution properties of a device equivalent to the MFE, known as Spherical Geodesic Waveguide (SGW), loaded with the perfect drain. In the SGW the source and drain are implemented with coaxial probes. The perfect drain is realized using a circuit (made of a resistance and a capacitor) connected to the drain coaxial probes. Super-resolution analysis for this device is done in Comsol Multiphysics. The results of simulations predict the super-resolution up to $\lambda/3000$ and optimum power transmission from the source to the drain.

1. Introduction

"Super-resolution" stands for the capacity of an optical system to produce images with details below the classic Abbe diffraction limit. In the last decade super-resolution has been shown experimentally with devices made of left-handed materials [1][2] (that is, materials with negative dielectric and magnetic constants) [3][4]. Unfortunately, high absorption and small (wavelength scale) source-to-image distance are both present in these experiments. Nevertheless, these devices have been claimed to reach the theoretical limit of infinite resolution [4].

An alternative device for perfect imaging has recently been proposed [6][7]: the Maxwell Fish Eye (MFE) lens. Unlike previous perfect imaging devices, MFE uses materials with a positive, isotropic refractive index distribution. This device is very well known in the framework of Geometrical Optics because it is an Absolute Instrument [5], so every object point has a stigmatic image point.

Leonhardt [6] analyzed Helmholtz wave fields in the MFE lens in two dimensions (2D). These Helmholtz wave fields describe TE-polarized modes in a cylindrical MFE, i.e., modes in which electric field vector points orthogonally to the cross section of the cylinder. Leonhardt found a family of Helmholtz wave fields which have a monopole asymptotic behavior at an object point as well as at its stigmatic image point. Each one of these solutions describes a wave propagating from the object point to the image point. It coincides asymptotically with an outward (monopole) Helmholtz wave at the object point, as generated by a point source, and with an inward (monopole) wave at the image point, as it was sunk by an "infinitely-well localized drain" (which we call a "perfect point drain"). This perfect point drain absorbs the incident wave, with no reflection or scattering. This result has also been confirmed via a different approach [8].

The physical significance of a passive perfect point drain has been controversial [9]-[18]. In references [5] and [6] the perfect point drain was not physically described, but only considered as a mathematical entity (a point drain is represented by Dirac-delta as the point source). However, a rigorous example of a passive perfect point drain for the MFE has recently been found, clarifying the controversy [19]. It consists of a dissipative region whose diameter tends towards zero and whose complex permittivity ε takes a specific value depending on the operation frequency.

Two sets of experiments have recently been carried out to support the super-resolution capability in the MFE. In the first one, super-resolution with positive refraction has been demonstrated for the very first time at a microwave-frequency (λ=3 cm) [20][21]. The experimental results showed that two sources with a distance of $\lambda/5$ from each other (where λ denotes the local wavelength $\lambda = \lambda_0/n$) could be resolved with an array made up of 10 drains spaced $\lambda/20$, which exceeded the $\sim\lambda/2.5$ classic diffraction limit. Results with closer sources were not reported, but it should be noted that this experiment was limited to the resolution of the array of drains.

The second set of experiments has been carried out for the near infrared frequency (λ = 1.55 μm), but resolution below the diffraction limit was not found [22]. The authors assume that the failure in the experimental demonstration is due to

manufacturing flaws in the prototype.

Although the perfect drain has not been used in these experiments, i.e. there was a reflected wave from the drain to the source, the MFE has shown super-resolution for microwave frequencies. This means that the perfect drain is not necessary for reaching the super-resolution (see [23]). However, in this paper we will show that the use of the perfect drain increases super-resolution.

Recently, a device equivalent to the MFE, Spherical Geodesic Waveguide (SGW) made for microwave frequencies has been presented [23][24]. The SGW is a spherical waveguide filled with a non-magnetic material and isotropic refractive index distribution proportional to $1/r$ ($\varepsilon = (r_0/r)^2$ and $\mu = 1$), r being the distance to the center of the spheres. Transformation Optics theory [25] proves that the TE-polarized electric modes of the cylindrical MFE are transformed into radial-polarized modes in the SGW, so both have the same imaging properties. When the waveguide thickness is small enough, the variation of the refractive index within the two spherical shells can be ignored resulting in a constant refractive index within the waveguide. In [23] the SGW has been analyzed using two coaxial probes (source and drain) loaded with the characteristics impedance. The results have shown the super-resolution up to λ/500 for a discrete number of frequencies, called notch frequencies, that are close to the well known Schumman Resonance frequencies of spherical systems. For other frequencies the system did not present resolution below diffraction limit. In these analysis the perfect drain has not been used, thus beside the incident wave, a reflected wave existed in the SGW as well. However, the super-resolution properties have been shown.

Herein, we present an improvement of the super-resolution using the SGW with the perfect drain. The perfect drain is realized using a circuit (made of a resistance and a capacitor) connected to the drain coaxial probe. The difference between the presented drain and the perfect drain proposed in [19] is the practical realization. While in [19] the perfect drain is made of a material with complex permittivity ε, here it is only a coaxial line loaded with a resistor and a capacitor of conventional values (for example, R=2.57Ω and C= 55.05pF for f=0.25 GHz). Using the circuital model for the perfect drain, the Comsol simulations have shown the super-resolution up to λ/3000 for the same discrete frequencies as in [23], which is much higher than the λ/500 obtained without perfect drain.
In section 2, it is described the complete microwave circuits. In section 3 modal analysis of the SGW is made including: the rigorous procedure used to find the perfect drain, the analysis of the transmitted and evanescent modes and the concept of voltage and current wave in the SWG. Discussion and conclusions are presented in section 4.

2. Microwave circuit and parameters of the simulation.

The SGW is bounded by two metallic spherical shells. The media between the shells is air. Two coaxial probes have been used to simulate the source and drain in the SGW. Consider the microwave circuit consists of the generator V_g with the impedance Z_g (on the source port side), coaxial lines, the SGW, and the load with the impedance Z_L (on the drain port side), as shown in Figure 1.

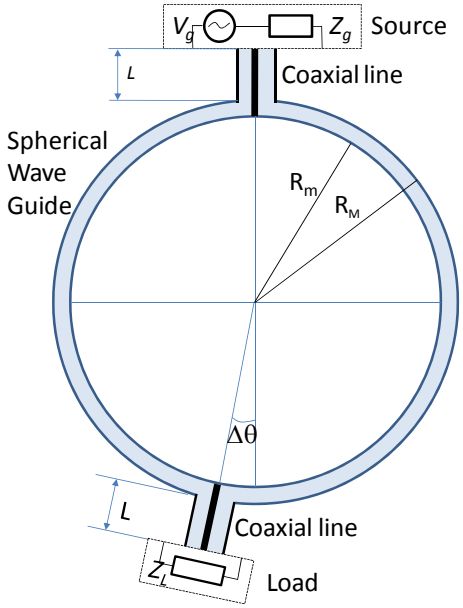

Figure 1 Complete microwave circuit analyzed in this paper formed by: the source (V_g and Z_g) connected to a coaxial transmission line of length L, the load connected (Z_L) to other identical transmission line and the spherical waveguide. R_M and R_m are radius of the external and internal metallic spheres.

The same circuit has been analyzed in [23] with the condition Z_L=Z_g=Z_0, where Z_0 is the characteristics impedance of the coaxial line, so we have:

$$|S_{21}|^2 = \frac{P_{load}}{P_{\max}} \qquad (1)$$

Where, S_{21} is the scattering parameter of the circuit [26], P_{load} is the power delivered to the load Z_L and P_{max} is the maximum power that can be delivered by the generator. In [23] the results have been presented using function $|S_{21}|^2$ obtained for different frequencies and displacements $\Delta\theta$.
Here, in Section 4, it is repeated the same procedure using the impedance that simulates the perfect drain (it will be calculated in Section 3 and will be called Z_{pd}). The circuit is designed in Comsol with the conditions Z_L=Z_g=Z_{pd} (see Figure 1). The super-resolution is analyzed via function P_{load}/P_{max} for different frequencies and displacements. Note, that now P_{load}/P_{max} is different from $|S_{21}|^2$.

3. Modal analysis of the structure and numerical procedure to find the perfect drain.

The perfect drain, defined by the impedance Z_L, absorbs all the incident radiation without reflection inside the SWG when the source and drain are placed in opposite pole ($\Delta\theta$=0). In this section we present a rigorous procedure to find this impedance for a wide band of frequencies. The structure does not depend on the cylindrical (coaxial) and spherical (SWG) coordinate ϕ, thus:

- The unique modes of the coaxial guide without ϕ dependence are the TEM modes, so in the interface between the coaxial and sphere only exist the TEM modes, incident and reflected [26].
- Inside the SGW the electric and magnetic fields are necessary of the form:

$$\mathbf{E}(r,\theta) = \mathrm{E}_r(r,\theta)\mathbf{r} + \mathrm{E}_\theta(r,\theta)\boldsymbol{\theta}$$
$$\mathbf{H}(r,\theta) = \mathrm{H}_\phi(r,\theta)\boldsymbol{\phi} \quad (2)$$

The complete analysis of the modes is done using the same procedure explained by Wu in [27] on a radial-line/coaxial-line junction. Figure 2 shows the complete region of the junction separated into three regions: the coaxial (region 1), the SGW (region 2) and the common region (region 3). The electronic field is calculated in each of these three regions using the procedure described below.

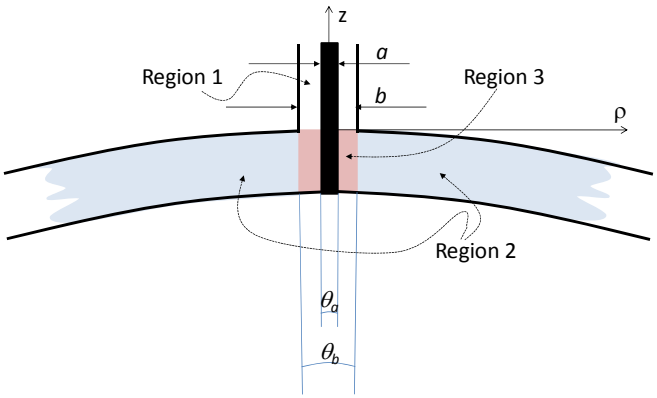

Figure 2 Three regions of the junction used for the analysis. The coaxial is the white region, the SGW the blue and the common region is the read. θ_a and θ_b are the angles in spherical coordinates covered by the inner and outer conductor of the coaxial.

The dimension of the structure analyzed here are (Figure 1 and Figure 2):

- R_M=1005 mm.
- R_m=1000 mm.
- a=5 mm (θ_a= 0.285º)
- b=10 mm (θ_b=0.57º)
- L=20 mm.

3.1. Field in the coaxial line (region 1).

Due to the symmetry of the structure, the field of the coaxial probe is completely described by the TEM modes of the line [26]:

$$\mathbf{E} = \left(\frac{V_e^+}{\rho Ln(b/a)}e^{-jk_o z} + \frac{V_e^-}{\rho Ln(b/a)}e^{jk_o z}\right)\boldsymbol{\rho}$$
$$\mathbf{H} = \frac{1}{\sqrt{\mu/\varepsilon}}\left(\frac{V_e^+}{\rho Ln(b/a)}e^{-jk_o z} - \frac{V_e^-}{\rho Ln(b/a)}e^{jk_o z}\right)\boldsymbol{\phi} \quad (3)$$

Where a and b are the diameters of the internal and external coaxial (Figure 2), ρ and z the cylindrical coordinates, k_o the propagation constant and V_e^+ and V_e^- constants. With the condition $b << R_M$, on the surface z=0 the approximation $\rho = R_M \sin(\theta)$ can be used (Figure 1and Figure 2).

$$\mathbf{E} = \left(\frac{V_e^+}{R_M sin(\theta) Ln(b/a)} + \frac{V_e^-}{R_M sin(\theta) Ln(b/a)}\right)\boldsymbol{\theta}$$
$$\mathbf{H} = \frac{1}{\sqrt{\mu/\varepsilon}}\left(\frac{V_e^+}{R_M sin(\theta) Ln(b/a)} - \frac{V_e^-}{R_M sin(\theta) Ln(b/a)}\right)\boldsymbol{\varphi} \quad (4)$$

3.2. Field in the SGW (Region 2).

With the condition $R_M - R_m << R_M$ one complete set of solutions inside the SWG fulfilling the boundary condition of metallic surfaces is [28]:

$$E_r(r,\theta) = \sum_n \left[A_n F_{\nu_n}(\cos(\theta)) + B_n R_{\nu_n}(\cos(\theta))\right] \left(\left(\frac{n\pi}{R_M - R_m}\right)^2 + k_0^2\right)\left(-\cos\left(\frac{(r-R_m)n\pi}{R_M - R_m}\right)\right)$$
$$E_\theta(r,\theta) = \sum_n \frac{1}{r}\left[A_n F'_{\nu_n}(\cos(\theta)) + B_n R'_{\nu_n}(\cos(\theta))\right] \frac{-n\pi}{R_M - R_m}\sin\left(\frac{(r-R_m)n\pi}{R_M - R_m}\right)$$
$$H_\varphi(r,\theta) = -j\omega\varepsilon_0 \sum_n \left[A_n F'_{\nu_n}(\cos(\theta)) + B_n R'_{\nu_n}(\cos(\theta))\right] \frac{1}{r}\cos\left(\frac{(r-R_m)n\pi}{R_M - R_m}\right)$$
$$\nu_n \approx -0.5 + 0.5\sqrt{1 + 4\left((R_M k_o)^2 - \left(\frac{R_M n\pi}{R_M - R_m}\right)^2\right)} \quad (5)$$

Where A_n and B_n are constants and $F_{\nu n}$ and $R_{\nu n}$, are called Forwards and Reverse Legendre functions defined as:

$$F_{\nu_n}(x) = P_{\nu_n}(x) + j\frac{2}{\pi}Q_{\nu_n}(x)$$
$$R_{\nu_n}(x) = P_{\nu_n}(x) - j\frac{2}{\pi}Q_{\nu_n}(x) \quad (6)$$

$P_{\nu n}$ and $Q_{\nu n}$, are the Legendre function of first and second kind.

3.3. Field in the common region of coaxial and SGW (region 3).

The solution in this region has the same form as the solution expressed in Equation (5), but now having an additional term, one particular solution, necessary to fulfill the boundary conditions at the common surfaces.

$$
\begin{aligned}
E_r(r,\theta) &= \sum_n \left[D_n F_{\nu_n}(\cos(\theta)) + E_n R_{\nu_n}(\cos(\theta)) \right] \\
&\left(\left(\frac{n\pi}{R_M - R_m} \right)^2 + k_0^2 \right) (-\cos(\frac{(r-R_m)n\pi}{R_M - R_m})) \\
E_\theta(r,\theta) &= \sum_n \frac{1}{r} \left[D_n F'_{\nu_n}(\cos(\theta)) + E_n R'_{\nu_n}(\cos(\theta)) \right] \\
&\frac{-n\pi}{R_M - R_m} \sin(\frac{(r-R_m)n\pi}{R_M - R_m}) + E_p(r,\theta) \\
H_\varphi(r,\theta) &= -j\omega\varepsilon_0 \sum_n \left[D_n F'_{\nu_n}(\cos(\theta)) + E_n R'_{\nu_n}(\cos(\theta)) \right] \\
&\frac{1}{r} \cos(\frac{(r-R_m)n\pi}{R_M - R_m}) + H_p(r,\theta)
\end{aligned}
\tag{7}
$$

Where the particular solution E_p and H_p has to fulfill the Maxwell equations and the boundary conditions at r=R_M and r=R_m.

$$
\begin{aligned}
&\mathbf{E_p} = E_p(r,\theta)\boldsymbol{\theta} \\
&\nabla \times \mathbf{E_p} = \frac{1}{r}\frac{\partial}{\partial r}(rE_p(r,\theta))\boldsymbol{\varphi} = -j\omega\mu \mathbf{H_p}(r,\theta) \\
&\nabla \times \mathbf{H_p} = \frac{-1}{j\omega\mu}\frac{1}{r^2\sin(\theta)}\frac{\partial}{\partial\theta}(\sin(\theta)\frac{\partial}{\partial r}(rE_p(r,\theta)))\mathbf{r} + \\
&\frac{1}{j\omega\mu}\frac{1}{r}\frac{\partial}{\partial r}(\frac{\partial}{\partial r}(rE_p(r,\theta)))\boldsymbol{\theta} = j\omega\varepsilon E_p(r,\theta)\boldsymbol{\theta}
\end{aligned}
\tag{8}
$$

From the second equation in (8), it is necessary:

$$
\begin{aligned}
&E_p(r,\theta) = f(r)\frac{1}{\sin(\theta)} \\
&\frac{d^2}{dr^2}(rf(r)) = -k_0^2 rf(r) \qquad k_0^2 = \omega^2\mu\varepsilon
\end{aligned}
\tag{9}
$$

Solving the differential Equation (9), the particular solution for the fields E_p an H_p is obtained:

$$
\begin{aligned}
E_p(r,\theta) &= \frac{a_1\frac{e^{jk_0 r}}{r} + a_2\frac{e^{-jk_0 r}}{r}}{\sin(\theta)} \\
H_p(r,\theta) &= \frac{-jk_0}{j\omega\mu}\frac{a_1\frac{e^{jk_0 r}}{r} - a_2\frac{e^{jk_0 r}}{r}}{\sin(\theta)}
\end{aligned}
\tag{10}
$$

Where a_1 and a_2 are two integration constants. These constants are obtained using the boundary conditions for E_p at r=R_M and r=R_m (E_p=0 for metallic surface):

$$
\begin{aligned}
a_1 &= (V_e^+ + V_e^-)\frac{1}{Ln(b/a)}\left(\frac{1}{e^{jk_0 R_M} - e^{jk_0(2R_m - R_M)}}\right) \\
a_2 &= (V_e^+ + V_e^-)\frac{1}{Ln(b/a)}\left(\frac{-e^{jk_0 2R_m}}{e^{jk_0 R_M} - e^{jk_0(2R_m - R_M)}}\right)
\end{aligned}
\tag{11}
$$

The fields defined in Equations (10) and (11) can be expresed as follow:

$$
\begin{aligned}
E_p(r,\theta) &= \frac{V_e^+ + V_e^-}{r\sin(\theta)}\sum_n d_n \frac{-n\pi}{R_M - R_m}\sin[\frac{(r-R_m)n\pi}{R_M - R_m}] \\
H_p(r,\theta) &= \frac{V_e^+ + V_e^-}{r\sin(\theta)}\sum_n e_n \cos[\frac{(r-R_m)n\pi}{R_M - R_m}]
\end{aligned}
\tag{12}
$$

Where d_n and e_n are the expansion constants satisfying $j\omega\varepsilon d_n$=-e_n. The complete field in this region is then:

$$
\begin{aligned}
E_r &= \sum_n \left[D_n F_{\nu_n}(\cos(\theta)) + E_n R_{\nu_n}(\cos(\theta)) \right] \\
&\left(\left(\frac{n\pi}{R_M - R_m} \right)^2 + k_0^2 \right) (-\cos(\frac{(r-R_m)n\pi}{R_M - R_m})) \\
E_\theta &= \sum_n \frac{1}{r}\left[D_n F'_{\nu_n}(\cos(\theta)) + E_n R'_{\nu_n}(\cos(\theta)) + \frac{V_e^+ + V_e^-}{\sin(\theta)}\frac{e_n}{-j\omega\varepsilon_0} \right] \\
&\frac{-n\pi}{R_M - R_m}\sin(\frac{(r-R_m)n\pi}{R_M - R_m}) \\
H_\varphi &= -\sum_n \left[D_n F'_{\nu_n}(\cos(\theta)) + E_n R'_{\nu_n}(\cos(\theta)) + \frac{V_e^+ + V_e^-}{\sin(\theta)}\frac{e_n}{-j\omega\varepsilon_0} \right] \\
&j\omega\varepsilon_0 \frac{1}{r}\cos(\frac{(r-R_m)n\pi}{R_M - R_m})
\end{aligned}
\tag{13}
$$

In the coaxial line (on the drain side) the term for the electric field has the same form (V_e has to be replaced by V_s, θ by π-θ, D_n by G_n and E_n by I_n):

3.4. Transmitted and not transmitted modes.

Different modes inside the sphere are defined by ν_n=α_n+jβ_n (see Equation (5)), which is in general a complex number. According to the asymptotic expression of Legendre functions $P_{\nu n}(x)$ and $Q_{\nu n}(x)$ for x close to 1 and -1 the following results are obtained [29]:

$$
\left.
\begin{aligned}
&\left| \frac{F_{\nu_n}(\cos(\pi-\theta))}{F_{\nu_n}(\cos(\theta))} \right| \to \frac{e^{-\beta_n}}{\Gamma(0)} \\
&\left| \frac{R_{\nu_n}(\cos(\theta))}{R_{\nu_n}(\cos(\pi-\theta))} \right| \to \Gamma(0)e^{-\beta_n}
\end{aligned}
\right\} \quad for \quad \theta \to 0
\tag{14}
$$

$\beta_n = \mathrm{Im}[\nu_n]$ $\Gamma(\theta)$, Gamma function

Having in mind the SGW dimension and the frequencies of interest (the microwave frequencies from 0.2 GHz to 0.4 GHz) the parameter ν_n is real only for n=0. For example for f=300 MHz, ν_0 =4.98, ν_1 =-0.5+631.4j, ν_2 =-0.5+1262.9j etc. Figure 3 shows for example the graphs for $\mathrm{Log}(|F_{\nu n}(\cos(\theta))/F_{\nu n}(\cos(\theta_b))|)$ and

Log($|R_{vn}(\cos(\theta))/R_{vn}(\cos(\theta_b))|$) respect to θ for one complex ν_n=-0.5+4.0j (θ_b is defined in Figure 2). Clearly $|F_{vn}(\cos(\theta))|$ suffers a near exponential attenuation between θ=θ_b and θ=π-θ_b as shown in Equation (14). The same occurs for $|R_{vn}(\cos(\theta))|$ between θ=π-θ_b and θ=θ_b. The similar results are found for every complex ν_n, so $F_{vn}(\cos(\theta))$ and $R_{vn}(\cos(\theta))$ can be considered evanescent waves. The SWG works as a single-mode with the electric and magnetic fields far for the interface region given by:

$$\mathbf{E}(r,\theta) = k_0^2\left[A_0 F_{\nu_0}(\cos(\theta)) + B_0 R_{\nu_0}(\cos(\theta))\right]\mathbf{r}$$
$$\mathbf{H}(r,\theta) = -j\omega\varepsilon_0\left[A_0 F'_{\nu_0}(\cos(\theta)) + B_0 R'_{\nu 0}(\cos(\theta))\right]\frac{1}{r}\boldsymbol{\phi} \quad (15)$$

The Poynting vector and transmitted power through a surface, defined by θ=cte, in the direction $\boldsymbol{\theta}$ have the following form:

$$\mathbf{S}(\theta) = \frac{1}{2}(\mathbf{E}\times\mathbf{H}^*) = k_0^2 j\omega\varepsilon(A_0 F_\nu(\cos(\theta)) + B_0 R_\nu(\cos(\theta)))$$
$$(A_0\frac{dF_\nu(\cos(\theta))}{d\theta} + B_0\frac{dR_\nu(\cos(\theta))}{d\theta})^*\boldsymbol{\theta} \quad (16)$$
$$P = \mathrm{Re}[\iint_{\substack{R_m<r<R_M\\ 0<\varphi<2\pi}} S(\theta) r\sin(\theta) dr d\varphi] =$$
$$2k_0^2\omega\varepsilon(R_M - R_m)(|A_0|^2 - |B_0|^2)$$

This equation explains clearly the concept of F_{v0} and R_{v0} as incident and reflected waves.

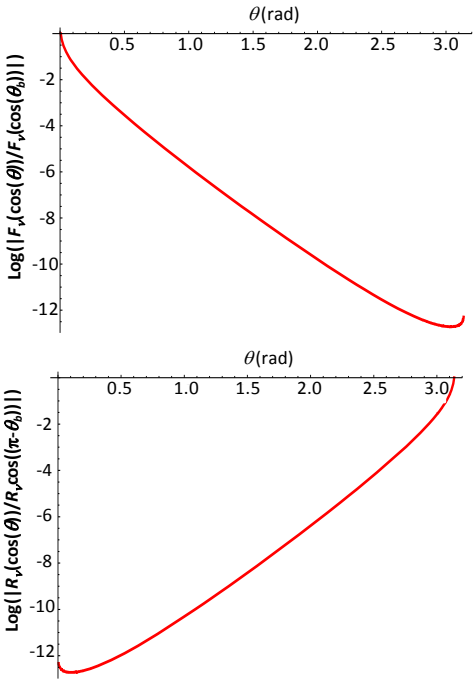

Figure 3 Graphs for Log($|F_{vn}(\cos(\theta))/F_{vn}(\cos(\theta_b))|$) and Log($|R_{vn}(\cos(\theta))/R_{vn}(\cos(\pi$-$\theta_b)|$) as function of θ for ν_n=-0.5+4.0j. $F_{vn}(\cos(\theta))$ and $R_{vn}(\cos(\theta))$ have a near exponential attenuation similar to the evanescent waves in conventional waveguides. The modes with complex ν_n are not transmitted. The only modes that exist inside the SWG far from the interface are the modes having real ν_n.

3.5. Boundary conditions.

The coefficients A_n and B_n from Equation (5), D_n, E_n, G_n and I_n from Equation (7) are obtained using the following boundary conditions (Figure 2):

- Tangent electric field in the inner conductor is null.
- Electric and magnetic field are the same in the common surface between regions 1 and 2.
- The same conditions in the coaxial at the drain side.

$$D_n F_{\nu_n}(\cos(\theta_a)) + E_n R_{\nu_n}(\cos(\theta_a)) = 0$$
$$D_n F_{\nu_n}(\cos(\theta_b)) + E_n R_{\nu_n}(\cos(\theta_b)) = A_n F_{\nu_n}(\cos(\theta_b)) + B_n R_{\nu_n}(\cos(\theta_b))$$
$$D_n F'_{\nu_n}(\cos(\theta_b)) + E_n R'_{\nu_n}(\cos(\theta_b)) + \frac{V_e^+ + V_e^-}{\sin(\theta_b)}\frac{e_n}{-j\omega\varepsilon_0} =$$
$$= A_n F'_{\nu_n}(\cos(\theta_b)) + B_n R'_{\nu_n}(\cos(\theta_b)) \quad (17)$$
$$G_n F_{\nu_n}(\cos(\pi-\theta_a)) + I_n R_{\nu_n}(\cos(\pi-\theta_a)) = 0$$
$$G_n F_{\nu_n}(\cos(\pi-\theta_b)) + I_n R_{\nu_n}(\cos(\pi-\theta_b)) =$$
$$= A_n F_{\nu_n}(\cos(\pi-\theta_b)) + B_n R_{\nu_n}(\cos(\pi-\theta_b))$$
$$G_n F'_{\nu_n}(\cos(\pi-\theta_b)) + I_n R'_{\nu_n}(\cos(\pi-\theta_b)) + \frac{V_s^+ + V_s^-}{\sin(\pi-\theta_b)}\frac{e_n}{-j\omega\varepsilon_0} =$$
$$= A_n F'_{\nu_n}(\cos(\pi-\theta_b)) + A_n R'_{\nu_n}(\cos(\pi-\theta_b))$$

Where θ_a and θ_b are defined in Figure 2. When the voltage in the two coaxial lines (V_e=V_e^++V_e^- and V_s=V_s^++V_s^-) are known, the system (17) can be solved for each n.

3.6. Perfect Drain.

According the previous analysis, the SGW work as a single-mode guide, so the condition for the perfect drain (there is no reflected wave in the guide) is satisfied when B_0=0 in Equation (15). The procedure to obtain the perfect drain consists of the following steps:

- In Equation (17) for n=0 it is imposed the condition B_0=0. Then A_0, D_0, E_0, G_0, I_0 and V_s^++V_s^- are calculated. V_s^++V_s^- is the necessary voltage (on the drain side coaxial) for perfect wave absorption in the SWG.
- The coefficient A_n, B_n, D_n, E_n, G_n and I_n are obtained using Equation (17) and the voltage V_s^++V_s^- calculated in the previous step.
- The field H_φ for r=R_M and $\theta_a < \theta < \theta_b$ is computed using Equation (13).
- For the sake of uniqueness of solution, this field has to depend on θ as in Equation (4). The voltage V_s^+-V_s^- is then obtained.
- The impedance of the coaxial line at r=R_M and the load are defined as:

$$Z_S = Z_0\frac{V_s^+ + V_s^-}{V_s^+ - V_s^-} \quad Z_L = Z_0\frac{V_s^+ e^{jk_oL} + V_s^- e^{-jk_oL}}{V_s^+ e^{jk_oL} - V_s^- e^{-jk_oL}} \quad (18)$$

Figure 4 shows the real and imaginary parts of the perfect drain impedance calculated for a band of frequencies of interest, the results show some oscillation due numerical error in the calculation. Linear approximation is presented. Figure 5 shows the comparison between the module of the theoretical electric field (in the case of the perfect drain, there exit only forward wave, given by the function $F_{v0}(\theta)$)

and the module of the electric field simulated in COMSOL. Although the theoretical value of the electric field at θ=0 and $\theta=\pi$ is infinite (due to the properties of the Legendre functions), for the sake of clearness of the graphs in Figure 5 we did not extend the theoretical graph to these points. Figure 5 shows perfect matching between the theoretical and simulated fields for f=0.25 GHz. The circuit parameters are calculated using the linear approximations presented in Figure 4, R=2.57Ω and C= 55.05pF.

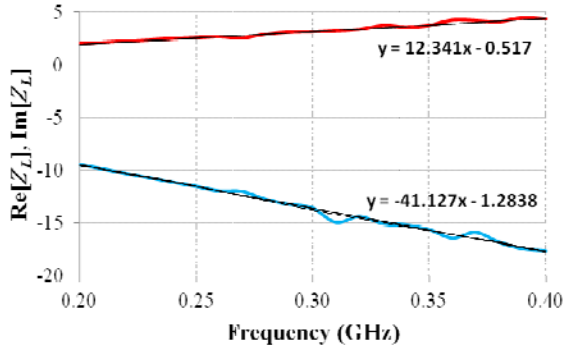

Figure 4 Real (in red) and imaginary (in blue) parts of the perfect drain impedance for different frequencies.

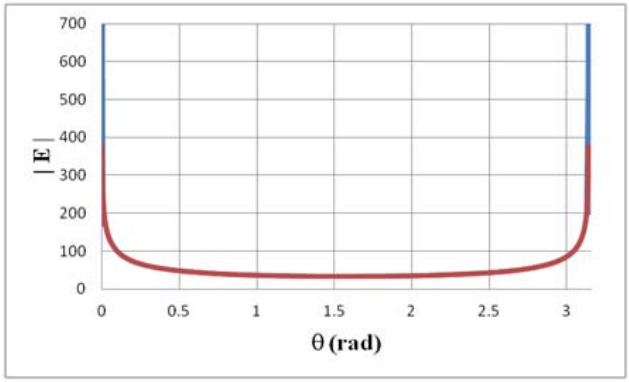

Figure 5 The module of the theoretic electric field (in red) and the modul of the electric filed simulated in Comsol (in blue) for the SGW with the perfect drain.

4. SR analysis of the SGW matched with the perfect drain.

The SGW with the perfect drain is designed and analyzed in Comsol, in the same way as described in [32] In order to show super-resolution properties of the SGW, we have made several simulations for different displacements of the drain port, and for different values of frequency.

4.1. P_{load}/P_{max} as function of frequencies for different drain port position.

We have computed Pload/Pmax using COMSOL for a frequency range between 0.2 GHz and 0.4 GHz for different positions of the drain port. The source port is fixed at the source's image point, that is, θ= 0, while the drain port is shifted λ/N (for λ=1m corresponding to 0.3 GHz and N>100) in the neighborhood of the image point, that is, θ= π, see Figure 1. When the drain port is placed in the image point, all the power is delivered perfectly. This can be achieved for all the frequencies using corresponding perfect drain impedance (Figure 4). However, when the drain is moved from the image point, some of the power reflects, so the power delivered to the drain decreases. This power drop is extremely abrupt for some frequencies very close to the Schumann frequencies, called notch frequencies (see also [23]).

Figure 6 shows P_{load}/P_{max} as function of the frequency in a narrow band around a notch frequency (close to ν=5) for different drain port positions. The notches get wider when the drain port is shifted further from the image point of the source, but the null of P_{load}/P_{max} remains fixed.The frequencies corresponding to these nulls are called notch frequencies.

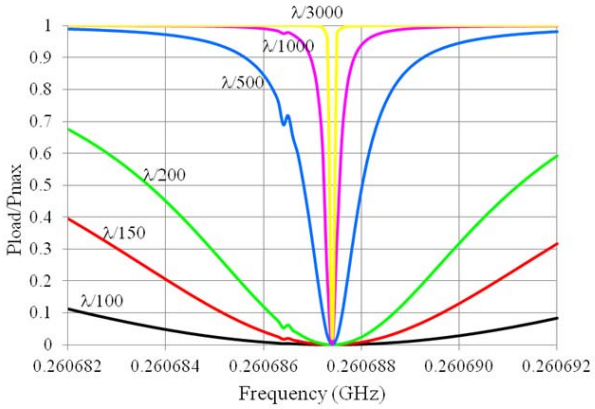

Figure 6 Detail of P_{load}/P_{max} as function of the frequency in a narrow band around a notch frequency for different drain port positions. The notch frequency is f=0.2606874 GHz. (ν=4.996). The nearest Schumann frequency is f=0.26086609 GHz (ν=5) which is out the range of this Figure.

The curves correspond to different shifts of the drain port. The shifts are in all cases much smaller than wavelength (from λ/100 to λ/3000 with λ=1.15084047 m that correspond to f=0.2606874 GHz, see Figure 6). These results are quite surprising, since close to a specific frequency the power transmitted to the drain port suddenly reduces to a value near zero.

4.2. P_{load}/P_{max} as function of drain port shift for different frequencies.

Since P_{load}/P_{max} is proportional to the transmitted power, the graph representing P_{load}/P_{max} versus the shift (Figure 7) is equivalent to the Point-Spread-Function (PSF) commonly used in Optics. This equivalence may seem surprising since the PSF is defined as the square of the electric field amplitude calculated in the absence of absorbers in the image space, and P_{load}/P_{max} is defined in terms of the power

transmitted to an absorber. However, the equivalence comes from the fact that, in Optics, the detection at the image is assumed to be made with a sensor which does not perturb the free-space fields; or that even if it does perturb the fields, it is assumed that still the sensor signal is proportional to the field amplitude (or its square, which is the PSF. Figure 7 shows P_{load}/P_{max} versus the drain port shifts for two frequencies. The blue curve corresponds to f=0.2847 GHz, i.e., far from a notch frequency (ν= 5.5).

Let us define "resolution" as the arc length (in wavelength units) that a drain port needs to be shifted so P_{load}/P_{max} drops to 10% (not far from the Rayleigh criteria in Optics, which refers to the first null). With this definition, the diffraction limited resolution given by the blue curve is $\lambda/3$. The red curve corresponds to notch frequency f=0.26068741 GHz (ν =4.996) which clearly shows a much better resolution.

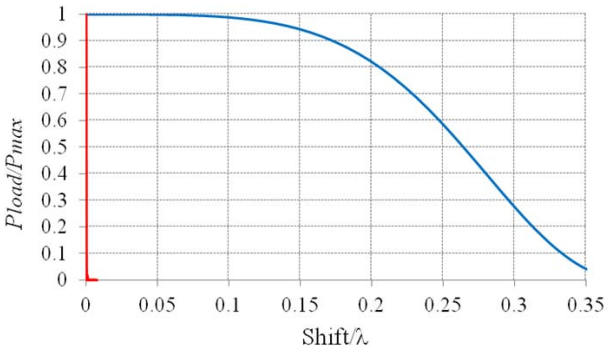

Figure 7 P_{load}/P_{max} as function of the drain port shift for a frequency near a notch one (red curve) and for a frequency far from the notch one (blue curve).

Figure 8 is a blow-up of Figure 7 in the upper neighborhood of a notch frequency. The graph for frequencies slightly below the notch frequency is similar. Note that Figure 8 shows the same information as Figure 6 but plotting P_{load}/P_{max} vs. the drain port shift (expressed in units of λ) and using the frequency as a parameter.

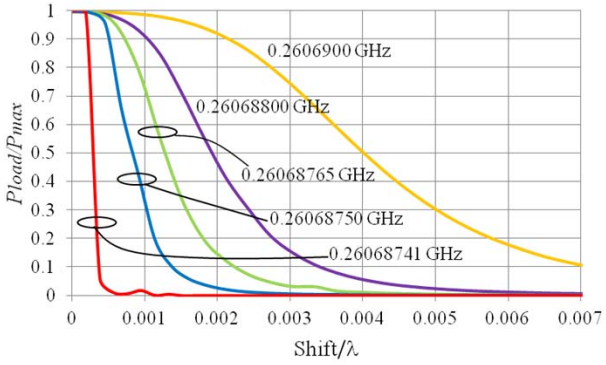

Figure 8 P_{load}/P_{max} as function of the drain port shift for different frequencies corresponding to super-resolution between λ/3000 and λ/140.

From the orange to the red curves, increasing resolutions are achieved: 0.007 λ (that is, λ/140) for the orange to λ/3000 for the red. The latter, whose frequency f=0.26068741 GHz corresponds to ν=4.99636) is the highest resolution that we have obtained. Computations for frequencies near the notch frequency show essentially null P_{load}/P_{max} values for shifts > λ/3000 (as in the red line in the picture). P_{load}/P_{max} values for shifts below λ/3000 (excepting no shift or shifts very near to zero) and frequencies near a notch frequency are inconsistent (the solver did not converge to a single solution due to numerical errors). It seems that Leonhardt's assertion of infinite resolution (i.e., perfect imaging) may occur for the discrete notch frequencies in the SGW, although the mentioned inconsistencies have prevented us from numerically predicting resolutions beyond λ/3000.

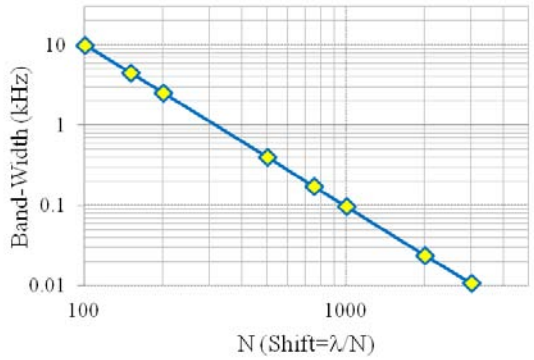

Figure 9 Bandwidth as a function of the resolution. The abscissa axis shows N, meaning that the resolution is better than λ /N.

The λ/3000 resolution is achieved only for a narrow bandwidth (≈ 10 Hz, which is much smaller than the notch frequency ≈0.3GHz). If larger bandwidths are needed, lower resolutions (but still sub-wavelength) may be achieved. Figure 9 shows the bandwidth vs. N, meaning that the resolution is better that λ/N. The bandwidth has been calculated as $f_{max}-f_{min}$ with f_{max} and f_{min} fulfilling P_{load}/P_{max} (f_{max})=P_{load}/P_{max} (f_{min}) =0.1, using the information of the curves in Figure 6. The linear dependence shown in Figure 9 (slope -2) reveals that the product N^2×bandwidth is constant in the range analyzed here.

5. Discussion.

Leonhardt in [6] and [7] suggested that MFE should produce perfect imaging for any frequency using perfect drains. However, the experiments in [20][21] and simulations from [23], have shown super-resolution properties of the MFE, although the perfect drain has not been used. In these references, the coaxial probes were loaded with their characteristic impedances, so the absorption of the incident wave was not perfect. Leonhardt assumed that the ability of the MFE to propagate the wave, generated by a point source, toward to a perfect point drain was enough to guarantee perfect imaging. This does not seem to be sufficient, since it does not provide information on how much power the drain will absorb when it is displaced out of the image point. The simulations presented here show that super-resolution only

happens for a particular set of frequencies known as notch frequencies, the same one as in [23]. The presented results have shown maximum super-resolution λ/3000, which is much higher than in the case where there were not perfect drains (λ/500, see [23]). Also, the frequency bandwidth has increased 20 times, e.g. for λ/500 the bandwidth is about 400 Hz (Figure 9), while in [23] it was only 20 Hz.

Acknowledgements

The authors would like to thank the Spanish Ministry MCEI (Consolider program CSD2008-00066, PERIMAGE: TEC2011-24019, TEC2010-16948) for the support given in the preparation of the present work.

References

[1] Fang N, Lee H, Sun C, Zhang X 2005 Sub-Diffraction-Limited Optical Imaging with a Silver Superlens *Science*, Vol 308, 534-537.

[2] Mesa F, Freire F, Marqués R, Baena J D 2005 Three dimensional superresolution in material slab lenses: Experiment and theory *Phy. Review B* 72, 235117.

[3] Pendry J B, 2000 Negative Refraction makes a Perfect Lens *Phy. Review Let.* Vol. 85, Nº 18. 3966-3989.

[4] Shelby R A., Smith D R, Schultz S 2001 Experimental verification of negative index of refraction *Science*, Vol 292, 79.

[5] M. Born, E. Wolf. *Principles of Optics*. Cambridge University Press. Sixth Edition, p.143.

[6] Leonhardt U 2009 Perfect imaging without negative refraction, *New J. Phys.* **11** 093040.

[7] Leonhardt U, Philbin T G, 2010 Perfect imaging with positive refraction in three dimensions, Phys. Rev. A 81, 011804.

[8] Benítez P, Miñano J C, González J C 2010 Perfect focusing of scalar wave fields in three dimensions *Optics Express* 18, 7650-7663.

[9] Blaike R.J. 2010 Comment on 'Perfect imaging without negative refraction' *New Journal of Physics*, 2010. **12**(5): p. 058001.

[10] Leonhardt U. 2010 Reply to comment on 'Perfect imaging without negative refraction' *New Journal of Physics*. **12**(5): p. 058002.

[11] Guenneau, S. A. Diatta, and R.C. McPhedran 2010 Focusing: coming to the point in metamaterials *Journal of Modern Optics*. **57**(7): p. 511-527.

[12] Merlin, R. 2010 Comment on "Perfect imaging with positive refraction in three dimensions" *Physical Review* A. **82**(5): p. 057801.

[13] F. Sun and S. He 2010 Can Maxwell's fish eye lens really give perfect imaging? *Progress In Electromagnetics Research*, Vol. 108, 307-322.

[14] F. Sun, X. C. Ge, and S. He 2010 Can Maxwell's fish eye lens really give perfect imaging? part II. the case with passive drains *Progress In Electromagnetics Research*, Vol. 110, 313-328.

[15] Leonhardt, U. and S. Sahebdivan 2010 Perfect imaging: they do not do it with mirrors *Journal of Optics*. **13**(2): p. 024016.

[16] Leonhardt, U. T.G. Philbin 2010 Reply to "Comment on `Perfect imaging with positive refraction in three dimensions" *Physical Review* A. **82**(5): p. 057802.

[17] P. Kinsler and A. Favaro 2010 Comment on: Reply to comment on `Perfect imaging without negative refraction' 2011 *New J. Phys.* 13 028001.

[18] U. Leonhardt 2011 Reply to Comment on Reply to Comment on `Perfect imaging without negative refraction' *New J. Phys.* 13 028002.

[19] González JC., Benítez P, Miñano JC. 2011 Perfect drain for the Maxwell Fish Eye lens *New Journal of Physics*.

[20] Ma YG, Ong CK, Sahebdivan S, Tyc T, Leonhardt U. 2010 Perfect imaging without negative refraction for microwaves *ArXiv:1007.2530v1*.

[21] Ma YG, Sahebdivan S, Ong CK, Tyc T, Leonhardt U. 2010 Evidence for subwavelength imaging with positive refraction *New J. Phys*. 13 033016.

[22] Gabrielli LH, Leonhardt U, Lipson M. 2010 Perfect imaging in the optical domain using dielectric materials *ArXiv:1007.2564v1*.

[23] Miñano J.C, Marqués R, González J.C, Benítez P., Delgado V., Grabovičkić D. and Freire M. 2011 Super-Resolution for a point source better than λ/500 using positive refraction *New Journal of Physics*. **13**(2011) 125009.

[24] Miñano J.C., Benítez P, González JC. 2010 Perfect imaging with geodesic waveguides *New Journal of Physics*. **12**(12): p. 123023.

[25] Leonhardt U, 2010 . *Geometry and Light: The Science of Invisibility*, Dover.

[26] Pozar David M. 2005 *Microwave Engineering*. John Wiley&Son Inc.

[27] Wu D. and Ruan C. 1998 Analysis on a radial-line/coaxial-line junction *Electronics Letters* Vol. 34, No.10 p.994.

[28] Akira Ishamuro 1991 *Electromagnetic wave propagation, radiation and scattering*. Prentice-Hall.

[29] Erdélyi A, Magnus W, Oberhettinger F and Tricomi F G 1953 *Higher Transcendental Functions vol I* (New York: McGraw-Hill).

[30] Jackson D.J. 1998 *Classical Electrodynamics.* John Wiley & Sons, *Inc.*3rd ed.

[31] Solimeno S, Crosignani B, DiPorto P, 1986 *Guiding, Diffraction and Confinement of Optical Radiation*, Academic Press.

[32] Grabovičkić D, Gonzalez J.C, Miñano J.C, and Benitez P., Super-resolution Properties of the Maxwell Fish-Eye, Proc. Comsol Conference, Stuttgart 2011

Plasmonic properties of silver nanocube monolayers on high refractive index substrates

Adam Bottomley[1], Daniel Prezgot[1], Anatoli Ianoul[1]

[1]Department of Chemistry, Carleton University, Canada
*corresponding author, E-mail: anatoli_ianoul@carleton.ca

Abstract

Extinction spectra of nanocubes supported by a symmetry breaking dielectric substrate are very different from those in solution. In this work we varied the refractive index of the substrate in order to optimize the refractive index sensitivity (RIS) of supported silver nanocube monolayers. We found that on thin (5-7 nm) silicon films the RIS is characterized by the figure of merit (FOM) for the quadrupolar plasmonic mode as high as 5.0, making silicon supported silver nanocube monolayers a promising sensing platform.

1. Introduction

Localized surface plasmon resonances (LSPR) of noble metal nanoparticles have been studied intensely in recent years. The ability to control and tune LSPRs is crucial to both understanding and application in the field of plasmonics [1]. Progress made in fabrication methods [2] and theory for metal nanoparticles has allowed for development of novel optical and sensing materials [3]. When the LSPRs of these particles are excited, a strong enhancement of their local electric fields occurs at the surface of the particles. This field enhancement allows for increased signal from optical techniques such as Raman [4,5], IR [6], and fluorescence [7-10] spectroscopy. The spectral extinction spectra of LSPRs are also very sensitive to the refractive index of their local environment making them an excellent platform for sensing [3,11]. The plasmonic signature of metal nanostructures can be influenced in several ways by modifying their size, shape, and material [1,12], but also through interparticle interactions [13] and particle substrate interactions [14,15]. Such investigations have shown unique properties such as collective modes and Fano like resonances [16].

Plasmonic signatures of nanoparticles that are supported by a dielectric material exhibit significant changes in their LSPRs when compared to particles in colloidal solutions. The most notable change is the splitting of a single dipolar plasmonic mode into two distinct modes [16-18]. When dealing with spherical nanoparticles these two new modes correspond to dipolar oscillations with orthogonal polarizations [18]. However, when nanocubes are deposited on a dielectric support their substrate interaction leads to plasmon mode hybridization, resulting in two distinct bands with corresponding charge oscillations located at the opposite sides of the nanocube [14,16-18]. Separation between the bands in the case of cubes was found to be greater than that for the spherical particles dependent on the size [17], edge and corner sharpness, as well as distance from the substrate [19]. Each of these hybrid bands present in the nanocubes is sensitive to the refractive index of their respective environments, one being the substrate and the other the surrounding medium in which the supported layer is immersed [14,16,17]. In the present work we fabricated quasi-periodic arrays of silver nanocubes on substrates with varying refractive indices. This allowed for a series of refractive index sensitivity measurements that relate the changes in refractive index of the substrate to changes in the surrounding medium.

2. Experimental

2.1. Chemicals

Silver nitrate 99+%, polyvinylpyrrolidone (PVP) with a molecular weight of 55000, anhydrous 99.8% ethylene glycol (EG), anhydrous sodium sulfide, and chloroform were purchased from Sigma-Aldrich and used as obtained. 1,2-dioleoyl-sn-glycero-3-phosphocholine (DOPC) was purchased from Avanti Polar Lipids, Alabaster, AL. Ethanol (95%) were obtained from Brampton and used without further purification.

2.2. Preparation of Nanocubes

Silver nanocubes (NC) with an edge length of 55 nm were synthesized according to the procedure described in the literature [20]. Typically, a 100 mL round bottom flask containing 35 mL of EG and a clean stir bar was placed in an oil bath set to 150°C and allowed to heat for 1 h. Using a glass syringe 5 mL of EG containing 0.4 g of dissolved PVP was injected. Five minutes later using a micropipette 400 μL of 3 mM sodium sulfide dissolved in EG was added. After an additional 5 min 2.5 mL of 282 mM silver nitrate dissolved in EG was injected slowly using a glass syringe. Upon addition of the silver nitrate the solution immediately turned black, slowly became a transparent yellow, and then changed to an ochre colour while some plating in the flask occurred. The reaction was monitored by periodically

taking small aliquots out of the reaction flask using a pasture pipette and dispersing it in a cuvette filled with ethanol for UV-visible spectroscopy. The reaction was quenched by placing the flask in an ice bath when the appearance of a small but distinct peak at 350 nm was observed in the spectra.

2.3. Purification of Colloidal Silver Nanocubes

The as-synthesized colloidal nanocubes contained unreacted EG, an excess of PVP. EG and PVP were removed by diluting the colloidal solution with ethanol (1:1 by volume) followed by centrifugation at 12 000 rpm. The precipitate was collected and redispersed in ethanol by sonication. This process was repeated 30 times for complete removal of EG and PVP. The purified silver NC solution was further subjected to washing with chloroform by centrifugation (at least 3 times) prior to LB film preparation. The final volume of the nanocube solution was 4 mL.

2.4. Preparation of LB Monolayers

Nanocube substrates were prepared according to the procedure reported previously [21]. Briefly, a NIMA 311D trough, filled with Milli Q water (18.2 mΩ cm), was used to prepare the Langmuir monolayers of different NC samples. In order to form monolayers, an appropriate amount of each sample was deposited onto the water surface using a micro syringe. Each monolayer was left for 20 min to allow chloroform evaporation. The surface pressure of the monolayer was measured with a paper Wilhelmy plate. Before transferring the monolayer onto solid supports several isotherm cycles were performed to anneal the films to surface pressures in the solid phase. Monolayers of nanocube/DOPC mixtures were transferred onto substrates cleaned with aqua regia and subsequently with mixture of chloroform and methanol at various surface pressures by vertical upward dipping at 2 mm/min at room temperature.

2.5. UV-Vis Measurements

UV-vis spectra of monolayers deposited on the substrates were recorded using a Shimadzu UV-2450 UV-vis spectrophotometer. Spectra were analyzed using GRAMS/AI spectral data processing software. Spectral deconvolution was performed using an appropriate number of mixed Gaussian-Lorentzian functions as well as a linear baseline to achieve the best fit to the original trace while minimizing χ^2 values. To determine the refractive index sensitivities (RIS), the monolayer slides were immersed in water/EG solutions with varying volume percentages and the extinction spectra measured. The refractive indices of the mixtures were calculated from the volume percentages of the ingredients according to the Lorentz-Lorenz equation [22]. The refractive indices of the pure solvents were 1.3334 and 1.4318, for water and EG respectively [22]. The plasmon shifts were plotted as a function of the refractive index. The refractive index sensitivities were obtained from the slope of the linear fitting.

2.6. Topographical Measurements

The topography of the NC monolayers, transferred onto substrates at different surface pressures, was obtained using an Ntegra (NTMDT, Russia) atomic force microscope in semi contact mode in air at 23 °C with 512x512 points per image. A 100x100 μm^2 scanner (Ntegra) and cantilevers with rotated monolithic silicon tips (125 μm long, 40 N/m spring constant Tap 300Al, resonance frequency 315 kHz, Budget Sensors) were used for all topographic measurements. The typical scan rate was 0.5 Hz. AFM images were further processed by Nova image processing software.

3. Results and Discussion

Colloidal silver nanocubes of ~55 nm edge size used in the present study are characterized by an extinction spectrum with a single dipolar LSPR peak at 443 nm, and a small peak at 350 nm [23]. Applications exploiting plasmonic properties often require nanoparticles to be deposited on a solid substrate. We have previously shown that Langmuir Blodgett monolayer technique allows not only effective deposition but also control of plasmonic properties of monolayers of silver nanocubes [14,15,17]. Such monolayers are proven to be effective in enhancing surface enhanced Raman scattering (SERS) signal but also in probing refractive index change in the environment, and therefore represent a powerful sensing platform. Plasmonic properties of supported by a dielectric nanocubes however differ significantly from those in a suspension [1,3,14,23]. LSPR- induced charges in such dielectric substrates disturb the nanocube electric field leading to plasmon mode hybridization with the appearance of two new bands: dipolar (D) and quadrupolar (Q). The charge oscillations for these new bands are located at the opposite sides of the cube: dipolar near the substrate and quadrupolar away from the substrate [1,3,14,23]. The degree of spectral separation between the two bands and the refractive index sensitivity depend on the distance between the substrate and the cubes, contact area and the refractive index (n_{RI}) of the substrate (Figure 1) [1,14,23].

In this work we prepared a monolayer of 55 nm silver nanocubes on several substrates with varying refractive indices. The samples were found to be very homogeneous with very uniform nanocubes (Figure 1a). In addition, to minimize interparticle dipolar coupling the monolayer was prepared from a mixture of nanocubes and a phospholipid DOPC. We have previously shown that by using mixtures consisting of nanocubes and lipids of different kind it is possible to pattern the nanocubes in monolayers. Depending on the lipid properties we were able to obtain homogeneously dispersed nanocubes, as shown in figure 1a. It turns out

that in such monolayers separation between the nanocubes was maintained at ~130 nm (Figure 1b). As a result extinction spectra of supported nanocubes contained only small long wavelength peaks corresponding to dipole-dipole coupling between adjacent cubes, observed at Figure 1c in the 550-700 nm spectral region. We used four substrates with increasing refractive indexes: glass, sapphire, 5 nm Si film deposited on glass, and a 7 nm Si film deposited on glass. Due to plasmonic band hybridization two bands visible in the spectra are observed and assigned to Q and D modes.

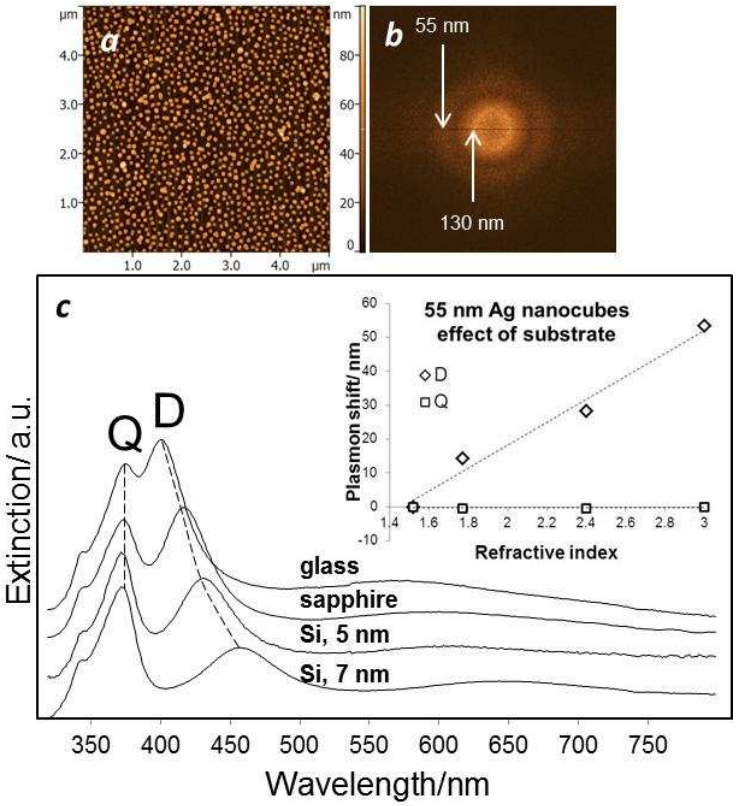

Figure 1: Supported silver nanocube monolayer prepared by Langmuir Blodgett technique: (a) AFM topography and (b) Fast Fourier transform (FFT) images indicate the size (55 nm) and the average inter-particle distance (130 nm); (c) extinction spectra of supported silver nanocube monolayers indicate strong dependence of the dipolar (D) but not quadrupolar (Q) mode on the substrate refractive index.

Since charge oscillations corresponding to the D mode are located near the substrate surface the dipolar band shows strong dependence on the substrate refractive index, and red-shifts by more than 50 nm when the refractive index of the substrate changes from 1.52 for glass to ~3.0 for a 7 nm silicon film (Figure 1c inset). In contrast the quadrupolar mode is insensitive to the substrate refractive index.

At the same time, both modes were found to be sensitive to the refractive index change of the medium (Figure 2). And, since change oscillations corresponding to the Q mode are located at the nanocube side away from eth substrate, it was found to have a stronger dependence than the D mode (Figure 2 inset) [14,23]. At the same time, the nature of the supporting dielectric substrates appears to play a crucial role in our ability to track spectral changes associated with the medium refractive index change. For example, when n_{RI} of the substrates is relatively low, as for glass, where n_{RI}=1.52, upon immersion in liquid plasmon mode hybridization disappears (Figure 2). This is due to insufficiently large refractive index change between the substrate and the medium to induce plasmon mode hybridization. As a result, plasmonic signature of glass supported silver nanocube monolayer immersed in water resembles that of colloidal nanocubes, mentioned before. The main band observed in such monolayer corresponds to dipolar oscillations and show modest sensitivity to the medium refractive index (Figure 2). At the same time, if the substrate has a sufficiently high n_{RI}, as with the 7 nm silicon film (n~3.0), the dipolar and quadrupolar bands remain clearly distinguished even when submerged in high refractive index liquids, such as ethylene glycol (Figure 2). The Q and D bands remain well separated in various solutions- pure water and ethylene glycol. By tracking the position of each band in solvents with increasing n_{RI} we were able to determine the refractive index sensitivity (RIS) of the quadrupolar band to be

~150 refractive index units/ nm, which is about twice as high as for the D mode (Figure 2 inset). Another parameter that is often used in evaluating sensitivity of various platforms to the refractive index change, namely the Figure of merit (FOM), was introduced as a ratio of RIS to the full width at half maximum for a band. From the data obtained in this work we were able to obtain the figure of merit for the quadrupolar band as high as ~5.0. This value is one of the highest reported so far for plasmonic nanostructures.

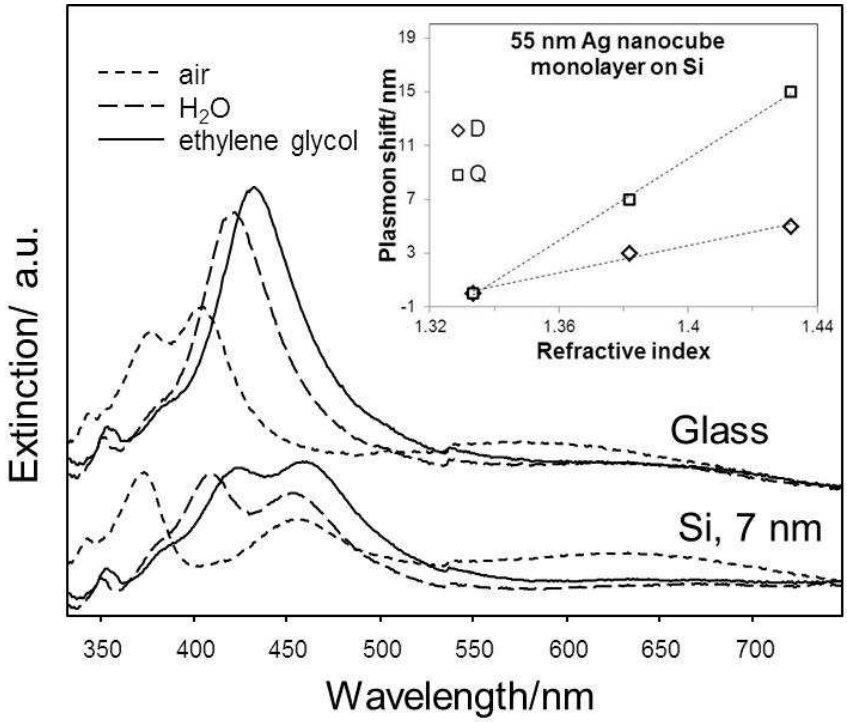

Figure 2: Solution refractive index sensing using nanocube monolayers deposited on glass and on a 7nm thick silicon film. Inset shows solution refractive index dependences of the dipolar (D) and quadrupolar (Q) peaks.

4. Conclusions

In this work we prepared monolayers of silver nanocubes on substrates with various refractive indexes in order to enhance the sensitivity of such plasmonic materials to the refractive index change. We found that by changing the refractive index of the substrate dipolar and quadrupolar plasmon mode hybridization can be carefully adjusted and fine-tuned. As a result, silicon supported silver nanocube monolayers are shown to represent a powerful platform for sensing the refractive index change.

Acknowledgements

Financial support was provided by MRI ERA, NSERC, and CFI.

References

[1] M. Rycenga, C.M. Cobley, J. Zeng, W. Li, C.H. Moran, Q. Zhang, D. Qin, Y. Xia. *Chem. Rev.* 2011, 111, 3669–3712

[2] M. Jones, K. Osberg, R. Macfarlane, M. Langille, C. Mirkin, *Chem. Rev.* 2011, 111, 3736–3827

[3] K. Mayer, J. Hafner, *Chem. Rev.* 2011, 111, 3828–3857

[4] P.C. Lee, D. Meisel, *J. Phys. Chem.* 1982, 86, 3391–3395

[5] M. Fleischmann, P.J. Hendra, A.J. McQuillan, *Chem. Phys. Lett.* 1974, 26, 163–166

[6] A. Hartstein, J.R. Kirtley, J.C. Tsang, *Phys. Rev. Lett.* 1980, 45, 201–204

[7] A. Ianoul, A. Bergeron, *Langmuir,* 2006, 22, 10217–10222

[8] A. Parfenov, I. Gryczynski, J. Malicka, C. Geddes, J.R. Lakowicz, *J. Phys. Chem. B,* 2003, 107, 8829–8833

[9] P. Anger, P. Bharadwaj, L. Novotny, *Phys. Rev. Lett.* 2006, 96, 113002

[10] H. Rigneault, J. Capoulade, J. Dintinger, J.; Bonod, N. Wenger, E. Popov, T.W. Ebbesen, P.F. Lenne, *Phys. Rev. Lett.* 2005, 95, 117401
[11] Y. Lee, H. Chen, Q. Xu, J. Wang, *J. Phys. Chem. C,* 2011, 115, 7997–8004
[12] C. Noguez*, J. Phys. Chem. C*, 2007, 111, 3806-3819
[13] P. Albella, B. Garcia-Cueto, F.G. alez, F. Moreno, P. Wu, T. Kim, A. Brown, Y. Yang, H. Everitt, G. Videen, *Nano Lett.* 2011, 11 (9), 3531–3537
[14] N. Ahamad, A. Bottomley, A. Ianoul, *J. Phys. Chem. C,* 2012, 116, 185–192
[15] N. Ahamad, D. Prezgot, A. Ianoul, *Journal of Nanoparticle Research*, 14, 2, 724
[16] S. Zhang, K. Bao, N. Halas, H. Xu, P. Nordlander, *Nano Lett.* 2011, 11, 1657–1663
[17] A. Bottomley, A. Ianoul, *ChemPhysChem*, 2011,12, 2912–2914
[18] M.W. Knight, Y. Wu, J.B. Lassiter, P. Nordlander, N. Halas, *Nano Lett.* 2009, 9, 2188–2192
[19] E. Ringe, J. McMahon, K. Sohn, C. Cobley, Y. Xia, J. Huang, G. Schatz, L. Marks, R. Van Duyne, *J. Phys. Chem. C*, 2010, 114, 12511–12516
[20] M.A. Mahmoud, M.A. El-Sayed, *Nano Lett.* 2011, 11, 946–953
[21] N. Ahamad, A. Ianoul, *J. Phys. Chem. C*, 2011, 115, 3587–3594
[22] H. Chem, X. Kou, Z. Yang, W. Ni, J. Wang, *Langmuir*, 2008, 24, 5233–5237
[23] L. Sherry, S. Chang, G. Schatz, R. Van Duyne, B. Wiley, Y. Xia, *Nano Lett.* 2005, 5, 2034–2038

Optimizing the Resolution of Nanohole Arrays in Metal Films for Refractive Index Sensing

Gabriela Andrea Cervantes Tellez, Aftab Ahmed, Reuven Gordon*

Department of Electrical Engineering, University of Victoria, Victoria, Canada
*corresponding author, E-mail: rgordon@uvic.ca

Abstract

We optimized the resolution of nanohole arrays in metal films for refractive index sensing by increasing the sensitivity with modifications to the hole-array parameters and by reducing the noise of the sensor system. The nanohole array parameters (including film thickness, periodicity and diameter) were first optimized by finite-difference time-domain simulations, and then fabricated and tested, showing good agreement between the two cases (theory and experiment) in terms of optimal parameters. To improve the sensitivity and to reduce the noise, the laser source wavelength was optimized (including the efficiency of the camera for detection) and the intensity was increased to reduce shot noise. A bulk resolution of 6×10^{-7} RIU was demonstrated. Due to the collinear microscope geometry and potential for multiplexing of nanohole arrays, these results are encouraging for future biosensing applications.

1. Introduction

Surface plasmon resonance (SPR) sensing is an established technology for monitoring refractive index changes due to mass loading at a surface of a metal film. Since the discovery of extraordinary optical transmission through nanohole arrays in metal films [1], it has been demonstrated that these arrays may be used for sensing applications [2-3]. Compared to Kretschmann-type SPR, sensing using the nanohole arrays is extremely promising for future technologies because it allows for: a small footprint for dense integration, a high degree of multiplexing, collinear optical detection for facile integration and combined optofluidic functionality [4-25].

The optimization of sensors includes sensitivity, resolution, reproducibility and accuracy. Sensitivity depends on the sensor output to the change in refractive index. Resolution is defined as the smallest change in refractive index that the nanohole array sensor can detect and is limited by the noise of the system [26]. Commercial SPR instruments have a resolution of 10^{-7} refractive index units (RIU) [27]. So far, the resolution of nanohole arrays has been demonstrated to be between 10^{-4}-10^{-6} RIU; however, those works used complicated optical setups [28-30].

In this work, we optimize the resolution of nanohole arrays in metal films for refractive index sensing by increasing the sensitivity with modifications to the hole-array parameters and by reducing the noise of the sensor system. We achieve a bulk resolution of 6×10^{-7} RIU. Due to the collinear microscope geometry and potential for dense multiplexing of nanohole arrays with optofluidic functionality [31-33], the results are encouraging for future biosensing applications.

2. Simulation methods and results

To have an idea of the optimal parameters for nanohole sensors, we performed comprehensive calculations of the transmission spectra of nanohole arrays using the finite-difference time-domain method (FDTD). To model the dispersive gold film a fit to the experimental data of Johnson and Christy was used [34]. The substrate was taken to have refractive index of 1.52 (for glass) and the refractive index of the background was varied to determine the sensitivity. The simulation domain used perfectly matched layer boundaries to prevent reflections and Bloch boundary conditions for the periodic structure. A plane wave source was used normally incident on the nanohole array. A frequency domain profile monitor collected the transmission through the holes in the visible and near infrared wavelength range. A mesh over-ride of 2 nm was used over the metal film, and this was confirmed to capture the surface plasmon dispersion by finite difference mode calculations. The sensitivity was determined by noting the change in the transmission characteristics for varying refractive index of the solution surrounding the holes.

Periodicity of the array, hole-diameter, and metal thickness were varied to obtain the best performance of the nanohole array sensor. FDTD simulations were carried out for hole-diameters from 140 nm to 250 nm, periodicities from 415 nm to 570 nm, and gold film thicknesses from 100 nm to 500 nm.

Fig. 1(a) shows the transmission spectrum of the optimized nanohole arrays for film thickness of 100 nm. The optimization was determined in terms of the resolution, assuming that shot noise is the dominant factor (for which the noise scales as the square root of the intensity). Considering this, the resolution, when changing the

refractive index from $n_1 = 1.330$ to $n_2 = 1.331$ will be proportional to the resolution parameter, R:

$$R = \left| \frac{I_{n1} - I_{n2}}{\sqrt{I_{n1}}} \right| \quad (1)$$

Using Equation (1), we compare the performance between the nanohole arrays, where I_{n1} and I_{n2} are the transmission intensities for the different refractive index values. Fig. 1(b) shows that the optimal wavelength for operation is at 648 nm for this film thickness, and this occurs for a hole-diameter of 150 nm and a periodicity of 425 nm.

Fig. 1. Results of FDTD simulations. (a) Spectrum of a circular nanohole array of diameter 150 nm and periodicity 425 nm in a gold film of 100 nm thickness. (b) Optimal wavelength for operation is at 648 nm.

It is interesting to note here that the optimal periodicity for the 100 nm film is close to the expected lowest order Bragg resonance of the plasmon dispersion for this wavelength; however, this is not the case for the thicker films. We will discuss this further in Section 6.

Fig. 2 shows equivalent results for a gold film of 300 nm thickness. The optimal parameters found were hole-diameter of 260 nm, periodicity of 570 nm. The wavelength for the best performance was 655 nm.

Fig. 2. Results of FDTD simulations. (a) Spectrum of a circular nanohole array of diameter 260 nm and periodicity 570 nm in a gold film of 300 nm thickness. (b) Optimal wavelength for operation 655 nm.

Fig. 3 shows the transmission spectrum and resolution parameter for a 500 nm gold film thickness. The optimal parameters for this thickness were hole-diameter of 260 nm and periodicity of 570 nm. The largest R value change is at the wavelength of 655 nm.

Fig. 3. Results of FDTD simulations. (a) Spectrum of a circular nanohole array of diameter 260 nm and periodicity 570 nm in a gold film of 500 nm thickness. (b) Optimal wavelength for operation is 655 nm.

Comparing Figs. 1-3, it is clear that the thicker films provide better performance. In practice, however, we are limited by the ability to make high-aspect nanoholes in thick films and the duration of milling, and so we do not attempt larger thicknesses than 500 nm in this work. It is also interesting to note that the optimal wavelength of operation was consistently around 650 nm for all of the film thicknesses, and this has important ramifications for the sensor performance, as discussed further in Section 6.

3. Fabrication procedure

The nanohole arrays were fabricated by using a FB-2100 (Hitachi) focused ion beam with a gallium ion source. The ion beam was set to 40 keV for milling, and a beam current of 0.01 nA. Fig. 4 shows a scanning electron microscope image of the circular nanohole array. To match the simulations, the nanohole arrays were milled in film thicknesses of 100 nm, 300 nm and 500 nm. Due to the cost of fabrication, the simulations were used to reduce the range of fabrication parameters. For the 100 nm film thickness, the periodicity was scanned from 415 nm to 435 nm in steps of 5 nm and the diameters used were 150 nm and 160 nm. For the 300 nm and 500 nm film thicknesses, the diameters used were 260 nm and 270 nm and the periodicity was scanned from 550 nm to 575 nm in steps of 5 nm.

Good verticality of the side-walls was confirmed by energy dispersive X-ray spectroscopy studies, which showed that the gold was removed from the region of precisely (to within 5 nm) the specified radius.

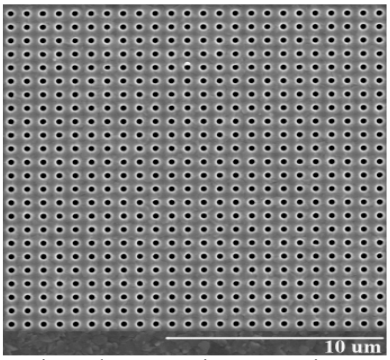

Fig. 4. Scanning electron microscope image of circular apertures with a diameter of 260 nm in a 500 nm thick gold film.

Fig. 5 shows the microfluidic chip. For measuring change in intensity due a change in the index of refraction we use a microfluidic flow channel which consists of a polydimethylsiloxane (PDMS) microchip made by rapid prototyping lithography [35]. The master mold of the channel was patterned on a silicon wafer using SU-8 50 photoresist. For the development of the microchip, a curing agent and PDMS (ratio 10:1) were used. The gold sample with PDMS flow channel was sandwiched between two acrylic layers to seal the flow channel.

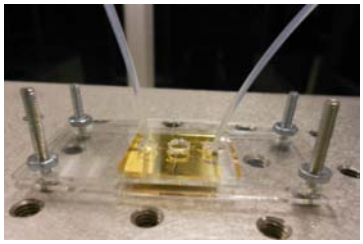

Fig. 5. Microchip of a 500 nm thick gold film sample and with PDMS microfluidic over-channel sandwiched between acrylic layers.

4. Experimental setup

Fig. 6 shows the experimental setup for measuring the fabricated gold samples. To enable scanning over a wide range of wavelengths, a supercontinuum light source (Fianium SC400) was used. With the acousto-optic tunable filter (AOTF), any desired wavelength ranging from 400 nm to 1100 nm could be obtained. This source illuminated the top surface of the sub-wavelength apertures. A spatial filter was used to improve the spatial/spectral quality of the laser beam. Two objective lenses had been set up to measure the transmission of the nanohole arrays. First, the laser beam was focused using a microscope objective of 0.1 NA, and then it was collected with a microscope objective of 0.5 NA. We experimented with various objective lens combinations, and we found that this is a good configuration. In particular, the high NA objective below the glass substrate helps to acquire a larger number of photons. By contrast, the low NA objective above the microfluidic channel ensures a low angular deviation in the incident photons, so that the resonances (that are angle-sensitive) are more spectrally pure [36].

A CCD camera (Thorlabs DCU224C) was used to record a video of the sub-wavelength structures while flowing solutions of slightly different refractive index over the sample. Any change in the refractive index of the solution appears as a change in intensity. A syringe pump (Harvard apparatus 11 series) was used for a stable liquid flow rate of 7 μL/min.

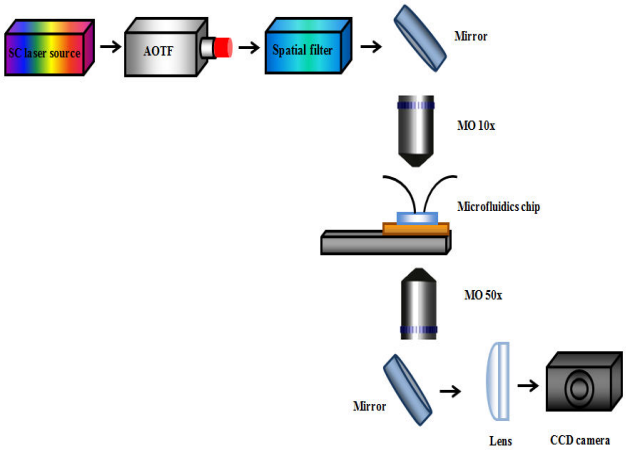

Fig. 6. Schematic of optical setup used for measuring the change in intensity of the fabricated gold samples with a super continuum laser source tunable over the visible near infrared region.

5. Results

In the experiments, the 100 nm thick gold film showed the largest sensitivity for a hole-diameter of 150 nm and periodicity of 425 nm, with a resolution of 2×10^{-6} RIU. The 300 nm thick film showed largest sensitivity for a hole-diameter of 260 nm and periodicity of 570 nm with a resolution of 8×10^{-7} RIU. The 500 nm thick film showed the largest sensitivity for a hole-diameter of 260 nm and periodicity of 570 nm, with a resolution of 6×10^{-7} RIU. These parameter values are all in close-agreement with the simulation results. It is clear also that the thicker film gives better resolution, as expected from the simulations.

Fig. 7 shows the best result obtained among all the arrays, varying the refractive index to determine the sensitivity. The curve in Fig. 7(a) has a staircase appearance because it was acquired by scanning the AOTF in 5 nm steps for 5 second duration at each step. For convenience, the figure is plotted versus wavelength instead of time.

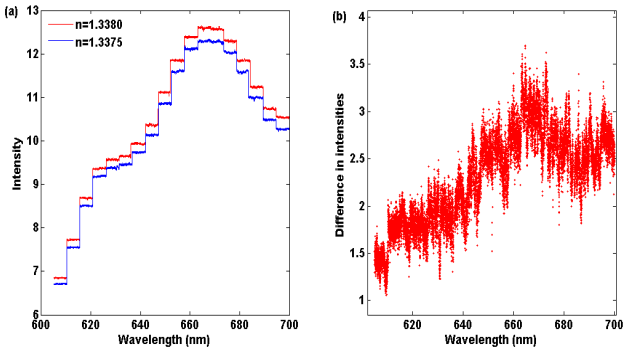

Fig. 7. (a) Representation in time of the spectrum of a nanohole array while flowing two different refractive index solutions. (b) Difference in intensities of two refractive index solutions.

After choosing the optimal wavelength of operation for the nanohole array sensor measurements, by the procedure in Fig. 7, bulk sensitivity measurements were carried out with a higher intensity of 3.6 mW and using a low-pass finite impulse response numerical filter. Fig. 8 shows the intensity change of the circular nanohole arrays subjected to refractive index change of 0.0005 operating at 655 nm. The numerical filtering reduced the time resolution to 0.5 frames per second. The highest resolution that was obtained was 6×10^{-7} RIU.

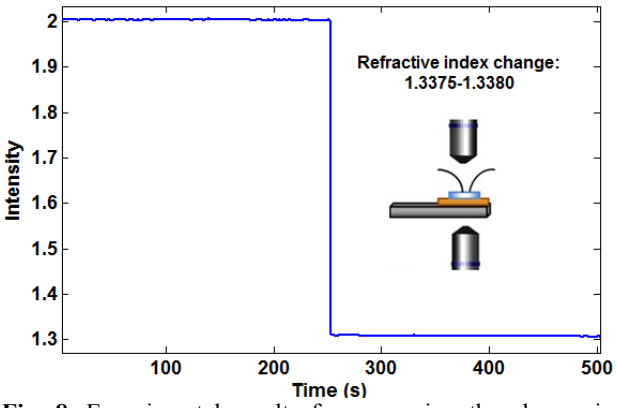

Fig. 8. Experimental results for measuring the change in intensity at 655 nm wavelength for a 500 nm thick gold film. An array of circular holes with diameter of 260 nm and periodicity of 570 nm were used.

6. Discussion

First we note that good agreement is seen between the simulation and the experiments. The achieved resolution of 6×10^{-7} RIU is a promising step towards competing with existing commercial SPR devices (10^{-7} resolution), while allowing for the integration, multiplexing and optofluidic advantages of nanohole SPR.

It is interesting to note that the optimum resolution found from the simulations was around 655 nm. This is believed to result from the gold dispersion for two reasons. First, gold has a low loss at 655 nm because this wavelength is past the interband absorption peak of gold (around 510 nm). Second, the magnitude of the relative permittivity at 655 nm is not too large (it is closer to the plasma frequency than further in the IR, for example), which allows for significant electromagnetic field penetration into the metal and pronounced plasmonic effects. It is fortuitous that the optimal operation considering the material properties of gold coincides fairly well with the optimal sensitivity of the CCD camera used in this experiment (~600 nm), because this allows for higher photon collection efficiency, and therefore reduced shot-noise signal-to-noise ratio.

It is common to use the SP Bragg relation to determine the optimal periodicity for nanohole array sensing:

$$\lambda_{SP}(i,j) = p\left(i^2 + j^2\right)^{-\frac{1}{2}}\left(\frac{\varepsilon_d \varepsilon_m}{\varepsilon_d + \varepsilon_m}\right)^{1/2} \qquad (2)$$

where ε_m and ε_d are the permittivities of metal and dielectric material, p is the periodicity, i and j are integers that represent Bragg resonance orders. This gives reasonable results for predicting the resonance wavelength for thinner films for the lowest order resonance. For example, the $i=0$, $j=1$ resonance of the 100 nm film with 425 nm periodicity on the water side is predicted to be 625 nm, and was observed to be 648 nm in the simulations. We see here, however, that larger periodicities are required for thicker films, and these do not seem to match the lowest order resonance. Indeed, they are closer to the $i=1$, $j=1$ resonance. The reason for this effect is still under investigation; however, this shows that future investigations should not simply chose the lowest order resonance wavelength as has been done in the past [37].

7. Conclusions

We optimized the resolution of circular nanohole arrays in metal films for refractive index sensing by increasing the sensitivity with modifications to the hole-array parameters (film thickness, periodicity and diameter), by determining the optimal wavelength of operation, and by reducing the noise of the sensor system (through increased collection efficiency, increased intensity and numerical filtering). We achieve a bulk resolution of 6×10^{-7} RIU. Due to the collinear microscope geometry, the potential for multiplexing of nanohole arrays and improved optofluidic functionality [32], these results are encouraging for future detection of chemical and biological species.

Acknowledgements

The authors are grateful for the support of the NSERC Strategic Network for Bioplasmonic Systems (Biopsys).

References

[1] T.W. Ebbesen, H.J. Lezec, H.F. Ghaemi, T. Thio, P.A. Wolff, Extraordinary optical transmission through sub wavelength hole arrays, *Nature* 391:667-669, 1998.

[2] W.L. Barnes, A. Dereux, T.W. Ebbesen, Surface plasmon subwavelength optics, *Nature* 424:824-830, 2003.

[3] A.G. Brolo, R. Gordon, B. Leathem, K.L. Kavanagh, Surface plasmon sensor based on the enhanced light transmission through arrays of nanoholes in gold films, *Langmuir* 20:4813-4815, 2004.

[4] R. Gordon, D. Sinton, K.L. Kavanagh, A.G. Brolo, A new generation of sensors based on extraordinary optical transmission, *Acc. Chem. Res.* 41:1049-1057, 2008.

[5] A. Lesuffleur, H. Im, N.C. Lindquist, S.H. Oh, Periodic nanohole arrays with shape-enhanced plasmon resonance as real–time biosensors, *Appl. Phys. Lett.* 90:243110, 2007.

[6] W.L. Barnes, W.A. Murray, J. Dintinger, E. Devaux, T.W. Ebbesen, Surface plasmon polaritons and their role in the enhanced transmission of light through periodic arrays of subwavelength holes in metal film, *Phys. Rev.* 92:107401, 2004.

[7] A. Lesuffleur, H. Im, N.C. Lindquist, K.S. Lim, S.H. Oh, Laser-illuminated nanohole arrays for multiplex plasmonic microarray sensing, *Opt. Express* 16:219-224, 2008.

[8] L. Pang, G.M. Hwang, B. Slutsky, Y. Fainman, Spectral sensitivity of two-dimensional nanohole array surface plasmon polariton resonance sensor, *Appl. Phys. Lett.* 91:123112, 2007.

[9] R. Gordon, A. G. Brolo, D. Sinton, K. L. Kavanagh, Resonant optical transmission through hole-arrays in metal films: Physics and applications, *Laser and Photonics Reviews* 4:311-335, 2010.

[10] J. Homola, S. Yee, G. Gauglitz, Surface plasmon resonance sensors: Review, *Sensor Actuat. B-Chem.* 54:3-15, 1999.

[11] A. De Leebeeck, L.K.S. Kumar, V. de Lange, D. Sinton, R. Gordon, A.G. Brolo, On-chip surface-based detection with nanohole arrays, *Anal. Chem.* 79:4094-4100, 2007.

[12] H. Gao, J. Henzie, T.W. Odom, Direct evidence of surface plasmon-mediated enhanced light transmission through metallic nanohole arrays, *Nano Lett.* 6:2104-2108, 2006

[13] N.C. Lindquist, A. Lesuffleur, H. Im, S.H. Oh, Sub-micron resolution surface plasmon resonance imaging enable by nano-hole arrays with surrounding Bragg mirrors for enhanced sensitivity and isolation, *Lab Chip* 9:382-387, 2009.

[14] Y. Liu, S. Blair, Fluorescence enhancement from an array of subwavelength metal apertures, *Opt. Express* 28:507-509, 2003.

[15] J. Dintinger, S. Klein, T.W. Ebbesen, Molecule-surface plasmon interaction in hole arrays: Enhanced absorption, refractive index changes, and all-optical switching, *Adv. Mater* 18:1267-1270, 2006.

[16] J.C. Sharpe, J.S. Mitchell, L. Lin, N. Sedoglavich, R.J. Blaikie, Gold nanohole array substrates as immunobiosensors, *Anal. Chem.* 80:2244-2249, 2008.

[17] T. Allsop, R. Neal, E.M. Davies, C. Mou, P. Bond, S. Rehman, K. Kalli, D.J. Webb, P. Calverhouse, I. Bennion, Low refractive index gas sensing a surface plasmon resonance fibre device, *Meas. Sci. Technol.* 21:094029, 2010.

[18] J. Ji, J.G. O'Connell, D.J. Carter, D.N. Larson, High-throughput nanohole array based system to monitor binding events in real time, *Anal. Chem.* 80:491-498, 2008.

[19] X. Shou, A. Agrawal, A. Nahata, Role of metal film thickness on the enhanced transmission properties of a periodic array aperture, *Opt. Express* 13:9834-9840, 2005.

[20] P.R.H. Stark, A.E. Halleck, D.N. Larson, Short order nanohole arrays in metals for highly sensitive probing of local indices of refraction as the basis for a highly multiplexed biosensor technology, *Methods* 37:37-47, 2005.

[21] K.L. Lee, S.H. Wu, P.K. Wei, Intensity sensitivity of gold nanostructures and its application for high-throughput biosensing, *Opt. Express* 17:23104-23113, 2009.

[22] C.J. Alleyne, A.G. Kirk, R.C. McPhedran, N.A.P. Nicorovici, D. Maystre, Enhanced SPR sensitivity using periodic metallic structures, *Opt. Express* 15:8163-8169, 2007.

[23] J. Homola, Present and future of surface plasmon resonance biosensors, *Anal. Bional. Chem.* 377:528-539, 2003.

[24] T. Akimoto, S. Sasaki, K. Ikebukuro, I. Karube, Refractive-index and thickness sensitivity in surface plasmon resonance spectroscopy, *Appl. Optics* 38:4058-4064, 1999.

[25] A. Dhawan, M.D. Gerhold, J.F. Muth, Plasmonic structures based on subwavelength apertures for chemical and biological sensing applications, *IEEE Sens. J.* 8:942-950, 2008.

[26] J. Homola, Surface plasmon resonace based sensors for detection of chemical and biological species, *Chem. Rev.* 108:462-493, 2008.

[27] Biacore www.biacore.com

[28] A.K. Tetz, L. Pang, Y. Fainman, High-resolution surface plasmon resonance sensor based on linewidth-optimized nanohole array transmittance, *Opt. Express* 31:1528-1530, 2006.

[29] A-P. Blanchard-Dionne, L. Guyot, S. Patskovsky, R. Gordon, M. Meunier, Intensity based surface plasmon resonance sensor using a nanohole rectangular array, *Opt. Express* 19:15041-15046, 2011.

[30] C. Escobedo, S. Vincent, A.I.K. Choudhury, J. Campbell, A.G. Brolo, D. Sinton, R. Gordon, Integrated nanohole array surface plasmon resonance sensing

device using a dual-wavelength source, *J. Micromech. Michroeng.* 21:115001, 2011.

[31] C. Escobedo, A.G. Brolo, R. Gordon, D. Sinton, Optofluidic concentration: Plasmonic nanostructure as concentrator and sensor, *Nano Lett.* ASAP 2012.

[32] F. Eftekhari, C. Escobedo, J. Ferreira, X. Duan, E.M. Girotto, A.G. Brolo, R. Gordon, D. Sinton, Nanoholes as nanochannels: Flow-through plasmonic sensing, *Anal. Chem.* 81:4308-4311, 2009.

[33] C. Escobedo, A.G. Brolo, R. Gordon, D. Sinton, Flow-through vs flow over: Analysis of transport and binding in nanohole array plasmonic biosensors, *Anal. Chem.* 82:10015-10020, 2010.

[34] P.B. Johnson, R.W. Christy, Optical constants of the noble metals, *Phys. Rev. B* 6:4370, 1972.

[35] D.C. Duffy, J.C. McDonald, O.J.A. Schueller, G.M. Whitesides, Rapid prototyping of microfluidic systems in poly(dimethylsiloxane), *Anal. Chem.* 70:4974-4984, 1998.

[36] H.F. Ghaemi, T. Thio, D.E. Grupp, T.W. Ebbesen, H.J. Lezec, Surface plasmons enhance optical transmission through subwavelength holes, *Phys. Rev. B* 58:6779-6782, 1998.

[37] A. Krishnan, T. Thio, T. J. Kim, H. J. Lezec, T. W. Ebbesen, P. A. Wolff, J. Pendry, L. Martin-Moreno, F. J. Garcia-Vidal, Evanescently coupled resonance in surface plasmon enhanced transmission, *Opt. Commun.* 200:1-7, 2001.

Exotic Properties and Potential Applications of Quantum Metamaterials

Romain Fleury[1], and Andrea Alù [1*]

[1]Department of Electrical and Computer Engineering, The University of Texas at Austin, Austin, TX, USA
*corresponding author, E-mail: alu@mail.utexas.edu

Abstract

We discuss here potential venues for applications and exotic features of quantum metamaterials. We explore the coupling of conventional electromagnetic metamaterials with quantum emitters and the wave properties of quantum metamaterials obtained by tailoring their effective band structure. We discuss anomalous enhancement effects in the quantum emission properties of individual and collections of small emitters in the presence of metamaterials, as well as matter-wave cloaking and anomalous tunneling phenomena for quantum mechanical waves in artificial materials with exotic band structures.

1. Introduction

The field of metamaterials and plasmonic materials has evolved tremendously in the past few years, expanding into a variety of novel fields and disciplines. Initially based on purely classical concepts, the trend of the last few years has been to consider smaller and more closely spaced nanoparticles, forcing scientists to consider quantum effects for the proper modeling of metamaterials [1]-[2], in particular for shorter wavelengths in fields like optics and plasmonics. In addition, combination of metamaterials with quantum sources and small optical emitters has tremendously expanded, together with the application of optical antennas for which quantum emitters may represent efficient localized power sources [3]. The field of metamaterials is currently mature to include quantum effects, also tailoring the effective band structure of composite materials to produce anomalous propagation properties for matter waves. In this paper, we theoretically discuss potential applications of quantum metamaterials, considering the coupling of small quantum sources with electromagnetic systems, and the tailoring of band structure to produce anomalous quantum effects.

As a first example of our investigations in this area, inspired by electromagnetic metamaterials, we discuss how low-constitutive parameters [4]-[8], compared to those available in nature, may be especially attractive to modify the quantum emission properties of small sources. Zero-permittivity (ENZ) metamaterial channels have been proposed to increase the spontaneous emission of small optical sources within a purely classical analysis [9]. We discuss here how these effects may be even more dramatic than what predicted based on purely classical mechanisms, including the effects of quantum super-radiance in systems that have a large physical area, but a small electrical size, due to the large phase velocity of the modes supported in an ENZ channel.

In addition, we discuss how, by modifying the effective band structure of metamaterials, we may be able to translate and extend established metamaterial effects to matter waves. ENZ tunneling and plasmonic cloaking will be discussed for matter waves, analyzing the potentials of these effects when translated into the quantum arena. To this end, transmission-line modeling of wave propagation in quantum metamaterials will be applied to anomalous constitutive parameters and composite systems, showing that the tools successfully used in conventional metamaterials may be theoretically extended also in the area of quantum metamaterials.

2. Quantum Metamaterials

Metamaterials are artificial materials characterized by a wave interaction not commonly available in nature. They have been mostly applied to electromagnetic and acoustic waves, but recent interest in the extension and application of these concepts to matter waves has been explored in a variety of scenarios. A design mimicking the Veselago's lens in optics has been proposed for matter waves, exploiting an electron focusing effect across a p-n junction in graphene [10]. Total transmission of cold Rubidium atoms through an array of sub-De Broglie wavelength slits has been theoretically demonstrated in [11]. Semiconductor heterostructures have been exploited to predict total transmission for electrons in a layered 1D quantum metamaterial [12]. Cloaking of matter waves using an invariant transformation of the Schrödinger equation has been theoretically demonstrated in [13].
In the case of periodic arrays, which make the vast majority of metamaterial geometries, at frequencies such that the wavelength is long compared to the periodicity of the metamaterial, the equations governing the wave propagation can be homogenized and effective constitutive parameters may be defined. By carefully designing the sub-wavelength periodic structure of the medium, materials with anomalous values of constitutive parameters may be engineered.

Metamaterials are therefore associated with exotic properties, not directly available in nature, like negative refraction, extreme parameters, fast or slow waves, and extraordinary tunneling. These properties make them particularly interesting for a wide range of applications including far-field imaging, sensing and cloaking. In this section we discuss how these concepts may be applied to matter waves and to electromagnetic waves interacting with quantum systems, both aspects belonging to the general area of quantum metamaterials (QMM), whose properties cannot be described within classical concepts.

2.1. Classification and general discussion

2.1.1. Type I quantum metamaterials

As a first type of QMM, we will consider quantum systems embedded in a conventional electromagnetic metamaterial, and strongly coupled to it. Here the quantum nature is brought by the quantum system, which for example may be represented by quantum dots and/or quantum wells. The fundamental idea behind type I QMM is that metamaterials can be exploited to dramatically enhance quantum effects. An example of type 1 QMM would be a system of quantum emitters radiating in an electromagnetic metamaterial. We will treat this type of QMM in section 3 of this paper, and show that very peculiar properties can be achieved when including quantum effects in the classical electrodynamic theory of metamaterials.

2.1.2. Type II quantum metamaterials

The second type of quantum metamaterial (type II QMM) consists of an artificial medium supporting quantum or matter waves. In order to further illustrate this concept, let's review how the motion of particles can be described by a wave equation with effective parameters. The time-independent Schrödinger equation for a particle can be written as

$$\left[-\frac{\hbar^2}{2m_0}\nabla^2 + V_c(\vec{r}) + U(\vec{r})\right]\Psi = \left[H_0 + U(\vec{r})\right]\Psi = E\Psi \,, \quad (1)$$

where we have assumed that the potential energy may be split into a periodic part $V_c(\vec{r})$ and a non-periodic part $U(\vec{r})$, which is assumed to be slowly varying on the scale of the lattice constant. H_0 represents the part of the full Hamiltonian that commutes with all the translation operators constructed from a lattice vector. By virtue of Bloch's theorem, it is possible to find a basis of common eigenvectors of H_0 and all the lattice translation operators. We denote this basis of Bloch's functions as $\Psi_{n\vec{k}} = e^{i\vec{k}.\vec{r}}u_{n\vec{k}}(\vec{r})$, where $u_{n\vec{k}}(\vec{r})$ has the lattice periodicity, and we use it to expand the solution Ψ of the full Schrödinger equation (1) as

$$\Psi = \sum_{n,k}\langle\Psi_{nk}|\Psi\rangle|\Psi_{nk}\rangle \cdot \quad (2)$$

It can be shown [14] that around a maximum or minimum in the band diagram, within the single band approximation and assuming that the strength of the potential is small compared with the fundamental bandgap, one term in the expansion (2) is dominant and the solution of equation (1) is in first approximation

$$\Psi = F(\vec{r})u_{n0}(\vec{r}) \cdot \quad (3)$$

$F(\vec{r})$ is the envelope function and satisfies the single-band effective mass equation:

$$\left[-\frac{\hbar^2}{2}\nabla(\hat{m}^{*-1}\nabla) + U(\vec{r})\right]F(\vec{r}) = \left(E - E_{c0}\right)F(\vec{r}) \quad (4)$$

where E_{c0} is the energy at the extremum, and the effective mass tensor is defined as:

$$\hat{m}^*_{ij} = \hbar^2\frac{\partial^2(E - E_{c0})}{\partial k_i \partial k_j} \quad (5)$$

If the potential energy changes very rapidly (for example, in a heterojunction between two direct band-gap semiconductors), the theory presented above is still valid if one considers the boundary condition [15]:

$$F \text{ and} \left(\hat{m}^{*-1}\frac{\partial}{\partial\hat{n}}\right)F \text{ continuous} \quad (6)$$

We see that all the effects from the periodic potential are absorbed into the effective-mass parameter. Considering the external potential U as a medium parameter (i.e., the energy difference at the band edge), we may consider the material to be an effective homogeneous medium for the envelope of the quantum particle. This justifies the term 'quantum metamaterial'.

Examples of type II QMM, for which the single band effective mass approximation is valid, include conduction electrons in direct band gap semiconductors operated close to their Γ point, or cold atoms in an optical lattice. The analogy between type II QMM and electromagnetic or acoustic metamaterials make them particularly suitable for translating and exploiting the most exotic effects discovered in these fields to matter waves. We will discuss specific examples of type II QMM in sections 4 and 5.

3. Boosting quantum super-radiance in an epsilon-near-zero medium

As example of type I QMM we will consider the emission properties of a system of identical 2-level quantum emitters in a metamaterial with extremely low value of effective permittivity. Consider a non-magnetic background medium with effective permittivity ε in which we embed a system of N identical 2-level quantum emitters, radiating at frequency ω_0, for instance quantum dots or atoms. We note N_0 the concentration of emitters, and d the off-diagonal matrix element of the dipole moment operator (chosen to be real). We will assume that at $t = 0$ all the 2-levels atoms are in their excited state. All the emitters are therefore expected to spontaneously radiate as a result of the interaction with the quantum fluctuations of the electric field. The background is considered as a classical metamaterial in which one can

achieve anomalous values of permittivity at the emission frequency of the 2-level atoms.

As was first pointed out by Dicke in his original paper [16] about coherent super-radiance, the independence of the spontaneous decay of several identical atoms is a wild assumption, and a more accurate description of the problem leads to quite different results. Interestingly, the interaction of the atoms through their radiation electromagnetic fields results in correlation between the atomic dipole moments, leading to the formation of macroscopic polarization, the latter being proportional to the total number of atoms in the system N. As a consequence, the total radiation intensity is considerably enhanced, and the spontaneous decay time is shortened. We shall now describe this effect more quantitatively, and explain how it can be further enhanced by decreasing the permittivity ε of the medium.

3.1. Model

To address the effect of the permittivity of the medium on the radiative properties of our quantum metamaterial we exploit a semi-classical model of super-radiance. This model is suitable for describing systems whose size exceeds the emission wavelength. We briefly review the basic assumptions of this model: we will assume that the system is a rectangular box whose size is smaller than the Arecchi-Courtens length (critical length beyond which the system splits up to several incoherent super-radiating segments) [17]. The system is opened at both ends along the x axis. In addition, we assume that all physical quantities depend only on one spatial coordinate x and that the quantum dipole moments and electric fields are polarized along the y direction. This simple model has been proven to describe with excellent accuracy experimentally measured super-radiant pulses [18].

The semi-classical approach that we follow combines the quantum mechanical treatment of the 2-level system with the classical treatment of the radiation field. His main result is the dimensionless Maxwell-Bloch non-linear PDE equations system [19]

$$\frac{\partial R}{\partial \tau'} = Z\mathrm{E} \tag{7}$$

$$\frac{\partial Z}{\partial \tau'} = -R\mathrm{E} \tag{8}$$

$$\frac{\partial \mathrm{E}}{\partial \xi} = R\,, \tag{9}$$

where Z is the population difference or inversion, R is the envelope of the non-diagonal element of the local average of the density matrix, which is linked with the local polarization of the medium, E is the normalized electric field, ξ is the normalized coordinate x and τ' is the normalized retarded time

$$\tau' = \tau - \xi \tag{10}$$

where τ is the normalized time. The way that these quantities are normalized is of crucial importance to determine the scaling properties of super-radiance and the effect of the background permittivity. We have

$$\tau = t\,\Omega_0\,,\ \xi = x\,x_0^{-1}\,,\ \mathrm{E} = e\,e_0^{-1} \tag{11}$$

where e is the electric field. The frequency Ω_0 gives information on the characteristic time of super-radiance

$$\Omega_0 = \sqrt{\frac{d^2\omega_0 N_0}{2\hbar\varepsilon}} \tag{12}$$

The characteristic length x_0 is the above-mentioned Arecchi-Courtens length which is given by:

$$x_0 = \frac{c}{\Omega_0} \tag{13}$$

where c is the phase velocity of light in the considered medium. Note than this length does not depend on the permittivity of the background medium. This implies that it is not possible to extend the spatial range of super-radiance by tailoring ε. This is simply related to the fact that when two emitters are separated by more than x_0, they cannot interact through their radiation field because the electromagnetic interaction cannot go faster than the speed of light in vacuum. As a consequence, they belong to two different uncorrelated super radiating segments. We therefore restrict ourselves to a single super-radiating segment by requiring that the system be smaller than x_0.

The normalization constant for the electric field is:

$$e_0 = \frac{i\Omega_0}{d} \tag{14}$$

The method for solving this system of equation has first been proposed by Burnham and Chiao when modeling the coherent resonant fluorescence excited by a short light pulse [20]. We consider the auto-modeling solution of the Maxwell-Bloch equation, and numerically solve the resulting differential equation with the appropriate boundary conditions. This yields the magnitude of the electric field as a function of x and t. From its value, we can compute the radiation intensity (number of photons per unit time radiated through one end of the system).

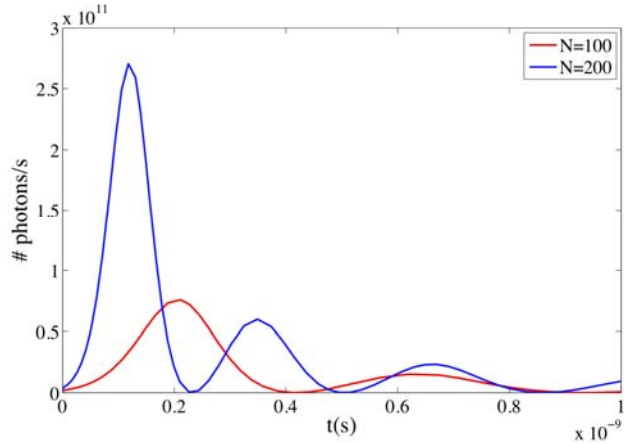

Figure 1: Output intensity versus time for different concentrations of emitters. The relative permittivity of the background medium is 1.

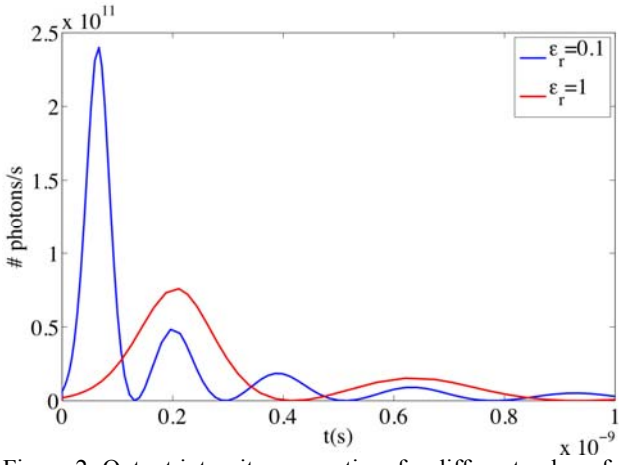

Figure 2: Output intensity versus time for different value of the relative permittivity of the background medium, for 100 emitters.

3.2. Results

In order to highlight the exotic features of our quantum metamaterial we plot in Fig. 1 the number of emitted photons versus time for different values of total number of emitters. Fig. 2 compares the output intensity for different values of the background permittivity. The energy levels of the identical quantum emitters are assumed to be separated by 3.1 eV, the dipole moment d is chosen to be 10^{-29} C.m, and the cross-sectional area of the system used in the intensity calculations is 4000 nm^2. We notice that the maximum peak value is proportional to N^2. This is the dramatic effect of interaction between the emitters through their common radiation field. One would indeed expect the output intensity to be proportional to N if the sources were independent. We also see that the super-radiance characteristic time is inversely proportional to the total number of atoms in the system. This suggests that the radiation decay time can be extremely short for sufficiently dense media.

The effect of decreasing the permittivity is also dramatic: both radiation intensity and characteristic time are roughly inversely proportional to $\sqrt{\varepsilon}$. This suggests the use of metamaterials as background media in order to achieve very low values of permittivity and further enhance both the maximum output intensity and the radiation time.

In summary, this very simple model predicts a significant boosting of spontaneous emission in quantum metamaterials made of confined identical quantum emitters in an ENZ background. This result is significantly larger than what predicted in [9] adopting a purely classical analysis.

4. Plasmonic cloaking of matter waves

As an example of a potential application of type-II QMM, we investigate the possibility of cloaking matter waves by cancelling the scattering cross-section of a given potential profile.

4.1. Preliminaries

Cloaking of matter waves has been theoretically predicted for spherical systems with given potential energy and effective mass, by considering an invariant transformation of the Schrödinger equation [13]. Here, we take a different approach, similar to what has been done in the field of plasmonic cloaking. Similar to what proposed for electromagnetic [21] and acoustic waves [22], the idea is to exploit the scattering cancellation based on the negative local polarizability of a cover made of low-permittivity or low-density metamaterial. The purpose of this cover is to cancel the dominant scattering terms in the multipole expansion of the scattered fields. This method is very robust to geometry since it does not rely on a resonance phenomenon. The first experimental realization of a cloaked device for a free-standing 3D object was based on this principle [23]. We discuss now how plasmonic cloaking may be translated to matter waves. For the purpose of clarity we will not consider motion in a periodic potential, and therefore we consider a quantum particle in vacuum impinging on a region with non-zero potential $U(\vec{r})$. This is equivalent to setting V_c to zero in equation (1). This situation corresponds to the usual quantum problem of scattering by a potential. We make the usual assumptions that the impinging particles are spinless and structureless. The potential is not necessarily central, but it is negligible outside a certain action zone Ω.

4.2. Cloaking condition

Let's start from the Lippmann-Schwinger equation in the position representation: the solution of the Schrödinger equation satisfies the following integral equation [24]:

$$\varphi(\vec{r}) = e^{ikz} + \int d^3\vec{r}\,' G_+(\vec{r} - \vec{r}\,')u(\vec{r})\varphi(\vec{r}), \tag{15}$$

where

$$G_+(\vec{r}) = -\frac{1}{4\pi}\frac{e^{ikr}}{r} \tag{16}$$

Is the Green's function associated with the linear operator $\nabla^2 + k^2$ and $u(\vec{r})$ is a normalized potential related to the potential $U(\vec{r})$ by

$$U(\vec{r}) = \frac{\hbar^2}{2m_0}u(\vec{r}). \tag{17}$$

Equation (14) can be solved by iteration, but if the potential $u(\vec{r})$ is small enough one can keep only the first term, following Born approximation

$$\varphi(\vec{r}) = e^{ikz} - \frac{1}{4\pi}\int d^3\vec{r}\,' u(\vec{r}\,')e^{i\vec{K}.\vec{r}\,'}, \tag{18}$$

where $\vec{K} = \vec{k}_s - \vec{k}_i$ is the difference between the scattered wave vector in the direction $\vec{r}\,'$ and the incident wave vector. Imagine now to be able to add a potential cover $u_c(\vec{r})$ around the action zone of the potential. Let's denote by Ω_c the finite domain where the potential cover is non-zero. Equation (15) becomes:

$$\varphi(\vec{r}) = e^{ikz} - \frac{1}{4\pi}\left(\int_{\Omega} d^3\vec{r}\,' u(\vec{r}\,')e^{i\vec{K}.\vec{r}\,'} + \int_{\Omega_c} d^3\vec{r}\,' u_c(\vec{r}\,')e^{i\vec{K}.\vec{r}\,'}\right) \tag{19}$$

Cloaking is achieved when the integral over the cover cancels the one over the initial potential:

$$\int_{\Omega_c} d^3\vec{r}\,' u_c(\vec{r}\,')e^{i\vec{K}.\vec{r}\,'} = -\int_{\Omega} d^3\vec{r}\,' u(\vec{r}\,')e^{i\vec{K}.\vec{r}\,'}. \tag{20}$$

For instance, for constant potentials and in the quasistatic limit, one has the simple condition:

$$u_c = -\frac{\Omega}{\Omega_c}u. \tag{21}$$

For spherical constant potentials, if γ denotes the ratio between the shell and the core radii, the cloaking condition becomes

$$\frac{U_c}{U} = -\frac{\gamma^3}{1-\gamma^3}. \tag{22}$$

The analogies with the case of plasmonic cloaking for electromagnetic or acoustic waves are evident. The multipole expansion is replaced by the Born expansion, and the dipole approximation by the Born approximation. Like in the electromagnetic case, the cover needs to have opposite local polarizability to cancel dipolar scattering. Alone, the cover or the core would scatter, but when combined and interfering with each other, they cancel each other, making the obstacle totally transparent to the impinging wave. The cloaking condition is robust to geometry imperfections or fluctuations in the potentials, since it does not rely on a resonance phenomenon. The associated low observability of the cloaked object may find potential application in electronics, sensing, and imaging.

5. Transmission-line theory of guided matter wave

Given the strong analogy between type II QMM and conventional electromagnetic or acoustic metamaterials, we strongly suspect that type-II QMM may be associated with similar anomalous tunneling phenomena as for classical metamaterials. These phenomena are well described by transmission-line (TL) theory. In this section, we first illustrate the need for a TL theory of matter waves. We show that TL theory is the most suitable tool to understand the extraordinary tunneling phenomena associated with electromagnetic metamaterials, through the examples of ENZ supercoupling and tunneling at the plasmonic Brewster angle. Then, we develop a transmission line theory for guided matter waves which may be directly applied to transpose those concepts into the quantum world, paving the way to a variety of exciting applications.

5.1. ENZ supercoupling

ENZ supercoupling is a peculiar transmission phenomenon which occurs between two waveguides of very different cross-sectional areas. Consider an infinite parallel-plate waveguide directly connected to another infinite waveguide with much smaller cross section. Intuitively, one would expect almost total reflection of the TEM waves at the junction between the two waveguides, because of the huge impedance mismatch introduced by the difference in cross-sections. From TL analysis, however, we find the condition for having zero reflection as [6]

$$\frac{h_1}{\sqrt{\varepsilon_1}} = \frac{h_2}{\sqrt{\varepsilon_2}}, \tag{23}$$

where h denotes the waveguide height and ε is the effective permittivity of the medium filling each waveguide. We have assumed that the permeability in the two waveguide is the same. If $h_2 \ll h_1$ and the permittivities are of the same order of magnitude, condition (22) is far from being fulfilled. But interestingly, if ε_2 is near zero, total transmission is paradoxically achieved for a waveguide of infinitely small h_2 [5]. The associated large field enhancement, uniform all along the small waveguide due to the ENZ quasistatic response, is peculiarly independent of its length and shape and has been proposed for novel concepts in light concentration and harvesting [25], sensing [26], boosting molecular emission [9] or optical non-linearity [27].

5.2. Plasmonic Brewster angle

Tunneling of electromagnetic waves at the plasmonic Brewster angle is another example of anomalous tunneling through a very small aperture. Like ENZ tunneling, it relies on impedance matching. Therefore, this phenomenon is best described by transmission line formalism. Consider a metallic screen corrugated by very narrow slits. It has been shown [28] that the impedance mismatch with a normally incident plane wave can be totally compensated if the angle of incidence satisfies the following matching condition:

$$\cos(\theta) = \frac{\beta_s w}{k_0 d}, \tag{24}$$

where β_s is the wave number inside the screen, w is the width of the slits, k_0 is the free space wave number and d is the periodicity of the grating. This phenomenon is of particular interest since the associated ultrabroadband tunneling can span from dc to the visible range for a fixed incidence angle.

5.3. TL theory of guided matter waves

TL theory for matter waves has been proposed to describe propagation of plane waves in one dimensional problems [29]. We propose to extend it to the description of guided matter waves, in order to enable easy transposition of the two above mentioned extraordinary tunneling. Imagine a rectangular matter waveguide made out of infinite potential walls filled up with a type-II QMM with effective parameters m^* and V. The solution of the time-independent Schrödinger equation for the envelope function can be written as

$$\varphi(x,y,z) = \varphi_0 \sin\left(\frac{n\pi x}{a}\right)\sin\left(\frac{m\pi y}{b}\right)e^{ik_z z} \tag{25}$$

where a and b are the rectangular cross-section dimensions in the x and y directions, φ_0 is a constant, and (n,m) is a pair of nonzero integers. We will restrict ourselves to the $(1,1)$ mode, for which the guided wave number k_z satisfies the dispersion relation

$$k_z^2 = \frac{2m^*}{\hbar^2}(E-V) - \left(\frac{\pi}{a}\right)^2 - \left(\frac{\pi}{b}\right)^2. \tag{26}$$

We propose the following TL model for the wave propagation along z. The line voltage $u(z)$ is defined as

$$u(z) = \varphi(\frac{a}{2},\frac{a}{2},z) = \varphi_0 e^{ik_z z} \tag{27}$$

and the line current as

$$i(z) = \frac{ab}{m^*}\frac{du}{dz} = iab\frac{\varphi_0}{m^*}k_z e^{ik_z z}. \tag{28}$$

The primary parameters of the line are the shunt line admittance Y_p and the series line impedance Z_s, given by

$$Z_s = -\frac{m^*}{ab} \tag{29}$$

$$Y_p = \frac{ab}{m^*}k_z^2. \tag{30}$$

The line impedance is therefore:

$$\eta = \sqrt{\frac{Z_s}{Y_p}} = i\frac{m^* k_z}{ab} \tag{31}$$

Note that this definition of voltage and current has been chosen to ensure the continuity of the probability and probability current along the line. With these definitions, the junction between two waveguides with different cross-section can be directly modeled by connecting the two TL models together. The condition for total transmission between two semi-infinite waveguides is obtained by equating the line impedances:

$$\frac{m_1^* k_{z1}}{a_1 b_1} = \frac{m_2^* k_{z2}}{a_2 b_2} \tag{32}$$

It is evident how this theory can be exploited to transpose epsilon-near-zero supercoupling to matter waves, with similar properties as described in Section 5.1. Moreover, this theory is obviously valid for plane waves in unbounded media (or particles with well-defined momentum), written in the form:

$$\varphi(x,y,z) = \varphi_0 e^{ik_z z} \tag{33}$$

An angle of incidence can be taken into account by appropriately inserting factors $\cos\theta_i$ in the definitions of the line voltage and current in order to ensure the continuity of the probability and probability current at the junctions between unbounded media and waveguides. This modification allows a translation of the plasmonic Brewster tunneling to matter waves, which we will explore in detail in an upcoming publication.

6. Conclusions

We have presented and theoretically explored exotic properties and applications of quantum metamaterials. Type I quantum metamaterials, which are constituted of a quantum system strongly coupled to a classical metamaterial, were illustrated by considering the spontaneous radiation properties of a system of identical quantum emitters in a near-zero permittivity medium. We have presented quantitative arguments to support the fact that super-radiance may be strongly enhanced in an epsilon-near-zero background. Type II quantum metamaterials are artificial media with exotic effective properties for matter waves. We have shown how such media can be constructed by tailoring the band structure of quantum particles in periodic potentials. Exotic properties of matter wave metamaterials have been illustrated through several promising examples. We have shown that in principle it is possible to achieve plasmonic cloaking for matter waves, by designing a cover to cancel the scattering from a region of non-zero potential. In addition, we have shown that the

applications of classical metamaterials may be successfully translated into the quantum arena. A transmission-line theory for matter waves has been presented and we have showed how this tool may be successfully applied to transpose ENZ supercoupling and plasmonic Brewster angle tunneling to the quantum wave functions. These phenomena may be of interest in a variety of applications including sensing, electronics, or imaging.

Acknowledgements

This work has been supported by the ONR MURI grant No. N00014-10-1-0942.

References

[1] N. I. Zheludev, The road ahead for metamaterials, *Science* 328: 582–583, 2010.

[2] J. Zuloaga, E. Prodan, and P. Nordlander, Quantum plasmonics: optical properties and tunability of metallic nanorods, *ACS Nano* 4: 5269–5276, 2010.

[3] J.J. Greffet, M. Laroche and F. Marquier, Impedance of a nanoantenna and a single quantum emitter, *Phys. Rev. Lett.* 105: 117701, 2010.

[4] A. Alù, M.G. Silveirinha, A. Salandrino and N. Engheta, Epsilon-near-zero metamaterials and electromagnetic sources: tailoring the radiation phase pattern, *Phys. Rev. B* 75: 155410, 2007.

[5] M. G. Silveirinha, and N. Engheta, Tunneling of electromagnetic energy through subwavelength channels and bends using ε-near-zero materials, *Phys. Rev. Lett.* 97: 157403, 2006.

[6] A. Alù, M.G. Silveirinha, and N. Engheta, Transmission-line analysis of ε-near-zero–filled narrow channels, *Phys. Rev. E* 78: 016604, 2008.

[7] R. W. Ziolkowski, Propagation in and scattering from a matched metamaterial having a zero index of refraction, *Phys. Rev. E* 70: 046608, 2004.

[8] B. Edwards, A. Alù, M.G. Silveirinha, and N. Engheta, Experimental verification of plasmonic cloaking at microwave frequencies with metamaterials, *Phys. Rev. Lett.* 103: 153901, 2009.

[9] A. Alù and N. Engheta, Boosting molecular fluorescence with a plasmonic nanolauncher, *Phys. Rev. Lett.*103: 043902, 2009.

[10] V.V. Cheianov, V. Fal'ko and B.L. Altshuler, The focusing of electron flow and a veselago lens in grapheme p-n junctions, *Science* 315:1252-1255, 2007.

[11] E. Moreno, A.I. Fernandez-Dominguez, J. Ignacio Cirac and L. Martin-Moreno, Resonant transmission of cold atoms through subwavelength apertures, *Phys. Rev. Lett.* 95: 170406, 2005.

[12] L. Jenilek, J.D. Baena, J. Voves and R. Marques, Metamaterial inspired perfect-tunneling in semiconductors heterostructures, *New Journal of Physics* 13: 083011, 2011.

[13] S. Zhang, D.A. Genov, C. Sun and X. Zhang, Cloaking of matter waves, *Phys. Rev. Lett.* 100:123002, 2008.

[14] J.M. Luttinger and W. Kohn, Motion of electrons and holes in perturbed periodic fields, *Phys. Rev.* 97: 869–883, 1955.

[15] L.C. Lew Yan Voon, M. Willatzen, *The k.p method, Electronic properties of semiconductors*, Springer, New York, 2009.

[16] R.H. Dicke, Coherence in spontaneous radiation processes, *Phys. Rev.* 93: 99–110, 1954.

[17] F.T. Arecchi and E. Courtens, Cooperative phenomena in resonant electromagnetic propagation, *Phys. Rev. A* 2: 1730-1737, 1970.

[18] N.Skribanowitz, I.P. Herman, J.C. MacGillivray and M.S. Feld, Observation of Dicke super-radiance in optically pumped HF gas, *Phys. Rev. Lett.* 30:309-312, 1973.

[19] M.G. Benedict, A.M. Ermolaev, V.A. Malyshev, I.V. Solokov and E.D Trifonov, *Super-radiance, multiatomic coherent emission*, Institute of Physics Publishing, Bristol, 1996.

[20] D.C. Burnham and R.Y. Chiao, Coherent resonance fluorescence excited by short light pulses, *Phys. Rev.* 178: 2025–2035, 1969.

[21] A. Alù and N. Engheta, Achieving transparency with plasmonic and metamaterial coatings, *Phys. Rev. E* 72: 016623, 2005.

[22] M. Guild, A .Alù and M.R. Haberman, Cancellation of acoustic scattering from an elastic sphere, *J. Acoust. Soc. Am*, 129:1355-1365, 2011.

[23] D. Rainwater, A. Kerkhoff, K. Melin, J. C. Soric, G. Moreno and A. Alù, Experimental verification of three-dimensional plasmonic cloaking in free space, *New Journal of Physics*, 14:013054, 2012.

[24] A. Bohm, *Quantum Mechanics, Foundations and Applications*, 3rd edition, Springer-Verlag, New York, 1994.

[25] A. Alù and N. Engheta, Light squeezing through arbitrarily shaped plasmonic channels and sharp bends, *Phys. Rev. B* 78: 035440, 2008.

[26] A. Alù and N. Engheta, Dielectric sensing in ε-near zero narrow waveguide channels, *Phys. Rev. B* 78: 045102, 2008.

[27] C. Argyropoulos, P.Y. Chen, G. D'Aguanno, N. Engheta and A. Alù, Boosting optical non-linearities in epsilon-near-zero plasmonic channels, *Phys. Rev. B* 85: 045129, 2012.

[28] A. Alù, G. D'aguanno, N. Mattiucci and M.J. Bloemer, Plasmonic Brewster angle: broadband extroadinary transmission through optical gratings, *Phys. Rev. Lett.* 106:123902, 2011.

[29] A.N. Khonder, M. Rezwan, A.F.M. Anwar, Transmission line analogy of resonance tunneling phenomena: The generalized impedance concept, *Journal of Applied physics*, 63:5191-5193, 1988.

Study and analysis of an electric Z-shaped meta-atom

Abdallah Dhouibi[1], Shah Nawaz Burokur[1*], André de Lustrac[2], and Alain Priou[1]

[1]LEME, Univ. Paris-Ouest, EA 4416, 92410 Ville d'Avray, France
[2]IEF, Univ. Paris-Sud, CNRS, UMR 8622, 91405 Orsay cedex, France
*corresponding author, E-mail: sburokur@u-paris10.fr

Abstract

A printed Z-shaped electric meta-atom is presented as an alternative design to the conventional electric-LC (ELC) resonator. We propose to redesign the ELC resonator pattern to get a compact and a low cost electric resonator exhibiting a strong electric response. Our approach consists in redressing the resonator shape to accommodate higher inductance and therefore leading to a lower resonance frequency without being limited by fabrication tolerances. Simulation and measurement results show that the Z meta-atom exhibits an electric response to normally incident radiation and can be used very effectively in producing materials with negative permittivity.

1. Introduction

Metamaterials offer remarkable properties that go beyond conventional natural materials and are actually used in novel class electromagnetic devices such as invisibility cloaks [1-5], rotators [6], retroreflectors [7], Luneburg lenses [8], waveguide tapers [9] and directive antennas [10-17]. A typical metamaterial is an artificially engineered structure made of a periodic array of sub wavelength metallic or dielectric inclusions called meta-atoms. Various forms of meta-atoms such as Split Ring Resonator (SRR) [18] or electric-LC (ELC) resonator [19] have been shown to be able to produce respectively a wide range of permeability or permittivity values in the vicinity of the resonance. Other metamaterial resonators such as the S-shaped structures [20, 21] and the asymmetric cut wire pairs [22-24] have shown a negative refractive index. In order to use such resonators in the effective medium regime, the ratio between the operating wavelength and the unit cell size must be greater than 4 [25]. Different approaches have been proposed to increase the latter ratio with the main goal to shift downwards the resonance frequency of the meta-atoms. For instance, solutions such as integrating interdigital capacitors [26] or using high permittivity or permeability host substrates [27] have been proposed. However, such attempts are very limited according to the fabrication technology when frequency shifts upwards.

It is our aim in this paper to investigate numerically and experimentally the electromagnetic properties of a Z-shaped meta-atom in the microwave regime. The latter meta-atom is obtained by changing the LC equivalent circuit topology of the ELC resonator. It is reported that the structure presents an electric resonance which occurs at a lower frequency than that presented by the ELC resonator for similar geometrical dimensions. A negative real part of ε is demonstrated in the vicinity of the resonance. Moreover, the experimental study of cross-polarization and magneto-electric coupling in such an electric Z-shaped resonator is presented. The results are further compared with those of completely symmetric ELC and electric I-shaped resonators. It is shown that cross-polarization is near zero in the resonance vicinity of the Z-shaped resonator, indicating that a purely electric response is obtained at resonance.

2. From ELC to Z-shaped resonator

We first consider the unit cell of the ELC resonator introduced in Ref. 19 and presented in Fig. 1(a). In the effective medium regime, where resonator size is much smaller than the operating wavelength, the ELC resonator can be described qualitatively in terms of its equivalent circuit as illustrated in Fig. 1(b). A capacitor-like structure couples to the electric field and is connected in parallel to two loops providing inductance to the circuit. In order to increase the ratio between the operating wavelength and the ELC unit cell size it has been suggested that the resonance frequency of the LC circuit expressed as $f_r = \frac{1}{2\pi\sqrt{LC}}$, can be tuned downwards by introducing additional inductive loops to accommodate more inductance. Similar to interdigital capacitors, adding inductive loops can be a difficult technological task at optical frequencies.

Thus, we propose to transform the LC topology of the ELC resonator with the main goal to lower the resonance frequency. This transformation presents also the advantage of facilitating the metamaterial fabrication process. Hence, the ELC resonator can be easily reduced to an I-shaped resonator by removing firstly the two side arms, causing the inductance of the element to considerably decrease. On the counterpart, a new capacitance is created between the two horizontal arms. However, this capacitance C is very weak compared to that of the gap in the middle of the structure, which suggests that the transformed resonator will show a higher resonant frequency than the ELC. Removing the gap in the middle of the resonator changes the LC circuit topology and the resulting I-shaped resonator presented in

Fig. 1(c) is equivalent to the circuit given in Fig. 1(d). In this case without the gap, the capacitance needed for the LC resonance is given by C_p created between two consecutive unit cells.

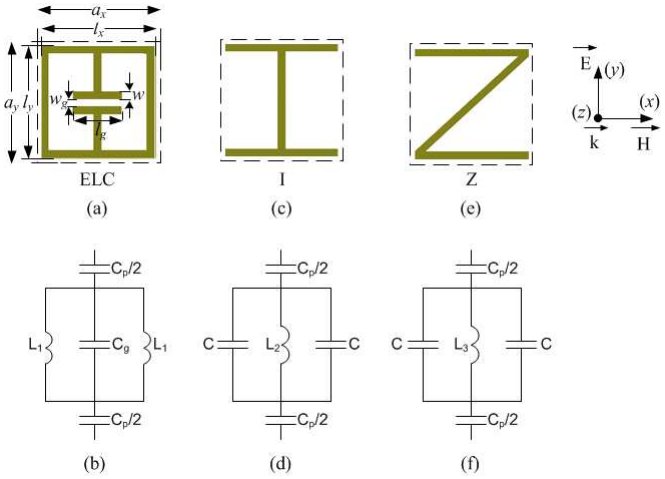

Figure 1: Unit cells and equivalent LC circuit models. (a)-(b) ELC resonator. (c)-(d) I-shaped resonator. (e)-(f) Z-shaped resonator. For all the resonators, the geometrical dimensions are: $a_x = a_y = 6$ mm, $l_x = 5.7$ mm, $l_y = 5.8$ mm, $w = 0.3$ mm, $w_g = 0.45$ mm and $l_g = 2$ mm.

Another practical shape transformation aiming to decrease the resonance frequency of the ELC resonator without changing the lattice constant consists in adding physical length to both inductive loops by using a slant line as presented in Fig. 1(e). Adding physical length when passing from I-shaped to Z-shaped structure shall produce a larger phase delay and increases the total inductance of the metamaterial without requiring additional fabrication steps. Due to this increase in inductance, the Z-shaped resonator shall present resonance at a lower frequency. The equivalent circuit model of the resulting Z-shaped structure is given in Fig. 1(f).

3. Parametric analysis of the resonators

To examine and compare the performances of the different resonators presented in Fig. 1, the properties of the structures are characterized numerically using a Finite Difference Time Domain (FDTD) Maxwell's equations solver, Microwave Studio Suite by CST. The dielectric spacer used throughout this study is single face copper-cladded epoxy with a relative dielectric constant of 3.9, a tangential loss of 0.02 and a thickness $t_s = 0.4$ mm. For the samples reported in this paper, the nominal length of the 17 μm thick copper wires along the x- and y-direction is respectively $l_x = 5.7$ mm and $l_y = 5.8$ mm and the nominal width is $w = 0.3$ mm in both simulations and experiments. For the capacitive gaps present in the ELC, the nominal width and length is respectively $w_g = 0.45$ mm and $l_g = 2$ mm. For the unit cell, $a_x = a_y = 6$ mm. For an electromagnetic wave incident with a wave vector and field polarization of Fig. 1, the different resonators will exhibit a strong electric response.

A parametric study of the resonators is performed in order to point out the importance of the different geometric parameters in the LC resonance frequency and to provide a guideline for design of such metamaterials. Three series of calculations are performed for each resonator; the first one concerns the width of the strip lines w, the second one for the length l_y and the third one concerns the length l_x. The transmission spectra under normal incidence are shown for each configuration. The parametric study is presented in the various parts of Fig. 2. Each column corresponds to a specific resonator and each row corresponds to the study of a physical parameter. In all subplots, the green traces correspond to the nominal values and the red and blue traces correspond respectively to upper and lower values. When considering only the resonance corresponding to nominal parameters (green traces), a resonance is clearly observed for each type of meta-atom. The I-shaped resonator presents a resonance frequency of 6.4 GHz, compared to 5.9 GHz for ELC. This shift toward higher frequencies was predictable since the inductance and capacitance are reduced when transforming ELC into I-shaped resonator. The shape transformation induces a change on the LC topology. In a quasi-static approximation, where resonator size is very small compared to operating wavelength, the I-shaped structure can be modeled in the form of the LC resonance circuit presented in Fig. 1(d). The equivalent capacitance in the I-shaped structure is then given by C_p since we neglect the capacitance C. According to the dimensions w_g and l_g used for the gap of the ELC, the capacitance of the latter (C_g) is almost half of the one created by the periodicity (C_p).

The resonance frequency of the Z-shaped resonator is expressed as $f_r = \dfrac{1}{2\pi\sqrt{L_3 C_p}}$ where the inductance is approximated by $L_3 \approx \mu_0 t_s \left(\dfrac{2w}{l_x} + \dfrac{\sqrt{l_x^2 + l_y^2}}{w} \right)$ and the inter-cell capacitance by $C_p \approx \dfrac{\varepsilon l_x}{\pi} \ln\left(\dfrac{2w}{a_y - l_y} \right)$ [18]. The circuit theory then predicts a resonance frequency equal to 5.2 GHz, which is in good agreement with the simulated value. Concerning the I-shaped resonator, the inductance is approximated by $L_2 \approx \mu_0 t_s \left(\dfrac{2w}{l_x} + \dfrac{l_y}{w} \right)$ and the calculated resonance frequency is 6.2 GHz. The equivalent capacitance of the ELC resonator is given by $\dfrac{C_p C_g}{C_p + C_g} \approx \dfrac{C_p}{3}$, and it's inductance is given by $L_1 \approx \mu_0 t_s \left(\dfrac{2w}{l_x} + \dfrac{2l_y}{w} + \dfrac{l_y - 2w - w_g}{w} \right)$. Hence, circuit theory predicts a resonance frequency of 6.3 GHz for the

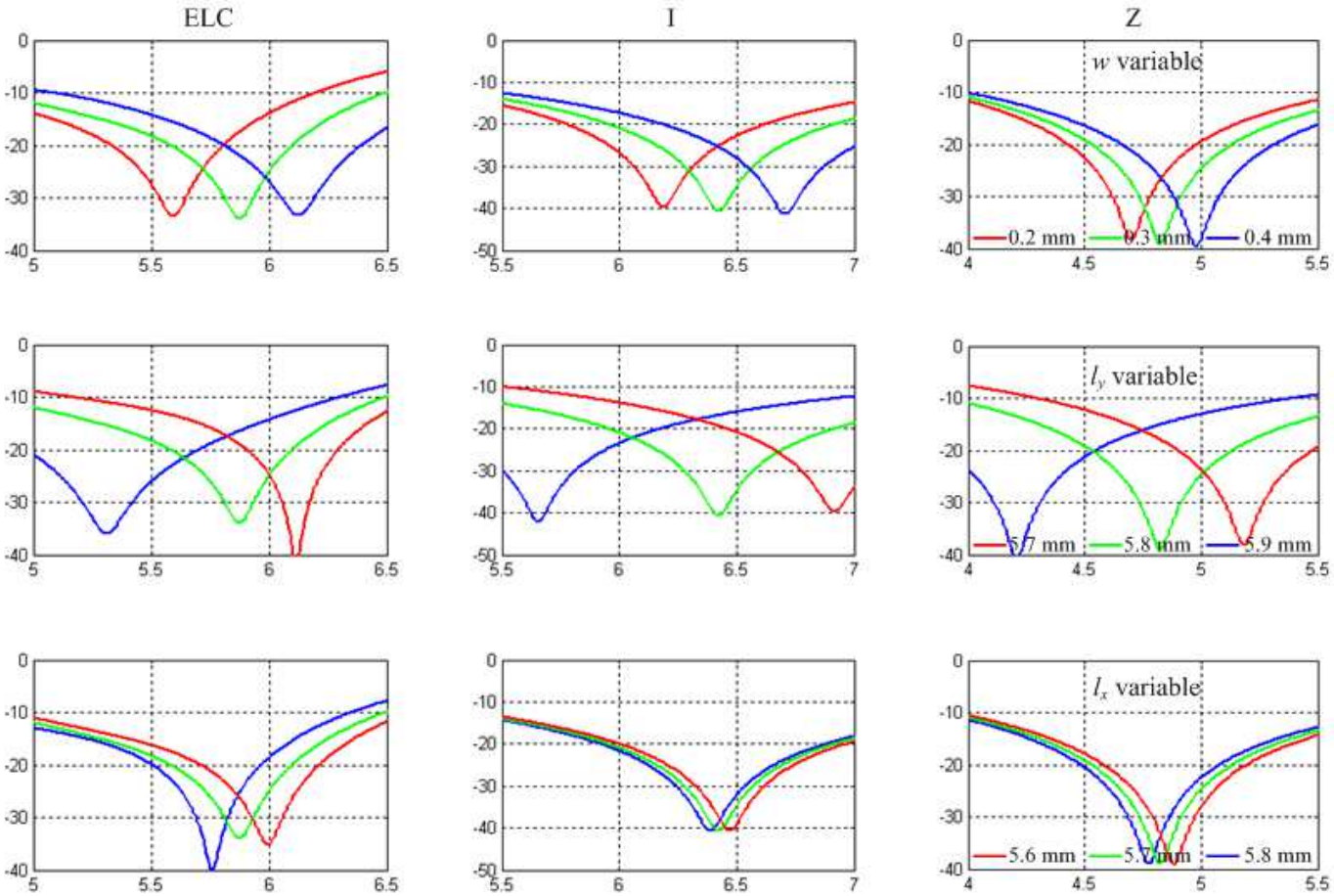

Figure 2: Parametric study of ELC, I-shaped and Z-shaped resonators. Variation of w, l_y and l_x.

ELC resonator. A good qualitative agreement can be observed with the resonance frequencies obtained from CST simulations as shown in Table I. The effective medium ratio λ/a, i.e. the ratio between the operating wavelength and the unit cell size, is also given for each meta-atom in Table I. We can clearly observe that parameters extraction is indeed possible with the different resonators since λ/a is greater than 4.

Table 1: Computed and measured resonance frequencies of the resonators (GHz).

Resonator	Simulated f_0	Calculated f_0	Measured f_0	Simulated λ/a
ELC	5.9	6.3	6	8.5
I	6.4	6.2	7	7.8
Z	4.9	5.2	4.9	10.2

Commenting on the parametric sweep, the first series of calculation given in Fig. 2 illustrate the influence of the strip lines width, w. We observe a shift toward higher frequencies for the three resonators when increasing w, since the inductance involved in the LC resonance is reduced. The second series of calculation is based on the variation of the vertical length l_y, and keeping a_y fixed to 6 mm. As l_y is increased, the resonance frequency of each meta-atom is decreased. This is because a higher capacitance value C_p is present between consecutive cells in the y-direction and also to higher inductance in the circuits. The third parametric sweep concerns the horizontal length l_x while keeping a_x fixed to 6 mm. An increase in l_x causes a decrease in resonance frequency for the different resonators. However, this decrease is more important in the ELC meta-atom since vertical arms are present in the structure and therefore a capacitance is created between consecutive cells in the x-direction. In the I- and Z-shaped resonators, the decrease is only slight due to the absence of vertical arms. A variation in lx causes inherently a variation in the length of the slant line in the Z-shaped resonator. On the other side, the length of the vertical lines does not vary in the I-shaped structure. Therefore a greater change in inductance is noted with the Z-type resonator and this explains why the Z-type resonator presents a larger shift in frequency than the I-shaped one when l_x varies.

4. Experimental measurement of the resonators

Prototypes based on the nominal dimensions have been fabricated for each resonator using standard lithography techniques. Total sample size is 18 × 18 cells on a 120 mm × 120 mm dielectric board. Microwave measurements based on the experimental setup described in ref. 28 have been done on the fabricated prototypes in an anechoic chamber using an Agilent 8722ES network analyser and two dual-polarized 2-18 GHz wideband band horn antennas. In this

case, the two horns are polarized similarly, with the wave vector and electric field polarization directed as shown in Fig. 1. Phase referencing and normalization have been performed in transmission by removing the sample from the signal path, and in reflection, by replacing the sample with a copper plate. Measured reflection and transmission coefficients are compared to the simulated ones in Fig. 3.

Calculated and measured magnitudes of S_{21} show clearly a resonance dip for each type of resonator. There is a very good qualitative agreement between simulations and measurements, except for I-shaped resonator. This discrepancy is due to the fact that the dimensions obtained with the fabricated prototype of the I-shaped structure do not correspond exactly to those used in simulations. Table I summarizes the numerical and experimental resonance frequencies.

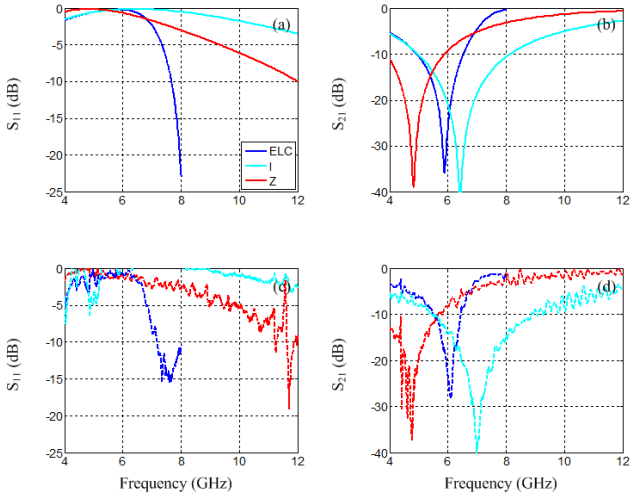

Figure 3: (a)-(b) Computed, and (c)-(d) measured reflection and transmission responses of the different resonators.

5. Study of magneto-electric coupling in the Z-shaped resonator

It can be clearly observed that the ELC and I-shaped resonators possess a high level of symmetry, implying both an electric coupling to an electric field and a magnetic coupling to a magnetic field. However due to the symmetric configuration, the two inductive loops are equivalent but opposite, cancelling the magnetic coupling in the structure [19]. Thus, a purely electric response is obtained from such structures. In the case of the Z-shaped resonator, the only apparent symmetry is a rotation of 180° around the z-axis. Because of the lack of mirror symmetry plane in the Z-type design, the eigenwave in such structures is not as simple as the *y*-direction linear polarized wave defined in Fig. 1. For this reason, cross-polarizing behaviour and magnetoelectric coupling study need to be addressed.

We first start by verifying the electromagnetic (EM) wave polarization of the Z-shaped structure. Two linear eigenmodes corresponding to *x*-polarized and *y*-polarized waves are considered in the numerical simulations. Therefore, four linear transmission coefficients T_{xx}, T_{yx}, T_{xy} and T_{yy} are obtained and used to calculate circular transmission coefficients T_{++}, T_{-+}, T_{+-} and T_{--} using the following equation [29]:

$$\begin{pmatrix} T_{++} & T_{+-} \\ T_{-+} & T_{--} \end{pmatrix} = \frac{1}{2}\times\begin{pmatrix} (T_{xx}+T_{yy})+i(T_{xy}-T_{yx}) & (T_{xx}-T_{yy})-i(T_{xy}+T_{yx}) \\ (T_{xx}-T_{yy})+i(T_{xy}+T_{yx}) & (T_{xx}+T_{yy})-i(T_{xy}-T_{yx}) \end{pmatrix} \quad (1)$$

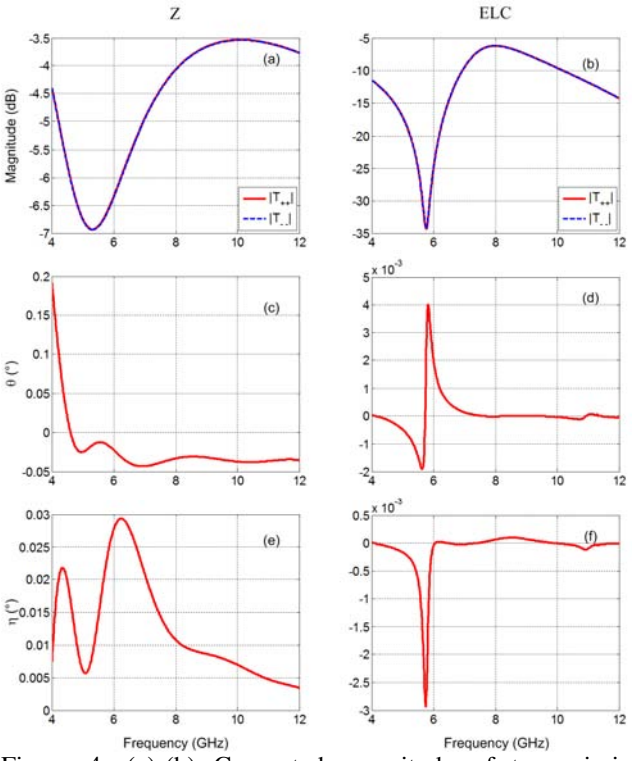

Figure 4: (a)-(b) Computed magnitude of transmission coefficient for the circularly polarized EM wave, (c)-(d) Computed polarization azimuth rotation (θ), (e)-(f) Computed ellipticity angle (η) for the Z-shaped and ELC resonators respectively.

Fig. 4(a) shows the calculated T_{++} and T_{--} coefficients for the Z-shaped meta-atom. We can note that conversely to the chiral metamaterial presented in Ref. 29, the right-handed and left-handed circularly polarized EM waves are similar in this case. The same behavior is observed for the ELC resonator as illustrated in Fig. 4(b). The polarization azimuth rotation $\theta = \left[\arg(T_{++}) - \arg(T_{--})\right]/2$, and the ellipticity $\eta = \frac{1}{2}\arcsin\left(\frac{|T_{++}|-|T_{--}|}{|T_{++}|+|T_{--}|}\right)$ of elliptically polarized light, are presented in Figs. 4(c) and 4(e) and Figs. 4(d) and 4(f) for the Z-shaped and ELC resonator, respectively. Compared to Ref. 29, the polarization rotation and the ellipticity present very low values close to zero for both the Z-shaped and the ELC resonators, suggesting that the structures do not possess chiral properties.

Further investigations about magnetoelectric coupling are performed by comparing the magnetic field vector distribution in the Z-shaped and ELC resonators at resonance. As it can be observed in Fig. 5, a magnetic loop is formed on each side of the central line in both resonators. The magnetic field vectors of the loops point in opposite

directions, cancelling the magnetic coupling in the resonators. It can therefore be deduced that similarly to the ELC resonator, a purely electric response can be obtained from the Z-shaped meta-atom.

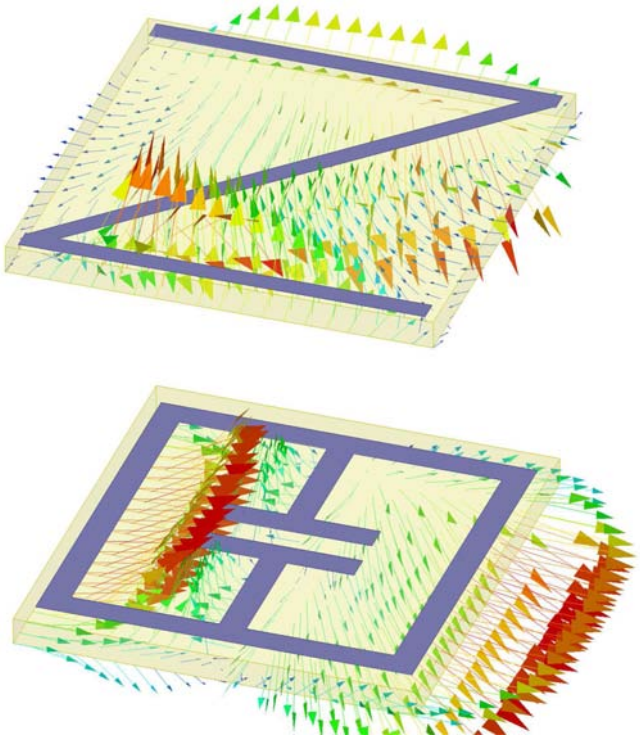

Figure 5: .Magnetic field vector distribution at resonance in the Z-shaped and ELC resonators.

6. Experimental measurement of bianisotropy

To experimentally verify bianisotropy effect in the Z-shaped meta-atom, cross-polarization transmission measurements are performed on the 18 × 18 cells fabricated sample as detailed in [30]. Conversely to co-polarization (or desired polarization) measurements performed in section 4, here the two horns are polarized orthogonally with respect to each other. The horn antenna used as emitter is polarized with an electric field along the y-direction whereas the one used as receiver is polarized with an electric field along the x-direction, such that the E-plane of one horn is oriented 90° with respect to the other.

Measurements on the various element samples are presented in Fig. 6(a)-(c) for normal incidence (0°) and in Fig. 6(d)-(f) for 45° incidence in E-plane. For normalization, co- and cross-polarization measurements are performed with no sample present. It can clearly be observed that in both incidence cases, cross-polarization level of the ELC sample is commensurate with that of no sample present. For the Z-shaped metamaterial sample, cross-polarization is considered negligible below 6 GHz since the level is almost the same as in free space (without the sample). However, the cross-polarization level tends to increase above 6 GHz, indicating the presence of magneto-electric coupling. The resonance frequency of the Z-shaped metamaterial sample having been experimentally measured at 4.9 GHz, we can therefore deduce that the latter resonance is purely electric similar to the ELC meta-atom, although the lack of symmetry in the design. Cross-polarization measurements have also been performed on the highly symmetric I-shaped metamaterial and results consistent with the ELC have been observed.

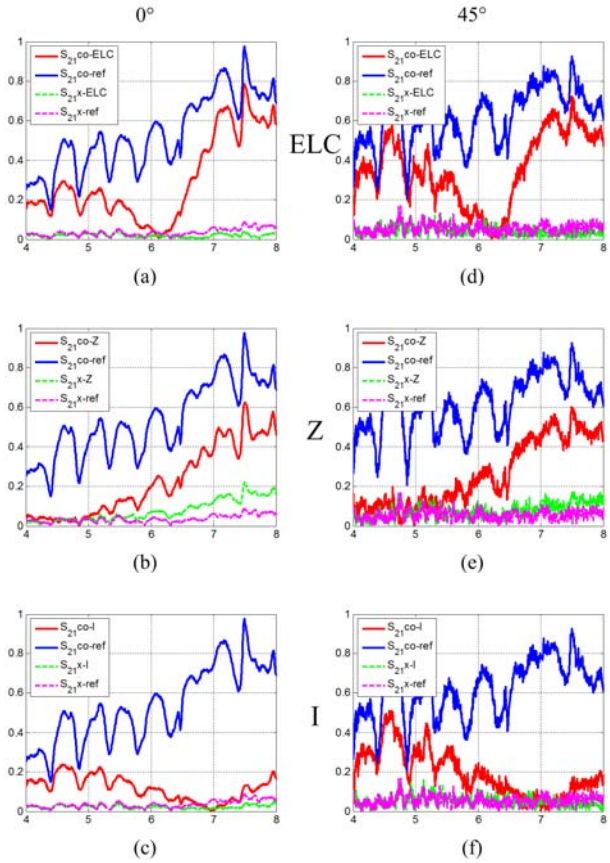

Figure 6: Comparison of cross-polarization measurements for the various ELC, Z-shaped and I-shaped designs. (a)-(c) 0° incidence. (d)-(f) 45° oblique incidence. For calibration, horns aligned and cross-polarization transmission measurements are shown for no sample present (blue and magenta colors).

7. Effective parameters retrieval

Using reflection and transmission responses from a single layer of the sample and considering a *y*-direction linear polarized wave, effective parameters can be extracted using the retrieval procedure described in [31]. This is possible since the structure period along the propagation direction is very small compared to the working wavelength. In performing the retrieval, we assume a z-direction size a_z = 6 mm corresponding to a cubic unit cell as proposed in Ref. 19. Extracted permittivity ε and permeability μ are shown for ELC, I-shaped, and Z-shaped resonators in the various parts of Fig. 7. Real and imaginary parts of μ are respectively shown in Fig. 7(a) and 7(b). As stated above, the ELC resonator presents an electric response but no magnetic response, i.e. the real part of μ is close to unity over the frequencies of interest. However, the retrieved parameters do not strictly comply with this principle. As shown in Fig. 7(a), the real part of μ becomes anti-resonant. In fact, this anomaly is an artifact introduced during parameter extraction in a frequency range where the

medium is highly spatially dispersive [19]. The two other resonators present similar responses. From Figs. 7(c)-7(f), we see a strong electric resonance, with the real part of the permittivity ranging from positive to negative values in the vicinity of the resonance. The values issued from measurement data agree very well with those calculated from numerical simulations. It must be noted that the extraction from the measured spectra are presented without any fitting. From the simulated and measured real parts of ε, it can also be noted that both Z-shaped meta-atoms (with and without gap) present a wider frequency band where the values are negative compared to the ELC resonator. Finally, we stress on the fact that the parameters extracted from the retrieval procedure described in [31] concerning the Z-shaped resonator are valid only in the vicinity of the resonance, *i.e.* for frequencies below 6 GHz, since presence of magneto-electric coupling has been observed for higher frequencies.

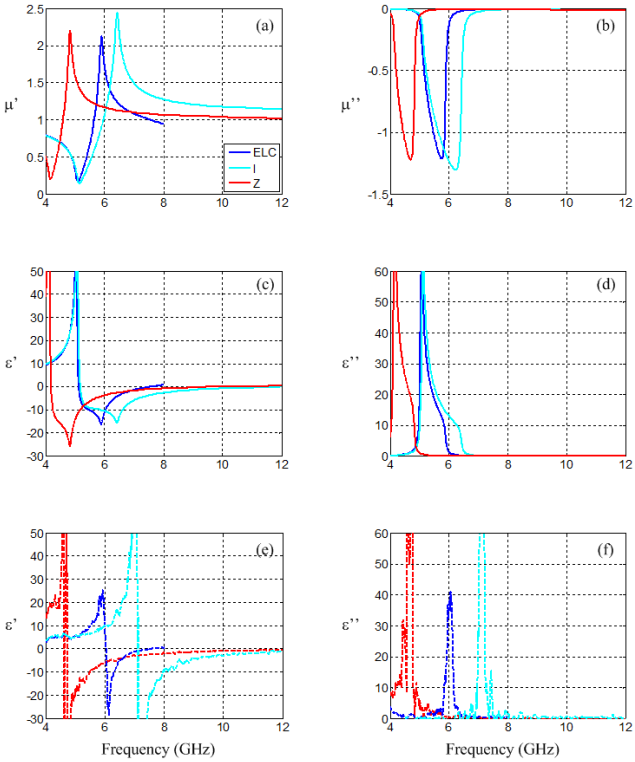

Figure 7: Computed effective parameters: (a) Re(μ), (b) Im(μ), (c) Re(ε), and (d) Im(ε). Measured effective parameters: (e) Re(ε) and (f) Im(ε).

8. Conclusions

We have presented an experimental demonstration of a negative permittivity from various meta-atoms in the microwave domain. The proposed structures, evolved from the transformation of conventional electric-LC (ELC) resonator, are simple to design and can be easily fabricated with standard techniques. A parametric study on the different parameters has also been presented so as to show the influence on the resonance frequency of the different resonators. In particular, a Z-shaped meta-atom has been shown to be an interesting alternative to the conventional ELC. This proposed electric resonator allows to considerably improve the effective medium ratio λ/a. Due to the simplicity of the structure geometry and to the absence of capacitive gap, a transposition of geometrical parameters can be considered for the optical domain.

Acknowledgements

This work was supported by the EADS Company Foundation through the METAQOPT project, contract No. 090-AO09-1006. One of the authors (A.D.) acknowledges support for his PhD scholarship from EADS Company Foundation. The authors thank T. Lepetit and A. Degiron for fruitful discussions on magneto-electric coupling.

References

[1] U. Leonhardt, Optical conformal mapping, *Science* 312(5781): 1777-1780, 2006.

[2] J. B. Pendry, D. Schurig, D. R. Smith, Controlling electromagnetic fields, *Science* 312(5781): 1780-1782, 2006.

[3] D. Schurig, J. J. Mock, B. J. Justice, S. A. Cummer, J. B. Pendry, A. F. Starr, D. R. Smith, Metamaterial electromagnetic cloak at microwave frequencies, *Science* 314(5801): 977-980, 2006.

[4] W. Cai, U. K. Chettiar, A. V. Kildishev, V. M. Shalaev, Optical cloaking with metamaterials, *Nat. Photon.* 1(4): 224-227, 2007.

[5] B. Kanté, A. de Lustrac, J.-M. Lourtioz, S. Burokur, Infrared cloaking based on the electric response of split ring resonators, *Opt. Express* 16(12): 9191-9198, 2008.

[6] H. Chen, B. Hou, S. Chen, X. Ao, W. Wen, C. T. Chan, Design and experimental realization of a broadband transformation media field rotator at microwave frequencies, *Phys. Rev. Lett.* 102(18): 183903, 2009.

[7] Y. G. Ma, C. K. Ong, T. Tyc, U. Leonhardt, An omnidirectional retroreflector based on the transmutation of dielectric singularities, *Nat. Mater.* 8(8): 639-642, 2009.

[8] N. Kundtz, D. R. Smith, Extreme-angle broadband metamaterial lens, *Nat. Mater.* 9(2): 129-132, 2010.

[9] P.-H. Tichit, S. N. Burokur, A. de Lustrac, Waveguide taper engineering using coordinate transformation technology, *Opt. Express* 18(2): 767-772, 2010.

[10] S. N. Burokur, M. Latrach, S. Toutain, Theoretical investigation of a circular patch antenna in the presence of a left-handed medium, *IEEE Antennas Wireless Propag. Lett.* 4: 183-186, 2005.

[11] P.-H. Tichit, S. N. Burokur, A. de Lustrac, Ultradirective antenna via transformation optics, *J. Appl. Phys.* 105(10): 104912, 2009.

[12] P.-H. Tichit, S. N. Burokur, D. Germain, A. de Lustrac, Design and experimental demonstration of a high-directive emission with transformation optics, *Phys. Rev. B* 83(15): 155108, 2011.

[13] P.-H. Tichit, S. N. Burokur, D. Germain, A. de Lustrac, Coordinate transformation based ultra-directive emission, *Elec. Lett.* 47(10): 580-582, 2011.

[14] C. Garcia-Meca, A. Martinez, U. Leonhardt, Engineering antenna radiation patterns via quasi-conformal mappings, *Opt. Express* 19(24): 23743-23750, 2011.

[15] E. Lier, D. H. Werner, C. P. Scarborough, Q. Wu, J. A. Bossard, An octave-bandwidth negligible-loss radiofrequency metamaterial, *Nat. Mater.* 10(3): 216-222, 2011.

[16] Z. H. Jiang, M. D. Gregory, D. H. Werner, Experimental demonstration of a broadband transformation optics lens for highly directive multibeam emission, *Phys. Rev. B* 84(16): 165111, 2011.

[17] P.-H. Tichit, S. N. Burokur, A. de Lustrac, Transformation media producing quasi-perfect isotropic emission, *Opt. Express* 19(21): 20551-20556, 2011.

[18] J. B. Pendry, A. J. Holden, D. J. Robbins, W. J. Stewart, Magnetism from conductors and enhanced non-linear phenomena, *IEEE Trans. Microwave Theory Tech.* 47(11): 2075-2084, 1999.

[19] D. Schurig, J. J. Mock, D. R. Smith, Electric-field-coupled resonators for negative permittivity metamaterials, *Appl. Phys. Lett.* 88(4): 041109, 2006.

[20] H. Chen, L. Ran, J. Huangfu, X. Zhang, K. Chen, T. M. Grzegorczyk, J. A. Kong, Left-handed materials composed of only S-shaped resonators, *Phys. Rev. E* 70(5): 057605, 2004.

[21] D. Wang, L. Ran, H. Chen, M. Mu, J. A. Kong, B.-I. Wu, Experimental validation of negative refraction of metamaterial composed of single side paired S-ring resonators, *Appl. Phys. Lett.* 90(25): 254103, 2007.

[22] A. Sellier, S. N. Burokur, B. Kanté, A. de Lustrac, Negative refractive index metamaterials using only metallic cut wires, *Opt. Express* 17(8): 6301-6310, 2009.

[23] S. N. Burokur, A. Sellier, B. Kanté, A. de Lustrac, Symmetry breaking in metallic cut wire pairs metamaterials for negative refractive index, *Appl. Phys. Lett.* 94(20): 201111, 2009.

[24] S. N. Burokur, T. Lepetit, A. de Lustrac, Incidence dependence of negative index in asymmetric cut wire pairs metamaterials, *Appl. Phys. Lett.* 95(19): 191114, 2009.

[25] T. Koschny, P. Markos, E. N. Economou, D. R. Smith, D. C. Vier, C. M. Soukoulis, *Phys. Rev. B* 71(24): 245105, 2005.

[26] W. Withayachumnankul, C. Fumeaux, D. Abbott, Compact electric-LC resonators for metamaterials, *Opt. Express* 18(25): 25912-25921, 2010.

[27] C. Caloz, A. Lai, T. Itoh, The challenge of homogenization in metamaterials, *New J. Phys.* 7, art. no. 167, 2005.

[28] J. Zhou, L. Zhang, G. Tuttle, T. Koschny, C. M. Soukoulis, Negative index materials using simple short wire pairs, *Phys. Rev. B* 73(4), 041101(R), 2006.

[29] J. Zhou, J. Dong, B. Wang, T. Koschny, M. Kafesaki, C. M. Soukoulis, Negative refractive index due to chirality, *Phys. Rev. B* 79(12): 121104(R), 2009.

[30] D. R. Smith, J. Gollub, J. J. Mock, W. J. Padilla, D. Schurig, Calculation and measurement of bianisotropy in a split ring resonator metamaterial, *J. Appl. Phys.* 100(2): 024507, 2006.

[31] D. R. Smith, S. Schultz, P. Markos, C. M. Soukoulis, Determination of effective permittivity and permeability of metamaterials from reflection and transmission coefficients, *Phys. Rev. B* 65(19): 195104, 2002.

Calculation of Effective Material Parameters by Field Averaging Over Lattices with Non-Negligible Unit Cell Size

Anthony K. Amert, Victor V. Gozhenko, Keith W. Whites*

Electrical and Computer Engineering Department, South Dakota School of Mines and Technology, Rapid City, USA
*corresponding author, E-mail: whites@sdsmt.edu

Abstract

The Pendry *et al*. field averaging method for calculation of effective material parameters is reviewed and its limits explored. The method is then extended so that it can accurately calculate the effective material parameters of lattices where the unit cell size is appreciable but still quasistatic ($d \sim 0.1\lambda_0$). The new algorithm is verified by calculating the effective material properties of periodically placed particles suspended in free space, as the unit cell size becomes appreciable. Results of our proposed formulation are then compared with the Pendry *et al*. and conventional volumetric averaging algorithms.

1. Introduction

Artificial materials for electromagnetic and optical applications typically consist of lattices of dielectric or metal inclusions of various shapes and sizes [1]. Many inclusion geometries such as dielectric spheres, metal cylinders, swiss rolls, and split-ring resonators have been investigated for their unique electromagnetic behaviors. Successful use of these materials hinges on the accurate calculation of the effective permittivity ε_{eff} and permeability μ_{eff} of the material.

The effective parameters of lattices can be calculated using a plurality of methods that have been proposed over the years (see, e.g., [2-5]). In the quasistatic regime, when the size d of the unit cell of a lattice is small compared to the operating wavelength, $d << \lambda$, and the inclusion volume is small, it is possible to calculate the effective permittivity and permeability of the lattices based on the Maxwell Garnett formula [6]. However, beyond the quasistatic regime and for high inclusion volume geometries one has to use more sophisticated approaches.

One often used method to compute effective materials parameters both in the lab and from computational data is to equate the scattering parameters of a plane wave incident on a finite thickness slab to the scattering parameters of an equivalent transmission line problem [7]. In the lab, free space measurement systems are used to measure such scattering parameters and computationally such problems can be solved trivially. However, contemporary work on artificial materials has focused on periodic materials that have lattice constants that are in the $0.05\lambda_0$ to $0.4\lambda_0$ range and are only a few layers thick in the direction of wave propagation. Calculation of effective material parameters from such geometries using transmission line equivalent problems is very difficult at best. As identified by others, periodic materials cannot be exactly modeled by a single section of homogeneous transmission line [8,9]. Near the edges of a finite thickness slab the truncation of the lattices cause the particles near the truncation to polarize differently than those in an infinite lattice. This edge effect results in both spatially varying and inherently anisotropic material parameters near the edge of the slab. To mitigate the effect this problem has on the calculated effective material problems one could create a finite thickness slab that is many cells thick in an attempt to average out the edge effect. However, this does not completely eliminate the error caused by the only approximate transmission line model and results in an unknown and unpredictable amount of inherent error in the calculated effective material parameters.

To avoid the inherent error of transmission line models, we instead chose to investigate methods of calculating effective materials using only the information contained within a single unit cell away from the lattice edges where the local electromagnetic behavior is nearly identical to that of the behavior of an infinite lattice. One particularly appealing method in the literature is proposed by Pendry *et al*. [5]. In the proposed method, effective material parameters of periodic materials are calculated using only the local E , D , H , and B fields averaged over unit cells. The average values of D and B fields are defined as surface integrals of the local field values while the averages of E and H fields are defined as line integrals of the local fields. These local fields can be obtained by numerically solving the corresponding boundary-value problem for Maxwell's equations with an appropriate solver.

Though this approach has been previously reported to give good results for lattices of some types, the proposers of the Pendry *et al*. method have identified two serious problems with the method [10,11]. First, it's only rigorously valid in the quasistatic limit and returns increasingly inaccurate material parameters as the size of the unit cell increases. Second, beyond the quasistatic limit it returns complex material parameters for lossless problems.

To eliminate these problems, we are proposing a modification to the Pendry *et al*. method. Our modification

is based on using surface averages instead of line averages for the definition of the averaged electric and magnetic fields.

In this communication, we first briefly discuss the Pendry *et al*. method and its limitations. Next our modification to the Pendry *et al*. method is described and how it is applied. We then apply the Pendry *et al*. method, our proposed modified method, and the conventional volume averaging method to three periodic materials consisting of (a) free space, (b) dielectric spheres, and (c) dielectric cubes. Lastly, we report the accuracy of the Pendry *et al*. method and our proposed modified method.

2. Pendry *et al.* and modified averaging methods

According to Pendry *et al*., the effective permittivity and permeability tensors of a lattice of inclusions can be calculated as [10,11]

$$(\varepsilon_{\text{eff}})_{ij} \equiv \frac{\langle D_i \rangle_S}{\langle E_j \rangle_L}, \qquad (\mu_{\text{eff}})_{ij} \equiv \frac{\langle B_i \rangle_S}{\langle H_j \rangle_L} \tag{1}$$

where F_i is the i th component of the respective field ($F = E, D, H, B$) and the averages $\langle F_i \rangle_S$, $\langle F_i \rangle_L$ are defined as surface and line integrals

$$\langle F_i \rangle_S \equiv \frac{1}{S} \iint_S F_i dS , \tag{2}$$

$$\langle F_i \rangle_L \equiv \frac{1}{L} \int_L F_i dL \tag{3}$$

with specific integration surface S and integration path L . The latter is designated along one of the edges of the unit cell and the surface S is designated as one of the cell's faces as illustrated in Fig. 1.

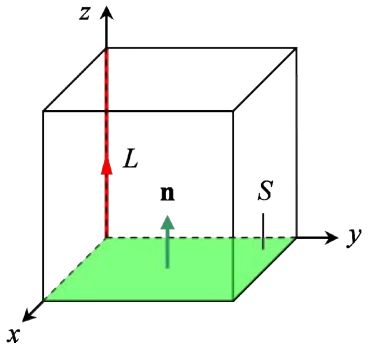

Figure 1: The integration surface S and integration path L used in Eqs. (2)-(3) to calculate the average values of z -components of the fields. For x - and y -components, both the line L and the surface normal **n** must be in the respective directions.

Eqs. (1)-(3) play a central role in the Pendry *et al*. averaging method. They define how to calculate the effective permittivity and permeability tensors ε_{eff} and μ_{eff} if the local distributions of all the fields E , D , H , and B are known. The distributions of E and H fields can be obtained by numerically solving the respective boundary value problem with a full wave solver. The distributions of D and B fields can then be calculated from those of E and H fields by using the constitutive relations

$$\mathbf{D} = \varepsilon_0 \varepsilon_r \mathbf{E}, \qquad \mathbf{B} = \mu_0 \mu_r \mathbf{H},$$

with $\varepsilon_0 = 8.85 \times 10^{-12}$ F/m and $\mu_0 = 4\pi \times 10^{-7}$ H/m being the permittivity and permeability of free space and ε_r and μ_r are the local *relative* permittivity and permeability within the unit cell.

Note the following advantages of the Pendry *et al*. method:

i) it only utilizes local field information and thus simulations can be created that have little or negligible edge effect problems;

ii) the field quantities used in the method can be easily calculated using an appropriate commercial software.

However, the Pendry *et al*. method also has the following limitation: it is only correct, strictly speaking, in the quasistatic case. For lattices with an appreciable unit cell size, it provides a poor description of their effective parameters [10,11].

As an illustration, we calculated, based on Eqs. (1)-(3), the effective parameters of a lattice of empty cells with non-negligible unit cell size when compared to the wavelength of the incident wave. The local field data sets used in Eqs. (2)-(3) were obtained from *CST Microwave Studio Suite* by simulating the propagation of a plane wave incident normally onto a slab of free space. The slab was split into simple cubic cells (SCCs) of cell size d . The total thickness of the slab was 9 unit cells and the necessary field calculations were performed on the unit cell at the center of the slab. The time domain solver was used to calculate the numerical results and was set to terminate after the energy of the system had run down to -80 dB. Automatic meshing of the geometry was set to 50 lines per wavelength (convergence of this and the geometries discussed later in this paper were verified but are not shown here). Once calculated, post processing templates within the software were used to calculate the necessary line and surface averages. Ratios of the averaged quantities were finally used to calculate the effective material parameters. The calculation results for both the real and imaginary parts of the relative values $\varepsilon_{\text{eff},r} \equiv \varepsilon_{\text{eff}} / \varepsilon_0$ and $\mu_{\text{eff},r} \equiv \mu_{\text{eff}} / \mu_0$ of ε_{eff} and μ_{eff} as functions of the unit cell size are presented in Fig. 2 (red dashed curves).

As seen from Fig. 2(a), the calculated values of the real parts of $\varepsilon'_{\text{eff},r} \equiv \text{Re}\,\varepsilon_{\text{eff},r}$ and $\mu'_{\text{eff},r} \equiv \text{Re}\,\mu_{\text{eff},r}$ progressively diverge away from the value $\varepsilon'_r = \mu'_r = 1$ of free space as the unit cell size increases from $d/\lambda = 0$ to approx. 0.7 and then converges in an oscillating manner to a final value of $\varepsilon'_{\text{eff},r} = \mu'_{\text{eff},r} = 0$. A similar oscillating behavior is observed for the imaginary parts $\varepsilon''_{\text{eff},r} \equiv \text{Im}\,\varepsilon_{\text{eff},r}$ and $\mu''_{\text{eff},r} \equiv \text{Im}\,\mu_{\text{eff},r}$, as seen in Fig. 2(b). Conversely, and purely coincidentally because of the loss free geometry, the final value of

calculated $\varepsilon''_{\text{eff},r}$ and $\mu''_{\text{eff},r}$ coincides with the true value $\varepsilon''_r = \mu''_r = 0$ for vacuum.

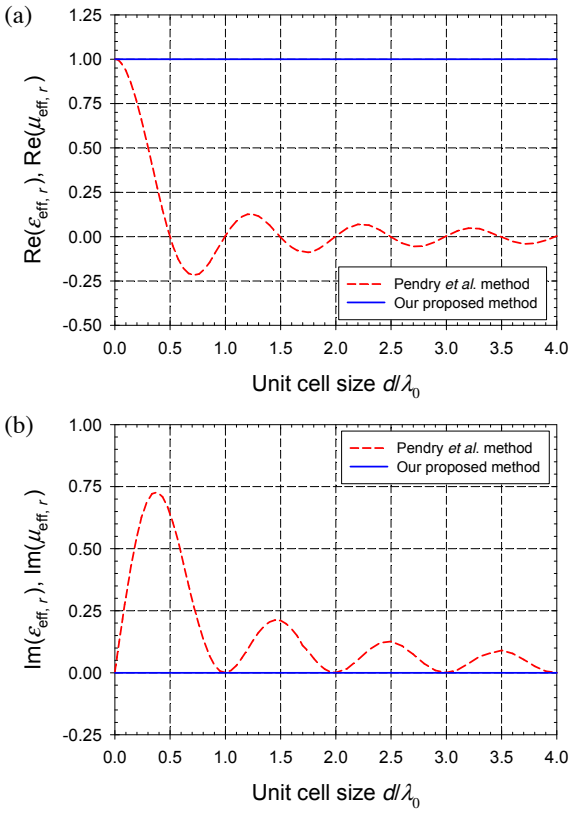

Figure 2: Computed (a) real and (b) imaginary parts of the relative effective permittivity and permeability of free space considered as a lattice of empty cells.

Dependence of the error in the real part of the computed permittivity value $\Delta \equiv (\varepsilon_0 - \varepsilon'_{\text{eff}})/\varepsilon_0$ on the unit cell size d is presented in Fig. 3. As seen from the plot, even at $d/\lambda = 0.2$, where one might expect the Pendry *et al.* method to give quite satisfactory results, the calculated value of $\varepsilon'_{\text{eff}}$ of free space contains an error approximately 25%.

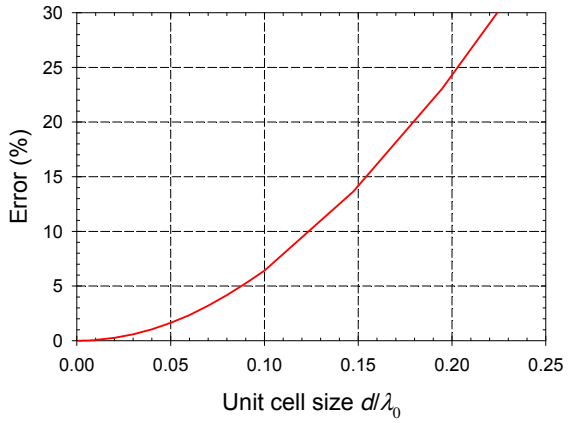

Figure 3: The error in the effective permittivity of free space computed by Pendry *et al.* method.

The discrepancy between the calculated and true values of ε_{eff}, μ_{eff} of free space has been explained [10,11] as caused by the spatial variation of the electric and magnetic fields of the incident wave over large enough unit cells. Due to this variation, the effective parameters of free space calculated from Eqs. (1)-(3) become [10]

$$\varepsilon_{\text{eff}} = \varepsilon_0 \frac{\exp(ikd) - 1}{ikd}, \qquad \mu_{\text{eff}} = \mu_0 \frac{\exp(ikd) - 1}{ikd}, \tag{4}$$

with their real parts [11]

$$\varepsilon'_{\text{eff}} = \varepsilon_0 \frac{\sin(kd)}{kd}, \qquad \mu'_{\text{eff}} = \mu_0 \frac{\sin(kd)}{kd}, \tag{5}$$

and imaginary parts

$$\varepsilon''_{\text{eff}} = \varepsilon_0 \frac{1 - \cos(kd)}{kd}, \qquad \mu''_{\text{eff}} = \mu_0 \frac{1 - \cos(kd)}{kd}, \tag{6}$$

where k is the wave number of the incident wave propagating along one of the lattice's axis. The oscillating behavior of both the real and imaginary parts of ε_{eff} and μ_{eff} as functions of the unit cell size d, which is predicted by analytical expressions (5)-(6), is exactly what is observed in our numerical results shown in Fig. 2.

It should be mentioned that the calculation of ε_{eff} and μ_{eff} of a lattice of empty cells was performed, within the Pendry *et al.* averaging method, for the first time in [10] and then repeated in [11]. However, the expressions (6) for the imaginary parts $\varepsilon''_{\text{eff}}$, μ''_{eff} are not given explicitly in either of these works.

Formally, the difference between $(\varepsilon_{\text{eff}}, \mu_{\text{eff}})$ and (ε_0, μ_0) is due to the oscillating factors appearing in Eqs. (4)-(6). To match the values of $(\varepsilon_{\text{eff}}, \mu_{\text{eff}})$ calculated by the Pendry *et al.* method to the values (ε_0, μ_0) of free space, it has been proposed [10,11] to simply remove the respective phase factors $[\exp(ikd) - 1]/(ikd)$ or $\sin(kd)/(kd)$ from Eqs. (4)-(5). However, such "handmade correction" is valid for only the case of empty cells considered here. For the general case of non-empty cells with arbitrary inclusions it is still not clear what is the "phase factor" that has to be eliminated from the calculation results to obtain correct values of ε_{eff}, μ_{eff}.

Since at large enough d/λ values the line integral definition (3) for the average E and H fields cannot take into account the phase variation of the fields over the unit cells in the direction of wave propagation, we propose to modify the Pendry *et al.* method in order to automatically account for the variation. Namely, we propose the use of surface averages for E and H fields instead of the line averages (3). Accordingly, Eqs. (1) are replaced by

$$(\varepsilon_{\text{eff}})_{ij} \equiv \frac{\langle D_i \rangle_S}{\langle E_j \rangle_{S'}}, \tag{7}$$

$$(\mu_{\text{eff}})_{ij} \equiv \frac{\langle B_i \rangle_S}{\langle H_j \rangle_{S'}}, \tag{8}$$

where the surface averages $\langle E_j \rangle_{S'}$, $\langle H_j \rangle_{S'}$ are calculated similarly to Eq. (2) but now over the surface S' selected as explained in Fig. 4. Note that our modified definitions for the averages of E and H in Eqs. (7)-(8) do not compute the average value normal to the plane as used in the definitions for the average electric or magnetic flux densities. Rather, it calculates the average tangential value in the i th direction over the plane S'.

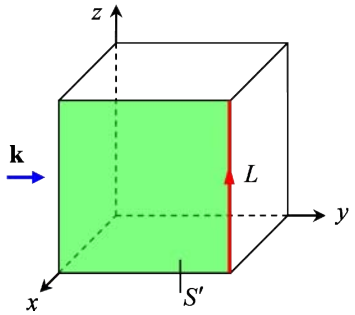

Figure 4: The integration surface S' used in Eqs. (7)-(8) to calculate the average values of z -components of E and H fields. For the other two components, surface S' is defined by the respective axis and the wave vector **k** of the incident wave.

Note that our approach can be proven rigorously (the proof will be published elsewhere) in the static approximation from first principles—the general properties of the static electric and magnetic fields and conventional spatial averaging of the local fields. Moreover, in the quasistatic limit our proposed method is identical to the Pendry *et al*. method. However, as the unit cell size increases, our approach provides more accurate results for lattices of larger unit cell size in the region of d/λ values where the Pendry *et al*. method fails.

To illustrate the advantages of our modified method, we first calculated, based on Eqs. (7)-(8), the effective parameters of free space. The results are presented in Fig. 2 by the blue solid curves. As seen from Fig. 2, our approach returns correct results for ε_{eff} and μ_{eff} of free space regardless of the unit cell size. Such perfect agreement between these calculated and theoretical results is a unique case and will not generalize to any other unit cell geometry. Generally, our proposed method will give only approximate values of the effective parameters, but far more accurate than the Pendry *et al*. method.

Lastly, the very concept of the effective parameters is questionably applicable to lattices with unit cells that are of the order of the wavelength of incident waves. Therefore, as the unit cell size becomes too large it should be expected that our averaging method will also fail.

3. Numerical results and discussion

To further investigate the validity of our proposed method, we have applied it to simple cubic lattices of dielectric spheres and cubes. For comparison, we have also implemented the Pendry *et al*. method as well as the rigorous volume averaging method where the effective material parameters are defined as [12]

$$(\varepsilon_{\text{eff}})_{ij} \equiv \frac{\langle D_i \rangle_V}{\langle E_j \rangle_V},$$

$$(\mu_{\text{eff}})_{ij} \equiv \frac{\langle B_i \rangle_V}{\langle H_j \rangle_V},$$

where

$$\langle F_i \rangle_V \equiv \frac{1}{V} \iiint_V F_i \, dV$$

and V is the entire volume of the unit cell under investigation. While volume averaging as defined above may be appear to be an appealing method, it should be noted that it becomes very difficult to implement once highly conducting materials are added to the unit cell design due to the polarization of the conducting object. However, since we are only dealing with dielectric materials here it provides highly accurate data to compare with our proposed method.

3.1. Dielectric spheres

A simple cubic lattice of dielectric spheres with a volume fill factor of 0.3 and relative permittivity of 8 was modeled and its effective permittivity was computed. The real and imaginary components of the effective permittivity are shown in Fig. 5. As seen from the data, our proposed method returns nearly identical effective permittivity parameters as the volume averaging method up to a unit cell size of 0.3 free space wavelengths. In contrast, the Pendry *et al*. method immediately diverges away. To quantify the divergence of both our proposed method and the Pendry *et al*. method away from the volume averaging method, we have computed the difference between the computations and normalized the resulting difference to that of the volume averaging method, $\Delta \equiv \left| (\varepsilon_{\text{eff},V} - \varepsilon_{\text{eff}}) / \varepsilon_{\text{eff},V} \right|$. This divergence is shown in Fig. 6 and is plotted in percent. As seen from the plot, the Pendry *et al*. method incurs significant error (up to approx. 210% at $d/\lambda_0 = 0.3$) while our proposed method incurs little error.

Note that the values of ε_{eff}, μ_{eff} computed by using the Pendry *et al*. method are complex even in cases of lossless inclusions such as those presented here. This is due first to the peculiarities of the Pendry *et al*. method itself and second the complex representation of the local electromagnetic fields provided by *CST Microwave Studio Suite* [which uses an $\exp(j\omega t)$ time convention, $j \equiv -i$] or any other electrodynamic solver. Within the Pendry *et al*. method, one might avoid the appearance of nonzero imaginary parts of the effective parameters of lossless lattices by using a real-valued representation of all the fields. This was actually done in [11] where a sinusoidal form of the incident wave has been used instead of the exponential one while deriving analytical expressions for the effective

parameters of free space. However, such an approach cannot be exploited in *numerical* calculations if complex values of the local fields provided by eigensolvers by default are used to calculate the average fields.

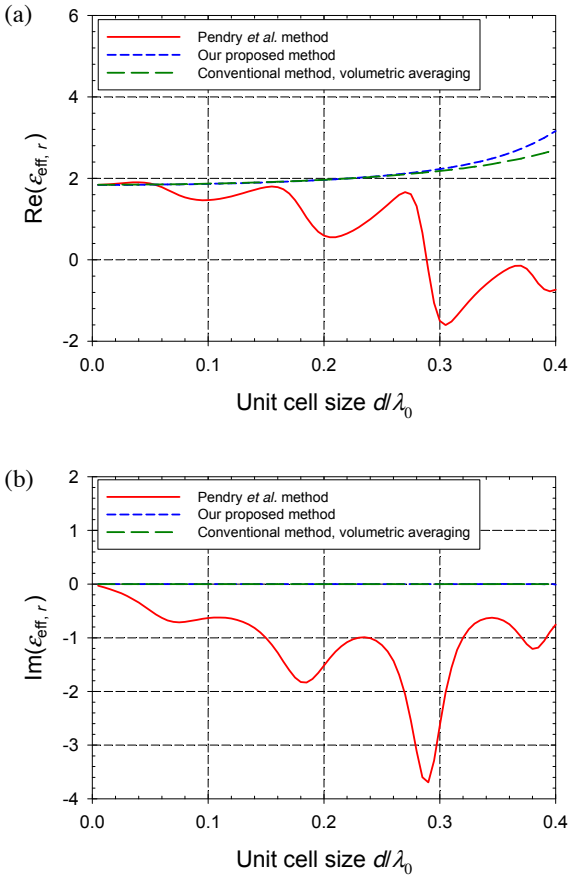

Figure 5: Computed (a) real and (b) imaginary parts of the relative effective permittivity of periodic material consisting of dielectric spheres of $\varepsilon_r = 8$ at a fill factor of 0.3 vs. normalized unit cell size of the material.

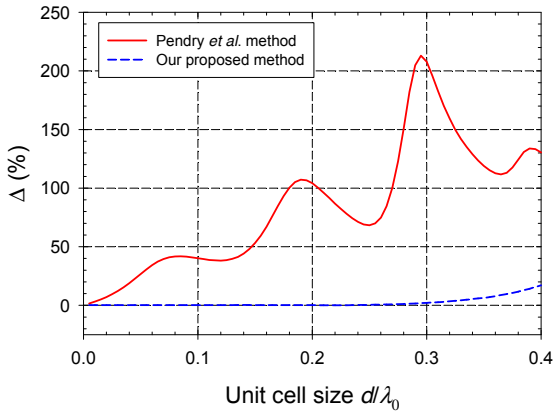

Figure 6: Difference between Pendry *et al*. method or our proposed method from the volume averaging method.

To avoid the appearance of nonzero imaginary parts of numerically calculated effective parameters of lossless lattices, Smith and Pendry proposed [11] to calculate the field averages at two phases of the incident wave 90° apart. This correction to the initial Pendry *et al*. method allows one to obtain plausible results on $\varepsilon''_{\text{eff}}, \mu''_{\text{eff}}$. Comparatively our modified method yields correct values $\varepsilon''_{\text{eff}} = 0$, $\mu''_{\text{eff}} = 0$ from complex local fields *automatically*, see Fig. 5(b), without invoking any additional correction procedures.

3.2. Dielectric cubes

A simple cubic lattice of dielectric cubes with a volume fill factor of 0.4 and relative permittivity of 8 was modeled and its effective permittivity was computed. The real and imaginary components of the effective permittivity are shown in Fig. 7.

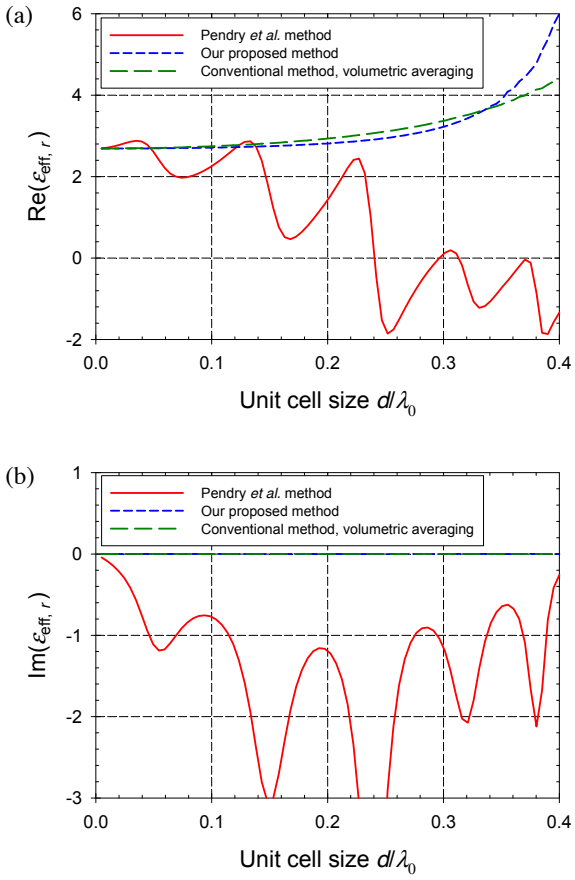

Figure 7: Computed (a) real and (b) imaginary parts of the relative effective permittivity of periodic material consisting of dielectric cubes of $\varepsilon_r = 8$ at a fill factor of 0.4 vs. normalized unit cell size.

As seen from the data, our proposed method returns effective permittivity parameters that are very close to those returned by the volume averaging method. In contrast, the Pendry *et al*. method immediately diverges away. The divergence of both our proposed method and the Pendry

et al. method away from the volume averaging method is shown in Fig. 8 and is plotted in percent. As seen from the plot, until a unit cell size of 0.35 wavelengths our proposed method incurs approximately 5% error or less. Comparatively, the Pendry *et al*. method incurs more than 5% error after a unit cell size of just 0.013 λ_0.

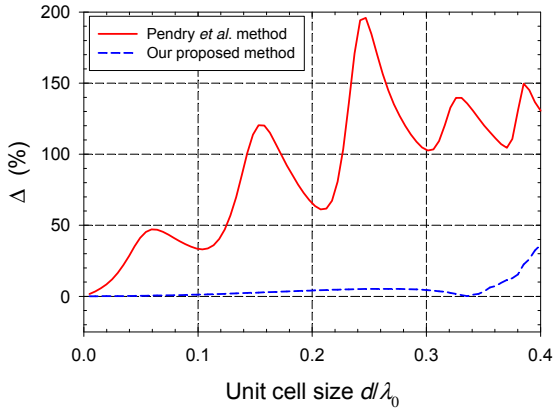

Figure 8: Difference between Pendry *et al*. method or our proposed method from the volume averaging method.

4. Conclusions

Our proposed modification to the averaging method of Pendry *et al*. allows one to calculate the effective material parameters of lattices of particles to a much higher degree of accuracy for the case of appreciable unit cell size. For small unit cell sizes, $d << \lambda_0$, our proposed method returns identical results to that of the Pendry *et al*. method as well as the conventional volume averaging method. For the intermediate region $0.02 < d/\lambda_0 < 0.3$, our method provides more favorable results than the Pendry *et al*. method. Our quantification of the error of the calculated effective material parameters of cube and sphere media show that the Pendry *et al*. method incurs 5% or more error for $d/\lambda_0 > 0.02$. Comparatively, our proposed method incurs more than 5% error for a much larger $d/\lambda_0 > 0.35$.

Acknowledgements

This work was supported by the National Science Foundation through a Communications, Circuits, and Sensing-Systems program grant (ECCS-0824034) and an EPSCoR Research Infrastructure Improvement program grant (EPS-0903804).

References

[1] W. Cai, V. Shalaev, *Optical Metamaterials*, Springer, 2010.

[2] J.W.S. Rayleigh, On the infuence of obstacles arranged in rectangular order upon the properties of the medium, *Phil. Mag*. 34: 481–502, 1892.

[3] R.C. McPhedran and D.R. McKenzie, The conductivity of lattices of spheres, *Proc. R. Soc. A* 359: 45–63, 1978.

[4] H.F. Contopanagos, C.A. Kyriazidou, W.M. Merrill, and N.G. Alexopoulos, Effective response functions for photonic bandgap materials, *JOSA A* 16: 1682–1699, 1999.

[5] J.B. Pendry, A.J. Holden, D.J. Robbins, and W.J. Stewart, Magnetism from conductors and enhanced nonlinear phenomena, *IEEE Trans. Microwave Theory Tech*. 47: 2075–2084, 1999.

[6] J.C. Maxwell Garnett, Colours in metal glasses and in metallic films, *Phil. Trans. R. Soc. Lond*. 203: 385–420, 1904.

[7] C. Caloz and T. Itoh, *Electromagnetic metamaterials: transmission line theory and microwave applications*, John Wiley and Sons, 2006.

[8] C.R. Simovski, S.A. Tretyakov, A.H. Sihvola, and M.M. Popov, On the surface effect in thin molecular or composite layers, *Eur. Phys. J.: Appl. Phys*. 9: 195–204, 2000.

[9] S.A. Tretyakov and A.H. Sihvola, On the homogenization of thin isotropic layers, *IEEE Trans. Antennas Propag*. 48: 1858–1861, 2000.

[10] D.R. Smith, D.C. Vier, N. Kroll, and S. Schultz, Direct calculation of permeability and permittivity for a left-handed metamaterial, *Appl. Phys. Lett*. 77: 2246-2248, 2000.

[11] D.R. Smith and J.B. Pendry, Homogenization of metamaterials by field averaging, *JOSA B* 23: 391–403, 2006.

[12] J.D. Jackson, *Classical Electrodynamics*, Wiley, 1999.

Transformation optics and infrared metamaterials for optical devices

R. Ghasemi[1], N. Dubrovina[1], P.-H. Tichit[1], A. Lupu[1,2], and A. de Lustrac[1,*]

[1]Univ. Paris-Sud, Institut d'Electronique Fondamentale, UMR 8622, 91405 Orsay Cedex, France
[2]CNRS, Orsay, F-91405, France
*corresponding author, E-mail: andre.de-lustrac@u-psud.fr

Abstract

The coordinate transformation approach is applied for the design of an optical mode adaptor between two different width waveguides in the near IR telecom optical domain. The control of the mode profile in the adaptor is achieved by considering a composite waveguide consisting of a thin metamaterial (MM) layer intercalated between 2µm thick SU8 photoresist slab and a glass substrate. We demonstrate that intercalated metafilm enables the realization of a space coordinate transformation and allows a precise control of the light propagation in the composite waveguide. Numerical simulations and experimental realizations of the metamaterial layer are performed in order to validate the device concept and realization feasibility .

1. Introduction

Metamaterials have recently attracted considerable interests because of their unusual properties, not encountered with conventional materials and allowing their applications in a novel class coordinate transformation based devices [1-10]. By using these new properties, it becomes possible the creation of innovative components such as "perfect lens" to produce images beyond the diffraction limit, modulators and cloaks that able to make the region of space invisible [1-8]. Despite these very attractive features, the there is a number of issues limiting MMs implementation, especially in the optical domain. These structures are often metallic with important losses due to the high absorption coefficient of metals in the infrared and visible domains. In addition, the fabrication of these composite materials having subwavelength dimensions requires nanoscale precision control[9]. Given the current state of nanotechnology, optical MMs can be realized in a simple way by planar monolayer structures. In a precedent study we have demonstrated that planar MMs can be used in guided wave configuration by placing a sheet of MMs on the top of the Silicon slab waveguide [10]. In this study we further extend the concept to a different kind of technological implementation. We aim to demonstrate that an efficient control of the light flow by a thin metamaterial layer can be also achieved in the case of lower index waveguides with different MM layer disposition.

2. Mode adaptor for the waveguides with low refractive index

The considered structure consists of two different width waveguides with an intermediate mode adaptor region between. The waveguides are made of SU8 photoresist which refractive index n=1.96. The width of the wide waveguide is around 10µm and that of the narrow one is 2µm. The intermediate region acting as mode adaptor is composed of a thin metafilm, and SU8 layer on a glass substrate(figure 1). To verify the operation of such a mode adaptor the following calculations are performed at the wavelength λ=1.55µm.

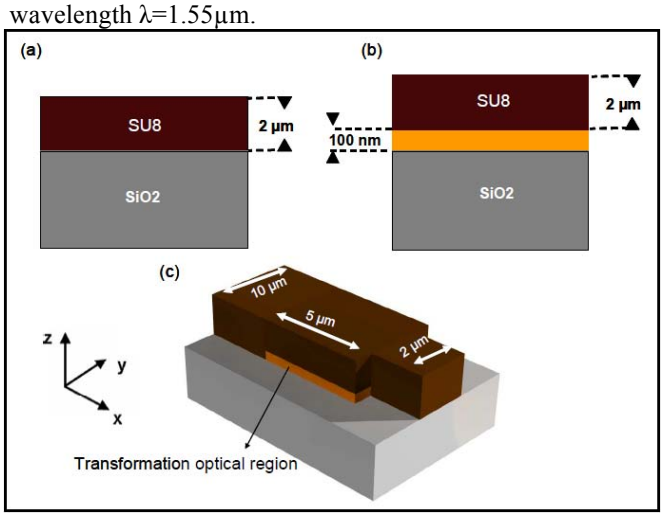

Figure 1: (a) Geometry of the mode adaptor considered in this study. (b) Cross-sectional view of the input wave guide, (c) cross- sectional view of the mode adaptor .

As we shown in [10], the first step corresponds to the calculation of the mode adaptor using Comsol multiphysics based on the finite elements method in 2D and then in the second step to the calculation of the transition in 3D. Figure 2 shows the calculated propagation of the light in the taper in 2D with HFSS and COMSOL respectively. We see that the signal was efficiently transmitted from the input waveguide to the output waveguide.

On the example shown in the figure 1, the adaptor metafilm is located beneath the SU8 layer (the region shown in orange in the figure 1). Another possible configuration would be

place the metafilm on the top of SU8 layer. To determine what configuration is optimal a series of simulation was performed in which the metafilm is placed in two positions, above and below the SU8 layer.

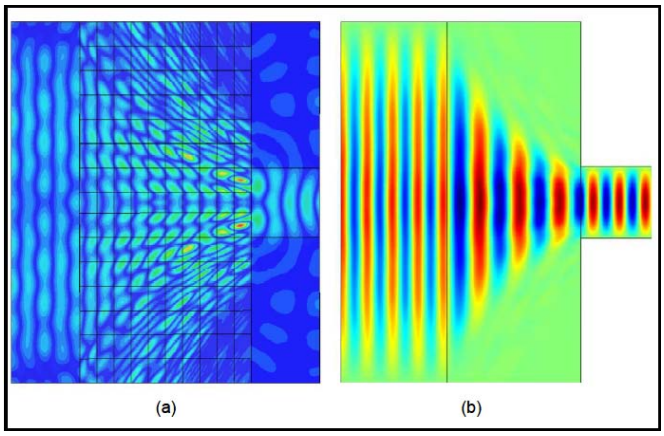

Figure 2: Propagation of the electric field (?) between two waveguides in presence of mode adaptor (a) with HFSS (b) with COMSOL.

Comparing the efficiency of two configurations, the transition between the two waveguides is more efficient when metafilm is located below the SU8, as represented in the figure 2. The thickness of the transformed region may be the cause of this result. The thickness of the transformed region plays an important role in the transmission. To find out the suitable thickness of the transformed layer different cases were tested.

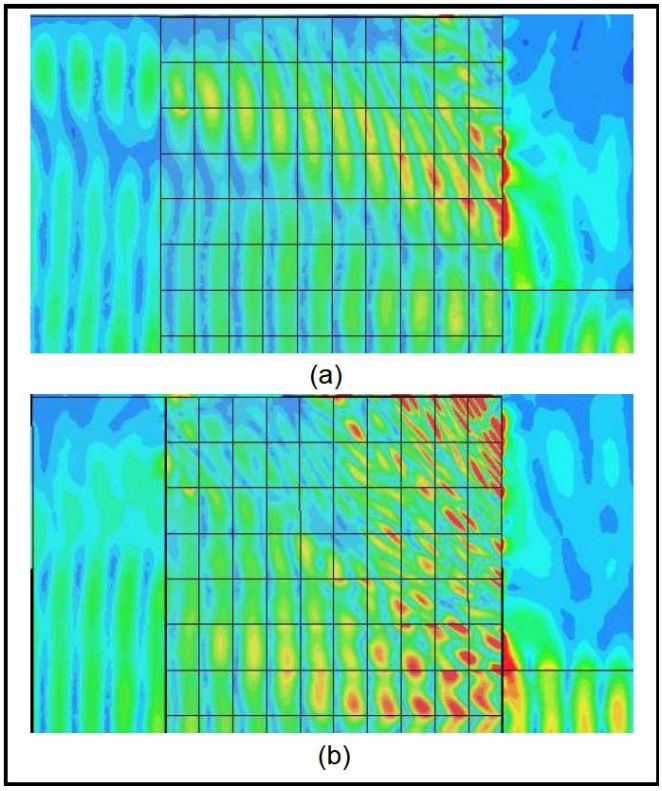

Figure 3: Propagation of the transversal energy in the structure (a) thickness of mode adaptor is about 30nm (b) thickness of mode adaptor is 100nm

In the figure 3 we compare the propagation with two optimized thicknesses of 30 (a) and 100 nm (b) respectively. It should be noted that to reduce the computational time and improve the results precision, we have exploited the symmetry of the structure to reduce the size of the computational domain. Initially, the considered cases seems identical but looking more closely at the distribution of the energy in XY plan, the metamaterial layer will tend to control the signal between the waveguides by compressing itself. But, as it demonstrated in figure 3, the role of mode adaptor is much more efficient for a thickness of 100nm, as compared to 30nm. In the case of 30nm we can say that the signal is less confined by the mode adaptor (metamaterial layer). One can explain this fact by the weak thickness of 30nm compared to 2µm height of the SU8 layer of the structure.

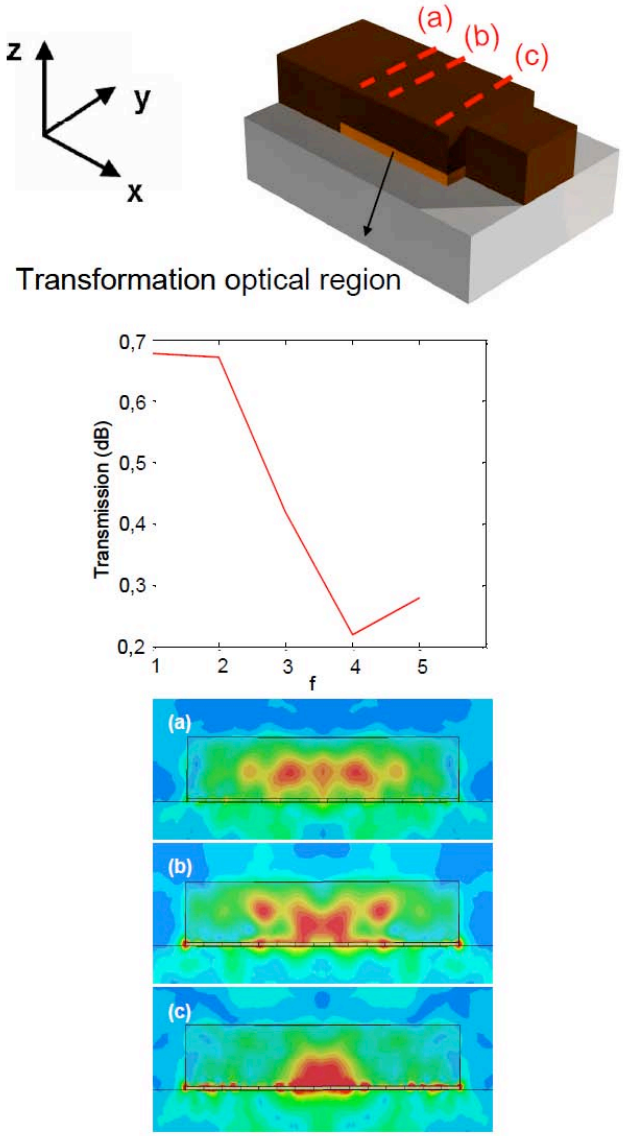

Figure 4: Top: Studied structure in 3D. Middle: Graph of the transmission in function with f. bottom: the distribution of transversal energy in different coordinate of x: (a) x=0.5µm, (b) x= 2.5µm and (c) x= 4.2 µm.

3. Results

As we demonstrate in the reference 10 the transmission critically depends on the proportionality factor in the expression of the permittivity (reminder: corresponds to a factor of space compression in the transformed region).

This result implies that the interactions between the transformed optical region and the SOI waveguide must be carefully adjusted. By plotting the transmission in function of ***f***, we find the optimized value of ***f*** is equal to 2. In the next figure this graph with its results in structure is presented. In the most favorable case, the signal is much more confined and symmetric, and the profile of the electric field remains quite Gaussian. At the end of the taper the signal is well confined in the small waveguide.

4. Discretization

The next figure shows the complete transition in 3D with a discretization of the metamaterial layer.

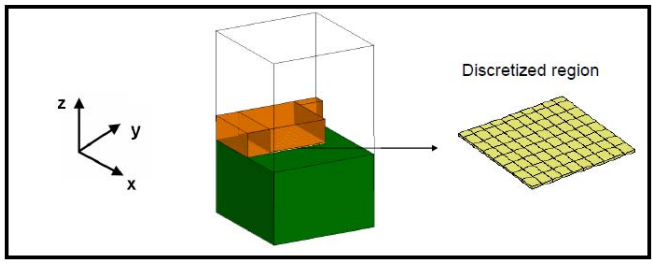

Figure 5: Geometry of the structure in 3D with a discretization of the metamaterial layer.

This discretization is the first step conducting to the design of a realistic device. The yellow layer contains the discretized units cells of the metamaterial layer. As in the reference 10 each cell corresponds to a different value of permittivity tensor. The next step will be the replacement of each cell by the real materials cell [11]. Regarding the sub-wavelength features, optical MMs can be reasonably described in terms of effective electromagnetic parameters. However, there are several experimental or fundamental difficulties to retrieve these parameters from the measurement of thin films of MMs. Generally speaking the dielectric permittivity and the magnetic permeability can be retrieved from the transmission and reflection of a single layer at normal incidence, provided by an interferometer technique which is used to simultaneously measurement of the phase and the amplitude of both coefficients [12-14]. But this procedure is not well applicable in our case [15]. Another difficulty is the fact that the layer of metamaterial has two different interfaces such as one with the air and the other with a dielectric substrate in our case. It should be noted that the retrieval method proposed by Smith et al. consider that the MMs as a homogeneous layer to which it is possible to reverse the scattering data to determine the refractive index and the impedance from transmission and reflection coefficients calculated for normal incidence. Lupu et al. [15] has shown that this method can be generalized through the inversion of the characteristic matrix of medium in the most general case of oblique incidence using a particular solution of Smith's generalized formula. In this study we are interested to this point.

5. Fabrication

In view of the realization of the mode adaptor adaptor, we start to develop the fabrication process of the MMs in a clean room. As show in figure 6, we think make the final device with a layer of metallic cut wire, whose dimensions vary to achieve the space transformation. At this stage of our study, we were able to fabricate a multilayer metamaterial made of metallic cut wires on planar substrate, as shown in the views of SEM in figure6. The dimensions and the period of the cut wires are sub-micron so that the entire layer behaves as a homogeneous medium in wavelength. Therefore, these structures can be performed by electron beam lithography followed by metallization (Ti-Au) and a lift-off procedure (figure 6(a)). Looking to develop the fabrication, we arrive to have the multilayer structures (4 layers) on the glass substrate (figure 6(b)).

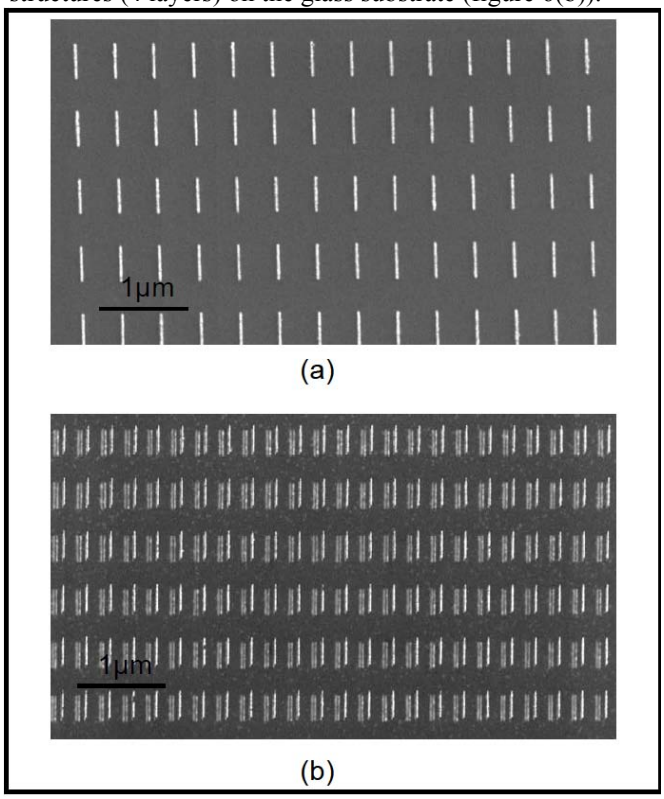

Figure 6: (a) monolayer of gold cut wire: length 440nm, width 30nm, and thickness 50nm (b) 4 layers of gold cut wire made on a glass substrate separated by a 65 nm dielectric layer.

We should mention that the thickness of the wires is 50nm; the width is about 30 nm and their length 440nm. We control the position of each wire layer with respect to its neighbors. So we can obtain different optical index easily [16, 17]. Figure 7 present the numerical simulations and experimental results of these structures.

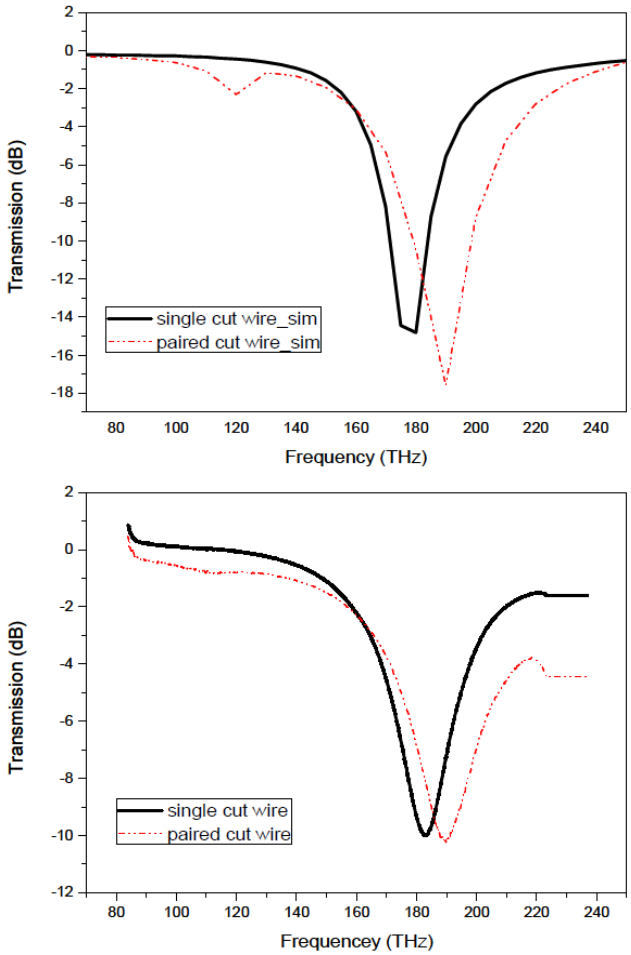

Figure 6: (a) monolayer of gold cut wire: length 440nm, width 30nm, and thickness 50nm (b) 4 layers of gold cut wire made on a glass substrate separated by a 65 nm dielectric layer.

The black curve correspond to the single cut wire with 440nm length, 30nm width and 50nm thickness and the red one to the paired cut wires with the same dimension and without any coordinate shifts with the respect to the first level. The transmittance and reflectance spectra were measured under normal incidence with a Fourier Transformed Infrared spectrometer Varian 600. As we can see in the figure 7, the numerical simulations are in excellent agreement with experimental results.

The fabricated multiplayer MMs structure represent the first step toward the realization of a of mode adaptor. Its utility is also quite important to develop the fabrication of devices designed by transformation optics on glass substrate.

6. Conclusions

The first important point of this study is the demonstration that a thin layer of MMs calculated by transformation optics and placed between two waveguides whatever of their refractive index (low or high) can control the signal propagation through the structure. On the other hand the considered approach can be applied to different geometries, suggesting that the planar MMs have great potential in integrated optics. The second point is the realization of multilayer metamaterial allowing the engineering of refractive index at infrared wavelengths

Acknowledgements

The authors thank X. Leroux for fruitful discussions. This work was supported by the French National Research Agency (ANR Metaphotonique, contract number 7452RA09).

References

[1] V. G. Veselago, The electrodynamics of substances with simultaneously negative values of e and m, Soviet Phys. USPEKHI, 10:509-514, 1968.

[2] J. B. Pendry, A. J. Holden, D. J. Robbins et al., Magnetism from conductors and enhanced nonlinear phenomena, IEEE TRANSACTIONS ON MICROWAVE THEORY AND TECHNIQUES, 47: 2075-2084, 1999.

[3] J. B. Pendry, A. J. Holden, D. J. Robbins et al., Low frequency plasmons in thin-wire structures, JOURNAL OF PHYSICS-CONDENSED MATTER, 10: 4785-4809, 1998.

[4] J. B. Pendry, Negative refraction makes a perfect lens, Phys. Rev. Lett., 85: 3966-3969, 2000.

[5] D. Schurig, J B. Pendry and D. R. Smith, Transformation-designed optical elements, Opt. Express., 15: 14772-14782, 2007.

[6] M. Rahm, D. A Roberts, J. B. Pendry et al., Transformation-optical design of adaptive beam bends and beam expanders Opt. Express., 16: 11555-11567, 2008.

[7] D. Schurig, J. J. Mock, B. Justice et al., Metamaterial electromagnetic cloak at microwave frequencies, Science, 314: 977-980, 2006.

[8] B. Kanté, D. Germain, and A. de lustrac, Experimental demonstration of a nonmagnetic metamaterial clock at microwave frequencies, Phys. Rev. Lett. B, 80:201104, 2009.

[9] M. C. Soukoulis and M. Wegener, Past achievements and future challenges in the development of three-dimensional photonic metamaterials, NATURE PHOTONICS, 5: 523-530, 2011.

[10] R. Ghasemi, P. H. Tichit, A. Degiron, A. Lupu and A. de Lustrac, Efficient control of a 3D optical mode using a thin sheet of transformation optical medium, Opt. Express., 18:20305, 2010.

[11] B.Kanté, J. M Lourtioz and A. de Lustrac, Infrared metafilms on a dielectric substrate, Phys. Rev. B, 80:205120, 2009.

[12] R. Mittra, C. H. Chan and T. Cwik, Techniques for analyzing frequency selective surfaces-A, review Proc. IEEE, 76:1593, 1988.

[13] D. R. Smith, S. Schultz, P. Markos and C. M Soukoulis, Determination of effective permittivity and permeability of metamaterials from reflection and transmission coefficients, Phys. Rev. B, 65:195104, 2002.

[14] S. G. Johnson, M. Ibanescu, M. Skorobogatiy, O. Weisberg, T. D. Engeness, M. Soljacic, S. A. Jacobs, J. D. Joannopoulos and Y. Fink, Low-loss asymptotically singlemode propagation in large-core OmniGuide fibers, Opt. Express, 9:748, 2001.

[15] A. Lupu, N. Dubrovina, R. Ghasemi, A. Degiron and A. de Lustrac, Metal-dielectric metamaterials for guided wave silicon photonics, Opt. Express, 19:24746, 2011.

[16] S. N. Burokure, A. Sellier, B. Kante, A. De Lustrac, Symmetry breaking in metallic cut wire pairs for negative refractive index, Appl. Phys. Lett,. 94:201111, 2009.

[17] B. Kante, S. N. Burokure, A. Sellier and A. De lustrac and J.-M Lourtioz, Controlling Plasmon Hybridization for Negative Refraction Metamaterials, Phys. Rev. Lett. B., 79:075121, 2009.